AGARD-CP-77-70

AGARD-CP-77-70

AGARD

ADVISORY GROUP FOR AEROSPACE RESEARCH & DEVELOPMENT

7 RUE ANCELLE 92 NEUILLY SUR SEINE FRANCE

AGARD CONFERENCE PROCEEDINGS No. 77

on

Electromagnetics of the Sea

NORTH ATLANTIC TREATY ORGANIZATION

DISTRIBUTION AND AVAILABILITY
ON BACK COVER

A G A R D

ADVISORY GROUP FOR AEROSPACE RESEARCH & DEVELOPMENT

Organisation du Traité de l'Atlantique Nord
7, rue Ancelle, 92, Neuilly-sur-Seine

presents

THE ELECTROMAGNETIC WAVE PROPAGATION PANEL SPECIALISTS MEETING

"ELECTROMAGNETICS OF THE SEA"

22-25 June 1970

Program Chairman
Collator-Coordinator
Capitaine de Frégate P. Halley, Chef de la
Division des Prévisions Ionosphériques du
Centre National d'Etudes des Communications
Chateau de la Martinière
91, Saclay, France

Co-Chairman-Collator
Dr. H. Hodara
Tetra Tech. Inc.
630 North Rosemead Blvd
Pasadena, Calif.,
91107, USA

EPP Chairman
Dr. Kenneth Davies
U.S. Department of Commerce
Environmental Science
Services Administration
Boulder, Colorado, 80302
USA

EPP Executive

CDR. C.R. Smith, USN
AGARD

The papers and discussion material in this publication were presented at the AGARD Electromagnetic Wave Propagation Panel Specialists' Meeting, "Electromagnetics of the Sea" held in Paris, 22 to 25 June 1970.

Published November 1970

621.317.32(26):551.46

Printed by Technical Typing and Reproduction Ltd
Barbara House, Charlotte St. London, W1P 1HL.

THE ELECTROMAGNETIC WAVE PROPAGATION PANEL SPECIALISTS MEETING

"ELECTROMAGNETICS OF THE SEA"

T H E M E

The growing interest and increased activity in exploiting ocean resources promotes this Specialists' Meeting for the dissemination exchange and integration of experimental and theoretical findings as well as formulating cooperation for problems remaining unsolved.

Underwater Electromagnetic Propagation has experienced a rebirth with increased activity beneath the oceans. Two portions of the electromagnetic spectrum fill the gap previously occupied by acoustics VLF/ELF and optics. This resulted from their common characteristic of propagation along air-sea transmission paths. Optics gives high resolution at short range. VLF offers low information rates at long ranges.

Typical optics applications for both military and commercial utilization are identification, recognition and salvage. VLF/ELF offers extensive communication possibilities and underwater remote control. Bottom mapping from the air with coherent radiation shows promise.

The Program has been divided equally between radio and optics as follows:

SESSION I	VLF/ELF Radiation and Propagation in Sea.
SESSION II	VLF/ELF Electromagnetic Noise.
SESSION III	Air Sea Interface and Scatter.
SESSION IV	MHD of the Ocean.
SESSION V	Round Table, ~~open forum.~~
SESSION VI	Optical Properties of Sea Water.
SESSION VII	Imagery.
SESSION VIII	Research Program in Optical Oceanography.
SESSION IX	Round Table, open forum.

Allocution de Bienvenue

de

Monsieur Louis RAGONNET

Ingénieur général de 1ère classe de l'Armement
chef du groupe Télécommunications du Service Technique des Constructions et Armes Navales

- Amiral,
- Messieurs les Présidents de la présente réunion,
- Mesdames, Messieurs.

Je voudrais tout d'abord m'associer à Monsieur le Professeur CURIEN pour vous souhaiter la bienvenue et pour remercier le "Comité de Propagation de l'Onde Electromagnétique" d'avoir organisé la présente réunion sur le thème de "l'Electromagnétisme de la Mer". Je voudrais également souligner après M. le V.A. d'O'GRADY combien ce thème est actuel et important, non seulement du point de vue de la Recherche Scientifique, mais encore pour tout ce qui concerne l'exploration des océans et l'exploitation de leurs immenses richesses potentielles, et aussi bien entendu pour les applications militaires.

De tout temps les militaires se sont intéressés au milieu marin, il est à peine utile de rappeler à cet égard la part prépondérante prise par les officiers et les ingénieurs des Marines Nationales des différents pays dans l'exploration des profondeurs. Pour m'en tenir aux Français les plus connus du grand public, je citerai : au début du siècle, Gustave Zédé et Laubeuf, et aujourd'hui Cousteau, Willm et Houot. Grâce à tous ces pionniers, ont été mis au point des matériels permettant de vivre, de se déplacer et de travailler sous l'eau, malgré le froid, le manque d'air et la terrible pression des profondeurs. Aujourd'hui, l'apparition des forces sous-marines de dissuasion augmente encore, et dans des proportions considérables, l'importance militaire du milieu marin. En tant que représentant du Ministère d'Etat chargé de la Défense Nationale, je ne puis donc que me réjouir de voir la présente réunion consacrée à l'étude de l'un des problèmes les plus importants concernant ce milieu : à savoir son comportement vis-à-vis des ondes électromagnétiques.

Les expressions "monde du silence" ou "monde sans soleil", utilisées pour populariser le milieu marin, illustrent l'isolement dans lequel se trouvent plongés les hommes qui explorent ce milieu pourtant si proche ; et l'on ne peut s'empêcher de mesurer le contraste avec la situation des cosmonautes, qui jusque sur la lune, restent en contact étroit avec leurs bases et dont les moindres gestes sont suivis à la télévision. En fait, les ondes électromagnétiques se propagent toutes fort mal dans la mer, ce qui explique que les applications, bien qu'importantes, en soient relativement limitées ; elles font appel généralement, soit aux très basses fréquences, soit aux fréquences du spectre visible. L'examen du programme de la présente réunion montre que la plupart des sujets qui y seront traités se rattachent à l'un ou l'autre de ces deux grands domaines.

Les ondes très longues ont à la fois la propriété de se propager très loin et très régulièrement autour de la terre et celle de pénétrer dans la mer. Cette double propriété est connue depuis longtemps et les marines militaires les ont largement utilisées pour transmettre des ordres à leurs sous-marins en plongée. Mais des progrès importants ont été réalisés au cours des dernières années tant sur le plan théorique notamment en ce qui concerne le mécanisme de la propagation et le rôle de la couche D de l'ionosphère, que sur le plan pratique notamment en ce qui concerne la technologie des systèmes d'émission et de réception. La profondeur de pénétration dépend de différents facteurs, notamment de la salinité de l'eau et de la fréquence : plus cette dernière est faible, plus la pénétration est profonde. Malheureusement, malgré l'ingéniosité des techniciens, il n'a pas été possible à ce jour de produire le rayonnement sans faire appel à des antennes dont les dimensions deviennent vite prohibitives lorsque la fréquence devient très basse ; aussi la profondeur de pénétration reste-t-elle toujours faible.

En ce qui concerne les ondes du spectre visible, il y a effectivement propagation dans l'eau de mer, mais celle-ci est contrariée par deux phénomènes distincts : l'absorption et la diffusion. L'absorption dépend des propriétés du milieu et la fréquence ; elle est donc sélective ; ce sont les ondes comprises entre 4.700 et 5.300 angstroems (bleu-vert) qui se propagent le mieux. La diffusion est due à la réflexion de la lumière sur les particules en suspension ; elle est l'ennemi principal de tous les systèmes de vision sous-marine à éclairement constant. Aujourd'hui, les techniques laser apportent dans ce domaine des perspectives de progrès considérables ; grâce à la possibilité d'obtenir des faisceaux cohérents puissants, étroits et modulés en impulsion.

Outre ces deux grands domaines, des recherches sont en cours dans différents pays sur un certain nombre de problèmes, parmi lesquels je citerai :

- L'étude des parasites dûs à la réflexion des ondes sur la mer.
- L'étude des liaisons entre points situés au voisinage de la limite de séparation de la mer et d'un autre milieu, c'est-à-dire près de la surface ou près du fond.
- L'étude des liaisons entre points profondément immergés, par propagation directe.

L'importance de toutes ces études me conduit, en conclusion, à constater que la présente réunion arrive au moment opportun, à celui où se manifeste de façon particulièrement pressante le besoin de transmettre les messages et la lumière sous l'eau et où les moyens nécessaires commencent à être prêts. Je suis persuadé aussi que les nombreux organismes qui en France s'intéressent à l'étude du milieu marin ou à l'étude des ondes électromagnétiques apprécient le choix qui a été fait de Paris pour la tenue de cette réunion. Nul doute que les discussions soient animées et qu'elles préparent les solutions aux problèmes qui se présentent et ceci, pour le plus grand intérêt de nos pays. C'est en même temps ma conviction et le voeu que je formule, au moment où s'ouvre cette réunion sur l'électromagnétisme de la mer.

INTRODUCTION

La réunion non classifiée de spécialistes scientifiques sur l'"Electromagnétisme de la Mer" est une suite au symposium AGARD sur les communications en dessous de la surface "Subsurface Communications" (AGARD Conference Proceedings N° 20), tenu à Paris en 1966, dont le sujet très vaste donnait au sol continental la place prépondérante. Il a paru logique de développer le même sujet en le particularisant à la mer, en l'étendant à l'ensemble du spectre et plus généralement à l'étude de tout phénomène électromagnétique intéressant le milieu marin. Partout se manifeste un intérêt croissant pour la mer, dont on peut dire qu'elle est un bien essentiel qui participe à l'entretien du mouvement et de la vie. Un bien jusque là presque ignoré, dont l'usage ou l'exploitation pose de nombreux problèmes qui restent, pour le moment, sans solution.

Sur le plan militaire, Monsieur le Vice-amiral O'Grady a souligné dans son allocution d'ouverture, l'importance de la détection, de l'identification et de la localisation des sous-marins au-delà des possibilités acoustiques.

La réunion de spécialistes de l'électromagnétisme de la mer avait pour but de revoir les résultats acquis, de constater l'existence de théories généralement ou partiellement applicables, de dégager les tout derniers progrès et de discuter les possibilités d'études futures.

Le programme des réunions a distingué le domaine radioélectrique et notamment les bandes EBF et TBF, qui permettent les communications à faible taux d'information mais à grande portée avec une pénétration sous-marine, du domaine optique infra-rouge et visible, qui permet à courte distance de hautes résolutions et dans lequel l'emploi du laser offre de nouvelles perspectives.

Il est clair que la surface de la mer ou l'interface Air/Mer est un sujet d'études important dans l'étendue du spectre. En radio, le rayonnement, la propagation à la surface et le franchissement de la surface conditionnent les communications à distance. En optique, le franchissement de la surface conditionne l'observation sous-marine et la photographie aérienne du fond.
Il aurait été possible de grouper les communications en conséquence. J'ai estimé préférable de considérer le milieu marin dans son ensemble, sans orienter particulièrement les exposés et les discussions sur une limite, même si pratiquement ce sont les problèmes relatifs à cette limite que l'on connait le mieux.

D'une manière générale, les communications qui ont été présentées, sont pour la plupart des études orientées vers l'aspect analytique et physique des questions traitées plus que vers l'aspect technologique des systèmes et des appareils.

Deux tables rondes ont été constituées, dont le lecteur trouvera les comptes-rendus au papier 26 pour le domaine radio et au papier 47 pour le domaine optique.
Il est certain que ces comptes-rendus écrits ne peuvent donner qu'une idée très médiocre d'une activité essentiellement orale où la spontanéité et la liberté d'expression sont nécessaires. Si les participants aux tables rondes, dont beaucoup peuvent être des observateurs, ont pu librement exposer l'objet de leurs préoccupations qui n'ont pas nécessairement rapport à une communication d'auteur et, si les auteurs ont pu librement discuter sur les points délicats des affaires qui les occupent, les tables rondes ont été utiles. Ainsi, sur le sujet de l'électromagnétisme de la mer, des opticiens ont pu discuter avec des radioélectriciens.

Au cours de la table ronde du domaine radioélectrique, à laquelle malheureusement n'assistait aucun océanographe, on a discuté à propos de presque toutes les communications.

Il est très regrettable que Monsieur le professeur COHN, empêché, n'ait pu présenter en séance sa communication sur "Magnetohydrodynamic wave phenomena in sea water" (paper 25), qui aurait sans doute fait l'objet de discussions intéressantes.

La table ronde d'optique océanographique fut très animée. Au cours des discussions, on s'est efforcé de dégager des idées fondamentales concernant cette discipline récente . J'en ai gardé l'impression qu'il y a encore beaucoup à faire. Il semble qu'il y ait un problème d'instrumentation. (Quel appareillage et quelle technique faut-il définir pour rendre les mesures significatives en vue d'une application déterminée ?). Les spécialistes de l'optique dans les milieux turbides et absorbants comme l'eau de mer, avec ou sans franchissement d'une surface, sont peu nombreux.

Cependant, l'éclairement et la visibilité dans l'eau, la photographie sous-marine constituent des domaines d'études dont l'importance est évidente.

Il est souhaitable que les recherches dans ces domaines soient encouragées et que, dans les prochaines années, on organise sur ce sujet une "Lecture Serie" de l'AGARD, avec l'approbation du Comité de Propagation des Ondes Electromagnétiques.

Pierre HALLEY

INTRODUCTION

The Scientific Specialists' meeting on "Electromagnetics of the Sea", which was unclassified, is a follow-up of the AGARD Symposium on "Sub-Surface Communications" (AGARD Conference Proceedings No. 20), held in Paris in 1966, and of the great interest shown in this subject by the European Continent. It seemed logical, therefore, to develop the same subject, giving particular attention to the sea and extending it to the whole spectrum, particularly to the study of electromagnetic phenomena in the sea atmosphere. Interest in the sea is increasing everywhere, particularly with regard to the benefits provided by the sea in sustaining life--a benefit which, until now, has been almost ignored. The use or exploitation of the sea, however, has presented many problems which, for the time being, remain unsolved.

Vice-Admiral O'Grady, in his opening remarks concerning the military viewpoint, pointed out the importance of detection, identification, and localization of undersea craft beyond present acoustical capabilities.

The primary purpose of the Electronics of the Sea meeting was to review results already obtained, to see the existence of the generally or partially applicable theories, to sort out the latest progress, and to discuss the possibilities of future studies. The program illustrated the possibilities of radioelectric field, particularly for the EBF and TBF bands, which allow feeble information rate communications but which have long-distance, undersea penetration; and of the infra-red and visible optic field, which permits short-distance high resolutions and in which the laser offers new uses and prospectives.

It was made clear that the surface of the sea or the interface of Air/Sea is an important subject in the studies of the spectrum. In radio, the radiation and propagation to the surface and the penetration through the surface are determining communications distances. In optics, this penetration through the surface is limiting under-sea observation and aerial photography of the sea bottom. It may have been possible to group the communications but it was thought preferable to consider the sea environment as a whole without orienting the presentations and discussions. This was done even though practical problems exist and limits are known. Generally, the presentations are oriented to the analytic and physic aspects of the questions treated rather than to the technological aspect of the systems or apparatus.

Two round-tables were arranged for the Radio field (see paper 26) and the Optic field (see paper 47). These papers illustrate only briefly the activity in these areas. Although responses were essentially oral, this spontaneous and free expression is necessary. Most of the participants at the round-table discussions were observers and they showed preoccupations which were not necessarily relative to the authors' presentations. The authors could also discuss freely the delicate points and matters of great concern to themselves; the Opticians could discuss "Electromagnetics of the Sea" with the Radio-electricians. Thus the round-tables proved to be very useful.

During the round-table on "Radio-electricalfields", to which unfortunately no oceanographer attended, the discussions followed the paper presentations. It was regretted that Prof. Cohn could not attend this round-table as his paper (No. 25, "Magnetohydrodynamic Wave Phenomena in Sea Water") created considerable interest and much discussion would have resulted.

The "Oceanographic-Optical" round-table was very lively with the sorting out of fundamental ideas in this very new discipline. The impression was gained that there is much to be accomplished in this area. It appears the problem is instrumentation -- which apparatus and which technique might be selected -- to give significant values to a determined application. The specialists of optics in the "turbide and absorbant" fields such as sea water, either or through the surface, appear to be very few. Nevertheless, the lighting and visibility in water and the under-sea photography -- both constitute fields of studies where the importance was very evident.

It is desirable that the research in these fields be further encouraged and that quite possibly an AGARD Lecture Series could be organized on this subject upon the recommendations of the "Electromagnetic Wave Propagation" Panel of AGARD.

Pierre HALLEY

REMERCIEMENTS

La réunion sur "L'Electromagnétisme de la Mer" a été projetée avec l'approbation et l'appui de Monsieur l'Ingénieur Général Libois directeur du Centre National d'Etudes des Télécommunications. Mais, un colloque international est une entreprise de groupe, qui nécessite de nombreux concours et une solide organisation. L'AGARD a apporté la sienne avec sa direction, son personnel et particulièrement l'assistance amicale et dévouée du Commander Smith. J'en remercie son directeur.

Je remercie le Centre National de la Recherche Scientifique d'avoir mis ses moyens à notre disposition avec l'approbation encourageante de Monsieur le Professeur Curien qui a bien voulu présider notre cérémonie d'ouverture, conjointement avec Monsieur le Vice-Amiral O'Grady de Saclant, Monsieur l'Ingénieur Général de l'Armement Ragonnet et Monsieur l'Ingénieur Général Hydrographe Mannevy.

En ce qui concerne la réunion proprement dite, j'ajouterai que :

Le Dr. Hodara m'a apporté un concours sans réserve dans le rassemblement des communications américaines, la préparation et le déroulement du programme. Monsieur le Professeur Bouix et Monsieur le Professeur Ivanoff m'ont efficacement conseillé et orienté dans la recherche des communications françaises. Monsieur Davies président de l'E.P.P. et Monsieur Kullback membre du comité ont soutenu et favorisé la préparation de la réunion. Monsieur Richard directeur de Thomson CSF a bien voulu organiser la visite de ses laboratoires et y recevoir les participants à la réunion.

Je leur adresse à tous de très sincères remerciements ainsi qu'à tous ceux, très nombreux que je ne puis nommer, qui ont bien voulu m'apporter leur collaboration.

Je remercie surtout les auteurs et les présidents de sessions qui ont fourni la substance même de la réunion avec leurs connaissances, la communication de leurs dernières recherches et de nouvelles idées.

J'espère que la série des exposés et les discussions qui ont suivi auront été pour eux à la fois un enseignement et un stimulant propres à favoriser le progrès.

ACKNOWLEDGEMENTS

The meeting on "Electromagnetics of the Sea" was the result of considerable interest generated by the AGARD Symposium on "Sub-Surface Communications" held in 1966 and the full approval and support of Monsieur l'Ingénieur Général Libois, director of the National Center for the Studies of Telecommunications.

An International Symposium is a large enterprise, requiring considerable organization and the cooperation of many persons. In this regard, many thanks are extended to the Director and the staff at AGARD, particularly to CDR Smith who gave his devoted and friendly assistance.

I would also like to thank the National Center of Scientific Research, Paris, which gave its full support and the encouraging approval of Professor Curien from the Center, who honored us by participating in the opening ceremony, along with Vice-Admiral O'Grady from Saclant, Monsieur l'Ingénieur Général of the Armament Ragonnet, and Monsieur L'Ingénieur Général Hydrography Mannevy.

With regard to the meeting itself, I would like to add that :

Dr. Hodara gave his full support to the collecting of U.S. contributions and to the preparation and organization of the program. Professor Bouix and Professor Ivanoff provided advice and assistance in obtaining French contributions. Dr. Davies, Chairman of the E.P.P., and Mr. Kullback, U.S. coordinator, assisted in the preparation of the meeting. Mr. Richard, Director of Thomson CSF, acted as host for participants during their technical tour of the laboratories.

I thank all of these persons and the many more who provided so much assistance to the successful completion of this symposium. Above all, I extend my appreciation to the Authors and Session Chairmen who provided the substance for this meeting by their presentations on the latest research and ideas in electromagnetics of the sea.

It is my hope that the papers presented and the related discussions will be useful to everyone present and to those who use the forthcoming publication, and that they will provide the stimulus to encourage further progress in this field.

Pierre HALLEY

NOTE ANNEXE

sur

LE CENTRE D'ETUDES THEORIQUES DE LA DETECTION ET DES COMMUNICATIONS

Le CETHEDEC (sigle désignant le Centre d'Etudes Théoriques de la Détection et des Communications) est un Centre de Recherches dépendant du Ministère d'Etat chargé de la Défense Nationale en France . Il a participé activement au symposium AGARD "Subsurface communications" (Paris 1966) et à la réunion de spécialistes scientifiques "Electromagnetics of the sea" . Aussi pensons nous que le lecteur sera intéressé par quelques informations sur ce centre .

Le CETHEDEC, dirigé par le professeur Maurice Bouix, travaille en liaison très étroite avec des professeurs et chercheurs de l'Université, ce qui lui permet d'aborder au niveau scientifique le plus élevé les problèmes théoriques de son programme . Il a un triple rôle :

-a) assurer une formation scientifique de niveau elevé à des chercheurs qui se destinent à l'étude de problèmes liés à la détection et aux communications .

-b) effectuer des travaux de recherche fondamentale orientée vers la détection et les communications .

-c) assurer une liaison avec des séminaires, des conférences et des publications d'une part entre tous les chercheurs de sa spécialité, d'autre part entre ces chercheurs et les ingénieurs utilisateurs .

Dans ce but, le CETHEDEC réunit sous une même direction des élèves, des chercheurs et un service de documentation et de publications .

La formation scientifique est assurée :
d'une part par l'enseignement du Troisième cycle de la Faculté des Sciences de Paris donné par le Laboratoire de Recherches de Mathématiques Statistiques du professeur FORTET, et une option particulière intitulée Théorie Probabiliste des Signaux de l'Information et de la Régulation, qui comporte en plus des cours spéciaux sur la Théorie de la Propagation ; cet enseignement est donné à des étudiants en fin d'études supérieures ;
d'autre part par des journées ou des semaines d'études soit de synthèse, soit d'exposés de résultats qui s'adressent à des ingénieurs ou chercheurs professionnels .

Les travaux de recherche proprement dits du CETHEDEC s'effectuent dans le cadre de groupes d'études, actuellement au nombre de cinq :
- 1) Groupe Support Physique du Signal (Propagation)
- 2) Groupe Théorie du Signal
- 3) Groupe Codes Correcteurs d'Erreurs
- 4) Groupe Tests non-Paramétriques
- 5) Groupe des Méthodes de Calcul (Analyse et Méthodes Numériques)

Certaines recherches sont menées en liaison avec le Département Mathématique de la Faculté des Sciences de Rouen, Le Laboratoire d'Astrophysique de la Faculté des Sciences de Paris, la Faculté des Sciences de Nice .

Quelques liaisons avec des chercheurs européens (allemands, italiens, hollandais) et américains vont être développées et renforcées dans un avenir immédiat afin d'éviter la dispersion des efforts .

Le CETHEDEC s'efforce de développer les liaisons avec tous les chercheurs qui s'intéressent à la recherche théorique relative aux sciences de la détection et des communications, soit parce qu'ils effectuent des recherches dans ces branches, soit parce qu'ils désirent en utiliser les résultats . C'est dans ce but qu'il publie depuis 1964 la Revue du CETHEDEC où l'on peut trouver aussi bien les travaux des chercheurs du Centre que des articles d'autres auteurs .

Le CETHEDEC a participé à la réunion "Electromagnetics of the sea" en la personne du Prof. M. BOUIX et de MM. BACH et POIREE . Le Dr. P. WIRGIN de l'institut d'optique leur a apporté une participation active .

CETHEDEC 5(bis) Av. de la Porte de Sèvres - PARIS 15ème - France

PROGRAM CHAIRMAN

Capitaine de Frégate (H) Pierre HALLEY
Ingénieur en chef au Centre National d'Etudes des Télécommunications
Château de La Martinière - SACLAY - 91 - ORSAY - France

CO - CHAIRMAN

Dr. Henri HODARA
Vice président Tetra Technics Inc.
630, North Rosemead Blvd Pasadena, Calif. 91107 U.S.A.

SESSION - CHAIRMEN

Part I : Radio

SESSION I	- ELF/VLF Propagation - Antennas immersed in a conducting medium	(Prof. E. SELZER (Institut de Physique du Globe de la (Faculté des Sciences de Paris (9 quai St Bernard, Paris 5ème, France
	- Transmission	(Prof. W. SCHÖNFELD (Technische Universität Hannover (3 Hannover, Welfengarten1, Germany
SESSION II	- VLF/ELF Electromagnetic Noise	(Prof. M. BOUIX (Cethedec - Direction des Recherches et (des Moyens d'Essais (5 (bis) Av. de la Porte de Sèvres (Paris 15ème, France
SESSION III	- Air Sea Interface	
	- HF/VHF Backscatter	(Prof. G. FRANCESCHETTI (University of Naples, Instituto Elettrotecnico, (via Claudio 21, 80125, Naples, Italy
	- Microwave Backscatter	(Dr. C. SWIFT (NASA Langley Research Center (Hampton, Va 23365, U.S.A.
SESSION IV	- Conductivity and Magnetohydrodynamics	(Dr. J. GALEJS (Sylvania Electronic Systems (77 "A" Street, Needham Heights, Mass 02194, U.S.A.
SESSION V	- Round table discussion	(Dr. J.R. WAIT (ESSA Research Lab. (Boulder, Colorado, 80302, U.S.A.

Part II : Optics

SESSION VI	- Experimental results	(Prof. A. IVANOFF (Faculté des Sciences de Paris (T. 24, 9 quai St Bernard Paris 5ème, France
SESSION VII	- Theoretical considerations	(Prof. J. TYLER, Visibility Lab., Scripps (Institution of Oceanography, San Diego (California 92037, U.S.A.
SESSION VIII	- Imagery	(Dr. W. CONDELL (Office of Naval Research (421) (800 N Quincy St, Arlington, Va, 22217, U.S.A.
SESSION IX	- Round table discussion	(Prof. J. TYLER and Dr. H. HODARA (see above).

CONTENTS

Part I

RADIO

E.L.F. PROPAGATION - REVIEW PAPER

by

Janis GALEJS
SYLVANIA ELECTRONIC SYSTEMS
77 "A" Street, Needham Heights, Massachusetts 02194

SOMMAIRE

Les décharges produites par les éclairs semblent constituer la principale source de radiations dans le domaine des fréquences extrêmement basses ; les variations temporelles des courants typiques permettent de déterminer le moment dipolaire effectif des sources et la forme des ondes émises. On rattache les statistiques portant sur l'amplitude d'une source à celles portant sur le bruit atmosphérique.

Après avoir étudié les représentations fondamentales des champs, on calcule les caractéristiques de propagation pour un certain nombre de modèles d'ionosphère stratifiés et anisotropes. Les modèles coniques de la basse ionosphère doivent également comporter des ions aux altitudes inférieures à la couche D. Pendant la nuit, les ondes pénètrent au-dessus de la couche D, et les paramètres de propagation du conducteur d'ondes terre-ionosphère dépendent de la structure détaillée de l'ionosphère en-dessous de la couche F. Les modèles individuels, de conception avancée pour l'ionosphère, ne sont pas représentatifs d'une propagation des ondes globales ou sur une longue distance, mais la moyenne des paramètres de propagation établis pour un certain nombre de géométries de propagation est comparable aux paramètres obtenus à partir d'un modèle ionosphérique isotrope correspondant aux heures de la nuit.

Les résonances se produisant dans le sens terre-ionosphère peuvent être analysées en une géométrie symétrique qui convient pour expliquer les fréquences de résonance, les facteurs Q, les spectres de puissance, les variations diurnes de puissance, et les changements de fréquences de résonance observés.

Les modes divisés résultant des différences entre hémisphère normaux de jour et de nuit sont d'une amplitude négligeable.

Au large, les champs révèlent un affaiblissement exponentiel au fur et à mesure que la profondeur s'accroît, mais au voisinage du littoral, ils tendent à nouveau à augmenter à proximité de la surface sous-marine.

Les vagues provoquent des fluctuations de signaux pour une station réceptrice immergée. Lorsque les vagues sont importantes et les fréquences élevées, les fluctuations de signaux correspondent aux changement de profondeur immédiatement au-dessus de l'antenne réceptrice.

Dans le cas de petites vagues et de fréquences plus faibles, ce sont les caractéristiques de surface d'une zone définie située au-dessus de la station réceptrice qui déterminent les fluctuations de signaux.

ELF PROPAGATION

Janis Galejs
SYLVANIA ELECTRONIC SYSTEMS
77 "A" Street, Needham Heights, Massachusetts 02194

SUMMARY

Lightning discharges appear as principal sources of radiation in the ELF range; time variations of typical currents determine the effective dipole moment of sources and the shape of the radiated waveforms. Amplitude statistics of a source are related to the statistics of atmospheric noise.

After reviewing the fundamental field representations propagation characteristics are calculated for a number of stratified and anisotropic model ionospheres. Tapered models of the lower ionosphere should include also ions at altitudes below the D-layer. During nighttime waves penetrate above the D-layer, and propagation parameters of the earth-to-ionosphere wave guide are dependent on the detailed ionospheric structure below the F-layer. The individual models advanced for the ionosphere are not representative of long distance or global wave propagation; but the average of the propagation parameters derived for a number of propagation geometries is comparable to the parameters deduced from an isotropic nighttime ionosphere model.

The resonances of the earth to ionosphere can be analyzed in a symmetrical geometry, which is adequate for explaining observed resonance frequencies, Q-factors, power spectra, diurnal variations of power, and changes of resonance frequencies. The split modes that result from differences between normal day and night hemispheres are of negligible amplitudes.

In an open ocean fields exhibit an exponential decay with increasing depth, but in the vicinity of the shore line the fields tend again to increase in the vicinity of the bottom surface. Waves cause signal fluctuations in a submerged reception. For large waves and the higher frequencies the signal fluctuates corresponding to the changes of the instantaneous depth above the receiving antenna. For small waves and lower frequencies the signal fluctuations are determined by surface characteristics in a finite area above the receiver.

1. INTRODUCTION

ELF propagation has been the subject for surveys by Galejs[1], Gendrin[2], and Fellman[3], which provide also a detailed historical account of the various developments.

This paper will attempt to illustrate the different problem areas and will mention only several of the many relevant investigations. Emphasis will be on results of theoretical studies; experimental data will be quoted to support the various theoretical findings. After reviewing the sources of ELF radiation and the fundamentals of field representations in the spherical shell between the earth and the ionosphere, some discussion will be devoted to long range propagation and to Schumann resonances. The air-to-sea interface and signal fluctuations below a wavy sea will be also treated.

2. SOURCES

Lightning discharges appear as effective sources of radiation in the VLF and ELF ranges of frequency. In the lower ELF range, the Schumann resonances of the earth-to-ionosphere cavity are excited almost exclusively by lightning discharges. In the ELF and VLF range, atmospherics associated with individual lightning discharges are found to propagate to large distances, and they provide convenient means for estimating the effective parameters of wave propagation. In communication systems, the radio signal must exceed the background noise provided by atmospherics; the noise statistics are also significant for determining the error rates of various communication channels.

The detailed structure of individual lightning discharges has been described in survey papers by Schonland[4], Horner[5], Jones[6], and electric near field measurements of Kittagawa and Brook[7] illustrate various processes of a typical lightning discharge.

Based on a number of measurements, probabilities of stroke current distributions have been estimated by McCann[8], Malan[9], Wagner[10], and Muller-Hillebrand[11]. The median current of the first return stroke is shown to be in the range of 15 to 25 kA with no measurement data available for currents exceeding 200 kA. The time variations of typical current waveforms investigated by Bruce-Golde[12], Hepburn[13], Williams[14], Berger[15] are illustrated in Figure 1. The return stroke model of Bruce and Golde[12], which provides significant radiation only for frequencies in the VLF range, can be supplemented by a model for corona currents between the leader sheath and the return channel in the first stroke[16]. Additional radiation is observed from so-called K-changes that are caused by the inhomogeneous charge distribution in the clouds. They are observed as small rapid field fluctuations, and the model of K-changes by Arnold and Pierce[17] are shown also in Figure 1.

Together with estimated velocity variations of the current waveforms, the data of Figure 1 are used for calculating the effective dipole moments of lightning discharges in Figure 2. The combination of the return stroke by Bruce and Golde[12] and of the corona current models of Rao[16] gives dipole moments comparable to those of Hepburn[13] over the frequencies of the ELF and VLF range. However, these estimates of ELF radiation are lower than in the work of Pierce[18] that are based on estimated gross time variations of the moments in a lightning discharge. Pierce[19] suggests a modification of the K-pulse waveform by additional more gradually decaying terms. The total charge of the modified K-pulse is increased 4 times and the spectral dipole moment would be increased sixfold for ELF in Figure 2.

Using standard propagation formulas it is possible to compute the atmospherics spectra and also waveforms at various distances from the source. The waveforms of Figure 3 have been computed by Jones[20] for a distance of 4000 km using the dipole moment of Williams[14] shown in Figure 2 or by assuming an impulse type source which exhibits a constant spectral dipole moment. The bandwidth of the waveform is limited by a 30 c/s or 3 c/s low pass filter. Such waveforms have been observed by Hepburn[13] or Hughes[21]. Wait[22] shows that a gaussian pulse propagated through the antipode undergoes a change in its shape; the latter pulse is proportional to the time derivative of the original waveform. Less drastic are the changes noted by Jones[20], but there appear to be no experimental observations of individual pulses propagated through the antipode.

A superposition of individual atmospherics of various amplitudes received from different distances gives rise to the atmospheric noise. The noise spectra measured by Maxwell[23] and Mikhaylova[24] are indicated in Figure 4 following Ishida[25]. The spectral measurements of Maxwell[23] can be explained using theoretical propagation models[1].

The amplitude statistics of the received noise can be related to the amplitude statistics of lightning discharges[26,27]. For a received noise that is caused by the activity of a single thunderstorm center the probability distribution is calculated in Figure 5 by assuming that n atmospherics overlap during the integration time of the receiver, where the scale factor β_1 is proportional to this integration time and inversely proportional to the median field strength of the received signal. In the log log versus log scale used for graphing the results, the exponential distribution of n = 1 has a slope of (-1) for r small, the Rayleigh distribution of n large and r small has a slope of (-2). The decay of the curves becomes more gradual for r large. Although curves similar to the one indicated by dashed lines have been reported in some ELF measurements[28], most measurements show AD, which are inversely proportional to the squared amplitudes for larger signals[29,30]. The dynamic range of the calculated noise can be increased by considering the contributions by sources at several distances. Figure 6 shows the effects of adding more frequent waveforms received from nearby sources. The calculated curves of Figure 6 compare with the measured probability distributions of Watt and Maxwell[29]. Alternately, one may also consider lower amplitude radiation processes of the lightning discharge of a single thunderstorm center[27].

The atmospheric noise may be also charecterized by the distribution of intervals between noise bursts. Such measurements have been reported by Watt and Maxwell[29] and Farstadt[28].

Manmade sources are relatively ineffective radiators in the ELF range. The characteristics of transmissions reported by Dunn et al[32], Gutton[33] and Gage et al[34] are summarized in Table 1. Horizontal wire antennas appear to be favored, but the transmission range is very limited for the lowest frequencies.

3. FIELD REPRESENTATIONS

ELF fields in a spherical shell can be discussed by idealizing ground surface and also the ionospheric boundary of the wave guide as homogeneous isotropic conductors. In the ELF range, TE modes do not propagate and the propagating TM n = 0 (or TEM) mode contains only E_r, E_θ, and H_ϕ field components for azimuthally symmetric (vertical electric dipole) excitation in an isotropic environment.

The ELF fields can be represented by a series of zonal harmonics. After expressing the radial functions in a Taylor series and neglecting the height variations of the fields, the radial electric fields E_r excited by a vertical electric dipole of moment Ids are expressed as

$$E_r \approx \frac{iIds}{4\pi\omega\epsilon_o h a^2} \sum_n \frac{n(n+1)(2n+1)}{n(n+1) - \nu(\nu+1)} P_n(\cos\theta) \qquad (1)$$

where

$$\nu(\nu+1) = (k_o aS)^2 = (k_o a)^2 \left[1 + \frac{i\Delta_e}{k_o h}\right] \qquad (2)$$

and $\Delta_e = Z_e/\eta$ is the normalized surface impedance of the ionosphere for TM field components, a is the radius of the earth and h is the height of the ionospheric boundary. The impedance of the ground surface Δ_g is much smaller than Δ_e, and the ground can be approximated by a perfect conductor for purposes of calculating the propagation parameter ν. The approximation (1) is valid only for $nh < a$, and it will become inaccurate for large values of n. The exponential approximation of the radial functions[35] shows that the terms of the sum should become proportional to $n^2 P_n(\cos\theta)$ for $n > k_o a$, and further manipulations of the summation are necessary to increase its rate of convergence.

More convenient for numerical work is the residue series representation of the fields which contains only one propagating terms for frequencies in the ELF range. It can be shown that

$$E_r = -\frac{iIds}{4\omega\epsilon_o h a^2} \frac{\nu(\nu+1)}{\sin\nu\pi} P_\nu(-\cos\theta) \approx \frac{Ids\,\eta}{2h\sqrt{a\lambda\sin\theta}} (iS)^{1.5} \exp(ik_o Sa\theta) \qquad (3)$$

where the last approximation is obtained by substituting the assymptotic expansion for Legendre function $P_\nu(-\cos\theta)$. The parameter ν is obtained from (2) as

$$\nu = -0.5 + \sqrt{0.25 + (k_o aS)^2} \approx k_o aS - 0.5 \qquad (4)$$

The latter approximation introduces an approximately 10 percent error in ν for frequencies near the fundamental Schumann resonance; however, the error becomes small at higher frequencies. The Legendre

function of (3) can be also expressed as a summation of Legendre polynomials, which gives

$$E_r = \frac{iIds\ \nu(\nu+1)}{4\pi\omega\epsilon_o h a^2} \sum_{n=0}^{\infty} P_n(\cos\theta) \frac{2n+1}{n(n+1) - \nu(\nu+1)} \tag{5}$$

For frequencies where Re ν approaches an integer value n, the resonant terms of equation (5) are approximately the same as in (1). However, the total field that is represented by (1) will generally differ from (5), where all the terms of the summation represent only one propagating wave-guide mode.

The horizontal magnetic field component H_ϕ can be obtained from the approximate form of (3) as

$$H_\phi \approx - E_r/(\eta S) \tag{6}$$

Using Legendre polynomials H_ϕ is expressed as

$$H_\phi = - \frac{Ids}{4\pi a h} \sum_n \frac{2n+1}{n(n+1) - \nu(\nu+1)} \frac{d}{d\theta} P_n \cos\theta) \tag{7}$$

There is only one rapidly convergent H_ϕ representation (7) which corresponds to two different E_r expressions (1) and (5).

In the actual earth-to-ionosphere waveguide the surface properties will vary along the direction of wave propagation and the guide boundaries will be stratified and anisotropic. The simple field expressions derived for homogeneous boundaries may still be used provided that the surface impedance of the ionospheric boundary accounts for the stratification and the possible existence of TE field components, which arise in the guide from ionospheric anisotropy. However, the gradual variations of boundary characteristics are ignored in this approach.

More complete field expressions containing also the various height-gain functions are listed by Galejs[35,36] for sources of horizontal and vertical electric dipoles.

4. PROPAGATION MODELS

The wave propagation in the spherical shell is characterized by the phase velocity v_{ph} and the attenuation rate α, which are related to the propagation parameters S of (2) by

$$v_{ph} = c/\mathrm{Re}\ S \tag{8}$$

$$\alpha = 0.02895\ \omega\ \mathrm{Im}\ S$$

where c is the free space velocity of electromagnetic waves and α is defined in decibels per 1000 km. The propagation parameters are illustrated for a number of ionosphere models.

The calculations for a sharply bounded homogeneous and isotropic ionosphere model do not account properly for phase velocity and attenuation rate variations over the ELF range. The stratifications of the lower ionosphere may be represented most simply by an exponentially varying conductivity. This idealization approximates the observed daytime characteristics. The nighttime attenuation rate is lower, and it appears as too low for frequencies in the Schumann resonance range[1].

The observed differences between the general East-to-West (EW) and West-to-East (WE) directions of propagation can be modeled most simply with a purely horizontal static magnetic field[37], but these directional effects can be accounted more accurately by allowing for the finite dip angle of the geomagnetic field. Significant differences between EW and WE directions of propagation are noted when the geomagnetic field is within 30° from the horizontal direction, but these differences are not necessarily the largest for a purely horizontal magnetic field[38]. The radial geomagnetic field component facilitates wave penetration in the nighttime ionosphere; and the nighttime attenuation rates are higher for frequencies in the Schumann resonance range, even when ignoring the presence of ions below the D-region.

Inclusion of ions increases the attenuation rates for the lower frequencies in Figure 7, and the static magnetic field affects the daytime data to a lesser degree than the nighttime data when the attenuation rates of the isotropic model ($B_o = 0$) are significantly lower. The isotropic nighttime ionosphere model yields propagation parameters in Figure 7 that are comparable to the average of Taylor's measurement data[39] that were obtained by observing atmospheric waveforms in a transpacific geometry. The experimental Re S and α figures are lower than in calculations, except for frequencies less than 40 c/s, where Taylor expects his data to become less accurate. The attenuation rates of 400 c/s measurement made by Dunn et al[32] over a 3000 km propagation path between California and New York are also indicated in Figure 7. The daytime attenuation rate is approximated by the calculations for the anisotropic model, but the nighttime attenuation rate is represented more closely by the isotropic model. The inclusion of a static magnetic field should provide more realistic propatation parameters, but it increases the difference between calculations and nighttime measurements. The magnetic field increases the attenuation rate, which may signify wave penetration above the upper boundary of the present nighttime model, where the ionosphere has been assumed to be homogeneous in the vertical (or radial) direction and where the presence of an increase of electron density near the F-layer has been ignored.

The effects of the F-layer will be investigated using several idealized electron density profiles. It is frequently assumed that the electron density which is of the order of 10^3 cm^{-3} at an altitude near 100 km is gradually increased in the height range between 100 and 200 km; a more rapid increase is observed near the bottom side of the F-layer, where N_e exceeds 10^4 following Hanson,[40] Prince and Bostick,[42]. Such electron density data are further idealized by the profiles A and B of Figure 8. For altitudes between 100 and 200 km, the electron density varies from experiment to experiment; and it is in the range from 300 to 5000 cm^{-3} following Wakai,[43] and Maeda[41]. An E-layer peak that is reported near 100 km with densities of 3000 to 10^4 cm^{-3} in the review of Maeda[41] is approximated by the profile C of Figure 8, which follows profile B at altitudes above 120 km. The profile D considered in conjunction with the electron density curve C represents lower densities than the profile B in the altitude range from 120 to $(h_F - \Delta h)$km.

The simplest sharply bounded and homogeneous F-layer model profile A of Figure 8 overemphasizes the effects of standing waves between D and F-layers, the characteristics of which are determined by the propagating magneto-ionic mode. There appear absorption peaks and phase velocity changes, the occurrence of which depends on electron density, boundary height of the F-layer, and the radial component of the static magnetic field; but in long distance or global propagation the conditions for absorption peaks may be satisfied only locally. More refined models include ions above 100 km, a gradual electron density buildup at the bottom side of the F-layer, and a residual nighttime E-layer; these factors tend to decrease but do not eliminate the standing-wave effects in a given ionosphere model, as may be seen from the data shown in Figure 9 for ionosphere models C and CD. It has not been possible to advance a single ionospheric model which produces gradually varying propagation parameters comparable to the ones obtainable from models of the lower ionosphere. The average of the calculated propagation parameters tends to approximate the propagation parameters of the isotropic nighttime ionosphere model, and <u>not</u> the parameters of the lower ionosphere model with a radial static magnetic field. Nighttime models of an anisotropic lower ionosphere may give excessive attenuation rates; and such simplified ionosphere models should be carefully justified by comparisons with available experimental data.

The propagation parameters of the daytime model of the lower ionosphere with a radial geomagnetic field and of the isotropic nighttime ionosphere of Figure 7 are indicated by the dashed lines in Figure 10. The isotropic nighttime model was shown in Figure 9 to approximate an average of propagation parameters derived for more elaborate models which consider ionospheric anisotropy and reflections from the F-layer. In the frequency range of Schumann resonances, the average of propagation parameters of the theoretical curves approximates the data of Chapman et al[44]; Taylor[39] does not consider his transpacific measurements accurate for frequencies less than 40 c/s, and for higher frequencies there is a reasonable agreement between the theoretical curves and the data of Taylor[39], the 400 c/s California to New York measurements of Dunn et al[32], and the atmospherics measurements of Chapman et al[44]. The measurements of Jean et al[45] made on a mixed day and nighttime path are intermediate between the day and nighttime measurements shown in Figure 10. The estimated propagation parameters of Jones[46], who does not distinguish between day and nighttime conditions, are intermediate between those of the present anisotropic day and isotropic nighttime models shown in Figure 10. The propagation parameters are affected by the selection of ion models of the lower ionosphere. An increase of ion density and/or a decrease of the ion-neutral collision frequency ν_{in} may lead to day and nighttime models[47] which exhibit $\alpha \approx 1$ db/1000 km for f = 30 c/s. If adopted for the analysis of global propagation phenomena, such ionosphere models would produce a rather high damping of Schumann resonances.

Propagation under perturbed conditions is discussed by Crain and Booker[48], Johler and Berry[49], or Field[47]. The conductivity of the lower ionosphere is determined principally by ions and ions will affect the characteristics of radio wave propagation under perturbed conditions and/or for the lower frequencies, but there are uncertainties in parameters that characterize the ion contributions to the total conductivity. The measurement data shown in Figures 8-18 and 8-20 of Valley[50] indicate that for moderate northern latitudes and for altitude range of 20 to 28 km, the small ion concentration is near 2500 cm^{-3} and the atmospheric conductivity σ is 2 to 5 x 10^{-12} mho/m with variations up to ±40 percent. Such conductivity figures can be reproduced in calculations if the ion collision frequencies ν_{in} exceed the neutral particle of collision frequency ν_{nn} and if molecular weights MW exceed MW = 29 of the typical lower atmosphere ions. For unperturbed and slightly perturbed ionosphere profiles, the phase velocity is practically unaffected by the presence of ions; but there is some increase in the attenuation rate α. The propagation parameters are shown to depend on the choice of MW and ν_{in} figures by Galejs[51].

5. SCHUMANN RESONANCES

The electromagnetic oscillations in the spherical shell between the earth and ionosphere that are due to azimuthal waves are frequently described as Schumann[52] resonances. These oscillations are excited by naturally occurring lightning discharges and are manifested by increased spectral field amplitudes near 8, 14, 20 c/s and higher frequencies. At these frequencies the wavelengths are large, and the resonances are affected by ionospheric parameters averaged over comparable distances. The essential characteristics of the resonances can be explained even by assuming a perfect symmetry of the cavity, and the elementary field representations of Section 3 can be used to calculate resonance frequencies and cavity quality (Q) factors and noise spectra.

There is a close agreement between measured and calculated resonance frequencies, but certain ambiguities are associated with an interpretation of Q-factors. The half-power width of resonance curves is affected by the presence of adjacent resonances and of near field noise, which may lead to low experimental Q estimates. A close agreement with measured power spectra may be obtained with Q figures which are higher than the usually accepted experimental values. When used in conjunction with estimated source distributions, similar theoretical models are also useful for explaining diurnal changes of power levels and differences of noise levels observed at various locations on the globe[1].

The nonsymmetrical structure of the earth-to-ionosphere cavity has been analyzed numerically with a network analog of the varying surface impedances[53], by perturbation techniques[54,55] or by a direct summation of the series of zonal harmonics, which allows for θ but no ϕ variations of the fields[56]. In a uniform or ϕ-symmetrical cavity, the fields are expressed using Legendre polynomials P_n (cos θ) while nonsymmetrical cavities can support additionally the so-called split modes characterized by Legendre

functions P_n^m (cos θ) with $m \leq n$. The various mode amplitudes of such a field representation are determined from a solution of linear equations the number of which increases quadratically with the number of modes $N \geq n$. The solution of the large number of linear equations is avoided by restricting N to two. In a geometry which distinguishes only between day and night hemispheres, the amplitudes of these additional split modes appear to be negligible under normal day and nighttime conditions.

The diurnal frequency variations differ when observing vertical electric or horizontal magnetic field components. The fundamental resonance frequency of the magnetic field is smoothly varying. The frequency variations of the electric field appear discontinuous near the null of the fields when the equatorial point source is separated from the observation point by 90° in longitude, but the magnitude of these frequency changes is decreased for sources spread out in the asimuthal direction. The diurnal frequency variations reported by Balser and Wagner[57] and Nelson[54] are shown in Figure 11. The complete observed frequency variation can be explained by noting that the peak activity of local thunderstorms, which occurs in late afternoon over land, is shifted to nighttime for sources over the Pacific Ocean. A similar difference in the peak activity of thunderstorms can be seen from the data of Maxwell and Stone[58], Solovyev[59] and Whipple[60] plotted in Figure 12.

In agreement with Madden and Thompson[53] or Nelson[54], the frequency shifts of resonance frequencies are explained by the interaction of adjacent resonance modes. Bliokh et al[55] proposed a mechanism where the difference in the response of day and nighttime hemispheres to an eccentric geomagnetic field caused frequency changes for a single mode. For such frequency changes, it is necessary that the nighttime phase velocity is decreased with an increased radial component of the geomagnetic field; but in multi-layer ionosphere models, which consider F-layer reflections, there can be also an increase of phase velocity following Figure 9.

6. AIR-TO-SEA INTERFACE

The subsurface fields near the air-to-sea interface will be discussed only at large distances from the source, where the fields of the airspace can be adequately represented by a single propagating waveguide mode as in (3) and (6). The subsurface fields will be described in a cartesian (x,y,z) coordinate system, where the x-axis is in the direction of wave propagation above the interface, y-axis is transverse and horizontal, and the vertical z-axis is oriented upwards. These x,y,z coordinates correspond to the θ, φ, r coordinates of the spherical system used in Section 3. The magnetic fields of the lossy half-space ($z \leq o$) will be of the form

$$H_y = H_y^o \exp (ik_o Sx - ik_z z) \tag{9}$$

with no field variations in the y-direction. The continuity of the H field representations (6) and (7) for z = 0 shows that

$$H_y^o = - \frac{Ids}{2h} \sqrt{\frac{i^3 S}{a\lambda \sin \theta}} \tag{10}$$

Also the E_x and E_z components of the field can be written in the form (9) as

$$E_j = E_j^o \exp (ik_o S_x - ik_z z) \tag{11}$$

with j = x or z. Substitution of (9) and (11) in Maxwell's equations shows that

$$(k_o S)^2 + k_z^2 = k_o^2 \left(\epsilon_r + i \frac{\sigma}{\omega \epsilon_o}\right) \tag{12}$$

$$\frac{k_z}{k_o} = \sqrt{\epsilon_r + \frac{i\sigma}{\omega \epsilon_o} - S^2} \tag{13}$$

where ϵ_r is the relative dielectric constant and σ is the conductivity of the medium. For sea water $\epsilon_r \approx 80$, $\sigma \approx 4$ mho/m and $\sigma/\omega\epsilon_o > 10^8$ for f < 720 c/s. S is of the order of unity and can be neglected in (13); the wave number k_z of wave propagation in the vertical direction is then the same as for a plane wave in a homogeneous medium. Although the wave propagates in the x-direction above the interface, the wave propagates downward in the lossy medium for z < 0.

The assumption of a homogeneous semi-infinite lossy medium neglects salinity changes with increasing depth. Pronounced conductivity variations have been observed in the shallow waters near Denmark, where the lower conductivity Baltic water may be found on top of higher conductivity water of the North Sea following Brock-Nannestad[61].

The exponential decrease of field intensity indicated in (9) and (11) is not necessarily observed with increasing depth near the short line. Soderberg[62] has observed the natural ELF noise in the 8 to 60 c/s range off the coast of Baja California at depths from 30 to 300 meters. The measured noise levels are compared with calculations for a semi-infinite conducting medium in Figure 13. The decay of the fields is nearly exponential in the vicinity of the surface, but the noise level is increased as the bottom is approached. This increase of the ambient electric field is apparently caused by energy conducted

from the shore along the ocean bottom. Soderberg[62] has also related the depth of the minimum noise value to the electric properties of the ocean bottom and to the distance from the shore.

Spence et al[63] have studied the electromagnetic fields in the ocean resulting from ground wave excitation over land. They present an approximate treatment of a two dimensional geometry and indicate the relative contributions to the noise field in ocean by energy propagated from above the surface and from below the ocean bottom.

7. EFFECTS OF WAVE MOTION

Wave motion of the ocean surface will cause some fluctuations of the subsurface fields.

Wait[64] considers a uniform plane wave in free space traveling in a direction parallel to the mean (plane) boundary of the conducting dielectric. The interface is taken to be a sinusoidal wave form with an amplitude much smaller than the period, with the magnitudes of both being much less than the free space wavelength. The fields in a reference plane through the wave troughs are computed by assuming that field penetration at any point along the conductor is the same as for a planar surface, which is depicted in the computational model A of Figure 14. The subsurface fields are then related to the fields in the reference plane. In this approach subsurface fields do not exceed the surface fields of a planar interface. In the limit of large wavelength L fields below the surface will depend on the instantaneous depth below the wave.

Winter[65] presents an elaborate statistical analysis of surface roughness described by a gaussian distribution, but he assumes that the surface fields at a given time on the wavy surface are the same as in an unperturbed geometry. This implies that the tangential electric field components on the wavy surface are essentially determined by the projection of the nearly vertical unperturbed fields. The tangential fields below the sloping part of the wave may be stronger than for a flat sea where the tangential field component is related to the normal component by the boundary condition

$$E_{tan}/E_{norm} \approx \sqrt{\frac{\omega\epsilon_o}{i\sigma}}$$

In this formulation the undersea fields become very weak for long waves when the maximum slope is decreased and there is no indication that the subsurface fields depend on the instantaneous depth in the limit of large L.

Lerner and Max[66] find a solution to the field problem above the sea surface on the assumption that the sea surface is perfectly conducting to the extent that the E-field is everywhere normal to the surface and that the water waves make the sea surface a trochoidal cylinder, the cross section of which is indicated in Figure 15. Then (dropping the assumption that sea water is a perfect conductor) they relate the subsurface fields to the fields and their normal derivatives at the sea surface. For underwater measurements made a few tens of feet below the troughs of the waves, the field variations due to one- or two-foot sea waves are averaged out. Figure 15 indicates slight field differences for EM wave propagation in directions perpendicular ($\perp$) and parallel ($\parallel$) to the wave crests, but the variations are small relative to the changes in nominal field strength that corresponds to the instantaneous antenna depth and is indicated by dashed lines. For storm waves the phase and amplitude of the underwater field varies with instantaneous depth, which is illustrated for waves of D = 25 ft. in Figure 15. These theoretical predictions have been confirmed experimentally in the VLF range.

Wetzel[67] has considered EM field fluctuations in submerged reception by postulating that the electric fields are normal to the wavy boundary. He distinguishes between big wave theory, when signal fluctuations are related to the instantaneous observer depth, and small wave theory, where the spectrum of signal fluctuations corresponds to the spectrum of ocean waves, but with an added high frequency cut-off. The small wave theory is valid for $k_z D \ll 1$ where k_z is the wave number of sea and D is the wave height. With $k_z \sim \sqrt{\omega}$, the small wave theory applies to larger wave heights D (or greater wind speeds) at the lower frequencies of the ELF range.

8. REFERENCES

1. Galejs, J., "Schumann resonances," Radio Sci. 69D(8), 1043-1055, 1965.

2. Gendrin, R., "ELF and micropulsations, Part I," (in French), Ann. de Geophys. 23(1), 145-152, 1967.

3. Fellman, E., "ELF noise" 16th General Assembly of URSI, Ottawa, 1969.

4. Schonland, B. F. J., "The lightning discharge," Handbuch der Physik, 22, 576-628, 1956.

5. Horner, F., ,Radio noise from thunderstorms," in Advances in Radio Research, edited by J. A. Saxton, Vol. 2, Academic Press, New York, 146, 1964.

6. Jones, D. L., "Atmospherics," MF, LF, and VLF Radio Propagation, IEE Conference Publication 36, 1967.

7. Kitagawa, N., and M. Brook, "A comparison of intercloud and cloud-to-ground lightning discharges," J. Geophys. Res., 65, 1189-1201, 1960.

8. McCann, G. D., "The measurement of lightning currents in direct strokes," Trans. IEE, 63, 1157-1164, see Figure 13, 1944.

9. Malan, D. J., ,Lightning counter for flases to ground," in Gas Discharges and the Electricity Supply Industry, Proc. Intern. Conf., Central Electricity Res. Lab., Leatherhead, Surrey, England, May 1962, edited by J. S. Forrest, Butterworths, London, 121, 1962.

10. Wagner, C. F., "The lightning stroke as related to transmission line performance," Elec. Eng., 82, 339-347, 1963.

11. Muller-Hillebrand, D., "Lightning protection," in Problems of Atmospheric and Space Electricity, Proc. 3rd Intern. Conf. Atmospheric and Space Electricity, Monteux, Switzerland, 1963, edited by S. C. Coroniti, Elsevier Publishing Company, New York, 408-429, 1965.

12. Bruce, C. E. R., and R. H. Golde, "The lightning discharge," Institution of Electrical Engineers Journal, 88, Part II, 487-505, 1941.

13. Hepburn, F., "Atmospheric waveforms with very-low-frequency components below 1 kc/s known as slow tails," J. Atmosph. Terr. Phys., 10, 266-287, 1957.

14. Williams. J. C., "Thunderstorms and VLF radio noise," Ph.D. Thesis, Harvard University, Div. Engr. and Applied Phys., 1959.

15. Berger, K., "Front duration and current steepness of lightning strokes to the earth," in Gas Discharges and Electricity in Supply Industry, Proc. Inter. Conf., Central Electricity Res. Lab., Leatherhead, Surrey, England, May 1962, edited by J. S. Forrest, Butterworths, London, 63-73, 1962.

16. Rao, M., "Corona currents after the return stroke and the emission of ELF waves in a lightning flash to earth," Radio Science, 2(2), 241-244, 1967.

17. Arnold, H. R., and E. T. Pierce, "Leader and junction processes in the lightning discharge as a source of VLF atmospherics," Radio Science, 68D(7), 771-776, 1964.

18. Pierce, E. T., "Excitation of earth-ionosphere cavity resonances by lightning flashes," J. Geophys. Res., 68(13), 4125-4127, 1963.

19. Pierce, E. T., "The thunderstorm as a source of atmospheric noise at frequencies between 1 and 100 kHz," Report DASA 2290, Stanford Research Institute, Menlo Park, California, 1969.

20. Jones, D. L., "Terrestrial electromagnetic wave propagation - theory and experiment in the time domain and application to "slow tail" atmospherics", Radio Science, 5, 1970.

21. Hughes, H. G., "A comparison at extremely low frequencies of positive and negative atmospherics," J. Atmosph. Terr. Phys. 29, 1277-1283, 1967.

22. Wait, J. R., "Distortion of an ELF pulse after propagation through an antipode," J. Geophys. Res. 74(11), 2982-2986, 1969.

23. Maxwell, E. L., "Atmospheric noise from 20 Hz to 30 Hz," Radio Sci. 2(6), 637-644, 1967.

24. Mikhaylova, G. A., "Spectra of atmospherics at ultra low frequencies during nighttime," Geomag. and Aeron., 7(2), 285-287, 1967.

25. Ishida, T., "Statistical characteristics of atmospheric noise," 16th General Assembly of URSI, Ottawa, 1969.

26. Galejs, J., "Amplitude distributions of radio noise at ELF and VLF," J. Geophys. Res., 71, 201-216, 1966.

27. Galejs, J., "Amplitude statistics of lightning discharge currents and ELF and VLF radio noise," J. Geophys. Res., 72(11), 2943-2953, 1967.

28. Farstadt, A. J., "Atmospheric noise," Final Report, Contract No. N00039-69-C-1541, Westinghouse Electric Corporation, Georesearch Laboratory, Boulder, Colorado, 1969.

29. Watt, A. D., and E. L. Maxwell, "Measured statistical characteristics of VLF atmospheric noise," Proc. IRE, 45, 55-62, 1957.

30. Crichlow, W. Q., C. J. Roubique, A. D. Spaulding and W. M. Berry, "Determination of the amplitude probability distribution of atmospheric radio noise from statistical moments," J. Res. NBS (Radio Propagation), 64D(1), 49-56, (1960).

31. Nakai, T., "On the time functions of atmospheric noise," Proc. Res. Inst. Atmospherics, Nagoya University, 15, 17-28, 1968.

32. Dunn, G. R., P. F. Kuhnle, and R. D. Smith, "Experimental research investigation of extremely low frequency propagation," Final Report, Space General Corp., El Monte, California, Contract AF19 628 1603, AD-437 777 Div. 8, 1964.

33. Gutton, H., "Experimental study of the electromagnetic field of the very low frequency 40 Hz," (in French), AGARD Symposium on Subsurface Propagation of Electromagnetic Waves, Paris, 20, 409-424, 1966.

34. Gøge, B. P., D. K. Reynolds and J. C. Rogers, "Artificial excitation of Schumann resonance in the earth-ionosphere cavity," J. Geophys. Res. 73(13), 4416-4420, 1968.

35. Galejs, J., "Near fields and antipodal fields in the terrestrial earth-to-ionosphere wave guide," Proc. IEE 116(7), 1150-1158, 1969.

36. Galejs, J., "ELF and VLF fields of a horizontal electric dipole," IEEE Trans. Ant. Prop. AP-16(6), 689-700, 1968.

37. Galejs, J., "Terrestrial extremely-low-frequency propagation," Natural Electromagnetic Phenomena Below 30 kc/s, ed. D. F. Bleil, Proc. NATO Advanced Study Institute, Bad Homburg, Germany, 1963, Plenum Press, New York, New York, 205-258, 1964.

38. Galejs, J., "Propagation of ELF and VLF waves below an anisotropic ionosphere with a dipping static magnetic field," J. Geophys. Res. 73(1), 339-352, 1968.

39. Taylor, W. L., "Observed directional effects in ELF, attenuation rates and phase velocities from slow tail components of atmospherics," Paper presented at the USNC - URSI Spring Meeting Washington, D. C., 1969.

40. Hanson, W. B., "Structure of the ionosphere," in Satellite Environment Handbook, ed. F. S. Johnson, Stanford University Press, Stanford, California, 27-46, 1961.

41. Maeda, K., "Mid-latitude electron density profile as revealed by rocket experiments," J. Geomagnetism and Geoelectricity 21(2), 557-567, 1969.

42. Prince, C. E., and F. X. Bostick, "Ionospheric transmission of transversely propagated plane waves at micropulsation frequencies and theoretical power spectrums," J. Geophys. Res. 69(15), 3213-3234, 1964.

43. Wakai, N., "Quiet and disturbed structure and variations of the nighttime F region," J. Geophys. Res. 72(17), 4507-4517, 1967.

44. Chapman, F. W., D. L. Jones, J. D. W. Todd, and R. A. Challinor, "Observations on the propagation constant of the earth-ionosphere waveguide in the frequency band 8 c/s to 16 kc/s," Radio Sci. 1(11), 1273-1282, 1966.

45. Jean, A. G., Jr., A. C. Murphy, J. R. Wait, and D. F. Wasmundt, "Propagation attenuation rates at ELF," J. Res. NBS 65D(5) (Radio Prop.), 475-479, 1961.

46. Jones, D. L., "Schumann resonances and ELF propagation for inhomogeneous isotropic profiles," J. Atmos. and Terr. Physics 29, 1037-1044, 1967.

47. Field, E. C., "The propagation of ELF waves under normally and naturally disturbed conditions," J. Geophys. Res. 74(14), 3639-3650, 1969.

48. Crain, C. M., and H. G. Booker, "The effects of ions on low frequency and very low frequency propagation in an abnormally ionized atmosphere," J. Geophys. Res. 69(21), 4713-4716, 1964.

49. Johler, J. R., and L. A. Berry, "On the effect of heavy ions on LF propagation, with special reference to the nuclear environment," Radio Sci. 1(3), 303-307, 1966.

50. Valley, S. L., ed., Handbook of Geophysics and Space Environment, Air Force Cambridge Research Laboratories, McGraw-Hill Book Company, Inc., 1965.

51. Galejs, J., "ELF and VLF propagation for models of a perturbed ionosphere," Radio Science, 5(5), 1970.

52. Schumann, W. O., "On the radiation free selfoscillations of a conducting sphere, which is surrounded by an air layer and a ionospheric shell," (in German), Z.Naturforsch 72, 149-154, 1952.

Schumann, W. O., "On the damping of electromagnetic selfoscillations of the system earth-air-ionosphere," (in German), Z. Naturforsch 72, 250-252, 1952.

53. Madden, T. R., and W. Thompson, "Low-frequency electromagnetic oscillations of the earth-ionosphere cavity," Rev. Geophys. 3, 211-254, 1965.

54. Nelson, P. H., "Ionospheric perturbations and Schumann resonance data," Ph.D. Dissertation (Geophysics), Massachusetts Institute of Technology, Cambridge, Massachusetts, 1967.

55. Bliokh, P. V., A. P. Nikolayenko, and YU. F. Fillippov, "Diurnal variations of the natural frequencies of the earth-ionosphere resonator in relation to the eccentricity of the geomagnetic field," Geomagnetism and Aeronomy 8(2), 198-206, 1968.

56. Large, D. B., and J. R. Wait, "Theory of electromagnetic coupling phenomena in the earth-ionosphere cavity," J. Geophys. Res. 73(13), 4335-4362, 1968.

57. Balser, M., and C. A. Wagner, "On frequency variations of the earth-ionosphere cavity modes," J. Geophys. Res. 67(10), 4081-4083, 1962.

58. Maxwell, E. L., and D. L. Stone, "VLF atmospheric noise predictions," Report 92-F-1 on Contract NObsr 93159, DECO Electronics, Inc., Boulder, Colorado, 1966.

59. Solovyev, V. A., "Time and space characteristics of thunderstorm activity," Planetary Electrodynamics, ed. S. C. Coroniti and J. Hughes, Gordon and Breach, New York, New York, 1969.

60. Whipple, F. J. W., "On the association of the diurnal variation of electric potential gradient in fine weather with the distribution of thunderstorms over the globe," Quart. J. Roy. Met. Soc. 55, 1-17, 1929.

61. Brock-Nannestad, L., "Determination of the electric conductivity of the sea bed in shallow waters with varying conductivity profile," Electronic Letters, 1(10).

62. Soderberg, E. F., "ELF noise in the sea at depths from 30 to 300 meters," J. Geophys. Res. 74(9), 2376-2387, 1969.

63. Spence, J. R., E. J. Sullivan and J. J. Beville, "Electromagnetic fields in the ocean near a shoreline," AGARD Symposium or Subsurface Propagation of Electromagnetic Waves, Paris, 20, 97-113, 1966.

64. Wait, J. R., "The calculation of the field in a homogeneous conductor with a wavy interface," Proc. IRE 47(6), 1959.

65. Winter, D. F., "Low-frequency radio propagation into a moderately rough sea," J. Res. NBS Radio Propagation, 67D(5), 551-562, 1963.

66. Lerner, R. M. and J. Max, "VLF and LF fields propagating near and into a rough sea," Radio Science, 69D(2), 273-286, 1965.

67. Wetzel, L. B., "Electromagnetic field fluctuations in transmission through the surface of the sea", Paper presented at the USNC - URSI Spring Meeting, Washington D.C., 1970.

TABLE

1

ELF Sources.

AUTHOR	FREQUENCY c/s	ANTENNA	LOCATION	DISTANCE km
Dunn et al [1964]	400	107 km power line	Calif. - N.Y.	3000
Gutton [1966]	40	1.2 km submerged insul. wire	So. France	40
Gage et al. [1968]	5.4	35 km insul wire on ice	Antarctica	18

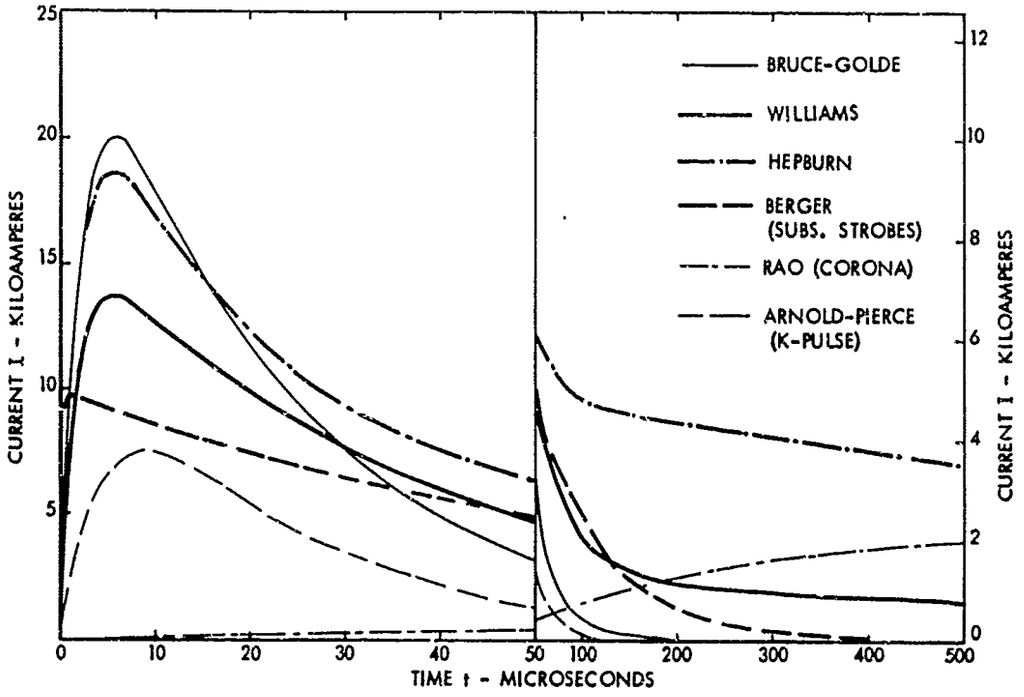

Fig. 1 Current Waveforms of Lightning Discharges.

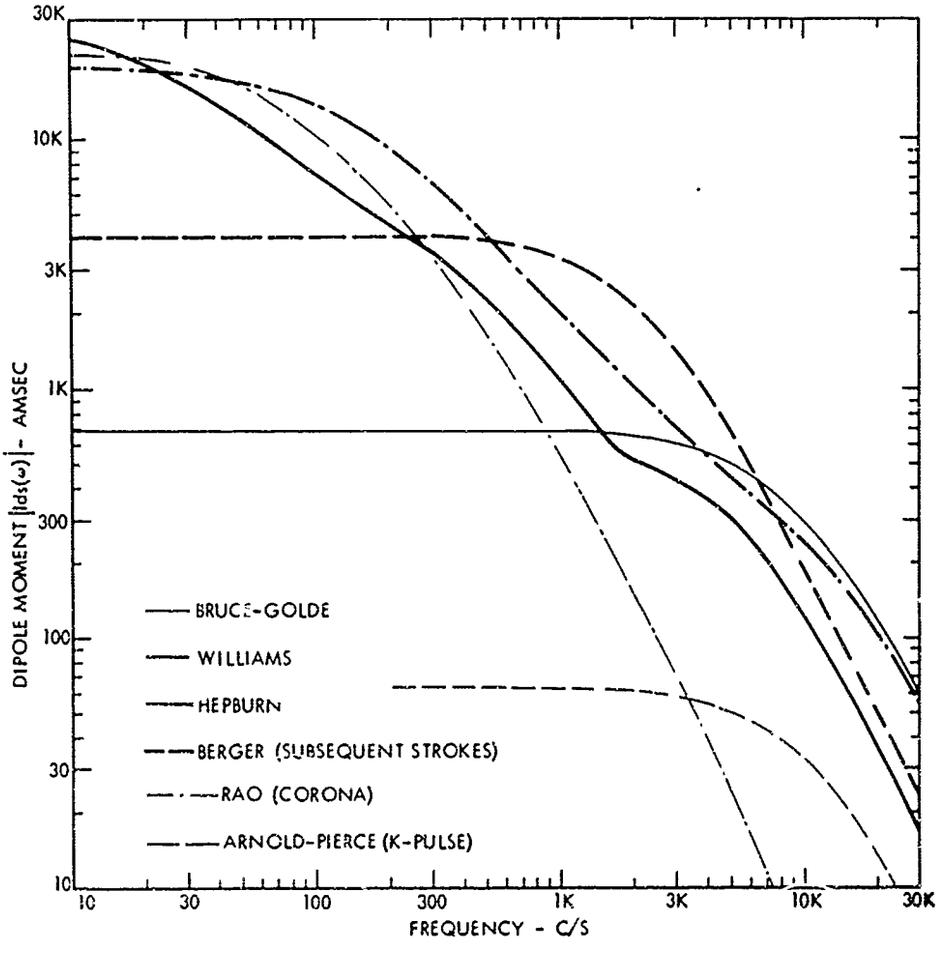

Fig 2 Spectrum of the Dipole Moment for a Median Lightning Flash.

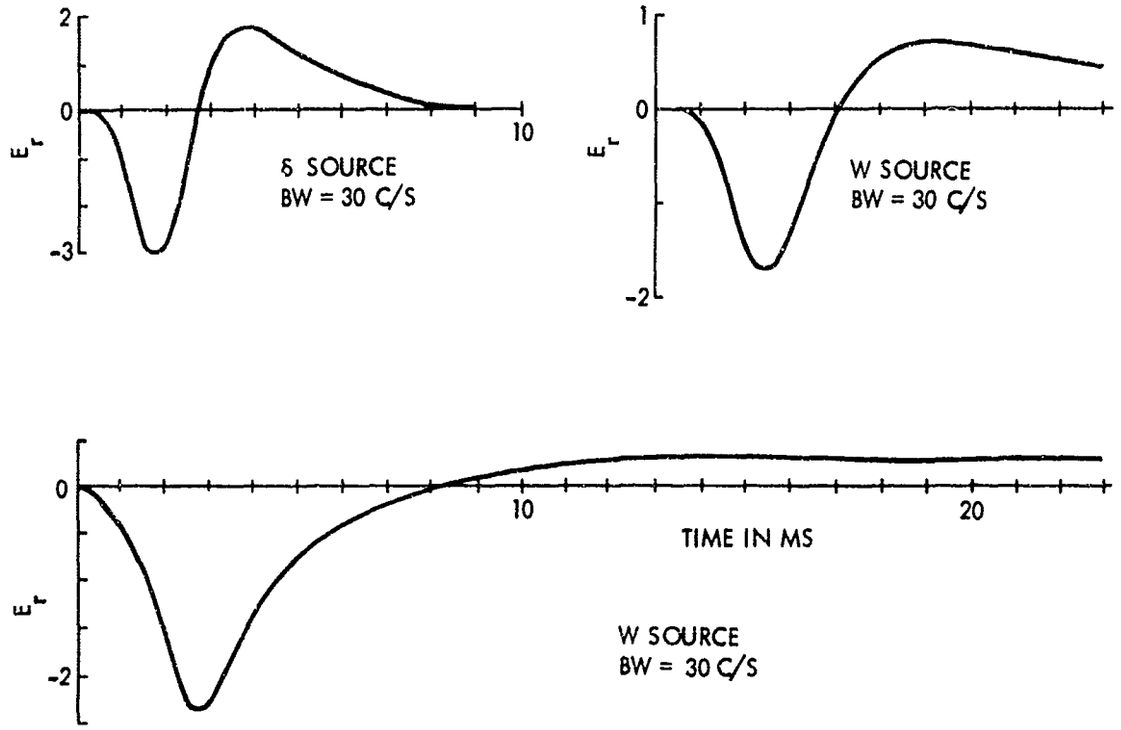

Fig.3 Atmospherics at a Distance of 4000 KM.
δ = Impulsive Source, W = Williams Source of Figure 2

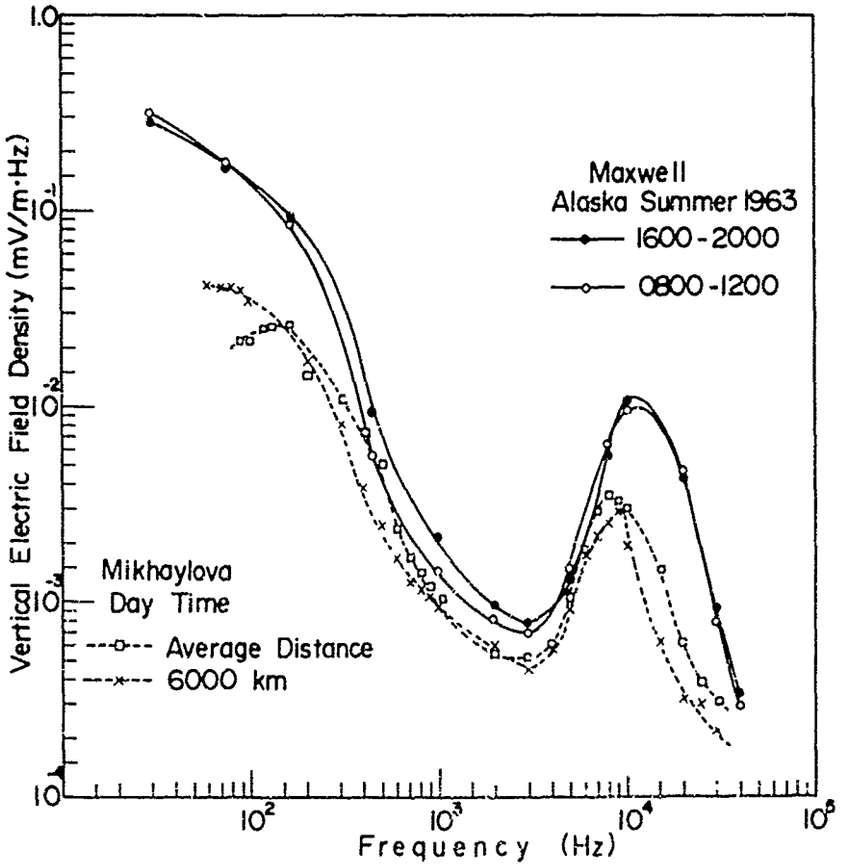

Fig 4 Frequency Spectrum of Atmospheric Noise in ELF Range.
(Adopted from Ishida [1969])

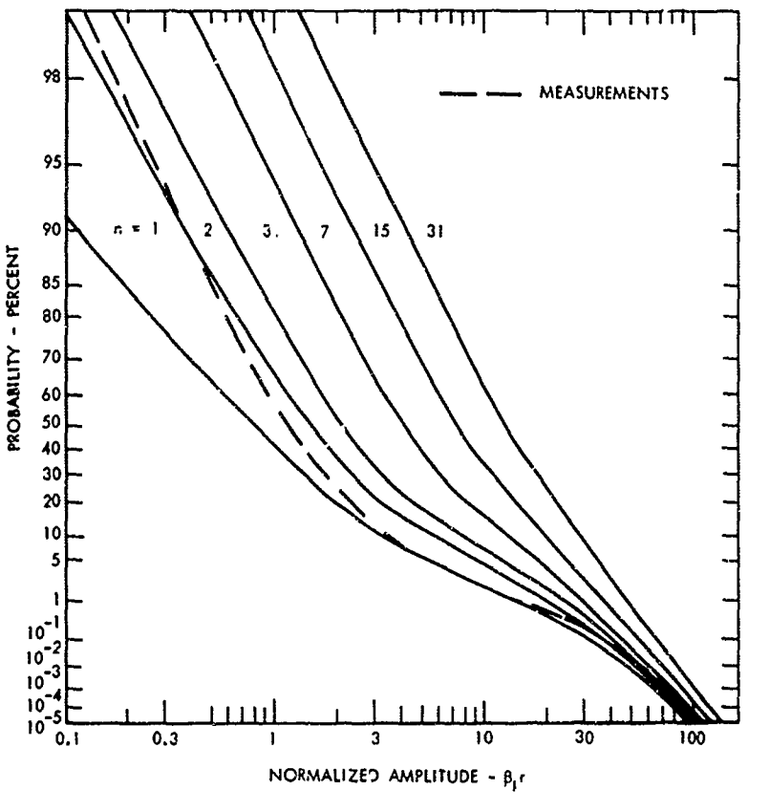

Fig.5 Probability Distribution of the Received Noise. Source Current Distribution Represented by Two Exponentials.

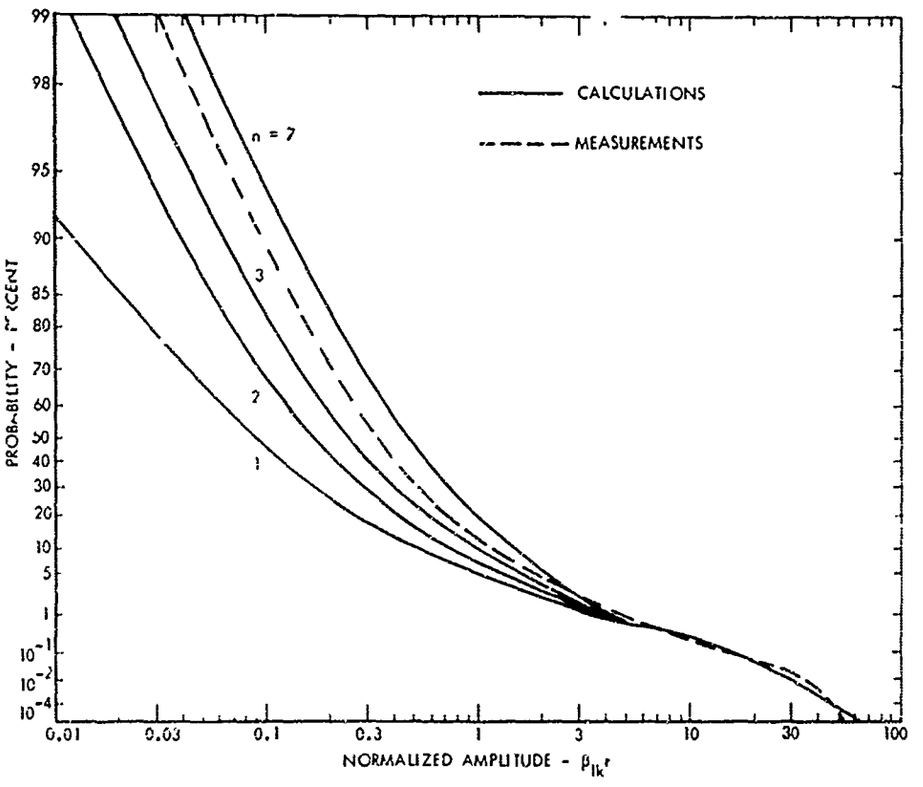

Fig 6 Probability Distribution of the Noise Received From Distances d_1 and $d_2 > d_1$. 90% of Time n Waveforms Received from d_2, 10% of Time 1 Waveform From d_1 is Added to (n-1) Waveform d_2; u = 10.

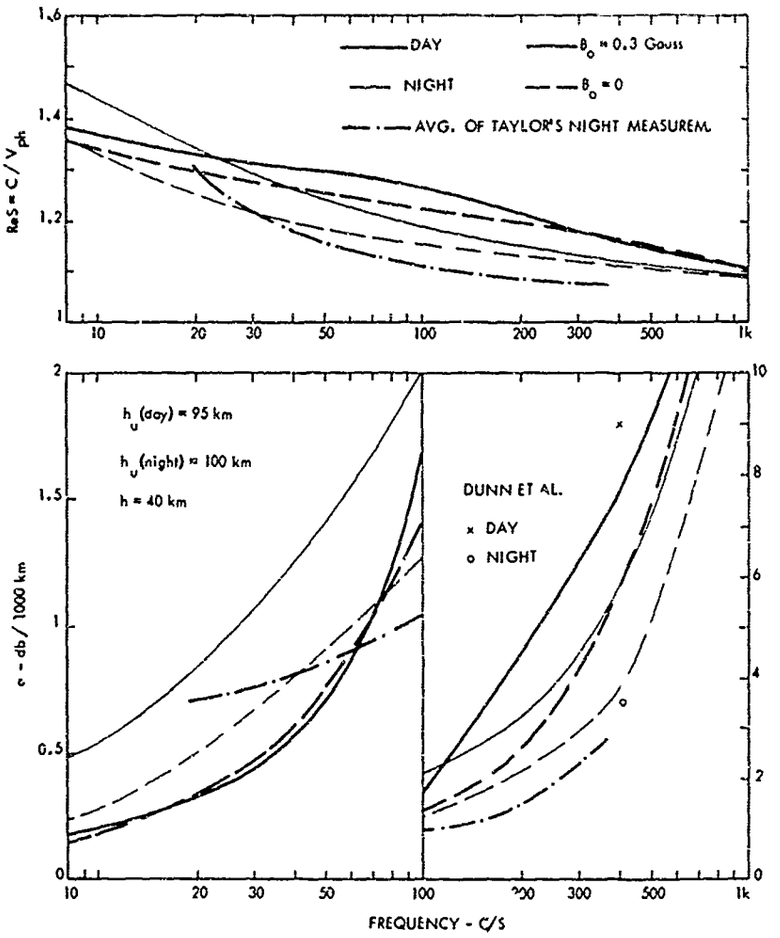

Fig. 7 Phase Velocity and Attenuation Rates of ELF Waves, Electron Profiles of Decks with Added Ions.

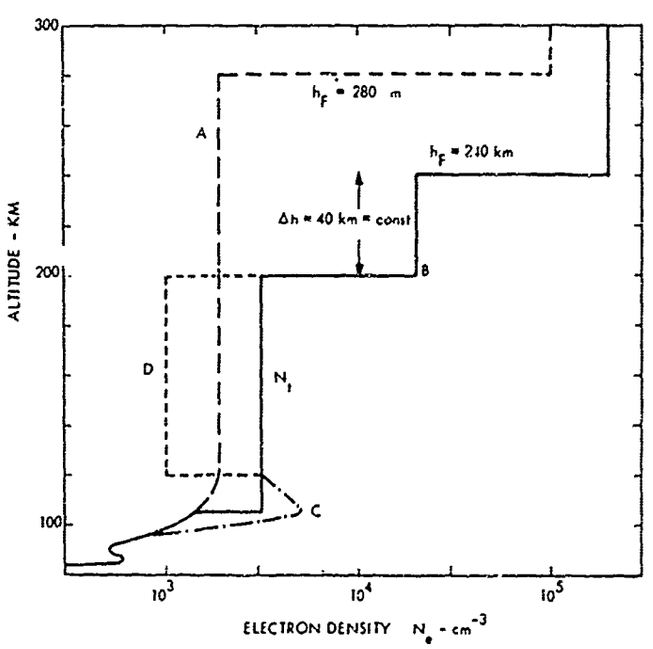

Fig 8 Models of Night Time Electron Density.

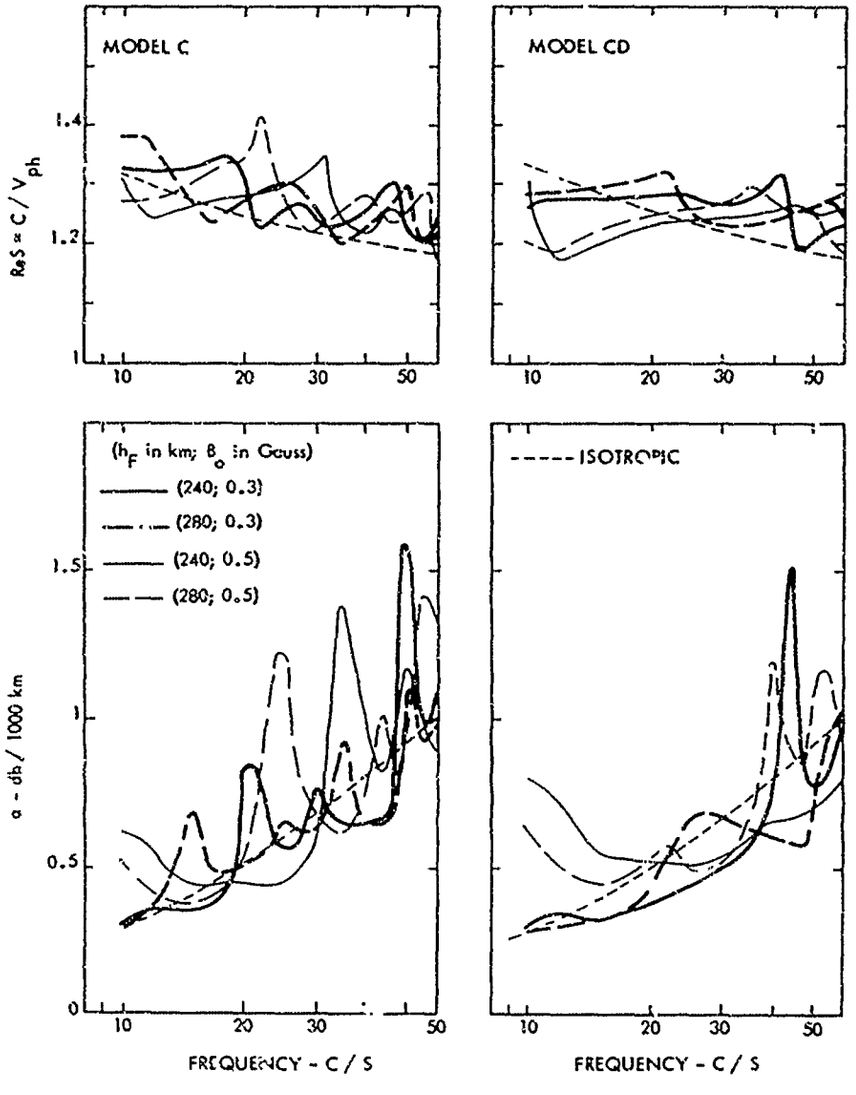

Fig 9 Phase Velocity and Attenuation Rates for Ionosphere Models C and D.

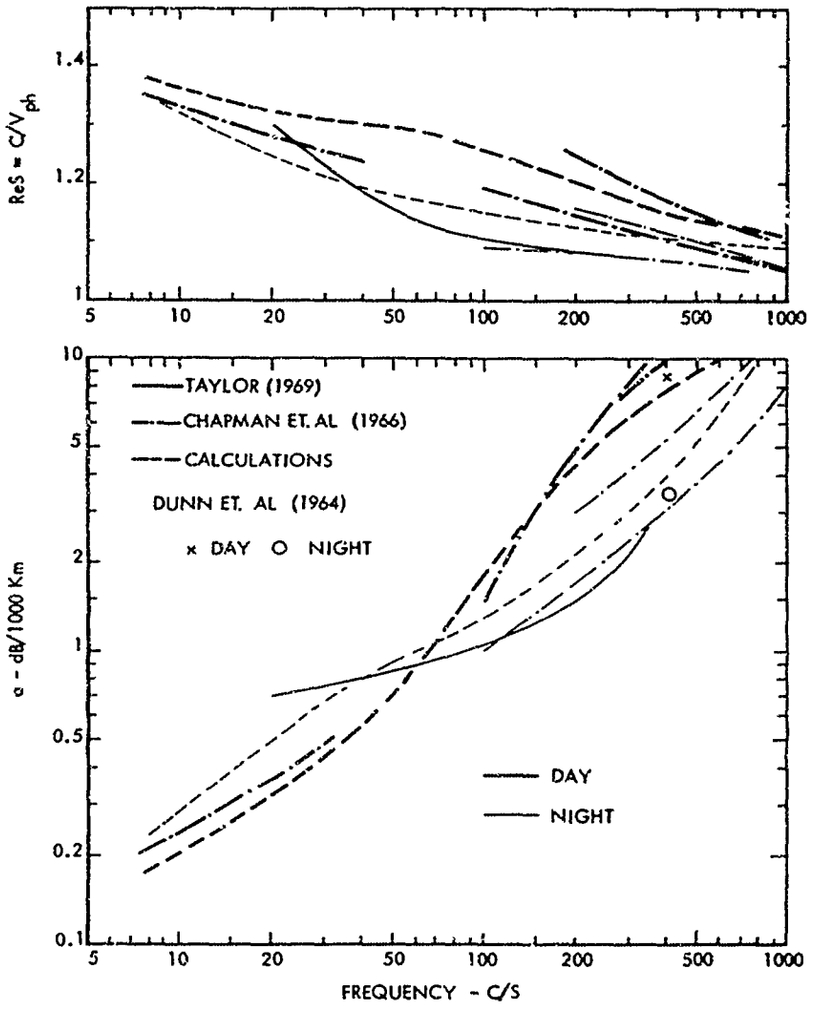

Fig. 10 Measured And Calculated ELF Propagation Parameters.

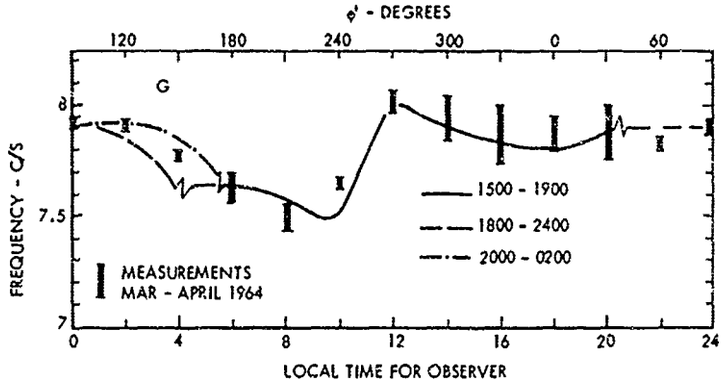

Fig. 11 Measured And Calculated Variations of Resonant Frequencies; Observer At 45° N, 70° W; Equatorial Sources Active During The Indicated Interval Of Local Time.

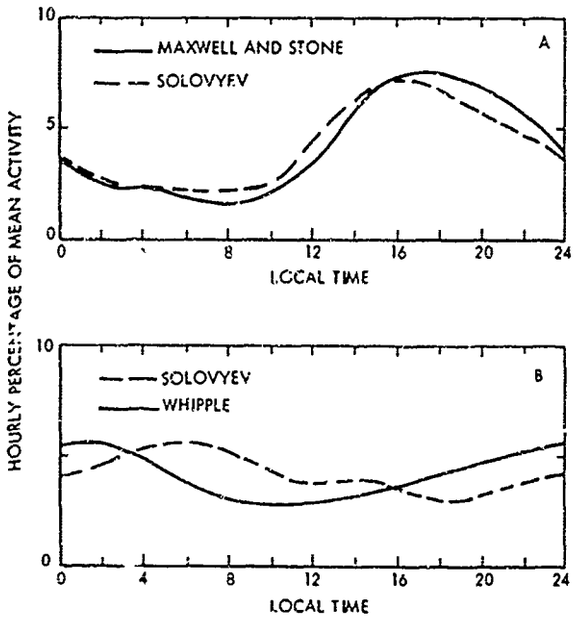

Fig 12 Diurnal Variations of Local Thunderstorm Activity.

A Over Land
B On Oceans

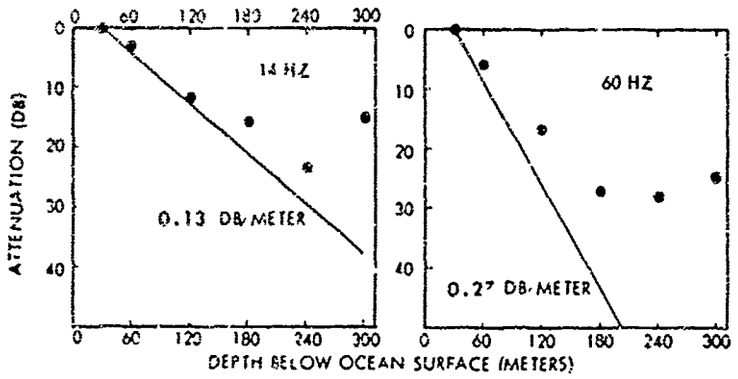

Fig 13 Attenuation Versus Depth for Two Frequencies. The Straight Lines Represented the Open Sea Attenuation (With Respect to a Reference Depth of 30 Meters). The Dots Represent Measurements of Soderberg (1969).

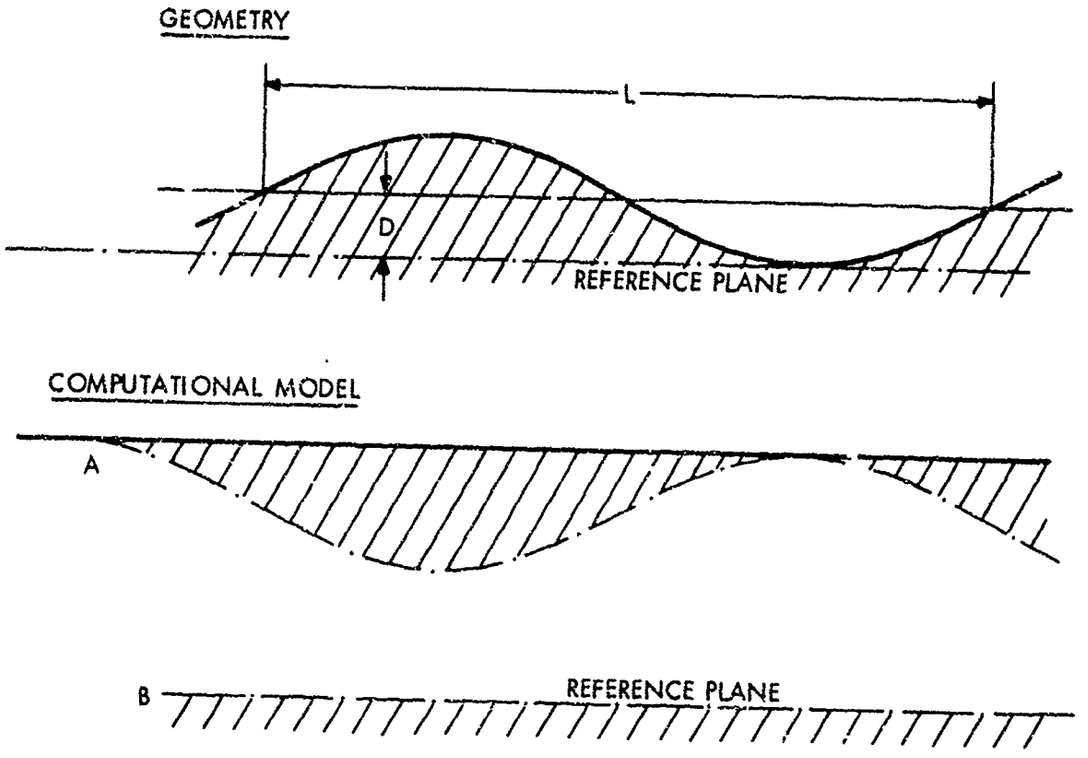

Fig. 14 Fields in a Conductor with a Wavy Interface.

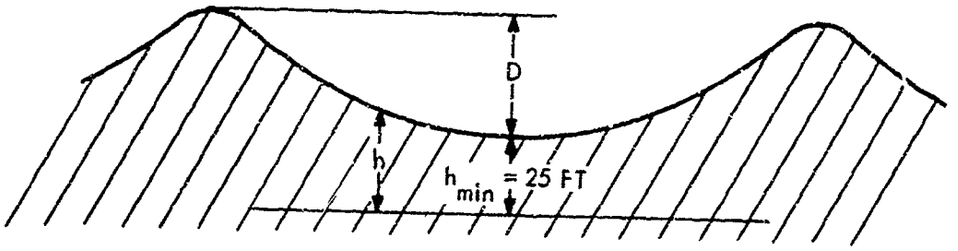

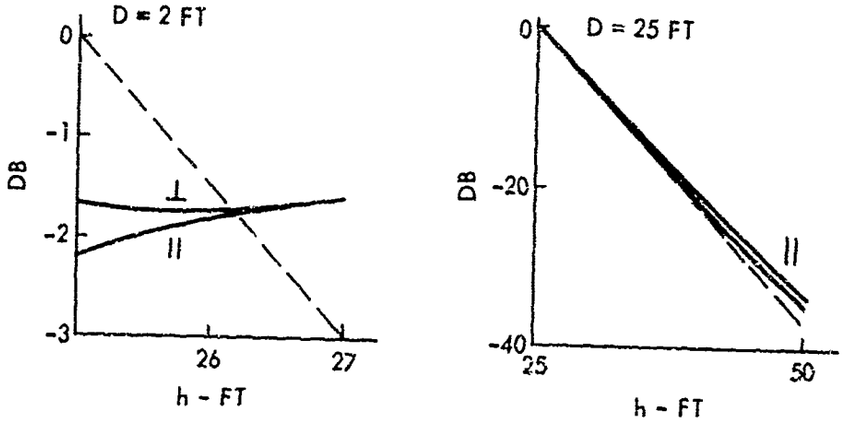

Fig 15 Subsurface Fields of Lerner and Max [1965] f = 20 Kc/s

PROPAGATION OF VLF ELECTROMAGNETIC WAVES ACROSS LAND/SEA BOUNDARIES

by

James R. WAIT

ESSA Research Laboratories, Boulder
Colorado 80302 - U.S.A.

SOMMAIRE

Pour les applications aux systèmes de radio-navigation et de communications, il est souhaitable de disposer d'une théorie d'ensemble relative à la propagation des ondes électromagnétiques le long d'une trajectoire mixte, à la fois terrestre et aquatique. Nous nous efforçons dans cet exposé, de formuler une équation générale intégrale, tenant compte à la fois des contrastes de conductivité et des caractéristiques topographiques du littoral. Nous étudions également l'influence d'une plage en pente et d'une profondeur d'eau variable. Des perfectionnements appropriés de cette théorie nous permettent d'étudier en outre la réflexion et la réfraction d'une onde se propageant sur le littoral selon une trajectoire oblique. Nous examinons enfin la forme du rayonnement d'une antenne basée au sol à proximité du littoral, du point de vue de l'émission optimale d'ondes d'espace à haute fréquence.

PROPAGATION OF VLF ELECTROMAGNETIC WAVES ACROSS LAND/SEA BOUNDARIES

James R. Wait
ESSA Research Laboratories, Boulder, Colorado 80302, U. S. A.

ABSTRACT

We consider a two-dimensional model of propagation of radio waves in the earth-ionosphere waveguide across a land/sea boundary. The surface impedance of the outer wall is uniform but there is a discontinuity in the surface impedance for the lower wall. Following a Wiener-Hopf procedure, the dual integral equations for the problem are solved exactly. Various limiting forms of the solution are discussed. In particular, it is shown that the exact expression for the mode conversion coefficient is closely related in form to the result obtained by Kirchhoff theory. The numerical results show that a land/sea boundary may cause excessive conversion of energy from the dominant to the higher modes. The resulting interference pattern can have serious consequences in VLF phase navigation systems.

1. INTRODUCTION

The Wiener-Hopf technique has been used extensively to examine wave propagation in non-uniform structures. The scope of the method has been the subject of two notable textbooks[1, 2] One of the earliest applications was carried out by Heins and Feshbach[3] who were interested in acoustic wave scattering in ducts with non-uniform walls. The application of the method to water waves in channels of non-uniform depth has been considered by Heins[4] and Keller and Weitz[5] An interesting problem in electromagnetics involving diffraction by an imperfectly conducting sheet was treated by Senior[6] using an elegant adaptation of the factorization method.

Recently, the Wiener-Hopf technique and related factorization methods have been applied to a host of electromagnetic problems involving boundaries with discontinuities in the surface impedance. Many of these are described by Weinstein[2] who has contributed extensively in this field. Propagation of radio waves across a coast line was treated by Clemmow[7] and Bazer and Karp[8] for a flat-earth model, and by Thompson[9] and Chang[10] for a curved-earth model. The coast line problem has also been treated by integral equation methods where approximate solutions are obtained by relatively simple iterative procedures [e.g., Feinberg[11], Wait[12, 13]] These latter approaches are closely related to the Kirchhoff method as pointed out only very recently.[14]

In the present paper, we wish to consider wave propagation in the earth-ionosphere waveguide which has a uniform upper boundary and a sectionally uniform lower boundary. To facilitate the solution, the problem is made two-dimensional by adopting a cylindrical model excited by a uniform magnetic line source in the axial direction. Thus, in effect, we are considering azimuthal propagation in the cylindrical cavity. Unlike earlier discussions [i.e., Wait[15], Chang[10]], we formulate the problem in terms of cylindrical wave functions so the final results are applicable to an unrestricted range of the parameters.

A special objective of the present work is to cast the exact solution into a form which can be easily compared with the corresponding Kirchhoff result. Actually, the latter can be derived directly from orthogonality considerations. Finally, some illustrative numerical results are presented. Also, we consider the approximate extension of the theory to any number of homogeneous sections.

2. BASIC FORMULATION FOR UNIFORM BOUNDARIES

In order to introduce the notation and to facilitate the analysis, we consider first the fields of a magnetic line source located in a concentric cylindrical cavity with uniform boundaries. The solution is cast in the form of a contour integral which is particularly suitable for treating the mixed-path problem by a factorization technique.

To be specific, we choose a cylindrical coordinate system (r, θ, z) with the z axis parallel to the cylindrical structure being considered. The inner and outer surfaces of the cavity are then defined by $r = a$ and $r = b$, respectively. A uniform magnetic line source of strength K is located within the cavity at $r = r_o$ and $\theta = 0$ where $a < r_o < b$. The direct or primary magnetic field at (r, θ) of the line source has only a z component H_z^p. For an implied time factor $\exp(i\omega t)$, it is given by

$$H_z^p = K H_o^{(2)}(kR) \qquad (1)$$

where $R = [r^2 + r_o^2 - 2 r r_o \cos\theta]^{\frac{1}{2}}$, $k = 2\pi/(\text{wavelength})$ and where $H_o^{(2)}$ is a Hankel function of the second kind of order zero.

NOTE - A longer version of this paper with complete mathematical details will be made available in the open literature.

We now construct an expression for the total field H_z within the cavity which behaves like (1) as $R \to 0$ and, at the same time, it satisfies appropriate boundary conditions on the cavity walls. In this connection, we assume that the tangential electric field E_θ is proportional to H_z at both walls. Thus,

$$E_\theta = -Z_1 H_z \quad \text{at} \quad r = a \qquad \text{and} \qquad E_\theta = Z_i H_z \quad \text{at} \quad r = b \tag{2}$$

where Z_1 and Z_i, by definition, are surface impedances. Because the fields do not vary in the z direction we know from Maxwell's equations that, within the cavity, $E_\theta = i\eta_o \partial H_z/\partial x$ where $x = kr$ and where $\eta_o = 120\pi$ ohms. Thus, the boundary conditions (2) are equivalent to

$$\partial H_z/\partial x = i\Delta_1 H_z\Big]_{x=ka} \quad \text{where } \Delta_1 = Z/\eta_o, \quad \text{and} \quad \partial H_z/\partial x = -i\Delta_i H_z\Big]_{x=kb} \quad \text{where } \Delta_i = Z_i/\eta_o .$$

The appropriate form of the solution, for $r < r_o$, is easily found to be

$$H_z = \frac{K}{2}\int_{-\infty}^{+\infty} \frac{\left[H_\nu^{(2)}(kr_o) + S_\nu H_\nu^{(1)}(kr_o)\right]\left[H_\nu^{(1)}(kr) + {}_1R_\nu H_\nu^{(2)}(kr)\right]}{\left[1 - {}_1R_\nu S_\nu\right]} e^{-i\nu\theta} \sum_q e^{-2\pi i q\nu}\, d\nu \tag{3}$$

where

$${}_1R_\nu = -\frac{H_\nu^{(1)\prime}(ka) - i\Delta_1 H_\nu^{(1)}(ka)}{H_\nu^{(2)\prime}(ka) - i\Delta_1 H_\nu^{(2)}(ka)} \tag{4}$$

and

$$S_\nu = -\frac{H_\nu^{(2)\prime}(kb) + i\Delta_i H_\nu^{(2)}(kb)}{H_\nu^{(1)\prime}(kb) + i\Delta_i H_\nu^{(1)}(kb)} . \tag{5}$$

[The primes over the Hankel function indicate differentiation with respect to the indicated argument.] The form of (3), valid for $r > r_o$, is obtained by merely exchanging r and r_o where they occur in (3).

3. RESIDUE SERIES FOR UNIFORM BOUNDARIES

While (3) is an exact solution for the cylindrical cavity with uniform walls, it is not useful for calculation. A more convenient form is obtained by deforming the contour about the singularities of the integrand. For the problem specified, these are poles at $\nu = \pm\nu_m$ where ν_m $(m = 1, 2, 3, \ldots)$ are the solutions of

$$1 - {}_1R_\nu S_\nu = 0 \tag{6}$$

which appear in the fourth quadrant of the complex ν plane. We retain only the contribution for $q = 0$. Thus, we obtain

$$H_z = \sum_m A_m e^{-i\nu_m\theta}\left[H_{\nu_m}^{(2)}(kr) + S_{\nu_m} H_{\nu_m}^{(1)}(kr)\right] \tag{7}$$

where

$$A_m = -\pi i K \frac{\left[H_{\nu_m}^{(2)}(kr_o) + S_{\nu_m}^{(1)}(kr_o)\right]{}_1R_{\nu_m}}{\left[1 - {}_1R_\nu S_{\nu_m}\right]'} , \tag{8}$$

where

$$\left[1 - {}_1R_{\nu_m} S_{\nu_m}\right]' = \left\{\frac{\partial}{\partial\nu}\left[1 - {}_1R_\nu S_\nu\right]\right\}_{\nu=\nu_m} .$$

The neglected terms (i.e., non-zero values of q) correspond to waves which have encircled the cylinder at least once.

4. FORMULATION FOR MIXED-PATH PROBLEM

We now turn out attention to the mixed-path problem depicted in Fig. 1a. Here, the surface impedance of the lower boundary at $r = a$ of the cylindrical cavity is sectionally uniform. For $\theta < \theta_o$, the surface impedance is Z_1 but, for $\theta > \theta_o$, the surface impedance is Z_2. On the other hand, the surface impedance at the upper boundary is Z_i and, as before, it is uniform for all θ.

For the posed mixed-path problem, we assume that the resultant magnetic field H_z' can be written

$$H_z' = H_z + \delta H_z \tag{9}$$

where H_z is the field for a fully uniform situation (i.e., $Z_2 = Z_1$) while δH_z is the modification resulting from the change of the surface impedance from Z_1 to Z_2 for $\theta > \theta_o$. From (3), we can readily deduce that

$$H_z\Big]_{r=a} = \frac{2K}{i\pi ka}\int_{-\infty}^{+\infty}\frac{\left[H_\nu^{(2)}(kr_o) + S_\nu H_\nu^{(1)}(kr_o)\right]e^{-i\nu\theta}}{\left[1 - {}_1R_\nu S_\nu\right]\left[H_\nu^{(2)\prime}(ka) - i\Delta_1 H_\nu^{(2)}(ka)\right]}\,d\nu \tag{10}$$

where the Wronskian relation

$$H_\nu^{(1)}(x)\,H_\nu^{(2)\prime}(x) - H_\nu^{(2)}(x)\,H_\nu^{(1)\prime}(x) = -4i/(\pi x) \tag{11}$$

has been used.

We now construct an integral representation for δH_z which, first of all, satisfies the required boundary condition at $r = b$. A suitable form for δH_z is

$$\delta H_z = \frac{2}{i\pi ka}\int_{-\infty}^{+\infty}\frac{\beta(\nu)\left[H_\nu^{(2)}(kr) + S_\nu H_\nu^{(1)}(kr)\right]}{\left[1 - {}_1R_\nu S_\nu\right]\left[H_\nu^{(2)\prime} - i\Delta_1 H_\nu^{(2)}\right]}\,e^{-i\nu(\theta-\theta_o)}\,d\nu \tag{12}$$

which certainly fulfills the condition

$$\left[\partial\,\delta H_z/\partial x = -i\Delta_i\,\delta H_z\right]_{x=kr=kb} . \tag{13}$$

The function $\beta(\nu)$ is yet to be determined and the other factors in (12) are introduced for later convenience. Also, for simplicity in (12) and in what follows, we use the following convention, for Hankel functions of argument ka,

$$H_\nu^{(1)(2)}(ka) = H_\nu^{(1)(2)} . \tag{14}$$

The boundary condition on the total field H_z' is now automatically satisfied at $r = b$ since both H_z and δH_z satisfy (13). The more difficult case is for the lower boundary at $r = a$. Here, we must have

$$\begin{aligned}\partial H_z'/\partial x &= i\Delta_1 H_z' \quad \text{for} \quad \theta < \theta_o \\ &= i\Delta_2 H_z' \quad \text{for} \quad \theta > \theta_o .\end{aligned} \tag{15}$$

But we know that

$$\partial H_z/\partial x = i\Delta_1 H_z \quad \text{for all } \theta . \tag{16}$$

Therefore, a compact statement for the boundary condition at $r = a$ is

$$\left[\left(\frac{\partial}{\partial x} - i\Delta_1\right)\delta H_z\right]_{x=ka} = 0 \quad \text{for } \theta < \theta_o \tag{17}$$

$$\left[\left(\frac{\partial}{\partial x} - i\Delta_2\right)\delta H_z\right]_{x=ka} = i(\Delta_2 - \Delta_1)\left[H_z\right]_{x=ka} \quad \text{for } \theta > \theta_o . \tag{18}$$

Using the integral representations (13) and (14), the boundary conditions in the form given by (17) and (18) readily yield

$$\int_{-\infty}^{+\infty}\beta(\nu)\,e^{-i\nu(\theta-\theta_o)}\,d\nu = 0 , \quad \text{for} \quad \theta < \theta_o \tag{19}$$

and

$$\int_{-\infty}^{+\infty}F(\nu)\,\beta(\nu)\,e^{-i\nu(\theta-\theta_o)}\,d\nu = i(\Delta_2 - \Delta_1)\int_{-\infty}^{+\infty}G(\hat{\nu})\,e^{-i\hat{\nu}\theta}\,d\hat{\nu} , \quad \text{for} \quad \theta > \theta_o , \tag{20}$$

where

$$F(\nu) = \frac{\left[1 - {}_2R_\nu S_\nu\right]}{\left[1 - {}_1R_\nu S_\nu\right]}\,\frac{\left[H_\nu^{(2)\prime} - i\Delta_2 H_\nu^{(2)}\right]}{\left[H_\nu^{(2)\prime} - i\Delta_1 H_\nu^{(2)}\right]} , \tag{21}$$

and

$$G(\nu) = \frac{H_\nu^{(2)}(kr_o) + S_\nu H_\nu^{(1)}(kr_o)}{\left[1 - {}_1R_\nu S_\nu\right]\left[H_\nu^{(2)\prime} - i\Delta_1 H_\nu^{(2)}\right]} . \tag{22}$$

In (21) and (22) above, ${}_1R_\nu$ and S_ν are defined by (4) and (5), respectively, while ${}_2R_\nu$, in (21) is defined by

$$2R_\nu = -\frac{H_\nu^{(1)\prime} - i\Delta_2 H_\nu^{(1)}}{H_\nu^{(2)\prime} - i\Delta_2 H_\nu^{(2)}} \tag{23}$$

where, in keeping with our convention, the arguments of the Hankel functions are ka unless otherwise indicated.

In order to reduce the dual integral equations (19) and (20) to simpler form, we introduce the integral representation

$$g(\nu) = \int_{-\infty}^{+\infty} g(\nu, \hat{\nu})\, d\hat{\nu} \tag{24}$$

and then assume that the order of integration may be inverted.

Then, (19) and (20) are equivalent to the pair

$$\int_{-\infty}^{+\infty} g(\nu, \hat{\nu})\, e^{-i\nu(\theta-\theta_o)}\, d\nu = 0 \qquad \text{for} \qquad \theta < \theta_o \tag{25}$$

and

$$\int_{-\infty}^{+\infty} F(\nu)\, g(\nu, \hat{\nu})\, e^{-i\nu(\theta-\theta_o)}\, d\nu = i(\Delta_2 - \Delta_1)\, G(\hat{\nu})\, e^{-i\hat{\nu}\theta} \qquad \text{for} \qquad \theta > \theta_o \quad . \tag{26}$$

5. SOLUTION BY FACTORIZATION METHOD

We now follow the standard Wiener-Hopf technique (e.g., Noble[1]) and obtain a solution for $g(\nu, \hat{\nu})$ by introducing the factorization

$$1/F(\nu) = M^+(\nu)\, N^-(\nu) \quad . \tag{27}$$

Here, the function $M^+(\nu)$ is regular except for poles in the finite part of the complex ν plane and has neither zeroes nor poles in the upper half plane. The function $N^-(\nu)$ is also regular except for poles in the finite part of the complex ν plane but it has neither zeroes nor poles in the lower half plane. Without difficulty, we can also show that $M^+(\nu)$ and $N^-(\nu)$ are bounded at infinity in the upper and lower half planes, respectively.

With the above conditions in mind, we can now write the formal solution as

$$g(\nu, \hat{\nu}) = -\frac{(\Delta_2 - \Delta_1)}{2\pi} e^{-i\hat{\nu}\theta_o}\, \frac{M^+(\nu)\, N^-(\hat{\nu})}{\nu - \hat{\nu}}\, G(\hat{\nu}) \tag{28}$$

under the provision that the contour of integration in (25) and (26) be indented above the pole at $\nu = \hat{\nu}$. This result for $g(\nu, \hat{\nu})$ is confirmed by closing the contour in (25) and (26) in the upper and lower half planes, respectively, and making use of Jordan's Lemma and Cauchy's theorem. Using (24), we see that

$$g(\nu) = -\frac{(\Delta_2 - \Delta_1)}{2\pi}\, M^+(\nu) \int_{-\infty}^{+\infty} \frac{N^-(\hat{\nu})}{\nu - \hat{\nu}}\, G(\hat{\nu})\, e^{-i\hat{\nu}\theta_o}\, d\hat{\nu} \quad , \tag{29}$$

where the integration is indented below the pole at $\nu = \hat{\nu}$. A series representation for $g(\nu)$ can be obtained by noting that since $\theta_o > 0$, the contour can be closed in the lower $\hat{\nu}$ half plane. Then contributions at the residues of the poles at $\hat{\nu} = \nu_m$ yield

$$g(\nu) = i(\Delta_2 - \Delta_1)\, M^+(\nu) \sum_m \frac{N^-(\nu_m)}{\nu - \nu_m}\, \frac{H_{\nu_m}^{(2)}(k r_o) + S_{\nu_m} H_{\nu_m}^{(1)}(k r_o)}{\left[1 - {}_1R_{\nu_m} S_{\nu_m}\right]\left[H_{\nu_m}^{(2)\prime} - i\Delta_1 H_{\nu_m}^{(2)}\right]}\, e^{-i\nu_m\theta_o} \quad . \tag{30}$$

When this result is inserted into (12) we have a solution for ${}^sH_z$.

By making use of (27), we obtain the following explicit result:

$${}^sH_z = \frac{2K(\Delta_2 - \Delta_1)}{\pi ka} \sum_m \int_{-\infty}^{+\infty} \frac{N^-(\nu_m)}{N^-(\nu)}\, \frac{\left[H_\nu^{(2)}(kr) + S_\nu H_\nu^{(1)}(kr)\right]}{\left[1 - {}_2R_\nu S_\nu\right](\nu - \nu_m)} \times$$

$$\times \frac{\left[H_{\nu_m}^{(2)}(k r_o) + S_{\nu_m} H_{\nu_m}^{(1)}(k r_o)\right]}{\left[1 - {}_1R_{\nu_m} S_{\nu_m}\right]'\left[H_{\nu}^{(2)\prime} - i\Delta_2 H_{\nu}^{(2)}\right]\left[H_{\nu_m}^{(2)\prime} - i\Delta_1 H_{\nu_m}^{(2)}\right]} e^{-i\nu(\theta-\theta_o)} e^{-i\nu_m\theta_o} d\nu \quad . \tag{31}$$

6. REDUCTION OF THE SOLUTION

The integral solution written in the form given by (31) is particularly convenient for evaluating the field when $\theta > \theta_o$. In this case, we close the contour in the lower half plane and sum the residues at the poles. There are two sets of these. First of all, we have the pole at $\nu = \nu_m$. The residue contribution from this set (summed over m) is identical to $-H_z$ where H_z is given by (7). To establish this equivalence, we use the following easily proved relation:

$$\left[\left(1 - {}_2R_\nu S_\nu\right)\left(H_\nu^{(2)\prime} - i\Delta_2 H_\nu^{(2)}\right)\right]_{\nu=\nu_m} = -\frac{4}{\pi k a}\frac{(\Delta_2 - \Delta_1)}{{}_1R_{\nu_m}}\frac{1}{H_{\nu_m}^{(2)\prime} - i\Delta_1 H_{\nu_m}^{(2)}} \quad . \tag{32}$$

Here, we have made repeated use of the definition of ${}_1R_\nu$ given by (4) and the pole condition ${}_1R_{\nu_m} S_{\nu_m} = 1$.

In view of the preceding development, we find that the sum of the residues at the second set of poles at $\nu = \mu_n$ yield directly the expression for $H_z + \delta H_z$ or H_z'. Thus, after some reordering of the terms we find that, for $\theta > \theta_o$,

$$H_z' = \sum_m A_m e^{-i\nu_m\theta_o} \sum_n T_{n,m} e^{-i\mu_n(\theta-\theta_o)}\left[H_{\mu_n}^{(2)}(k r) + S_{\mu_n} H_{\mu_n}^{(1)}(k r)\right] \tag{33}$$

where A_m is given by (8), and

$$T_{n,m} = i(\Delta_1 - \Delta_2)\frac{\nu_m + \mu_n}{\nu_m^2 - \mu_n^2}\frac{N^-(\nu_m)}{N^-(\mu_n)}\frac{H_{\nu_m}^{(2)} + S_{\nu_m} H_{\nu_m}^{(1)}}{\left[1 - {}_2R_{\mu_n} S_{\mu_n}\right]'\left[H_{\mu_n}^{(2)\prime} - i\Delta_2 H_{\mu_n}^{(2)}\right]} \tag{34}$$

where

$$\left[1 - {}_2R_{\mu_n} S_{\mu_n}\right]' = \frac{\partial}{\partial\nu}\left[1 - {}_2R_\nu S_\nu\right]_{\nu=\mu_n} \tag{35}$$

and μ_n are solutions of

$$1 - {}_2R_\nu S_\nu = 0$$

in the lower half ν plane.

In order to discuss the result for (34), we define the wave function $Z_\nu(k r)$ by

$$Z_\nu(k r) = H_\nu^{(2)}(k r) + S_\nu H_\nu^{(1)}(k r) \quad , \tag{36}$$

which also holds for $\nu = \nu_m$ and $\nu = \mu_n$. Then, we can write (34) in the fully equivalent form

$$T_{n,m} = i\frac{\nu_m + \mu_n}{\nu_m^2 - \mu_n^2}\frac{N^-(\nu_m)}{N^-(\mu_n)}\frac{(\Delta_1 - \Delta_2) Z_{\nu_m}(k a)}{\left\{\frac{\partial}{\partial\nu}\left[Z_\nu'(k a) - i\Delta_2 Z_\nu(k a)\right]\right\}_{\nu=\mu_n}} \quad . \tag{37}$$

The physical interpretation of (33) is that modes of order m incident on the coast line at $\theta = \theta_o$ are converted to modes of order n. Thus, $T_{n,m}$ is a mode conversion coefficient.† In fact, it may be shown that

$$T_{n,m} = Q_{n,m}\hat{T}_{n,m} \tag{38}$$

† In order to obtain an expression for the secondary field δH_z scattered back toward the source, we would return to the contour integral representation (12). For $\theta < \theta_o$, we would close the contour in the upper half plane and then sum the residues at the enclosed poles at $\nu = -\nu_p$.

where
$$\hat{T}_{n,m} = i \frac{2\mu_n}{\nu_m^2 - \mu_n^2} \frac{(\Delta_1 - \Delta_2) Z_{\nu_m}(ka)}{\left\{ \frac{\partial}{\partial \nu} \left[Z'_\nu(ka) - i \Delta_2 Z_\nu(ka) \right] \right\}_{\nu = \mu_n}} , \tag{39}$$

where
$$Q_{n,m} = \frac{\nu_m + \mu_n}{2\mu_n} \frac{N^-(\nu_m)}{N^-(\mu_n)} = \frac{\nu_m + \mu_n}{2\mu_n} \frac{\left(1 + \frac{\nu_m}{\nu_s}\right)\left(1 + \frac{\mu_n}{\mu_s}\right)}{\left(1 + \frac{\nu_m}{\mu_s}\right)\left(1 + \frac{\mu_n}{\nu_s}\right)} . \tag{40}$$

Here, we have made use of the infinite product theorem in order to decompose $N^-(\nu_m)$ and $N^-(\mu_n)$. The function $Q_{n,m}$ can be approximated by unity in many cases of practical interest. In fact, this corresponds physically to using a Kirchhoff approach in order to estimate the forward mode conversion at the land/sea boundary.

7. AIRY FUNCTION FORM OF THE SOLUTIONS

The solutions obtained here for the fields of the magnetic line source in the cylindrical cavity can be cast in a form suitable for numerical work if the Airy function representations for the Hankel functions are employed. These may be written as follows:

$$H_\nu^{(1)}(x) \cong -(i/\pi^{\frac{1}{2}})(2/x)^{\frac{1}{3}} w_2(\tau) , \tag{41}$$

$$H_\nu^{(2)}(x) \cong (i/\pi^{\frac{1}{2}})(2/x)^{\frac{1}{3}} w_1(\tau) , \tag{42}$$

where $\tau = (\nu - x)(2/x)^{\frac{1}{3}}$ and $w_1(\tau)$ and $w_2(\tau)$ are Airy functions.† These representations are valid provided $x \gg 1$ and $|\nu - x| \ll x^{2/3}$ which means that the low-order modes of greatest physical interest are adequately described. Also, to within the same approximation, the derivatives of the Hankel functions may be approximated by the derivatives of the Airy functions. Thus,

$$H_\nu^{(1)'}(x) \cong (i/\pi^{\frac{1}{2}})(2/x)^{2/3} w_2'(\tau) , \tag{43}$$

$$H_\nu^{(2)'}(x) \cong -(i/\pi^{\frac{1}{2}})(2/x)^{2/3} w_1'(\tau) . \tag{44}$$

We are now in the position to express the final result for H'_z or $H_z + \delta H_z$ in a form which is familiar in the development of VLF propagation theory for the earth-ionosphere waveguide. Thus, we write for the uniform waveguide

$$H_z = H_z^\infty W \tag{45}$$

and for the non-uniform waveguide

$$H'_z = H_z^\infty W' \tag{46}$$

where
$$H_z^\infty = 2K H_o^{(2)}[ka\theta] \simeq 2K \left(\frac{2i}{\pi ka\theta} \right)^{\frac{1}{2}} e^{-ika\theta} . \tag{47}$$

Here, H_z^∞ is a reference field which is numerically equal to the field of the magnetic line source of strength K located on the surface of a flat perfect conductor at a linear distance $ka\theta$. Then, if the fields are normalized in this manner, W and W' are the "attenuation functions" which are applicable to the earth-ionosphere waveguide in spherical geometry[15].

In order to proceed, we introduce some of the appropriate naturalized parameters such as $x_o = (ka/2)^{\frac{1}{3}} \theta_o$, $x = (ka/2)^{\frac{1}{3}} \theta$, $y_o = [2/(ka)]^{\frac{1}{2}} k(b-a)$, $y = [2/(ka)]^{\frac{1}{2}} k(r-a)$, $\hat{y} = [2/(ka)]^{\frac{1}{2}} k(r_o - a)$, $q_1 = -i(ka/2)^{\frac{1}{3}} \Delta_1$, $q_2 = -i(ka/2)^{\frac{1}{3}} \Delta_2$ and $q_i = -i(ka/2)^{\frac{1}{3}} \Delta_i$. The meaning of these parameters is illustrated in Fig. 1b.

Omitting numerous details of a straightforward nature, we can write down the expressions of the attenuation functions mentioned above.

$$W \cong \frac{2}{y_o} (\pi x)^{\frac{1}{2}} e^{-i\pi/4} \sum_{m = 1, 2, 3, \ldots} A_m^{(1)} \exp(-i x t_m^{(1)}) G_m^{(1)}(\hat{y}) G_m^{(1)}(y) \tag{48}$$

and for $\theta > \theta_o$,

$$W' \cong \frac{2}{y_o} (\pi x)^{\frac{1}{2}} e^{-i\pi/4} \sum_m (A_m^{(1)})^{\frac{1}{2}} \exp(-i x t_m^{(1)}) G_m^{(1)}(\hat{y}) ,$$

† These are related to the more conventional Airy functions defined by Miller[16] as follows:

$$w_{1,2}(\tau) = \pi^{\frac{1}{2}} [Bi(\tau) \pm i Ai(\tau)] .$$

$$\times \sum_n \hat{S}_{n,m} \exp\left[-i(x-x_o)\, t_n^{(2)}\right] \left(\Lambda_n^{(2)}\right)^{\frac{1}{2}} G_n^{(2)}(y) \quad , \tag{49}$$

where

$$\hat{S}_{n,m} = \frac{2}{y_o}\left[\Lambda_m^{(1)}\, \Lambda_n^{(2)}\right]^{-\frac{1}{2}} \frac{q_1 - q_2}{t_m^{(1)} - t_n^{(2)}}\, Q_{n,m} \quad . \tag{50}$$

Here, $t_m^{(1)}$ and $t_n^{(2)}$ are solutions of the mode equations

$$A(\tau)\, B^{(1)}(\tau) = 1 \quad , \tag{51}$$

and

$$A(\tau)\, B^{(2)}(\tau) = 1 \quad , \tag{52}$$

respectively. Here,

$$A(\tau) = -\left[\frac{w_1'(\tau - y_o) + q_i\, w_1(\tau - y_o)}{w_2'(\tau - y_o) + q_i\, w_2(\tau - y_o)}\right] \tag{53}$$

and

$$B^{(1,2)}(\tau) = -\left[\frac{w_1'(\tau) - q_{1,2}\, w_2(\tau)}{w_1'(\tau) - q_{1,2}\, w_1(\tau)}\right] \quad . \tag{54}$$

We also note that in terms of the previous notation,

$$\nu_m \cong ka + (ka/2)^{\frac{1}{3}}\, t_m^{(1)} \tag{55}$$

and

$$\mu_n \cong ka + (ka/2)^{\frac{1}{3}}\, t_n^{(2)} \quad . \tag{56}$$

The "excitation functions" occurring in (48), (49), and (50) are defined as follows:

$$\Lambda_m^{(1)} = y_o\left[2\, f\left(t_m^{(1)},\, q_1\right)\right]^{-1} \quad , \tag{57}$$

$$\Lambda_n^{(2)} = y_o\left[2\, f\left(t_n^{(2)},\, q_2\right)\right]^{-1} \quad , \tag{58}$$

where

$$f(t,q) = t - q^2 - \frac{(t - y_o - q_i^2)\left[w_1'(t) - q\, w_2(t)\right]^2}{\left[w_2'(t - y_o) + q_i\, w_2(t - y_o)\right]^2} \quad . \tag{59}$$

Also, the "height-gain" functions occurring above are defined by

$$G_m^{(1)}(y) = \frac{w_1\left(t_m^{(1)} - y\right) + A\left(t_m^{(1)}\right) w_2\left(t_m^{(1)} - y\right)}{w_1\left(t_m^{(1)}\right) + A\left(t_m^{(1)}\right) w_2\left(t_m^{(1)}\right)} \tag{60}$$

and

$$G_n^{(2)}(y) = \frac{w_1\left(t_n^{(2)} - y\right) + A\left(t_n^{(2)}\right) w_2\left(t_n^{(2)} - y\right)}{w_1\left(t_n^{(2)}\right) + A\left(t_n^{(2)}\right) w_2\left(t_n^{(2)}\right)} \tag{61}$$

8. AN ILLUSTRATIVE EXAMPLE

A key parameter in this study is the mode conversion coefficient defined by (50). It involves the infinite product function $Q_{n,m}$ given by (40). In the discussion which follows, we can set $Q_{n,m}$ equal to unity.

In order to discuss a concrete example, we consider transmission at a frequency of 20 kHz from a land surface (with a conductivity $\sigma_1 = 10^{-2}$, 10^{-3} or 10^{-4} mhos/meter and a relative dielectric constant $K_1 = 15$) to a sea surface (with a conductivity $\sigma_2 = 4$ mhos/meter and a relative dielectric constant $K_2 = 80$). The ionosphere conductivity parameter $\omega_r = 2 \times 10^5$ and the reflecting height $h = b - a = 70$ km are representative of daytime conditions.[15] Numerical values of the attenuation rates, phase velocities and excitation factors along with the conversion coefficients are given in an earlier report.[17] Here, we will merely indicate a sample of the results in graphical form.

The magnitude of the conversion coefficient $\hat{S}_{n,m}$ is plotted in Fig. 2 for a typical case. Not surprisingly, the conversion coefficient becomes more marked as the conductivity contrast between land and sea is increased. The corresponding frequency dependence of the conversion coefficient is illustrated in Fig. 3 for a fixed set of the parameters. From this, it appears that the mode conversion is generally stronger for the higher frequencies.

9. FINAL REMARKS

In our discussions, we have been considering explicitly a two-section path. However, in principle, there is no difficulty in extending the present theory to a multi-section path. For example, we might consider the four-section path depicted in Fig. 4 which is a generalization of the situation shown in Fig. 1b. The surface impedance parameters are q_1, q_2, q_3, and q_4 as indicated, while the distances of the three boundaries from terminal A are described by the parameters x_1, x_2, and x_3. On the assumption that all reflections can be neglected, the two-section solution may be applied in succession to each separation boundary. Thus, without difficulty, we find that the resultant attenuation function at terminal B is given by

$$W' = \frac{2(\pi x)^{\frac{1}{2}}}{y_o} e^{-i\pi/4} \sum_m \left(\Lambda_m^{(1)}\right)^{\frac{1}{2}} G_m^{(1)}(y_a) \exp\left(-i x_1 t_m^{(1)}\right) \sum_n \hat{S}_{n,m}^{(1)} \exp\left[-i(x_2 - x_1) t_n^{(2)}\right]$$

$$\times \sum_p \hat{S}_{p,n}^{(2)} \exp\left[-i(x_3 - x_2) t_p^{(3)}\right] \sum_q \hat{S}_{q,p}^{(3)} \exp\left[-i(x - x_3) t_q^{(4)}\right] \left(\Lambda_q^{(4)}\right)^{\frac{1}{2}} G_q^{(4)}(y) \quad , \tag{62}$$

which is an obvious generalization of (49). Here, $\hat{S}_{n,m}^{(j)}$, for $j = 1, 2, 3$, is the mode conversion coefficient for the jth separation boundary and is given by

$$\hat{S}_{n,m}^{(j)} = \frac{q_j - q_{j+1}}{\left[f\left(t_m^{(j)}, q_j\right) f\left(t_n^{(j+1)}, q_{j+1}\right)\right]^{\frac{1}{2}} \left(t_m^{(j)} - t_n^{(j+1)}\right)} \quad , \tag{63}$$

where $f(t, q)$ is defined by (59).

A mixed path of any number of sections can be treated by cascading the two-section results in the manner indicated above. The summations in (62) may each be truncated after only a few terms if the distance increments x_1, $x_2 - x_1$, $x_3 - x_2$, and $x - x_3$ are all of the order of one or larger. Thus, the method works well when the individual sections are not too short.

The ionospheric model we have chosen is very rudimentary. While it is adequate for the present purpose, we call attention to recent VLF mode calculations for homogeneous earth but with very realistic D-region profiles [e.g., Galejs[18]]. It is believed that such model calculations can be readily extended to include land/sea boundary effects using the method in the present paper.

10. REFERENCES

1. B. Noble, "The Wiener-Hopf Technique," Pergamon Press, New York, 1968.
2. L. A. Weinstein, "The Theory of Diffraction and the Factorization Method," Golem Press, Boulder, Colo., 1969.
3. A. E. Heins and H. Feshbach, "The coupling of two acoustical ducts," J. Math. Phys. 26, pp. 143-155 1947.
4. A. E. Heins, "Water waves over a channel of finite depth with a dock," Amer. J. Math. 70, pp. 730-748, 1948.
5. J. B. Keller and M. Weitz, "Reflection and transmission coefficients for waves entering or leaving an ice field," Commun. Pure Appl. Math. 6 (3), pp. 415-417, 1953.
6. T. B. A. Senior, "Diffraction by a semi-infinite metallic sheet," Proc. Roy. Soc. A213, pp. 436-458, 1952.
7. P. C. Clemmow, "Radio propagation over a flat earth across a boundary separating two different media," Phil. Trans. Roy. Soc. (London) A246 (905), pp. 1-55, 1953.
8. J. Bazer and S. N. Karp, "Propagation of electromagnetic waves past a shore line," J. Res. NBS 66D (3), pp. 319-333, 1962.
9. J. R. Thompson, "Radio propagation over a sectionally homogeneous surface," Proc. Roy. Soc. A267 (1329, pp. 183-196, 8 May 1962.
10. D. C. Chang, "Propagation along a mixed path in the curved earth-ionosphere waveguide," Radio Sci. 4 (4), pp. 335-345, 1969.
11. E. L. Feinberg, "Propagation of radio waves along an inhomogeneous surface," Nuovo Cimento, Ser. X 11 (Supplement), pp. 60-91, 1959.
12. J. R. Wait, "Electromagnetic surface waves," in Advances in Radio Research (ed. J. A. Saxton) 1, pp. 157-217, Academic Press, London, 1964.

13. J. R. Wait, "Influence of an inhomogeneous ground on the propagation of VLF radio waves in the earth-ionosphere waveguide," Radio Sci. J. Res. NBS 69D (7), pp. 969-975, 1965.

14. J. R. Wait, "On mode conversion of VLF radio waves at a land-sea boundary," IEEE Trans. AP-17 (2), pp. 216-220, 1969.

15. J. R. Wait, "Recent theoretical advances in the terrestrial propagation of VLF electromagnetic waves, in Advances in Electronics and Electron Physics (ed. L. Marton) 25, pp. 145-209, Academic Press, New York and London, 1968.

16. J. C. P. Miller, "The Airy Integral," Cambridge University Press Cambridge, 1946.

17. J. R. Wait and K. P. Spies, "VLF mode calculations for propagation across a land/sea boundary in the earth-ionosphere waveguide," ESSA Technical Report ERL 87-OD 2, Sept. 1968.

18. J. Galejs, "Propagation of ELF and VLF waves below a generally anisotropic ionosphere," Radio Sci. 3 (8), pp. 781-786, 1968.

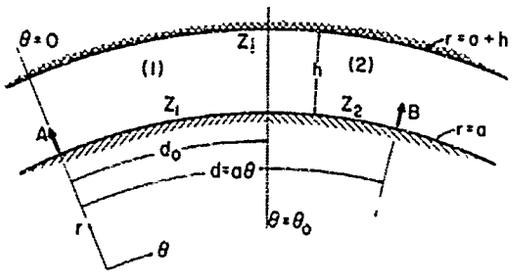

Fig. 1(a) The model of the earth-ionosphere waveguide illustrating the physical parameters

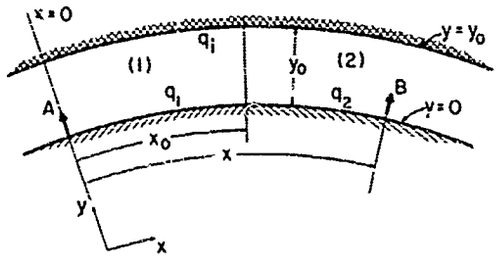

Fig 1(b) The model of the earth-ionosphere waveguide illustrating the "natural" parameters

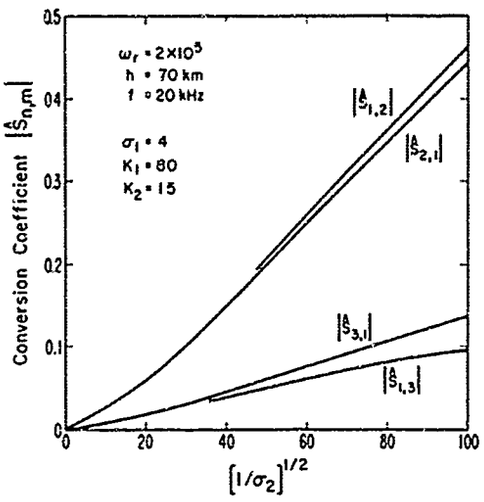

Fig. 2 Conversion coefficient as a function of the land conductivity σ_2

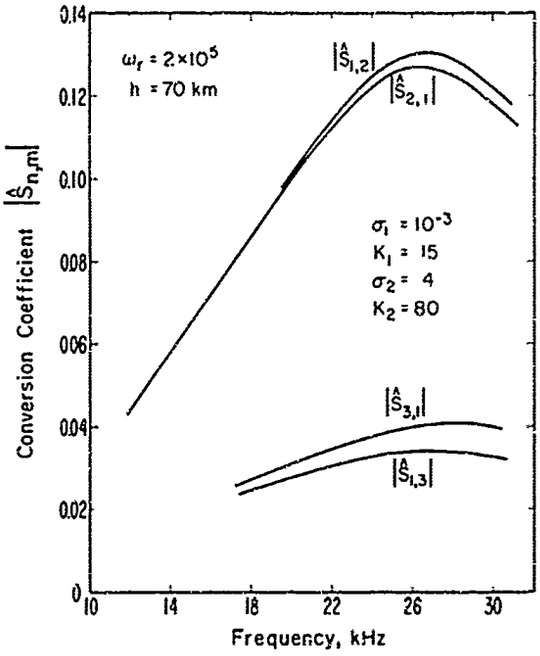

Fig. 3 Conversion coefficient as a function of frequency

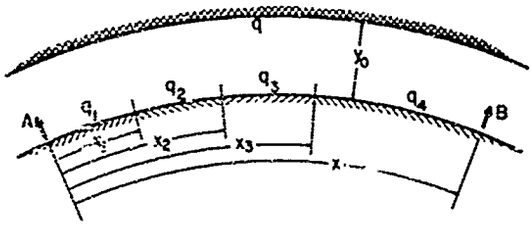

Fig. 4 Multi-section path in the earth-ionosphere waveguide

PROPAGATION OF ACOUSTIC OR ELECTROMAGNETIC WAVES IN AN INHOMOGENEOUS SEA-TYPE MEDIUM WITH ROUGH FRONTIERS

by

Marie France VERHAEGHE and Armand WIRGIN
Groupe d'Etudes sur la Diffraction I.O.- E.S.E.
Institut d'Optique, 3 Bd. Pasteur, 75 - PARIS 15e, France

SOMMAIRE

Cet exposé traite de la propagation des ondes acoustiques ou électromagnétiques à travers la mer. Cette dernière est considérée comme un milieu conducteur d'ondes, de contenu non homogène, aux frontières non lisses et non opaques. La paroi supérieure est constituée par la surface de séparation entre l'air et l'eau considérée comme un plan auquel est superposée une perturbation ondulée stationnaire créée par les courants aériens et marins. La paroi inférieure est également un plan auquel est superposée une perturbation appropriée destinée à simuler l'inégalité de la croûte terrestre. On tient compte de l'inhomogénéité de la mer en utilisant une stratification verticale comportant un certain nombre de couches homogènes séparées par des surfaces intermédiaires planes.

On étudie l'interaction du champ d'onde avec chaque surface intermédiaire en faisant appel à l'approximation physique optique qui est valable pour les aspérités à faible pente.

Les résultats numériques relatifs à l'étendue des effets de diffraction sont donnés pour le cas d'une onde d'espace incidente et d'un modèle marin consistant en un milieu conducteur d'ondes de contenu homogène et aux parois comportant des aspérités de place en place.

PROPAGATION OF ACOUSTIC OR ELECTROMAGNETIC WAVES IN AN INHOMOGENEOUS SEA-TYPE MEDIUM WITH ROUGH FRONTIERS

Marie France Verhaeghe and Armand Wirgin

Groupe d'Etudes sur la Diffraction I.O.-E.S.E.
Institut d'Optique , 3 Bd. Pasteur , 75-Paris 15e, France

SUMMARY

This paper concerns the propagation of acoustic or electromagnetic waves in the sea. The latter is considered as an inhomogeneously-filled waveguide with rough non-opaque frontiers. The top waveguide wall is the air-water interface considered to be a plane surface on which is superimposed a stationary wavy perturbation due to air and sea currents. The bottom wall is also a plane surface with an appropriate perturbation designed to simulate the uneveness of the earth's crust. The inhomogeneity of the sea is taken into account by considering the waveguide to be filled with a number of horizontal piecewise homogeneous layers separated by flat or perturbed interfaces which are mutually parallel to each other in the mean. A homogeneous plane wave propagates towards the sea in the air which is considered as a homogeneous medium extending upwards towards infinity. Similarly, the earth's crust is treated as a homogeneous medium extending downwards toward infinity. The interaction of the wave field at each interface is examined by a perturbation method based on the assumptions that the spatial frequency spectrum of the interface profiles have a high spatial frequency cutoff and that the smallest spatial period of the interface profiles is large compared to the wavelength in air of the incident monochromatic wave. Numerical results pertaining to the extent of diffraction effects are given for a model of the sea consisting of a homogeneously-filled waveguide with periodically rough walls.

1. INTRODUCTION

Among the many factors which can affect the propagation of acoustic or electromagnetic waves in or above the sea are the sea surface and bottom roughnesses and the temperature-pressure-salinity inhomogeneity of the water. Wait (1) and others have already treated the problem of propagation in and above an inhomogeneous medium which is considered as being composed of a number of horizontal piecewise homogeneous layers separated by flat mutually parallel interfaces. On the other hand, Beckmann (2) and others have treated the problem of the propagation of waves in the presence of one rough interface separating two homogeneous media. However, the Wait model does not account for interface roughness and the Beckmann model neglects either the top or bottom rough interface and the effects of inhomogeneities of the media.

The theoretical considerations which follow offer the first opportunity to study the interaction of an acoustic or electromagnetic wave field with a rather complete model of the sea which takes into account interface roughnesses as well as inhomogeneities in the water medium.

2. PHYSICAL MODEL

The air, the water, and the earth's crust are considered to be linear, isotropic, time-invariant media describable by a set of scalar physical constants which are the complex indices of refraction, the electrical parameters σ, ϵ, μ (electromagnetic case) and/or the densities ρ (acoustic case). The air and earth's crust are homogeneous media of infinite extent in the horizontal (XOY) plane and of half-infinite extent in the vertical (Z) direction. (Fig. 1) The complex indices of refraction of these two media are denoted by N_1 and N_{L+1} respectively; these parameters, as well as the other pertinent electrical of acoustical parameters for the two media in question, are independent of the x,y or z coordinates. The sea is considered to be composed of a number (L- 1) of piecwise homogeneous horizontal layers whose complex indices of refraction $N_2, N_3, \ldots, N_L$ and other pertinent electrical or acoustical parameters are independent of x,y and z. The interfaces of this structure are infinite cylindrical surfaces whose generators are parallel to the y axis and whose generating curves $C_k(x,z)$, $k=1,2,\ldots,L$ are described by the equations

$$2.1 \quad C_k(x,z): \quad z=f_k(x) \qquad \forall x \ , \ k=1,2,\ldots,L$$

with $f_1,\ldots,f_L$ single-valued continuous fuctions of x for all x. In addition, the interfaces are, on the average, flat mutually parallel horizontal planes which means $z=(f_k(x))_{avg}$ describe a set of planes parallel to the XOY plane (Fig. 2).

A plane homogeneous monochromatic wave propagates in air towards the sea such that its propagation vector $\vec{K}_0$ lies in the XOZ plane. In view of the linear, homogeneous, isotropic nature of the media, and in view of the geometry of the interfaces and of the plane incident wave, the total wave field possesses cylindrical symmetry, with y the ignorable coordinate.

3. STATEMENT OF THE BOUNDARY-VALUE PROBLEM

Consider a monochromatic wave field which we shall designate by the vector $\vec{\mathcal{F}}(x,z,t)$ in the electromagnetic case and by the scalar $\mathcal{F}(x,z,t)$ in the acoustic case. We shall assume that the temporal variation of this field is of the form $\exp -i\omega t$ with ω the angular frequency. Let $\vec{F}(x,z)$ and $F(x,z)$ denote the spatial parts of $\vec{\mathcal{F}}$ and $\mathcal{F}$ respectively; in the electromagnetic case, $\vec{F}$ will represent either the transverse electric (TE) field

$$3.1 \qquad \vec{F}(x,z) = \vec{E}(x,z) = (0, U(x,z), 0)$$

or the transverse magnetic (TM) field

$$3.2 \qquad \vec{F}(x,z) = \vec{H}(x,z) = (0, U(x,z), 0)$$

whereas in the acoustic case, F will represent the product of the density $\rho(x,z)$ and the velocity potential ψ

$$3.3 \qquad F(x,z) = U(x,z) = \rho(x,z)\psi(x,z)$$

The incident field is described by

$$3.4 \qquad U_0(x,z) = \exp i k_1 (x \sin\theta_0 - z\cos\theta_0) \quad ; \quad |\theta_0| < \pi/2$$

where

$$3.5 \qquad k_1 = 2\pi/\lambda$$

is the wavenumber in air, λ the wavelength in air, and θ_0 the angle of incidence in the XOZ plane measured from the positive z axis.

We shall identify u(x,z) with the functions $u_1, u_2, \ldots, u_{L+1}$ in the plane domains $S_1, S_2, \ldots, S_{L+1}$ defined by:

$$3.6 \qquad S_k(x,z): \begin{cases} z > f_1(x) & ; \ k = 1 \\ f_{k-1}(x) > z > f_k(x) & ; \ k = 2,3,\ldots,L \\ f_L(x) > z & ; \ k = L+1 \end{cases} \quad ; \ \forall x$$

The integer k is equal to 1 in air, 2 in the first water layer, 3 in the second water layer,...., L in the last water layer, and L+1 in the earth's crust, whereas $f_k, k=1,2,\ldots,L$ are the successive interface profile functions and u_k the total wave field in the k-th medium.

The physics of the boundary value problem is embodied in the following partial differential equations and constraints which permit the unique determination of u_k, $k=1,2,\ldots,L+1$:

$$3.7 \qquad U_k, \nabla U_k, \Delta U_k \quad \text{continuous for} \quad (x,z) \in S_k \ , \ k = 1,2,\ldots,L+1$$

$$3.8 \qquad (\Delta + k_k^2) U_k(x,z) = 0 \qquad (x,z) \in S_k \ , \ k = 1,2,\ldots,L+1$$

$$3.9 \qquad k_k^2 = \omega^2 \mu_k \epsilon_k + i\omega\mu_k\sigma_k \ , \quad \mu_k, \epsilon_k, \sigma_k \ \text{constant in } S_k$$

$$3.10 \qquad U_k(x,f_k) - U_{k+1}(x,f_k) = 0$$

$$3.11 \qquad \alpha_k D_k U_k(x,f_k) - \alpha_{k+1} D_k U_{k+1}(x,f_k) = 0 \qquad \Big\} \ k = 1,2,\ldots,L$$

where

$$\alpha_k = \begin{cases} \rho_k^{-1} & \text{acoustic case} \quad (\rho_k = \text{density} = \text{constant in } S_k) \\ \mu_k^{-1} & \text{TE case} \quad (\mu_k = \text{magnetic permeability} = \text{constant in } S_k) \\ \mu_k k_k^{-2} & \text{TM case} \end{cases}$$

$$D_k = \dot{f}_k \partial_x - \partial_z \ , \quad \dot{f}_k = \frac{df_k(x)}{dx}$$

$$3.12 \qquad \exists \ A = \text{constant such that}$$

$$(\partial_r - ik_1)[U_1(x,z) - U_0(x,z) - AU_0(x,-z)] = o(r^{-1/2}) \quad ; \quad r = \sqrt{x^2+z^2} \to \infty$$

$$3.13 \qquad (\partial_r - ik_k) U_k(x,z) = o(r^{-1/2}) \quad ; \quad r \to \infty \ , \ k = 2,3,\ldots,L+1$$

4. GREEN'S FUNCTION FIELD REPRESENTATIONS

It has been shown elsewhere (3) that the field can be rigorously represented by the following expression

$$4.1 \quad U_K(x',z') = \gamma_K U_0(x',z') - U_K \int_{-\infty}^{\infty} K_{K,K,K-1}(x',z';x,f_{K-1}) U_K(x,f_{K-1})\,dx + \\ + U_K \int_{-\infty}^{\infty} K_{K,K,K}(x',z';x,f_K) U_K(x,f_K)\,dx \qquad ; \begin{matrix}(x',z')\in S_K \\ K=1,2,3,\ldots,L+1\end{matrix}$$

where

$$4.2 \quad \begin{matrix}\gamma_K = \delta_{K,1} \\ U_K = 1-\delta_{K,1} \\ \nu_K = 1-\delta_{K,L+1}\end{matrix} \qquad (\delta_{ij} = \text{Kronecker delta}),$$

K_{lmn} is the operator

$$4.3 \quad K_{lmn}(x',z';x,z) = G_l(x'-x,z'-z)\frac{\alpha_m}{\alpha_l} D_n - D_n G_l(x'-x,z'-z) \;,$$

and G_1 is the Green's function

$$4.4 \quad G_l(x'-x,z'-z) = \frac{i}{4} H_0^{(1)}[k_l(x'-x,z'-z)] \qquad (H_0^{(1)} = \text{Hankel function}) .$$

In (3) it was also shown that the $2L$ unknown functions

$$4.5 \quad \begin{matrix}U_K(x) \equiv U_K(x,f_K(x)) \\ V_K(x) \equiv D_K U_K(x,f_K(x))\end{matrix} \qquad ; K=1,2,\ldots,L$$

are solutions of one of four sets of $2L$ coupled integral or integrodifferential equations. Straightforward numerical techniques can be employed (4) (at least in the case of periodic interface profile functions) to solve these equations but such an approach is both costly and cumbersome (in addition to being difficult to generalize to aperiodic interface profile functions). The approach that will be used here is to search for approximate solutions to the integral equations by means of a perturbation technique.

5. PLANE WAVE FIELD REPRESENTATIONS

By replacing G_1 in 4.1 by its plane wave integral representation

$$5.1 \quad G_l(x'-x,z'-z) = \frac{i}{4\pi}\int_{-\infty}^{\infty} \exp i k_l[s(x'-x) + \sqrt{1-s^2}\,|z'-z|]\,\frac{ds}{\sqrt{1-s^2}} \;,$$

it can be shown that, within the domains S_k' defined as follows:

$$5.2 \quad S_K' : \begin{cases} z > (f_1)_{MAX} & ; K=1 \\ (f_{K-1})_{MIN} > z > (f_K)_{MAX} & ; K=2,3,\ldots,L \\ (f_L)_{MIN} > z & ; K=L+1 \end{cases} \qquad \forall x \;,$$

the field can be expressed by

$$5.3 \quad U_K(x',z') = \gamma_K U_0(x',z') + \nu_K \int_{-\infty}^{\infty} R^K(s)\exp i k_K[\sigma_K(s)x + W_K(s)z]\,ds + \\ + U_K \int_{-\infty}^{\infty} T^K(s)\exp i k_K[\sigma_K(s)x - W_K(s)z]\,ds \qquad ; \begin{matrix}(x',z')\in S_K' \\ K=1,2,\ldots,L+1\end{matrix}$$

where

$$5.4 \quad \sigma_K(s) = k_1 k_K^{-1} s$$

$$5.5 \quad W_K(s) = +\sqrt{1-\sigma_K^2(s)}$$

and

$$5.6 \quad \begin{Bmatrix} R^K(s) \\ T^K(s)\end{Bmatrix} = \begin{Bmatrix}+\\-\end{Bmatrix}\frac{ik_1}{4\pi k_K W_K(s)}\int_{-\infty}^{\infty}\left\{\begin{matrix}[V_K(x) + ik_K(\sigma_K(s)f_K' - W_K(s))U_K(x)] \\ [\frac{\alpha_{K-1}}{\alpha_K}V_{K-1}(x) + ik_K(\sigma_K(s)f_{K-1}' + W_K(s))U_{K-1}(x)]\end{matrix}\right\} e^{-ik_K[\sigma_K(s)x + W_K(s)\begin{Bmatrix} f_K \\ -f_{K-1}\end{Bmatrix}]}\,dx$$

$R^K(s)$ and $T^K(s)$ are the amplitudes of the reflected and transmitted plane waves in the domain S_K'; these reduce, in the case in which all the interfaces are flat (in which case $S_K'=S_K$) to the well-known result

$$5.7 \quad \begin{Bmatrix} R^K(s) \\ T^K(s)\end{Bmatrix} = \begin{Bmatrix} R^K \\ T^K\end{Bmatrix}\delta(s-s_0) \;,$$

with $s_0=\sin\theta_0$, R^K, T^K constants; and δ the Dirac distribution. Eq. 5.7 expresses the fact that the field ^{0} reduces to the incident wave plus one specularly reflected plane wave in S_1, to one refracted plane wave plus one reflected plane wave in each of the domains $S_2, S_3, \ldots, S_L$ and to one refracted plane wave in S_{L+1}. In all other cases, that is, when the interfaces are rough surfaces, the fields in the domains S_K' must be expressed as continuous infinite spectra of plane waves.

It is $R^1(s)$ which is of particular interest to us here, $|R^1(s)|^2$ for $|s| = |\sin\theta| < 1$ representing the scattering diagram of reflected flux in air. To determine this function, we will have to evaluate $u_1(x)$ and $v_1(x)$ which are, of course, related to $u_k(x)$, $v_k(x)$, k=2,...,L.

In the special case in which all the profile fuctions f_k are periodic in x

$$5.8 \qquad f_K(x) = f_K(x+\Delta_K) \qquad ; K = 1,2,\dots,L$$

such that

$$5.9 \qquad f_K(x+\Delta_K) = f_K(x+\Delta) \qquad ; K = 1,2,\dots,L$$

with Δ such that

$$5.10 \qquad \Delta = M_1\Delta_1 = M_K\Delta_K \qquad ; K = 2,3,\dots,L \qquad M_1, M_k \text{ integers,}$$

the continuous spectrum of 5.3 reduces to the discrete spectrum

$$5.11 \qquad U_K(x,z) = \gamma_K \exp i k_1(\sigma_{10}x - w_{10}z) + \sum_{n=-\infty}^{\infty} [U_K A_n^K \exp i k_K(\sigma_{Kn}x - w_{Kn}z) + v_K B_n^K \exp i k_K(\sigma_{Kn}x + w_{Kn}z)] \qquad ; (x,z) \in S_K' \quad K = 1,2,\dots,L+1$$

with

$$5.12 \qquad \begin{cases} \sigma_{Kn} = k_1 k_K^{-1} s_n \\ s_n = s_0 + 2n\pi/k_1\Delta \qquad \text{(grating formula (5))} \\ w_{Kn} = +\sqrt{1-\sigma_{Kn}^2} \\ k_K = \frac{2\pi}{\lambda} N_K \end{cases}$$

Eq. 5.11 was obtained for the first time (for L=1) by Lord Rayleigh (5).

6 . FUNDAMENTAL HYPOTHESES

In the following, we shall assume, when considering the case of periodic interface profile functions, that 5.11 is a valid representation of the total fields throughout and in each of the domains S_k (that is, not only in the subdomains S_k'). It turns out (6) that even though this is not strictly true, 5.11 and 4.1 are equivalent representations throughout S_k in the asymptotic sense to be defined later on.

Secondly, 5.11 will be used to obtain approximate expressions for $u_k(x), v_k(x)$ in the case of periodic interface profiles and it will be assumed that these expressions are fundamentally the same whether the interface profiles are periodic or aperiodic functions of x. This hypothesis can be justified a posteriori by applying to 5.3, which is valid for aperiodic profiles, the same perturbation technique as will be applied to 5.11.

It is necessary, as concerns the use of the perturbation method with 5.11, to add additional constraints to the functions f_k. As the latter are periodic functions of x in the case considered, they can be expanded in the Fourier series

$$6.1 \qquad f_K(x) = f_K(x+\Delta_K) = A_0 + \sum_{\ell=1}^{\infty} [A_\ell \cos\frac{2\pi\ell}{\Delta_K}x + B_\ell \sin\frac{2\pi\ell}{\Delta_K}x] \qquad (\Delta_K = \text{period of } f_k).$$

First of all, we shall assume that f_k has a high spatial frequency cutoff; this means that

$$6.2 \qquad A_\ell = B_\ell = 0 \qquad \text{for} \qquad \ell > L_K$$

The spatial period of the L_k-th harmonic is

$$6.3 \qquad p_K = \Delta_K/L_K \qquad ; K = 1,2,\dots,L$$

and our second assumption will be that

$$6.4 \qquad p_K >> \lambda \qquad ; K = 1,2,\dots,L$$

But, as $\Delta_K = \Delta/M_K$, 6.4 is equivalent to

$$6.5 \qquad \Delta >> M_K L_K \lambda \qquad ; K = 1,2,\dots,L$$

or, in other words,

$$6.6 \qquad 0 < C = \frac{\lambda}{\Delta} << (M_K L_k)^{-1}_{MAX} < 1$$

C will be chosen as the perturbation parameter in the following analysis.

In order to conform as much as possible with the assumptions made in the periodic profile case, we shall assume, in the aperiodic profile case, that the Fourier spectrum of f_k, k=1,...,L contains no spatial frequencies higher than $\bar{\nu} = \Delta^{-1}$, which means that

$$6.7 \qquad f_K(x) = \int_0^{\bar{\nu}} [A^K(\nu)\cos 2\pi\nu x + B^K(\nu)\sin 2\pi\nu x]\,d\nu = \Delta^{-1}\int_0^1 [A^K(\frac{\eta}{\Delta})\cos\frac{2\pi}{\Delta}\eta x + B^K(\frac{\eta}{\Delta})\sin\frac{2\pi}{\Delta}\eta x]\,d\eta$$

where, as before, it is assumed that

6.8 $$0 < C = \frac{\lambda}{\Delta} \ll 1$$

7. FORMAL SOLUTION OF THE PERIODIC PROFILE PROBLEM

Let us substitute 5.11 into 3.10-3.11, multiply 3.10 and 3.11 by

$$\Delta^{-1}dx \exp -ik_K(\sigma_{Km}x + w_{K0}f_K)$$

or

$$-\Delta^{-1}dx\, a_{K+1}^{-1} \exp -ik_{K+1}(\sigma_{K+1,m}x - w_{K+1,0}f_K) \qquad ; \; m = 0, \pm 1, \ldots, \pm\infty$$

respectively, and integrate the resulting equations over one period Δ. These operations lead to the following linear system of equations

7.1 $$-\gamma_K \overset{-}{I}{}^{K1}_{m0} = \sum_{n=-\infty}^{\infty}\left[\nu_K B_n^K \overset{+}{I}{}^{KK}_{mn} + \upsilon_K A_n^K \overset{-}{I}{}^{KK}_{mn} - \nu_{K+1} B_n^{K+1} \overset{\pm}{I}{}^{K,K+1}_{mn} - \upsilon_{K+1} A_n^{K+1} \overset{-}{I}{}^{K,K+1}_{mn}\right] \quad K = 1, \ldots, L$$

7.2 $$-\gamma_K \overset{-}{J}{}^{K1}_{m0} = \sum_{n=-\infty}^{\infty}\left[\nu_K B_n^K \overset{+}{J}{}^{KK}_{mn} + \upsilon_K A_n^K \overset{-}{J}{}^{KK}_{mn} - \nu_{K+1} B_n^{K+1} \overset{+}{J}{}^{K,K+1}_{mn} - \upsilon_{K+1} A_n^{K+1} \overset{-}{J}{}^{K,K+1}_{mn}\right] \quad ; m = 0, \pm 1, \ldots ,$$

which is equivalent to the matrix equation of order $2L\infty$

7.3 $$\mathbb{E}_L \mathbb{F}_L = \mathbb{G}_L \qquad ,$$

where

7.4 $$\mathbb{E}_L = \left[\begin{array}{c|c} \mathbb{E}_{L-1} & \mathbb{E}_{L,12} \\ \hline \mathbb{E}_{L,21} & \mathbb{E}_{L,22} \end{array}\right] \; ; \; L = 2, 3, \ldots \quad ; \quad \mathbb{E}_1 = \mathbb{E}_{1,22} \qquad ,$$

7.5 $$\mathbb{E}_{L,22} = \begin{bmatrix} \overset{+}{\mathbb{I}}{}^{LL} & -\overset{-}{\mathbb{I}}{}^{L,L+1} \\ \overset{+}{\mathbb{J}}{}^{LL} & -\overset{-}{\mathbb{J}}{}^{L,L+1} \end{bmatrix} , \quad \mathbb{E}_{L,21} = \left[\overbrace{\begin{array}{cc|c|cc|} \mathbb{O} & \mathbb{O} & & \mathbb{O} & \mathbb{O} \\ & & \cdots & & \\ \mathbb{O} & \mathbb{O} & & \mathbb{O} & \mathbb{O} \end{array}}^{L-2 \text{ series}} \begin{array}{cc} \mathbb{O} & \overset{-}{\mathbb{I}}{}^{LL} \\ & \\ \mathbb{O} & \overset{-}{\mathbb{J}}{}^{LL} \end{array}\right] \qquad ,$$

7.6 $$\mathbb{E}_{L,12} = \left.\begin{bmatrix} \mathbb{O} & \mathbb{O} \\ \mathbb{O} & \mathbb{O} \\ \hdashline & \vdots \\ \hdashline \mathbb{O} & \mathbb{O} \\ \mathbb{O} & \mathbb{O} \\ \hdashline -\overset{+}{\mathbb{I}}{}^{L-1,L} & \mathbb{O} \\ -\overset{+}{\mathbb{J}}{}^{L-1,L} & \mathbb{O} \end{bmatrix}\right\} L-2 \text{ series} \quad , \quad \mathbb{F}_L = \left[\begin{array}{c} \mathbb{F}_{L-1} \\ \hdashline \mathbb{F}_{L,2} \end{array}\right] , \; \mathbb{F}_1 = \mathbb{F}_{1,2} \; , \; \mathbb{F}_{L,2} = \begin{bmatrix} \underline{\mathbb{B}}^L \\ \underline{\mathbb{A}}^{L+1} \end{bmatrix}$$

$$\mathbb{G}_L = \left[\begin{array}{c} \mathbb{G}_{L-1} \\ \hdashline \mathbb{G}_{L,2} \end{array}\right] , \; \mathbb{G}_1 = \begin{bmatrix} -\overset{-}{\underline{\mathbb{I}}}{}^{11} \\ -\overset{-}{\underline{\mathbb{J}}}{}^{11} \end{bmatrix} , \; \mathbb{G}_{L,2} = \begin{bmatrix} \underline{\mathbb{O}} \\ \underline{\mathbb{O}} \end{bmatrix} \qquad ,$$

$$\mathbb{O} = \begin{bmatrix} 0 & \cdots & 0 \\ 0 & \cdots & 0 \end{bmatrix} \qquad \underline{\mathbb{O}} = \begin{bmatrix} 0 \\ \vdots \\ 0 \end{bmatrix}$$

7.7 $$\overset{\pm}{\mathbb{I}}{}^{Kj} = \left\{\overset{\pm}{I}{}^{Kj}_{mn}\right\} = \left\{\int_0^\Delta \frac{dx}{\Delta} \exp i\left[\frac{2\pi}{\Delta}(n-m)x + (\pm k_j w_{jn} - k_K w_{K0}) f_K\right]\right\} \qquad ,$$

7.8 $$\overset{\pm}{\mathbb{J}}{}^{Kj} = \left\{\overset{\pm}{J}{}^{Kj}_{mn}\right\} = \left\{\frac{-a_j}{a_{K+1}} \int_0^\Delta \frac{dx}{\Delta}\left[\dot{f}_K \frac{\sigma_{jn}}{w_{j0}} \mp \frac{w_{jn}}{w_{j0}}\right] \exp i\left[\frac{2\pi}{\Delta}(n-m)x + (\pm k_j w_{jn} + k_{K+1} w_{K+1,0}) f_K\right]\right\} \qquad ,$$

7.9 $$\underline{\mathbb{B}}^K = \left\{B_n^K\right\} \quad , \quad \overset{\pm}{\underline{\mathbb{I}}}{}^{Kj} = \left\{\overset{\pm}{I}{}^{Kj}_{m0}\right\} \qquad ,$$

7.10 $$\underline{\mathbb{A}}^K = \left\{A_n^K\right\} \quad , \quad \overset{\pm}{\underline{\mathbb{J}}}{}^{Kj} = \left\{\overset{\pm}{J}{}^{Kj}_{m0}\right\} \qquad ,$$

7.11 $$a_K = k_K \kappa_K w_{K0} \qquad ,$$

whereas $\{e_{mn}\}$ signifies the matrix whose elements are e_{mn} for m,n varying from 0 to $\pm\infty$, and $\{e_m\}$ signifies the vector whose elements are e_m for m varying from 0 to $\pm\infty$.

It will be noticed that $\mathbb{E}_L$ is a partitioned hypermatrix whose four submatrices are themselves hypermatrices of infinite order such that the order of $\mathbb{E}_L$ is $2L\infty$. More interesting is the fact, well-known to those familiar with thin-film analysis in optics (7), that $\mathbb{E}_L$ is expressible in terms of $\mathbb{E}_{L-1}$. This suggests that the solution $\mathbb{F}_L$, for L interfaces, can be obtained by an iterative process from the solutions $\mathbb{F}_1, \mathbb{F}_2, \ldots, \mathbb{F}_{L-1}$ for 1,2,...,L-1 interfaces. This is seen more clearly from the following analysis. The solution of 7.3 is formally

7.12 $$\mathbb{F}_L = \mathbb{E}_L^{-1}\mathbb{G}_L \qquad ,$$

where $\mathbb{E}_L^{-1}$ is the inverse of $\mathbb{E}_L$ which can be written as

$$7.13 \qquad \mathbb{E}_L^{-1} = \left[\begin{array}{c|c} \mathbb{C}_{L,11} & \mathbb{C}_{L,12} \\ \hline \mathbb{C}_{L,21} & \mathbb{C}_{L,22} \end{array}\right] ,$$

and where, by the rules for the inversion of a four-fold partitioned matrix,

$$7.14 \qquad \left\{\begin{array}{l} \mathbb{H} = -\mathbb{E}_{L-1}^{-1}\,\mathbb{E}_{L,12} \\ \mathbb{C}_{L,22} = (\mathbb{E}_{L,22} + \mathbb{E}_{L,21}\,\mathbb{H})^{-1} \\ \mathbb{C}_{L,12} = \mathbb{H}\,\mathbb{C}_{L,22} \\ \mathbb{C}_{L,21} = -\mathbb{C}_{L,22}\,\mathbb{E}_{L,21}\,\mathbb{E}_{L-1}^{-1} \\ \mathbb{C}_{L,11} = \mathbb{E}_{L-1}^{-1} + \mathbb{H}\,\mathbb{C}_{L,21} \end{array}\right. .$$

This result shows the relation between $\mathbb{E}_L^{-1}$ and $\mathbb{E}_{L-1}^{-1}$.

Unfortunately ,it is not possible to proceed any further with this analysis--analysis which should have led to the actual solution of the problem-- since it is not possible to invert even $\mathbb{E}_1$ in closed form.

8. PERTURBATION SOLUTION

With C the perturbation parameter, let us expand $\mathbb{E}_L$, $\mathbb{F}_L$ and $\mathbb{G}_L$ in series of powers of C

$$8.1 \qquad \left\{\begin{array}{c} \mathbb{E}_L \\ \mathbb{F}_L \\ \mathbb{G}_L \end{array}\right\} = \sum_{l=0}^{\infty} \left\{\begin{array}{c} \mathbb{E}_L^{(l)} \\ \mathbb{F}_L^{(l)} \\ \mathbb{G}_L^{(l)} \end{array}\right\} C^l .$$

The index l, in these expressions, denotes the order of perturbation. By inserting 8.1 into 7.3, and by comparing powers of C, we obtain

$$8.2 \qquad \mathbb{E}_L^{(0)}\,\mathbb{F}_L^{(0)} = \mathbb{G}_L^{(0)}$$

$$8.3 \qquad \mathbb{E}_L^{(0)}\,\mathbb{F}_L^{(l)} = \mathbb{G}_L^{(l)} - \sum_{q=0}^{l-1} \mathbb{E}_L^{(l-q)}\,\mathbb{F}_L^{(q)} \qquad ; \; l = 1,2,\ldots .$$

This defines a useful recourrence relation provided that $\mathbb{E}_L^{(0)}$ can be inverted in closed form. However $\mathbb{E}_L^{(0)}$ is expressible as

$$8.4 \qquad \mathbb{E}_L^{(0)} = \left[\begin{array}{c|c} \mathbb{E}_{L-1}^{(0)} & \mathbb{E}_{L,12}^{(0)} \\ \hline \mathbb{E}_{L,21}^{(0)} & \mathbb{E}_{L,22}^{(0)} \end{array}\right] \qquad ; \; L = 2,3,\ldots ,$$

with

$$8.5 \qquad \mathbb{E}_1^{(0)} = \left[\begin{array}{cc} \mathbb{1} & -\bar{\mathbb{U}}^{12(0)} \\ \check{\mathbb{U}}^{11(0)} & \mathbb{1} \end{array}\right] , \quad \mathbb{E}_{L,22}^{(0)} = \left[\begin{array}{cc} \mathbb{1} & -\bar{\mathbb{U}}^{L,L+1(0)} \\ \check{\mathbb{U}}^{LL(0)} & \mathbb{1} \end{array}\right] ,$$

$$8.6 \qquad \mathbb{F}_{L,12}^{(0)} = \left[\begin{array}{cc} \mathbb{0} & \mathbb{0} \\ \mathbb{0} & \mathbb{0} \\ \hline & \vdots \\ \hline \mathbb{0} & \mathbb{0} \\ \mathbb{0} & \mathbb{0} \\ \hline -\bar{\mathbb{U}}^{L-1,L(0)} & \mathbb{0} \\ -\check{\mathbb{U}}^{L-1,L(0)} & \mathbb{0} \end{array}\right] , \quad \mathbb{E}_{L,21}^{(0)} = \left[\begin{array}{ccc|c|cc} \mathbb{0} & \mathbb{0} & & & \mathbb{0} & \mathbb{0} \\ \mathbb{0} & \mathbb{0} & \cdots & \mathbb{0} \; \mathbb{0} & \mathbb{0} & \bar{\mathbb{U}}^{LL(0)} \\ & & & & & \\ & & & & & \check{\mathbb{U}}^{LL(0)} \end{array}\right] ,$$

8.7 $$\mathbb{1} = \{ \delta_{mn} \} \quad ,$$

8.8 $$\overset{\pm}{\mathbb{I}}{}^{kj(o)} = \left\{ \overset{\pm}{I}{}^{kj(o)}_{mn} \right\} = \left\{ \int_0^1 d\zeta \exp i [2\pi(n-m)\zeta + (\pm k_j w_{jo} - k_k w_{ko}) g_k(\zeta)] \right\} \quad ,$$

8.9 $$\overset{\vee}{\mathbb{J}}{}^{kj(o)} = \left\{ \overset{\vee}{J}{}^{kj(o)}_{mn} \right\} = \left\{ \pm \frac{a_j}{a_{k+1}} \int_0^1 d\zeta \exp i [2\pi(n-m)\zeta + (\pm k_j w_{jo} + k_{k+1} w_{k+1,o}) g_k(\zeta)] \right\} \quad ,$$

8.10 $$\zeta = \frac{x}{\Delta} \quad , \quad g_k(\zeta) = f_k(x) \quad .$$

Therefore the inversion of $\mathbb{E}_L^{(o)}$ follows the same rules as that of $\mathbb{E}_L$ and depends on the possibility of inverting $\mathbb{E}_1^{(o)}$ in closed form. It turns out that

8.11 $$\mathbb{E}_1^{(o)-1} = \left(\frac{a_1}{a_1 + a_2} \right) \begin{bmatrix} \mathbb{1} & \bar{\mathbb{D}}^{12(o)} \\ \overset{\vee}{\mathbb{J}}{}^{11(o)} & \mathbb{1} \end{bmatrix} \quad .$$

Closed-form expressions for $\mathbb{E}_2^{(o)}, \mathbb{E}_3^{(o)}, \ldots$ then follow by the iterative analysis described in 7.14.

The general result of all these operations is that the l-th perturbation order coefficients of B_n^k and A_n^k are expressible as the Fourier integrals

8.12 $$\begin{Bmatrix} B_n^k \\ A_n^k \end{Bmatrix} = \int_0^\Delta \frac{dx}{\Delta} \begin{Bmatrix} r^{k(l)}(x) \\ t^{k(l)}(x) \end{Bmatrix} \exp -i\frac{2\pi n}{\Delta} x \quad ; \quad \begin{matrix} l = 0, 1, 2, \ldots . \\ k = 1, 2, \ldots, L+1 \\ n = 0, \pm 1, \pm 2, \ldots . \end{matrix} \quad ,$$

where, for three or less interfaces ($L \leq 3$) and to the zeroth order of perturbation (8):

8.13
$$r^{1(o)}(x) = b_{11}^{-2} [(a_1 - a_2)(a_2 \overset{+}{\rho} + a_3 \bar{\rho}) b_{21}^{-2} b_{22}^2 + (a_1 + a_2)(a_2 \overset{+}{\rho} - a_3 \bar{\rho})] / \chi \quad ,$$

$$t^{2(o)}(x) = b_{11}^{-1} b_{21}^{-1} b_{22}^2 \, 2a_1 (a_2 \overset{+}{\rho} + a_3 \bar{\rho}) / \chi \quad ,$$

$$r^{2(o)}(x) = b_{11}^{-1} b_{21}^{-1} \, 2a_1 (a_2 \overset{+}{\rho} - a_3 \bar{\rho}) / \chi \quad ,$$

$$t^{3(o)}(x) = b_{11}^{-1} b_{21}^{-1} b_{22} b_{32} \, 4 a_1 a_2 / \chi \quad ,$$

$$r^{3(o)}(x) = b_{11}^{-1} b_{21}^{-1} b_{22} b_{32} b_{33}^{-2} \, 4 a_1 a_2 (a_3 - a_4) / [\chi (a_3 + a_4)] \quad ,$$

$$t^{4(o)}(x) = b_{11}^{-1} b_{21}^{-1} b_{22} b_{32} b_{33}^{-1} b_{43} \, 8 a_1 a_2 a_3 / [\chi (a_3 + a_4)] \quad ,$$

$$\chi = (a_1 + a_2)(a_2 \overset{+}{\rho} + a_3 \bar{\rho}) b_{21}^{-2} b_{22}^2 + (a_1 - a_2)(a_2 \overset{+}{\rho} - a_3 \bar{\rho}) \quad ,$$

$$\overset{\pm}{\rho} = 1 \pm b_{32}^2 b_{33}^{-2} (a_3 - a_4)(a_3 + a_4)^{-1} \quad ,$$

$$b_{jk} = \exp i k_j w_{jo} f_k(x) \quad .$$

The case of two or one interfaces can be deduced from the preceding relations by posing $a_3 = a_4$ or $a_2 = a_3 = a_4$ respectively.

9. NUMERICAL EXAMPLES

In Figs. 3 and 4 we have plotted $|B_0^{1(o)}|^2$, ie., the zeroth perturbation order flux in the zeroth (specular) grating order in air, as a function of the incident angle θ_0. The upper set of curves, in each case, refer to the situation in which the two interfaces are perfectly flat, ie.,

9.1 $$\begin{cases} f_1(x) = 0 \\ f_2(x) = -E \end{cases}$$

whereas the lower curves refer to the case of two rough periodic interfaces, ie.,

9.2 $$\begin{cases} f_1(x) = h_1 \cos \frac{2\pi}{\Delta_1} x \\ f_2(x) = -E + h_2 \cos \frac{2\pi}{\Delta_2} x \end{cases}$$

In both cases, the sea is considered to be a homogeneous medium whose complex index of refraction is N_2, and the incident field is either a TE or TM electromagnetic wave whose wavelength in air is λ. The pertinent parameters are given in the table below:

	Fig.3	Fig.4
h_1	0.1 m	0.1m
h_2	0.25 m	0.25 m
Δ_1	5.0 m	5.0 m
Δ_2	10.0 m	10.0 m
N_1	1.0	1.0
N_2	12.9+9.3 i	9.045+1.32o i
N_3	1.533+0.59 i	1.41o+o.33x10^{-2} i
E	300 m	300 m
λ	1 m	0.1 m

It turns out, that at the chosen wavelengths, the absorption of the water (related to the imaginary part of the refractive index) is so large that the refracted waves in the water are, for all practical purposes, completely attenuated before they reach the bottom; this means that nothing is reflected from the bottom so that the incident wave is "blind" to the earth's crust. However, the roughness of the air-sea interface makes itself felt, since there is a large difference in specularly reflected flux with respect to the flat interface for practically all angles of incidence up to near grazing incidence.

10. APPROXIMATIONS FOR THE INTERFACE FIELDS

Approximations for $u_k(x)$ and $v_k(x)$ can be obtained from 5.11 by the use of a straightforward perturbation technique which employs the previously-obtained expressions $B_n^{\kappa(l)}$ and $A_n^{\kappa(l)}$. Let us illustrate this procedure for $u_k(x)$. From 5.11 we have

$$10.1 \quad U_k(\zeta) = u_k(x)\exp -ik_1 w_{10} x = \gamma_k \exp -ik_1 w_{10} g_k(\zeta) + \sum_{n=-\infty}^{\infty} \left[v_k A_n^k \exp i[2\pi n\zeta - k_k w_{kn} g_k(\zeta)] + \right.$$
$$\left. + v_k B_n^k \exp i[2\pi n\zeta + k_k w_{kn} g_k(\zeta)] \right] \qquad (\zeta = \tfrac{x}{\Delta})$$

By expanding all functions that depend on C in series of powers of C, we obtain the relation

$$10.2 \quad \gamma_k^{(l)}(\zeta) = U_o^{\kappa(l)}(\zeta) + \sum_{l=0}^{l} \sum_{n=-\infty}^{\infty} \left[\bar{U}_n^{\kappa(l-s)}(\zeta) A_n^{\kappa(l)} + \bar{U}^{\kappa(l-s)}(\zeta) B_n^{\kappa(l)} \right] \exp i 2\pi n\zeta \quad ; \begin{matrix} \kappa = 1,2,\dots,L \\ l = 1,2,\dots \end{matrix}$$

with

$$10.3 \quad U_o^{\kappa(l)} = \gamma_\kappa \delta_{l,o} \exp -ik_1 w_{10} g_1$$

$$10.4 \quad \bar{U}^{\kappa(l)} = \frac{1}{l!} \left[\partial_c^l (\exp \pm i k_\kappa w_{\kappa n} g_\kappa) \right]_{c=0}$$

and with $B_n^{\kappa(l)}$, $A_n^{\kappa(l)}$ as given in 8.12.

The quantities of interest, $u_1(x)$, $v_1(x)$, obtained in this manner, to the zeroth order of perturbation, are of the form

$$10.5 \quad U_1^{(o)}(x) = [1 + r^{1(o)}(x)] u_o(x, f_1)$$

$$10.6 \quad V_1^{(o)}(x) = -[1 - r^{1(o)}(x)] \partial_g u_o(x, f_1)$$

where, for example, in the case of two interfaces,

$$10.7 \quad r^{1(o)}(x) = \left[\frac{(a_1 - a_2)(a_2 + a_3) + (a_1 + a_2)(a_2 - a_3) \exp 2i k_2 w_{20} (f_1 - f_2)}{(a_1 + a_2)(a_2 + a_3) + (a_1 - a_2)(a_2 - a_3) \exp 2i k_2 w_{20} (f_1 - f_2)} \right] \exp -2ik_1 w_{10} f_1$$

Eqs. 10.5-10.6 constitute the so-called horizontal-plane-physical-optics approximation for the interface fields. Beckmann (2) has previously obtained an equivalent expression for one interface only (take $a_2=a_3$ in 10.7).

11. APERIODIC INTERFACE PROFILES

After identifying w_{k_0} with $w_k(s_o)$ and inserting $u_1^{(o)}(x)$ and $v_1^{(o)}(x)$ into the perturbation expansions of $R^1(s)$, we obtain

$$11.1 \qquad R^{1(o)}(s) = \frac{k_1}{2\pi} \int_{-\infty}^{\infty} r^{1(o)}(x) \exp i k_1 (s_o - s) x \, dx$$

A similar procedure can be used for the other reflection and transmission functions to all orders of perturbation by using the $u_K^{(1)}(x)$, $v_K^{(1)}(x)$ obtained from the periodic interface profile perturbation analysis.

12. CONCLUSIONS

The theory outlined in this paper is applicable to any rough-interface stratified medium provided that the smallest spatial period of the spectrum of the interface profile functions is large compared to the wavelength of the incident field in air. The results are valid for both periodic and aperiodic rough surfaces and they can be used to evaluate the influence of the air-water and water-earth interface roughnesses as well as the influence of inhomogeneities of the sea on the signal sent into the sea from the air.

The perturbation method explains the origin of the oft-used physical optics approximation and shows how this approximation can be improved (6,8,9). It can be shown (6) that the perturbation expansions of $u_k(x)$ and $v_k(x)$ are asymptotic series for $C \to 0$ and they are the same asymptotic series one obtains by application of the perturbation method to the rigorous Green's function representations of the fields ; this explains why it was permissible to use the plane wave field representations in the perturbation analysis.

Finally, the physical optics approximation has been obtained for an arbitrary number of rough interfaces whereas only the single interface physical optics approximation has until now been given in the litterature.

REFERENCES

(1) Wait, J.R., Electromagnetic waves in stratified media, Pergamon, London, 1962

(2) Beckmann,P. and Spizzichino, A., The scattering of electromagnetic waves from rough surfaces, Pergamon, London, 1963

(3) Wirgin, A., Propagation d'une onde électromagnétique dans un milieu stratifié, Rev. CETHEDEC, No. 15, 1968, p.101

(4) Wirgin, A., Réflexion d'une onde plane homogène sur un réseau métallique recouvert d'une couche diélectrique, Rev. CETHEDEC, No.15, 1968, p.131

(5) Rayleigh, L., The theory of sound, Dover, N.Y., 1945, Vol.2, p.89

(6) Wirgin, A., Théorie électromagnétique de la diffraction d'une onde par une surface quasiment plane, Thèse, Faculté des Sciences d'Orsay, Juin 1967

(7) Born,M. and Wolf,E., Principles of optics, Pergamon, London, 1959

(8) Verhaeghe, M.F., Réflexion et transmission d'une onde plane par les interfaces à rugosités périodiques d'un milieu stratifié, to appear in Optica Acta

(9) Croce,P., Devant,G., Sere, M.G., and Verhaeghe, M.F., Thin-film surface studies by x-ray reflection, 3rd conference on thin films, York, England, 1969, to appear in Surface Science

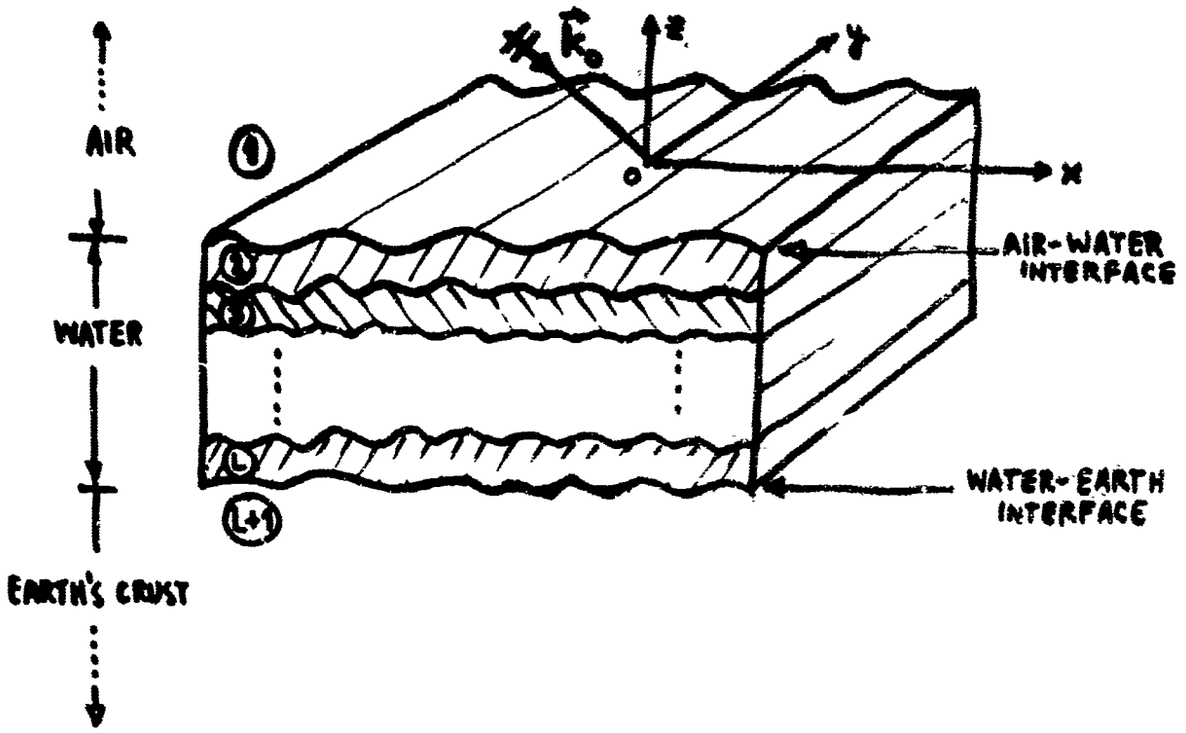

Figure 1

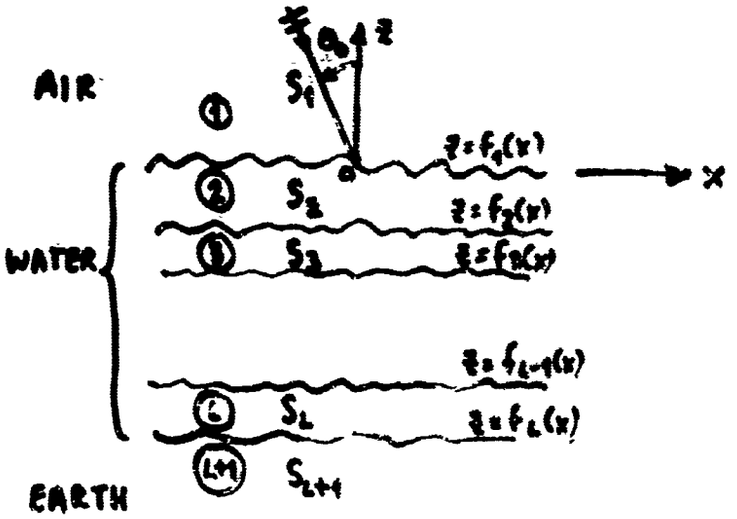

Figure 2

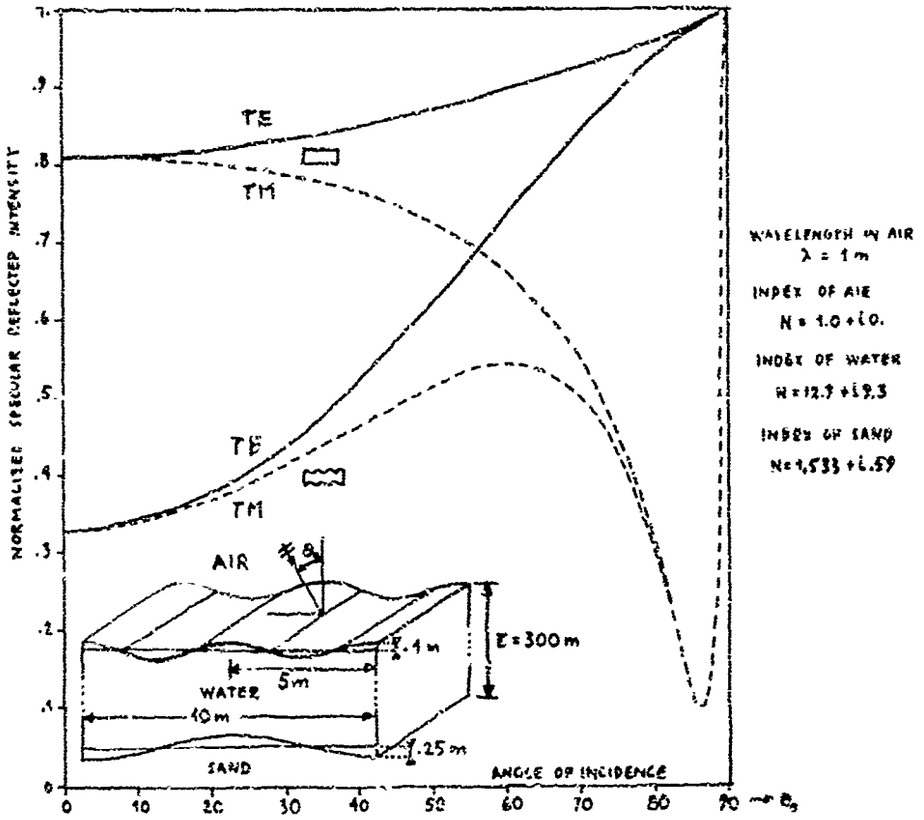

Figure 3

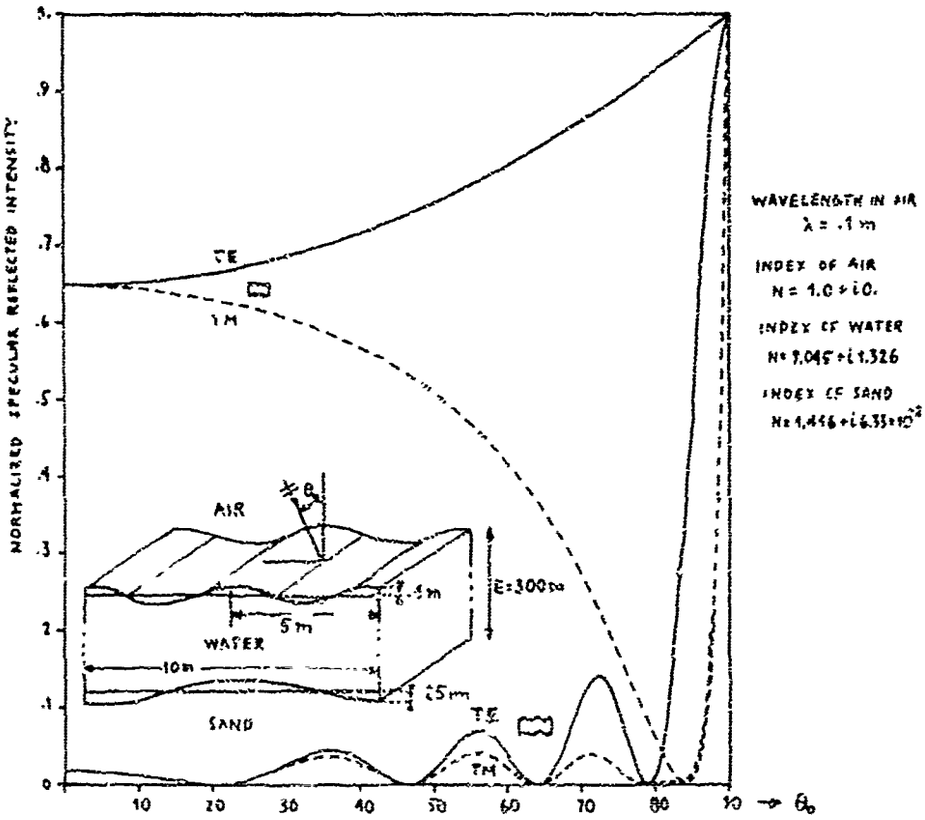

Figure 4

RAYONNEMENT DES SOURCES ELECTROMAGNETIQUES PLACEES DANS DES MILIEUX ABSORBANTS ANALYSE BIBLIOGRAPHIQUE

par

Robert GABILLARD - Université de LILLE - FRANCE
Pierre DEGAUQUE - " "
James R. WAIT - ESSA - BOULDER (Colo) U.S.A.

RAYONNEMENT DES SOURCES ELECTROMAGNETIQUES PLACEES DANS DES MILIEUX ABSORBANTS ANALYSE BIBLIOGRAPHIQUE

Robert GABILLARD - Université de LILLE - FRANCE
Pierre DEGAUQUE - " "
James R. WAIT - ESSA - BOULDER (Colo) - U.S.A.

Introduction

Cet article est une revue de la littérature dans laquelle nous nous sommes efforcés d'être le plus complet possible. Le rayonnement des sources électromagnétiques placées dans des milieux absorbants ne constitue en effet que l'une des rubriques de la bibliographie que nous donnons et qui contient 424 références d'articles. Ce nombre de publications qui n'est certainement pas complet et qui ne comprend pas (à part quelques uns) les auteurs des pays de l'Est, mesure l'importance des efforts qui ont été consacrés depuis le début du 20ème siècle à la compréhension des mécanismes qui régissent la propagation des ondes électromagnétiques dans le sol et dans la mer. Nous traitons à part les travaux expérimentaux et les travaux théoriques et dans chaque rubrique, les références sont classées par ordre chronologique.

L'étude du fonctionnement des appareils de télécommunication radioélectrique lorsque l'émetteur ou le récepteur (ou les deux) sont placés au sein d'un milieu absorbant a déjà fait l'objet de très nombreuses études théoriques et expérimentales.

L'une des motivations de ces recherches a été le désir d'établir des communications avec les sous-marins en plongée. On trouve sur ce problème des publications antérieures à 1920 (Réf. (1) à (5)).

Mais les recherches sur la propagation des ondes radioélectriques à travers les milieux absorbants ont été stimulées par beaucoup d'autres possibilités d'applications qu'il est intéressant de citer.

Dans le domaine de la prospection géophysique, les publications sont innombrables. A l'époque où SCHLUMBERGER et STEFANESCU (Réf. (6) à (12)) développaient leurs méthodes de prospection en courant continu ou à très basse fréquence, d'autres chercheurs, en particulier EVE et KEYS[13], proposaient déjà l'utilisation d'ondes de fréquences relativement élevées. La période qui s'étend de 1930 jusqu'à la seconde guerre mondiale a vu paraître un assez grand nombre de travaux concernant des procédés électriques et radioélectriques de prospection géophysique (Réf. (14) à (25)). La même période a vu se développer des procédés de prospection utilisant des courants impulsifs (Réf. (26) à (29)), mais ces procédés n'ont pas eu d'avenir à cause des difficultés d'interprétation. Toutes ces méthodes électromagnétiques de prospection géophysique sont décrites et discutées dans le livre de HEILAND paru en 1946[31].

Parallèlement au développement des procédés de prospection géophysique, que certains de leurs promoteurs tel que BARRET (Réf. (30) à (32)) prétendaient faire fonctionner jusqu'à des profondeurs interdites par la théorie, de nombreux expérimentateurs ont cherché à établir par des mesures directes effectuées dans des carrières, dans des mines, dans des cavernes, ou dans des forages, les lois physiques de la propagation des ondes électromagnétiques à travers le sol. Les premières expériences semblent avoir été faites par ILSLEY, FREEMAN et ZELLERS du U.S. Bureau of Mines [34] en 1928, puis en 1929 et 1930 par EVE, KEYS et LEE dans les grottes du Mamouth au Kentucky (Réf. (35) à (37)). Ces expérimentateurs furent suivis par beaucoup d'autres (Réf. (38) à (63)) parmi lesquels nous citerons FRITSCH (Réf. (64) à (67)) qui a observé dans des mines de potasse des portées de 14 km à 3,5 MHz, et PRITCHETT[60] qui mesura à l'aide d'émetteurs et récepteurs descendus dans des forages l'atténuation dans le sol d'une onde de 1652 Kcs.

Après la seconde guerre mondiale, le développement des armes nucléaires a obligé les postes de commandement militaire à s'enterrer. Cette nécessité a provoqué une recrudescence des travaux à la fois théoriques et expérimentaux dont le but était de développer des moyens de télécommunications radioélectriques entre des stations enterrées ou submergées.

Certains de ces travaux ont commencé à être publiés à partir de 1960.

En FRANCE l'équipe du Professeur GABILLARD a effectué en collaboration avec l'Institut Français du Pétrole, et en partie pour le compte de la D.R.M.E.*, de nombreux travaux expérimentaux (Réf. (68) à (89)). Ceux-ci concernent : la propagation d'ondes basse fréquence (100 Hz à 20 kHz) à travers les roches ; verticalement entre une station à la surface du sol et une galerie de mine (carrière de gypse) située à 80 m. de profondeur (Réf. (68) à (72)), et à 520 m. dans une houillère [78] ; la propagation entre deux stations souterraines en utilisant un guide d'onde géologique [80] ; la mesure directe de la vitesse de propagation d'un groupe d'ondes entre deux stations souterraines (Réf. (73) à (76)); la propagation à travers les roches d'impulsions électromagnétiques brèves (4µs) (Réf. (81) à (84)) ; la propagation par ondes de surface [79] . La plupart de ces travaux expérimentaux ont été résumés en 1966 au Congrès de l'A.G.A.R.D. [77]. Ils ont conduit à la réalisation d'appareils pratiques de télécommunication à travers le sol (Réf. (85) à (89)).

En FRANCE également il faut parler des essais de GUTTON [90] qui a étudié en mer et sur terre la propagation d'une onde de surface à 40 Hz. Enfin beaucoup de travaux qui ont été effectués par des organismes militaires ou par des sociétés industrielles n'ont pas été publiés (Travaux de la C.G.G., de la S.E.R.E.B., de la C.S.F., etc...).

* Direction des Recherches et Moyens d'Essais

Aux U.S.A. les travaux expérimentaux concernant la propagation radioélectrique à travers le sol et la mer ont été très nombreux depuis 1960. L'ampleur de ces travaux a été révélée en 1963 par un numéro spécial des I.E.E.E. Transactions on Antennas and Propagation édité par J.R. WAIT [156]. Depuis, le 12ème Symposium de l'Avionics Panel de l'AGARD qui s'est tenu à PARIS en Avril 1966 a permis de faire le point [150]. Le lecteur trouvera dans ces documents de nombreuses références. Elles ont été récemment mises à jour par J.R. WAIT dans le Chapitre 24 du livre "Antenna Theory" publié par R.E. COLLIN et F.J. ZUCKER [151].

Les références que nous donnons ne sont qu'un extrait des travaux expérimentaux américains. Il faut citer les articles de GHOSE[92, 93], de KRAICHMAN [95], de C.K.H. TSAO et J.T. de BETTENCOURT [101, 102, 110 à 113 et 115 à 118] qui ont étudié la propagation d'ondes de surface émises par des dipôles placés dans des forages ; et de A.W. GUY et G. HASSERJIAN [98, 99, 105 à 107] qui ont particulièrement étudié les réseaux d'antennes. L'article de AMES, FRAZIER et URANGE[114] contient de nombreuses références. J. GA[illegible][120] a étudié le rayonnement en haute fréquence (1 à 160 MHz) d'antennes enterrées à faible profondeur. Enfin E.SODERBERG[121, 122] à bord d'une "soucoupe plongeante" du type développé par le Commandant COUSTEAU a mesuré dans la mer l'intensité des ondes électromagnétiques naturelles jusqu'à 300 m de profondeur.

Parmi les travaux effectués en ITALIE, nous citerons ceux de E. CORTI, G. FRANCESCHETTI et G. LATHIRAL concernant des essais d'antennes sphéroïdales[123].

Enfin il est intéressant de constater que la propagation des ondes électromagnétiques à travers le sol et à travers la mer commence à avoir des applications civiles importantes. Notamment dans les techniques de forage[89 - 124], pour la télécommande des vannes de puits de pétrole sous-marins et comme télécommunications de survie dans les mines[87 - 125].

En FRANCE les études de propagation ont donné naissance à des méthodes d'analyse des gisements de pétrole[127] et à des procédés de détection des cavités souterraines utilisés en génie civil (réf. (128) à (131)).

Les travaux théoriques sont également très nombreux. Nous les avons classés dans plusieurs rubriques : D'abord nous donnons la liste des livres auxquels les auteurs se réfèrent le plus souvent ou dans lesquels des chapitres sont consacrés au problème du rayonnement électromagnétique dans les milieux absorbants (Réf. (132) à (161)). Ensuite nous passons en revue les publications consacrées au rayonnement des antennes placées au sein d'un milieu conducteur supposé homogène et infini et à la propagation des ondes électromagnétiques dans ces milieux (Réf. (162) à (200)).

Ces études débutent en 1947 avec les publications de TAI[162, 163] qui a étudié le rayonnement du dipôle élémentaire au sein d'un milieu conducteur homogène et infini. Il a le premier montré la nécessité de placer le dipôle à l'intérieur d'une sphère isolante pour pouvoir calculer son impédance d'entrée. Le modèle théorique le plus simple étant alors l'antenne biconique de faible ouverture. Puis en 1952 WAIT[167] calcule la puissance rayonnée par un dipôle magnétique placé au centre d'une sphère isolante entourée d'un milieu conducteur infini. Apparaissent ensuite dans la littérature les travaux de KING[173, 174] qui étudie encore le dipôle, puis HARRISON, GOOCH, WU, DESCHAMPS[172, 175, 176] entreprennent l'étude d'antennes dont les dimensions ne sont plus petites vis-à-vis de la longueur d'onde. Les boucles circulaires nues et isolées sont l'objet de nombreuses études de la part de WAIT[171, 187], puis de WU, CHEN, TIZUKA, KRAICHMAN, KING, HARRISON et TINGLEY (Réf. (177) à (184), (189), (190), (193), (198)). GALEJS[192] s'intéresse plus particulièrement au fonctionnement en haute fréquence. Enfin les antennes de forme sphéroïdale sont étudiées par WAIT[168, 197] et par CORTI, FRANCESCHETTI et LATHIRAL en ITALIE[199]. En FRANCE il faut citer les publications de BLACHIER[196] sur les antennes de réception et de GABILLARD[185] qui en 1963 montre comment les variations avec la fréquence de la conductivité et de la constante diélectrique du milieu absorbant vont influer sur la pénétration des ondes qui s'y propagent. Le papier de BURROWS[194] est consacré à la propagation en milieu absorbant d'ondes planes décomposées de type TM et TE.

Puis nous abordons les travaux consacrés à l'étude plus délicate de la propagation des ondes dans les milieux inhomogènes. Nous trouvons d'abord en 1902 le travail de LEVI-CIVITA[201] sur le rayonnement d'un fil de longueur infinie posé sur un plan conducteur arbitrairement grand, puis en 1909 la publication historique de SOMMERFELD[202] qui le premier a indiqué la méthode correcte de résolution du problème du rayonnement d'un dipôle vertical placé à la surface du sol. Ce problème, qui a été obscurci par une erreur de

signe dans le calcul initial de SOMMERFELD, a été étudié par d'autres auteurs (Réf. (203) à (212)), WEYL en particulier[203], et a reçu une solution claire et définitive de la part de NORTON (Réf. (206) à (209)).

Le phénomène de l'induction mutuelle entre des câbles téléphoniques posés sur le sol ou suspendus à faible hauteur, devait susciter dans les laboratoires des Bell System les travaux de CAMPBELL[213] ; CARSON[214, 215] ; FOSTER[216, 218] ; RICORDAN et SUNDE[217]. Nous avons classé avec ces études qui se sont déroulées de 1930 à 1940 les travaux plus récents de WAIT et KURSS consacrés au couplage de dipôles magnétiques placés au-dessus du sol ou posés à sa surface (Réf. (220) à (224)). Ces travaux avaient pour motivation l'étude de procédés de prospection géophysique.

La rubrique suivante de notre bibliographie est consacrée aux études des dipôles et antennes électriques et magnétiques placées au-dessus du sol (Réf. (225) à (256)). L'intérêt des auteurs est l'étude de l'influence d'une éventuelle stratification du sol sur le rayonnement atmosphérique de ces sources. Cette série de publications débute en 1946 avec celle de WOLF[225], et on y remarque particulièrement l'importante contribution de J.R. WAIT.

Les 10 dernières références de cette rubrique sont des communications présentées à la Conférence "Environmental effects on antennas performances" tenue à BOULDER (Colorado) en juillet 1969. Elles traitent surtout du problème du calcul de l'impédance et du rayonnement d'antennes ou de systèmes d'antennes V.L.F.

Nous abordons enfin les publications consacrées à l'analyse du fonctionnement des antennes submergées ou enterrées dans un demi-milieu conducteur. Cette série d'études a débuté en 1951 par le travail de MOORE[258], puis en 1953 on trouve les contributions de LIEN[259], puis de WAIT et CAMPBELL[260, 261]. Il faut encore citer les papiers de : WHEELER[257, 265, 266, 269, 272] ; de KING[276] ; de MOORE et BLAIR[278] ; d'ANDERSON[279] ; de BANNISTER[292, 294, 296, 297] ; et en FRANCE ceux de ROBIN et POINCELOT [274, 295] et de GABILLARD[293].

En 1966 le livre de BANOS[291] faisait le point sur le problème du rayonnement d'un dipôle en présence d'un demi-milieu conducteur.

Enfin dans les publications de WEEKS et FENWICK[280, 283] ; SIVAPRASAD et KING[286] ; GHOSE[288] ; GUY et HASSERTIAN[287, 105, 106] et GALEJS[290], on aborde l'étude du fonctionnement en haute fréquence des antennes immergées ou enterrées et on abandonne les antennes simples pour s'intéresser aux réseaux de dipôles résonnants enfouis à faible profondeur dans le sol ou dans la mer.

La rubrique suivante de notre bibliographie est consacrée aux systèmes de télécommunications entre terminaux submergés ou souterrains. Nous abordons ici les applications de tous les travaux théoriques et expérimentaux consacrés à la propagation radioélectrique dans les milieux absorbants. Nous trouvons d'abord en 1951 la publication fondamentale de MOORE[302] qui constituait sa thèse de Doctorat consacrée aux communications Radio entre sous-marins immergés, puis en 1960 le travail de GHOSE[303] est consacré à l'émission VLF à longue distance à partir d'une antenne horizontale placée dans une station souterraine.

La possibilité de tirer partie de la résistivité probablement très élevée des roches du socle cristallin pour y réaliser des télécommunications à l'échelle mondiale a fait l'objet de nombreuses investigations de la part principalement de WHEELER[304] ; HARMON[305] ; BURROWS[307, 310] ; WAIT[311, 323, 324, 325] ; MOTT et SIGGS[312].

Plusieurs papiers sur ce sujet (Réf. (318) à (322)) ont été présentés en 1965 à la Conférence de l'A.G.A.R.D. consacrés aux "Sub-Surface communications".

Les travaux de AMES, de BETTENCOURT et TSAO, FRAZIER et ORANGE ((314), (306) et (110) à (118)) sont consacrés à la propagation dans des couches sédimentaires moins profondes, en tirant partie du contraste de conductivité entre une couche résistante et des épontes conductrices. C'est ce sujet que traitent également les publications de WIGGS[313] et de GABILLARD et LOUAGE[326, 331, 334].

Les publications de DURRANI[308, 309] et BOUIX[317] sont à nouveau orientées vers les télécommunications avec les sous-marins immergés. Enfin HALLEY[315, 316] traite du cas où l'émission destinée au sous-marin provient non plus d'une station VLF située en surface, mais d'un satellite de télécommunication

évoluant à très haute altitude. Enfin les publications de GABILLARD, FONTAINE et DEGAUQUE[327, 328, 330, 334, 333, 335], traitent de l'optimisation des liaisons VLF obtenues à partir d'une station émettrice souterraine.

Nous abordons enfin la partie de la littérature consacrée aux propriétés électromagnétiques de la mer et des roches et aux méthodes de mesure de la conductivité en surface et en profondeur. La liste des auteurs commence en 1924 avec GRANIER[336] et nous trouvons à partir de 1953 les publications sur la méthode magnéto-tellurique de mesure de la résistivité des couches profondes, principalement les travaux de CAGNIARD[342] et de WAIT[347]. En 1963-64, nous trouvons les travaux de KELLER[350] consacrés à l'évaluation des propriétés électriques des couches profondes, et les mesures de de BETTENCOURT et FRAZIER[351] ; LAVTWELL et NELSON[352] et celles de TSAO[353, 354, 355]. Enfin en 1966 à la Conférence de l'A.G.A.R.D. on note 4 communications à ce sujet (Réf. (356) à (359)).

La rubrique suivante de notre bibliographie est consacrée à l'étude de la propagation dans les milieux absorbants d'ondes électromagnétiques de caractère impulsif. On y remarque surtout les contributions de WAIT (17 publications) et de BHATTACHARYYA[372, 375, 382]. Rappelons aussi dans ce domaine les travaux expérimentaux de GABILLARD et MARCHANT (Réf. (81) à (84)). Enfin nous citons quelques travaux consacrés à la propagation des ondes dans le guide terre-ionosphère (Ref. (39) à (412))

La dernière partie de notre bibliographie donne quelques références sur le bruit dans la bande V.L.F. (Publication de MAXWELL (Réf. (414)) ; sur l'optimisation de l'inclinaison d'un dipôle placé dans une couche peu absorbante surmontant un milieu conducteur (travaux de WAIT, BIGGS et WAIT (Réf. (415) à (421)) ; sur l'influence du relief et sur le procédé de simulation sur modèles de la propagation électromagnétique dans les milieux absorbants.

BIBLIOGRAPHIE ANALYTIQUE

« Dans chaque rubrique les références sont classées par ordre chronologique »

I. TRAVAUX EXPERIMENTAUX

I.1. Publications initiales

1. R.H. BATCHER — Loop antenna for submarines
Wireless Age, Vol. 7, p. 28, 1920

2. L. BOUTHILLON — Contribution à l'étude des radiocommunications sous-marines
Rev. Gén. élect., Vol.7, p. 696-700, May 1920

3. A.H. TAYLOR — Short-wave reception and transmission on ground wires (subterranean and submarine)
Proc. IRE, Vol. 7, p. 337-362, Aug. 1919

4. A.H. TAYLOR — Long wave reception and the elimination of streys on ground wires (subterranean and submarine)
Proc. IRE, Vol. 7, p. 559-583, Dec. 1919

5. J.A. UTLLOUGHBY, P.D. LOWELL — Development of loop acrials for submarine radio communication
Phys. Rev., Vol. 14, p. 193-194, Aug. 1919

I.2. Travaux de SCHLUMBERGER et STEFANESCU vers 1930

6. S. STEFANESCU, R.M. SCHLUMBERGER — Sur la distribution électrique potentielle autour d'une prise de terre ponctuelle dans un terrain à couches horizontales, homogènes et isotropes
J. Phys. Radium, Vol. 1, p. 132-140, 1930

7. S. STEFANESCU — Etudes théoriques sur la prospection électrique du sous-sol
I. Série. Institut Géologique de Roumanie

8. S. STEFANESCU, C et M. SCHLUMBERGER — Etudes théoriques sur la prospection électrique du sous-sol
II. Série. Institut Géologique de Roumanie, 1932

9. S. STEFANESCU — Sur les déformations d'un champ électromagnétique inductif provoquées par un sous-sol à stratification horizontale.
Bull. Soc. Roum. de Phys., Vol. 36, p. 63-64, 169-179, 1934

10. S. STEFANESCU — Sur la mesure des résistivités apparentes par la méthode de la spire circulaire
Beitr. angew. Geophys., Vol.5, n° 2, p. 182-192, 1935

11. S. STEFANESCU — Sur les fondements théoriques de la prospection électromagnétique par courant alternatif à très basse fréquence
Beitr. angew. Geophys., Vol. 6, n°2, p. 168-201, 1936

12. S. STEFANESCU — Théorie du plan conducteur pour l'émetteur alternatif de longueur finie
Beitr. angew. Geophys., Vol. 4, p. 169-186, 1934

I.3. Procédés de prospection électromagnétique développés entre 1930 et la seconde guerre mondiale

I.3.1. Procédés de prospection au courant alternatif

13. A.S. EVE, D. KEYS — Applied Geophysics
Cambridge University Press, London, 1929

14. J. GROSSKOPF, K. VOUT — Uber die Messung der Boden Leitfähigkeit
Telegraphen-Fernsprech Funk Fernseh Tech., Vol. 29, p. 164, June 1940

15. A. PETROWSKY — Uber die Anwendung der elektromagnetischen Wellen zur Bodenforschung in der USSR
Beitr. angew. Geophysik, vol. 5, p. 149-204, 1933

16. V. FRITSCH — Detection of caverns in karst formation by radiation-absorption method
Beitr. angew. Geophysik., vol. 4, p. 416-425, 1934

17. K. SUNDBERG — Principles of the swedish geo-electric methods
Beitr. angew. Geophysik, vol.1, n° 3, p. 298, 1931

18. K. SUNDBERG, H. HEDSTROM — Structural investigations by electromagnetic methods
Proc. World Petrol. Congr., B(I), p. 107, 1934

19. J.C. KARCHER, E.A. McDERMOTT — Deep electrical prospecting
Am. Assoc. Petrol. Geol. Bulletin, Vol.19 (I), p. 64-77, Jan. 1935

20. H. LUNDBERG — Geo-electrical prospecting methods
Mining Mag.(London) p.245-248, Oct. 1930 ; p. 310-313 Nov. 1930

21. C.H. FOCKEN — The sundberg inductive method of electrical prospecting
Colo. School Mines Quart., Vol. 32, p. 225-251, 1937

22. H.M. EVJEN — Utility of the electric methods in geophysical exploration
Geophysics, p. 146-156, 1945

23. W.B. LEWIS — Working depths for low frequency electrical prospecting
Geophysics, Vol. X, (1), p. 63-75, 1945

24. C.W. HORTON — On the use of electromagnetic waves in geophysical prospecting
Geophysics, Vol. 11, p. 505, 1946

25. L. KERWIN — Use of the broadcast band in geologic mapping
J. Appl. Phys., Vol. 18, p. 407-413, 1947

I.3.2. Procédés de prospection en courant impulsif

26. G. WHITE — Application of rapid current surges to electric transient prospecting
AIME Tech. Pub., 1216, Vol. 4, Feb. 1940

27. L. STATHAM — Electric earth transients in geophysical prospecting
Geophysics, Vol. 1, p. 271-277, 1936

28. P.F. HAWLEY — Transients in electrical prospecting
Geophysics, Vol. 3, p. 247-257, July 1938

29. P.W. KLIPSCH — Recent developments in eltran prospecting
Geophysics, Vol. 4, p. 283-291, Oct. 1939

I.3.3. Procédés de prospection en haute fréquence

30. W.M. BARRET — Exploring earth with radio waves
World Petrol., Vol. 20, p. 52-53, Apr.1949

31. W.M. BARRET — Salt mine tests prove earth penetration by radio waves
World Petrol., Vol. 20, p. 62-63, 1949

32. W.M. BARRET — Note on the radio-transmission demontration at Grand Saline, Texas
Geophysics, Vol. 17, p. 544-549, 1952

33. C.A. HEILAND — Geophysical exploration
Prentice-Hall Inc., Englewood Cliffs, N.J., p. 667, 1946

I.4. Mesure directe des paramètres électromagnétiques du sol ou de la mer et expériences de transmission électromagnétique à travers le sol et la mer.

I.4.I. Travaux expérimentaux classés par ordre chronologique : 1928 à 1954

34. L.C. ILSLEY, H.B. FREEMAN, D.H. ZELLERS — Experiment in underground communication through earth strata
Dept. of Commerce, Bur. of Mines, Tech. Paper, p. 433, 1928

35. A.S. EVE, D.A. KEYS, F.W. LEE — The penetration of rock by electromagnetic waves at audio frequency
Proc. I.R.E., Vol. 17, p. 2072, Nov. 1929

36. A.S. EVE, D.A. KEYS, F.W. LEE — Penetration of rocks by electromagnetic waves
Nature, Vol. 124, n° 3118, p. 178-179, 1929

37. A.S. EVE — Absorption of electromagnetic induction and radiation by rocks
Amer. Inst. of Mining and Met. Eng. Tech. Pub., Vol. 316, 1930 and
Vol. 97, p. 160-168, 1932

38. A.R. PETROVSKY — R. SKARIATIN, A. SELESNEW, B.N. DOSTAVALOV, L. KLEINMANN
Über die ondometrischen Arbeiten des Institutes fur die angewandte Geophysik
Arbeiten des J.A.G., p. 45-69, 1930 (in russian)

39. J.A. RATCLIFFE, F.W.G. WHITE — The electrical properties of the soil at radio frequencies
Phil. Mag., Vol. 7, 10, n° 65, p. 667-680, 1930

40. J.W. JOYCE — Electromagnetic absorption by rocks with some experimental obsevationstaken at Mammoth Cave in Kentucky
Bur. of Mines, Tech. Paper, 497, 1931

41. R.L. SMITH-ROSE — The electrical properties of sea-water for alternating currents
Proc. Roy. Soc., A, Vol. 143, p. 135-146, 1933

42. R.L. SMITH-ROSE — Electrical measurements on soil with alternative currents
J. Inst. Elec. Engrs, LONDON, Vol. 75, p. 221-237, 1934

43. R.L. SMITH-ROSE — The electrical properties of soil at frequencies up to 100 megacycles per second
Proc. Phys. Soc., Vol. 47, p. 923, 1935

44. J.N. HUMMEL — Unterlagen der geoelektrischen Aufschliessungsmethoden
Beitr. Ang. Geophys., Vol. 5, p.32, 1935

45. S.G. BIMALENDU, S.R. KHASTGIR — Direct determination of the electric constants of soil at radio-frequency
Phil. Mag., (7), Vol. 22, n° 146, p. 265-273, 1936

46. D. DOBORZYNSKI — Uber den Radioempfang in der ojcow-Hölen (in polish.)
Przegląd. Radjotechn., n° 7-8, 1936

47. D. DOBORZYNSKI — Experimenteller Beitrag zum Problem des unterirdischen Rundfunkempfanges
Hochfrequenztechn. u. E.47, 12, 1936

48. D. DOBORZYNSKI — Uber das Problem der Radiokommunikation in Bergwerken (in polish)
Przegladu-Gornizco-Huntniczego, 1937

49. S.R. KHASTGIR, M.K. CHAKRAVARTY — Direct determination of the electr. constants of soil at ultra high radio frequencies - Phil. Mag., (7), Vol. 25, p.793, 1938

50. S.S. BANERJEE, R.D. JOSHI — Dielectric constant and conductivity of soil at high radio frequencies
Phil. Mag. (7), Vol. 25, n° 172, p. 1025-1033, 1938

51. J.L. ALBERT — V.V. MIGULIN and P.A. RYASIN
Investigation of the phase structure of the electromagnetic field and the velocity of radio-waves. J. Phys. U.S.S.R., Vol. 4, n°12 , p. 11-13, 1941

52. D. SILVERMAN, D. SHEFFET — Note on the transmission of radio waves through the earth. Geophysics, Vol. 7, p. 406-413, 1942

53. B.F. HOWELL — Some effects of geologic structure on radio reception. Geophysics, Vol. 8, p. 165-176, 1943

54. E.P. TROUNSON, S.J. RAFF — The attenuation of plane electromagnetic waves in sea-water. U.S.N.O.L., Memo, n° 8936, Jan. 1947

55. T.L. WADLEY — Underground communication by radio in gold mines on the witwatersrand. South African Council for Sci. and In. Res., Rept. T.R.L.3., Nov. 1946

56. A. PETROVSKY — Der erste Versuch uber die Fortpflanzung Hertzscher Wellen durch ewig gefrorenen Boden (in russian). Trudy Inst. Merzlotovendenija Imeni, V.A. Obrucheva, 5

57. E.W. FELEGY, E.J. COGGESHALL — Applicability of radio to emergency mine communications. U.S. Bur. of Mines, Rept. R. I.42 94, May 1948

58. R.I.B. COOPER — The attenuation of ultra-high frequency electromagnetic radiation by rocks. Proc. Phys. Soc., Vol. 61, p. 40-47, p. 482-483, 1948

59. O.C. HAYCOCK — E.C. MADSEN, S.R. HURST. Propagation of electromagnetic waves in the earth. Geophysics, Vol. 14, n° 2, p. 162-171, Apr. 1949

60. W.C. PRITCHETT — Attenuation of radio frequency waves through the earth. Geophysics, Vol. 17, n° 2, p. 193-217, 1952

61. C.A. BAYS — Study of the propagation of electromagnetic waves through lithologic formations. Quart.Prog. Rept., Signal Corps Project, n°26, 182B, 1952

62. E.W. FELEGY — Underground radio communication in lake Superior District Mines. Mining Engng., Vol. 5, p. 518-521, 1953

63. McGEHEE Jr.F.L. — Propagation of radio frequency energy through the earth. Geophysics, Vol. 19, n° 3, p. 459-477, 1954

I.4.2. Travaux de FRITSCH

64. V. FRITSCH — Beitrag zum Studium der Ausbreitung elektromagnetischer Felder in unterirdischen Hohlräumen. Hochfrequenztechn. u.E. Vol. 39, n° 4, p. 136-139, 1932

65. V. FRITSCH — Lo smorzamento delle onde Hertziane attraverso i conduttori geologici. Geofisica pura appl., Vol. 4, n° 1, p. 15-37, 1942

66. V. FRITSCH — Beiträge zur Funkgeologie VIII. Ausbreitung hertzscher Wellen in geologischen Leitern. Beitr. angew. Geophysik, Vol. 11, n° 2, p. 163-199, 1943

67. V. FRITSCH — Propagation of radiofrequency electromagnetic fields in geological conductors. Nat. Bur. Stands. J. Res., Vol. 67D, n° 4, p. 161-178, 1963

I.4.3. Travaux expérimentaux français postérieurs à 1960

68. R. DESBRANDES, G. MOREL — Prospection électromagnétique. Etude expérimentale 1959. Rapport I.F.P., n° 3983, 1960

69. R. GABILLARD — R. DESBRANDES, Y. MORINEAU. Prospection électromagnétique. Etude de la propagation des ondes électromagnétiques dans le sol. Rapport I.F.P., n° 6945, 1961

70. R. DESBRANDES — Prospection électromagnétique. Mise au point au 1er Janv. 1962. Rapport I.F.P., n° 7061, 1962

71. R. GABILLARD — Résultats et interprétation des expériences de propagation d'ondes électromagnétiques effectuées à TRIEL en Mai et Juin 1964. Rapport I.F.P., n 11117, 1964

72. R. GABILLARD — Rapport trimestriel d'activité. Contrat D.R.M.E. 19[illegible]. Rapport I.F.P., n° 11650, 1965

73. R. GABILLARD — Méthode de mesure de la vitesse de propagation des ondes électromagnétiques dans le sol et appareillage pour sa mise en oeuvre. Brevet I.F.P., n° 10593, 1965

74. J.P. DUBUS — Etude et réalisation d'un appareillage permettant la mesure de la vitesse de propagation d'une onde électromagnétique dans le sol. Thèse C.N.A.M., LILLE, 1965

75. J. FONTAINE — Contribution à l'étude théorique et expérimentale de la vitesse de propagation des ondes électromagnétiques dans le sol. Thèse 3ème Cycle, LILLE, 1966

76. R. GABILLARD — Mesure directe de la vitesse de propagation des ondes électromagnétiques en milieu géologique. Semaine d'études du CETHEDEC (VAIS-les-BAINS - 28 juin - 3 juillet 1965). Publié dans la Revue du CETHEDEC, n° 8, p. 119-145, 4ème tr. 1966

77. R. GABILLARD — Communications à travers le sol. AGARD Conf. Proc. n° 20, Sub-surface Communications, p. 355-386, 1966

78. R. GABILLARD — Compte rendu succinct des expériences de propagation d'ondes électromagnétiques effectuées dans la fosse de Vieux Condé des Houillères du Nord- Pas-de-Calais (8p.) Contrat D.R.M.E. n°196-64 - Rapport I.R.E.L 66-002 Mars 1966

79. R. GABILLARD — Expériences de propagation d'ondes électromagnétiques effectuées [illegible] teau de Vaucluse.
Contrat D.R.M.E. n° 196-64 - Rapport I.R.E.L. 66.004 - Avr. 1966 [illegible].

80. R. GABILLARD — R. DESBRANDES, F. LOUAGE and J. FONTAINE
Experimental and theoretical study of electromagnetic propagation in a geological waveguide
I.E.E. Conf. on MF, LF and VLF Radio Propagation, LONDON,
Nov. 1967, Conf. Publ. n° 36, p. 320-325

81. R. GABILLARD — J. MARCHANT and R. DESBRANDES
Experimental and theoretical study of the propagation of electromagnetic pulses of short duration through the earth I.E.E. Conf. on MF, LF and VLF Radio Propagation, LONDON, Nov. 1967, Conf. Publ. n° 36, p. 326-330

82. R. GABILLARD — Compte-rendu succint des expériences de propagation d'impulsions électromagnétiques effectuées dans la fosse de Vieux-Condé des Houillères du Nord Pas-de-Calais Contrat D.R.M.E. n° 201-65 - Rapport I.R.E.L. 67-102, Fév. 1967, 6 p.

83. R. GABILLARD, J. MARCHANT — Etude expérimentale et théorique de la propagation d'une impulsion électromagnétique brève dans le sol
Contrat D.R.M.E. n° 201-65, Rapport I.R.E.L. 67-107, Juin 1967, 24p.

84. J. MARCHANT — Etude expérimentale et théorique de la propagation d'une impulsion électromagnétique brève dans le sol. Thèse Docteur-Ingénieur, LILLE, Juillet 1967

85. R. GABILLARD — Démonstration de transmission d'ordres par ondes électromagnétiques se propageant à travers le sol - TAVERNY - 11 mars 1967 - Contrat D.R.M.E. n° 173-66. Rapport I.R.E.L. 67-104, Mars 1967, 4 p.

86. R. GABILLARD — Démonstration de télécommunication télex par ondes électromagnétiques se propageant à travers le sol.TAVERNY - Octobre 1967 - Contrat D.R.M.E. n° 173-66. Rapport I.R.E.L. 67-111, Oct. 1967, 7 p.

87. R. GABILLARD, J.P. DUBUS — Méthode de repérage et de télécommunications de survie ou de service pour mineurs et spéléologues et appareillage pour sa mise en oeuvre
Brevet français n° 1.553.455, PV n° 139.061, Fév. 1968

88. R. GABILLARD — Etude de la transmission des ondes électromagnétiques entre terminaux souterrains - Contrat D.R.M.E. n° 173 - 66.
Rapport I.R.E.L. 69-001, Janv. 1969, 52 p.

89. Ch. CLARISSE — Conception et réalisation pratique d'un système de transmission d'informations à travers le sol. Application aux télémesures pétrolières
Thèse Docteur-Ingénieur, LILLE, Juillet 1969

90. H. GUTTON — Propagation des fréquences très basses. Compte-rendu d'expériences de transmission à 40 Hz. AGARD - Conf. Proc. n° 20 Sub-surface communications, p. 409-424, 1966.

I.4.4. Travaux expérimentaux postérieurs à 1960 effectués aux U.S.A.

91. E.J. KIRKSCETHER — Ground constant measurements using a section of balanced two-wire transmission line
I.R.E. Trans. on Ant. and Prop., Vol. AP-8, p.307-312, May 1960

92. R.N. GHOSE — The radiator to medium coupling in an underground communication system
Proc. Natl. Elec. Conf., p. 279-282, 1960

93. R.N. GHOSE — The long range sub-surface communication system
Proc. VIth IRE Natl. Commun. Symp., p. 110-120, 1960

94. G.S. SARAN, G. HELD — Field strenght measurements in fresh water
J. Res. NBS, Vol. 64D, p. 435-437, Sep.-Oct. 1960

95. M.B. KRAICHMAN — Basic experimental studies of the magnetic field from electromagnetic sources immersed in a semi-infinite conducting medium
J. Res. NBS, Vol. 64D, p.21-25, Jan.Feb. 1960

96. T.C. LAMTER — M.E. LOUAPRE, A.P. STOGRYN
Laboratory simulation of VLF Propagation and underground antenna performance
1961 IRE WESCON Convention, Los Angeles, Calif., paper 31/1, Aug. 1961

97. G.J. HARMON — Radio wave propagation through the earth's rock strata-a new medium of communication - IRE Globecom Convention Record, p. 31-34, 1961

98. A.W. GUY — Experimental data on buried antennas
Boeing Aircraft Co, Seattle, Wash. Preliminary Rept., D2-11190

99. A.W. GUY, G. HASSERJIAN — Design criteria for buried antennas
Boeing Aircraft Co, Seattle, Wash., Preliminary Rept., D2-7760, Janv. 1961

100. K. IIZUKA, R.W.P. KING — Apparatus for the study of the properties of antennas in a conducting medium
Cruft Lab., Harvard U., Cambridge, Mass. Sci, Rept. N° 1, May 1961

101. J.T. de BETTENCOURT, R.A. SUTCLIFFE — Studies in deep strata communication - Communications and data processing operation. The Raytheon Co, Norwood, Mass., Contrat n° AF19 (604)-8359, Oct. 1962 (Final rept. for U.S. Air force Cambridge Res. Lab.)

102. J.T. de BETTENCOURT — Resistivity investigation on Cape Cod
Geoscience Inc., Natick, Mass. U.S. Air Force Rept. GAF 13-26, Aug. 1962

103. K. IIZUKA — An experimental study of the insulated dipole antenna immersed in a conducting medium. Gordon Mckay Lab. Sci. Rept.3, HARVARD UNIVERSITY, 1962

104. K. IIZUKA, R.W.P. KING — An experimental study of the half-wave dipole antenna immersed in a stratified conducting medium. IRE Trans. Antenna Prop., Vol. AP-10, p. 393-399, 1962

105. A.W. GUY, G. HASSERJIAN — Design criteria for buried antennas. Boeing Airplane Co, Doc. D2-7760, 1961

106. A.W. GUY, G. HASSERJIAN — Impedance properties of large subsurface antenna arrays, I.E.E.E. Trans. Antennas Propag., Vol. AP-11, p. 232-240 May 1963

107. G. HASSERJIAN, A.W. GUY — Low-frequency subsurface antennas. I.E.E.E. Trans. Anten. Prop., Vol. AP-11, p. 225-231, May, 1963

108. W.E. BLAIR — Experimental verification of dipole radiation in a conducting half-space. I.E.E.E. Trans. Anten. Prop., Vol. AP-11, n° 3, p. 269-275, May 1963

109. K. IIZUKA — An experimental study of the insulated dipole antenna immersed in a conducting medium. I.E.E.E. Trans. Anten. Prop., Vol.AP-11,p.518-532, Sept.1963

110. J. CAROLAN, J.T. de BETTENCOURT — Radio waves in rock near overburden rock interface. I.E.E.E. Trans. Anten. Prop., Vol. AP-11, p. 336-338, May 1963

111. J.T. de BETTENCOURT, J.W. FRAZIER — Rock electrical characteristics deduced from depth attenuation rates (in drill holes). I.E.E.E. Trans. Anten. Prop., Vol. AP-11, n° 3, p.358-363 May 1963

112. C.K.H. TSAO, J.T. de BETTENCOURT — Conductivity measurements in dissipative media with electrically short probes. Sci. Rept. n°6, Raytheon Co, Equipment Div., CADPO, Contrat AF19(628)-2362 Aug. 1964

113. C.K.H. TSAO — Subsurface radio transmission tests in Cheyenne Mountain. Sci. Rept. n°7, Raytheon Co, Equipment Div., CADPO, Contrat AF19(628)-2362, Feb. 1965

114. AMES L.A. — J.W. FRAZIER, A.S. ORANGE. Review of the earth mode communication program at Air Force Cambridge Res. Lab. - Paper presented at NATO, 12th AGARD Symp., PARIS-FRANCE Apr.1966

115. C.K.H. TSAO, J.T. de BETTENCOURT — Subsurface radio propagation experiments. NATO, 12th AGARD Symp., PARIS, FRANCE, Apr. 1966. Subsurface communications Conf. Proc. n° 20, p. 471-490, 1966

116. J.T. de BETTENCOURT — Review of radio propagation below the earth's surface. Paper presented at URSI XVth General Assembly, Com.2, MUNICH, GERMANY, Sept. 1966

117. C.K.H. TSAO, J.T. de BETTENCOURT — Measurement of phase constant for rock propagated signals. I.E.E.E. Trans. on Comm. Tech., Vol. COM-15, n°4, Aug. 1967

118. C.K.H. TSAO, J.T. de BETTENCOURT — Subsurface radio communication. I.E.E. Conf. on MF, LF and VLF Radio propagation, LONDON, Nov. 1967, I.E.E. Conf. Publ. n° 36, p. 313-319

119. R.M. WUNDT — New results on buried antennas for use at medium and high frequencies. Northeast Electron. Res. and Engng Meetg (NEREM) BOSTON, Mass., Nov. 1964

120. J. GALEJS — Impedance and radiation efficiency of buried dipole type and loop antennas. AGARD Conf. Proc. n°20, Sub-surface Communications, p.629-657, 1966

121. E. SODERBERG — ELF Measurements in the sea off the Baja California Coast. Paper presented at 47th Annual Meetg, AGU, Wash.D.C., 19-22 Apr. 1966

122. E. SODERBERG — Undersea ELF measurements of the horizontal electromagnetic field to depths of 300 meters. AGARD Conf. Proc., n° 20, Sub-surface Communications, 1966, p. 453-470

7.5. Références complémentaires et applications diverses

123. E. CORTI — G. FRANCESCHETTI, G. LATMIRAL. Oblate spheroidal antennas for conducting media. URSI Symp. on electromagnetic waves, STRESA, June 1968. Paper n° 93, session 5

124. J.C. GOSSELIN — Transmission des paramètres de fond par ondes électromagnétiques guidées le long du train de tiges. Rapport I.F.P., n° 17812, Fév. 1970

125. Committee on Mine rescue and survival techniques — Mine rescue and Survival. Interim Rept. of the Committee on Mine Rescue and survival techniques. National Acad. of Engng (2101 Constitution Avenue, Wash.D.C. 20418), Nov.1969

126. P. CORNILLE — Phase measurements of electromagnetic field components . Conf. on Environmental effects on antenna performance ESSA, BOULDER, July 1969, 6p.

127. R. GABILLARD — F. LOUAGE et R. DESBRANDES. Procédé de prospection des terrains situés autour d'un forage. Brevet français de l'I.F.P., PV n°156.220, Juin 1968

128. R. GABILLARD, J.P. DUBUS — Procédé de détection des cavités souterraines et appareillage pour sa mise en oeuvre. Brevet français n°1.510.996, PV n° 18795 Nord, Déc. 1966

129. J.P. DUBUS — Recherche théorique et expérimentale des possibilités d'adaptation de certaines méthodes de prospection électromagnétique à la détection des cavités souterraines. Thèse 3ème Cycle, LILLE, Oct. 1968

130. R. GABILLARD — J.P. DUBUS, F. LOUAGE
Procédé électromagnétique pour la détection des carrières souterraines. Simulation sur une cuve électrolytique HF Onde Electrique, n° 503, p. 3-8, Fév. 1969

131. M. CAUTERMAN — Contribution à l'étude et à la réalisation d'un appareillage électronique permettant le repérage systématique de cavités souterraines à faible profondeur. D.E.A., LILLE, Juillet 1969

2. ETUDES THEORIQUES

2.1. *Livres et numéros spéciaux de revues*

132. O. HEAVISIDE — Electrical papers. Vol. I and 2, Macmillan. Co, LONDON, ENGLAND, 1892

133. O. HEAVISIDE — Electromagnetic theory
Vol.I., The Electrician Printing and Publishing Co, LONDON, ENGLAND, 1893

134. O. HEAVISIDE — Electromagnetic theory. Vols. 2 and 3., Ernest Benn, Ltd, England, 1922

135. J.C. MAXWELL — A treatise on electricity and magnetism. Clarendon Press, OXFORD, 1893

136. N.W. McLACHLAN — Bessel functions for engineers. Clarendon Press. OXFORD, 1934

137. J.A. STRATTON — Electromagnetic theory. McGRAW-HILL Book Co Inc., New York, N.Y., 1941

138. S.A. SCHELKUNOFF — Electromagnetic waves. D. Van Nostrand Co, Inc., 1943

139. E.T. WHITTAKER, G.N. WATSON — A course of modern analysis. 4th ed., Cambridge University Press, LONDON, 1944

140. G.N. WATSON — A treatise on the theory of Bessel functions
2d ed., Cambridge University Press, LONDON, 1944

141. R.V. CHURCHILL — Modern operational mathematics in Engineering
Tables of Laplace Transforms, Mc Graw-Hill Co, NEW YORK, 1944

142. R.W.P. KING — Electromagnetic Engineering
Mc Graw-Hill Book Co, New York, N.Y., Vol. I., 1945

143. E. JAHNKE, F. EMDE — Tables of functions
4th ed, Dover Publ., Inc., New York, 1945

144. C.A. HEILAND — Geophysical exploration. Prentice Hall, Inc., Englewood Cliffs, N.J., 1946

145. HARVARD Univ. — Tables of the generalized exponential-integral functions
Ann. Computation Lab., Vol. 21, 1949

146. E.D. SUNDE — Earth conduction effects in transmission systems
D.VAN NOSTRAND Co, Inc. Princeton, N.J., 1949

147. E.C. JORDAN — Electromagnetic waves and radiating systems
Prentice-Hall, Inc., New York, N.Y., 1950

148. S.A. SCHELKUNOFF — Advanced antenna theory. J. WILEY, New York, 1952

149. S.A.SCHELKUNOFF, H.T. FRIIS — Antennas theory and practice
J. WILEY, New York, 1952

150. R.W.P. KING — The theory of linear antennas. Harvard Univ. Press, Cambridge, Mass., 1956

151. L.M. BREKHOVSKIKH — Waves in layered media. Academic Press, New York, 1960

152. R.F. HARRINGTON — Time-Harmonic electromagnetic fields. Mc Graw Hill Co, New York, 1961

153. H. JASIK — Antenna Engineering handbook. Mc Graw Hill Co, New York, 1961

154. Y.L. LUKE — Integrals of Bessel functions. Mc Graw Hill Co, New York, 1962

155. J.R. WAIT — Electromagnetic waves in stratified media. Pergamon Press, New York, 1962

156. J.R. WAIT — May 1963 issue of I.E.E.E. Trans. Antennas Propagation
Vol.AP-11, n°3 devoted to electromagnetic waves in the earth

157. A. BANOS Jr. — Dipole radiation in the presence of a conducting half-space
Pergamon Press, New York 1966

158. AGARD Conf. — Sub-Surface Communications
Selected papers from the 12th Symposium of the Avionics Panel of AGARD held in PARIS, FRANCE on 25-29 April 1966 AGARD Proc. n°20, 1966

159. M. BOUIX — Les discontinuitésdu rayonnement électromagnétique. DUNOD, PARIS, 1966

160. J. GALEJS — Antennas in inhomogeneous media. Pergamon Press, New York, 1968

161. R.E. COLLIN, F.J. ZUCKER (ed.) — Antenna theory
Vol. I and II, Mc Graw Hill Co, New York, 1969

2.2. *Antennes et propagation dans un milieu conducteur homogène et infini*

162. C.T. TAI — Radiation of a hertzian dipole immersed in a dissipative medium
Cruft Lab., Harvard Univ., Cambridge, Mass. Rept. n°TR21, Oct. 1947

163. C.T. TAI — On radiation and radiating systems in the presence of a dissipative medium
Cruft Lab. Harvard Univ., Cambridge, Mass. Rept n°TR77, May 1949

164. J.R. WAIT — Electromagnetic radiation in the earth (a theoretical investigation)
Univ. of TORONTO, 1-69, 1950

165. J.R. WAIT — A note on dipole radiation in a conducting medium
Geophysics, Vol. 17, p. 978-979, Oct. 1952

166. J.R. WAIT — Electromagnetic fields of current-carrying wires in a conducting medium
Can. J. Phys., Vol. 30, p. 512-523, Sept. 1952

167. J.R. WAIT — The magnetic dipole antenna immersed in a conducting medium
Proc. I.R.E., Vol. 40, p. 1244-1245, Oct. 1952

168. J.R. WAIT — The receiving loop with a hollow prolate spheroidal core
Can. J. Tech., Vol. 31, p. 132-139, June 1953

169. J.E. STORER — Impedance of thin-wire loop antennas
Trans. AIEE, Vol. 75 (Communication and Electronics) p. 606-619, Nov. 1956

170. S. ADACHI, Y. MUSHIAKE — Studies of large circular loop antennas
Sci. Rep. Res. Inst. Tohoku Univ. Sér. B (Elec.Comm.) Vol. 9, p.79, n°2, 1957

171. J.R. WAIT — Insulated loop antenna immersed in a conducting medium
J. Res. NBS, Vol. 59, p. 133-137, Aug. 1957

172. R.W.P. KING, C.W. HARRISON — Half-wave cylindrical antenna in a dissipative medium ; current and impedance
J. Res. NBS, Vol. 64D, p. 365-380, July-Aug. 1960

173. R.W.P. KING — Dipoles in dissipative media
Cruft Lab. Harvard Univ., Cambridge, Mass., Tech. Rept.n° 336, Feb.1, 1961

174. R.W.P. KING — Dipoles in dissipative media in ELECTROMAGNETIC WAVES
R.E. LANGER, Ed. U. of Wisconsin Press, Madison, Wis., p. 199-241, 1962

175. D.W. GOOCH — C.W. HARRISON, R.W.P. KING, T.T.WU
Impedances and admittances of long antennas in air and in dissipative media with tables of the functions $\sqrt{1 \pm ip}$
Cruft Lab. Tech. Rept. 353, Harvard University, 1962

176. G.A. DESCHAMPS — Impedance of an antennain a conducting medium
I.R.E. Trans. Antennas Propagation, Vol. AP-10, p. 648-650, 1962

177. T.T. WU — Theory of thin circular loop antenna
J. Math. Phys., Vol. 3, p. 1301-1304, Nov. Déc. 1962

178. K. IIZUKA, R.W.P. KING — The dipole antenna immersed in a homogeneous conducting medium
I.R.E. Trans. Antennas Propagation, Vol.AP-10, p.384-392, 1962

179. M.B. KRAICHMAN — Impedance of a circular loop in an infinite conducting medium
J.Res.Natl.Bur.Std.U.S,Vol.66D(radio prop.), p. 499-503, 1962

180. C.C. CHEN — The small loop antenna immersed in a dissipative medium
Cruft Lab. Tech. Rept., 369, Harvard University, 1962

181. S. CHEN, C.T. TAI — The input impedance of thin biconical antennas immersed in a dissipative or an ionized medium
Antenna Lab. Tech. Rept., 1021-14, Ohio State University, 1962

182. R.W.P. KING — Dipoles in dissipative medium
Symp. Electromag. Waves, U. of Wisconsin Press, Madison, Wis., p.199-241,1962

183. R.W.P. KING, K. IIZUKA — The complete electromagnetic field of a half-wave dipole in a dissipative medium
I.E.E.E. Trans. Antennas Propagation, Vol. AP-11, p.275-285, May 1963

184. C.L. CHEN, R.W.P. KING — The small bare loop antenna immersed in a dissipative medium
I.E.E.E. Trans. Antennas Prop., Vol. AP-11, p.266-269, May 1963

185. R. GABILLARD — Réflexions sur le problème de la propagation d'une onde électromagnétique dans le sol.
Revue de l'I.F.P., Vol. 18, n° 9, p. 1137-1164, Sept. 1963

186. R.H. WILLIAMS — Charge density response in a lossy medium
I.E.E.E. Trans. Antennas Prop., Vol. AP-11,n°3, p.372, May 1963

187. J.R. WAIT, K.P. SPIES — A note on the insulated loop antenna immersed in a conducting medium
Radio Sci. J. Res. NBS/USNC-URSI, Vol. 68D, n° 11 p.1249-1250, Nov. 1964

188. J.R. WAIT — Electromagnetic fields in lossy media
The U.S. National Committee Rept. for Commission 6 of URSI, Subcomm. 6.3. Electromagnetics, Radio Sci.J.
Res. NBS/USNC-URSI, Vol. 68D, n°4, p.463-465, Apr. 1964

189. R.W.P. KING — C.W. HARRISON, D.G. TINGLEY
The admittance of bare circular loop antennas in a dissipative medium
I.E.E.E. Trans. on Antennas and Propagation, Vol. AP-12, p.434-438, July 1964

190. K. IIZUKA — The circular loop antenna immersed in a dissipative medium
I.E.E.E. Trans. Anten. Prop., Vol. AP-13, p.43-47, Jan.1965

191. R. ROW — Insulated loop antenna in a conducting spherical shell
I.E.E.E. Trans. Anten.Prop., Vol.AP-13,p.216-218, March 1965

192. J. GALEJS — Admittance of insulated loop antennas in a dissipative medium
I.E.E.E. Trans. Anten.Prop.,Vol.AP-13,p.229-235, March 1965

193. R.W.P. KING — C.W. HARRISON, D.G. TINGLEY
The current in bore circular loop antennas in a dissipative medium
I.E.E.E. Trans. Anten.Prop.,Vol.AP-13, n°4, p.529-531, July 1965

194. C.R. BURROWS — Plane waves in dissipative media
I.E.E.E. Trans. Anten.Prop.,Vol.AP-13, n°5, p. 759-774, Sept. 1965

195. C.J. BENNING — Impedance of a loop antenna in a conducting medium
I.E.E.E.Trans.Anten.Prop.,Vol.AP-14, n°2,p.242-243, March 1966

196. B. BLACHIER — Etude de la réception dans la mer par dipôle et antenne volumétrique
A.G.A.R.D. Conf.Proc.,n°20, Sub-surface communications p.621-628, 1966

197. J.R. WAIT — Theories of prolate spheroidal antennas
Radio Sci., Vol. 1(new series), n°4, p. 475-512, Apr.1966

198. K. IIZUKA — R.W.P. KING, C.W. HARRISON
Self and mutual admittances of two identical circular loop antennas in a conducting medium and in air
I.E.E.E. Trans.Anten.Prop., Vol.AP-14, n°4, p.440-450, July 1966

199. E. CORTI — G. FRANCESCHETTI, G. LATMIRAL
Oblate spheroidal antennas for conducting media
URSI Symp. on electromagnetic waves, STRESA, paper n°93 session 5, June 1968

200. J.R. WAIT — Electromagnetic fields of sources in lossy media in Antenna theory
Ed. by R.E. COLLIN and F.J.ZUCKER, Mc Graw Hill Co. New York, 1969

2.3. Rayonnement des antennes placées dans l'atmosphère au-dessus de la mer ou d'un sol homogène ou stratifié

2.3.1. Premières publications sur la propagation des ondes radio au-dessus d'un sol de conductivité finie

201. T. LEVI-CIVITA — Influence di un schemo conduttorre sul campo elettromagnetic
R.Acc.Lincie, Ser. 5A, Vol. XI, p. 163, 191, 228, 1902

202. A. SOMMERFELD — Uber die Ausbreitung der Wellen in der drahtlosen Telegraphie
Ann. Physik, Vol. 28, p. 665, 1909

203. H. WEYL — Ausbreitung elektromagnetischer Wellen über einem ebenen Leiter
Ann. Physik, sér.4, Vol. 60, p. 481-500, 1919

204. A. SOMMERFELD — Uber die Ausbreitung der Wellen in der drahtlosen Telegraphie
Ann. Physik, sér.4, Vol.81, n°17, p. 1135-1153, Déc. 1926

205. M.J.O. STRUTT — Strachlung von Antennen unter den Einfluss der Erdbodeneigenschaften
Ann. Physik., Vol.1, n°1, p.721-750, 1929

206. K.A. NORTON — Propagation of radio waves over a plane earth
Nature, Vol. 135, p. 954-955, June 8, 1935

207. K.A. NORTON — The propagation of radio waves over the surface of the earth and in the upper atmosphere
Pt.I., Proc.IRE, Vol. 24, p. 1367-1387, Oct. 1936
Pr.II., Proc. IRE, Vol.25, p. 1203-1236, Sept. 1937

208. K.A. NORTON — Space and surface waves in radio propagation
Phys. Rev. Vol.52, p. 132-133, July 15, 1937

209. K.A. NORTON — Physical reality of space and surface waves in the radiation field of radio antennas
Proc.IRE, Vol.25, p. 1192-1202, Sept. 1937

210. C.R. BURROWS — The surface wave in radio propagation over plane earth
Proc. IRE, Vol. 25, p. 219-229, 1937

211. W.H. WISE — The physical reality of Zenneck's surface wave
Bell System Tech. J., Vol.16, p.35-44, Jan. 1937

212. S.O. RICE — Series for the wave function of a radiating dipole at the earth's surface
Bell System Tech. J., Vol.16, p.101-109, Jan. 1937

2.3.2. Couplage mutuel entre des câbles et des boucles placés à la surface du sol

213. G.A. CAMPBELL — Mutual impedancesof grounded circuits
Bell System Tech. J., Vol.2., p. 1, 1923

214. J.R. CARSON — Wave propagation in overhead wires with ground return
Bell System Tech.J., Vol.5, p.539-554, Oct. 1926

215. J.R. CARSON — Ground return impedance : underground wire with earth return
Bell System Tech.J., Vol.8, p. 94-98, Jan. 1929

216. R.M. FOSTER — Mutual impedance of grounded wires lying on the surface of the earth
Bell System Tech.J., Vol.10, p.408-419, July 1931

217. J. RIORDAN, E.D. SUNDE — Mutual impedance of grounded waves for horizontally stratified two-layer earth
Bell System Tech. J., Vol.12, p. 162-177, Apr. 1933

218. R.M. FOSTER — Mutual impedance of grounded wires lying on or above the surface of the earth. Bell System Tech. J., Vol. 12, p. 264-287, July 1933

219. S.S. WEST — Mutual impedance of collinear grounded wires
Geophysics, Vol. 8, p. 157-164, Apr. 1943

220. J.R. WAIT — Mutual inductance of circuits on a two layer earth
Can. J. Phys., Vol. 30, p. 450-452, Sept. 1952

221. J.R. WAIT — Mutual coupling of loops lying on the ground
Geophys., Vol.19, p. 290-296, Apr. 1954

222. J.R. WAIT — Mutual electromagnetic coupling of loops over a homogeneous ground
Geophys., Vol.20, n°3, p. 630-637, July 1955

223. J.R. WAIT — Mutual electromagnetic coupling of loops over a homogeneous ground - an additional note
Geophys., Vol. 21, n°2, p. 479-484, Apr. 1956

224. H. KURSS — Electromagnetic coupling of horizontal loops over a stratified ground
ESSA and Adelphi U., Garden City, N.Y., Conf. on environmental effects on antennas performances, BOULDER, COLORADO, July 1969

7.3.3. Rayonnement de dipôles et antennes électriques et magnétiques placés au-dessus du sol

225. A. WOLF — Electric field of an oscillating dipole on the surface of a two-layer earth
Geophysics, Vol.11, p. 518-534, Oct. 1946

226. W.B. LEWIS — Discussion on electric field of an oscillating dipole on the surface of a two-layer earth
Geophysics, Vol. 11, p. 535-537, Oct. 1946

227. J.R. WAIT — The magnetic dipole over the horizontally stratified earth
Can. J. Phys., Vol. 29, p. 577-592, Nov. 1951

228. J.R. WAIT — Current-carrying wire loops in a simple inhomogeneous region
J. appl. Phys., Vol.23, p.497-498, Apr. 1952

229. J.R. WAIT — Radiation resistance of a small circular loop in the presence of a conducting ground. J. appl. Phys., Vol.24, p. 646-649, May 1953

230. J.R. WAIT — The fields of a line source of current over a stratified conductor
Appl. Sci. Res., Vol. B3, p. 279-292, 1953

231. J.R. WAIT — Induction by a horizontal oscillating magnetic dipole over a conducting homogeneous earth
Trans. amer. Geophys. Union, Vol. 34, n°2, Apr. 1953, p. 185-188

232. J.R. WAIT — Radiation from a vertical electric dipole over a stratified ground
IRE Trans. Anten Prop., Vol. AP-1, p. 9-11, July 1953

233. J.R. WAIT, W.C.G. FRASER — Radiation from a vertical electric dipole over a stratified ground
Part. II, IRE Trans. Anten. Prop., Vol. AP-2, p.144-146, Oct.1954

234. J.R. WAIT — Radiation from a ground antenna. Can. J. Tech., Vol.32, p.1-9, Jan.1954

235. R.W.P. KING — Antennas over a conducting region in "Theory of linear Antennas"
Harvard Univ. Press, Cambridge Mass., 1956

236. F. MINAW — La résistance de rayonnement d'une antenne placée au-dessus d'un plan conducteur, étudiée au point de vue de la prospection géophysique
C.R. Acad. Sci. fr., p. 1603-1605, 1956

237. J.R. WAIT — Induction by an oscillating magnetic dipole over a two layer ground
Appl. Sci. Res., Section B, Vol.7, p.73-80, 1958

238. L.B. SLICHTER, L. KNOPOFF — Field of an alternating magnetic dipole on the surface of a layered earth
Geophys., Vol. 24, p. 77-88, Feb. 1959

239. J.R. WAIT — On the impedance of long wire suspended over the ground
Proc. IRE, Vol. 49, p. 1576, Oct. 1961

240. B.K. BHATTACHARYYA — Input resistances of horizontal electric and vertical magnetic dipoles over a homogeneous ground
I.E.E.E. Trans. Anten. Prop., Vol. AP-11, n°3, p. 261-266, May 1963

241. J.R. WAIT — Electromagnetic fields of a dipole over an anisotropic half-space
Can. J. Phys., Vol.44, p. 2387-2401, 1966

242. J.R. WAIT — Fields of a horizontal dipole over a stratified anisotropic half-space
I.E.E.E. Trans. Anten. Prop. Vol.AP -14, n°6, p. 790-792, Nov. 1966

243. J.R. WAIT, G.A. SCHLAK — New asymptotic solution for the electromagnetic fields of a dipole over a stratified medium
Electron. Letters, Vol. 3, n°9, p. 421-422, Sept. 1967

244. J.R. WAIT — Asymptotic theory for dipole radiation in the presence of a lossy slab lying on a conducting half-space
I.E.E.E. Trans. Anten. Prop., Vol.AP-15, n°3, p. 645-648, 1967

245. J.R. WAIT — Characteristics of antennas over lossy earth, in Antenna Theory (Ed. by R.E. COLLIN and F.J. ZUCKER), Mc Graw Hill Co, New York, 1969

246. J.R. WAIT, K.P. SPIES — On the image representation of the quasi static fields of a line current source above the ground. Can. J. Phys., Vol. 47, n°23, p. 2731-2733, 1969

Conference on Environmental effects on antennas performances, BOULDER, COLORADO, U.S.A. JULY 1969

247. W.J. SURTEES — The impedance of a finite horisontal antenna above ground
Defence Research Board, Ottawa, Canada

248. A.N. SMITH, E.J. JACKSON — Performance of valley spanning VLF antennas based on electromagnetic modelling
Westinghouse Electric. Corp., Boulder, Colo., U.S.A.

249. E.W. SEELEY — VLF transmitting antennas using fast wave dipoles
Naval Weapons Center Corona Lab., Corona, Calif., U.S.A.

250. D.C. CHANG — Finite tubular antenna above a conducting half-space
Univ. of Colorado, Boulder, U.S.A.

251. R.J. KING — Electromagnetic propagation over a constant impedance plane
Univ. of Wisconsin, Madison, U.S.A.

252. R.J. KING — On the surface impedance concept
Univ. of Wisconsin, Madison, U.S.A.

253. D.C. CHANG, J.R. WAIT — Near field solutions for a vertical hertzian dipole over a finitely conducting earth
Univ. of Colorado and ESSA, Boulder, Colo., U.S.A.

254. D.B. LARGE, L. BALL — Magnetic field excited by a long horizontal wire antenna near the earth's surface. Westinghouse Electric Corp., Boulder, Colo., U.S.A.

255. C.K.H. TSAO — Distributed shunt admittance of horizontal dipole over lossy ground
Raytheon Co, Norwood, Mass., U.S.A

256. J.R. WAIT — Impedance of a hertzian dipole over a conducting half-space
ESSA Res. Lab., Boulder, Colo., U.S.A.

2.4. Rayonnement des antennes submergées ou enterrées dans un sol homogène ou stratifié

257. H.A. WHEELER — Fundamental limitations of small antennas
Proc.IRE, Vol. 35, p. 1479-1484, Déc. 1947

258. R.K. MOORE — Antennas in conducting media. URSI-IRE Spring Meeting, Wash. D.C., Apr.17,1951

259. R.H. LIEN — Radiation from a horizontal dipole in a semi-infinite dissipative medium
J. appl. Phys., Vol. 24, p. 1-4, Janv. 1953

260. J.R. WAIT, L.L. CAMPBELL — The fields of an electric dipole in a semi-infinite conducting medium
J. Geophys. Res., Vol.58, p.21-28, March 1953

261. J.R. WAIT, L.L. CAMPBELL — The fields of an oscillating magnetic dipole immersed in a semi-infinite conducting medium
J. Geophys. Res., Vol.58, p.167-178, June 1953

262. J.R. WAIT — The radiation fields of a horizontal dipole in a semi-infinite dissipative medium
J. appl. Phys., Vol.24, p.958-959, July 1953

263. A. BANOS, J.P. WESLEY — The horizontal electric dipole in a conducting half-space
Scripps Inst.of Oceanography, La Jolla, Calif., Pt.I.
Scripps Rept.53-35, Sept. 1953 - Pt.II. Scripps Rept.54-31, Aug.1954

264. J.R. WAIT — Radiation resistance of dipoles in an interface between two dielectrics
Can. J. Phys., Vol.34, p.24-26, Jan.1956

265. H.A. WHEELER — Fundamental limitations of a small VLF antenna for submarines
IRE Trans. Ant.Prop., Vol.AP-6, p. 123-125, Janv. 1958

266. H.A. WHEELER — The spherical coil as an inductor, shield or antenna
Proc. IRE, Vol.46, p. 1595-1602, Sept. 1958

267. J.R. WAIT — Radiation from a small loop immersed in a semi-infinite conducting medium
Can. J.Phys., Vol.37, p. 672-674, May 1959

268. P.W. TURNER — Submarine communication antenna systems. Proc.IRE, Vol.47, p.735-739,May1959

269. H.A. WHEELER — The radiansphere around a small antenna. Proc.IRE, Vol.47, p.1325-1331, Aug.1959

270. R.N. GHOSE — The radiator-to-medium coupling in an underground communication system
Proc. Natl. Electronics.Conf.,Vol. 16, p.279-289, Oct.10-12, 1960

271. G.J. MONSER, W.D. SABIN — Antenna design for maximum LF radiation
Electronics, Vol.33, p.84-86, June 1960

272. H.A. WHEELER — Useful radiation from an underground antenna
J. Res. NBS, Vol. 65 D, p. 89-91, Jan. Feb.1961

273. J.W. POWERS, D.E. ROSS — Near-zone field strength of a buried horizontal dipole near an interface
1961 IRE-PGMIL Winter Conv., Los Angeles, Calif. Feb. 1-3, 1961

274. L. ROZIN — Etude du champ électromagnétique créé par un doublet magnétique en présence de deux milieux séparés par un plan
Ann. Télécom., T.16, n°3-4, Mars-Avril 1961, p. 96-104. Suite dans : Ann. Télécom., T.19, n°3-4, Mars-Avril 1964, p. 81-86

275. G.J. MONSER — Pickup devices for VLF reception. Electronics, Vol.34, p.68-69, Apr. 1961

276. R.W.P. KING — Dipoles in dissipative media
Proc. Symps. on Electromagnetic waves, Math. Res. Center U. of Wisconsin, Madison, Wis, Apr. 1961, U. of Wisconsin Press, Madison, p.199-241, 1962

277. J.R. WAIT — The electromagnetic fields of a horizontal dipole in the presence of a conducting half-space. Can. J.Phys., Vol.39, p. 1017-1028, July 1961

278. R.K. MOORE, W.E. BLAIR — Dipole radiation in a conducting half-space
J. Res.NBS, Vol. 65D, p.547-563, Nov.Dec.1961

279. W.L. ANDERSON — Fields of electric dipoles in sea water - the earth-atmosphere ionosphere problem. J. Res. NBS, Vol.66D, p.63-72, Jan.Feb.1962

280. W.L. WEEKS, R.C. FENWICK — Submerged antenna performance
1962 IRE International Convention Record, pt. 1, p. 108-135

281. A.W. BIGGS — Radiation fields from a horizontal dipole in a semi-infinite medium
IRE Trans. Anten. Prop., Vol.AP-10, p. 358-362, 1962

282. A.W. BIGGS, H.M. SWARM — Radiation fields of an inclined electric dipole immersed in a semi-infinite conducting medium. IEEE Trans. Anten.Prop., Vol. AP-11, p.306-310, May 1963

283. R.C. FENWICK, W.L. WEEKS — Submerged antenna characteristics
IEEE Trans. Anten. Prop., Vol.AP-11, P.296-305, May 1963

284. R.K. MOORE — Effects of a surrounding conducting medium on antenna analysis
IEEE Trans. Anten. Prop., Vol. AP-11, p. 216-225, May 1963

285. R.C. HANSEN — Radiation and reception with buried and submerged antennas
IEEE Trans. Anten. Prop., Vol.AP-11, p.207-216, May 1963

286. K. SIVAPRASAD, R.W.P. KING — A study of arrays of dipolesin a semi-infinite dissipative medium
IEEE Trans. Anten. Prop., Vol. AP-11, p.240-256, May 1963

287. G. HASSERJIAN, A.W. GUY — Low frequency subsurface antennas
IEEE Trans. Anten. Prop., Vol. AP-11, p.225-231, May 1963

288. R.N. GHOSE — Mutual couplings among subsurface antenna array elements
IEEE Trans. Anten. Prop., Vol. AP-11, p. 257-261, May 1963

289. J.R. WAIT — Theory of radiation from sources immersed in anisotropic media
J. Res. NBS, Vol. 68B, n°3, Jul.Sep. 1964

290. J. GALEJS — Driving point impedance of linear antennas in the presence of a stratified dielectric. IEEE Trans. Anten. Prop., Vol.AP-13, p.725-737- Sep.1965

291. A. BANOS — Dipole radiation in the presence of a conducting half-space
Pergamon Press, Oxford, 1966

292. P.R. BANNISTER — Surface to surface and subsurface to air propagation - quasi-static and near field ranges
AGARD/NATO Symp. on Subsurface Communications, PARIS, FRANCE 25-29 Avril 1966

293. R. GABILLARD — Propagation des ondes électromagnétiques dans les milieux conducteurs. Application aux télécommunications souterraines T.1. : Propagation dans un milieu infini et dans un demi-milieu. Rapport I.R.E.L. 67-110, 185 p., Juillet 1967

294. P.R. BANNISTER — The quasi-near fields of dipole antennas
IEEE Trans. Anten. Prop., Sept.1967 also presented at the Spring 1967 URSI Meetg, Ottawa, Ontario, Canada

295. L. ROBIN, P. POINCELOT — Rayonnement d'un dipôle électrique en présence de deux milieux séparés par un plan. Ann. Télécom., T.22, n°9-10, Sept.Oct.1967, p.243-248

296. P.R. BANNISTER — Subsurface to air and air to subsurface propagation with dipole antennas - quasi near and near field ranges. IEE Conf. on MF, LF and VLF Radio Propagation, LONDON, Nov.1967, Conf. Publ. n°36, p.306-312

Conference on environmental effects on antenna performance - BOULDER - COLO., July 14-18, 1969

297. P.R. BANNISTER — Quasi-static fields of subsurface horizontal electric antennas
U.S. Navy Underwater sound Lab., New London, Conn., U.S.A.

298. R.J. LYTLE — Prolate spheroidal and linear antennas in lossy media
Lawrence Radiation Lab., U. of California, Livermore, USA

299. G. FRANCESCHETTI — C. BUCCI, E. CORTI, G. LATMIRAL
Metallic and dielectric antennas in conducting media
U. of Naples, and Istituto Universitario Navale, Naples, ITALY

300. C.K.H. TSAO, J.T. de BETTENCOURT — Impedance of a finite length insulated dipole in dissipative media
Raytheon Co, Norwood, Mass., U.S.A.

301. H.L. BERTONI — L.B. FELSEN, A. HESSEL
Complex rays and the local properties of radiation in lossy media
Polytechnic Inst. of Brooklyn, Brooklyn, N.Y., U.S.A.

2.5. Systèmes de télécommunications entre terminaux submergés ou souterrains

302. R.K. MOORE — The theory of radio communication between submerged submarines
Ph. D. Dissert., Cornell Univ., Ithaca, N.Y., 1951

303. R.N. GHOSE — The long range sub-surface communication system
Proc. 6th Natl Comm. Symp., p. 110-120, 1960

304. H.A. WHEELER — Radio-wave propagation in the earth's crust
J. Res.NBS, Vol. 65D, p. 189-191, March-Apr. 1961

305. G.J. HARMON — Radio wave propagation through the earth's rock strata. A new medium of communication. IRE Globecom. Conv. Rec., p. 31-34, 1961

306. J.T. de BETTENCOURT, R.A. SUTCLIFFE — Studies in deep strata radio communications. Commun. and data processing operation. The Raytheon Co, Norwood, Mass., Contrat n°AF19 (604)-8359 ; Oct. 1962 (Final rept. for the U.S. Air Force Cambridge Res. Lab.)

307. C.R. BURROWS — D.C. Signaling in conducting media. IRE Trans. Anten.Prop.,Vol.AP-10, p. 328-334, 1962

308. S.H. DURRANI — Air-to-undersea communication. Proc. IRE, Vol. 50, p. 96-97, 1962

309. S.H. DURRANI — Air-to-undersea communication with electric dipoles
IRE Trans. Anten. Prop., Vol. AP-10, p. 524-528, 1962

310. C.R. BURROWS — Radio communication within the earth's crust
IEEE Trans. Anten. Prop., Vol. AP-11, p.311-317, May 1963

311. J.R. WAIT — The possibility of guided electromagnetic waves in the earth's crust
IEEE Trans. Anten.Prop., Vol.AP-11, n°3, p.330-335, May 1963

312. H. MOTT, A.W. BIGGS — Very-low-frequency propagation below the bottom of the sea
IEEE Trans. Anten. Prop., Vol.AP-11, p.323-329, May 1963

313. M.E. VIGGH — Modes in lossy stratified media with application to underground propagation of radio waves. IEEE Trans.Anten.Prop., Vol.AP-11, p.318-323, May 1963

314. L.A. AMES — J.T. de BETTENCOURT, J.W. FRAZIER, A.S. ORANGE
Radio communications via rock strata
IEEE Trans.Communic.Sys.,Vol.CS-11, n°2, p.159-169, June 1963

315. P. HALLEY — Le problème air-sol à trois milieux. Calcul des champs dans le sol conducteur parfait, produits par une source électrique polarisée verticalement, élevée en altitude. Applications numériques.
AGARD Conf. Proc. n° 20, Sub Surface Communications, 1966 p. 17-56

316. P. HALLEY — Effets importants d'une discontinuité physique diélectrique métal sur la propagation de l'onde électromagnétique qui la franchit
AGARD Conf. Proc.n°20, Sub Surface Communications, 1966 p. 57-96

317. M. BOUIX — Résultats numériques concernant une onde de surface guidée par la surface de la mer.
AGARD Conf. Proc., n°20, Sub Surface Communications, 1966 p. 1-16

318. S.B. LEVIN — Lithospheric radio propagation : a review
AGARD Conf. Proc., n°20, Sub Surface Communications, 1966 p. 147-178

319. A.M. RJAZANCEV, A.V. SHADEL'NIKOV — La propagation des ondes radioélectriques dans l'écorce terrestre (exposé d'ensemble). AGARD Conf.Proc., n°20, Sub Surface Communications, 1966 p. 179-210

320. A.F. GANGI — Model results in underground communications
AGARD Conf.Proc., n°20, Sub Surface Communications, 1966 p.387-408

321. A.D. WATT — G.F. LEYDORF, A.M. SMITH
Notes regarding possible fields strength versus distance in earth crust wave guides. AGARD Conf. Proc., n°20, Sub Surface Communications, 1966 p.491-520

322. D.R. WORD — F.X. BOSTICK, L.A. AMES
ULF ELF earth mode communications via horizontal electric dipoles at the surface. AGARD Conf. Proc., n° 20 Sub Surface communications, 1966 p.521-542

323. J.R. WAIT — Electromagnetic propagation in an idealized earth crust waveguide
Radio Sci., Vol.1, n°8, Aug.1966, p.913-924

324. J.R. WAIT — Some factors concerning electromagnetic wave propagation in the earth's crust
IEEE Proc., Vol.54, n°8, Aug.1966, p. 1020-1025

325. J.R. WAIT — Radiation and Propagation of electromagnetic waves in the earth's crust
URSI XVth General Assembly Commission, 2, MUNICH, GERMANY, Sept. 1966

326. R. GABILLARD — F. LOUAGE, J. FONTAINE, J.P. DUBUS
Théorie matricielle de la propagation dans un terrain stratifié d'une onde électromagnétique émise par une antenne verticale souterraine
URSI Symp. sur les ondes électromagnétiques, STRESA, ITALY, Juin 1968

327. P. DEGAUQUE — Champ électromagnétique créé par une longue antenne enterree D.E.A. LILLE Juillet 1968

328. R. GABILLARD — J. FONTAINE, P. DEGAUQUE
Sur le choix de la disposition des antennes lors d'une télécommunication entre stations souterraines. C.R. Acad. Sci. fr., t.262,p.1061-1063, 1968

329. J.R. WAIT — Optimisation of the ground wave over a stratified earth
Electron. Letters, Vol.4, n°26, p.575-576, 27 Déc. 1968

330. R. GABILLARD — J. FONTAINE, P. DEGAUQUE
Sur le choix de la fréquence pour l'établissement d'une télécommunication entre stations souterraines
C.R. Acad. Sci. fr., t.268, p.837-840, 1969

331. F. LOUAGE — Théorie et vérification expérimentale de la propagation des ondes électromagnétiques dans un guide d'ondes géologique
Thèse de Doctorat d'Etat, LILLE, Juillet 1969

332. R. GABILLARD — J. FONTAINE, P. DEGAUQUE
Optimum frequency for a VLF telecommunication system using buried antennas
Conf. on Environmental effects on antenna performance,
BOULDER, COLO., U.S.A., July 1969

333. J. FONTAINE — Contribution à la théorie du rayonnement des dipôles électriques enterrés et au développement de méthodes d'optimisation des liaisons électromagnétiques entre terminaux souterrains. Thèse de Doctorat d'Etat, LILLE, Oct. 1969

334. R. GABILLARD
F. LOUAGE — Télécommunications à travers le sol dans un terrain stratifié. Théorie générale. Ann. Télécom., T.25, n°1-2, Janv.Fév. 1970, p. 15-21

335. P. DEGAUQUE — Contribution à l'étude théorique du rayonnement d'une antenne électrique horizontale enterrée. Thèse de Docteur-Ingénieur, LILLE, Mars 1970

2.6. Propriétés électromagnétiques de la mer et des roches - Méthodes de mesure -

336. J. GRANIER — Absorption des ondes électromagnétiques par la glace
C.R. Acad. Sci. fr., t. 179, n° 23, p. 1313-1316, 1924

337. L.B. SLICHTER — An inverse boundary value problem in electrodynamics
Physics, Vol. 4, n°12, p.411-418, Déc.1933

338. Mc PETRIE — A determination of the electrical constants of the earth's surface at wavelengths of 1.5 and 0.46 m. Proc. Phys.Soc., Vol. 46, n°5, p.637-648, 1934

339. A.F. STEVENSON — On the theoretical determination of earth resistance from surface potential measurements. Physics, Vol.5, n°4, p.114-124, Apr.1934

340. [illegible] H. CARD — Correlation of earth resistivity with geological structure and age
AIME Tech. Bull., p. 829, 1937

341. K.A. McKINNON — Radiofrequency measurements of ground conductivity in Canada.
Can. J. Res. Vol.A.18, p.123, 1940

342. L. CAGNIARD — Basic theory of the magneto-telluric method of geophysical prospecting.
Geophys., Vol. 18, p.605-635, July 1953

343. K.E. ELIASSEN — A survey of ground conductivity and dielectric constant in Norway within the frequency range 0.2-10Mc/s
Geofysiske Publ.Norske VidenskapsAkademi, Vol.19, n°11, OSLO

344. J.R. WAIT — The effective electrical constants of soil at low frequencies
Proc.IRE, Vol.45, n°10, 1p., Oct. 1957

345. J.R. WAIT
A.M. CONDA — On the measurement of ground conductivity at VLF
IRE Trans. Anten.Prop., Vol. AP-6, p.273-277, July 1958

346. S.H. YUNGAL — Magneto-telluric sounding three-layer interpretation curves
Geophys., Vol.26, p. 465-476, Aug. 1961

347. J.R. WAIT — Theory of magneto-telluric fields. J.Res.NBS, Vol.66D, p.509-541,Sept.Oct.1962

348. T.R. MADDEN — T. CANTWELL, D. GREENEWALT, A. KELLY, A. REGIER
Progress Report on Geomagnetic studies and electrical conductivity in the earth's crust and upper mantle. M.I.T. Geophys.Lab., Cambridge, Mass., Project Rept. NR-371-401, Apr.15, 1962

349. K. IIZUKA — The dipole antenna as a probe for determining the electrical properties of a stratified medium. IRE Trans. Anten.Prop., Vol.AP-10,p.783-784, Nov.1962

350. G.V. KELLER — Electrical properties in the deep crust
IEEE Trans.Anten.Prop., Vol.AP-11, p.344-357, May 1963

351. J.T. de BETTENCOURT
J.W. FRAZIER — Rock electrical characteristics deduced from depth attenuation rates in drill holes. IEEE Trans.Anten.Prop.,Vol.AP-11, p.358-363, May 1963

352. T. CANTWELL
P. NELSON — Deep resistivity investigation in northern New York state
Sci.Rept.n°4, Geosci. Inc., Contrat AF19(628)-2351, Sept.1963

353. C.K.H. TSAO — Investigation of electrical characteristics of rock medium on Cape Cod
Sci.Rept.n°1, Raytheon Co, Equipment Div. CADPO,
Contract AF19(628)-2362, Dec.1963

354. C.K.H. TSAO — Investigation of electrical characteristics of rock in northern New York State
Sci.Rept.n°3, Raytheon Co, Equipment Div., CADPO,
Contrat AF19(628)-2362, Janv.1964

355. C.K.H. TSAO — Investigation of electrical characteristics of the Subsurface rock medium in Essex County, New York. Sci.Rept.n°5, Raytheon Co, Equipment Div., CADPO,
Contract AF19(628)-2362, Apr.1964

356. M. ACKER
L.J. MUELLER — Some measured electrical characteristics of the earth's crust
AGARD Conf. Proc., n°20, Sub-Surface Communications, 1966 p.211-238

357. A.S. ORANGE — W.F. BRACE, R.T. MADDEN
The electrical resistivity of water saturated crystalline rocks
AGARD Conf.Proc., n°20, Sub-surface communications, 1966 p.265-288

358. K. VOZOFF — T. CANTWELL, H. LAHMAN, A. ORANGE
Results of in-situ rock resistivity measurements
AGARD Conf. Proc., n°20, Sub-surface communications, 1966 p.287-308

359. E.L. MAXWELL, R.R. MORGAN
A 10 kHz effective conductivity map of North America
AGARD Conf. Proc., n°20, Sub-surface communications, 1966 p.239-264

360. J.R. WAIT
Comments on "the variation of ground constants for the frequency range of 30 to 70 MHz". Proc. IEEE, Vol.55, n°1, p.85, Jan. 1967

361. W.L. TAYLOR
Effective ground conductivity measurements at radio frequencies using small loop antennas(ITS, ESSA)
Conf. on environmental effects, BOULDER, COLO., USA, 1969

2.7. Rayonnement et propagation d'ondes de caractère impulsif

362. J.R. CARSON
Electric circuit theory and the operational calculus
Mc Graw-Hill Co, New York, 1926

363. L.C. PETERSON
Transients in parallel-grounded circuits, one of which is of infinite length
Bell System. Tech.J., Vol.9, p.760-769. Oct. 1930

364. J. RIORDAN
Transients in grounded wires lying on the earth's surface
Bell System Tech.J., Vol.10, p.420-431, July 1931

365. G.A. CAMPBELL, R.M. FOSTER
The practical application of the Fourier integral
Bell System Tech.J., p.639-707, Oct.1928
Fourier integrals for practical application
Bell System Monograph B-584, 1931

366. Y.W. LEE
Synthesis of electric networks by Fourier transformations of Laguerre's functions. J. Math.Phys., Vol.11, p.83-113, June, 1932

367. J.R. WAIT
Transient electromagnetic propagation in a conducting medium
Geophysics, Vol.16, p.213-221, Apr.1951

368. J.R. WAIT
Transient coupling in grounded circuits
Geophysics, Vol.18, p.138-141, Janv.1953

369. J.R. WAIT
A transient magnetic dipole source in a dissipative medium
J. appl. Phys., Vol.24, p.341-343, March 1953

370. J.R. WAIT
An approximate method of obtaining the transient response from the frequency response. Can J. Tech., Vol.31, p.127-131, June 1953

371. J.R. WAIT, C. FROESE
Reflection of a transient electromagnetic wave at a conducting surface
J. Geophys. Res., Vol.60, n°1, p.97-103, March 1955

372. B.K. BHATTACHARYYA
Propagation of transient electromagnetic waves in a conducting medium
Geophys., Vol.20, p.959-961, 1955

373. J.R. WAIT
Transient fields of a vertical dipole over a homogeneous curved ground
Can.J.Phys., Vol.34, p.27-35, Jan.1956

374. J.R. WAIT
Shielding of a transient electromagnetic dipole field by a conductive sheet
Can.J.Phys., Vol.34, p.890-893, Aug. 1956

375. B.K. BHATTACHARYYA
Propagation of transient electromagnetic waves in a medium of finite conductivity. Geophys., Vol.22, p.75-88, Jan.1957

376. J.R. WAIT
The transient behavior of the electromagnetic ground wave on a spherical earth. IRE Trans.Anten.Prop., Vol.AP-5, p.198-202, Apr.1957

377. J.R. WAIT
Propagation of a pulse across a coast line. Proc. IRE, Vol.45, n°11, 1p. Nov.1957.

378. B.R. LEVY, J.B. KELLER
Propagation of electromagnetic pulses around the earth
IRE Trans.Anten.Prop., Vol.AP-6, p.56-61, Jan.1958

379. J.R. JOHLER
Transient radio-frequency ground waves over the surface of a finitely conducting plane earth. J. Res.NBS, Vol.60, p.281-285,Apr.1958

380. P.I. RICHARDS
Transients in conducting media. IRE Trans.Anten.Prop., Vol.AP-6, p.178-182, Apr. 1958

381. J.R. JOHLER, L.C. WALTERS
Propagation of a ground wave pulse around a finetely conducting spherical earth from a damped sinusoidal source current
IRE Trans.Anten.Prop.Vol.AP-7, p.1-10, Jan.1959

382. B.K. BHATTACHARYYA
Electromagnetic fields of a transient magnetic dipole on the earth's surface
Geophys., Vol.24, p.89-108, Feb.1959

383. A. GRUMET
Penetration of transient electromagnetic fields into a conductor
J. appl. Phys., Vol.30, p. 682-686, May 1959

384. J. KIELSON, R.V. ROW
Transfer of transient electromagnetic surface waves into a lossy medium
J. appl.Phys., Vol.30, p. 1595-1598, Oct. 1959

385. J. GALEJS
Impulse excitation of a conducting medium
IRE Trans.Anten.Prop., Vol.AP-8, p.227-228, March 1960

386. S.H. ZISK
Electromagnetic transients in conducting media
IRE Trans. Anten.Prop., Vol.AP-8, p.229-230, March 1960

387. J.R. WAIT
Propagation of electromagnetic pulses in a homogeneous conducting earth
Appl. Sci.Res., Ser.B, Vol.8, p.213-253, 1960

388. J.R. WAIT, R.K. MOORE — Frequency spectra of transient electromagnetic pulses in a conducting medium. IRE Trans.Anten.Prop., Vol.AP-8, p.603, 1960

389. S.H. ZISK — Electromagnetic transients in conducting media. IRE Trans. Anten.Prop., Vol.AP-8, p.229-230, 1960

390. P.E. MIJNARENDS — Propagation of electromagnetic step functions over conducting media. J. appl. Phys., Vol.33, p.2556-2564, 1962

391. J.R. WAIT — A note on the propagation of electromagnetic pulses over the earth's surface. Can.J. Phys., Vol.40, p.1264-1268, 1962

392. C.R. BURROWS — Transient response in an imperfect dielectric. IEEE Trans.Anten.Prop., Vol.AP-11, p. 286-296, May 1963

393. J.R. WAIT — Propagation of electromagnetic pulses in terrestrial waveguides. IEEE Trans. Anten. Prop., Vol.AP-13, n°6, p.904-918, Nov.1965

394. J.R. WAIT — Propagation of pulses in dispersive media. Radio Sci.J. of Res.NBS/USNC-URSI, Vol.69D, n°11, p.1387-1401 Nov. 1965

395. J.R. WAIT, K.P. SPIES — On the theory of transient wave propagation in a dispersive medium. Appl. Sci. Res., Vol.16, p.455-465, 1966

396. W.L. CURTIS — Pulse propagation into the ground. Boeing Co, Seattle, Washington - Conf. on Environmental effects on antennas performances, BOULDER, COLO, USA, 1969

397. J.R. WAIT, K.P. SPIES — Transient magnetic field of a pulsed electric dipole in a dissipative medium. To be published in IEEE Trans. Sept.1970

398. J.R. WAIT, K.P. SPIES — Transient fields for an electric dipole in a dissipative medium. To be published in Can. J. Phys., 1970

2.8. *PROPAGATION DANS LE GUIDE TERRE-IONOSPHERE (bibliographie partielle)*

399. WATSON — The transmission of electric waves round the earth. Proc. Roy. Soc., 95, p. 546, 1919

400. RYDBECK — On the propagation of radio waves. Trans. Chalmers University, 34, 1944

401. BUDDEN — The propagation of very low frequency radio waves to great distances. Phil. Mag., 44, 1953

402. SCHUMANN — Uber die elektrische Eigenschwingungen des Hohlraumes Erde-Luft-Ionosphere arrogt durch blitzenbadungen. Z. Angew. Phys., Vol.6.,p.225, 1957

403. AL'PERT — Radiowave propagation and the ionosphere. Consultants Bureau, N.Y., 1960

404. VOLLAND — Comparison between mode theory and ray theory of V.L.F. propagation. J. Res.N.B.S., Vol. 65D, n°4, 1961

405. J.R. WAIT — A new approach to the mode theory of V.L.F. propagation. J. Res. N.B.S., Vol. 65D, n°1, 1961

406. BUDDEN — Radiowaves in the ionosphere. Cambridge Univ.Press, 1961

407. JOHLER, BERRY — A complete mode sum for L.F., V.L.F., E.L.F. terrestrial radio wave fields. V.L.F. Symposium, Boulder, Colo., U.S.A., Aug.1963

408. J.R. WAIT — Review of mode theory of radio propagation in terrestrial waveguides. Geophysics, V.1, n°4, p.481-505, 1963

409. WAIT, SPIES — Characteristics of the earth-ionosphere waveguide for V.L.F. radiowaves. N.B.S. Technical Note, n°300, 1964

410. LEE — Wave propagation in earth-ionosphere waveguide. Appl. Sci.Res., Vol.17, p.115, 1967

411. J.R. WAIT — Comments on S.W. LEE wave propagation in earth-ionosphere waveguide. Appl. Sci. Res., Vol.18, p.458-459, 1968

412. HARARI — Le guide d'onde terre-couche D. Revue du CETHEDEC, 1968

2.9. *REFERENCES SUPPLEMENTAIRES DIVERSES*

2.9.1. *Bruits*

413. L. BROCK-MANNESTAD — Electromagnetic background noise in the E.L.F. range. AGARD Conf. Proc., n°20, Sub-surface communications, p. 543-556, 1966

414. E.L. MAXWELL — Atmospheric noise from 20 Hz to 30 kHz. AGARD Conf. Proc., n°20, p.557-594, 1966 et Radio Science, Vol.2, n°6, 1967

2.9.2. *Emission par dipole incliné dans un milieu à deux couches*

415. T. TAMIR, L.B. FELSEN — On lateral waves in slab configurations and their relation to other wave types. IEEE Trans. Anten.Prop., Vol.AP-13, p.410-422, May 1965

416. J. TAYLOR — A note on the computed radiation patterns of dipole antennas in dense vegetation. Stanford Res.Inst.,Special Tech.Rept., 16, Feb.1966

417. D.L. SACHS, P.J. WYATT — A conducting-slab model for electromagnetic propagation within a jungle medium. Defense Res.Corp., Tech. Memo 376 and Internal Memo IMR-471, 1966

418. C.R. BURROWS — Ultra-short wave propagation in the jungle. IEEE Trans.Anten.Prop., Vol.AP-14, p.386-388, May 1966

419. D. STAIMAN, T. TAMIR — The nature and optimization of the ground (lateral) wave excited by submerged antennas. Proc. IEE(London), Vol. 113, p. 1299-1310, Aug.1966

420. T. TAMIR — On radio-wave propagation in forest environments. IEEE Trans. Anten. Prop., Vol. AP-15, p. 806-817, Nov. 1967

421. T. TAMIR, A.W. BIGGS — On the optimization of the ground wave above a dissipative half-space. IEEE Trans. Anten. Prop., Vol. AP-16, p.607-608, 1968

2.9.3. Influence du relief

422. J.J. EGLI — Radio propagation above 40 Mc over irregular terrain. Proc. IRE, Vol. 45, p. 1383-1391, Oct. 1957

423. P. BECKMANN, A. SPIZZICHINO — The scattering of electromagnetic waves from rough surfaces. PERGAMON PRESS, 1963

2.9.4. Mesures sur modèles (bibliographie très partielle)

424. G.L. BROWN, A.F. GANGI — Electromagnetic modeling studies of lithospheric propagation. IEEE Trans. on Geosci. Electron., Vol.GE-1, p.17-23, Déc. 1963

RAYONNEMENT DES ANTENNES PLACEES DANS DES MILIEUX ABSORBANTS - REVUE

par

Robert GABILLARD - Université de LILLE - FRANCE
Pierre DEGAUQUE - "
James R. WAIT - ESSA - BOULDER (Colo) U.S.A.

RAYONNEMENT DES ANTENNES PLACEES DANS DES MILIEUX ABSORBANTS - REVUE

Robert GABILLARD - Université de LILLE - FRANCE
Pierre DEGAUQUE - " "
James R. WAIT - ESSA - BOULDER (Colo.) -U.S.A.

PLAN

INTRODUCTION

Cet article de mise au point est consacré à un exposé didactique du fonctionnement des antennes placées dans des milieux absorbants. Nous étudions d'abord le cas des milieux homogènes d'étendue infinie. Puis ensuite le cas où l'espace offert à la propagation des ondes est formé de plusieurs milieux homogènes séparés par des plans. Ce cas constitue l'idéalisation théorique la plus fidèle du milieu hétérogène formé par la mer ou un terrain stratifié surmonté par l'atmosphère. Nous abandonnons dans cette partie l'ordre historique des travaux des auteurs au bénéfice de la clarté d'exposition.

1. DIPOLE ELECTRIQUE PLACE AU SEIN D'UN MILIEU CONDUCTEUR HOMOGENE ET INFINI

1.1. Champ créé par un élément de courant

"L'élément de courant" qui intervient dans la théorie classique des antennes comme élément differentiel, est un morceau de fil isolé de longueur $d\ell$ parcouru par un courant uniforme I. Dans un milieu conducteur, il est possible de brancher les deux extrêmités du fil sur des "prises de masse" d'admittance électrique non nulle. Si sa longueur est petite par rapport à la longueur d'onde, il pourra alors être parcouru d'une extrêmité à l'autre par un courant uniforme. Il est ainsi possible dans un milieu conducteur de réaliser physiquement un "élément de courant" : $Id\ell$.

Cette antenne élémentaire produit dans tout l'espace un potentiel de Hertz électrique donné par la formule (voir Réf. (185), (293), (200)) :

$$\vec{\Pi} = \frac{I\vec{d\ell}}{4\pi(\sigma+j\omega\varepsilon)} \quad \frac{e^{-\gamma r}}{r} \tag{1}$$

r est la distance joignant dans le système de coordonnées sphériques de la figure 1. le point d'observation P à l'origine où se trouve placé l'élément de courant orienté suivant l'axe polaire oz.

σ est la conductivité et ε la constante diélectrique du milieu et le courant I est harmonique du type :

$$I = I_o \, e^{j\omega t} \tag{2}$$

I_o étant une constante.

Les composantes $\vec{E}$ et $\vec{H}$ du champ électromagnétique au point P sont obtenues à partir du potentiel de Hertz par les formules (voir Réf. (200), (293)) :

$$\vec{E} = -\gamma^2\vec{\Pi} + \text{grad div } \vec{\Pi} \tag{3}$$

$$\vec{H} = (\sigma+j\omega\varepsilon) \text{ rot } \vec{\Pi} \tag{4}$$

L'application de ces formules conduit aux expressions suivantes pour les composantes non nulles du champ :

$$E_\theta = \frac{Id\ell}{4\pi(\sigma+j\omega\varepsilon)} \quad \frac{\sin\theta}{r^3} \quad (1 + \gamma r + \gamma^2 r^2)e^{-\gamma r} \tag{5}$$

$$E_r = \frac{Id\ell}{2\pi(\sigma+j\omega\varepsilon)} \quad \frac{\cos\theta}{r^3} \quad (1 + \gamma r)e^{-\gamma r} \tag{6}$$

$$H_\phi = \frac{Id\ell}{4\pi} \quad \frac{\sin\theta}{r^2} \quad (1 + \gamma r)e^{-\gamma r} \tag{7}$$

Dans ces formules γ est le facteur de propagation relié à la fréquence et aux constantes électromagnétiques du milieu par :

$$\gamma^2 = -\varepsilon\mu\omega^2 + j\omega\mu\sigma \qquad (8)$$

μ étant la perméabilité magnétique du milieu.

Les deux "prises de masse " de l'élément de courant peuvent être considérées comme une source et un puits injectant et drainant le courant I dans le milieu conducteur. Ces deux "pôles" espacés de la distance $d\ell$ constituent donc un dipôle électrique.

D'après la formule (8) γ est nul pour le courant continu ($\omega = 0$). En faisant $\omega = 0$ dans les formules (5) à (7) on retrouve effectivement les composantes du champ électrique et magnétique créé par un dipôle alimenté en courant continu dans un milieu conducteur :

$$E_{\theta_o} = \frac{I_o d\ell}{4\pi\sigma} \frac{\sin\theta}{r^3} \qquad (9) \qquad E_{r_o} = \frac{I_o d\ell}{2\pi\sigma} \frac{\cos\theta}{r^3} \qquad (10)$$

$$H_{\phi_o} = \frac{I_o d\ell}{4\pi} \frac{\sin\theta}{r^2} \qquad (11)$$

Dans la suite de notre étude nous allons surtout nous intéresser à l'influence de la fréquence. C'est pourquoi nous allons définir des paramètres égaux aux rapports des intensités des composantes du champ à la fréquence angulaire ω aux intensités de ces mêmes composantes en courant continu :

$$e_\theta = \frac{E_\theta e^{-j\omega t}}{E_{\theta_o}} = \frac{1}{1 + j\frac{\omega\varepsilon}{\sigma}} (1 + \gamma r + \gamma^2 r^2) e^{-\gamma r} \qquad (12)$$

$$e_r = \frac{E_r e^{-j\omega t}}{E_{r_o}} = \frac{1}{1 + j\frac{\omega\varepsilon}{\sigma}} (1 + \gamma r) e^{-\gamma r} \qquad (13)$$

$$h_\phi = \frac{H_\phi e^{-j\omega t}}{H_{\phi_o}} = (1 + \gamma r)\, e^{-\gamma r} \qquad (14)$$

I.2. Notion de fréquence caractéristique et de longueur caractéristique du mi.. ..conducteur (Voir Réf. (185))

Nous voyons apparaître dans les formules (12)et (13) la variable :

$$\beta = \frac{\omega\varepsilon}{\sigma} \qquad (15)$$

Cette variable peut aussi s'écrire :

$$\boxed{\beta = \frac{f}{f_c}} \qquad (16) \qquad \text{avec} \qquad \boxed{f_c = \frac{1}{2\pi} \frac{\sigma}{\varepsilon}} \qquad (17)$$

f_c est un paramètre dont la dimension physique est celle d'une fréquence et qui ne dépend que des caractéristiques σ et ε du milieu conducteur.
Nous appellerons donc f_c la *fréquence caractéristique du milieu.*

β est ainsi une *fréquence relative* égale au rapport de la fréquence du courant alimentant le dipôle à la fréquence caractéristique du milieu entourant ce dipôle. β est aussi le rapport du courant de déplacement au courant de conduction dans le milieu et la *fréquence caractéristique* est la fréquence pour laquelle le courant de déplacement devient égal au courant de conduction.

La fréquence intervient encore dans le facteur de propagation γ et il convient de l'exprimer en fonction de β. D'après (8) nous avons en choisissant la détermination positive du radical :

$$\gamma = \sqrt{j\omega\mu\sigma(1 + j\beta)} \qquad (18)$$

et puisque $\omega = \beta \frac{\sigma}{\varepsilon}$:

$$\gamma = \frac{1}{L_c} 2\sqrt{j\beta(1 + j\beta)} \qquad (19)$$

avec :

$$\boxed{L_c = \frac{2}{\sigma} \sqrt{\frac{\varepsilon}{\mu}}} \qquad (20)$$

L_c est un paramètre qui, tout comme f_c, ne dépend que des caractéristiques σ, ε, et μ du milieu conducteur. Ses dimensions physiques étant celles d'une longueur nous l'appellerons *longueur caractéristique du milieu.*

γ peut aussi s'écrire : $\gamma = \frac{1}{L_c} (a + jb)$ (21)

avec :

$$a = (2\beta[\sqrt{1+\beta^2} - \beta])^{1/2} \qquad (22)$$

$$b = (2\beta[\sqrt{1+\beta^2} + \beta])^{1/2} \qquad (23)$$

I.3. Variations de l'intensité du champ électromagnétique en fonction de la fréquence

Appelons *distance relative* le rapport :

$$\boxed{x = \frac{r}{L_c}} \qquad (24)$$

nous voyons que les formules (12) à (14) peuvent s'exprimer en fonction uniquement des deux variables sans dimensions physiques β et x.

Nous avons : (voir Réf. (185))

$$e_\theta = \frac{1}{1+j\beta}\left[1 + (a+jb)x + 4x^2\beta(j-\beta)\right] e^{-(a+jb)x} \qquad (25)$$

$$e_r = \frac{1}{1+j\beta}\left[1 + (a+jb)x\right] e^{-(a+jb)x} \qquad (26)$$

$$h_\phi = \left[1 + (a+jb)x\right] e^{-(a+jb)x} \qquad (27)$$

Les figures (2), (3) et (4) montrent pour plusieurs valeurs de x, les variations en fonction de β des modules de e_θ, e_r et h_ϕ. Considérons par exemple le réseau des courbes de $|e_\theta|$. Nous voyons que $|e_\theta|$ qui est supérieur à 1 pour les faibles valeurs de β diminue rapidement lorsque β se rapproche de l'unité. Mais lorsque β devient plus grand que 1, $|e_\theta|$ augmente et peut atteindre pour les valeurs de β assez élevées des valeurs plus grandes que 1.

Ceci signifie que le milieu conducteur, qui se laisse assez bien traverser par le courant continu, devient opaque lorsque la fréquence des ondes augmente et se rapproche de la fréquence caractéristique. *Mais, au-delà de la fréquence caractéristique, lorsque le courant de déplacement l'emporte sur le courant de conduction, le milieu conducteur redevient transparent.*

Ce regain de transparence d'un milieu absorbant à fréquence très élevée est un phénomène connu : une feuille d'aluminium qui est un obstacle infranchissable aux ondes hyperfréquences, se laisse facilement traverser par des rayons X ; l'eau de mer dans laquelle des ondes de 20 kHz sont déjà affaiblies de 55 dB après un parcours de 11 m se laisse traverser par la lumière du jour jusqu'à des profondeurs supérieures à 100 m.

Or les rayons X tout comme la lumière sont des ondes électromagnétiques obéissant aux équations de Maxwell et ne différant des ondes de la gamme radio que par leur fréquence.

Si nous examinons l'une des courbes de la figure (2) nous voyons que $|e_\theta|$ est supérieur à 1 dans deux domaines de fréquences :

- pour β compris entre 0 et β_m
- pour β supérieur à β_M.

A ces deux domaines correspondent deux fenêtres possibles pour les télécommunications à travers le milieu conducteur : l'une en basse fréquence ; l'autre en très haute fréquence.

Les frontières β_m et β_M de ces deux fenêtres dépendent de la distance relative x. La figure (5) montre les deux fonctions $\beta_m(x)$ et $\beta_M(x)$ dont le calcul est détaillé en annexe.

I.4. Etude particulière de la fenêtre de transmission basse fréquence

La frontière β_m de la fenêtre de transmission basse fréquence correspond à la valeur $\eta_o = 3{,}16$ de la distance relative $\eta = r/\delta$ définie dans l'annexe. Elle dépend donc à la fois de la fréquence et de la distance.

La *bande passante à 3 dB* disponible pour une liaison de distance r_o donnée à travers le milieu conducteur correspond, elle, à la valeur $\eta_c = 3{,}85$. Pour cette valeur de la variable η on a en effet $|e_\theta| = 0{,}707$ correspondant à l'affaiblissement de 3 décibels. L'allure de la bande passante est celle de la fonction $F(\eta)$ représentée figure (6).

Nous avons avec $\mu = \mu_o = 4\pi.10^{-7}$:

$$\Delta f = \frac{\eta_c^2}{\pi\mu}\,\frac{1}{\sigma r_o^2} = \frac{3{,}75}{\sigma r_o^2}\,10^6 \text{ Hz} \qquad (28)$$

La bande passante est généralement imposée par la nature des télécommunications que l'on désire établir à travers le milieu conducteur (téléphone ; télétype ; télécommande ; etc ...).

Pour une bande passante Δf_o donnée la *distance maximum* r_m à laquelle la liaison pourra être établie à travers le milieu conducteur sera :

$$r_m = \frac{\eta_c}{\sqrt{\pi\mu}} \quad \frac{1}{\sqrt{\sigma\Delta f_o}} = \frac{1,94.10^3}{\sqrt{\sigma\Delta f_o}} \text{ m} \tag{29}$$

Même si l'on se contente d'une bande passante Δf_o très petite, la distance maximum possible r_M pour la liaison sera déterminée par la nécessité d'obtenir à la réception un rapport signal/bruit suffisant. L'analyse de cette condition a été faite par GABILLARD et CLARISSE (Réf. (88) et (89)) dans le cas d'une transmission télétype à travers un massif calcaire. D'une manière générale r_M sera donnée à partir de la formule (9) par :

$$r_M = \left[\frac{1}{4\pi\sigma} \quad \frac{I_o d\ell}{E_\theta}\right]^{1/3}_{max} \tag{30}$$

Dans le rapport $\left(\frac{I_o d\ell}{E_\theta}\right)_{max}$ I_o est le courant maximum alimentant le dipôle de longueur $d\ell$ et E_θ est le plus petit signal exploitable par le récepteur. La valeur maximum de ce rapport dépend de la technologie de construction des appareils utilisés et de l'intensité des bruits parasites perturbant la réception. Pratiquement et avec la technologie actuelle, on ne peut guère dépasser pour ce rapport la valeur :

$$\left(\frac{I_o d\ell}{E_\theta}\right)_{max} \simeq 10^9 \quad \frac{\text{Amp.m}^2}{\text{Volt}} \tag{31}$$

Nous avons donc approximativement :

$$\boxed{r_M = 4,3.10^2(\sigma)^{-1/3} \text{ m}} \tag{32}$$

I.5. *Exemples*

Nous allons illustrer les considérations qui précèdent avec trois exemples : l'eau de mer ; un terrain sédimentaire de résistivité moyenne ; un massif calcaire de résistivité élevée :

I.5.1. *Eau de mer*

Les paramètres électromagnétiques de l'eau de mer sont :

$$\mu = \mu_o \qquad \varepsilon = 80\,\varepsilon_c \qquad \sigma = 4 \text{ mho/m}$$

Les formules (17) et (20) nous donnent donc :

$$f_c = 900 \text{ MHz} \qquad L_c = 1,4 \text{ cm}$$

<u>En basse fréquence</u> : La portée maximum donnée par (32) est r_M=270 m, mais la bande passante disponible n'est à cette distance que : $\Delta f = 13$ Hz.
La distance maximum à laquelle une liaison phonie de 3 kHz de bande passante peut être établie est (formule (29)) : $r_m = 18$ m.

<u>En haute fréquence</u> on pourrait croire que la fenêtre de transmission est inexploitable. En effet, à seulement 29 cm de la source (x = 21), la formule (15.1) donne déjà : $\beta_M = 5,75.10^5$. La fréquence de l'onde correspondante à cette valeur de β est $f = 5,2.10^{14}$ Hz : c'est de la lumière jaune.

Or une lampe jaune immergée se voit dans la mer à une distance bien supérieure à 29 cm.

Ceci signifie que l'hypothèse qui assimile la mer à un milieu homogène de conductivité constante devient fausse au-delà d'une certaine fréquence (voir Réf. (185)). En particulier, aux fréquences optiques, l'eau de mer ne suit plus la loi d Ohm.

I.5.2. *Terrain sédimentaire moyen*

Considérons des galeries de mine (figure (7)) situées dans un terrain de paramètres électromagnétiques:

$$\mu = \mu_o \qquad \varepsilon = 10\,\varepsilon_o \qquad \sigma = 2.10^{-2} \text{ mho/m}$$

Ces caractéristiques sont par exemple celles de sable argileux saturé d'eau douce.

Nous avons : $f_c = 36$ MHz $\qquad L_c = 80$ cm

Les caractéristiques <u>basse fréquence</u> sont :

$r_M = 1,6$ km $\rightarrow$ $\Delta f = 73$ Hz

$r_m = 250$ m $\rightarrow$ $\Delta f = 3$ kHz

<u>En haute fréquence</u> : à 10 m de la source (x = 12,5) nous avons $\beta_M = 2,34.10^2$ et la fréquence correspondante est f = 8,4 GHz.

Dans ce cas la théorie est contredite par l'expérience en sens inverse du cas de l'eau de mer : *des ondes de radar de 3,6 cm de longueur d'onde ne traversent pas 10 m de sable argileux.* La faute en est cette fois aux bandes d'absorption diélectrique de l'argile qui augmentent la conductivité apparente en très haute fréquence (voir Réf. (185)).

I.5.3. *Massif calcaire*

On rencontre, en particulier dans le Sud de la France, des massifs calcaires dont l'ordre de grandeur

des paramètres électromagnétiques est :

$$\mu = \mu_o \qquad \varepsilon = 5\,\varepsilon_o \qquad \sigma = 2.10^{-4} \text{ mho/m}$$

Nous avons dans ce cas :

$$f_c = 720 \text{ kHz} \qquad L_c = 60 \text{ m}$$

Les possibilités de transmission électromagnétique à travers un tel milieu sont excellentes.

En basse fréquence nous obtenons : $r_M = 7{,}5$ km → $\Delta f = 330$ Hz

$r_m = 2{,}5$ km → $\Delta f = 3$ kHz

En haute fréquence la fenêtre de transmission semble parfaitement utilisable. En effet à 480 m de la source ($x = 8$), on trouve $\beta_M = 11$ et la fréquence correspondante de 7,9 MHz est dans la gamme des ondes courtes.

Or, bien qu'à notre connaissance l'expérience n'ait pas été faite, la propagation d'ondes de cette fréquence sur une telle distance dans le calcaire paraît invraisemblable. Il y a toutefois lieu de porter à l'actif de la théorie les observations de FRITSCH (Réf. (67)).

1.6. Possibilités d'utilisation de la fenêtre de transmission haute fréquence

La théorie qui montre la remontée en haute fréquence de l'intensité des composantes E_θ et H_ϕ du champ d'un dipôle électrique reçu à une distance donnéene peut pas être suspectée. Il faudrait pour cela admettre la non validité des équations de Maxwell.

Mais les courbes des figures (2) à (4) impliquent trois hypothèses dont il y a lieu de vérifier la validité en haute fréquence :

1. La longueur $d\ell$ du dipôle reste petite vis-à-vis de la longueur d'onde
2. Les paramètres électromagnétiques σ, μ et ε sont des constantes indépendantes de la fréquence
3. Le moment électrique du dipôle $Id\ell$ est maintenu constant dans toute la gamme de fréquences explorée.

La condition 1 est la plus facile à satisfaire, car on peut toujours diminuer la longueur du dipôle mais il faut augmenter le courant en proportion et on peut se trouver dans l'impossibilité de satisfaire la condition 3.

Nous avons attribué à la non satisfaction de la condition 2. les discordances entre les prévisions théoriques et les constatations expérimentales concernant la propagation de la lumière dans la mer et des ondes radar dans la terre. Il est évident qu'une étude de la pénétration des ondes de fréquence élevée dans les milieux absorbants est indissociable d'une étude des variations de σ, μ et ε en fonction de la fréquence. Ces variations sont liées à la nature microphysique des mécanismes d'absorption. Elles dépendent de la structure moléculaire et cristalline du milieu et du rôle des défauts et des impuretés qu'il renferme.

Le respect de la condition 3 dépend de la puissance de l'émetteur dont on dispose. La puissance nécessaire pour alimenter un dipôle avec un courant I est proportionnelle à sa résistance d'entrée. Pour savoir si la condition 3 peut être satisfaite, il faut donc au préalable déterminer comment varie la résistance d'entrée du dipôle dans la gamme de fréquence intéressée.

2. DIPOLE MAGNETIQUE DANS UN MILIEU CONDUCTEUR HOMOGENE ET INFINI

2.1. Champ créé par un dipôle magnétique.

Le dipôle magnétique élémentaire est constitué par une boucle de surface dS parcourue par un courant I.

Il produit dans tout l'espace un potentiel de Hertz magnétique donné par la formule (voir Réf. (293), (200)) :

$$\vec{\Pi}^* = \frac{I\vec{dS}}{4\pi} \frac{e^{-\gamma r}}{r} \tag{33}$$

$\vec{dS}$ est orienté suivant l'axe de la boucle,
γ est le facteur de propagation du milieu donné par (8) et le courant I est du type (2).

Les composantes $\vec{E}$ et $\vec{H}$ du champ électromagnétique au point de réception P sont obtenues par les formules bien connues :

$$\vec{E} = -\,j\omega\mu\, \text{rot}\, \vec{\Pi}^* \tag{34}$$

$$\vec{H} = -\gamma^2 \vec{\Pi}^* + \text{grad div}\, \vec{\Pi}^* \tag{35}$$

L'application de ces formules conduit alors aux expressions suivantes pour les composantes non nulles du champ.

$$H_\theta = \frac{IdS}{4\pi} \frac{\sin\theta}{r^3} (1 + \gamma r + \gamma^2 r^2) e^{-\gamma r} \tag{36}$$

$$H_r = \frac{IdS}{2\pi} \frac{\cos\theta}{r^3} (1 + \gamma r) e^{-\gamma r} \tag{37}$$

$$E_\phi = \frac{-j\omega\mu IdS}{4\pi} \frac{\sin\theta}{r^2} (1 + \gamma r) e^{-\gamma r} \tag{38}$$

En courant continu ($\omega = \gamma = 0$) ces formules se réduisent à :

$$H_{\theta_o} = \frac{I_o dS}{4\pi} \frac{\sin\theta}{r^3} \tag{39}$$

$$H_{r_o} = \frac{I_o dS}{2\pi} \frac{\cos\theta}{r^3} \tag{40}$$

$$E_{\phi_o} = 0 \tag{41}$$

Pour étudier l'influence de la fréquence, nous définirons les rapports :

$$h_\theta = \frac{H_\theta e^{-j\omega t}}{H_{\theta_o}} = (1 + \gamma r + \gamma^2 r^2) e^{-\gamma r} \tag{42}$$

$$h_r = \frac{H_r e^{-j\omega t}}{H_{r_o}} = (1 + \gamma r) e^{-\gamma r} \tag{43}$$

$$e_\phi = \frac{E_\phi e^{-j\omega t}}{\sqrt{\frac{\mu}{\varepsilon}} H_{\theta_o}} = -2j\beta x (1 + \gamma r) e^{-\gamma r} \tag{44}$$

2.2. *Variations de l'intensité du champ en fonction de la fréquence*

Comme dans le cas du dipôle électrique le produit γr peut s'écrire :

$$\gamma r = x(a + jb) \tag{45}$$

a et b étant donnés en fonction de β par (22) et (23).

Les courbes des figures (10) et (11) montrent les variations des modules $|h_\theta|$ et $|e_\phi|$ en fonction de la variable "fréquence relative β" et du paramètre "distance relative x".

Les courbes de $|h_\theta|$ montrent l'existence de deux fenêtres de transmission. L'une en basse fréquence pour β compris entre 0 et β_m^* ; l'autre en haute fréquence pour β supérieur à β_M^*. Lorsque β est très petit les deux expressions (12) et (42) deviennent identiques. Il en résulte que :

$$\beta_m = \beta_m^* \tag{46}$$

Par contre, pour x constant, $|h_\theta|$ augmente en haute fréquence proportionnellement à β^2. Il en résulte que β_M^* est plus petit que β_M. La figure (5) donne β_M^* en fonction de x.

3. IMPEDANCE D'UNE ANTENNE PLACEE DANS UN MILIEU CONDUCTEUR HOMOGENE ET INFINI

3.1 *Définition de la "résistance d'entrée"*

Bien que les résultats que nous allons donner se rapportent uniquement aux dipôles, les définitions sont valables pour une antenne quelconque.

La "résistance de rayonnement" d'une antenne est définie par :

$$R_r = \frac{W_r}{I^2} \tag{47}$$

I est le courant du générateur alimentant l'antenne et W_r est l'integrale du vecteur de Poynting sur toute la surface d'une sphère de rayon r entourant l'antenne.

Dans le cas d'un milieu non absorbant la diminution de l'intensité du champ avec la distance est due seulement à l'épanouissement de l'onde. L'énergie émise dans un angle solide déterminé se conserve, et pour r assez grand W_r est une constante indépendante du rayon de la sphère.

Mais dans un milieu conducteur, chaque coquille sphérique traversée par l'onde lui prélève une partie de son énergie. W_r diminue donc constamment lorsque r augmente. La *résistance de rayonnement* définie par (47) est alors une fonction décroissante de r qui n'a plus aucune utilité.

Pratiquement le milieu absorbant n'occupe pas tout l'espace, car il faut bien au minimum y creuser une petite cavité pour y placer l'antenne. Ceci est évident pour une antenne enterrée, et, dans le cas de la mer, la cavité épouse exactement le volume de l'antenne recouverte de son isolant.

Supposons donc l'antenne placée au centre d'une cavité sphérique de rayon ρ. Appelons W_i la *puissance injectée* qui pénètre dans le milieu absorbant à travers la paroi de cette cavité. Si l'on y ajoute la puissance W_o perdue par effet joule dans l'antenne elle-même (fils conducteurs et prises de terre éventuelles), on obtient la puissance totale débitée par le générateur.

Par définition la *résistance d'entrée* de l'antenne sera :

$$R_e = \frac{W_i + W_o}{I^2} \tag{48}$$

3.2. *Calcul de la puissance injectée W_i*

Le calcul de W_i s'effectue en imposant la continuité des composantes tangentielles du champ électromagnétique de part et d'autre de la paroi de la cavité. Ces conditions aux limites permettent de relier les composantes de l'onde progressive qui s'éloigne de la cavité à travers le milieu absorbant, aux composantes de l'onde stationnaire qui existe dans la cavité. On peut ainsi exprimer le champ dans le milieu absorbant en fonction du courant de l'antenne.

Ce calcul a été fait par TAI (Voir Réf. (162) - (163)) pour un dipôle électrique qu'il assimile à une antenne biconique de faible ouverture placée dans une cavité sphérique (voir figure (8)). Pour le dipôle magnétique ce calcul a été fait par WAIT (Voir Réf. (167)-(171)-(187)-(200)).

La figure (9) représente une boucle de rayon d à l'intérieur de la cavité sphérique. On la suppose parcourue par un courant I uniforme. Dans son travail de 1957, (Réf. (171)), WAIT résoud le problème en décomposant en harmoniques sphériques le potentiel vecteur produit par la boucle. Cette analyse reprise dans une publication plus récente (Réf.(187)), conduit à une formule rigoureuse pour la puissance injectée dans le milieu absorbant :

$$W_i = \frac{(IdS)^2}{2} \frac{(\omega\mu)^2}{6\pi\rho} (\sigma+j\omega\varepsilon) \left[1 + \frac{9}{280} \left(\frac{d}{\rho}\right)^4 + \ldots\right] \tag{49}$$

Le premier terme négligé de la série étant de l'ordre de grandeur de $(d/\rho)^8$.

Pour un dipôle élémentaire ($d/\rho \ll 1$) la partie réelle de W_i qui correspond à l'énergie active fournie par le générateur au milieu environnant est :

$$W_i = \frac{\sigma(\omega\mu)^2}{12\pi\rho} (IdS)^2 \tag{50}$$

Ce résultat suppose seulement la condition :

$$\rho \ll \frac{1}{\omega\sqrt{\mu_o\varepsilon_o}} = \frac{\lambda}{2\pi} \tag{51}$$

ce qui nécessite que le rayon ρ de la cavité soit toujours beaucoup plus petit que la longueur d'onde dans l'isolant qui la constitue.

L'expression (50) de W_i avait déjà été obtenue par WAIT en 1952 par une approche mathématique différente (Voir Réf. (167)). Dans cette publication WAIT montre également que les composantes du champ dans le milieu absorbant entourant la cavité sont encore données par les expressions (36) à (38) sous réserve que l'on y remplace le moment IdS du dipôle magnétique par le moment équivalent :

$$(IdS)_e = IdS \frac{3\, e^{\gamma\rho}}{3 + 3\gamma\rho + \gamma^2\rho^2} \tag{52}$$

Cette expression suppose également la validité de (51).

Nous avons ensuite ce résultat remarquable :

L'expression (50) de W_i, calculée rigoureusement en tenant compte de l'effet réflecteur des parois de la cavité est identique à $W_r(\rho)$.

$W_r(\rho)$ étant simplement l'intégrale sur une sphère de rayon ρ de la partie réelle du vecteur de Poynting :

$$P_m = \frac{1}{2} R_e(E_\phi H_\theta^*)_{r=\rho} \tag{53}$$

H_θ^* est la quantité complexe conjuguée de H_θ, donné ainsi que E_ϕ par les expressions (36) et (38) *qui ne supposent nullement l'existence d'une cavité dans le milieu entourant le dipôle.*

L'effet de la cavité se manifeste seulement par le terme correctif (52) mais celui-ci tend vers 1 si γρ est très petit.

3.3. *Variations de la puissance injectée en fonction de la fréquence*

$W_r(\rho)$ est relié au vecteur de Poynting par :

$$W_r(\rho) = 2\pi\rho^2 \int_0^\pi P(\rho) \sin\theta d\theta \tag{54}$$

En prenant pour $P(\rho)$ l'expression P_m donnée par (53) pour le dipôle magnétique et l'expression P_e donnée pour le dipôle électrique par :

$$P_e = \frac{1}{2} R_e(E_\theta H_\phi^*)_{r=\rho} \tag{55}$$

(E_θ étant l'expression (5) et H_ϕ^* la quantité complexe conjuguée de l'expression (7)).

Nous obtenons :

Pour le dipôle magnétique :

$$W_r(\rho)_m = \frac{(IdS)^2}{12\pi} \frac{\sigma\mu}{\varepsilon\rho^3} P_m(\beta x_o) \tag{56}$$

avec :

$$P_m(\beta x_o) = \frac{9\,\beta b x_o \left[2\,a x_o + x_o^2\,(a^2 + b^2)\right]}{\left[3 + 3a x_o + x_o^2(a^2 - b^2)\right]^2 + \left[3b x_o + 2ab x_o^2\right]^2} \qquad (57)$$

a et b étant les fonctions de β (22) et (23).

et

$$x_o = \frac{\rho}{L_c} \qquad (58)$$

Pour le dipôle électrique :

$$W_r(\rho)_e = \frac{(Id\ell)^2}{12\pi} \quad \frac{1}{\sigma\rho^3}\; P_e(\beta x_o) \qquad (59)$$

avec :

$$P_e(\beta x_o) = \frac{\left[(1 + a x_o - \beta b x_o)(1 + a x_o + x_o^2(a^2 - b^2)) + b x_o(1 + 2a x_o)(\beta(1 + a x_o) + b x_o)\right] e^{-2a x_o}}{1 + \beta^2} \qquad (60)$$

Ces formules ne sont valables que si l'hypothèse (51) reste vérifiée , ce qui implique la condition:

$$2\beta x_o = \rho\omega\sqrt{\mu\varepsilon} = \frac{2\pi\rho}{\lambda}\sqrt{\varepsilon_r} \ll 1 \qquad (61)$$

λ étant la longueur d'onde dans la cavité et ε_r étant la constante diélectrique relative du milieu absorbant par rapport à l'isolant de la cavité.

Si l'on admet que la condition (51) est encore satisfaite pour :

$$\rho = 10^{-1}\,\frac{\lambda}{2\pi} \qquad (62)$$

β ne devra pas dépasser vers les hautes fréquences la valeur :

$$\beta_{max} = \frac{10^{-1}\sqrt{\varepsilon_r}}{2x_o} \qquad (63)$$

Ceci implique, si l'on désire pouvoir utiliser les formules (56) et (59) à des fréquences correspondant à la fenêtre de transmission haute fréquence, d'avoir x_o suffisamment petit, c'est-à-dire d'avoir :

$$\rho \ll L_c \qquad (64)$$

La figure (12) montre les variations en fonction de β des rapports :

$$w_m = 3\pi\sigma\rho^3 L_c^2\,\frac{W_r(\rho)_m}{(IdS)^2} \qquad (65)$$

et

$$w_e = 12\pi\sigma\rho^3\;\frac{W_r(\rho)_e}{(Id\ell)^2} \qquad (66)$$

Pour β très petit et pour β très grand, les formules (56) (57) et (59) (60) se simplifient. Nous avons :

<u>Pour le dipôle magnétique</u>

$$w_m = (2\beta x_o)^2 \qquad \text{pour } \beta \ll 1 \qquad (67)$$

$$w_m = (2\beta x_o)^2\,(1 + 2\beta^2 x_o) \qquad \text{pour } \beta \gg 1 \qquad (68)$$

<u>Pour le dipôle électrique</u>

$$w_e = 1 \qquad \text{pour } \beta \ll 1 \qquad (69)$$

$$w_e = \beta^{-2} \qquad \text{pour } \beta \gg 1 \qquad (70)$$

Si l'on remplace dans (67) β et x_o par leurs valeurs, on trouve :

$$w_m = \omega^2\rho^2\mu\varepsilon \qquad (71)$$

et en portant cette valeur de w_m dans (65) on obtient :

$$W_r(\rho)_m = \frac{\sigma(\omega\mu)^2}{12\pi\rho}\;(IdS)^2 \qquad \text{pour } \beta \ll 1 \qquad (72)$$

On retrouve bien ainsi l'expression (50) de la puissance injectée W_i donnée par le calcul de WAIT.

Pour le dipôle électrique la valeur (69) de w_e portée dans (66) nous donne :

$$W_r(\rho)_e = \frac{1}{12\pi\sigma\rho^3}\;(Id\ell)^2 \qquad \text{pour } \beta \ll 1 \qquad (73)$$

Cette valeur de la puissance injectée par le dipôle électrique coïncide elle aussi avec un résultat donné par WAIT (formule (24-30) de la Réf. (200)).

3.4. *Exemples*

Reprenons l'exemple du massif calcaire du § 1.5.3. Si nous creusons dans le calcaire une cavité sphérique de 1 m de rayon pour y placer nos antennes, nous aurons : $x_o = 1{,}6.10^{-2}$ et la valeur de β à ne pas dépasser pour rester dans le domaine de validité de nos formules, sera d'après (63) : $\beta_{max} = 6{,}7$.

Utilisation de la fenêtre de transmission basse fréquence

Supposons que nous désirions établir à travers le calcaire une liaison électromagnétique avec une autre cavité située à 600 m. Cette distance de propagation correspond à la valeur $x = 10$ du paramètre *distance relative* et la figure (5) nous donne pour cette valeur de x : $\beta_m = 5.10^{-2}$. Nous disposons donc d'une fenêtre basse fréquence ouverte entre 0 et 36 kHz. A cette fréquence, l'intensité du champ électromagnétique sera la même que si nous alimentions les dipôles en courant continu. Les formules (9) et (39) nous donnent alors respectivement dans les cas des deux types de dipôles les moments nécessaires pour obtenir un champ donné à 600 m. Pour avoir $E_\theta = 1$ µV/m ou $H_\theta = 1$ µA/m il nous faudra avoir :

soit $Id\ell = 0{,}55$ A.m (dipôle électrique)

soit $IdS = 2{,}7.10^3$ A.m^2 (dipôle magnétique)

A l'aide des formules (65) (66) (67) et (69) ou en utilisant la figure (12) nous obtenons alors la puissance injectée W_i : 40 Watts pour le dipôle électrique et seulement 3 Watts pour le dipôle magnétique.

Mais le générateur alimentant les dipôles n'aura pas seulement à fournir la puissance W_i, il lui faudra aussi fournir la puissance dissipée en chaleur dans les prises de terre du dipôle électrique et dans le fil du dipôle magnétique.

Supposons les prises de terre constituées par des hémisphères de cuivre de 10 cm de rayon en contact avec le calcaire sur toute leur surface. La résistance électrique de chacune d'elle sera de 8 kΩ, soit au total $R_o = 16$ kΩ. Comme nous disposons pour le dipôle électrique d'une longueur $d\ell = 2$ m, il suffira d'y faire passer un courant de 225 mA. La puissance perdue dans les prises de terre sera alors $W_o = 800$ Watts.

En basse fréquence la résistance d'entrée du dipôle électrique est donc pratiquement celle de ses prises de terre et son rendement émissif est très mauvais.

Examinons maintenant le cas du dipôle magnétique. Dans une cavité de 1 m de rayon, il peut avoir une surface de 2,7 m^2. Avec 100 spires et un courant de 10 Ampères nous obtenons alors le moment nécessaire.

La réalisation technologique de ce dipôle résultera d'un compromis entre le poids, l'encombrement et le souci d'obtenir une faible résistance électrique. Le résultat est pour celle-ci un ordre de grandeur de 10 Ω. La puissance perdue dans le fil du dipôle est alors : $W_o = 1$ kW.

Ainsi, bien que le dipôle magnétique semble plus avantageux du point de vue émissif (3 W seulement sont nécessaires au lieu de 40 W), il est en définitive moins intéressant que le dipôle électrique. Un autre désavantage du dipôle magnétique est la valeur élevée de la partie réactive de son impédance. Un simple examen des formules (5) (7) et (36) (38), permet de se rendre compte qu'au voisinage des dipôles ($r \to 0$), les composantes électriques et magnétiques du champ sont en phase pour le dipôle électrique et en quadrature pour le dipôle magnétique. Ceci explique la différence des formules donnant l'énergie injectée dans le milieu absorbant par ces deux types de dipôles : le dipôle magnétique dissipe moins d'énergie dans son voisinage mais il faut lui fournir une énergie réactive importante. Il en résulte une partie selfique élevée de son impédance d'entrée qui crée des surtensions posant pour sa mise en oeuvre des problèmes technologiques délicats.

Utilisation de la fenêtre de transmission haute fréquence

A la limite $\beta_{max} = 6{,}7$ donnée par (63) correspond la fréquence : $f = 4{,}8$ MHz.

Supposons que nous désirions établir à cette fréquence une liaison électromagnétique sur une distance de 360 m à travers le calcaire. Nous avons à cette distance $x = 6$. Les limites inférieures des fenêtres de transmission haute fréquence sont données par les courbes de la figure (5). Pour $x = 6$ nous avons $\beta_M = 2{,}6$ (dipôle électrique) et $\beta_M^* = 1{,}15$ (dipôle magnétique). La fréquence de 4,8 MHz est donc située à l'intérieur des fenêtres de transmission haute fréquence des deux types de dipôles.

Pour $\beta = 6{,}7$ et $x = 6$, les courbes des figures (2) et (10) nous donnent : $|e_\theta| = 2{,}6$ et $|h_\theta| = 16{,}5$.

L'intensité du champ à la distance r sera :

$$H_\theta = h_\theta \frac{IdS}{4\pi r^3}$$ pour le dipôle magnétique

et

$$E_\theta = e_\theta \frac{Id\ell}{4\pi\sigma r^3}$$ pour le dipôle électrique

On extrait de ces formules les moments dipolaires nécessaires pour obtenir à 360 m un champ magnétique $H_\theta = 10^{-6}$ A/m et un champ électrique $E_\theta = 10^{-6}$ V/m :

$$IdS = 35 \text{ A.m}^2 \qquad Id\ell = 4{,}5.10^{-2} \text{ A.m}$$

La réalisation de moments dipolaires de cette intensité en haute fréquence est possible (surtout pour le dipôle électrique). Le calcul des puissances injectées dans le sol au moyen de la figure (12) et des formules (65) et (66) nous donne 18 Watts pour le dipôle magnétique et seulement $2{,}8.10^{-2}$ Watt pour le dipôle électrique.

Ces chiffres semblent indiquer que *l'utilisation de la gamme des ondes courtes serait possible pour réaliser sur de courtes distances des télécommunications à travers des milieux relativement peu conducteurs.*

Mais cette possibilité n'existe en fait que pour des milieux qui conservent jusqu'à des fréquences de quelques MHz une conductivité apparente très faible.

4. ANTENNE ELECTRIQUE HORIZONTALE PLACEE DANS UN DEMI-MILIEU CONDUCTEUR

4.1. Principe des liaisons à grande distance utilisant des dipôles enterrés ou immergés.

L'étude précédente nous a montré qu'un dipôle électrique ou magnétique placé dans un milieu conducteur rayonnait dans ce milieu une énergie électromagnétique décelable jusqu'à quelques centaines de mètres. C'est la conductivité électrique du milieu qui détermine les portées possibles et les gammes de fréquences permises. Ce type de télécommunication à travers les roches presente un intérêt évident pour l'industrie minière.

Il permet en particulier la réalisation de liaisons de secours utilisables en cas de catastrophes. Mais il ne présente pas d'intérêt pour les marins qui sont surtout désireux d'entrer en communication avec des sous-marins immergés à plusieurs milliers de kilomètres de leur base.

La propagation d'une onde électromagnétique sur une telle distance ne peut se faire qu'à travers un milieu présentant une conductivité nulle. La formule (20) montre en effet que dans ce cas la longueur caractéristique est infinie. Il faut donc nécessairement pour réaliser des liaisons à grande distance faire appel à la propagation dans l'atmosphère d'une onde électromagnétique.

La figure (13) montre qu'un dipôle électrique enterré ou immergé à une profondeur n'excédant pas la portée r_m permise à travers le sol ou à travers la mer, crée au-dessus de lui à la surface du sol ou de la mer, une nappe de courant. Celle-ci agit comme une antenne qui donne naissance à une onde qui se propage dans l'atmosphère. Cette onde, en se réfractant à travers l'interface air-mer ou air-sol, peut atteindre à une grande distance un récepteur situé dans un sous-marin ou dans une galerie de mine.

La figure (13) montre aussi que le dipôle doit être horizontal. En effet, si il est vertical (fig. 13.b.), il donne naissance en surface à deux nappes de courant de sens opposés qui ne peuvent engendrer qu'un rayonnement quadrupolaire de faible portée.

4.2. Importance de la littérature consacrée au rayonnement du dipôle électrique horizontal placé sous la surface.

La méthode d'analyse mathématique développée en (1926) par *SOMMERFELD* (Ref. (204)) et en (1937) par *NORTON* (Réf. (207)) pour l'étude du rayonnement de l'antenne électrique horizontale placée au-dessus du sol, a été adaptée en (1951) par *MOORE* (Réf. (302)) au cas d'un dipôle horizontal immergé. Cette étude a été en (1953) reprise et améliorée dans divers cas d'approximation par *LIEN* (Ref. (259)) ; *BANOS* et *WESLEY* (Réf. (263)) ; *WAIT* (Réf. (262)) ; *WAIT* et *CAMPBELL* (Réf. (260)) ; à nouveau *WAIT* en (1961) (Réf. (277)), puis de très nombreux auteurs dont les travaux sont cités dans la rubrique 2.4. de notre bibliographie.

En 1966 le livre de *BANOS* (Réf. (157)) donnait la somme de ces travaux qui sont d'un niveau mathématique élevé.

En raison précisément de ses applications importantes (en particulier pour les liaisons avec les sous-marins en plongée) le rayonnement des antennes horizontales souterraines ou sous-marines a été tellement étudié qu'il semble impossible d'apporter à cette étude une contribution originale. Nous nous contenterons donc de donner quelques formules pratiques et de citer des exemples numériques empruntés aux thèses de Doctorat de *FONTAINE* (Réf. (333)) et *DEGAUQUE* (Réf. 335)).

4.3. Zones d'approximation

La figure (14) montre le système de coordonnées cylindriques utilisé. Le dipôle électrique horizontal (deh) est dirigé suivant ox et placé à la profondeur h. La surface du sol coïncide avec le plan (xoy).

Les composantes $\vec{E}$ et $\vec{H}$ du champ électromagnétique sont encore données par les formules (3) et (4). Mais le potentiel de Hertz que nous écrirons $\vec{\Pi}_1$ dans le sol ou la mer et $\vec{\Pi}_2$ dans l'atmosphère possède dans chacun de ces deux milieux deux composantes :

$$\begin{cases} \Pi_{2x} \text{ et } \Pi_{2z} & \text{dans l'atmosphère} \\ \Pi_{1x} \text{ et } \Pi_{1z} & \text{dans le demi-milieu conducteur} \end{cases} \qquad (74)$$

Les expressions de ces composantes sont données par des formules que l'on trouvera dans les Réf. (333) et (157) et qui s'expriment en fonction des intégrales classiques de *SOMMERFELD*.

Pour simplifier la forme mathématique des résultats et rendre plus faciles les applications numériques *WAIT* (Réf. (277)) et *BANOS* (Réf. (157)) ont introduit trois distances caractéristiques R_A, R_B et R_C telles que :

$$|\gamma_1 R_A| = 1 \qquad |\gamma_2 R_B| = 1 \qquad |n^2 \gamma_2 R_C| = 1 \qquad (75)$$

γ_1 et γ_2 sont respectivement les facteurs de propagation des deux milieux : *

$$\gamma_1 = \sqrt{j\omega\mu(\sigma_1 + j\omega\varepsilon_1)} \qquad (76)$$

$$\gamma_2 = j\omega\mu\varepsilon \qquad (77)$$

et on pose :

$$n = \frac{\gamma_2}{\gamma_1} \qquad (78)$$

on suppose que : $|n|^2 << 1$ (ce qui revient à l'hypothèse $\sigma_1 >> \omega\varepsilon$), et que la distance r de la liaison est supérieure à plusieurs longueurs d'onde dans le sol : soit $|\gamma_1 r| >> 1$. Enfin la somme a des profondeurs du récepteur et de l'émetteur est bien inférieure à r.

* on pose : $\mu_1 = \mu_2 = \mu$ $\quad \varepsilon_2 = \varepsilon$

En explicitant les constantes de propagation, on obtient :

$$R_A = \frac{1}{4\pi}\sqrt{\frac{2.10^7}{\sigma_1 f}} \qquad (79)$$

$$R_B = \frac{3.10^8}{2\pi f} \qquad (80)$$

$$R_C = \frac{2,7.10^{18}}{\pi}\,\frac{\sigma_1}{f^2} \qquad (81)$$

On définit alors ainsi quatre zones d'approximation :

- zone très basses fréquences : $r < R_B/10$
- zone proche : $5R_A < r < R_B/5$
- zone intermédiaire : $R_B/5 < r < R_C/5$
- zone asymptotique : $r > 5R_C$

Nous avons représenté sur la figure (15) les limites de ces différentes zones pour un exemple concret où la conductivité du sol est $\sigma_1 = 3,3.10^{-4}$ mho/m.

Si nous choisissons pour fixer les idées une fréquence de 1 kHz, la zone très basses fréquences correspond à une distance r < 5 km, la zone proche a 3 km < r < 10 km et la zone intermédiaire à r > 10 km. Par contre à 50 kHz on est en zone intermédiaire entre 200 m et 20 km.

Les formules exprimant les composantes du champ au point de réception sont différentes dans chacune des zones d'approximation. Elles sont données dans les références (157) et (333).

4.4. Optimisation des liaisons en "zone intermédiaire"

La figure (16) montre une exploitation numérique de ces formules. On s'est fixé la distance de la liaison : r = 15 km ; trois valeurs de la conductivité σ_1 du sol et deux valeurs de a = 500 m et a = 200 m de la somme des profondeurs de l'émetteur et du récepteur. On remarque l'excellent raccordement des formules de la zone TBF et de celles de la zone intermédiaire.

Pour recevoir le maximum de champ les antennes d'emission doivent être parallèles. Mais leur direction commune peut être parallèle ou perpendiculaire à la droite joignant l'émetteur au récepteur. Le champ reçu dans le premier cas sera noté $E_{//}$ il est représenté sur la figure (16) par les courbes en trait plein. Les courbes pointillées montrent les variations de $E_{\perp}$ correspondant à la seconde orientation des antennes.

En T.B.F. on a toujours $E_{\perp} = 2E_{//}$. Mais au-delà d'une certaine fréquence f_{cr} $E_{//}$ devient supérieur à $E_{\perp}$. *GABILLARD, FONTAINE* et *DEGAUQUE* (Réf. (328), (332), (333)), ont montré que la fréquence f_{cr} était indépendante de la conductivité du sol et était donnée par la formule très simple :

$$f_{cr} = 2,35\,\frac{c}{2\pi r} = \frac{1,14.10^8}{r}\ \text{Hz} \qquad (82)$$

c étant la vitesse de la lumière.

Cette formule permet pour une liaison de distance et de fréquence données de prévoir l'orientation optimum des antennes.

Les courbes de la figure (16) montrent aussi que pour une liaison donnée : (r et a fixées) $E_{//}$ passe par un maximum pour une fréquence f_{opt} de la bande V.L.F. Les mêmes auteurs (Réf. (330), (332), (333)), ont montré que cette fréquence ne dépendait pas de la distance r mais uniquement de a et σ_1. On a avec une très bonne approximation :

$$f_{opt} = \frac{32}{2\pi\mu a^2\sigma_1} = \frac{4.10^6}{a^2\sigma_1}\ \text{Hz} \qquad (83)$$

$E_{//}$ pour f_{opt} peut être supérieur ou inférieur à $E_{\perp}$ pour $f \to 0$. Les abaques de la figure (17) permettent de calculer en fonction de σ_1 et de a pour les deux distances r = 15 km et r = 30 km le rapport :

$$\theta = \frac{E_{//}\ \text{pour}\ f = f_{opt}}{E_{\perp}\ \text{pour}\ f \to 0} \qquad (84)$$

Si l'on obtient $\theta > 1$ on a intérêt à effectuer la liaison sur la fréquence f_{opt} et à adapter la disposition parallèle des antennes.

Exemple :

Pour fixer les idées considérons un massif calcaire de conductivité $\sigma_1 = 3,3.10^{-4}$ mho/m (resistivité 3000 Ωm) qui correspond à un exemple réel et cherchons le champ produit en surface à 15 km par un émetteur enterré à 500 m dans le calcaire (a = 500).

Sur la figure (17) nous trouvons $\theta = 2,9$ et la figure (16) nous donne pour $f \to 0$ $E_{\perp} = 2,3.10^{-10}$ V/m.La figure (16) est normalisée pour un moment électrique Idℓ = 1 du dipôle émetteur. Supposons que nous puissions réaliser (ce qui est technologiquement facile) dℓ = 100 m et I = 25 A. Nous aurons en surface à 15 km :

$$E_{//} = 1,7\ \mu V/m$$

La fréquence d'émission sera donnée par (83) :

$$f = f_{opt} = 48,5\ \text{kHz}$$

(Pour cette même liaison, la fréquence f_{cr} donnée par (82) est 7,6 kHz, et la figure (15) montre que la liaison se situe en zone "intermédiaire").

4.5. Diagrammes de rayonnement des antennes longues

L'exemple précédent de liaisons à quelques dizaines de kilomètres trouve des applications dans certains problèmes militaires particuliers et en protection civile. Mais pour intéresser les marins il faut pouvoir réaliser à partir d'un émetteur enterré des portées de plusieurs milliers de kilomètres. Pour cela on est amené à augmenter le moment électrique de l'antenne en augmentant sa longueur (ce qui ne consomme pratiquement pas de puissance). On obtient alors une antenne longue le long de laquelle le courant n'est plus uniforme. On a alors à résoudre plusieurs problèmes :

- L'étude de la distribution du courant le long de l'antenne
- La détermination de l'impédance d'entrée de l'antenne et de son efficacité de rayonnement
- Le tracé des diagrammes de rayonnement dans le plan horizontal et dans le plan vertical.

Le diagramme de rayonnement dans le plan vertical est particulièrement important à connaître car il détermine la manière dont l'antenne va exciter le guide d'ondes Terre-Ionosphère sans lequel les portées envisagées de plusieurs milliers de kilomètres ne seraient pas possibles.

Les résultats que nous allons donner ont été obtenus par *DEGAUQUE* (Réf. (335)) qui a exploité numériquement les formules de *BANOS* (Réf. (157)).

Dans le plan horizontal le diagramme de rayonnement d'une antenne longue dépend de la zone d'approximation dans laquelle se situe la liaison. La figure (18) montre ce diagramme dans le cas d'une émission très basse fréquence : f = 300 Hz. On retrouve le fait qu'en T.B.F. $E_{\perp} = 2E_{//}$ (l'antenne de réception est supposée toujours orientée dans la direction de la composante horizontale du champ électrique). La figure (19) montre le même diagramme dans le cas de l'approximation de la "zone intermédiaire" : f = 30 kHz. Le diagramme possède une forme très voisine de celui de l'approximation de la "zone T.B.F." mais on remarque qu'il a pivoté de $\pi/2$ par rapport à la direction de l'antenne. Le fait que l'on ait une antenne résonnante en $\lambda/4$ diminue seulement l'intensité du champ (courbe (2)) sans modifier la forme, qui est semblable à celle du diagramme de rayonnement du dipôle (courbe (1)).

En "zone asymptotique" la composante $E_{\perp}$ devient très faible et dans le plan horizontal le diagramme a la forme d'un 8.

La figure (20) montre dans le plan vertical les diagrammes des composantes E_r et E_z du champ électrique et le champ résultant E. Ces diagrammes sont obtenus dans l'approximation asymptotique en supposant le point de réception situé à 500 km de l'antenne. Cette hypothèse fait abstraction de l'ionosphère. Nous voyons que si cette couche n'existait pas toute l'énergie émise par l'antenne horizontale serait rayonnée vers le haut et se perdrait dans l'espace. *DEGAUQUE* montre (Réf. (335)) que l'énergie rayonnée le long de la surface du sol dans la petite couronne sphérique correspondant à $\theta_m < \theta < \pi/2$ est négligeable par rapport à l'énergie rayonnée dans la calotte sphérique $0 < \theta < \theta_m$. Ainsi, sans l'ionosphère qui réfléchit l'énergie émise vers le haut et l'oblige à se canaliser le long de la surface terrestre des liaisons à grande distance ne seraient pas possibles en utilisant une antenne horizontale enterrée.

4.6. "Impédances" et "rendements" de l'antenne horizontale enterrée

Si l'on assimile l'ionosphère à un réflecteur parfait, l'énergie totale rayonnée à grande distance dans le guide terre-ionosphère sera la même que celle rayonnée dans la calotte sphérique $0 < \theta < \theta_m$. On dispose ainsi d'un moyen commode pour calculer la résistance de rayonnement.

DEGAUQUE (Réf. (335)) a déterminé la puissance W_r rayonnée dans cette calotte sphérique en calculant sur sa surface l'intégrale du vecteur de Poynting. Puisque l'on se trouve dans l'atmosphère (milieu non absorbant), on trouve pour W_r une valeur limite lorsque $r \to \infty$. Il devient ainsi possible de définir pour l'antenne enterrée une "résistance de rayonnement" par la formule :

$$R_r = \frac{W_r}{I^2} \qquad (85)$$

En supposant le courant I constant ce qui correspond au cas de l'antenne électriquement courte, on obtient :

$$R_r = 9{,}8.10^{-25}\, \ell^2 f^3 \sigma^{-1} e^{-2h/\delta} \qquad (86)$$

ℓ est la longueur de l'antenne, σ la conductivité du terrain dans lequel elle est enterrée à la profondeur h et δ la *longueur de pénétration* :

$$\delta = (\pi\mu\sigma f)^{-1/2}$$

L'antenne horizontale enterrée est constituée par un fil de diamètre d placé dans une galerie que nous assimilerons à un tunnel cylindrique de diamètre D. Le fil doit être relié à chaque extrémité à une prise de terre si la longueur de la galerie n'est pas suffisante pour obtenir une résonance de l'antenne. L'ensemble est assimilable à un coaxial dont la gaine serait un mauvais conducteur.

La puissance W_i injectée dans le sol par ce type d'antenne se calcule en intégrant le vecteur de Poynting sur toute la surface des parois de la galerie. La figure (21) montre le principe de cette intégration.

La puissance injectée W_i donne naissance à une onde qui se propage dans le sol, et qui, si la galerie n'est pas trop profonde, crée à la surface la nappe de courant qui engendre le rayonnement atmosphérique de l'antenne. On définit le *rendement radiatif* de l'antenne comme le rapport :

$$\rho_r = \frac{W_r}{W_i} \qquad (87)$$

Le calcul de W_i est relativement classique et figure en particulier dans les livres de *STRATTON* (Réf. (137)) et *GALEJS* (Réf. (160)) qui étudient le cas du conducteur cylindrique isolé placé dans un milieu absorbant d'étendue infinie.

L'analyse de l'influence de l'interface air-sol est moins classique. Elle a été effectué par *GUY* et *HASSERJIAN*(Réf. (106)) et par *WHEELER* (Réf. (272)). Elle a été reprise par *DEGAUQUE* dans sa thèse (Réf. (335)). Ce calcul relativement long et complexe conduit à un résultat remarquablement simple. Sous réserve que sa profondeur h soit égale ou supérieure à la longueur de pénétration δ, l'antenne peut être assimilée à une ligne de transmission placée dans un milieu conducteur infini. *GHOSE* (Réf. (92)) a montré que cette ligne possédait alors une impédance série par unité de longueur :

$$Z_s = \frac{\omega\mu}{8} + j\,\frac{\omega\mu}{2\pi}\,\mathrm{Log}(1{,}59\,\frac{\delta}{d}) \qquad (88)$$

Cette formule est valable sous les deux conditions :

$$D \ll \delta \qquad (89) \qquad\qquad \mathrm{Log}(1{,}59\,\frac{\delta}{d}) > 5 \qquad (90)$$

Si la longueur ℓ de l'antenne est petite par rapport à la longueur d'onde, la puissance W_i injectée dans le sol est alors donnée par :

$$W_i = R_i\ \overline{I^2} \qquad (91)$$

avec
$$R_i = \frac{\pi\mu f}{4}\,\ell \qquad (92)$$

Ainsi W_i ne dépend, ni de la profondeur de l'antenne, ni de ses dimensions géométriques, ni de la conductivité du terrain.

Mais une antenne électriquement courte doit nécessairement être branchée à ses extrêmités sur des prises de terre. Le générateur doit donc en plus de W_i fournir la puissance W_o qui est dissipée en pure perte dans les prises de terre et dans le fil de l'antenne. On a :

$$W_o = (\ell R_o + R_p)\ \overline{I^2} \qquad (93)$$

R_o étant la résistance par unité de longueur du conducteur central et R_p la résistance des prises de terre.

Nous appellerons *rendement propre* de l'antenne, le rapport : $\rho_p = \dfrac{W_i}{W_i + W_o}$ (94)

Le rendement global est alors le produit : $\rho = \rho_r\,\rho_p$ (95)

D'après (86) et (90) nous avons : $\rho_r = \dfrac{R_r}{R_i} = 10^{-18}\ \dfrac{\ell f^2}{\sigma}\ e^{-2h/\delta}$ (96)

et par suite le rendement global de l'antenne courte est :

$$\rho = 9{,}8.10^{-25}\ \frac{\ell^2 f^3 \sigma^{-1}\ e^{-2h/\delta}}{(\frac{\pi\mu}{4} f + R_o)\ell + R_p} \qquad (97)$$

L'impédance d'entrée est :

$$Z_e = R_e + jX_e \qquad (98)$$

avec :

$$\begin{cases} R_e = (\frac{\pi\mu}{4} f + R_o)\ell + R_p & (99) \\ X_e = \mu f \ell\,\mathrm{Log}(1{,}59\,\frac{\delta}{d}) & (100) \end{cases}$$

Cas d'une antenne résonnante

Si la longueur de l'antenne n'est plus petite vis-à-vis de la longueur d'onde il est possible de laisser son extrêmité en circuit ouvert et ainsi d'éliminer la prise de terre. La théorie classique des lignes donne alors pour l'impédance d'entrée :

Résonance en $\lambda/4$

$$Z'_e = R'_e + jX'_e \qquad (101)$$

avec :

$$\begin{cases} R'_e = \frac{15\pi^2}{4}\ \frac{1}{\psi} + R_o\ell' + R'_p & (102) \\ X'_e = -\frac{14}{\mathrm{Log}(\frac{D}{d})}\ \frac{1}{\psi^2} & (103) \end{cases}$$

Résonance en $\lambda/2$

$$Z''_e = R''_e + jX''_e \qquad (104)$$

avec :

$$\begin{cases} R''_e = \frac{15\pi^2}{2}\ \frac{1}{\psi} + R_o\ell'' & (105) \\ X''_e = -\frac{28}{\mathrm{Log}\,(\frac{D}{d})}\ \frac{1}{\psi^2} & (106) \end{cases}$$

Ces formules supposent que l'antenne a des pertes relativement faibles et que les conditions (89) et (90) sont vérifiées.

ψ est le *facteur de ralentissement* égal au rapport de la vitesse de propagation des ondes dans l'atmosphère à la vitesse de propagation v le long de l'antenne.

On a :

$$\psi = \frac{c}{v} = \left[\frac{\text{Log}(1{,}59\ \frac{\delta}{d})}{\text{Log}\ \frac{D}{d}} \right]^{1/2} \qquad (107)$$

La puissance injectée dans le sol par une antenne résonnante est donnée par la formule (91) dans laquelle il faut remplacer $\overline{I^2}$ par l'intégrale :

$$\overline{I^2} = \frac{1}{\ell} \int_0^{\ell} I(\ell)^2\, d\ell \qquad (108)$$

A cette modification près, les formules donnant les rendements de l'antenne courte sont valables pour l'antenne résonnante.

Efficacité d'une antenne enterrée

On peut se faire une idée de l'efficacité d'une antenne horizontale enterrée en comparant ses performances à celles d'une antenne verticale aérienne. Cette comparaison est donnée par le rapport F de leurs résistances de rayonnement.

La résistance de rayonnement du demi-doublet de Hertz vertical posé à la surface du sol est :

$$R_v = 40\ (\frac{2\pi H}{\lambda})^2 \qquad (109)$$

H étant la hauteur de la nappe de fils constituant la capacité terminale et λ la longueur d'onde dans l'air. On a donc :

$$F = \frac{R_r}{R_v} = 5{,}6.10^{-11}\ \frac{f}{\sigma}\ \frac{\ell^2}{H^2}\ e^{-2h/\delta} \qquad (110)$$

Cette formule est valable pour une antenne électriquement courte.

Considérons par exemple une antenne de 2 km enterrée à la profondeur h = 200 m dans un terrain de conductivité $\sigma = 3{,}3.10^{-4}$ mho/m. La formule (110) donne $F = 2.10^{-2}$ pour une fréquence de 18 kHz si l'on compare cette antenne à une antenne verticale de 300 m. de haut.

4.7. Champ produit à grande distance

La détermination de l'intensité des composantes du champ électromagnétique produit à quelques milliers de kilomètres de l'antenne émettrice nécessite le calcul de la propagation dans le guide Terre-Ionosphère. L'étude théorique de ce type de propagation a fait l'objet depuis le travail original de *WATSON* (Réf. (399)) en 1919 de publications que leur très grand nombre nous empêche de citer intégralement. Nous donnons cependant dans la partie complémentaire de notre bibliographie quelques références (Réf. (399) à (412)).

DEGAUQUE (Réf. (335)) a calculé le champ produit par une antenne électrique horizontale enterrée pour des distances de 500 à 3000 km. Il utilise la théorie des modes de *WAIT* (Réf. (405)) dans l'approximation de la terre plate et d'une ionosphère homogène. Cette hypothèse est valable pour les fréquences inférieures à 20 kHz qu'il envisage.

La figure (22) montre la composante verticale E_z à la surface du sol pour la fréquence 18 kHz. La courbe est similaire à celle obtenue avec une antenne aérienne verticale. La figure (23) montre pour 4 distances les variations de E_z en fonction de la fréquence.

Il est intéressant de constater que des champs de l'ordre de grandeur de 1 µV/m sont obtenus avec un dispositif émetteur relativement modeste : Antenne de 2 km enterrée à 200 m dans un massif calcaire ou granitique de conductivité $\sigma = 3{,}3.10^{-4}$ mho/m. Le courant nécessaire et la puissance du générateur sont de l'ordre de 100 A et 100 kW.

Un sous-marin en plongée ne dispose que de l'onde qui s'est réfractée dans la mer et qui s'atténue exponentiellement en fonction de la profondeur. La figure (24) montre qu'au voisinage de la surface le champ magnétique de l'onde qui pénètre dans la mer est le même que celui de l'onde aérienne, tandis que la composante E_z du champ électrique dans la mer est beaucoup plus petite que la composante E_z dans l'air. Une antenne sensible au champ magnétique sera donc préférable à une antenne sensible au champ électrique.

La faisabilité d'une liaison avec un sous-marin en plongée dépend aussi du bruit parasite à la réception. Le choix des fréquences de transmission optimum doit être fait en tenant compte de la répartition spectrale du bruit dans la bande V.L.F. (Voir *MAXWELL* (Réf. (414)) et *BROCK NANNESTAD* (Réf. 413)).

5. PROGRES ET RECHERCHES A EFFECTUER CONCERNANT LES ANTENNES EMETTRICES ENTERREES

La longue antenne horizontale enterrée parallèlement à la surface du sol constitue le procédé classique d'émission à partir d'une station souterraine. Il y a maintenant 19 années que les bases de l'étude théorique de ce dispositif ont été établies par MOORE (Réf. (302)).

Il faut probablement rechercher dans le très petit nombre de réalisations pratiques de ce type d'emetteur (et dans le fait que les réalisations existantes n'ont donné lieu qu'à des études classifiées), l'explication du peu de progrés apparents accomplis depuis le mémoire original de MOORE. Néanmoins certaines études sont susceptibles de faire évoluer cette technique d'émission.

5.1. Influence de la stratification et du relief du terrain

Une antenne immergée peut être considérée comme étant placée dans un demi-milieu conducteur infini. La raison en est la bonne homogénéité de la conductivité de l'eau de mer et sa valeur élevée qui provoque l'absorption totale des ondes avant qu'elles aient atteint le fond de la mer. Il en est différemment des antennes enterrées, car l'épaisseur des stratifications du terrain peut être petite par rapport à la longueur de pénétration des ondes dans le sol.

Le cas d'une couche peu conductrice et d'épaisseur D $\leq \delta$ surmontant un demi-milieu infini fortement

conducteur a été particulièrement etudi , à cause probablement de l'importance des applications pratiques. Un dipôle placé dans cette couche est en effet dans l'environnement physique qui est celui d'un émetteur, au milieu de la jungle, ou enterre dans la couche de glace qui recouvre les régions polaires.

L'excitation d'une onde latérale par un dipôle placé dans cette couche de conductivite intermediaire a été étudiéepar *TAMIR* et *FELSEN* (Réf. (415)) ; *TAYLOR* (Ref. (416)) ; *SACHS* et *WYATT* (Ref. (417)) ; *BURROW* (Réf. (418));*STAIMAN* et *TAMIR* (Réf. (419)) ; *TAMIR* et *BIGGS* (Ref. (421)) ; et par *WAIT* (Réf. (155), (244), (329)).

Le résultat le plus intéressant de ces investigations est qu'il existe un angle optimum de l'inclinaison du dipôle qui assure le rayonnement maximum dans une direction donnée. La figure (25) extraite de l'article de *TAMIR* (Réf. (420)) montre les divers modes de propagation entre un émetteur et un recepteur placés dans une forêt.

La figure (26) fait comprendre intuitivement la raison physique pour laquelle il existe une inclinaison préférentielle du dipôle émetteur pour l'excitation d'un mode determine du guide "terre-ionosphère". Ici les lois de l'optique viennent en aide à la compréhension des phénomènes. Enfin, *WAIT* a montré (Réf. (329)) que si le dipôle était placé tout en bas de la couche de faible conductivite, la disposition verticale redevenait préférable. Les figures (27 a et b) montrent l'évidence physique de ce resultat mathématique. En effet si l'on fait tendre vers zéro la conductivite de la première couche d'epaisseur H, on se retrouve dans le cas de la figure(27 a),qui est celui de l'antenne verticale placée à la surface du sol.

Ces résultats conduisent à penser que l'antenne horizontale n'est peut être pas la meilleure solution pour la réalisation des stations souterraines destinées à communiquer avec les sous-marins. En effet, les massifs calcaires de faible conductivite où il est favorable de placer ces stations surmontent assez souvent des terrains sédimentaires très épais et très conducteurs. L'épaisseur de calcaire n'etant que de 1000 à 2000 m, on est exactement placé dans le cas de structure de la figure (27 b.). Il y aurait alors lieu de comparer l'efficacité et le prix de revient d'une antenne horizontale à celui d'une antenne verticale placée dans un forage atteignant le terrain conducteur sous-jacent. Il serait possible d'y placer une excellente prise de terre (Voir figure (28)).

Enfin le relief de la surface du terrain situé au-dessus de l'antenne n'est certainement pas sans influence sur son rayonnement. Nous savons en effet que ce sont les nappes de courant qui circulent à la surface du sol qui produisent le rayonnement atmosphérique de l'antenne.

L'influence du relief du terrain a eté très étudiée en ce qui concerne la propagation des ondes courtes et la réflexion des ondes radar (Réf. (422) ; (423)), mais à notre connaissance il n'existe pas encore de publications consacrées à l'influence du relief sur le rayonnement des antennes souterraines. Il n'est certainement pas sans importance que celle-ci soit surmontee d'une montagne ou d'une plaine. Nous pensons que de telles études évidemment difficiles à entreprendre mathématiquement, devraient être effectuées au moins sur maquettes (Voir Réf. (424) ; (320)).

A cette influence du relief s'ajoute l'effet des changements de terrains le long du parcours de l'onde. Ces changements sont dûs soit à une variation de l'altitude de l'ionosphère (passage du jour à la nuit), soit à la traversée d'une ligne de côtes (passage de la terre à la mer). L'effet de ces facteurs a été particulièrement bien étudié. Ce sujet est celui de la communication du Professeur WAIT à la Session I. de la présente conférence.

5.2. *Utilisation des ondes courtes*

Nous avons vu qu'il existait pour la propagation des ondes à travers les roches la possibilité d'une fenêtre de transmission haute fréquence. Il n'est donc pas impossible d'obtenir un rayonnement d'ondes courtes dans l'atmosphère à partir d'antennes souterraines. Pratiquement l'antenne ne doit pas être enterrée à une profondeur dépassant beaucoup la longueur caractéristique L_c du terrain. Ceci exclut la mer (L_c = 1,4 cm) des milieux au sein desquels cette technique serait possible. Mais pour certaines roches, surtout si elles sont situées dans des régions désertiques, L_c peut atteindre et dépasser une centaine de mètres. Il serait alors possible d'enterrer l'émetteur à une profondeur lui apportant une protection efficace.

Les études à conduire pour évaluer la faisabilité d'un tel projet seraient l'analyse des variations des paramètres σ et ε de la roche dans les bandes d'ondes courtes. Il faudrait également reprendre toute l'étude du rayonnement des antennes souterraines en abandonnant l'hypothèse $\sigma \gg \omega\varepsilon$.

GALEJS (Réf. (290), (120)) a montré que dans ce cas la méthode du calcul de *MOORE* assimilant l'antenne immergée à une ligne coaxiale n'était plus valable, et que la supériorité du dipôle électrique horizontal sur d'autres types d'antennes n'était plus évidente.

GALEJS (Réf. (120)) a donné des résultats à la fois théoriques et expérimentaux concernant le type d'antenne représenté figure (21 b.). Cette antenne peut être assimilée à une cavité cylindrique couplée au milieu extérieur par une fente circulaire. Enterrée à une profondeur de 1 m dans un terrain ayant une conductivité $\sigma = 2.10^{-2}$ mho/m et une constante diélectrique $\varepsilon = 10\,\varepsilon_0$ cette antenne rayonne plus efficacement qu'un dipôle horizontal dans la bande de fréquence 2 à 30 MHz.

Les caractéristiques du terrain de couverture calculées à l'aide des formules (17) et (20) sont : f_c = 36 MHz et L_c = 80 cm. A 30 MHz, l'antenne travaillait donc avec x = 1,25 et β = 0,83.

La courbe de la figure (2) ne s'applique évidemment pas au type d'antenne etudié par *GALEJS*. Mais si l'on suppose que chaque élément de surface de la fente circulaire se comporte comme un dipôle infinitésimal, on voit que pour x inférieur à 2, l'intensité du champ électrique se maintient constante dans toute la partie basse fréquence et commence juste à augmenter à β = 0,83. Ceci est en accord avec le résultat rapporté par *GALEJS*.

Des antennes de ce type enterrées à très faible profondeur ont de nombreuses applications militaires et civiles (antennes de piste d'aéroport par exemple).

5.3. *Réseaux d'antennes*

Nous conclurons cette revue des antennes enterrées en donnant quelques références concernant les réseaux d'antennes enterrées. *GUY* et *HASSERJIAN*(Réf. (106)) ; *GHOSE* (Ref. (288)) et d'autres auteurs

(Réf. (286)), ont étudié des projets de stations d'émission souterraines formées de plusieurs antennes horizontales disposées parallèlement. Si ces antennes sont enterrées près de la surface et séparées d'une distance supérieure à la longueur de pénétration δ elles n'ont pratiquement pas d'influence les unes sur les autres. Mais comme δ est beaucoup plus petit que la longueur d'onde dans l'air, elles rayonnent à grande distance comme une antenne unique parcourue par un courant I = n i, n étant le nombre des antennes et i le courant dans chacune d'elles. Si w est la puissance nécessaire à chaque antenne, l'ensemble du réseau consomme une puissance W = nw. Pour obtenir le même rayonnement avec une seule antenne, la puissance perdue dans les prises de terre augmentant avec le carré du courant, il faudrait une puissance égale à $n^2 w$.

A puissance de générateur égale, un réseau de n antennes permet donc de gagner un facteur n sur l'intensité du champ rayonné.

Il est certain que la conception de stations émettrices destinées à la communication avec les sous-marins doit s'inspirer de cette technique des réseaux.

ANNEXE

Calcul de la fonction $\beta_m(x)$

L'examen de la figure (2) montre qu'il y a deux valeurs de la variable β pour laquelle $|e_\theta| = 1$.

$$\beta_m << 1 \qquad (1)\text{-I} \qquad \text{et} \qquad \beta_M >> 1 \qquad (2)\text{-I}$$

β_m étant petit, l'expression (21) de γ peut se simplifier. Nous avons en effet si β est négligeable devant 1 :

$$a = b = (2\beta)^{1/2} \qquad (3)\text{-I}$$

et par suite :

$$\gamma = (1 + j)\frac{1}{\delta} \qquad (4)\text{-I}$$

avec :

$$\delta = \frac{L_c}{\sqrt{2\beta}} = \sqrt{\frac{2}{\omega\mu\sigma}} \qquad (5)\text{-I}$$

δ est un nouveau paramètre qui dépend à la fois des caractéristiques μ et σ du milieu conducteur et de la fréquence. Ses dimensions physiques sont celles d'une longueur et on l'appelle *la longueur de pénétration*. L'intérêt de ce paramètre est que si nous définissons une nouvelle distance relative par :

$$\boxed{\eta = \frac{r}{\delta}} \qquad (6)\text{-I}$$

il devient possible d'exprimer $|e_\theta|$ en fonction de la seule variable η. Nous avons :

$$|e_\theta| = F(\eta) = \left[(1 + \eta)^2 + \eta^2(1 + 2\eta)^2\right]^{1/2} e^{-\eta} \qquad (7)\text{-I}$$

La figure (6) montre la fonction F(η), égale à 1 pour η = 0 elle croît et passe par un maximum égal à 1,45 pour η = 1,62. Elle décroît ensuite et est à nouveau egale à 1 pour $\eta = \eta_o = 3{,}16$.

Nous aurons donc $|e_\theta| = 1$ pour $\frac{r}{\delta} = \eta_o$, soit, en tenant compte de l'expression (5) de δ pour :

$$\boxed{\beta = \beta_m = \frac{1}{2}\frac{\eta_o^2}{x^2} \# \frac{5}{x^2}} \qquad (8)\text{-I}$$

La formule (8)-I n'est évidemment valable que pour x > 10 car il faut que l'inégalité (1)-I reste satisfaite. Pour x < 10 nous avons extrait β_m d'une résolution numérique de l'équation obtenue en faisant dans (25) $|e_\theta| = 1$.

Calcul de la fonction $\beta_M(x)$

Si β est beaucoup plus grand que 1 nous avons :

$$a = 1 \qquad (9)\text{-I} \qquad\qquad b = 2\beta \qquad (10)\text{-I}$$

et par suite :

$$\gamma r = x(1 + j2\beta) \qquad (11)\text{-I}$$

En portant cette valeur de γr dans la formule (12) et en tenant compte de (2)-I nous avons :

$$|e_\theta| = \left[4x^2 + \frac{1}{\beta^2}(4\beta^2x^2 - 1)^2\right]^{1/2} e^{-x} \qquad (12)\text{-I}$$

cette formule se simplifie si nous avons :

$$2\beta x >> 1 \qquad (13)\text{-I}$$

En remplaçant dans cette inégalité L_c et β par leurs valeurs (15) et (20) celle-ci devient :

$$r >> \frac{1}{\omega\sqrt{\mu\varepsilon}} = \frac{\lambda}{2\pi} \qquad (14)\text{-I}$$

λ étant la longueur d'onde dans un milieu non absorbant de perméabilité μ et de constante diélectrique ε.

Si (14)-I est satisfait nous obtenons alors en faisant, dans (12)-I, $|e_\theta| = 1$:

$$\boxed{\beta_M = \frac{e^x}{4x^2}} \qquad (15)\text{-I}$$

Cette formule commence à être valable pour x > 7. Pour x < 7, nous avons extrait β_M d'une resolution numérique de l'équation obtenue en faisant dans (12)-I $|e_\theta| = 1$.

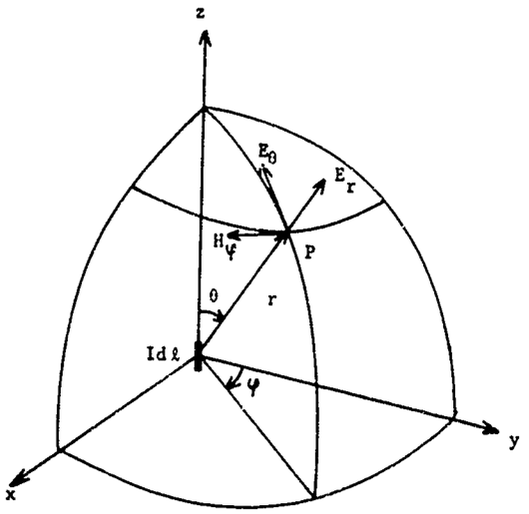

Fréquence caractéristique $f_c = \frac{1}{2\pi} \frac{\sigma}{\varepsilon}$

Longueur caractéristique $L_c = \frac{2}{\sigma}\sqrt{\frac{\varepsilon}{\mu}}$

Figure 1

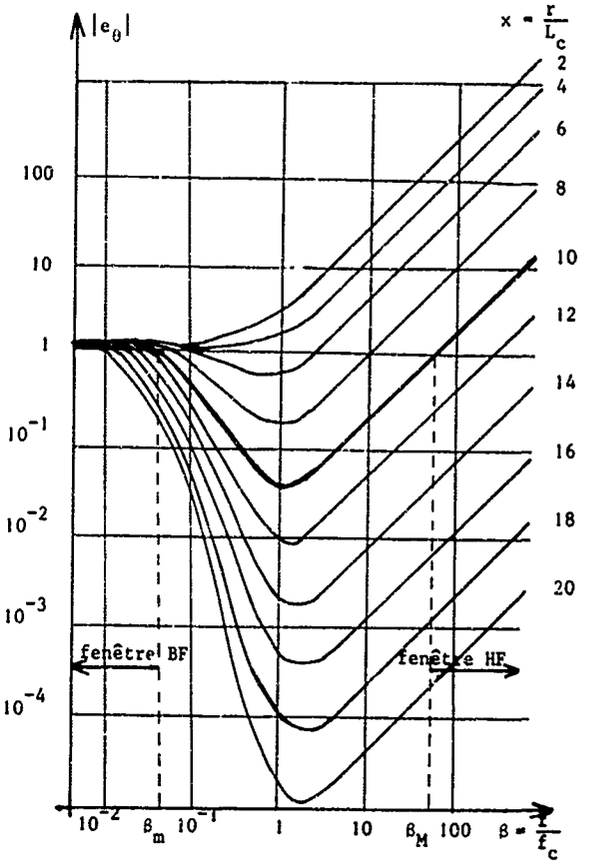

Figure 2

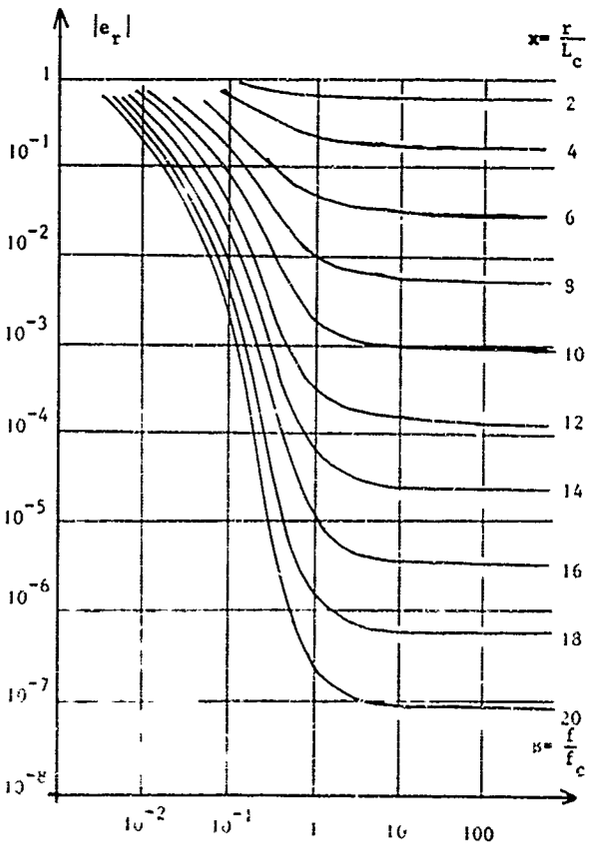

Figure 3

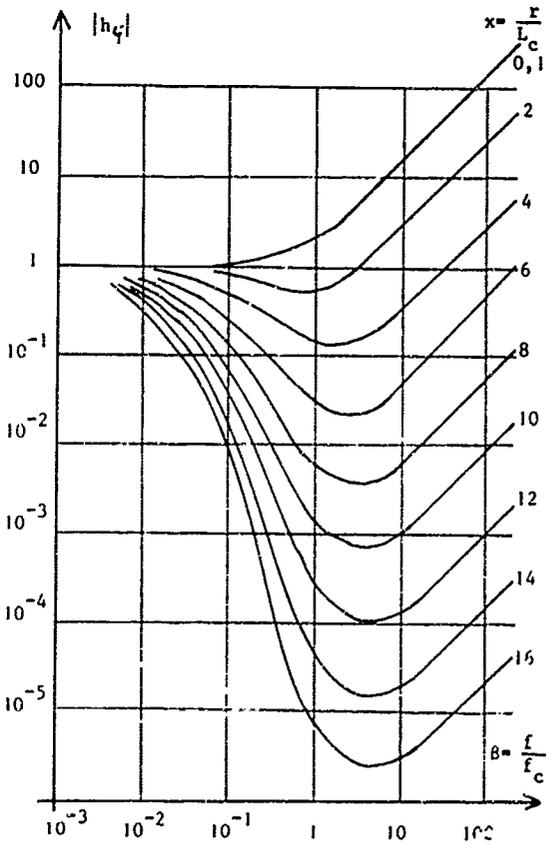

Figure 4

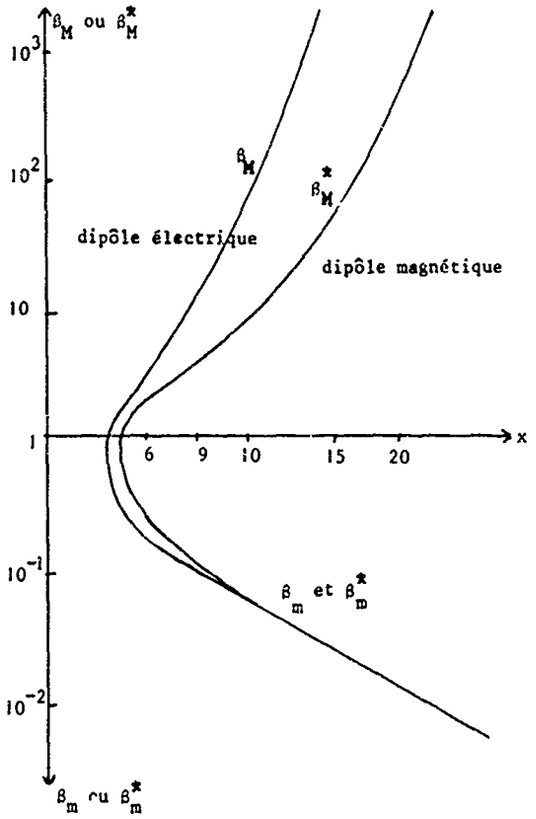

Figure 5

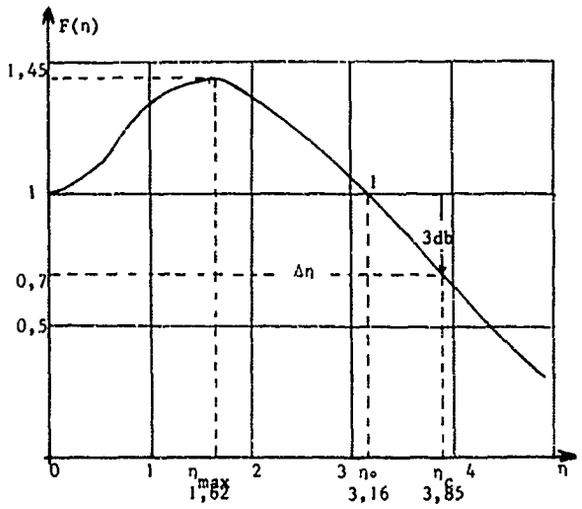

Figure 6

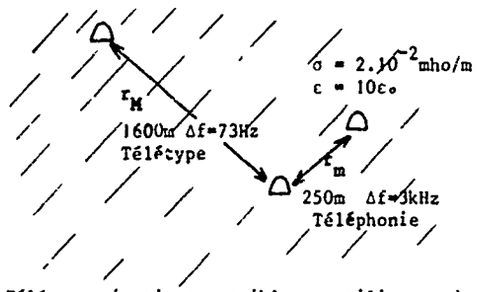

Télécommunications possibles en milieu conducteur et infini

Figure 7

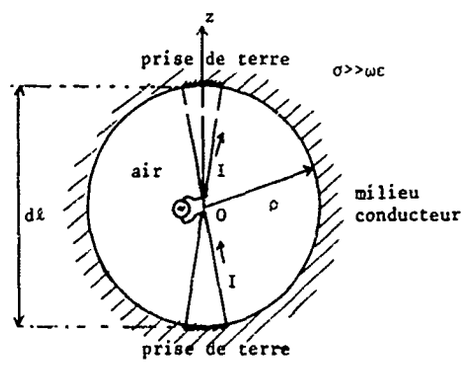

Figure 8

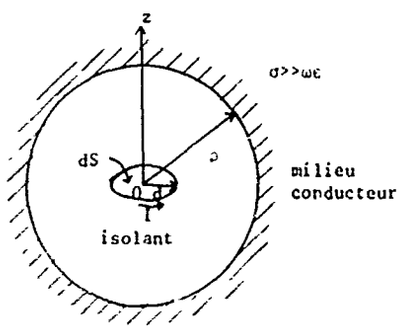

Figure 9

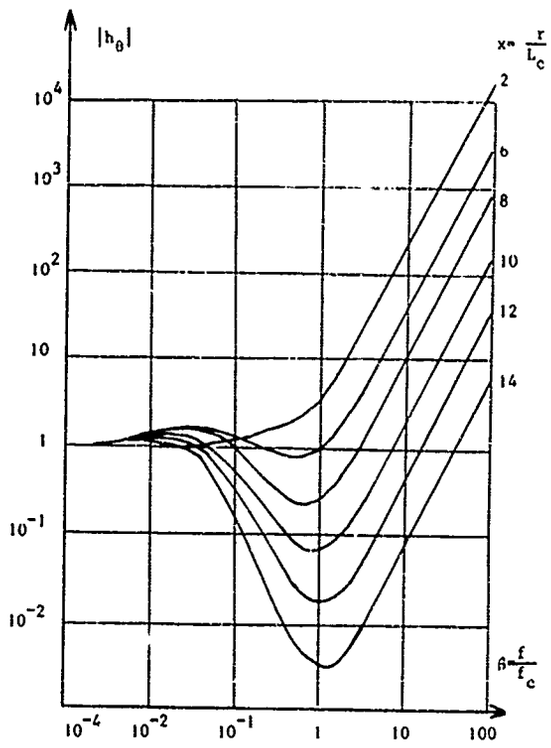

Figure 10

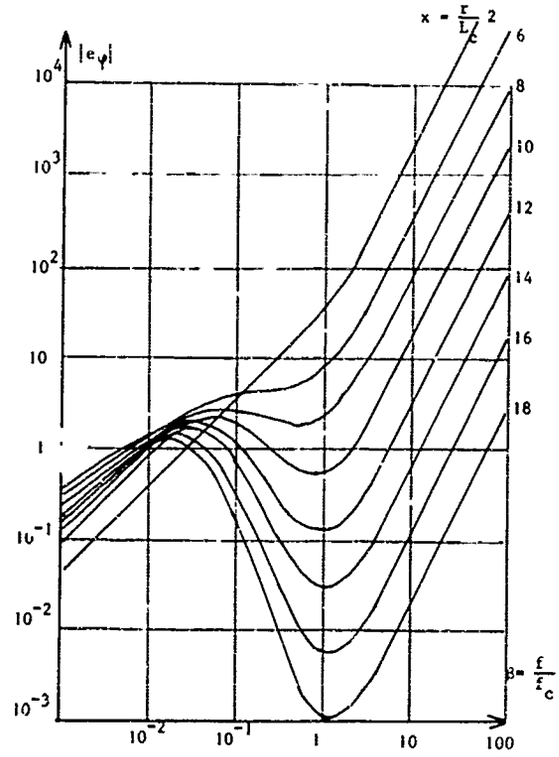

Figure 11

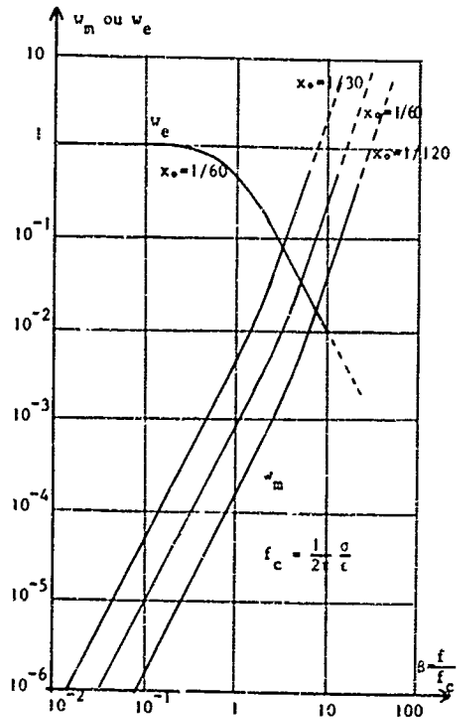

Figure 12

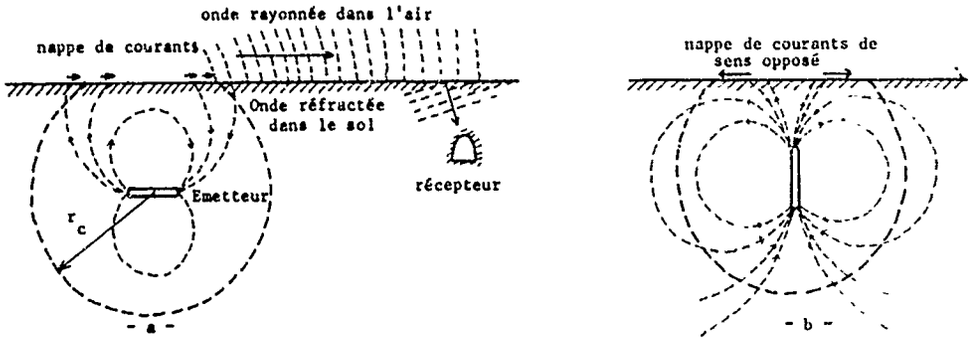

Figure 13

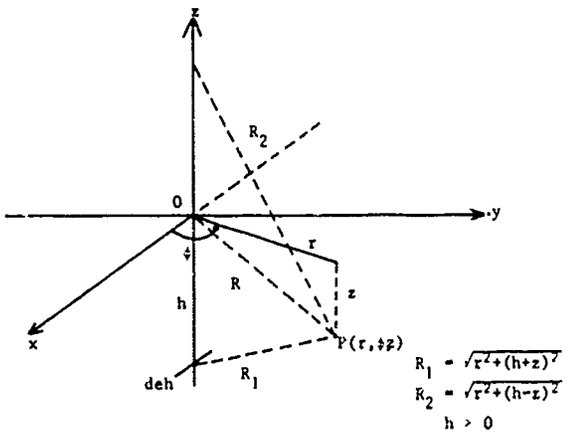

Figure 14

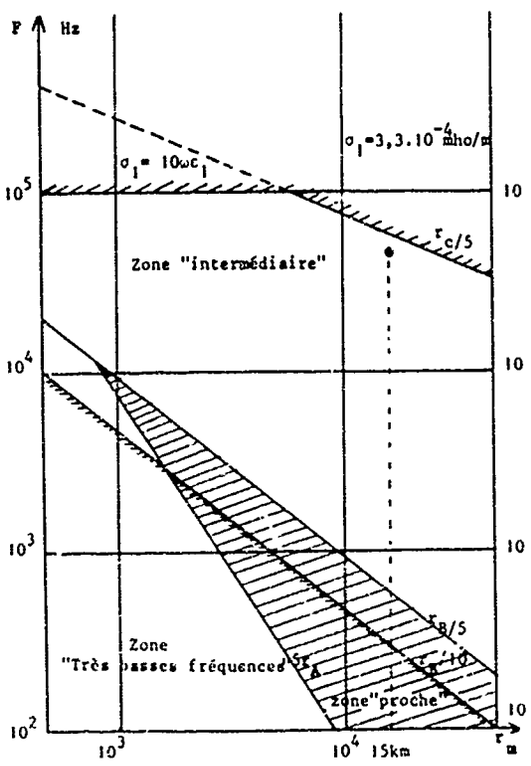

Figure 15

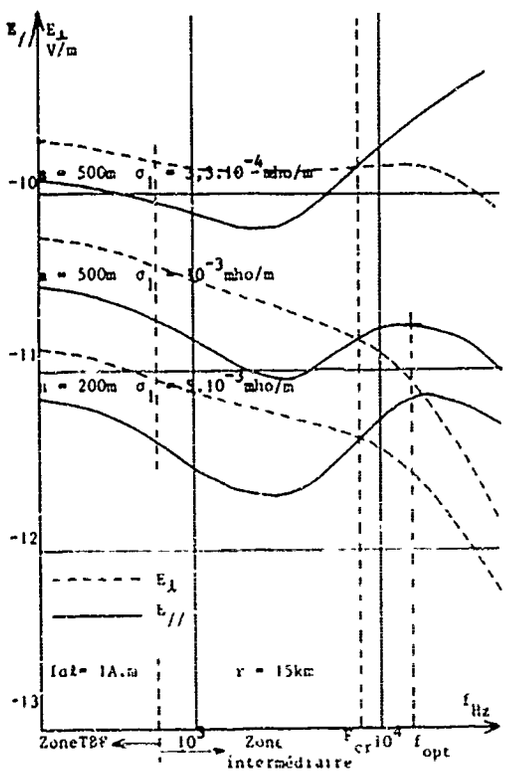

Figure 16

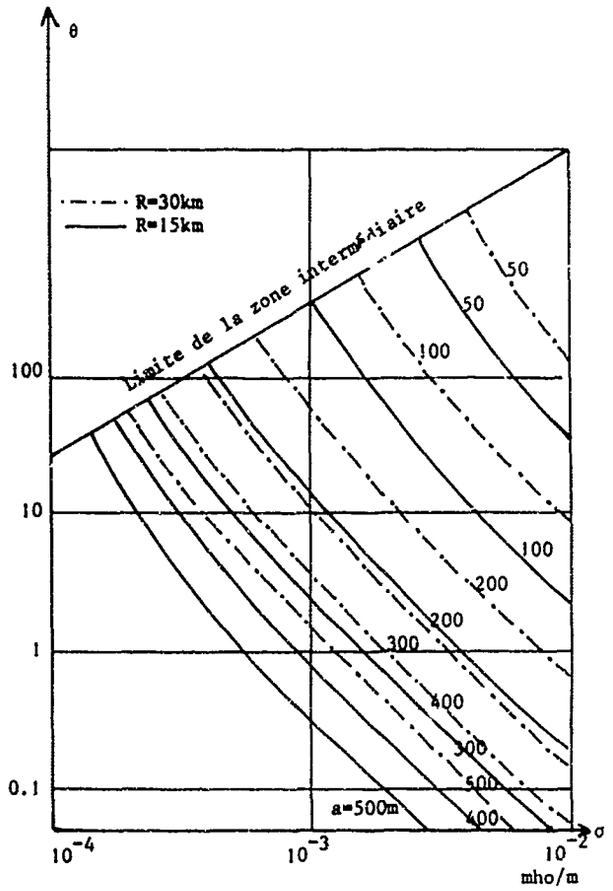

Figure 17

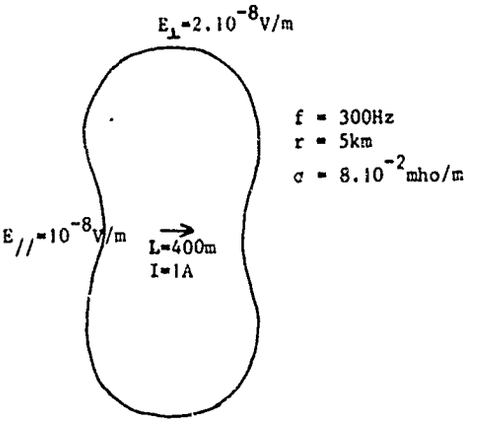

Figure 18

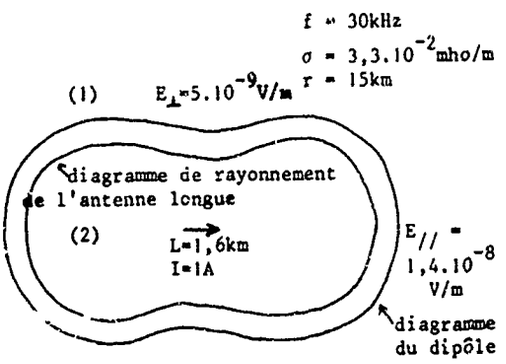

Figure 19

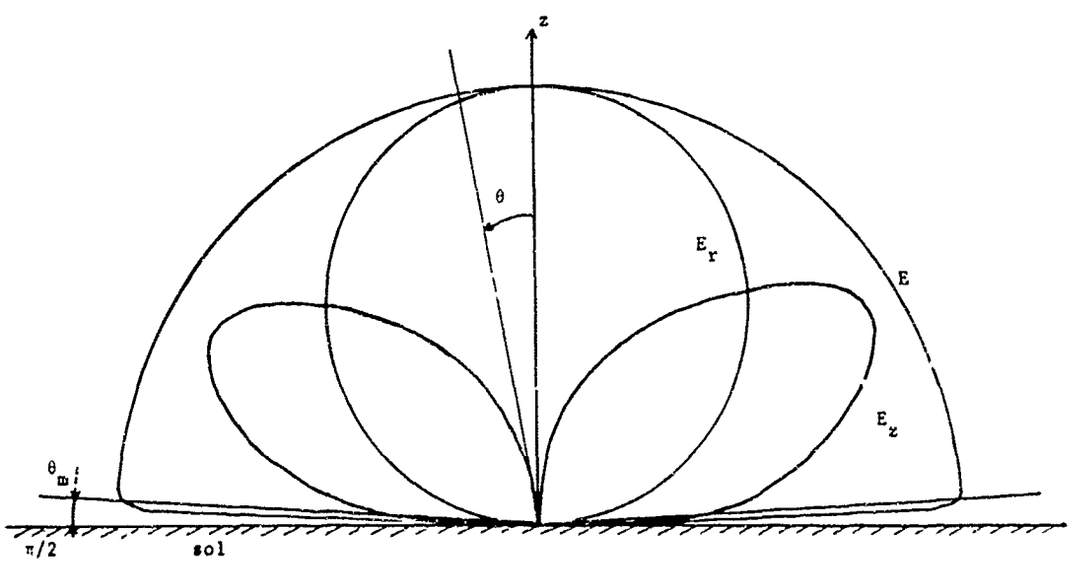

Figure 20

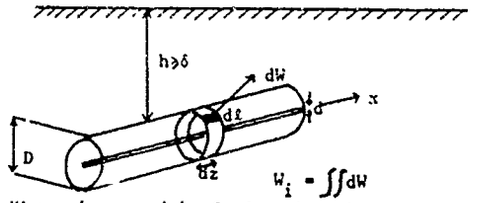

dW : puissance injectée dans le sol par la surface dS = dℓ.dz

Antenne galerie pour ondes VLF f < 100kHz

- a -

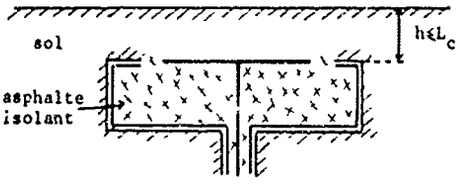

- b -

Antenne HF 2MHz < f < 30Mhz

Figure 21

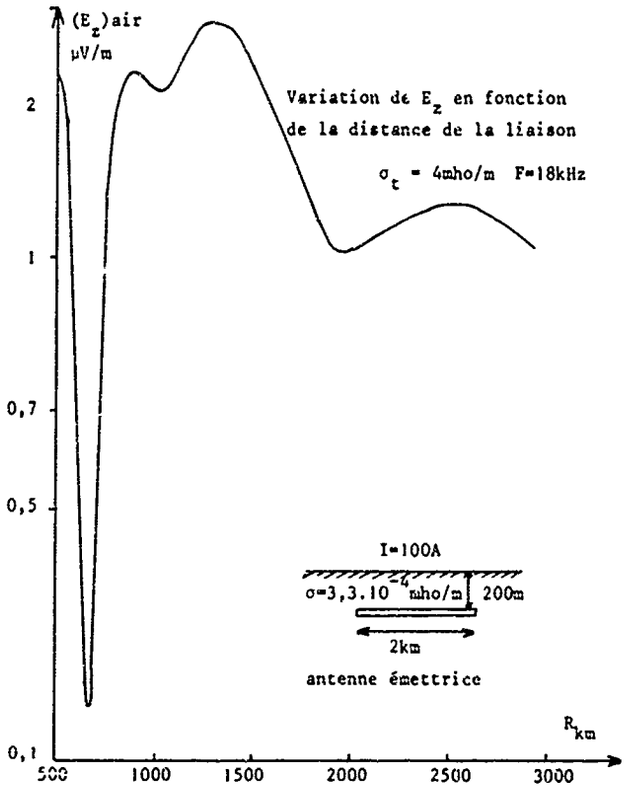

Figure 22

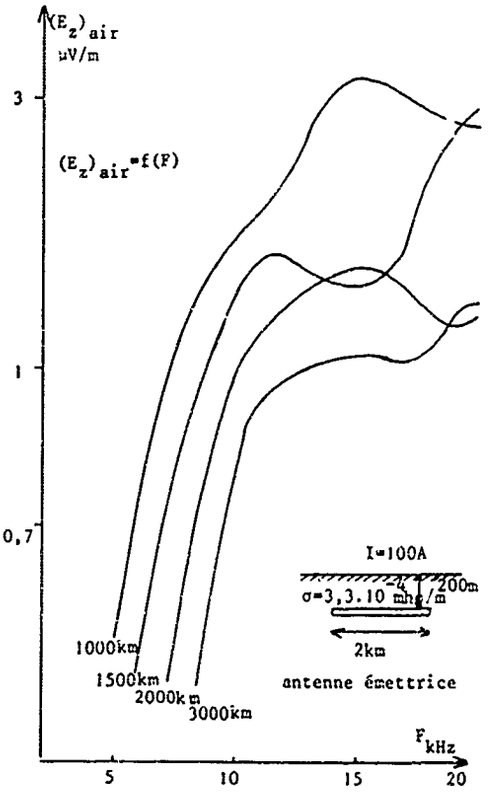

Figure 23

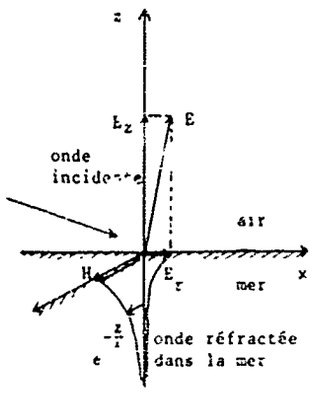

Figure 24

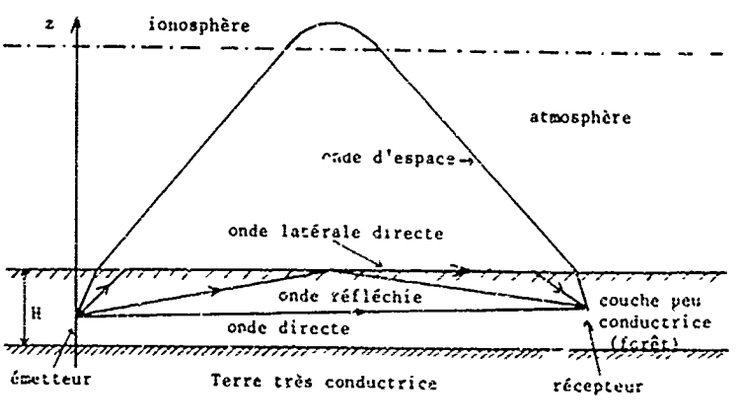

Figure 25

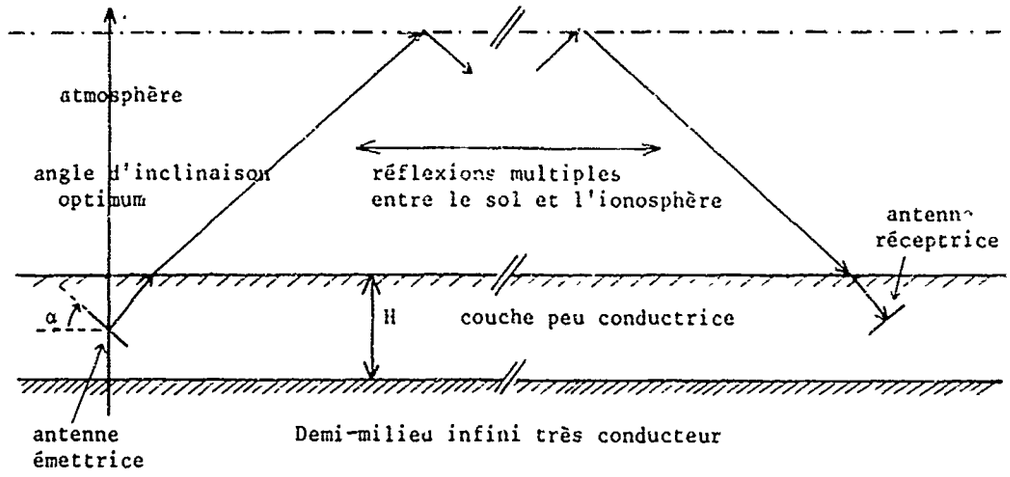

Figure 26

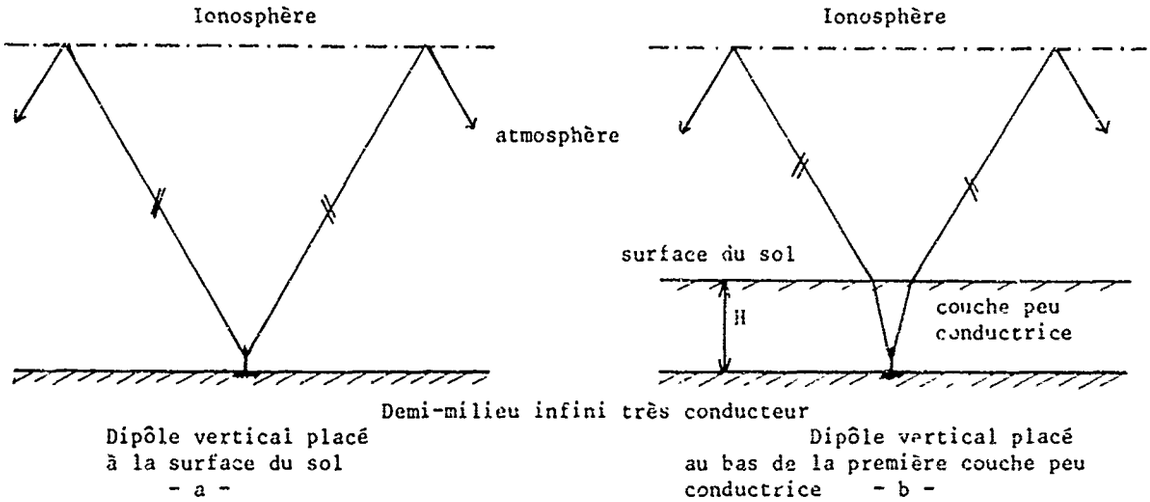

Figure 27

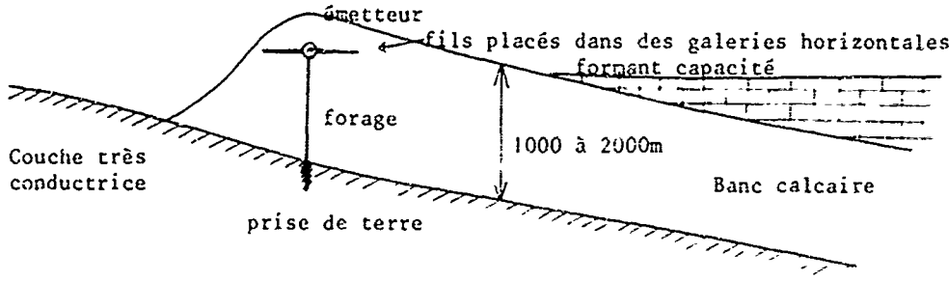

Figure 28

METHODE DE CALCUL EXACTE DE LA REPARTITION DES COURANTS SUR UNE ANTENNE

par

Maurice BOUIX, D.R.M.E.
CETHEDEC
5bis, Avenue de la Porte de Sèvres - 75 - Paris 15è

METHODE DE CALCUL EXACTE DE LA REPARTITION DES COURANTS SUR UNE ANTENNE

par M. BOUIX, DRME,
CETHEDEC

SOMMAIRE

En utilisant la définition des sources électromagnétiques ponctuelles donnée par l'auteur dans son livre "les discontinuités du rayonnement électromagnétique", on trouve une équation intégrale vectorielle pour la détermination exacte des courants sur une antenne formée d'un conducteur de forme quelconque portant une ligne de sources. On applique cette méthode à une antenne de révolution épaisse quelconque alimentée par une fente ; l'équation intégrale est alors scalaire. Une méthode numérique est donnée dans le cas de l'antenne cylindrique épaisse avec des bouts plats ou sphériques.

L'intérêt de cette résolution est qu'elle s'étend à des problèmes très divers de propagation dans des milieux stratifiés et avec des conditions aux limites variées.

SUMMARY

ACCURATE METHOD FOR COMPUTING THE CURRENT DISTRIBUTION ON AN ANTENNA

Based on the definition of the pinpoint electromagnetic sources as given by the author in this book entitled : "Discontinuities in Electromagnetic Radiations", an integral vectorial equation is derived for the accurate determination of currents on an antenna consisting of a waveguide of any shape, bearing a line of sources. This method is applied to any thick axisymetrical antenna supplied through a slot ; then, the integral equation is of the scalar type. A numerical method is given for the case of the thick cylindrical antenna with flat or spherical ends.

The advantage of this solution lies in the fact that it can be extended to very different propagation problems in stratified media with various boundary conditions.

1- GENERALITES

Nous nous proposons de calculer les courants sur une antenne parfaitement conductrice connaissant les sources pour une fréquence donnée $\omega/(2\pi)$.

On utilisera les notations des références [1] et [2], rappelées brièvement ici : $\vec{E}$, $\vec{H}$: champs électrique et magnétique ; $\vec{M}$, $\vec{J}$: sources magnétique et électrique ; ε,μ,σ : permittivité diélectrique, perméabilité magnétique, conductivité ; système d'unités MKS Giorgi normalisé.

Les équations de Maxwell s'écrivent :

$$(1)\quad \mathrm{rot}\,\vec{E} + i\omega\mu\vec{H} = \vec{M}\ ;\ \mathrm{rot}\,\vec{H} - (i\omega\varepsilon+\sigma)\vec{E} = \vec{J}$$

et on en déduit les équations aux divergences

$$(2)\quad \mathrm{div}(i\omega\mu\vec{H}) = \mathrm{div}\,\vec{M}\ ;\ \mathrm{div}\,[(i\omega\varepsilon+\sigma)\vec{E}\,] = \mathrm{div}\,\vec{J}$$

ε,μ sont supposés constants dans tout l'espace ; σ sera supposé infini dans un milieu parfaitement conducteur, nul en dehors. Si S est une surface qui sépare un milieu conducteur de l'espace non conducteur, si $\vec{n}$ est le vecteur unitaire de la normale à S orientée vers le milieu non conducteur et si $\vec{I}$ désigne la densité superficielle de courant sur S, on a :

$$(3)\quad \vec{I} = \vec{n}\wedge\vec{H}_S$$

$\vec{H}_S$ étant le champ magnétique dans le milieu non conducteur sur S (dans le milieu conducteur $\vec{E}$, $\vec{H}$ sont nuls). Si ρ est la densité superficielle de charge électrique sur S, on a encore [1].

$$(4)\quad \rho = 1/(i\omega\varepsilon)\ \vec{n}.\vec{E}_S = \mathrm{div}\,\vec{I}$$

On posera dans ce qui suit :

$$(5)\quad k = \omega(\varepsilon\mu)^{1/2}\ ;\ \eta = (\mu/\varepsilon)^{1/2}$$

Si on élimine $\vec{E}$ entre les deux relations de Maxwell (1), on a l'équation en $\vec{H}$

$$(6)\quad \mathrm{rot\ rot}\,\vec{H} - k^2\vec{H} = \mathrm{rot}\,\vec{J} + i\omega\varepsilon\vec{M}$$

Considérons maintenant une surface régulière idéale Σ partageant l'espace $\mathbb{R}^3$ en deux domaines D et D' et en chaque point M de Σ considérons le vecteur unitaire $\vec{n}$ de la normale orientée vers le domaine D ; soit l une abscisse portée sur cette normale à partir de M.

.../...

On désigne par U et U' les fonctions caractéristiques des domaines D et D' (si $P \in D$, alors $U(P) = 1$, $U'(P) = 0$; si $P \in D'$, alors $U(P) = 0$, $U'(P) = 1$).

Si $\vec{H}$ et $\vec{H}'$ désignent la fonction vectorielle $\vec{H}$ dans D et D', on voit à partir de (6) et des formules d'analyse vectorielle [1], [2], que le champ égal à $\vec{H}$ dans D et à zéro dans D' satisfait à l'équation de Helmholtz à second membre.

$$\Delta(U\vec{H}) + k^2(U\vec{H}) = [2(\partial\vec{H}/\partial l + H \operatorname{div} \vec{n}]\,\delta(1) + \vec{H}\delta'(1) + \operatorname{rot} \vec{J}$$

$$(7) \qquad + i\omega\vec{\varepsilon M} + (i\omega\mu)^{-1} \operatorname{grad} \operatorname{div} \vec{M}$$

(cela signifie, par exemple, que, si le "support" des sources $\vec{M}$, $\vec{J}$ est dans D', la distribution portée par la surface Σ annule exactement l'effet de ces sources du côté D' de Σ ; et que pour calculer le champ du côté D, on peut remplacer les sources par la distribution sur Σ).

Soit alors V une solution arbitraire de l'équation de Helmholtz scalaire

(8) $\Delta V + k^2 V = -4\pi\delta$ (δ distribution de Dirac de l'origine).

A chaque solution V de (8), on voit, en formant la différence des produits de convolution $V * \Delta(U\vec{H}) - \Delta V * (U\vec{H}) = 0$

et en tenant de l'égalité $\delta * (U\vec{H}) = U\vec{H}$, que l'on peut tirer de (7) et (8)

$$U\vec{H} = -\frac{1}{4\pi}\{ V * [2\partial\vec{H}/\partial l + \vec{H} \operatorname{div} \vec{n}]\,\delta(1) + \vec{H}\delta'(1)$$

$$(9) \qquad + V * [\operatorname{rot} \vec{J} + i\omega\vec{\varepsilon M} + (i\omega\mu)^{-1} \operatorname{grad} \operatorname{div} \vec{M}].$$

Or, à une fonction régulière près, si les coordonnées cartésiennes orthogonales du point $A \in \mathbb{R}^3$ sont x, y, z, la solution générale de (8) est donnée par :

(10) $V = [\alpha \exp(-ikr) + \beta \exp(ikr)]/r$

avec $r = [x^2+y^2+z^2]^{1/2}$.

Donc si $P \in \mathbb{R}^3$, $M \in \Sigma$, si maintenant r désigne la distance PM, si on désigne alors V par V(P,M) et si $\vec{n}$,l se rapportent au point $M \in \Sigma$, la relation (9) devient :

$$(11) \quad U(P)\,\vec{H}(P) = [-1/(4\pi)]\{\int [V(P,M)\,\partial\vec{H}(M)/\partial l - \vec{H}\partial V(P,M)/\partial l]\,d\Sigma$$

$$+ V * [\operatorname{rot} \vec{J} + i\omega\vec{\varepsilon M} + (i\omega\mu)^{-1} \operatorname{grad} \operatorname{div} \vec{M}]\}.$$

Si on avait fait un calcul analogue pour le domaine D', on aurait en désignant par $\vec{f}(M)$ et $\vec{g}(M)$ les discontinuités de $\vec{H}$ et de $\partial\vec{H}/\partial l$ sur Σ, soit :

(12) $\vec{f}(M) = \vec{H}(M) - \vec{H}'(M)$; $\vec{g}(M) = \partial\vec{H}(M)/\partial l - \partial\vec{H}'(M)/\partial l$:

$$U(P)\vec{H}(P) + U'(P)\vec{H}'(P)$$

$$= -[1/(4\pi)]\{\int_\Sigma [V(P,M)\,\vec{g}(M) - \vec{f}(M)\partial V(P,M)/\partial l]\,d\Sigma$$

$$(13) \qquad + 2V * [\operatorname{rot} \vec{J} + i\omega\vec{\varepsilon M} + (i\omega\mu)^{-1} \operatorname{grad} \operatorname{div} \vec{M}].$$

On a démontré à la réf : [2] que lorsque P traverse la surface Σ au point M_0 de D' vers D le premier terme du deuxième membre subit une discontinuité de $(1/2)\,f(M_0) = (1/2)[\vec{H}(M_0) - \vec{H}'(M_0)]$

et donc que l'on peut écrire, en étudiant la limite de l'expression (13) lorsque P tend vers M_0 soit du côté D, soit du côté D'

$$(13) \quad \vec{H}(M_0) + \vec{H}'(M_0) = -[1/(2\pi)]\{\int_\Sigma [V(M_0,M)\,\vec{g}(M) - \vec{f}(M)\partial V(M_0,M)/\partial l]\,d\Sigma$$

$$+ 4V * [\operatorname{rot} \vec{J} + i\omega\varepsilon\vec{M} + (i\omega\mu)^{-1} \operatorname{grad} \operatorname{div} \vec{M}]$$

où $\vec{f}$ et $\vec{g}$ ont les valeurs des relations (12)

Cette relation vectorielle constitue trois relations scalaires entre les douze composantes de $\vec{H}$, $\vec{H}'$, $\partial\vec{H}/\partial l$, $\partial\vec{H}'/\partial l$.

2. MODELE D'ANTENNE

Considérons une antenne constituée par une surface métallique fermée partagée en deux coquilles par une fente. On pourra en faire une antenne en plaçant une ligne de sources sur la fente. Les modèles de lignes de sources sont très variés et il peut être assez délicat de les décrire dans le cas général, nous en préciserons trois types au N° 3. Si nous prenons la surface parfaitement conductrice sauf sur la fente comme surface Σ, on devra écrire, que, sauf peut-être sur la fente, le champ électrique est normal à S, soit :

(14) $\vec{n} \wedge \operatorname{rot} \vec{H} = \vec{n} \wedge \operatorname{rot} \vec{H}' = 0$ sur S

.../...

ce qui suffit à assurer que la divergence est nulle partout.

On obtient ainsi neuf relations relatives à treize inconnues que sont les douze composantes déjà envisagées et le rapport β/α de la relation (10). Mais on sait [1] que (14) et (15) entraînent que $\vec{n}.\vec{H} = \vec{N}.\vec{H}' = 0$. Il reste donc seulement onze inconnues. Pour les déterminer il faudra écrire une condition de Sommerfeld pour le milieu extérieur D. (Cela s'exprime [1] uniquement au moyen de $\vec{H}$ et $\partial H/\partial l$ sur la surface Σ), ce qui **fournira** une dixième relation. Quant à la onzième, si la fente est constituée par une ligne de sources actives, on **écrira** que la puissance active qui traverse la fente est nulle.

Si la fente est raccordée à une ligne de transmission unimode, raccordée elle-même à une source et adaptée à cette source, le tout entièrement situé à l'intérieur du domaine D, les équations sont un peu différentes. Les inconnues sont les cinq composantes extérieures à Σ, le rapport β/α et le taux d'onde stationnaire sur la ligne de transmission. On aura trois équations de type (13) avec $H' = 0$; $\partial H/\partial l = 0$ deux équations du type (14), une du type (15) et une relation de Sommerfeld à l'intérieur.

3. ANTENNE DE REVOLUTION

Pour une antenne de révolution alimentée par des sources de type électrique à symétrie de révolution placée suivant une fente percée le long d'un parallèle, le problème se simplifie si on impose de plus aux courants d'être longitudinaux et aux sources d'être électriques suivant les méridiennes. Les seules inconnues qui restent sont a etb) les composantes du champ magnétique extérieur suivant les parallèles, fonction seulement de l'abscisse le long de la méridienne, c) le rapport β/α, et on n'a-qu'une seule équation intégrale suivant la méridienne provenant de la relation (13).

4. REMARQUE

Lorsque l'on fait un développement du champ rayonné par une antenne suivant une suite de champs orthogonaux (ainsi I. ROBIN a étudié le rayonnement d'une antenne sphéroïdale dans un exposé au CETHEDEC (Centre d'Etudes Théoriques de la Détection et des Communications)). Le problème est plus simple, car on sait a priori qu'on obtiendra un champ électromagnétique et on n'a pas besoin de préciser trop la nature de la source. Mais pour le problème général toutes les précautions prises ici sont utiles. Il faut encore remarquer que les diverses formes de sources liées à une même antenne vont peut-être conduire à des rayonnements assez différents.

==========

BIBLIOGRAPHIE

[1] M. BOUIX "Les discontinuités du rayonnement électromagnétique" Dunod 1966 PARIS.

[2] M. BOUIX - Détermination d'une solution des équations de Maxwell harmoniques extérieure à une surface. Application au rayonnement d'une antenne métallique. Revue du CETHEDEC 1968-4 N° 16.

[3] M. BOUIX "Fonction généralisée ou distribution". Masson 1964.

[4] GUELFAND et CHILOV - Tome 1 "Les distributions" Dunod 1970 PARIS.

[5] HORMANDER "Partial differential operators" Springer Verlag 1964.

==========

ON THE INFLUENCE OF THE THICKNESS OF EXCITATION GAP ON ANTENNA PERFORMANCE

by

G. Franceschetti
Dept. of El. Eng., Via Claudio 21, 80125 Napoli, Italy

and

Istituto Universitario Navale, Via Acton 38, 80133 Napoli, Italy

SOMMAIRE:

Dans un récent ouvrage de Franceschetti (1969), le comportement d'une vaste categorie d'antennes immergées dans un milieu conducteur a été etudié sous l'angle à la fois théorique et expérimental. Pour ces diverses antennes (sphériques, en forme d'ellipses allongées ou aplaties, rectangulaires), on a calculé la conductance d'entrée G et la hauteur effective h pour le cas statique limitatif où $\omega = 0$, on a obtenu :

$$G = A\sigma a\left(1 + C \ln\left[Da/s\right]\right) \quad , \quad h = \frac{Fa}{1+C \ln\left[Da/s\right]} \quad , \qquad (1)$$

σ étant la conductivité du milieu externe, "a" une dimension typique de l'antenne, s la largeur de l'intervalle d'excitation, et A, F, C et D des constantes connues.

La question qui se pose est la suivante : dans quelle mesure les résultats statiques peuvent-ils être appliqués au cas dynamique ?

Considérons un cas particulier, celui d'une antenne sphérique de rayon a. Pour l'admission d'entree Y, nous avons obtenu :

$$Y = G + j\,B = 2(\sigma + j\omega\varepsilon)(1 + \ln\left[a/4s\right] + \pi\Sigma) \quad , \qquad (2)$$

où Σ est une série à convergence rapide.

Dans le cas où $\sigma \neq 0$ et $\omega \to 0$, nous déduisons de (2) que les résultats statiques de (1) sont pratiquement valables, pourvu que $a \leq \delta/5$, $\delta = \sqrt{2/\omega\mu_o\sigma}$ représentant la pénétration de l'onde. En outre, on peut rendre B égal à zéro sur une très large bande si l'on choisit correctement a et s. Dans ce cas, le terme logarithmique s'applique à la fois à G et à B, lorsque $\sigma = 0$, il s'applique seulement à B.

En ce qui concerne h, il n'est pas facile de comparer les cas statique et dynamique lorsqu'on se réfère aux champs. Cependant, reportons nous au pseudopotentiel a (Schelkunoff, 1952 ; Wait, 1966), de façon que :

$$\underline{E} = -\frac{1}{r \sin\theta}\,\underline{i}_\phi \times \nabla a \quad . \qquad (3)$$

Ainsi, pour $r \to \infty$, nous avons, pour le terme bipolaire :

$$a_1 = -\frac{I\,h_d}{4\pi(\sigma+j\omega\varepsilon)} \sin^2\theta\left[\frac{1}{4} + jk\right] \exp\left[-jkr\right] \qquad (4)$$

où la hauteur dynamique effective h_d montre une dépendance logarithmique à l'égard de la largeur de l'intervalle et s'assimile à h lorsque $a<\delta/5$.

Nous obtenons, par exemple, à partir de (3) et (4) :

$$E_\theta = \sqrt{\frac{j\omega\mu_o}{\sigma+j\omega\varepsilon}}\,\frac{I\,h_d}{4\pi r}\,\sin\theta\left[jk + \frac{1}{r} + \frac{jk}{r^2}\right] \exp\left[-jkr\right] \quad , \qquad (5)$$

qui est le même E_θ que pour un bipôle élémentaire de hauteur h_d.

L'analyse qui précède peut être étendue à d'autres types d'antennes, couvrant ainsi une vaste catégorie d'antennes à nu ou isolées.

L'un des résultats importants de ces travaux, que nous n'avons pas trouvé dans les ouvrages publiés, est l'analyse de la dépendance de Y et de h à l'égard de la largeur de l'intervalle à la fois dans le cas dissipatif et non dissipatif. Nous avons également démontré l'importance et l'applicabilité des resultats statiques.

ON THE INFLUENCE OF THE THICKNESS OF EXCITATION GAP ON ANTENNA PERFORMANCE

G. Franceschetti
Dept. of El. Eng., Via Claudio 21, 80125 Napoli, Italy
and
Istituto Universitario Navale, Via Acton 38, 80133 Napoli, Italy

SUMMARY

The input admittance and the effective height of a spherical antenna in a lossless or conducting environment is computed. The antenna is assumed to be excited by means of a voltage applied to a small equatorial gap.

The explicit dependence of the antenna's parameters on the excitation gap thickness is found and discussed. Analytical expressions and graphs of the above parameters are shown. It is found that an approach in the zero-frequency limit should be very useful for these studies.

For the situation of both antennas,or of one of them, submerged or buried, the radio-link equation is computed. The optimum frequency which maximizes the ratio between the received and the transmitted power is found. The influence of the excitation gap thickness on the radio-link is demonstrated.

1. STATEMENT OF THE PROBLEM AND DISCUSSION OF PRINCIPAL RESULTS.

In a recent work (1) the behaviour of a large class of antennas (spherical, oblate and prolate spheroidal, strip antennas) immersed in a conducting medium was studied, in the limiting case of zero frequency excitation. By using special summation techniques on the series solution for the input conductance G, it was possible to extract the dependence of G on the excitation gap thickness; the remaining series turned out to be fairly rapidily convergent. The input conductance G and the effective height h both turned out to be dependent on the log of the gap thickness, as well as on the other dimensions of the antenna.

It should be interesting to enquire to what extent the static results could be applied in the dynamical case; or, more generally, to what extent the summation techniques adopted in the static could be applied in the dynamical case. This would be very useful for antennas not only in a conductive but also in a lossless environment. As a matter of fact, for this last case, fairly rapidily convergent series for the input susceptance should be obtained.

In order to make an initial approach to this problem, a spherical antenna was considered. The antenna (fig.1) was assumed to be excited with a constant voltage along a small equatorial gap; the time dependence of the applied voltage was assumed to be of type $\exp[j\omega t]$; the external medium was assumed to be isotropic, homogeneous, of permittivity ε, permeability μ, and conductivity σ; and the general solution for the input admittance y and effective heights h_n of the dipolar (n=1) and multipolar terms of radiation was found.

Although the solution obtained is valid in general, emphasis was placed, in the discussion of results on an antenna in a highly conductive medium such that $\sigma \gg \omega\varepsilon$.

It is believed that the results of this study can be enlarged to cover the more complex case of a spherical antenna in a layered environment, or immersed in a magnetized cold or warm plasma (2). More generally, it is believed that the main results are valid for all other antennas, apart from analytical complexities of the related study.

As far as the input admittance Y of the antenna is concerned, it was expressed as the sum of three terms, save a multiplicative factor; the first term shows explicitily the dependence of Y on the gap thickness; the second term is frequency independent, and in the form of a series whose convergence is of the type $1/n^2$, n being the summation index; the third term is frequency dependent and in the form of a series whose convergence is of the type $(ka/n)^3$ for $|ka|>n$, "a" being the radius of the antenna and $k^2=-j\omega\mu(\sigma+j\omega\varepsilon)$. The first two terms are exactly those that would be obtained by using a purely static approach (1); and this point emphasizes the usefulness of such a study in the zero-frequency limit, provided that $|ka|\ll 1$. The dependence of the gap thickness is on the input conductance G, when $\sigma \gg \omega\varepsilon$ (lossy case); on the contrary, it is on the input susceptance B when $\sigma=0$ (lossless case). A fairly interesting result for the lossy case is that B is negative (inductive), and can be exactly compensated in the range $|ka|\ll 1$ by means of a lumped capacitance. Therefore the antenna can be made to have a very flat response within a wide band.

As far as the effective height h of the dipolar term of radiation is concerned, it was computed for both the lossless and the lossy case. As the frequency is made to approach zero, the value of the effective height goes into that very value which would be computed by means of a static approach.

The dynamical behaviour of the field is conveniently described by a pseudopotential (3). In order to get the components of the field in the dynamical, or in the static case, different expansions for each term of the pseudopotential should be made in general. However, it is shown how to get expressions for the field, valid over all the frequency range, by a singe suitable asymptotic expansion for the pseudopotential.

For the computation of a radio link in practical situations of buried or submerged antennas,two cases are of interest (4): both the antennas are buried or submerged (up-over-and-down mechanism of propagation), or a single antenna is buried or submerged, and the other is upon the earth surface (up-and-over mechanism of propagation). The system equation for the radio link can be obtained by substituting for the buried or submerged antennas equivalent elementary dipoles of momentum I h, I being the input current of the antenna. It is thus possible to compute the very frequency for which the ratio between the received and the transmitted power reaches its maximum value. For the up-over-and-down case, it is found that optimum condition are obtained provided that $(h_1 + h_2) = 4\delta$, h_1 and h_2 being the depths of the antennas, and δ the skin depth of the wave (inversely proportional to the square root of the frequency). For the up-and-over case the optimum conditions are reached provided that $h = 7\delta$.

In both cases the received power is reduced if the gap thickness decreases. This fact suggests the use of insulating layers protruding from the gap in order to enhance the behaviour of the radio link. The dimensions of such layers can be optimized experimentally.

The work reported herein was sponsored by the Italian Consiglio Nazionale delle Ricerche, under the Contract 115.0615.03748.

2. COMPUTATION OF THE INPUT ADMITTANCE.

2.1. Formal solution to the problem.

Let us consider the spherical antenna of fig.1, immersed in a homogeneous infinite medium of conductivity σ, permittivity ε and permeability μ, which is excited by a constant voltage V along a small gap $2s = 2a\alpha$.

The electromagnetic field relative to this antenna is described by the following components, with reference to a spherical system of coordinates (r,θ,ϕ), centered on the centre of the antenna (5):

$$E_r = \sum_1^\infty t_n \frac{(2n-1)\, H^{(2)}_{2n-1/2}(kr)}{(\sigma+j\omega\varepsilon)\, r^{3/2}} \frac{}{\sin\theta} \left[P^1_{2n}(\eta) - \eta\, P^1_{2n-1}(\eta)\right]$$

$$E_\theta = \sum_1^\infty t_n \frac{P^1_{2n-1}(\eta)}{(\sigma+j\omega\varepsilon)\, r^{3/2}} \left[(2n-1)\, H^{(2)}_{2n-1/2}(kr) - kr\, H^{(2)}_{2n-3/2}(kr)\right] \qquad (1)$$

$$H_\phi = \sum_1^\infty t_n \frac{P^1_{2n-1}(\eta)}{r^{1/2}} H^{(2)}_{2n-1/2}(kr) \quad ,$$

P^1_n being the associate Legendre polinomial, $H^{(2)}_n$ the Hankel functions of second kind, and η equal to $\cos\theta$.

The coefficients t_n of the series expansion for the field are such as to satisfy the boundary conditions at r=a, and are therefore given by:

$$t_n = \frac{(\sigma+j\omega\varepsilon)\, a^{1/2}}{ka\, H^{(2)}_{2n-3/2}(ka) - (2n-1)\, H^{(2)}_{2n-1/2}(ka)} \frac{4n-1}{4\, n^2\, (2n-1)} \frac{V}{\sin^{-1}\eta_o} \int_o^{\eta_o} P^1_{2n-1}(\eta)\, d\eta \quad , \qquad (2)$$

where $\eta_o = \cos(\pi/2-\alpha) = \sin\alpha$.

The input admittance Y of the antenna can be obtained from Eq.(1) and (2) as follows:

$$Y = \frac{2\pi a\, H_\phi(a,o)}{V} = \pi a(\sigma+j\omega\varepsilon)\cos\alpha \sum_1^\infty \frac{4n-1}{2n(2n-1)^2} S_n(ka) \frac{P^1_{2n-1}(\eta)}{\sin^{-1}\eta_o} \int_o^{\eta_o} P^1_{2n-1}(\eta)\, d\eta \quad , \qquad (3)$$

where:

$$S_n(ka) = \frac{1}{1 - \dfrac{ka\, H^{(2)}_{2n-3/2}(ka)}{(2n-1) H^{(2)}_{2n-1/2}(ka)}} \quad .$$

It should be noted that the complex power radiated by the antenna is given by:

$$P = \frac{1}{2}\int_o^\pi d\theta \int_o^{2\pi} d\phi\, E_\theta(a,\theta)\, H^*_\phi(a,\theta)\, 2\pi a \sin\theta = \frac{1}{2}\,\frac{V}{s}\, s\, 2\pi a\, H^*_\phi\left(a,\frac{\pi}{2}\right) = \frac{1}{2}\, Y^*\, |V|^2 \quad , \qquad (4)$$

where the equality is valid in the limiting case of a very small gap.

By taking into account the properties of the Legendre polonomial (6), we obtain up to first-order terms in η_o:

$$\frac{P^1_{2n-1}(\eta_o)}{\sin^{-1}\eta_o} \int_o^{\eta_o} P^1_{2n-1}(\eta)\, d\eta = \frac{2n-1}{4n(n-1)} P_{2n-2}(\eta_o) \left[(2n^2 - 4n-1)\, P_{2n}(\eta_o) - (4n^2-2n-1)\, \frac{P_{2n+1}(\eta_o)}{\eta_o}\right] . \qquad (5)$$

For n fixed, and η_o sufficiently small, we get:

$$\frac{P^1_{2n-1}(\eta_o)}{\sin^{-1}\eta_o} \int_o^{\eta_o} P^1_{2n-1}(\eta)\, d\eta \to 4n^2\, [P_{2n}(o)]^2 \quad ; \qquad (6)$$

while, for η_o fixed and n sufficiently large, we get:

$$\frac{P^1_{2n-1}(\eta_o)}{\sin^{-1}\eta_o} \int_o^{\eta_o} P^1_{2n-1}(\eta)\, d\eta \to \frac{1}{\pi} \frac{\sin\left[4n \sin^{-1}\eta_o\right]}{\sin^{-1}\eta_o} \quad . \qquad (7)$$

Therefore the series of Eq.(3) can be recast in the following form:

$$Y = \pi a(\sigma+j\omega\varepsilon) \left\{ \sum_1^N \frac{2n(4n-1)}{(2n-1)^2} [P_{2n}(o)]^2 S_n(ka) + \sum_{N+1}^\infty \frac{1}{2\pi n^2} \frac{\sin\left[4n \sin^{-1}\eta_o\right]}{\sin^{-1}\eta_o} \right\} \quad , \qquad (8)$$

N being a (yet unspecified) suitable number, such that for $n<N$ the asymptotic expression of Eq.(6) could be used; on the contrary for $n>N$ the asymptotic expression of Eq.(7) should be appropriate, together with

the limiting value of $(4n-1)/2n(2n-1)^2 \to 1/2n$.

Adding and subtracting a same suitable quantity in Eq.(8) we get:

$$Y = a(\sigma+j\omega\varepsilon) \sum_{1}^{N} \frac{2n(4n-1)}{(2n-1)^2} \left\{ \left[P_{2n}(o)\right]^2 S_n(ka) - \frac{1}{2\pi n^2} \frac{\sin\left[4n \sin^{-1} n_o\right]}{\sin^{-1} n_o} \right\} +$$

$$+ \pi a(\sigma+j\omega\varepsilon) \sum_{1}^{\infty} \frac{1}{2\pi n^2} \frac{\sin\left[4n \sin^{-1} n_o\right]}{\sin^{-1} n_o} \qquad (9)$$

In the first summation the terms $(\sin x)/x$ can be put equal to x, since $n<N$. Furthermore we have, for n even moderately large:

$$S_n(ka) \frac{1}{1 - 0.35 \left(\frac{ka}{n}\right)^2} \approx 1 \quad ; \quad \left[P_{2n}(o)\right]^2 \to \frac{1}{\pi n} \quad . \qquad (10)$$

It is seen that the general term of the summation behaves as $1/n^2$, therefore rendering the summation fairly rapidly convergent. It follows that this summation can be converted into a series letting $N \to \infty$.

The second series can be totaled exactly (7). After some rearrangement, we get:

$$Y = 2\pi a (\sigma+j\omega\varepsilon) \left(\frac{1}{\pi} + \sum_{1}^{\infty} \left\{ \frac{n(4n-1)}{(2n-1)^2} \left[P_{2n}(o)\right]^2 - \frac{1}{\pi n} \right\} + \frac{1}{\pi} \ln \frac{a}{4s} \right) +$$

$$+ 2\pi a (\sigma+j\omega\varepsilon) \sum_{1}^{\infty} \frac{n(4n-1)}{(2n-1)^2} \left[P_{2n}(o)\right]^2 \left[S_n(ka)-1\right] = 2\pi a(\sigma+j\omega\varepsilon)\, y \quad . \qquad (11)$$

The normalized input admittance y consists essentially of three parts.

The first part, comprising the first two terms inside the first large bracket, is independent of both the frequency and the geometry of the antenna. This part can be totaled and is found to be equal to 0.85. The second part, comprising the last term inside the first large bracket, is only dependent on the length of the excitation gap normalized to the radius of the antenna. The third part is only dependent on the parameter ka. This last series is fairly rapidly convergent, since its general term behaves, for n large, as $(ka)^2/(2n)^3$, provided that $|ka|<2n$.

2.2. The lossy case.

When the antenna is immersed in a conductive medium, such that $\sigma \gg \omega\varepsilon$, we have from Eq.(10):

$$Y = G + jB = 2\pi a\sigma \left(0.85 + \frac{1}{\pi} \ln \frac{a}{4s} + \sum_{1}^{\infty} \frac{n(4n-1)}{(2n-1)^2} \left[P_{2n}(o)\right]^2 \left[S_n(ka) - 1\right] \right) \qquad (11)$$

where $ka = (1-j)a/\delta$, δ being the skin depth of the wave.

Examination of Eq.(11) shows that the input conductance G of the antenna is dependent on the gap thickness, while the input susceptance is not affected by this factor. The input conductance at zero frequency, say G_o, is exactly the same as that obtained by solving the static problem (1) directly.

A series expansion of Eq.(11) in the neighbourhood of $ka \to o$, up to terms of order $(ka)^3$ included, leads to the following results:

$$G = G_o - \frac{3}{2} \left(\frac{a}{\delta}\right)^3 \approx G_o \quad ; \quad B = -2\pi\sigma a \frac{3}{2} \left(\frac{a}{\delta}\right)^2 \left[1 - \frac{a}{\delta}\right] \approx -\frac{3\pi}{4} (\sigma a)^2 \omega\mu a \quad . \qquad (12)$$

The input susceptance of the antenna is inductive, and less than $2\pi\sigma a/10$, provided that $a<\delta/3$. The input conductance is exactly that computed in the static case. These results emphasize the importance of static computation for the study of problems of this kind.

It should be remarked that the inductive susceptance B, which increases linearly with the frequency, can be exactly compensated by means of a shunt lumped capacitance of value $C = 3\pi(\sigma a)^2 \mu a/4$ in the range $|ka| \ll 1$. For $a = 1m$, $\mu = 1.256 \cdot 10^{-6}$ F/m, $\sigma = 10^{-2}$ Siemens/m (soil), we get C=300pF; for $\sigma = 5$ (sea water), we get C=75μF; in all cases very reasonable values. It follows that the spherical antenna can be made to have a very flat response over a very wide band.

The graphs of the normalized conductance $g = G/2\pi\sigma a$ and susceptance $b = B/2\pi\sigma a$ are represented in fig.2 as a function of the ratio a/δ, up to values $a/\delta = 2$.

2.3. The lossless case.

When the antenna is immersed in a lossless medium, we have from Eq.(10):

$$Y = G + jB = j \frac{4\pi^2}{\zeta} \frac{a}{\lambda} \left\{ 0.85 + \frac{1}{\pi} \ln \frac{a}{4s} + \sum_{1}^{\infty} \frac{n(4n-1)}{(2n-1)^2} \left[P_{2n}(o)\right]^2 \left[S_n\left(\frac{2\pi}{\lambda}\right) - 1\right] \right\} \quad , \qquad (13)$$

λ being the wavelength, and ζ the intrinsic impedance in the external medium.

Examination of Eq.(13) shows that the input conductance G of the antenna is independent of the gap thickness, while the input susceptance is affected by this factor.

A series expansion of Eq.(13) in the neighbourhood of $2\pi/\lambda \to o$, leads to the following result:

$$G = \frac{(2\pi)^5}{\zeta}\left(\frac{a}{\lambda}\right)^4 \quad ; \quad B = \frac{4\pi^2}{\zeta}\,\frac{a}{\lambda}\left[0.85 + \frac{1}{\pi}\,\mathrm{Ln}\,\frac{a}{4s} + 6\pi^2\left(\frac{a}{\lambda}\right)^2\right] \quad . \tag{14}$$

The results of Eq.(14) are in fairly good agreement with some experimental measurements on satellite antennas (5).

3. COMPUTATION OF THE EFFECTIVE HEIGHT.

3.1. Formal solution to the problem.

For the considered problem, the electromagnetic field can be derived from a pseudo potential $\underline{A}$ as follows:

$$\underline{A} = A\,\underline{i}_\phi = \frac{r\sqrt{1-\eta^2}\,H_\phi(r,\theta)}{\sigma+j\omega\varepsilon}\,\underline{i}_\phi \quad , \tag{15}$$

where:

$$\underline{E} = -\frac{1}{r\sqrt{1-\eta^2}}\,\underline{i}_\phi \times \nabla A \quad , \quad \underline{H} = \frac{\sigma+j\omega\varepsilon}{r\sqrt{1-\eta^2}}\,\underline{A} \tag{16}$$

i.e.

$$E_r = \frac{1}{r^2}\,\frac{\partial A}{\partial \eta} \quad ; \quad E_\theta = -\frac{\sqrt{1-\eta^2}}{r}\,\frac{\partial A}{\partial r} \quad , \quad H_\phi = \frac{\sigma+j\omega\varepsilon}{r\sqrt{1-\eta^2}}\,A \quad , \tag{17}$$

$\underline{i}_\phi$ being the unit vector along the ϕ coordinate, and H_ϕ being given by the third relation of Eq.(1).

The general term of the series expansion for A can be put in the following form:

$$A_{2n-1} = j\,\zeta\,\frac{I\,h_{2n-1}(ka)^{2n-1}}{4\pi}\,\frac{P^1_{2n-1}(\eta)}{\sqrt{1-\eta^2}}\,kr\,R^{(4)}_{2n-1}(kr) \quad , \tag{18}$$

where:

$$R^{(4)}_{2n-1}(kr) = (-1)^n\sqrt{\frac{\pi}{2kr}}\,H^{(2)}_{2n-1/2}(kr) \quad , \quad \zeta = \sqrt{\frac{j\omega\mu}{\sigma+j\omega\varepsilon}} \quad , \tag{19}$$

$R^{(4)}_{2n-1}$ is the spherical Bessel function of order $2n-1$, I is the input current of the antenna, and:

$$h_{2n-1} = \frac{3a}{2}\,\frac{j\sqrt{2/\pi}}{(ka)^{2n-1/2}\,H^{(2)}_{2n-1/2}(ka)}\,S_n(ka)\,\frac{2(4n-1)}{3(2n-1)^2}\,|P_{2n}(o)|\,\frac{1}{y} \quad . \tag{20}$$

In order to understand the meaning of h_{2n-1}, let us first consider the case n=1.

Expanding asymptotically $kr\,R^{(4)}_{2n-1}(kr)$ for $kr \to o$, stopping at terms of order 1/kr included, we get from Eq.(18):

$$A_1 \to j\,\zeta\,\frac{I\,h_1}{4\pi}\,\frac{1}{\sqrt{1-\eta^2}}\,\sin\theta\,\exp[-jkr]\left[1+\frac{1}{jkr}\right] \quad ; \tag{21}$$

and consequently for E_θ:

$$E_\theta = \zeta\,\frac{I\,j\,h_1}{4\pi r}\,\sin\theta\,\exp[-jkr]\left[jk + \frac{1}{r^2} + \frac{1}{jkr^3}\right] \quad , \tag{22}$$

i.e. exactly the field of an elementary electric dipole of effective height h_1. Expression (22) is valid even in the zero frequency limiting case $k \to o$.

In the general case, the asymptotic expansion for $kr\,R^{(4)}_{2n-1}(kr)$ must be performed up to terms of order $(1/kr)^{2n-1}$ included.

It should be remarked that h_{2n-1} assumes the following value in the zero frequency limiting case:

$$h_{2n-1} \to \frac{3a}{2}\,|P_{2n}(o)|\,\frac{2(4n-1)}{3\,(2n-1)^2}\,[1.3.5.\ldots.\,(4n-3)]\,\frac{1}{y_o} \quad , \tag{23}$$

y_o being the limiting value of (11) for $k \to o$.

3.2. The lossy case.

Let us assume, as in Sect.2.2., $\sigma \gg \omega\varepsilon$ and let us consider the case n=1 (dipolar term).

The effective height is dependent on the gap thickness via the factor y in the denominator of (20). Therefore the effective height decreases as the gap thickness decreases, and consequently also the radiated power, as will be shown in Sect.4.

A series expansion of Eq.(20) in the neighbourhood of ka→o, up to terms of order $(ka)^2$ included, leads to the following result :

$$h_1 \to \frac{3a}{2}\frac{1}{s_o}\left[1 + j\,\frac{\ln\frac{a}{4s} - 2.04}{\ln\frac{a}{4s} + 2.68}\left(\frac{a}{\delta}\right)^2\right] \quad . \tag{24}$$

The value of h_1 for ka=o is exactly that computed in the static case (1). These results emphasize the importance of static computation for the study of problems of this kind.

The graphs of the normalized effective height $2h_1/3a$ are reported in fig.3 as a function of the ratio a/δ, up to values $a/\delta=2$.

3.3. The lossless case.

Also in this case, it is evident from Eq.(20) that the effective height h_1 is dependent on the gap thickness. However, this does not necessarily means that the radiated power is reduced when the gap thickness is decreased, as will be shown in Sect.4. This apparent contradiction is related to the fact that only the input susceptance, and not the input conductance, is dependent on the gap thickness.

A series expansion of Eq.(20) in the neighbourhood of (ka)→o, up to terms of order $(ka)^2$ included, leads to the following result :

$$h_1 = \frac{3a}{2j}\,\frac{1}{0.85 + \frac{1}{\pi}\ln\frac{a}{4s}}\left[1 - 2\pi^2\, j\,\frac{\ln\frac{a}{4s} - 2.04}{\ln\frac{a}{4s} + 2.78}\left(\frac{a}{\lambda}\right)^2\right] \quad . \tag{25}$$

4. COMPUTATION OF THE RADIO LINK.

4.1. Formal solution to the problem.

Let us now compute the radio link equation between two matched sperical antennas, oriented for the maximum received field, and let us use subscript T and R for transmitting and receiving antennas respectively. The transmitted power P_T is given by:

$$P_T = \frac{1}{2}\,G_T\,|V_T|^2 = \frac{1}{2}\,G_T\left|\frac{I_T}{Y_T}\right|^2 \quad , \tag{26}$$

V being the voltage applied to the shunt of the antenna input admittance Y_T and the matching susceptance $-B_T$.

The electric field at the receiving antenna, say E_{TR}, will be given by:

$$E_{TR} = K\,I_T\,h_T \quad , \tag{27}$$

K being a suitable constant depending on the radio-link type and geometry and h_T the effective height h_1 of the transmitting antenna (the dipolar term of radiation is assumed to be the dominant one).

The induced current at the input terminals of the receiving antenna is given by:

$$I_R = E_{TR}\,h_R\,Y_R \quad ; \tag{28}$$

and consequently the received power by:

$$P_R = \frac{1}{2}\,\frac{|I_R|^2}{G_R} \quad . \tag{29}$$

From Eq.(26), through (29), we get:

$$\frac{P_R}{P_T} = |K|^2\,\frac{|h_T\,Y_T|^2}{G_T}\,\frac{|h_R\,Y_R|^2}{G_R} = |K|^2\,\alpha_T\,\alpha_R \quad . \tag{30}$$

The radio-link parameter α can be computed for the spherical antenna via Eq.(20). Thus:

$$\alpha = 9\pi^2\,a^2\,\left|\frac{ka}{\zeta}\right|^2\left|\frac{\exp[jka]}{1+jka-(ka)^2}\right|\,\frac{1}{G} \quad . \tag{31}$$

It is noted that the dependence of α on the gap thickness is only related to the eventual dependence of G on this same parameter. This is what happens in the lossy case, but not in the lossless case. Therefore a decreases in the gap thickness lowers the efficiency of the radio-link in the lossy case and does not lower the efficiency in the lossless case, provided that the antennas are matched.

For the lossy case, the graph of the radio link parameter α is given in fig.4 as a function of the ratio a/δ.

4.2. The up-over-and-down radio-link.

For this case the constant K can be computed for the intermediate range as follows (4):

$$|K| = \frac{1}{2\pi r} \frac{4}{\zeta_o^2 \sigma^3} \frac{1}{\delta^4} \exp\left[-\frac{d_1+d_2}{\delta}\right] \quad , \qquad (32)$$

where $\zeta_o = \sqrt{\mu_o/\varepsilon_o}$, and d_1, d_2 are the depths of the two antennas respectively.

Note that the value $|ka/\zeta|^2 = (\sigma a)^2$ is frequency independent; the frequency dependence of the remaining term is of order $|ka|^2$.

When this dependence can be neglected, it is easy to get the optimum frequency which maximizes the ratio P_R/P_T, by differentiating Eq.(30) with respect to $1/\delta$.

The condition is the following one:

$$d_1 + d_2 = 4\delta \quad . \qquad (33)$$

4.3. The up-and-over radio-link.

For this case the constant K can be computed for the intermediate range as follows:

$$|K_i| = \frac{1}{2\pi r} \frac{2\sqrt{2}}{\zeta_o \sigma^2} \frac{1}{\delta^3} \exp\left[-\frac{d}{\delta}\right] \quad ; \qquad (34)$$

d being the depth of the submerged or buried antenna.

In order to compute the optimum frequency of the radio link, we must compute the value of α for the antenna in air. Assuming this antenna to be an elementary dipole, we have that Y is proportional to ω, while G is inversely proportional to the square of ω. It follows that α is proportional to ω^4, and therefore to $1/\delta^8$. By taking this factor into account, we get the new condition which replaces that of Eq.(33):

$$d = 7\delta \quad .$$

5. REFERENCES.

1. Franceschetti, G., O.M. Bucci, E. Corti, G. Latmiral, "Metallic and Dielectric Antennas in Conducting Media", Conference on Environmental Effects on Antenna Performance, Boulder 1969.
2. Wait, J.R., "Electromagnetics and Plasmas", Holt, Rinehart and Weston, 1968.
3. Wait, J.R., "Theories of Prolate Spheroidal Antennas", Radio Science, Vol.1, p.475-512.
4. Baños, A. Jr., "Dipole Radiation in the Presence of a Conducting Half-Space", Pergamon Press, 1966.
5. Checcacci, P.F., P. Fabeni, G. Pazzi, A. Ranfagni, "Spherical Dipole for the Italian San Marco Satellite", Alta Frequenza, Vol.36, p.403-407.
6. Angot, A., "Complément de Mathematique", Revue d'Optique, 1957.
7. Collin, R.E., "Field Theory of Guided Waves", McGraw Hill, 1960.
8. Schelkunoff, S.A., "Advanced Antenna Theory", J. Wiley, 1952.

6. ACKNOWLEDGMENTS.

The author is very indebted to Dr. Maria R. Crisci, of the Numerical Computing Centre of the Faculty of Science, and to Ing. Catello Savarese, of the Dept. of Electrical Engineering, for their help in performing the numerical computations. Many thanks are also due to Miss Gherarda Tomasella for the careful typing of the manuscript.

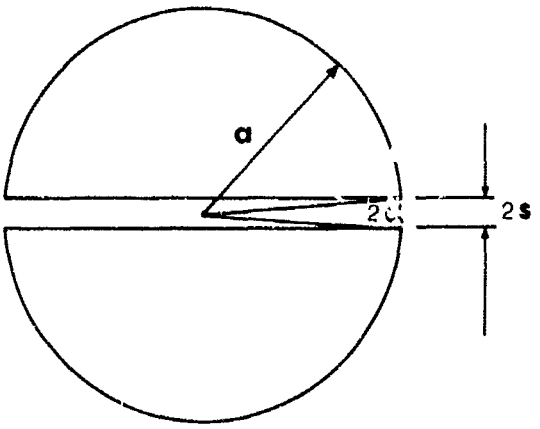

Fig.1 - A sketch view of the spherical antenna excited by a constant voltage V at its equatorial gap.

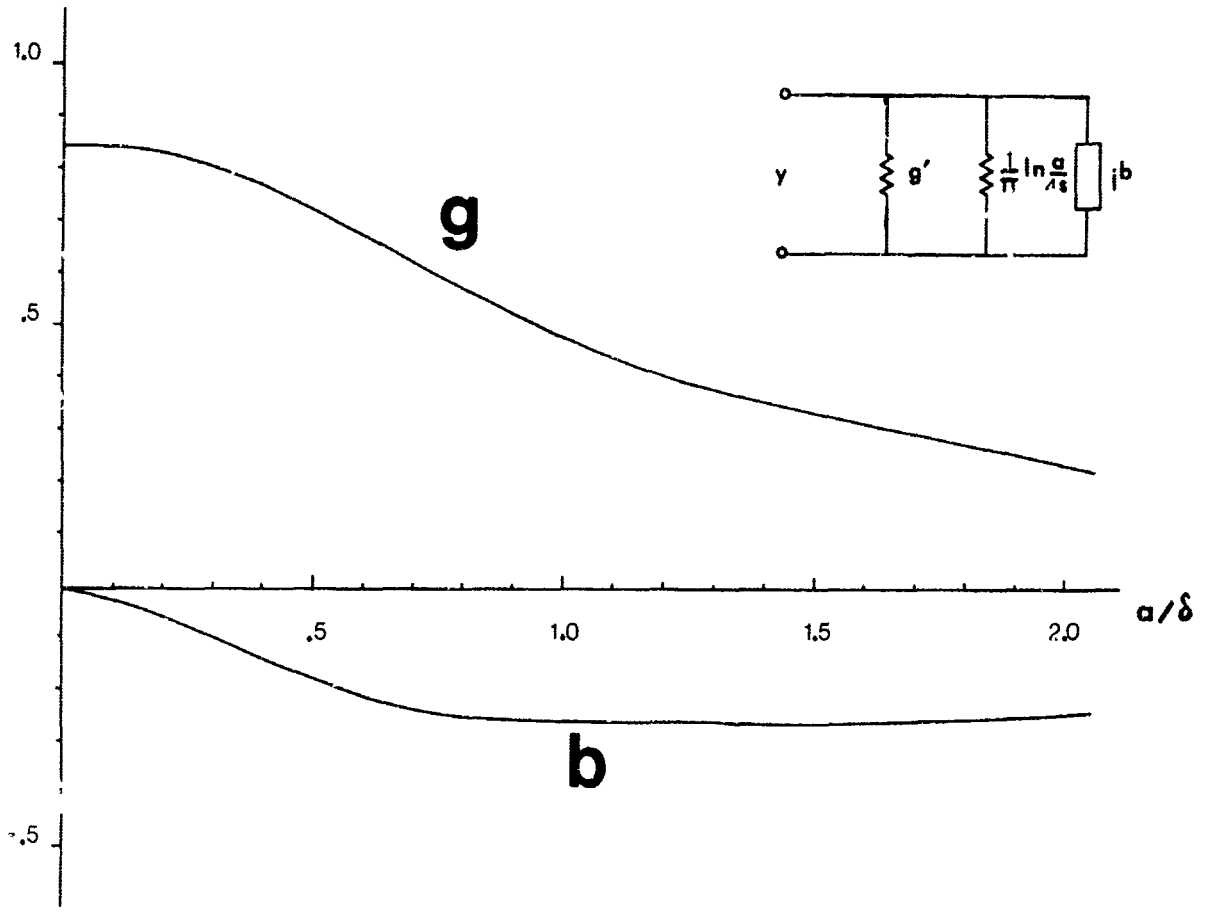

Fig.2 -Graphs of the gap independent part normalized conductance $g'=G/2\pi\sigma a$ and susceptance $b=B/2\pi\sigma a$, as a function of the ratio a/δ (antenna's radius on the skin depth of the wave). The effective normalized conductance g is obtained by adding to g' the "gap term" $(\ln\frac{a}{4s})/2\pi^2\sigma a$.

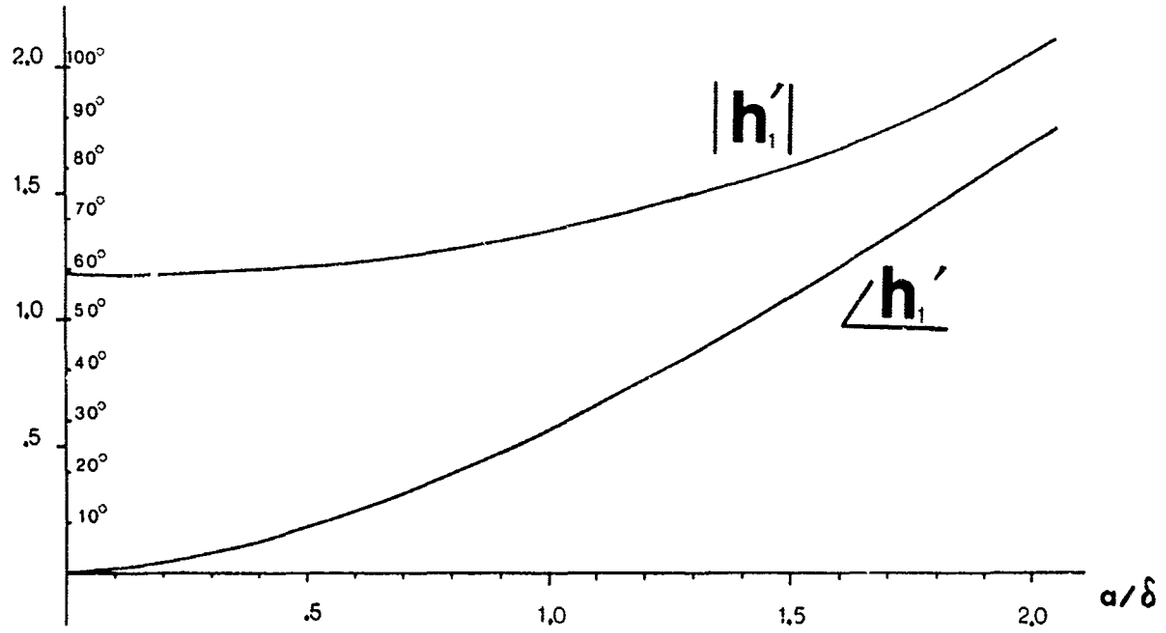

Fig.3 -Graphs of the module and of the phase (in degrees) of the normalized modified affective height (of the dipolar term of radiation) $h_1'=(2h_1y)/(3ay')$ as a function of the ratio a/δ (antenna's radius on the skin depth of the wave). The effective height h_1 can be easily computed when the ratio y'/y is known. This in turn is given by $(g'+jb)/(g+jb)$, and can be easily obtained by using the graphs of fig.1, once the gap of the antenna has been chosen.

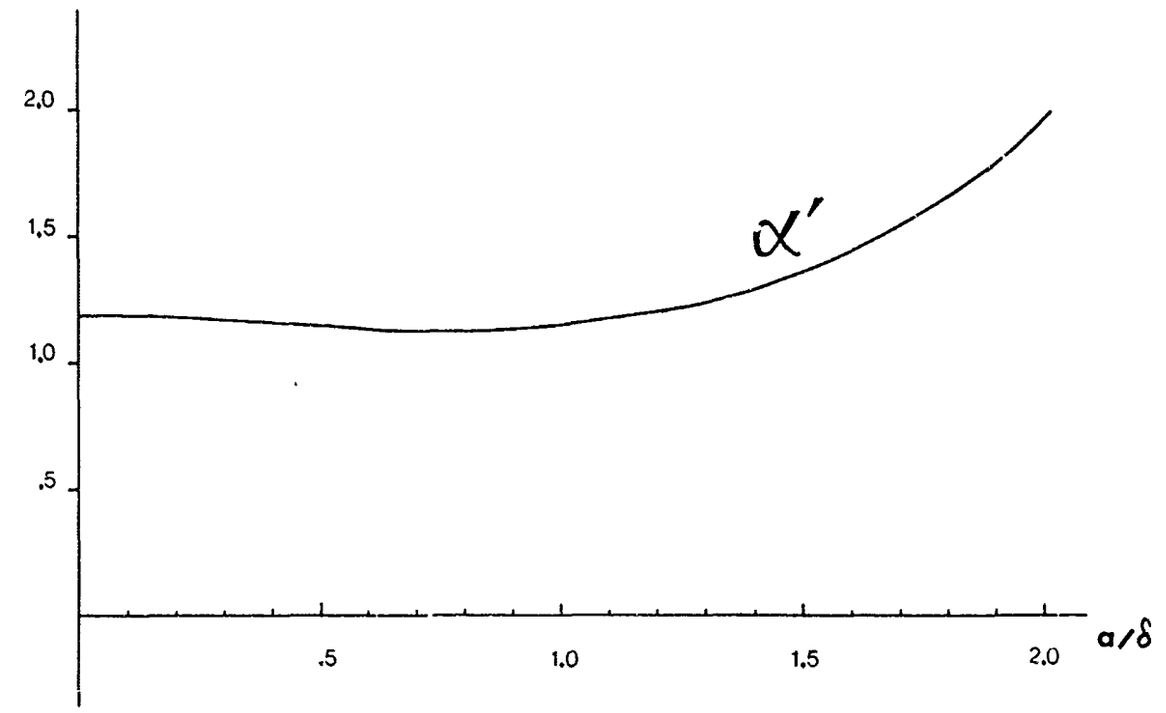

Fig.4 -Graph of the modified link parameter $\alpha'=\alpha g'/g$ as a function of the ratio a/δ (antenna's radius on the skin depth). The radio link α can be easily computed when the ratio g/g' is known. This in turn can be easily obtained by using the graph of fig.3, once the gap of the antenna has been chosen.

CALCUL EN MILIEU ABSORBANT DE CHAMP REFLECHIE PAR UNE SURFACE METALLIQUE

par

M. Bouix et L. T. Bach

Centre d'Etudes Théoriques de la Détection et des Communications
5bis, avenue de la Porte de Sèvres, 75, Paris 15e, France

RESUME

On se propose de schématiser la détection électromagnétique d'un obstacle dans un milieu absorbant à partir d'une source ponctuelle du type dipôle magnétique comme émetteur, et d'un récepteur ponctuel du même type dont l'axe est situé dans le plan de symétrie du premier, de façon à recevoir un champ nul en milieu indéfini; la présence d'un obstacle représenté par un plan conducteur indéfini produit un champ non nul. Ce schéma trop simple qui correspondrait à une puissance infinie issue de l'émetteur est modifié par l'introduction d'un milieu non absorbant entourant l'émetteur et limité par une sphère, ce qui permet de faire un calcul complet, généralisable à toute autre source ponctuelle, et à tout milieu absorbant homogène et isotrope.

SUMMARY

It is planned to schematize the electromagnetic detection of an absorbing medium, from a pinpoint source, like a magnetic dipole, as a sender, and a pinpoint receiver of the same type, with its axis in the symmetry plane of the former, so as to receive a zero field in an undefined medium; the presence of an obstacle represented by an undefined conducting plane creates a zero field. This excessively simple diagram, which would correspond to an infinite power issuing from the sender is modified by the introduction of a non-absorbing medium surrounding the sender and limited by a sphere, which makes it possible to perform a complete calculation, likely to be extended to any other pinpoint source, or to any homogeneous and isotropic absorbing medium.

CALCUL EN MILIEU ABSORBANT DE CHAMP REFLECHIE PAR UNE SURFACE METALLIQUE

M. Bouix et L. T. Bach

1. ENONCE DU PROBLEME

Nous nous proposons d'étudier les conditions de la détection électromagnétique d'un objet métallique plongé dans un milieu absorbant par un dispositif constitué d'un système emetteur agissant comme un doublet magnétique qui, placé seul dans le milieu absorbant supposé indéfini produirait dans un plan Q perpendiculaire au doublet un champ magnétique transversal nul. La présence d'un obstacle modifie la répartition du champ électromagnétique dans le milieu et crée un champ longitudinal non nul dans le plan Q, champ que l'on peut mettre en évidence par un système de réception détectant le champ longitudinal en un point de cet axe; pour que le système permette la détection d'un obstacle, l'émetteur et le récepteur doivent être construits en respectant soigneusement les symétries requises par le principe du procédé. Nous schématiserons encore davantage le problème en supposant

1. que l'obstacle à détecter est constitué par un plan parfaitement conducteur (sous la réserve qu'il ait une grande épaisseur par rapport à λ ou qu'il soit conducteur parfait, sinon il faudrait tenir compte du milieu qui est derrière et de l'onde diffuse)
2. que l'émetteur est réduit à une source ponctuelle.

2. ETUDE DE L'ENERGIE ELECTROMAGNETIQUE PRODUITE PAR UN DOUBLET MAGNETIQUE EN MILIEU ABSORBANT

Un doublet megnétique d'axe Oz fonctionnant avec une pulsation ω dans un milieu de constantes caractéristiques ϵ, μ, σ, produit un champ électromagnétique dont les composantes en coordonnées sphériques sont données par (Réf. 1, page 71).

$$
\begin{aligned}
E_r &= E_\theta = H_\varphi = 0 \\
E_\varphi &= \frac{A\eta}{kr}\left(1 + \frac{1}{ikr}\right) e^{-ikr} \sin\theta \\
H_r &= A \sim \frac{2i}{k^2 r^2}\left(1 + \frac{1}{ikr}\right) e^{-ikr} \cos\theta \qquad (2\text{-}1) \\
H_\theta &= \frac{1}{kr}\left(1 + \frac{1}{ikr} - \frac{1}{k^2 r^2}\right) e^{-ikr} \sin\theta
\end{aligned}
$$

formules dans lesquelles on a

$$
k = -i\omega\mu(i\omega\epsilon + \sigma) \qquad \eta^2 = \frac{i\omega\mu}{i\omega\epsilon + \sigma} \qquad \mathrm{Re}(k) > 0 \qquad \mathrm{Re}(\eta) > 0 .
$$

La puissance active qui sort d'une sphère S de rayon f centrée sur le doublet est donnée par le flux de la partie réelle du vecteur de Poynting à travers cette sphère soit:

$$
W = \int_S \mathrm{Re}\left[\vec{r} \wedge \tfrac{1}{2}\, \vec{E} \wedge \vec{H}^*\right] r^2 \sin\theta \, d\theta \quad (\bullet)
$$

On a ici:

$$
\begin{aligned}
\mathrm{Re}\left[\tfrac{1}{2}\vec{E}\wedge\vec{H}^*\right] &= \tfrac{1}{2}\left[\mathrm{Re}(\vec{E}) + i\ \mathrm{Im}(\vec{E})\right] \wedge \left[\mathrm{Re}(\vec{H}) - i\ \mathrm{Im}(\vec{H})\right] \\
&= \tfrac{1}{2}\left[\mathrm{Re}(\vec{E}) \wedge \mathrm{Re}(\vec{H}) + \mathrm{Im}(\vec{E}) \wedge \mathrm{Im}(\vec{H})\right] .
\end{aligned}
$$

(•) Le signe "$\wedge$" veut dire: produit vectoriel

Ici $\vec{\varphi}\Lambda\vec{\theta} = -\vec{r}$ et $-\mathrm{Re}[\frac{1}{2}\vec{E}\Lambda\vec{H}^*] = \frac{1}{2}[\mathrm{Re}(E_\varphi)\mathrm{Re}(H_\theta) + \mathrm{Im}(E_\varphi)\mathrm{Im}(H_\theta)]$. On a alors:

$$Q = \text{Val.moy. sur } S \text{ de } \frac{4\pi}{3}(-E_\varphi H_\theta)$$

$$= A^2 \frac{4\pi}{3} \mathrm{Re}\left\{\frac{\eta}{kk^*r^2}\left(1-\frac{i}{k^2}\right)\left(1+\frac{i}{k^*r}-\frac{1}{k^{*2}r^2}\right)e^{-ikr}\, e^{+ik^*r}\, r^2\right\}$$

$$= A^2 \frac{4\pi}{3} e^{2\,\mathrm{Im}(kr)}\, \mathrm{Re}\left\{\frac{\eta}{|k|^2}\left[1-\frac{2\mathrm{Im}(k)}{|k|^2 r}+\frac{1}{|k|^4 r^2}|k|^2-k^2\right]+\frac{i\mathrm{Re}(k)-\mathrm{Im}(k)}{|k|^4 r^3}\right\}$$

$$= A^2 \frac{4\pi}{3} e^{2\,\mathrm{Im}(kr)}\, \mathrm{Re}\left\{\frac{1}{|k|^2}[\mathrm{Re}(\eta)+i\,\mathrm{Im}(\eta)]\left(1-\frac{2\mathrm{Im}(k)}{|k|^2 r}+\right.\right.$$

$$\left.\left.+\frac{1}{|k|^4 r^2}[\mathrm{Re}^2(k)+\mathrm{Im}^2(k)-\mathrm{Re}^2(k)+\mathrm{Im}^2(k)-2i\,\mathrm{Re}(k)\mathrm{Im}(k)]\,\frac{i\,\mathrm{Re}(k)-\mathrm{Im}(k)}{|k|^4 r^3}\right)\right\}$$

$$= A^2 \frac{4\pi}{3} e^{2\,\mathrm{Im}(kr)}\, \frac{1}{|k|^2}\left\{\mathrm{Re}(\eta)\left[1-\frac{2\mathrm{Im}(k)}{|k|^4 r^2}-\frac{\mathrm{Im}(k)}{|k|^4 r^3}\right]+\mathrm{Im}(\eta)\left[\frac{2\mathrm{Re}(k)\mathrm{Im}(k)}{|k|^4 r^2}-\frac{\mathrm{Re}(k)}{|k|^4 r^3}\right]\right\}$$

$$= A^2 \frac{4\pi}{3} e^{2\,\mathrm{Im}(kr)}\, \frac{1}{|k|^2}\left\{-\frac{\mathrm{Re}(\eta)\mathrm{Im}(k)+\mathrm{Im}(\eta)\mathrm{Re}(k)}{|k|^4 r^3}+\frac{2\mathrm{Im}(k)[\mathrm{Re}(\eta)\mathrm{Im}(k)+\mathrm{Im}(\eta)\mathrm{Re}(k)]}{|k|^4 r^2}-\frac{2\,\mathrm{Re}(\eta)\mathrm{Im}(k)}{|k|^2 r}+\mathrm{Re}(\eta)\right\} .$$

Or Im k est toujours négatif, on a

$$\eta k = \left(\frac{i\omega\mu}{i\omega\epsilon+\sigma}\right)^{1/2}[-i\omega\mu(i\omega\epsilon+\sigma)]^{1/2} = \omega\mu .$$

Si μ est réel, on a donc ηk réel donc

$$\eta k = \mathrm{Re}(\eta k) = \omega\mu , \qquad \mathrm{Im}(\eta k) = 0 = 2(\mathrm{Re}\,\eta\,\mathrm{Im}\,k + \mathrm{Re}\,k\,\mathrm{Im}\,\eta) .$$

On voit alors que la puissance active à traverse la sphère s'exprime par

$$W = A^2 \frac{4\pi}{3} e^{2\,\mathrm{Im}\,k.\,r}\, \frac{\mathrm{Re}\,\eta}{|k|^2}\left[1-\frac{2\mathrm{Im}\,k}{|k|^2 r}\right] . \qquad (2\text{-}2)$$

Si k n'est pas réel, c'est-à-dire si $\sigma \neq 0$, l'expression de W contient un terme en 1/r et devient donc infiniment grande lorsque le rayon de la sphère tend vers zéro. Donc le champ H_{01} écrit ne pourrait être engendré que par une source ponctuelle de puissance infinie. En fait ceci n'est pas physique; sans entrer dans des considérations trop compliquées, disons simplement qu'un émetteur est toujours placé dans un compartiment séparé du milieu absorbant par une certaine surface. Pour trouver les ordres de grandeur on supposera que cette surface est l'une des sphères S , que la puissance active qui en sort est la puissance de l'émetteur, et que la distribution du champ électromagnétique sur cette surface est celle de champ à symétrie sphérique H_{01} .

Si μ était complexe, on aurait trouvé un terme en $1/r^3$ pour W , mais le même raisonnement permet d'éviter la difficulté de la source ponctuelle en milieu absorbant.

3. CALCUL DE L'EFFET D'OBSTACLE CONSTITUE PAR UN PLAN INDEFINI PARFAITEMENT CONDUCTEUR

Considérons (fig.3 1) un émetteur placé à l'origine du repère orthonormé Oxyz de la figure 2.1 assimilable à un doublet magnétique situé en O orienté suivant Oz placé dans un milieu non absorbant limité par une sphère de rayon a centrée à l'origine: cet émetteur émet à la fréquence $f = \omega/(2\pi)$ une puissance telle que la puissance active qui sort de la sphère de rayon a soit égale à W_0 . Le milieu extérieur à la sphère est le milieu de constantes caractéristiques ϵ , μ , σ . En l'absence de tout obstacle le champ électromagnétique à l'extérieur de la sphère est le champ sphérique des formules (2-1), le coefficient A étant déterminé à partir de la formule (2-2) par

$$W_0 = A^2 \frac{4\pi}{3} e^{2(\mathrm{Im}\,k)a}\, \frac{\mathrm{Re}\,\eta}{|k|^2}\left[1-\frac{2\mathrm{Im}\,k}{|k|^2 a}\right] . \qquad (3\text{-}1)$$

Le champ électromagnétique dans le plan xOy est tel que $H_r = 0$(car $\cos\theta = 0$) ; il en est ainsi au point R de l'axe Ox tel que OR = d

Si l'on introduit maintenant un obstacle représenté par un plan P infiniment conducteur, situé à la distance ρ de l'origine, il superpose au champ précédent un champ de même structure produit par un doublet magnétique symétrique de l'origine par rapport à P, mais dont la puissance est multipliée par le facteur d'attenuation $e^{2p\ \mathrm{Im}\,k}$. Le dispositif de réception devra mettre en évidence la composante de ce deuxième champ suivant Ox. C'est cette composante que nous allons calculer.

Pour cela, il faut écrire par rapport au repère Oxyz les composantes du champ image symétrique du champ incident par rapport au plan P.

Remarquons, afin de simplifier le calcul, que, puisque les équations du Maxwell sont linéaires, on peut décomposer un doublet magnétique placé suivant un axe en la somme de deux ou plusieurs doublets magnétiques dont il est la résultante (Cf. form.3.12.17 Réf.1) et le champ du doublet initial est la somme des champs des composantes.

Or si un doublet magnétique est parallèle à un plan conducteur, la nullité de la composante du champ magnétique dans le plan normal au doublet en son centre sera conservée par la présence du plan conducteur.

Donc si, en présence du plan conducteur, on décompose un doublet magnétique en un doublet parallèle au plan et en un doublet perpendiculaire au précédent et situé dans le plan passant par le doublet initial et perpendiculaire au plan conducteur, c'est seulement cette deuxième composante qui pourra fournir une valeur non nulle au champ magnétique détecté par le dispositif récepteur.

Aussi, nous étudierons seulement la disposition suivante: le doublet magnétique étant placé suivant Oz, on mesure la composante du champ magnétique suivant Ox en un point R de Ox tel que $\overline{OR} = d$. Le plan P sera déterminé par l'angle α que fait le vecteur unitaire $\vec{u}$ de sa normale avec Oz et par sa distance p à l'origine; si H est le pied de la normale à P issue de O, on orientera u dans un sens tel que $\overline{OH} = p > 0$.

Si O' est l'image de O par rapport à P les coordonnées de O' seront:

$$x_0 = 2p \sin\alpha \qquad y_0 = 0 \qquad z_0 = 2p\cos\alpha \ .$$

Le champ électromagnétique image sera rapporté à un repère direct d'origine O', de vecteurs unitaires $\vec{I}'$, $\vec{J}'$, $\vec{K}'$ liés aux vecteurs unitaires $\vec{I}$, $\vec{J}$, $\vec{K}$ du repère du O par

$$\vec{I} - \vec{I}' = 2\vec{u}\sin\alpha \qquad \vec{J} + \vec{J}' = 0 \qquad \vec{K} - \vec{K}' = 2\vec{u}\cos\alpha \ .$$

Or on a:

$$\vec{u} = \vec{I}\sin\alpha + \vec{K}\cos\alpha \ .$$

Donc:

$$\begin{aligned} \vec{I}' &= (1 - 2\sin^2\alpha)\vec{I} - 2\vec{K}\sin\alpha\cos\alpha \\ \vec{J}' &= -\vec{J} \\ \vec{K}' &= -2\sin\alpha\cos\alpha\,\vec{I} + (1 - 2\cos^2\alpha)\vec{K} \ . \end{aligned} \tag{3-2}$$

Si r', θ', φ' sont les coordonnées sphériques d'un point M de l'espace associées au repère de O', elles seront liées aux coordonnées du repère de O, soit sphériques r, θ, φ, soit cartésiennes x, y, z par des relations tirées de

$$\overrightarrow{O'M} = \overrightarrow{O'O} + \overrightarrow{OM} = -2p\vec{u} + \overrightarrow{OM}$$

ce qui donne:

$$r'[\vec{I}'\sin\theta'\cos\varphi' + \vec{J}'\sin\theta'\sin\varphi' + \vec{K}'\cos\theta'] = -2p(\vec{I}\sin\alpha + \vec{K}\cos\alpha) + \vec{I}x + \vec{J}y + \vec{K}z$$

ce qui donne en tenant compte de (3-2)

$$r'[(1 - 2\sin^2\alpha)\sin\theta'\cos\varphi' + 2\sin\alpha\cos\alpha\cos\theta']\vec{I} + r'[-2\sin\alpha\cos\alpha\sin\theta'\cos\varphi' + (1 - 2\cos^2\alpha)\cos\theta']\vec{K} -$$

$$- r'\sin\theta'\sin\varphi'\,\vec{J} = (-2p\sin\alpha + x)\vec{I} + \vec{y}j + (-2p\cos\alpha + z)\vec{K} \ .$$

Or on s'intéresse seulement à un point de Ox par lequel $y = z = 0$.

On a donc les relations d'identification

$$\begin{cases} r'[(1-2\sin^2\alpha)\sin\theta'\cos\varphi' - \sin^2\alpha\cos\theta'] = -2p\sin\alpha + x \\ r'\sin\theta'\sin\varphi' = 0 \\ r'[-\sin 2\alpha\sin\theta'\cos\varphi' + (1-2\cos^2\alpha)\cos\theta'] = -2p\cos\alpha\ . \end{cases}$$

Comme $\sin\theta'$ n'est pas identiquement nul sur Ox, c'est qu'on aura $\sin\varphi' = 0$, soit en choisissant une bonne origine des arcs

$$\varphi' = 0$$

il reste:

$$r'[(1-2\sin^2\alpha)\sin\theta' - \sin 2\alpha\cos\theta'] = -2p\sin\alpha + x$$

$$r'[-\sin 2\alpha\sin\theta' + (1-2\cos^2\alpha)\cos\theta'] = -2p\cos\alpha\ .$$

On tire de ces deux relations $r'\cos\theta'$ et $r'\sin\theta'$ par les formules de résolution des équations linéaires, ce qui donne:

$$\begin{aligned} r'\cos\theta' &= -2p\cos\alpha + x\sin 2\alpha \\ r'\sin\theta' &= -(2p\sin\alpha + x\cos 2\alpha) \end{aligned} \qquad (3\text{-}3)$$

et il en résulte:

$$r' = [4p^2 - 4px\sin\alpha + x^2]^{1/2}\ ; \qquad (3\text{-}4)$$

il est a remarquer que $c' \to \infty$ quand $p \to \infty$.

Si on affecte d'accents les champs provenant du doublet image, le champ suivant Ox est

$$H'_x = \vec{i}(\vec{r}'\vec{H}'_r + \vec{\theta}'\vec{H}'_\theta)$$

avec:

$$\vec{r}' = \vec{i}'\sin\theta\cos\varphi' + \vec{j}'\sin\theta'\sin\varphi' + \vec{k}'\cos\theta'$$

$$\vec{\theta}' = \vec{i}'\cos\theta'\cos\varphi' + \vec{j}'\cos\theta'\sin\varphi' - \vec{k}'\sin\theta'$$

soit en tenant compte de (3-2) et de $\varphi' = 0$

$$\vec{r}' = [(1-2\sin^2\alpha)\sin\theta' - \sin 2\alpha\cos\theta']\vec{i} + [-\sin 2\alpha\sin\theta' + (1-2\cos^2\alpha)\cos\theta']\vec{k}$$

$$\vec{\theta}' = [\cos\theta'(1-2\sin^2\alpha) + \sin^2\alpha\sin\theta']\vec{i} + [-\sin^2\alpha\cos\theta' - \sin\theta'(1-2\cos^2\alpha)]\vec{k}\ .$$

Pour avoir la composante de $\vec{H}'$ suivant l'axe des x, il suffit de garder les termes en i ; on a:

$$H'_x = H'_r[(1-2\sin^2\alpha)\sin\theta' - \sin 2\alpha\cos\theta'] + H'_\theta[\cos\theta'(1-2\sin^2\alpha) + \sin 2\alpha\sin\theta']\ .$$

Il suffit de remplacer dans cette expression $\cos\theta'$, $\sin\theta'$, r' par leurs valeurs tirées de (3-3) et (3-4) pour avoir H'_x connaissant p, x et α.

Remarquons que, si $\alpha = \pi/2$, alors $H'_x = 0$.

4. CAS PARTICULIER

Afin de déterminer les ordres de grandeur nous traiterons le cas où le plan P est parallèle à Ox, soit $\alpha = 0$. On a alors:

$$r'^2 = (4p^2 + x^2)\ , \qquad \cos\theta' = \frac{2p}{r'}\ ; \qquad \sin\theta' = \frac{x}{r'}\ ; \qquad \varphi' = 0\ .$$

Donc en tenant compte de l'atténuation due à l'absorption en θ et θ', on a à partir des formules (2-1) les composantes en coordonnées sphériques (r', θ, φ') d'un champ électromagnétique $\vec{E}'$, $\vec{H}'$ reçu

$$E_{r'} = E_{\theta'} = H_{\varphi'} = 0$$

$$E_{\varphi'} = -\frac{\eta A}{kr'}\left(1+\frac{1}{ikr'}\right)e^{-ikr'}\sin\theta' ,$$

$$H_{r'} = -\frac{2iA}{k^2r'^2}\left(1+\frac{1}{ikr'}\right)e^{-ikr'}\cos\theta' ,$$

$$H_{\theta'} = A\frac{1}{kr'}\left(1+\frac{1}{ikr'}-\frac{i}{k^2r'^2}\right)e^{-ikr'}\sin\theta' .$$

La puissance dirigée suivant l'axe Ox est $W = \mathrm{Re}(\vec{I}.\vec{P}')$, c'est-à-dire: $W = \frac{1}{2}\mathrm{Re}\,\vec{I}(\vec{E}'\wedge\vec{H}^{*\prime})$ et nous obtenons:

$$W = \frac{A^2}{2}\frac{\omega\mu\, e^{2(\mathrm{Im}\,k)r'}}{|k|^4r'^3}\sin\theta'\left\{\mathrm{Re}\left[-2\left(1+\frac{k^*}{|k|^2r'}\right)\left(1+\frac{ik}{|k|^2r'}\right)\cos\theta'(\vec{I}.\vec{\theta}') + r'|k|^2\left(1-\frac{ik^*}{|k|^2r'}\right)\left(\frac{k^*}{|k|^2}+\frac{i}{|k|^2r'}-\frac{k}{|k|^4r'^2}\right)\sin\theta'(\vec{I}.\vec{r})\right]\right\}$$

avec $(\vec{I}.\vec{\theta}') = \cos\theta'$; $(\vec{I}.\vec{r}') = \sin\theta'$.

On obtient finalement:

$$W = \frac{A^2}{2}\omega\mu\frac{e^{2\mathrm{Im}(k)r'}}{|k|^4r'^2}\sin^3\theta'\cdot\mathrm{Re}(k)\left[1-\frac{2\mathrm{Im}(k)}{|k|^2r'}\right] \quad \text{avec} \quad \theta' = \frac{x}{r'} .$$

L'atténuation entre la puissance reçue et la puissance émise tirée de (2-2) est donc:

$$10\ \mathrm{Log}\ \frac{W}{W_0}\ \text{décibels}$$

avec

$$\frac{W}{W_0} = \frac{3}{8\pi}\frac{ax^3\omega\mu\,\mathrm{Re}(k)}{r'^4|k|^2\mathrm{Re}(\eta)}\cdot\frac{|k|^2r'-2\mathrm{Im}(k)}{|k|^2a-2\mathrm{Im}(k)}\cdot\exp[2\mathrm{Im}(k)(r'-a)] ,$$

expression dans laquelle on doit tenir compte de:

$$r' = (4p^2+x^2)^{1/2} .$$

CONCLUSION

Les formules établies ci-dessus permettent de calculer la puissance arrivant sur une antenne de réception lorsqu'on connaît la puissance d'émission, et la disposition de l'obstacle par rapport à l'émetteur et au récepteur.

Ces formules de principe sont généralisables à des dispositifs réels plus compliqués.

REFERENCES

1. Bouix, M. — *Les Discontinuités du Rayonnement Electromagnétique.* Dunod, 1966.

2. Bouix, M. — *Détermination d'une Solution des Equations de Maxwell Harmoniques Extérieure à une Surface.* Rev. CETHEDEC 1968, no. 16, p. 1-50.

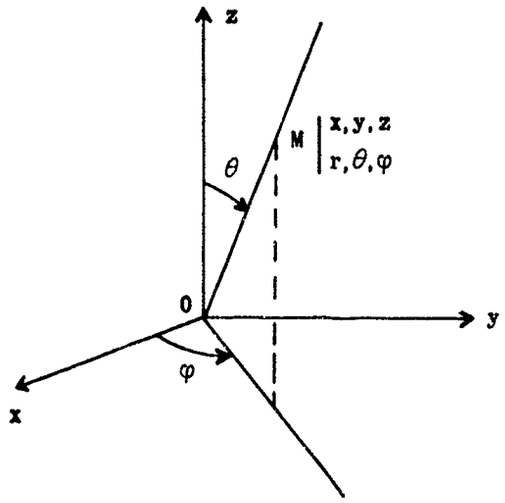

Figure 2.1

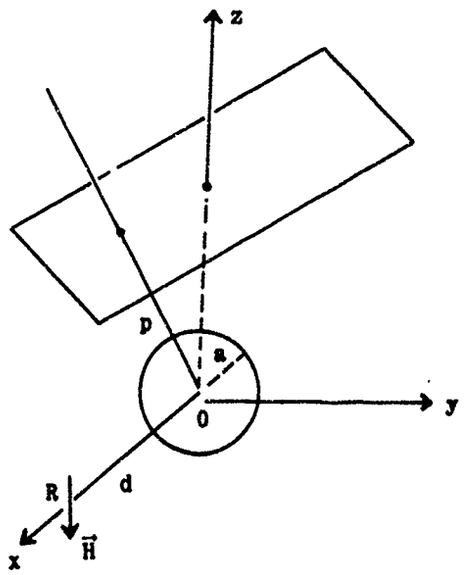

Figure 3.1

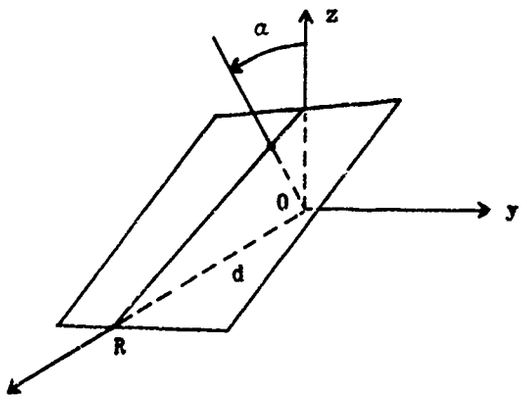

Figure 3.2

SURFACE WAVE PROPAGATION FROM VLF ARRAYS IN POLAR SEAS

by

Albert W. BIGGS
University of Kansas
Lawrence, Kansas 66044 U.S.A.

SOMMAIRE

L'auteur de cet exposé étudie plusieurs aspects de la propagation des ondes à très basse fréquence. Les milieux de propagation sont constitués par des étendues marines, des ilôts de glace flottant sur la mer, et des glaces emprisonnées à l'intérieur des terres. Ce choix de milieux donne des résultats anormaux car il correspond aux caractéristiques physiques de l'Arctique ou de l'Antarctique. Ces résultats anormaux sont obtenus en raison de la présence de trajectoires mixtes, de modes d'ondes de surface, de caractéristiques inhérentes à la glace flottante, et des effets de ces milieux sur les réseaux à très basse fréquence. On trouve, en passant de la mer à la glace flottante à sa surface (et vice-versa), des trajectoires de propagation mixtes.

Les modes d'ondes de surface se retrouvent dans la glace flottante en raison de l'indice de réfraction inférieur de la glace, mais ces modes sont beaucoup plus faibles que ceux des glaces plus épaisses (Groenland et Antarctique) du fait de la longueur d'ondes considérable des ondes à très basse fréquence. Les caractéristiques des glaces en milieu marin dépendent de leur âge, des poches d'eau salée qu'elles renferment et du volume d'eau. L'auteur étudie des réseaux composés de trois à cinq éléments situés en terrain arctique (glace ou toundra) et decrit les variations de forme de leur rayonnement suivant les paramètres du milieu où ils se trouvent. Ces paramètres, qui varient avec le temps, sont la température de la glace, son épaisseur, et son contenu en eau, salée ou non.

Les résultats relatifs aux antennes et à la propagation à très basse fréquence sont étendus au spectre des micro-ondes (mais non aux fréquences intermédiaires) en ce qui concerne les ondes de surface ou les "ducts" troposphériques, les phénomènes de relaxation dans l'eau de mer (par contraste avec les phénomènes de relaxation de la glace marine aux très basses fréquences), et les effets sur les réseaux en phase.

Ces résultats sont ainsi étendus parce qu'ils peuvent être appliqués aux deux régions. On peut également les utiliser à des fins de diagnostic pour la glace marine et les milieux de propagation.

SURFACE WAVE PROPAGATION FROM VLF ARRAYS IN POLAR SEAS

Albert W. Biggs
University of Kansas
Lawrence, Kansas 66044 U.S.A.

SUMMARY

This paper describes VLF surface wave propagation over open ocean, sea ice, and glacier ice path segments. These propagation path segments provide mixed path effects in the Arctic, where ice depths range from those in new sea ice to that of the Greenland ice cap. The ice layers introduce surface waves to complement mixed path propagation. Some of the parameters include frequency, ice depth, and distribution of brine pockets, ice spheroids, water content, density, and temperature in the ice. Antenna pattern distortion of a linear array of horizontal dipoles illustrates the dependence of the radiation field as well as propagation loss on these parameters. Extension of VLF results to higher frequencies is made for related phenomena.

1. INTRODUCTION.

Analyses of radio wave propagation in polar regions are useful when the models simulate the actual terrain. Although the subsequent discussion relates to the Arctic, the sea ice, the Greenland ice cap, and snow covered tundra have their counterparts in Antarctica. In some cases, Greenland can be represented as a homogeneous medium (1) of ice with low electrical conductivity. A more realistic model of Arctic terrain is a two layer medium, especially with sea ice. The upper layer of sea or glacier ice above a lower layer of sea water, rock, slightly frozen soil, or fresh water describes much of the polar terrain. The remaining terrain is sea water, either in open stretches of ocean or in leads (openings in the ice) in sea ice.

The source is a horizontal electric dipole on the surface of the ice. At very low frequencies (VLF), 3 to 30 kHz, the ice would be glacier ice in Greenland. At high frequencies (HF), 300 kHz to 3 MHz, sea ice would be adequate if it was more than five meters in depth (at the higher end of the HF spectrum). The advantages of horizontal over vertical dipoles are in antenna efficiencies and input impedances. With increasing conductivity, vertical dipoles are better, but with decreasing conductivity, horizontal dipoles are better (1). Another advantage with either dipole is the ability to formulate radiation fields for any linear antenna or array by superposition of fields from one dipole element.

Both sky and ground waves are present, but only the ground wave is considered in order to illustrate surface wave and mixed path phenomena in the Arctic. Although horizontal and vertical polarizations may be present, the high attenuation of the horizontally polarized wave removes it from the ground wave mode. The high conductivity of the sea water paths support the vertically polarized ground wave and severely attenuate the horizontally polarized ground wave. This phenomena suggests the use of horizontal dipole transmitting and receiving antennas on ice islands in the ocean.

2. SEA AND GLACIER ICE.

The major forms of ice in the Arctic Ocean are sea and glacier ice, differing in their origin in the sea and on land, respectively. The electrical properties of glacier ice (fresh water ice) are empirical formulations (2), predicted from simple theories of dielectric relaxation. They yield a complex dielectric constant

$$\epsilon^* = \epsilon' + i\epsilon'' = \epsilon_\infty + \frac{(\epsilon_0 - \epsilon_\infty)}{(1 - i\omega\tau)}, \quad (1)$$

where the values for ϵ_0, ϵ_∞, and τ for different temperatures T are

T(°C)	ϵ_0	ϵ_∞	τ (seconds)
- 0.1	91.5	3.1	2.2×10^{-5}
-10.8	95.0	3.08	6.0×10^{-5}
-20.9	97.4	3.1	1.64×10^{-4}
-32.0	100	3	5.7×10^{-4}
-44.7	104	3.1	2.52×10^{-3}
-56.8	114	3.1	1.2×10^{-2}
-65.8	133	3.1	4.5×10^{-2}

The important characteristics of VLF are the dependences on both temperature and frequency.

Sea ice has many forms (3). Although the Arctic Ocean may appear to be open water (in some places) in early autumn, the surface appears oily because of the formation of ice crystals. As this "frazil ice" increases, it forms into large areas of "sludge". The sludge can reach a four to six inch thickness overnight, and will form a smooth "ice field" over a foot in thickness.

In the spring, ice fields reach a thickness of five to six feet, but become rough and broken from actions of tides, winds, and currents. Pressures from these forces buckle the ice field and long "pressure ridges" are formed. "Rafted floes" result from the action of one piece sliding over another. Release of pressure may break the ice fields into floes with "leads" of open water between them. Shore locked ice is called "fast ice". These "ice sheets" and "ice islands", up to 200 square miles in area, do have some conductivity (lossy dielectrics) because of entrapped brine pockets formed during the ice growth.

The usual physical properties of sea ice come from the growth of ice in the presence of salty sea water. At equilibrium at a given temperature, pure (fresh water) ice co-exists with brine of a specified composition. Salinity profiles show that sea ice is very salty when it first forms, the salinity of a given segment of ice gradually decreases with time, and the vertical salinity profile at any given time has a characteristic "C" shape.

The brine pockets in sea ice have their corollary in ice crystal spheroids in glacier snow or lightly packed ice. These mixtures of heterogeneous particles (including water) produce changes in dielectric properties and, at microwave frequencies, create volume scatter phenomena.

Sea ice is dynamic in motion. A path over an ice island and an open lead on one day will see a new lead (opening in the ice) and a closed lead on the next day. Lack of information on Arctic sea ice is from relative inaccessibility and severe weather. One estimate for ice cover (4) in February is shown in Figure 1.

3. GROUND WAVE PROPAGATION.

The vertically polarized field intensity found with a modified saddle point method (5), is

$$E_z = -i60Idl\frac{M}{n_1}k_0\cos\phi\, F(x_0)\frac{e^{ik_0R}}{R}, \quad (2)$$

where $F(x_0)$ is the ground wave attenuation function

$$F(x_0) = 1 + i\sqrt{\pi x_0^2/2}\, e^{-x_0^2/2}\, \mathrm{erfc}(ix_0/\sqrt{2}), \quad (3)$$

and x_o is the Sommerfeld distance,

$$\frac{1}{2} x_o^2 \simeq \frac{i k_o R}{2} \left(\frac{M}{n_1}\right)^2 \tag{4}$$

In equations (2) and (4), the dipole moment is Idl, k_o is the free space wave number, n_1 is the refractive index of the ice, ϕ is the azimuth angle measured from the dipole axis, R is the distance from the antenna source, and M is a depth parameter

$$M = \frac{k_1 - i k_2 \tan k_1 D}{k_2 - i k_1 \tan k_1 D} \simeq -i \tan k_1 D, \tag{5}$$

where the depth D and wave number k_1 for ice appear. Since k_2 is much greater than k_1, the approximation follows. With the relationship for k_1

$$k_1^2 = k_o^2 \{\epsilon' + i\epsilon''\}, \tag{6}$$

where ϵ_1 and ϵ' appear in equation (1), the relaxation phenomena in ice at VLF produces wide changes with temperature and frequency.

The influence of M on $F(x_o)$ is seen in Figures 2 and 3 where the magnitude and phase of F(p) are described. The numerical distance p is used as the independent variable. The positive angles are the phases of p for ground wave propagation over homogeneous earth, identical with conventional ground wave curves. The negative angles are ground wave propagation over layered earth. The curve for -90° is a ground wave over lossless ice above infinitely conducting sea water, increasing with the square root of distance. When F(p) is divided by the distance, the curve for -90° is a ground wave proportional to the inverse square root of distance. The increase in intensity can be compared with waves in free space, where F(p) is unity. Curves above unity are waves with less attenuation than those in free space. A decrease in F(p) is found for increasing positive phases of p. The asymptotic F(p) varies inversely with p except at -90°. Fluctuations in the magnitude of F(p) have been observed by King (6) in similar studies. As the phase approaches -90°, the fluctuations and asymptotic behavior in F(p) occur at larger values of p.

The phase of F(p) is presented in Figure 3 as a function of the magnitude and phase of p. In homogeneous earth, where the phase of p varies from 0° to +90°, the phase of F(p) increases monotonically to an asymptotic value when the magnitude of p exceeds 10.0. In layered terrain, represented by phase variations from 0° to -90°, the phase of F(p) reaches a maximum value and then exhibits moderate oscillations before smoothing out to an asymptotic value. The fluctuations in the phase of F(p) coincide with those in the corresponding magnitude of F(p). If the magnitude and phase of F(p) are desired for a phase of p in the negative range, these curves cannot be interpolated for intermediate points.

4. MIXED PATH EFFECTS.

A vertically polarized ground wave over homogeneous ice attenuates at a rate described by the ground wave attenuation function for the ice (7) until it reaches the boundary of an adjacent ocean. At the shoreline, it increases as a "recovery effect" for a short distance and then attenuates at a rate described by the ground wave attentuation function for the sea. If the wave originates at sea, then it experiences a "dropoff effect" after passing the shoreline to the ice. The dropoff effect is a decrease in field intensity for a short distance followed by attentuation determined by the ground wave attenuation function for the ice.

When the homogeneous ice corresponds to Greenland, the mixed path described may be satisfactory. When the ice is not homogeneous, but is an upper layer of sea ice above a lower layer of sea water, brine, or highly (relatively with respect to the ice layer) conducting soil, then the dropoff effect may change to a recovery effect, create no change at all, or oscillate in both amplitude and phase. The instabilities in amplitude and phase in the ground wave result from the surface wave generated in a stratified medium where the upper layer has a lower refractive index than

that of the lower layer. These instabilities are frequently encountered in the Arctic, at high frequencies (HF) where sea ice is encountered almost continuously through the year. Communication instabilities have been encountered in the Arctic Ocean at HF (8) and in the vicinity of Point Barrow, Alaska at medium frequencies (MF) (9).

When one path (sea water) has a large refractive index, p will be less than unity for the entire mixed path. In the left side of Figure 4, p_2 for sea is much less than 1.0, and p_1 for ice is greater than 2.0. The dropoff and recovery effects appear in the upper and lower parts of the curves.

5. RESULTS.

The influence of layer depth is seen in Figure 5, where the magnitude of F(p) appears for a variable layer of soil with 0.0001 mhos per meter (m/m) above a layer of soil with 0.1 m/m. The frequency of 10.0 kHz, for this and subsequent examples, has a wavelength of 30 km, and the depth and distance are in units of λ_o, the free space wavelength. For example, a depth of 0.0037 λ_0 is 111 meters (m). A distance of 100 λ_o is 3000 km. In the HF range, λ_o is 300 m for 1.0 MHz, and the depth drops to 1.11 m. Although these depths are large at VLF, they drop to practical values at rising frequencies. Even at 30 kHz, the above depth drops to 37 m.

In Figure 6, F(p) is given for an upper layer of ice at -0.1° C above sea water at 5.0 m/m. A change of temperature to -20.9° C appears in Figure 7. In Figure 8, the depth is fixed at 0.0267 λ_o for different ice temperatures above sea water.

Homogeneous ice is presented in Figure 9 as part of a mixed path for a ground wave. The ice has a temperature of -20.9° C. Since the refractive index of sea water is high at VLF, p is less than unity in the mixed path distance and F(p) is a horizontal line equal to 1.0 for sea water paths. The lowest curve is Figure 9 is for homogeneous ice paths.

Initial path lengths of 4, 10, 40, 100 λ_o's over ice are followed with the balance over sea water. The recovery effects for the ice to sea paths are heavy lines superposed on the F(p) curve for the ice part of the path. The dropoff effects are presented for initial path lengths of 4, 10, 40, 100 λ_0's over sea with the balance over ice. The curves for each path are horizontal along the "sea" curve until the boundary is reached. Their pattern over the remaining ice is shown in dashed lines.

The influence of stratification is shown in Figure 10. The curve for F(p) is for ice with a depth of 1000 meters or 0.04 λ_o. The lower layer is sea water. The horizontal line at F(p) equal to 1.0 represents sea water as it did for the homogeneous ice and sea path. The curve for the layer of ice is different from the curve for homogeneous ice in four aspects. It exceeds the free space attenuation of inverse distance at F(p) equal to unity for several wavelengths, an increase in F(p) is observed near the source, fluctuations are encountered with increasing distance, and higher attenuations than inverse distance squared are present. These differences result in mixed path effects in variable forms. The same ice to sea paths are followed as in the homogeneous ice curves. Instead of recovery effects, dropoff effects are found in the curves for 4 and 10 λ_o's. The recovery effects are found in the ice to sea paths when the distance over ice was large enough for F(p) to be much smaller than unity. The increase in the recovery effect with distance is not found in the same sequence as that for homogeneous ice. The asymptotic curves are following the F(p) curve for layered ice, but are located on both sides of it. The phase associated with the mixed path are shown in Figures 11 and 12. Figure 11 is a parametric set of phase lags for paths from homogeneous ice to sea water with distances of 0.1, 0.25, 0.5, 1.0, 2.0, and 4.0 λ_o's on the ice. Figure 12 is similar except for stratification effects. The anomalous phase effect is evident in Figure 12 for the layered path segment.

6. VLF ARRAYS.

In the development of a linear array, the variables in each element are the amplitude and phase of the radiated fields with respect to the remaining elements. Modulating the amplitude or/and the phase creates a pattern with desired characteristics. When the elements are horizontal electric dipoles on ice at VLF, the space of a few miles will be sufficient to cause distortion because of non-uniform temperature conditions, sinking of elements into the ice (causing a phase shift), or physical changes in the terrain. The major consideration in VLF arrays is the impact of the environment on the pattern.

7. CONCLUSIONS.

Mixed path and surface wave propagation in Arctic terrain creates anomalies in measurements if these phenomena are not considered. The neglect of sky wave modes would be more critical as distance from the source increases. As indicated in the paper, the transition region between propagation paths was assumed to be abrupt. A linear transition from the conductivity and dielectric constant of one path to those of the next path would be more relevant. Also, a linear transition between layers would also be more relevant.

8. ACKNOWLEDGEMENT.

Dr. James R. Wait, ESSA, Boulder, Colorado, has written several excellent papers on both mixed path and layered media effects. Although not listed in the references, they should be consulted for additional and more detailed insight into these phenomena.

REFERENCES

1. Biggs, A. W. and Swarm, H. M., "Radiation Fields from an Electric Dipole in Homogeneous Antarctic Terrain," IEEE Trans. Antennas and Prop., vol. AP-16, pp. 201-208, March 1968.

2. Auty, R. P. and Cox, R. H., "Dielectric Properties of Ice and Solid D_2O," J. Chem. Phys., vol. 20. pp. 1309-1314, August 1952.

3. Neumann, G. and Pierson, W. J., Jr., "Principles of Physical Oceanography," Prentice Hall, Inc., Englewood Cliffs, New Jersey, pp. 70-84, 1966.

4. U. S. Navy Hydrographic Office, "Ice Altlas of the Northern Hemisphere," 1st Edition, 1946.

5. Biggs, A. W., "Dipole Antenna Radiation Fields in Stratified Antarctic Media," IEEE Trans. Antennas and Propagation, vol. AP-16, pp. 445-448, July 1968.

6. King, R. J. and Schlak, G. A., "Groundwave Attentuation Function Over a Highly Inductive Earth," Radio Science, vol. 2, pp. 687-694, July 1967.

7. Millington, G., "Ground Wave Propagation Over an Inhomogeneous Smooth Earth," Proc. IEEE, vol. 96, Pt. III, pp. 53-64, 1949.

8. Bourne, I. A., Ross, D. G. and Segal, B., "Phase Instability in Radio Waves Propagation Across Ice-Covered Seas." presented at the Thirteenth NATO/AGARD Symposium on Phase and Frequency Instability in Electromagnetic Wave Propagation, 9-12 October 1967, Ankara, Turkey.

9. Stanley, G. M., "Layered Earth Propagation in the Vicinity of Point Barrow, Alaska," J. Research, NBS, vol. 64D, pp. 95-97, January 1960.

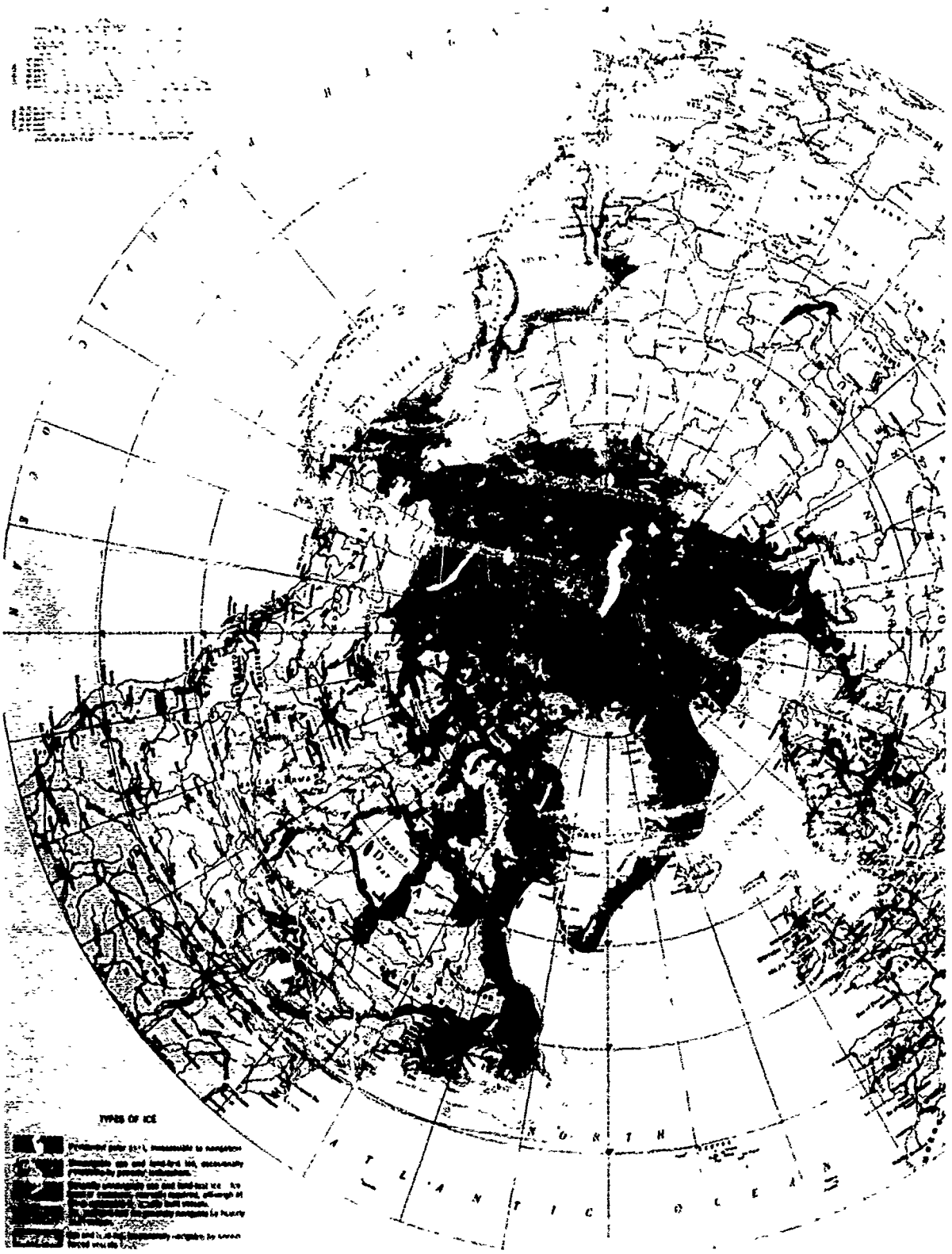

Fig. 1 Polar projection map of Northern Hemisphere average ice cover for the month of February – ice limits furtherest south (Reference 4)

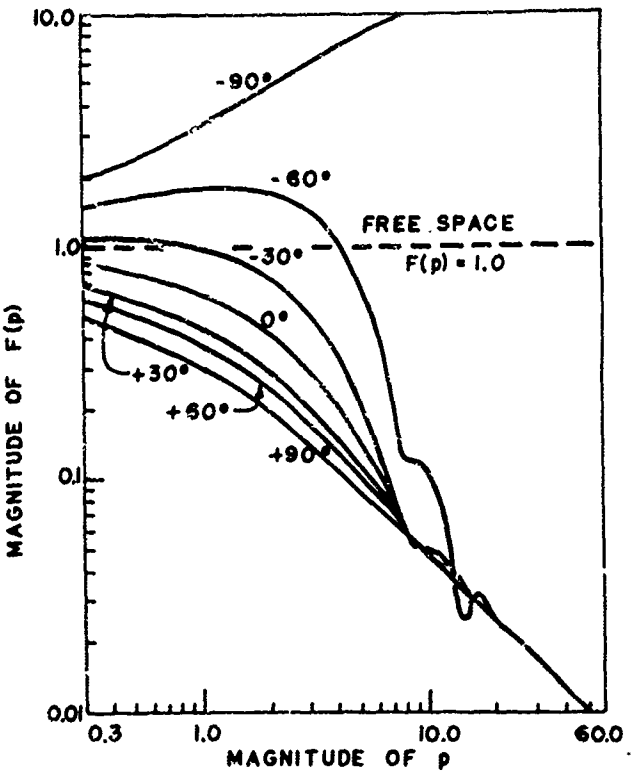

Fig. 2 Magnitude of the ground wave attenuation function F(p) for phases of p from -90° to $+90^{\circ}$

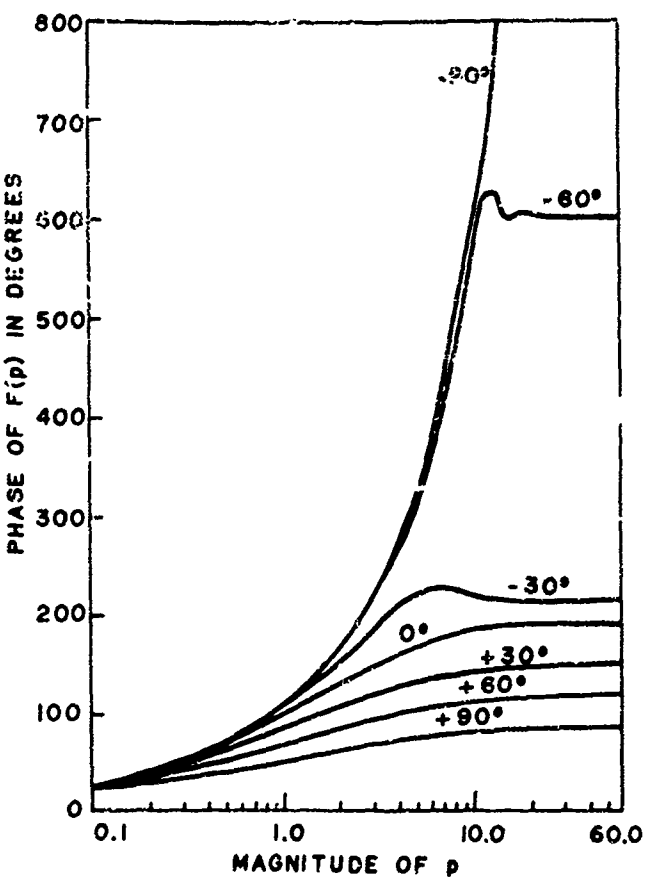

Fig. 3 Phase of the ground wave attenuation function F(p) for phases of p from -90° to $+90^{\circ}$

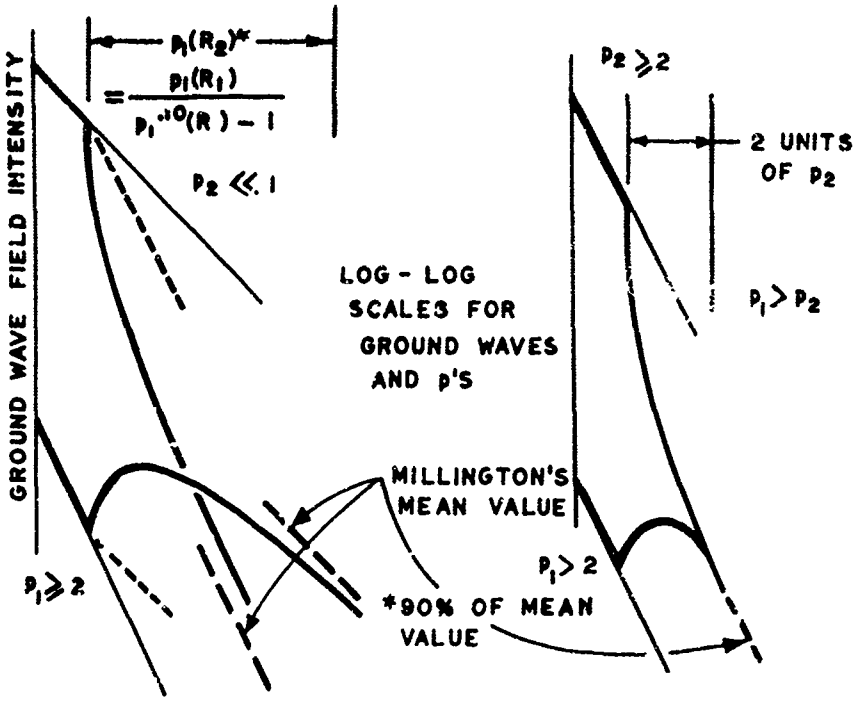

Fig. 4 Mixed path propagation for large and small p in the path segments, and for large p in both segments

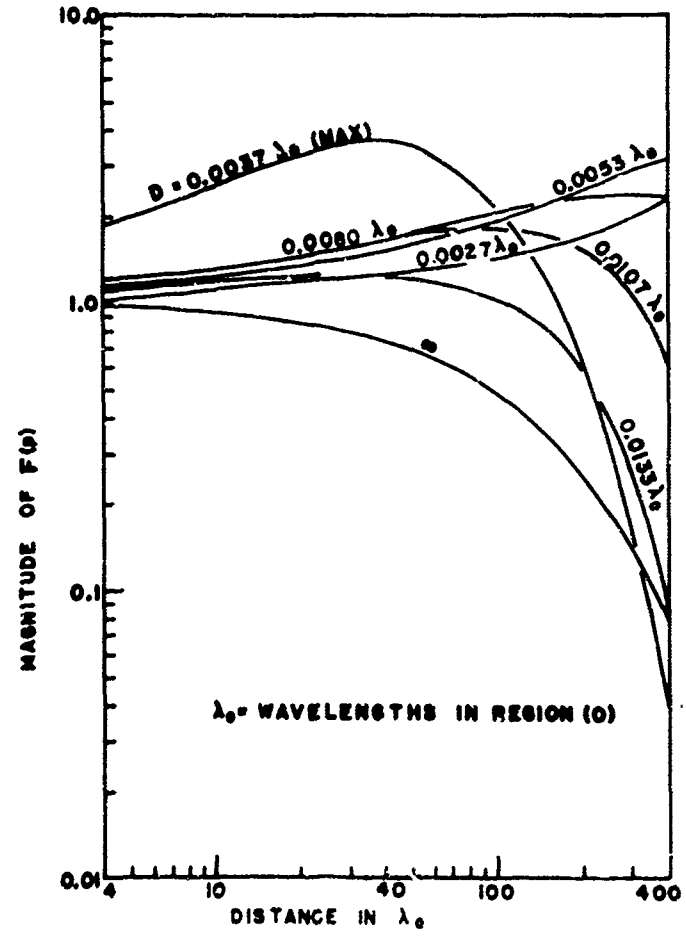

Fig. 5 Ground wave attenuation for a verying layer of 0.0001 m/m soil abo/e 0.10 m/m soil

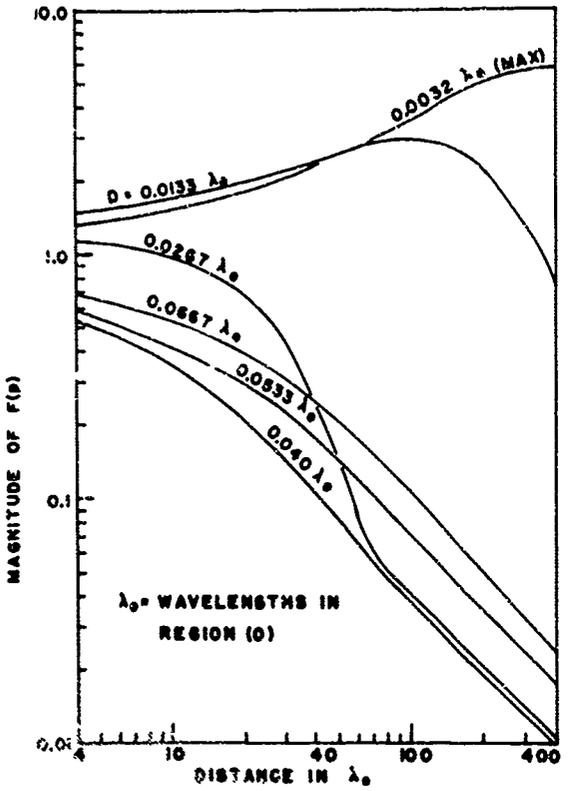

Fig. 6 Ground wave attenuation for a varying layer of −0.1°C ice above 5.0 m/m sea water

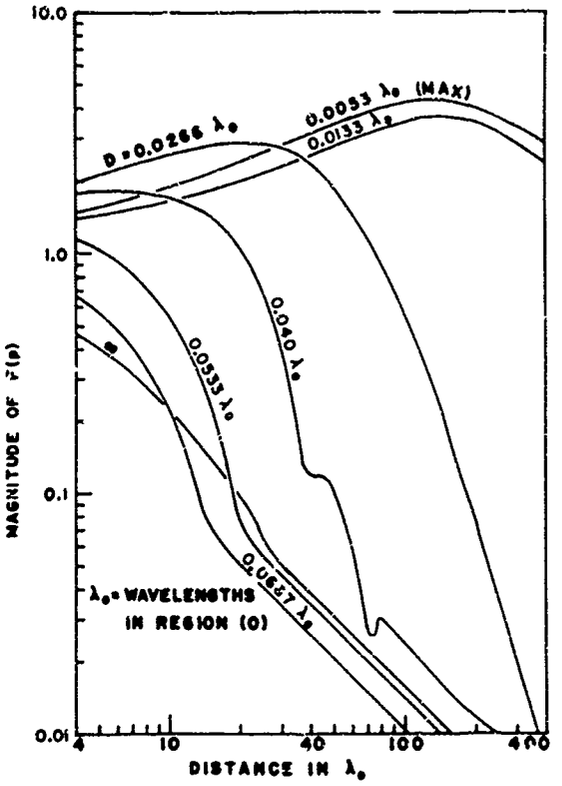

Fig. 7 Ground wave attenuation for a varying layer of −20.9°C ice above 5.0 m/m sea water

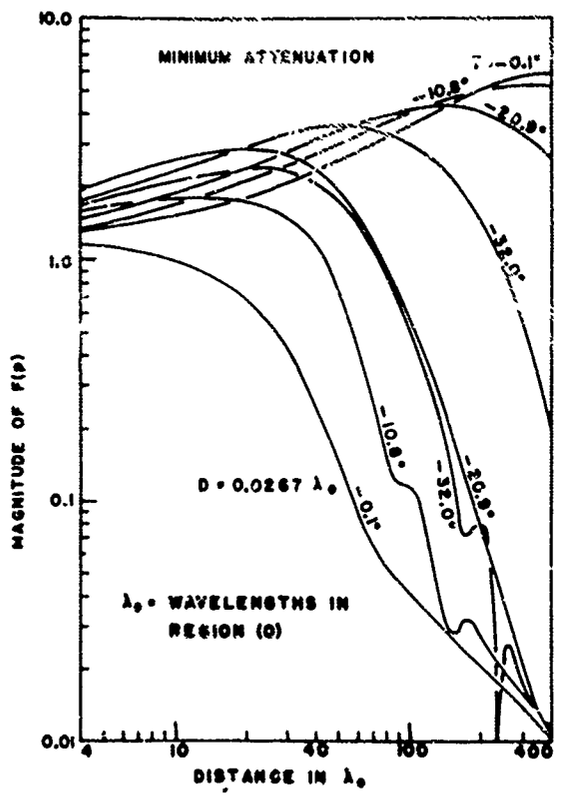

Fig. 8 Ground wave attenuation for a fixed layer of ice at varying temperatures above 5.0 m/m sea water

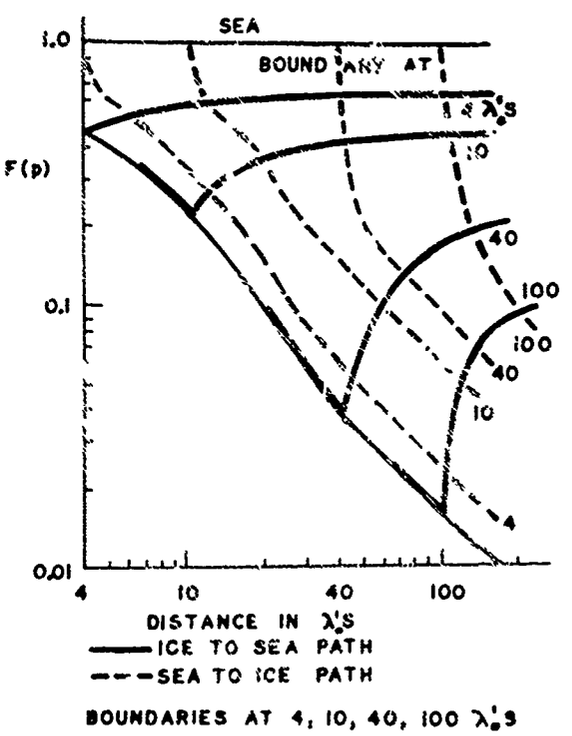

Fig. 9 Amplitude variation from homogeneous ice to sea water paths

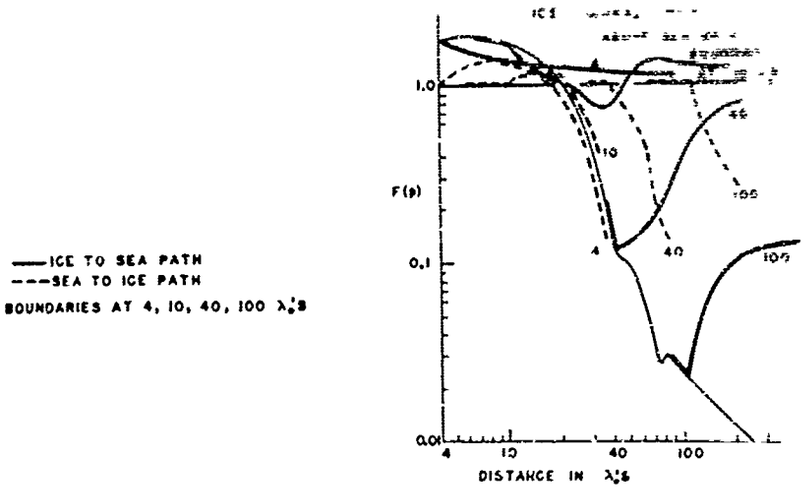

Fig. 10 Amplitude variation instabilities from floating sea ice to sea water paths

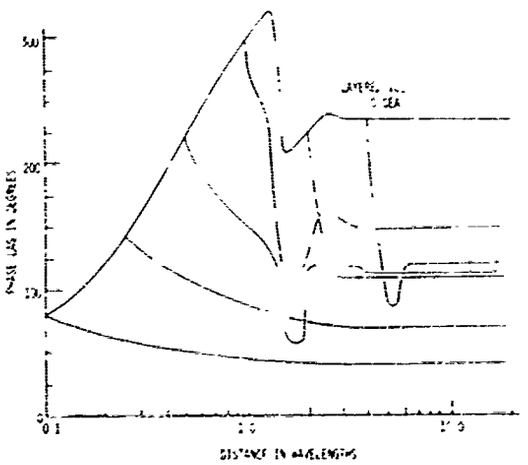

Fig. 11 Phase variation from homogeneous ice to sea water paths

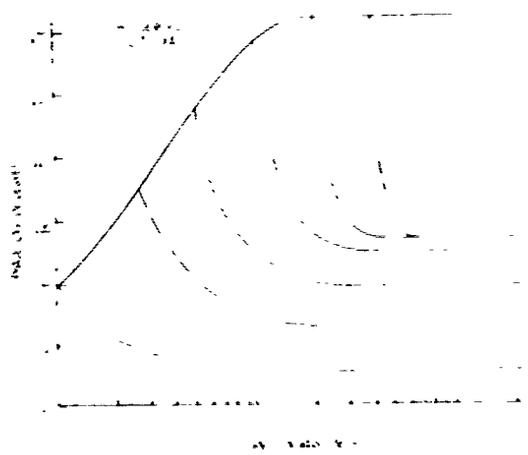

Fig. 12 Phase variation instabilities from floating sea ice to sea water paths

SOME RESULTS IN CONNECTION WITH A SEARCH FOR MAXIMUM UNDERWATER LF/VLF COVERAGE

by

Rune Lindquist
Research Institute of National Defence,
FOA 346
S-104 50 Stockholm, Sweden

SOMMAIRE

Les recherches en cause avaient pour objectif essentiel la mise au point d'une méthode simple et raisonnable permettant de déterminer la zone sous-marine susceptible d'être couverte par une station radio émettant dans le domaine des basses et très basses fréquences. Nous avons eu recours à cette méthode pour choisir l'emplacement et la fréquence optima d'une station qui fonctionnerait dans une zone définie entourant la Suède.

Nous avons utilisé comme base de calculs, une carte indiquant la répartition de la salinité des eaux entourant la Suède. L'intensité de champ des ondes de surface en fonction de la fréquence et de la distance a été calculée à l'aide de méthodes classiques. Des corrections ont été faites pour tenir compte de l'influence de l'interférence des ondes d'espace. Nous avons également tenu compte des variations diurnes et saisonnières intervenant dans la position du minimum principal. L'intensité de champ nécessaire, au niveau de la mer, à la réception à une certaine profondeur a été déterminée en considérant à la fois les bruits thermiques et atmosphériques.

Sur la base de ces données, nous procédons à des calculs sur échantillons pour déterminer la somme de puissance émise qui est requise en fonction de la fréquence pour plusieurs combinaisons d'emplacement d'émetteur et de récepteur. Nous montrons en outre comment une hauteur maximale fixe d'antenne influence les résultats.

Nous étudions enfin certaines méthodes simples, semi-graphiques, permettant de déterminer les diverses profondeurs de réception pour l'ensemble de la zone considérée.

SOME RESULTS IN CONNECTION WITH A SEARCH FOR MAXIMUM UNDERWATER LF/VLF COVERAGE

Rune Lindquist
Research Institute of National Defence,
FOA 346
S-104 50 Stockholm, Sweden

SUMMARY

The main objective of this investigation has been to find a reasonable simple method of determining the underwater coverage from a radiostation in the LF/VLF range. The sea water attenuation is computed from a map showing the distribution of salinity in the waters surrounding Sweden. The ground wave field strength as a function of frequency and distance has been computed by classical methods. Corrections have been added to take account of the influence of sky wave interference. The field strength required at sea level to permit reception at a certain depth has been determined by considering both thermal and atmospheric noise.

The use of the method is demonstrated in a search for optimum choice of frequency for a station serving a specified area around Sweden. It is further shown how a fixed maximum antenna height will influence the results. Finally, we discuss some simple semi-graphical methods for determining the various reception depths in the whole area.

1. INTRODUCTION

This paper deals with computations of the coverage of an LF-transmitter intended for under-water communications. Rigorous computations can be made with a computer program and a detailed knowledge of all the physical parameters. However, many times this method is too sophisticated, it is ofter quite satisfactory to obtain the final results with an accuracy of a few decibels. For those cases will the methods discussed in this paper be sufficient.

As an example, we will carry through a computation of the required radiated power at the best choice of frequency for a transmitter placed at a hypothetical fixed location in Sweden. Further is specified which area around Sweden it is supposed to cover and to what depth communication should be possible. Some data are given stating the sensitivity and noise-factor of the receiver and its ferrite-antenna.

The minimum field strength required for communication is ultimately determined by noise. Depending on the type of modulation used, one requires a certain signal/noisevalue in order to have a specified reliability in the communication system. We have chosen to determine the field strength that is equal to the noise power in the same bandwidth as the minimum required field strength. This way the user can afterwards compute the transmitted power that is required for the actual choice of modulation-system.

Two types of noise have been considered, thermal noise at the receiver input and atmospheric noise at sea level above the receiver. The latter is frequency dependent and also depending on time of day and season. The former is only frequency dependent.

2. FIELD STRENGTH REQUIRED TO OVERCOME THE THERMAL NOISE

Wave propagation from the transmitter to the receiver under water takes place along the surface to a point immediately above the receiver. From there it goes vertically down through the water to the receiver. It is therefore natural to start by computing the field strength at sea level which is required in order to obtain a signal level at the receiver input equal to the thermal noise.

The propagation path is shown in fig 41-1. We assume that the receiving antenna is a rod of ferrite material. The electromagnetic field at the antenna will then induce a voltage, V(z), at the input of the receiver

$$V(z) = h \cdot E(z) \qquad (41\text{-}1)$$

where

h = effective antenna length in meters
E(z) = electric wave field at receiving antenna

$$h = \frac{2\pi \cdot N \cdot A \cdot f \cdot \mu_{rod}}{3 \cdot 10^8} \qquad (41\text{-}2)$$

where

N = number of turns
A = area in m^2
f = frequency in Hz
μ_{rod} = relative permeability of rod material

In air we have

$$E = 120\,\pi \cdot H \qquad (41\text{-}3)$$

where

H = magnetic field strength.

The magnetic field is continuous when passing through the boundary between air and water. We can therefore write the following expression, valid for a ferrite antenna both above and below the boundary

$$V(z) = 120 \pi \cdot h \cdot H(z) \qquad (41\text{-}4)$$

The signal power, P(z), available from the antenna at a certain depth, z, is

$$P(z) = \frac{V^2(z)}{4 R} \qquad (41\text{-}5)$$

where R = resistive part of antenna impedance.

From Eq (41-4) and (41-5) we get

$$P(z) = \frac{120 \pi \cdot h^2}{4 R} \cdot E_o \cdot H_o \cdot A(z) \qquad (41\text{-}6)$$

where E_o and H_o = electric and magnetic field components in air at the boundary
A(z) = attenuation function for the field in water

$$A(z) = e^{-4\pi \cdot 10^{-4} \cdot z \cdot \sqrt{10 f \sigma}} \qquad (41\text{-}7)$$

where

z = depth in m below sea level
f = frequency i Hz
σ = conductivity of water, in S/m.

Let P_{tn} be the thermal noise power at the receiver input in the chosen bandwidth. The penetration depth is then given by

$$P(z) = P_{tn} \qquad (41\text{-}8)$$

or from Eq (41-6)

$$E_o = \frac{2\sqrt{R \cdot P_{tn}}}{h \sqrt{A(z)}} \qquad (41\text{-}9)$$

Knowing the values of R and P_{tn} for the actual receiver installation it is easy to compute the required field strength at the surface, E_o, for communication to a certain depth, z, as a function of frequency and the conductivity of the sea water.

Some results are given in Table 41-1. They apply to a typical receiver with a bandwidth of 200 Hz and give the required field strength for communication to a depth of 10 meters. The values are also shown in Fig 41-2.

Table 41-1. Required field strength, E_o, at sea level for communication (signal = thermal noise) to a depth of 10 meters as a function of salinity, conductivity and frequency. Receiver bandwidth is 200 Hz.

Salinity at 10°C o/oo	Conductivity S/m	Frequency kHz	Req. field strength, E_o, at sea level in dBμV/m
4,0	0,5	25	23,9
		50	23,9
		100	31,3
8,1	1	25	32,1
		50	35,6
		100	47,4
16,8	2	25	43,6
		50	51,4
		100	69,4
36,5	4	25	59,4
		50	73,4
		100	101,5

3. FIELD STRENGTH REQUIRED TO OVERCOME THE ATMOSPHERIC NOISE

It is a wellknown fact that the atmospheric noise is depending on location, time of day and season. The world distribution of the atmospheric noise and its variations can be found in CCIR Report 322 [41-1]. As the geographic area which is of interest in this investigation is rather small, we have assumed that the noise is constant within this area. Inspection of the variations in noise field strength with time of day and season showed that it would be sufficient to consider three cases. They are June day, November day and June night. With the use of Ref [41-1] we found the noise values as a function of frequency and corrected them to give the upper decile values. Some samples are given in Table 41-2.

Table 41-2. Atmospheric noise field strength not exceeded during 90% of the time.

Freq. kHz	Atmospheric noise field strength, bandwidth 200 Hz dB/ 1 μV/m		
	Day		Night
	June	Nov.	
15	57,5	45,5	48,5
30	50,5	39,0	43,5
60	43,5	29,5	38,0

The atmospheric noise during night hours shows very small variations with the season. The noise values are also shown in Fig 41-2.

4. COMPUTATION OF THE TRANSMITTED POWER REQUIRED FOR A SPECIFIED CIRCUIT

4.1 Method of calculation

Suppose we want to compute the transmitted power that is required in order to produce a signal equal to the thermal or atmospheric noise at a certain depth and at a certain distance from the transmitter. The method for doing this computation is rather straighforward. First, using the information given in a preceeding chapter, we compute the equivalent field intensity, E_o, required at the surface, to give a signal equal to the noise at the input of the receiver. Then, using the information on atmospheric noise, we compute the equivalent field intensity of the atmospheric noise, E_n, at the surface of the sea and as a function of season and time of day. Whichever is highest, E_n, or E_o, determines the required field intensity from the transmitter. Using conventional methods we then can compute the field strength at this point from a transmitter with an output power of say 1 kW. This time we have to take account of both ground- and sky-wave propagation. The resulting field is compared with the required, the difference given the required actual transmitted power.

4.2 Computing the required field strengths E_o and E_n.

In order to compute E_o at a certain receiver location, we must have knowledge of the salinity of the water in this area. The salinity of the water around Sweden varies within wide limits, from 2‰ on the extreme westcoast to 2‰ in the northern part of the Gulf of Botnia. Further, there are local variations and also variations with the time of year. The salinity has also a general tendency of increasing with the depth. The electrical conductivity as a function of salinity is also temperature-dependent. By using all the information we could get from primarily coast guard stations, light-houses and weather-stations we have drawn a map showing the approximate distribution of salinity in the waters around Sweden.

This map has been converted into a map showing the distribution of the values of electrical conductivity, Fig 41-3. At this point, we have assumed that the surface temperature has been 10°C. We know that temperature is decreasing with depth but we have assumed that this will be compensated by the increase in salinity. We have considered the values given in Fig 41-3 as beeing constant both with time of day and time of year. For a more precise determination it is always possible to add correction terms to take care of the yearly fluctuations. The map of the electrical conductivity in Fig 41-3 is the basis for all computations of the attenuation of the electromagnetic waves in the sea water.

The atmospheric noise-field has on the other hand a very pronounced dependence on the time of day and year. A study of these variations showed that it was necessary to make the computations for three different cases, local noon in June, local noon in November and for night conditions. Another reason for making the computations for three different time intervals, is that the received field strength also is depending on time of day and year. Typical values of the strength of the atmospheric noise field are shown in Table 41-2. In Fig 41-4 curves are presented which show the atmospheric noise amplitudes as a function of frequency for three different seasons.

4.3 Computing the received field strength, E_m, at sea level.

The principal component of the received field at these comparatively short distances is determined by the ground wave. The field strength of the ground wave as a function of conductivity, frequency and distance can easily be found in the literature [41-2]. We have used this material to draw curves showing the field strength as a function of distance for various frequencies in the band 15 - 60 kHz. All the curves are drawn for $\sigma = 4$ S/m. Some of the paths are along ground with much lesser conductivity, however for the comparatively short distances involved the error when using $\sigma = 4$ instead of the actual conductivity is rather

small. When dealing with longer paths, it is necessary to go to the trouble of taking full account of the influence of the various conductivities. A sample of ground wave field strength as a function of distance is shown in Fig 41-5. It is assumed that the radiated power is 1 kW. We also assume that the ground wave is independent of time of day and year.

We have also taken account of the influence of the sky wave component. The amplitude of this component is strongly influenced by time of day, time of year and frequency. There is of course also to be expected variations in the field strength in connection with magnetic storms or similar phenomena, these cases have not been considered. A study of the variations at different times and seasons shows that we will cover the extreme cases if we make calculations of the sky wave field as a function of distance and frequency for the same time periods as used for the atmospheric noise fields.

A very suitable method for predicting the sky wave field strengths is published by Belrose [41-3], this method will also be published in an updated version in a report from CCIR, IWP VI/5. A sample of the computed sky wave field strength as a function of distance is also shown in Fig 41-5.

At the receiving point, sky wave and ground wave will add vectorially. We have here considered the static case, i.e. only used the phase difference between the ground wave and sky wave which is due to different geometrical path lengths. A sample of the resulting combined field is also shown in Fig 41-5. However, this curve will not be very suitable in the practical case. Due to several factors, for example turbulence in the ionosphere, the phase of the sky wave will be continuously shifting in a random manner around the geometrical value. It is then better to compute a factor with which the field strength of the ground wave should be reduced in order to compensate for the influence of the sky wave.

This factor will be depending on the required percentage of time the resulting field strength should be exceeded. We have choosen to set this limit at 90 % of the time. The factor is determined by the ratio of the amplitudes of the ground wave and the sky wave. The reduction factor in dB as a function of this ratio is shown in Fig 41-6. As can be seen from Fig 41-6, the ground wave can be reduced up to 10 dB. This happens within the region where the amplitudes of the ground wave and the sky wave are of the same order of magnitude, this is often referred to as the chief minimum. Theoretically, the field strength would be reduced to zero, however due to the instabilities in the phase of the sky wave we discussed before, this will happen only momentarily. Beyond this region the sky wave will dominate. In order to avoid the resulting severe fading conditions in that region, we have limited the service area of the transmitter to slightly beyond the chief minimum. An example of the corrected ground wave field strength, E_m, as a function of distance and at different times of the year is given in Fig 41-7.

4.4. Computation of the optimum frequency when covering a certain area.

As a hypothetical case we have assumed that we want to place a transmitter at the location marked on the map shown in Fig 41-8. The transmitter shall be able to furnish a received signal equal to the noise level at the receiver within an area where the outermost points are marked A, B and C. The reception depth is assumed to be 10 meters.

From the preceeding information we can first determine the conductivity of the sea water at the different receiving points and also the distance from the transmitter. We find from the map in Fig 41-3

Receiving point	Conductivity S/m	Distance, transm.-receiver, km
A	3,2	200
B	1,0	400
C	0,8	500

We can then determine the values of E_o, E_n and E_m for each of the three receiving points at a number of frequencies within the frequency band of interest. This has to be repeated for the three different times we discussed before, i.e. June day, November day and June night. For each frequency and for all three receiving points we compare the received field intensity at sea level from a transmitter of 1 kW with the highest required field intensity, determined by E_o or E_n. This gives the required transmitter power. The highest of the three values for A, B or C will be the resulting required transmitter power for that particular frequency in order to cover the intended area. An example of this calculation for a frequency of 25 kHz and on a June day is shown in Table 41-3.

Table 41-3. Calculation of E_o, E_n, E_m and the resulting required transmitter power in dB/1 kW for a June day and on a frequency of 25 kHz.

Receiving point	E_o dB/1 µV/m	E_n dB/1 µV/m	E_m dB/1 µV/m	Req. increase in transm. power dB/1kW	Result.increase in transm, power dB/1 kW
A	54,0	52,0	61,5	- 7,5	
B	32,0	52,0	51,0	+ 1,0	+ 5,5
C	29,0	52,0	46,5	+ 5,5	

In Fig 41-9 is shown the resulting required increase in transmitter power above 1 kW for the three different times of the year as a function of frequency. In order to be able to communicate with a reliability of 90 % during the whole year we have to choose the worst case for each frequency.

The resulting curve is also shown in Fig 41-9. From that curve we can see that a suitable frequency band would be from 29 kHz to 45 kHz with an optimum around 35 kHz. This can seem to be a surprisingly high frequency, however, one must recall that we have only required a rather modest penetration depth, 10 meters. At the optimum frequency we would need a radiated power of about 1,0 kW(-0,5 dB/1kW) in order to produce a signal equal to or greater than the noise at the receiver input. To this we have to add power equal to the required signal/noise ratio.

4.5 Influence of a realistic trancmitting antenna.

In the preceeding paragraph we have considered the case of an ideal transmitting antenna, i.e. we have set the radiated power equal to output power of the transmitter. In practical applications one has also to take account of the efficiency of the transmitting antenna. In our hypothetical case we have decided that a realistic practical solution would be to use an antenna of the top-loaded type with an height of 200 meters. The theoretical efficiency of this antenna compared to an isotropic radiator can easily be computed, the result as a function of frequency is given in Fig 41-10.

We have now to correct the resulting curve given in Fig 41-9 in order to obtain the corrected curve of required increase in transmitter output power as a function of frequency. This new curve is also shown in Fig 9. From this new curve we see that the recommended frequency range now is from 32 to 52 kHz with an optimum around 40 kHz. At the optimum we will need about 10 kW(9,5 dB/1 kW) in order to have a signal equal to the noise at the receiver input.

5. A METHOD FOR MAKING MAPS SHOWING THE MAXIMUM DEPTH OF RECEPTION WITH A GIVEN RADIATED POWER

5.1 Determining the geographical distribution of F .

We have earlier shown that the maximum depth of reception is a function of the thermal noise at the receiver input and the attenuation in the sea water. With a knowledge of these parameters we can compute the field strength, E_o, that is required immediately above the sea-air interface in order to produce a signal equal to the thermal noise for a specified depth of penetration in the sea water. We repeat Eq (41-9),

$$E_o = \frac{2\sqrt{R\,P_{tn}}}{h\sqrt{A(z)}}$$

This can be written as

$$E_o = E_t \cdot B \qquad (41\text{-}10)$$

where

$$E_t = \frac{2\sqrt{R\,P_{tn}}}{h}$$

and

$$B = \frac{1}{\sqrt{A(z)}}$$

E_t is the field strength required at the receiver input, it is depending on the technical characteristics of the receiver and its antenna and includes also the polarization losses at the air-sea boundary. It is frequency dependent, in Fig 41-11 we have shown E_t as a function of frequency for the receiver we specified earlier in the paper. E_t is here expressed in dB/ 1 µV/m.

If we express E_o, E_t and B in dB we can write

$$E_o = E_t + B \qquad (41\text{-}11)$$

where now B will be the total attenuation in dB to the specified depth, z meters. As shown in Eq (41-7), B is a function of depth, frequency and conductivity. This relationship is shown in Fig 41-12 for a few typical frequencies and assuming a penetration depth of 18 meters.

Using Fig 41-3, 41-11 and 41-12 it is now easy to construct a new map showing E_o at a specified frequency and with a penetration depth of 18 meters. We have choosen to draw the map for a frequency of 50 kHz, this choice is of course quite arbitrarily. The result is shown in Fig 41-15.

The relationship represented by Fig 41-15 can be written as

$$E_o(50\text{ kHz}) = B(50\text{ kHz}) + E_t(50\text{ kHz}) \qquad (41\text{-}12)$$

with all parameters expressed in dB

$E_o(50\text{ kHz})$ = required field strength at sea level and at 50 kHz, expressed in dB/1 µV/m

$B(50\text{ kHz})$ = total attenuation to 18 meters depth in dB.

$E_t(50\text{ kHz})$ = equivalent field strength required at the receiver input in dB/1 µV/m

It is now easy to convert the map in Fig 41-15 to an arbitrary frequency. We can write the general expression

$$E_o(f\ kHz) = B(f\ kHz) + E_t\ (f\ kHz) \qquad (41\text{-}13)$$

We choose one of the lines on the map, representing a constant value of E_o. With the aid of Fig 41-11 and Eq (41-12) we can determine the corresponding value of the total attenuation to 18 meters depth and at 50 kHz, B(50 kHz). This number is then converted with the aid of figur 41-12 into the new value of E_t(f kHz) valid for the frequency f kHz. By adding the new value of E_t(f kHz) from Fig 41-11 one finally gets the new value of E_o, now valid for the frequency f kHz. In this manner the whole map can be redrawn for any frequency.

5.2 Determining the coverage from a specified transmitter.

We now have maps showing the required field intensity at sea level. If we want to find the coverage from a specified transmitter, we have to consider the worst condition for the wave propagation, i.e. night conditions. Following the method outlined earlier in this paper we can compute the expected field strength, E_m, as a function of distance, using the actual radiated power. On a transparent paper we draw circles corresponding to different values of received field intensities, the distance scale used must be exactly the same as for the map. This overlay is placed with its center above the transmitting station on the map. By marking all the points where the received and required field strengths are equal, we get contour lines showing the coverage for a penetration depth of 18 meters (as used in this example).

This method can also be used to locate the best position for maximum coverage from a new station. By sliding the overlay over the map it is very easy by a cut and try - method to find the best position for the transmitter.

5.2. Limitations of the method.

The reasoning above is based on the fact that the thermal noise is determining the required field strength. As was shown earlier we have also to consider the atmospheric noise. It is therefore necessary to check afterwards if the atmospheric noise has been dominating in some areas. In those cases the radiated power has to be modified accordingly.

5.3. Determining the position of an arbitrarily choosen depth of penetration.

It is often of interest to find the position of an arbitrarily choosen penetration depth, b meters. This can be done with the aid of Fig 41-14. Here we have computed E_o as a function of B_m, where B_m is the attenuation in dB/meter and with the frequency as parameter. E_o is, as before, the field strength required at sea level in order to produce a signal in the receiver input equal to the thermal noise level and at a reception depth of 18 meters. From Fig 41-14 we can determine the value of B_m that corresponds to an arbitrarily chosen value of E_o. If we now want to find a place where reception depth only is b meters, this point is determined by the requirement that the field strength at sea level, $E_{c,b}$, shall be

$$E_{o,b} = E_{o,18} - (18 - b) \cdot B_m$$

The practical procedure is that one uses the same transparent paper with circles corresponding to different received field strengths as was mentioned in an earlier paragraph. One selects a line of constant $E_{o,18}$, follows this line until it crosses a field strength circle with the required new field strength, $E_{o,b}$. This because the validity of Eq (41-14) is based on the fact that the conductivity is kept constant.

6. CONCLUSIONS

The purpose of this paper has been to outline some methods for making fast and still quite accurate computations of transmitter coverage in connection with underwater communications. We have only quoted a few applications, the use of the methods can easily be expanded to cover a lot more applications.

7. ACKNOWLEDGEMENT

The author would like to thank Mr Göran Svennérus of the same institute who also has taken an active part in this project.

8. REFERENCES

41-1 C.C.I.R. Report 322, World Distribution and Characteristics of Atmospheric Radio Noise, ITU, Geneva, 1964.

41-2 C.C.I.R. Documents of the XIth Plenary Assembly, Vol IV, Propagation, pp 17-23, ITU, Geneva, 1967.

41-3 Belrose, J.S., Lecture no 33, Low-frequency Propagation, NBS, Course in Radio Propagation, CRPL, NBS, Boulder, Summer 1962. (Will also be published in an updated version within C.C.I.R)

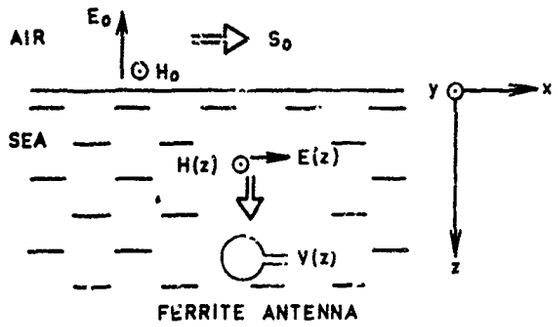

Fig. 1 Showing the penetration of electromagnetic waves into the sea (simplified)

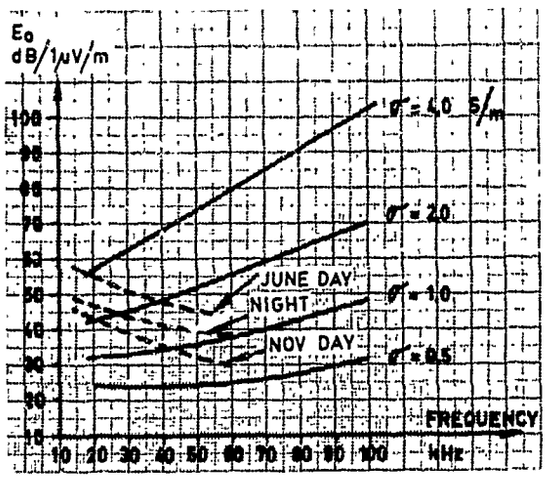

Fig. 2 Field strength required at sea level in order to give a signal at the receiver input equal to the thermal noise. Depth of receiver is 10 meters. The dotted lines show the atmospheric noise level at different seasons

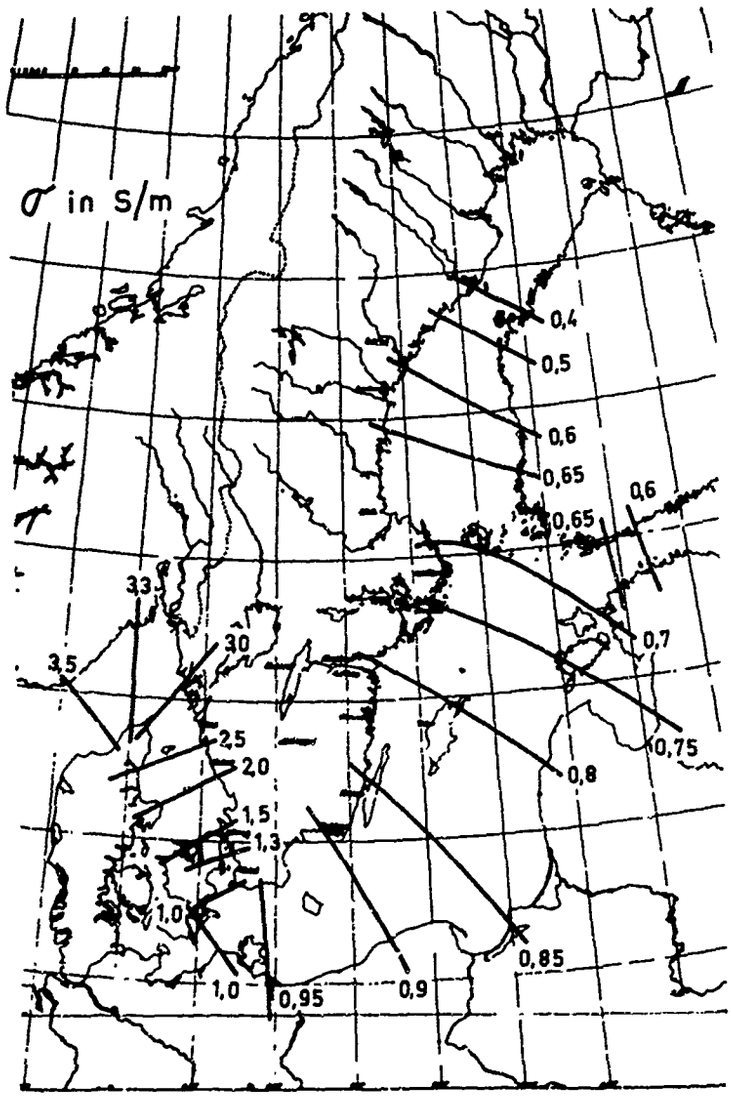

Fig. 3 Map showing the conductivity in S/m in the waters surrounding Sweden

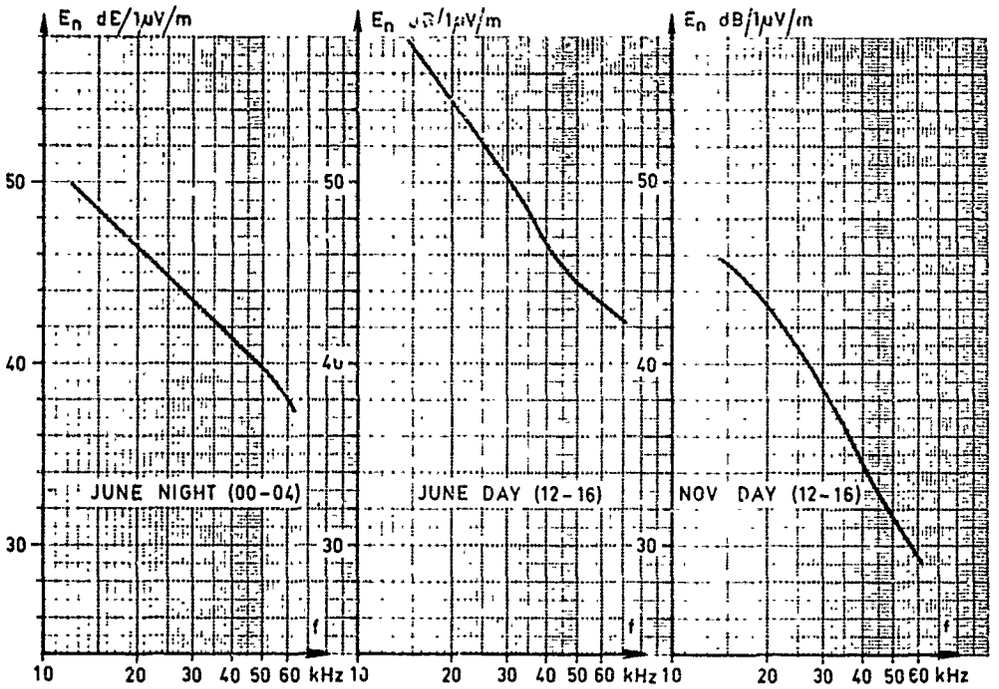

Fig. 4 Equivalent atmospheric noise field strength, E_n, as a function of frequency at three different times of year Receiver bandwidth is 200 Hz. The curves give the field strength not exceeded during 90% of the time

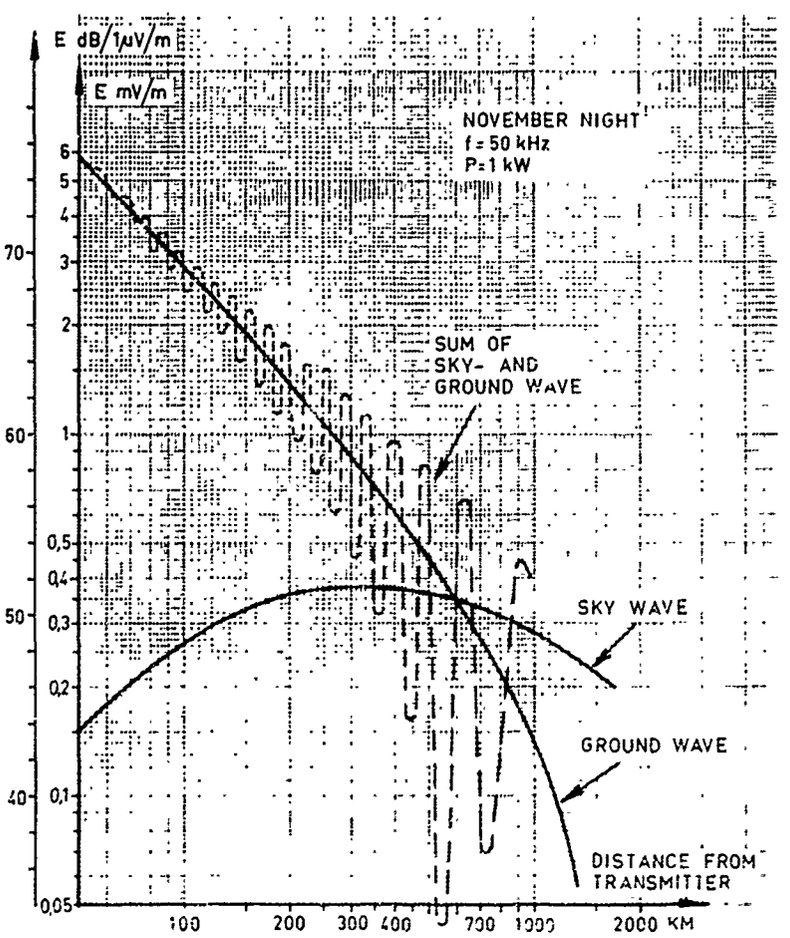

Fig. 5 Field strength of ground wave and sky wave during night conditions as a function of distance. The figure also shows the resulting received signal, i e. the vectorial sum of ground and sky wave Radiated power is 1 kW

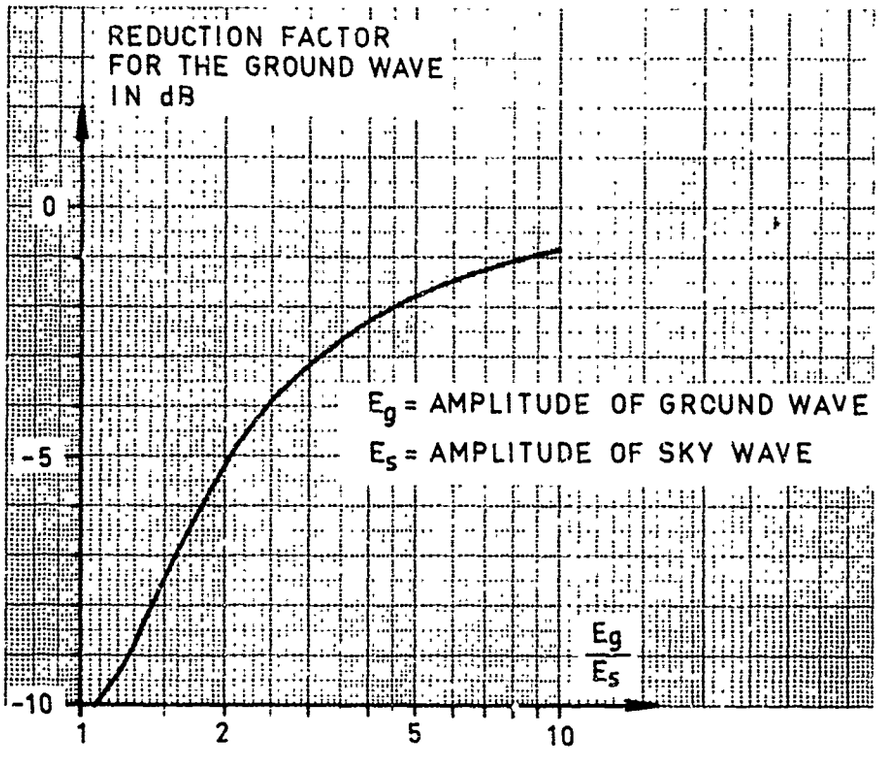

Fig.6 Reduction factor used to correct the received ground wave field intensity for the influence of the sky wave

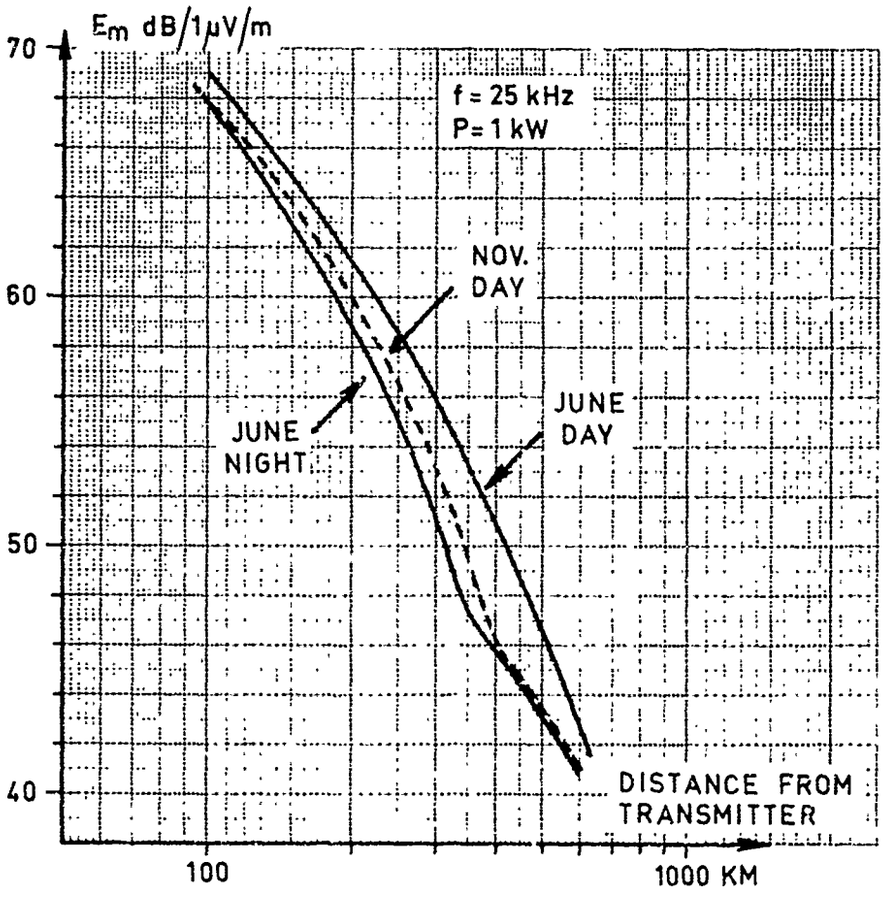

Fig.7 The resulting field strength, E_m, i e ground wave corrected for the influence of the sky wave as a function of the distance for three different seasons

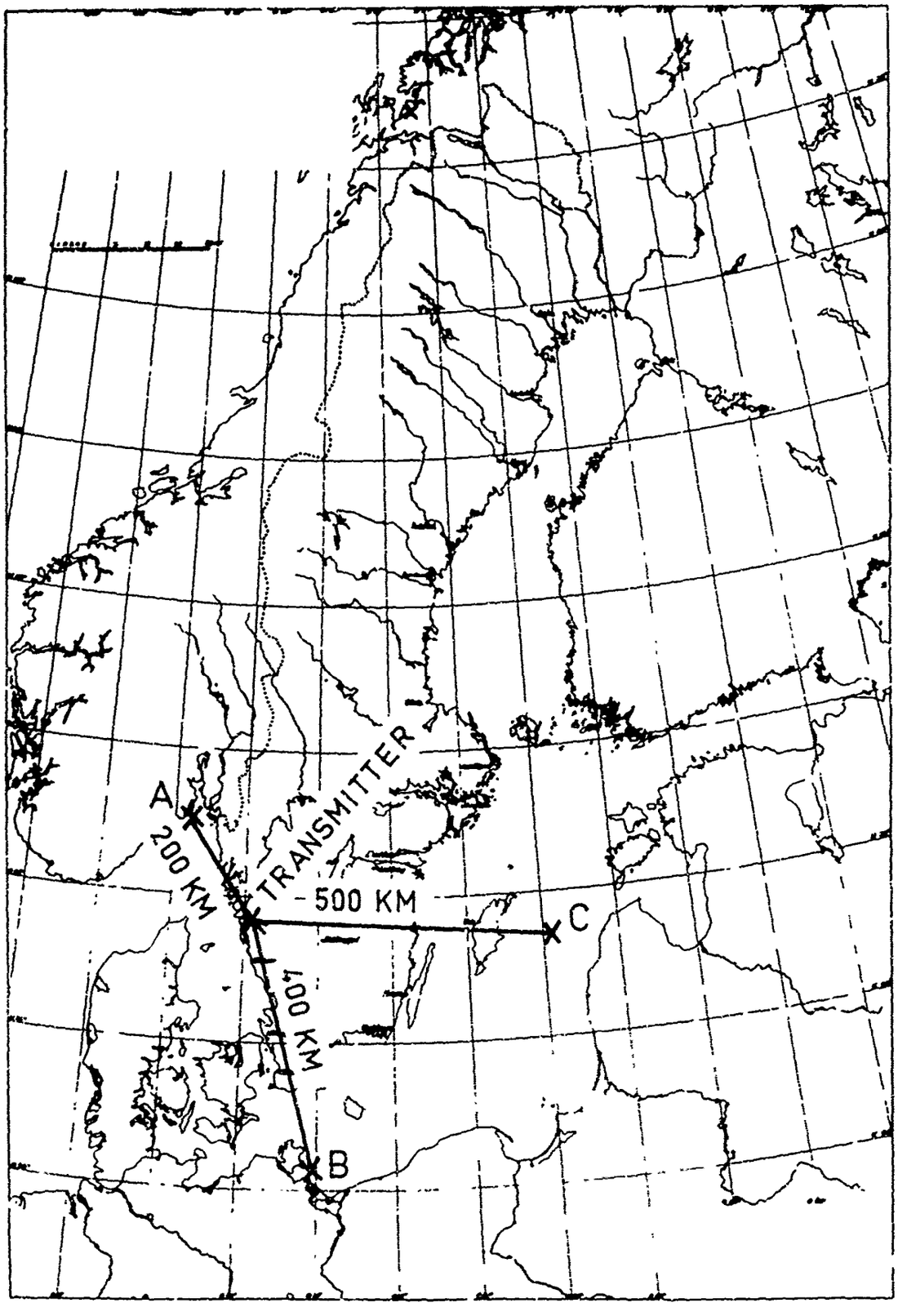

Fig 8 Map showing the suggested position of the transmitter and also three receiving points, A, B and C, which determine the outer area of expected coverage

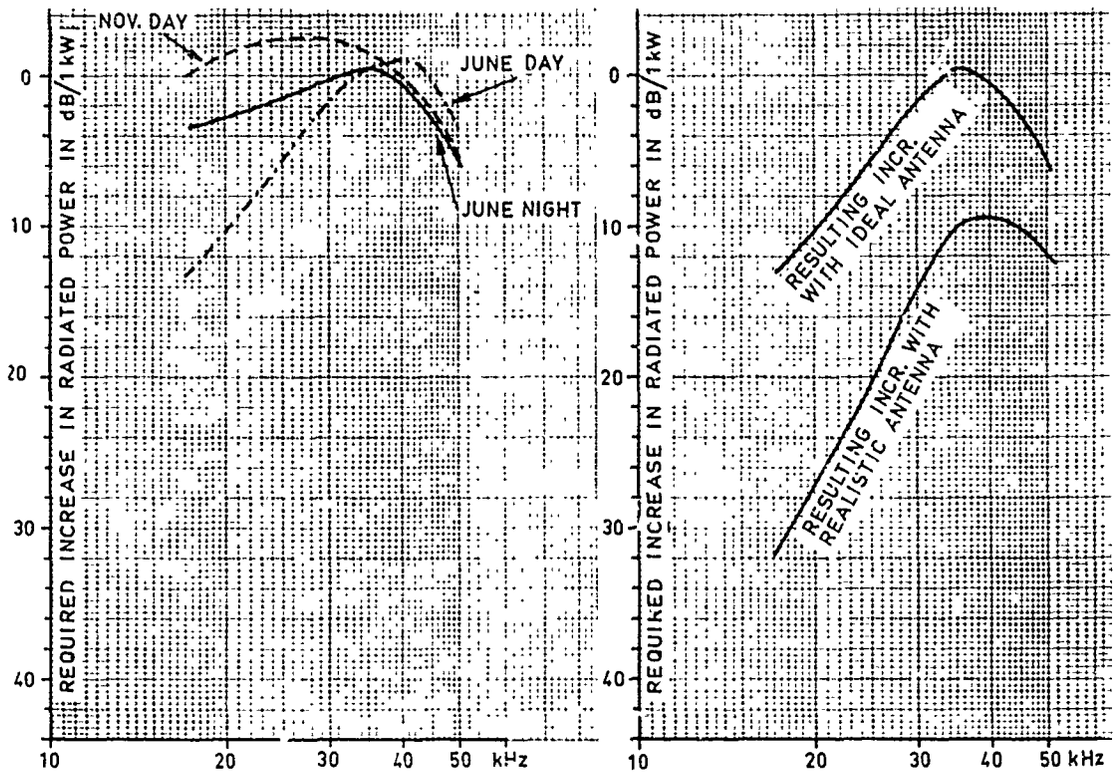

Fig. 9 Required increase in radiated power in dB/1kW in order to have a reception depth of 10 meters within the whole area The curves are shown for three different seasons in the year. In the figure is also shown the resulting curve when the requirement should be fulfilled throughout the whole year. The top curve is with an ideal antenna and the bottom curve is for a top loaded vertical antenna with a height of 200 meters

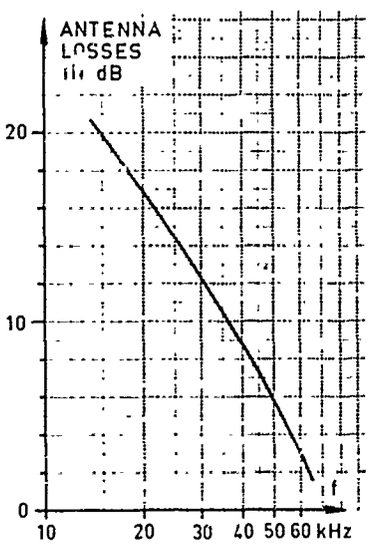

Fig. 10 Antenna losses as a function of frequency The curve applies to a top loaded vertical antenna with a height of 200 meters

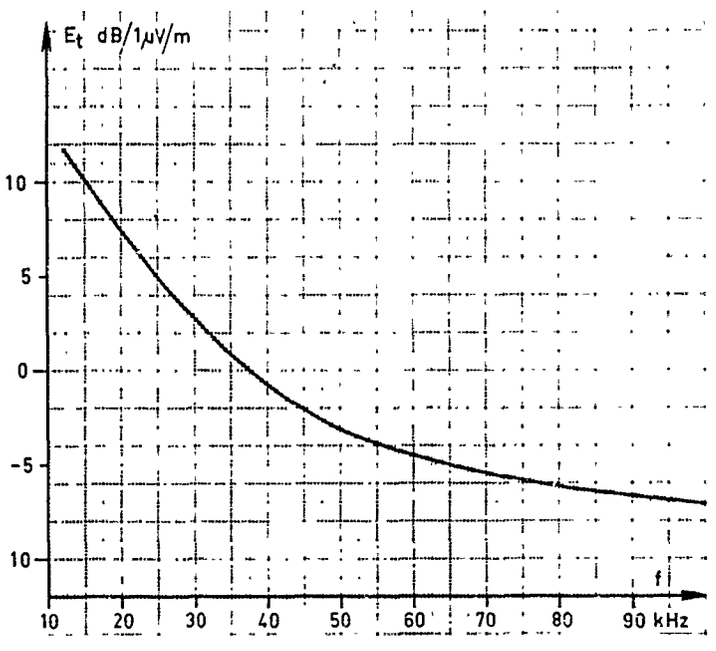

Fig. 11 The equivalent field strength, E_t , required at the input of the specified receiver installation when the received signal is equal to the thermal noise The curve applied to a reception depth of 18 meters

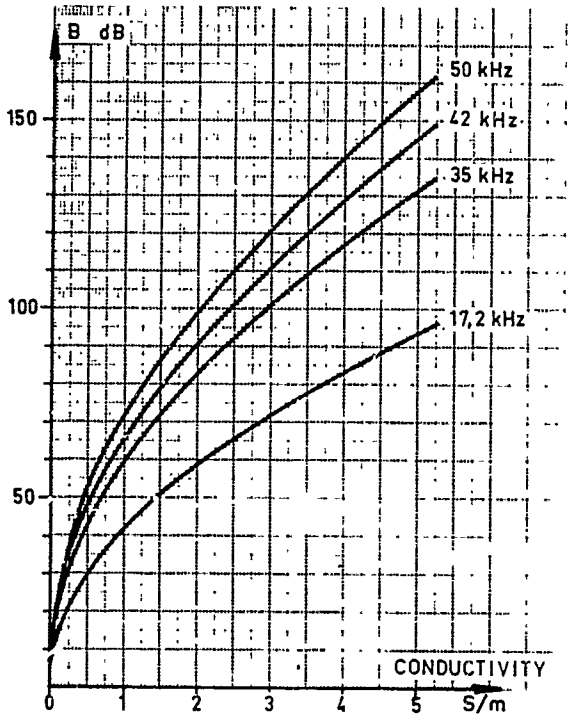

Fig. 12 Shows the total attenuation down to 18 meters depth, B , as function of the conductivity. The relationship is given for a few sample frequencies

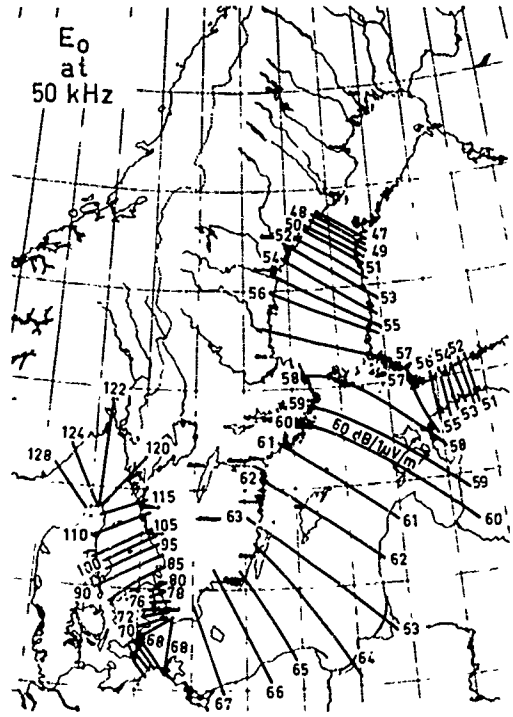

Fig. 13 The field strength, E_0 , required at sea level in order to produce a signal at the receiver input equal to the thermal noise and at a reception depth of 18 meters. E_0 is given in dB/1 μV/m and is computed for a frequency of 50 kHz

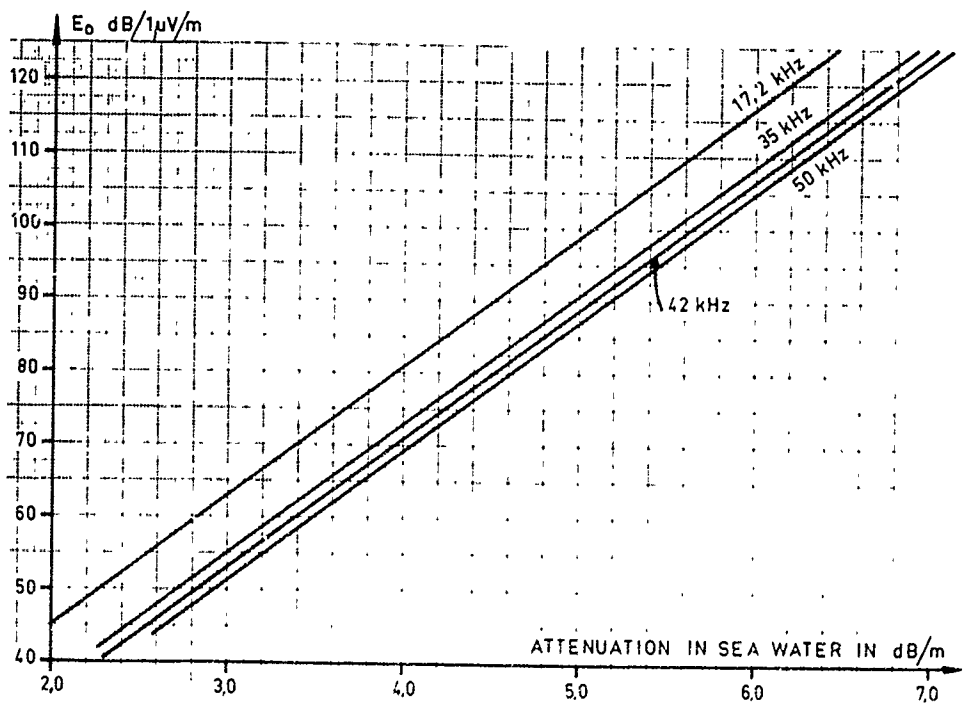

Fig. 14 Shows the relationship between E_0 in dB/1 μV/m and the attenuation in sea water in dB/meter Curves are drawn for the typical frequencies and apply to the specified receiving installation

DISCUSSION ON THE PAPERS PRESENTED IN SESSION I
(VLF/ELF Propagation in the Sea)

Discussion on paper 1 : "ELF Propagation", by J. GALEJS.

Dr. R.D. HOLLAND : I asked for the radiated power levels for the slide

(Bunn	400 Hz	3000 km)
(Gutton	40	40 km)
(Gage	5.4	15 km)

Dr. J. GALEJS : I do not recall the power level of the 400 Hz transmission. Gutton used a 40 KVA generating system. Gage apply about 12 kW to the antenna and estimate that 500 W are transmitted on the fundamental frequency of a pulse excited antenna.

Dr. Albert BIGGS : Were the works by Gage in 1968 in Antarctica published ?
Where were the results ?

Dr. J. GALEJS : Journal of Geophysical Research 1968, Vol. 73 n° 13, pp. 4416-4420.

Dr. A. ESSMANN : L'orateur a décrit l'effet de la houle sur l'amplitude du champ dans l'eau. En pratique cet effet n'apparait de façon significative que pour les très petites profondeurs d'immersion. A 10 m. de profondeur et aux fréquences de quelques centaines de Hz l'effet est à peine observable.

Dr. J. GALEJS : In figure 15 there is a 35 dB change in the signal level at f = 20 kc/s as the instantaneous depth of observation point below the waves is changed from 25 to 50 ft. Such fluctuations of the signal level have been also experimentally verified at VLF. However the corresponding signal changes would be smaller at ELF.

Dr. A. WIRGIN : What do you mean by the reference plane approximation ?

Dr. J. GALEJS : Fields in an assumed reference plane through the troughs of a sinusoidal wave are computed by assuming that field penetration through the wavy surface is the same as for a flat surface.
Fields of deeper depths are then expressed in terms of the fields in this reference plane.

Discussion on paper 2 : "Propagation of VLF electromagnetic waves across land : sea boundaries", by JR. WAIT.

Dr. FRANCESCHETTI : What about the accuracy of radio-aids to navigation as LORAN C, due to the problems you have spoken about ?

Dr. J.R. WAIT : The same method may be applied to this case but at the Loran-C frequency (ie, 100 kHz) it is more convenient to treat the ground wave and sky waves separately. The Wiener-Hopf analysis for ground wave propagation over a multiple mixed-path on a curved earth is described in a forthcoming paper in the journal of Mathematical physics. It confirms the previously employed integral equation methods referenced in this (Agard) Paper.

Dr. T. SWIFT : The next to the last slide showing mode conversion $(1/\sigma_2)^{\frac{1}{2}}$ indicates that (2,1) conversion curves are monotonically increasing. What asymptotic value do they reach as $\sigma_2 \to 0$

Dr. J.R. WAIT : About 0.835689 Maybe.

Dr. D.D. CROMBIE : Is the behaviour of the mode conversion coefficient with oblique propagation across the coastline the same as for an oblique path through a day/night transition, when the angle of the path across the boundary varies.

Dr. J.R. WAIT : Yes, more or less. Coast-lines, however, are more abrupt than sunrise and sunset boundary lines in the ionosphere where VLF radio waves are reflected.

Dr. D.E. BARRICK : Would Dr. Wait please comment on two variations of the coast-line problem, estimating the seriousness of these effects and also mentioning previous work if it is available :

1) a straight coastline oblique to the propagation path, and
2) a curved coastline

Dr. J.R. WAIT : Oblique propagation across a coast-line has been treated theoretically by E. Feinberg in the USSR and the author in a series of papers in NBS Journal of Research (Radio Propagation) 1963, 1964 and 1965. Curved coast-lines have not been treated explicitly as far as I am aware. But a general formulation and many literature references are given in J.R. Wait "Electromagnetic Surfaces Waves" Advencer in Radio Research, Vol. I, 157-217 Academic Press, London 1964.

Discussion on paper 3 : "Propagation of acoustic or electromagnetic waves in an inhomogeneous sea-type medium with rough frontiers"by M.F. Verhaeghe and A. Wirgin.

Dr. J.R. WAIT : Please explain the applicability of your results to the attenuation of grazing wave propagation of H.F. Radio waves over the rough sea.

Dr. A. WIRGIN : An excitation field radiated from some physical source density can be represented as a plane wave spectrum containing both homogeneous and inhomogeneous waves. Our analysis is based on determining the response to one of these plane (homogeneous) waves ; since Maxwell's equations are linear, the response of the sea to the source distribution will be the sum of the responses to the individual plane homogeneous and inhomogeneous plane waves that appear in the source spectrum. For instance, we showed that the zeroth order approximation of the field on the air-water interface for a plane homogeneous wave of incident angle θ_i was

$$U_1^{(o)}(X, \theta_i) = \left[1 + r^{1(o)}(X, \sin\theta_i)\right] \exp ik_1(X \sin\theta_i - f_1(X)\cos\theta_i)$$

$$V_1^{(o)}(X, \theta_i) = \left[1 - r^{1(o)}(X, \sin\theta_i)\right] ik_1 \cos\theta_i \exp ik_1(X \sin\theta_i - f_1(X)\cos\theta_i)$$

If the source spectrum is of the form,

$$U_o(X, f_1) = \int_{-\infty}^{+\infty} A(S) \exp ik_1 \left[SX - \sqrt{1 - S^2}\, f_1\right] dS$$

at the air/water interface, then we have by the superposition principle

$$U_1^{(o)}(x) = \int_{-\infty}^{+\infty} A(S) \left[1 + r^{1(o)}(X, S)\right] \exp ik_1 \left[SX - \sqrt{1 - S^2}\, f_1\right] dS$$

$$V_1^{(o)}(x) = \int_{-\infty}^{+\infty} A(S)\, ik_1 \sqrt{1 - S^2} \left[1 - r^{1(o)}(X, S)\right] \exp ik_1 \left[SX - \sqrt{1 - S^2}\, f_1\right] dS$$

where $S = \sin\theta$ for $|S| < 1$

Note that for an incident plane wave (the case treated in our paper)

$$A(S) = \delta(S - \sin\theta_i)$$

and we fall back onto our original expression.

For a line source localized at (X_o, Z_c) above the air/water interface

$$U_o(X, f_1) = \frac{i}{4} H_o^{(1)}\left[k(X - X_o, f_1 - Z_o)\right] \qquad (H_o^{(1)} = \text{Hankel function})$$

$$" = \frac{i}{4\pi} \int_{-\infty}^{+\infty} \frac{1}{\sqrt{1 - S^2}} \exp ik_1 \left[S(X - X_o) - \sqrt{1 - S^2}\,(f_1 - Z_o)\right]$$

whereupon

$$A(S) = \frac{i}{4\pi\sqrt{1-S^2}} \exp - ik_1 (SX_o - \sqrt{1-S^2}\, Z_o)$$

and

$$U_1^{(o)}(X) = \frac{i}{4\pi} \int_{-\infty}^{+\infty} \frac{\left[1 + r^{1(o)}(X,S)\right]}{\sqrt{1-S^2}} \exp ik_1 \left[S(X - X_o) - \sqrt{1-S^2}\,(f_1 - Z_o)\right] dS$$

$$V_1^{(o)}(X) = \frac{-k_1}{4\pi} \int_{-\infty}^{+\infty} \left[1 - r^{1(o)}(X, S)\right] \exp ik_1 \left[S(X - X_o) - \sqrt{1-S^2}\,(f_1 - Z_o)\right] dS$$

of course we now have to cope with the problem of performing the S - integrals ($r^{1(o)}(X,S)$ being a non-analytic function), but this is a classical problem of integration in the complex plane with which Dr. Wait is very familiar. Thus our apprcach can be generalized to take into acount the physical sources which generate ground waves.

Dr. E. BARRICK : In your perturbation development was it necessary to assume the surface height small compared to a radio wavelength in free space ?

Dr. A. WIRGIN : The perturbation method used here is based only on the assumption that the lowest spatial periods of the spectrum of the interface profile functions are of an order of magnitude greater than the wavelength . However if the surface heights are of the order or greater than the wavelength it might become necessary to take into account many terms in the perturbation series (inconvenient) or the series might cease to have any sense . In fact it seems probable that limiting the perturbation series to its first terms only is justified only in the case when the surface slopes are rather small . But by keeping the second term of the perturbation series which is equivalent to the inclined plane physical optics approximation, the restrictions on the slopes probably become less severe . It should be pointed out that a perturbation solution has been obtained by M.F. Verhaeghe (Optica Acta, to appear,) based on the fact that he surface heights are an order of magnitude less than the wavelength .

Dr. G. FRANCESCHETTI : I should like to have more informations about the definition of the reflection coefficient .

Dr. A. WIRGIN : We represent the field in air above the plane Z = (f1)max as a spectrum of plane waves both homogeneous and inhomogeneous . This spectrum is discrete in the periodic irregularity case and continious in the aperiodic irregularity case . The graphs pertain to a sandwich with periodic walls . Thus the reflected diffraction field in air is composed of a series of plane waves (or grating orders) one of which corresponds to the specularly reflected wave from the plane (f_1)average . The amplitude of this wave is the amplitude reflection coefficient and the modulus squared of this amplitude normalized with respect to the intensity of the incident plane wave is the intensity reflection coefficient which is the ordinate in our graphs .

Discussion on paper 4 : Rayonnement des sources electromagnétiques placées dans des milieux absorbants, par le Prof. R. GABILLARD .

C.F. P. HALLEY : Dans la réception sous-marine, est-il plus intéressant pour atteindre une réception à grande profondeur d'utiliser un capteur magnétique plutôt qu'un capteur électrique ?

Pr. R. GABILLARD : L'impédance E/H de l'onde dans l'atmosphère est de 377 ohms . Dans la mer l'impédance de l'onde réfractée est de l'ordre du dixième d'ohm . On a donc intérêt à capter la composante H qui est bien plus intense que la composante E . Bien entendu ceci n'est vrai que si le bruit propre de l'antenne ou du récepteur intervient . Si le bruit provient entièrement de l'atmosphère on aura le même rapport S/B en captant le champ H, qu'en captant le champ E .

Prof. M. BOUIX : Le rapport des composantes électrique et magnétique est le même pour le bruit que pour le signal à la même fréquence .

Pr. R. GABILLARD : C'est exact, mais seulement dans la mesure où le bruit provient entièrement de l'atmosphère . Si le bruit de l'antenne intervient on a intérêt à capter le champ magnétique qui est bien plus intense . Il faut aussi tenir compte des possibilités technologiques de construction de l'antenne . Une antenne électrique formée d'un très long fil tiré en remorque par le sous-marin peut en définitive avoir des performances meilleures qu'une antenne magnétique utilisant des barreaux de ferrite .

Dr. A. ESSMANN : Dans le cas de réception dans l'eau par dipôle électrique ou magnétique les bruits ne sont pas spécialement produits par l'eau, mais créés par le sous-marin lui-même . Ce sont les bruits des courants de corrosion et les pertes du réseau du bord .

Prof. R. GABILLARD : Il est certain que le sous-marin engendre par son fonctionnement propre (et en particulier par les courants de corrosion qu'il envoie dans la mer) un bruit important . La seule solution semble être d'éloigner les antennes du sous-marin en les traînant au bout d'une remorque .

Discussion on paper 6 : "Méthode exacte de calcul de la distribution de courant sur une antenne" , par M. BOUIX .

Prof. EL SELZER : Par des réseaux d'antennes pourrait-on gagner en directivité ?

Prof. M. BOUIX : Certainement, par un phénomène de groupement en réseau . Mon but est de faire un calcul de forme d'antenne, avec un but déterminé à l'avance . On peut sans doute augmenter la directivité, sans augmenter les dimensions de l'antenne . Mais, on aura une impédance qui ne sera certainement pas la meilleure .

Discussion on paper 7 : "On the influence of the thickness of excitation gap on antenna performance" , by G. FRANCESCHETTI .

Dr. J. WAIT : Are induced polarization effects important at the metal-fluid interface in the actual E.L.F. applications in the sea ?

Prof. G. FRANCESCHETTI : The induced polarization effects, as well as contact resistance effects, are very important . For this reason we have switched from 1 Kc/s to 10 Kc/s the operating frequency in laboratory experiments .

Dr. J. GALEJS : Could you clarify the assumptions used in deriving the optimum transmitter and receiver depth and frequency or skin-depth ?

Prof. G. FRANCESCHETTI : For a fixed frequency , i.e. skin depth, the optimum ratio P_R/P_T is obviously obtained for $d_1 + d_2 = 0$. However for a fixed depth $d_1 + d_2$, it exists an optimum frequency, i.e. an optimum skin depth for which P_R/P_T is maximized .

Dr. A. ESSMANN : Vous avez mentionné que l'antenne devait être courte en comparaison de la profondeur de pénétration . Mais pour les applications pratiques dans l'eau de mer il faut réaliser une antenne aussi grande que possible . Si l'antenne est trop petite il est impossible de trouver de l'énergie rayonnée à l'extérieur .

Prof. G. FRANCESCHETTI : The assumption of the antenna's dimension small with respect to the skin depth was made only for finding simple optimization conditions . However, in the general case, these optimization conditions can always be obtained, eventually numerically starting from the results reported in the printed version of the paper .

Discussion on paper 9 : "Surface wave propagation from VLF arrays in polar seas", by A.W. BIGGS .

Dr. J. WAIT : a) Please explain why you can use the Millington theory for the present application .

b) Can you justify neglect of elevation changes at the coast line .

Dr. BIGGS : a) It has been supported by analytical work of Clemmov Bremmer, and Wait . Some variations occur due to mathematical approximation .

b) We must assume flat interfaces with elevation changes, the path variables change .

Discussion on paper 10 : "Some results in connection with a search for maximum underwater LF/VLF coverage", by Dr. LINDQUIST .

Dr. J.R. WAIT : Does the inhomogeneous ground-sea condition affect the calculation ?

Dr. LINDQUIST : Yes, if you want an exact determination of the field strength . However, we are only dealing with comparatively short distances . The results will be accurate within a few dB even when neglecting the effects of land-sea boundaries .

HIGHLY SENSITIVE ANTENNA COIL AND BALL ANTENNA FOR ELF-ATMOSPHERICS

H.L. Koenig

Elektrophysikalisches Institut der Technischen Hochschule Muenchen

8 Muenchen 2, Arcisstr. 21, Germany

SOMMAIRE

L'auteur décrit la réalisation d'une antenne-bobine destinée à l'enregistrement de parasites atmosphériques à très basse fréquence. On a calculé les lois d'échelle de ce type de bobine ; elles ont révélé que le rapport signal/bruit augmente comme la puissance 3/2 du diamètre pour une section transverse donnée du bobinage. On a donc fabriqué une bobine de vinyl de 2 m de diamètre, comportant 40 000 tours de fil N° 32. La bobine présente une inductance de 6 600 Hy, une fréquence de résonance naturelle (avec sa résistance de capacité répartie) de 74 Hz et une résistance en courant continu de 12 120 kΩ . Pour éviter la formation de signaux parasites dans la bobine sous l'influence des vibrations mécaniques de cette bobine dans le champ magnétique naturel terrestre, on a construit un montage anti-choc supportant l'essieu. La fréquence de résonance du tore du système de support absorbant les chocs de la bobine pourrait être amenée en dessous de 2 Hz et, par conséquent, en dessous de la portée de transmission. Des étalonnages effectués à l'aide d'une bobine similaire, et des calculs ont montré que l'on peut obtenir une sensibilité de 9 V pour 1 A/m.

HIGHLY SENSITIVE ANTENNA COIL AND BALL ANTENNA FOR ELF-ATOMSPHERICS

H.L.Koenig
Elektrophysikalisches Institut der Technischen Hochschule Muenchen
8 Muenchen 2, Arcisstr. 21, Germany

SUMMARY

Construction of an antenna-coil for the reception of ELF (Extremely Low Frequency)-atmospherics is described. The scaling laws of such a coil were calculated and showed that the signal to noise ratio increases with the 3/2 power of the diameter for a given winding cross section. The construction of a vinyl coil form of 2 m diameter which is wound with 40 000 turns of # 32 wire is described. The coil has an inductance of 6600 Hy, a natural resonance frequency (with its distributed capacitance) of 74 Hz and a d.c. resistance of 120 kΩ . To avoid parasitic signals in the coil due to mechanical vibrations of the coil in the natural magnetic field of the earth, a shock mount (torsional resonance frequency below 2 Hz) to support the axle was developed. Calibrations and calculations showed that a sensitivity of 9 V per 1 A/m can be obtained.

For the reception of the electric field component of ELF-signals a ball antenna was constructed. This is advantageous because, due to the long wave length of the signals, the antenna signal depends only on the capacitance between the antenna and free space. As a protection against bad weather conditions the outside conducting layer of the antenna is surrounded by an insulation material. In order to reduce the noise produced by ionized rain drops a distance of 5 cm between the outside insulation material and the conducting layer of the antenna itself was provided.

During recent years natural electromagnetic signals of extremely low frequency (ELF-signals) have been studied by several investigators. Experiments have shown that such signals appear in connection with electromagnetic waves of similar frequency. As shown by the calculations of SCHUMANN (1) (Schumannresonance) these waves are reinforced by the resonant properties of the earth's spherical ionosphere. First of all the existence of ELF-signals was demonstrated by measurements of the electric component as well as of the magnetic component (2,3). Simultaneous measurements of electric and magnetic fields (3) have shown that the signals are produced by electromagnetic waves, since the E/H-ratio (characteristic impedance) equals that of electromagnetic waves propagating in air.

Present objects of the investigation (see also ref. (4)) are the identification of ELF-noise sources, the identification of the pertinent propagation phenomena, and the identification of other processes which determine properties of ELF noise such as diurnal and seasonal variation of its amplitude and frequency spectrum. The work is carried on in cooperation with Dr. CH. Polk and Dr. H. Etzold at the Department of Electrical Engineering of the University of Rhode Island in Kingston, R. I. USA. The experimental data obtained at field stations in Germany and USA are to be analyzed and published (5) in the USA.

Possible applications of the observation and analysis of ELF-noise (6) which have become apparent in the course of this work are (a) the possibility of continously locating the position of the major thunderstorm regions on the surface of the earth, (b) "early warning" prediction (three to twenty hours in advance) of some types of solar proton events and associated major ionospheric disturbances and (c) identification of changes in the effective conductivity profile (i. e. electron and ion density and collision frequency profile) over large regions of the lower ionosphere.

In order to increase the quality of the ELF-recordings special H- and E-antennas were constructed.

1. ANTENNA COIL FOR H-MEASUREMENTS

First calculations (7) showed that the signal to noise ratio of an ironless coil (for H-field measurements) increases with the 3/2 power of the coil diameter d for a given winding cross section A_w

$$\frac{U_S}{U_N} = C_1 \, d^{3/2} \sqrt{A_w} \qquad (1)$$

or increases proportionally with d for a given total copper weight G_{cu}

$$\frac{U_S}{U_N} = C_2 d \sqrt{G_{Cu}} \, . \qquad (2)$$

The noise voltage U_s is assumed to be produced by thermal processes in the copper wire.

For technical reasons a diameter of 2 meters was chosen for the coil. From

consideration of the noise of the preamplifier connected with the coil 4o ooo turns of #32 wire (o,2 mm Ø) were wound on a vinyl coil form resembling a spoked wheel. This insulating material was used to avoid shorted turns by the total wheel or parts of it (2 spokes and a part of the circumference). The coil has an inductance of 66oo Hy, a natural resonance frequency (due to its distributed capacitance) of 74 Hz, a Q = 1o.5 and a d.c. resistance of 12o kΩ.

To avoid parasitic signals in the coil due to mechanical vibrations of the coil in the natural magnetic field of the earth, a shock mount supporting the axle was developed. The mechanical resonance frequency of the coil/shock mount system could be brought below 2 Hz and therefore below the transmission range. The total weight of the coil is 153 kp including 69 kp copper wire.

Calibrations and calculations showed a sensitivity of 9 V per 1 A/m (= o.o125 Gauß or 125oγ in air) at 8 Hz. At this frequency a magnetic flux density of 1.25 mγ induces in the coil a voltage of 9μV . This is to be compared with o.3μV thermial noise of 4o Hz bandwidth produced in the copper wire.

Therefore, the noise level in the signal to noise ratio of the total measuring apparatus is (in practice) determined only by the input noise of the preamplifier.

2. BALL-ANTENNA FOR E-MEASUREMENTS.

For the reception of the vertical electric field a ball antenna was constructed (8).

Due to the wave length of the order of 4o ooo km of the recorded signals, only the capacitance between the antenna and the free space in connection with the antenna-load (capacitance and resistance antenna ground) determines the signal level on the antenna.

Replacing a horizontal long wire antenna by a ball antenna offers several advantages.

a) The antenna can be mounted at a single point (e.g. a mast) and does not need two mounting points separated from each other by a relatively large distance.

b) The capacitance of a ball system to free space can easily be made of the same order as that of the relatively long and thick antenna wire otherwise necessary.

c) The high impedance preamplifier connected inside the sphere is well protected and weather proof.

d) Ion motion is particularly pronounced within the first two meters above ground. By mounting the antenna which is electrically isolated from ground at a height of 1o meters spurious signals due to ion motion are largely eliminated.

e) Furthermore the capacitance to ground of a relatively small sphere (radius a = o.2 meter) is rather insensitive to small changes in height h, since (for $a/h < 1/10$)

$$C = 2\pi\varepsilon_0 \cdot a\,(2 + a/h). \qquad (5)$$

Consequently C and the received field intensity should not be affected by motion or bending of the supporting mast during heavy winds.

f) The dielectric coating surrounding the antenny system at a distance of .o5 meter acts as a "radome". Thus the antenna may be usable even during moderate precipitation.

g) The dielectric coating may increase the antenna capacitance.

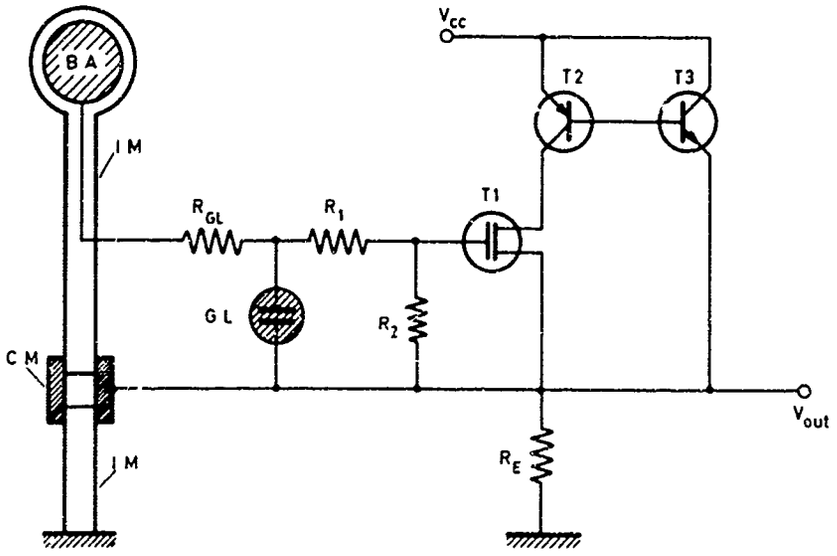

Fig.1 Ball antenna system

Due to the high reactance between the antenna and free space the input impedance of the preamplifier has to be > 1 GΩ. This results in an insulating problem in some parts of the antenna. Therefore the possibility of impedance transformation by an emitter follower stage is utilized (see fig. 1). For this purpose any material insulating the antenna (I.M.) is separated into two parts by a metal-layer (C.M.) which is connected with the emitter potential of the input stage (R_E).

In this way the total input impedance (including conductivity and capacitance of the insulating material) between antenna (B.A.) and this intermediate layer of metal (C.M.) is transformed approximally with the current amplification rate defined for the current amplification between input (T_1) and the emitter of the input stage (T_3, R_E).

The impedance of the insulation (I.M.) situated between the intermediate layer of metal (C.M.) and ground is not transformed but is shunted by the emitter resistor (R_E) of the input stage. This resistor is in the order of several KΩ, so that insulating problems will never arise.

Normally as input transistor (T_1) a FET or MOSFET type is used. Applying the impedance transformation technique described above this transistor can be protected against voltage overloading by inserting a small glow discharge lamp (G.L.) between antenna (B.A.) and emitter (R_E). The glow discharge lamp (G.L.) is followed by a resistive voltage divider (R_1, R_2) which reduces the conducting voltage of the lamp to the maximum allowed transistor (T_1) input voltage V_{EB}. The impedances of the glow discharge lamp and the voltage divider will be transformed to higher values and are therefore only a negligibly small load for the input. Practical measurements confirmed the utility of the antenna.

The work is sponsered by the USAF under Contract AF 61 (052)-836.

REFERENCES:

(1) W.O. Schumann: Ueber die strahlungslosen Eigenschwingungen einer leitenden Kugel, die von einer Luftschicht und einer Ionospherenhuelle umgeben ist, Z.f. Naturforschung, 7a, 15o (1952);
(2) W.O. Schumann u. H.L. Koenig: Atmospherics geringster Frequenzen, Die Naturwissenschaften 41, 183 (1954);
(3) H.L. Koenig: Athmospherics geringster Frequenzen Z. angew. Physik 11, 264 (1959);
(4) T.J. Keefe, C. Polk, H.L. Koenig: Results of Simultaneous ELF Measurements at Brannenburg (Germany) and Kingston, R.I. USA, Contr. no. 12 in NBS Techn. Report no. 8815, U.S. Dept. of Commerce, NBS, Boulder, Colorado, 1965;
(5) A.J. Carrigan, N.J. Oliver (Editors): Geophysical and Space Data Bulletin, AFCRL;
(6) C. Polk: Research on Extremly Low Frequency Propagation with particular emphasis on Schumann resonance and related phenomena, dep. no 18, Contract AF 19 (628)-495o, 3o oct. 1969;
(7) H.L. Koenig: Hochempfindliche Empfangsspule für ELF-Atmospherics, Z. angew. Physik 25, 14 (1968);
(8) T. Ogawa et al.: Observations of Natural ELF and VLF Electromagnetic Noises by Using Ball Antennas, J. of Geomagnetism and Geoelectricity 18, 443 (1966).

SUR QUELQUES OBSERVATIONS DU BRUIT RADIOELECTRIQUE DANS LA BANDE T.B.F. FAITES AU COURS D'UNE CROISIERE DANS L'ATLANTIQUE

par

G. MATTERN

Taunus - Observatorium
6241 - Kleiner Feldberg/Ts

SUMMARY

During a four week voyage between Hamburg and Guyaquill (Ecuador), in November 1967, atmospheric radio noise was recorded with a 500 Hz to 5 KHz bandpass receiver.

Diurnal intensity variations recorded, and radio noise spectrum patterns give an overall idea of Africa and South America Storms.

The data collected also reveal that, below latitude 40° N, the other atmospheric noise components (whistler, hiss, dawn chorus, etc.). do not significantly contribute to the average noise intensity.

SUR QUELQUES OBSERVATIONS DU BRUIT RADIOELECTRIQUE DANS LA BANDE T.B.F. FAITES AU COURS D'UNE CROISIERE DANS L'ATLANTIQUE

par

G. MATTERN

Taunus - Observatorium
6241 - Kleiner Feldberg/Ts

SUR QUELQUES OBSERVATIONS DU BRUIT RADIOELECTRIQUE DANS LA BANDE T.B.F. FAITES AU COURS D'UNE CROISIERE DANS L'ATLANTIQUE*

G. MATTERN
Taunus Observatorium, 6241 Kleiner Feldberg/Ts

On sait, depuis longtemps, que le bruit radioélectrique atmosphérique, dans la gamme T.B.F., est dû essentiellement à l'activité orageuse de l'atmosphère. Il est bien connu que cette activité est concentrée, pour une grande part, dans les zones tropicales d'Asie Orientale, d'Afrique et d'Amérique du Sud. En été, dans l'hémisphère nord, on doit également tenir compte de foyers orageux localisés en Europe et en Amérique du Nord. La contribution des foyers orageux qui se situent au-dessus des océans est encore très insuffisamment connue, bien moins connue, certainement, que la contribution des orages continentaux.

Le bruit radioélectrique atmosphérique, qui possède des composantes dans toute la gamme E.B.F. et T.B.F., est une source naturelle importante d'émission dans le domaine des très basses fréquences et est, de ce fait, souvent utilisé pour l'étude des conditions de propagation de ce type d'ondes au-dessus du et dans le milieu marin.

D'autre part, puisque le bruit se présente, pour les radiocommunications utilisant les très basses fréquences, comme une forte source de perturbation, il est intéressant de définir la répartition temporelle et spatiale de l'activité radio atmosphérique au-dessus des mers.

Au cours d'une série d'observations concernant l'activité orageuse mondiale, l'Institut de Météorologie de l'Université de Francfort/Main a entrepris, en novembre 1967, de faire enregistrer le bruit radioélectrique atmosphérique, par un cargo qui reliait Hambourg à l'Amérique du Sud. Cette croisière fut organisée au cours du mois de novembre, car l'activité orageuse étant faible, à cette époque, en Europe et en Amérique du Nord, seuls les foyers orageux localisés en Afrique et en Amérique du Sud pouvaient déterminer l'intensité et la répartition dans le temps du bruit atmosphérique le long du trajet.

On recevait les atmosphériques au moyen d'un récepteur, installé sur la passerelle de navigation du navire le "Persimmon" et raccordé à une antenne verticale de deux mètres. La gamme de réception se situait entre 500 Hz et 5 kHz. La dynamique du récepteur était de 80 dB, variable par échelon. Toutes les quatre heures (et même toutes les deux heures pendant quelques jours) les atmosphériques, repartis suivant les différents échelons d'énergie, furent comptés chaque fois pendant une minute, à l'aide d'un compteur électronique. En outre, des enregistrements sur rubans magnétiques furent effectués, plusieurs fois par jour, en vue d'analyses ultérieures concernant la forme des atmosphériques.

Comme on le voit sur la figure 1, le voyage aller conduisait de Hambourg à Savannah (U.S.A.), en passant par les Açores, puis, par le canal de Panama, aboutissait à Guyaquil (Equateur). Le voyage retour (ligne interrompue sur la figure 1) s'effectuait directement de Panama, par les Açores, vers Hambourg.

Au cours de l'exploitation des enregistrements, on a pu sélectionner trois positions spécialement intéressantes du navire.

1.- Au départ de Hambourg, en novembre, les orages d'Afrique provoquaient un maximum dans l'activité des atmosphériques, au cours des heures précédant minuit.

2.- Dans la zone des Açores, équidistante, en novembre, des foyers orageux d'Afrique et d'Amérique du Sud, on observe alors un déroulement diurne équilibré de l'activité des atmosphériques.

3.- Dans la zone du canal de Panama, les orages d'Amérique du Sud apportent la contribution principale à l'activité des atmosphériques.

La figure 2 indique les écarts par rapport à la moyenne journalière du nombre d'impulsions par minute, obtenus toutes les deux heures, au cours d'une journée, pour les trois positions ci-dessus. On n'a tenu compte, pour établir ces courbes, que des atmosphériques dont le niveau de champ était supérieur ou égal à 0,1 mV/m. La courbe continue montre l'évolution de l'activité des atmosphériques, telle qu'elle fut observée en novembre 1967 à la station de Hambourg-Halleg. Un faible maximum dans les heures suivant minuit, conséquence des orages d'Amérique du Sud, est suivi, au lever du soleil, par une diminution du taux des atmosphériques. Pendant toute la journée, l'affaiblissement des ondes apporté par la présence de la basse ionosphère, empêchait la réception d'une partie importante de l'activité orageuse issue d'Afrique. Ceci explique la présence d'un minimum au voisinage de 12 h. G.M.T. Après le coucher du soleil, la réception devient possible vers 18 h. G.M.T., ce qui provoque un accroissement rapide du taux des impulsions et un maximum absolu de l'activité des atmosphériques dans les premières heures du soir. Cependant, l'activité orageuse diminuant, en moyenne, rapidement, après 18 h. G.M.T. et la voie de transmission vers le foyer orageux (lequel est alors maximal en Amérique du Sud) se trouvant encore partiellement sous l'effet du soleil, il y a, vers minuit, un second minimum relatif dans l'activité des atmosphériques.

On peut observer une évolution diurne analogue des mesures prises au voisinage de l'équateur, représentée, sur la figure 2, par une courbe discontinue.

Le diagramme étant établi en heures G.M.T., le premier maximum se situe un peu après minuit. La décroissance de l'activité avec un minimum vers 12 h G.M.T. correspond à la décroissance de l'activité orageuse continentale, un peu avant le coucher du soleil. On peut expliquer ainsi le maximum secondaire observé vers 16 h. G.M.T.

L'évolution de l'activité des atmosphériques dans la zone des Açores, est beaucoup plus régulière, comme le montre la courbe en pointillé de la figure 2.

Les foyers orageux d'Afrique et d'Amérique du Sud sont alors, bien captés en moyenne, ce qui, par suite du décalage dans le temps des instants d'activité maximum de chaque foyer, conduit à une évolution diurne régulière, qui possède un faible maximum vers 20 h. G.M.T.

Un bilan statistique des nombres d'impulsions par minute, comptés dans différentes plages d'énergie, est représenté par les figures 3 et 4.

La figure 3 présente ce bilan, établi à partir de mesures prises dans la zone des Açores, le 2 novembre 1967, à bord du "Persimmon". Une comparaison de ces mesures avec les valeurs journalières moyennes simultanées, mesurées à Hambourg, montre que celles-ci peuvent différer de celles-là dans un rapport de 1 à 100 et plus, pour les atmosphériques de forte énergie. Ces différences ne sont certainement pas uniquement une conséquence des distances entre foyers orageux et récepteur. On peut penser que la présence de la mer, qui favorise la propagation des ondes, est une cause supplémentaire.

Les mesures enregistrées le 5 novembre 1967 font apparaître des différences encore plus importantes (figure 4). Le navire se trouvait alors à la hauteur des Iles Bermudes, et captait ainsi une grande partie des orages d'Amérique du Sud.

La comparaison des enregistrements pris sur le navire, du 2 au 5 novembre, montre une forte augmentation du taux des atmosphériques dans la zone d'intensité de champ inférieure ou égale à 1 mV/m. Ceci pourrait être une conséquence de l'affaiblissement de propagation diurne, qui peut, lors de la réception dans la zone des Bermudes, déplacer dans une zone d'intensité de champ plus faible, les impulsions créées au cours de la période orageuse maximale de l'après-midi, en Amérique du Sud.

La figure 5 présente un bilan des taux d'atmosphériques, observés aux trois positions signalées précédemment, pendant la période d'activité orageuse principale de 16 h. locale. On a utilisé la moyenne mensuelle des taux d'atmosphériques pour la station de Hambourg, et des moyennes de chaque fois 4 jours (pendant les voyages aller et retour) dans les zones des Açores et de l'équateur. Les courbes obtenues montrent qu'au voisinage de l'équateur, le pouvoir de résolution du récepteur est atteint, avec des intensités de champ de 1 mV/m. Il est en outre remarquable que des fréquences d'impulsions de 100 par minute aient été observées à l'équateur, avec des intensités de champ de 0,1 V/m. Comme il n'y avait, aux Açores, en novembre 1967, d'activité orageuse, dans la zone des fortes intensités de champ, les impulsions y sont moins fréquentes qu'aux environs de l'équateur. Au-dessous de 1 mV/m, on obtient des fréquences comparables à celles de la station équatoriale, ce qui prouve la position favorable des Açores pour des essais de surveillance des foyers orageux Africains et Sud Américains.

La courbe de la station de Hambourg est, à 16 h H.C.E. (heure de l'Europe Centrale) masquée par une absorption encore efficace, intervenant le long des voies de propagation des atmosphériques. Une partie essentielle du groupe des orages africains apparaît sous des intensités inférieures à 0,5 mV/m.

Les valeurs indiquées montrent que l'activité orageuse aux environs de l'équateur est suffisante pour produire une intensité moyenne de champ assez forte pour permettre une réception des atmosphériques aux grandes profondeurs marines.

En vue de l'observation des foyers orageux d'Afrique et d'Amérique du Sud, une station de réception installée aux Açores semble offrir les meilleures conditions. En effet, on peut y mesurer des taux d'atmosphériques provenant des deux foyers d'orage, assez élevés pour permettre des observations statistiques.

Il sera nécessaire de procéder à un grand nombre d'autres mesures à bord de navires, pour obtenir dans cette bande de fréquence, une vue d'ensemble de l'activité des atmosphériques au-dessus de l'Atlantique.

* La communication 12B est associée à la communication 12A.

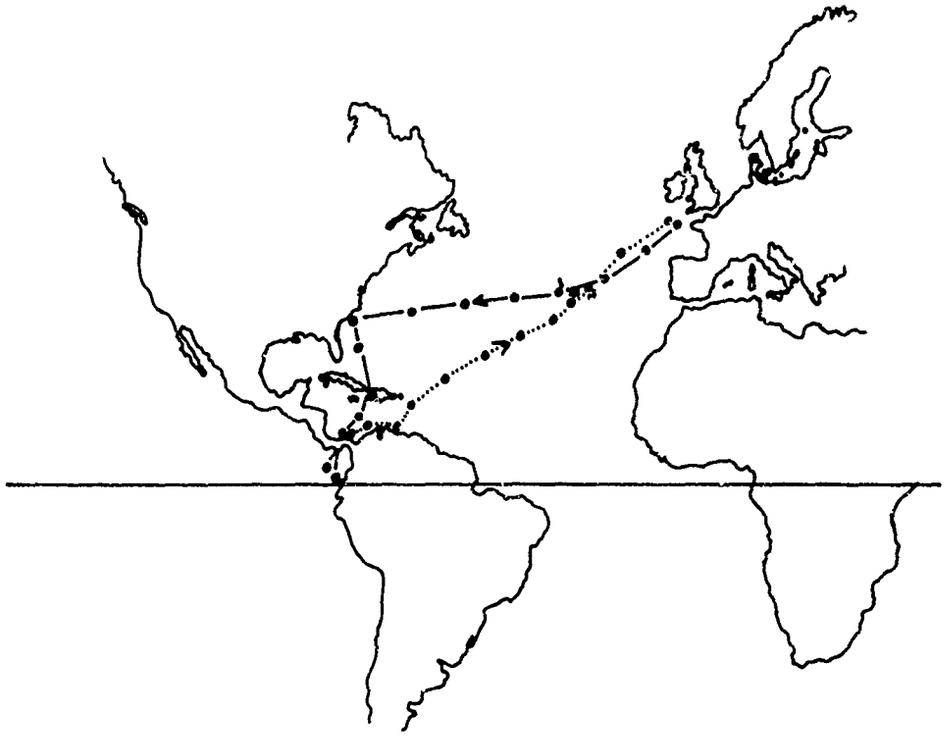

Fig. 1 La route du vapeur 'Persimmon'

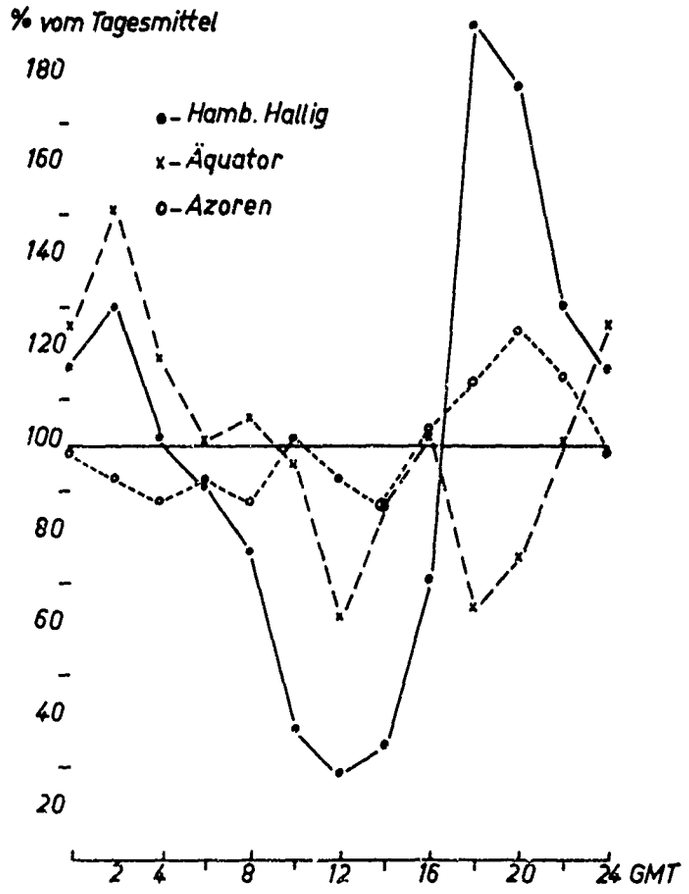

Fig 2 La déviation des nombres des parasites par minute de leurs moyenne quotidienne chez les stations 'Hamburg', 'Equateur' et 'Azores' en temps universelle

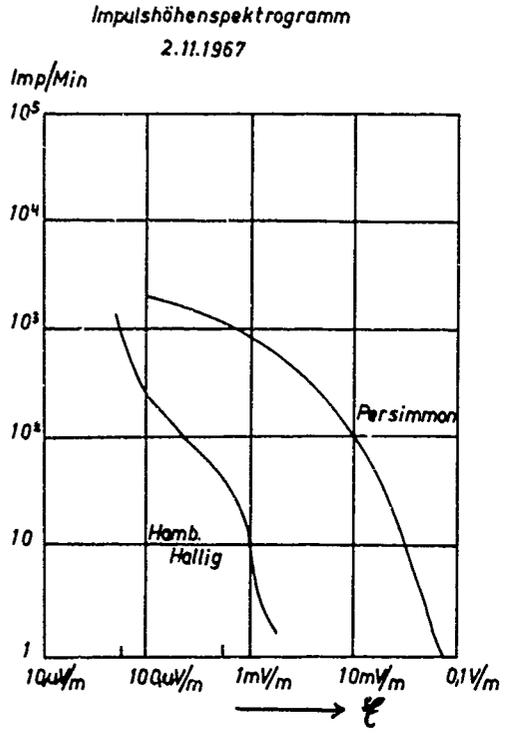

Fig. 3 Les nombres de parasites par minute en function de la force du champ électromagnétique.
2 Novembre 1967

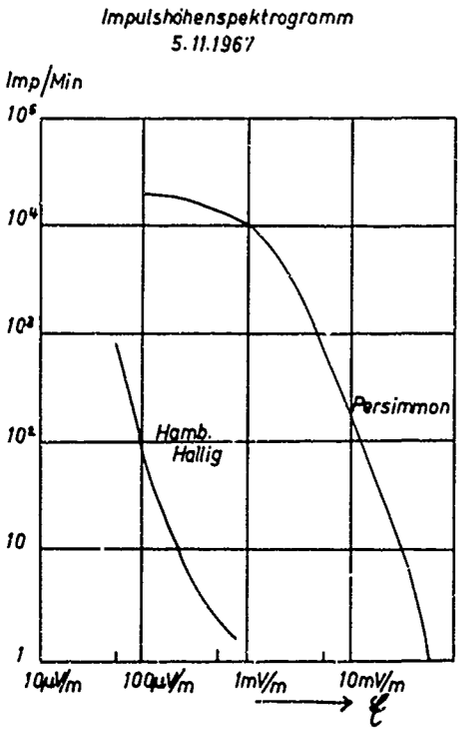

Fig. 4 Les nombres de parasites par minute en function de la force du champ électromagnétique
5 Novembre 1967

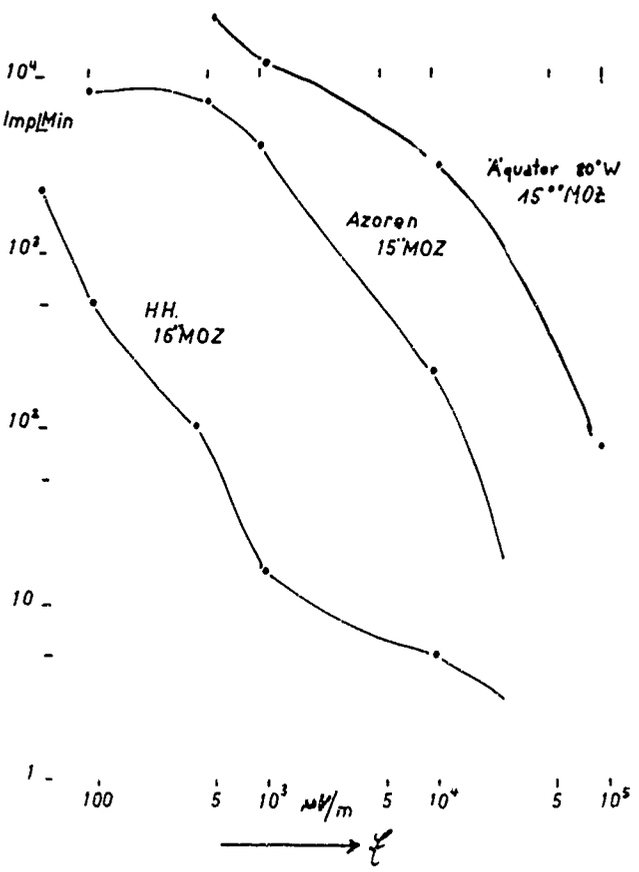

Fig. 5 Les nombres de parasites par minute, en temps local chez diverses champs électromagnétiques et diverses positions du vapeur 'Persimmon'

A COMPARISON OF ELF ATMOSPHERIC NOISE SPECTRA MEASURED ABOVE AND IN THE SEA

by

Emil F. Soderberg and Manuel Finkle

Navy Underwater Sound Laboratory
New London, Connecticut 06320

A COMPARISON OF ELF ATMOSPHERIC NOISE SPECTRA MEASURED ABOVE AND IN THE SEA

Emil F. Soderberg and Manuel Finkle
Navy Underwater Sound Laboratory
New London, Connecticut 06320

SUMMARY

Extremely low frequency (ELF) electromagnetic noise arising from worldwide atmospheric electrical disturbances was measured at sea, using a ship-mounted whip antenna to sense the vertical electric fields in air and a towed cable with a widely spaced pair of tandem electrodes to sense the corresponding horizontal electric fields in the sea. The outputs of these sensors were recorded simultaneously on multichannel magnetic tape as the ship proceeded on courses of magnetic east and magnetic south. This paper reports some results of these measurements and illustrates some of the features that characterize ELF electric fields above and in the sea. Comparison between the spectra of vertical electric fields in air and horizontal electric fields in the sea shows that the omnidirectionality (in azimuth) of the whip antenna tends to smooth the spectrum whereas the directionality of the electrode pair enhances the spectrum characteristics of sources located in the direction of the electrode pair axis.

1. INTRODUCTION

The source of extremely low frequency (ELF) electromagnetic noise in the sea is predominantly of atmospheric origin. Electromagnetic waves, arising from atmospheric electrical activity in various parts of the world, dissipate a small amount of energy into the sea as they travel along the ocean surface, thereby producing an ambient electromagnetic noise background in the sea which decays exponentially with depth below the surface. It is of interest to compare the electric fields in air as measured with a vertical whip antenna to the resulting electric fields underwater as measured with a horizontally oriented pair of electrodes.

In air, the total electric field sensed by a whip antenna is the combination of the vertical electric field components of all the arriving waves. Underwater, however, the resultant electric field sensed by a horizontal electrode pair represents only a part of the horizontal electric fields that are present. Each of these horizontal electric field components is oriented in the direction of propagation of the wave that created it, and, since the waves traveling along the surface have arrived from a number of different directions, many of the underwater horizontal components fall in a direction off-axis with respect to the electrode pair. The results presented here indicate that the directionality of the electrode pair provides a means for reducing the electric field contributions from directions normal to the axis of the electrode pair, thus enhancing the spectrum characteristics of sources lying in the general direction of the axis of the electrode pair. This feature is of value for such applications as the study of worldwide thunderstorm location through observations of the Schumann resonances. The ratio of the magnitudes of successive peaks of the Schumann resonances may be used to determine the angular separation between a thunderstorm region and the location of the sensor(1, 2).

Previous work has been done on measurements of ELF electric fields over the ocean (3) and ELF electric fields in the ocean (4, 5), but the data reported here offer the first opportunity for direct comparison of simultaneous measurements of electric fields above and in the sea.

2. THEORETICAL CONSIDERATIONS

If we assume that a single vertically polarized wave is incident on the ocean surface at a grazing angle, a portion of the wave will be refracted into the medium in a direction practically straight downward. Let the incident wave, traveling in a direction x, have a vertical electric field $E_y = E_o e^{-ikx}$ and a horizontal magnetic field $H_z = H_o e^{-ikx}$, where $k = \omega\sqrt{\mu_o \epsilon_o}$. The horizontal magnetic field H_z is continuous across the air-sea boundary and therefore relates the vertical electric field E_y above the sea to the horizontal electric field E_x below the surface:

$$H_z = \frac{E_y}{\eta_o} = \frac{E_x}{\eta_s},$$

where η_o and η_s are the intrinsic impedances of air and sea water, respectively. The ratio of the vertical electric field to the horizontal electric field is then

$$\frac{E_y}{E_x} = \frac{\eta_o}{\eta_s} = \frac{(\mu_o/\epsilon_o)^{1/2}}{(i\omega\mu/(\sigma + i\omega\epsilon))^{1/2}} = \left(\frac{\mu_o \sigma}{i\omega\mu\epsilon_o} + \frac{i\omega\mu_o\epsilon}{i\omega\mu\epsilon_o}\right)^{1/2} = \left(\frac{\sigma}{i\omega\epsilon_o} + \epsilon_r\right)^{1/2}$$

where σ = the electrical conductivity of sea water ≈ 1
ϵ_o = the permittivity of free space = $(36\pi \times 10^9)^{-1}$
ϵ_r = the relative permittivity of sea water = ϵ/ϵ_o = 81 (dimensionless)
$\mu \cong \mu_o$ = the permeability of free space = $4\pi \times 10^{-7}$ henry/meter

For $\sigma >> \omega\epsilon_o$, ϵ_r may be neglected. For example, if $\sigma = 4$ mhos/meter and frequency $f = \frac{\omega}{2\pi} = 100$ Hz, the ratio is

$$\frac{\eta_o}{\eta_s} = \left(\frac{4 \cdot 36\pi \cdot 10^9}{j2\pi \cdot 100} + 81\right)^{1/2} = \left(\frac{7.2 \times 10^8}{j} + 81\right)^{1/2} = 2.68 \times 10^4 \angle -45°$$

The ratio of the magnitudes of these fields is

$$\left|\frac{E_y}{E_x}\right| = \left(\frac{\sigma}{\omega\epsilon_o}\right)^{1/2} = 1.342 \times 10^5 \sqrt{\sigma}\sqrt{\frac{1}{f}} .$$

The ratio $\frac{E_y}{E_x}$, where E_y and E_x can be the root mean square voltages representing their respective fields, is plotted as a function of frequency in Fig. 1 for several values of sea water conductivity.

The rate of attenuation of the refracted wave as it progresses downward through the seawater may be expressed as the reciprocal of the "skin depth" δ:

$$\frac{1}{\delta} = \alpha = \sqrt{\frac{\omega\mu\sigma}{2}} \quad \text{(nepers/meter of depth)}$$

where $\omega = 2\pi \times$ frequency, $\mu = 4\pi \times 10^{-7}$ henry/meter, and σ = sea water conductivity in mhos/meter. The attenuation rate α is therefore

$$\alpha = 0.00199 \sqrt{\sigma}\sqrt{f} \text{ nepers/meter}$$
$$= 0.0173 \sqrt{\sigma}\sqrt{f} \text{ db/meter (1 neper = 8.686 db).}$$

Figure 2 is a graph of attenuation rate versus frequency for several values of sea water conductivity.

ELF electromagnetic waves which are due to sources that excite the earth-ionosphere cavity are believed to propagate mainly in the transverse magnetic mode (i.e., no component of magnetic field radial to the earth), so that at large distances from the sources only the vertical electric field is significant (6). It is assumed here that the waves sensed by the whip antenna were vertically polarized and that, consequently, the voltages developed on the whip were truly representative of the ELF electric fields present. This assumption is encouraged by the absence of local atmospheric electrical activity, so that the sources were presumably far distant from the measurement area.

It is assumed that the presence of the ocean bottom has no effect on the fields considered here. The ocean depths encountered during this particular set of measurements ranged from 2400 to 3000 fathoms (4390 to 5480 meters). A depth of 2400 fathoms corresponds to thirty "skin depths" at 3 Hz and 303 "skin depths" at 300 Hz. The measurements reported here are therefore considered to be "open ocean" measurements as opposed to "shallow water" or "near shore" measurements.

It is assumed that the sea surface was flat. The sea states during these measurements were reasonably low, and it may be assumed that there were no significant perturbations due to ocean waves.

3. MEASUREMENTS

The measurements were made in the open ocean at a position of approximately 40°N 65°W, some 300 nautical miles southeast of the mainland of New England. The oceanographic ship that carried the instrumentation proceeded slowly along magnetic east-west and magnetic north-south courses while recordings were made of the vertical electric field in air and the horizontal electric field in the sea. A 2-meter whip antenna aboard ship and a tandem 60-meter electrode pair towed 255 meters behind the ship were used to measure these respective fields. Figure 3 shows the locations of the sensors with respect to the ship. The trailing dummy antenna consisted of a transmission line identical to that used as the lead-in cable from the electrodes, except that it was terminated in a resistance which simulated the impedance of the electrode pair. A depressor was used to force the towed line down so that the neutrally buoyant line would be maintained in a horizontal attitude at the desired depth. The speed of the ship was varied to adjust the depth of the depressor and thus the depth of the electrodes. The output of the pressure transducer showed that the line was indeed maintaining a stable path at the desired depth.

The procedure used was to record ELF noise for a one-half hour period while the ship proceeded in one direction, then to change course 90° and record for another half-hour period in that direction. The ELF noise could not be recorded in both directions at once, of course, as would be the case if two ships had been available for towing two separate electrode pairs, and it was hoped that atmospheric conditions would not change too drastically from one half-hour period

to the next. Comparison of ELF spectra from the whip antenna (which is omnidirectional and quite independent of the ship's course) showed that changes did occur, however, but not so much in level as in the shape of the spectrum. For purposes of this report this variation with time does not matter when we are making a comparison between simultaneously recorded portions of the ELF noise data.

Some changes of ocean characteristics were encountered. Nansen casts were made periodically during the cruise to determine the temperature and the salinity of the water at depths of interest for the measurements. Depth profiles of temperature and electrical conductivity are shown in Fig. 4 for the four Nansen casts closest in time to the measurement periods reported here. There was a significant change in the depth profile between times 1600 and 1900, with conductivity values changing from 4.2 to 3.2 mhos/meter, and care must be taken in dealing with the data obtained during this time period.

4. INSTRUMENTATION

The instrumentation aboard the ship included four measurement channels and a WWV time channel into a multi-channel magnetic tape recorder. Two of the measurement channels amplified the outputs of the whip antenna and the electrode pair. A third channel monitored the amount of noise picked up on the cable of the trailing dummy antenna. The fourth channel was used to establish a base line for system noise. A resistor terminated the input of this channel right at the input of the amplifier itself.

The frequency response of the whip channel was 3 db down at 6 Hz and 950 Hz, with a fall-off of 80 db per decade below 4 Hz. The responses of the remaining three measurement channels were all similar: 3 db down at 40 Hz and 910 Hz, with a fall-off of 20 db per decade below 20 Hz. All of the following data have been corrected for the frequency responses of their respective channels.

5. THE DATA

The data selected for presentation consist of samples from four time periods (local time):

Starting Time	Ship's Course	Electrode Depth
1154:30	magnetic south	22.8 meters
1207:00	magnetic east	22.3 meters
1731:00	magnetic east	25.0 meters
1815:40	magnetic south	23.7 meters

Each of these samples is displayed in three ways: as broadband amplitude versus time, as frequency versus time, and as mean square voltage versus frequency (spectral density).

Figure 5 shows a 1-minute section of a chart recording of logarithmic amplitude versus time for the outputs of four sensors recorded simultaneously on the magnetic tape. The output of the whip antenna is seen to be characterized by a relatively high level of background hiss which, in this type of presentation, masks all but the highest impulsive noise bursts. In contrast, the output of the electrode pair is seen to consist mainly of distinguishably separate impulses, a result of the filtering out of the higher frequency atmospheric hiss by the sea water attenuation. The outputs of the trailing dummy and of the system noise channel show the constant level that is characteristic of this nearly normally distributed noise. Figures 6, 7, and 8 are amplitude versus time chart recordings for the other three samples. Part of the data shown in this figure was selected for analysis in the form of sonagrams, which are representations of the noise frequency spectrum as a function of time, with amplitude being represented by the intensity of the marks on the paper.

Figure 9 shows a set of sonagrams representing simultaneous 22-second samples of the outputs of the four sensors, analyzed over the frequency range from 1 to 500 Hz. Many of the ELF bursts are seen to appear simultaneously on both the whip antenna and electrode pair presentations, as is to be expected. Some bursts that appear on the whip antenna channel but not on the electrode pair channel are presumed to have arrived from directions approximately normal to the axis of the electrodes, i.e., in a null of the sensitivity pattern of the electrode pair. The background hiss that was mentioned earlier is clearly visible in the whip antenna sonagram and is noticeably subdued in the electrode pair sonagram. The horizontal traces in the electrode pair and trailing dummy presentations are power line harmonics from the 60-Hz ship's power that have been coupled into the lead-in cables of both channels because of their proximity to power lines at some point along the cable way. Although these tonals are visible in this type of presentation, their relative levels are low with respect to the ELF noise. Figures 10, 11, and 12 are the sonagrams for the other three samples.

Figure 13 shows the power spectra obtained for the noise outputs from the four sensors for the frequency range of 3 to 300 Hz. Again, these represent simultaneous samples from the four sensors, with the sample length in this case being 152 seconds. The data on each of the four tape channels were re-recorded onto a closed-loop tape for individual analysis on a power spectrum analyzer. Each data point represents the mean square voltage in a 1.25-Hz bandwidth averaged over the 152-second sample period. Each revolution of the closed-loop tape through the analyzer automatically printed out the result and advanced the analysis frequency by 1 Hz, thus progressing cycle-by-cycle up to 300 Hz. (The frequency range of 3 to 25 Hz was analyzed in 1/4-Hz steps, that of 25 to 75 Hz in 1/2-Hz steps, and that of 75 to 300 Hz in 1-Hz steps). The curves shown here have been corrected for the frequency response characteristics of the four measurement systems and are plotted as a function of the mean square voltage that would have been measured at the terminals of each sensor, as calculated from the output back through the gains and responses of each channel.

The system noise curve establishes the lowest possible spectrum levels obtainable with the amplifiers used here. The spectrum of the trailing dummy antenna indicates that although it has no sensor with which it can detect underwater fields, there is a certain amount of noise, presumably ship's electrical noise, that is inductively coupled into the lead-in cable itself. There is also an indication of a triboelectric effect at the frequencies of ship vibration (here centered about 32 Hz and 68 Hz). That is, the vibration of portions of the lead-in cable itself gives rise to frictional effects in the cable which produce voltages at the frequencies of vibration. As large as these triboelectric voltages appear to be in this spectrum, they are far below the voltages that are developed across the electrode pair by the underwater ELF electric fields. The spectrum obtained with the electrode pair is at least 15 to 20 db greater than the largest extraneous system noise and is therefore satisfactorily uncontaminated by ship noises.

The spectra of the vertical electric field in air and the horizontal electric field in the sea sensed by the whip antenna and the electrode pair, respectively, are represented by the two upper curves. The mean square voltage levels (read from the left-hand ordinate) have been corrected for the effective height (or length) of each sensor and converted to values of equivalent field strength in rms volts per meter (right-hand ordinates). The gap in the curve of the whip antenna spectrum is due to the intentional omission, for clarity, of two large resonance peaks, at 52 Hz and 60 Hz, which would otherwise dominate the appearance of the spectrum. Both of these resonances are from 25 to 30 db above the adjacent spectrum level in all four of the samples. The peak at 52 Hz appears to be caused by a mechanical resonance of the whip antenna, and that at 60 Hz by the ambient field of the ship's 60-Hz power line system. The presence of these peaks is shown in the sonagrams (Figs. 9 through 12) but, as with all of the other tonals and resonances arising from system or ship noise, their effects upon the spectra of interest is negligible and may be ignored for the purposes of this discussion.

6. DISCUSSION

Examination of the instantaneous characteristics of the over-water ELF noise fields sensed by the whip antenna and the underwater ELF noise fields sensed by the electrode pair has shown that these fields have essentially the same structure, thus ensuring that it is valid to make comparisons between them. Further, it was seen that, with the exception of the large peaks at 52 and 60 Hz in the whip antenna spectra (omitted from the curves), the data are otherwise uncontaminated by system noise or ship noise, so that the noise levels which were measured really do represent the ELF fields above and in the sea.

In order to determine the total horizontal electric field that would have been sensed by an omnidirectional (instead of bi-directional) antenna at the depths at which the electrode pair was located, the vertical electric field values at five frequencies were extrapolated down into the sea, with corrections made for the refraction ratio across the air-sea boundary and for the attenuation through the sea water. These calculated values are represented by the open circles lying along the spectra of the electrode pair data. The nominal values of sea water conductivity, using the data of Fig. 4, were taken to be 4 mhos/meter for the sample periods of Figs. 13 and 14, and 3.3 mhos/meter for the periods of Figs. 15 and 16. The calculated values of total horizontal electric field in Figs. 13 and 14 bear a reasonable relationship to the measured values of the horizontal electric field in view of the fact that some of these fields were not sensed by the electrode pair. The measured values in Figs. 15 and 16, however, appear to be somewhat high (judging from the calculated values), which suggests that during these sample periods the ship may have passed through an eddy of sea water even colder (thus less conductive) than that indicated by the "Time 1900" curve of Fig. 4. The results of these comparisons are satisfactorily close, but a more detailed analysis of the differences must be put off until additional data have been processed.

It should be noted here that the close agreement between calculated and observed values of the underwater ELF fields tends to verify the accuracy of calibration of both the whip antenna system and the electrode pair system. That is, the ELF levels in each medium were evaluated independently, each system was calibrated in its own unique way, and the results were found to be compatible when compared by means of their theoretical relationships.

A comparison of the shapes of the ELF spectra shows that the most interesting features lie in the region between 10 and 40 Hz. During the sample period represented by Fig. 13 (near local noon), the electrode pair was oriented in a north-south (magnetic) direction. Three distinctive peaks occur in the electrode pair spectra at approximately 14, 25, and 32 Hz, coinciding with the second, fourth, and fifth Schumann resonances. A fourth peak, less distinct, is seen near 21 Hz. The whip antenna spectrum does not have any particularly distinctive peaks in this case. The curves of Fig. 14 show the spectra that were obtained approximately 13 minutes later, during which time the electrode pair was oriented in an east-west direction. The vertical electric field spectrum has not changed significantly since the previous sample. The electrode pair, however, is now directed toward sources whose combined spectra produce dominant resonances at approximately 20, 26, and 32 Hz, corresponding to the third, fourth, and fifth modes.

The curves in Figs. 15 and 16 represent data taken during late afternoon. In Fig. 15, the vertical electric field spectrum is shown to have changed to such an extent that resonances near 14, 25, and 32 Hz have become dominant. The underwater electrode pair, however, now oriented in an east-west direction, does not sense these resonances, which indicates that the sources of these peaks lie in a southerly (or northerly) direction (i.e., generally normal to the electrode pair axis). In Fig. 16, data taken 45 minutes later show that the peaks in the over-water spectrum sensed by the whip antenna have disappeared. The electrode pair, oriented in a north-south direction, now senses sources having peaks near the second, third, and fourth modes, at approximately 14, 20, and 26 Hz, respectively.

These illustrations have been intended to suggest how each of these methods of measuring ELF noise may be used to advantage: the whip antenna provides the total level of noise due to the vertical electric fields over the sea, whereas the electrode pair system provides some enhancement of the spectra of noise sources lying generally in the direction of its axis.

7. CONCLUSION

Spectra of vertical electric fields above the sea and horizontal electric fields in the sea have been compared to illustrate differences that may be used to advantage in the study of ELF noise. The vertical electric field, sensed by the whip antenna, represents the total level above the sea of ELF noise arriving from distant sources. The underwater electrode pair does not sense the total horizontal electric field in the water because of its bi-directional sensitivity to the fields, but this feature may be used to enhance the spectra of ELF noise arriving from thunderstorm areas by aligning the axis of the electrode pair in the direction of the sources of interest.

In studying ELF noise spectra, amplitude versus time chart recordings and frequency versus time sonagrams are of value in describing the instantaneous features of the noise that goes to make up the power spectra.

Future measurements using two horizontal electrode pairs whose axes are orthogonal are expected to provide information on both the total horizontal electric field in the sea and the directional characteristics of the noise.

8. REFFRENCES

1. Polk, C., "Relation of ELF Noise and Schumann Resonances to Thunderstorm Activity," in Planetary Electrodynamics, vol. 2, edited by S. C. Coroniti and J. Hughes, Gordon and Breach Science Publishers, New York, 1969, pp. 55-82.

2. Toomey, J., and C. Polk, "Research on Extremely Low Frequency Propagation with Particular Emphasis on Schumann Resonance and Related Phenomena," Final Report, Part II (Location of Sources), on Contract No. AF 19(628) -4950, University of Rhode Island, Kingston, April 1, 1970.

3. Koenig, H. L., M. Finkle, and C. Polk, "Measurements of Electric Fields Between 3 cps and 10,000 cps with a Vertical Antenna over the Atlantic Ocean Near the East Coast of Florida," University of Rhode Island Rept. 396(10)/1, University of Rhode Island, Kingston, December 1964.

4. Soderberg, E. F., "ELF Noise in the Sea at Depths from 30 to 300 Meters," J. Geophys. Res., vol. 74, no. 9, May 1969, pp. 2376 - 2387.

5. Launay, L., S. W. Lichtman, and E. Selzer, "ULF Environment of the Ocean Floor," Paper presented at the Symposium on Ultra Low Frequency Electromagnetic Fields, Boulder, Colorado, August 1964.

6. Wait, J. R., "Electromagnetic Waves in Stratified Media," Pergamon Press, The Macmillan Company, New York, 1962.

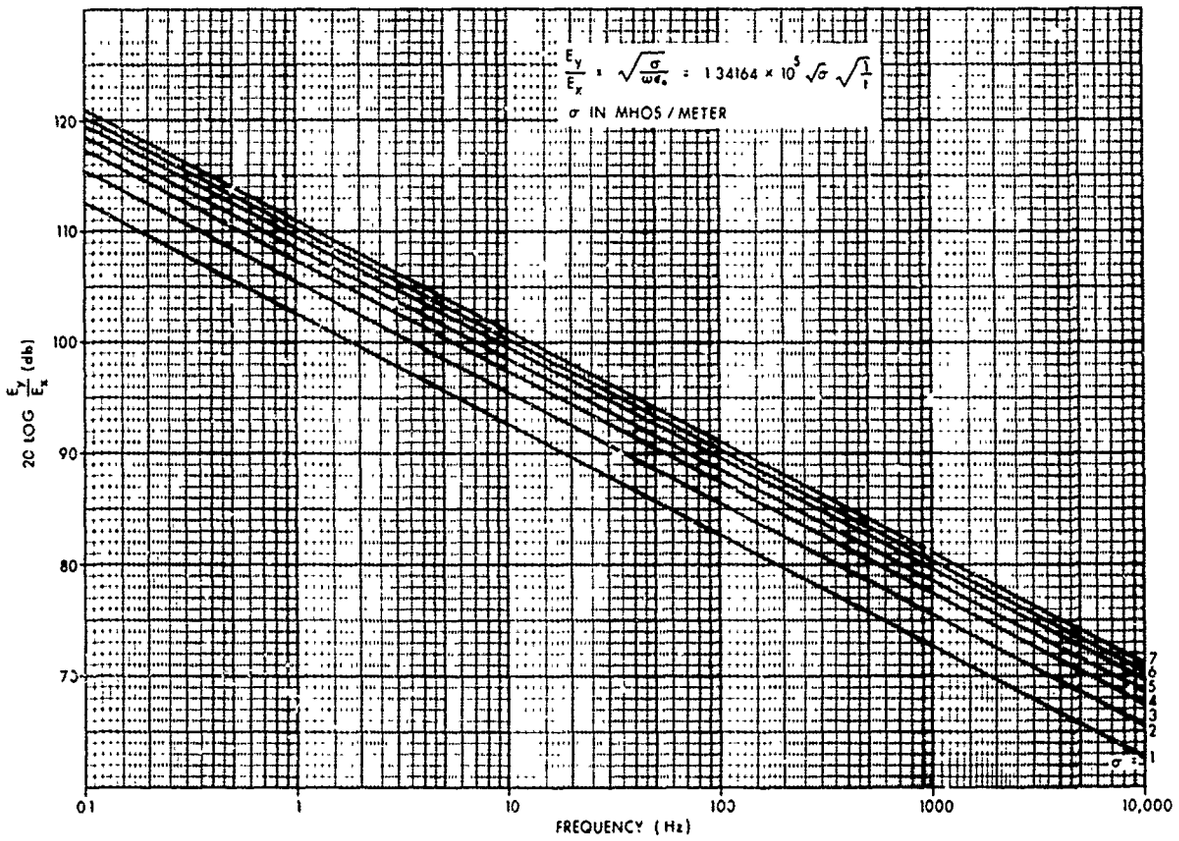

Fig.1 Refraction ratio vs frequency for various values of sea water conductivity

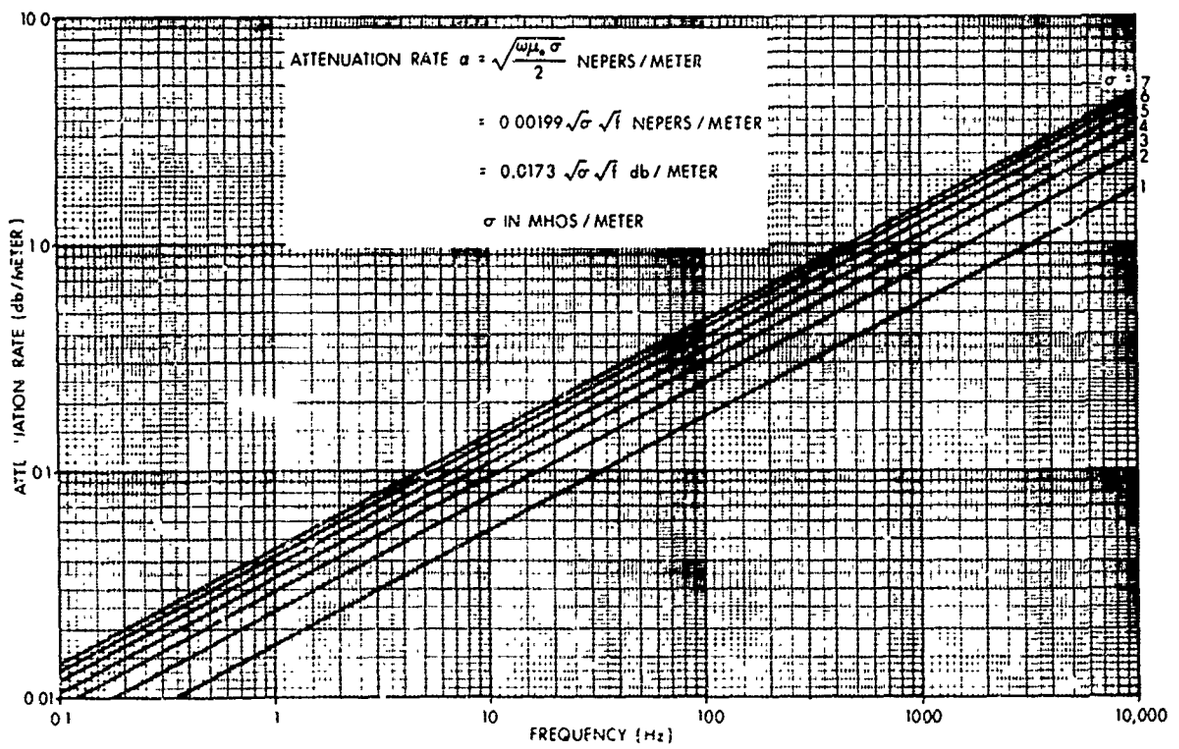

Fig.2 Attenuation rate in sea water for various values of sea water conductivity

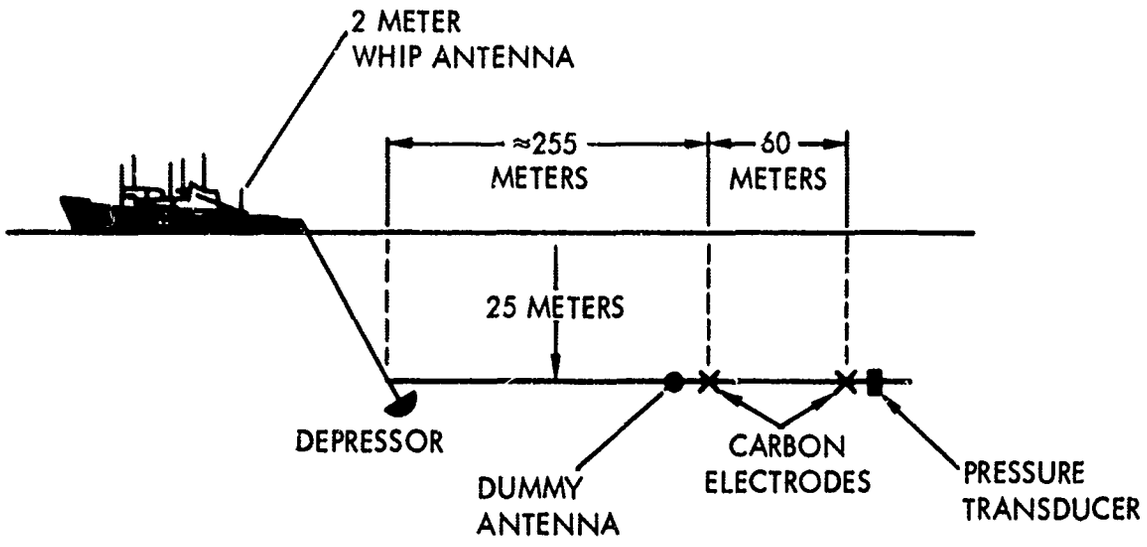

Fig.3 Locati n of sensors with respect to the ship

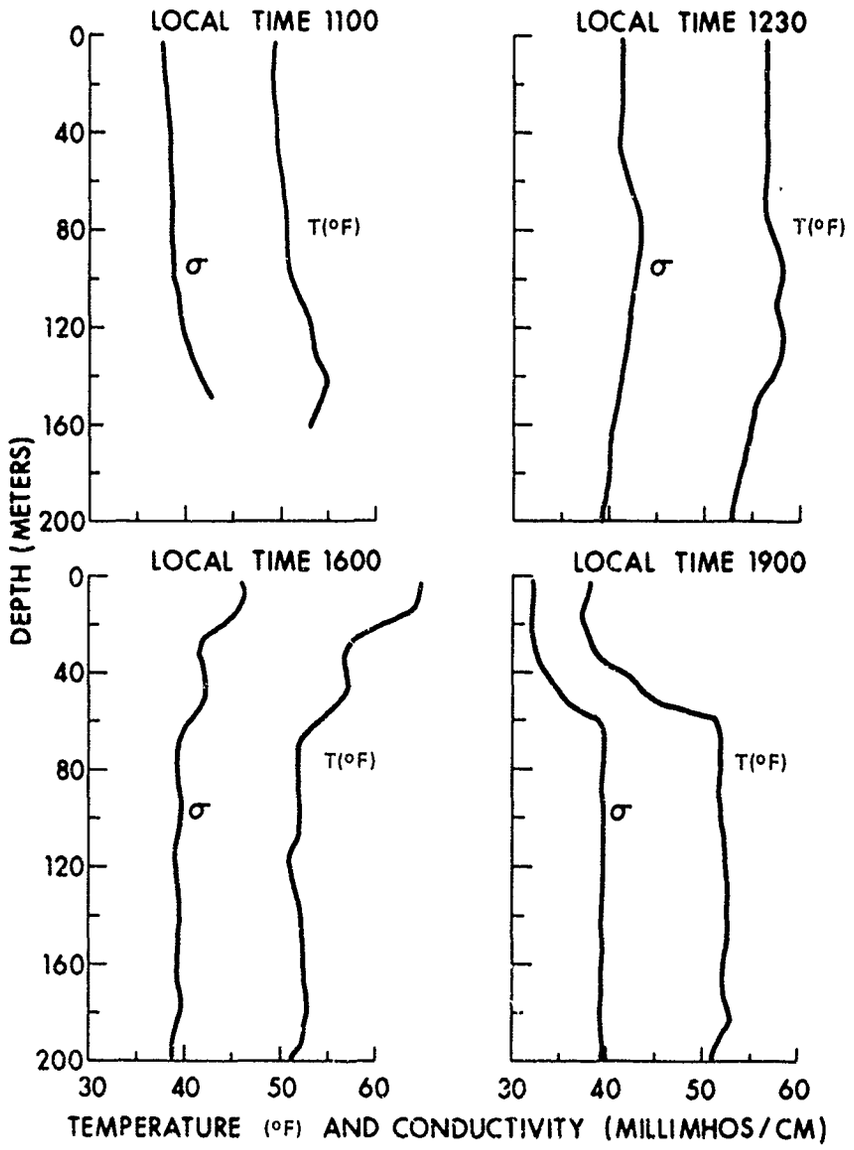

Fig.4 Depth profiles of temperature and electrical conductivity

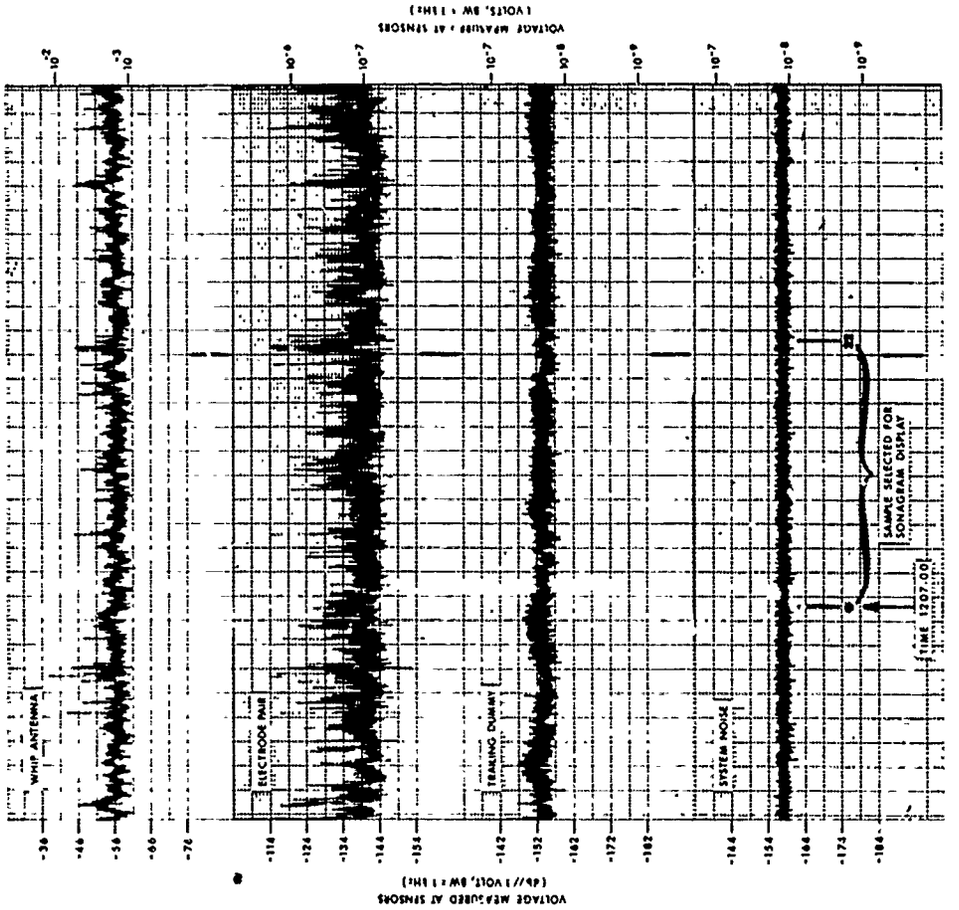

Fig.6 Amplitude vs time sample recordings: local time 1207:00, ship's course 090° magnetic

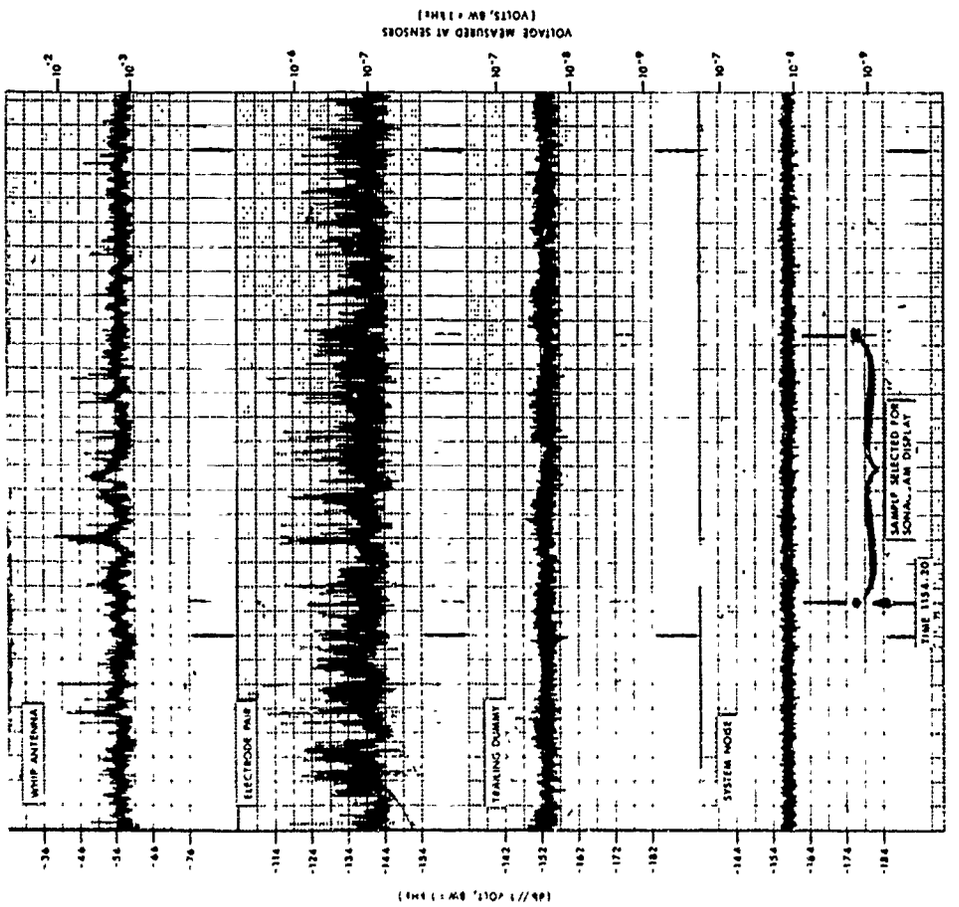

Fig 5 Amplitude vs time sample recordings: local time 1154:30, ship's course 180° magnetic

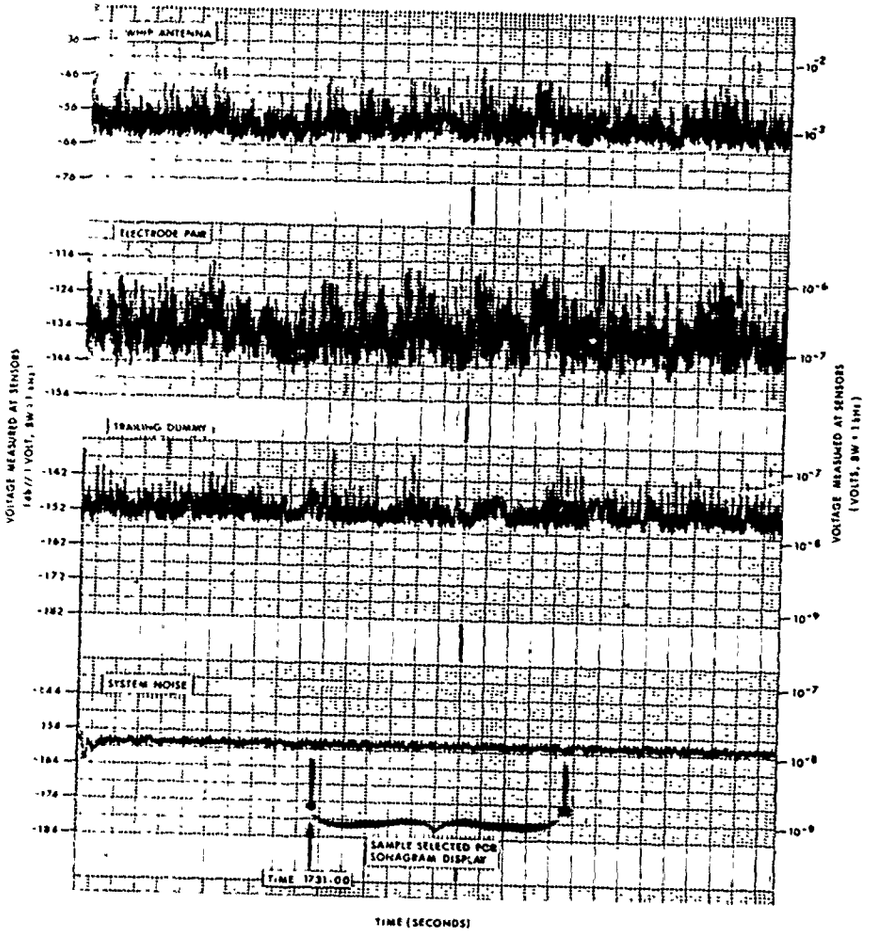

Fig.7 Amplitude vs time sample recordings: local time 1731:00, ship's course 090° magnetic

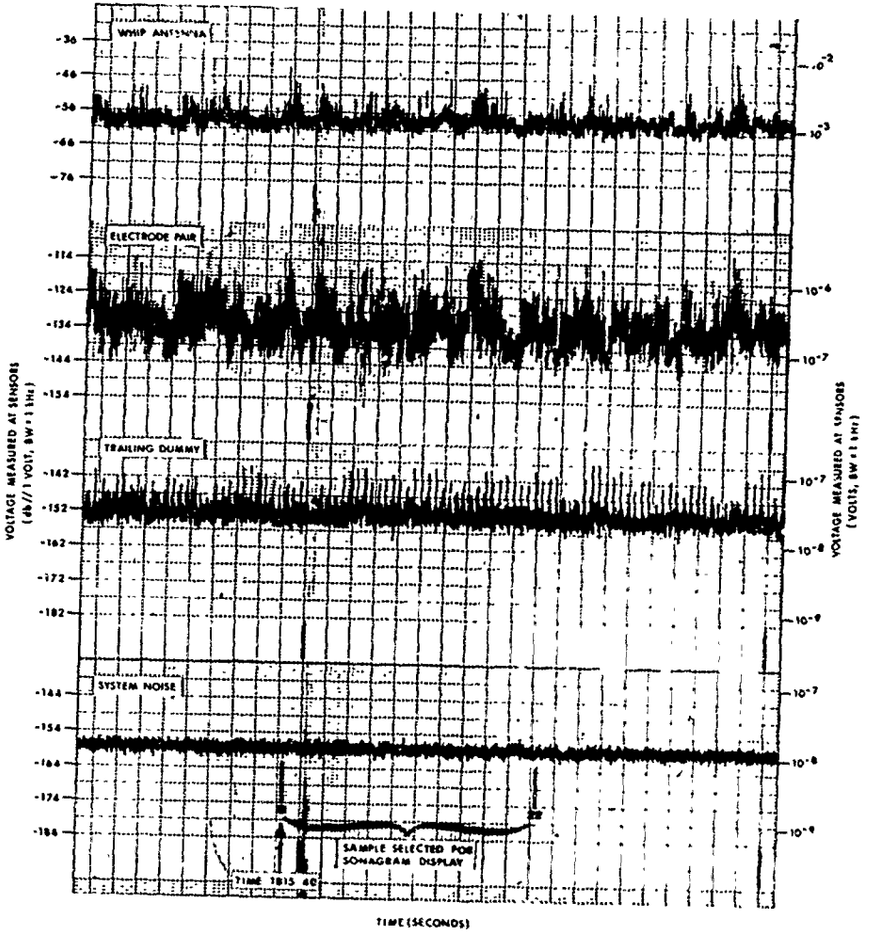

Fig.8 Amplitude vs time sample recordings: local time 1815:40, ship's course 180° magnetic

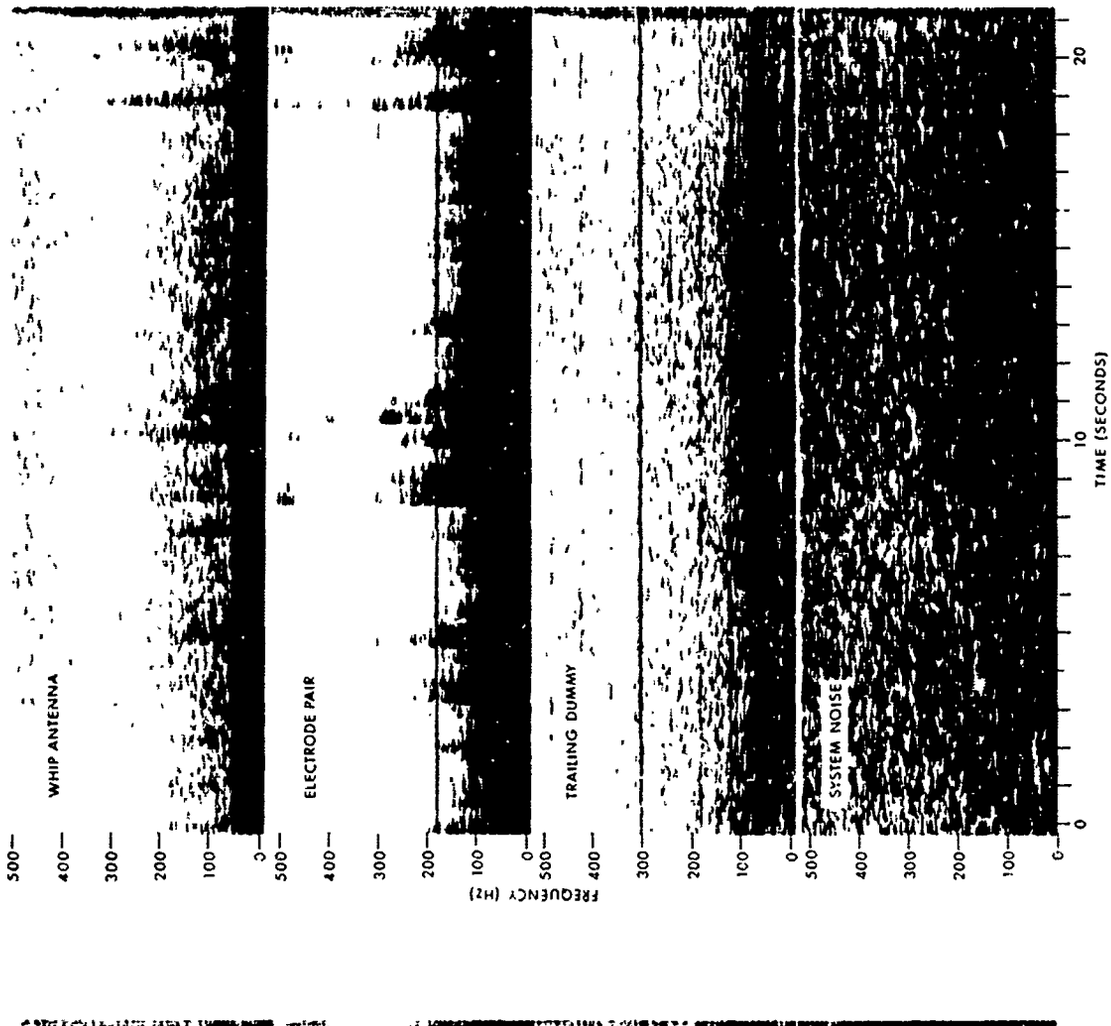

Fig.10 Frequency vs time sonagrams: local time 1207:00, ship's course 090° magnetic

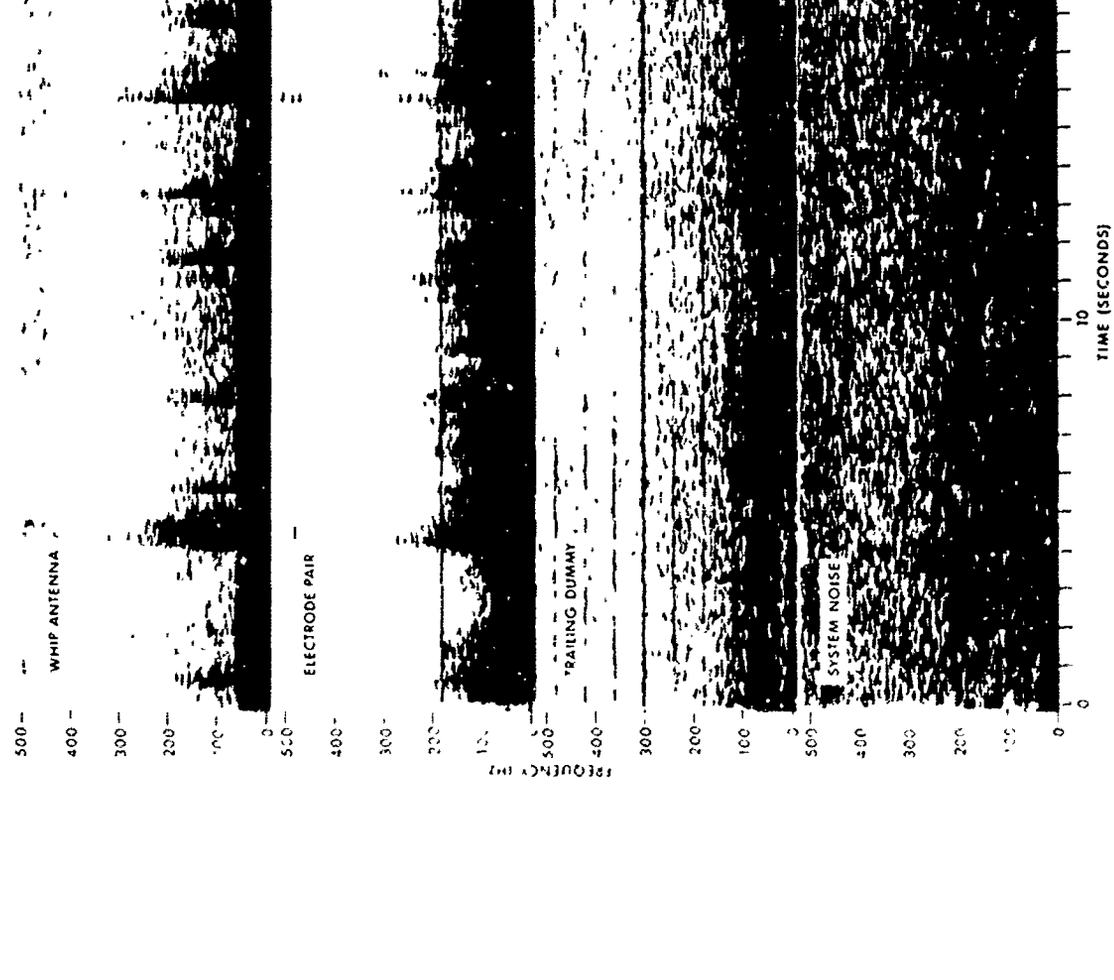

Fig.9 Frequency vs time sonagrams: local time 1154:30, ship's course 180° magnetic

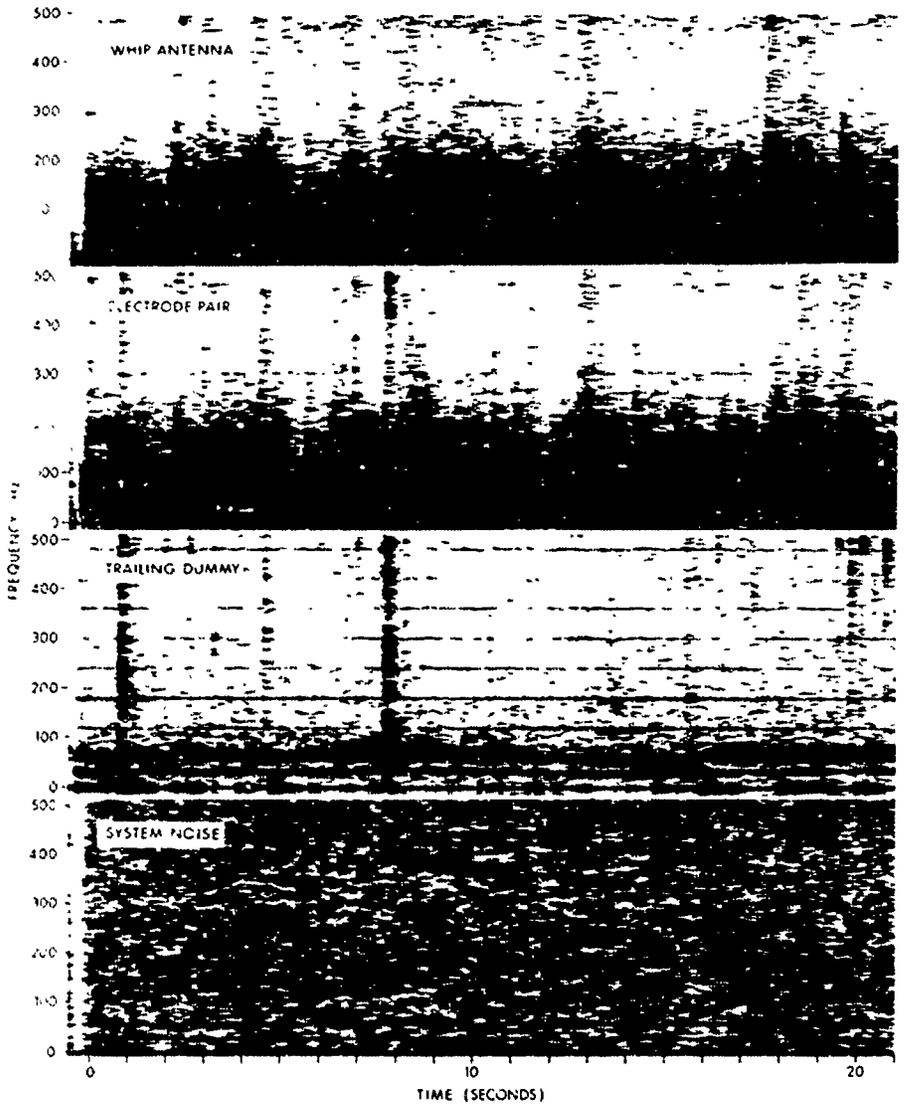

Fig. 11 Frequency vs time sonagrams: local time 1731:10, ship's course 090° magnetic

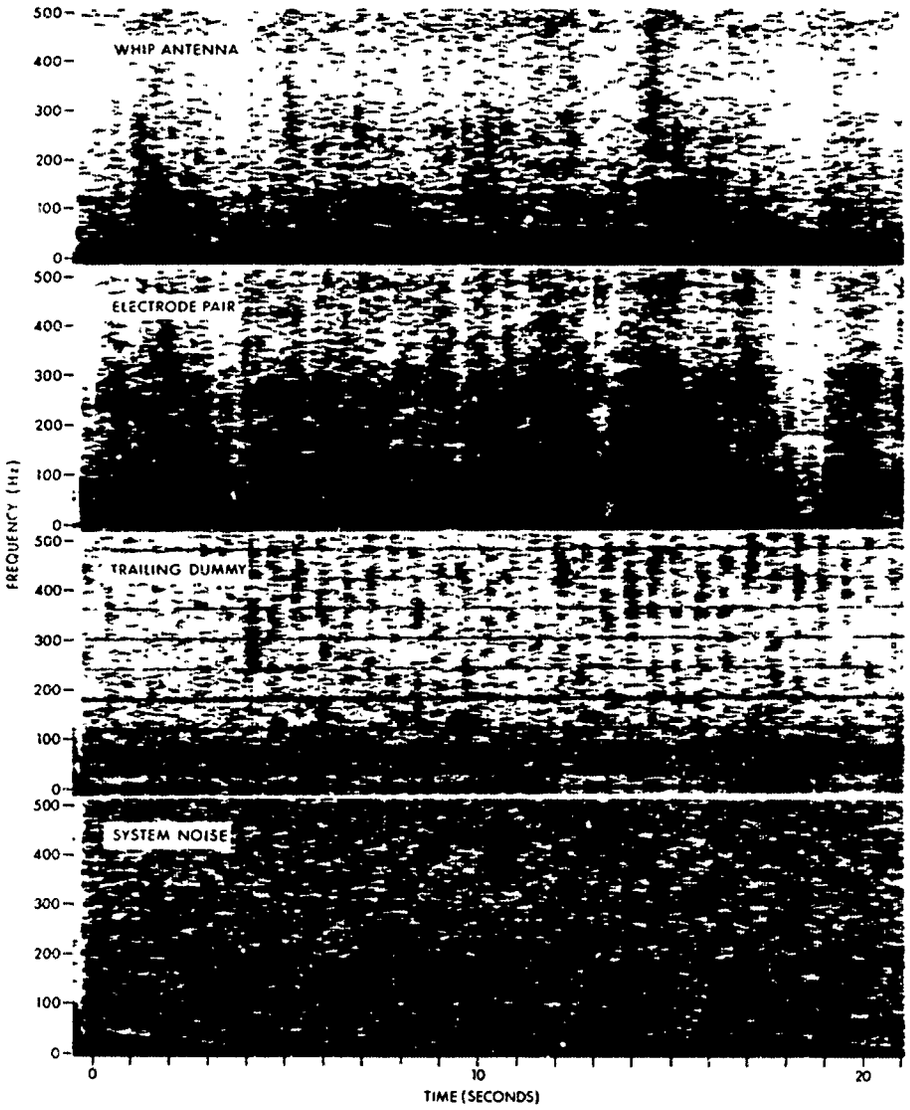

Fig.12 Frequency vs time sonagrams: local time 1815:40, ship's course 180° magnetic

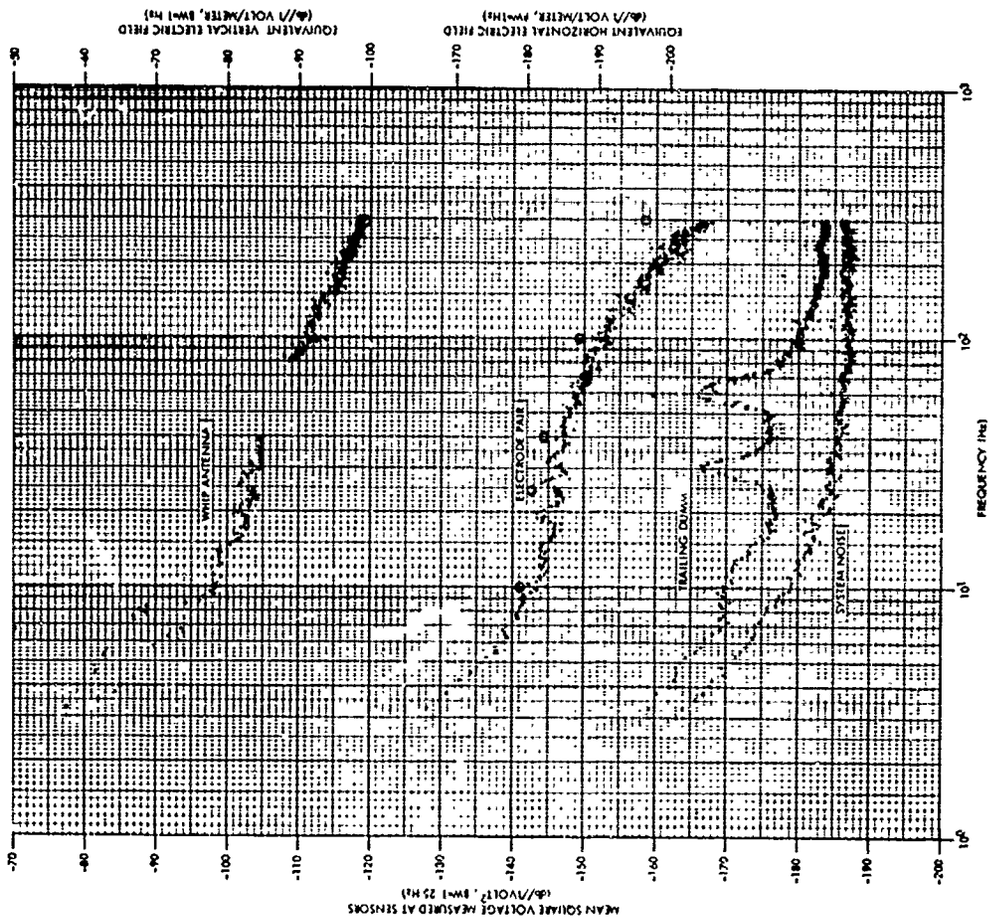

Fig.14 Power spectra for the four channels: local time 1207·00, ship's course 090° magnetic

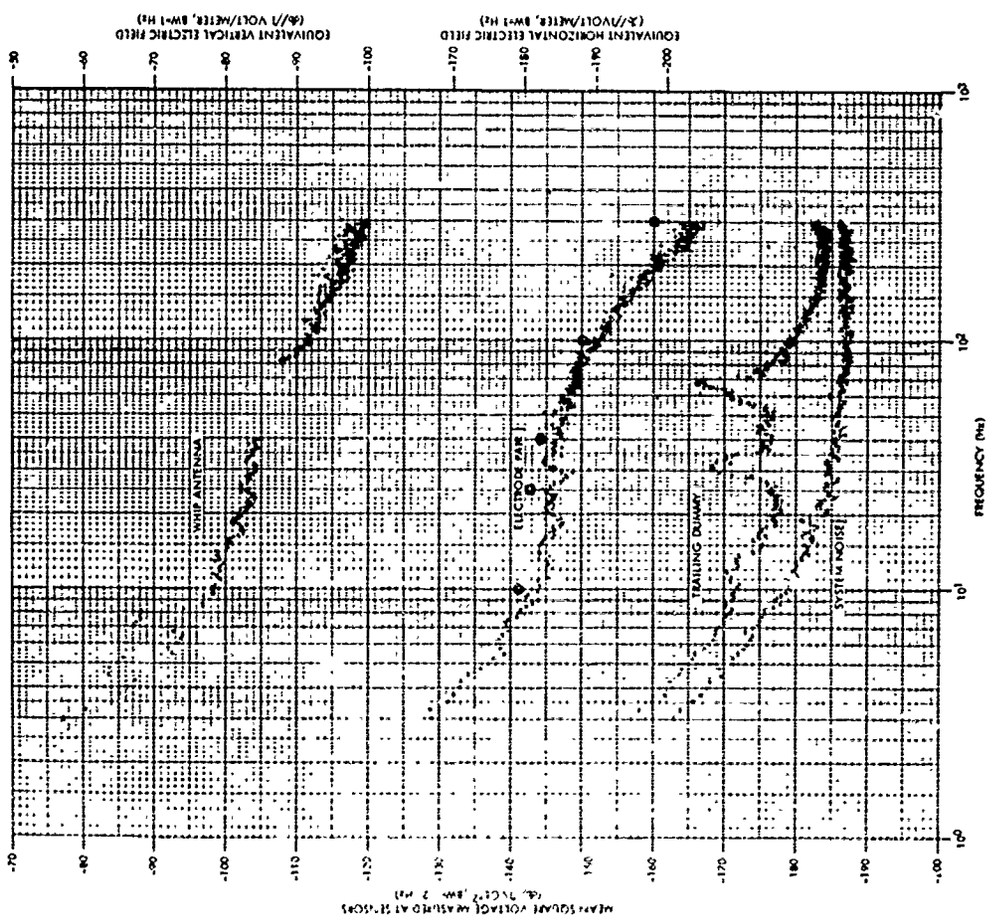

Fig.13 Power spectra for the four channels: local time 1154:30, ship's course 180° magnetic

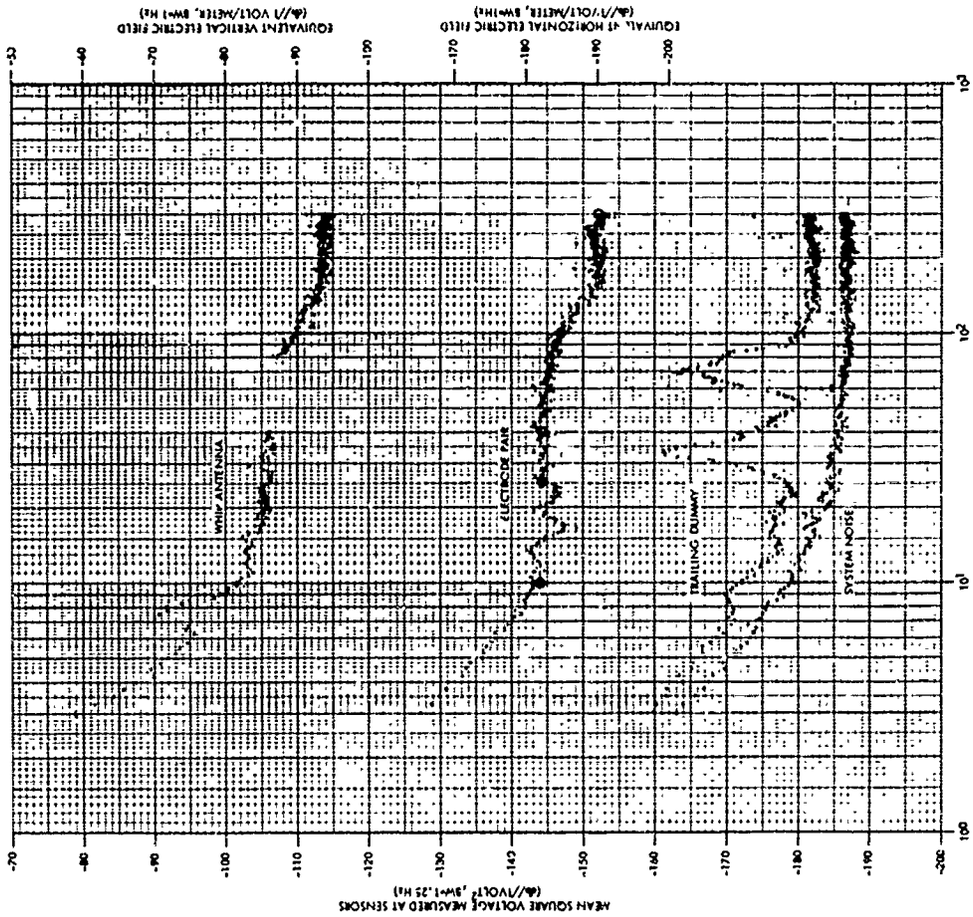

Fig.16 Power spectra for the four channels: local time 1815:40, ship's course 180° magnetic

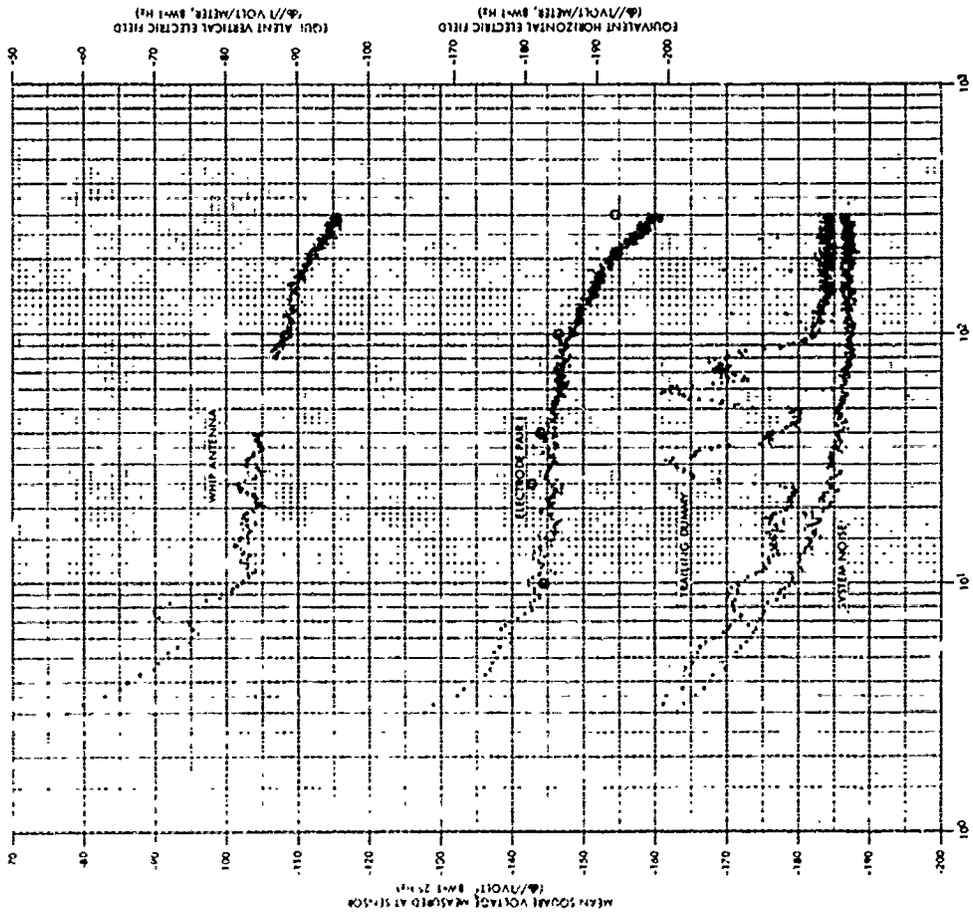

Fig.15 Power spectra for the four channels: local time 1731:00, ship's course 090° magnetic

NIVEAUX CARACTERISTIQUES DU BRUIT ELECTROMAGNETIQUE NATUREL DANS LA GAMME UBF, AU SEIN DES MERS, EN FONCTION DE LA PROFONDEUR

par

E. SELZER

Institut de Physique du Globe
de la Faculté des Sciences de Paris

SUMMARY

If we confined ourselves to the simplest basic principles (water masses assumed to be homogeneous and completely passive from the electromagnetic viewpoint ; inactive sea bottoms ; tabular and coherent external excitation sources ; no discontinuities between continents and oceans, etc.), the electromagnetic noise levels that we might expect to find in the oceans could be expressed in a particularly simple way, in terms of the depth and spectral composition of the incident radiation, as a direct application of the "skin effect". This way, at frequencies approximating 1 Hz, we might expect to find an attenuation of the order of 170 DB at a depth of 5000 m. Such an electromagnetic "quiet" is likely to stimulate various projects ; it is therefore important to verify it experimentally. However, we come up against critical practical difficulties which prevent us from obtaining the final accurate information required. Therefore, direct "in situ" absorption measurements have been successfully carried out mostly in some fresh water lakes (for instance, by Prof. Dessoulavy in the lake of Geneva, with the "Mesoscaph").

In this paper, a synthesis is made of the results obtained during successive campaigns on board the "Archimedes" bathyscaph (from 1964 to 1967), combined with those provided by the complete recording of a magnetic storm by means of a probe immersed at 5om. depth in the bay of Villefranche (L. Launay), and taking account of various calculations on the hydromagnetic effects related to sea kinetics (waves, currents, etc.). We have found that real conditions may diverge to a large extent from the theoretical conditions often assumed. Taking into account, as far as possible, the overall factors involved, we propose likely thresholds for the natural noise levels that should be expected, in actual fact, in seawater, within the range of electromagnetic variations considered.

NIVEAUX CARACTERISTIQUES DU BRUIT ELECTROMAGNETIQUE NATUREL DANS LA GAMME UBF, AU SEIN DES MERS, EN FONCTION DE LA PROFONDEUR

par

E. SELZER

Institut de Physique du Globe
de la Faculté des Sciences de Paris

SOMMAIRE

Dans le présent exposé nous faisons la synthèse des résultats de mesures de bruit électromagnétique obtenus au cours des campagnes successives effectuées depuis 1964 par le bathyscaphe "Archimède", associés à ceux d'un enregistrement intégral d'un orage magnétique au moyen d'une sonde immergée par 60 m de fond dans la baie de Villefranche (L. Launay). Tenant compte également de divers effets hydromagnétiques liés à la cinétique des mers (vagues, courants, etc.), nous trouvons que les conditions réelles peuvent s'écarter dans de larges mesures des conditions de principe souvent postulées (ne tenant compte que du "skin effect"). Considérant, dans toute la mesure du possible, l'ensemble des facteurs en jeu, nous proposons des seuils probables pour les niveaux de bruit naturel que l'on doit s'attendre à trouver réellement au sein des mers dans la gamme des variations électromagnétiques considérée.

SUMMARY

In this paper, a synthesis is made of the results concerning electromagnetic measurements obtained during successive campaigns on board the "Archimedes" bathyscaph since 1964, combined with those provided by the complete recording of a magnetic storm by means of a probe immersed at 60 m depth in the bay of Villefranche (L. Launay). Taking account of various hydromagnetic effects related to sea kinetics (waves, currents, etc.), we have found that real conditions may diverge to a large extent from the theoretical conditions often assumed which take only in consideration the classical skin effect. Taking into account, as far as possible, the overall factors involved, we propose likely thresholds for the natural noise levels that should be expected, in actual fact, in seawater, within the range of electromagnetic variations considered.

1. INTRODUCTION

Le bruit électromagnétique naturel au sein des mers n'est pas une grandeur dont la détermination précise en fonction de la profondeur puisse être clairement exprimée. Si l'on s'en tenait aux conditions de principe les plus simples (masses d'eaux supposées homogènes et totalement passives du point de vue électromagnétique; fonds des mers inactifs; sources d'excitation externes tabulaires et cohérentes; absence de discontinuités continents-océans; etc.) les niveaux de bruit électromagnétique naturel que l'on pourrait s'attendre à trouver s'exprimeraient d'une façon particulièrement simple par application directe de l'effet de peau ("skin effect") en tenant compte, avec la profondeur, de la composition spectrale de la radiation incidente. C'est ainsi que, aux environs de la fréquence 1 Hz , on pourrait s'attendre à trouver un affaiblissement de l'ordre de 170 dB à une profondeur de 5000 m . Un tel "calme électromagnétique" étant susceptible d'encourager divers projets, sa vérification expérimentale est importante. Nous allons essayer de faire la synthèse de diverses mesures que nous avons faites dans ce sens et des données actuelles sur cette question. Nous serons ainsi conduits à tenir compte d'un nombre plus grand de paramètres et de phénomènes plus complexes que ne le demande la théorie classique du skin effect.

C'est en 1960, à l'occasion de la soumission de projets concernant les objectifs scientifiques que l'on pourrait se donner pour l'utilisation la plus spécifique des possibilités nouvelles qu'allait apporter la mise en service du bathyscaphe "Archimède, que nous nous sommes intéressés directement à ces questions. On ne s'étonnera donc pas que notre étude expérimentale ait été conduite d'abord, exclusivement, de 1964 à 1966, au cours de plongées effectuées avec l'Archimède. Malgré la préparation - aussi minutieuse que possible - que nous avions faite pour ces expériences, ceci a donné lieu à un certain nombre de critiques que nous classerons comme suit :

1° Pourquoi avoir opté pour des expériences avec présence même de l'observateur, alors qu'étant donné les progrès de l'automatisme les mesures faites à partir du bathyscaphe auraient pu être conduites, plus convenablement, à partir de la surface ?

2° Par sa seule présence, le bathyscaphe doit perturber le milieu à explorer.

3° Le caractère relativement exceptionnel des plongées doit empêcher des expériences "sérieuses" d'être accomplies.

Nous nous permettrons de ne répondre que brièvement à la première de ces critiques car - bien qu'elle

ait trait à une question d'une importance primordiale, sa discussion fait partie maintenant d'un des aspects les plus classiques des méthodes expérimentales de la science moderne. Il nous suffira de rappeler, à titre d'exemple, les diatribes - maintenant bien dépassées - entre partisans des explorations lunaires par engins habités et ceux qui estimaient que des engins automatiques feraient tout aussi bien. Tout dépend de la catégorie logique de la méthode d'étude que l'on entend appliquer à l'exploration envisagée : si l'on entend essentiellement vérifier la validité, ou préciser, des idées déjà conçues, des engins automatiques pourront remplir d'une façon satisfaisante les missions qui leur seront imparties ; mais s'il s'agit d'aller au devant de nouvelles conceptions, la présence personnelle d'un observateur ou d'un expérimentateur sera nécessaire. A cette philosophie générale relative à la façon de concevoir la recherche que l'on désire entreprendre, nous ajouterons une considération beaucoup plus particulière relative à notre cas précis : une fois admis - indépendamment de notre activité propre - la mise en place des campagnes de l'Archimède, le fait de greffer nos expériences sur ces plongées n'entraînait pour nous qu'une charge budgétaire réduite, alors que la mise en place de mesures équivalentes destinées à être faites à partie de la surface, aurait nécessité des moyens considérables que notre laboratoire - non spécialisé en océanographie - n'aurait jamais pu rassembler.

En ce qui concerne la deuxième des objections, celle relative aux perturbations apportées à l'état magnétique et électromagnétique du milieu à explorer par le bathyscaphe lui-même, il est évident qu'elle s'appuie sur des faits indéniables dont, en premier lieu, l'apport de la sphère d'acier constituant l'habitacle du bathyscaphe. Cette circonstance rendrait, en effet, illusoire tout essai de mesure de la valeur statique du champ magnétique principal existant au voisinage de notre engin d'exploration. Une mesure de ce genre ne pourrait être faite que par des procédés détournés tels que l'usage d'une remorque construite en matériaux non magnétiques, ou par le dépôt du magnétomètre en un point du fond de la mer dont on s'éloignerait pendant la durée des mesures. Ces manières de faire sont parmi les choses possibles mais moyennant - tout au moins pour la première - des réalisations onéreuses et qui nécessiteraient des mises au point compliquées. Nous ne nous y arrêterons pas, car de telles mesures du champ magnétique statique n'étaient pas dans nos projets. Nous avions, par contre, choisi d'étudier le "bruit électromagnétique" - donc, des variations magnétiques - dans des bandes de fréquences à l'intérieur desquelles les perturbations apportées par le bathyscaphe ne devaient pas être prohibitives, soit depuis quelques Hertz jusque vers 200 Hertz. En fait, nous avons découvert que la sphère d'acier de l'Archimède provoquait bien une perturbation importante à l'intérieur de cette bande de fréquence et que cette perturbation pouvait être très gênante, mais au fur et à mesure de notre étude et de la connaissance plus précise - et même très précise - que nous avons pu avoir sur cet effet, nous nous sommes rendus capables d'éliminer les défauts qu'il nous causait. Il s'agissait, en effet, d'une variation électromagnétique centrée sur une raie spectrale très étroite (ceci, pour une profondeur déterminée), par exemple, comprise entre 39,5 et 40,5 Hz à une profondeur de l'ordre de 5000 mètres (plongées de la campagne de Grèce et de celles au voisinage de Madère), ce qui permettait de la reconnaître facilement sur les enregistrements quand ceux-ci sont soumis aux méthodes de l'analyse spectrale, sans qu'elle puisse entâcher des signaux de fréquences différentes. (Je passe ici sur certains inconvénients techniques, tels que les saturations des amplificateurs d'entrée, que cette raie a pu provoquer, mais auxquels il a été possible de parer). Le problème le plus délicat que nous ayons eu à résoudre relativement à cette raie a été d'établir avec certitude son origine : une fréquence de résonance propre (oscillations libres) de la sphère d'acier qui constitue un système mécanique oscillant ayant un coefficient de qualité élevé, ce qui lui permet de présenter une amplitude d'oscillations quasi permanente (et même pseudo constante quand on s'attache à réaliser une immobilité aussi complète que possible de tout l'intérieur de la sphère) qui se transmet alors à l'eau par un mécanisme de couplage mécano-magnétique. (Il est probable que ce type de couplage se produit dans les deux sens : de légers mouvements de l'eau - très faibles courants, tourbillons peut-être ? - excitent mécaniquement, et entretiennent, les vibrations de la sphère, qui retransmettent à l'eau - par le mécanisme indiqué ci-dessus - l'énergie reçue). Nous comptons revenir d'une façon plus précise, dans la suite de notre exposé, sur cet effet, mais ajoutons seulement ici que les analyses spectrales des enregistrements ont souvent fait apparaître d'autres raies plus ou moins étroites que nous avons également reconnues comme étant d'origine artificielle et causées par diverses parties du bathyscaphe. Comme pour la raie voisine de 40 Hz , ces autres raies ne sont pas gênantes une fois leur existence bien reconnue et "cataloguée".

Des phénomènes perturbateurs d'une autre nature ont été aussi mis en évidence au cours de nos plongées, mais ils étaient relatifs, essentiellement, à des états dynamiques du bathyscaphe : prises d'immersion (avec les inconvénients que cela comporte pour la stabilité des phénomènes de polarisation des électrodes servant à mesurer les champs électriques), descentes de plongées, tourbillons et nuages de vase lors des arrivées sur le fond, etc.. Une perturbation particulière, mais qui n'a pas été sans intérêt, a été celle - observée lors de plongées à profondeurs moyennes (2000 à 2500 m) en Méditerranée - causée par l'agitation microsismique et transmise par le fond au bathyscaphe lui-même. D'une façon générale, les diverses perturbations que nous avons évoquées ont compliqué considérablement notre travail de dépouillement et de compréhension préalable des phénomènes; elles nous ont forcé à perfectionner nos moyens d'analyse et à répéter - lors de plongées successives - les expériences et les mesures de contrôle, mais nous pensons avoir réussi maintenant, grâce à ce souci de rigueur, à éliminer la plupart de leurs conséquences nocives pour une interprétation correcte de nos mesures.

Enfin, quant au dernier type des critiques que l'on pouvait faire à nos expériences, à savoir que l'on pouvait difficilement imaginer que des mesures précises pouvaient être mises en oeuvre - pour autant qu'elles n'avaient pas été rendues automatiques - dans les conditions de séjour et de confort relativement précaire que l'on s'attend à trouver dans la sphère-habitacle d'un bathyscaphe, c'est celui auquel nous pouvons répondre de la façon la plus formelle : une fois bien posés sur le fond, le bathyscaphe et sa sphère constituent un excellent laboratoire de physique qui assurent aux expérimentateurs un calme et des facilités de travail très remarquables, la seule limitation venant de la durée toujours trop courte - cinq à six heures au maximum - des séjours au fond. En vue d'expériences futures, il y aurait certainement un intérêt majeur à pouvoir augmenter d'une façon substancielle cette durée.

Nous ne nous étendrons pas plus avant, ici, sur les circonstances générales de ces campagnes de plongées avec l'Archimède. Nous rappelerons simplement les époques de ces campagnes et l'ordre de grandeur des profondeurs correspondantes auxquelles se rapportent les mesures : Fosse de Porto Rico en 1964, pour des profondeurs de l'ordre de 7 et 8000 mètres ; Méditerranée orientale (au voisinage des côtes de Grèce) en 1965, avec des plongées à 3000 mètres ; environs de l'île de Madère en 1966, sur des fonds compris entre 4000 et 4500 mètres ; campagne du Japon en 1967 (expériences confiées à J. JARRY, Chef du

Laboratoire du Bathyscaphe) avec des plongées de 8000 et 9000 mètres ; enfin, quelques mesures (effectuées également par J. JARRY) ont pu être faites au cours de cinq plongées de la dernière campagne aux Açores, en 1969, par des fonds atteignant les 3000 mètres ; il faut mentionner également divers essais, hors campagnes, en Méditerranée, à des profondeurs comprises entre 2000 et 3000 mètres. Les conditions et les buts précis relatifs à toutes ces plongées n'étaient pas strictement uniques (on les trouvera exposés dans les publications parues précédemment, (1), (2), (3), (4)), mais nous avons toujours eu le souci que chaque expérience nouvelle permette également la vérification des points les plus douteux laissés en suspens par les précédentes. C'est à ce sujet qu'apparaît la critique peut-être la plus fondée que l'on puisse faire à nos séries d'essais successifs : la difficulté qu'il y a à assurer une bonne continuité dans le temps de toutes les vérifications suggérées par les expériences qui viennent de se dérouler et dont on dépouille les résultats, ou nécessitées par les expériences suivantes, projetées ; ceci, étant donné les contingences logistiques entraînées par l'usage du bathyscaphe.

Nous avons essayé de remédier à ces difficultés, d'abord en développant les essais d'appareillages à terre, au laboratoire, et surtout en prévoyant des enregistrements continus à partir de sondes sensibles immergées à demeure - bien qu'à faible profondeur seulement : une soixantaine de mètres - dans la baie de Villefranche. Un des buts recherchés était, entre autre, de permettre un réglage de la chaîne d'enregistrement quand elle est poussée à son maximum d'amplification, ce qui est la plupart du temps quelque chose d'impossible à exécuter avec des sondes sensibles à terre (même en dehors de locaux de laboratoires) étant donné la rareté des sites non perturbés. Une mise en oeuvre de ce type a pu être faite durant quelques semaines en Août 1966 (L. LAUNAY opérant à partir de la station de géodynamique sous-marine de Villefranche) et a donné de bons résultats du point de vue magnétique (avec notamment un enregistrement complet de l'orage magnétique des 29/30 Août sur lequel nous reviendrons); malheureusement, un enregistrement sismique conjugué sur lequel nous comptions pour éclaircir certaines ambiguïtés, a été victime d'incidents de fonctionnement (détérioration accidentelle d'un des câbles de raccordement ayant provoqué un défaut d'isolement).

En résumé, étant donné la difficulté bien connue des mesures électriques (et électromagnétiques) en mer, il ne suffisait pas de conduire un programme coordonné, mais unique, d'expériences, pour avancer avec quelque sûreté dans la voie que nous nous étions tracée. Un ensemble très vaste et très varié de vérifications de toutes sortes était aussi indispensable. Bien que l'exécution de cet ensemble ne puisse pas être considéré comme terminé définitivement, nous pensons qu'il est maintenant suffisamment avancé pour que, tenant compte des conclusions auxquelles il nous a amenés, nous soyons à même de faire part de ces dernières. C'est ce à quoi nous allons nous employer maintenant.

2. RAPPEL DES PROBLEMES POSES — RESULTATS EXPERIMENTAUX CORRESPONDANTS

Nous avons bien donné déjà, dans l'INTRODUCTION, la ligne générale des recherches que nous désirions suivre, mais la manière de suivre cette ligne peut être tellement variée dans le choix des faits ou des hypothèses par lesquels nous aborderons d'une façon tangible nos études, que nous devons ici les préciser. Nous pourrons les classer comme suit :

1° Admettant que nous opérons à des profondeurs telles qu'aucun signal électromagnétique perceptible ne puisse nous atteindre à partir de la surface, ceci par les voies directes, est il possible de recevoir de tels signaux par voie indirecte, au voisinage immédiat des fonds marins ? Dans l'affirmative, par quel processus cela se produirait-il et jusqu'à quelles distances ? En dehors de tels signaux, un niveau de bruit électromagnétique appréciable est il rayonné vers le haut par les fonds marins ?

2° La mer elle-même est-elle, dans son sein propre, génératrice de bruit électromagnétique, et rayonne-t-elle dans sa masse un tel bruit ?

3° Quelles sont les sources et les niveaux de bruit électromagnétique engendrés par l'interface mer-air ?

4° Y a-t-il une répartition de nappes de courant électrique (plus ou moins horizontales) au sein des mers et, dans la mesure où ces courants comporteraient une composante continue (ou pseudo continue) importante, une telle composante a-t-elle une influence importante - ou tout au moins appréciable - sur la distribution de la Déclinaison Magnétique au dessus des étendues océaniques : hypothèse de SHULEIKIN (5) ?

5° Comment les variations magnétiques (et électromagnétiques) naturelles venant de l'environnement spatial de la Terre, pénètrent-elles réellement dans les masses océaniques et comment - à des profondeurs faibles ou moyennes, ne devant pas dépasser, dans l'état actuel des possibilités techniques, 2000 à 3000 m - peuvent elles être utilisées pour des sondages magnéto-telluriques du sous-sol marin ?

Ne pouvant pas traiter tous ces problèmes, nous nous limiterons à ceux pour lesquels nous pensons que nos efforts ont pu apporter quelque contribution efficace, aussi petite soit elle, en donnant les conclusions correspondantes.

Bruit rayonné par les fonds marins. L'hypothèse fondamentale est celle suivant laquelle un guide d'ondes sub-terrestre (couche de haute resistivité électrique comprise entre deux masses conductrices) serait capable de permettre la propagation d'ondes électromagnétiques de fréquences extrêmement basses (au maximum, quelques dizaines ou quelques centaines de Hertz) sur des distances assez grandes (des centaines ou des milliers de kilomètres). Bien entendu, il ne suffit pas que ce guide existe, encore faut-il qu'une émission électromagnétique (naturelle ou artificielle) puisse y pénétrer. Au point de réception (supposé assuré par le bathyscaphe), il convient aussi que la transmission du guide vers les couches d'eau surmontant le fond, puisse se faire sans trop d'atténuation. Cette dernière condition - bien qu'impérative - paraît cependant la plus facile à remplir : nous savons que les quelques mètres qui séparent les sondes réceptrices du niveau du fond où s'est posé le bathyscaphe, imposent une atténuation modérée pour des ondes dont la fréquence ne dépasserait pas une centaine de Hertz (de l'ordre de 8,6 db - correspondant à la dite "profondeur de pénétration" de 25 m à 100 Hz , la plus grande partie de ces 25 m pouvant être consacrée à la traversée de la portion des sédiments très imbibée d'eau de mer et qui présente, de ce fait, une conductivité du même ordre de grandeur). En fait, tout dépendra sur ce point de l'épaisseur totale des sédiments de haute conductivité et de la profondeur (soit qu'elle soit seulement d'une dizaine de kilomètres, soit qu'elle soit plusieurs fois supérieure à ce chiffre) à laquelle la couche de haute résistivité passerait au dessous du fond. Indiquons qu'il est arrivé un petit nombre de fois que le bathyscaphe se

pose sur des plaines abyssales à fond rocheux (en dehors du cas - peu intéressant pour nos études et qui a été réalisé assez souvent lors de plongées destinées à des recherches géologiques - où il a exploré et s'est posé au fond de ravins rencontrés sur les talus côtiers et leurs éboulis), mais il est difficile d'être sûr de la continuité rocheuse d'un tel support car il arrive que de grandes dalles rocheuses reposent, en fait, sur une couche sous-jacente de sédiments.

En ce qui concerne le guide lui-même, les discussions relatives à son existence éventuelle n'ont guère progressé depuis le Symposium AGARD de 1966 (6). Tout dépend des résistivités maximales prévisibles pour la couche intermédiaire, car en ce qui concerne les deux milieux conducteurs qui la bornent au-dessus et au-dessous d'elle, leur présence n'est plus mise en doute : au-dessus, se trouvent évidemment les couches sédimentaires plus ou moins humides et les mers elles-mêmes ; au-dessous, se trouve (comme on peut le considérer comme définitivement établi maintenant) la couche à haute conductibilité dite "couche conductrice intercalaire" (7), que l'on situe dans le Manteau Supérieur à une profondeur assez variable qui, sous les océans, pourrait n'être que de deux ou trois dizaines de kilomètres (alors qu'on la situe entre 40 et 100 km en diverses régions continentales) et présente une résistivité aussi faible que 30 ou 40 ohm.m (8) et (9). Pour que les propriétés du guide puissent se manifester, il conviendrait de pouvoir tabler sur une résistivité au moins égale à 10^8 ohm.m pour la couche qui le constituerait.

Le point le plus délicat, et le plus douteux, reste celui de l'injection des fluctuations électromagnétiques externes à l'intérieur de la couche. Il faut pour cela qu'une masse compacte et suffisamment résistante puisse assurer la liaison électromagnétique entre d'assez vastes portions du sol continental et les portions intéressées du Manteau Supérieur. De telles masses existent, la preuve de ce fait pouvant être considérée comme établie par le succès même des déterminations de la couche conductrice intercalaire (du Manteau Supérieur), obtenues par la méthode des sondages profonds magnéto-telluriques. En effet, si ces sondages ont pu donner des résultats affirmatifs c'est, obligatoirement, que les ondes électromagnétiques naturelles (venant de l'extérieur de la Terre : cavité Terre-Ionosphère, Ionosphère, Magnétosphère, etc.) qui constituent les signaux d'excitation utilisés exclusivement dans ce type de sondages, avaient pu atteindre cette couche conductrice intercalaire, donc - à fortiori - les couches très résistantes formant le guide d'ondes recherché (s'il existe). Le problème du choix des sites convenant à une exploration magnéto-tellurique profonde du Manteau Supérieur et de ceux qui permettraient une injection de signaux naturels dans ce guide, est donc bien unique dans son principe. Il y a cependant une distinction importante à faire dans les deux faces de cette question : le géophysicien qui désire mettre en oeuvre un sondage magnéto-tellurique profond peut se contenter d'une étendue relativement moyenne (domaines linéaires de quelques centaines de kilomètres) pour la région de surface de haute résistivité convenant à la pénétration des ondes (puisqu'il capte à un même site les effets "aller-retour", si on peut ainsi s'exprimer, des signaux d'excitation ; au contraire, s'il s'agit d'escompter une injection suffisamment efficace de ces mêmes ondes dans un guide sub-terrestre de grande étendue, de très larges surfaces sont requises pour que cette injection puisse mettre en jeu des flux énergétiques suffisants. De telles surfaces, ayant les ordres de résistivités requises, existent bien en diverses régions du Globe, mais jusqu'à présent, les campagnes du bathyscaphe n'ont pas eu lieu à proximité, ce qui aurait facilité la recherche de l'effet envisagé. La campagne la plus favorable à ce sujet a été celle de 1967 au Japon - de vastes régions du Nord-Est de la Sibérie pouvant constituer la zone d'injection (avec des résistivités superficielles de l'ordre de 10^3 ohm.m). Le "bouclier canadien", le massif du Hoggar en Afrique, de vastes portions de l'Australie, devraient pouvoir assurer une bonne pénétration, avec des résistivités superficielles pouvant atteindre 3.10^5 ohm.m . Des zones d'injection encore plus efficaces doivent être constituées par les grandes carapaces glacières recouvrant le Groenland et le Continent Antarctique, avec des résistivités de l'ordre de 10^7 ohm.m pour les masses de glace, que l'on peut supposer raccordées directement à des masses granitiques sous-jacentes de résistivités comprises entre 10^6 et 10^7 ohm.m . Mais des lieux de plongées commodes ne se trouvent pas à proximité.

Nous résumerons la discussion précédente en remarquant que l'existence d'un guide d'ondes pseudo-horizontal pourrait être considéré comme le prolongement latéral de la pénétration suivant la verticale des ondes électromagnétiques naturelles servant à la prospection magnéto-tellurique profonde. A périodes (ou fréquences) égales pour les ondes en cause, on doit donc s'attendre à trouver des distances de propagation horizontale ayant au moins le même ordre de grandeur que les profondeurs de pénétration verticale atteintes, c'est-à-dire une centaine de kilomètres. En fait, on est en droit d'espérer une propagation dans le guide horizontal sur des distances beaucoup plus élevées; d'une part, à cause des résistivités plus grandes, d'autre part, parce que la propagation dans un guide - donc avec parois réfléchissantes - donne, à résistivités et périodes égales, des distances de propagation plus lointaines que celles imposées par la simple considération du "skin effect", valable pour des ondes planes se propageant dans un milieu présentant de vastes dimensions latérales.

Nous retiendrons aussi de cette comparaison entre notre problème de propagation et celui des sondages magnéto-telluriques profonds, des données utiles concernant l'ordre de grandeur des fréquences à utiliser. On trouvera, en particulier, dans les abaques établis par H. FOURNIER (10), la détermination de ces fréquences en fonction des résistivités de surface admises pour les régions d'injection, et des profondeurs supposées nécessaires pour atteindre le guide d'ondes sub-terrestre. On verra que, si on laisse de côté le cas, particulièrement avantageux d'une pénétration en surface à partir d'un glacier, ce qui conduirait à une fréquence de l'ordre de 100 Hz pour atteindre une profondeur minimale de 70 km, des fréquences inférieures à 1 Hz (c'est-à-dire des périodes supérieures à la seconde) paraissent nécessaires. Ceci semble devoir réduire notre champ d'action pour la recherche d'une émission par le guide qui serait détectée au fond des mers, à celui des variations magnétiques naturelles dites "rapides", comprenant toute la gamme des phénomènes pulsatoires plus ou moins réguliers dont l'enregistrement à la surface du Globe rentre maintenant dans la routine d'un grand nombre d'observatoires. Certaines de ces pulsations sont quasi-permanentes (si on considère leurs diverses bandes de fréquences), d'autres seulement épisodiques. Il conviendrait de leur ajouter la plupart des variations de plus grandes amplitudes liées aux perturbations magnétiques (naturelles) de toutes sortes, notamment aux "baies" - ou orages magnétiques élémentaires - et aux grands orages magnétiques mondiaux.

Si l'on se reporte à nos expériences passées, on se rend compte, à la lumière de nos connaissances actuelles, que notre choix de bande passante - donc de phénomènes - n'était pas parfait, l'ayant axé sur des fréquences trop élevées (donc, ayant fait preuve d'un "optimisme" que l'on peut trouver maintenant exagéré) : nos plongées de Porto-Rico étaient dévolues à la recherche des pertes (toujours par le fond de la mer) du 60 Hz des réseaux de distribution d'énergie du continent américain ; celles des campagnes

suivantes ont été orientées - suivant une suggestion de H. FOURNIER (11) - sur la recherche des fréquences résonance de Schumann, c'est-à-dire sur les possibilités d'un couplage entre la résonance de la cavité externe Terre-Ionosphère et la "cavité" électromagnétique sub-terrestre dont nous essayons de mettre en évidence l'existence. Ceci nous a conduits à faire descendre en fréquence les possibilités de notre appareillage, de façon à être à même d'observer la résonance fondamentale (sur environ 8 Hz) et les "supérieurs" (ou pseudo-harmoniques", sur 14, 20, 26, 32 Hz, etc.) susceptibles de se présenter. Ceci a été réalisé, en particulier, en passant du type d'enregistrement sur bande magnétique dit "direct" (qui ne permet guère de descendre en fréquence au dessous d'environ 30 Hz) à un enregistrement en modulation de fréquence ("MF"). (Remarquons que, de toute façon, il eut été impossible, en pratique, de prolonger lors des campagnes de Grèce et de Madère, nos essais de Porto-Rico axés sur les fréquences des réseaux d'alimentation en énergie électrique, car s'il a été relativement aisé - par des analyses spectrales faites au laboratoire, en France - de rechercher la présence d'un éventuel signal sur 60 Hz sur les bandes magnétiques enregistrées à Porto-Rico, il eut été tout à fait illusoire d'espérer pouvoir décider - en continuant à faire les dépouillements en ce même laboratoire - si un signal sur 50 Hz avait été, ou non, collecté et enregistré sur ces mêmes bandes, en Grèce ou à Madère. Il aurait donc fallu, si nous avions voulu pousser cette question, compléter parfaitement la symétrie des opérations en faisant faire les analyses spectrales de nos enregistrements dans un laboratoire américain alimenté en énergie électrique exclusivement sur 60 Hz !).

Passons aux résultats en ces matières : En ce qui concerne le 60 Hz , la réponse expérimentale a été très nettement négative. Nos enregistrements de Porto-Rico ne portent aucune trace de 60 Hz, ceci jusqu'au seuil détectable de 2.10^{-15} watt/m^2. D'ailleurs, même en surface, le 60 Hz issu du Continent Américain (par ses côtes) est très rapidement courtcircuité par la mer à une distance de ces côtes ne dépassant pas une vingtaine de kilomètres. Il est donc géographiquement inexact de considérer que la surface de notre Globe soit polluée dans sa plus grande part par les pertes d'énergie électrique d'origines industrielles ou humaines, que ce soit sur 60 Hz ou sur 50 Hz. L'idée contraire, que nous avions avant que nos mesures ne nous amènent à cette conclusion, venait de ce que, effectivement, la plupart des lieux où un expérimentateur - physicien , géomagnéticien, etc. - désire en général s'établir commodément pour faire ses mesures ou observations délicates, sont presque toujours pollués à un degré tel qu'il est difficile d'en protéger efficacement ces mesures. Mais, abstraction faite de ces commodités, et raisonnant dans un concept de pure géophysique, nous pourrions constater que toute la surface des mers et leur sein même, si on fait exception de quelques dizaines de kilomètres au voisinage des côtes, échappent encore, actuellement, à ces perturbations. Ceci ne veut pas dire qu'il soit toujours commode d'en profiter; sans oublier que les expérimentateurs eux-mêmes apportent souvent, par la mise en oeuvre d'installations électriques de fortune, des perturbations localisées mais d'un niveau élevé.

Quant aux oscillations correspondant à la résonance de Schumann, les plongées des deux campagnes de Grèce (1965) et de Madère (1966) ont été tout spécialement orientées en vue de leur détection, ainsi que les analyses spectrales les plus poussées qui ont été faites ensuite au laboratoire. Malgré cela, il est difficile d'apporter une conclusion parfaitement nette. Indépendamment des soins que nous avions donné à ces mesures, deux circonstances défavorables rendaient, en effet, les signaux que l'on pouvait attendre plus faibles que ceux, qu'en d'autres circonstances, on pourrait essayer de capter : d'une part, l'éloignement trop grand des zones de plongées des régions continentales les plus propices aux injections électromagnétiques venant de l'extérieur ; d'autre part, l'absence de mesures sur fonds rocheux. Les spectres d'énergie obtenus à partir des enregistrements montrent presque tous une légère bosse entre 24 et 26 Hz - qui pourrait ainsi être la trace du quatrième harmonique de la résonance de Schumann - mais l'absence du fondamental et des harmoniques précédents rend cette conclusion incertaine. Lors des plongées de la campagne du Japon, les circonstances géographiques et géologiques étaient, en principe, plus favorables, mais les enregistrements qui - pour d'autres raisons - avaient été faits en "direct" et non en "modulation de fréquence", ont été plus difficiles à analyser avec sûreté dans la bande de fréquence intéressée et, de ce fait, n'ont pas pu nous apporter de conclusion plus définitive. On peut retenir de cet examen que - en dehors de "raies" perturbatrices dont l'origine artificielle est maintenant bien établie (et qui - ainsi bien connues - ne sont plus guère gênantes pour nos recherches, ne serait-ce que par leur finesse même (leur inconvénient le plus sérieux est de provoquer des saturations des amplificateurs d'entrée si on n'a pas réussi à les filtrer convenablement), un certain nombre de "bosses", dont l'origine paraît être naturelle, se retrouvent à place à peu près fixe dans les analyses spectrales de nos enregistrements, mais ceci avec des intensités très variables qui - quand ces intensités sont trop basses - les fait passer au-dessous des seuils de bruit aléatoire que comportent également nos enregistrements (soit le bruit ultime de nos appareillages, soit des bruits naturels sur lesquels nous reviendrons plus loin). Dans la mesure où l'on peut voir dans ces "bosses" les effets de l'excitation d'ensemble de tout le Globe Terrestre par cette activité électromagnétique externe d'origine météorologique responsable également de la résonance de Schumann, on peut comprendre que - la "cavité électromagnétique" interne supposée ne pouvant avoir, dans aucune hypothèse vraisemblable, des qualités de résonance comparables à celles de la cavité externe - le couplage, direct ou indirect, s'il existe entre ces deux "cavités", ne doit guère pouvoir produire des signaux bien organisés dans la cavité interne. Ce couplage reste, cependant, une source de bruit dont le niveau peut être nettement supérieur aux seuils, très bas, de bruit naturel auxquels on pouvait s'attendre à grande profondeur.

Bien qu'en cette matière les évaluations quantitatives restent précaires indiquons, à titre d'exemple, comment nous pouvons déterminer, à partir du résultat des analyses spectrales, les ordres de grandeur des énergies mises en jeu correspondant à la bosse centrée (approximativement) sur 25 Hz . Les spectres obtenus donnent, en

$(\text{gauss})^2$/ Hertz la répartition spectrale de la puissance captée.

Prenant un résultat moyen de plongées, nous trouvons ainsi une bosse s'étalant entre 23 et 27 Hz , dont l'ordonnée moyenne est de l'ordre de

(1 / 100 de gamma)^2 , soit (10^{-7} gauss)^2, (le "gamma" - " γ " - unité usuelle des géomagnéticiens, valant 10^{-5} gauss) . Nous en déduisons la valeur $10^{-14} \times 4 \times 1/8\pi$ erg/cm^3 pour la densité énergétique correspondante (tenant compte de la bande passante de 4 Hz suivant laquelle s'étale la bosse), valeur qu'il suffira de multiplier par la vitesse de propagation moyenne dans l'eau de mer, pour les ondes de la fréquence considérée, pour - tenant compte des unités utilisées - obtenir le flux d'énergie correspondant.

Pour la fréquence de 25 Hz la vitesse de propagation, déduite de la formule :

$v = (2\omega/\sigma\mu)^{1/2}$ valable dans tout système e.m. rationalisé, dans laquelle v est la vitesse de propagation, ω la pulsation, σ la conductivité, μ la perméabilité (prise ici avec le facteur 4π provenant de la rationalisation), prend la valeur $9.\ 10^3$ m/s .

En exprimant toutes les données en unités M.K.S.A. , nous obtenons ainsi pour le flux d'énergie (plus exactement, il s'agit d'un <u>flux de puissance</u>) correspondant à l'ensemble de la bosse, l'expression numérique suivante :

$$(\ 10^{-14} \times 4 \times 1/8\pi \times 10^{-1}\ )\ \text{joule/m}^3 \times (\ 9.\ 10^3\ )\ \text{m/s} \quad \text{soit} \quad 1{,}4\ .\ 10^{-12}\ \text{watt/m}^2$$

On voit que la valeur obtenue est largement supérieure à l'ordre de grandeur des flux de puissance détectables par nos enregistrements. Bien entendu, les conclusions précédentes comportent une large part d'incertitudes dues essentiellement au fait que - dans l'ignorance des mécanismes exacts et des causes précises des fluctuations enregistrées - il n'y a pas qu'une voie unique pour déboucher sur des conclusions numériques.

<u>Bruits sismiques - Bruit blanc rayonné au voisinage du fond</u>. La conclusion précédente s'applique, en particulier, à divers bruits que nous avons enregistrés, soit posés sur le fond, soit en nous approchant du fond, qui - bien que dépassant nettement les seuils limites, valables, que pouvaient assurer nos enregistrements - n'ont pu être étudiés suffisamment. Nous nous limiterons donc, en ce qui les concerne, à de brèves données .

Les plus précises concernent, non pas un bruit proprement dit, mais un balancement rythmique auquel est soumis le bathyscaphe posé sur le fond (même quand il appuie sur ce fond avec un poids effectif de plusieurs centaines de kilos). Ces oscillations sont pseudo-périodiques, les périodes étant comprises entre 4 et 6 secondes. Ce phénomène n'a été mis en évidence que lors de plongées sur des fonds de Méditerranée au large de Toulon (profondeurs de 2000 et 2500 mètres) pour lesquelles l'appareillage utilisé permettait leur mise en évidence, mais il est probablement général et attribuable à l'agitation microsismique.

Ainsi que nous l'avons exposé lors du Symposium AGARD de 1966 (6) - rejoignant les résultats donnés par E.F. SODERBERG à cette même réunion - un bruit e.m. de type incohérent apparaît quand le bathyscaphe se rapproche du fond (quelle que soit la profondeur de celui-ci) et persiste même après plusieurs heures d'immobilité sur le fond. (Nous faisons abstraction, ici, d'un bruit artificiel provoqué par les nuages de vase soulevés par l'approche du bathyscaphe). Ce bruit, qui a les caractères généraux, plus ou moins parfaits, d'un <u>bruit blanc</u>, peut, dans une certaine mesure, être considéré comme le renforcement du bruit qui accompagne d'une façon quasi-permanente le bathyscaphe en plongée. (Bien que ce bruit ait tous les caractères d'un phénomène aléatoire, il y a corrélation entre ses deux composantes enregistrées, respectivement, par voie magnétique - sonde - et tellurique - électrodes sur perches - ce qui, les deux voies étant traitées en toute indépendance d'appareillage, confirme leur caractère "externe", naturel). Il y aurait donc là un effet de renforcement (par exemple par réflexion) par le fond.

Une autre portion de ce bruit paraît avoir son origine typiquement sur le fond lui-même. Nous ne développerons pas ce sujet ici, mais nous rappellerons les conclusions auxquelles nous étions arrivés précédemment (3), (4), à savoir : qu'une partie de ce bruit doit être imputable aux courants marins (hydrodynamiques) toujours présents sur le fond - ainsi que le met en évidence l'observation directe - et aux micro-tourbillons qui les accompagnent ; qu'une autre partie pourrait vraisemblablement être causée par l'activité - à la fois chimique, physico-chimique, et biologique - qui anime l'interface sol-mer, interface particulièrement active sur certains fonds sédimentaires, ou sur des fonds où affleurent des minerais (12).

D'une façon globale, on peut évaluer - en fonction des "résidus spectraux de caractère aléatoire" explicités par nos analyses spectrales - à un niveau de l'ordre de 10^{-14} à 10^{-13} watts/m^2 les flux de puissance attribuables à ces bruits. (Dans le cas d'effets dus à des gisements de minerais ces niveaux pourraient être beaucoup plus élevés).

<u>Bruit qui aurait sa source dans la masse même des mers</u>. C'est là un aspect important de notre problème général et il conviendrait, en conséquence, d'être à même de l'étudier soigneusement. Cependant, ceci nous entraînerait très au-delà des limites de notre exposé par le fait que la discussion qui devrait être mise en oeuvre devrait aborder et tenir compte d'un nombre important de phénomènes physiques dont plusieurs ne sont que très imparfaitement éclaircis au stade du laboratoire. D'autre part, nos propres expériences - une fois élagués certains phénomènes perturbateurs dont la manifestation nous avait intrigués - ne peuvent pour l'instant apporter de contribution précise sur ce point. Les phénomènes perturbateurs auxquels nous faisons allusion sont les raies fines que nous obtenions dans nos analyses spectrales (y compris celle sur 40 Hz environ). L'origine de ces raies a été entièrement éclaircie maintenant (raies de résonance de diverses parties du bathyscaphe, dont la sphère-habitacle) et il n'y a pas à la rechercher dans des effets naturels. Ceci ne signifie pas que de tels effets n'existent pas et il est possible qu'ils contribuent à la constitution du <u>bruit blanc</u> dont nous nous sommes occupés précédemment. Sans pousser plus loin cet examen, signalons parmi les causes dont les effets seraient susceptibles d'être appréciables : d'une part, l'agitation <u>mécanique</u>, aléatoire, que l'on sait maintenant exister au sein des mers (courants de convection, turbulence, tourbillons, etc. (13)); d'autre part, les irrégularités auxquelles pourraient être soumises des nappes de courants <u>électriques</u> qui - suivant l'hypothèse de SHULEIKIN (5)(14) - circuleraient à certaines profondeurs dans les mers (principalement entre 600 et 1000 m de profondeur). Nous reviendrons sur ce deuxième effet, mais à un autre point de vue. En ce qui concerne le premier type d'action, il s'agit d'effets mécaniques (hydrodynamiques), mais on sait que, se produisant en présence de la partie fixe du champ magnétique terrestre (qui, étant continue, peut pénétrer à toute profondeur) ils se transformeront par induction en effets électriques et électromagnétiques. Les mesures directes, cinématiques, étant elles-mêmes très délicates, il se pourrait que des mesures électromagnétiques spécialement conçues à cette fin, puissent les épauler utilement.

<u>Bruit en provenance de l'interface air mer</u>. Nous en distinguerons deux types, de natures et d'importances très différentes. Il y a d'une part, le bruit engendré par l'interface elle-même, principalement par toute la gamme des vagues ; d'autre part, le bruit qui vient des régions situées au-dessus de l'interface (atmosphère, ionosphère, magnétosphère, espace interplanétaire, etc.) et qui la traversant de

haut en bas pénètrent dans la mer.

Le premier de ces effets a été étud' par plusieurs auteurs dont WEAVER (15),et WARBURTEN et CAMINITI (16). En particulier, WEAVER a montré que, dans le cas de la grande houle océanique, l'effet était plus important qu'on ne l'avait estimé précédemment. Cependant, ainsi que le remarque DUFFUS (17), même des vagues assez importantes ne produisent que des champs magnétiques très faibles (d'une fraction de gamma) dès que l'on dépasse une profondeur d'une centaine de mètres : 0,05 γ pour des vagues de 2,5 m de haut et de 8 s de période. Il convient cependant de distinguer,dans cet examen de l'effet de profondeur, entre le cas d'une descente au-dessus d'un fond profond et celui où l'on rejoint rapidement un fond. Les résultats des calculs ne s'appliquent - sous leur forme première - qu'au premier de ces deux cas (dans lequel on peut négliger l'influence du fond puisqu'il reste toujours très au-dessous des profondeurs atteintes. Dans le deuxième cas, nous retrouvons une influence considérable du fond (à condition qu'une fraction appréciable des signaux lui parvienne) qui agit en déformant considérablement l'onde de perturbation pour l'étaler parallèlement à lui-même, c'est-à-dire horizontalement dans le cas le plus simple. Dans ces conditions, un renforcement considérable (plus de dix fois) de la perturbation (mesurée le long du fond) se manifeste généralement. Ce cas est important, car c'est celui qui viendra en application chaque fois que des installation auront été faites à même le fond d'une mer peu profonde : un effet perturbateur pourra ainsi se manifester jusqu'à plusieurs centaines de mètres de profondeur.

Le bathyscaphe, engin conçu pour les grandes profondeurs, ne convient pas - ne serait-ce que par l'utilisation désastreuse de ses budgets de fonctionnement qui en résulterait - pour étudier ces conditions relatives aux faibles profondeurs. A ce point de vue des explorations en soucoupes seraient plus indiquées ainsi que cela a été étudié par DUFFUS et LAUNAY (17). Sans attendre ces possibilités nous avons tenté, au cours de l'été 1966 , de mettre en place une expérimentation fixe permettant de nous initier à ces problèmes. La mise en oeuvre en a été assurée par L. LAUNAY qui a pu ainsi obtenir l'enregistrement complet de l'orage magnétique mondial des 29/30 Août 1966 , à partir d'un capteur (une sonde analogue à celle que nous utilisons en bathyscaphe) immergé par environ 60 m de fond en rade de Villefranche. Quelques extraits de cet enregistrement sont donnés en ANNEXE. On y remarque, en dehors des variations importantes (et parfois abruptes) dues à l'orage (il s'agit de la composante horizontale H parallèle au méridien magnétique) des fluctuations pulsées, quasi permanentes, d'une période voisine de 7 secondes, et d'une amplitude de l'ordre de 0,15 γ . Un dépouillement plus détaillé portant sur les trois journées enregistrées sans discontinuité (celles des 29, 30 et 31 Août) nous montre que l'amplitude de ces oscillations croît dans l'ensemble avec leur période (avec cependant assez d'irrégularités dans les résultats d'observations individuelles), ce qui est un indice important nous conduisant à penser que ces pulsations sont un effet direct, magnétique, de la houle de faible amplitude (pour les journées considérées), mais régulière et d'assez longue période, qui se propageait dans la baie. Ceci est contraire à certaines premières conclusions (voir notamment la réf. 17 , p. 17, loc. cit.) d'après lesquelles l'effet observé aurait été créé par une action mécanique des vagues (ou de la houle) sur la sonde ... ce qui est par ailleurs peu probable la sonde ayant été fixée rigidement par des colliers sur un gros bloc de ciment immergé en même temps qu'elle. D'autre part, une action micro-sismique naturelle paraît exclue car elle ne pourrait donner que des amplitudes d'un ordre de grandeur plus faible et des périodes un peu plus courtes que celles observées.

Le tableau suivant résume, en les classant en trois catégories, les résultats de ces observations, et permet leur comparaison avec les valeurs déduites des calculs de WEAVER (15) en les appliquant à la profondeur et aux périodes concernées et en les rapportant à une amplitude nominale de la houle de 0,50 m . Cette dernière valeur pourra paraître très faible et, de plus, il est évident que nous ne pouvons pas réduire notre examen à une relation unique entre l'effet magnétique de la houle et sa période, tout en supposant son amplitude constante. Mais, en l'absence d'enregistrement de la houle au cours de nos trois journées d'expérience, et tenant compte de ce que la mer dans la baie était particulièrement calme (par temps pluvieux et vent du Sud-Est) il paraît assez valable d'admettre que l'amplitude des effets magnétiques engendrés par la houle résiduelle était surtout sous la dépendance de la période exacte de celle-ci et non sous celle d'une variation d'amplitude de cette houle. Les diagrammes établis par WEAVER (cf. réf. 15, fig. 7 bis) montrent d'ailleurs clairement que l'effet magnétique est beaucoup plus sensible à la période de la houle qu'à son amplitude (les calculs font d'ailleurs intervenir des relations exponentielles dans le premier cas, et simplement linéaires dans le second).

	VALEURS OBSERVEES	VALEURS CALCULEES pour les mêmes périodes et pour une amplitude nominale de 0,50 m
Périodes (s)	Amplitudes en gammas	Amplitudes en gammas
6,25	0,19	0,015
7,14	0,15	0,04
8,33	0,20	0,11

Les amplitudes observées sont donc très supérieures aux amplitudes calculées. Evidemment, cela peut être dû à l'amplitude nominale adoptée arbitrairement pour la hauteur de la houle. Cependant il serait difficile d'admettre - pour arriver à égaliser plus ou moins les ordres de grandeur mesurés et calculés pour les effets magnétiques - que la houle à l'intérieur de la baie de Villefranche ait, par mer calme, dépassé les hauteurs de l'ordre du mètre qui seraient nécessaires pour cela. De plus, les valeurs mesurées et calculées ne sont pas proportionnelles les unes aux autres, ce qui fait que pour les périodes les plus courtes - pour lesquelles l'écart est le plus grand - il faudrait des amplitudes de houle de plus de 3 m . Nous pensons donc que cette comparaison des deux séries de valeurs met en évidence "l'effet de fond" dont nous avons parlé précédemment. Il reste cependant à expliquer pourquoi cet effet de fond serait plus marqué pour les courtes périodes que pour les longues, à moins d'admettre que - sans avoir recours, comme nous venions de l'envisager, à des ordres de grandeur absolus de la houle nettement plus forts que ceux que nous avons supposés - l'amplitude de la houle de courte période ait été, en moyenne (ceci n'étant pas forcément un cas général et ne s'appliquant, peut-être que pour les trois journées considérées) plus forte que celle de la houle de période plus longue. Il y a là tout un ensemble de déductions dont certaines peuvent conserver un aspect paradoxal, mais qui illustre quand même le rôle important joué par les fonds.

Ces expériences - ou d'autres analogues - devraient être reprises pour arriver à préciser ce rôle. Il conviendrait d'opérer dans une gamme plus étendue de profondeurs et - si possible - de fréquances.

Bruit provenant des régions situées au-dessus de l'interface air-mer. Ce sujet est important, mais comme il se trouve traité dans un grand nombre d'articles traitant du "Magnétisme Externe" et constitue la matière de base des chapitres sur les "variations géomagnétiques" qui figurent dans la plupart des traités de Magnétisme Terrestre, nous ne ferons que quelques brèves remarques à son sujet. Le lecteur pourra consulter, par exemple, le précis récent de J. JACOBS (18) ou, sous une forme résumée mais adaptée à notre problème, la communication (19) présentée l'an dernier par l'auteur. Nous tiendrons seulement à rectifier une idée quelque peu inexacte - ou tout au moins incomplète - que l'on voit souvent exposée par des spécialistes de l'électromagnétisme marin, non magnéticiens, quant aux sources principales des actions électromagnétiques perturbatrices pénétrant dans la mer à partir de l'atmosphère. Ils réduisent la plupart du temps ces sources à une seule : les "atmosphériques" ... (ces derniers étant, évidemment, envisagés sous leurs diverses formes et comprenant, en particulier, les oscillations de Schumann dont nous avons déjà parlé). On reconnaît là le souci majeur des spécialistes des transmissions radiotélégraphiques aériennes, qui- opérant à des fréquences en général de plusieurs kilo-Hertz - ne sont gênés qu'exceptionnellement, dans leurs transmissions, par les perturbations proprement magnétiques.

Le problème est très différent pour les transmissions e.m. sous la surface des mers : comme il faut alors s'adresser à des fréquences extrêmement basses, qui atteignent celles des variations géomagnétiques dites "rapides" (disons, de 1/100 Hz à 100 Hz), la pénétration dans la mer de ces variations naturelles doit être prise en considération. Pour fixer les idées sur leur importance,donnons quelques ordres de grandeur des amplitudes qui peuvent être ainsi mises en jeu ; comme notre élargissement du sujet à partir des fréquences radio va dans le sens des fréquences les plus basses, c'est également dans ce sens que nous allons procéder.

Nous partirons des fréquences de résonance de Schumann, domaine déjà traité. Dès que nous arrivons à des fréquences ne dépassant pas quelques Hertz nous passons des phénomènes d'origine météorologique à ceux plus spécifiquement géomagnétiques. La frontière entre ces deux domaines est d'ailleurs fluctuante, les phénomènes magnétiques montant en fréquence quand s'élève l'activité qui les concerne. (A noter que nous n'avons pas retenu dans notre examen,des émissions naturelles dans la gamme "T.B.F." - de quelques centaines de Hertz à 20 ou 30 Kilo-Hertz - dont les relations avec les "situations géomagnétiques" sont certaines, mais qui, étant donné l'ordre de grandeur de leurs fréquences, ne pénètrent pas d'une façon tant soit peu appréciable au-dessous de l'interface air-mer). Nous trouvons alors toute la gamme des pulsations "régulières" (nomenclature "pc" - "pulsations continues"- allant de pc 1 autour de la fréquence de 1 Hz , jusqu'à pc 5 s'étendant jusqu'à des périodes de 600 s) et celle des "irrégulières" (nomenclature "pi", comprenant les pi 1 - de 1 à 40 s - et les pi 2 - de 40 à 150 s). Les amplitudes que peuvent atteindre ces pulsations s'étagent entre quelques centièmes de gamma pour les pi 1 (d'ailleurs peu fréquentes), jusqu'à plusieurs dizaines de gammas pour les pc 5 et les pi 2 , en passant par quelques gammas pour les plus fréquentes, pc 3 et pc 4 , dont les périodes dominantes sont alors, respectivement, de l'ordre de 25-30 et 45-55 secondes. En fonction des données précédentes, il devient facile - par application de la théorie classique électromagnétique (équations de Maxwell) - de calculer les niveaux susceptibles d'être atteints, dans telle ou telle bande de fréquences, à des profondeurs données, par les variations électromagnétiques issues de variations géomagnétiques naturelles telles que nous les avons envisagées. On retiendra comme élément favorable pour ces calculs, le fait que la plupart de ces variations nous parviennent à partir de la très haute atmosphère (ionosphère, magnétosphère) dans de bonnes conditions de cohérence couvrant de vastes étendues géographiques (organisation en ondes planes); bien que ce fait ait été souvent controversé il est vérifié dans la grande majorité des cas (19). Par contre, pour savoir si telle ou telle manifestation (ou "émission") se produit effectivement à un instant déterminé, il conviendrait de s'adresser à des sources d'information spécialisées (c'est un des rôles dévolus aux observatoires géomagnétiques).

En plus des pulsations , d'autres types de variations affectent plus ou moins fréquemment le champ magnétique terrestre. Nous citerons notamment les "baies magnétiques" (de durées de l'ordre de l'heure et d'amplitudes pouvant dépasser 100 γ ... ces amplitudes pouvant être beaucoup plus fortes dans les régions de hautes latitudes) et les "orages magnétiques" , notamment les grands orages mondiaux, qui peuvent s'étendre sur plusieurs jours et dépasser 1000 γ en amplitudes. Aussi bien "baies" qu' "orages" ont des compositions spectrales souvent complexes - que l'on sait déterminer à partir de leurs enregistrements sur bandes magnétiques faits dans certains observatoires - dont il conviendra de tenir compte pour calculer (toujours par application des lois de l'électromagnétisme classique) leur pénétration dans la mer.

Certaines variations naturelles encore plus lentes (notamment les variations diurnes "S_q" avec leur cas particulier de l' "électrojet équatorial") sont susceptibles de jouer un rôle important - bien qu'on ne puisse guère les considérer comme un "bruit", mais étant donné leur grande profondeur de pénétration dans la mer - dans l'électromagnétisme marin et ses applications (notamment en ce qui concerne la méthode de sondage "magnéto-tellurique"). Nous allons y revenir dans notre CONCLUSION.

Cas des courants électriques marins - Hypothèse de SHULEIKIN. Nous avons insisté à plusieurs reprises sur le fait que les calculs de pénétration de bruit e.m. dans les profondeurs marines se faisaient suivant les lois de l'électromagnétisme classique. Ceci ne veut pas dire que tout soit prévisible - nous l'avons bien vu en ce qui concerne les sources de bruit émanant des fonds - car la mise en équation des phénomènes, parfois très peu connus, qui se présentent à notre analyse, est au moins aussi importante que la conduite des calculs. Cet aspect des recherches en électromagnétisme marin est particulièrement valable en ce qui concerne l'influence des courants électriques en mer, telle qu'elle a été postulée il y a une quinzaine d'années par V.V. SHULEIKIN et son Ecole (5 loc.cit.)(20,21).Les hypothèses de SHULEIKIN ont une double base expérimentale : d'une part, les anomalies de la distribution de la déclinaison magnétique à la surface du Globe, anomalies qui ne paraissent qu'imparfaitement expliquées par des causes totalement internes (intérieures à la partie solide de la Terre) , ou ionosphériques ; d'autre part, l'augmentation très importante des différences de potentiel telluriques mesurées, à l'horizontale, à l'occasion de plusieurs campagnes océanographiques soviétiques (campagnes de l'"Ob" dans l'Océan Indien, du "Sedov" et du "Mikhail Lomonosov" dans l'Atlantique) quand on enfonce les électrodes à des profondeurs qui ont été comprises entre 250 et 900 mètres. SHULEIKOV a déduit de ces résultats de mesures telluriques que d'importantes nappes de

courants électriques devaient circuler dans la plupart des océans avec des densités croissant en fonction de la profondeur (tout au moins jusqu'à un millier de mètres). De plus, il a vu dans la présence de ces courants une possibilité d'expliquer - au moins en partie - les anomalies de la distribution de la déclinaison. Des cartes mondiales de ces courants électriques sous-marins et des anomalies de la déclinaison ont pu ainsi être esquissées et présentent une certaine harmonie. Les densités de courant mises en jeu sont de l'ordre de $3{,}6 \cdot 10^{-4}$ A/m^2 vers 250 m de profondeur et de $6 \cdot 10^{-4}$ A/m^2 vers 700 m (ces valeurs ne sont données ici qu'à titre indicatif des ordres de grandeur, car il s'agit en fait de données déduites des expériences - en tenant compte également des conductivités locales mesurées indirectement à partir de la température et de la salinité des couches océaniques correspondantes - et elles sont fonction de diverses données géographiques. Quant aux anomalies dans la distribution de la déclinaison , ce sont celles qui - à partir de mesures en surface - figurent dans les recueils de données magnétiques. Cependant, un autre aspect, nouveau, de la question, consiste en ce que l'on peut prévoir que la déclinaison magnétique devrait présenter, au-dessous de la surface des mers, une variation plus ou moins systématique en fonction de la profondeur. Il s'agirait là d'un fait qui - s'il s'avérait exact - pourrait jouer un rôle important dans les opérations de navigation, de géodésie et de topographie sous-marines (bien que les compas gyroscopiques puissent assurer, en principe, les mêmes opérations). Les collaborateurs de SHULEIKIN ont fait, également, des efforts expérimentaux pour éclaicir cette question, mais aucun résultat définitif n'a été publié à notre connaissance.

On trouvera dans les références (1) (2) (3) (4) et (6), les mesures que nous avons faites au moyen du bathyscaphe pour essayer de résoudre la première partie (nappes de courants) de ce problème. Pour l'instant nous n'avons relevé aucune discontinuité nette, systématique, des différences de potentiel telluriques mesurées, en fonction de la profondeur. Il est vrai que de grosses difficultés expérimentales, en passe d'être résolues, nous ont empêchés de tirer le meilleur parti des mesures faites au cours des premières centaines de mètres de descente en plongée (les plus intéressantes au point de vue considéré). Il est aussi possible que l'étude statistique - non encore faite à l'heure actuelle - du grand nombre de mesures analogues (enregistrées sous une forme digitalisée) faites au cours de la dernière campagne des Açores (par J. JARRY) nous apporte quelque précision à ce sujet.

3. CONCLUSIONS

Arrivés à ce stade de notre exposé nous devons nous demander sous quelle forme il paraît possible de répondre aux promesses contenues dans son titre et de donner au lecteur la possibilité de déterminer les niveaux caractéristiques et les seuils de bruit (d'origine naturelle) qu'il peut s'attendre à trouver au sein des mers, dans des circonstances données. Nous avons souligné ce dernier point car il résulte, d'une façon assez évidente, je pense, de l'examen de toutes les conditions de bruit que nous avons envisagées, que l'association des diverses circonstances possibles peut donner un nombre de cas tellement élevé, qu'il nous serait matériellement impossible de donner numériquement les seuils de bruit correspondant à chacun d'eux. Ceci tient, en particulier, à ce que - en dehors de l'influence bien définie, en général, de la profondeur (mais nous avons rencontré une exception si l'on tient compte de nappes de courant !) - la plupart des autres données sont sous la dépendance de divers états aléatoires (à notre échelle) de la nature. Nous avons donc cherché avant tout à permettre à ce lecteur d'effectuer lui-même son bilan numérique de bruit. Nous allons cependant faire à ce sujet quelques dernières remarques qui, nous l'espérons, éclaireront mieux les méthodes à employer, et devraient faciliter l'interprétation des résultats et leur utilité.

Tout d'abord, relativement à la notion de "bruit" elle-même, n'oublions pas qu'il s'agit d'un bruit naturel, que la manifestation correspondante n'est pas forcément d'un caractère aléatoire mais peut, aussi, être organisée, et qu'elle n'est pas, non plus, obligatoirement, une chose nuisible, certaines applications pouvant, au contraire, lui être rattachées. D'ailleurs, en ce qui concerne la détermination des seuils, elle peut se faire indépendamment de la nature nuisible, ou utile, du "bruit", sauf en ce qui concerne les marges d'erreur ou les approximations, qui ne seront pas discutées tout à fait de la même façon dans les deux cas.

Par contre, il sera indispensable dans la préparation des calculs, de bien séparer les données physiques - en général, d'origine expérimentale ou d'observation - relatives aux sources (localisation, extension, cohérence, composition spectrale de l'émission, etc.), de celles relatives aux conditions de propagation. Ce seront ces dernières que l'on pourra confier aux méthodes, et aux résultats, de l'électromagnétisme "classique". Ceci ne veut pas dire que ce qui concerne les sources (auquel il faudrait d'ailleurs ajouter, également, ce qui concerne les modes de réception) il faille mettre en défaut les équations de Maxwell ... , il suffit simplement de remarquer qu'elles n'ont rien à voir avec cette partie du problème. L'exemple le plus frappant de cette distinction qui s'impose nous est encore donné par l'hypothèse de SHULEIKIN sur les nappes de courant sous-marines : on ne peut prendre argument des équations de Maxwell pour démontrer que ces nappes de courant ne devraient pas exister (en particulier, le "skin—effect" ne leur est en aucun cas applicable), mais il faudrait pouvoir démontrer expérimentalement que les diverses conditions physiques requises - et assez compliquées - pour permettre l'établissement et la stabilité de tels courants (répartitions particulières de la température et de la salinité, donc des conductivités, en fonction de la profondeur), sont effectivement réalisées.

Venons en maintenant aux effets, bons ou mauvais, des bruits auxquels on peut s'attendre dans telle ou telle condition. Ces jugements de qualité dépendront non seulement des buts poursuivis, mais - essentiellement - (en dehors de l'effet, évident, des niveaux) de la double évolution, spectrale et temporelle, de ces bruits. Il y aura, par exemple, le cas, des bruits épisodiques (à faible probabilité d'occurence) tels que ceux causés par les orages magnétiques, que l'on pourra, en général, totalement éviter en dépit de leurs niveaux élevés. Ce sera aussi le cas des pulsations pc 1 (dont la "profondeur de pénétration" est de l'ordre de 250 m) qui, pour un instant quelconque, ont une faible probabilité d'occurence. Ce ne sera pas le cas des pulsations pc 3 (une profondeur de pénétration de l'ordre de 1000 à 1500 m , pour des périodes centrées plus ou moins sur 25 s) dont les probabilités d'occurence sont - de jour - supérieures à 1/2 . Il nous faudrait donc passer en revue tous les autres phénomènes analogues, et en déduire - en fonction de la profondeur - les probabilités d'avoir, sur telle ou telle fréquence, un niveau de bruit donné. Encore faudra-t-il tenir compte de la proximité éventuelle du fond.

Enfin, pensant maintenant aux applications, nous rappelerons l'exemple des sondages magnéto-tellu-

riques , qui seront pratiqués avantageusement à partir du fond s'il s'agit de déterminer les structures géologiques sous-jacentes. Ces sondages utilisant uniquement des signaux naturels, il convient qu'il en arrive encore à un niveau suffisant, pour les bandes spectrales à utiliser (elles-mêmes fonction des profondeurs sous-jacentes à explorer). Cela limite évidemment les possibilités, et d'autant plus que le fond à partir duquel on opère sera situé à une plus grande profondeur. Dans le cas des grands fonds, par exemple de 4000 m , c'est une onde de période d'environ 150 s qui arriverait sur le fond avec une atténuation de l'ordre de 1/e en amplitude (correspondant à la,dite,"profondeur de pénétration"). En conséquence, le sondage ne pourrait être fait qu'à partir d'une période dont la valeur ne serait pas une fraction trop faible de la précédente. C'est ainsi qu'une onde dix fois plus courte en période (15 s) n'arriverait sur le fond qu'affaiblie environ 25 fois en amplitude. Cette limitation du côté des courtes périodes empêchera de sonder efficacement les premières couches du sous-sol sous-marin et ceci d'autant plus qu'on aura à opérer à une profondeur plus importante. La solution qui consisterait - pour parer à cet inconvénient - à opérer à partir de la surface de la mer, serait encore moins avantageuse : on disposerait bien, au départ, de la totalité des émissions naturelles présentes - ceci dans toute leur bande de fréquances - mais l'absorption des ondes se produirait quand même et, cette fois, aussi bien sur le trajet de retour que sur le trajet aller. Nous pouvons conclure à propos de la méthode magnéto-tellurique, même mise en oeuvre à partir du fond, qu'elle demande l'emploi de détecteurs extrêmement sensibles , ceux justement qui seraient considérés comme susceptibles d'être "perturbés" par le "bruit" si - dans ce cas - ce bruit n'était pas justement le signal utilisé. Des premiers essais d'enregistrements magnéto-telluriques, destinés à déterminer les conditions expérimentales d'une mise en pratique ultérieure de sondages, ont été faits en Méditerranée à partir de l' "Archimède", au cours de deux plongées effectuées à des profondeurs de 2000 et 2500 m , avec la participation effective,pour l'une d'elles,de Mme V.A. TROITSKAYA de l'Institut de Physique du Globe de Moscou (Février 1966).

C'est ici l'occasion d'associer à cet exposé des travaux que nous avons pu faire et aux conclusions, modestes, que nous avons pu tirer dans ce secteur de recherche difficile, les autres membres de notre équipe : Mme L. LAUNAY qui, à partir de la station et de la rade de Villefranche, a pu procéder à un grand nombre de vérifications et de calibrages de notre appareillage - aussi bien celui de nos enregistrements que celui de nos analyses ; le Dr. S. W. LICHTMAN, qui était à l'époque "Senior Scientist" à la Hughes Aircraft Company en Californie et qui a permis une collaboration active Franco-Américaine dans ce domaine ; le Dr. J. DUFFUS, de Victoria, British Columbia, Canada, qui a pu passer une grande partie de l'année 1967 à la station de Villefranche et y conduire, en collaboration avec Mme Launay, toute une série d'expérimentations de contrôle dont j'ai tenu compte dans cet exposé, ainsi que d'une enquête approfondie sur les possibilités offertes par les"Soucoupes plongeantes" pour prolonger vers les faibles (ou moyennes) profondeurs nos expériences et nos mesures poursuivies avec l' "Archimède". Enfin, rappelons que J. JARRY, maintenant Chef de la Section Bathyscaphe du C.N.E.X.O., a assuré personnellement toutes les mesures des plongées des campagnes du Japon et des Açores.

REFERENCES

1. LAUNAY L., LICHTMAN S. W., SELZER E. — U.L.F. Environment of the Ocean Floor. N.B.S. Report 8815, Boulder, 1965.

2. SELZER E., LAUNAY L., LICHTMAN S. W. — Enregistrements E.M. à très basses fréquences, faits en bathyscaphe, en eaux profondes. AGARD Conference Proceedings N° 20 - " Sub-Surface Communications " (Paris, Avril 1966), pp. 595-606.

3. LAUNAY L., LICHTMAN S. W., SELZER E. — Electrical environment determinations at great ocean depths. I.E.E.E. Technical Proceedings, Ocean Electronics Symposium, Honolulu, Aug. 1966, Western Periodicals Co, Hollywood, Cal.

4. SELZER E. — Mesures électromagnétiques effectuées en mer profonde à bord du bathyscaphe ARCHIMEDE (Campagne de Grèce, 1965). Annales de l'Institut Océanographique, Tome XLVI, 1968, Fasc. 1, pp. 19-28.

5. SHULEIKIN V. V. — The Terrestrial Magnetic Field and the world Ocean. Dok. Akad. Nauk, vol. 76, N° 1, pp. 57-60, 1951.

   Telluric currents in the Ocean and Magnetic Declination. Dok. Akad. Nauk, vol. 119, N° 2, pp. 257-260, 1958.

6. " AGARD " CP No. 20 — Sub-Surface Communications. 12ème Symposium AGARD, Paris, 25-29 Avril 1966, 661 pages.

7. SODERBERG E. F. — Undersea ELF Measurements of the Horizontal E-Field to Depths of 300 meters. AGARD Conference Proceedings N° 20 - "Sub-Surface Communications", Paris, Avril 1966, pp. 453-470.

8. FOURNIER H. — Thèse de Doctorat d'Etat déposée à la Faculté des Sciences de l'Université de Paris, Juin 1970, Tome I (Texte, 122 pages) et Tome II (Figures, 136 pages).

9. LAUNAY L., TOUITOU J., GRENET G. — La conductibilité électrique du Manteau Supérieur. Annales de Géophysique, Tome 19, N° 2, Avril-Juin 1963, pp. 180-183.

10. FOURNIER H. — Thèse, loc.cit., Fig. 65, Tome II, p. 123.

11. FOURNIER H. — Communication personnelle, 1965.

12. DUFFUS H. J., LAUNAY L. — The Use of Diving Saucers for Measurements of the Electromagnetic Fields in the Sea. Rapport interne entre le Laboratoire de Géodynamique Sous-Marine de Villefranche-sur-Mer et l'Institut de Physique du Globe de Paris, Avril 1967, 49 pages (consulter notamment pp. 4, 18 et 19).

13. BOWDEN K. F. — Chapitre VI, "Turbulence", du livre " The Sea ", vol. I, Interscience Publishers, New York - London, 1962, General Ed. M.N. Hill, 864 pages, cf. pp. 802-825.

14. KORNEVA L. A. — The anomalous geomagnetic field and the equivalent system of currents in the world Ocean. Dok. Akad. Nauk, vol. 76, N° 1, pp. 49-52, 1951.

15. WEAVER J. T. — Magnetic Variations associated with Ocean Waves and Swell. J. Geophys. Res. vol. 70, 1965, p. 1921.

16. WARBURTON F., CAMINITI R. — The Induced Magnetic Field of Sea Waves. J. Geophys. Res., vol 69, N° 20, 1964, pp. 4311-4318.

17. DUFFUS H. J., LAUNAY L. — The Use of Diving Saucers for Measurements of the Electromagnetic Fields in the Sea. Rapport interne loc. cit., pp. 17 et 18.

18. JACOBS J. A. — Geomagnetic Micropulsations. Springer-Verlag, Berlin Heidelberg New York, 1970, 179 pages.

19. SELZER E. — Limites imposées par le bruit magnétique naturel dans la mesure des champs faibles. Colloque international sur les Champs magnétiques faibles d'intérêt géophysique et spatial, Paris, Mai 1969, publié dans la Revue de Physique Appliquée, Tome 5, N° 1, 1970, pp. 233-238.

20. SHULEIKIN V. V., SIGACHEV N. I. — A new verification of a hypothesis on the nature of magnetic declination. DoK. Akad. Nauk, vol. 140, N° 1, 1961, pp. 107-110.

21. " ATD " Report P-64-56 — Geomagnetic Research by the Soviet Ship MIKHAIL LOMONOSOV. Review Article, oct. 1964, 13 pages.

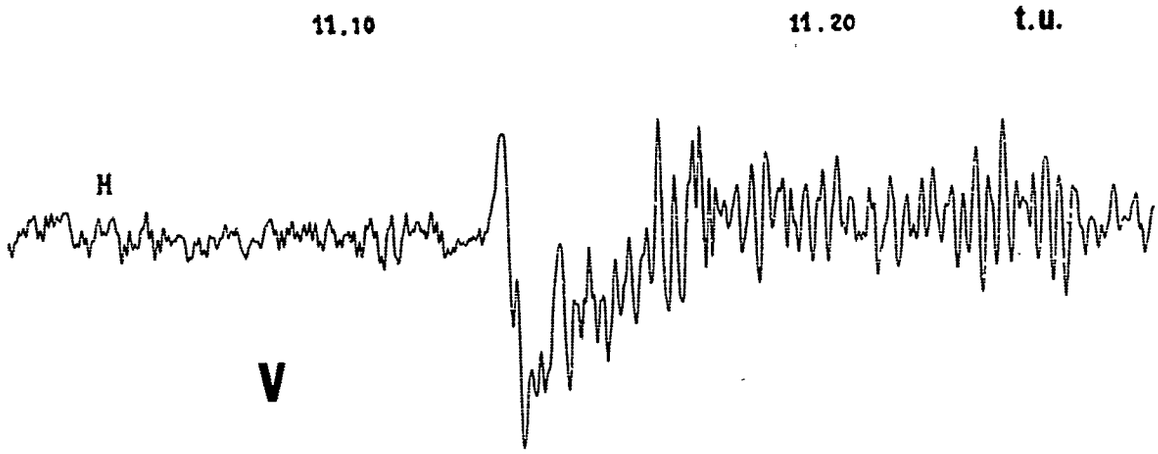

Fig. 1 Villefranche-sur-Mer (V)

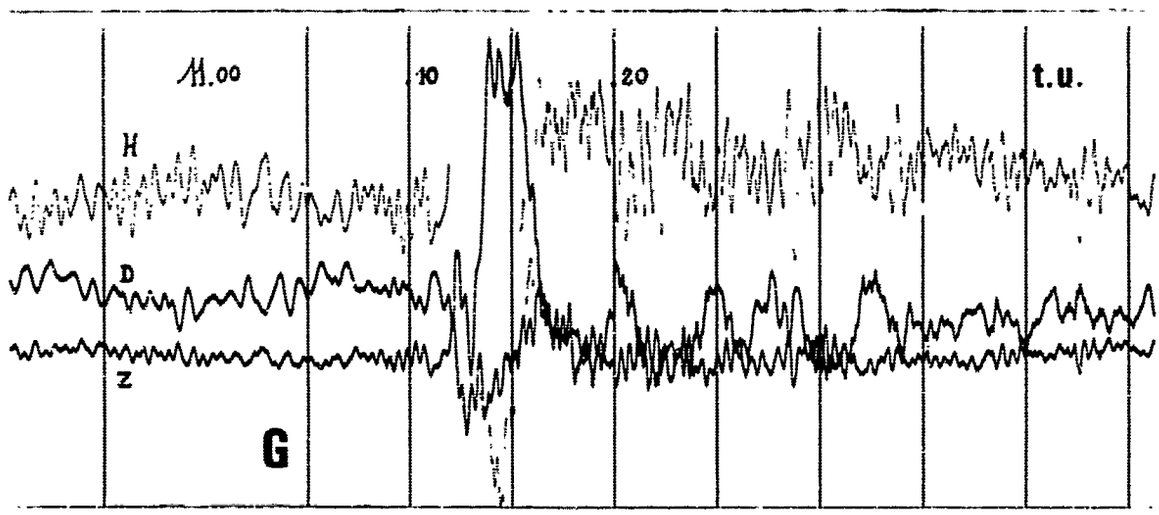

Fig. 1 bis Garchy (G)

Fig. 1 et Fig. 1 bis Enregistrements en Baie de Villefranche-sur-Mer (profondeur - 60 m) et à l'Observatoire de Chambon-la-Forêt (station auxiliaire de Garchy) du "Début Brusque", "SSC" ("Storm Sudden Commencement") du 2 ème orage de la période 29-31 Août 1966, le 30 Août à 11 h 12 m T.U.

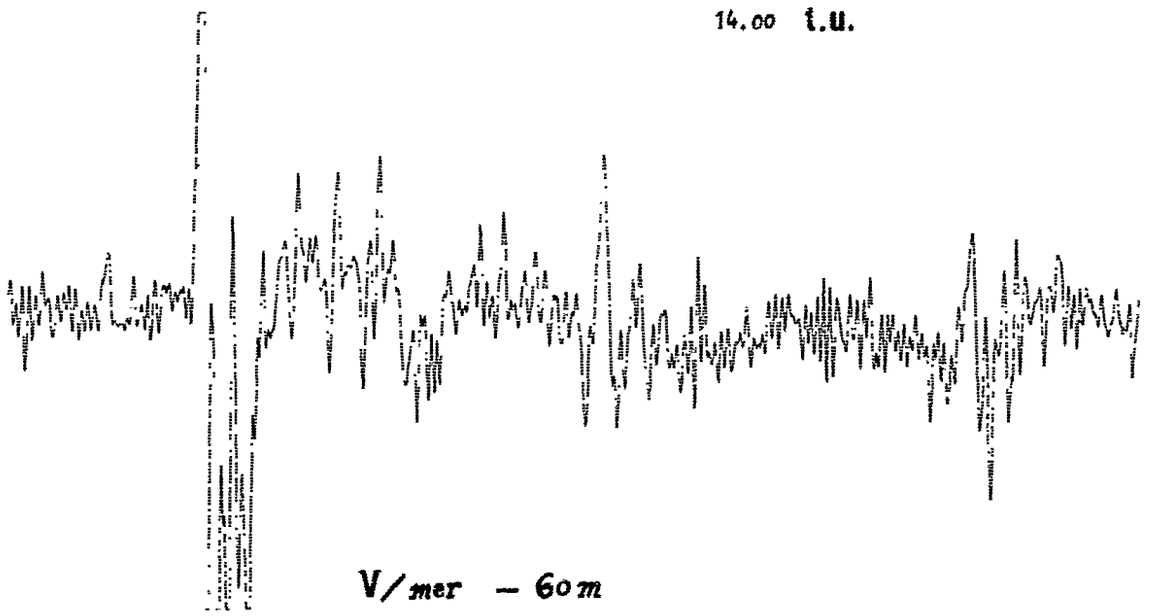

Fig. 2 Enregistrement en Baie de Villefranche-sur-Mer (profondeur – 60 m), d'une série de décrochements orusques ("SI", pour "Sudden Impulse") se produisant vers la fin des orages des 29-31 Août, le 31 Août vers 14 h T.U. – Composante H, comme dans la Figure 3. (Cliché L. Launay)

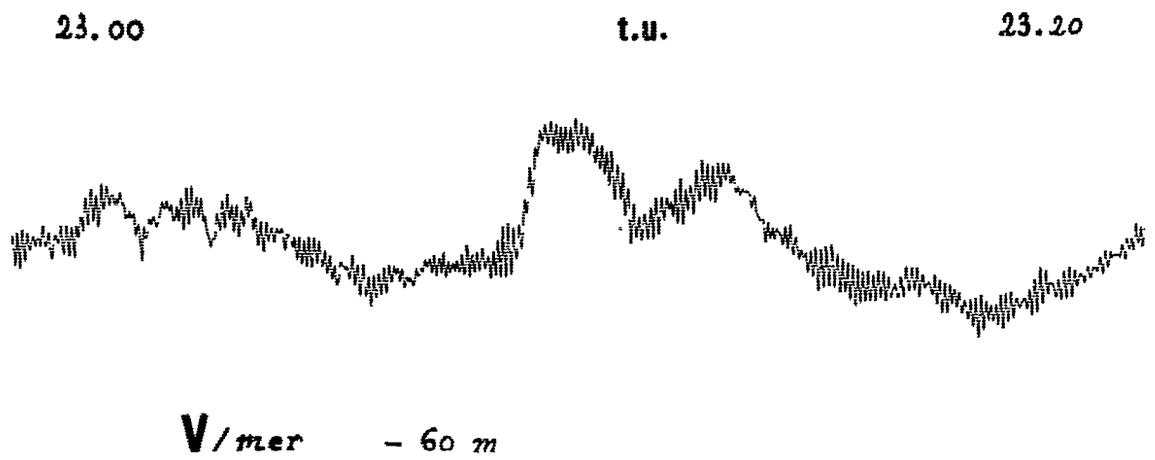

Fig 3 Enregistrement de la composante magnétique H (dans le plan du méridien magnétique), par 60 m de fond dans la baie de Villefranche-sur-Mer Le 30 Août 1966, entre 23 h et 23 h 20 m T.U. On y remarque les pulsations d'environ 6,2 s de période, engendrées par une faible houle et qui sont superposées à des variations naturelles, en général de plus grandes amplitudes. (Cliché L. Launay)

DISCUSSION ON PAPERS PRESENTED IN SESSION II

(VLF/ELF electromagnetic noise)

Discussion on paper 12-A : "Highly sensitive antenna-coil and ball antenna for ELF atmospherics", by H. L. KOENIG.

Dr. L. BROCK-NANNESTAD : Have you considered the use of coils with a high permeability core ?

Is Barkhausen noise considered a more serious problem than the vibrations of the coil in the static earthfield ?

Prof. E. SELZER : Au sujet du bruit de Barkhausen notre expérience des sondes à noyaux de mumétal (1 à 2 m. de long et 1 à 3 cm. de diamètre) nous a permis de vérifier que ce bruit est au-dessous des seuils gênants dans le cas d'usage d'"alliages massifs" au lieu de "fils". Ceci, bien entendu, n'est pas contraire à certaines qualités spécifiques des sondes à air (sans noyau perméable).

Dr. H.L KOENIG : We seriously discussed the problem of using a coil with or without iron with our american friends of the University of Rhode-Island. Certainly a coil with a mu-metal core has the advantage of the smaller size. The increase of inductance using mu-metal may be about the factor 25. Older experiments were done with coils which have an iron core. Applying the scaling law discribed above it could be seen that a 2 meter diameter coil is necessary for the signal to noise ratio and sensitivy wanted for the recordings (for a given copper weight). The use of mu-metal has the following disadvantages : although for a given sensitivity the ironless coil could be reduced in diameter to about 40 cm by using a mu-metal core, there are construction difficulties in doing this (a core of 40 cm diameter and a length of 1 m or 2 m, disregarding the costs). Also, modulation by strong interference (existing in the vicinity of the german field station) via the hysteresis characteristics of the mu-metal seemed possible. The E-field picked up by the core itself had to be considered. It was also not feasible to determine whether the Barkhausen effect would produce noise in the order of small signal levels. The shock mount system would be expected to be complicated. But the final decision in favor of an ironless coil involved the idea of the two completly identically equipped field stations for simultaneous elf-measurements. The use of ironless coils ensured that the measurements can be compared without any ambiguity with respect to absolute values of signals or to noise due to pickup by mu-metall core.

Discussion on paper 13 : "A comparison of ELF atmospheric noise spectra measured above and in the sea", by E.F. SODERBERG.

Prof. E. SELZER : In the curve of the trailing dummy, what was the method of transmission of the ship's vibration to the measurement channel ? Was it through the water to the sensor ?

Dr. E.F. SODERBERG : The noise peaks appearing at 32 Hz and 68 Hz were due to the mechanical coupling of ship's vibration to the input cables via the cable clamps securing the cables in place on the ship. The noise was not picked up via the water path, as is seen by comparing the relative levels of noise on the trailing dummy charnel with the ELF noise on the electrodes channel.

Dr. J.R. WAIT : I believe it is not entirely justified to calculate the sub-surface horizontal E field from the vertical E field using a simple exponential depth law. The latter assumes the surface field is equivalent to a grazing plane wave. It would be preferable to compare the sub-surface field with the horizontal E or H field on the surface.

Dr. E.F. SODERBERG : I agree that it would have been valuable to have had a horizontal sensor at the surface, but such equipment was not available. I expect that there is relatively insignificant error in assuming that, because of the absence of local electrical activity, the ELF sources were far enough distant to be nearly plane waves, with a constant wave tilt, due to the conductivity of the medium, over the ocean in the area of consideration.

Dr. A. EGSMANN : Quel était le type et le montage des antennes utilisées ?

Dr. E.F. SODERBERG : 2 meters whip-antenna with base 10 meters above the water.

Discussion on paper 14 : "Characteristic levels of natural electromagnetic noise in the ELF range, in sea water, as a function of depth", by E. SELZER.

Cap. Frég. P. HALLEY : Avez-vous pu utiliser les câbles sous-marins pour vos observations ? Par exemple celles de différences de potentiel créées par les marées ou d'autres causes ?

Prof. E. SELZER : Non. Le professeur DUFUS (Canada) a à sa disposition un câble transatlantique désaffecté mais je ne suis pas au courant de ses expériences. Il a fait par ailleurs un rapport très complet sur les bruits aussi bien artificiels que naturels dont il s'occupe.

Dr. L. BROCK-NANNSTAD : At the Agard meeting in 1966 spectral peaks around 9 Hz were reported. At that time no explanation was available. Can it be confirmed that these peaks were not real ?

Prof. E. SELZER : Oui à l'époque nous avons signalé un renforcement à 9 et à 14 Hz surtout à 14. Aujourd'hui je ne suis ni davantage ni moins certain qu'il s'agit d'une résonance de Schumann provenant du fond.

Dr. A. ESSMANN : On connait l'existence des effets dus aux marées et aux courants d'eau de mer sur le champ magnétique. Avez-vous pu constater ces effets à grande profondeur ?

Prof. E. SELZER : Nous avons trouvé beaucoup de choses mais nous n'avons pas eu le temps de les inclure dans ce rapport. Nous avons trouvé au fond de la mer un effet des microséismes. Quand le bathyscaphe est au fond de la mer il suit très bien les ondes microsismiques.

Dr. H. L. KOENIG : Since calculating the Schumann-resonances, Schumann has also made calculations of radiation from the sun as a spherical radiator. The result showed a fundamental period of the radiation to be about 20 seconds. There may be some relation between the signals you observed and the radiation from the sun.

Prof. E. SELZER : Peut-etre.

SPECTRAL CHARACTERISTICS OF HF GROUND WAVE SIGNALS BACKSCATTERED FROM THE SEA

by

D.D. Crombie, J.M. Watts, and W.M. Beery

Institute for Telecommunication Sciences
Environmental Science Services Administration
Boulder, Colorado, U.S.A. 80302

SOMMAIRE

Le phénomène de rétrodiffusion avec résonance des ondes radio à haute fréquence, à partir de la surface de la mer est maintenant bien connu. Il résulte de la diffusion cohérente qui s'effectue à partir d'un composant spatial de la surface de la mer dont la longueur d'onde est la moitié de la longueur d'onde radio, et qui se propage selon une trajectoire radiale dirigée vers le radar, ou en provenance de celui-ci. L'un des traits caractéristiques de ce signal rétrodiffusé réside dans le fait que son déplacement par effet Doppler a une valeur très proche de celle que l'on attendrait de signaux rétrodiffusés à partir d'ondes marines ayant la vitesse de phase théorique des ondes à longueur résonnante.

Un examen plus approfondi des spectres des signaux rétrodiffusés révèle cependant qu'il existe des différences systématiques par rapport aux valeurs théoriques, et que la forme des spectres n'est pas conforme à la simple théorie.

Ces points seront illustrés à l'aide de spectres observés à des fréquences variant entre 1,7 et 12, 37 MHz, et les causes des différences seront étudiées. En outre, l'auteur examinera les preuves de la présence de raies spectrales d'un ordre supérieur à l'unité, et le comportement d'autres ondes de gravité non linéaires de surface.

SPECTRAL CHARACTERISTICS OF HF GROUND WAVE SIGNALS BACKSCATTERED FROM THE SEA

D. D. Crombie, J. M. Watts, and W. M. Beery
Institute for Telecommunication Sciences
Environmental Science Services Administration
Boulder, Colorado, U.S.A. 80302

SUMMARY

The phenomenon of resonant backscattering of HF radio waves from the surface of the sea is now well known. It occurs because of coherent scattering from a spatial component of the sea surface having a wavelength of half the radio wavelength and travelling radially towards or away from the radar. A characteristic feature of the backscattered signal is that its Doppler shift is very near the value which would be expected for signals backscattered from sea waves having the theoretical phase velocity for waves of resonant length. Closer examination of the spectra of backscattered signals shows, however, that there are systematic differences from the theoretical values, and that the shapes of the spectra do not conform to simple theory.

These points will be illustrated using spectra observed at frequencies between 1.7 and 12.37 MHz, and explanations for the differences discussed. In addition, evidence for spectral lines of order higher than unity and other nonlinear surface gravity wave behavior will be discussed.

1. INTRODUCTION.

In the last three years the Institute for Telecommunication Sciences has made sporadic observations of the spectrum of HF ground wave signals coherently backscattered from the sea. This work was done near Eglin Air Force Base, Florida. From this data it became apparent that it might be used to obtain considerable information of oceanographic importance. Verification of this idea, however, required simultaneous backscattering data and actual data on the power spectrum of the sea surface measured in the area from which backscattering was observed.

Recently, the opportunity to take data during the Barbados Oceanographic and Meteorological Experiment (BOMEX) in which measurements of sea state, power spectrum, and wind were being made became available. The purpose of this paper is to report on some of the preliminary backscatter results obtained. Unfortunately, correlation of the backscatter data with the appropriate oceanographic data must await receipt of the latter.

2. INSTRUMENTATION.

The instrumentation used at Barbados, West Indies consisted of a modified C3 ionosphere sounder operating with broadband vertical monopole antennas. The ionosonde was modified to be coherent, and provisions for changing frequency between adjacent pulses were made by replacing the VFO with a synthesizer which could be rapidly switched in sequence through eight preset frequencies in the range of 1.7 to 12.4 MHz. The transmitter pulse rate was 60/sec and pulse length 40 μsec. The peak radiated power of the transmitting antenna varied from about 20 watts to 2 kW, depending on frequency.

Two spaced receiving antennas were used to collect data concerning the azimuthal angle of arrival of the backscattered signals. Because of this, each frequency was transmitted on two successive pulses; the receiver being switched from one antenna to the other between pulses. Data from one antenna (which is all that will be discussed here) were sampled at the rate of 3-3/4 samples/sec, a frequency very much greater than the maximum Doppler shift expected from the sea.

The output of the receiver was sampled at four ranges, 22.5, 45.0, 67.5, 90.0 km, and the samples were recorded using a 10-bit digital magnetic tape recorder. Recordings were made for 30 minutes, four to five times a day for about 30 days during a six-week period, on the eight frequencies.

The recorded data were then returned to Boulder where the individual power spectra for each sample was obtained using fast Fourier transform procedures. The resulting power spectra have a resolution of ~ 0.002 Hz with 6 degrees of freedom.

The equipment was operated on the east coast of Barbados within 100 yards of the sea. The nominal field of view of the sea was ~ 180 degrees centered on an east direction.

3. SAMPLE DATA.

Figures 1 and 2 show samples of the resulting data. It should be noted that the receiving system introduces a frequency shift of + 0.5 Hz so that signals having negative Doppler shifts can be separated. Thus signals having zero Doppler shift in figures 1 and 2 appear at a frequency of 0.5 Hz and frequencies below 0.5 represent negative Doppler shifts, those above represent positive Doppler shifts.

These two figures illustrate the features shown by the data. They represent simultaneous recordings taken at a range of 45 km. Figure 1 was taken at a frequency of 2.90 MHz. It shows the three main

spectral peaks of interest at frequencies of ~ 0.32, 0.68, and 0.75 Hz. These correspond to signals having Doppler shifts of - 0.18, + 0.18, and + 0.25 Hz. As shown in the next section, the negative peak corresponds to resonant scattering from sea waves which are travelling radially away from the equipment. The very narrow peak at + 0.18 Hz is the coherent scattered component travelling radially towards the equipment. It is much stronger than the negative peak, presumably because at Barbados the dominant wind, and hence dominant directions of wave travel, is from the east. The third peak at + 0.25 Hz $\simeq \sqrt{2} \times 0.18$ Hz will be discussed later. Note that the dominant peak is about 40 dB above the noise level.

Figure 1 also shows a minor peak at 0.5 Hz corresponding to a signal having zero Doppler shift. Since at a range of 45 km none of the island should be visible to the radar, and since this signal is also seen at greater ranges, it is unlikely to be a result of scattering from the island. On the other hand it is difficult to account for it as arising from the sea, particularly if one assumes only single scattering, or linear processes in the sea.

Figure 2 shows data taken at a frequency of 8.37 MHz at the same time as figure 1 was obtained. It shows characteristics similar to those of figure 1 except that the Doppler shifts are greater, the line widths are greater, and there is evidence of a third positive peak at a frequency of $\sqrt{3}$ times that of the main peak. The zero frequency component in this case is about 3 times as strong, relative to the main positive peak as it was at 2.90 MHz.

4. RESULTS.

4.1 Magnitude of Doppler Shifts

It was originally suggested[1] that the Doppler shift Δf of signals coherently backscattered from the sea was of the form

$$\Delta f = \sqrt{g/\pi\lambda} = 1.02 \times 10^{-4} \sqrt{f} \quad \text{Hz} \qquad (1)$$

in water deep compared with the wavelength. Here g is the acceleration of gravity, λ is the radar wavelength, and f is the radar frequency in Hz. This result has been approximately confirmed[2] by many workers over a wide range of frequencies.

In the present situation, Doppler shifts could be determined with considerable precision (~ 0.001 Hz). Results of measurements on several occasions are shown in figure 3 in which the solid line represents the theoretical value of Δf versus f. The observed values of Δf for both the approaching and receding components are shown. It is very clear that the Doppler shift of the approaching component is greater than the theoretical value, while that of the receding component is less. The differences from the theoretical value increase with frequency.

The cause of these differences from simple theory is believed to be due to four factors:

(1) Nonlinear interaction between the waves causing the coherent backscatter and the rest of the sea spectrum,

(2) Changes in phase velocities depending on wave amplitude (Stokes' effect),

(3) Drifts induced by the wind, and

(4) Tidal drifts.

The first effect is a result of the change in the phase velocity of the sea waves caused by the nonlinear interaction[3]. The other three effects are a result of the waves travelling on a moving sea surface. However, it should be noted that figure 3 shows that the discrepancy in Doppler shift is less at 90 km than at 22.5 km, an effect which may be associated with the varying water depths at the two ranges. These depths are very much greater than the lengths of wind-induced sea waves.

In the case of the data labelled 7/15/69, 1400 LT, the discrepancies between the observed and theoretical Doppler shifts could be accounted for if it is assumed that the surface of the water was moving radially with a velocity of approximately 0.4 m/sec. This value is much greater than would be expected from (1) above, while the second mechanism would produce an equivalent velocity which depended on the wave frequency.

4.2 Spectral Line Shapes

It can be readily shown that the signal E backscattered from a plane radio wave by a single long-crested sinusoidal gravity-wavetrain on the surface of the sea travelling in the direction of the radio wave (or against it) is of the form

$$E \propto \left[(\omega+\sigma)\,t - 2kd + \theta\right] \frac{\sin\left[(\beta+2k)D\right]}{(\beta+2k)} + \cos\left[(\omega-\sigma)\,t - 2kd - \theta\right] \frac{\sin\left[(\beta-2k)D\right]}{(\beta-2k)} \,, \qquad (2)$$

where ω is the angular radio frequency, k is the radio wave number, σ is the angular gravity wave frequency, β is its wave number, d is the distance between the radar and the patch of sea under consideration, and D is the radial length of the wave illuminated by the incident pulse. Provided that D is large, the first term is negligible when β and k are both positive, i.e., when the incident radio wave and the gravity wave are travelling in the same direction. Then the Doppler shift of the backscattered signal is negative and equal to the wave frequency. When $\beta = 2k$ the backscattered signal is maximum, a result consistent with eq. 1. When the two waves are travelling in opposite directions, β and k have opposite signs, and then the second term of eq. 2 is negligible, giving a signal having positive Doppler shift.

Equation 2 shows that as the frequency σ of the gravity wave is changed, the amplitude of the backscattered signal varies as

$$\frac{\sin(\beta - 2k)D}{\beta - 2k} \quad \text{where } \beta = \frac{\sigma^2}{g} \quad .$$

Thus, with a realistic sea of constant spectral density in the vicinity of $\beta = 2k$, the spectrum of the returned signal near the resonant peak should be of the form

$$E^2(\beta) \propto \frac{\sin^2(\beta - 2k)D}{(\beta - 2k)^2} \quad . \tag{3}$$

Reference to figures 1 and 2, obtained for D = 12 km shows that the shape of the peak signal is not of this form. These and other similar data indicate that a Gaussian spectral profile is a much better approximation than eq. 3.

A simple explanation of this is that eq. 3 assumes that the surface of the sea can be decomposed into Fourier components which propagate without change of amplitude or phase during the observation time (or through the observing region). The Gaussian form of the spectrum suggests that instead, each Fourier component only persists for a finite time (or has a finite length) before either the amplitude or phase changes significantly. The width of the spectral peak is much greater than would be expected from eq. 3. Thus the "coherence" length of these Fourier components is much less than the illuminated length D. Alternatively the "lifetime" of the Fourier components is much less than the time required for them to move through the illuminated area.

Some data giving observed bandwidths of the main spectral peak are shown in figure 4. The bandwidth is $\propto 1/$"lifetime." In figure 4 the bandwidth is defined as being the bandwidth at a level 10 dB below the spectral peak. The figure shows that the bandwidths increase markedly with radio frequency and that the rate of increase can vary markedly from one day to another.

4.3 Nonlinear Effects

Attention has been drawn to the presence of minor spectral peaks in figures 1 and 2 at angular frequencies of $\sqrt{2}\,\sigma$ and $\sqrt{3}\,\sigma$. It was originally suggested[1], before eq. 2 was developed, that this was a result of backscattering from gravity waves of two or three times the resonant wavelength given by $\beta = 2k$. In other words, it was due to scattering from waves of length $L = \lambda, 3\lambda/2$, etc. However, reference to eq. 2 shows that such scattering will have negligible amplitude when $kD \gg 1$.

A better explanation involves the fact that gravity waves of finite amplitude (Stokes' waves) are not sinusoidal but consist of a fundamental component of length L, together with higher order harmonics. These higher order harmonics have wavelengths of $L/2$, $L/3$, etc. and travel with the phase velocity of the fundamental. Thus, it can be argued that the frequency components at $\sqrt{2}$, $\sqrt{3}$, etc. of the resonant backscatter frequency arise as scattering from the second, third, etc. harmonic of waves having lengths of 2L, 3L, etc. where $L = \lambda/2$.

In view of this argument, it is expected that with sufficient sensitivity, frequency peaks of higher order than 3 should also be observable. The upper limit to their detectability would depend on λ and the upper cutoff wavelength of the gravity waves.

5. CONCLUSIONS.

The data presented here show that HF ground wave signals backscattered from the sea provide valuable information about certain features of sea waves. In particular, the phase velocity of waves having a length determined by the radar wavelength in use, the relative amplitude of Stokes' "harmonics" and the "lifetime" or "coherence length" of the wavetrains can be determined with considerable precision. Furthermore, the relative amplitudes of receding and approaching waves can be readily obtained. None of these properties can be easily obtained using more conventional approaches.

REFERENCES

1. Crombie, D. D., "Doppler Spectrum of Sea Echo at 13.56 Mc/s," Nature, Lond. 175, 681 (1965).

2. Crombie, D. D. and J. M. Watts, "Observations of Coherent Backscatter of 2-10 MHz Radio Surface Waves from the Sea," Deep-Sea Research 15, [illegible] (1968).

3. Longuet-Higgins, M. S. and O. M. Phillips, "Phase Velocity Effects in Tertiary Wave Interactions," J. Fluid Mechanics 12, 333 (1962).

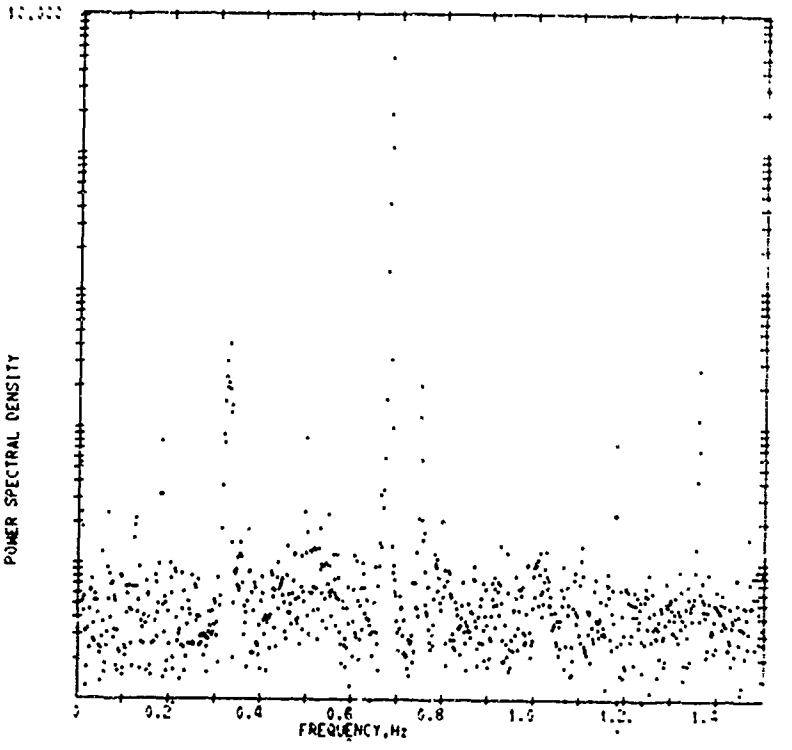

POWER SPECTRAL DENSITY OF SEASCATTER SIGNAL,
FREQUENCY IS 2.90 MHz, RANGE IS 45.0 KM 7/15.69 1[illegible]
BOMEX 0024 FILE 4

Fig. 1 Spectral density at 2.9 MHz

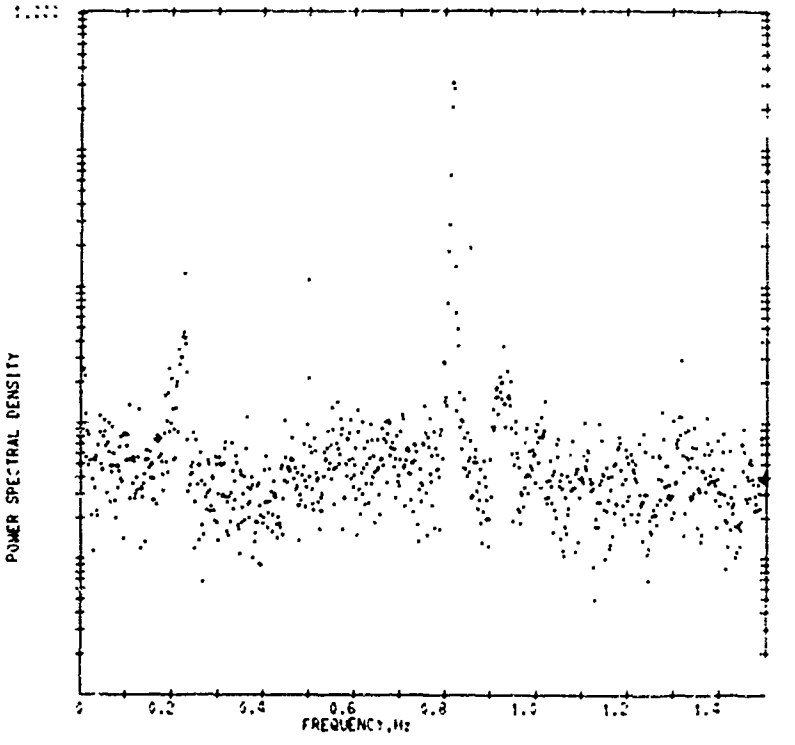

POWER SPECTRAL DENSITY OF SEASCATTER SIGNAL,
FREQUENCY IS 8.37 MHz, RANGE IS 45.0 KM 7/15.69 1[illegible]
BOMEX 0024 FILE 4

Fig. 2 Spectral density at 8.37 MHz taken at the same time as figure 1

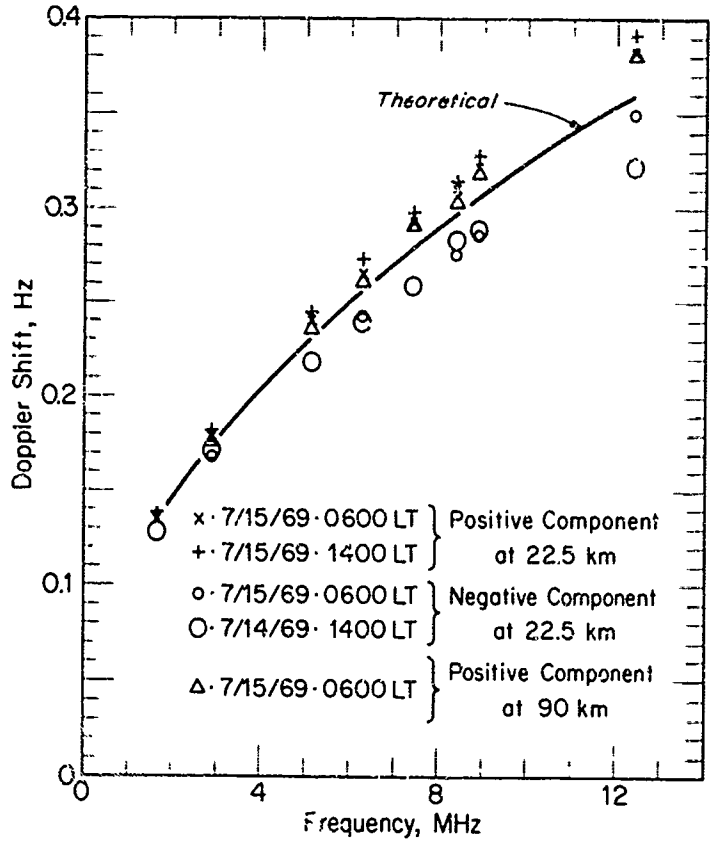

Fig. 3 Observed Doppler shifts

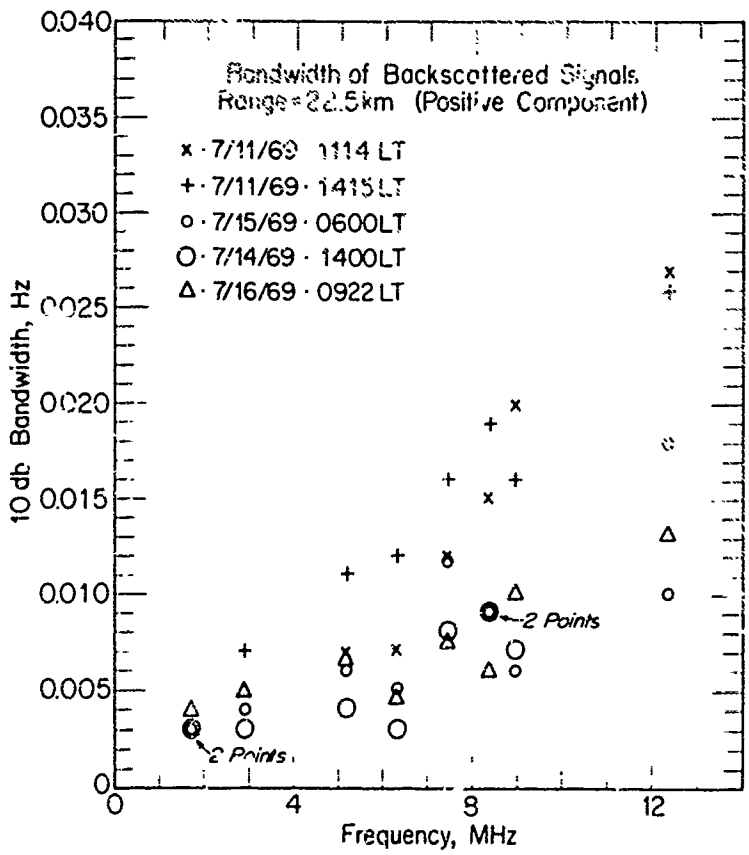

Fig. 4 Observed bandwidths of Doppler shifted signals

THE REFLECTIVITY OF THE SEA SURFACE AT RADAR FREQUENCIES

by

W.H. Schönfeld

Technical University, Hannover

SOMMAIRE

L'auteur présente les résultats de mesure d'intensité de la diffusion par une mer agitée (sea clutter). Les amplitudes dépendent de divers paramètres tels que la portée, la force du vent par rapport à celle du pinceau éclairant du radar, la hauteur de l'antenne, etc... Les fonctions typiques sont comparées aux considérations théoriques appropriées. L'auteur étudiera les problèmes posés par une extinction par interférence qui, dans des conditions connues, peut se produire dans le cas d'une cible ponctuelle aussi bien que dans celui de cibles ayant une certaine étendue tant en profondeur qu'en largeur.

Les signaux rétrodiffusés par la mer peuvent être décrits par un groupe de dipoles sur la surface agitée de la mer. L'auteur présentera des résultats récents qui révèlent un comportement différent de la part de la surface marine lorsqu'elle est illuminée simultanément à l'aide de deux fréquence (entre 8,5 et 24 KMHz) ou de deux polarisations différentes (verticale et horizontale). Il donnera également les résultats de mesures effectuées à partir de bouées sur mer calme, d'une part, et sur mer agitée, d'autre part, avec illuminations simultanées à double fréquence.

Une analyse océanographique récente du spectre de fréquence des vagues conduit à considérer de nouveau l'emploi d'antennes à révolution rapide qui peuvent présenter des avantages lorsqu'il s'agit de localiser dans une mer agitée, des cibles de petites dimensions comme des bouées ou des canots de sauvetage.

On peut escompter que l'utilisation d'un instrument de mesure spécial pour échos radar, actuellement en cours de réalisation aux Laboratoires de Haute Fréquence de l'université Technique de Hanovre, permettra de progresser dans ce domaine.

Summary

Reflections from the rough surface of the sea generate clutter, this means a conglomeration of unwanted signals in radar receivers, which may mask the signals from small targets.

An attempt is made to describe and explain observed phenomena of clutter signals by abstract models and theories. The results of theories are compared with measurements. A summary of known attempts of suppression of clutter signals with references is given in appendix 2. For many applications the improvement of the signal-to-clutter ratio is not yet sufficient. Two special measuring instruments, developped at Hannover Technical University, are described in appendix 1. Results of our measurements and future plans of investigations are discussed.

The Reflectivity of the Sea Surface at Radar Frequencies

W.H. Schönfeld
Technical University Hannover

Introduction

The reflectivity of the sea is of special interest in radar applications, because a sea, which is not calm but rough, reflects signals back to the radar receiver. Those reflections (see fig.1) give rise to a conglomeration of unwanted radar echos, which we call clutter. This paper will deal with sea clutter, its phenomenology, its strength, proposed methods of improving the signal-to-clutter ratio, results of measurements, proposals for future investigations and possible means of new improvements.

Clutter energy versus distance

The difference between a normal target and the sea surface is that the normal target always has the same radar cross section whereas the illuminated surface of the sea increases with distance. That has been the reason why all the scattering elements on the same illuminated surface have been put together to the sum

$$\sum_i \sigma_i = \sigma^\circ R \Theta \frac{c\tau}{2} \qquad (1)$$

so that the radar cross section has to be replaced by the term (1). By introducing that into the radar formula we find that because of the increasing cross section with distance the received power is not inverse to R4 but to R3.

$$P_r = \frac{P_t G_t G_r \lambda^2 \Theta \frac{c\tau}{2} \sigma^\circ}{(4\pi)^3 R^3} \qquad (2)$$

This fact has been verified by calculations of several authors, specially by Katzin and also by Müller in my institute and has been verified by measurements which we have made with our analog radar reflection measuring instrument, which is described in appendix 1.

Fig.2 shows as results of our measurements the received power in dB as a function of distance with the height of the waves as parameter. The exponents to the distance, written above the different curves, are a bit higher than 3 up to distances of between two and four kilometers. After this the strength of the echos drops at a quite higher rate with exponents of the inverse distance of 7.9 to 10.3. This is due to the fact that with the normal antenna heights on ships and the height of the waves at those distances the rays become so flat that by interference and two-path propagation the amplitude decreases rather quickly.

The factor σ°, which is a pure figure, can be calculated out of those measurements. Fig.3 shows measurements of Goldstein and measurements of my institute evaluated from our echo measurements.

Influence of two-path propagation

The curves of radar echos versus distance, as shown in fig.2, represent only the envelope of the maximum values. Fig.6 shows such an envelope as a dotted line, whereas because of the two-path propagation the true values oscillate between maxima and minima.

We have calculated a few maxima and minima for the simplified case of a single point-target at a height h_{so} above sea-level. The results are plotted versus distance in fig.4. The first minimum lies always on the surface of the sea. The target has been drawn in a position, where we would observe a minimum, in this case the second one. If we draw any target of a certain height at a chosen distance position, then we can read in the chart, whether we will receive from this target a maximum or a minimum value of energy or a value in between. A similar plot in fig.5 shows the positions of maxima and minima for an extended target, which consists of a conglomeration of small individual scattering elements. This model corresponds in some way to the rough surface of the sea.

Experimental proof of the two-path propagation theory

The question is, whether this description of sea clutter corresponds to what really happens. Fig.7 shows a P-scope of sea clutter. The radar aerial was fixed, whilst the

deflection coils have been rotating at a normal speed. We exposed the photo during 50 revolutions of the antenna corresponding to a time of 120 seconds. The range was 3 nautical miles, the wind strength 7 Beaufort. You find even in this long time of 120 seconds clearly dark and bright zones, that means maxima and minima, an effect which, because of the ever changing surface of the sea, only can be explained by the two-path propagation. Fig.8 shows a similar photo of a P-scope of sea clutter with a range of 1000 to 2000 m.

We have tried to check the observed four maxima at the four different distances 1210, 1378, 1682 and 1756 m and have calculated the theoretical positions of maxima with the simple model of fig.4 at a wind strength of 7 Beaufort. All the maxima are corresponding to the theory with slight tolerances in the height of the waves of a few centimeters.

The fact is a bit different with the minima. There are some more minima than can be calculated with the theory with one height of waves. Fig.9 shows the spectrum of water waves. It can be seen, that there is a sum of different wavelengths with different heights which give an irregular surface with lower and higher waves. The maxima are apparently coming from the highest waves, whereas the lower parts give the necessary reflecting surface. Some of the lower waves also produce some of the other minima. Therefore this seems to be a satisfactory explanation. We will come back to some possibilities to make use of those facts of a two-path propagation in a later part of this paper.

Doppler frequency shift

Another phenomenon of sea clutter is that there is a Doppler frequency shift because of the orbital movement on the surface of the waves. Fig.10 shows as result of a Russian publication, which is cited on fig.10, the Doppler frequency shift of the sea clutter as a function of the radar wavelength with the wind velocity as parameter. We have not been interested so much in making use of the Doppler frequency shift because we have been interested mainly in the recognition of small targets in sea clutter, like buoys, whose fluctuations in the sea may lead to a Doppler shift of the same order. We have no experience, whether the Doppler effect of the sea-movement may be of interest in other applications.

Frequency dependence of clutter

The question which we want to discuss now is, whether the effect of the two-path propagation is the only effect which we have to take account of. Maxima of reception are to be found at different distances. Formula (3) shows a simplified model for interference action:

$$\frac{\Delta l}{\lambda} = \frac{2 H_o H_t}{R \lambda} \qquad (3)$$

You can see that the different points of maxima or minima are dependent on the height of the radar antenna, the height of the target, the distance and the radio wavelength. By a change of frequency, that means of the wavelength, we can shift a maximum of a sea clutter response to another place so that a target which has a different height, possibly a higher height than the sea waves, may appear again on the screen because of the diminuished clutter response. But the change of frequency which is necessary is rather high and not very practical in many cases. That leads us to the question, whether this two-path propagation is the only effect responsible for building up maxima and minima of clutter signals. Fig.12 shows an oscillogram of the same sea clutter simultaneously received with two different frequencies with only a moderate change of frequencies. You see that the clutter response is not equal on both frequencies. This effect can be explained by using a model which is shown on fig.11.

ΔR is the distance which is illuminated at a certain moment by the pulse sent out by the radar station. In this example we assume 12 statistically distributed small surface elements which reflect independently of each other, and which are distributed in distances between one and ten wavelengths. We have been able to show that such a model is dependent of frequency, and gives maxima and minima which are quite the same as those which we could measure with our measuring instrument.

Fig.13 and 14 show the results of our measurements. The back-coming signals of the two frequencies transmitted to the sea have been said to be equal, if their difference in amplitude was less than 10 dB. They have been said not to be the same, if the difference was higher than 10 dB. With less than 10 dB difference we say that there is coincidence in both channels. The probability of coincidence is shown in fig.13 plotted versus distance. You can see that at higher distances the probability of having the same signal in both channels is rather low. At low distances the overloading of the receiver gives no proper answer to the problem.

In fig.14 you see the same probability of coincidence plotted versus the difference in frequency. And with rather small frequency differences you have already only 40 % to 50 % probability of coincidence between the two frequencies. That gives another possibility of having remedies against sea clutter by making use of a frequency diversity.

Frequency diversity

In fig.15 you can see an A-scope of a target and clutter at the same time. We have shown different scans, one above the other. The differences between a target and the big peaks of the sea clutter are not really visible. On the other hand our measurements of coincidence with different frequencies have shown some aspects. But in our model we have different target elements, which reflect independently of each other. The sea surface illuminated by the radar is rather large. The target, which we want to detect, may be rather small. So the target itself may be part of the elements and by changing the frequency to such a degree that the clutter signal disappears, the target itself may disappear at the same time.

Those deliberations have led to a new series of experiments, where we have been trying to explore the behaviour of a rough sea itself in comparison to a target in the rough sea at the same wind conditions and the same distance and the same azimuth. The philosophie of our measurements has been the following. We have compared all signals in the two channels which came in at the same time and have been higher than a certain threshold.

Fig.16 shows the results of our measurements. We have counted the number of signals surmounting a given threshold under different conditions. When receiving a signal from a small cell, defined by distance and azimuth, where a buoy has been laid out, you cannot discriminate between target response and false alarm in the presence of sea clutter. But if you compare the result with the one of a cell, where there is only clutter, then you get a statistical answer. We measure for instance the probability of signals in one frequency-channel alone. When sending out two frequencies simultaneously, we measure both the probabilities for getting signals in at least one channel and for coincident signals in both channels.

It may be sufficient to compare in the lefthand diagram of fig.16 only the curves b2 and c2, which show the probability to get equal response in both channels with a target in the clutter and the clutter alone. The probability of coincidences is higher with a target in the clutter than with the clutter itself. The differences in those curves decrease with rising wind strength. On the righthand side you see the improvement factor which can be reached by using two different frequencies at the same time. The improvement shows that it may be possible to recognize a target in the clutter by using suitable correlation methods with a two-frequency radar. As we have only evaluated signals which all have been hardly above the noise level, the value of our results is restricted. The necessary observation time, to get the necessary confidence level, is still too high for practical purposes. But we hope that, by changing the comparison level, we may come to observation times which are reasonable and can be used in pratice.

Measurements of targets in clutter

We may state finally that we think that the comparison of recordings of sea clutter signals to signals from targets in sea clutter has to be an essential part of future investigations. We will use for this purpose in our future program a new digital measuring instrument, which is described in appendix 1.

Life duration of clutter-signals

Another essential point in finding new methods of improving the signal-to-noise ratio in the presence of sea clutter is the question of the life duration of clutter signals. Fig.17 and fig.18 show A-scope photos of sea clutter. Several scans are superimposed and show the change of clutter signals with time. Some of them have a life duration of more than 50 ms, some of them have a lower life duration.

Discussion of measuring results from appendix 1

To begin with analog peak values fig.21 shows the response of different targets in comparison to the sea clutter. You see that small targets, seen scan by scan, show an envelope, which corresponds to the antenna diagram. The distribution of amplitudes of the sea clutter itself is quite different. That shows other feasibilities of improving the signal-to-noise ratio by correlating values scan by scan.

Synopsis of results and proposals

My paper until this state has given a certain description of the phenomenology of sea clutter, has given some results of our recent deliberations and measurements.
In appendix 2 of this paper I have made a synopsis of all the methods proposed until now for improvement of the signal-to-noise ratio in sea clutter. You see that the problem seems to be so difficult that a lot of intelligent people in the whole world have dealt with that problem without having results which are fully satisfactory. We believe that in the next generation of radar sets, which will work with automatic evaluation of signals, connected with computers, we have to deal with the clutter problem again. For certain purposes, like coastal radar stations, we may be able to have a next generation of radar sets which are much more complicated and sophisticated. Because of the

higher costs they may not be suitble as ship-borne equipment, but for the radar-chaines of fixed radar stations planned by many administrations for the next future, the improvement may justify the higher costs.

Appendix 2 shows a comparison of what has been done in the past with all the necessary references and some critical remarks. Many authors, who have found improvements, only gave a qualitative description. Some of the quantitative evaluations show that the results are rather unsatisfactory, because values in the order of 6 dB are not satisfactory at all, as the whole dynamics of the sea clutter is at about 90 dB and the sea clutter dynamics inside a certain distance-cell is about 30 dB.

In the table in appendix 2 we have included some proposals of ours, which haven't yet been proved to be valuable. This is rather a program than a report of results. We think that some diversity programs may be prospective. One possibility is the antenna diversity with two antennas at different heights. The second one is the frequency diversity. Polarization diversity doesn't show the same aspects following our experience.

That is why we didn't include them in this list of proposals. From all the results, reported in appendix 2, a report of Mr. Harrison is most interesting, where the chirp radar has shown real good aspects. Unfortunately Harrison has only shown results of one single experiment.

It has to be investigated, whether radar sets with chirp or with an inner-pulse modulation system perhaps a Barker code, could improve the signal-to-noise ratio in the presence of sea clutter.

First tests of a digital measuring instrument.

We have built meanwhile a new instrument with digitalisation of radar signals. Because of the high frequencies involved, we only can digitalize video signals after an envelope detection with a sampling frequency of 10 MHz. The measurement with this new instrument has been described in appendix 1. Fig.23 shows PCM-signals after demodulation by a computer. Fig.24 and fig.25 show correlation functions computed with an electronic computer. We see the main advantage of this new instrument in the fact that we can go to the field during a period where we have the necessary high clutter. Later we can evaluate the signals, which are recorded on a magnetic tape, on a computer several times with different simulated evaluation methods instead of going out to the field again and again with different evaluation methods as hard-ware.

I am at the end of my report, and I believe that because of the difficulty of the problem we could not yet show aspects of final results. But we have shown methods with which we want to go into the field. And we hope, at least, we will get some results which will lead to improvement in the future.

Notation

c	Light velocity
G_r	Gain of the receiving antenna
G_t	Gain of the transmitting antenna
H_a	Height of the antenna
H_t	Height of the target
Δl	Difference between the direct path and the path of the wave reflected on the sea surface
λ	Radar wavelength
P_r	Received power
P_t	Transmitted power
R	Range
σ_i	Radar cross section of target i
σ^o	Normalized radar cross section of clutter
τ	Radar pulselength
θ	Antenna beamwidth

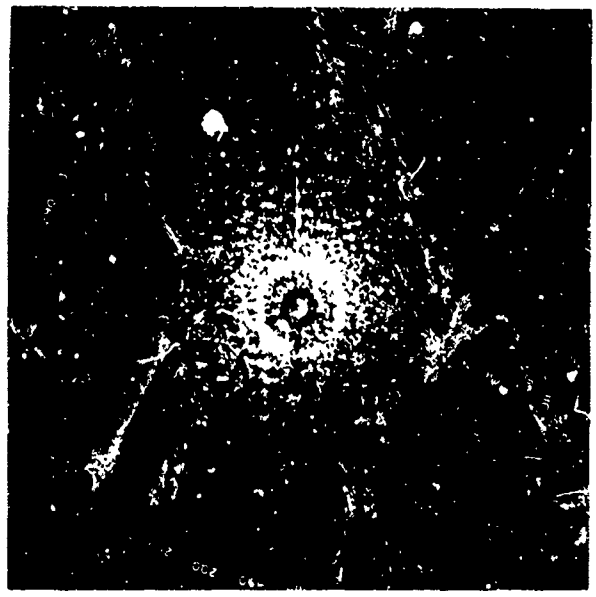

Fig 1 Sea-clutter on PPI-screen

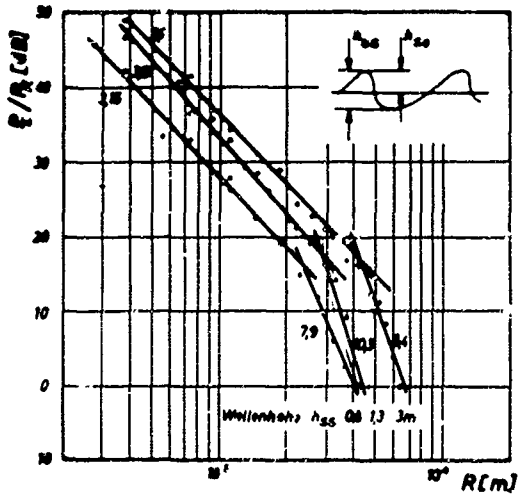

Fig.2 Clutter distance from random noise as a function of range and waveheight (h_{ss})

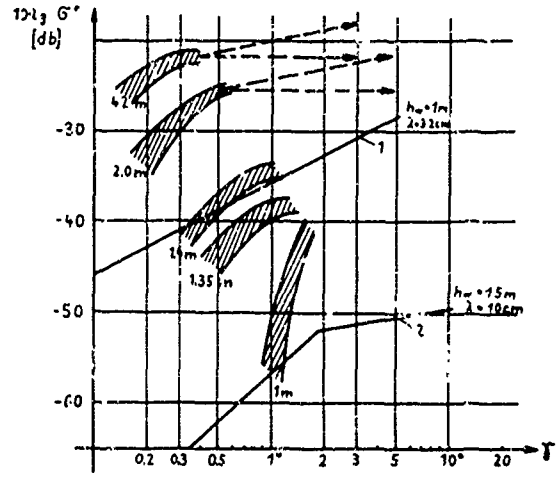

Fig.3 σ^0 for different states of the sea. (Parameter: waveheight.) Curves 1 and 2 are results described by Goldstein (MIT Rad. Lab. Ser Vol.13)

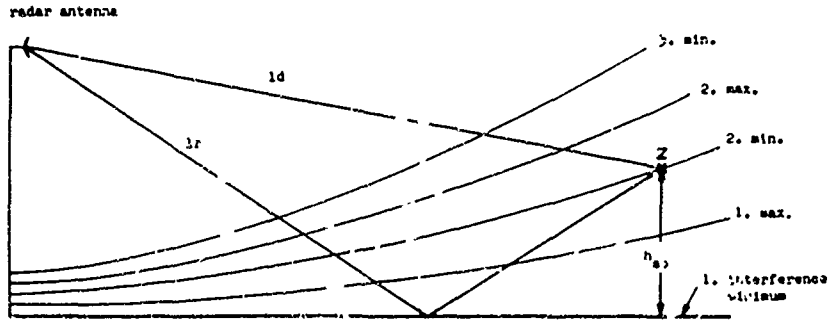

Fig 4 Two-path propagation with regard to a point target If either the height of the radar antenna or the wavelength of the radar frequency are halved (or doubled) the 1 max. (2. max) will lie exactly on the line of the 2 min in this diagram

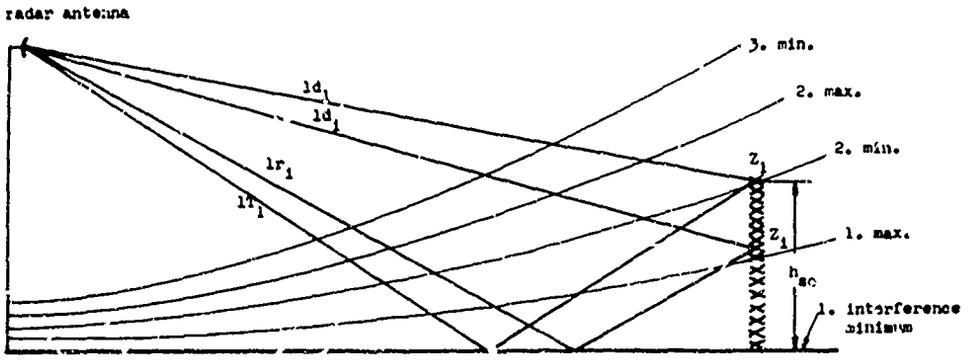

Fig 5 Two-path propagation with regard to a vertical plane

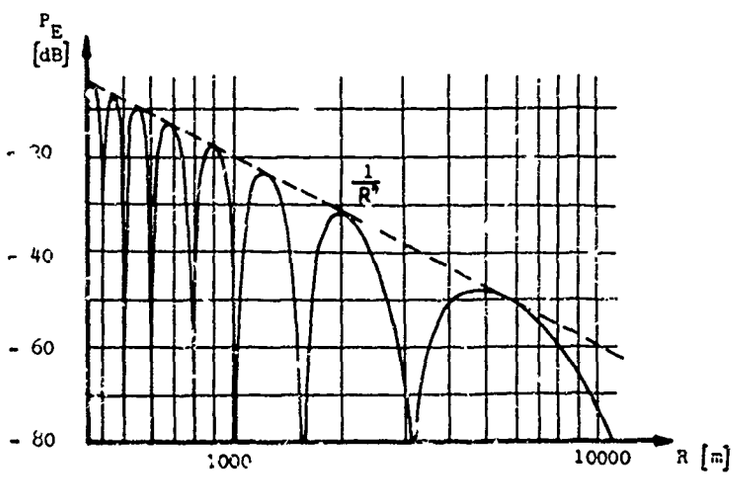

Fig.6 Example for the dependence of the received echopower of a point target from range (h_a = 24 m; h_t = 2 m, = 0,032 m)

Fig 7 p-scope of sea-clutter Radar aerial fixed deflection coils rotating 50 revolutions corresponding 120 seconds Rang 3 nm 7 Beaufort

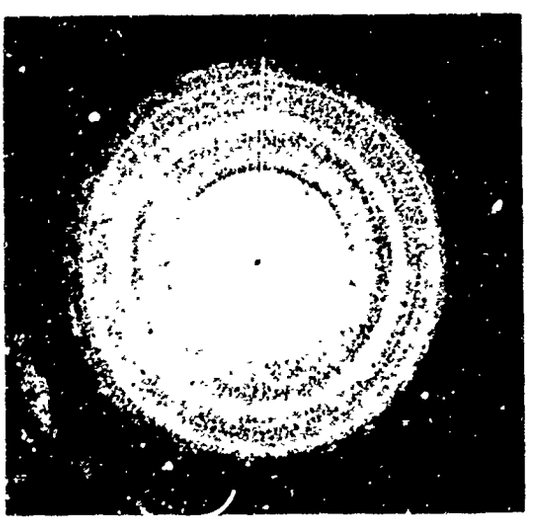

Fig.8 p-scope of sea-clutter Aerial fixed, deflection coils rotating 50 revolutions corresponding 120 seconds Range 1000 m to 2000 m 7 Beaufort

Minima at			Maxima at	
1147 m	1630 m		1210 m	
1357 m	1735 m		1378 m	
1451 m	1838 m		1682 m	
1588 m			1756 m	

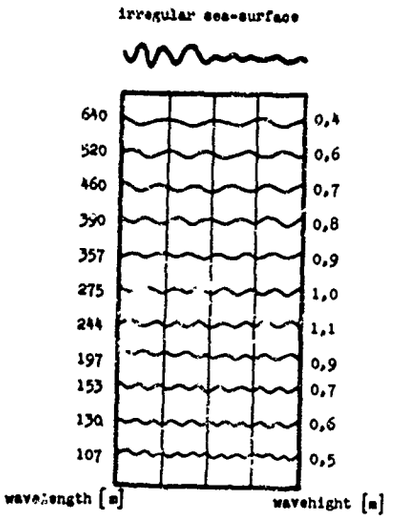

Fig. 9 Example for the Fourier-spectrum of a waterwave. [From: Life, Wunder der Wissenschaft. Schiffe.]

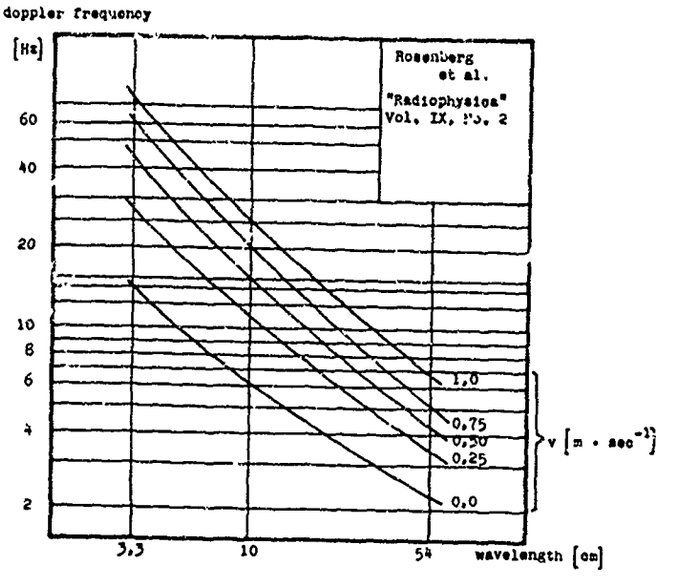

Fig. 10 Doppler frequency-shift of sea-clutter over radar-wavelength. Parameter: velocity of the sea-surface

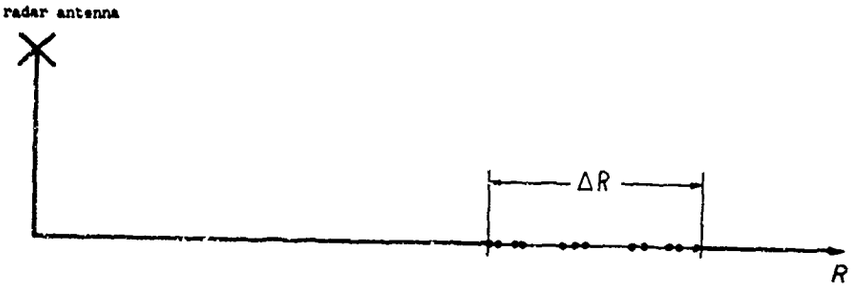

Fig. 11 Backscatter model with 12 statistically distributed "high-lights"

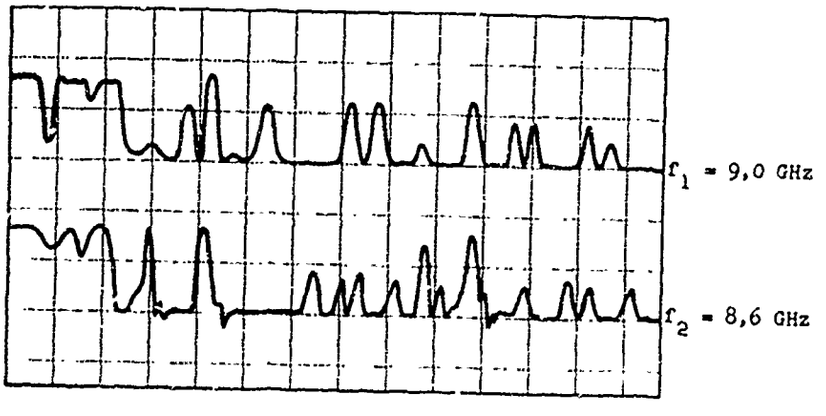

Fig. 12 Two simultaneously received clutter-signalchains.
($2\ \frac{\mu sec}{cm}$ = 4000 m total signal length)

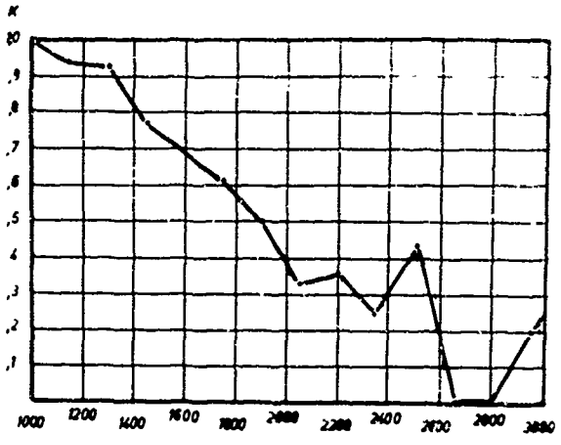

Fig. 13 Two-frequency-radar. Coincidence (probability) K = f(R) Δf = const.

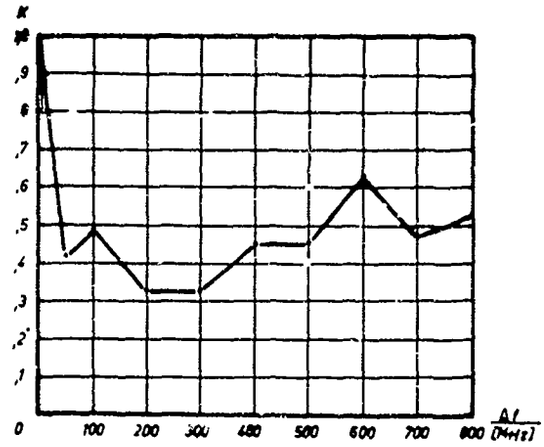

Fig. 14 Two-frequency-radar. Coincidence (probability) K = f (Δf)

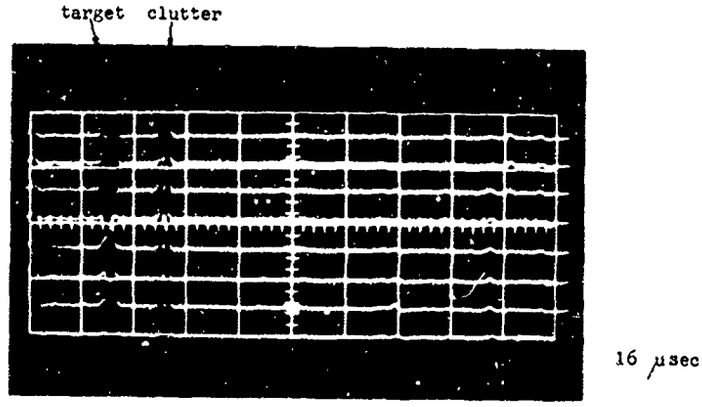

Fig. 15 A-scope (2 Volt/cm, 2 μsec/cm). Target and clutter

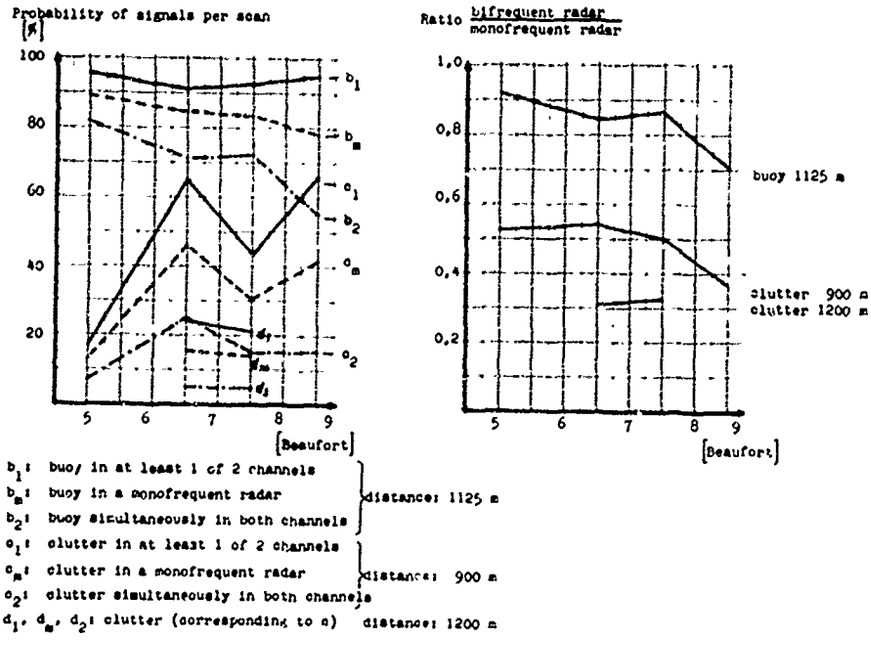

Fig. 16 Mono- and bifrequent radarechos of a small buoy (with radarreflector) and clutter

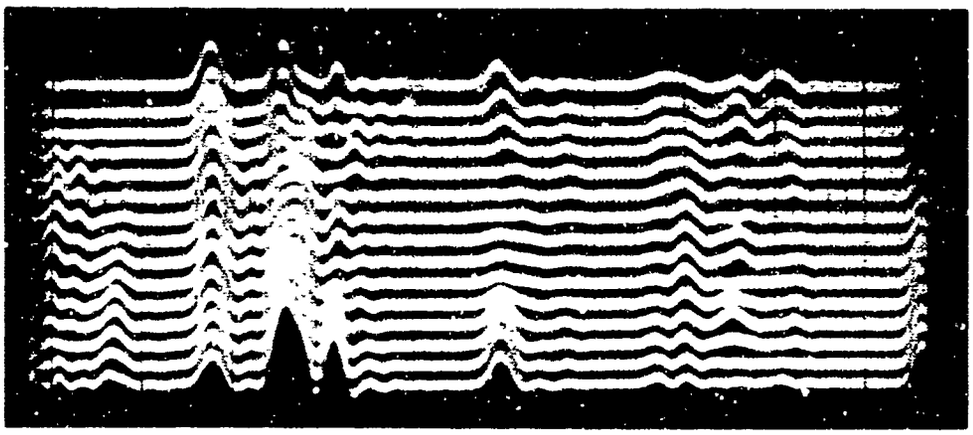

Fig. 17 Life duration of clutter-peak values A-scope 15 msec observation time 5 V/cm, 0.5 μsec/cm, 7 Beaufort

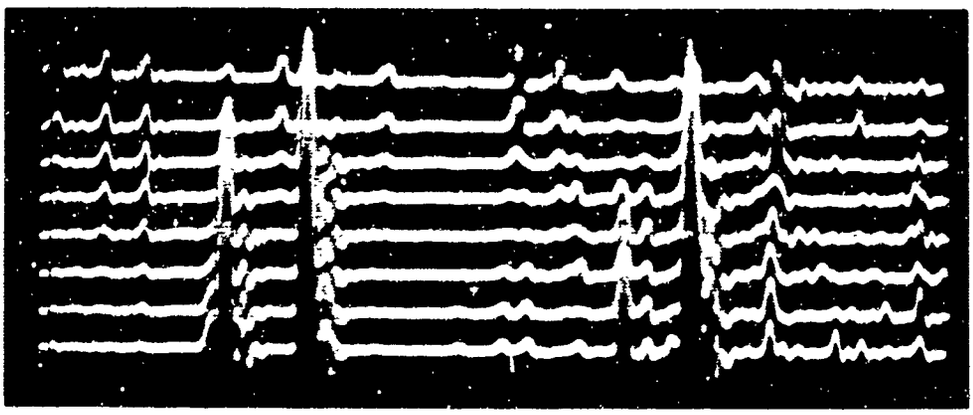

Fig. 18 Life duration of clutter-peak values A-scope 8 msec observation time. 2 V/cm, 1 μsec/cm, 3 + 4 Beaufort

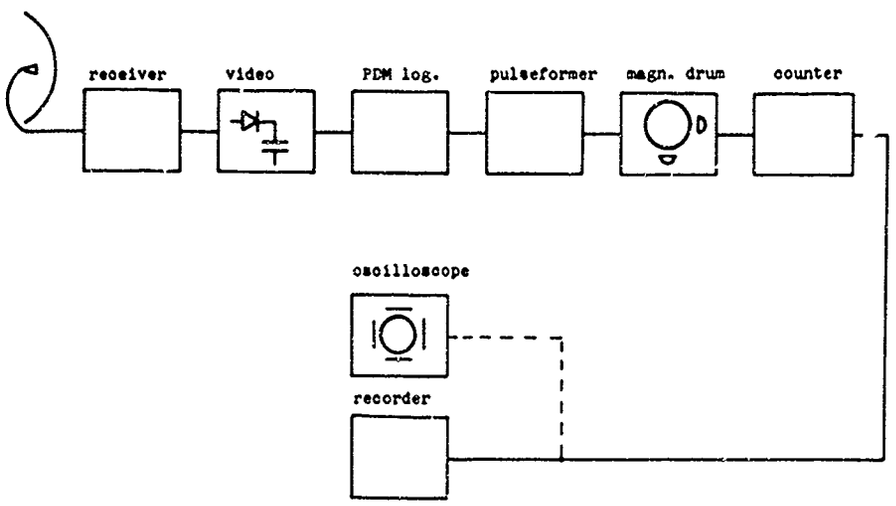

Fig. 19 Block diagram of a measuring instrument for the strength of radarechos

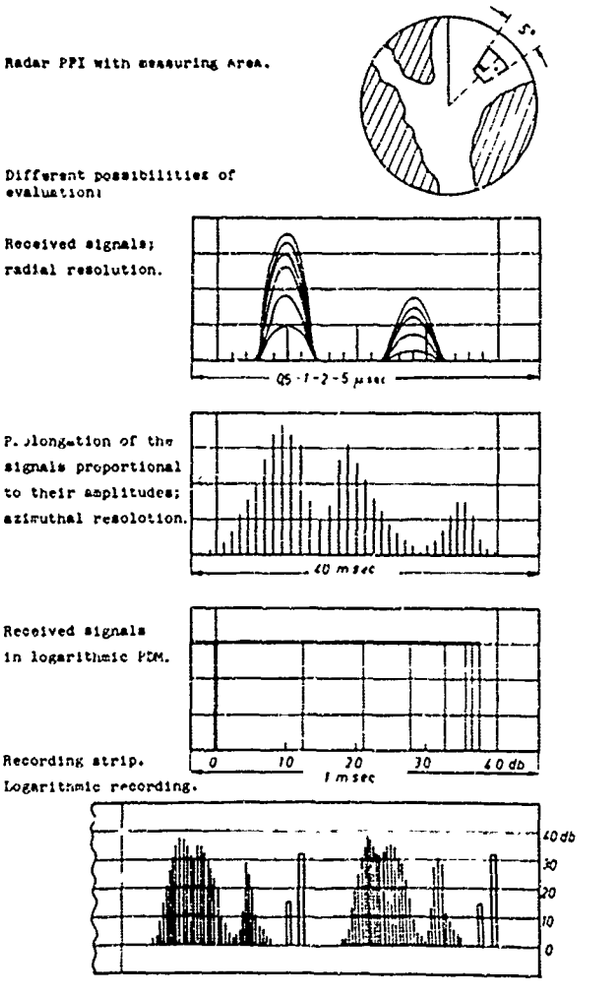

Fig. 20 The evaluation of data, measured with the instrument of Figure 19

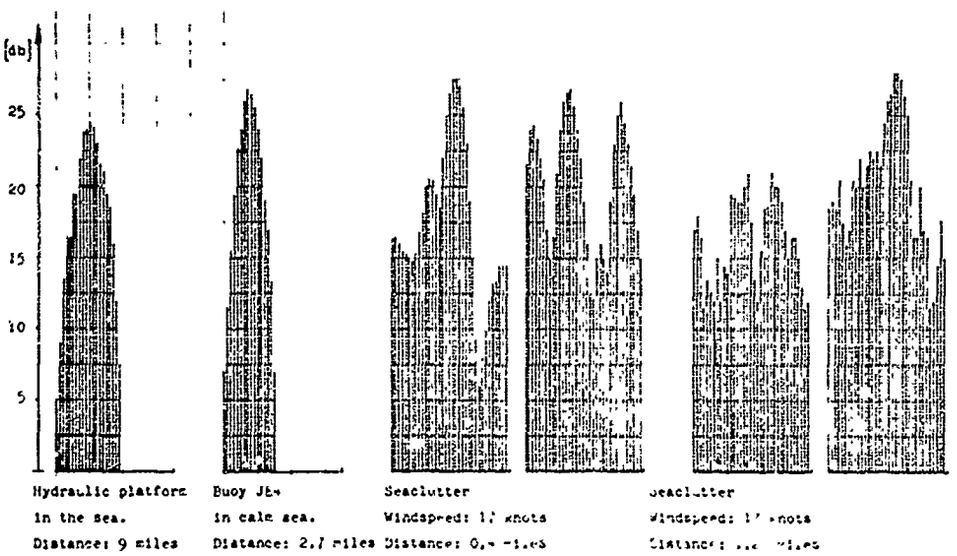

Fig. 21 Relative echoamplitudes of some different targets. (Antenna 24 $\frac{\text{rev.}}{\text{min.}}$, 1.2° Puise repetition frequency 1000 Hz)

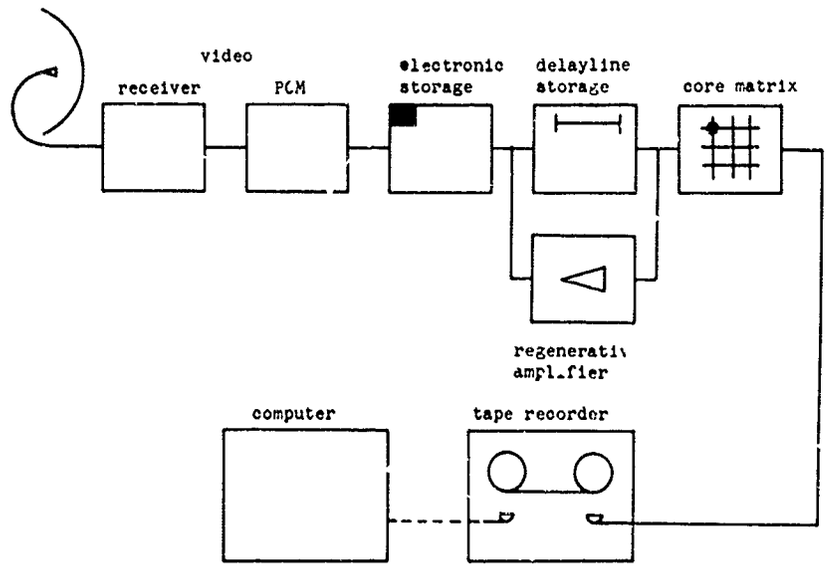

Fig. 22 Block diagram of a measuring instrument for radarechos

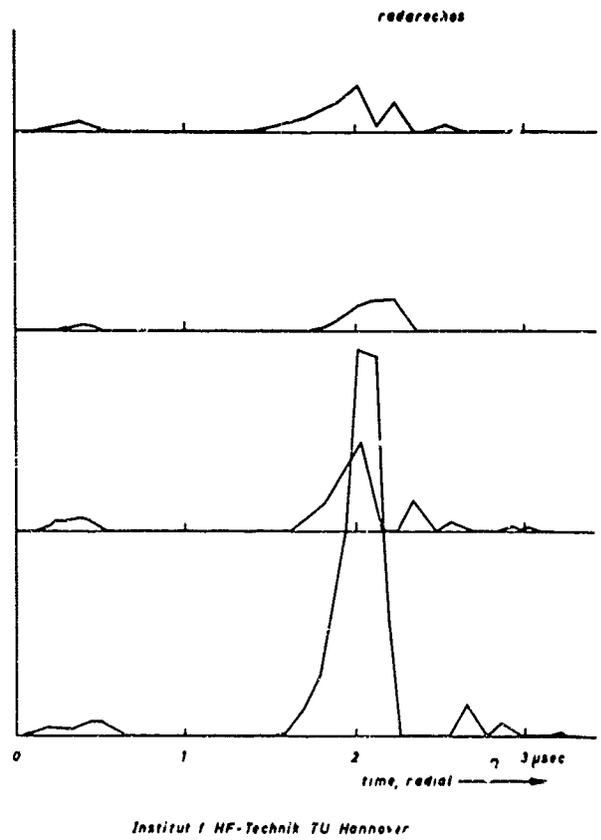

Fig. 23 PCM signals, analogue plot of a computer

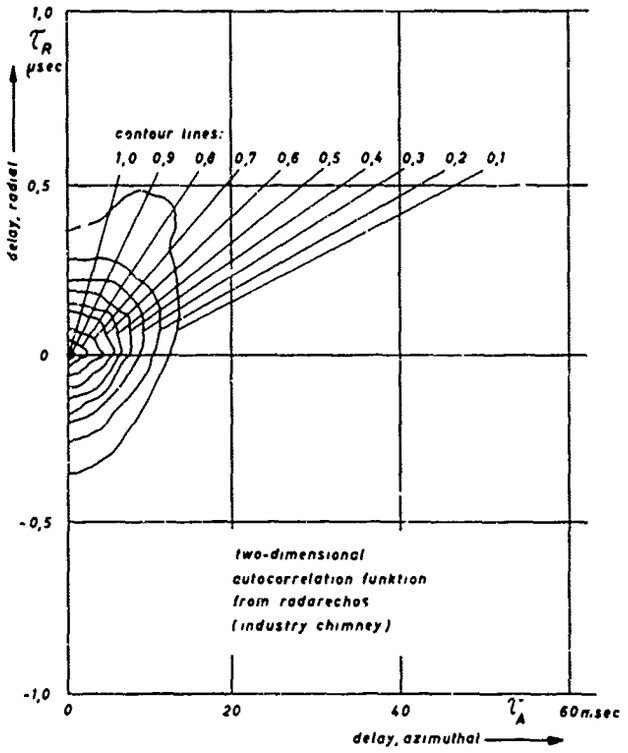

Fig. 24 Two-dimensional autocorrelation-function of radarechos (Factory chimney)

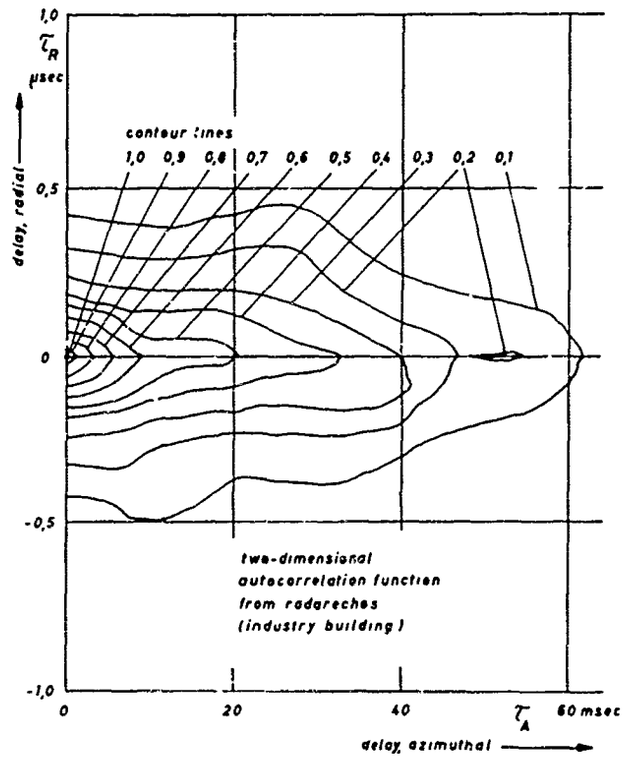

Fig. 25 Two-dimensional autocorrelation function of radarechos. (Industrial building)

Description of an analog instrument measuring and recording the echopower received at a radar from intentionally chosen targets.

Reference: Jahrbuch der Technischen Hochschule Hannover 1960/1962
W.H. Schönfeld und H. Kaune

"Entwicklung eines Gerätes zur objektiven Messung und Registrierung der Reflexionseigenschaften von Radarzielen".

The instrument has been developed at about 1958 for the Federal Ministry of Traffic in Bonn. It can be connected to any radar set, which can continue its normal operation during measurements. Exchangeable moduls (e.g. IF-Amplifiers) are available to adapt the instrument to the special radar set. A trigger-synchronized pulse program is used to mark the chosen target on the PPI-screen (see fig.20 above). The "window" can be moved by means of a simple manual control in case of relative movement between target and radar station, to hold the chosen target inside the "window". The pulses forming the "window" are in addition used as gate pulses. Via the gates only those signals can pass to the evaluation part of the instrument, which are received from the chosen target. Fig.19 shows a block diagram of the evaluation part.

The IF-signal is rectified. The peak-value of the target response on each radius is lengthened by means of delay lines without change of its amplitude. Thereafter the pulse-amplitude modulation is transformed into a pulse-duration modulation at logarithmic scale. An oscilloscope is available to check the function of the equipment. Fig.20 shows in the middle three different kinds of display of the signals. A zero-pulse of a duration of 60 µsec is added to the PDM-pulses, to guarantee a constant number of 36 pulses inside the window independent whether the target reflects energy at all radii or not. If there is a response from the target the zero-pulse is suppressed again. The longest pulse, representing the highest amplitude (40 dB above zero) has to be a bit shorter than the inverse of the pulse repetition frequency, e.g. 900 µsec, if the prf is 1 kHz. The 36 pulses are recorded thereafter on a magnetic drum. By means of a preset electronic counter one pulse after the other is picked up from the drum, one for each revolution of the drum. By this means the frequency is divided by 36. The pulses then have a frequency of roughly 28 Hz, which means that they can be recorded with an ordinary pen recorder. At the bottom of fig.20 and fig.21 you see typical recordings of different targets.

Description of a digital instrument measuring and recording the echopower received at a radar from intentionally chosen target areas.

Reference: Doctor-Thesis of K.A. Lothar Krisch,
Institut für Hochfrequenztechnik, Technische Universität Hannover,
to be published in autumn 1970.

Clutter research needs such a high amount of measured values, that they can only be evaluated by a computer. We decided therefore to develop a digital measuring instrument. Integrated circuits and other modern components made it possible to use a PCM-code with 8 bits and a sampling frequency of 10 MHz. As we have the intention to investigate, whether diversity methods will lead to improvement of the signal-to-noise ratio in the presence of sea clutter, we have built two equal channels. We think of antenna-diversity (two antennas at different heights) and frequency-diversity. The channels can, in addition, work together with interlaced sampling pulses resulting in a sampling-frequency of 20 MHz. Similar to the analog instrument a certain measuring area can be chosen and be indicated on the PPI-display simultaneously. The area can be rather large in the radial direction. The limitation of the area makes it possible to use the dead time for a frequency-band-compression by means of storage devices (see fig.22). The tape recorder is a normal audio-recorder.

The main advantage of this kind of recording is:

1.) The recorded data can directly be handled by a computer to evaluate all wanted statistical data.

2.) The computer can be used as a digital-to-analog converter, to make the entire video-signal visible by means of an x-y-recorder (see fig.23).

3.) The computer can be used as a simulator for different evaluation methods. The same set of data can be processed at home in different ways, without the necessity of repeated measurements under different conditions in the field. Fig.24 and fig.25 show autocorrelation-functions calculated by a computer and plotted with an x-y-recorder.

4.) With a decoder an analog signal can be used for further experiments.

Sea clutter measurements with the new instrument are planned during the storm-period in autumn 1970.

Synopsis of methods and proposals to improve the signal-to-noise ratio in the presence of sea clutter with related references.

	Proposal	Reference	Results
1	Sensitivity-Time-Control (STC) and logarithmic IF-amplifiers	Merill I. Skolnik Introduction to Radar Systems McGraw-Hill 1962	Difficult to adjust, when target signal is only slightly stronger than clutter. Compromise because clutter varies with direction of observation.
2	Integration		
2a	Post detection integration	See reference 1	Integration of n = 10 hits leads to an improvement of 6 dB.
2b	Digital integration	1. Mellberg Video-Korrelator. ENT Vol.39, No.4,1964 2. Hobbard Digital Automatic Radar Data Extraction. J.Brit.IRE Nov. 1963 3. Child Digital Data Processing Considerations in Radar. The Radio and Electronic Eng. Jan. 1964	Less efficient than the analog integration method.
2c	Integration by a special two-layer luminiscent screen	Harrison Methods of Distinguishing Sea Targets from Clutter on a Civil Marine Radar. The Radio and Electronic Eng. April 1964	No quantitative Information of factor of improvement.
2d	Integration by the storage capacity of a vidicon	Harrison see reference 2c	Unsufficient dynamical properties of vidicons. Unsufficient integration with moving targets.
2e	Integration on foto-film (Fotoplott of Kelvin Hughes)	H.G. Möller 1964 not published	Similar difficulties than 2d, additional delay because of processing time of film.
3	Correlation methods	Boring, Flynt, Long, Widerquist Sea Return Study, Final Report, Department of the Bureau of hips. Georgia Institute of Technology, August 1957	Improvement 6 dB with horizontal polarisation 16 dB with vertical polarisation. Lower factors if the target itself is fluctuating. Value of this investigation is more to the side of phenomenology
4	Fast motion effect. (Six storage vidicons energized by a mechanical scanning system)	Crost A Motion-Enhancement Display by Time Compression. US Army Signal Research and Development Laboratory Fort Monmouth NJ	No quantitative evaluation. Expensive Equipment. Mechanical Scanning.

	Proposal	Reference	Results
5	Special radars		
5a	Doppler radar	Rosenberg, Ostrovsky, Kalmykow Frequenzverschiebung von Radarwellen, die von der rauhen Meeresoberfläche zurückgestreut werden. Radiophysika, Vol.9, No.2, 1966	Doppler shift too small in comparison to the Doppler shift of small fluctuating targets, e.g. buoys in the sea.
5b	Chirp radar	1. Harrison see reference 2c	Harrison reports that a chirp radar improves the signal-to-noise ratio by 13 dB in a snow storm.
		2. Sclater New "Shirping" Schemes sharpen Radar Returns. Electronic Design, Vol.15, No.19, Sept.1967	Sclater mentions a submarine-periscop found in sea clutter.
5c	Pulse coded radar	Proposal of W.H. Schönfeld	Not yet tested.
6	Antenna speed		
6a	Slow antenna	No known reference	Integration time corresponding to life duration of clutter signals. Disadvantage: If antenna rotation frequency is equal or a full part of the frequency of the sea wave a small target may disappear always in a wave trough.
6b	High speed antenna (20 to 1400 rpm)	Croney Improved Radar Visibility of small Targets in Sea Clutter. The Radio and Electronic Eng. Sept. 1966	Improvement by 6 dB. The disadvantage of 6a is avoided.
7	Diversity systems		
7a	Jumping-frequency radar	Gustafson System properties of jumping-frequency radars. Philips Telecommunication Review, Vol.25, No.1, Juli 1964	No quantitative evaluation.
7b	Frequency diversity with two simultaneous frequencies	W.H. Schönfeld, V. Müller, K.D. Schwarz Report on the state of arts in sea clutter reduction. Ortung und Navigation, Vol.II, 1968 W.H. Schönfeld, V. Müller Detection of active Radar Targets in the Presence of Sea-Return Echos. 7-2-5 VIIth Int. Conf. on Lighthouses, Rome, 1965	Details see this paper.
7c	Polarisation diversity	See references 3 and 7b correlation methods	Experience of author of this paper: less efficient than frequency diversity.
7d	Antenna diversity	See 7b	Results not yet available.
7e	Two divergent beams	See 7b	Correlation and other methods of comparison are possible. No results yet. High costs.

THE INTERACTION OF HF/VHF RADIO WAVES WITH THE SEA SURFACE AND ITS IMPLICATIONS

by

Donald E. Barrick

The Electrical Engineering Department
The Ohio State University
Columbus, Ohio 43210

and

Battelle Memorial Institute
Columbus Laboratories
Columbus, Ohio 43201

SOMMAIRE

Pour étudier l'interaction des ondes radio à hautes fréquences avec la mer, l'auteur analyse les perturbations aux limites. Il voit l'influence de l'agitation de la mer sur la propagation des ondes terrestres à travers l'océan comme une augmentation de l'impédance effective à la surface. A l'aide du spectre des ondes de vent de Phillips, il procède à des estimations quantitatives de la déperdition supplémentaire due à l'état de la mer. Il montre que la diffusion à partir de la mer est due à l'effet Bragg. Il extrait par dérivation, puis examine, l'intensité et le spectre du signal diffusé. Il analyse enfin plusieurs configurations bistatiques de radar utilisées pour la mesure des spectres des ondes océaniques. Ces configurations impliquent diverses conbinaisons de bateaux, de bouées, d'avions, de satellites et de stations côtières. Il examine sous une forme assez détaillée les possibilités de réalisation de deux systèmes de ce genre, et conclut que le matériel dont on dispose semble en permettre le développement.

THE INTERACTION OF HF/VHF RADIO WAVES WITH THE SEA SURFACE AND ITS IMPLICATIONS

Donald E. Barrick

The Electrical Engineering Department
The Ohio State University
Columbus, Ohio 43210

and

Battelle Memorial Institute
Columbus Laboratories
Columbus, Ohio 43201

SUMMARY

The interaction of HF and VHF radio waves with the sea is examined using a boundary perturbation analysis. The effect of ocean roughness on ground-wave propagation across the ocean is seen as an increase in the effective surface impedance. Quantitative estimates are made of the added loss due to sea state using the Phillips wind-wave spectrum. Scatter from the sea is shown to arise from the Bragg effect. Both the scattered signal intensity and spectrum are derived and examined. Finally, several bistatic radar configurations for measuring ocean-wave spectra are analyzed. These involve various combinations of ships, buoys, aircraft, satellites, and shore stations. The feasibility of two such systems is examined in some detail, and their implementation appears possible with present-day hardware.

1. INTRODUCTION.

Winds blowing at speeds greater than 10 knots over the ocean excite the longer and higher ocean waves. For example, a 10-knot wind can create waves about 20 meters in length, while a 30-knot wind will arouse waves about 200 meters long. Since wind speeds between these limits are highly indicative of the meteorological conditions over the ocean, the remote sensing of the characteristics of ocean waves with these lengths will provide valuable data concerning the weather over the sea.

Elementary physical principles indicate that electromagnetic waves whose wavelengths are comparable to the longer ocean wavelengths should interact significantly with these water waves. Such electromagnetic waves lie in the HF and VHF regions of the spectrum. These suspicions were confirmed and the interaction mechanism was discovered experimentally by Crombie in 1955[1]. He observed that near-grazing backscatter at 13.56 MHz is Doppler-shifted by a discrete increment above and below the carrier. The velocities required to produce these shifts are possessed only by ocean waves whose lengths are precisely one-half the electromagnetic wavelength and whose crestlines lie perpendicular to the transmission path. Hence, the mechanism was seen to be Bragg scatter from ocean-wave trains moving toward and away from the radar in much the same manner as a set of translating diffraction gratings. In an accompanying paper, Crombie presents recent experimental observations of this phenomenon and interprets the two spectral shifts in terms of advancing and receding water waves at a number of HF frequencies.

Quantitative theoretical estimates of the interaction, however, lagged the measurements by many years. Now, however, applying the classical boundary perturbation approach of Rice[2] to a random surface, we are able to predict the magnitude of scatter and propagation across the sea at HF and VHF. Both high-angle reflection and scatter as well as near-grazing propagation (i.e., ground-wave propagation) and scatter can and will be analyzed in this manner here. The sea surface at HF/VHF is very amenable to analysis by this technique because it satisfies all of the necessary assumptions inherent in the derivation: (i) its height, ζ, above a mean plane is small in terms of the wavelength; (ii) its slopes (i.e., $\zeta_x = \partial\zeta/\partial x$ and $\zeta_y = \partial\zeta/\partial y$) are small for these longer ocean waves; and (iii) the ocean-water medium is highly conducting, and hence an impedance boundary condition can be employed.

In the next section, we show that the ocean roughness can affect a vertically polarized ground wave propagating above it. Such an effect should be expected, since corrugations have long been used to guide waves along the conducting surface of antennas, wires, and other structures. It is shown that the random roughness changes the effective surface impedance; this corrected impedance can then be used in any of the ground-wave treatments to estimate the field strength attenuation with distance. We present such curves based on the Phillips isotropic wind-wave spectrum.

The subsequent section deals with scattering of HF/VHF waves by the longer ocean waves. Both near-grazing (ground-wave) incidence and the higher incidence angle regions are considered. An expression for σ^0, the scattering cross section per unit surface area is derived for the Phillips ocean wave-height model. We also obtain an expression for the scattered signal spectrum, to the first order, and show the discrete, Doppler-shifted frequencies measured by Crombie and others are predicted. The expressions are general and can be applied to backscatter as well as bistatic radio geometries.

In the final section, we discuss possible methods of sensing the ocean wave-height spectrum by measuring the electromagnetic scattered signal and its Doppler spectrum. Several have already suggested the use of HF ionospherically propagated sea scatter as a method of ocean-wave sensing[3]. We suggest nonionospheric techniques here involving combinations of ships, buoys, aircraft, and shore stations in bistatic modes to measure the ocean-wave spectrum. The signal processing techniques currently available permit the resolution necessary to sort out the presence and strengths of ocean waves of various lengths and directions; hence, such techniques can offer a valuable input to real-time global oceanography/meteorology.

2. GROUND-WAVE PROPAGATION ACROSS THE SEA.

2.1 Derivation of Effective Surface Impedance of a Slightly Rough Surface.

Much attention has been given to radiation from a dipole above a smooth, finitely conducting medium. Sommerfeld[4] first solved the problem for a planar interface; Norton[5] later interpreted his results and reduced them to a convenient graphical form for engineering calculations. Others, including

van der Pol and Bremmer[6] and Fock[7], obtained asymptotic solutions to the problem of radiation above a smooth spherical earth, and Norton generated curves to facilitate the use of these results[8]. A thorough review of the subject by Wait[9] is recommended to the reader.

Essentially, Wait[9] shows that one can formulate the ground-wave radiation and propagation problem in terms of the impedance of the surface normalized to that of free space, i.e., $\Delta = Z_s/Z_o$, where Z_s is the impedance of the surface in ohms, and $Z_o \simeq 120\ \pi\ \Omega$ is the impedance of free space. The quantities Δ and Z_s are functions of the grazing angle and material properties. For the earth and sea, Δ is much less than unity, and hence vertical polarization is favored for near-grazing or ground-wave propagation.

It was established by Norton[10] and Wise[11] that vertically polarized waves propagating near grazing and near the surface of the ground appear to be guided waves locally, even though macroscopically they do not exhibit this guided (or Zenneck-wave) nature.* Hence, we shall derive in this section the effective impedance of a slightly rough surface, treating the propagation field at a mean planar interface as a locally guided wave.

First, we write the expression for the planar field guided by a flat, smooth, highly conducting surface. The geometry is shown in Figure 1. Jordan[12] can be consulted for this straightforward derivation:

$$E_z \simeq E_0 \exp\{ik_0\sqrt{1 - \Delta^2}\, x - ik_0 \Delta Z - i\omega_0 t\} \quad , \tag{1a}$$

$$E_x \simeq E_0 \Delta \exp\{ik_0\sqrt{1 - \Delta^2}\, x - ik_0 \Delta Z - i\omega_0 t\} \quad , \tag{1b}$$

$$H_y \simeq \frac{-E_0}{120\pi} \exp\{ik_0\sqrt{1 - \Delta^2}\, x - ik_0 \Delta Z - i\omega_0 t\} \quad , \tag{1c}$$

where E_0 is the E-field amplitude constant, and k_0 is the wavenumber in free space, i.e., $2\pi/\lambda$, where λ is the wavelength. The normalized surface impedance at grazing for a medium below the smooth interface of complex permittivity ϵ_1 and permeability μ_1 can be written as

$$\Delta = \frac{1}{120\pi}\sqrt{\frac{\mu_1}{\epsilon_1}} \times \sqrt{1 - \frac{\epsilon_0\mu_0}{\epsilon_1\mu_1}} \simeq \frac{1}{120\pi}\sqrt{\frac{\mu_1}{\epsilon_1}} \text{ for } \epsilon_1 \gg \epsilon_0 \quad .$$

Included in ϵ_1 is the effect of conductivity, i.e., $\epsilon_1 = \epsilon_{r1} + i\,\sigma_1/\omega_0$, where ϵ_{r1} is the real dielectric constant of the medium and σ_1 is its conductivity. For sea water at 10 MHz, for example, $\epsilon_{r1} \simeq 80\ \epsilon_0$, $\sigma_1 \simeq 4$ mhos/meter, $\epsilon_1 \simeq \epsilon_0(80 + i7200)$, and $\Delta \simeq 1.18 \times 10^{-2} \exp(-i\pi/4)$.

Now, we write the total field above a slightly rough surface (see Figure 2) as follows:

$$E_x = \Delta E(h,0,z) + \sum_{m,n=-\infty}^{\infty}{}' A_{mn}\, E(m + h,n,z) \quad , \tag{2a}$$

$$E_y = \sum_{m,n=-\infty}^{\infty}{}' B_{mn}\, E(m + h,n,z) \quad , \tag{2b}$$

$$E_z = E(h,0,z) + \sum_{m,n=-\infty}^{\infty}{}' C_{mn}\, E(m + h,n,z) \quad , \tag{2c}$$

where

$$E(m + h,n,z) = E_0 \exp\{ia(h + m)x + iany + ib(m + h,n)z\} \quad , \tag{3a}$$

and

$$b(h + h,n) = \sqrt{k_0^2 - a^2(m + h)^2 - a^2n^2} \quad . \tag{3b}$$

The definition of b above is such that Equations (2) satisfy the Helmholz wave equation. The Cartesian components of the H-field are not given here, but are readily determined from Maxwell's equations.

In the above equations, the presence of roughness manifests itself as the summation terms. As the roughness height approaches zero, A_{mn}, B_{mn}, C_{mn}, will vanish, and $b(h,0) \to -k_0\Delta$; Equations (2) then become identical with Equations (2) then become identical with Equations (1) for a guided wave over a smooth impedance boundary.

Also, C_{00} is taken to be identically zero in (2c). This choice is possible; what it really means is that all of the remaining constants are normalized so that the 0,0 mode appearing in (2c) is removed from the summation and grouped with the preceding term, E(h,0,z) with amplitude E_0. Physically, the guided-wave portions of the field appearing in Equations (2) are all terms having the E(h,0,z) structure. These are

$$E_x^G = (\Delta + A_{00})\, E(h,0,z) \quad , \tag{4a}$$

*This is analogous to the fact that a spherical wave appears planar locally, i.e., within the area of a Fresnel zone, but macroscopically it is spherical in nature.

$$E_y^G = B_{oo}E(h,0,z) \quad , \tag{4b}$$

$$E_z^G = E(h,0,z) \quad . \tag{4c}$$

The remaining portions of Equations (2) consist of modes generated by the roughness. These modes, to be termed the scattered field here, actually include both propagating and evanescent modes.

The guided-wave portions of the perturbed fields are given by Equations (4). When one compares (4a) and (4c) with (1b) and (1a) for a smooth impedance boundary, one is lead to define an "effective" or average impedance guided-wave propagation across a roughened surface as

$$\bar{\Delta} = \langle \Delta + A_{oo} \rangle = \Delta + \langle A_{oo} \rangle \tag{5}$$

i.e., the effective impedance consists of the constant impedance of a smooth interface plus $\langle A_{oo} \rangle$, which accounts for the roughness. The braces $\langle\ \rangle$ denote an average. This convenient definition will in fact be used, and the goal of the analysis will be to derive an expression for $\langle A_{oo} \rangle$. If the roughness is to contribute to the impedance, we expect this average to be nonzero. Physically, (5) says that the average wave front and polarization tilt at the surface is

$$\langle E_x^G \rangle / \langle E_z^G \rangle = \bar{\Delta} = \Delta + \langle A_{oo} \rangle \quad ,$$

which is another way of defining the effective surface impedance.

In solving for A_{oo}, we expand the surface height itself in a Fourier series, valid over a square of side L:

$$\zeta(x,y) = \sum_{m,n=-\infty}^{\infty} P(m,n) \exp[ia(mx + ny)] \tag{6}$$

where $a = 2\pi/L$. We can also write the surface slopes $\partial\zeta/\partial x$ and $\partial\zeta/\partial y$ by differentiating (6).

We intend to solve for A_{oo} by a standard perturbation approach. Equations (2) for the fields are to be substituted into the Leontovich boundary condition at the surface. This condition is:

$$\vec{E}^T - (\hat{n} \cdot \vec{E}^T)\hat{n} = \eta_o \Delta (\hat{n} \times \vec{H}^T) \quad .$$

Here, $\vec{E}^T$ and $\vec{H}^T$ are the total electric and magnetic fields above the surface, as given in Equations (2) with $z = \zeta$. The quantity $\hat{n}$ is the unit normal to this surface. It is expressible in terms of the surface slopes as

$$\hat{n} = \frac{-\frac{\partial\zeta}{\partial x}\hat{x} - \frac{\partial\zeta}{\partial y}\hat{y} + \hat{z}}{\sqrt{1 + \left(\frac{\partial\zeta}{\partial x}\right)^2 + \left(\frac{\partial\zeta}{\partial y}\right)^2}} \quad . \tag{7}$$

The determination of A_{oo} proceeds by ordering the terms in the resulting series in order of smallness. The following quantities are assumed to be small, and hence serve as perturbation parameters: (1) $(k_o\zeta)^2 \ll 1$ -- i.e., roughness height is small compared to wavelength; (2) $(\partial\zeta/\partial x)^2$, $(\partial\zeta/\partial y)^2 \ll 1$ -- i.e., the surface slopes are relatively small; and (3) $|\Delta| \ll 1$ -- i.e., the normalized impedance of the medium below the surface is small.

All of the above conditions are satisfied by the sea at HF/VHF.

Sparing the algebraic drudgery (the details of which can be found in Reference 13), the above procedure shows that to the first order in the perturbation parameters, $A_{oo} = 0$. To the second order,

$$A_{oo} \simeq \sum_{m,n}{}' \left[\frac{k_o a^2 m^2}{b(m+h,n)D(m,n)} + \Delta\left[\frac{a^2m^2 + a^2n^2 - k_o am}{D(m,n)} + k_o am + \left(\frac{a^2m^2 - a^2n^2}{2}\right)\right]\right] |P(m,n)|^2 \tag{8}$$

where

$$D(m,n) = 1 + \frac{k_o}{b(m+h,n)}\Delta\left[\frac{b^2(m+h,n)}{k_o^2} + 1\right] \quad . \tag{9}$$

The above expression for A_{oo} is valid for deterministic, periodic surfaces as well as random rough surfaces. For example if the surface is sinusoidal in the x-direction with period L, then A_{oo} consists of only two terms, the ones for $m = \pm 1$, $n = 0$. When A_{oo} is then added to Δ, one has the effective surface impedance of this sinusoidal surface.

When the surface is random, as in the case of the sea, the $P(m,n)$ are random variables. In this case, we are interested in the average value of A_{oo}, and the $P(m,n)$ are related to the wave height spectrum of the surface, $W(p,q)$ as follows:

$$\langle |P(m,n)|^2 \rangle = \frac{\pi^2}{L^2} W(p,q) \tag{10}$$

where $p = am = 2\pi m/L$ and $q = an = 2\pi n/L$. If we then take the average of A_{oo} in (8), use (10), and

substitute $\langle A_{00} \rangle$ into (5) we obtain:

$$\bar{\Delta} = \Delta + \frac{1}{4} \int_{-\infty}^{\infty} \int_{-\infty}^{\infty} F(p,q)\, W(p,q)\, dp\, dq \tag{11}$$

where

$$F(p,q) = \frac{p^2 + b'\Delta(p^2 + q^2 - k_o p)}{b' + \Delta(b'^2 + 1)} + \Delta\left(\frac{p^2 - q^2}{2} + k_o p\right) \tag{12a}$$

$$b' = \frac{1}{k_o}\sqrt{k_o^2 - (p + k_o)^2 - q^2} \quad . \tag{12b}$$

The definition of W(p,q) follows that of Rice[2], as does most of the notation used here; this is done to facilitate reference to his classic perturbation treatment.

As a check on (11), if we permit Δ to approach zero in (12) we obtain $F(p,q) = p^2/b'$, and

$$\bar{\Delta} = \Delta + \frac{1}{4} \int_{-\infty}^{\infty} \int_{-\infty}^{\infty} \frac{p^2 W(p,q)\, dp\, dq}{b'} \tag{13}$$

This result was derived from an integral equation technique by Feinberg[14]. If we allow Δ to approach zero, Equation (13) becomes identical to that obtained by Rice[2] for a perfectly conducting surface.

To interpret the simpler form, (13), let us refer to Figure 3. We separate the contribution to $\bar{\Delta}$ of the integral into two parts, R_Δ and $-iX_\Delta$. The contribution R_Δ comes entirely from that part of the height spectrum lying within the circle centered at $p/k_o = -1$, $q/k_o = 0$. If there are no roughness spatial frequencies, or waves, within this region, then the resistive contribution is zero; these spatial frequencies must thus be less than $2k_o$. Physically, this statement means that only ocean waves longer than $\lambda/2$ can contribute to the resistive portion. From a study of scatter from this type of surface,[15,16] it has been shown that waves whose lengths are greater than $\lambda/2$ are responsible for scatter. Hence the interpretation of the resistive portion becomes clearer; longer ocean waves whose wavenumbers lie within the circle are responsible for removal of energy from the guided wave and scatter of this energy into all directions in the upper hemisphere. This energy removal produces an increase in the resistive term of the surface impedance.

On the other hand, if there are no ocean waves whose lengths are greater than a half-wavelength (i.e., that lie outside the unit circle), then the roughness contribution to $\bar{\Delta}$ is purely reactive; in addition, it is always an inductive reactance. Roughness waves of these shorter lengths do not scatter (at least to the first order in $k_o\zeta$, the roughness height). Hence, this higher-frequency roughness produces a perturbation on the local field at the surface that exists only at and near the region between the waves; since there are no scattered propagating fields removing energy from the guided wave, this effect should be evident only very near the surface. The perturbed modes in this case are not propagating, but evanescent.

2.2 Effective Surface Impedance of the Sea Using the Phillips Wind-Wave Spectrum.

The presence of roughness on the ocean is due to winds blowing across the sea. The full growth of the longer waves (20-200 meters) by winds (10-50 knots), however, requires several hours to fully develop. After the winds have ceased, the higher longer waves do not immediately abate. They decrease in amplitude only as they travel to other areas of the ocean and as they break at their crests.

Thus, the longer waves at a given patch on the ocean originate from two sources: (i) winds which have blown across that patch for the several hours prior to the observation, and (ii) waves which have been developed at other times and places and which may be considerably weaker in magnitude than at their origins; these latter are called swell. Only in the case of the former are there available simple mathematical models relating the wave heights to their meteorological sources, the winds.

Hence the best we can do in attempting to estimate the effect of sea state on radio-wave propagation and scatter is to use a simple wind-wave model and neglect the effect of swell. The error involved will almost certainly be one of overestimation. Roughness heights due to swell are bound to be less than those due to the recent, local winds, since "swell" is actually "sea" in the process of dissipation. Therefore, the predictions of the effects presented here represent "worst-case" estimates, and should be treated as such.

The Neumann-Pierson ocean-wave spectrum was suggested some fifteen years ago[17], and predictions based on it can be found in (13). Ocean-wave data gathered in recent years, however, have led many oceanographers to search for a more accurate model. Phillips[18] and Munk[19] have presented convincing evidence to show that the spatial spectrum should behave as $(p^2 + q^2)^{-2}$, instead of the $(p^2 + q^2)^{-9/4}$ dependence of the Neumann-Pierson model. More important, however, measurements show that the lower-end cutoff is much more pronounced than the artificial exponential factor attached to the Neumann-Pierson spectrum. Slope measurements by Cox and Munk[20] show that the spectrum is closer to being isotropic than the cosine-squared directionality often assumed with the Neumann-Pierson model[17].

Hence, we employ the following spectrum[18]:

$$W(p,q) = \frac{4B}{\pi(p^2 + q^2)^2} \tag{14}$$

where $B \approx 0.005$, $g = 9.81\ m/s^2$ (acceleration of gravity), and U is the wind speed in m/s. The spectrum is identically zero for $\sqrt{p^2 + q^2} < g/U^2$ and also in the half-space from which the wind is coming.

We use (14) in a numerical evaluation of Equation (11), and the results for the normalized resistive and reactive portions of effective surface impedance are shown in Figure 4. We divide the spectrum, (14), by two and integrate over all p,q space, rather than only over the forward wind half. This is necessary because at a given instant the sea profile will appear "frozen" to a radio wave, and it will not be possible to tell from this profile whether the waves are moving forward or backward. For the spectrum of Equation (14), the mean-square height is $h^2 = 1/2\ B\ U^4/g^2$. Since the curves are meaningful only for $k_0^2 h^2 \ll 1$, they can be used for frequencies up to about 50 MHz with a wind speed of 25 knots. The conductivity of the sea is taken as $\sigma = 4$ mhos/meter.

2.3 Basic Transmission Loss Across the Sea Using the Phillips Wind-Wave Spectrum.

We can now employ the effective surface impedance, $\bar{\Delta}$, accounting for roughness in any of the more-or-less standard techniques for calculating ground-wave propagation. In particular, we employ a modified version of a FORTRAN IV program available from ESSA[21] for propagation over a spherical earth. Their program is modified to the extent that it will accept the resistive and reactive portions of the surface impedance rather than the ground conductivity and dielectric constant; the output is modified so that it prints basic transmission loss as well as the other variables.

Basic transmission loss is a concept widely publicized by Norton[22],[23] in the 1950's. Formally, it is defined as

$$L_b = 10\ \mathrm{Log}_{10}\left(\frac{P_{ti}}{P_{ri}}\right) \quad , \qquad \text{(decibels)} \qquad (15)$$

where P_{ti} is the power transmitted by an isotropic radiator and P_{ri} is the power received by an isotropic radiator. In a simple communication problem, one must merely subtract out the free-space antenna gains (in dB) in order to determine the overall power loss. For example, the basic transmission loss between two points in free space separated by distance d is $10\ \mathrm{Log}_{10}(4\pi d/\lambda)^2$; if the same two points are located above a flat, perfectly conducting ground plane, the 4 is replaced by 2 in the parentheses. The presentation of ground-wave attenuation in the form of basic transmission loss appears to be more readily interpretable and useful than many of the ground-wave normalizations (e.g., unity electric dipole, 1 kW transmitted power, field strength one mile from the transmitter, etc.).

Figure 5 shows this basic transmission loss between two points at the surface of a perfectly smooth sea as a function of range. These were computed from the program using a water conductivity $\sigma = 4$ mhos/m (typical of the Atlantic), and effective earth radius factor of 4/3 (accounting for atmospheric refractivity in an idealized manner). In Figures 6-8, we show the added transmission loss due to sea state. These curves were calculated using the same program and subtracting the results from those of Figure 5 for a smooth sea. In all these cases, the transmitter and receiver points are located near the surface.

Figures 9-11 show the basic transmission loss to various points above the earth when the transmitter is located at the surface. The first number at each height-range grid point is the loss when the sea is perfectly smooth, while the second represents the loss when the sea is fully excited by a 25-knot wind. The "height-gain" effect is clearly in evidence as one moves upward at a given range; one first observes a drop in signal of 2-3 dB and then a monotonic increase as he moves out of the surface-wave region into the lit, or space-wave region. In the lit region, such curves and computer programs are not necessary, because the transmission loss becomes simply the inverse-distance relation given after Equation (15).

One should observe from Figure 6 that the added "loss" due to sea roughness in some cases is negative, indicating an <u>increase</u> in signal level. This effect is expected, because at these lower frequencies, most of the ocean wavelengths are still small compared to the radio wavelength. Thus the contribution to the surface impedance is almost entirely reactive, rather than resistive. Small corrugations on an otherwise conducting surface have long been known to contribute to its reactance, with a resulting effect of "trapping", or guiding the energy near the surface. Wait[9] discusses this trapping mechanism. The effect here is not strong, however, because the resistive portion is already high due to the finite water conductivity. Also, it should be noted by comparing the curves at 10 MHz and 30 MHz (Figures 7 and 8) that losses due to sea state would seem to be less pronounced above about 15 MHz. This arises from the fact that the simple increase in impedance due to water conductivity with frequency overshadows the increase due to roughness.

Again, it should be mentioned that the curves presented here are based on the Phillips isotropic wind-wave spectrum. As such, the losses are believed to represent an upper limit, because (i) it takes many hours for a strong wind to fully arouse the sea; (ii) the length of ocean over which an intense wind is blowing (termed "fetch") may be less than the range between transmitter and receiver, and (iii) the gentler, ever-present swell contribution to roughness is neglected.

3. SCATTER OF A GROUND WAVE BY THE MOVING SEA SURFACE.

3.1 Derivation of the Scattered Field Mode Coefficients.

In the preceding section, we examined the structure of the ground wave propagating across a rough sea. We represented the electric field above the slightly rough surface by Equations (2), and we saw that the influence of the roughness on ground-wave propagation manifested itself in the second-order A_{00} term of the series of (2a). In this section, we wish to examine the remaining perturbed field coefficients A_{mn}, B_{mn}, and C_{mn}. The existence of these coefficients is due to the roughness on the surface. The series represent plane-wave modal expansions of the "scattered" field, although the modes of this "scattered" field may not be propagating. When m and n are such that b(h + m,n), defined in (3b), is imaginary, the modes are evanescent, or nonpropagating. When m and n are sufficiently small, however, that b(h + m,n) is real, the scattered modes propagate upward, away from the surface, in directions

related to m and n. In the wavenumber space of Figure 3, this corresponds to p/k_o ($= am/k_o$), q/k_o ($= an/k_o$) falling inside the displaced unit circle.

We generalize the previous expansions at this point to include time. The slightly rough surface varies in height with time as

$$\zeta(x,y,t) = \sum_{m,n,\ell=-\infty}^{\infty} P(m,n,\ell)\exp\{ia(mx + ny) + iw\ell t\} \quad , \tag{16}$$

where $w = 2\pi/1$, T being the basic time period of the Fourier expansion. The remaining terms are as defined in (6). The perturbed fields arising from a vertically polarized wave at grazing incidence passing over the surface are still represented as in Equations (2), but with the added subscript ℓ (i.e., $A_{mn\ell}$, $\cdots$, $E(m + h,n,\ell,z)$). In addition, (3a) is expanded to show this time dependence as

$$E(m + h,n,\ell,z) = E_o\exp\{ia(h + m)x + iany + ib(m + h,n)z + i(w\ell - \omega_o)t\} \quad , \tag{17}$$

where the time dependence of the incident field on the carrier ω_o is $e^{-i\omega_o t}$.

The solution of the problem here then consists of finding $A_{mn\ell}$, $B_{mn\ell}$, and $C_{mn\ell}$. This is done in the straightforward perturbation manner. We again employ the Leontovich, or impedance, boundary condition given before Equation (7), since this condition is fulfilled by sea water below UHF. The assumptions involved in the perturbation parameters are as given after Equation (7). The general coefficients* for arbitrary m, n, and ℓ are of first-order in these perturbation parameters, and are:

$$A_{mn\ell} = \frac{N_A}{D(m,n)} P(m,n,\ell) \quad ; \quad B_{mn\ell} = \frac{N_B}{D(m,n)} P(m,n,\ell) \quad ; \quad C_{mn\ell} = \frac{-a(m + h)\, N_A - anN_B}{b(h + m,n)\, D(m,n)} P(m,n,\ell) \quad , \tag{18a,b,c}$$

where

$$N_A = -iam\left[1 + \frac{\Delta k_o}{b}\left(1 - \frac{a^2(h + m)^2}{k_o^2}\right)\right] + ian\,\frac{\Delta k_o}{b}\cdot\frac{a^2n(m + h)}{k_o^2} \quad , \tag{19a}$$

$$N_B = -ian\left[1 + \frac{\Delta k_o}{b}\left(1 - \frac{a^2n^2}{k_o^2}\right)\right] + iam\,\frac{\Delta k_o}{b}\cdot\frac{a^2n(m + h)}{k_o^2} \quad , \tag{19b}$$

and D(m,n) is as given in Equation (9).

Throughout the derivations of the above coefficients, only first-order terms in $k_o\zeta$, ζ_x, ζ_y, and Δ (the perturbation parameters) were retained. The second-order corrections have been derived by Rice[2] for perfectly conducting surfaces, and these are complex in general and difficult to interpret. When one reaches the point where the second-order terms are necessary to correct the above expressions, the entire perturbation technique has been pushed to the limit of its expected validity.

The first-order coefficients of the scattered field give particularly enlightening interpretations of the interaction mechanism. The direction of propagation of the scattered m,n,ℓ mode is directly related to the Fourier component of the surface, and for propagation modes, this direction is the Bragg direction required by a periodic surface with wavenumbers am and an.

3.2 The Far-Field Scatter from a Sea Surface Patch.

In Equations (2) and (18), we have modal, plane-wave expansion for the fields above a surface of infinite extent. We wish now to apply the preceding results to a patch of sea surface of finite extent. In particular, let us choose a square patch of side L. In most practical situations, L will be considerably larger than the wavelength, λ, but considerably smaller than R_o, the distance from the patch to the observation point. It is this situation which is of interest here, i.e., $\lambda \ll L \ll R_o$.

When the scattering patch is considerably smaller in extent than R_o, the far-zone distance from the patch center (See Figure 12), we can employ the following equation for the scattered magnetic field[24]:

$$\bar{H}^s(R_o,t) \simeq \frac{ik_o e^{ik_o R_o}}{4\pi R_o}\int_{-L/2}^{L/2}\int_{-L/2}^{L/2}\left[\hat{k}_o^s \times (\hat{n} \times \bar{H}^s) - \sqrt{\frac{\varepsilon_o}{\mu_o}}(\hat{n} \times \bar{E}^s) + \sqrt{\frac{\varepsilon_o}{\mu_o}}\,\hat{k}_o^s \cdot (\hat{n} \times \bar{E}^s)\hat{k}_o^s\right] e^{-ik_o\hat{k}_o^s \cdot \bar{r}'}\, dS' \quad , \tag{20}$$

where $\bar{E}^s$ and $\bar{H}^s$ in the integrand are the fields evaluated at the surface element dS'. Here $\hat{k}_o^s$ is a unit vector pointing in the desired observation direction, i.e., $\hat{k}_o^s = \sin\theta_s\cos\varphi_s\,\hat{x} + \sin\theta_s\sin\varphi_s\,\hat{y} + \cos\theta_s\,\hat{z}$, where the angles are as defined in Figure 12. The vector $\bar{r}'$ points from the origin to the local area increment, dS', on the surface of integration.

The perturbation approach of the preceding section shows that the slight roughness produces a scattered E-field, $\bar{E}^s$, whose three Cartesian components are represented by the three summations of Equations (2). It also makes it possible to choose our surface of integration as the $z = 0$ plane by writing $\bar{E}^s$ and $\bar{H}^s$ in the integrand evaluated on this plane. Then $dS' = dxdy$, and $\hat{n} = \hat{z}$; $\bar{H}^s$ is simply determined from $\bar{E}^s$ using Maxwell's equations. Also, we restrict our interest at this point to the $\hat{\varphi}_s$

*The method of solution follows directly that of Rice[2]. The algebra is straightforward and hence omitted here.

component of $\overline{H}^s(R_o,t)$, i e., the scattered H-field normal to the scatter plane. Then the integral becomes:

$$H_\varphi^s(R_o,t) = \frac{ik_o e^{ik_o R_o}}{4\pi R_o} \sum_{m,n,\ell}^{\infty} \int_{-L/2}^{L/2}\int_{-L/2}^{L/2} P(m,n,\ell) f_\varphi(m,n) e^{ia(m+h)x + iany + i(w\ell - \omega_o)t}$$

$$\times e^{-ik_o \sin\theta_s \cos\varphi_s x - ik_o \sin\theta_s \sin\varphi_s y} dxdy \quad , \tag{21}$$

where $f_\varphi(m,n)$ is a factor containing N_A, N_B, and $\hat{k}_o^s$, determined from (20).

Equation (21) can be integrated over the square patch to give

$$H_\varphi^s(R_o,t) = \frac{ik_o L^2 e^{ik_o R_o}}{4\pi R_o} G_\varphi \quad , \quad \text{where} \tag{22a}$$

$$G_\varphi = \sum_{m,n,\ell}^{\infty} P(m,n,\ell) f_\varphi(m,n) \left[\frac{\sin(k_o \sin\theta_s \cos\varphi_s - am - ah)\frac{L}{2}}{(k_o \sin\theta_s \cos\varphi_s - am - ah)\frac{L}{2}}\right] \left[\frac{\sin(k_o \sin\theta_s \sin\varphi_s - an)\frac{L}{2}}{(k_o \sin\theta_s \sin\varphi_s - an)\frac{L}{2}}\right] \times e^{i(w\ell - \omega_o)t} \tag{22b}$$

As yet, no statistics have been introduced. Equation (22) can apply for a deterministic periodic surface with Fourier expansion coefficients $P(m,n,\ell)$ as well as to a random surface. We could square H_φ^s and average at this point to obtain the scattering cross section per unit area. However, since we will ultimately be interested an expression valid near grazing (i.e., $\theta_s \to \pi/2$), we shall defer the averaging process, and first study the effect of scatter above a plane with nonzero surface impedance, Δ.

3.3 Application of the Compensation Theorem to Scatter.

King[25,26] has recently applied the Compensation Tneorem to the problem of radiation from a dipole above a plane with surface impedance, Δ. We shall apply it in the same manner to our problem: reradiation from a scattering patch on the surface to a far-zone point above a plane with effective surface impedance, Δ. The reader is referred to King's papers for details on the technique.

The derivation shows that the general radiation problem can be reduced to the following integral equation (Equations (6) and (7) of King[26]):

$$H_\varphi^{s\prime} = H_\varphi^s + \frac{ik_o}{2\pi} \int_S \bar{\Delta} H_\varphi^{s\prime} \left(\frac{e^{ik_o R_2}}{R_2}\right) \sin\delta \cos\gamma \, dS \quad , \tag{23}$$

where the indicated angles are shown in Figure 13.

Here, H_φ^s (the first term on the right side of (23)) is the "unperturbed" $\hat{\varphi}$ component of the H-field at the observation point, the left side of (23) represents the "perturbed" $\hat{\varphi}^s$ component of the H-field at the observation point, and $H_\varphi^{s\prime}$ in the integrand is the $\hat{\varphi}_1$ component of the "perturbed" H-field at dS, the integration point on the plane.

The terms "perturbed" and "unperturbed" as used with the Compensation Theorem have different meanings than used previously with the technique for scatter from a slightly rough surface. The "perturbed" field here is the unknown quantity, and its nature depends upon the surface over which it propagates. The "unperturbed" solution to the problem is presumed known. Thus (23) is an integral equation in $H_\varphi^{s\prime}$, the desired "perturbed" field.

Analogous to King[26], we select for our "unperturbed" field the far-zone H_φ^s component reradiated from the surface patch when the remainder of the surface is perfectly conducting (i.e., $\Delta = 0$). This is given by Equation (22a) when we set $\Delta = 0$ in Equation (22b) for $f_\varphi(m,n)$. Thus, the reradiated H-field to be used as the unperturbed solution in (23) is

$$H_\varphi^s = \frac{ik_o L^2 e^{ik_o R_o}}{2\pi R_o} G_\varphi^c \quad , \tag{24}$$

where G_φ^c represents G_φ of (22b) but with $\Delta = 0$. This expression is doubled from that of (22a) because of the location over the perfectly conducting plane.

Now, analogous to King[26] we define the "perturbed" or unknown field as equal to the "unperturbed" field times a slowly varying attenuation function, i.e.,

$$H_\varphi^{s\prime} = H_\varphi^s F'(d,z,\bar{\Delta}) \quad . \tag{25}$$

Then Equation (23) can be rewritten as an integral equation in F', obtaining:

$$F'(d,z,\bar{\Delta}) = 1 + \frac{ik_o R_o e^{-ik_o R_o}}{2\pi G_\varphi^c(0)} \int_S \bar{\Delta} G_\varphi^c(\varphi_1) \left(\frac{e^{ik_o(R_1+R_2)}}{R_1 R_2}\right) F'(R_1,0,\bar{\Delta}) \cdot \sin\delta \cos\gamma \, dS \quad , \tag{26}$$

where $G_\varphi^c(0)$ is G_φ^c evaluated at θ_s, φ_s and $G_\varphi^c(\varphi_1)$ is G_φ^c evaluated at $\theta_s = \pi/2$, $\varphi_s + \varphi_1$.

We now note that for highly conducting surfaces where $|\bar{\Delta}| \ll 1$, that F' is close to unity and the above integral is very nearly zero. It is only in the vicinity of grazing (i.e., $\pi/2 - \theta_s \simeq z/d \to 0$) that the incident and reflected waves reradiated by the patch cancel and only the Norton surface wave remains. Therefore, the integral in (26) is important only at very small grazing angles, typically 0°-0.5° for sea water (i.e., below the Brewster angle). In this region, Δ in the integrand is nearly a constant, and also $G_\varphi^c(\varphi_1)$ is nearly constant over the important region of integration near $\varphi_1 = 0$, $\theta_s \simeq \pi/2$. Also, $\sin \zeta \simeq 1$ and $\cos \gamma \simeq 1$, so that the integral equation simplifies to

$$F'(d,z,\bar{\Delta}) \simeq 1 + \frac{ik_0R_0e^{-ik_cR_0}}{2\pi}\,\bar{\Delta}\int_S F'(R_1,0,\bar{\Delta})\left(\frac{e^{ik_0(R_1+R_2)}}{R_1R_2}\right)dS \quad . \tag{27}$$

The remaining solution to (27) is performed by King[25,26]. Using an elliptic coordinate system as a basis for the surface integral and performing a stationary phase integration in the φ_1 direction, the result is reduced to an inhomogeneous Volterra integral equation of the second kind. This is then solved, and F' is shown to be identically the Norton attenuation factor.

The point of this section is the following: a patch of sea scattering or reradiating vertically polarized electromagnetic energy over an imperfect surface does so in a manner identical to a vertical dipole located on the same plane. Within the restrictions of the problem, therefore, all one must do is evaluate Equation (22a) at $\Delta = 0$ (i.e., the perfectly conducting limit) and multiply by 2F', the Norton attenuation factor.

In terms of L_b, the basic transmission loss derived and discussed previously, 2F' becomes $2F' = 2k_0R_0 10^{L_b/20}$, where L_b is defined and presented on those curves in decibels. Hence the field scattered by the patch of sea can be expressed as

$$H_\varphi^s(R_0,t) = \frac{ik_0L^2e^{ik_0R_0}}{2\pi R_0}\,F'\,G_\varphi^c \quad , \quad \text{or alternately} \tag{28a}$$

$$H_\varphi^s(R_0,t) = \frac{ik_0^2L^2e^{ik_0R_0}}{2\pi}\cdot 10^{L_b/20}\,G_\varphi^c \quad , \tag{28b}$$

where F' is the Norton attenuation function, L_b is the basic transmission loss derived in the preceding section, and G_φ^c is G_φ of (22b) evaluated at $\Delta \to 0$.

3.4 Derivation of the Average Scattered Signal Spectrum.

At this point, we are ready to consider averaging over ensembles of surfaces whose Fourier expansion coefficients $P(m,n,\ell)$ are random variables. To this end, we form $H_\varphi^s(R_0,t_1)H_\varphi^{s*}(R_0,t_2)$ from (28), (the star denotes complex conjugate) and average to obtain $R^s(\tau)$, where $\tau = t_1 - t_2$. This implies stationarity in the temporal sense so that $R^s(\tau)$ depends only on the difference, τ, and not upon t_1 or t_2.

$$R^s(\tau) = \frac{k_0^2L^4F'^2}{32\pi^2R_0^2}\int_{-\infty}^{\infty}\int\int\int \left|f_\varphi^c(p,q)\right|^2 \left[\frac{\sin(k_0\sin\theta_s\cos\varphi_s - k_0 - p)\frac{L}{2}}{(k_0\sin\theta_s\cos\varphi_s - k_0 - p)\frac{L}{2}}\right]^2 \times$$

$$\times \left[\frac{\sin(k_0\sin\theta_s\sin\varphi_s - q)\frac{L}{2}}{(k_0\sin\theta_s\sin\varphi_s - q)\frac{L}{2}}\right]^2 W(p,q,\omega)e^{i(\omega-\omega_0)\tau}\,dpdqd\omega \quad . \tag{29}$$

In the above, the six summations have been reduced to the triple integral by using the statistical independence of the Fourier coefficients and the definition of the spatial and temporal surface height spectrum:

$$\langle P(m_1,n_1,\ell_1)P(m_2,n_2,\ell_2)\rangle \equiv \begin{cases} \frac{\pi^3}{L^2T}\,W(p,q,\omega) & \text{for } m_2 = -m_1,\ n_2 = -n_1 \\ & \ell_2 = -\ell_1 \\ 0 & \text{otherwise} \end{cases} \quad , \tag{30}$$

Also, in the merging of series into integrals, we employ $p = am$, $q = an$, $\omega = w\ell$. Since all quantities in the integrand now apply to a perfectly conducting surface, ah becomes k_0, as seen from a preceding section. The quantity $f_\varphi^c(p,q)$ represents $f_\rho(m,n)$ of (22b) evaluated for $\Delta \to 0$, $am \to p$, $an \to q$.

Equation (29) can be simplified further by employing an assumption we made earlier: the scattering patch size, L, is much greater than wavelength, so that $k_0L \gg 1$. Under these conditions, the $[\sin x/x]^2$ functions in the integrand become impulse functions:

$$L\left[\frac{\sin(k_0\sin\theta_s\cos\varphi_s - k_0 - p)\frac{L}{2}}{(k_0\sin\theta_s\cos\varphi_s - k_0 - p)\frac{L}{2}}\right]^2 \Longrightarrow 2\pi\,\delta[p - k_0(\sin\theta_s\cos\varphi_s - 1)] \quad ,$$

with a similar expression for the other factor. These impulse functions permit integration over p and q to give

$$R^s(\tau) = \frac{k_o^2 L^2 F'^2}{8R_o^2} \left| f_{\varphi}^{c}\left[k_o(\sin\theta_s \cos\varphi_s - 1),\ k_o \sin\theta_s \sin\varphi_s\right]\right|^2 \int_{-\infty}^{\infty} W[k_o(\sin\theta_s \cos\varphi_s - 1),$$

$$k_o \sin\theta_s \sin\varphi_s, \omega]\ e^{i(\omega - \omega_o)\tau}\, d\omega \quad . \tag{31}$$

Rather than the correlation function of the scattered signal, we are interested in its power density spectrum; this is simply the Fourier transform of $R^s(\tau)$, where*

$$P^s(\omega) = \frac{1}{\pi} \int_{-\infty}^{\infty} R^s(\tau) e^{-i\omega\tau}\, d\tau \quad .$$

Making this transformation, we obtain

$$P^s(\omega) = \frac{k_o^2 L^2 F'^2}{4R_o^2} \left| f_{\varphi}^{c}\left[k_o(\sin\theta_s \cos\varphi_s - 1),\ k_o \sin\theta_s \sin\varphi_s\right]\right|^2 \times$$

$$\times\ W[k_o(\sin\theta_s \varphi_s - 1),\ k_o \sin\theta_s \sin\varphi_s,\ \omega - \omega_o] \quad . \tag{32}$$

We now simplify f_{φ}^{c} by noting that as $\Delta \to 0$, $N_A \to -ip = -ik_o(\sin\theta_s \cos\varphi_s - 1)$, $N_B \to -iq = ik_o \sin\theta_s \sin\varphi_s$, and $D(m,n) \to 1$. Carrying through the algebra, we arrive at the following

$$P^s(\omega) = \frac{k_o^4 L^2 H_o^2 F'^2}{4\pi\omega_o^2} (\sin\theta_s - \cos\varphi_s)^2\, W[k_o(\sin\theta_s \cos\varphi_s - 1),\ k_o \sin\theta_s \sin\varphi_s,\ \omega - \omega_o] \quad ,$$

where $H_o = \frac{k_o}{\omega_o \mu_o} E_o$. Now, the above result can be converted to $\sigma(\omega)$, the range-independent bistatic scattering cross section per unit surface area per radian/sec bandwidth by multiplying by $4\pi R^2/L^2 H_o^2 F'^2$ to obtain

$$\sigma(\omega) = \pi k_o^4 (\sin\theta_s - \cos\varphi_s)^2\, W[k_o(\sin\theta_s \cos\varphi_s - 1),\ k_o \sin\theta_s \sin\varphi_s,\ \omega - \omega_o] \quad . \tag{33}$$

To obtain σ^o, the average bistatic scattering cross section per unit area, we integrate over all frequencies to obtain

$$\sigma^o = \frac{1}{2} \int_{-\infty}^{\infty} \sigma(\omega) d\omega \quad , \quad \text{or}$$

$$\sigma^o = \pi k_o^4 (\sin\theta_s - \cos\varphi_s)^2\, W[k_o(\sin\theta_s \cos\varphi_s - 1),\ k_o \sin\theta_s \sin\varphi_s] \quad , \tag{34}$$

where in (34) we have reduced the surface height spatial-temporal spectrum $W(p,q,\omega)$ appearing in (33) to the surface height spatial spectrum, $W(p,q)$.

Let us recall that we have in (33) and (34) the average scattered signal spectrum and bistatic cross section per unit area of a surface illuminated by a ground wave propagating along the x-direction and scattering into the direction θ_s, φ_s. The polarization (E-field direction) retained in both the incident and scattering directions is vertical (i.e., lying in the planes of incidence and scatter). The imperfect nature of the surface is taken into account by the Norton attenuation factor, F', appearing in the equations. Thus, if we can find $W(p,q)$ and $W(p,q,\omega)$ for the sea surface, we have expressions for the scattering cross section and signal spectrum expressed directly in terms of these surface-height spectra. Conversely, by measuring $\sigma(\omega)$ for various scattering angles and frequencies, we might hope to deduce estimates of the ocean wave-height spectrum.

Equation (34) can be compared with previous results by Barrick and Peake[15],[16],[27], where the incidence angle has not been taken as grazing (i.e., θ_i is not $\pi/2$ as we assume in this paper). However, one should take note of the different normalization: we normalize here by dividing by the <u>total</u> ground-wave field intensity, E_o or H_o, over the scattering patch. In the case of sky-wave clutter ($\theta_i \neq \pi/2$) discussed in the above references, the conventional normalization divides by the downcoming incident field. At grazing the latter is one-half of E_o, the total ground-wave field. Hence, the results for σ^o in the above references have an added factor of 4 present in (34). Unfortunately there appears to be more diversity than convention on how to define scattering cross sections of surface objects at near-grazing angles, and one must be wary in using others results because of the constant presence or absence of factors 2, 4, and even 16 in the definitions.

Finally, we call attention to the scattering mechanism in evidence in Equations (33) and (34): Bragg scatter. The bistatic radar responds to only those roughness waves with wavenumbers $p = k_o(\sin\theta_s \cos\varphi_s - 1)$, $q = k_o \sin\theta_s \sin\varphi_s$, as seen from the arguments of the wave-height spectrum in those equations. These roughness wave crests are of precisely the correct length and orientation direction for a diffraction grating which is to scatter a wave at grazing incidence along the x-axis into directions θ_s, φ_s.

3.5 First-Order Ocean Wave-Height Spatial-Temporal Spectrum.

To a first order, we can relate $W(p,q)$ to $W(p,q,\omega)$ for the ocean. This is possible because deep-water waves of a given length, L, travel at a speed $v_w = \sqrt{gL/2\pi}$, where $g \simeq 9.81$ m/s^2 is the accel-

*It should be cautioned that the normalizations used here in the definitions of the Fourier transforms do not conform to many used in communication theory. We employ these in order to permit reference to Rice's work[2].

eration of gravity. This is correct to a first order in the waveheight/wavelength ratio. Studies have shown, however, that this ratio is always small, for when it exceeds 0.14, wave crests tend to be unstable and break, dissipating energy and reducing the height of the waves. Hence, to this first order, the temporal wavenumber, ω, is related uniquely to the spatial wavenumbers by the following dispersion equation:

$$\omega_{\pm} = \pm [g\sqrt{p^2 + q^2}]^{1/2} = \pm [g\sqrt{a^2m^2 + a^2n^2}]^{1/2} \quad , \tag{35}$$

where the $\pm$ signs arise from ambiguity in the direction of travel of the ocean waves.

Therefore, Equation (16) for first-order ocean waves may be rewritten as follows:

$$\zeta(x,y,t) = \sum_{m,n=-\infty}^{\infty} P_{\pm}(m,n) e^{iamx + iany + i\omega_{\pm}t} \quad , \tag{36}$$

where $\omega_{\pm}$ is given in (35).

We can now determine $W(p,q,\omega)$ by multiplying $\zeta(x_1,y_1,t_1)$ by $\zeta(x_2,y_2,t_2)$, averaging, and taking the Fourier transform, i.e.,

$$W(p,q,\omega) = \frac{1}{\pi^3} \iiint_{-\infty}^{\infty} \langle \zeta(x_1,y_1,t_1)\zeta(x_2,y_2,t_2) \rangle \, e^{ip\tau_x + iq\tau_y + i\omega\tau} \, d\tau_x d\tau_y d\tau \quad ,$$

where $\tau_x = x_1 - x_2$, $\tau_y = y_1 - y_2$, and $\tau = t_1 - t_2$. Using the definitions of the spatial spectrum given in (10), the spatial-temporal spectrum then becomes:

$$W(p,q,\omega) = 2W_{+}(p,q)\delta[\omega + \omega_{+}] + 2W_{-}(p,q)\delta[\omega + \omega_{-}] \quad , \tag{37}$$

where again the $\pm$ signs refer to the direction of motion of the waves, and $\omega_{\pm}$ is given in (35).

The above indicates that the spatial-temporal wave-height spectrum for a given p,q (spatial wavenumbers) consists of only two possible discrete temporal frequencies, ω_{+} and ω_{-}, which are related to p and q through (35).

3.6 Radar Scatter and the Phillips Isotropic Wind-Wave Spectrum.

Let us now combine Equation (33) for the scattered signal spectrum with (37) for the first-order spatial-temporal spectrum of the ocean. Recall that (33) represents the vertically polarized signal scattered in a direction θ_s, φ_s from a ground wave (vertically polarized) per unit area of sea per radian/second bandwidth.

$$\sigma(\omega) = 2\pi k_0^4 (\sin\theta_s - \cos\varphi_s)^2 \{ W_{+}[k_0(\sin\theta_s \cos\varphi_s - 1), k_0 \sin\theta_s \sin\varphi_s]\delta(\omega + \omega_{+} - \omega_0)$$

$$+ W_{-}[k_0(\sin\theta_s \cos\varphi_s - 1), k_0 \sin\theta_s \sin\varphi_s]\delta(\omega + \omega_{-} - \omega_0) \} \quad . \tag{38}$$

Notice that this scattered signal spectrum consists of two spikes centered at ω_0, the carrier, but shifted by an amount

$$\omega_{\pm} = \pm \sqrt{gk_0} \left[\sin^2\theta_s - 2\sin\theta_s \cos\varphi_s + 1 \right]^{1/4} \quad . \tag{39}$$

These Doppler shifts correspond to the velocities of ocean waves with the proper lengths for Bragg scatter, i.e., $L = \lambda/[\sin^2\theta_s - 2\sin\theta_s \cos\varphi_s + 1]^{1/2}$, where $\lambda = 2\pi/k_0$ is the radio wavelengths.

The frequency shift, $\omega_{\pm}$, is zero in the forward direction, where $\theta_s \to \pi/2$, $\varphi_s \to 0$. It is largest in the backscatter direction, where $\theta_s \to \pi/2$, $\varphi_s \to \pi$. Here, $\omega_{\pm} = \pm\sqrt{2k_0 g}$, and the lengths of the water waves responsible for scattering becomes the shortest, i.e., $L = \lambda/2$.

For backscatter at 10 MHz, for example, $f_{\pm} = \omega_{\pm}/2\pi = \pm 0.322$ Hz, and L = 15 meters. The observation of such shifts in the received signal is entirely possible with the processing techniques available in present day receivers. In fact, Crombie clearly observed these shifts as early as 1955[1]. Here, of course, the + sign in front of the shift arises from receding waves and the - sign, from approaching waves. The strength of each spectral line gives a quantitative indication of the strengths of ocean waves approaching and receding from the radar.

Let us now specialize these equations to the case of backscatter ($\theta_s = \pi/2$, $\varphi_s = \pi$) and employ the Phillips model for an isotropic, wind-driven fully developed sea. Equation (14) gives the functional form for W(p,q), and using this, we have the following particularly simple results:

$$\sigma(\omega) = 2B\left[f_{+}\delta(\omega - \omega_0 + \sqrt{2gk_0}) + f_{-}\delta(\omega - \omega_0 - \sqrt{2gk_0}) \right] \quad , \text{ and} \tag{40}$$

$$\sigma^0 = B = 0.005 \tag{41}$$

In Equation (40), (giving the signal spectrum), f_{+} and f_{-} represent the fraction of spectral energy in the advancing and receding waves, with $f_{+} + f_{-} = 1$.

Equation (41) is valid for the average bistatic scatter--as well as backscatter--cross section per unit area. Based on the Phillips isotropic wind-wave spectrum, it represents a very concise expression for

the scatter cross section. The quantity, σ^o, is commonly used in radar systems analysis to estimate the clutter power received. Expressed in decibels, Equation (41) becomes $\sigma^o \simeq -23$ dB; this result has been noted also by Munk and Nierenberg[19]. Values for σ^o between -20 dB and -30 dB have been reported for sea clutter at HF using vertical polarization. A significant aspect of this model for σ^o is its lack of dependence on frequency. Insufficient data are available at HF to deduce any clear frequency dependence, but observations tend to confirm a relatively weak frequency dependence. Had we used a Neumann-Pierson ocean-wave model, σ^o would have varied as $k_o^{-1/2}$, being -21 dB at 10 MHz.

Let us recall what we have in Equation (41) and the Phillips spectrum. We have at best a crude estimate of fully developed ocean roughness based on the wind above the surface. The ocean-wave direction is assumed to be isotropic, but is identically zero for wind speeds less than $\sqrt{g/2k_o}$ meters/second as discussed after Equation (14). Hence, σ^o for backscatter would be identically zero for winds below this velocity, and -23 dB for winds exceeding this velocity. In practice, one would not expect to observe this abrupt drop in σ^o with wind speed. In addition, the wind-wave spectrum would appear to represent an overestimate of $W(p,q)$ and hence, σ^o, because the model neglects swell and also the finite fetch over which a patch of ocean is likely to be fully aroused.

3.7 The Received Power and Signal Spectrum.

In (34) and (38) we have the backscattering cross section per unit area and its time spectral density for the sea. These are related to the received signal power through the radar range equation as follows:

$$dP_R(\omega) = \frac{4P_T G_T G_R \lambda^2}{(4\pi)^3 R_T^2 R_T^2} F_T'^2 F_R'^2 \sigma(\omega) ds \quad ; \quad \text{and} \quad dP_k = \frac{4P_T G_T G_R \lambda^2}{(4\pi)^3 R_T^2 R_R^2} F_T'^2 F_R'^2 \sigma^o ds \quad , \qquad (42a,b)$$

where $dP_R(\omega)$ and dP_R are the amounts of power per rad/s and power received from a patch of sea of area ds. The quantity P_T is the transmitted power, G_T and G_R are the transmitting and receiving antenna (free-space) gain functions in the direction of the patch, R_T and R_R are the distances, transmitter-to-patch and patch-to-receiver. F_T' and F_R' are the Norton attenuation factors for the transmitter-to-target path and target-to-receiver path, respectively--the target being the patch of sea, ds. The quantities $\sigma(\omega)$ and σ^o, as related to (34) and (38), must be evaluated at the bistatic angles θ_s, ψ_s at the patch.

The received power spectral density, $P_R(\omega)$, is related to the total average power in the following way:

$$P_R = \frac{1}{2} \int_{-\infty}^{\infty} P_R(\omega) d\omega \qquad (43)$$

Equations (42) can alternately be expressed in terms of the basic transmission loss discussed in Section II by the following equations:

$$dP_R(\omega) = \frac{\pi P_T G_T G_R}{\lambda^2 \ell_{bT} \ell_{bR}} \sigma(\omega) ds \quad , \quad \text{and} \quad dP_R = \frac{\pi P_T G_T G_R}{\lambda^2 \ell_{bT} \ell_{bR}} \sigma^o ds \quad , \qquad (44a,b)$$

where

$$\ell_{bT} = 10^{-L_{bT}/10} = \left[\frac{F_T'}{k_o R_T}\right]^2 \quad , \quad \ell_{bR} = 10^{-L_{bR}/10} = \left[\frac{F_R'}{k_o R_R}\right]^2 \quad ,$$

L_{bT} and L_{bR} being the basic transmission losses in decibels over the transmitter-target and target-receiver paths. Again, several of the parameters in the above equations may be functions of the bistatic angles at the patch, dS.

To obtain the total received signal power or power spectral density, one then integrates over all areas of the sea. Frequently, however, such patches are limited in extent by the use of a short-pulse (or an equivalent time-coded) signal and finite antenna beamwidths. In such cases the integrations can often be simplified.

4. MEASUREMENT OF THE OCEAN-WAVE SPECTRUM WITH A BISTATIC RADAR.

4.1 General Considerations.

The simple relationship between the scattered signal and the ocean wave-height spatial spectrum expressed in (38) suggests possibilities for quantitative measurement of the state of the sea surface. While oceanographers have devised several techniques for measuring the temporal wave-height spectrum of the surface (from which the nondirectional spatial spectrum may be obtained), very few practical and reliable methods permit measurement of the directional spatial spectrum, $W(p,q)$. Hence a new sensing technique which can measure this quantity should provide oceanographers with welcome knowledge about the nature of ocean waves.

Where less detail about the surface spectrum is needed, the use of HF radar in conjunction with ships, aircraft, satellites, or other telemetry/relay devices could yield frequent estimates of sea state on a global basis. At present there are no operable sensors which provide such data, and most proposed schemes suffer serious deficiencies in this respect. We feel that the HF radar as an ocean-surface remote sensor will prove to be a workable solution to this problem.

A study of Equation (38) shows that several radar parameters appear in the arguments of $W(p,q)$ which might be exploited. By varying the frequency of operation, we change k_o. A suitable range of variation might lie between 3 and 30 MHz since the more important, longer ocean waves have lenghts

corresponding to the radio wavelengths in this region. At HF, devices with such a range of operation are not impractical; ionosounders presently provide a continuous sweep over nearly a decade in frequency. Probing the ocean with different frequencies will provide information about the lower-end cutoff of the spectrum, indicating whether or not longer ocean waves are present.

The Doppler shift in frequency from the carrier is contained in the scattered signal spectrum. By observing this spectrum for a given transmitted frequency, one can obtain information about the directional nature of W(p,q). The use of short-pulse signals and time delay at the receiver defines an area over which the integration of (38) (as shown in Equation (42a)) takes place, and the impulse functions uniquely relate the angles and arguments of W(p,q) to the Doppler-frequency shift of the received signal from the carrier.

Finally, the use of a stationary transmitter and moving receiver, such as an aircraft or satellite, provides another means of varying θ_s, φ_s, and the Doppler shift to various parts of the illuminated area. Several such schemes can be analyzed by the use of Equations (38) and (42) along with the geometries involved in the particular bistatic arrangement. Two different bistatic arrangements will be considered and discussed here.

At microwave frequencies, backscatter radars tend to be more practical than bistatic systems. At HF, however, the implementation of a simple, stationary, backscatter radar to measure W(p,q) is difficult. Unless one has a narrow antenna beamwidth so as to illuminate a small angular patch of sea, one obtains no directionality information about the sea. Narrow antenna beamwidths at these frequencies, require antenna arrays up to a mile long. Such antennas must be land-based and are thus useful only for measurement of offshore waves approaching the beach. Size precludes their use in midocean applications. The requirement for operation over decade frequency ranges compounds the complexity and already considerable expense involved in electronic beam scanning with such a phased array. Hence, schemes involving short, single-wire antennas with (nearly) omnidirectional radiation patterns are much more practical at HF, recommending the use of bistatic configurations to obtain directional information.*

4.2 A Bistatic Surface-Surface Configuration.

We shall examine here a bistatic radar configuration as shown in Figure 14. The transmitting and receiving antennas we take to be half-wave vertical whips, located a distance d apart on (nearly) stationary surface platforms. In practice, these may be ships, buoys, islands, shore stations, or combinations of these. The spacing, d, should be less than 200-300 km; otherwise the sea surface may vary considerably statistically between these points.

We also assume that the radar employs a short-pulse signal of duration τ (or an equivalent time-coded signal). Defining $t_d = d/c$ as the time delay for reception of the direct transmitter pulse, signals arriving at later times represent sea scatter originating from confocal elliptical annuli, as shown shaded in Figure 14. The foci of the ellipses are the transmitter and receiver points separated by d. Thus by observing the received signal spectrum for a given time delay, one can separate the scatter arising from different portions of the elliptical ring. This scatter originates from ocean waves of the proper Bragg length whose crestlines are tangent to the ellipse. Positive Doppler shifts originate from waves moving across the elliptical ring toward the baseline, while negative shifts are due to motion away from the baseline. The greatest Doppler shifts are due to the shorter waves at the ends of the ellipse moving along the baseline, while the shortest shifts are due to waves crossing the ellipse at the midpoint, with motions perpendicular to the baseline.

Nierenberg and Munk[28] have examined the arguments of W(p,q) in (38) (with $\theta_s = \pi/2$ for surface-surface propagation). They have numerically generated lines showing the transformation between the time-delay and Doppler observables and the p,q ocean-wave spatial wavenumbers. To show this transformation, let us normalize the observed Doppler frequency to that for ocean-wave backscatter, i.e., $f_N = f_d/f_{db}$, where $f_{db} = 1/2\pi\sqrt{2gk_o}$ is the Doppler shift for backscatter. Since the observed Doppler shift is greatest for backscatter, $0 \le f_N \le 1$. Nierenberg and Munk[28] then define a quantity K equal to f_N^2; it is exactly equal to the magnitude of the spatial wavenumber of the ocean waves producing the Bragg scatter at a given point on the ellipse divided by $2k_o$. Hence, $0 \le K \le 1$, with K = 1 occurring for backscatter (i.e., $\varphi_s = \pi$). The other radar observable, time delay, is also normalized, dividing by the direct baseline time delay, i.e., $S = t/t_d$. Then $1 \le S < \infty$. We also normalize the ocean spatial wavenumbers by dividing by $2k_o$, i.e., $U = p/2k_o$, $V = q/2k_o$. Then the transformation of interest relates K or f_N (Doppler shift) and S(time delay) for a point on the elliptical annulus to the ocean wavenumbers U and V responsible for scatter. Since $0 \le |U|, |V| \le 1$, we would like to be able to determine the ocean wave-height spectrum for all U, V in this range by observing K and S. Figures 15 and 16 show this transformation. As can be seen, there are no ocean wavenumbers that cannot be determined from some combination of time delay and Doppler shift. The normalized ocean wavenumbers, U and V can correspond to any actual wavenumbers, p and q, between zero and infinity; one measures the shorter wavenumbers by increasing the transmitted frequency.

In order to show how the actual received signal spectrum might look using this system, we employ the Phillips isotropic ocean-wave mode; we assume that all ocean waves which can scatter the radio waves are fully aroused†. We employ Equation (44a) along with (40), (with $f_+ = f_- = 1/2$) integrating over an elliptical annulus. The radar parameters selected are the following. The antennas are vertical ground-fed quarter-wave whips with equivalent free-space gains of 0.82. They are located 100 km apart. Two frequencies are considered: 5 and 10 MHz. The signal pulse length is taken as $\tau = 12.5$ μs, and we consider the elliptical annulus representing a delay $t_d + \tau$, i.e., one pulse length after the arrival of the direct pulse.

*An exception will be discussed in Section 4.3, in which a single-element omnidirectional antenna can be used on a moving ship to obtain directional information about the ocean waves.

†Hence, we obtain an upper limit on scattered power in this manner.

For this configuration the integration is best performed in elliptical coordinates, where $ds = R_R R_T d\mu d\theta$, $R_R = d/2\ (\cosh\mu + \cos\theta)$, $R_T = d/2\ (\cosh\mu - \cos\theta)$. Then integration over the annulus represents an integration over θ between 0 and 2π, where $\mu = 0.274$, $d\mu = 0.1352$ for the pulse length and time delay chosen. The integration can be performed exactly because of the impulse functions, and we obtain:

$$\frac{\omega_{db} P_R(\omega)}{P_T} = \frac{BG_T G_R k_o^3 d^2 \sinh^2\mu d\mu}{2\pi \ell_{bT} \ell_{bR} \left(\frac{f - f_o}{f_{db}}\right)^5 \sqrt{1 - \left(\frac{f - f_o}{f_{db}}\right)^4} \sqrt{\left(\frac{f - f_o}{f_{ds}}\right)^4 - 1}} \tag{45}$$

where f_{db} is the backscatter Doppler shift given previously and f_{ds} is the Doppler shift from waves at the side of the ellipse; it is $f_{ds} = f_{db}\sqrt{\tanh\mu}$. The free-space gains ℓ_{bT} and ℓ_{bR} are functions of R_T and R_R, the ranges to the part of the patch scattering the frequency f. These ranges are given in terms of f as

$$R_T = \frac{d}{2}\cosh\mu \times \left[1 - \sqrt{1 - \left(\frac{f_{ds}}{f - f_o}\right)^4}\right] \text{ and } R_R = \frac{d}{2}\cosh\mu \left[1 + \sqrt{1 - \left(\frac{f_{ds}}{f - f_o}\right)^4}\right]$$

The basic transmission losses may then be determined from the results of Section 2.

The received spectrum defined is (43) in nonzero only for frequencies in the range $f_{ds} \le |f - f_o| \le f_{db}$. Plots of this dimensionless quantity at 5 and 10 MHz are shown in Figures 17 and 18. Shown also there are the ocean wavelengths, ocean-wave directions with respect to the baseline, and wind speed required to excite the waves responsible for scatter at the indicated Doppler shift. The "ears" near the endpoints are due to scatter from the "stationary" regions of the ellipse, viz., the sides and ends. The heights observed for these "ears" will depend upon the resolution of the spectral processor.

In practice, the received signal spectrum will be lower than that shown in Figures 17 and 18 for the fully developed wind-wave model. The dashed curves show more typical shapes; the signal at the lower Doppler frequencies is likely to be weaker because these longer ocean waves are likely to be present less of the time.

The total sea-scattered power received from the ellipse is approximately $1.5 \times 10^{-11}\ P_T$ at 5 MHz. This should be compared with a received signal power direct from the transmitter of about $3.2 \times 10^{-9}\ P_T$. Hence the sea-scattered signal is down about 23 dB from the direct signal, which places no stringent demands on the receiver dynamic range.

4.3 A Bistatic Surface-to-Surface Configuration.

Here we consider a bistatic radar as shown in Figure 19. The transmitter is a quarter-wave vertical whip on a buoy or ship. The receiver in this case is a nonstationary satellite, and short pulses (or equivalent coded signals) are employed. In general, ocean areas of constant time delay are represented by the intersection of confocal spheroids with the ocean surface. The foci of these spheroids are the transmitter and receiver points. The intersection curves are nonconfocal ellipses. So as not to be bogged down in mathematical details of nonconfocal elliptical strips, let us specialize here to the situation when the satellite is directly overhead, for then these strips become circular annuli.

The principle of operation with this configuration is different from that of the preceding system, in that here we exploit the motion of one of the antennas to separate the scatter from different parts on the circular ring. The Doppler shift from different points on the ring varies because the range-rate to these points is different. Satellite speeds are sufficient that one can separate Doppler shifts due to satellite motion from the Doppler shifts due to water-wave motion (the mechanism used in the preceding system).

Let us assume satellite motion along the x-direction with the orbital plane coinciding with the x-z plane. Again, we employ frequencies of 5 to 10 MHz. The antenna on the satellite is assumed to have a free-space gain, G_R, of a half-wave dipole, i.e., 1.64. The gain of the quarter-wave transmitting antenna is, as before, 0.82. We assume that the satellite is at altitude $R_R \simeq 300$ km and moving with velocity 8000 m/s. We select a pulse length $\tau = 10\ \mu s$, yielding a clutter ring width of $dR_T = 3$ km. Let us also pick a time delay $t - t_d = 50\ \mu s$, corresponding to $R_T = 15$ km (t_d is the time delay of the direct signal from the transmitter to the satellite). We also select the Phillips isotropic wind-wave spectrum as an example; it represents the most intense sea-scatter situation. Employing Equations (42a) and (40) and employing the pertinent bistatic angles, $\theta_s = 0$, $\phi_s = 0$, we have the following for the received signal spectrum:

$$\frac{\omega_{dm} P_R(\omega)}{P_T} = \frac{BG_T G_R \lambda^2 dR_T}{\pi^3 R_R^2 R_T \sqrt{1 - \left(\frac{f - f_o}{f_{dm}}\right)^2}} \tag{46}$$

In obtaining the above from (40), it is assumed $f_+ = f_- = 1/2$. Also, f_{dm}, the maximum Doppler shift due to satellite motion ($f_{dm} \simeq f_o(R_T/R_R)v/c$) is considerably larger than f_{db}, the Doppler shift due to wave motion described in the preceding section. At 5 MHz, this shift f_{dm} is 6.67 Hz in contrast with $f_{db} = 0.228$ Hz for the ocean-wave Doppler. The above equation is valid for the range $-f_{dm} \le f - f_c \le f_{dm}$; outside this range, the first-order spectrum is zero.

Plots of this dimensionless quantity are shown in Figures 20 and 21 at 5 and 10 MHz. Shown also is the angular direction from the orbital plane to the point on the ring responsible for scatter at a given frequency. The ocean waves responsible for scatter are all of lengths $L = \lambda = 60$ meters and 30 meters at the two frequencies. They also cross the ring radially; hence the angle ϕ gives us the directional wave-height spectrum at the wavenumbers $p = k_o \cos\phi$ and $q = k_o \sin\phi$. By varying the

frequency (and hence k_o) and observing the signal spectrum (and hence φ), we can obtain the complete directional spectrum of the surface.

In the system of the last section, ocean waves of many lengths were observed at a given frequency; here, a given frequency permits observation of waves of only one wavelength--the radar wavelength.

The total received sea-scattered power for this configuration is $P_r \simeq 2.5 \times 10^{-12} P_T$ at 5 MHz. This compares to the received signal direct from the buoy, which is considerably less than $10^{-9} P_T$, typically of the order $10^{-11} P_T$. This reduced direct power occurs because the satellite overhead is in the null of the pattern of the vertical whip transmitting antenna; theoretically the direct component should drop to zero, but practically, a drop of 20 dB from the main antenna lobe might be expected. The lower the direct signal compared with the sea-scattered signal, the better, for the dynamic range and interference problems will be reduced.

A problem which must be recognized in connection with this system at lower HF frequencies is the presence of the ionosphere. It may be only at nighttime that frequencies as low as 5 MHz can penetrate the ionosphere. The favored region for satellite reception will occur when it is close to the overhead position, since this region offers the best chances for penetration and lowest attenuation by the ionosphere.

Several alternates to the satellite receiver could operate on the same moving Doppler principle. A lower, slower flying aircraft receiver could accomplish the same task as the satellite. A second alternative would have the transmitter and receiver mounted on the same ship; the ship's Doppler would be used to resolve the sea scatter directionally. However, the ship's velocity will lie in the same range as the speeds of the ocean waves responsible for scatter, and both must be taken into account in the equations.

The buoy/transmit, satellite/receive configuration suggested could also be used reciprocally. However, larger transmitter powers should be available from a buoy. In addition, the possibility of the satellite selecting and interrogating a buoy, recording the signal, and then transmitting it to earth for processing at a more convenient point in the orbit indicates that the arrangement here is more desirable than its reciprocal configuration.

5. SUMMARY AND CONCLUSIONS.

The longer ocean waves (i.e., 20-200 meters) interact significantly and predictably with radio waves in the HF/VHF region. The scattering mechanism deduced theoretically and confirmed experimentally is the Bragg effect. The theoretical basis for this effect is developed and reviewed here. The problem is analyzed using the boundary perturbation approach of Rice [2] along with a Leontovich boundary condition at the surface. This approach is valid as long as the ocean wave-height is small in terms the radio wavelength and the surface slopes of the longer ocean waves are small. Both of these conditions are met by ocean waves in the HF and lower-VHF regions. In addition, the restrictions required for the application of the Leontovich boundary condition are easily satisfied by ocean water at these frequencies. As long as the technique is not pushed beyond its intended limits, the results and interpretation obtained therefrom will be valid.

Using the perturbation technique, we derive an expression for the effective surface impedance of a slightly rough planar surface. It consists of two parts: the impedance of the surface when it is perfectly smooth, along with a second term due to the presence of roughness. We apply it to the sea using the Phillips isotropic ocean-wave spectrum for a model. Calculations show that at 5-20 MHz, the change in impedance due to roughness can be as much as 100% of its unperturbed value for a smooth ocean-water surface. These effective surface impedances are then used in a standard ground-wave program to determine curves of added transmission loss due to sea state. The curves show that below about 2 MHz, ocean roughness can be neglected, but at 15 MHz, the increase in one-way loss can be as much as 15 dB at 100 nmi.

Scatter of HF/VHF waves from the sea is also analyzed using the perturbation approach. The random ocean surface is considered a function of time as well as space, and expressions are derived for the bistatic scattered signal intensity and spectrum. They are valid in the region near grazing (as well as at higher angles) for vertically polarized waves. To a first order, water waves of a given length travel at a given speed; when this restriction is used in the ocean wave-height spectrum, the scattered signal from a patch of sea is shown to consist of two impulse functions, equidistant from the carrier in the frequency domain. These impulses represent ocean-wave trains of the required Bragg length moving at the corresponding discrete velocity toward and away from the radar. These impulse functions have been observed over 15 years ago in HF backscatter data from the sea. Furthermore, the use of the Phillips isotropic ocean-wave spectrum gives an upper limit at σ^o (backscatter cross section per unit area) of -23 dB, a value in agreement with several measurements.

The possible use of bistatic radar configurations for study of sea surface is explored. Two techniques are briefly analyzed: one employing a stationary surface transmitter and receiver and the other using a stationary surface transmitter and orbiting receiver. In the first case, the observables are the processed signal spectrum and the time delay at which it is computed; these are then related simply to the spatial wavenumbers of the directional ocean wave-height spectrum. In the second system, the receiver motion permits directional resolution of the ocean waves, and frequency variation provides the magnitude of the ocean wavenumbers. Many variations of these systems are possible, employing ships, aircraft, buoys, shore stations, and satellites. Power requirements and antenna sizes are not design limitations for the bistatic configurations discussed, and the processing requirements for the received signal are within the state of the art. HF/VHF radars appear to be one of the most promising systems both for monitoring the sea state and for detailed study of the nature of ocean waves.

REFERENCES

1. Crombie, D. D., "Doppler Spectrum of Sea Echo at 13.56 Mc/s", Nature, Vol. 175, p. 681 (1955).

2. Rice, S. O., "Reflection of Electromagnetic Waves from Slightly Rough Surfaces", in Theory of Electromagnetic Waves, M. Kline, Editor, p. 351, Interscience Publishers, New York (1957); also Dover Publications, New York (1963).

3. Ward, J. F., "Power Spectra from Ocean Movements Measured Remotely by Ionospheric Radio Backscatter", Nature, Vol. 223, p. 1325 (1969).

4. Sommerfeld, A., "The Propagation of Waves in Wireless Telegraphy", Annalen der Physik, Vol. 28, p. 665 (1909).

5. Norton, K. A., "The Propagation of Radio Waves over the Surface of the Earth and in the Upper Atmosphere, Part I - Ground Wave Propagation from Short Antennas", Proc. IRE, Vol. 24, p. 1367 (1936); "..., Part II - The Propagation from Vertical, Horizontal, and Loop Antennas over a Plane Earth of Finite Conductivity", Proc. IRE, Vol. 25, p. 1203 (1937).

6. van der Pol, B., and H. Bremmer, "The Diffraction of Electromagnetic Waves from an Electrical Point Source Round a Finitely Conducting Sphere", Philosophical Mag., Series 7, Vol. 24, pp. 141-176, pp. 825-864; Vol. 25, pp. 817-834; Vol. 26, pp. 261-275 (1937, 1938, 1939).

7. Fock, V. A., "Diffraction of Radio Waves Around the Earth's Surface", J. Phys. (USSR), Vol. 9, p. 256 (1945).

8. Norton, K. A., "The Calculation of Ground Wave Field Intensity over a Finitely Conducting Spherical Earth", Proc. IRE, Vol. 29, p 623 (1941).

9. Wait, J. R., "Electromagnetic Surface Waves", in Advances in Radio Research, J. A. Saxton, Editor, Vol. 1, pp. 157-217, Academic Press, New York (1964).

10. Norton, K. A., "The Physical Reality of Space and Surface Waves in the Radiation Field of Radio Antennas", Proc. IRE, Vol. 25, p. 1192 (1937).

11. Wise, W. H., "The Physical Reality of the Zenneck Surface Wave", Bell System Tech. J., Vol. 16, p. 35 (1937).

12. Jordan, E. C., Electromagnetic Waves and Radiating Systems, Prentice-Hall, Englewood Cliffs, New Jersey (1950).

13. Barrick, D. E., "Theory of Ground-Wave Propagation Across a Rough Sea at Dekameter Wavelengths", Research Report, Battelle Memorial Insticute, Columbus, Ohio (January 1970).

14. Feinberg, E., "On the Propagation of Radio Waves Along an Imperfect Surface", J. Phys. (USSR), Vol. 8, p. 317 (1944).

15. Barrick, D. E., and W. H. Peake, "Scattering from Surfaces with Different Roughness Scales: Analysis and Interpretation", Research Report, Battelle Memorial Institute, Columbus, Ohio (November 1967), AD 662751; also published under separate cover by the ElectroScience Laboratory, Ohio State University, Columbus, Ohio (September 1967), N67-39091.

16. Barrick, D. E., and W. H. Peake, "A Review of Scattering from Surfaces with Different Roughness Scales", Radio Science, Vol. 3 (New Series), p. 865 (1968).

17. Kinsman, Blair. Wind Waves, Prentice-Hall, Englewood Cliffs, New Jersey, pp. 386-403 (1965).

18. Phillips, O. M., Dynamics of the Upper Ocean, Cambridge University Press, London, pp. 109-139 (1966).

19. Munk, W. H., and W. A. Nierenberg, "High Frequency Radar Sea Return and the Phillips Saturation Constant", Nature, Vol. 224, p. 1285 (1969).

20. Cox, C., and W. Munk, "Measurement of the Roughness of the Sea Surface from Photographs of the Sun's Glitter", J. Opt. Soc. Am., Vol. 44, p. 838 (1954).

21. Berry, L. A., and M. E. Chrisman, "A FORTRAN Program for Calculation of Ground Wave Propagation Over Homogeneous Spherical Earth for Dipole Antennas", Report 9178, National Bureau of Standards, Boulder, Colorado (1966).

22. Norton, K. A., "Transmission Loss in Radio Propagation: II", Report 5092, National Bureau of Standards, Boulder, Colorado (1957).

23. Norton, K. A., "Transmission Loss in Radio Propagation", Proc. IRE, Vol. 41, p. 146 (1953)

24. Ruck, G. T., D. E. Barrick, W. D. Stuart, and C. K. Krichbaum, Radar Cross Section Handbook, Vol. 1, Plenum Press, New York, p. 53 (1970).

25. King, R. J., "An Introduction to Electromagnetic Surface Wave Propagation", IEEE Trans. on Education, Vol. 11, p. 59 (1968).

26. King, R. J., "Electromagnetic Wave Propagation Over a Constant Impedance Plane", Radio Science, Vol. 4, p. 255 (1969).

27. Ruck, G. T., D. E. Barrick, W. D. Stuart, and C. K. Krichbaum, Radar Cross Section Handbook, Vol. 2, Plenum Press, New York, pp. 703-709 (1970).

28. Nierenberg, W. A., and W. H. Munk, "Sea Spectra and Radar Scattering", Working Paper, 1969 JASON Summer Study, Boulder, Colorado.

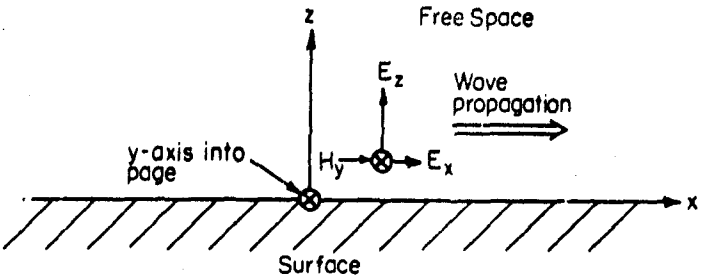

Figure 1. Guided Wave Above a Planar Impedance Boundary.

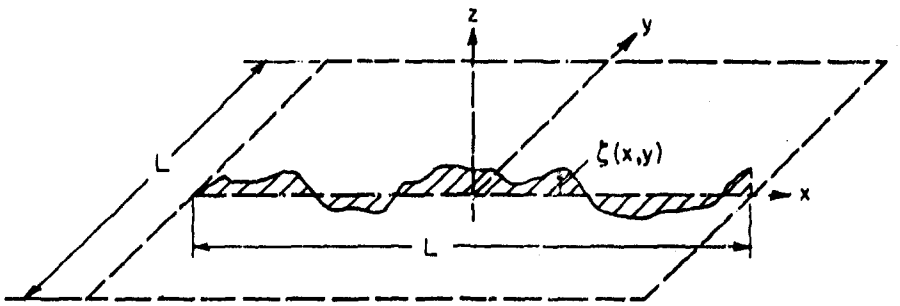

Figure 2. Slightly Rough Surface Geometry.

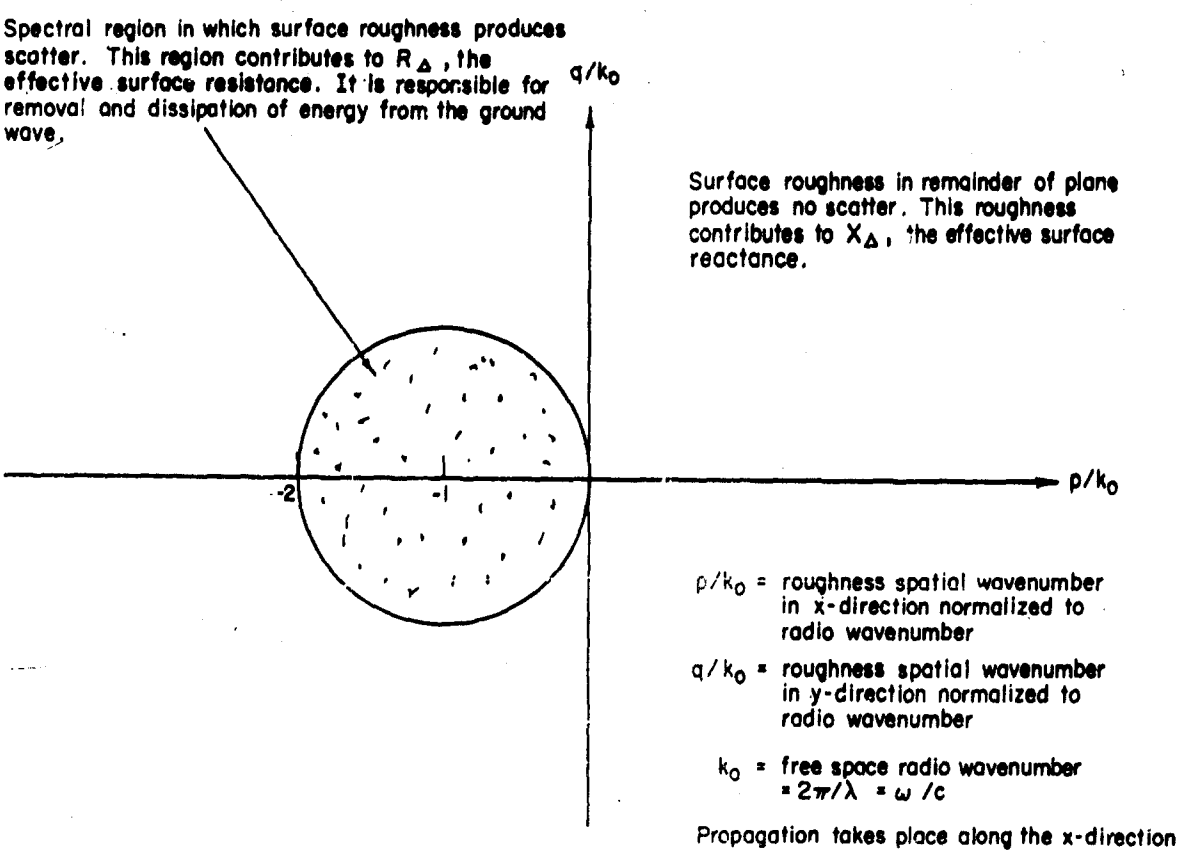

Figure 3. Effect of Various Regions of Spatial Roughness Spectrum on Effective Surface Impedance.

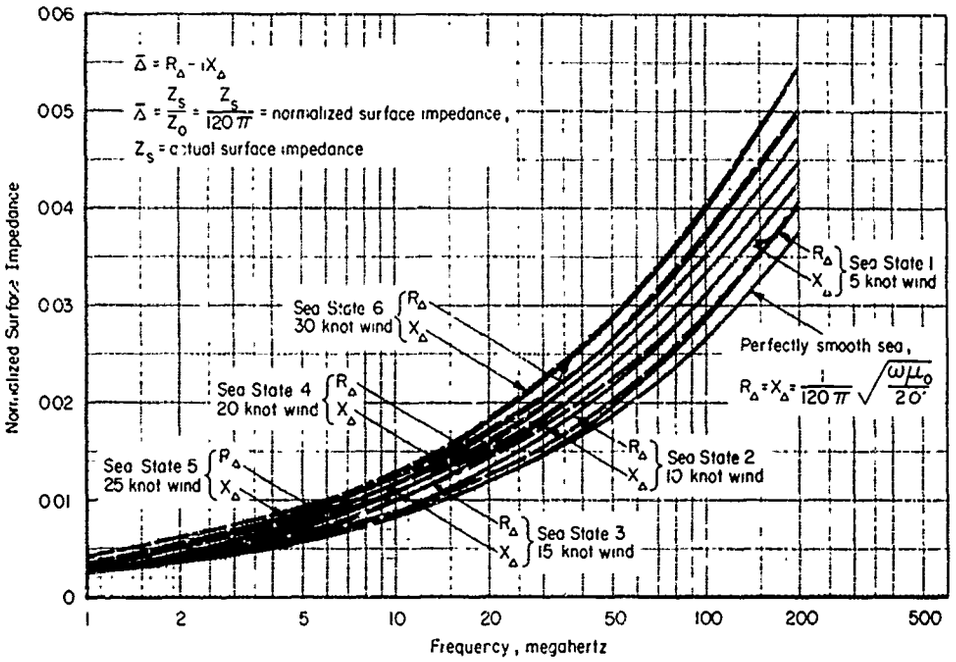

Figure 4. Effective Surface Impedance, $\bar{\Delta}$, vs Wind Speed and Frequency. Phillips Isotropic Wave Spectrum.

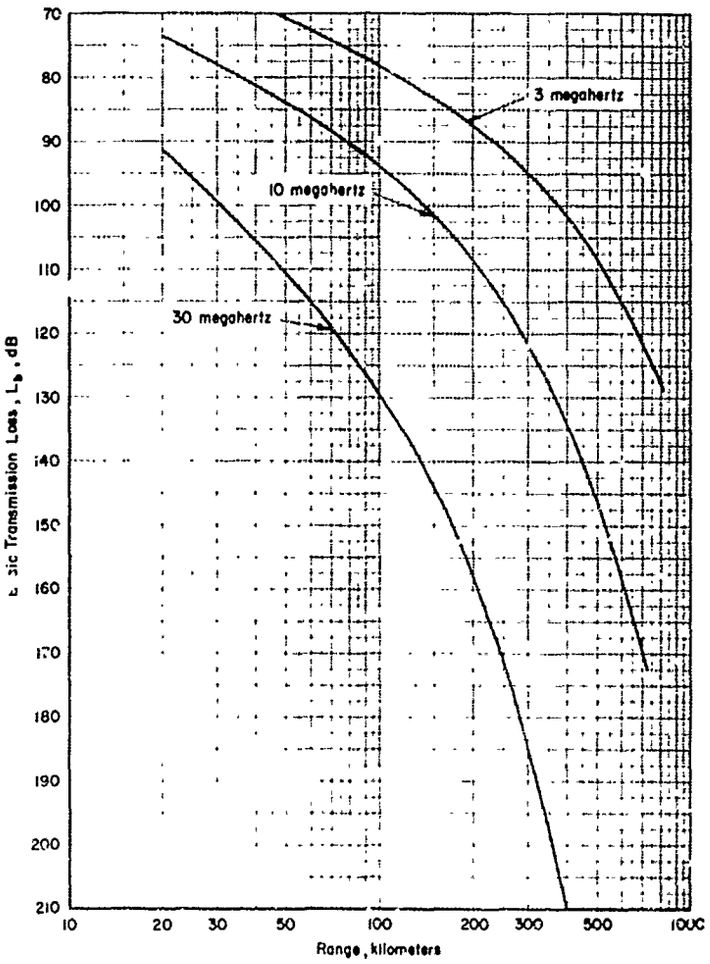

Figure 5. Basic Transmission Loss Across the Ocean Between Points at the Surface of Smooth Spherical Earth. Conductivity is 4 mhos/meter and an Effective Earth Radius Factor of 4/3 is Assumed.

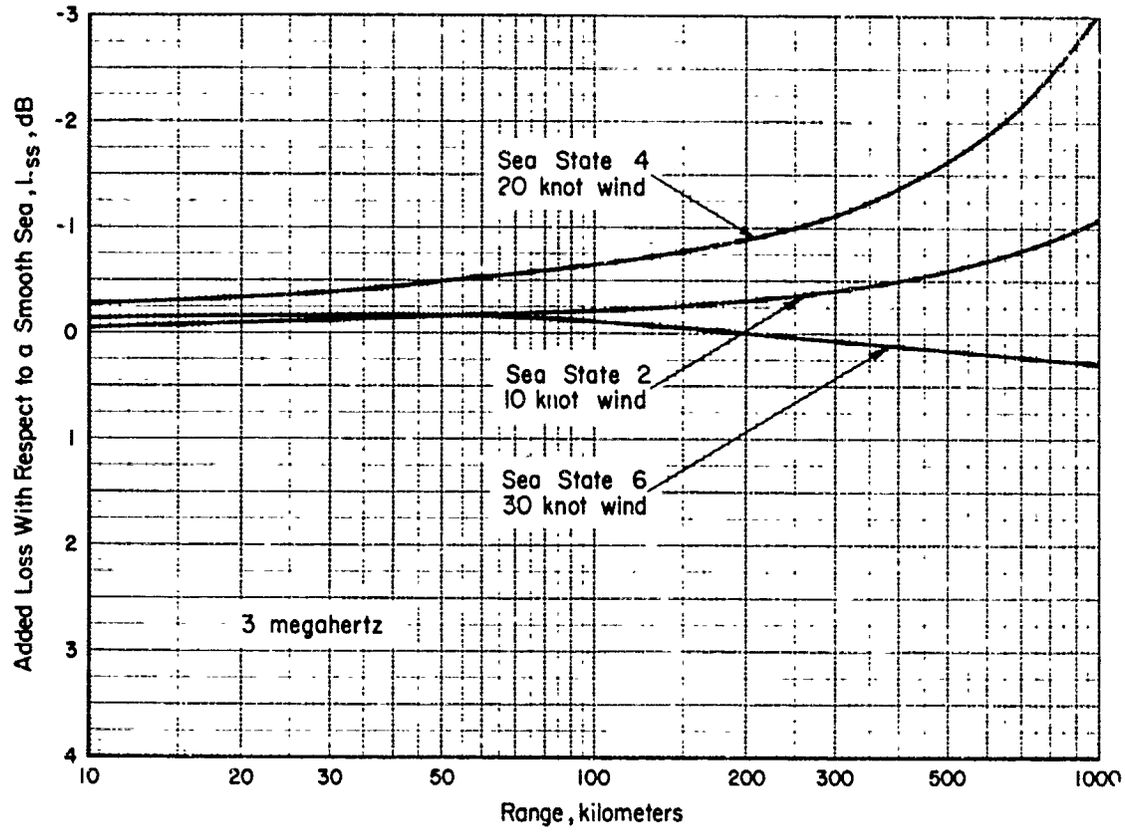

Figure 6. Added Transmission Loss Due to Sea State at 3 MHz. Antennas are Located Just Above Surface. Phillips Isotropic Ocean-Wave Spectrum.

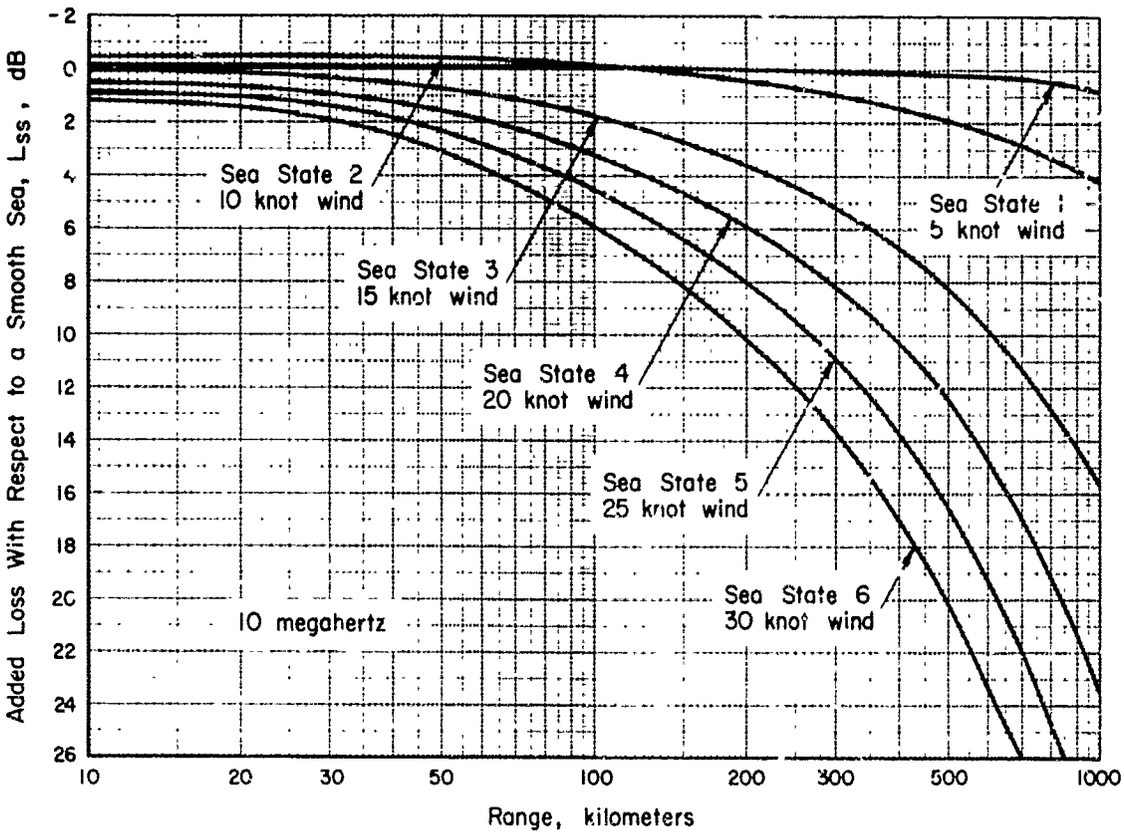

Figure 7. Added Transmission Loss Due to Sea State at 10 MHz. Antennas are Located Just Above Surface. Phillips Isotropic Ocean-Wave Spectrum.

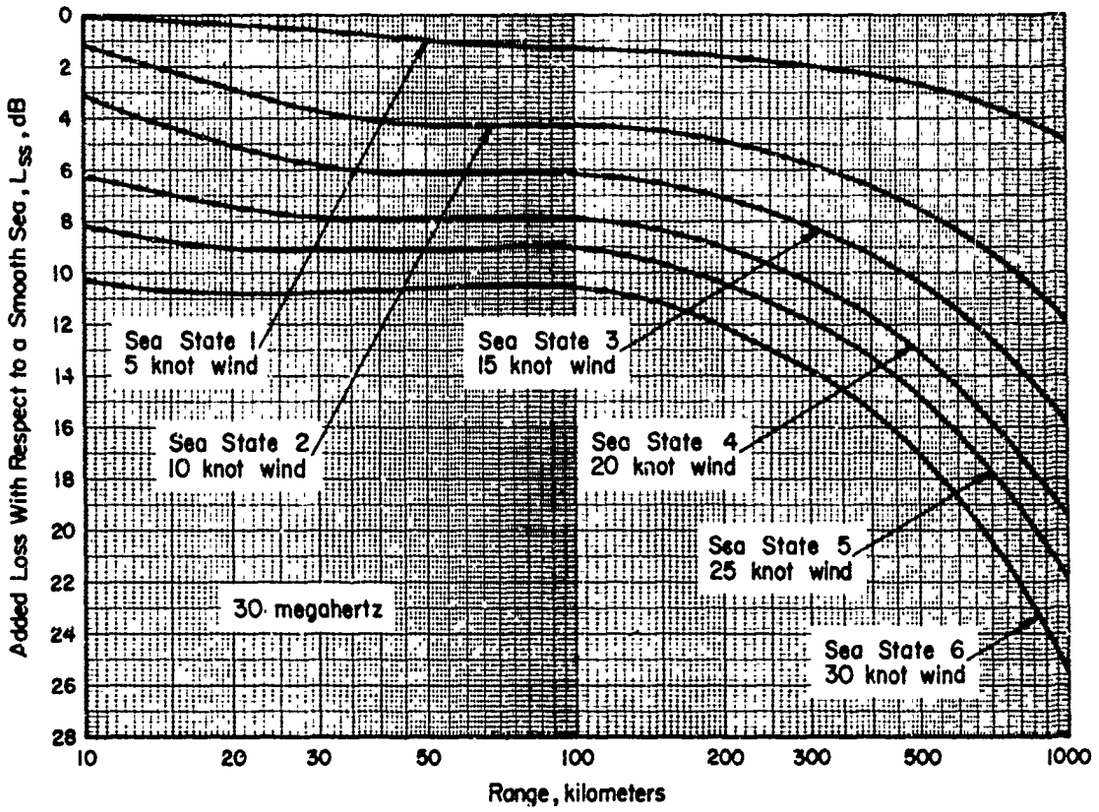

Figure 8. Added Transmission Loss Due to Sea State at 30 MHz. Antennas are Located Just Above Surface. Phillips Isotropic Ocean-Wave Spectrum.

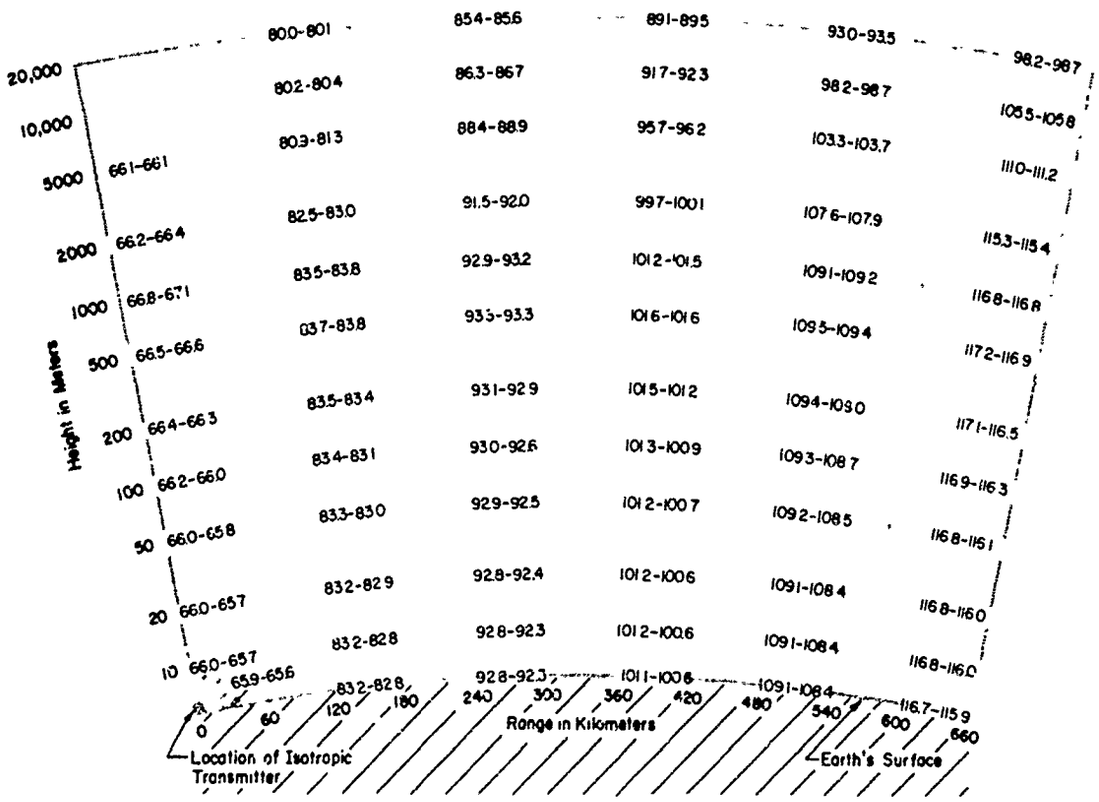

Figure 9. Basic Transmission Loss to Points at Various Heights and Ranges Above the Ocean at 3 MHz. First Number is for Perfectly Smooth Sea, Second is for Sea State 5 (25 knot wind) Using Phillips Ocean-Wave Spectrum.

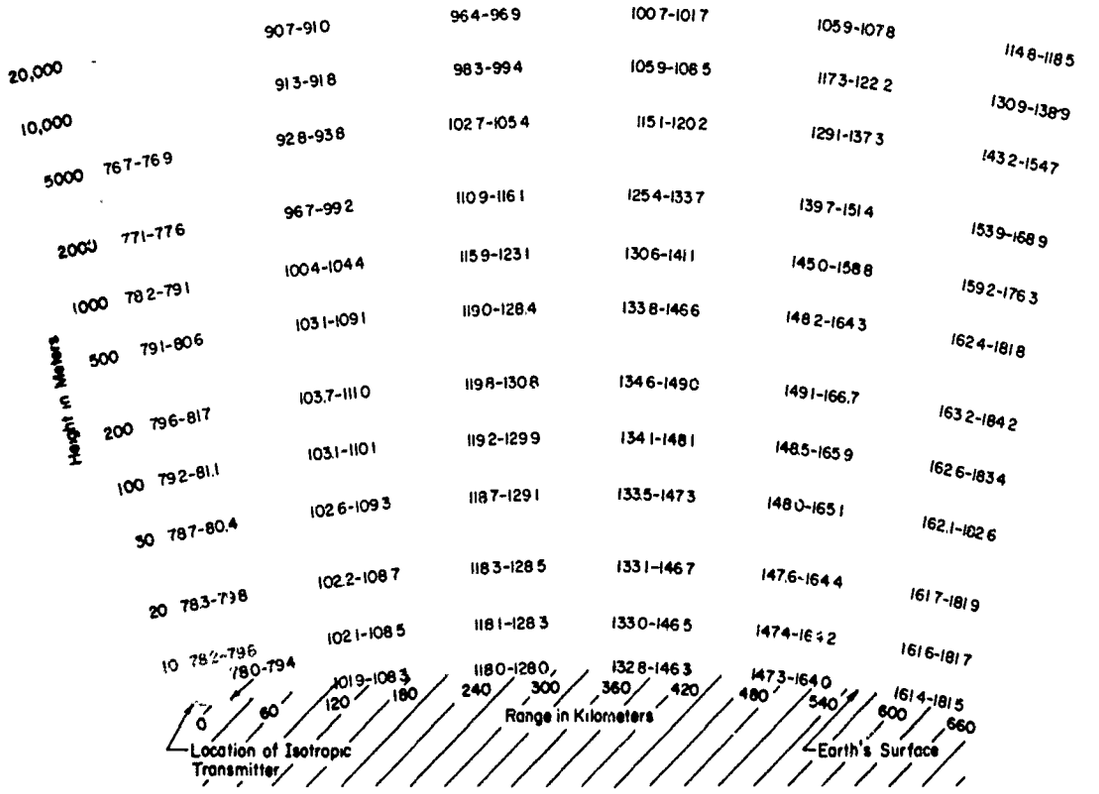

Figure 10. Basic Transmission Loss to Points at Various Heights and Ranges Above the Ocean at 10 MHz. First Number is for Perfectly Smooth Sea, Second is for Sea State 5 (25 knot wind) Using Phillips Ocean-Wave Spectrum.

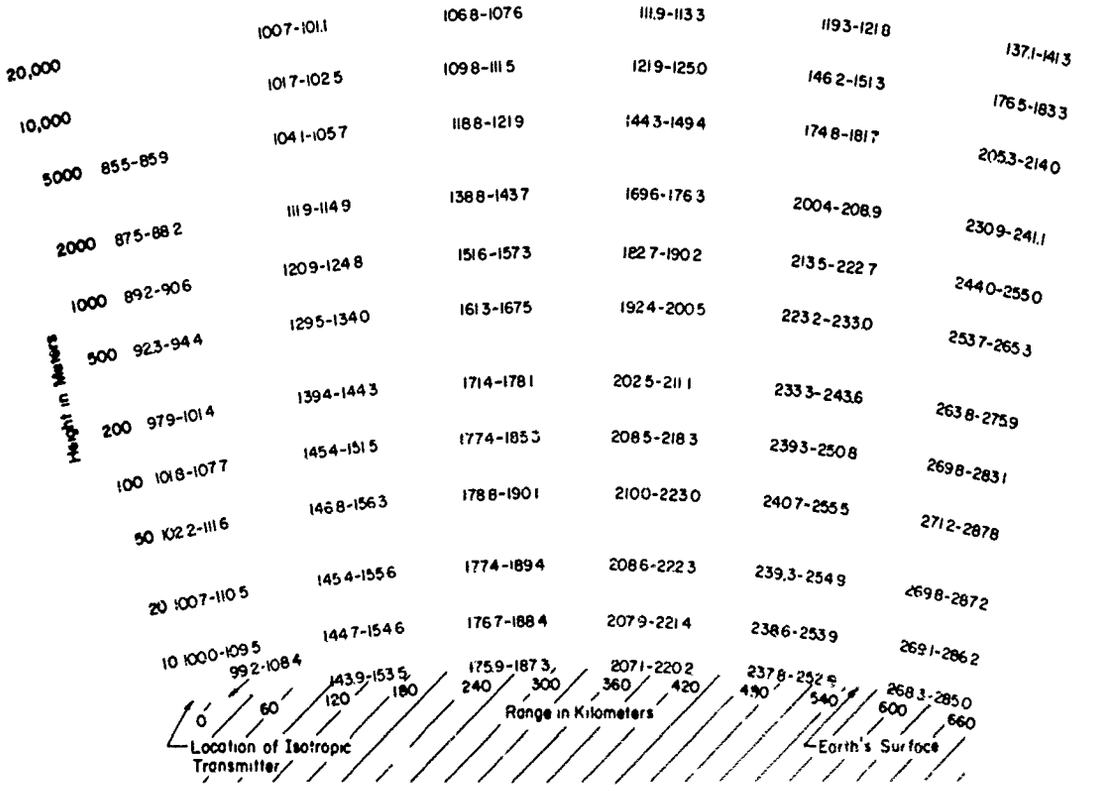

Figure 11. Basic Transmission Loss to Points at Various Heights and Ranges Above the Ocean at 30 MHz. First Number is for Perfectly Smooth Sea, Second is for Sea State 5 (25 knot wind) Using Phillips Ocean-Wave Spectrum.

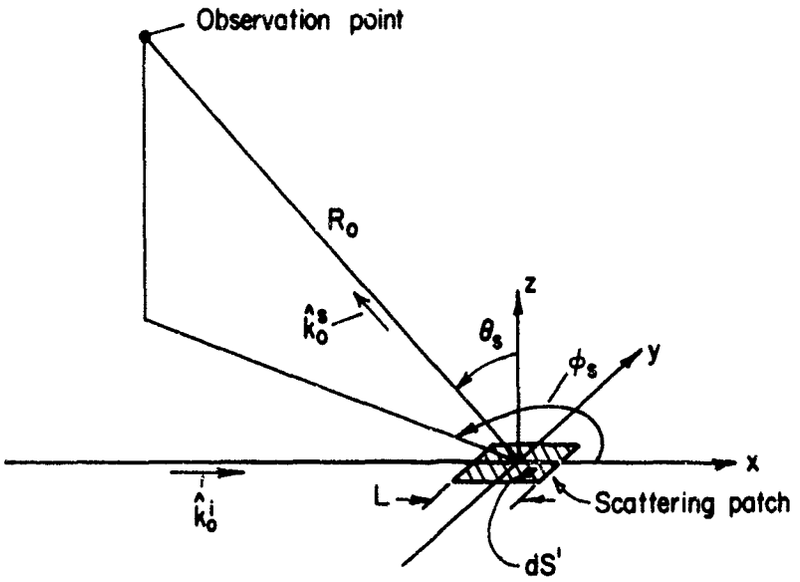

Figure 12. Far-Zone Scatter Geometry.

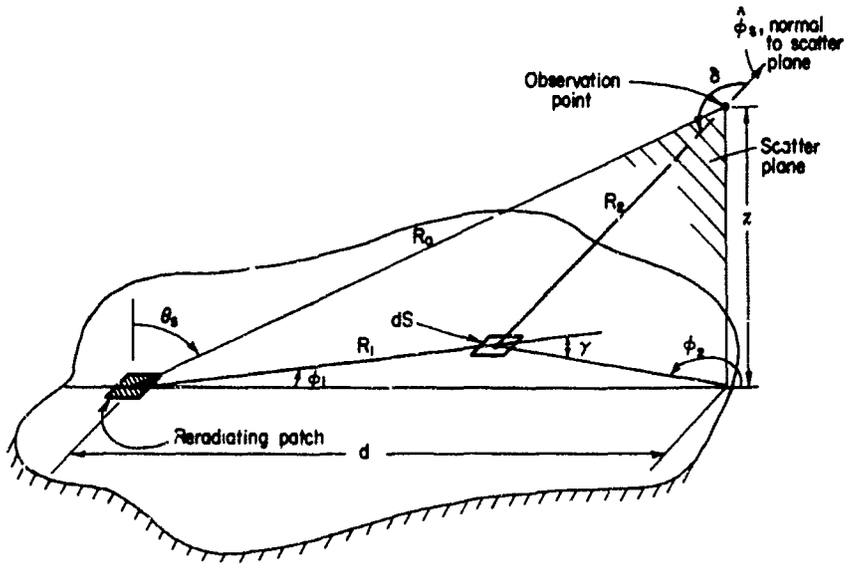

Figure 13. Geometry for Compensation Theorem.

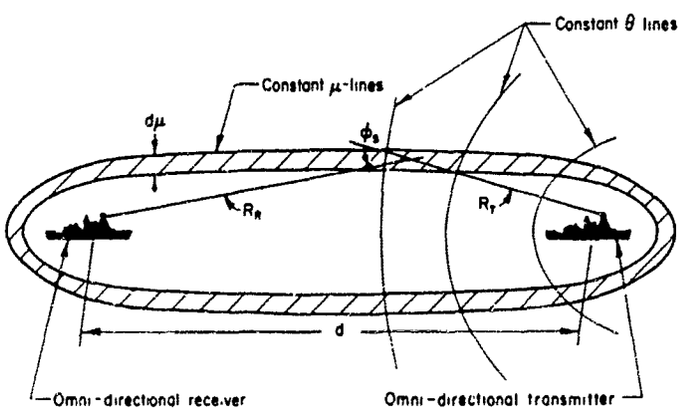

Figure 14. Bistatic Surface-to-Surface Radar.

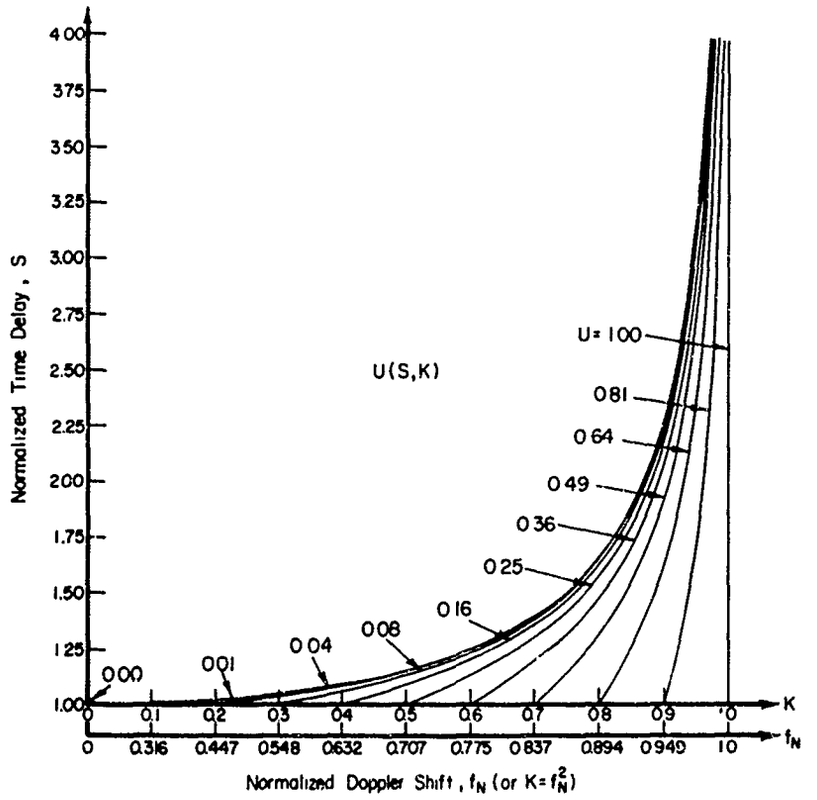

Figure 15. Transformation between U (Normalized Spatial x-Wavenumber), and f_N (Normalized Doppler Shift) and S (Normalized Time Delay) Radar Observables.

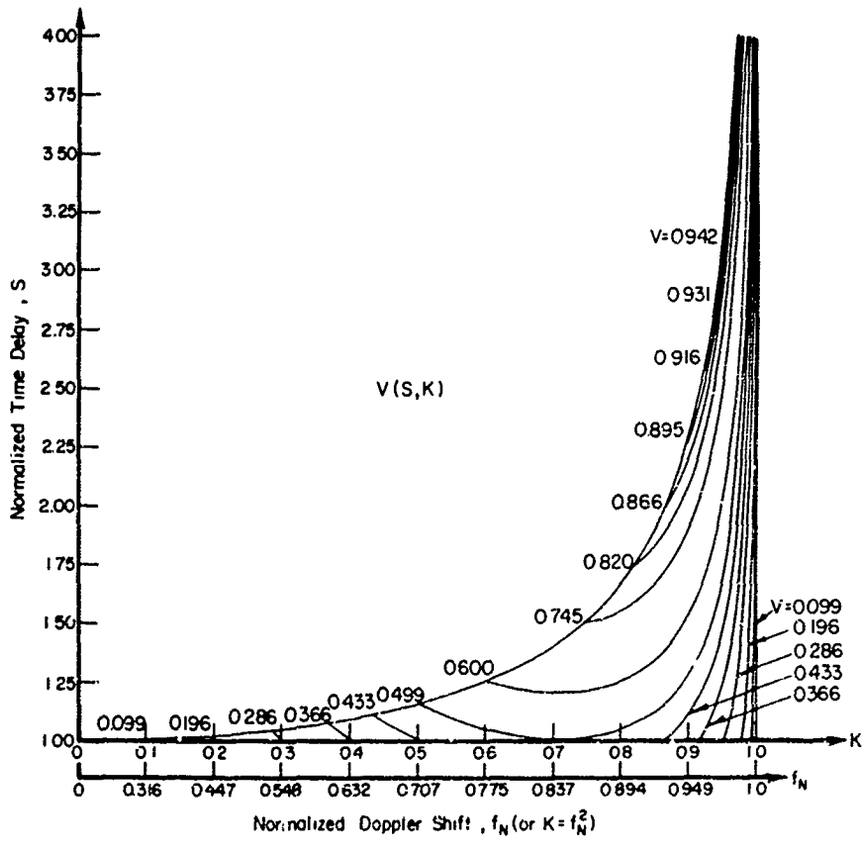

Figure 16. Transformation between V (Normalized Spatial y-Wavenumber), and f_N (Normalized Doppler Shift) and S (Normalized Time Delay) Radar Observables.

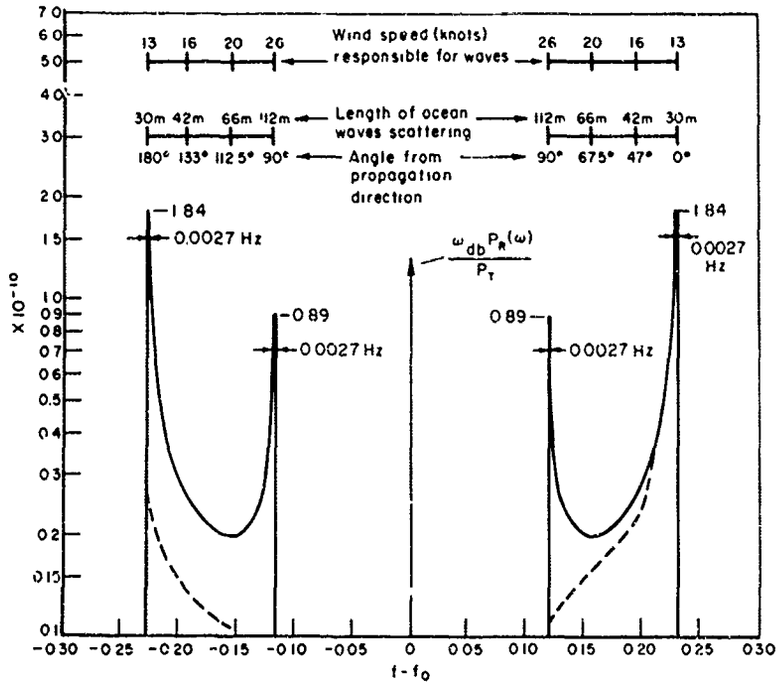

Figure 17. Received Signal Spectrum at 5 MHz for Sea Scatter Configuration of Figure 14. Solid Lines Were Computed for Fully Aroused Phillips Isotropic Ocean-Wave Spectrum. Dashed Curves Represent Expected Measurements from Non-Isotropic Sea.

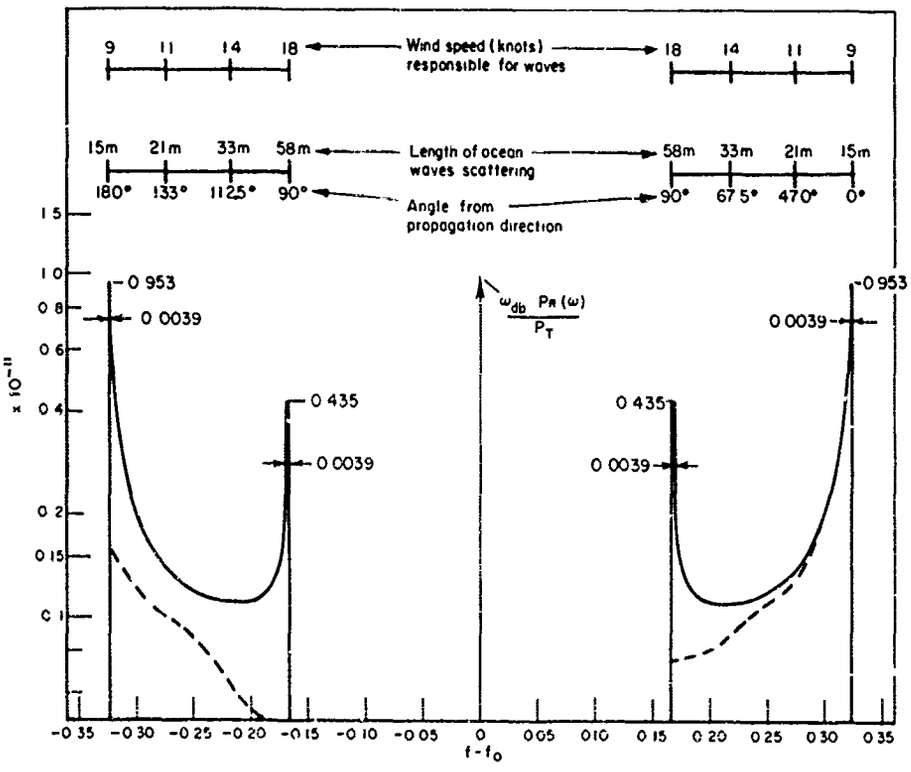

Figure 18. Received Signal Spectrum at 10 MHz for Sea Scatter Configuration of Figure 14. Solid Lines Were Computed for Fully Aroused Phillips Isotropic Ocean-Wave Spectrum. Dashed Curves Represent Expected Measurements from Non-Isotropic Sea.

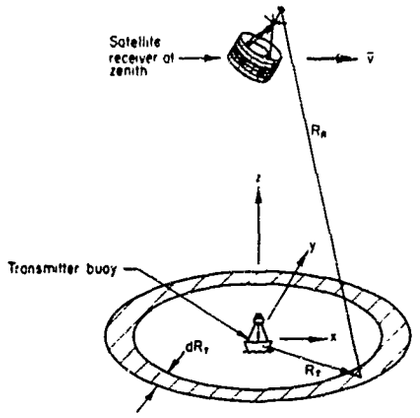

Figure 19. Bistatic Surface-to-Satellite Radar.

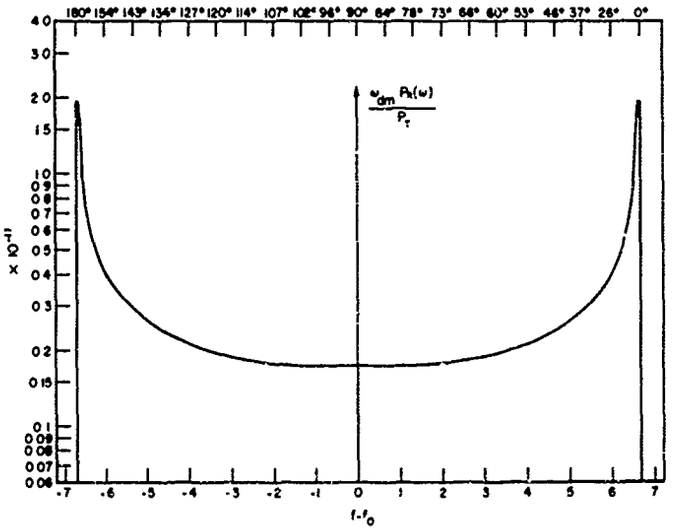

Figure 20. Received Signal Spectrum at 5 MHz for Sea Scatter Configuration of Figure 19; Computed for Fully Aroused Phillips Isotropic Ocean-Wave Spectrum.

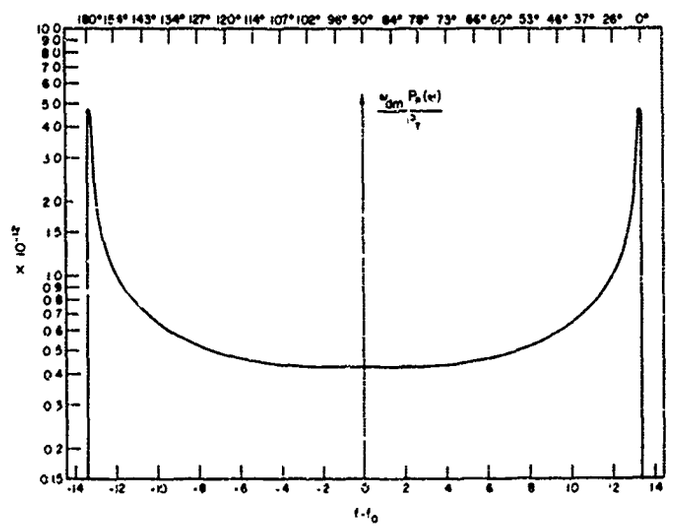

Figure 21. Received Signal Spectrum at 10 MHz for Sea Scatter Configuration of Figure 19; Computed for Fully Aroused Phillips Isotropic Ocean-Wave Spectrum.

DOPPLER SPECTRA IN MICROWAVE SCATTERING FROM WIND WAVES

by

J.W. Wright & W.C. Keller

Naval Research Laboratory
Washington, D.C. 20390

DOPPLER SPECTRA IN MICROWAVE SCATTERING FROM WIND WAVES

J.W. Wright & W.C. Keller
Naval Research Laboratory
Washington, D.C. 20390

SUMMARY

Doppler spectra in microwave backscattering from wind waves have been measured at X band (3.2 cm) and K band (1.25 cm) in a short fetch laboratory wind wave tank. The scattering can be accounted for as low order Bragg scattering and the spectral bandwidth is proportional to Bragg wavenumber and to windspeed.

1. INTRODUCTION.

It is now fifteen years since observation of doppler spectra (i.e., backscattered power spectral density) of sea echo at 13 MHz led Crombie[1] to identify Bragg scattering as a primary mechanism in radar scattering by wind generated waves. The essential correctness of this insight is shown by the fact that the Bragg scattering mechanism is incorporated in recent successful calculations of the mean scattering cross sections of the sea. Subsequent measurements of doppler spectra at sea at higher radar frequencies have been, comparably, rather less perspicuous to the scattering problem. We have learned[2,3,4] that doppler bandwidths may be correlated with estimates of orbital velocities of the wave system and Pidgeon[5] reports that the mean doppler shift itself is so correlated. However, successful measurements of doppler spectra at sea have, for practical reasons, been limited to low grazing angles. Furthermore, accurate measurements of surface velocities are difficult to obtain at sea. We have attempted to avoid these limitations by taking recourse to the laboratory and have obtained doppler spectra on vertical polarization at X band (3.2 cm) and K band (1.25 cm) for depression angles between 15° and 80° and windspeeds between 4 and 15 knots, in the short fetch tank and scattering range described in Section 2.

Although there are many similarities between waves in a tank and those at sea[6], the experimental situation in the tank differs from that at sea in at least three important respects which are particularly relevant to our measurements. First, due to the short range and small water wave amplitude, the nature of the illumination pattern, including the Fresnel zone structure, is much more important than is normally the case at sea. This requires an examination of the convolution which is the mathematical representation of our measurement. This is done in Section 4. Second, in the short fetch tank the mean surface drift is large compared to the RMS orbital velocity which is qualitatively the reverse of the situation at sea. This conspicuous difference is delineated by the measurements of mean drift and RMS particle velocities by stroboscopic photography which are reported in Section 3. Finally, the value of the mean squared height spectrum is significantly greater at short fetches than at sea[6]. We have measured the directional mean squared slope spectra by an optical Fourier transform technique and some results of these measurements are also given in Section 3.

The main conclusion to be drawn from the results presented in Sections 3 and 5 is that the doppler bandwidth is proportional to the windspeed and to Bragg wavenumber, $2 k_o \cos\theta$ (k_o the microwave propagation number, θ the depression angle) while its value near grazing correlates well with the orbital velocity as is the case at sea. This observed dependence on depression angle cannot be explained by the customary assumption that the scatterers are moving in circular trajectories as this latter assumption yields a doppler bandwidth nearly independent of depression angle. In Section 6 it is suggested that a more appropriate interpretation may be that the doppler bandwidth is an inverse scatterer lifetime.

2. WIND WAVE TANK, DOPPLER SPECTROMETER, AND SCATTERING RANGE

The wind wave tank, of plywood and fiberglass construction and shown schematically in Figure 1, is installed in an ordinary sized, air-conditioned laboratory room and is 16 feet long and 30 inches wide. An overflow baffle at the downwind end and the inletting of a trickle of water maintains the depth at 11 inches and permits contaminant surface films to be driven off by the wind. The wind is produced by a centrifugal fan blowing through a wind tunnel 6 feet long, the underside of the top of which, covered with a microwave absorbent material, is five inches above the static water level. A grill, constructed of rectangular tubes of resistive paper (surface resistance ~ 377 ohms) one inch by 1/2 inch in cross section and 3 inches long, fills the inlet to the wind tunnel. This serves the dual purpose of increasing the homogeneity of the air flow and absorbing any microwave energy reaching the end of the tunnel. The windspeed is varied by inserting a shutter across the outlet of the blower. The maximum windspeed is 7.9 m/sec.

The area illuminated by the horn antennas is centered midway in the channel and four feet downwind from the end of the tunnel. The windspeed at this position and two inches above the static water level, which is approximately the position of the maximum in the vertical wind profile, is measured with an Alnor velometer, denoted by the symbol, U, and given as the measure of the windfield. However, the expansion of the airstream upon leaving the tunnel results in a gradient in the windspeed which is very nearly constant along the tank. The windspeed, U, and the gradient measured at the same position are given in TABLE I.

TABLE I

GRADIENT IN THE WINDSPEED AT VARIOUS WINDSPEEDS

WINDSPEED U(m/sec)	GRADIENT OF WINDSPEED $\frac{1}{U}\frac{dU}{dx}$ (m^{-1})	GRADIENT IN SURFACE DRIFT $\frac{1}{V_d}\frac{dV_d}{dx}$ (m^{-1})
2.25	0.50	.57
3.5	0.38	.64
4.8	0.40	.39
6.0	0.38	.47
7.9	0.36	

The microwave and audio frequency circuitry is similar at both microwave frequencies. The principles and operation of the circuitry are discussed elsewhere[7] for the case of measurements on mechanically generated waves. The principal modification for measurements on wind generated waves is the introduction of an integrator after the audio frequency filter. The integration time used is 15 seconds which is long compared to the period of any wind generated wave in the tank and about three times the period of the fundamental seiche. The equivalent statistical bandwidth of the filter is 2.2 Hz so that the normalized standard error in the measured power spectral density as given by Bendat and Piersall[8] is 0.2. Scan rates between 2 Hz/min and 8 Hz/min were utilized.

The antennas are long tapered horns and are mounted on a circular arch such that the range is 140 cm at X band and 150 cm at K band. A dimensionless backscattering cross section σ^0 and an effective illuminated area A_i are defined in the following way. Let $E_i(x,y)$, $H_i(x,y)$ be the complex amplitudes (time factor $e^{j\omega t}$ omitted) of the electromagnetic fields incident on the undisturbed water surface in the plane of which are situated the cartesian coordinates x, y, z (Figure 1) with origin at the center of illumination and let $E_i^0 = E_i(0,0)$ and $H_i^0 = H_i(0,0)$. Then:

$$A_i \equiv \iint \frac{\left| E_i(x,y) H_i(x,y) \right|^2}{\left| E_i^0 \, H_i^0 \right|^2} \, dx \, dy \qquad (1)$$

We assume that the product $E_i H_i$ vanishes slowly but inexorably at large distances so that the limits of this and subsequent integrals over the x,y plane may be considered to be unbounded. Then we define:

$$\sigma^0 \equiv \sigma / A_i \qquad (2)$$

where the cross section σ is obtained by comparing the backscattered power due to the wind waves with that from a target of known cross section. The measured values of A_i at normal incidence are 200 cm^2 and 360 cm^2 at X band and K band respectively. It was found that, for all practical purposes, the value of A_i at other angles could be obtained from those values by division by sin θ.

3. AUXILIARY MEASUREMENTS

Two types of auxiliary measurements were made to aid in the interpretation of the doppler spectra. First, the directional slope spectra of the waves were obtained by a photometric technique combining the methods of Cox[9] and Stilwell[10]. These results will be described in detail elsewhere but for ready reference, the upwind/downwind slope spectra as a function of upwind/downwind wave number for various windspeeds obtained from those measurements are given in Figure 2. Second, we used stroboscopic photography to obtain the mean and mean squared vertical and horizontal velocities of small paraffin and polyethylene floats as well as measuring the mean drift following the methods of Keulegan[11] and Wu[12]. Figure 3 gives the mean upwind/downwind drift velocity of a series of 1/2 inch diameter paraffin disks as a function of windspeed and thickness of disk. The abscissa, labeled depth of submergence, is the calculated centroid of the submerged portion of the disk. The two points plotted at very small depth of submergence at windspeeds of 2.25 m/s and 7.9 m/s were obtained with 1/4 inch squares of 2 mil polyethylene sheet. These measurements are clearly in excellent agreement with the value of surface velocity found by extrapolation of the paraffin disk velocities. We also made mean drift measurements at the low windspeeds with 1/8", 1/4" and 1/2" diameter paraffin disks and at most windspeeds with 1/8", 3/16" and 1/4" diameter polyethylene spheres and found no significant dependence on float shape or size other than the dependence on depth of submergence like that shown in Figure 3. We therefore believe that the mean surface drift is well characterized by the values and linear dependence on windspeed exhibited by the data of Figure 4. The same cannot be said for the variances of the horizontal and vertical velocities also shown in Figure 4. There the open squares and triangles are the square roots of the two variances obtained from photographs taken from the side of the tank of the trajectories of 1/8" and 1/4" diameter polyethylene spheres under stroboscopic lighting at a repetition rate of 20 per second. Each point is the average obtained from 8-10 tracks each 30-60 cm long. Only at intermediate windspeeds were the measurements made with both 1/8" and 1/4" diameter spheres and the data are insufficient to expose any significant dependence on sphere size. However, definitely greater values were obtained from stroboscopic photographs made looking vertically downward of trajectories of 1/4" diameter by .073" thick paraffin disks. At

least some of the difference between horizontal and vertical velocities is explained by the upwind/downwind gradient in the mean drift for, under suitably simplifying assumptions, the total variance in horizontal velocity,

$\overline{\Delta V_t^2}$, is the sum of a term due to the (constant) gradient and the variance in horizontal velocity, $\overline{\Delta V_h^2}$, in the absence of the gradient:

$$\overline{\Delta V_t^2} = \frac{(\Delta V)^2}{12} + \overline{\Delta V_h^2} \tag{3}$$

where ΔV is the change in mean drift over the track. We were able to estimate the gradient in the mean drift at windspeeds of 6 m/sec and less by averaging slopes obtained from least mean squares linear fits to the velocity vs time trajectories, and these estimates are given in TABLE I. Though larger than the corresponding gradients in the windspeed the measured gradients in the mean drift are too small to explain the observed differences in horizontal and vertical velocities. We surmise that when the mean drift is larger than the orbital velocity and the horizontal and vertical gradients in the mean drift appreciable, the interpretation of the RMS horizontal float velocity is uncertain and it is better to characterize the orbital velocity of the wind wave system by the variance in vertical float velocity.

4. THEORY OF THE SCATTERING MEASUREMENT

The results to be reported here were all obtained on vertical polarization and, owing to this and the short fetch, the effects of large scale roughness calculable from composite surface theory[2,7,13,14,15,16] are largely outweighed by the influence of the illumination pattern. Thus, if one calculates the backscattering from a slightly rough surface on which is incident an approximately spherical wave one finds that the cross section is proportional to the convolution of the mean squared height spectrum with the Fourier transform of the illumination pattern. More precisely, it can be shown that

$$\sigma^o = 16\pi K_o^4 \, gg^* \int_{-\infty}^{\infty}\int_{-\infty}^{\infty} W(K_x',K_y') \, V(2K_o\cos\theta - K_x', K_y') \, dK_x' \, dK_y' \tag{4}$$

where g is the function of depression angle, dielectric constant and polarization similarly denoted and defined by Wright[13]. $W(K_x,K_y)$ is the mean squared height spectrum of the surface displacements such that the total mean squared height, $\overline{h^2}$, is given by

$$\overline{h^2} = \int_{-\infty}^{\infty}\int_{-\infty}^{\infty} W(K_x,K_y) \, dK_x \, dK_y \tag{5}$$

and

$$V(K_x,K_y) = (2\pi)^{-2} \frac{\left| \iint e_i(x,y) h_i(x,y) e^{jk_x x} e^{jK_y y} \, dxdy \right|^2}{\iint \left| e_i(x,y) h_i(x,y) \right|^2 dxdy} \tag{6}$$

with
$$E_i \equiv e_i \, e^{j(K_o\cos\theta)x}$$
$$H_i \equiv h_i \, e^{j(K_o\cos\theta)x} \tag{7}$$

To proceed further, suppose the incident fields are given in terms of the fields in the plane of the aperture by Silver's[17] expression specialized to the case of narrow beam and assuming the aperture is a plane of constant phase. In that case $V(K_x,K_y)$ can be obtained in the following way:

$$V(K_x,K_y) = C \int_{-\infty}^{+\infty}\int_{-\infty}^{+\infty} v(K_x',K_y') v(K_x - K_x', K_y - K_y') \, dK_x' \, dK_y' \tag{8}$$

where $v(K_x,K_y)$ is itself the convolution of two functions $F(K_x,K_y)$ and $W(K_x,K_y)$

$$F(K_x,K_y) = e^{-j\left(\frac{\beta K_x}{2}\right)^2} e^{-j\left(\frac{\gamma K_y}{2}\right)^2} \quad (9)$$

$$W(K_x,K_y) = u_a\left(\frac{\beta^2 K_x \sin\theta}{2}, \frac{\gamma^2 K_y}{2}\right) e^{j\left(\frac{\beta K_x}{2}\right)^2} e^{j\left(\frac{\gamma K_y}{2}\right)^2} \quad (10)$$

where $\gamma^2 = 2R_o/K_o$, $\beta^2 = 2R_o/K_o \sin^2\theta$, $u_a(x',y')$ is the amplitude of the yield in the plane of the aperture of the horn, and the constant, C, may be obtained from the condition

$$\int_{-\infty}^{+\infty}\int_{-\infty}^{+\infty} V(K_x,K_y)\,dK_x\,dK_y = 1 \quad (11)$$

Since $u_a(x',y')$ is assumed to be zero outside the aperture of the horn, $W(K_x,K_y)$ vanishes if

$$\left|\gamma^2 K_y\right| > D_h \; ; \; \left|\beta^2 K_x \sin\theta\right| > D_e \quad (12)$$

where D_h and D_e are the linear dimensions of the aperture in the H and E planes respectively. Since $F(K_x,K_y)$ and $W(K_x,K_y)$ are (except for a multiplicative factor) functions of $K_x/\sin\theta$, $V(K_x,K_y)$ at one depression angle may be obtained from its value at any other angle by a scale change. Furthermore, the convolution of $F(K_x,K_y)$ and $W(K_x,K_y)$ tends to small values only for such large values of its argument that $W(K_x,K_y)$ spans a sufficient number of zero crossings of $F(K_x,K_y)$. Hence, except in cases of severe under-illumination (antenna beamwidth small compared to $(K_o/R)^{-\frac{1}{2}}$) the Fresnel zone structure substantially broadens the convolving function $V(K_x,K_y)$ in the expression (equation (4)) for the backscattering cross section of the slightly rough surface.

Values of $V(K_x,0)$ for the cases of 70° depression angle at K band and 30° depression angle at X band, calculated from equations (8)-(10) assuming that the fields in the aperture of the horn are uniform in the E plane, are shown in Figure 5 together with the measured mean squared height spectra at maximum and minimum windspeeds. The solid portions of these latter curves are computed from the photometrically measured spectra of Figure 2 and the dashed portions, which are really only estimates, are inferred from the orbital velocity measurements. The two representations of $V(K_x,0)$ are shown with arbitrary normalization, i.e., there is no significance to their vertical positions on the graph. Important features of $V(K_x,0)$ shown in Figure 5 can be discerned in the measured spectra, some examples of which are shown in Figure 6. In order to compare these measured spectra with the calculations given above, it is necessary to assume the existence of a dispersion relation, $\omega(K)$, or for small changes $\Delta\omega$ and ΔK:

$$\Delta\omega/\omega \cong (V_{group}/V_{phase})\ \Delta K/K \quad (13)$$

where for water waves in the transition region between capillary and gravity waves the bracketed ratio is near unity. Referring then to Figure 6a, a measured spectrum for K band, 70°, 2.25 m/s, we note two main peaks. The peak shifted furthest from zero frequency, which is indicated by the arrow at the top of photo and the vertical slash on the photo, is the Bragg resonant peak as can be inferred from the fact that it is shifted by the same amount as is the case, X band, 30°, 2.25 m/s shown in Figure 6c. The other major peak is due to the "sidelobe" of $V(K_x,0)$ shown in Figure 5 whereas the minor peak on the opposite side of zero frequency is due to reflection of the dominant water wave by the imperfect beach, a fact discerned by degrading the beach and enhancing this minor peak. On the other hand, the subsidiary peaks in Figure 6c are not due to either of these causes. Rather, the peak at zero frequency is largely due to the residual unbalance of the microwave bridge whereas the two peaks spaced symmetrically about it result from rescattering by stationary objects of energy Bragg scattered slightly above and below the specular direction by the dominant water wave. The "sidelobes" of $V(K_x,0)$, being lower and nearer the main lobe in this case, are masked by the broadening of the spectrum. On the other hand, for the comparable pair of spectra shown in Figure 6b and 6d, it is

found that, owing to the greater steepness of the mean squared height spectrum in the region near $K_x \approx 2.5$, the Bragg wavenumber for this case, the "sidelobe" dominates at K band and is large enough to be clearly discernible at X band.

Increasing windspeed and formation of larger waves destroys the influence of the Fresnel zone structure, which results from the phase differences between the spherical wave front and a plane water surface. The sidelobes, which are entirely dependent on the Fresnel zone structure, tend to vanish and, as illustrated in Figure 5 for 70° K band, the main lobe contracts toward the inner curve, which is entirely due to the amplitude distribution or "gain function" of the horn. In this case, the region ΔK over which the scattering measurement tends to average can be estimated from equation (12):

$$(\Delta K/2K_o \cos\theta)_{horn} \cong (D_e/4R_o) \tan\theta \qquad (14)$$

At the same time the tilting of the Bragg resonant waves by the larger waves causes an averaging, Wright[13], qualitatively similar to that expressed by the convolution integral, equation (4), resulting in a relation analogous to equation (14):

$$(\Delta K/2K_o \cos\theta)_{tilt} \cong \overline{(m^2)}^{\frac{1}{2}} \tan\theta \qquad (15)$$

where $\overline{(m^2)}^{\frac{1}{2}}$ is the RMS upwind/downwind slope due to the large waves. In truth, the quantity, $\overline{(m^2)}^{\frac{1}{2}}$ is not independently determinate because in composite surface scattering theory, the dichotomy between long and short waves must be made ad hoc. The total mean square slope in our tank is not greater than about 0.1 radian and $\overline{(m^2)}^{\frac{1}{2}}$ can be only a fraction of that value so that the effects expressed by equations (14) and (15) may be comparable. As the windspeed increases, however, the spectral broadening due to other causes much exceeds that due to these two effects and the only discernible vestige of these effects is a slight asymmetry in the spectra as seen in Figure 6e.

5. EXPERIMENTAL RESULTS

The examples of measured spectra shown in Figure 6 were chosen not to be "typical" nor "exemplary" but rather to illustrate perturbing or distorting features. Thus in analyzing these spectra, we first computed a mean frequency for each spectra neglecting portions of the spectra clearly identifiable as resulting from the distortions discussed in Section 4. Then we computed two RMS bandwidths, one using the same data as in the calculation of the mean frequency shift and the other, almost invariably slightly smaller, using only the data for frequencies greater than the mean. The average of these two bandwidths for both the K-band and X-band measurements for five different windspeeds is plotted vs Bragg wavenumber, $2K_o \cos\theta$, in Figure 7. In cases where these two bandwidths differed by more than 0.4 Hz, the extend of the horizontal line through the point indicates this difference. From the discussion of Section 4, it is clear that the bandwidths for the smallest values of $2K_o \cos\theta$ and the lower windspeeds should be eliminated since the convolving function, $V(K_x, 0)$ then spans the peak of the mean squared height spectrum. They have been eliminated from Figure 7, though, in truth, their inclusion would make little or no difference in the overall picture. The straight lines through the data points in Figure 7 result from a least mean squares fit to the data so that (with $\omega = 2\pi f$) the doppler bandwidth may be written:

$$\left[\overline{(\omega-\bar{\omega})^2}\right]^{\frac{1}{2}} = \omega_o + 2K_o V_o \cos\theta \qquad (16)$$

Both ω_o and V_o depend on windspeed and in Figure 8, it is seen that V_o is closely proportional to windspeed. In magnitude V_o is almost exactly equal to the square root of the variance in the horizontal surface velocity measured with 1/4" and 1/8" diameter spheres which may be coincidental in view of the apparent dependence of the latter velocity on shape and size of float. The portion of ω_o due to the filter bandwidth is $2\pi \times 1.4$ Hz and the remainder may be due to the "tilt" discussed in Section 4.

Most obvious sources of doppler broadening yield bandwidths which either decrease or, as in the case of scatterers borne in circular trajectories, are constant with decreasing depression angle. One exception is the gradient in the mean drift which would yield a bandwidth

$$\left[\overline{(\omega-\bar{\omega})^2}\right]^{\frac{1}{2}} \cong 2K_o V_d \cot\theta \qquad (17)$$

where ΔV_d is the increment in the mean drift over the illuminated area at normal incidence and the proportionality is to cot θ because the total increment in drift increases inversely as sin θ. However, there is no vestige of the angular dependence of equation (17) even at 15°. The data for 15° are not shown in Figure 7, because the range variation in the illumination pattern does introduce some distortion into the measured spectra at this low angle, but the measured bandwidths at 15° are very nearly equal to those at 30°. Furthermore, early in the experimental program, we measured K-band spectra with a thin film cover continuing the wind tunnel downwind of the illuminated area, thus eliminating the gradient in the windspeed and drift. These measurements were made at a shorter fetch and higher windspeed so that the magnitude of the bandwidth is not directly comparable to that shown in Figure 7. The bandwidth is, however, very clearly proportional to cos θ, differs little in magnitude from that reported for a windspeed of 7.9 m/s in Figure 7. In view of the size of the estimate of the gradient in the drift given in TABLE I it is a little surprising that no trace of its influence on the bandwidth can be discerned and it may be that these estimates are in fact too large.

Figure 9 shows a phase velocity computed from the measured mean frequency for wind generated and mechanically generated waves. The solid and open points refer, respectively, to measurements made at two different periods of time approximately 15 months apart. The lower curve, A, is the phase velocity for linearized, irrotational water waves, and it is seen that, if this curve is shifted upwards about 6 cm/s (curve B) rather than 10 cm/s, which is the measured surface drift, a fair fit to the data is obtained. However, it seems likely that these wind waves should be considered to be a perturbation of the wind induced drift rather than as classical irrotational waves. Some preliminary calculations seem to show that the measured phase velocities at the low windspeed can indeed be explained on this basis. At the high windspeed the situation is complicated by the possibility of higher order Bragg scattering which would lead to a still different relationship[18]. The dashed curve, C, is such a relationship for second order scattering again based on linear irrotational wave motion and arbitrarily shifted upwards 25 cm/s. The determination of the true nature of these wind waves, as well as the possible influence of higher order Bragg scattering, clearly requires further experimentation.

The mean squared height spectra at minimum and maximum windspeeds multiplied by $(2K_o \cos \theta)^4$ to yield a dimensionless form and calculated, after integration of the doppler spectra, from the relation:

$$\sigma_o = 16\pi K_o^4 \, gg^* \, \Psi(2K_o \cos \theta, 0) \tag{18}$$

are shown in Figure 10, together with the photometrically determined spectra. Actually, we have made some corrections based on the more exact relationship (equation (4)) but, except in the case of the high angle K band points at the minimum windspeed, these corrections were 1.3 dB or less. The significance of the open and solid data points is the same as in Figure 9. It is evident from the excellent reproduction of the sharp dip in the spectrum near $K_x = 3.5$ that at the low windspeed the cross section is very satisfactorily accounted for by first order Bragg scattering. This is also true at the lower angles at the maximum windspeed but at higher angles, despite some scatter, there appears to be a significant discrepancy between the photometrically and electromagnetically determined spectra again suggesting the possibility of higher order scattering. Final resolution of this question will depend on further measurements.

6. DISCUSSION

The fact that the magnitudes of the doppler bandwidth and the orbital velocity are very similar at sea as well as in the wave tank does not, of course, establish a causal link between them. It does, however, suggest that the doppler bandwidth at low angles scales with fetch in much the same way as does the orbital velocity. If this is so, then the question whether the angular dependence of doppler bandwidth observed in the tank will also be observed at sea devolves on the fetch dependence of ω_o in equation (16). Unless ω_c increases more rapidly with increasing fetch than the orbital velocity (which it will not, e.g., if it depends on the tilt or mean squared slope) a decrease of doppler bandwidth on approach to normal incidence will also be observed at sea.

Of even more interest perhaps is the question of the origin of the doppler bandwidth. In this respect, it is suggestive if, neglecting ω_o, we divide both sides of equation (16) by the angular frequency, ω, of the water wave of wave number $2K_o \cos \theta$:

$$\Delta\omega/\omega = V_o/V_{phase}(2K_o \cos \theta) \tag{19}$$

Thus, the relative bandwidth associated with a water wave is a maximum for the water wave with minimum phase velocity. Now, as can be seen in Figure 2, the water wave spectrum has a partial null which in fact, occurs in the region of minimum phase velocity. The origin of this null can be observed in a simple demonstration in which one slowly sweeps the frequency of small amplitude mechanically generated water waves through the region of minimum phase velocity. With proper illumination, one then observes that in the region of minimum phase velocity the water waves are unstable and tend toward the production of harmonics. This phenomenon has been discussed theoretically by numerous authors[19,20]. Qualitatively it may be understood as a result of the fact that whereas the phase velocity of finite amplitude gravity waves is greater than that for infinitesimal waves, the reverse is true for capillary waves. At all events the null in the spectrum can be interpreted to be the result of an instability

or decreased lifetime for water waves in the transition region. This notion can be retained at higher windspeeds when the null is filled in because in that case there are sufficient capillary waves which, slowing as they grow in amplitude, tend to feed energy back into the transition region. Of course, the foregoing considerations do not prove that the doppler bandwidth is an inverse lifetime, but the applicability of equation (16) to both gravity and capillary waves seems to preclude an explanation based solely on the relative motions of a composite surface. In the absence of more plausible explanations then, this hypothesis seems well worth pursuing. Finally, it is interesting to compare the results given here for wind waves with the measurements reported by Mee[21] for doppler spectra at X band on plunger generated, narrow band water waves in a wave tank. Mee's interpretation shows that the component of orbital velocity along the line of sight determines the width of the doppler spectra which is thus essentially independent of depression angle for the reported range of angles, 40°-90°. Gross features of Mee's results are qualitatively understandable on the basis of geometrical optics[22]. The difference between the cases of wind generated and plunger generated waves comes about because it is the mean squared slope, which is the second moment of the height spectrum, and the mean squared curvature, which is the fourth moment, that are the parameters important in the scattering. These quantities are distributed very differently in a K^{-4} wind generated spectrum than in a narrow band plunger generated spectrum and there may be little similarity in the scattering in the two cases.

7. CONCLUSIONS

As a result of the work reported herein, we have come to the following conclusions and speculations to be tested by further study:

a. Microwave backscattering from wind waves in a short fetch tank is largely explainable on the basis of low order Bragg scattering.

b. The doppler bandwidth is proportional to the Bragg wavenumber, $2K_o \cos\theta$, and to the windspeed. The magnitude of the doppler bandwidth (in velocity units) at low angle, is very similar to the orbital velocity and probably scales with fetch like the orbital velocity.

c. An explanation for the doppler bandwidth requiring further investigation is that the bandwidth is a kind of inverse lifetime of the Bragg resonant water wave.

8. ACKNOWLEDGEMENTS

The authors gratefully acknowledge the aid of Ernest Mabrey who conducted many of the scattering measurements and of Roger Pilon and Raymond Bovet who did the stroboscopic photography. We are especially indebted to Dr. Gaspar Valenzuela for many enlightening discussions concerning scattering from water waves and to Dr. Omar Shemdin for a particularly productive conversation concerning the water wave spectra in the transition region.

9. REFERENCES

1. Crombie, D.D., "Doppler Spectrum of Sea-Echo at 13.56 Mc/s," Nature, 175, 681-682, 1955.
2. Hicks, B.L., N. Knable, J.J. Kovaly, G.S. Newell, J.P. Ruina, and C.W. Sherwin, "The Spectrum of X-Band Radiation Backscattered from the Sea Surface," J. Geophys. Res., 65(3), 825-837, 1960.
3. Fuks, I.M., "On the Theory of Radio Wave Scattering by a Ruffled Sea Surface," Radio Physics (USSR), 9, 876, 1966.
4. Valenzuela, G.R. and M.B. Laing, "Study of Doppler Spectra of Radar Sea Echo," J. Geophys. Res., 75(3), 551-563, 1970.
5. Pidgeon, V.W., "The Doppler Dependence of Radar Sea-Return," J. Geophys. Res., 73(4), 1333-1341, 1968.
6. Hess, G.D., G.M. Hidy, and E.J. Plate, "Comparison Between Wind Waves at Sea and in the Laboratory," J. Marine Res., 27(2), 216, 1969.
7. Wright, J.W., "Backscattering from Capillary Waves with Application to Sea Clutter," IEEE Trans., AP-14(6), 749-754, 1966.
8. Bendat, J.S. and A.G. Piersol, Measurement and Analysis of Random Data, John Wiley and Sons, New York, 1966.
9. Cox, C., "Measurement of Slopes of High Frequency Wind Waves," J. Marine Res., 16(3), 199, 1958.
10. Stilwell, D., Jr., "Directional Energy Spectra of the Sea from Photographs," J. Geophys. Res., 74(8), 1974-1986, 1969.
11. Keulegan, G., "Wind Tides in Small Closed Channel," J. Res. Natl. Bur. of Std. (U.S.), 46, 358, 1951.
12. Wu, J., "Laboratory Studies of Wind Wave Interaction," J. Fluid Mech., 34, 91, 1968.
13. Wright, J.W., "A New Model for Sea Clutter," IEEE Trans., AP-16(½), 217-233, 1968.
14. Bass, F.G., "Contribution to the Theory of the Combination Scattering of Waves by a Rough Surface," Radio Physics (SSR), 4, 58, 1961.
15. Bass, F.G., I.M. Fuks, A.I. Kalmykov, I.E. Ostrovsky, and A.D. Rosenberg, "Very High Frequency Radiowave Scattering by a Disturbed Sea Surface," IEEE Trans., AP-16(5), 554-568, 1968.
16. Barrick, D.E. and W.H. Peake, "A Review of Scattering from Surfaces with Different Roughness Scales," Radio Science, 3(8) (new series), 865-868, 1968.
17. Silver, S., Microwave Antenna Theory and Design, McGraw-Hill, New York, 167, 1949.
18. Rosenberg, A.D., I.E. Ostrovsky, and A.I. Kolmykov, "Frequency Shift of Radiation Scattered by a Ruffled Sea Surface," Radio Physics (USSR), 9, 234, 1966.
19. Wilton, J.R., "On Ripples," Phil. Mag., 6th series, 29(173), 688, 1915.
20. Pierson, W.J. and P. Fife, "Some Nonlinear Properties of Long Crested Periodic Waves with Lengths Near 2.44 Centimeters," J. Geophys. Res., 66(1), 163, 1961.
21. Mee, T.R., Jr., "An Investigation of the Dynamics of Water Waves," Cornell Aeronautical Lab., Inc. Report No. RG-1623-P-1, 1963.
22. Camnitz, H.G. and R.P. Rogers, "An Experimental and Theoretical Study of Scattering from Water Waves," Cornell Aer. Lab., Inc. Report No. RM-1933-P-1, 1965.

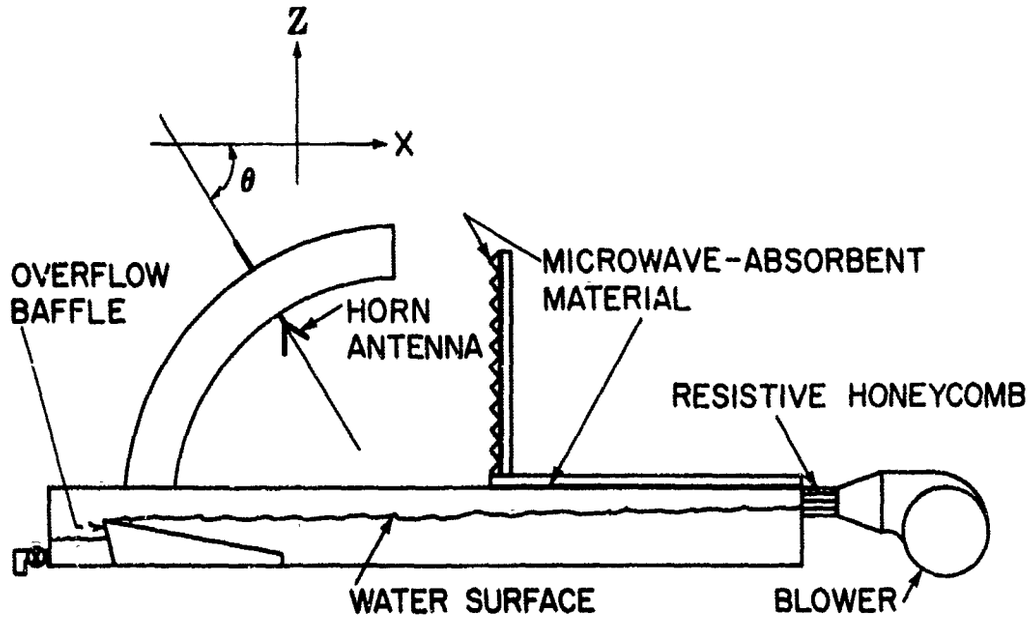

FIGURE 1 Schematic representation of the wind/wave tank and scattering range.

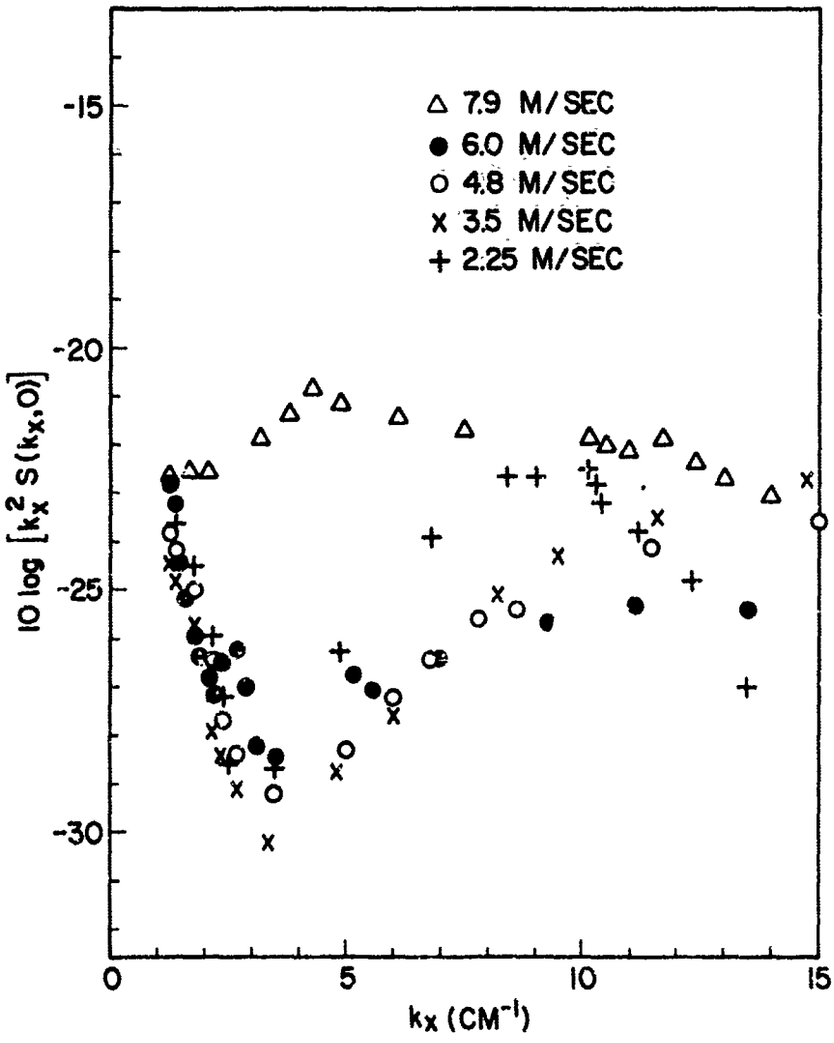

FIGURE 2 Upwind-downwind slope spectrum as a function of upwind-downwind wavenumber.

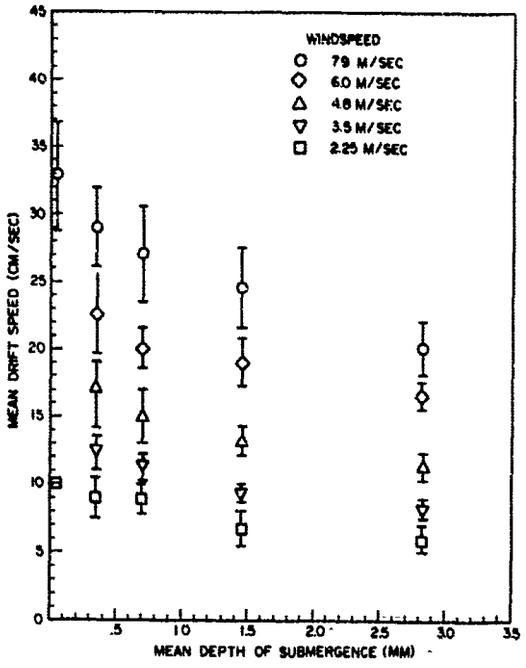

FIGURE 3 Mean upwind-downwind drift velocity of a series of 1/2" diameter paraffin disks of varying thickness. The extent of the vertical bar through the data points is the standard deviation in a series of 10-15 consecutive measurements.

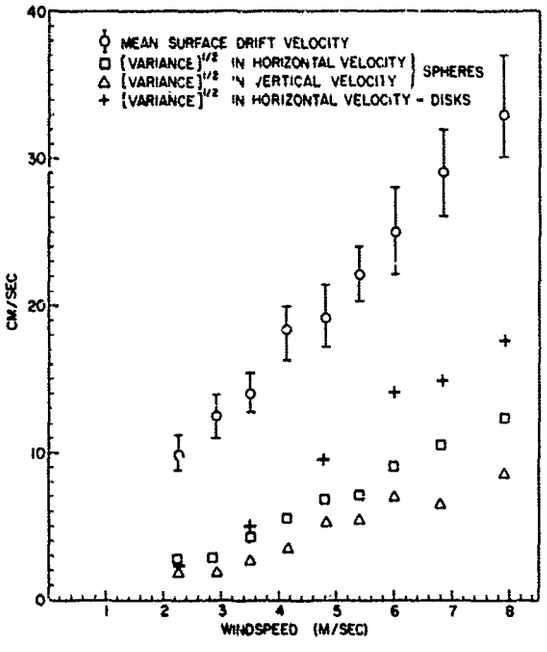

FIGURE 4 Various characteristic velocities as a function of windspeed.

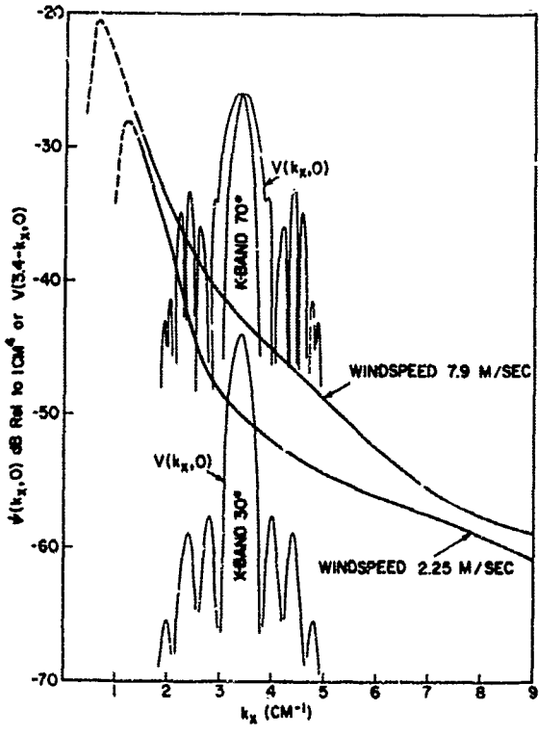

FIGURE 5 Mean square height spectra and Fourier transforms of illumination patterns.

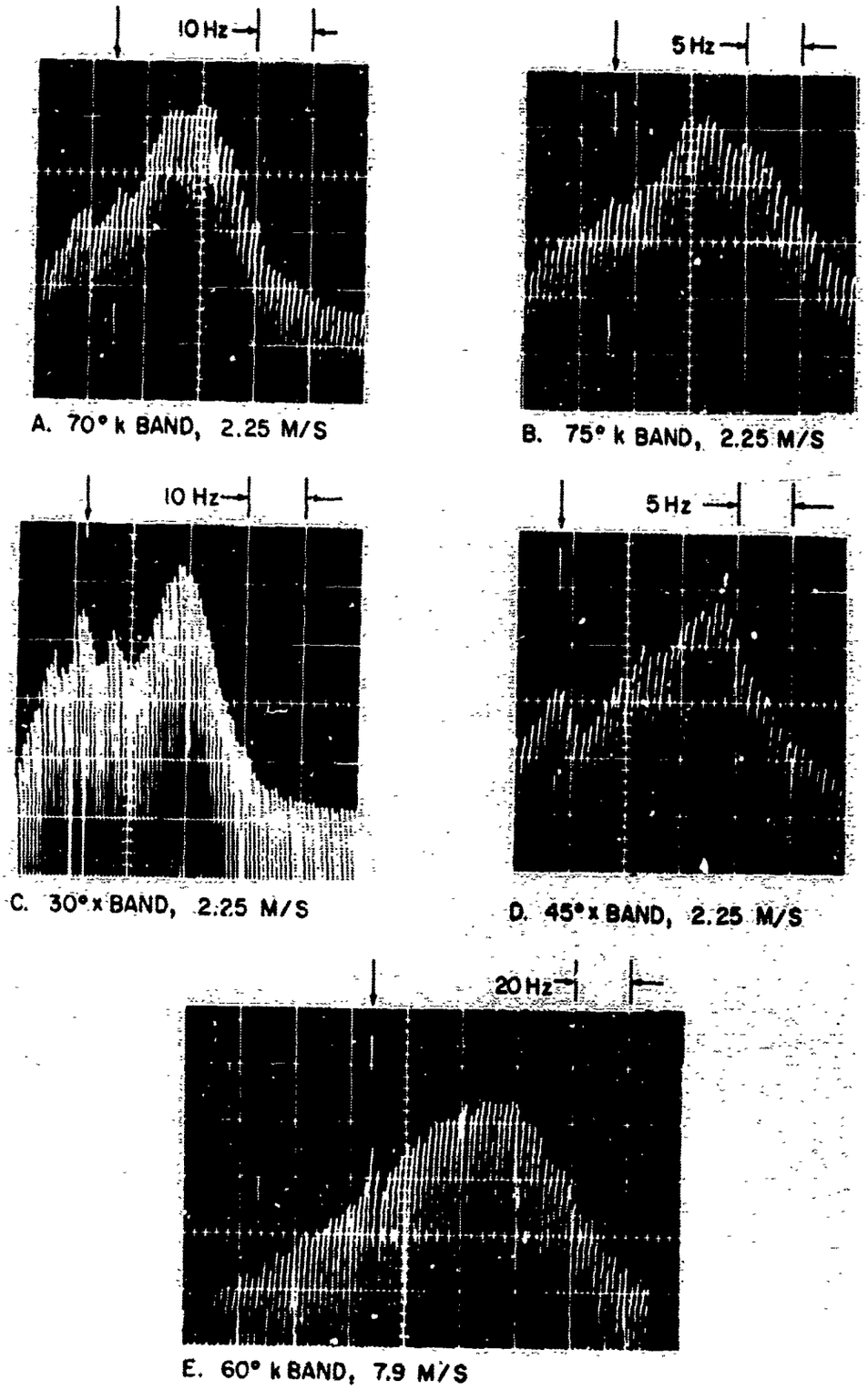

FIGURE 6 Measured doppler spectra showing the influence of the illumination pattern and other perturbing effects. The vertical scale is 10 dB/large division in each case.

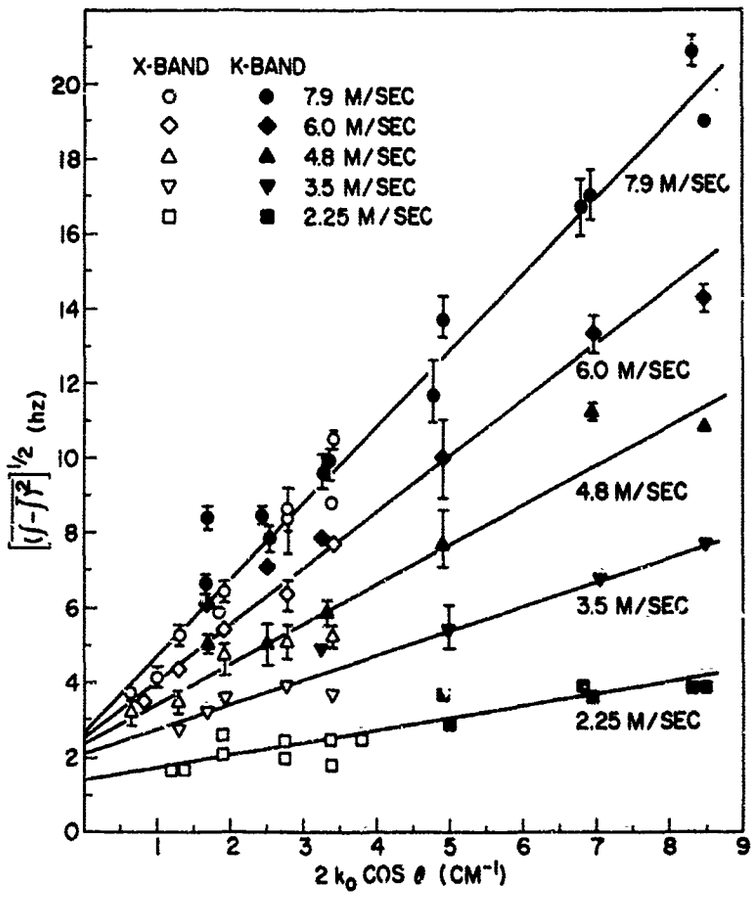

FIGURE 7 Doppler bandwidths as a function of Bragg wavenumber for various windspeeds.

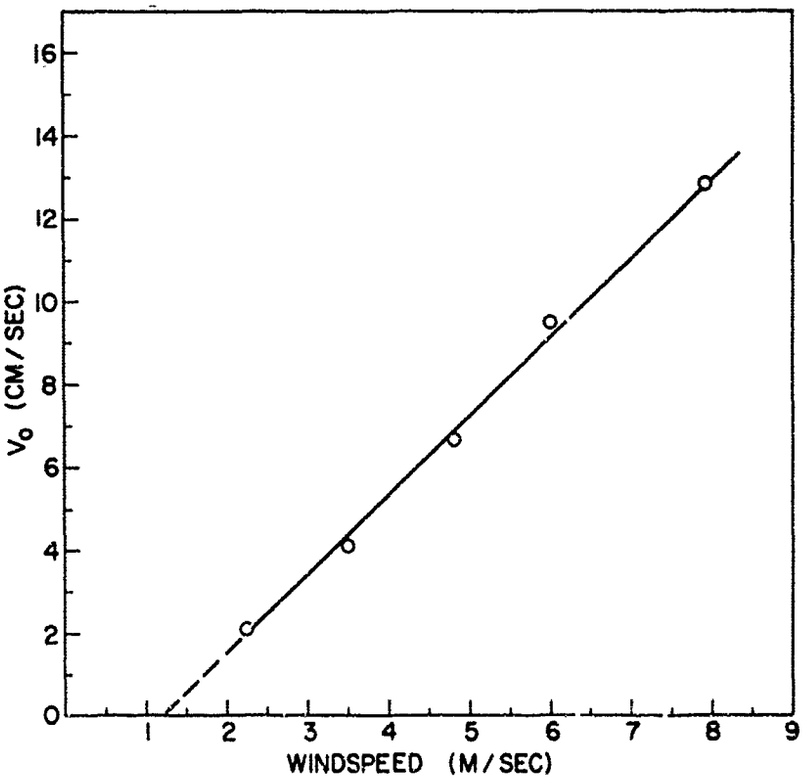

FIGURE 8 Doppler velocity, V_o, as a function of windspeed.

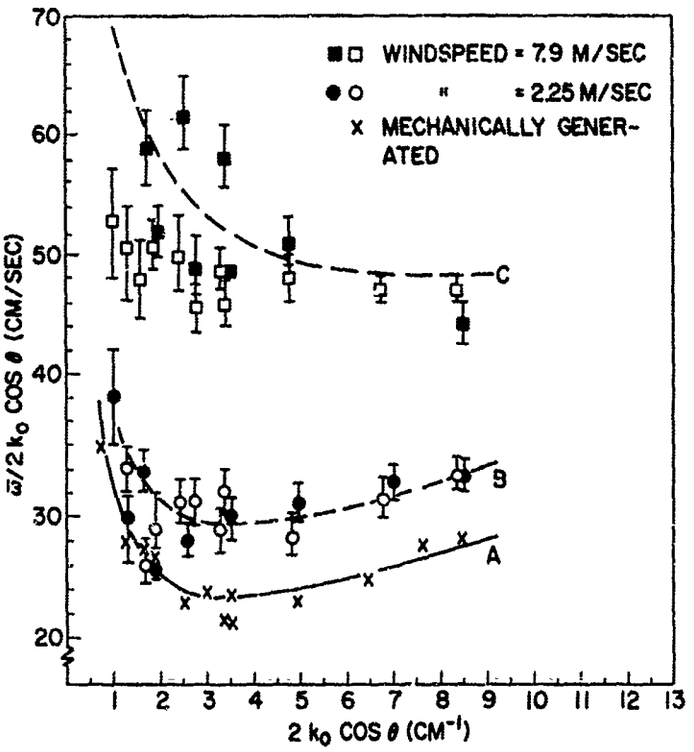

FIGURE 9 Calculated phase velocity vs Bragg wavenumber for wind generated and mechanically generated water waves.

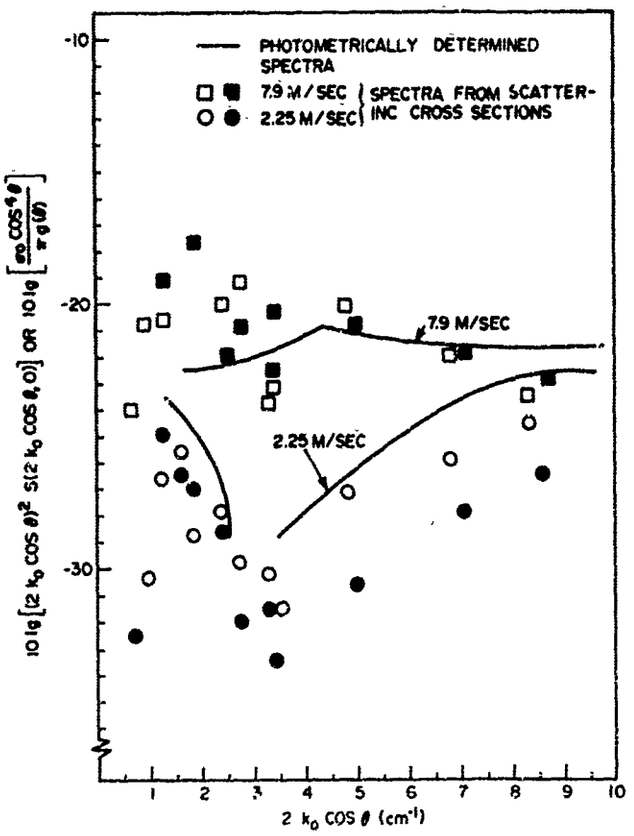

FIGURE 10 Comparison of water wave spectra determined photometrically with spectra determined from scattering measurements.

WORLDWIDE OCEANIC WIND AND WAVE FORECASTS USING A SATELLITE RADAR-RIOMETER

by

Richard K. MOORE
Professor of Electrical Engineering
Director, Remote Sensing Laboratory
The University of Kansas
Lawrence, Kansas, U.S.A.

and

Willard J. Pierson
Professor of Oceanography
Department of Meteorology
& Oceanography
New York University
New York, New York, U.S.A.

SOMMAIRE

L'accroissement de la rétrodiffusion radar qui accompagne les augmentations de vitesse des vents et d'amplitude des vagues constitue un fait connu depuis de nombreuses années. Ce n'est que recemment, toutefois, que les théories ont commencé à apporter des explications satisfaisantes de la diffusion due a la mer.

En outre, les mesures par instruments aéroportés, de la diffusion due aux vitesses de vents élevees sont récentes. L'augmentation du coefficient de diffusion à des longueurs d'ondes centimétriques, avec des vitesses de vents allant jusqu'à 50 noeuds, semble indiquer que l'on peut avoir recours a la mesure du coefficient de diffusion pour déterminer la vitesse du vent. Si l'on peut effectuer ces mesures à partir d'un satellite, on pourra établir la structure globale des vents soufflant à la surface des océans et prédire ainsi les houles des océans du monde entier. L'atténuation des ondes centimétriques peut être compensée par la mesure de la température effective vue par l'antenne radar.

Une théorie quantitative des images radar de l'océan fut d'abord proposée au début des années 50. Cette théorie a été récemment améliorée grâce à la méthode des perturbations, suggérée a l'origine par Rice, et à la méthode de Kirchoff, que Davies fut le premier à utiliser pour la solution de ce problème.

On peut attribuer la plupart des divergences observées autrefois entre la théorie et l'expérience à l'emploi de descriptions de la surface, choisies davantage parce qu'elles se prêtaient a un traitement mathématique que pour leur exactitude.

Malheureusement, il n'existe pas encore de descriptions adéquates de la surface des océans pour les vitesses de vent élevées et les phénomènes à petite échelle, particulièrement importants pour les radars à ondes centimétriques. Toutefois, l'emploi, dans les deux cas de la théorie, d'approximations du spectre de surface des océans a permis d'améliorer, récemment, la description théorique des images océaniques reçues par l'écran radar. L'auteur examine certaines de ces nouvelles methodes et la comparaison établie entre celles-ci et les résultats expérimentaux.

C'est seulement au cours de ces deux dernières années que l'on a procédé à des mesures des images de l'océan reçues par radar dans le cas de vents soufflant à des vitesses supérieures a 30 noeuds environ (si l'on excepte quelques mesures antérieures effectuées au voisinage du littoral ou à partir de bateaux sous un très faible angle d'incidence. Des mesures récemment effectuées par le laboratoire de Recherche de la Marine des Etats-Unis et par la NASA ont fourni des informations sur la diffusion, pour des fréquences allant de 0,4 GHz à 13,3 GHz, au dessus de surfaces marines où les vents variaient de moins de 10 noeuds à environ 50 noeuds.

Pour une fréquence de 0,4 GHz, la forme de courbe du coefficient de diffusion varie peu avec la vitesse du vent. Les observations effectuées à la fois par le laboratoire de Recherche Naval pour 9 GHz et par la NASA pour 13,3 GHz révèlent que la diffusion augmente avec la vitesse du vent pour des angles de quelques dizaines de degrés avec la verticale : par contre, les observations relatives a la frequence de 13,3 GHz indiquent un effet de vent supérieur à celles effectuées pour 9 ..... bien qu'il soit possible de rendre la technique expérimentale utilisée en partie responsable de cette difference, celle-ci semble être réelle et montre que l'on devrait, pour mesurer les vents de surface, utiliser des radars à fréquences supérieures à la bande X.

On a proposé un système de mesure des vents à partir de satellite ; ce système permettrait de déterminer les vents sur toute la surface marine du globe, à des intervalles suffisamment fréquents pour etablir des prévisions du temps et de l'état des mers à l'intention des marins, pêcheurs et autres usagers de l'océan.

Pour obtenir des résultats optimaux, il faudrait qu'un tel système dépende de mesures absolues, de puissance et utilise des radars capables d'effectuer un bon balayage latéral de la trajectoire du satellite de façon à ce que l'on puisse observer une vaste portion d'océan à chaque passage de ce satellite.

L'emploi d'un récepteur Doppler semblable au radiomètre de Dicke utilisé par les radio-astronomes permettra à un système de ce genre de fonctionner avec une précision satisfaisante, même avec des rapports signal/bruit, approchant de l'unité. Un rapport signal/bruit aussi peu élevé permettra d'utiliser des émetteurs de puissance relativement faible, même à des fréquences supérieures à 10 GHz.

L'utilisation de ces hautes fréquences implique que le signal radar subira une atténuation en traversant d'épais nuages ou de pluie. De récentes mesures effectuées à l'aide des radiomètres à micro-ondes ont montré que l'on peut utiliser la température effective mesurée par le radiomètre (en grande partie déterminée par les radiations émises à partir de la région d'atténuation) pour etablir l'atténuation dans l'atmosphère.

L'association d'un radar et d'un radiomètre serait donc plus efficace pour étudier les vents marins qu'un radar seul.

Les données tant théoriques qu'expérimentales obtenues au cours de ces deux dernières années indiquent qu'un concept tel que celui décrit plus haut sera certainement valable pour la mesure des vents si l'on peut établir l'image reçue par l'écran radar sous deux angles d'incidence pour chaque point situé sous le satellite. Un tel système ne pourrait pas couvrir une aussi vaste portion d'océan pour chaque passage du satellite, et donnerait, pour les vitesses de vent observées, un quadrillage moins serré qu'un système faisant appel à des mesures absolues du coefficient de diffusion. La théorie semble indiquer que la technique des mesures absolues peut-être satisfaisante, mais il faut procéder a un complément d'expériences. (Il se peut que l'on dispose des résultats de ces expériences à la date de la réunion).

WORLDWIDE OCEANIC WIND AND WAVE FORECASTS USING A SATELLITE RADAR-RADIOMETER

Richard K. Moore
Professor of Electrical Engineering
Director, Remote Sensing Laboratory
The University of Kansas
Lawrence, Kansas, USA

and

Willard J. Pierson
Professor of Oceanography
Department of Meterology & Oceanography
New York University
New York, New York, USA

SUMMARY

The relationship between radar return from the sea at 2.25 cm wavelength and the speed of the wind disturbing the sea offers an opportunity for a satellite system to provide information for a global wave forecasting system. Results of measurements over seas with surface winds of 12.5 knots to 49 knots presented here indicate that the radar return at angles of incidence in the 25°-40° range increases rapidly with windspeed up to about 25 knots and less rapidly at higher speeds. Comparison of the observations with computations based on application of physical optics to a new composite model of the ocean wave spectrum indicates at least qualitative agreement.

The brightness temperature measured by a microwave radiometer looking at the sea is also proportional to wind speed, but the effect of atmospheric attenuation is much greater on brightness calibration for the radar scatterometer is suggested. A proposed instrument uses a scanning antenna and a common receiver for the radar and radiometer.

An example of the benefits to be gained by using the more plentiful satellite observations of wind speed is presented for the South Atlantic. Because of the sensitivity of both the radar return and the wave spectrum to wind direction, other information, such as that gained from satellite cloud photographs, must be used to perform the forecasts, and the radar data cannot be used alone.

INTRODUCTION

Forecasts of ocean wave spectra permit optimum routing of ships to allow greater speed and prevent storm damage. These forecasts, and meteorological forecasts, depend on knowledge of the surface wind field over the oceans. The relationship between radar backscattering and the winds permits global wind monitoring from a satellite, provided proper wavelengths are chosen and cloud attenuation is small. Combining a microwave radiometer with the radar scatterometer allows use of the greater sensitivity of the radiometer to cloud attenuation for removing most of the effect of attenuation of the backscatter signal.

Forecasting ocean wave spectra requires knowledge of the wind field over a large area and long time. Waves can propagate to long distances, and the effect local winds remains long after the winds have ceased. Numerical forecasting depends upon iterative solution of the appropriate equations over a period of about a week prior to the forecast time. Updating at about 6 hour intervals permits continuous extension of the forecast. A 120 km point spacing is used for forecasting, since a finer grid would require too much computer storage and time. This widely spaced grid permits use of a satellite instrument with resolution of 10s of km, which makes design simpler for the instrument.

Radar observations of backscatter from the sea have been made for nearly 30 years, but recent measurements from aircraft flying to stormy areas in the North Atlantic have permitted significant improvement in the available information. The data presented here were obtained by aircraft of the U. S. National Aeronautics and Space Administration (NASA) in March of 1968 and 1969. We had hoped to present data from flights in February of 1970, but data reduction is not yet complete. The 1968 data were only at 13.3 GHz (2.25 cm) with vertical polarization, and the 1969 data are from the same system plus a multipolarization 0.4 GHz (75 cm) system. The experimental results at 13.3 GHz are compared with theoretical computations based on a new composite wave spectrum.

A scanning radar-radiometer is proposed as an operational system for space. The radar will operate in an ICW mode, permitting use of low signal-to-noise ratio and radiometer-like calibration. Although both systems may use the same receiver, the radar bandwidth is smaller, as optimum S/N occurs when radar bandwidth is equal Doppler bandwidth of the signal.

A sample integration of satellite data into a forecast is presented to illustrate the major advantages of the satellite system.

RADAR BACKSCATTER OBSERVATIONS

Most previous measurements of radar backscatter were (1) near grazing incidence, or (2) near coastlines, or (3) without adequate information on the ocean conditions. Apparently the NASA measurements and U. S. Naval Research Laboratory (NRL) measurements within the last two years are the first to overcome these restrictions. The NRL measurements are reported elsewhere.[1] Here we report primarily on the NASA measurements.

Various observers have indicated some sort of "saturation" in the increase of radar return with windspeed, and Wright[2] has predicted this saturation on the basis of a perturbation theory for radar scatter and the Phillips expression for the "high-frequency tail" of the ocean wave spectrum. Apparently the validity of Wright's approach depends on the wavelength of the radar, for the measurements reported here show no saturation for 2.25 cm radar up to about 50 knots windspeed, whereas saturation does occur in our 75 cm measurements. NRL's 3.3 cm measurements show much smaller variation with windspeed than found at 2.25 cm.

THE RADAR SCATTEROMETER

The radar scatterometer used for the measurements reported here has a fan beam directed along the flight path of the aircraft, as shown in Slide 1. Returns from different angles within this beam are separated by filtering the appropriate Doppler frequencies. Isodops for horizontal flight are hyperbolas as shown on the slide, so a filter of width Δf_d can separate all returns between θ_1 and θ_2.[3]

Slide 2 shows a block diagram of the simple CW-Doppler radar system used. A klystron transmitter also provides a local oscillator signal, so the receiver is a homodyne. The Doppler frequencies received are amplified in an audio amplifier, and the results recorded on magnetic tape. On the ground the tape may be spectrum-analyzed either in analog or digital fashion. Two channels are used in quadrature to provide the phase information required to separate positive and negative Doppler frequencies. A calibration signal

was inserted with a ferrite modulator driven by an audio frequency outside the Doppler frequency band. Since the output of this calibrator is proportional to the transmitted signal, and since it passes through the same receiver/recorder channel as the received signal, it can provide an accurate calibration. Unfortunately, the ferrite modulator is somewhat temperature sensitive and subject to remanent-magnetism errors, so an uncertainty of about ±3 dB occurs in the absolute level of the signal. A calibrate source using PIN diodes and modulation at a different level was used in the 1970 flights, so the absolute calibration should be better for these data when they become available.

13.3 GHz SACTTEROMETER DATA

Because of the potential errors in absolute level, the data were normalized by presenting the ratio of differential scattering coefficient at any incident angle to that at 10°. Slide 3 shows a representative group of observations normalized in this fashion. Clearly the 49 knot upwind return is much higher than the crosswind return for the same wind speed, as would be expected. Comparable results were also found at lower wind speeds down to the 12.5 knot level, where little difference can be seen.

Slide 4 shows a more extensive set of observations for the upwind condition. The increase in normalized radar return with windspeed is evident, although some other effect must also be present to cause the difference between the 12.5 and 13 knot curves. Repeatability between the two years was amazingly good in the 20-30 knot range, where most data were available. Other curves are not shown here because they are so like the ones shown and would make the graph hard to interpret.

Recently an error was found in the antenna pattern used in the data reduction, so some changes in shape of the curves will result when the reprocessed data are available. Nevertheless, the separation between curves for different wind speeds will remain exactly the same. For data presented in this way the only change that would affect the relative postions of the curves would be a drift in the amplitude-vs-frequency characteristic of the audio amplifier, and this is certainly a very stable characteristic--as shown by the remarkable agreement between data taken a year apart.

For windspeed measurement, the observations should be plotted vs windspeed at a fixed angle. Slide 5 shows this. Although the variation at 15° is not significant, variation with windspeed at both 25° and 35° is quite strong. For the upwind case, the scattering at 35° varies as $v^{2.85}$ below 25.5 knots as as $v^{2.15}$ above 25.5 knots (v is windspeed). For the cross wind case, the scattering at 35° varies only linearly with v above 25.5 knots. With measurements of sufficient accuracy, this should permit windspeed determination over this range of speeds, provided the direction is known from other information.

0.4 GHz SCATTEROMETER DATA

The 0.4 GHz scatterometer also uses the fan-beam Doppler technique, but uses a superheterodyne rather than a homodyne receiver. Absolute accuracy should be better with this system than at 13.3 GHz. Slide 6 shows the vertically polarized observations with this system, compared with similar observation by NRL. All wind speeds give nearly the same results, although both the NASA and the NRL data show a slight tendency for the signal to be lower at 49 knots than at 12 knots. Slide 7 shows the horizontally polarized observations, and the same conclusions can be drawn. Because of this lack of sensitivity to wind speed, this frequency is not likely to be useful for wing measurement.

THEORY AND EXPERIMENT

Various theories have been used to describe the radar backscatter from the ocean. Geometric optics, of facet theories have been used in the past. Wright[2], Fung[4], and a group of Russian authors[5] have used perturbation techniques. Others have used physical optics, based on the Kirchhoff approximation that the field on the surface is the same as it would be for an infinite plane tangent to the surface at that point. Perturbation techniques alone give amazingly good results when considered in light of the breakdown of the approximation involved for any surface-height variation of the order of $\lambda/2\Pi$, but we do not believe the first-order perturbation can possibly give a true description of scatter from the open ocean. On the other hand, the fact that this method works at all indicates that the phenomenon causing return from the ocean must be strongly influenced by the very smallest waves, and that Bragg scatter from these small waves is significant.

The key point in any theory is the surface description used. The theoretical results presented here are based on application of physical optics to a new wave-spectrum model. The elements of this model are given in Slide 8. Region 1 is the now-standard Pierson-Moskowitz model, which gives a good description of large-scale structure on the fully-developed sea. In the high frequency limit this model, like that due to Phillips, is assymptotic to k^{-3}. Region 2 is associated with dynamic equilibrium between wind and waves. In this region the spectrum is proportional to wind speed v and to $k^{-2.5}$. The transition between Regions 1 and 2 is at a frequency (or k) that must be determined somewhat arbitrarily on the basis of experiment; the appropriate parameter is γ. Region 3 involves capillary (surface tension) waves, which are much smaller than the gravity waves of Region 1. In this region, however, the shape of the spectrum is the same as that for the high-frequency gravity waves, but the amplitude is about 8 times as great. The 4th region is the viscosity range, and is unimportant to this discussion.

Apparently the significant size of structures on the ocean for a radar of 2.25 cm wavelength are those associated with Regions 2 and 3, depending somewhat on the wind speed. Certainly these sizes are the same order of magnitude as those required for Bragg scattering of such radar frequencies. Chia[6] originally applied the Pierson-Moskowitz spectrum and physical optics to the long-crested case; he obtained results (assuming unit reflection coefficient) much like those shown in Slide 9. With this spectrum there is little effect of wind speed on the backscattering. Chia also applied a spectrum like that of Region 2 and showed considerable variation with windspeed, but his curves were the wrong shape. Now we have applied the entire spectrum of Regions 1, 2, and 3, obtaining the results shown in Slide 10. Although this was a crude attempt (unity reflection coefficient and long-crested waves), it clearly is in general accord with the experimental observations previously shown.

The comparison between this theory and experiment is illustrated in Slide 11. Because of uncertainties in absolute levels, the data have been normalized so that all points coincide for 25 knots. With this approach, the crude theory seems to fit the crosswind data quite well. The increase with windspeed for the upwind data is more rapid than the theory indicates. Since γ was selected somewhat arbitrarily for this set of theoretical curves, the agreement is surprisingly good. Work is now in progress to extend the calculations for short-crested waves and for the reflection coefficients appropriate to the cases of vertical and horizontal polarization.

THE MICROWAVE RADIOMETER

Several investigators have recently shown that a microwave radiometer, although highly sensitive to cloud attenuation, is also sensitive to winds at sea. This result is not surprising, since the microwave radiometer obtains much of its signal by scatter from the surface of the ocean. Fung and Ulaby[7] have recently developed a theory thst explains the observations near vertical incidence much better than the earlier theory of Stogryn[8]. The principal difference between the theories is that Stogryn used a Gaussian autocorrelation function of surface heights in the physical optics computation of scatter, whereas Fung and Ulaby used an exponential. Slide 12 shows the comparison of the two theories with some observations by Nordberg of NASA/Goddard Space Flight Center.

Because of the sensitivity of the radiometer to the atmosphere, the system proposed here uses it to calibrate the scatterometer, even though it could be used for windspeed measurement in its own right if the atmosphere were absent. A relatively small increase in attenuation causes a quite large increase in radiometer brightness temperature. Wilson (Slide 13) has shown how this can be used to calculate the atmospheric attenuation causing the increase in brightness, using an upward-looking radiometer. For attenuations below about 8 dB, this method appears quite attractive.

SPACECRAFT SYSTEM

A spacecraft wind-measuring system should cover as much ocean surface as possible in each orbit; accordingly a side-to-side scan seems appropriate. Because of the uncertainties in the absolute calibration of the NASA data a system that uses only one angle is still conjectural, but a system that measures the scattering cross-section at two angles seems guaranteed of success.

Slide 14 shows a system permitting measurements at two angles. The spacecraft radiates at 10° and 35° incident angles, using either a fan beam or two pencil beams. The time of travel between the two positions shown for the spacecraft is only a few minutes or less, so the ocean conditions remain statistically the same. Hence the spacecraft measures the scatter at 10° in its second position for the same ocean area from which the 35° measurement was made at its first position. By correlating these measurements, the wind speed at the surface may be determined, but only along the sub-satellite track.

If further measurements show, as we expect, that data are required from only a single angle to establish the wind speed, a scan like that in Slide 15 can be used. In this scan, the antenna uses a pencil beam that moves from side-to-side of the spacecraft in a plane tilted somewhat ahead of the nadir. With this method the angle of incidence can be kept within the region of maximum variability with sea state. A scan for a 1000 km orbit can readily be 1200 km long, thus providing 11 points at 120 km intervals for the forecasting computer.

Slide 16 shows a sample set of incident angles for 1000 km height of the satellite. Ordinarily the scan would be kept within about 600 km of the ground track; so that, for a 25° tilt of the antenna, the incident angle remains within the 30-40° range.

RADIO-RADIOMETER SYSTEM

The radar scatterometer using a narrow beam antenna like that shown in Slide 15 can be operated in a nearly-CW mode. Because of the difficulty with isolation, the signal is transmitted only until the first return signal appears, and then is turned off during the receiving period. This near-CW operation permits use of a narrow-band receiver, since the harmonics of the long-pulse fundamental rate are insignificant compared with the Doppler frequency spread. Thus, the band width of the receiver is determined by the Doppler spread, which is of the order of kiloHertz for practical cases.

Slide 17 illustrates how the post-detection signal-to-noise ratio can be made high with low predetection S/N by operating the scatterometer much like a radiometer/radio-telescope receiver.[9] Integrating a large enough number of independent samples of signal + noise and a like (or greater) number of noise samples reduces the variance of each so that very small differences can be measured reliably. The equation on the slide shows the signal-to-noise ratio improvement possible with this system. The number of independent samples r is approximately twice the time-bandwidth product of the receiver. With this method signal-to-noise ratio of unity or less at the input may be used successfully in a space system, and the result is a peak power requirement of the order of 10-50 watts, with average power of 2-10 watts.

The radar and radiometer systems may share time or may operate at slightly different frequencies within the capabilities of the antenna and pre-amplifiers. A simplified version of the block diagram of such a system is shown in Slide 18. An actual system would probably use more switches to provide the calibration signal for the radiometer, and would contain a provision to pass an attenuated version of the transmitter output through the receiver to calibrate the scatterometer. The Dicke switch in the radiometer alternately connects the radiometer receiver to the hot load (at accurately known temperature) and the antenna, with calibration by switching to a cold load at less frequent intervals. The scatterometer needs no such switch, since its noise calibration is provided by simply recording the output during a time when no scattered signal is present. The <u>noise</u> for the scatterometer is the <u>signal + noise</u> for the radiometer.

APPLICATION TO FORECASTING

The output of a side-to-side scanning system like that proposed will average about 2,500 pairs of σ° and T_b per orbit, if only data over ocean are counted. Forecasts are normally made on a 6-hour repetition period, and present data used for the purpose consist of ship reports radioed into meteorological centers at either 6 or 12 hour intervals and cloud information from weather satellites. Enough ship reports to permit adequate forecasts are present only in heavy shipping lanes such as those from North America to Europe. Even in these areas the forecasts often fail because insufficient information is available on storms moving in from regions having little shipping. Hence, this input of over 30,000 data points per day can have a major impact on forecasting weather and waves.[10]

Since the data must be combined with wind direction information to provide accurate reports of surface wind speeds, the operational system will need a combination of updating past weather reports and forecasts on an iterative basis with use of the available ship reports and of cloud photographs from satellites.

Another problem that must be overcome is the use of non-synoptic data. Forecasting presently is based on measurements made by all ships and coastal stations at the same time. The satellite, on the other hand, provides coverage in a continuous strip. The NIMBUS satellite always collects data at <u>local</u> noon or or midnight.

Computer programs to solve both the non-synopticity problem and the wind direction problem are presently being developed at New York University.

An example of the kind of analysis that might result from use of such a system is illustrated with Slide 19 and Slide 20. In Slide 19 a portion of an actual surface analysis for the South Atlantic area is shown. The dots indicate locations of reporting ships and shore weather stations, and the remainder of the analysis is based on combining these data with satellite cloud photographs. Note the high in the upper left and the two lows. Slide 20 shows a hypothetical set of observations from a satellite pass across this region, with the resulting modification to the pressure patterns shown. These changes in size and intensity of the main features of the pattern are quite reasonable to expect with the improved data coverage to be obtained using the satellite.

CONCLUSIONS

The use of a combined radiometer-scatterometer in a satellite to provide surface wind information on a global scale over the oceans has been shown feasible, based on observations of radar sea return at 2.25 cm and of the success of use of radiometers to estimate attenuation through clouds. Reasonably good agreement has been shown between backscatter observations at sea and predictions of a simplified theory based on a long-crested (one-dimensional) 4-part wave spectrum applied to a perfectly-reflecting physical optics formulation of the radar scatter problem.

Additional measurements are under way with a Doppler radar scatterometer operated by NASA Manned Spacecraft Center, and observations of frequency dependence of the ocean backscatter are planned with a radar-radiometer to be used by NASA/Langley Research Center. A radar-radiometer will probably be tested in space in 1972 on the Skylab to be flown by NASA.

This work was supported by the U.S. Naval Oceanographic Office under contract N62306-67-C-0044 and by NASA/MSC under contract NAS9-10261 with The University of Kansas and by the U.S. Naval Oceanographic Office under contract N62306-70-A-0075 with New York University.

REFERENCES

1. Guinard, N. W. and J. C. Daley, "An Experimental Study of a Sea Clutter Model," Proc. IEEE, vol. 58, pp. 543-550, April, 1970.
2. Wright, J. W., "A New Model for Sea Clutter," Transactions of the IEEE, vol. AP-16, pp. 217-223, 1968.
3. Moore, R. K., "Ground Echo," Chapter 25 in Skolnik, M., Radar Handbook, McGraw-Hill Book Company, Inc., New York, pp. 25-20, 25-21, 1970.
4. Fung, A. K. and H. L. Chan, "Backscattering of Waves by Composite Rough Surfaces," Transactions of the IEEE, vol. AP-17, pp. 590-597, 1969.
5. Bass, F. G., I. M. Fuks, A. I. Kalmykov, I. E. Ostrovsky, and A. D. Rosenberg, "Very High Frequency Radiowave Scattering by a Disturbed Sea Surface," Transactions of the IEEE, vol. AP-16, pp. 554-568, 1968.
6. Chia, R. C., "The Theory of Radar Scatter from the Ocean," Ph.D. Dissertation, The University of Kansas, 1968. Also published as Technical Report 112-1, CRES, University of Kansas, October, 1968.
7. Ulaby, F. T. and A. K. Fung, "Effects of Roughness on Emissivity of Natural Surfaces in the Microwave Region," 1970 Southwest IEEE Conference (SWIEEECO), CRES Reprint 133-8.
8. Stogryn, A., "The Apparent Temperature of the Sea at Microwave Frequencies," IRE Transactions Antennas and Propagation, vol. Ap-15, pp. 278-286, March, 1967.
9. Moore, R. K. and F. T. Ulaby, "The Radar Radiometer," Proceedings of the IEEE, vol. 57, pp. 587-590, 1969.
10. Pierson, W. J., L. J. Tick, and L. Baer, "Computer Based Procedures for Preparing Global Wave Forecasts and Wind Field Analyses Capable of using Wave Data Obtained by a Spacecraft," Sixth Symposium Naval Hydrodynamics, ONR Department of the Navy, ACR-136, 1966.

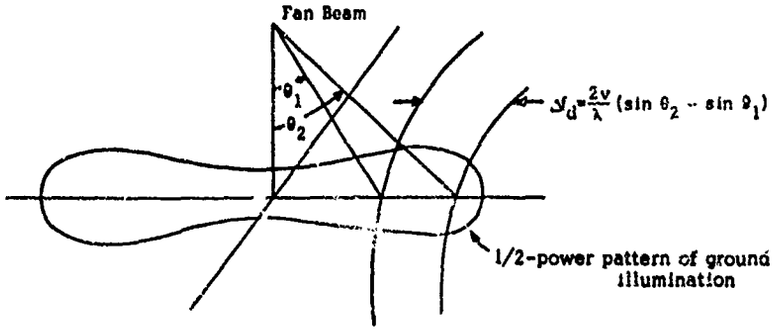

Fig.1 Operation of a fan-beam CW-Doppler scatterometer

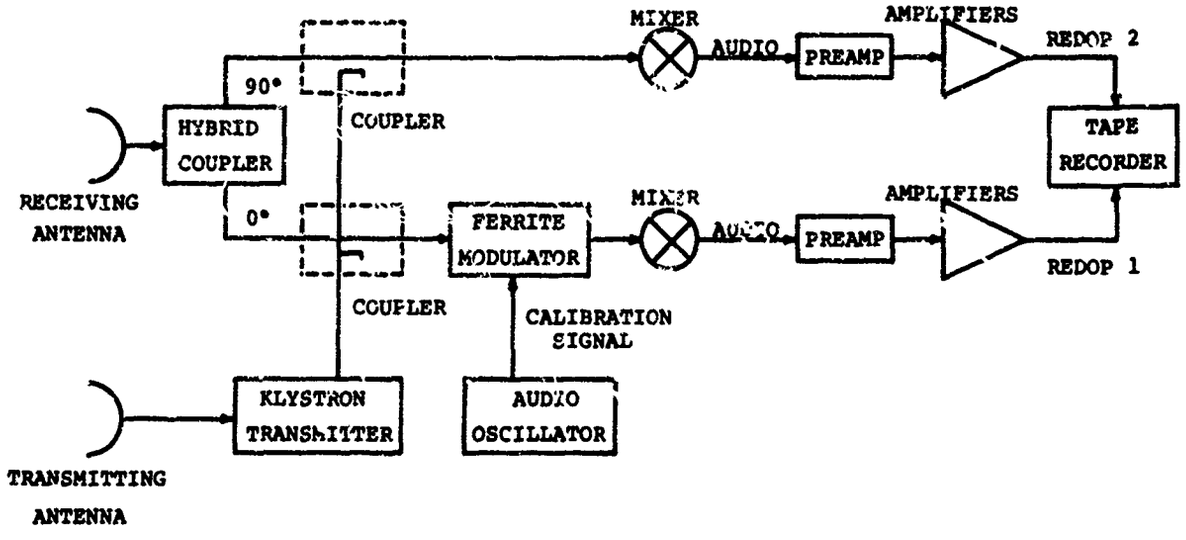

Fig.2 13.3 GHz radar scatterometer block diagram

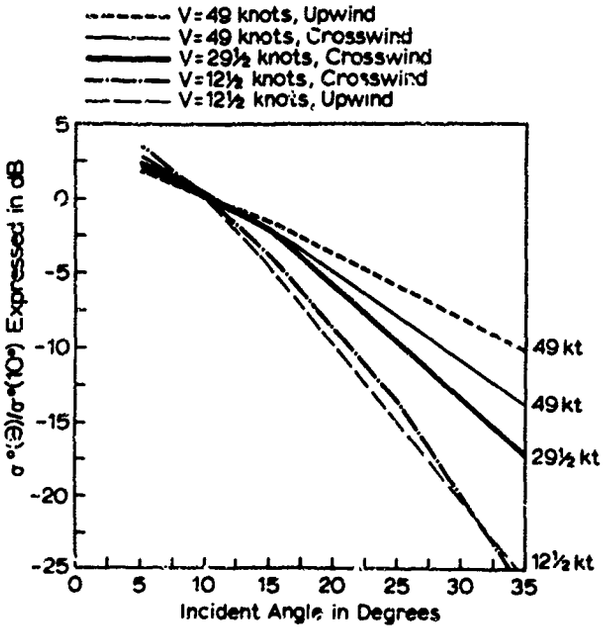

Fig.3 Comparison of crosswind and upwind normalized scattering coefficients at 2.25 cm wavelength, (March 1969 data)

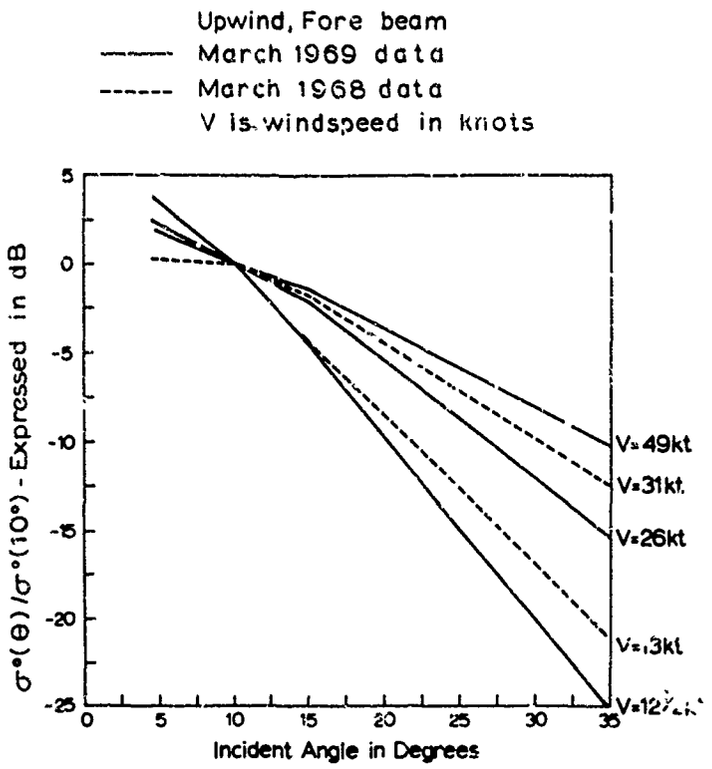

Fig.4 Differential scattering coefficient of ocean at 2.25 cm wavelength normalized to Odb at 10^0

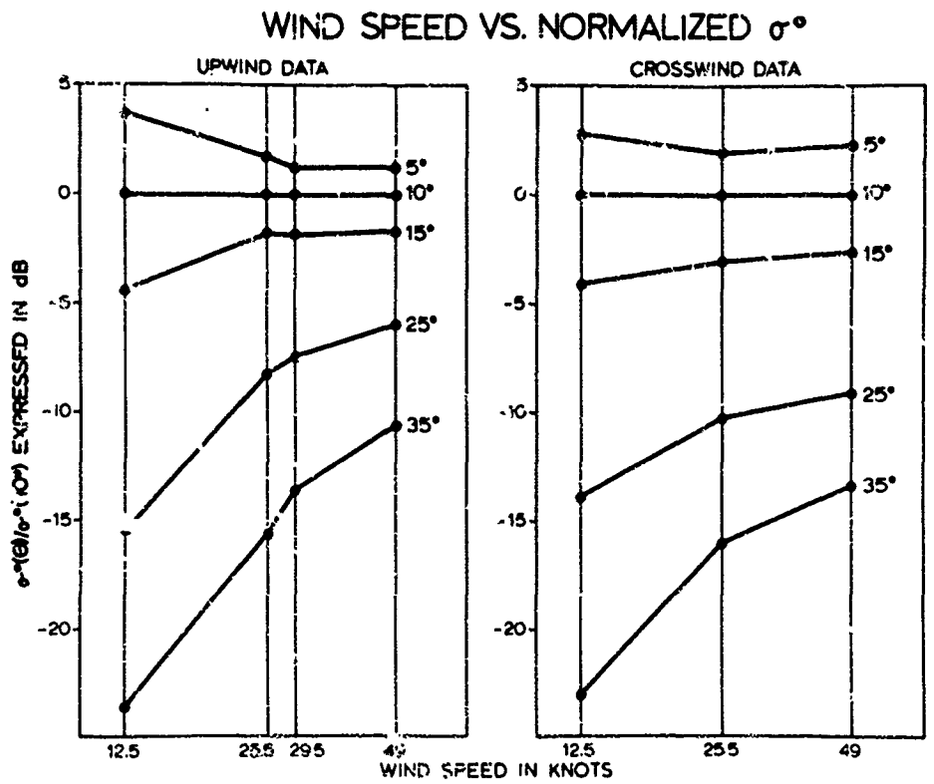

Fig.5 Normalized radar scattering coefficient vs. wind speed and direction at 13.3 GHz. (2.25 cm wavelength)

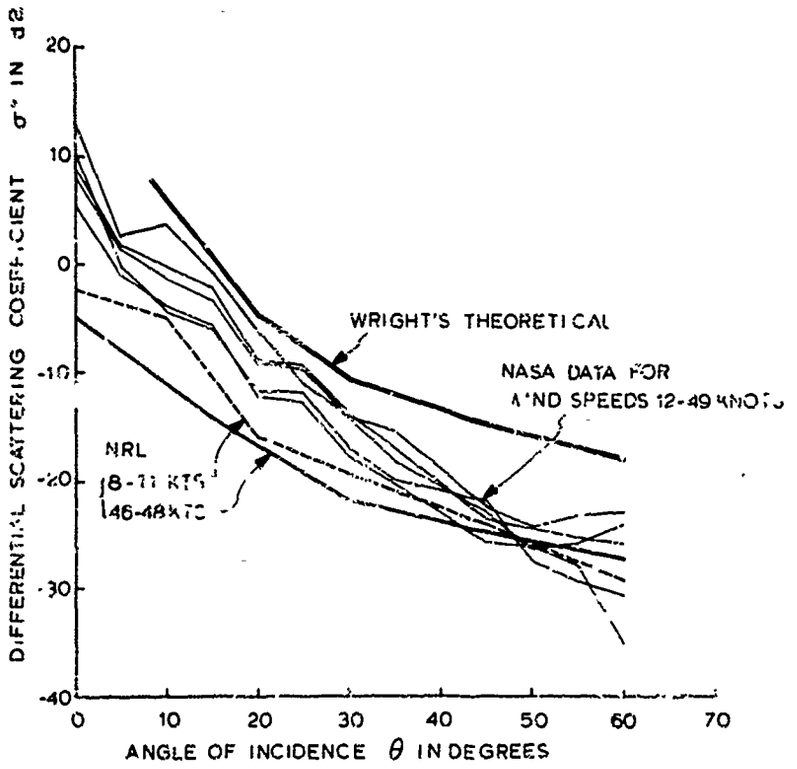

Fig.6 Vertically-polarized 400 MHz radar back-scatter from the ocean

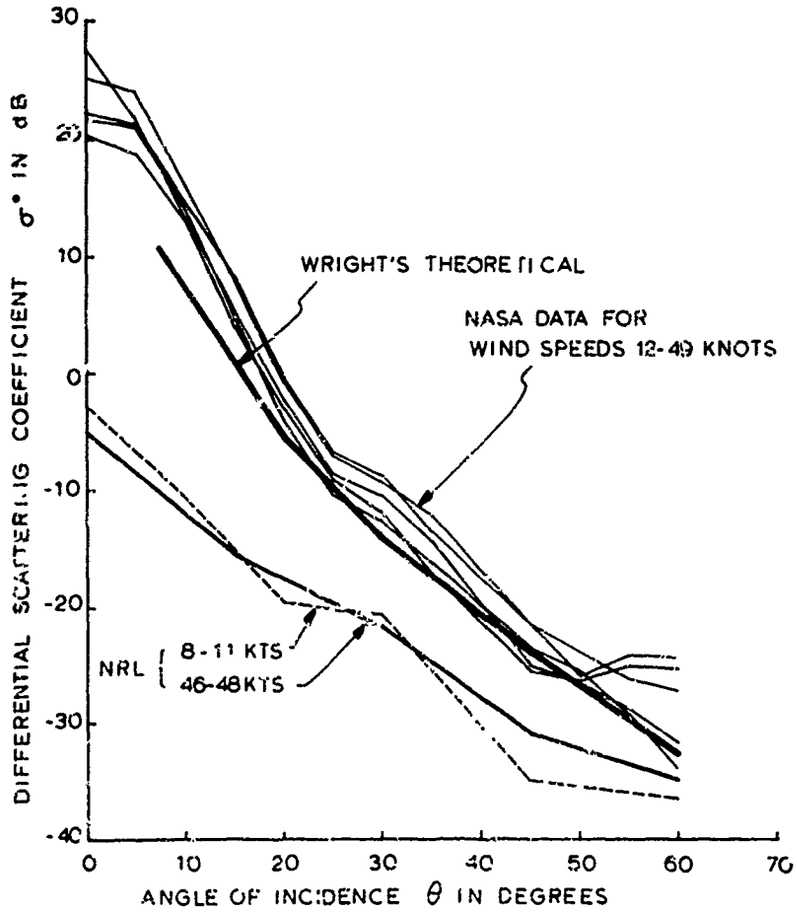

Fig.7 Horizontally-polarized 400 MHz radar back-scatter from the ocean

REGION 1 - SMALL K - PIERSON-MOSKOWITZ FORM ASYMPTOTIC TO AK^{-3}

REGION 2 - INTERMEDIATE K - DYNAMIC EQUILIBRIUM RANGE ASYMPTOTIC TO $BVK^{-2.5}$

TRANSITION REGION 2 - REGION 2 AT $\omega = \frac{\gamma g}{V}$

V = WIND VELOCITY

g = GRAVITATIONAL ACCELERATION

γ = PARAMETER TO BE SELECTED

REGION 3 - CAPILLARY WAVES SPECTRUM $8AK^{-3}$

REGION 4 - VISCOSITY RANGE (MILLIMETER WAVELENGTHS)

Fig.8 Composite wave spectrum

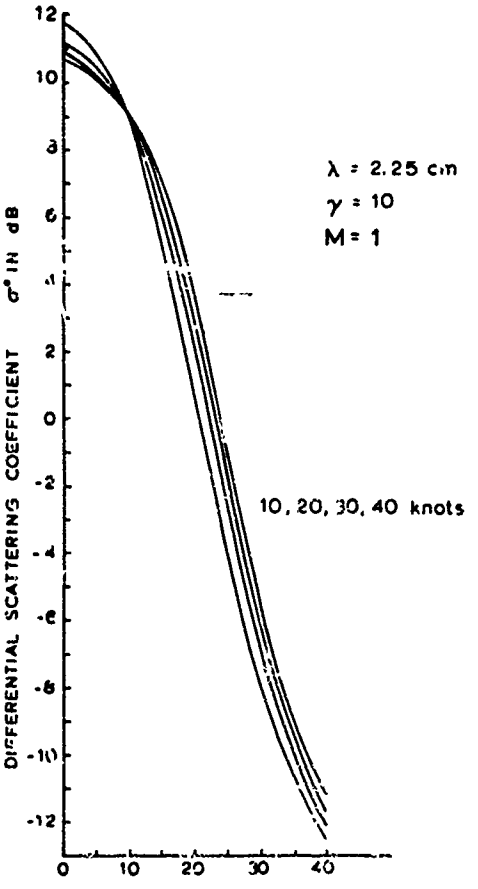

Fig.9 Angle of incidence θ in degrees
Differential scattering coefficient from physical optics (Kirchhoff approximation) Pierson-Moskowitz spectrum (asymptotic to Phillips theory) (long crested waves)

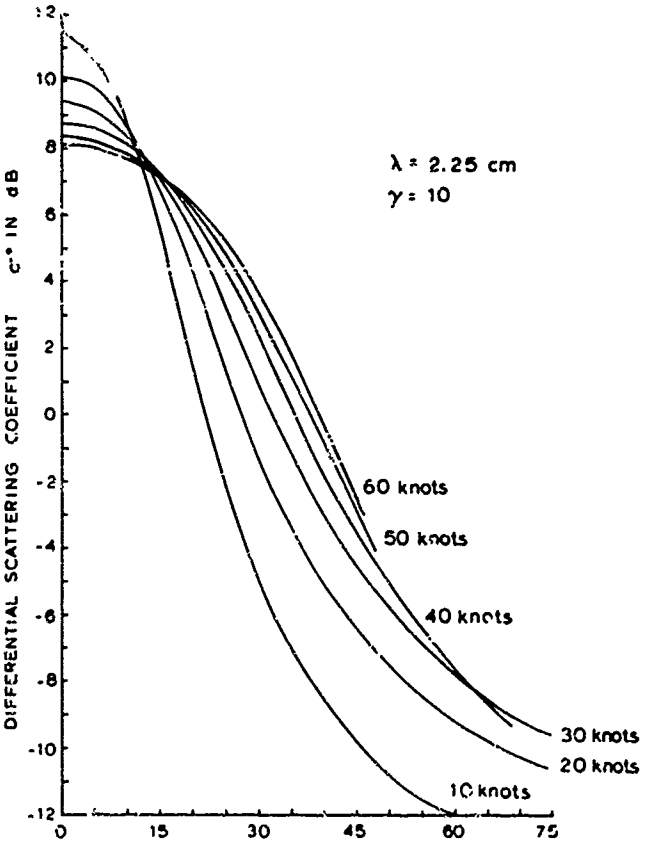

Fig.10 Angle of incidence θ in degrees
Differential scattering coefficient from physical optics (Kirchhoff approximation) composite spectrum (long crested waves)

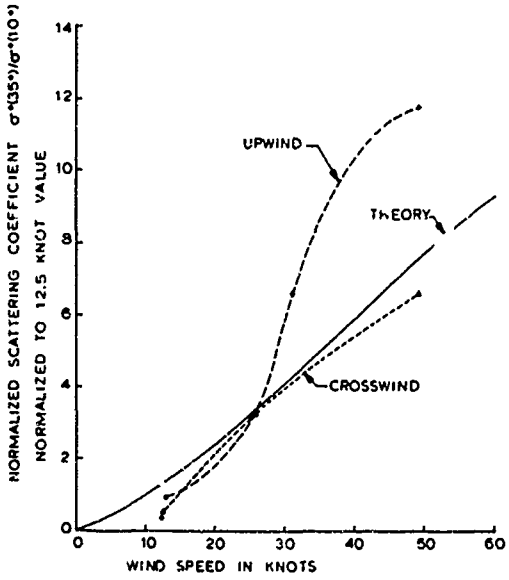

Fig. 11 Comparison of composite-spectrum theory with NASA experimental data. Absolute levels adjusted for coincidence at 25 knots

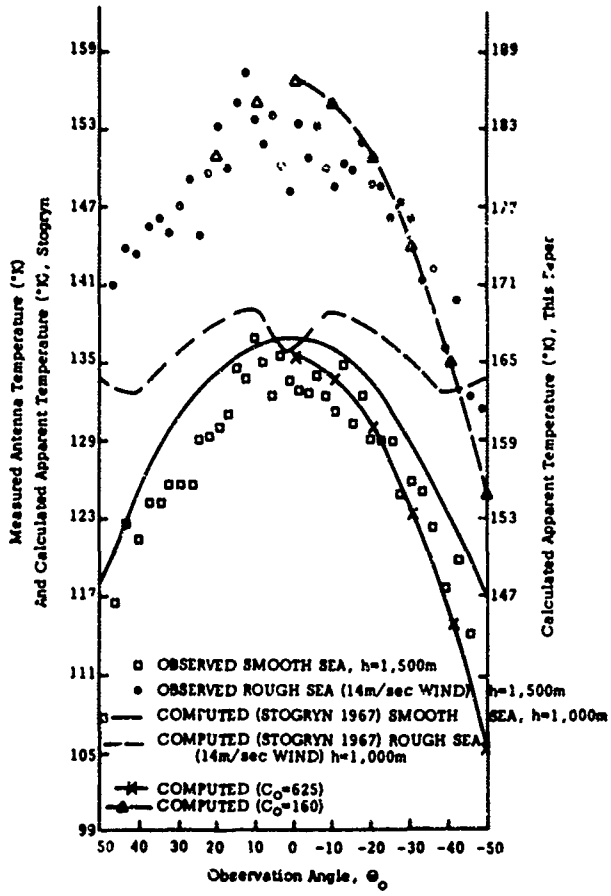

Fig. 12 Measured and calculated horizontally polarized apparent temperature of the ocean at 19.4 GHz. (From Fung and Ulaby, 1970)

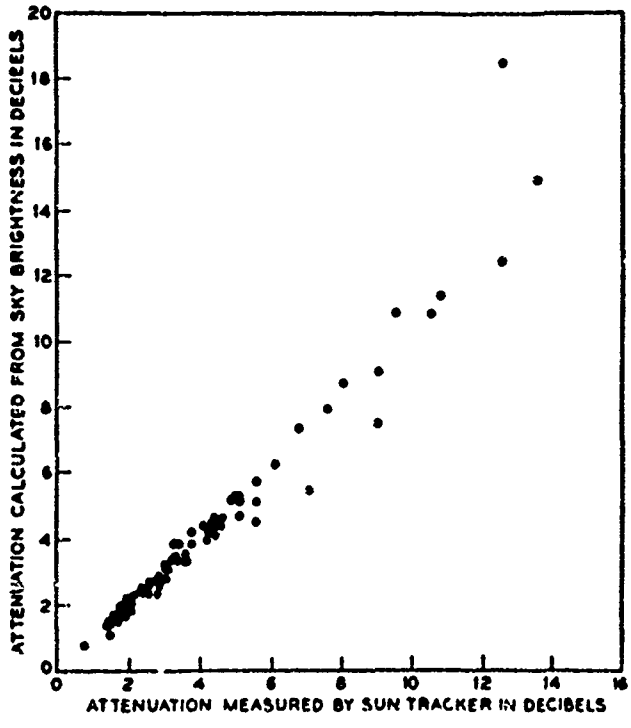

Fig. 13 Comparison of measured attenuation with values calculated from upward-looking microwave radiometer (16 GHz) (from Wilson, 1969)

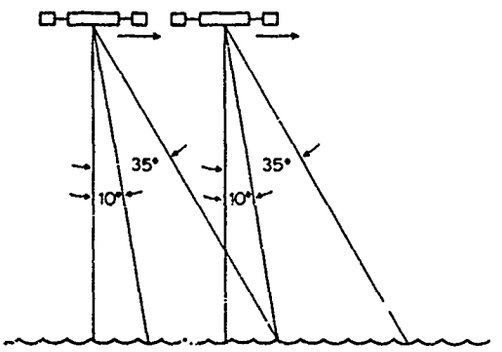

Fig. 14 Satellite mounted scatterometer for sea-state measurements

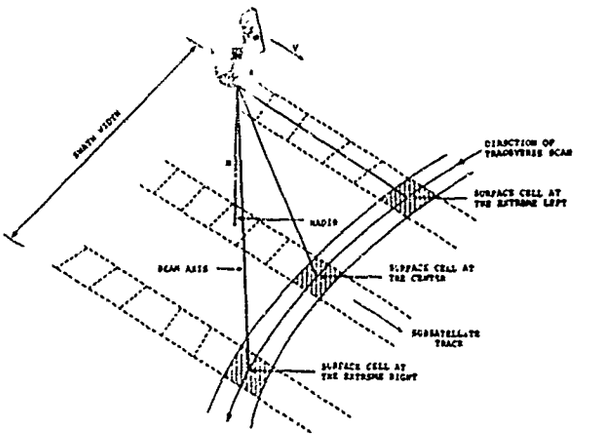

Fig. 15 Scan for an operational radiometer-scatterometer for sea-state measurement

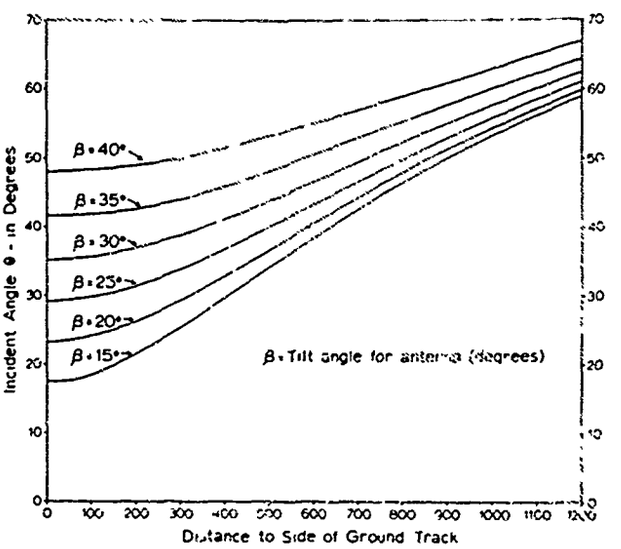

Fig. 16 Incident angle at the earth for a wave from a scanning antenna on a 1000 km altitude satellite

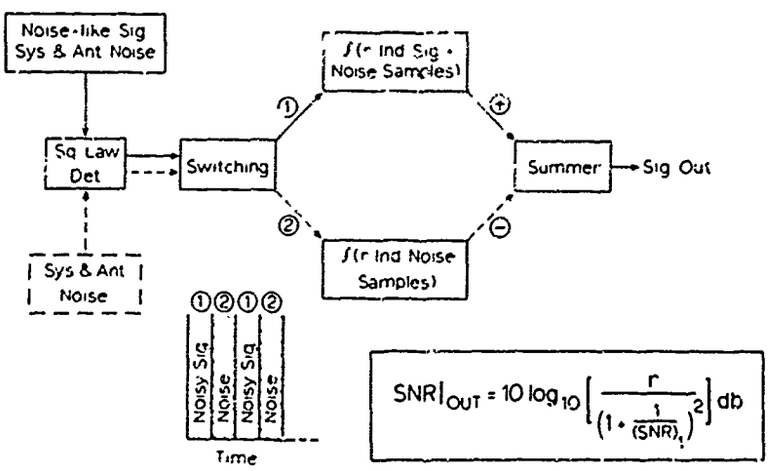

Fig. 17 S/N enhancement scheme for noise-like signals

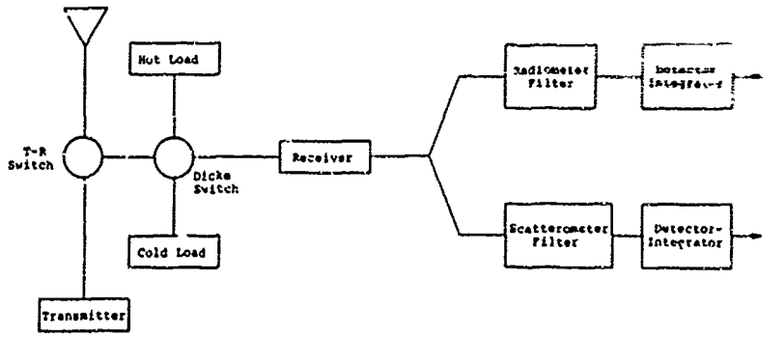

Fig. 18 Elements of a radiometer-scatterometer

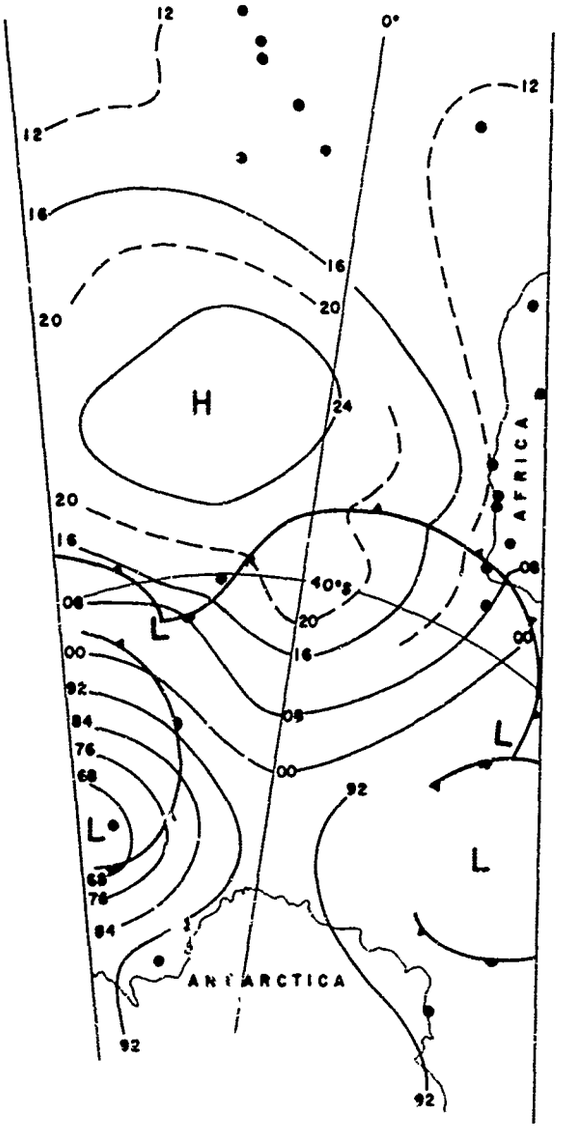

Fig. 19 Portion of the national meteorological center southern hemisphere surface analysis for January 18, 1968. The dots represent points where surface reports were available for the analysis. The analysis is based on these surface points, the southern hemisphere cloud mosaic patterns prepared by ESSA, and continuity considerations

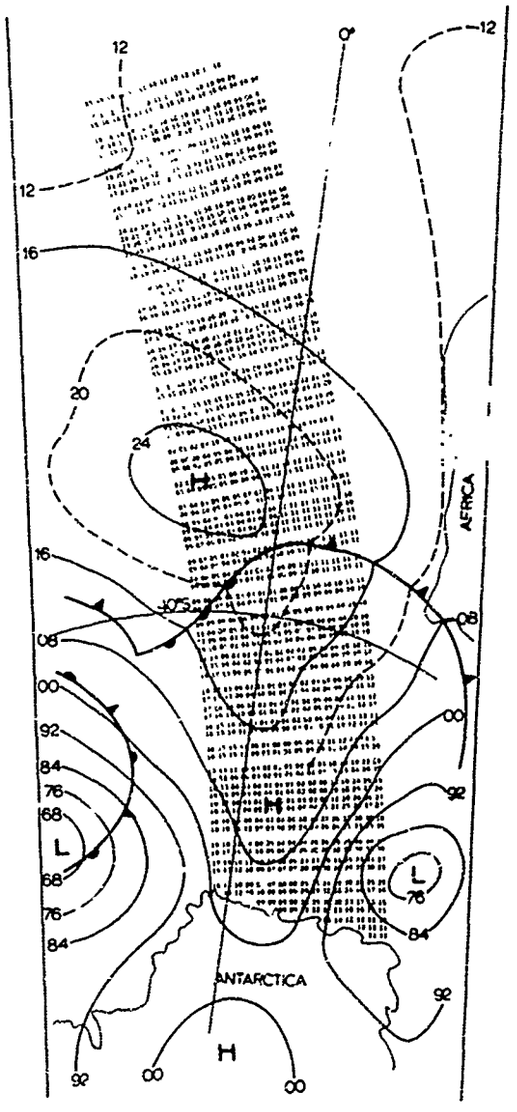

Fig. 20 Hypothetical data that might be obtained from one portion of one pass of a NIMBUS spacecraft with a scatterometer and dual antenna system. The numbers represent the wind speed in knots on a grid that approximates the actual coverage

SEA ECHO AT LASER WAVELENGTHS OF 1.06 MICRONS AND 10.6. MICRONS

by

A.V. Jelalian

and

R.G. Mc Manus

Raytheon Company
Sudbury, Massachusetts, U.S.A.

SEA ECHO AT LASER WAVELENGTHS OF 1.06 MICRONS AND 10.6 MICRONS

A. V. Jelalian
and
R. G. McManus
RAYTHEON COMPANY
Sudbury, Massachusetts, U.S.A.

ABSTRACT

This paper will discuss the results of two laser flight test programs conducted over the ocean for the purpose of determining system operation for (1) a vertically oriented 1.06 micron laser altimeter; and (2) a 10.6 micron optical Doppler radar at a variety of depression angles. The experimental data for a variety of sea states for the vertically oriented altimeter system established that the return signal was definitely range square dependent and that the effective target cross sections (σ^o) were 0.15 and 0.24 for smooth and rough surface water conditions, respectively. The 10.6 micron optical Doppler radar system established that, for a six inch spot size on the ocean surface: (1) the probability of achieving returns decreased as the depression angle decreased, and (2) as the sea state increased the corresponding probability of return increased.

1. INTRODUCTION.

In order to optimize electro-optical system performance over the ocean surface, one must consider the effect of the sea surface upon the backscattered signal. Through the years, significant study and experimentation have been performed at the microwave wavelengths[1-5] to determine the effective radar cross-section per unit area (σ^o). Additional evaluation of sea surface reflection at optical wavelengths has utilized the sun as a transmitting source to obtain optical reflection properties and sea surface slope distributions of the ocean[6-11]. More recently, evaluation of ocean scattering properties has been performed utilizing lasers as transmitting sources[12-13]. This paper will discuss the results obtained from two such flight test programs, one utilizing a 1.06 micron pulsed YAG solid state laser and the other utilizing a 10.6 micron CW carbon dioxide gaseous laser.

2. OCEAN SCATTERING.

The backscatter signal strength of an electromagnetic wave incident upon the ocean surface is related to the transmitted wavelength, polarization, depression angle, wind direction and the state of the sea surface. Environmental effects result in the ocean surface being composed of regular and irregular waves, small ripples, spray and other irregularities. Correspondingly the value of the ocean target cross-section fluctuates as the sea surface changes and the number and size of the scatterers within an illuminated region varies.

An appreciation of the ocean scatterer may be obtained by noting the ocean interaction effects upon signal backscatter. If one neglected environmental effects, one could envision the ocean surface as a flat specular reflector and, as such, the laser beam divergence would be the same before and after reflection. As wind and tidal effects occur, the sea surface is perturbed and becomes a more complicated scatterer. One might consider this complex scatterer to be composed of a distribution of flat facets oriented at different angles on the sea surface. Evaluation of measured ocean wave records have resulted in approximate Gaussian probability functions indicating ocean surface slopes having three sigma limits less than ±0.3 radians[14]. The orientation of these inclined facets[11,15] could contribute to diffusing or broadening of the scattering steradian volume of the sea surface. However, in order for this diffusing effect to occur, several such facets must be illuminated. The summation of the scattering signal from all illuminated scatterers would then constitute the amount of energy collected by the receiving system. For most laser systems, the spot size at the ocean surface typically is quite small with respect to ocean wave dimensions and, subsequently, the specularity or diffusivity of the ocean scatterer has a direct bearing upon the extent of signal drop-out conditions at the receiver.

3. SCATTERING CROSS SECTION CONSIDERATIONS.

The general equation for the received signal power P_R is:

$$P_R = \frac{P_T G_T \sigma A_{EFF} L}{(4\pi)^2 R^4} \tag{1}$$

where: P_T = Peak transmitter power (watts)

G_T = Directional gain of transmitter compared to an isotropic source $\approx (4\pi/\theta_T^2)$

R = System range

A_{EFF} = The effective capture area of the receiver

L = System transmission efficiency

θ_T = Transmitted beamwidth

The scattering cross section (σ) is defined to be 4π times the ratio of the power per unit solid angle scattered back toward the transmitter to the power per unit area in the wave incident upon the target and may be expressed as:

$$\sigma = 4\pi \frac{\rho(\gamma)}{\Omega} \sin(\gamma)\, da \tag{2}$$

where: $\rho(\gamma)$ = Reflection coefficient

γ = Grazing angle measured from the horizontal

Ω = Effective solid angle (of return)

da = Target area

The target cross section per unit area (σ^o) for a vertical path is defined as:

$$\sigma^o = \frac{\sigma}{da} \tag{3}$$

For a vertical path this reduces to:

$$\sigma^o = \frac{4\pi\, \rho(90^o)}{\Omega} \tag{4}$$

Substituting equations (3) and (4) in equation (1), the received signal power, at normal incidence for an extended target may be expressed as:

$$P_R = \frac{P_T \times \sigma^o \times A_{EFF} \times L}{4\pi R^2} \tag{5}$$

Knowing the refractive index of ocean water[16], one may calculate the reflection coefficient utilizing the Fresnel reflection formula to be 0.021 for vertical incidence.

The remaining function Ω in equation (4) remains to be defined. It is this function in the radar equation that is effected by the angular orientation of the inclined facets and the size and number of such scatterers within the transmitter beamwidth. Should the ocean appear highly specular, the scattering steradian volume would be small. Correspondingly, if the scatterer is diffuse, the scattering steradian volume would be large. In practice, most surfaces will have different degrees of specularity and diffusivity and, therefore, one must be concerned with a relatively broad classification of surface scatterers. If the reflected signal is scattered equally over a spherical volume, the surface may be termed an isotropic scatterer. Correspondingly, if the target causes the total reflected signal to be compressed into a smaller steradian

volume, then the radiation versus angle becomes peaked in some directions and diminished in others, compared to the referenced isotropic surface. This peaking effect may be expressed as a directional gain. The reflectivity of the surface would then determine the amount of energy reflected from the surface, whereas the directional gain expression indicates the intensity of the returned radiation as a function of angle.

In the radar field, the scattering steradian volume (Ω) is referenced to that of an isotropic scatterer (has equal radiation over a 4π steradian volume). One then refers to a directional gain over isotropic (Gi) as:

$$Gi = \frac{4\pi}{\Omega} \tag{6}$$

Typically, diffuse-type targets (sand, MgO), which appear as Lambertian scatterers (π steradians), have a directional gain over isotropic (4π steradian) of four. For a specular target where the beam divergence remains nearly the same before and after reflection, the directional gain over isotropic is very large.

Utilizing the Rayleigh surface smoothness criterion[1] (i.e., a surface may be considered smooth if $h \sin \Psi = \lambda/8$, where h is a measure of the peak-to-trough irregularity height, Ψ is the grazing angle, and λ is the wavelength), we may readily observe that as the transmission wavelength becomes shorter and shorter the surface smoothness requirements become more difficult to obtain. To the extent that this criterion is not met over the illuminated area, the backscattered radiation becomes diffused.

4. LABORATORY REFLECTIVITY MEASUREMENTS.

In order to illustrate the effect of specular- and diffuse-type target returns, a laboratory experiment was performed and the results may be observed in Figure 1. The experiment consisted of utilizing a helium-neon gas laser operating at 6328 angstroms which was amplitude modulated at a 1000-Hz rate by a mechanical chopping wheel. The resulting signal was transmitted to a mirror surface and the received signal was then collected by a photomultiplier and observed through an electronic filter on an oscilloscope. Figure 1A demonstrates this result. Figure 1B is the same system except that the mirror reflector was replaced by a container of water. The very narrow 5/16 inch spot size of the laser on the water surface allowed an investigation of the water surface on a "laboratory scale". By setting the water in sufficient motion to get a "rolling wave" one may observe in Figure 1C that the return signal suffered alternate conditions of signal return and signal drop-out for the specular water surface.

Figure 1D illustrates the effect of random turbulence on this rolling wave and one may observe here that the signal level begins to increase in amplitude in the previously noted regions of signal drop-out.

Having obtained an indication of the effect of specular and diffuse-type target returns, the 1.06 micron flight test system was prepared.

5. ALTIMETER FLIGHT TEST SYSTEM.

The altimeter flight test system consisted of a neodymium-doped, yttrium-aluminum-garnet (YAG) laser having the following system parameters:

(a) TRANSMITTER:	Max peak power	1 megawatt
	Pulse duration	20 nanoseconds
	PRF	0.3 pulses/second
	*Beam divergence	6 milliradians
	Wavelength	1.06 microns
	Pumping source	xenon flashlamp
	"Q" switch	Pockels cell
	Photodiode	EG+G Model SD-100
	Polarization	Vertical

*In order to allow the flight test altimeter system beamwidth to encompass a relatively large ocean area (and, thereby, minimize signal drop-outs) the transmitter divergence was deliberately broadened by removing the collimating optics.

(b) RECEIVER:

Optical Band Pass Filter	20Å filter
Photomultiplier	RCA 7102
Collecting optics	3 inch, f/2.5 objective
Polarization	unpolarized

5.1. Calibration Tests.

In order to monitor the transmitted power, an SD-100 photodiode, which normally views the rear mirror of the laser cavity and yields an output voltage which is utilized to trigger a type "A" scope display, was calibrated. By utilizing a calibrated light detector to actually measure the output laser energy, a calibration curve of transmitter power versus the SD-100 diode trigger voltage was attained. Periodic monitoring of the trigger voltage during the flight test allowed an indication of transmitter power to be obtained.

Additional calibration tests were performed on the laser system in order to:

(a) Calibrate transmitter and receiver responses using a known reflective surface.

(b) Determine the dynamic and linear range limitation of the equipment

(c) Perform range measurements against fixed targets.

(d) Assure operational functioning during the actual flight test.

5.2. Flight Test Results.

Subsequent to the calibration tests the equipment was installed in the Raytheon-owned B-26 aircraft.

Figure 2 is a picture of the coast and geodetic map of the flight test area, and one may observe from the lines drawn on this chart as to how a typical flight test was run. The numbered lines correspond to flight test runs 1-11 and 15-21 of the second flight test experiment. Basically, measurements were made over Plum Island Sound, the Atlantic Ocean, the Merrimac River, sand dunes and wooded areas. We were able on two flight tests to obtain pilot estimates of sea states varying from International one to three[16] and to obtain calm water estimates varying from "millpond smooth" to ripple surfaces.

During the flight tests aircraft height was determined by both an APN/22 microwave altimeter and the 1.06μ laser altimeter, transmitter power was monitored by the calibrated SD-100 diode, the receiving optics were masked by the aircraft mounting fixture to a 5 cm square, resulting in a collection optics area of 2.5×10^{-3} square meters, and the atmospheric and system losses were estimated to be 3db. As a result of the instrumentation and calibration of the receiving system the only remaining unknown in equation (5) was the effective target cross-section (σ^o).

Figure 3 is a composite plot of all of the averages (μ) of the flight test data for the various ocean situations. The diagonal lines indicate the least square curve fit to the data. The triangles in this figure illustrate the results of the first flight test. Data obtained during the second flight test are noted by X's. Above each of the data marks is the International sea state for that particular average.

The transmitter power was measured to be 150 kW and was noticed to vary slightly during the flight tests. However, we were able to maintain close correlation between the first and second flight tests. This may be noted by the following data points where the triangle at 3000 feet (915 meters) gave a return of approximately 6 1/2 mV at International sea state one. The two measurements performed at 3000 feet (915 meters) during the second flight test over sea states two and three (International) straddled that point.

Analysis of the flight test results indicated that the return signal was definitely range square dependent as expected and that the target cross-section per unit area (σ^o) was 0.24 for calm water and 0.15 for sea states one to three International.

Figure 4 shows the standard deviation (σ_1) about the mean for the ocean return over the various sea states. If the measured signal voltages were due to specular-type

targets, resulting in intermittent signal strength, the value of the standard deviation about the mean would be large. Correspondingly (as the laboratory experiments indicated) as the ocean becomes more turbulent, the signal intensity becomes more constant and, therefore, smaller values of standard deviation should be noted. Here the standard deviations may be noted to be within a factor of 2 of the mean and, therefore, significant variation was not concluded to exist.

Figure 5 shows the ocean return over calm water. Again the standard deviations about the mean were slight and not indicative of specular return or signal drop-outs.

To provide a means of understanding the scattering function, the beach sand of Plum Island was assumed to be a diffuse-type target. By comparing the ocean returns against the return of the beach sand, we were able to obtain a further indication as to whether the target was diffuse or specular; and, here one may see that the standard deviations about the mean for the beach sand returns were approximately the same as those obtained for the ocean returns (Reference Figure 6).

6. 10.6 MICRON DOPPLER RADAR FLIGHT TEST RESULTS.

In order to assess the capability of an optical Doppler radar system, a flight test program was conducted over land and water surfaces. Evaluation of some of the test data obtained over the ocean surface near the New England coast line, Figure 7, yielded the signal drop-out rate for a variety of depression angles and sea states. Basically the 10.6 micron optical Doppler system had the following system parameters:

(a)	TRANSMITTER:	Wavelength	10.6 microns
		Output power	10 watts
		Beam divergence	0.1 milliradian
		Transmit/receive optics diameter	15 CM
		Polarization	vertical
(b)	RECEIVER:	Detector	Copper doped germanium
		Detection technique	Optical heterodyne
		Display	Spectrum analyzer
		Altitude	305 meters
		Polarization	vertical

The 10.6 micron single mode single frequency laser signal was transmitted through a coaxial, 15 centimeter, F/2 optical system. The received backscatter signal from the ocean surface was then collected by this same optical system and combined on a copper doped germanium detector with a portion of the transmitted signal. The resultant Doppler shifted signal was then processed by suitable receiver electronics and observed on a spectrum analyzer, which portrayed the returned signal intensity as a function of the Doppler frequency. The entire system was mounted in a Raytheon C-26 aircraft and flight tested over the New England coast line. At the operating altitude of 305 meters the illuminated spot size was approximately 15 centimeters due to operation within the near field of the optical system. The optical system was inclined at depression angles of 70, 75, 80 and 85 degrees and tests were performed over a variety of sea states varying from International 0 to 4. Sea state assessment was performed by an experienced flight test pilot who has had much experience with such estimates. Synchronous 16 millimeter movies were made of the spectrum analyzer display and the terrain being traversed by the laser beam to provide test information for post flight processing. The flight test data was evaluated by random sampling of the flight test film recordings for a variety of sea states and depression angles. A typical film strip was visually evaluated by determining the number of times a received signal intensity was observed as opposed to the number of total consecutive frames examined, for upwind, downwind and crosswind conditions. Evaluation of this data as a function of angle and sea state may be noted in Figure 8. These figures indicate that near vertical incidence the probability of return signals being obtained was quite high even for relatively smooth sea conditions. However, as the depression angle decreased from 85 degrees to 70 degrees, a significant reduction in the percent of return signals resulted. Further, as the sea states increased from International 0 to 4, the probability of signal reception increased dramatically. Referring to Figure 9 for a 70 degree depression angle, significant changes in the probability of achieving a return signal is definitely noted for the various sea states, and suggests that potential sea state indications might be obtained by monitoring the return signal data rate at a variety of depression angles.

7. CONCLUSIONS.

The results of the 1.06 micron laser altimeter system with a deliberately broadened beamwidth at near vertical incidence indicated that: the return signal was definitely range squared dependent; adequate controls were maintained to allow a measurement of the effective ocean target cross-section; and that a sufficient number of scatterers were included within the illuminated beamwidth to allow continuous reception of received signal. This appears consistent with flight test data obtained for the 10.6 micron Doppler laser system utilizing a highly collimated beamwidth where a high data rate at near vertical incidence was obtained. However, the 10.6 micron flight tests also indicated frequent occurrence of signal drop-out conditions, due to the inclination and limited number of scatterers located within the 15 cm transmitted beamwidth at depression angles around 70 degrees.

Combined results of both test programs suggest that at near vertical incidence signal drop-out conditions decrease with increasing system beamwidths and that as the spot size on the ocean is broadened to illuminate a homogenous area of ocean surface that signal drop-out conditions may be eliminated. Additionally, these results indicate that as the sea state conditions increase to present a more turbulent ocean surface, received signal data rate at a given depression angle and spot size increases. This would appear to be consistent with the wider angular distribution of inclined facets anticipated for more turbulent ocean conditions.

Results of these two flight test conditions strongly suggest that electro-optical system operation over water surfaces should take into account the scattering effects of the ocean surface if reliable system operation is to be achieved.

8. ACKNOWLEDGEMENTS.

The authors would like to express their appreciation to Mr. Joe Day, Optical Doppler Navigator Project Engineer for the United States Air Force, Wright Patterson Air Force Base, Ohio; Mr. Cullen Lee, Laser Altimeter Project Engineer for the National Aeronautics and Space Administration, Marshall Space Flight Center, Alabama and to the members of the Electro-Optics Laboratory, Raytheon Company, Sudbury, Mass., for their technical contribution to these two flight test programs.

REFERENCES

(1) Kerr, D. E., Propagation of Short Radio Waves, New York: McGraw-Hill, 1951.

(2) Grant, C. R., Yaplee, B. S., "Backscattering from Water and Land at Centimeter and Millimeter Wavelengths", Proc. IRE, July 1957.

(3) Wiltse, J. C., Schlesinger, S. P., "Backscattering of the Sea in the Region from 10 to 50 KMC", Proc. IRE, February 1957.

(4) Katz, I., "Radar Reflectivity of the Earth's Surface", The Johns Hopkins University Applied Physics Laboratory Technical Digest, January-February 1963.

(5) Davies, H., Macfarlane, G. G., "Radar Echoes from the Sea Surface at Centimetre Wavelengths", Proc. Phys. Soc., 1946.

(6) Gordon, J. I., "Optical Properties of Objects and Backgrounds", Applied Optics, May 1964.

(7) Fritz, S., Solar Radiant Energy and its Modification by the Earth and its Atmosphere, Baltimore, Md., Waverly Press, 1960.

(8) Duntley, S. Q., et al., "Visibility", Applied Optics, May 1964.

(9) Boileau, A. R., Gordon, J. I., "Atmospheric Properties and Reflectances of Ocean Water and Other Surfaces for a Low Sun", Applied Optics, May 1966.

(10) Duntley, S. Q., "Oceanography from Manned Satellites by Means of Visible Light", Oceanography from Space, Washington, D. C., U. S. Government Printing Office, 1965.

(11) Cox, C. and Munk, "Statistics of the Sea Surface Derived from Sun Glitter", J. Marine Research, November 1954.

(12) Jelalian, A. V., "Sea Echo at Laser Wavelengths", Proc. IEEE, May 1968.

(13) Doppler Optical Navigator Program, Technical Report, AFAL-TR-68-211, October 1968.

(14) Hill, M. N., The Sea, New York, John Wiley and Sons, 1962.

(15) Katzin, M., "On the Mechanisms of Radar Sea Clutter", Proc. IRE, January 1957.

(16) American Institute of Physics Handbook, New York, McGraw-Hill, 1957.

(17) Bowditch, "American Practical Navigator", Washington, D. C., U. S. Government Printing Office, 1958.

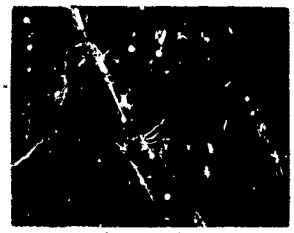

MIRROR TARGET

0.05 V/cm
1 ms/cm
0.275 V

Figure 1A

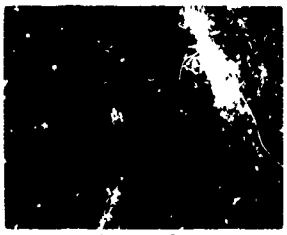

WATER RETURN

0.005 V/cm
1 ms/cm
0.005 V

Figure 1B

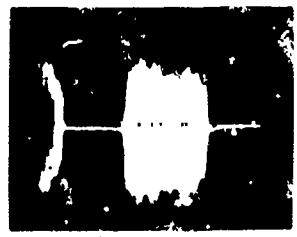

ROLLING WAVE
0.02 V/cm
0.1 sec/cm

Figure 1C

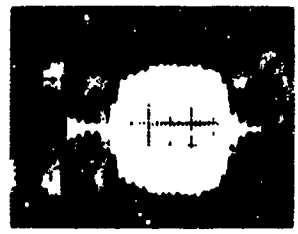

ROLLING WAVE WITH SOME RANDOM TURBULENCE
0.02 V/cm
0.1 sec/cm

Figure 1D

Figure 1. Laboratory Water Return from Helium-Neon Laser

Figure 2. Coast and Geodetic Map of the Flight Test Area

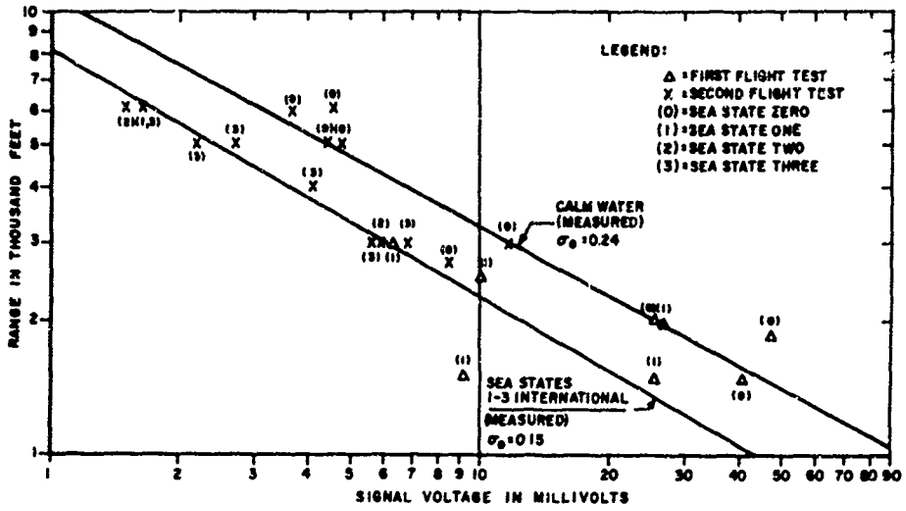

Figure 3. Ocean Return at 1.06 Microns

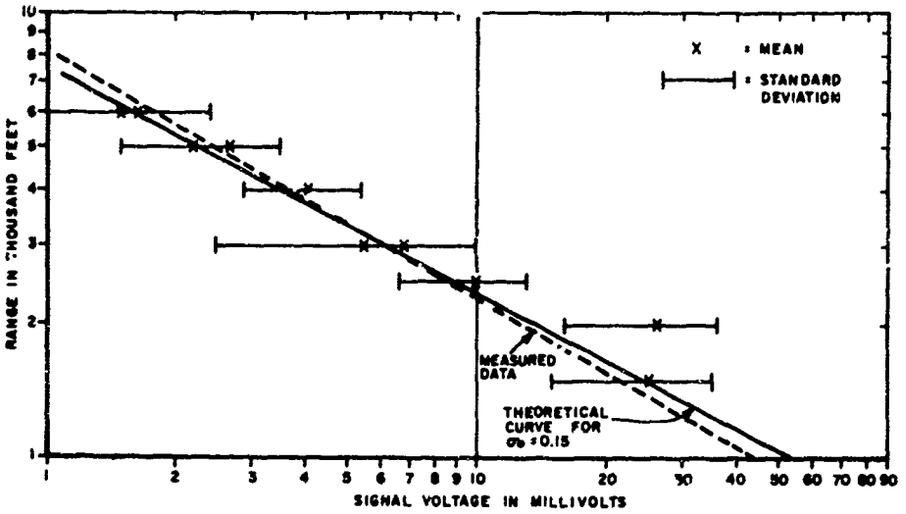

Figure 4. Ocean Return Over Sea State 1 - 3

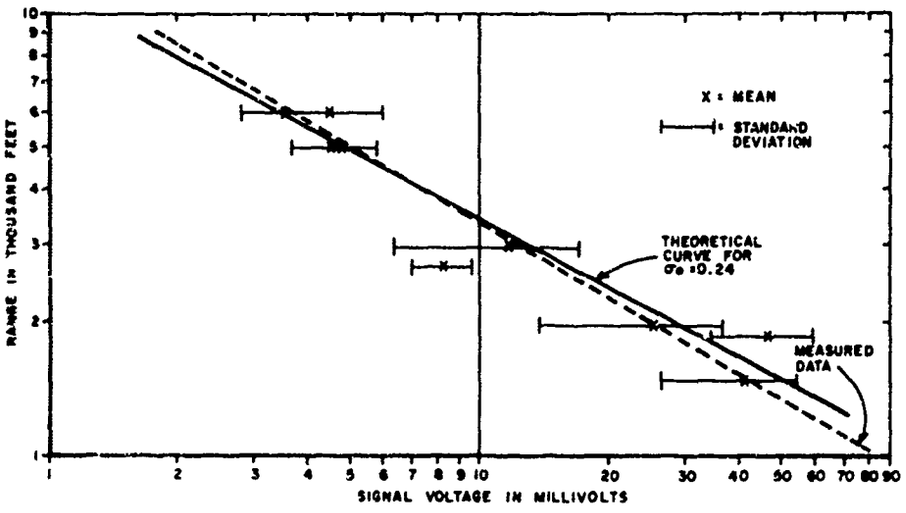

Figure 5. Ocean Return Over Calm Water

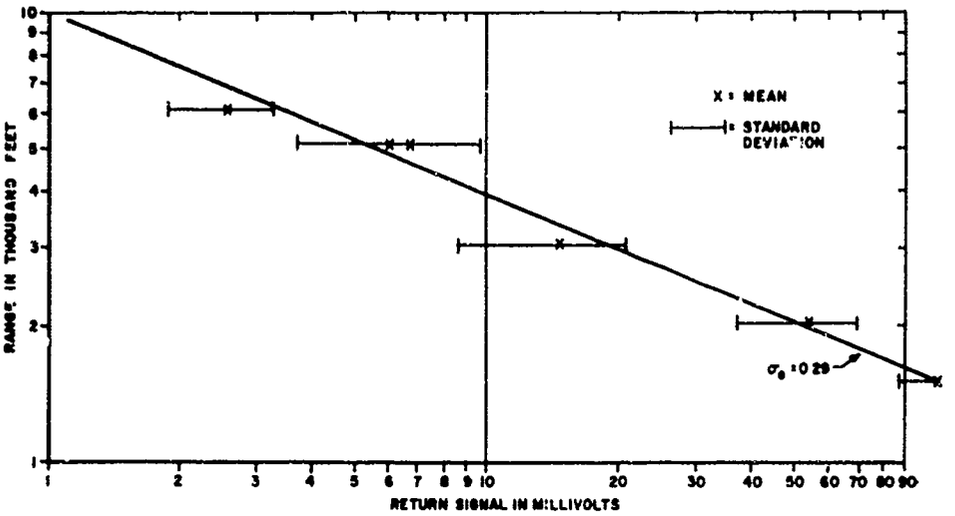

Figure 6. Return Over Beach Sand

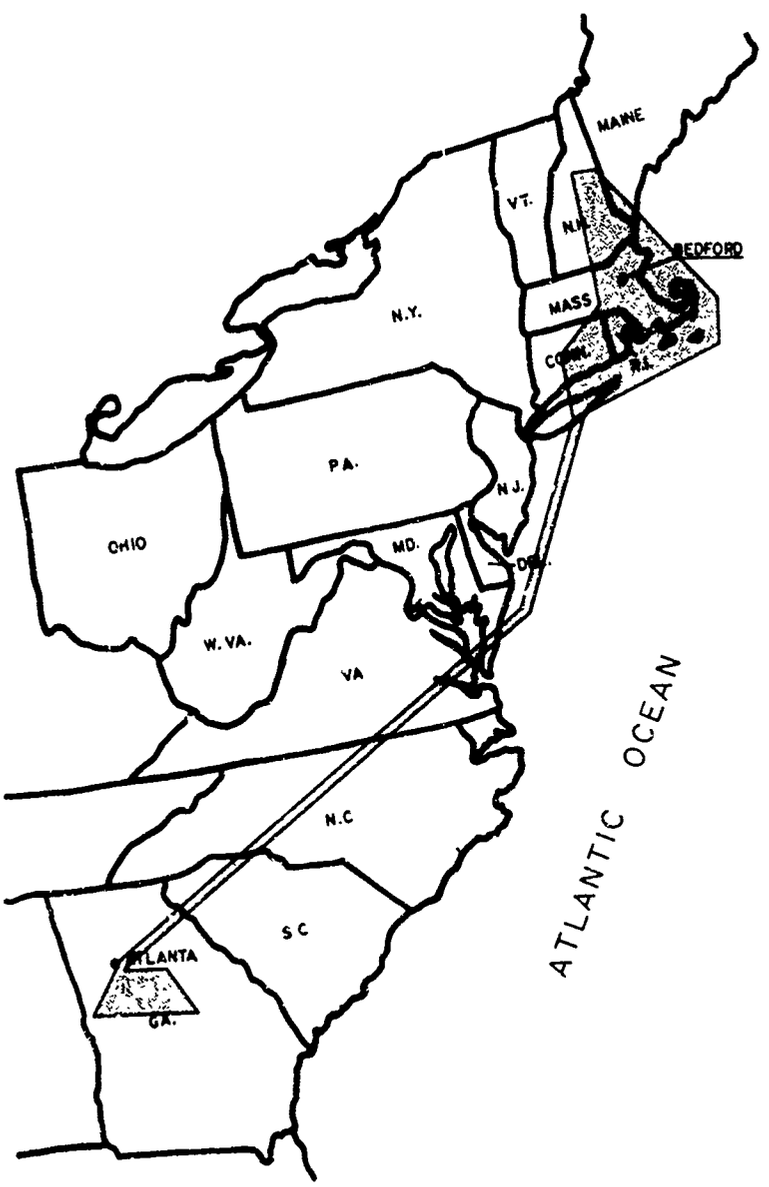

Figure 7. 10.6 Micron Flight Test Area

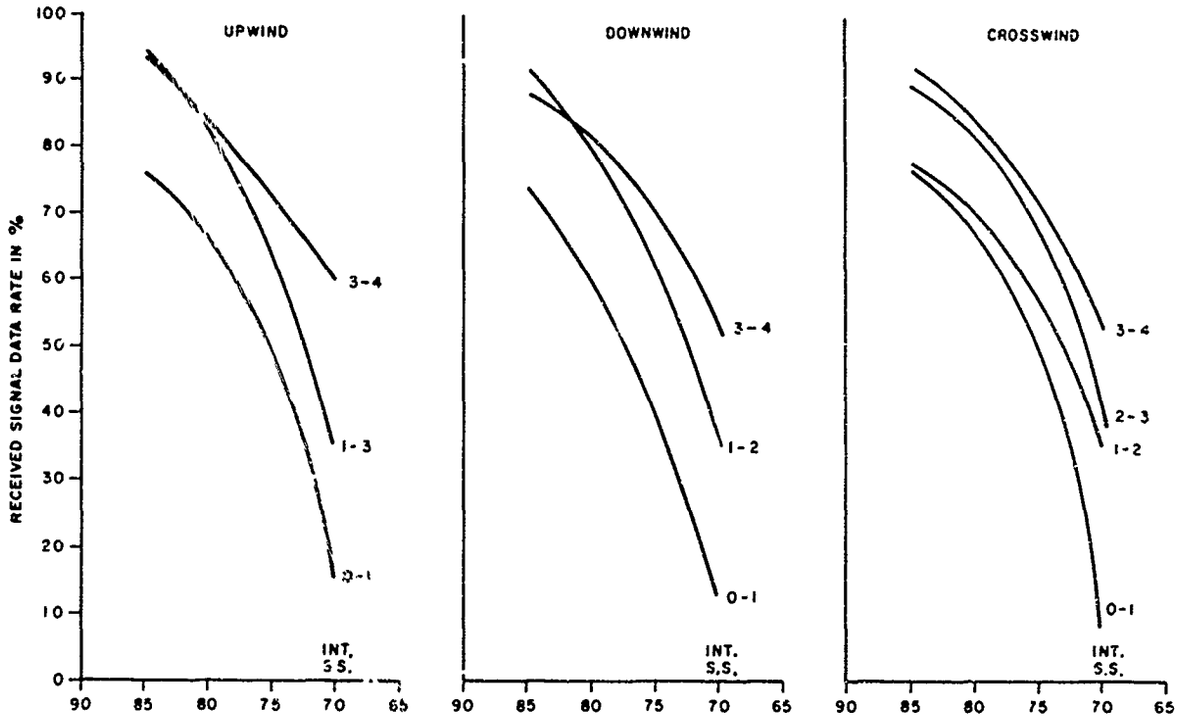

Figure 8. 10.6 Micron Laser Data Rate vs. Depression Angle

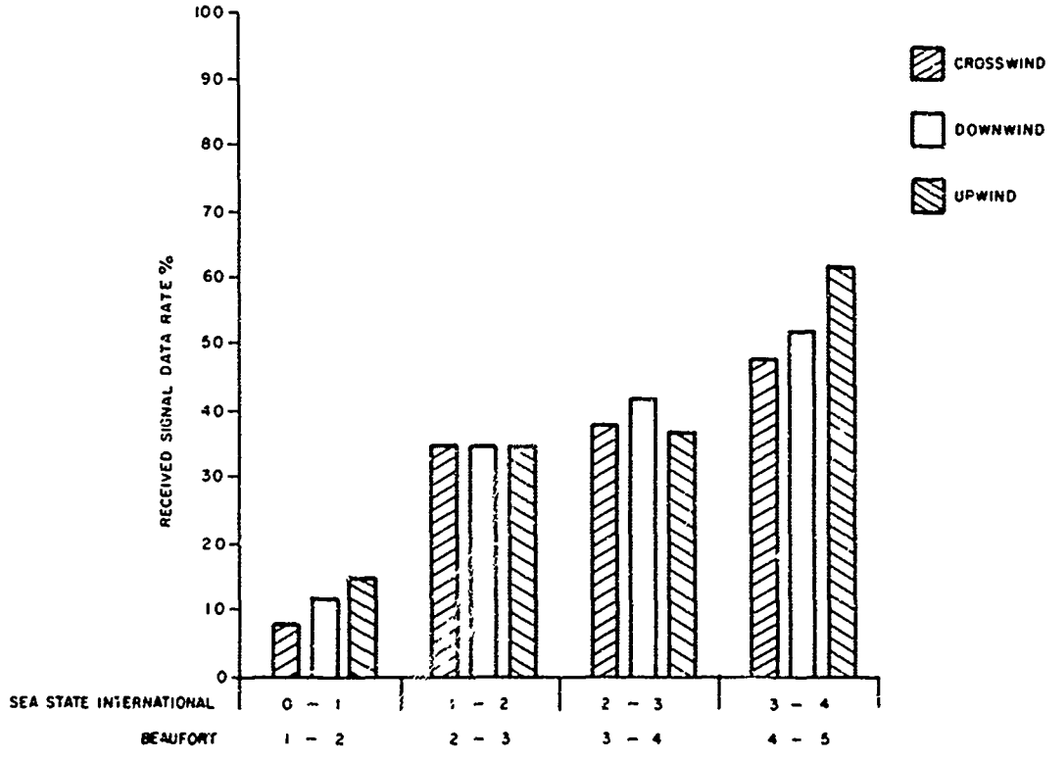

Figure 9. 10.6 Micron Data Rate vs. Sea State at 70° Depression Angle

ELECTROMAGNETIC FIELD FLUCTUATIONS IN TRANSMISSION THROUGH THE SURFACE OF THE SEA

by

Lewis Wetzel

Naval Research Laboratory
Washington, D. C. 20390, USA

ELECTROMAGNETIC FIELD FLUCTUATIONS IN TRANSMISSION THROUGH THE SURFACE OF THE SEA

Lewis Wetzel
Naval Research Laboratory
Washington, D. C. 20390, USA

SUMMARY

Due to the high conductivity of sea water, propagation of electromagnetic (radio) waves across the air-seawater interface is of practical interest only at relatively low frequencies (10^3 - 10^5 Hz). At such frequencies the relationship between subaqueous signal wavelengths and the characteristic dimensions of the perturbed sea surface permit reasonable approximations in the electromagnetic boundary conditions, which lead to useful expressions for the rms amplitude and power spectrum of the underwater field fluctuations. These expressions contain the sea wave spectrum and are functions of the signal frequency and the depth and velocity of the observation point. For example, the fluctuation spectrum seen by a stationary observer is a filtered version of the sea wave spectrum, the transfer function resembling that of a low pass filter in which the cut-off frequency and roll-off rate are determined by the signal frequency and the depth of the observer. The approximations are shown to cover a significant regime of depths and sea states over the given range of signal frequencies. The theory is illustrated by examples based on current models of the sea wave spectrum.

I. INTRODUCTION

Electromagnetic communication with a terminal below the surface to the sea is of practical interest only at very low frequencies, where the skin-depth is appreciable, or at very high (optical) frequencies, where the sea water is transparent. The interface problem in both cases is straightforward for an ideally smooth surface, but becomes difficult - and interesting - when the actual dynamic sea surface is introduced. In this paper we will restrict our attention to the very low frequencies (ELF to LF, or about 100 to 100,000 Hz) and find how the signal fluctuations at a submerged terminal are related to the spectrum of sea waves at the surface. Related work in the past has already been referenced in the review paper by Galejs found earlier in these proceedings (1): Wait (2) has considered the effect of a single sinusoid, Max and Lerner dwell on matching boundary conditions at a trochoidal surface (3), and Winter concentrates on Gaussian processes (4). While the treatment in this paper will inevitably contain elements of this earlier work, its major virtue is felt to be the introduction of the actual sea wave spectrum into the fluctuation problem, thereby linking the electromagnetic phenomena to the oceanographers' characterization of the sea surface.

It is obvious at the outset that the electromagnetic formulation of the problem will involve approximations, so the relationships among various characteristic lengths will be of interest. Although the surface of a wind-driven sea is highly irregular, it is often convenient - and instructive - to discuss its gross features in the nomenclature of a single sinusoidal process - i.e. in terms of wave "amplitudes", "frequencies", "wavelengths". There is usually sufficient regularity in at least the large-scale features to give some credence to this procedure, which means, simply, that the frequency spectrum of the surface fluctuations is rather peaked at the appropriate frequency.

While there is no uniform agreement on precise values for the pseudo-sinusoidal parameters mentioned above, the following are derived from several sources (e.g. Munk (5), Kinsman (6)) and will be adequate for our purposes:

Wave "Amplitude"	:	"A" $\approx 0.015\ W^2$
Wave "Length"	:	"λ" $\simeq 0.64\ W^2$
Min. "Rad. of Curv."	:	"ρ" $\simeq 0.7\ W^2$

Where W = wind speed in m/sec.

In the electromagnetic part of the problem, the parameter giving the scale of the underwater field variations will be the "skin-depth", defined by

$$\delta = (2/\sigma_1 \omega)^{1/2} \qquad (1)$$

The approximations to be used in formulating the electromagnetic problem will require this skin depth to be greater than the wave "amplitude", but less than both the "length" and minimum "radius of curvature" of the sea waves, thus placing both upper and lower limits on the wind-speed W for which approximate solutions may be found. These limits are indicated in the last column of Table I for several signal frequencies f_0 of interest.

f_0	λ_0	δ	"A" < δ < "ρ" ;"Λ"
100 Hz	3,000 km	25 m	W = 12 - 80 knots
10 kHz	30 km	2.5 m	W = 4 - 25 knots
100 kHz	3 km	0.8 m	W = 2 - 14 knots

Table I: Some relevant numbers

The wavelength λ_0 gives the scale of the variation of the electromagnetic field above the sea surface.

II. A SIMPLE MODEL FOR BIG WAVES

A very simple, yet instructive, model valid for certain restricted conditions may be constructed by imagining a low frequency electromagnetic field above a smooth sea surface and an observer at a depth h looking up at this surface. The field at the observer can always be represented as some combination of the surface fields times a propagation kernel (Green's function) integrated over the surface. The propagation constant entering this kernel will, for frequencies such as those in Table I, take the form

$$k = (i - 1)/\delta \qquad (z < 0) \tag{2}$$

where δ is the skin depth given in Eq. (1). Since the contributions from surface field elements thus decay exponentially with distance from the observer, the major contributions come from surface elements directly overhead, while surface elements at distances greater than $(h + \delta)$ from the observer contribute relatively little. The situation is illustrated in Fig. 1, from which it is clear that for an observer at depth h, there is a "circle of major influence" of radius

$$a = (2h\delta)^{1/2} \tag{3}$$

representing the area from which the major contributions arise - much in the nature of the primary Fresnel zone in non-dissipative propagation.

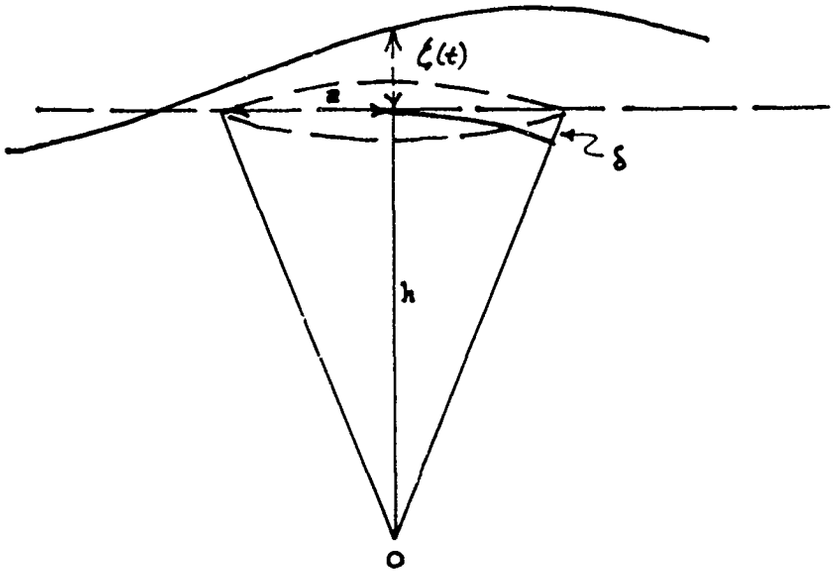

Fig. 1

(It should be noted that by using an appropriate integral formulation of the problem these arguments can be placed on a more rigorous basis - but there is little point in doing so here.)

We now observe that if the scale of the sea surface undulations is much larger than the radius of this "circle of major influence", the effect at the observer is simply as if the entire sea surface moved up and down overhead or, conversely, as if the observation point moved down and up under a flat surface. That is, if

$$\text{"K" } a << 1 \quad (\text{"K"} = 2\pi/\text{"}\Lambda\text{"}) \tag{4}$$

then

$$H(-h) \approx H_0 e^{ik(h + \zeta(t))} \tag{5}$$

where k is given in (2), H_0 is an electromagnetic field component (such as the magnetic field) at the surface, and ζ (t) is the displacement of the surface over the observation point as a function of time.

This model should almost always be valid for surface "swell" (long-wavelength quasi-sinusoidal wave components left over from distant storms), and might describe the major field fluctuations in wind-driven seas for which the inequality (4) is satisfied. Substituting into (4) from (1), (3) and the definition of "A" in the Introduction, we find that the wind speed W must satisfy

$$W > 9\, h^{1/4}\, (10/f_0)^{1/8} \text{ knots} \tag{6}$$

where h is the depth in meters and f_0 the signal frequency in kilohertz.

For the sake of future comparisons, let us imagine that the surface displacement is a simple sinusoid

$$\zeta\,(t) = A \cos \Omega t \tag{7}$$

and, further, that

$$kA < 1 \tag{8}$$

Under the conditions (4) and (8), then, the field H (-h) can be approximated by

$$H\,(-h) \approx H_0\, e^{+ikh}\left[1 + i(kA)\, \cos\Omega t\right] \tag{9}$$

That is, the fluctuation component is of order (kA).

III. ANOTHER SIMPLE MODEL DUE TO WAIT (2).

Wait's treatment of the problem as a boundary value problem using the Leontovich boundary conditions was described in reference (1) and will not be repeated here. The surface was represented by a spatial sinusoid Acos(Kx), and the application of the Leontovich boundary conditions required that the inequalities

$$k\rho > 1 \quad \rho > A \tag{10}$$

be satisfied, where ρ is the minimum radius of curvature of the surface.

By appropriately introducing time into Wait's formulation, and placing the observer at x = o, Wait's first-order approximation (kA < 1) to the underwater field can be put into a form permitting comparison with Eq. (9) above:

$$H\,(-h) \approx H_0\, e^{+ikh}\left[1 + i(kA)\, e^{-\left[(k^2 + K^2)^{1/2} - k\right](h - A)\, \cos\Omega t}\right] \tag{11}$$

(The frequency Ω is an appropriate function of surface wavenumber K.) The new feature which emerges here is the exponential factor multiplying the fluctuation amplitude (kA). This factor is close to unity as long as k >> K, or as the surface wavelengths are much larger than the skin depth. However, as the surface wavelengths shorten and become comparable to the skin depth, the associated signal fluctuations are strongly attenuated; the more so, the deeper the observer. This "filtering" behavior is an important feature of the phenomenon, and will emerge again in the more complicated treatment to follow.

IV. A FORMULATION INCLUDING THE SEA WAVE SPECTRUM

In order to introduce the sea wave spectrum into the problem, it is advantageous to utilize the conventional Stratton-Chu formulation of the vector boundary-value problem in the space beneath the sea surface. The geometry is illustrated in Fig. 2 below:

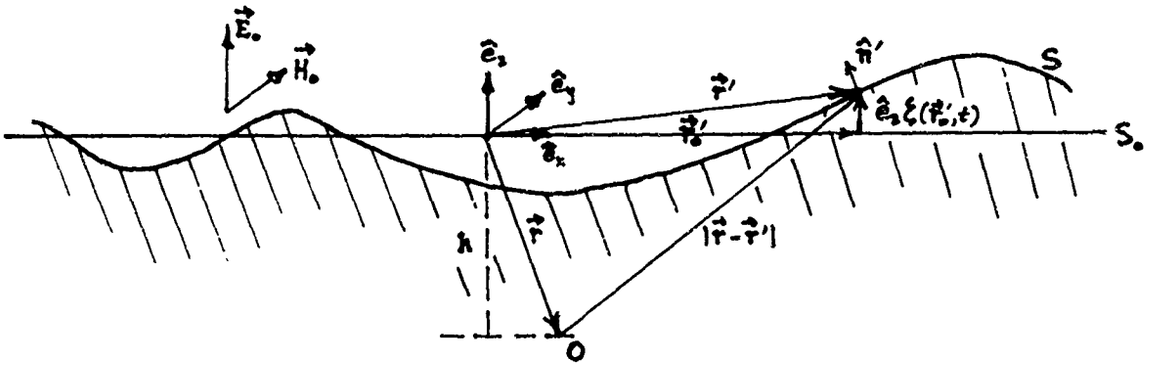

Fig. 2

The observer is designated as O and is located at the point $\vec{r}$ at a depth h beneath the mean surface. It is assumed the external low-frequency field ($\vec{E}_0$, $\vec{H}_0$) is that which would exist above the mean surface S_0. The electromagnetic field at O may be written in terms of the field quantities just under the actual sea surface S (as well as on the bottom - but we assume this to be far enough away from the sea surface and the observer that these "surface" elements can be ignored.) Let us restrict our attention to the magnetic field H at the point $\vec{r}$. This can be written (7)

$$\vec{H}(\vec{r}) = \int_S \left[i\omega\epsilon\, (\hat{n}' \times \vec{E}')\Phi\,(\vec{r}, \vec{r}') - (\hat{n}' \times \vec{H}') \times \nabla'\Phi\,(\vec{r}, \vec{r}') - (\hat{n}' \cdot \vec{H}')\, \nabla'\Phi\,(\vec{r}, \vec{r}') \right] dS' \qquad (12)$$

The prime denotes field values as viewed from below at the surface S, $\hat{n}'$ is the outward-drawn normal at $\vec{r}'$, and ϵ is the complex dielectric constant $\epsilon_w + \sigma/i\omega$ of the sea water, $\Phi(\vec{r}, \vec{r}')$ is the free-space Green's function for the water:

$$\Phi(r, r') = e^{-ik\,|\vec{r} - \vec{r}'|}/4\pi\,|\vec{r} - \vec{r}'| \qquad (13)$$

where -k is given in (2).

The boundary fields $\vec{E}'$ and $\vec{H}'$ will be approximated on the basis of the following simple arguments. Under most situations met in practice, the primary signal above the water will originate from a vertical radiator in the far distance, so the electric field will be mainly vertical and the magnetic field mainly horizontal. Since the wavelengths (thus the scale of major variations) of the fields above the surface are so large compared with the "circle of major influence" from which contributions to (12) are collected, the external fields $\vec{E}_0$ and $\vec{H}_0$ may be viewed as quasi-static. Due to the high conductivity of the sea water, the sea surface S may be viewed as a quasi-equipotential and local perturbations in S will produce local deformations of the quasi-static electric field $\vec{E}_0$ as it attempts to remain quasi-normal to the surface. The local distortion of the external electric field $\vec{E}_0$ due to a surface perturbation having a radius of curvature ρ can be estimated by introducing a fictitious electric dipole of moment $\vec{p} = 4\pi\epsilon_0 \rho^3 \vec{E}_0$ at the center of curvature. The relevant magnetic field perturbation due to this oscillating dipole is easily shown to be of the following size:

$$\begin{aligned} \Delta H/Ho &\approx k_0 \rho \qquad \rho < a \\ \Delta H/Ho &\approx k_0 a \qquad \rho > a \end{aligned} \qquad (14)$$

where $\underline{a}$ is given in Eq. (3) and $k_0 = 2\pi/\lambda_c$. Since $\underline{a}$ is at most a few tens of meters, these perturbations are insignificant and $\vec{H}_0$ can be regarded as uniform over the surface above the point of observation. Moreover, since sea water is non-magnetic and imperfectly conducting, the total magnetic field is continuous across its surface, and we may put

$$\vec{H}' = \vec{H}_0 \qquad (15)$$

in Eq. (12).

The only other field quantity entering (12) is the tangential component of the electric field, which is also continuous across the surface. The Leontovich boundary condition can be used if the inequalities in Eq. (10) are satisfied, and we write

$$(\hat{n}' \times \vec{E}') = (\hat{n}' \times \vec{E}_0) = (k/\sigma)\,(\hat{n}' \times \hat{n}' \times \vec{H}_0) \qquad (16)$$

which casts the entire integrand in Eq. (12) in terms of the uniform, unperturbed external magnetic field $\vec{H}_0$. Generally the slopes of the sea surface will be sufficiently small that we may approximate the components of the surface normal $\hat{n}'$ by the following (x'_0, y'_0 refer to coordinates on S_0):

$$n'_x \approx -\frac{\partial\zeta}{\partial x'_0}; \quad n'_y \approx -\frac{\partial\zeta}{\partial y'_0}; \quad n'_z \approx 1 \qquad (17)$$

Under the further conditions that

$$k\,|\zeta|_{max} < 1, \quad kh > 1 \qquad (18)$$

the gradient of the Green's function becomes, to first order in $k\,|\zeta|_{max}$

$$\nabla'\Phi\,(\vec{r}, \vec{r}') \approx \nabla'\Phi\,(\vec{r}, \vec{r}_0') + \zeta\,(\vec{r}_0')\,\frac{\partial}{\partial z'}\,\nabla'\Phi(\vec{r}, \vec{r}_0') \qquad (19)$$

Substituting all of these approximations into the original integral in Eq. (12) produces a horrendous expression of rather specious generality. We will not record here in detail all of the manipulations required to wrest a useful result from this formalism, but simply outline the sequence of steps taken.

1. Implicit in (17) and (18) is the requirement that the perturbation ζ of the sea surface be small compared with the wavelengths of both the sea waves and the subaqueous signal. For this reason we retain terms only through first order in ζ and its derivatives.

2. A subaqueous observer will tend to orient his sensor for maximum signal, so if we take the external magnetic field $\vec{H}_0$ to lie along the y-axis, we will select the y-component $\hat{e}_y' \cdot \vec{H}(\vec{r})$ of the underwater signal.

3. As long as the motion of the observer is small compared with the signal velocity in the water, this motion can be introduced into the formalism simply by replacing $\vec{r}$ with $\vec{r} + \vec{V}t$. Moreover, there is no loss of generality if we let $x = y = o$ at $t = o$; i.e. if we set $\vec{r} = -h\hat{e}_z$, where h is the depth of the observer.

4. Since the sea surface displacement is a random variable, and we want ultimately to express it in terms of its spectrum, we replace $\zeta(\vec{r}_0', t)$ by its expansion in gravity waves:

$$\zeta(r_0', t) = \iint_{-\infty}^{\infty} d\vec{K}\, \mathcal{E}(\vec{K})\, e^{i(\vec{K}\cdot\vec{r}_0' - \Omega(K)t)} \tag{20}$$

where Ω is related to $\vec{K}$ by the dispersion relation for (small-amplitude) gravity waves:

$$\Omega^2(K) = g|\vec{K}| \tag{21}$$

with g the acceleration of gravity. The wave amplitude $\mathcal{E}(\vec{K})$ is, of course, a stochastic variable.

5. The integrations involved in (12) are most conveniently performed if we use the three-dimensional Fourier transform of the Green's function:

$$\Phi(\vec{r}, \vec{r}_0') = \frac{1}{(2\pi)^3} \iiint_{-\infty}^{\infty} d\vec{q}\, \frac{e^{-i\vec{q}\cdot(\vec{r} - \vec{r}_0')}}{(k^2 - q^2)} \tag{22}$$

where $k^2 = -i\omega\mu\sigma = -ik_1^2$; comparing with (2) we note that $k_1 = \sqrt{2}/\delta$.

When all of these representations and approximations and specializations are put into Eq. (12) and the simple integrations performed, we find that the magnetic field perturbation may be written

$$\delta H_y(-h, \vec{V}) \approx \frac{H_0}{2\pi} \iint_{-\infty}^{\infty} d\vec{K}\, \mathcal{E}(\vec{K})\, e^{-i(\vec{K}\cdot\vec{V} - \Omega(K)t)} \times \int_{-\infty}^{\infty} dq_z \left[K^2 + q_z^2\right] \frac{e^{iq_z h}}{\left[(k^2 - K^2) - q_z^2\right]} \tag{23}$$

The integral on q_z contains a pole that is a function of the sea wavenumber K. The behavior of this pole, and the appropriate contour for performing the integration, is shown below

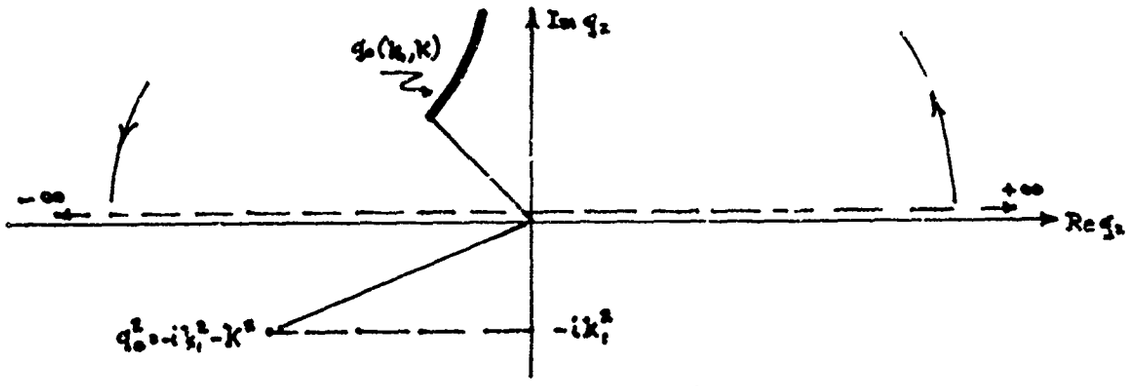

Replacing the q_z integral by its residue at the pole $q_z = +(\kappa^2 - K^2)^{1/2}$, the magnetic field perturbation takes the final form

$$\delta H_y(-h, t) \simeq -\frac{H_0}{2i} \iint_{-\infty}^{\infty} d\vec{K}\, \mathcal{E}(\vec{K})\, \frac{k_1^2}{\sqrt{ik_1^2 + K^2}}\, e^{-h\sqrt{ik_1^2 + K^2} + i(\vec{K}\cdot\vec{V} - \Omega(K)t)} \tag{24}$$

Amplitude and Spectrum of the Field Fluctuations

The sea surface is a random process described by a spectral density function. Therefore, we are interested not in the field perturbation for an instantaneous distribution of surface heights, but rather in the rms value of the field fluctuations for an ensemble average of the surface distributions. The random variable in (24) is the (complex) surface transform $\mathcal{E}(\vec{K})$, and the random process is stationary. Let us first find the covariance of δH_y, which is

$$C_H(h;\tau) = \langle \delta H_y(-h,t)\ \delta H_y^*(-h,t+\tau)\rangle \tag{25}$$

In performing the averaging on the RHS of (25) we encounter the ensemble average $\langle \mathcal{E}(\vec{k})\mathcal{E}^*(\vec{k}')\rangle$. Note, however, that

$$\langle \zeta\zeta^*\rangle = \langle \zeta^2\rangle = \int_{-\infty}^{\infty} d\vec{K}\, G(\vec{K}) \tag{26}$$

where $G(\vec{K})$ is the spectral density of the surface heights in wave-number space (the so-called "power spectrum") which, this being the surface of the ocean, is the oceanographers' "directional wave spectrum". Comparing with (20) we may write

$$\langle \mathcal{E}(\vec{K})\mathcal{E}^*(\vec{K}')\rangle = \delta(\vec{K}-\vec{K}')\, G(\vec{K}) \tag{27}$$

which reduces (25) to

$$C_H(h;\tau) = \frac{H_0^2 k_1^2}{4}\iint_{-\infty}^{\infty} d\vec{K} G(\vec{K})\ \frac{k_1^2}{|ik_1^2+k^2|}\ e^{-2h\,\mathrm{Re}\,(\sqrt{ik_1^2+K^2})}\ e^{-i(\vec{K}-\vec{V}-\Omega(K))\tau} \tag{28}$$

This is the basic expression from which all blessings flow. For example:

$$\langle|\delta H_y(-h)|^2\rangle = C_H(h;o) = \frac{H_0^2 k_1^2}{4}\iint_{-\infty}^{\infty} d\vec{K} G(\vec{K})\ \frac{k_1^2}{|ik_1^2+K^2|}\ e^{-2h\,\mathrm{Re}\,(\sqrt{ik_1^2+K^2})} \tag{29}$$

is the mean of the square of the field fluctuations. These may now be referenced either to the surface fields H_0, or to the unperturbed field $H_{un}(-h)$ existing at a depth h. We know that

$$|H_{un}(-h)|^2 = H_0^2\, e^{-2h\,\mathrm{Re}\,(\sqrt{ik_1^2})} \tag{30}$$

so by dividing (29) by (30) and taking the square root, we obtain the relative magnitude of the rms field fluctuations referred to the unperturbed field at depth h:

$$\left[\frac{\langle|\delta H_y(-h)|^2\rangle}{|H_{un}(-h)|^2}\right]^{1/2} = \frac{k_1}{2}\left\{\iint_{-\infty}^{\infty} d\vec{K} G(\vec{K})\ \frac{k_1^2}{|ik_1^2+K^2|}\ e^{-2h\,\mathrm{Re}\left[\sqrt{ik_1^2+K^2}-\sqrt{ik_1^2}\right]}\right\}^{1/2} \tag{31}$$

We see that this measurable quantity depends upon depth (through h), frequency (through k_1) and the state of the sea (through $G(\vec{K})$).

Next, let us find the power spectrum of the fluctuations by taking the Fourier transform of the covariance (Wiener-Khintchine Relation):

$$S(h,\vec{V};\omega) = \int_{-\infty}^{\infty} d\tau\ C_H(h;\tau)\ e^{-i\omega\tau} \tag{32}$$

Substituting from (28), we get

$$S(h,\vec{V};\omega) = \frac{\pi}{2} H_0^2 k_1^2 \iint_{-\infty}^{\infty} d\vec{K} G(\vec{K})\ \frac{k_1^2}{|ik_1^2+K^2|}\ \delta\left[(\Omega(K)-\vec{K}\cdot\vec{V})-\omega\right] e^{-2h\,\mathrm{Re}\,(\sqrt{ik_1^2+K^2})} \tag{33}$$

This is a very intractable expression as it stands, because the δ function says that for each value of ω the integral is performed over those values of K_x and K_y satisfying the equation

$$\sqrt{g}(K_x^2+K_y^2)^{1/4} - K_x V_x - K_y V_y - \omega = 0 \tag{34}$$

However, the picture simplifies significantly for a stationary terminal, since then (34) simply selects the magnitude of the sea wave vector K corresponding to the frequency ω. To illustrate what this means, let us make the transformation from Cartesian to Polar coordinates in the K-plane by setting $K_x = K\cos\theta$, $K_y = K\sin\theta$, $G(\vec{K}) \to G(K,\theta)$ and $d\vec{K} = KdKd\theta$. Putting $\vec{V} = O$ we now write

$$S(h,o;\omega) = \frac{\pi}{2} H_o^2 k_1^2 \int_0^{2\pi}\int_0^{\infty} d\theta dK K G(K,\theta) \frac{k_1^2}{|ik_1^2 + K^2|} \delta(\Omega(K) - \omega) e^{-2h\,\mathrm{Re}\,(\sqrt{ik_1^2 + K^2})} \quad (35)$$

Here the K-integration is trivial, since K is simply replaced everywhere by (ω^2/g), and we get

$$S(h,o;\omega) = \frac{\pi}{2} \frac{H_o^2 k_1^4}{|ik_1^2 + \frac{\omega^4}{g^2}|} \left(\frac{\omega^2}{g}\right) e^{-2h\,\mathrm{Re}\left(\sqrt{ik_1^2 + \frac{\omega^4}{g^2}}\right)} \int_0^{2\pi} d\theta\, G\left(\frac{\omega^2}{g}, \theta\right) \quad (36)$$

However, it can be shown that

$$\int_0^{2\pi} d\theta G(K,\theta) = K^{-3/2} E\left[\omega(K)\right] \frac{\sqrt{g}}{2} = \frac{1}{2} \frac{g^2}{\omega^3} E(\omega) \quad (37)$$

where $E(\omega)$ is the frequency spectrum of the ocean waves - as would be measured by a wave staff at a fixed location. Therefore (36) can be written

$$S(h,o;\omega) = \frac{\pi}{4} \frac{H_o^2 k_1^4}{|ik_1^2 + \omega^4/g^2|} \left(\frac{g}{\omega}\right) e^{-2h\,\mathrm{Re}\left(\sqrt{ik_1^2 + \omega^4/g^2}\right)} E(\omega) \quad (38)$$

That is, the power spectrum of the field fluctuations is a weighted version of the "power" spectrum of the sea waves producing the fluctuations.

The reader should keep in mind that (38) represents the fluctuation spectrum only; that is, $\omega = o$ corresponds to the signal frequency $2\pi f_o$. Moreover, S contains the unperturbed field at depth h as a scale factor, so it is convenient to define a normalized spectrum

$$\hat{S}(h,o;\omega) = S(h,o;\omega) \Big/ H_o^2 e^{-2h\,\mathrm{Re}\sqrt{ik_1^2}} = T(h;\omega)\, E(\omega) \quad (39)$$

where we have now displayed the electromagnetic fluctuation spectrum as an operation (transfer function) $T(h;\omega)$ upon the sea wave spectrum $E(\omega)$. Explicitly, the transfer function $T(h;\omega)$ is

$$T(h;\omega) = \frac{\pi}{4} \left(\frac{g}{\omega}\right) \frac{k_1^4}{|ik_1^2 + \omega^4/g^2|} e^{-2h\,\mathrm{Re}\left[\sqrt{ik_1^2 + \omega^4/g^2} - \sqrt{ik_1^2}\right]} \quad (40)$$

The major effect of this transfer function is to attenuate the high-frequency components of the sea-wave spectrum. That is, the intervening water acts as a low-pass filter for the sea-wave components. (The fluctuation spectrum $\hat{S}$ doesn't really have a pole at $\omega = o$; the sea-wave spectrum is such that $E(\omega)/\omega \to o$ as $\omega \to o$.)

The high-frequency roll-off point ω_c for the function $T(h;\omega)$ can be estimated by putting the argument of the exponential factor equal to unity:

$$2h\,\mathrm{Re}\left[\sqrt{ik_1^2 + \omega_c^4/g^2} - \sqrt{ik_1^2}\right] = 1 \quad (41)$$

For depths $h > \delta$, this can be approximated by

$$\frac{h\omega_c^4}{\sqrt{2}\, k_1 g^2} \approx 1 \quad (42)$$

or

$$\omega_c \approx \left(\sqrt{2}\, k_1 g^2/h\right)^{1/4} \quad (43)$$

Another interesting result is found by substituting $K_o^2 = \omega_o^4/g^2$ into (42) and rearranging to obtain

$$\sqrt{2h\delta'} \approx \Lambda_o/\pi \tag{44}$$

where Λ_o is the sea-wave length corresponding to the cut-off frequency ω_o. Recognizing the LHS of (44) as the radius of the "circle of major influence" defined in Eq. (3), we conclude that only those sea waves whose lengths are equal to or greater than the diameter of the "circle of major influence" will contribute significantly to the signal fluctuations at a submerged terminal.

V. SOME EXAMPLES

To obtain some idea of the magnitude of the electromagnetic fluctuations, let us consider the simple case of "swell", for which the directional spectrum in (31) can be written:

$$G(\vec{K}) = A^2\,\delta\,(\vec{K}_o - \vec{K}) \tag{45}$$

where the wave is a simple sinusoid of amplitude A and propagation vector $\vec{K}_o$.

If we choose the reasonable parameters A = 1 m, $K_o = 0.04\,m^{-1}$, and f_o = 10kHz, we obtain from Eq. (31):

$$\left[\frac{\langle|\delta H|^2\rangle}{|H_{un}|^2}\right]^{1/2} \approx 0.28\,e^{-\frac{h}{1000}} \tag{46}$$

Thus the magnitude of the fluctuation is not insignificant, and the dependence on depth is very weak (and consistent with the last paragraph of the previous section.)

In this simple case we can use Eq. (33) directly, and find the spectrum for a moving terminal:

$$S(h,\vec{V};\omega) = \frac{\pi}{2}\,H_o^2\,(k_1A)^2\,e^{-0.25h}\,\delta\,\left[(\Omega(K_o) - \vec{K}_o\cdot\vec{V}) - \omega\right] \tag{47}$$

The spectrum in this case shows a Doppler shift depending upon the relative motion of the observer and the wave. We would expect a similar shift in the components of the continuous sea-wave spectrum in a wind-driven sea.

By choosing a particular form for the spectrum $\mathcal{E}(\omega)$, we can illustrate the effect on the electromagnetic fluctuation spectrum of changing depth, signal frequency and wind speed. This has been done in Figs. 3, 4 and 5 for the so-called Pierson-Moskowitz spectrum (8)

$$\mathcal{E}(\omega) = 8.1 \times 10^{-3}\,g^2\omega^{-5}\,e^{-0.74\,(\Omega_o/\omega)^4} \tag{48}$$

where $\Omega_o = g/W$, with W the wind speed in m/sec. For ω well above Ω_o, the argument of the exponential factor vanishes, and the spectrum is controlled asymptotically by ω^{-5}. This asymptotic behavior has been sketched (relative ordinate) on each Figure to illustrate the nature of the high-frequency roll-off.

Since $\hat{S}$ is the fluctuation spectrum only, the complete signal spectrum would contain a δ function at the origin, corresponding to the unperturbed signal at frequency f_o. Since the fluctuations are essentially an amplitude modulation of the steady signal, we would expect symmetric sidebands for a stationary observer. However, this symmetry is destroyed in a complicated way if the observer is in motion with respect to the directional spectrum of the sea waves (see Eq. (34); in fact, if the observer were to move under the sea with the wind velocity above the sea ($\vec{W}$), we might expect the unperturbed signal spike to move into the center of one of the spectral bumps displayed in Figs. 3, 4 and 5.

REFERENCES

1. Galejs, Janis, "ELF Propagation", Paper I-1, these Proceedings.

2. Wait, J. R., "The Calculation of the Field in a Homogeneous Conductor with a Wavy Interface", Proc. IRE, Vol. 47, No. 6, p. 1155, 1959.

3. Lerner, R. M. and Max, J. "VLF and LF Fields Propagating Near and Into a Rough Sea", Radio Science, 69D(2), pp. 273-286, 1965.

4. Winter, D. F., "Low-Frequency Radio Propagation Into a Moderately Rough Sea", J. Res. NBS Radio Propagation, 67D(5), pp. 551-562, 1963.

5. Munk, W., "Water Waves", Encyclopaedia Britannica, 1965 Edition.

6. Kinsman, B., "Wind Waves, Their Generation and Propagation on the Ocean Surface", Prentice-Hall, 1965.

7. Stratton, J., "Electromagnetic Theory", McGraw-Hill, p. 464ff, 1941.

8. Pierson, W. J., Jr. and Moskowitz, L., "A Proposed Spectral Form for Fully Developed Wind Seas Based on The Similarity Theory of S. A. Kitaigorodskii", J. Geophys. Res., Vol. 69, pp. 5181-5190, December, 1964.

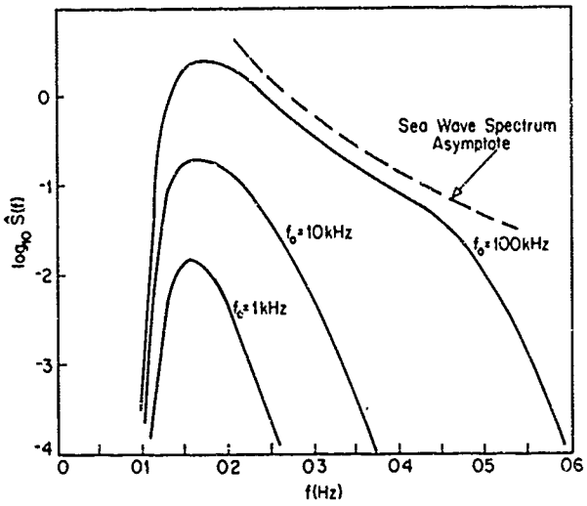

Fig 3. Fluctuation Spectrum vs. Signal Frequency f_0 (W = 15 knots, h = 10m)

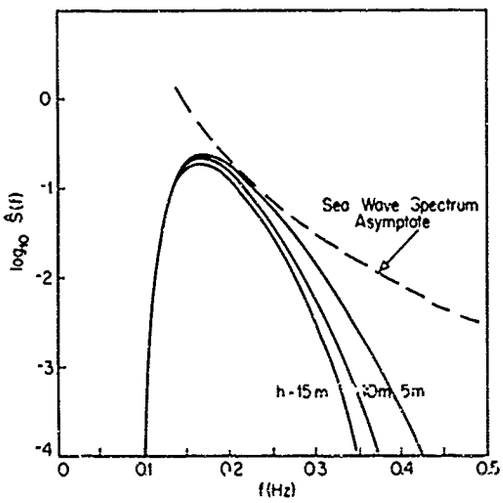

Fig. 4. Fluctuation Spectrum vs. Observation Depth h (W = 15 knots, f_0 = 10kHz)

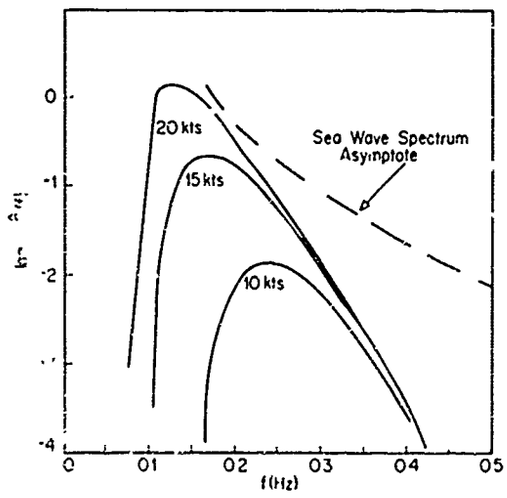

Fig. 5. Fluctuation Spectrum vs. Wind Speed W (h = 5m, f_0 = 10kHz)

DISCUSSION ON THE PAPERS PRESENTED IN SESSION III
(Air Sea Interface)

Discussion on paper 16 : "Spectral characteristics of HF ground wave signals backscattered from the sea" by D.D.CROMBIE, J.M. WATTS and W.M. BEERY .

Dr. J.R. WAIT : Have you observed zero doppler-shifted echoes on occasions ? A second order theory would predict the existence of this . (J.R.WAIT.ESSA.Report.OD-2,1969)

Dr. D.D.CROMBIE : Yes but it has not yet been possible to determine whether it comes from the sea .

Dr. W. HALLIDAY : 1) Have doppler shifts from moving surface waves been observed at frequencies significantly lower than those in the MHz range dealt with . The smaller shifts (in Hz) might be offset by the higher velocity of the longer ocean waves . Velocities of 100 - 200 knots are possible . However the amplitude of these long waves is low .

2) How do the results of radio measurements of wave size and velocity correlate with those using ordinary physical measurements .

Dr. D.D. CROMBIE : Use of frequencies down to a few 100 kHz would allow most wind waves to be observed . Waves having speeds of 100 - 200 knots fall in the Tsunani range have wavelengths of 100 s of km. ELF-VLF transmission would have to be used to see these . However they might have somme effect on the spectra of shorter waves observed with higher frequencies .

Prof. I. RANZI : By measuring the phase variation of backscattered radio-waves, we observed some years ago, that the radiowaves backscattered from the coastal sea present no phase variation but a periodic fading, having a frequency equal to the doppler frequency shifted from the open sea . We thought that this was due to a system of stationary sea waves which is present at the coastal boundary . Did you observe anything similar ?

Dr. D.D. CROMBIE : When one looks at the total received amplitude (without frequency resolution) beat between stationnary echoes and Doppler shifted sea echo will cause the amplitude to vary at the Doppler frequency . When both approaching and receeding waves are present they will also beat giving an amplitude variation at twice the Doppler frequency .

Prof. J. RANZI : An important point is the dependence of the backscattering cross section on the seastate and its variation with the radio frequency . We observed that such a dependence, which is very strong at low frequencies (2 MHz) is rapidly vanishing at frequencies higher than 20 MHz .

Dr. D.D. CROMBIE : I have one reason for thinking that for fully developed seas the spectral density at short wavelengths is constant . This would account for your observations.

Dr. G. FRANCESCHETTI : Is there any hope to measure the transverse Doppler shift ? (I suppose this is an academic question, since the deviation should be extremely small.)

Dr. D.D. CROMBIE : No .

Discussion on paper 17 : "The reflectivity of the sea surface at radar frequencies", by W. SCHONFELD

Prof. R. MOORE : We (and others) find a frequency spacing (150/D)MHz for statistically independent samples, where D is range dimension of the target . Thus, for clutter D is range cell of radar ($c\tau/2$), whereas for small targets D is their range dimension . Question : What is pulse length ?

Prof. W. SCHONFELD : We made measurements in the X band with frequency differences between 0 and 800 MHz . From a difference of $\geq$ 80 MHz we have no significant difference in behaviour .
The pulse length was 200 nanoseconds .

Discussion on paper 18 : "The interaction of HF/VHF radiowaves with the sea surface and its implications, by D. BARRICK .

Dr. C.T. SWIFT : 1) Does the theory you presented predict the return of signals scattered by ocean waves of length $nL/2$ as suggested by Mr. CROMBIE ?

2) Have you calculated the depolarized component using a second order perturbation expansion .

Dr. D.E. BARRICK : 1) No, the first order ocean wave theory did not include this effect . Use of a second order spectral estimate shows scatter from the "root two" component, or from waves of length nL/2 where n = 2 .

2) I have not interpreted depolarization at HF from the theory, since vertical polarization is much more important in ground-wave systems at these frequencies. In the microwave region, reference 15 of the text discusses depolarization effects deduced from this theory .

Dr. J.R. WAIT : this paper appears to be a fundamental contribution . However I believe the power scattered into the higher order grating modes (i.e. m and n > 0) may not be properly accounted for in the deterministic calculation for the attenuation of the total ground wave over a rough spherical earth .

Dr. D.E. BARRICK : For the purposes of simplicity in the paper, I defined the effective surface impedance $\bar{\Delta}$ as $\Delta + A_{00}$ with little explanation . Looking at the roughness contribution, A_{00}, it is not obvious that higher-order modes (i.e., m, n>0) are properly accounted for . An alternate, and perhaps more meaningful way of defining $\bar{\Delta}$ places in evidence the role of these higher-order modes . This definition is based upon a fact pointed out by Norton and Wise in 1937 for dipole radiation over a flat plane : the ratio between the Poynting vector downward into the surface to the Poynting vector in the forward direction at the surface is identically the normalized surface impedance (to the first order) . If we employ this definition for $\bar{\Delta}$ and compute the Poynting vectors averaged spatially over (at last) one period of the surface, we obtain identically the same result for $\bar{\Delta}$, i.e., $\Delta + A_{00}$.
Furthermore, if we compute the total upward Poynting vector at the surface (representing the complex power density scattered into the upper half-space by all propagating and evanescent modes with m, n > 0) and divide by the forward Poynting vector, the result is A_{00} In others words, the addition of the effective surface impedance produced by roughness is actually the result of scattering in all modes into the upper half space, the real part of $\bar{\Delta}$ being contributed by the upward propagating modes, while the reactive part of $\bar{\Delta}$ contributed by the upward evanescent modes . As a third check on the technique, Feynberg (1944) derived a similar result (neglecting conductivity) for radiation over slightly rough plane, using perturbation with an exact integral equation formulation for the fields If I convert my $\bar{\Delta}$ into an effective surface conductivity and allow the actual ohmic conductivity to approach infinity in my equations, I obtain identically the same result as Feynberg, indicating that two entirely different formulations lead to the same result . I prefer my formulation because I feel it allows a clearer physical interpretation of the local interaction mechanism with the surface .

The remaining question concerns the use of $\bar{\Delta}$, or effective independence boundary condition, valid strictly only for flat surfaces, in a formulation for a spherical surface such as the earth . Strictly speaking, for a sphere only moderately large in terms of wavelength, such an approximation is not possible and one must use instead "modal impedances" which differ for every term of the exact Mie series solution . For very large spheres, however, (such as the earth at HF) the Watson transformation of the Mie series and its ensuing asymptotic evaluation show that the modal impedances of importance in the solution are very well approximated by using a simple "flat-plane" impedance in place of them (Found in many works by van der Pol, Bremmer, and Wait) . This flat-plane impedance is the one employed to find the poles of the integrant and hence their residues, as used in the residue series solution . Stated simply, for a very large sphere, the diffracted wave interacts with the surface locally (i.e., over two or three "numerical distances") as though the surface were flat .

Obviously it would be more satisfying and correct to perturb the solution for a spherical earth rather than that for a plane earth ; this would provide errors bounds on the "first" order" approximation used here . Algebraic complexity has thus far precluded my solution to this more exact problem .

Prof. R.K. MOORE : 1) What is effect of ionosphere ?

2) How about Doppler shifts on through ionosphere or ionosphere-reflected waves ?

Dr. D.E. BARRICK : 1) The ionosphere will definitively pose limitations on propagation to a satellite, especially in the lower HF region and during the day time . I discuss this further in the written text .

2) We irvestigated Doppler broadening due to through-ionosphere propagation and found it to be negligible compared to the expected satellite-motion-induced Doppler shifts . Ionospherically-reflected waves can be a problem, and one would hence use short pulses and gating techniques to eliminate this multipath problem .

Dr. A.W. BIGGS : Have you compared your paper with similar studies by Yabroff (S.R.I.) about 4 - 5 years ago ?

Dr. D.E. BARRICK : I have compared my results with other theories appearing in the open literature and comparisons of these results are found in the written paper, and also in

reference 13 of that paper . I am not aware of the above work, and if I can obtain the pertinent report, I shall be most interested in making such a comparison . Thank you for calling attention to this work .

Discussion on paper 20 : "Worldwide oceanic wind and wave forecasts using a satellite radar radiometer", by R.K. MOORE and W.J. PIERSON .

Dr. J.W. WRIGHT : Data obtained both with radar over the sea at 400, 1200, 4400, 2900 MHz and 9300 and 24 000 MHz in a wave tank show that cross-sections at a given Bragg wave number are the same for depression angles less than 70° . Thus the wind speed dependence of the cross-section at 13,3 GHz and 55° depression angle should be much like that at 30° at 8.9 GHz . For the latter case NRL results in the North Atlantic and Puerto Rico show a wind speed dependence of about $(V \text{ wind})^{.6}$ for wind speeds between 10 and 50 knots .

Prof. R.K. MOORE : (from the magnetic tape)

According to what I know about the two systems, I am more confident with the data 13.3 than I am of the NRL data 8.9 .
However I believe that if the phenomena are quite frequency sensitive, it seems reasonable to consider that , then we must consider going to the shorter wavelength of course we don't know what is the best two and a quarter, two one and a half or 2.75 centimeters . But it does not appear that 2.5 is the best , 3.3 could be the best using the NRL data . On the other hand if I look the NRL data I can go to the conclusion that the wind speed dependency is of one half power of the velocity.

Dr. D.E. BARRICK : It would seem that unfortunatly the higher sea states and wind speeds would be often accompanied by heavy cloud covers and rain . Is two-way propagation from a satellite through rain to the earth a significant system limitation ?

Prof. R.K. MOORE : No . The number of hours year with rain, heavy enough to cause attenuation more than, says 5 dB, is at worst less than 10C and is far less in most places . Most of the interesting effects are in cloud-covered areas but cloud attenuation is not important at near vertical angles of transmission proposed here .

Discussion on paper 22 : "Electromagnetic field fluctuation in transmission through the surface of the sea", by L.B. WETZEL .

Dr. D.E. BARRICK : In the perturbation approach you employed, does the ocean wave height have to be small compared to the radiowavelength inside the sea water ?

Dr. L. WETZEL : Yes . As indicated in the first slide, this condition is satisfied over a rather large range of wind speeds for the span of frequencies from E.L.F. up to L.F.

DE L'INFLUENCE DES ECARTS A LA LOI DE DITTMAR SUR LA CONDUCTIVITE ELECTRIQUE DE L'EAU DE MER

par

A. Poisson et J. Chanu
Laboratoire d'Océanographie Physique
Faculté des Sciences de Paris
9, Quai St Bernard - Paris 5°
Laboratoire de Thermodynamique des milieux ioniques et biologiques
43, Rue Cuvier - Paris 5°

SUMMARY

Determining the salinity of sea-water samples from conductimetric measurements raises the problem of the contribution of each ionic species present to the overall electric conductivity.

Experimental results indicate that this contribution varies appreciably with the nature of the electrolyte, which implies a certain amount of uncertainty regarding the salinity values obtained through routine measurements when Dittmar's law is not strictly checked.

The experimental law used leads to determining the partial equivalent conductivity of the main ionic sea-water components, even in the case of hydrated or thermally unstable salts.

DE L'INFLUENCE DES ECARTS A LA LOI DE DITTMAR SUR LA CONDUCTIVITE ELECTRIQUE DE L'EAU DE MER

A. Poisson et J. Chanu
Laboratoire d'Océanographie Physique
Faculté des Sciences de Paris
9 Quai StBernard - Paris 5 ème
Laboratoire de Thermodynamique des milieux ioniques et biologiques
43 rue Cuvier - Paris 5 ème

SOMMAIRE

La détermination de la salinité des échantillons de l'eau de mer à partir des mesures conductimétriques soulève le problème de la contribution de chaque espèce ionique présente, à la conductivité électrique globale.

Les résultats expérimentaux obtenus par addition d'un électrolyte à l'eau de mer montrent que cette contribution varie notablement avec la nature de l'électrolyte, ce qui permet de prévoir une incertitude sur les valeurs de la salinité obtenue dans les mesures de routine lorsque la loi de Dittmar n'est pas rigoureusement vérifiée. La méthode expérimentale utilisée conduit à déterminer les conductivités équivalentes partielles des principaux constituants salins de l'eau de mer, même dans le cas des sels hydratés ou thermiquement instables.

1 . INTRODUCTION

La salinité S°/₀₀ demeure l'un des paramètres fondamentaux sur lequel repose encore l'identification des masses d'eau de l'océan mondial et l'évaluation de la densité utilisée en hydrodynamique marine. Actuellement les salinomètres basés sur la détermination de la conductivité $\varkappa$ sont universellement employés dans les mesures de routine, car cette grandeur est étroitement liée à la composition ionique du milieu.

Si la loi de Dittmar était rigoureuse, il existerait un rapport constant entre les concentrations des différentes espèces ioniques et la salinité ; les anciennes mesures de chlorinité auraient alors permis d'estimer la salinité avec une grande précision. Mais cette loi n'est qu'approchée et la conductivité est beaucoup plus étroitement corrélée à la salinité que la chlorinité (Cox et coll. 1962[1]). Toutefois la correspondance $\varkappa \rightarrow$ S°/₀₀ S°/₀₀ $\rightarrow \varkappa$ n'étant pas biunivoque, des échantillons de salinités différentes peuvent avoir même conductivité, de même que des eaux ne présentant pas exactement la même conductivité pourraient avoir la même salinité.

Afin de recueillir des informations précises à partir de la mesure de la conductivité $\varkappa$, il est donc de première nécessité de déterminer avec exactitude la manière dont elle varie en fonction de la teneur de l'eau de mer en ses principaux constituants. Le travail présenté ici a trait à l'étude de cette importante question.

Dans l'hypothèse où l'on considère un échantillon d'eau de mer artificielle obtenue par dissolution de j électrolytes dans l'eau on peut, avec Lewis[2], introduire la conductivité molaire partielle du sel i par

$$(1) \qquad \Lambda_i = \left(\frac{\partial L}{\partial n_i}\right)_{P,T,n_i',n_{eau}}$$

où L désigne la conductance de l'eau de mer et n le nombre de moles de ses divers constituants.

La conductivité molaire partielle du constituant eau s'exprime dans ces conditions par

$$(2) \qquad \Lambda_{eau} = \left(\frac{\partial L}{\partial n_{eau}}\right)_{P,T,n_i}$$

Ces grandeurs représentent le taux de variation de la conductance de l'échantillon considéré rapporté à une mole de chaque constituant.

2 . CONSIDERATIONS THEORIQUES

Dans l'étude des conductivités molaires partielles le cas des systèmes à constituants multiples peut être extrapolé à partir de considérations sur les systèmes binaires.

D'une part en électrochimie on définit la conductivité molaire $\Lambda_{élect.}$ d'une solution aqueuse d'un sel indépendamment de la présence du solvant par

$$(3) \qquad \Lambda_{élect} = \frac{1000\,\varkappa}{C}$$

où C désigne la concentration molaire du sel.

D'autre part on peut définir par la même solution la conductivité molaire thermodynamique Λ par

$$(4) \qquad \Lambda = \frac{L}{n_1 + n_{eau}}$$

où n est le nombre de moles de chacun des 2 constituants.

Si L est la conductance mesurée sur un volume V(cm^3) d'électrolyte placé entre 2 électrodes planes de grande surface distantes de 1cm, on a

$$(5) \qquad L = \varkappa V$$

et L est une grandeur extensive au sens thermodynamique.

Il s'ensuit que

$$(6) \qquad L = n_1 \Lambda_{élect} = (n_1 + n_{eau})\Lambda$$

et

$$(7) \qquad \Lambda = N_i \Lambda_{élect} \ ,$$

si $N_1 = \dfrac{n_1}{n_1 + n_{eau}}$ est la fraction molaire du sel.

En utilisant les définitions des conductivités molaires partielles (éq.(1) et(2)) on obtient d'une part(3)

$$(8) \qquad \begin{cases} \bar{\Lambda}_1 = \Lambda + (1 - N_1)\dfrac{\partial \Lambda}{\partial N_1} \\ \bar{\Lambda}_{eau} = \Lambda + (1 - N_{eau})\dfrac{\partial \Lambda}{\partial N_{eau}} \end{cases}$$

et d'autre part

$$(9) \qquad \begin{cases} \bar{\Lambda}_1 = \Lambda_{élect} + (1 - N_1)(1 - N_{eau})\dfrac{\partial \Lambda_{élect}}{\partial N_1} \\ \bar{\Lambda}_{eau} = (1 - N_{eau})^2 \dfrac{\partial \Lambda_{élect}}{\partial N_{eau}} \end{cases}$$

Si la concentration est définie en salinité par

$$S = \frac{n_1 M_1 \times 1000}{n_1 M_1 + n_{eau} M_{eau}} ,$$

M étant la masse molaire de chacun des 2 constituants, on obtient

$$(10) \qquad \begin{cases} \bar{\Lambda}_1 = \Lambda + M_1(1000 - S)\dfrac{\partial \Lambda}{\partial S} \\ \bar{\Lambda}_{eau} = \Lambda - M_{eau} S\left(S + 1 - \dfrac{S}{1000}\right)\dfrac{\partial \Lambda}{\partial S} \end{cases}$$

et

$$(11) \qquad \begin{cases} \bar{\Lambda}_1 = \Lambda_{élect} + \dfrac{S}{1000}(1000 - S)\dfrac{\partial \Lambda_{élect}}{\partial S} \\ \bar{\Lambda}_{eau} = -\dfrac{M_{eau} S^2}{1000 M_1}\dfrac{\partial \Lambda_{élect}}{\partial S} \end{cases}$$

L'échantillon d'eau de mer étant considéré comme un système à $j+1$ constituants (solution aqueuse de j sels), les conductivités molaires sont alors données par

$$(3') \qquad \Lambda_{élect} = \frac{1000\,\kappa}{\sum_i C_i}$$

où C_i est la concentration molaire du sel i, et

$$(4') \qquad \Lambda = \frac{L}{\sum_i n_i + n_{eau}}$$

de sorte que

$$(6') \qquad L = \sum_i n_i \Lambda_{élect} = \left(\sum_i n_i + n_{eau}\right)\Lambda$$

et

$$(7') \qquad \Lambda = \sum_i N_i \Lambda_{élect}$$

Un calcul identique à celui développé pour les mélanges binaires conduit à

$$(8') \qquad \begin{cases} \bar{\Lambda}_i = \Lambda + (1 - N_i)\dfrac{\partial \Lambda}{\partial N_i} \\ \bar{\Lambda}_{eau} = \Lambda + (1 - N_{eau})\dfrac{\partial \Lambda}{\partial N_{eau}} \end{cases}$$

et à

$$(9') \qquad \begin{cases} \bar{\Lambda}_i = \Lambda_{élect} + (1 - N_i)(1 - N_{eau})\dfrac{\partial \Lambda_{élect}}{\partial N_i} \\ \bar{\Lambda}_{eau} = (1 - N_{eau})^2 \dfrac{\partial \Lambda_{élect}}{\partial N_{eau}} \end{cases}$$

Ces relations montrent que, conformément aux idées de Gibbs, l'échantillon envisagé en tant que système à constituants multiples se comporte comme un mélange binaire.

Si on utilise la définition de la salinité

$$(12) \qquad S = \frac{\sum_i n_i M_i \times 1000}{\sum_i n_i M_i + n_{eau} M_{eau}}$$

les relations obtenues sont très complexes et peu maniables.

Le problème que nous nous sommes posé se ramène donc à la détermination des conductivités partielles et les valeurs obtenues seront données dans le paragraphe 4.

3 . METHODE EXPERIMENTALE

3.1 Montage expérimental

Nos mesures de conductance ont été faites à l'aide d'un pont de Kohlrausch qui, dans le domaine de concentration exploré présente une sensibilité de l'ordre de $2.10^{-2}(\mu\Omega)^{-1}$. Cette sensibilité nous imposait une stabilisation de la température de l'ordre de quelques millièmes de degré C. Pour atteindre ce résultat un bain thermostatique à deux étages a été réalisé. La régulation du premier étage, soigneusement calorifugé, est obtenue par chauffage intermittent, commandé par un thermomètre à contact, du liquide de circulation. Ce dernier est soumis en permanence à un apport continu de froid.

Le premier étage assure la stabilité thermique d'un récipient en laiton rempli d'huile de faible constante diélectrique contenant la cellule de mesure et qui constitue le second étage du bain thermostatique.

Ce procédé assure avec une efficacité suffisante l'amortissement des oscillations thermiques à l'intérieur de la cellule de mesure.

La cellule utilisée dont les électrodes étaient platinées suivant la méthode de Jones et Bollinger(1935)(4), a été associée à un erlenmeyer de un litre formant réservoir (cf. paragraphe 3.2).

3.2 Technique de mesure

Nous avons dans un premier temps vérifié la méthode de Connors et Weyl (1968)(5). Pour obtenir la conductivité équivalente partielle Λ_i de l'électrolyte i, des masses connues du sel dissous dans l'eau de mer de référence sont successivement ajoutées à un même échantillon de cette eau de mer. Des variations $\Delta\varkappa_i$ correspondant au nombre d'équivalents Δn_i ajouté, on déduit alors Λ_i par la formule

$$(13) \qquad \Lambda_i = \varkappa \bar{v}_i + v\left(\frac{\Delta\varkappa_i}{\Delta n_i}\right)_{n_i \to 0}$$

où v et $\bar{v}_i$ sont respectivement le volume massique de l'eau de mer de référence et le volume équivalent partiel du sel i dans cette eau de mer. Les volumes sont calculés par la méthode de Duedall et Weyl (1963)(6).

La méthode de Connors ne va pas sans inconvénients, notamment lorsqu'il faut faire appel aux sels hygroscopiques ou thermiquement instables. Nous avons préféré introduire des masses connues d'une solution aqueuse préalablement dosée d'un sel (solution primaire) dans un même échantillon d'eau de mer de référence, ce qui revient à ajouter Δn_i équivalent du sel i et Δn_{eau} équivalent d'eau par gramme d'eau de mer de référence.

La conductance d'un gramme d'eau de mer se déduit de la relation (5) et s'écrit

$$(14) \qquad \mathcal{L} = \varkappa v \quad .$$

A pression et température constantes on a

$$d\mathcal{L} = \frac{\partial \mathcal{L}}{\partial n_i} dn_i + \frac{\partial \mathcal{L}}{\partial n_{eau}} dn_{eau}$$

et

$$d\mathcal{L} = d(\varkappa v) = v\, d\varkappa + \varkappa\left[\frac{\partial v}{\partial n_i} dn_i + \frac{\partial v}{\partial n_{eau}} dn_{eau}\right]$$

d'où l'on tire

$$(15) \qquad \Lambda_i = v\frac{d\varkappa}{dn_i} + \varkappa \bar{v}_i + \left[\varkappa \bar{v}_{eau} - \Lambda_{eau}\right]\frac{dn_{eau}}{dn_i} \quad .$$

De la même manière on trouve

$$(16) \qquad \Lambda_{eau} = v\frac{d\varkappa}{dn_{eau}} + \varkappa \bar{v}_{eau} \quad .$$

Si (m_i) est la molalité de la solution du sel i d'électrovalence z_i ajouté à l'eau de mer, on a

$$\frac{dn_i}{dn_{eau}} = \frac{1000}{(m_i)\, z_i}$$

et l'équation (15) devient

$$(17) \qquad \bar{\Lambda}_i = v\frac{d\varkappa}{dn_i} + \varkappa \bar{v}_i + \left[\varkappa \bar{v}_{eau} - \bar{\Lambda}_{eau}\right] \frac{1000}{(m_i)z_i}.$$

Les valeurs de v, $\bar{v}_{eau}$ et $\bar{v}_i$ ont été déduites des résultats de Duedall et Weyl (1967)[6]. On a également utilisé la méthode de Millero (1969)[7] pour estimer les valeurs de $\bar{v}_i$.

L'eau de mer artificielle employée dans les expériences, a été préparée suivant le procédé préconisé par Kester et coll. (1967)[8] selon la formule de Lyman et Fleming (1940)[9]. Les salinités ont été déterminées à l'aide d'un "thermostat salinity meter" N.I.O.

4 . RESULTATS ET DISCUSSION

Dans le tableau I nous avons rassemblé les résultats obtenus dans la détermination des conductivités équivalentes partielles $\bar{\Lambda}_i$ des principaux électrolytes qui entrent dans la composition de l'eau de mer artificielle.

Tableau I

1 électrolyte	2 $\bar{v}_i$ Duedall	3 $\bar{v}_i$ Millero	4 $\bar{\Lambda}_i$ (éq.17) $\bar{v}_i$ Duedall $cm^2\ \Omega^{-1}éq^{-1}$	5 $\bar{\Lambda}_i$ (éq.17) $\bar{v}_i$ Millero $cm^2\ \Omega^{-1}éq^{-1}$
NaCl	18,90	16,60	79,0	78,9
NaBr		23,50		82,3
NaF		-2,30		35,5
$NaHCO_3$	27,07	21,70	40,0	39,8
KCl	29,20	26,80	100,8	100,7
KBr		33,70		104,7
$KHCO_3$	37,38	31,90	61,7	61,3
$MgCl_2$	9,81	7,25	63,9	63,8
$CaCl_2$	11,00	8,85	67,9	67,9
$SrCl_2$		8,95		67,4
Na_2SO_4	10,52	5,75	44,7	44,4
K_2SO_4	20,82	15,95	67,9	67,6
$MgSO_4$	1,43	-3,60	29,0	28,8

Les volumes équivalents partiels qui interviennent dans nos calculs (cf. éq.(17)) figurent dans les colonnes 2 et 3 et permettent, sur la base de nos données expérimentales d'atteindre les valeurs des $\bar{\Lambda}_i$ des colonnes 4 et 5.

L'ensemble de ces résultats appelle plusieurs remarques :

a) Une imprécision relativement grande sur l'appréciation des volumes équivalents partiels des électrolytes (cf. colonnes 4 et 5) ne retentit pas d'une manière notable sur les conductivités partielles et ne dépassent pas en importance les erreurs de mesure.

b) D'une manière générale, l'erreur commise sur les déterminations expérimentales demeure de l'ordre de grandeur de celles que signalent Connors et Weyl[5] dans leur propre expérimentation.

c) Une comparaison significative de nos résultats avec l'ensemble des travaux effectués dans le même domaine, notamment ceux de Connors et Weyl[5], ou dans des domaines connexes ne peut être envisagée que dans le cadre d'une analyse détaillée des mesures

directes liée à l'établissement de formules de lissage. Cette question, qui ne peut être abordée ici, sera présentée dans une publication ultérieure.

Dans le tableau II on a calculé les différences des conductivités équivalentes partielles des électrolytes possédant un ion commun. Pour chaque couple d'ions comparés, on obtient un ordre de grandeur bien caractéristique de ce couple, lequel constitue une fraction souvent très conséquente des conductivités équivalentes partielles propres des électrolytes envisagés.

Ce résultat important justifie l'intérêt que l'on doit porter à l'étude du problème que nous avons abordé ici, à savoir de l'influence des écarts à la loi de Dittmar sur la conductivité globale mesurée, eu égard aux informations que l'on a pris l'habitude d'en tirer sur la composition de l'eau de mer.

Tableau II

	$\bar{\Lambda}_i$ $\pm$0,5éq. $\bar{v}_i$ Duedall	$\bar{\Lambda}_i$ $\pm$0,5éq. $\bar{v}_i$ Millero
$\bar{\Lambda}(K^+-Na^+)Br^-$		22,4
$\bar{\Lambda}(K^+-Na^+)Cl^-$	21,8	21,8
$\bar{\Lambda}(K^+-Na^+)SO_4^{2-}$	23,2	23,2
$\bar{\Lambda}(K^+-Na^+)HCO_3^-$	21,7	21,5
$\bar{\Lambda}(Mg^{2+}-Na^+)Cl^-$	-15,1	-15,1
$\bar{\Lambda}(Mg^{2+}-Na^+)SO_4^{2-}$	-15,7	-15,6
$\bar{\Lambda}(SO_4^{2-}-Cl^-)Na^+$	-34,3	-34,5
$\bar{\Lambda}(SO_4^{2-}-Cl^-)K^+$	-32,9	-33,1
$\bar{\Lambda}(SO_4^{2-}-Cl^-)Mg^{2+}$	-34,9	-35,0
$\bar{\Lambda}(HCO_3^-Cl^-)Na^+$	-39,0	-39,1
$\bar{\Lambda}(HCO_3^-Cl^-)K^+$	-39,1	-39,4

Notons pour terminer que la comparaison effectuée ici sur des couples de grandeurs expérimentales semble, aux erreurs d'expérience près, beaucoup plus significative que celle faite à partir de grandeurs issues de formules de lissage (Connors et Weyl)(5). Toutefois ce travail n'est en fait qu'une étape dans l'étude du problème posé car il est évident que c'est au niveau des conductivités ioniques partielles, problème non encore résolu de manière satisfaisante dans les mélanges à composants multiples, que les renseignements que l'on pourra recueillir seront les plus instructifs.

Bibliographie

1. Cox R.A., Culkin F., Greenhalgh R. and Riley J.P. Chlorinity, Conductivity and Density of sea water. Nature 193, (1962), 578-520.

2. Lewis G.N. and Randall .Thermodynamics . 2nd edition (1961).

3. Mehta O.P., Lantelme F. et Chemla M. Electrochimica Acta, 14, (1969), 505-513

4. Jones G., Bollinger D.M. The measurement of the conductance of the electrolytes. VII. On platinization. J. of Am. Soc. 57, (1935) 280-284.

5. Connors D.N., Weyl P.K. The partial equivalent conductances of salts in sea water and the density/conductance relationship.. Limnology and Oceanography 13, (1968) 39-50.

6. Duedall I.W. and Weyl P.K. The partial equivalent volume of salts in sea water. Limnology and Oceanography 12, (1967) 52-59.

7. Millero F.J. The partial molal volume of ions in sea water. Limnology and Oceanography 14, (1969) 376-385.

8. Kester D.R., Duedall I.W., Connors D.N., Pytkowicz R.M. Preparation of artificial sea water. Limnology and Oceanography 12, (1967) 176-179.

9. Lyman . and Fleming R.H. Composition of sea water. J. of Marine research 3, (1940) 134-146.

MAGNETOHYDRODYNAMIC WAVE PHENOMENA IN SEA WATER

by

George I. Cohn

Prof. of Engineering, Calif. State College, Fullerton

SUMMARY

The various types of waves which can propagate in any media depends on the types of energy storage modes which the media can support and on the physical mechanisms available by which energy can be exchanged between the different energy storage modes. A different type of wave is supported by each combination of energy storage modes for which two-way energy exchange mechanisms exist. The greater the number of different energy storage modes which can interact the more complex the wave.

In the ocean medium the energy storage modes available are the :

1) electric field, 2) magnetic field, 3) mass density velocity field, 4) pressure field and 5) gravity field. The simplest types of waves consist of dual energy interchange between only two types of energy storage modes. The dual interchange of energy between the electric field and the magnetic field via electromagnetic and magnetoelectric induction comprises an ordinary electromagnetic wave. The dual interchange of energy between the pressure field and velocity field via Newton's law constitutes an ordinary sonic wave. The simplest MHD waves, Alfven waves, consist of the dual interchange of energy between the mass density velocity field and the magnetic field via action described by Ampere's law, Newton's law, Ohm's law and Faraday's law.

Simultaneous transference of energy between pressure, magnetic and kinetic energy storage modes constitutes magnetic ionic sound waves or magneto-hydrodynamic sound waves and between pressure, electric and kinetic energy storage modes constitutes electroionic sound waves or electrohydrodynamic waves. Simultaneous interactions of all four energy modes gives still more general magnetoelectrohydrodynamic waves.

In normal ocean type conditions the gravitational energy storage mode interacts significantly at a surface. Hence an even richer variety of surface waves are possible.

This initial phase of this paper will present the energy storage mode interaction mechanisms in a form which graphically illustrates the processes occurring in wave propagation in each case. The second phase will be concerned with the wavelength and attenuation frequency characteristics. The third phase is concerned with methods of generation and detection.

SOMMAIRE

Les divers types d'ondes susceptibles de se propager dans un milieu quelconque dépendent des modes d'accumulation d'énergie que ce milieu peut abriter et des mécanismes physiques existants permettant des échanges d'énergie entre les différents modes d'accumulation d'énergie. Un type d'onde différent est porté par chaque combinaison de modes d'accumulation d'énergie comportant des mécanismes d'échange d'énergie dans les deux sens. Plus le nombre de modes différents d'accumulation d'énergie susceptibles d'interactions est élevé, plus l'onde est complexe.

Les formes dans lesquelles l'énergie se manifeste dans le milieu marin sont les suivantes :

1) champ électrique, 2) champ magnétique, 3) champ de vitesse de la densité de matière, 4) champ de pression et 5) champ de gravité. Les types d'ondes les plus simples consistent en double échange d'énergie entre deux types seulement de modes d'accumulation d'énergie. Le double échange d'energie entre champ électrique et champ magnétique, par l'intermédiaire de l'induction électromagnétique et magnéto-électrique constitue une onde électromagnétique ordinaire. Le double échange d'énergie entre le champ de pression et le champ de vitesse, par l'intermédiaire de la loi de Newton, constitue une onde sonique ordinaire.

Les ondes magnétohydrodynamiques les plus simples (ondes Alfven) consistent en un double échange d'énergie entre le champ de vitesse de densité massique et le champ magnetique par l'intermédiaire du processus décrit par la loi d'Ampère, la loi de Newton, la loi d'Ohm et la loi de Faraday.

Le transfert simultané d'énergie entre les modes d'accumulation d'energie par pression, magnétique et cinétique, donne lieu à des ondes sonores magnéto-ioniques, ou magnétohydrodynamiques ; le type de transfert, entre les modes d'accumulation d'énergie électrique et cinétique donne lieu à des ondes sonores électro-ioniques ou électro-hydrodynamiques. Des interactions simultanées de ces quatre modes d'énergie donnent naissance à des ondes magnétoélectro-hydrodynamiques encore plus générales.

Dans les conditions océaniques normales, le mode d'accumulation d'énergie gravitationnelle est caractérisé par des interactions considérables en surface. Il est donc possible de trouver une gamme encore plus étendue d'ondes de surface.

Au cours de la première partie de cet exposé, l'auteur presentera le mecanisme d'interaction des modes d'accumulation d'énergie sous une forme qui illustre graphiquement les processus survenant, dans chaque cas, au cours de la propagation des ondes. La seconde partie sera consacrée aux caractéristiques de fréquence des longueurs d'ondes et du phénomène de l'atténuation. Au cours de la troisième partie, l'auteur exposera les méthodes de production et de détection.

MAGNETOHYDRODYNAMIC WAVE PHENOMENA IN SEA WATER

George I. Cohn

Prof. of Engineering, Calif. State College, Fullerton

1. Introduction

The waves which can propagate in a media depend on the types of energy storage modes which the media can support and on the physical mechanisms available by which energy can be exchanged between the different energy storage modes. A different type of wave is supported by each combination of energy storage modes for which two-way energy exchange mechanisms exist. The greater the number of different energy storage modes which can interact the more complex the wave.

In the ocean medium the energy storage modes available are the: 1) electric field, 2) magnetic field 3) mass density velocity field, 4) pressure field and 5) gravity field. The simplest types of waves consist of dual energy interchange between only two types of energy storage modes. The dual interchange of energy between the electric field and the magnetic field via electromagnetic and magnetoelectric induction comprises an ordinary electromagnetic wave as depicted in Fig. 1. The dual interchange of energy between the pressure field and velocity field via Newton's law constitutes an ordinary sonic wave. The simplest MHD waves, Alfven waves, consists of the dual interchange of energy between the mass density velocity field and the magnetic field via action described by Ampere's law, Newton's law, Ohm's law and Faraday's law.

Simultaneous transference of energy between pressure, magnetic and kinetic energy storage modes constitutes magnetic ionic sound waves or magnetohydrodynamic sound waves as depicted in Fig. 2. Simultaneous transfer of energy between pressure, electric and kinetic energy storage modes constitutes electronic sound waves or electrohydrodynamic waves. Simultaneous interactions of all four energy modes give still more general magnetoelectronydrodynamic waves.

The objective of this paper is in part tutorial and in part to broaden the conference scope (consideration of electromagnetic waves in the ocean medium) by considering the broader variety of waves which can be generated by the interchange of energy between a greater variety of energy storage modes. Physical descriptions of the basic interactions that provide a qualitative comprehension of the wave phenomena are given in the next two sections for the most basic MHD wave types. This is followed by a more quantitative development of the properties of the more general MHD wave.

2. Alfven Waves

Idealized Alfven waves can only exist in a perfectly conducting incompressible media immersed in a DC magnetic field. If the media is highly conducting and relatively incompressible a good approximation to the idealized Alfven wave can exist. In this type of wave there is a mutual interchange of stored energy between the AC magnetic field and the mass velocity field. If the fluid medium were compressible, a sonic type wave may also exist, in which case a more involved magnetohydrodynamic wave would result.

An understanding of the waves can be provided from a number of different viewpoints, of which two are stressed here. Comprehension of cause and effect on an intensive or local basis is facilitated by the flow graph equation format depicted in Fig. 3. Physical visualization of the extensive phenomena comprising Alfven wave propagation is facilitated by the sequence of sketches in Fig. 4.

Alfven waves (Fig. 3) can be explained by two cause and effect loops which have Ohm's law as their common causal link. Although the explanation can start at any point, consider first the current density and the upper loop. The applied magnetic field, B_0, exerts force on the current density. This electric motor type force accelerates the fluid, thereby giving it a velocity u. The conducting fluid moving thru the applied magnetic field creates a Lorentz force (motionally induced electromotance intensity) on the charge carriers in the conducting fluid. This electric generator type distributed voltage, $u \times B_0$, causes part of the current density, as described by Ohm's law. Next consider the lower causal loop. The current density, $\hat{n}, j$ duces a variable magnetic field, B_1, as dictated by Ampere's law. The time-varying magnetic field produces an electric field, E, as described by Faraday's electromagnetic induction law. This electric field causes another part of the current density, as described by Ohm's law. The idealized Alfven wave occurs if the conductivity is essentially infinite. In this case a negligible fraction of the induced electromotance intensity is consumed by the ohmic drop and hence the electromagnetically generated electric field intensity is essentially equal and opposite to the motionally induced electromotance intensity. Applying small signal theory in the simultaneous solution for the monochromatic plane wave gives the Alfven wave as propogating in the direction of the applied magnetic field with speed

$$(1) \qquad V = \frac{B_0}{\sqrt{\mu\rho}}$$

in terms of the inductivity μ, mass density ρ, and applied magnetic field B_0. For the case of sea water, with a mass density of approximately 1,000 kg per m^3 and the earth's field of approximately ½ Gauss or $\frac{1}{2} \times 10^{-4}$ weber/m^2, the Alfven speed is slightly greater than one mm per second. It should be noted that the conductivity of sea water is moderately low, approximately 4 mhos/m, hence the ocean does not provide the conditions for idealized Alfven waves. Nevertheless the idealized case provides a very instructive basis for comprehending the more complicated cases.

The flow graph only provides an intensive type explanation of Alfven waves, i.e., in terms of simultaneous relationships between field quantities at a point. An extensive explanation is required in order to visualize how the field propagates. This is facilitated by Fig. 4. To accomplish this explanation

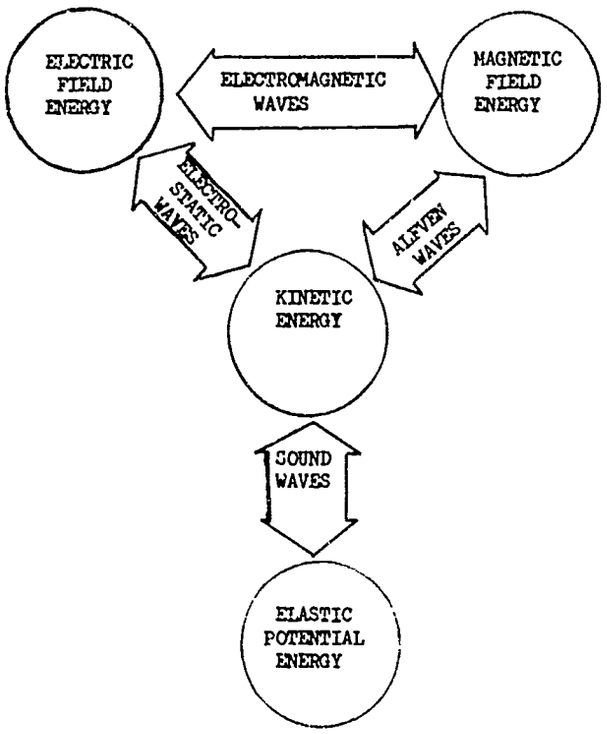

FIG. 1 WAVES BASED ON ENERGY INTERCHANGE BETWEEN TWO ENERGY STORAGE MODES

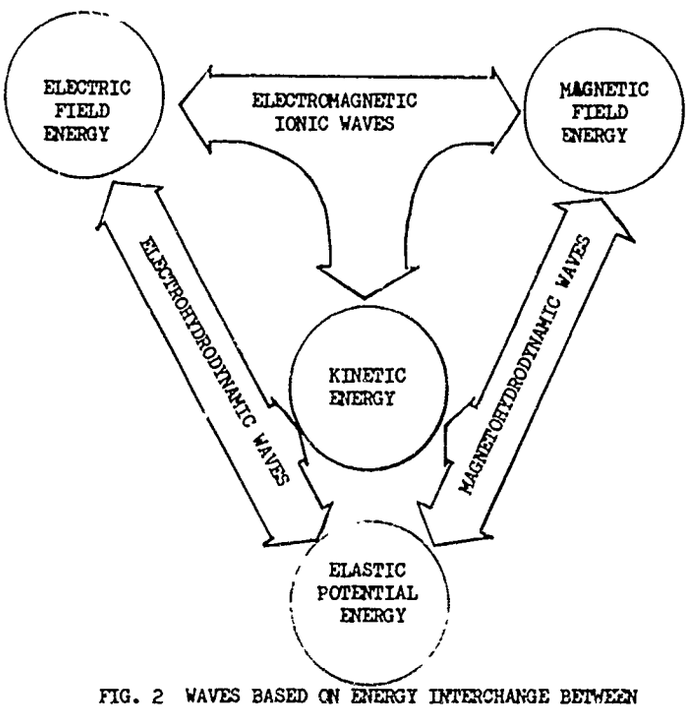

FIG. 2 WAVES BASED ON ENERGY INTERCHANGE BETWEEN THREE ENERGY STORAGE MODES

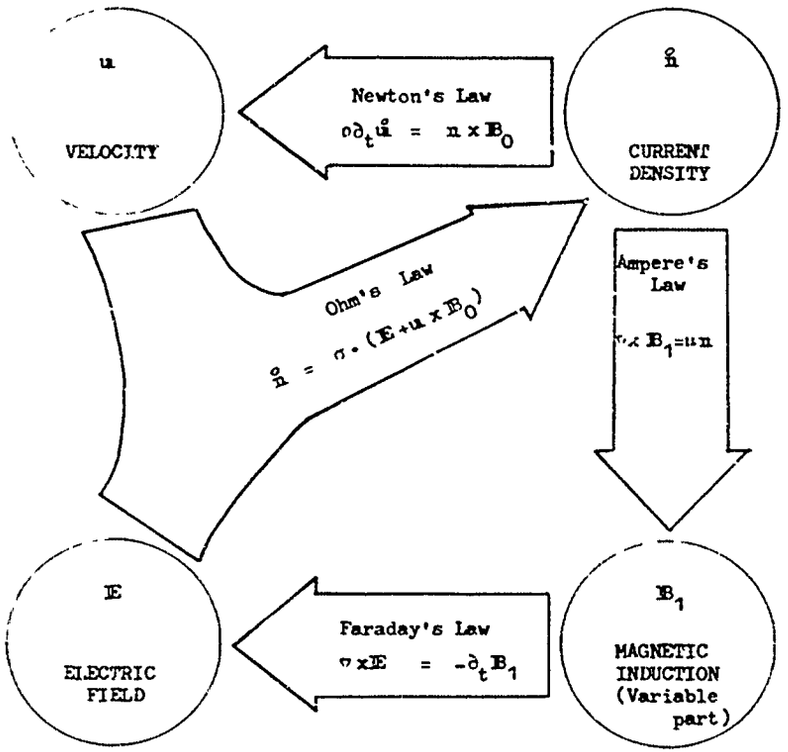

Fig. 3. Alfven Wave Intensive Causality Flow Graph

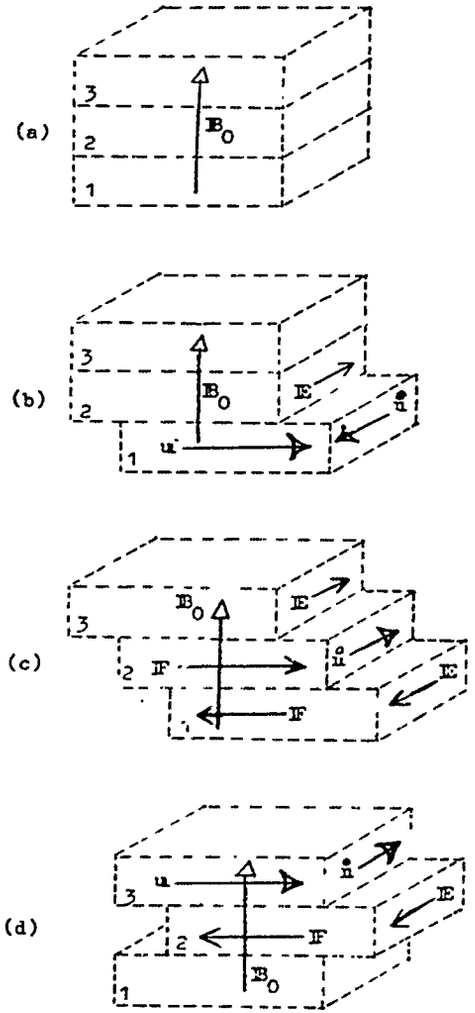

Fig. 4. Extensive Causality Slab Motion Model for Alfven Waves

with a reasonable economy of figures and words, the volume of space is subdivided into thin parallel slabs which are perpendicular to the direction of propagation, which is upward in Fig. 4. Of the variety of ways in which the wave can be initiated consider mechanical displacement of the lowest slab, slab-1, as depicted in Fig. 4b. The motion of slab-1 thru the applied magnetic field generates a Lorentz force on the charge carriers which produces a current in slab-1 (Fig. 4b). The applied magnetic field exerts a force on the current in slab-1, which opposes the applied driving force. The induced current in slab-1 varies with time and hence the time varying magnetic field it produces in slab-2, generates an electric field in slab-2, which drives a current in slab-2 in the opposite direction to the initial current in slab-1. The current in slab-2 produces a force on slab-2 which drives it to the right as depicted in Fig. 4c. The motion of slab-2 to the right generates a Lorentz force which bucks the electric field and hence reduces the current in slab-2. This varying current in slab-2, as well as that in slab-1, produces a varying magnetic field which extends into slab-3 and generates an electric field there. This electric field produces a current in slab-3 which produces a force on slab-3 thereby causing it to accelerate to the right as depicted in Fig. 4d. This is the manner in which the fields propagate along the direction of the applied magnetic field. In the course of propagation the currents produced in successive slabs have also reacted back on the previous slabs to decelerate their motions and cause them to be displaced in the opposite direction. Thus, the propagation phenomena is oscillatory.

The Alfven wave has been classified here as only involving two energy storage modes. The average energy stored in the variable magnetic field is equal to the average energy stored in the kinetic energy field. Since the Alfven wave requires an electric field for its existence, and since energy is stored in an electric field, it might appear reasonable to classify Alfven waves as a three energy storage mode type. However, the average energy stored in the electric field is negligible since it is smaller than the kinetic energy by a factor equal to the square of the ratio of the Alfvens wave speed to the speed of light,

$$(2) \qquad w_E = \frac{A^2}{c^2} w_k$$

Hence Alfven waves are classified as a two energy storage mode type of wave.

3. Transverse Magnetosonic Waves

Magnetosonic waves can be supported by a conducting compressible media with an impressed magnetic field. Such waves involve the interchange of energy between three types of energy storage modes: magnetic, kinetic and elastic. Magnetosonic waves can be considered as sonic waves whose characteristics are modified by the presence of the magnetic field and the conductivity of the media. The flow graph for sonic waves is given in Fig. 5. The speed of small amplitude monochromatic waves is given in terms of the bulk modulus K and the density ρ_0 by

$$(3) \qquad c = \sqrt{\frac{K}{\rho_0}} \quad .$$

The flow graph for magnetosonic waves is the composite of Figs. 3 and 5 obtained by superimposing the velocity in Fig. 3 on the velocity in Fig. 5. Understanding propagation of a magnetosonic wave by first considering propagation of an ordinary sound wave as provided by the slab model depicted in Fig. 6. The space is divided into parallel slabs which are perpendicular to the direction in which the wave propagates, which in Fig. 6 is to the right.

This illustration is restricted to the case of propagation perpendicular to the applied magnetic field. Understanding the magnetosonic wave is easily achieved by examining how the magnetic field modifies the ordinary sonic wave. The sonic wave can be considered as being initiated by applying a force to slab-1 which slightly compresses it, giving a velocity to the mass in slab-1, as depicted in Fig. 6b. The pressure increase in slab-1 exerts a force on slab-2 moving its material contents to the right. The pressure in slab-2 is thus increased. As slab-1 expands its pressure decreases, Fig. 6c. The increased pressure in slab-2 exerts a force on slab-3, and in turn slab-3 becomes compressed, Fig. 6d. This mode of pressure, velocity and density propagation is a sonic type wave.

Now reconsider this sonic wave in a conductive medium with an applied dc magnetic field as depicted in Fig. 7. The velocity, density, and pressure propagation picture is essentially the same as for the pure sonic wave except that the magnetic field produces a Lorentz force on the charge carriers. The force exerted by the applied magnetic field on the resulting current in the moving slab opposes the driving force, thereby making the slab appear stiffer than that due to compression of the material alone. The induced current in slab-1 produces a magnetic field in slab-2 which varies with time. This time-varying magnetic field generates an electric field in slab-2 which causes a current as shown in Fig. 7b. The applied magnetic field exerts a force on this current which acts in the same direction as the wave is propagating and acts in advance of the arrival of the kinetic pressure. Thus the magnetic field impressed on a sonic wave in a conducting medium makes the wave propagate faster.

The spatial relationship between the field components for an Alfven wave and a transverse magnetosonic wave are depicted in Fig. 8.

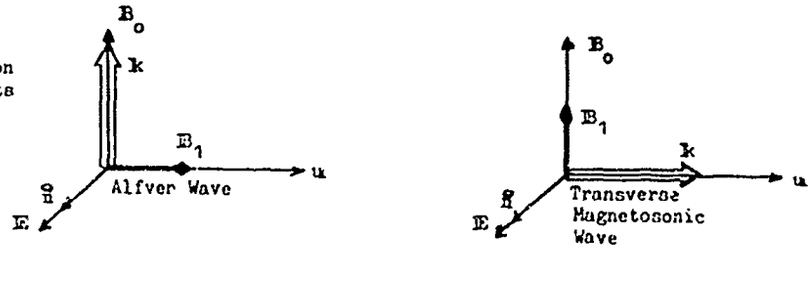

Fig. 8 Orientation of Field Components

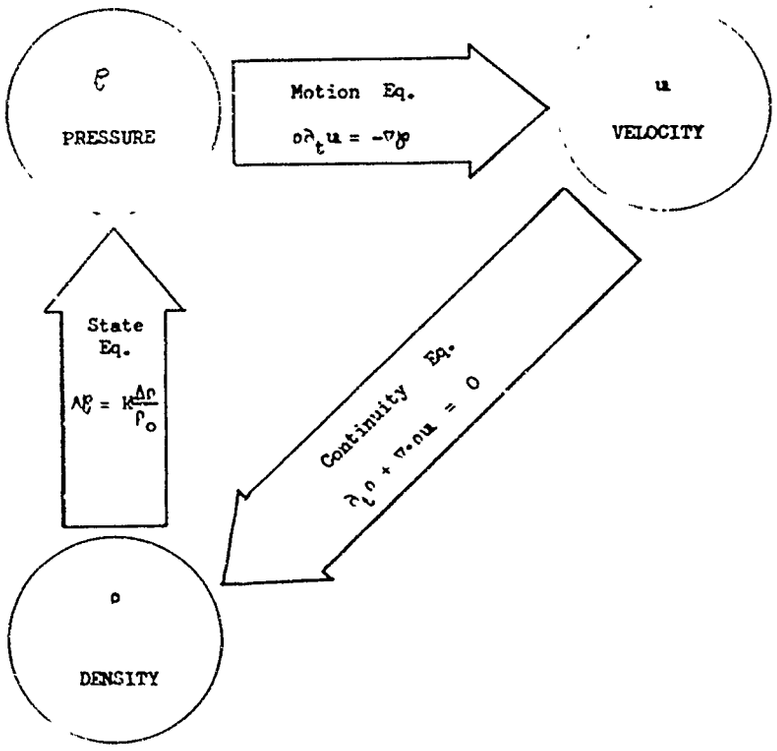

Fig. 5. Sonic Wave Causality Flow Graph

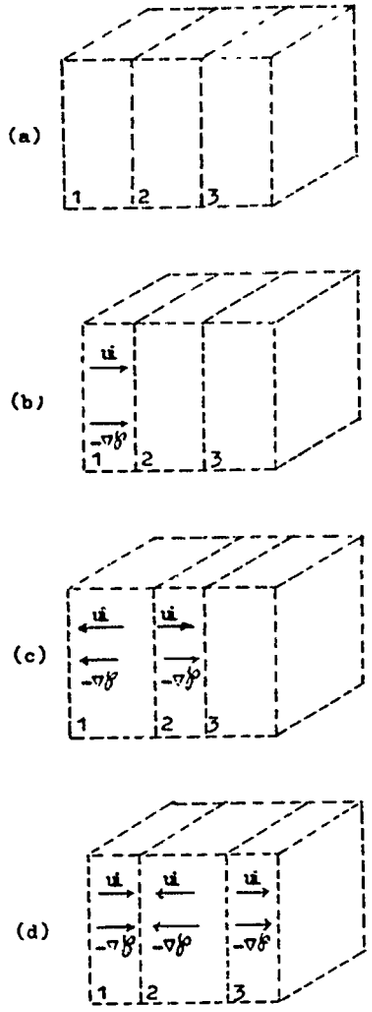

Fig. 6. Extensive Causality Slab Motion Model for Sonic Compression Waves

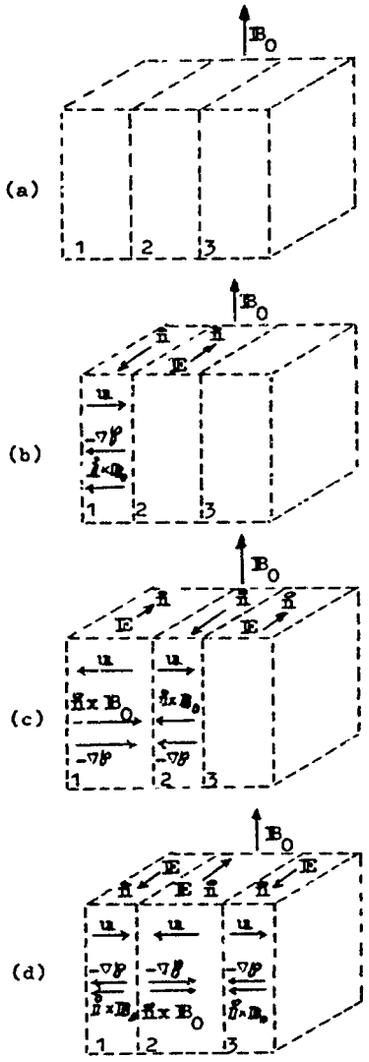

Fig. 7. Extensive Causality Slab Motion Model for Transverse Magnetosonic Waves

4. Magnetohydrodynamic Waves

The field equations for magnetohydrodynamic waves are solved for all directions of propogation of the waves with respect to the earth's magnetic field, in Appendix A. There are three types of MHD waves which exist that are slight modifications of the elementary acoustic shear wave, acoustic compression wave, and the electromagnetic eddy current wave. The speeds and attenuation factors for these waves are distinguished by the use of the subscripts s, c and e respectively. The dissipation mechanisms have a greater affect on the speeds and attenuation factors of the various modes than does the earth's magnetic field. As a consequence the first two terms in the power series expansion of the Alfven wave speed, A, of the phase speeds and attenuation factors provide adequate accuracy.

For graphical representation it is convenient to plot the two terms on separate graphs. The first term represents the particular mode in the absence of the earth's magnetic field and is designated by means of a subscript '0'. The second term gives the contribution to the MHD mode resulting from the presence of the earth's magnetic field and is designated by the subscript '2' since it is proportional to the square of the earth's magnetic field. For the acoustic shear type MHD wave (a91) and (A92) give

$$(4)\quad V_{s0} = \sqrt{2D}$$

$$(5)\quad \frac{V_{s2}}{V_{s0}} = \frac{A^2}{2}\,\frac{\cos^2\theta}{Q_c^2 - D}$$

$$(6)\quad \alpha_{s0} = \frac{\omega}{\sqrt{2D}}$$

and

$$(7)\quad \frac{\alpha_{s0}}{\alpha_{s0}} = \frac{A^2}{2}\,\frac{\cos^2\theta}{Q_c^2 - D}$$

where

- θ is the angle between the direction of propogation and the earth's magnetic field
- A is the Alfven wave speed
- Q is the electrical quality factor of sea water
- D is the viscosity dissipation factor see (A33)
- c is the speed of light in water
- C is the speed of sound in water .

For the acoustic compression type MHD wave (A93) and (A94) give

$$(8)\quad V_{c0} = C\Bigg/\sqrt{2\,\frac{1+\left(\frac{2D}{3C^2}\right)^2}{\sqrt{1+\left(\frac{2D}{3C^2}\right)^2}+1}}$$

$$(9)\quad \frac{V_{c2}}{V_{c0}} = \frac{A^2}{2}\,\frac{\sin^2\theta}{C^4+\left(Q_c^2-\frac{2D}{3}\right)^2}\left[C^2+\left(Q_c^2-\frac{2D}{3}\right)\sqrt{\frac{\sqrt{1+\left(\frac{2D}{3C^2}\right)^2}-1}{\sqrt{1+\left(\frac{2D}{3C^2}\right)^2}+1}}\right]$$

$$(10)\quad \alpha_{c0} = \frac{\omega}{C}\sqrt{\frac{1}{2}\,\frac{\sqrt{1+\left(\frac{2D}{3C^2}\right)^2}-1}{1+\left(\frac{2D}{3C^2}\right)^2}}$$

and

$$(11)\quad \frac{\alpha_{c2}}{\alpha_{c0}} = \frac{A^2}{2}\,\frac{\sin^2\theta}{C^4+\left(Q_c^2-\frac{2D}{3}\right)^2}\left[-C^2+\left(Q_c^2-\frac{2D}{3}\right)\sqrt{\frac{\sqrt{1+\left(\frac{2D}{3C^2}\right)^2}+1}{\sqrt{1+\left(\frac{2D}{3C^2}\right)^2}-1}}\right].$$

For the electromagnetic eddy current type or MHD wave (A95) and (A96) give

$$(12)\quad V_{e0} = \sqrt{2Q_c^2}$$

$$(13)\quad \frac{V_{e2}}{V_{e0}} = \frac{A^2}{2}\,\frac{C^4\cos^2\theta + \left(Q_c^2-\frac{D}{3}\right)C^2\sin^2\theta + \left(Q_c^2-\frac{2D}{3}\right)\left(Q_c^2-\frac{2D}{3}+\frac{D}{3}\sin^2\theta\right)}{(Q_c^2-D)\left[C^4+\left(Q_c^2-\frac{2D}{3}\right)^2\right]}$$

$$(14)\quad \alpha_{e0} = \frac{m}{\sqrt{2Qc^2}}$$

and

$$(15)\quad \frac{\alpha_{e2}}{\alpha_{e0}} = \frac{A^2}{2}\,\frac{C^4\cos^2\theta - \left(Qc^2-\frac{D}{3}\right)C^2\sin^2\theta + \left(Qc^2-\frac{2D}{3}\right)\left(Qc^2-\frac{2D}{3}+\frac{D}{3}\sin^2\theta\right)}{\left(Qc^2-D\right)\left[C^4+\left(Qc^2-\frac{2D}{3}\right)^2\right]}$$

In sea water the lossess and the speeds of the unmodified modes have only moderate ranges of values, consequently the primary independent variables over which graphs are desirable are the frequency and the propagation direction. As shown in Appendix A

$$(16)\quad D << Qc^2$$

and

$$(17)\quad \frac{2D}{3C^2} << 1 \quad \text{for } f < 10 \text{ terrahertz} \quad ,$$

hence the above expressions for the acoustic shear type MHD wave reduces to

$$(18)\quad V_{s0} = \sqrt{2D}$$

$$(19)\quad \frac{V_{s2}}{V_{s0}} = \frac{A^2\cos^2\theta}{2Qc^2}$$

$$(20)\quad \alpha_{s0} = \frac{m}{\sqrt{2D}}$$

$$(21)\quad \frac{\alpha_{s2}}{\alpha_{s0}} = \frac{A^2\cos^2\theta}{2Qc^2} \quad ,$$

the acoustic compression type MHD wave reduces to

$$(22)\quad V_{c0} = \left[C\left(1+\frac{3}{8}\left(\frac{2D}{3C^2}\right)^2\right)\right]$$

$$(23)\quad \frac{V_{c2}}{V_{c0}} = \frac{A^2\sin^2\theta}{2}\,\frac{C^2+\frac{DQc^2}{3C^2}}{C^4+Q^2c^4}$$

$$(24)\quad \alpha_{c0} = \frac{mD}{3C^3}\left[1-\frac{1}{2}\left(\frac{2D}{3C^2}\right)^2\right]$$

$$(25)\quad \frac{\alpha_{c2}}{\alpha_{c0}} = \frac{A^2\sin^2\theta}{2}\,\frac{-C^2+\frac{3Qc^2C^2}{D}}{C^4+Q^2c^4} \quad ,$$

and the electromagnetic eddy current type MHD wave reduces to

$$(26)\quad V_{e_0} = \sqrt{2Qc^2}$$

$$(27)\quad \frac{V_{e2}}{V_{e0}} = \frac{A^2}{2Ac^2}\,\frac{C^4\cos^2\theta + Qc^2C^2\sin^2\theta + Q^2c^4}{C^4+Q^2c^4}$$

$$(28)\quad \alpha_{e0} = \frac{m}{\sqrt{2Qc^2}}$$

and

$$(29)\quad \frac{\alpha_{e2}}{\alpha_{e0}} = \frac{A^2}{2Qc^2}\,\frac{C^4\cos^2\theta - Qc^2C^2\sin^2\theta + Q^2c^4}{C^4+Q^2c^4}$$

Expressing the mode parameters explicitly in terms of the frequency for nominal value of sea water parameters and the earth's magnetic field gives, for the acoustic shear type MHD wave

(30) $V_{s0} \approx 3.5 \times 10^{-4} \sqrt{f}$ m/sec

(31) $\frac{V_{s2}}{V_{s0}} \approx 10^{-22} \frac{\cos^2\theta}{f}$

(32) $\alpha_{s0} \approx 1.6 \times 10^{5}\sqrt{f}$ db/m

(33) $\frac{\alpha_{s2}}{\alpha_{s0}} \approx 10^{-22} \frac{\cos^2\theta}{f}$,

for the acoustic compression type MHD wave

(34) $V_{c0} \approx C$ m/sec

(35) $\alpha_{c0} \approx 5.2 \times 10^{-15} f^2$ db/m

(36) $\frac{V_{c2}}{V_{c0}} \approx 5 \times 10^{-22} \sin^2\theta \frac{1+4.4\times10^{-15} f^2}{1+2\times10^{3} f^2}$

(37) $\frac{\alpha_{c2}}{\alpha_{c0}} \approx 5 \times 10^{-22} \sin^2\theta \frac{-1+5\times10^{15} f^2}{1+2\times10^{3} f^2}$,

and for the electromagnetic eddy current type MHD wave

(38) $V_{e0} \approx 1.4\times10^{4}\sqrt{f}$ m/sec

(39) $\frac{V_{e2}}{V_{e0}} \approx \frac{5\times10^{-30}}{f} \frac{\cos^2\theta + 44f \sin^2\theta + 2\times10^{3} f^2}{1+2\times10^{3} f^2}$

(40) $\alpha_{e0} \approx 3.8\times10^{-3}\sqrt{f}$ db/m

(41) $\frac{\alpha_{e2}}{\alpha_{e0}} \approx \frac{5\times10^{-30}}{f} \frac{\cos^2\theta - 44f \sin^2\theta + 2\times10^{3} f^2}{1+2\times10^{3} f^2}$.

These mode parameters are graphed as functions of the frequency in Figs 9 thru 12. The effects of the earth's magnetic field on the properties of the various waves are extremely small.

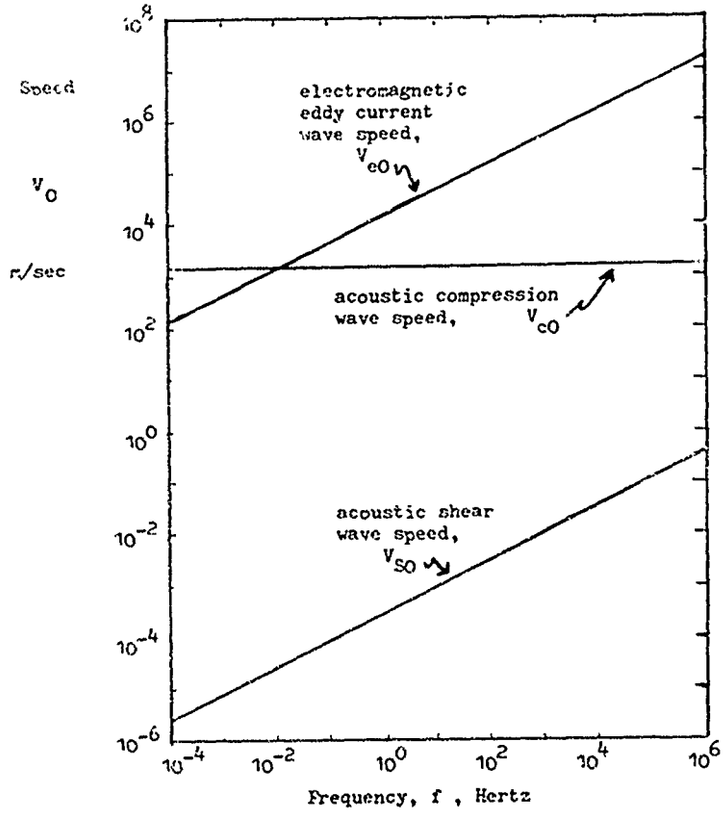

Fig. 9. Speed Dependence On Frequency of the various Uncoupled Waves in Bulk Sea Water

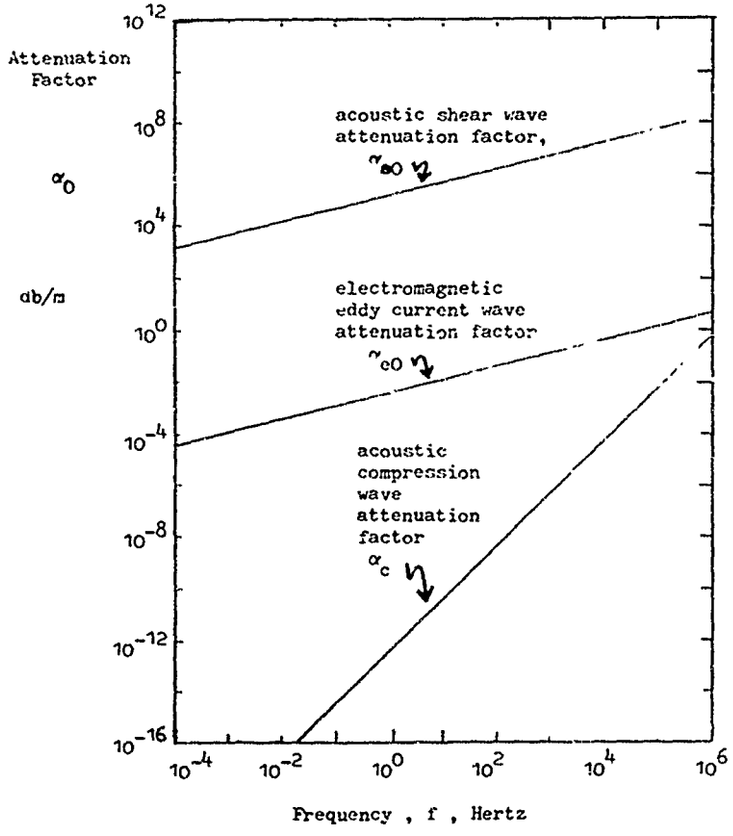

Fig. 10. Attenuation Factor Dependence On Frequency Of the Various Uncoupled Waves In Bulk Sea Water

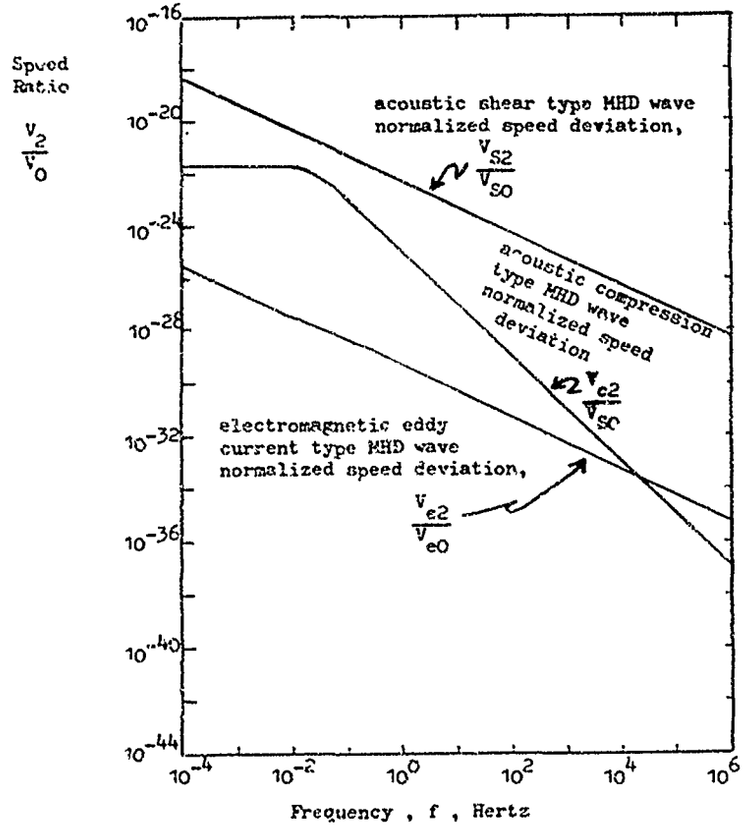

Fig. 11. Magnetohydrodynamic Wave Speed Deviation From Uncoupled Wave Speed Normalized with Respect To The Uncoupled Wave Speed As A Function Of Frequency For Propogation at 45° to The Earth's Magnetic Field In Bulk Sea Water

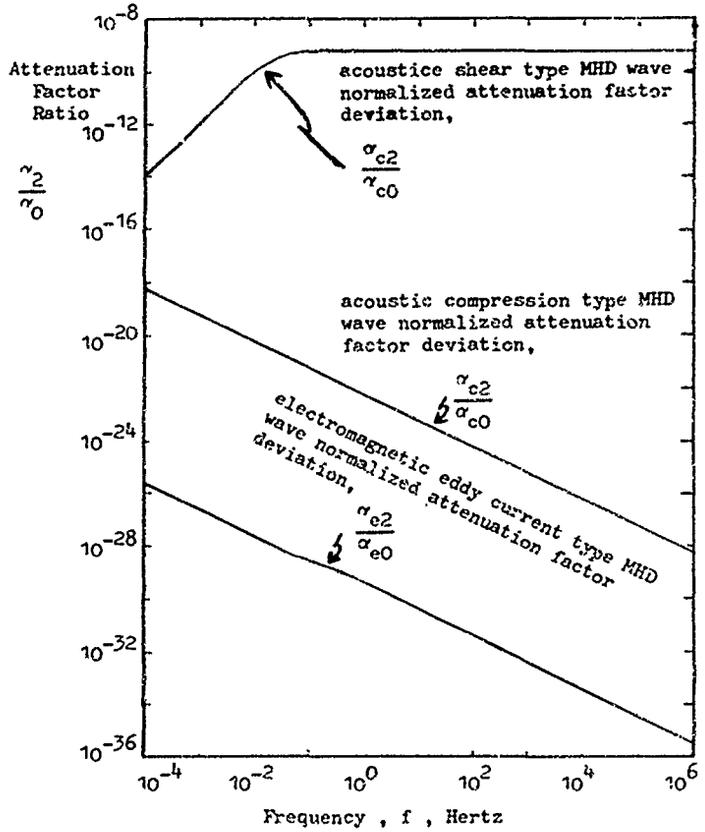

Fig. 12. Magnetohydrodynamic Wave Attenuation Factor Deviation From The Uncoupled Wave Attenuation Factor Normalized With Respect To The Uncoupled Wave Attenuation Factor As A Function Of Frequency For Propagation At 45° To The Earth's Magnetic Field In Bulk Sea Water

APPENDIX A: MHD WAVES

A.1 Field Equations

The six vector fields

$\mathbf{u}$	velocity
$\mathbf{J}$	current density
$\mathbf{B}$	magnetic induction
$\mathbf{E}$	electric field intensity
$\mathbf{D}$	electric displacement
$\mathbf{H}$	magnetic field intensity

and the three scalar fields

p	pressure
ρ	mass density
ρ	charge density

are interrelated by nine field equations, four of which are constitutive relations. There is an additional constraining relation imposed on the magnetic induction field making a total of ten field equations in the set. The constitutive parameters are

K	bulk modulus
η	viscosity
ϵ	capacitivity
μ	inductivity
σ	conductivity

The motion of the ocean fluid continum is approximated by the Navier-Stokes equation

$$\rho(\partial_t \mathbf{u} + \mathbf{u}\cdot\nabla\mathbf{u}) = -\nabla p + \eta\nabla^2\mathbf{u} + \frac{\eta}{3}\nabla\nabla\cdot\mathbf{u} + \rho\mathbf{E} + \mathbf{J}\times\mathbf{B} \quad \text{(A1a)}$$

Conservation of mass is expressed by the equations of continuity

$$\partial_t\rho + \nabla\cdot\rho\mathbf{u} = 0 \quad . \quad \text{(A1b)}$$

Relationships between the electromagnetic fields are:
Faraday's electromagnetic induction law

$$\nabla\times\mathbf{E} = -\partial_t\mathbf{B} \quad , \quad \text{(A1c)}$$

Maxwell-Ampere's magnetoelectric induction law

$$\nabla\times\mathbf{H} = \mathbf{J} + \partial_t\mathbf{D} \quad , \quad \text{(A1d)}$$

Gauss' law for the electric displacement fields

$$\nabla\cdot\mathbf{D} = \rho \quad , \quad \text{(A1e)}$$

and Gauss' law for the magnetic induction field

$$\nabla\cdot\mathbf{B} = 0 \quad . \quad \text{(A1f)}$$

The constitutive equations interrelating the fields are:
Hook's law

$$\nabla p = K\frac{\Delta\rho}{\rho_0} \quad , \quad \text{(A1g)}$$

the generalized Ohm's law

$$\mathbf{J} = \sigma(\mathbf{E} + \mathbf{u}\times\mathbf{B}) \quad , \quad \text{(A1h)}$$

the electric constitutive relation

$$\mathbf{D} = \epsilon\mathbf{E} \quad \text{(A1i)}$$

and the magnetic constitutive relation

$$\mathbf{B} = \mu\mathbf{H} \quad . \quad \text{(A1j)}$$

This set of equations, (A1) describe the wave phenomena involving energy interchange between the four energy storage modes: elastic, kinetic, magnetic, and electric.

A.2 Restriction to MHD Waves

If the energy stored in the electric field is negligible compared to the energy stored in the other fields the phenomena logical description is reduced from magnetoelectrohydrodynamic (MEHD) to magneto-hydrodynamic (MHD). This is the case if the net free electric charge density is negligible

$$\rho \approx 0 \quad \text{(A2a)}$$

and if the displacement current is negligible

$$|\partial_t\mathbf{D}| \ll |\mathbf{J}| \quad . \quad \text{(A2b)}$$

The conductivity of sea water is sufficiently high to cause any net free charge density to rapidly diffuse to a negligible level. The conductivity combined with the restriction to moderate frequencies causes the displacement current to be negligible compared to the conduction current. These restrictions reduce the Navier-Stokes equation to

$$\rho(\partial_t\mathbf{u} + \mathbf{u}\cdot\nabla\mathbf{u}) = -\nabla p + \eta\nabla^2\mathbf{u} + \frac{\eta}{3}\nabla\nabla\cdot\mathbf{u} + \mathbf{J}\times\mathbf{B} \quad , \quad \text{(A2a')}$$

Maxwell-Ampere equation to Ampere's law to

$$\nabla\times\mathbf{H} = \mathbf{J} \quad \text{(A2b')}$$

and Gauss' law for the electric field to

(A3c) $\nabla \cdot \mathbb{D} = 0$,

the other field equations remaining the same.

A.3 Reduced Set of Field Equations

It is convenient to reduce the number of field variables and field equations by using three of the constitutive equations to eliminate $\mathbb{H}$, $\mathbb{D}$, and ρ from the other equations. The remaining set of equations is

(A4a) $$\rho(\partial_t \mathbf{u} + \mathbf{u} \cdot \nabla \mathbf{u}) = -\nabla K \frac{\rho}{\rho_0} + \eta \nabla^2 \mathbf{u} + \frac{\eta}{3} \nabla \nabla \cdot \mathbf{u} + \mathfrak{J} \times \mathbb{B}$$

(A4b) $$\partial_t \rho + \nabla \cdot \rho \mathbf{u} = 0$$

(A4c) $$\nabla \times \mathbb{E} = -\partial_t \mathbb{B}$$

(A4d) $$\nabla \times \mathbb{B} = \mu \mathfrak{J}$$

(A4e) $$\nabla \times \epsilon \mathbb{E} = 0$$

(A4f) $$\nabla \cdot \mathbb{B} = 0$$

(A4g) $$\mathfrak{J} = \sigma(\mathbb{E} + \mathbf{u} \times \mathbb{B}) \quad .$$

A.4 Linearization

The fields can be expressed as the sum of a known part (designated by a subscript 0), and an unknown part (designated by a subscript 1). If the magnitudes of the products and powers of unknown parts are small compared to the magnitudes of the unknown parts the field equations can be accurately approximately by the following set of equations which is linear in the unknowns:

(A5a) $$(\rho_0 + \rho_1)(\partial_t \mathbf{u}_0 + \mathbf{u}_0 \cdot \nabla \mathbf{u}_0) + \rho_0(\partial_t \mathbf{u}_1 + \mathbf{u}_1 \cdot \nabla \mathbf{u}_0 + \mathbf{u}_0 \cdot \nabla \mathbf{u}_1) =$$
$$-\nabla K(1 + \frac{\rho_1}{\rho_0}) + \eta \nabla^2(\mathbf{u}_0 + \mathbf{u}_1) + \frac{\eta}{3} \nabla \nabla \cdot (\mathbf{u}_0 + \mathbf{u}_1) + \mathfrak{J}_0 \times \mathbb{B}_0 + \mathfrak{J}_1 \times \mathbb{B}_0 + \mathfrak{J}_0 \times \mathbb{B}_1$$

(A5b) $$\partial_t(\rho_0 + \rho_1) + \nabla \cdot (\rho_0 \mathbf{u}_0 + \rho_1 \mathbf{u}_0 + \rho_0 \mathbf{u}_1) = 0$$

(A5c) $$\nabla \times (\mathbb{E}_0 + \mathbb{E}_1) = -\partial_t(\mathbb{B}_0 + \mathbb{B}_1)$$

(A5d) $$\nabla \times (\mathbb{B}_0 + \mathbb{B}_1) = \mu(\mathfrak{J}_0 + \mathfrak{J}_1)$$

(A5e) $$\nabla \cdot \epsilon(\mathbb{E}_0 + \mathbb{E}_1) = 0$$

(A5f) $$\nabla \cdot (\mathbb{B}_0 + \mathbb{B}_1) = 0$$

(A5g) $$\mathfrak{J}_0 + \mathfrak{J}_1 = \sigma[\mathbb{E}_0 + \mathbb{E}_1 + \mathbf{u} \times \mathbb{B}_0 + \mathbf{u}_1 \times \mathbb{B}_0 + \mathbf{u}_0 \times \mathbb{B}_1]$$

A.5 Homogenization

The considerations are further restricted to the case for which the constitutive parameters and the known portions of the field are homogeneous in space and time. With this restriction the temporal and spatial derivatives of the known portions of the fields vanish thereby reducing the field equations to

(A6a) $$\rho_0(\partial_t \mathbf{u}_1 + \mathbf{u}_0 \cdot \nabla \mathbf{u}_1) = -\frac{K}{\rho_0} \nabla \rho_1 + \eta \nabla^2 \mathbf{u}_1 + \frac{\eta}{3} \nabla \nabla \cdot \mathbf{u}_1 + \mathfrak{J}_0 \times \mathbb{B}_0 + \mathfrak{J}_1 \times \mathbb{B}_0 + \mathfrak{J}_0 \times \mathbb{B}_1$$

(A6b) $$\partial_t \rho_1 + \mathbf{u}_0 \cdot \nabla \rho_1 + \rho_0 \nabla \cdot \mathbf{u}_1 = 0$$

(A6c) $$\nabla \times \mathbb{E}_1 = -\partial_t \mathbb{B}_1$$

(A6d) $$\nabla \times \mathbb{B}_1 = \mu(\mathfrak{J}_0 + \mathfrak{J}_1)$$

(A6e) $$\nabla \cdot \mathbb{E}_1 = 0$$

(A6f) $$\nabla \cdot \mathbb{B}_1 = 0$$

(A6g) $$\mathfrak{J}_0 + \mathfrak{J}_1 = \sigma[\mathbb{E}_0 + \mathbb{E}_1 + \mathbf{u}_0 \times \mathbb{B}_0 + \mathbf{u}_1 \times \mathbb{B}_0 + \mathbf{u}_0 \times \mathbb{B}_1] \quad .$$

A.6 Streamless Case

If the magnetic field has a known fixed part

(A7) $$\mathbb{B}_0 \neq 0$$

but there is no dc fluid flow

(A8) $$\mathbf{u}_0 = 0$$

and no dc current

(A9) $$\mathfrak{J}_0 = 0$$

there will also be no dc electric field intensity

(A10) $$\mathbb{E}_0 = 0 \quad .$$

Without dc streaming the field equations reduce to

(A11a) $$\rho_c \partial_t u_1 = -\frac{K}{\rho_0}\nabla\rho_1 + \eta\nabla^2 u_1 + \frac{\eta}{3}\nabla\nabla\cdot u_1 + \mathfrak{f}_1 \times B_0$$

(A11b) $$\partial_t \rho_1 + \rho_0 \nabla \cdot u_1 = 0$$

(A11c) $$\nabla \times \mathbf{E}_1 = -\partial_t \mathbf{B}_1$$

(A11d) $$\nabla \times \mathbf{B}_1 = u\mathfrak{f}_1$$

(A11e) $$\nabla \cdot \mathbf{E}_1 = 0$$

(A11f) $$\nabla \cdot \mathbf{B}_1 = 0$$

(A11g) $$\mathfrak{f}_1 = \sigma[\mathbf{E}_1 + u_1 \times B_0] \quad .$$

A.7 Steady State Waves

The transient solution can be obtained by superpositions of steady state solutions which are monochromatic plane waves. The phasor representation of the steady state solution is characterized by the fact that

t	time
$\mathbf{r}$	position

only occur in the linear combination

(A12) $$\text{phase} = \omega t \pm \check{\boldsymbol{\beta}} \cdot \mathbf{r}$$

where

ω	the angular frequency
$\check{\boldsymbol{\beta}}$	the complex phase factor

The complex phase factor can be expressed in terms of

β	phase factor
α	attenuation factor

thus

(A13) $$\check{\boldsymbol{\beta}} = \boldsymbol{\beta} - j\boldsymbol{\alpha} \quad .$$

To examine the basic properties of the steady state waves only the positively traveling wave need be considered. With phasor representation the time derivative operator is replaced by jω

(A14) $$\partial_t \longrightarrow j\omega$$

and the gradient operator is replaced by $-j\check{\boldsymbol{\beta}}$

(A15) $$\nabla \longrightarrow -j\check{\boldsymbol{\beta}} \quad .$$

This reduces the set of partial differential field equations to a set of algebraic field equations

(A16a) $$j\omega\rho_0 u_1 = j\frac{K}{\rho_0}\check{\boldsymbol{\beta}}\rho_1 - j\eta\check{\boldsymbol{\beta}}^2 u_1 - j\frac{\eta}{3}\check{\boldsymbol{\beta}}\check{\boldsymbol{\beta}}\cdot u_1 + \mathfrak{f}_1 \times B_0$$

(A16b) $$\omega\rho_1 = \rho_0\check{\boldsymbol{\beta}}\cdot u_1$$

(A16c) $$\check{\boldsymbol{\beta}} \times \mathbf{E}_1 = \omega\mathbf{B}_1$$

(A16d) $$-j\frac{\check{\boldsymbol{\beta}}}{\mu} \times \mathbf{B}_1 = u\mathfrak{f}_1$$

(A16e) $$\check{\boldsymbol{\beta}}\cdot \mathbf{E}_1 = 0$$

(A16f) $$\check{\boldsymbol{\beta}}\cdot \mathbf{B}_1 = 0$$

(A16g) $$\frac{1}{\sigma}\mathfrak{f}_1 = \mathbf{E}_1 + u_1 \times B_0 \quad .$$

A.8 Relative Directions of the Fields

The algebraic form of Gauss law for the electric field, (A16e), and for the magnetic field, (A16f), show that the electric and magnetic fields of the wave are perpendicular to the direction of propagation. The algebraic form of Faraday's electromagnetic induction law shows that the magnetic field is perpendicular to the electric field. Thus, the electric field, magnetic field and direction of propagation are mutually orthogonal just as for an elementary plane electromagnetic wave in free space. The algebraic form of Ampere's law (A16d), shows that the current density is perpendicular to both the magnetic field and the direction of propagation. Consequently, the current density is in the same direction as the electric field intensity. Since the current density and electric field intensity are in the same direction, Ohm's law (A16g), shows that both the ac fluid velocity and the dc magnetic field are in the plane perpendicular to the electric field intensity. Consequently, the dc magnetic field and the ac fluid velocity are coplanar with the magnetic field and the direction of propagation. These spacial relationships are summarized in Fig. A.1

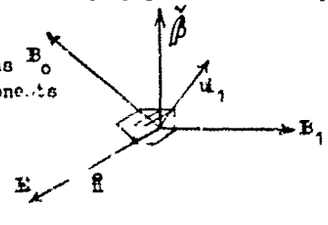

Fig. A.1 Spatial Relations of an MHD Wave Field Components at Point

A.9 Separation of Variables

Among the set of field variables, $\{\rho_1, \mathbf{u}_1, \mathbf{B}_1, \mathbf{E}_1, \hat{\mathbf{n}}_1\}$, the most convenient variable for expressing the others in terms of is $\mathbf{u}_1$. The continuity equation directlygives the variable mass density in terms of the fluid velocity

$$\rho_1 = \frac{\rho_0}{\omega}\check{\boldsymbol{\beta}}\cdot\mathbf{u}_1 \tag{A17}$$

Using the algebraic form of Faraday's law to eliminate the variable magnetic field from the algebraic form of Ampere's law gives

$$\check{\boldsymbol{\beta}}\times(\check{\boldsymbol{\beta}}\times\mathbf{E}_1) = j\omega\mu\hat{\mathbf{n}}_1 \quad . \tag{A18}$$

Expanding the triple cross product and using the algebraic form of Gauss law for the electric field gives

$$\check{\beta}^2\mathbf{E}_1 = -j\omega\mu\hat{\mathbf{n}}_1 \tag{A19}$$

Using this equation with Ohm's law gives

$$\mathbf{E}_1 = \frac{j\omega\mu\sigma\mathbf{B}_0\times\mathbf{u}_1}{j\omega\mu\sigma+\check{\beta}^2} \tag{A20}$$

and

$$\hat{\mathbf{n}}_1 = -\frac{\sigma\check{\beta}^2\mathbf{B}_0\times\mathbf{u}_1}{j\omega\mu\sigma+\check{\beta}^2} \quad . \tag{A21}$$

The variable magnetic field can now be expressed in terms of the velocity

$$\mathbf{B}_1 = \frac{j\mu\sigma\check{\boldsymbol{\beta}}\times(\mathbf{B}_0\times\mathbf{u}_1)}{j\omega\mu\sigma+\check{\beta}^2} \quad . \tag{A22}$$

A.10 Dispersion Relations

Eliminating the variable mass density and the current density from the algebraic form of the Navier-Stokes equation of motion gives

$$j\omega\rho_0\mathbf{u}_1 = j\frac{K}{m}\check{\boldsymbol{\beta}}\check{\boldsymbol{\beta}}\cdot\mathbf{u}_1 - \eta\check{\beta}^2\mathbf{u}_1 - \frac{\eta}{3}\check{\boldsymbol{\beta}}\check{\boldsymbol{\beta}}\cdot\mathbf{u}_1 + \frac{\sigma\check{\beta}^2\mathbf{B}_0\times(\mathbf{B}_0\times\mathbf{u}_1)}{\check{\beta}^2+j\omega\mu\sigma} \quad . \tag{A23}$$

Expanding the last term and factoring out the velocity gives

$$\left[(j\omega\rho_0+\eta\check{\beta}^2)\mathbf{1}-\left(\frac{\eta}{3}+j\frac{K}{m}\right)\check{\boldsymbol{\beta}}\check{\boldsymbol{\beta}}+\sigma\check{\beta}^2\frac{B_0^2\mathbf{1}-\mathbf{B}_0\mathbf{B}_0}{\check{\beta}^2+j\omega\mu\sigma}\right]\cdot\mathbf{u}_1 = 0 \quad . \tag{A24}$$

For a nontrivial solution to exist the determinent of the coefficients of the components of the velocity must vanish,

$$\left|(j\omega\rho_0+\eta\check{\beta}^2)\mathbf{1}-\left(\frac{\eta}{3}+j\frac{K}{m}\right)\check{\boldsymbol{\beta}}\check{\boldsymbol{\beta}}+\sigma\check{\beta}^2\frac{B_0^2\mathbf{1}-\mathbf{B}_0\mathbf{B}_0}{\check{\beta}^2+j\omega\mu\sigma}\right| = 0 \quad . \tag{A25}$$

Expressing the vector complex phase factor and the dc magnetic field in terms of their magnitudes and directions gives a more appropriate form for the dispersion relationship

$$\left|(j\omega\rho_0+\eta\check{\beta}^2)\mathbf{1}-\left(\frac{\eta}{3}+j\frac{K}{m}\right)\check{\beta}^2\mathbf{1}_{\beta\beta}+\sigma\check{\beta}^2B_0^2\frac{\mathbf{1}-\mathbf{1}_{B_0B_0}}{\check{\beta}^2+j\omega\mu\sigma}\right| = 0 \quad . \tag{A26}$$

A.11 Velocity Parameterization

Alfven waves and sonic waves are actually specialized cases of the more general category of MHD waves. Consequently it is convenient to eliminate the dc magnetic field and the bulk modulus in favor of the Alfven's wave speed

$$A = \frac{B_0}{\sqrt{\mu\rho_0}} \tag{A27}$$

and the sound wave speed

$$C = \sqrt{\frac{K}{\rho_0}} \tag{A28}$$

thereby giving the following expressions for the dispersions relationship

$$\left|\left(\frac{\omega^2}{\check{\beta}^2}-\frac{j\omega\eta}{\rho_0}\right)\mathbf{1}+\left(\frac{j\omega\eta}{3\rho_0}-C^2\right)\mathbf{1}_{\beta\beta}-A^2\frac{\mathbf{1}-\mathbf{1}_{B_0B_0}}{1-\frac{j\check{\beta}^2}{\omega\mu\sigma}}\right| = 0 \quad . \tag{A29}$$

Along with the preceeding characteristic speeds it is also convenient to use the electric quality factor of the medium

$$Q = \frac{\omega\epsilon}{\sigma} \tag{A30}$$

and the speed of light

(A31) $$c = \frac{1}{\sqrt{\mu\epsilon}} ,$$

which occur in the combinations

(A32) $$Qc^2 = \frac{\omega}{\sigma\mu} .$$

It is also convenient to represent the remaining constitutive parameters bunched with the viscosity as a single factor

(A33) $$D = \frac{m\mu}{\rho_0} .$$

The dispersion relation can now be expressed in terms of the more conveniently used parameters

(A34) $$\left| \left(\frac{\omega^2}{\beta^2} - jD \right) \mathbb{1} + \left(j\frac{D}{3} - c^2 \right) 1_{\beta\beta} - A^2 \frac{\mathbb{1} - 1_{B_C B_O}}{1 - jQc^2 \frac{\beta^2}{\omega^2}} \right| = 0 .$$

A.12 Scalar Dispersion Relation

The spacial relationships between the vector fields, depicted in Fig. A-1, make it convenient to use a rectangular coordinate system with the x-axis oriented along the electric field and the z-axis oriented along the dc magnetic field. In this case

(A35) $$1_{B_D} = 1_z$$

and

(A36) $$1_\beta = 1_z \cos\theta + 1_y \sin\theta .$$

The dispersion relation can now be expressed in the form

(A37) $$\left| \left(\frac{\omega^2}{\beta^2} - jD \right) \mathbb{1} - \left(c^2 - j\frac{D}{3} \right) \left(1_{zz} \cos^2\theta + \{1_{zy} + 1_{yz}\} \cos\theta \sin\theta + 1_{yy} \sin^2\theta \right) - A^2 \frac{\mathbb{1} - 1_{zz}}{1 - jQc^2 \frac{\beta^2}{\omega^2}} \right| = 0 .$$

Since there are no cross terms between the x-components and other components the conditional equation conveniently splits into two simpler conditional equations

(A38) $$\frac{\omega^2}{\beta^2} - jD - \frac{A^2}{1 - jQc^2 \frac{\beta^2}{\omega^2}} = 0$$

and

(A39) $$\left| \left(\frac{\omega^2}{\beta^2} - jD \right) (1_{yy} + 1_{zz}) - \left(c^2 - j\frac{D}{3} \right) (1_{yy} \sin^2\theta + \{1_{yz} + 1_{zy}\} \sin\theta \cos\theta + 1_{zz} \cos^2\theta) - A^2 \frac{1_{yy}}{1 - jQc^2 \frac{\beta^2}{\omega^2}} \right| = 0 .$$

Expressing the second dispersion relation in terms of scalar quantities only gives

(A40) $$\begin{vmatrix} \frac{\omega^2}{\beta^2} - jD - (c^2 - j\frac{D}{3})\sin^2\theta - \frac{A^2}{1 - jQc^2 \frac{\beta^2}{\omega^2}} & -(c^2 - j\frac{D}{3})\sin\theta\cos\theta \\ -(c^2 - j\frac{D}{3})\sin\theta\cos\theta & \frac{\omega^2}{\beta^2} - jD - (c^2 - j\frac{D}{3})\cos^2\theta \end{vmatrix} = 0 .$$

A.13 Longitudinal Waves

Because of the general complexity it is desireable to consider selected simple cases first. For propagation in the direction of the dc magnetic field

(A41) $$\theta = 0$$

the dispersion relations reduces to

$$(A42)\qquad \left[\frac{\omega^2}{\beta^2} - jD - \frac{A^2}{1 - jQc^2\frac{\beta^2}{\omega^2}}\right]\left[\frac{\omega^2}{\beta^2} - j\frac{2}{3}D - c^2\right] = 0 \quad .$$

The waves which can propagate have complex phase factors given by the roots of

$$(A43)\qquad \frac{\omega^2}{\beta^2} - j\frac{2D}{3} - c^2 = 0$$

and

$$(A44)\qquad \frac{\omega^2}{\beta^2} - jD - \frac{A^2}{1 - jQc^2\frac{\beta^2}{\omega^2}} = 0 \quad .$$

The first of these represents an ordinary sonic wave whose complex phase factor is

$$(A45)\qquad \check{\beta} = \frac{\omega}{\sqrt{c^2 + j\frac{2D}{3}}} = \frac{\omega}{c}\left[1 + j\frac{2D}{3c^2}\right]^{-1/2} \quad .$$

The phase and attenuation factors are given by

$$(A46)\qquad \beta = \frac{\omega}{c}\frac{\sqrt{\sqrt{1 + \left(\frac{2D}{3c^2}\right)^2} + 1}}{\sqrt{2}\sqrt{1 + \left(\frac{2D}{3c^2}\right)^2}} \qquad \text{radians/m}$$

and

$$(A47)\qquad \alpha = -j\frac{\omega}{c}\frac{\sqrt{\sqrt{1 + \left(\frac{2D}{3c^2}\right)^2} - 1}}{\sqrt{2}\sqrt{1 + \left(\frac{2D}{3c^2}\right)^2}} \qquad \text{nepers/m} \quad .$$

For small losses

$$(A48)\qquad \left(\frac{2D}{3c^2}\right)^2 \ll 1$$

the phase and attenuation factors reduce to

$$(A49)\qquad \beta \simeq \frac{\omega}{c}\left[1 - \frac{D^2}{6c^4}\right] \qquad \text{radians/m}$$

and

$$(A50)\qquad \alpha \approx \frac{\omega D}{3c^3} \qquad \text{nepers/m}$$

For water the viscosity is the order of one centipose (10^{-5} Newton sec/m^2), the density is the order of one thousand kilogram/m^3 and the speed of sound is the order of 1500 m/sec giving

$$(A51)\qquad \frac{2D}{3c^2} \approx 2 \times 10^{-14} f$$

Hence the approximations for β and α are valid up to terahertz frequencies.

The other factor in the dispersion relation represents waves traveling with the complex phase factors

$$(A52)\qquad \check{\beta} = \pm\omega\sqrt{\frac{-A^2 - jD - jQc^2 \pm \sqrt{(A^2 + jD + jQc^2)^2 + 4DQc^2}}{2DQc^2}} \quad .$$

If there were no losses at all the dispersion relation, (A14) would directly give

$$(A53)\qquad \check{\beta} = \omega A$$

in which case the phase speed is

$$(A54)\qquad V = A$$

and wave is an ideal Alfvén wave. However, in sea water the conductivity is approximately four mohs per meter, the relative capacitivity is approximately 81 and consequently

$$(A55)\qquad Qc^2 \approx 10^8 f$$

which is enormous compared to

(A56) $D \simeq 6 \times 10^{-8} f$

which is enormous compared to the square of the Alfven wave speed

(A57) $A^2 \simeq 2 \times 10^{-14}\ m^2/sec^2$

As a result the longitudinal MHD waves which exist in sea water have phase factors accurately given by

(A58) $\overset{v}{\beta} = \frac{m}{\sqrt{jD}}$

and

(A59) $\beta = \frac{\omega}{\sqrt{jQc^2}}$

The attenuation factors for these highly damped waves are equal to the phase factor

(A60) $\beta = \alpha = \frac{\omega}{\sqrt{2D}} \approx 2 \times 10^{4}\sqrt{f}$ m^{-1}

and

(A61) $\beta = \alpha = \frac{\omega}{\sqrt{2Qc^2}} \approx 6 \times 10^{-4}\sqrt{f}$ m^{-1}

The phase speeds of these waves are

(A62) $V = \sqrt{2D} \approx 3.5 \times 10^{-4}\sqrt{f}$ m/sec

and

(A63) $V = \sqrt{2Qc^2} \approx 1.4 \times 10^{4}\sqrt{f}$ m/sec

The second of these is the ordinary eddy current wave in the conducting sea water that results when the displacement current can be neglected compared to the conduction current.

A.14 Transverse Waves

For propagation in a direction perpendicular to the dc magnetic field

(A64) $\theta = \frac{\pi}{2}$

the dispersion relation reduces to

(A65) $\left(\frac{\omega^2}{\overset{v}{\beta}^2} - jD\right)\left(\frac{\omega^2}{\overset{v}{\beta}^2} - j\frac{2D}{3} - c^2 - \frac{A^2}{1 - jQc^2\frac{\overset{v}{\beta}^2}{\omega^2}}\right) = 0$.

The first factor represents the same highly damped uncoupled wave found in the longitudinal direction represented by (A58), A(60), and (A61). The second factor represents waves whose complex phase factors are given by

(A66) $\overset{v}{\beta} = \pm m\sqrt{\frac{-c^2 - A^2 - jQc^2 - j\frac{2D}{3} \pm \sqrt{(c^2 + A^2 + jQc^2 + j\frac{2D}{3})^2 - j4Qc^2(c^2 + j\frac{2D}{3})}}{j2Qc^2(c^2 + j\frac{2D}{3})}}$.

If there were no losses at all the dispersion relation from the second factor in (A64) would yield

(A67) $\overset{v}{\beta} = \frac{m}{\sqrt{c^2 + A^2}}$

hence the magnetosonic wave speed is given by

(A68) $V = \sqrt{c^2 + A^2}$.

With the Alfvén speed small compared to the sonic speed this reduces to

(A69) $V = c\left(1 + \frac{A^2}{2c^2}\right)$.

With the nominal strength of the earth's magnetic field in sea water the difference between the sonic speed and the magnetosonic speed would not be discernable. If the Alfven speed squared is neglected compared to the other terms the resulting waves are the same as the sonic waves and the eddy current waves discussed for the longitudinal propagation case.

A.15 Waves with Arbitrary Propagation Direction

To simplify writing it is convenient to introduce the abbreivation

$$(A70) \qquad C_m^2 = c^2 - j\frac{D}{\omega}$$

in terms of which the dispersion relation can be expressed as

$$(A71) \qquad \left[\frac{m^2}{\omega^2\beta^2} - jD - C_m^2\sin^2\theta - \frac{A^2}{1 - jQc^2\frac{\omega^2\beta^2}{m^2}}\right]\left[\frac{m^2}{\omega^2\beta^2} - jD - C_m^2\cos^2\theta\right] - C_m^4\sin^2\theta\cos^2\theta = 0$$

Rearranging the expression so that all like trigonometric functions are grouped together reduces the dispersion relation to

$$(A72) \qquad \left(\frac{m^2}{\omega^2\beta^2} - jD\right)\left(\frac{m^2}{\omega^2\beta^2} - jD - C_m^2 - \frac{A^2}{1 - jQc^2\frac{\omega^2\beta^2}{m^2}}\right) + \frac{C_m^2A^2\cos^2\theta}{1 - jQc^2\frac{\omega^2\beta^2}{m^2}} = 0 \quad .$$

Since the square of the Alfven speed is small compared to the other parameters, for waves in the sea, it is convenient to group together all terms multiplied by A^2, giving

$$(A73) \qquad \left(\frac{m^2}{\omega^2\beta^2} - jD\right)\left(\frac{m^2}{\omega^2\beta^2} - C_m^2 - jD\right) - A^2\frac{\frac{m^2}{\omega^2\beta^2} - jD - C_m^2\cos^2\theta}{1 - jQc^2\frac{\omega^2\beta^2}{m^2}} = 0 \quad .$$

For extracting the roots it is more convenient to reexpress the dispersion relation in the form

$$(A74) \qquad \left(\frac{m^2}{\omega^2\beta^2} - jD\right)\left(\frac{m^2}{\omega^2\beta^2} - C_m^2 - jD\right)\left(\frac{m^2}{\beta^2} - jQc^2\right) - A^2\frac{m^2}{\omega^2\beta^2}\left(\frac{m^2}{\omega^2\beta^2} - C_m^2\cos^2\theta - jD\right) = 0 \quad .$$

If there were no magnetic field present the dispersion relation would reduce to

$$(A75) \qquad \left(\frac{m^2}{\omega^2\beta^2} - jD\right)\left(\frac{m^2}{\omega^2\beta^2} - C_m^2 - jD\right)\left(\frac{m^2}{\beta^2} - jQc^2\right) = 0$$

The solutions to this are just the uncoupled acoustic shear wave

$$(A76) \qquad \frac{m}{\omega\beta_s} = \pm\sqrt{jD}$$

the uncoupled acoustic compression wave

$$(A77) \qquad \frac{m}{\omega\beta_c} = \pm\sqrt{C_m^2 + jD} \quad ,$$

and the uncoupled electromagnetic eddy current wave

$$(A78) \qquad \frac{m}{\omega\beta_e} = \pm\sqrt{jQc^2} \quad .$$

The subscripts, s, c, and e have been attached to designate that the complex phase factors are respectively for the acoustic shear wave, the acoustic compressional wave and the electromagnetic eddy current wave. The earth's magnetic field causes coupling between these three types of propagation modes giving rise to the MHD modes. However, since the square of the Alfven wave speed is small the coupling between the basic wave types are small and hence the resulting MHD modes are very similar to the three basic modes in the absence of coupling. The small coupling allows an accurate solution for the MHD mode characteristics in the sea to be obtained with the first two terms of an expansion in powers of the Alfven wave speed squared, where the first term represents the mode in the absence of the coupling dc magnetic field.

Solving the dispersion relation is facilitated by letting x be the variable $m^2/\omega^2\beta^2$, x_1, x_2, x_3 be the coupled roots, and δ_1, δ_2, δ_3 be the corrections due to coupling. With this notation change the dispersion relation has the form

$$(A79) \qquad (x - x_1)(x - x_2)(x - x_3) - \epsilon a(x - a) = 0$$

where ϵ is a small quantity, A^2, and $a = C_m^2\cos^2\theta + jD$ reexpressing the cubic equations in the form

$$(A80) \qquad (x - x_1 - \delta_1)(x - x_2 - \delta_2)(x - x_3 - \delta_3) = 0$$

gives

$$(A81) \qquad \delta_i = \frac{\epsilon x_i(x_i - a)}{(x_i - x_j)(x_i - x_k)} \quad , \qquad i \neq j \neq k \neq i \quad .$$

This gives

$$(A82)\qquad \frac{\beta^2}{\beta_s^2} = jD + \frac{A^2\cos^2\theta}{1 - \frac{Qc^2}{D}}$$

$$(A83)\qquad \frac{\beta^2}{\beta_c^2} = C_m^2 + jD + \frac{A^2\sin^2\theta}{1 - \frac{jQc^2}{C_m^2 + jD}}$$

and

$$(A84)\qquad \frac{\beta^2}{\beta_e^2} = jQc^2 + \frac{A^2}{1 - \frac{D}{Qc^2}} \frac{C_m^2\cos^2\theta + jD - jQc^2}{C_m^2 + jD - jQc^2}$$

Consequently

$$(A85)\qquad \check{\beta}_s = \pm \frac{\omega}{\sqrt{jD}}\left[1 + \frac{j}{2}\frac{A^2\cos^2\theta}{D - Qc^2}\right]$$

$$(A86)\qquad \check{\beta}_c = \pm \frac{\omega}{\sqrt{C_m^2 + jD}}\left[1 - \frac{1}{2}\frac{A^2\sin^2\theta}{C_m^2 + jD - jQc^2}\right]$$

and

$$(A87)\qquad \check{\beta}_e = \pm \frac{\omega}{\sqrt{jQc^2}}\left[1 + \frac{j}{2}\frac{A^2}{Qc^2 - D}\frac{C_m^2\cos^2\theta + jD - jQc^2}{C_m^2 + jD - jQc^2}\right] .$$

Considering only the positively traveling waves and preparing the expressions for separation of the attenuation and the phase factors gives

$$(A88)\qquad \check{\beta}_s = \frac{\omega}{\sqrt{2D}}(1 - j)\left[1 - \frac{j}{2}\frac{A^2\cos^2\theta}{Qc^2 - D}\right]$$

$$(A89)\qquad \check{\beta}_c = \frac{\omega}{C\sqrt{2}\sqrt{1 + \left(\frac{2D}{3C^2}\right)^2}}\left[\sqrt{\sqrt{1 + \left(\frac{2D}{3C^2}\right)^2} + 1} - j\sqrt{\sqrt{1 + \left(\frac{2D}{3C^2}\right)^2} - 1}\right]\left[1 - \frac{A^2\sin^2\theta}{2}\frac{C^2 + j(Qc^2 - \frac{2D}{3})}{C^4 + (Qc^2 - \frac{2D}{3})^2}\right] .$$

and

$$(A90)\qquad \check{\beta}_e = \frac{\omega}{\sqrt{2Qc^2}}(1-j)\left[1 + \frac{\frac{1}{2}A^2}{Qc^2 - D}\frac{\left(Qc^2 - \frac{D}{3}\right)C^2\sin^2\theta + j\left[C^4\cos^2\theta + \left(Qc^2 - \frac{2D}{3}\right)\left(Qc^2 - \frac{2D}{3} + \frac{D}{3}\sin^2\theta\right)\right]}{C^4 + \left(Qc^2 - \frac{2D}{3}\right)^2}\right]$$

The phase speed and attenuation of the acoustic shear type MHD are given by

$$(A91)\qquad V_s = \sqrt{2D}\left[1 + \frac{1}{2}\frac{A^2\cos^2\theta}{Qc^2 - D}\right]$$

and

$$(A92)\qquad \alpha_s = \frac{\omega}{\sqrt{2D}}\left[1 + \frac{1}{2}\frac{A^2\cos^2\theta}{Qc^2 - D}\right]$$

The phase speed and attenuations of the acoustic compression type MHD mode are given by

$$(A93)\qquad V_c = C\sqrt{2}\sqrt{\frac{1 + \left(\frac{2D}{3c^2}\right)^2}{\sqrt{1 + \left(\frac{2D}{3C^2}\right)^2} + 1}}\left[1 + \frac{1}{2}\frac{A^2\sin^2\theta}{C^4 + (Qc^2 - \frac{2D}{3})^2}\left\{C^2 + (Qc^2 - \frac{2D}{3})\frac{\sqrt{1 + \left(\frac{2D}{3C^2}\right)^2} - 1}{\sqrt{1 + \left(\frac{2D}{3C^2}\right)^2} + 1}\right\}\right]$$

and

$$(A94)\qquad \alpha_c = \frac{\omega}{C\sqrt{2}\sqrt{1 + \left(\frac{2D}{3C^2}\right)^2}}\left[\sqrt{\sqrt{1 + \left(\frac{2D}{3C^2}\right)^2} - 1}\left\{1 - \frac{1}{2}\frac{A^2C^2\sin^2\theta}{C^4 + (Qc^2 - \frac{2D}{3})^2}\right\} + \frac{1}{2}A^2\sin^2\theta\sqrt{\sqrt{1 + \left(\frac{2D}{3C^2}\right)^2} + 1}\frac{Qc^2 - \frac{2D}{3}}{C^4 + (Qc^2 - \frac{2D}{3})^2}\right] .$$

The phase speed and attenuation of the electromagnetic eddy current type MHD wave are given by

$$(A95)\qquad V_e = \sqrt{2Qc^2}\left[1 - \frac{\frac{1}{2}A^2}{-Qc^2-D}\,\frac{c^4\cos^2\theta + (Qc^2 - \frac{D}{3})c^2\sin^2\theta + (Qc^2 - \frac{2D}{3})(Qc^2 - \frac{2D}{3} + \frac{D}{3}\sin^2\theta)}{c^4 + (Qc^2 - \frac{2D}{3})^2}\right]$$

and

$$(A96)\qquad \alpha_e = \frac{m}{\sqrt{2Qc^2}}\left[1 - \frac{\frac{1}{2}A^2}{Qc^2-D}\,\frac{c^4\cos^2\theta - (Qc^2 - \frac{D}{3})c^2\sin^2\theta + (Qc^2 - \frac{2D}{3})(Qc^2 - \frac{2D}{3} + \frac{D}{3}\sin^2\theta)}{c^4 + (Qc^2 - \frac{2D}{3})^2}\right] .$$

ELECTROMAGNETICS OF THE SEA

RADIO ROUND TABLE DISCUSSION

RADIO ROUND TABLE DISCUSSION

Chairman : Dr James WAIT
Reporters : Drs Albert BIGGS and Pierre DEGAUQUE

SUMMARY EDITED BY CHAIRMAN

WAIT : The key point of Dr. Galejs' review was to identify the sources of the ELF waves and how they propagate. The ionospheric models were also of interest. Maybe he could have further comments.

GALEJS : I have very little to add - Dr. Wait and others may have some.

WAIT : A great deal of work has been done by Dr. Galejs and others on situations where the antennas are buried, or above ground, and where the signal propagates via the earth ionospheric waveguide. People should be aware of this relevant work.

ESSMANN : We have natural noise originating in thunderstorm centers. The wavelength is so large at ELF that we can't use the earth-ionosphere waveguide. What mechanism can we use ? Is the wave mode a surface wave or a space mode ?

GALEJS : If you start near a source, you can use ground and sky waves. As you move away, you have more of a sky wave. Only one mode is present in the sky wave as you move away. The others attenuate rapidly.

WAIT : Dr. Galejs is saying that a mode series is a more rapidly convergent representation at great distances from the source, but it remains valid at all distances. At short distances, it is more convenient to use wave hop series where the first term is the ground wave.

LOKKEN : Do man-made signals verify these theories for the first few hundred km ?

GALEJS : Only California to New York paths were used. In France, distances were very short.

WAIT : The next topic on mixed paths was covered by Wait and Biggs. It is important to consider the inhomogeneities in any path, such as coast-lines and pronounced topographical features. This is true even when the major portion of the path is over the sea.

WETZEL : We would like more measurements on the theoretical subjects discussed above, but funds are low for supporting such investigations.

BARRICK : What is the effect of sea wave distortions on communications above and below the surface - digital and voice ?

WETZEL : This is a problem depending on the channel used - at low frequencies, lower distortion occurs - it rises with frequency.

WAIT : In the present context, what is the "hammer and tong" manner referred to by Dr. Wetzel ?

WETZEL : It alludes to a blacksmith - in hammering the problem to fit the solution.

WAIT : Use of pressure sensors might be worthwhile. Recent unpublished work has shown that close correlations exist with electromagnetic fields in the ocean. Possibilities exist for noise cancellation if such correlations could be established.

BROCK-NANNESTAD : Most papers deal with deep water effects - but the sea bottom should also be considered. Much of the continental shelf is in shallow water and the sea bed influence is significant (e.g., at depths of the order of 150 meters).

WIRGIN : Isn't this a multi-layer problem ?

BROCK-NANNESTAD : Not entirely. The sea bed itself is irregular and sub-surface layering provides further distortions.

WAIT : In Brock-Nannestad's investigations in the Kattegat, mixtures of Baltic and North Sea waters are also present. These have different characteristics. Is this a problem ?

ESSMANN : In our measurements, signals from buried dipoles near banks resulted in minor changes. Only effects were near the bank.

BROCK-NANNESTAD : Was only one component measured above, or the total ? Some components (i.e., vertical H) are affected more than others.

WAIT : We would like Dr. Barrick to talk about the physical meaning of his boundary perturbation approach. Can he explain the significance of his effective surface impedance ? Also, is it proper to use this in a deterministic description of what is actually a random rough surface

BARRICK : I will discuss some alternatives. I looked at a guided wave over an impedance plane. It looks like a Zenneck wave. We used a plane wave above a field with and without roughness. A series expression was used to cover roughness perturbations. How does this relate to spherical modes ? I used a method like that of Rice in 1951. The justification is that a sphere looks locally flat. This is only valid for amplitudes small in comparison with spatial wavelengths.

WAIT : A surface impedance can be used with ground waves. But, how is energy scattered into the higher grating modes accounted for in the present problem (see also discussion after Barrick's paper) ?

BIGGS : What do we mean by modes ?

WAIT : Different things !

BARRICK : We retain only the ground wave because of the high attenuation of the HF sky waves. No ionosphere is present in the analysis !

WIRGIN : You can use a perturbation technique for a spherical earth.

BARRICK : The perturbation technique could be used with a MIE series and the Watson transform.

SWIFT : It is easier to deal with flat surfaces.

WAIT : Rayleigh treated the sinusoidal surfaces in 1902 - and this is the starting point for much of the current work on the subject. In principle, Rayleigh's method can be applied even if the mean level of the surface is curved.

WIRGIN : The perturbation method used by Barrick does not seem valid for non-sinusoidal profiles such as a trochoid.

BARRICK : Any profile can be treated, provided it has a valid Fourier expansion ; however, the process breaks down for high sea states.

CROMBIE : The sea is a sum of sine waves of infinitesimal amplitude - do we go from sines to trochoids as the sea gets rougher ?

WIRGIN : If we use Fourier series, we have sines and cosines. Barrick uses Fourier series and he only uses sinusoids. How does Barrick justify this procedure ?

BARRICK : I used the sinusoidal form (or superposition thereof) because of restrictions on trochoidal surfaces.

LOKKEN : What about internal waves ? These have been observed in high density areas, like the Straits of Georgia.

SCHONFELD : We don't know much about the theory. Small rivers flow on the surface of the ocean.

WRIGHT : Oceanographers can learn many things from radar people.

CROMBIE : Backscatter can measure sea states a few hundred km from coastlines. Relatively low frequencies must be used. Nonlinear interactions between waves need to be studied. Only wave tank experiments have been used to demonstrate this, but it is possible that nonlinear effects can be observed using coherent backscatter.

MATTERN : Subsurface ships need to know about subsurface waves. Can we detect these ? They have important applications - like crushing submarines.

WAIT : MHD or Alfven waves can be supported in conducting media. A paper by Cohen on this subject was not presented. In my early work on this subject, I had found that the classical skin-depth calculations are only modified by MHD effects if the wave periods exceeded hours ! Thus my interest in the problem dropped.

HODARA : In 1956-1957, I made calculations of these effects. The results were worthless because of such slow velocities. I know of no associated work.

WAIT : Any other wavy interface problems ?

SWIFT : How do we feel about monitoring sea states ?

CROMBIE : I think resonant backscatter measurements at appropriate radio wavelengths can be used to measure sea state. I think this is a much more direct method of finding waveheights, etc., than by inference drawn from guesses of the local wind velocity and history. This is particularly the case since recent observations of wave growth with distance, under fetch limited conditions, show results which are much greater than theory would predict.

MOORE : Oceanographers use wave forecasting programs - the U.S. uses them for the North Atlantic and saves travel time and cargo. Not enough wind data is available. With better forecasts, ships stay away from high wind areas - so the data drops with better forecasts - a dilemna.

CROMBIE : Is wind decided by pressure gradient ?

MOORE : It's easier to measure wind. You want to know about ocean waves. We looked at radar systems to do this. The waves seen depend on wavelength. The longest feasible from satellites is 75-80 cm - longer have ionospheric trouble. At 13.3 GHz, we apparently see small waves, which are proportional to wind. The best wavelength for waves depends on your likes - for winds, centimeters, and for waves, meters.

WRIGHT : There is no evidence to show that small waves are proportional to wind. Temperature effects and other factors are complicated problems. I think that the problem of winds will be solved in my wave tank. We don't know enough about short gravity waves.

MOORE : As Wright says, there are many complications that must be investigated ; but although wave-tank measurements are important, the will not settle what happens with real seas for winds above 20 knots or so. Mr. Crombie's measurements cover a different problem. Other (than NASA and NRL) measurements exist on wind and backscatter data, and often show the effects seen in NASA data. The NRL system is accurate to $\pm$ 2 dB, and the NASA system is accurate to $\pm \frac{1}{2}$ dB for relative measurements.

HALLET : The small surface irregularities are important, and they have a temporal nature. Differences in water characteristics can occur over even a short distance.

END OF SESSION

PARTICIPANTS IN "ROUND TABLE" DISCUSSION

Name	Address
Barrick, D	Batelle Memorial Institute 505 W. King Avenue Columbus, Ohio, 43201, U.S.A.
Biggs, A.	University of Kansas C. R. E. S. Lawrence, Kansas, 66044, U.S.A.
Brock-Nannestad, L.	DDRB Osterbrogades Kaserne DK 2100 Copenhagen O, Denmark
Crombie, D.D.	ESSA Research Laboratories Boulder, Colorado, 80302, U. S. A.
Degauque, P.	Département E.E.A. Faculte des Sciences, 59 Lille, France
Essmann, A.	Hagenuk Vormals, 2300 Kiel Postfach 500, Germany
Galejs, J.	Sylvania Electronic Systems 77 "A" Street Needham Heights, Massachusetts, 02194, U.S.A.
Halley, P.	C.N.E.T. Château de la Martinière 91 - Saclay - France
Hodara, H.	Tetra Tech. Inc. Rosemead Blvd. Pasadena, California, 91107, U.S.A.
Lokken, J.	Defence Research Establishment Pacific, F. M. O. Victoria, B. C., Canada
Mattern, G.	Taunus Observatorium 6241 Kleiner Feldberg Germany
Moore, R. K.	University of Kansas C.R.E.S. Marvin Hall Lawrence, Kansas, 66044, U.S.A.
Schonfeld, W.	Technische Universitat Hannover 3 Hannover, Welfengarten1, Germany
Swift, C.	NASA Langley Research Center Hampton, Virginia, 23365, U.S.A.
Wait, J.R.	ESSA Research Laboratories Boulder, Colorado, 80302, U.S A.
Wetzel, L.	Naval Research Laboratory Washington, D.C. 20390, U.S.A.
Wirgin, A.	Institut d'Optique 3, Bld Pasteur 75, Paris - 15ème France
Wright, J.	Naval Research Laboratory Code 5272 Washington, D.C. 20390, U.S.A.

PART II - OPTICS

MEASUREMENTS OF THE SPATIAL COHERENCE OF A LASER BEAM PROPAGATING THROUGH WATER

by

S.G. Varnado and A.H. LaGrone

Antennas and Propagation Laboratory
The University of Texas at Austin
Austin, Texas 78712

SOMMAIRE

On a mesuré la cohérence spatiale du rayonnement emis par un laser à argon, à onde continue, après propagation à travers l'eau. On a déterminé expérimentalement la valeur du degré normalisé de cohérence en calculant la visibilité de la configuration des franges par un faisceau laser lorsque, après s'être propagé à travers l'eau, il frappe deux ouvertures ponctuelles .

On a procédé à des mesures en laboratoire sur un échantillon d'eau du robinet, et deux échantillons d'eau naturelle, fraîche. Outre la cohérence, on a mesuré pour chaque échantillon, le coefficient d'atténuation du rayon, sur deux des fréquences que l'on peut obtenir avec le laser à argon.

Les résultats obtenus indiquent que les propriétés de cohérence spatiale du rayon laser ne sont pas dégradées de façon importante par la propagation du rayon à travers les échantillons d'eau étudiés, du moins pour des longueurs de trajectoire de propagation atteignant 12,25 longueurs d'atténuation.

MEASUREMENTS OF THE SPATIAL COHERENCE OF A LASER BEAM PROPAGATING THROUGH WATER*

S. G. Varnado[+] and A. H. LaGrone

Antennas and Propagation Laboratory
The University of Texas at Austin
Austin, Texas 78712

SUMMARY

The spatial coherence of the radiation from an argon laser after propagation through water has been measured. Measurements were performed for one sample of tap water and two samples of natural, fresh water. The results indicate that the spatial coherence properties of the laser beam are not significantly degraded by propagation through the water samples considered, at least for propagation path lengths of up to 12.25 attenuation lengths.

1. INTRODUCTION

The propagation of light in water has been a subject of continuing interest for many years. Duntley[1] has presented a very complete account of the optical nature of ocean water, the distribution of light intensity in the field of underwater incandescent light sources, and the propagation of collimated beams of light from incandescent underwater sources. Duntley[2] has also reported underwater measurements of the irradiance distribution in the field of a pulsed, neodymium-doped glass laser operating at a wave length of 0.53 microns. Since one of the exciting properties of laser signals is spatial coherence, a study of this property under various propagation conditions is highly desirable. Such a study would contribute significantly to Duntley's investigation of the propagation characteristics of laser radiation in water.

Measurements of the spatial coherence of the radiation from a pulsed, frequency-doubled neodymium-doped glass laser operating in lake water were attempted by Gilber, Stoner, and Jernigan[3]; however, no reliable conclusions were drawn from their data inasmuch as they failed to observe any interference fringes that could not be attributed to noise. There is, however, little reason to expect much spatial coherence in the output of such a laser because of the wave front distortion which results from the signal passing through the frequency-doubling KDP crystal[2]. Hodara[4] reported measurements of the spatial coherence of radiation from a helium-neon laser in tap water. He reported that no degradation in the spatial coherence properties of the radiation was detected for water path lengths of up to four attenuation lengths in the clear tap water.

It is well known[5,6,7] that the spatial coherence properties of a laser signal propagating through the atmosphere are degraded by random fluctuations in the index of refraction of the atmosphere due to turbulence. Hodara[4] has pointed out that due to the relative incompressibility of water the refractive index fluctuations of clear water and the resultant loss of spatial coherence should be negligible compared to those encountered in air. In natural water, however, suspended particulate matter and marine biological organisms in the water cause refractive index discontinuities along the propagation path resulting in scattering of the incident radiation[1]. The measurements reported here were performed in order to determine the effects of the suspended particulate matter and marine biological organisms in the water on the spatial coherence properties of the signal passing through the water.

2. THEORY

In order to adequately represent a wave field produced by a partially coherent source, such as a laser, it is necessary to introduce some measure for the correlations that exist between the field components at different points in the field. Born and Wolf[8] have formulated these correlation functions in terms of the complex analytic signal representation of the field amplitudes. Using this representation the normalized degree of coherence between two points, P_1 and P_2, is defined as

$$\gamma(P_1, P_2; \tau) = \frac{\langle V_1(t+\tau)\, V_2^*(t)\rangle}{\sqrt{I_1}\sqrt{I_2}} \qquad (1)$$

where V_j is the complex analytic signal associated with the field at point P_j, I_j is the irradiance of the field at point P_j, τ is the time delay between observations of the fields at point P_1 and P_2, and the angular brackets denote a time average. The spatial coherence of the radiation field is found by taking $\tau = 0$ in Eq. (1)[9].

*This work was sponsored in part by NSF Grant GZ974. Sandia Laboratories participated by lending the researchers an argon laser to use in the measurements.

[+]S. G. Varnado is now with Sandia Laboratories, Albuquerque, New Mexico 87115.

The experimental determination of the magnitude of the normalized degree of coherence can be accomplished by analyzing the results of a suitably designed interference experiment[8]. In such an experiment, the radiation is allowed to fall upon two apertures, usually slits or pinholes. Located at points P_1 and P_2. Interference fringes are then formed in the field of the apertures, and the visibility of the fringes is an indication of the spatial coherence of the radiation incident upon the apertures. If a point Q is taken such that it is located in the field of the apertures equidistant from P_1 and P_2, the magnitude of the normalized degree of coherence between P_1 and P_2 can be expressed in terms of measurable quantities as[8]

$$\gamma(P_1, P_2; 0) = \left[\frac{I_{max} - I_{min}}{I_{max} + I_{min}}\right] \left[\frac{I^{(1)}(Q) + I^{(2)}(Q)}{2\sqrt{I^{(1)}(Q)}\sqrt{I^{(2)}(Q)}}\right] \qquad (2)$$

Here I_{max} and I_{min} are the maxima and the minima of irradiance near point Q in the interference pattern, and $I^{(j)}(Q)$ is the irradiance at point Q due to radiation from the aperture at point P_j alone. The expression in the first bracket on the right-hand side of Eq. (2) denotes the visibility of the interference fringes. Eq. (2) is the basis for the experimental work described in this paper.

3. EXPERIMENTAL EQUIPMENT AND PROCEDURE

The experimental arrangement used to study the propagation characteristics of the spatial coherence of laser radiation in water is shown schematically in Fig. 1. The water tank was constructed of plywood and fiber glass of dimensions 3.05 meters x 0.610 meters x 0.610 meters and having a water capacity of approximately 350 gallons. The laser signal entered the water by means of a movable periscope which allowed the water path length to be varied as desired. A plate glass window served as the exit port for the laser beam. A maximum water path distance of 2.5 meters was obtainable with the equipment shown.

The laser used for the measurements reported here was a Spectra-Physics Model 141 continuous wave argon-ion laser. The two primary output wavelengths (4880 Å and 5145 Å) of this laser are located in the blue-green portion of the frequency spectrum for which the absorption of light by water is a minimum. The beam diameter of this laser was 2 millimeters.

The pinhole apertures used in these measurements were 400 microns in diameter and were mounted in a micrometer positioner which allowed the pinholes to be placed in the center of the beam. For each measurement the pinholes were placed as close to the plate glass window of the tank as possible. Two pinhole assemblies were constructed with separation distances between the pinholes of one millimeter and two millimeters. Two mirrors, M_1 and M_2, Fig. 1, were used to increase the path length between the pinholes and the photomultiplier to allow for proper formation of the fringe pattern.

The fringe patterns were recorded using an RCA 5819 photomultiplier which was equipped with an adjustable slit aperture. In all cases the slit width was much smaller ($<1/50$) than the width of the interference fringes. The photomultiplier was mounted on a linear translation stage to allow scanning of the interference pattern. The photomultiplier voltage, which is a direct measure of the light irradiance, was recorded on the y-axis of an x-y recorder while the x-axis of the recorder was driven by the voltage from a potentiometer which indicated the position of the photomultiplier in the fringe pattern. A typical interference pattern recording is shown in Fig. 2. The pattern shown was obtained for propagation over an all air path with a pinhole separation distance of one millimeter and the pinholes located a distance of 0.2 meters in front of the laser. The discontinuities observed in the pattern at a photomultiplier position of -6.0 millimeters are due to noise in the x-axis potentiometer of the x-y recorder. The normalized degree of coherence for the argon laser for the stated conditions can be obtained from the curves in Fig. 2 in accordance with Eq. (2).

Radiation at optical frequencies experiences exponential attenuation with distance in water. The rate of attenuation varies for different bodies of water and depends upon the amount of particulate matter and marine life in the water[1]. The power remaining in a laser beam after propagation through a water path of length z is given by

$$P_T = P_L e^{-bz} \qquad (3)$$

where P_L is the transmitted power, and b is called the beam attenuation coefficient. The coefficient b includes the effects of both scattering and absorption. The quantity 1/b is termed the attenuation length of the water.

The measurement of the beam attenuation coefficient for each water sample reported here was accomplished by measuring the power contained in the laser beam after propagation through various water path lengths. The measurements were performed with an EG&G Model 580 Radiometer which was placed at the position of mirror M_1 in Fig. 1. The radiometer, with a restricting aperture placed in front of the detector to keep out scattered light, intercepted all of the main beam so that the total attenuation coefficient was measured and no correction was needed for beam spreading loss. Measurements of b were made at the two wavelengths of 4880 Å and 5145 Å for each water sample.

The degree of spatial coherence of the argon laser signal was measured as a function of water path length for each of three water samples. The spatial coherence measurements were made at a signal wavelength of 5145 Å.

The minimum water path distance at which spatial coherence measurements were made was 0.07 meters, while the maximum water path distance was limited by the attenuation of the signal for a given water sample and, therefore, varied from water sample to water sample. In the lake water, for example, the maximum physical water path distance over which spatial coherence measurements could be made was 1.57 meters; however, this is a distance of 12.25 attenuation lengths.

For each water sample, the spatial coherence was measured first at the minimum water path distance for pinhole separation distances of one millimeter and two millimeters. The water path distance was then increased by sliding the periscope toward the laser a prescribed distance, usually 0.2 meters, and the measurements repeated. This procedure was repeated until the attenuation of the water reduced the signal to the point where photomultiplier noise precluded any further increase in water path length.

Due to the exponential attenuation of the signal by the water, large variations in the power incident upon the pinhole apertures were experienced as the water path distance was changed. To avoid saturating the photomultiplier at short water path distances, neutral density filters were inserted in the beam as needed prior to the beam entry into the periscope. These filters had no effect on the coherence properties of the beam, and their use made it possible to maintain the photomultiplier slit width at a constant value as the water path distance increased.

4. DESCRIPTION OF THE WATER SAMPLES

Measurements were performed for three different water samples. The first sample investigated was ordinary tap water. The attenuation length, $1/b$, for this sample, as obtained from the radiometer data in Fig. 3, was 3.01 meters at 4830 Å and 3.41 meters at 5145 Å.

In addition to the tap water samples, two samples of natural, fresh water were collected. The primary causes of light scattering in natural water are marine biological organisms and particulate matter in the water[1]. Tyler and Richardson [10] have pointed out that large changes in the marine population occur in samples of ocean or lake waters upon removal from their natural habitat, and they have emphasized the desirability of performing in situ measurements of the optical properties of natural water. In situ measurements are, however, difficult to make and require considerable logistic support. In order to approximate the actual conditions found in natural water, two precautions were taken in carrying out the experiments reported here. First, the water samples were collected from bodies of water located near The University of Texas at Austin to insure that measurements could be made shortly after collection of the sample. Secondly, large samples (2000 gallons) were collected to insure minimum disturbance of marine ecology. In the two cases reported, measurements were made within two to four hours of sample collection. The two samples were obtained from the Colorado River and from a spring-fed creek, both at Austin, Texas.

Attenuation measurements for each sample were made at the time of delivery and again several days after delivery. Fig. 4 is a plot of the radiometer data obtained for the Colorado River water at three different times. Measurements were made at the time of delivery of the sample, forty-eight hours after delivery, and nine days after delivery. The decrease in attenuation with time is due to the settling of particulate matter and the decrease in the population of the marine biological organisms. The attenuation coefficient decreased by 36.5 per cent in the first 48 hours and by 330 per cent in the nine day period.

Fig. 5 is a similar plot for the spring-fed creek sample. The attenuation coefficient for this sample was less than that of the Colorado River water by a factor of approximately 3 at the time of delivery. The change in attenuation coefficient over the first forty-eight hour period was 21.4 per cent indicating less particulate matter in this sample than in the river water sample.

In all water samples studied, the attenuation was slightly less at the 5145 Å wavelength than at the 4880 Å wavelength.

5. RESULTS AND CONCLUSIONS

With the equipment arranged as shown in Fig. 1 and the tank empty, measurements were made of the spatial coherence of the argon laser signal after it had passed through the periscope and the plate glass window. The purpose of this set of measurements was to determine the effect, if any, of moving the periscope on the coherence properties of the laser signal. Fig. 6 is a plot of the measurements which shows that the magnitude of the normalized degree of coherence was constant as the periscope was moved from one end of the tank to the other. Variations obtained in the degree of coherence are well within the experimental error. In view of the above results, any change in the degree of coherence with distance when the tank is filled with water can be attributed to the effect of the water.

The normalized degree of coherence was found to be approximately 0.94 for the one millimeter pinhole separation distance and approximately 0.86 for the two millimeter pinhole separation distance for most of the measurements reported. The exact value, however, depended upon the setting of the wavelength selection prism within the laser cavity[11] and was slightly different for each water sample.

Fig. 7 is a plot of the coherence measurements for the tap water. As expected from the results reported by Hodara[4], no degradation in spatial coherence is evident over the 2.5 meter path (0.725 attenuation lengths). The scatter in the data points is within the experimental error and is due primarily to vibrations of the mirrors M_1 and M_2 of Fig. 1. Figs. 8 and 9 show coherence measurements for the two samples of natural water. These measurements were made after each sample had been in the tank for forty-eight hours. Initial measurements made immediately after delivery of the water samples showed the same coherence as the later measurements. Measurements at distances greater than 10 attenuation lengths were difficult to make due to the signal being attenuated to the point where the photomultiplier noise was a problem.

In the two samples of natural water, the light was severely scattered by particulate matter and marine life; however, this apparently had no effect on the coherence properties of the signal. Attempts were made to measure the degree of coherence of the scattered light near the beam axis; however, no conclusions could be drawn from the measurements.

The results of this study show that any deterioration in the spatial coherence of the argon laser signal, for transmission through the water samples considered, is less than the experimental error. The maximum water path length considered was 12.25 attenuation lengths.

REFERENCES

1. S. Q. Duntley, J. Opt. Soc. Am. 53, 214 (1963).
2. S. Q. Duntley, Letter Report, Defense Documentation Center No. AD 631033 (1966).
3. G. D. Gilbert, T. R. Stoner, and J. L. Jernigan, Seminar on Underwater Photo Optics (Society of Photo-Optical Instrumentation Engineers, San Diego, 1966), p. A-II-1.
4. H. Hodara, R Marquedant, A. Merrill, and S. Swiadek, Tetra Tech Report No. 104 (Tetra Tech, Inc., Pasadena, 1967), p. 37.
5. P. Beckman, Radio Science, J. Res. Natl. Bur. Standards, 64D, 629 (1965).
6. H. Hodara, Proc. IEEE, 56, 2130 (1968).
7. J. W. Strohbehn, Proc. IEEE, 56, 1301 (1968).
8. M. Born and E. Wolf, Principles of Optics (Pergamon Press, Inc., New York, 1965). Chapter 10.
9. H. Hodara, Proc. Third International Conf. on Quantum Electronics (Columbia University Press, New York, 1964), p. 121.
10. J. E. Tyler and W. H. Richardson, J. Opt. Soc. Am. 48, 354 (1958).
11. S. G. Varnado, Ph. D. Dissertation, (The University of Texas at Austin, Austin, Texas. 1969).

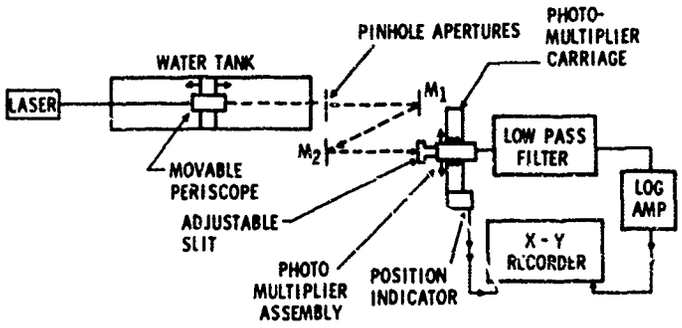

Fig. 1 Experimental arrangement for the measurement of the magnitude of the normalized degree of coherence.

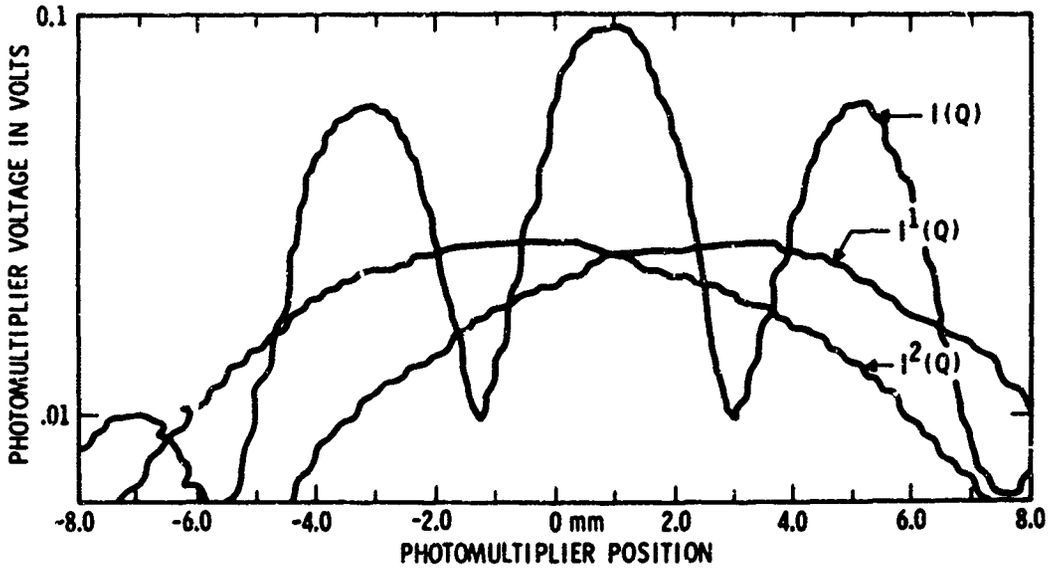

Fig. 2 Recording of the interference pattern produced by the argon laser.

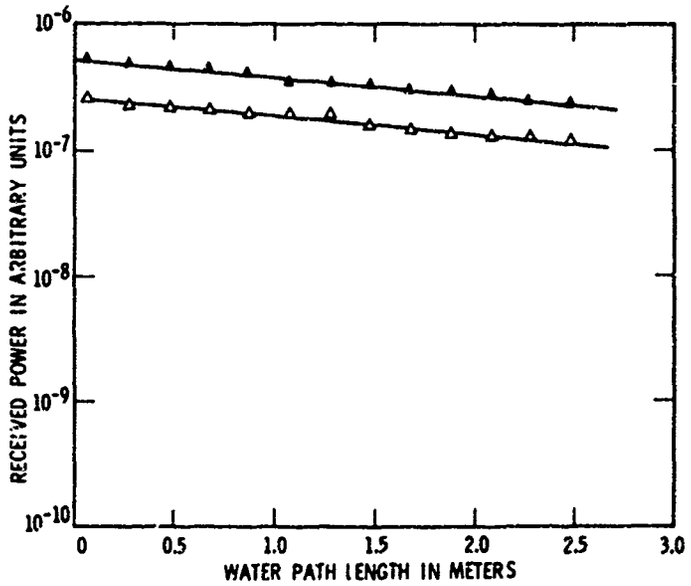

Fig. 3 Received power as a function of water path length for the tap water sample.

▲ 4880 Å wavelength Δ 5145 Å wavelength

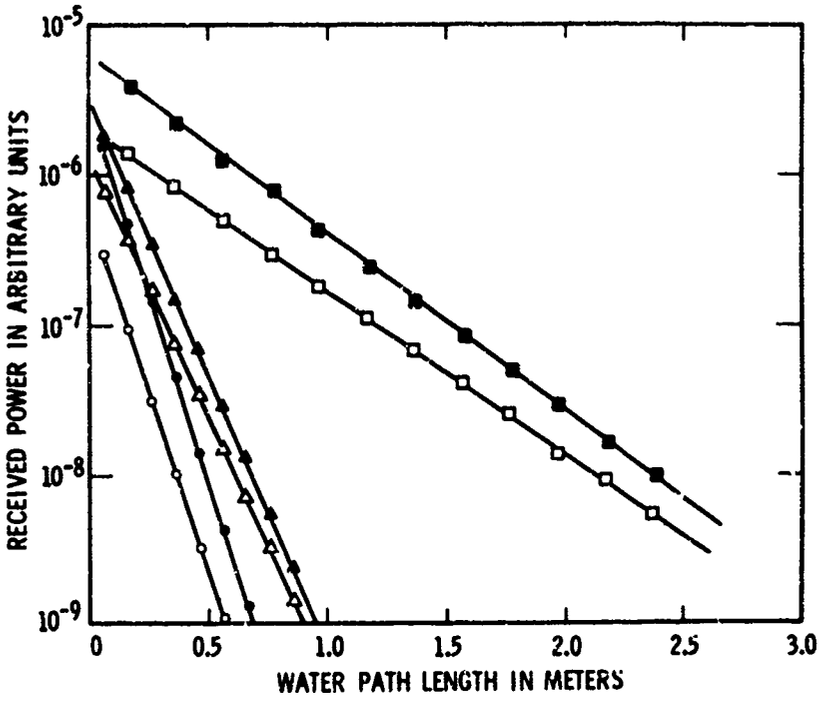

Fig. 4 Received power as a function of water path length for the Colorado River water sample.

● - 4880 Å wavelength, at delivery.
○ - 5145 Å wavelength, at delivery.
▲ - 4880 Å wavelength, 48 hours after delivery.
△ - 5145 Å wavelength, 48 hours after delivery.
■ - 4880 Å wavelength, 9 days after delivery.
□ - 5145 Å wavelength, 9 days after delivery.

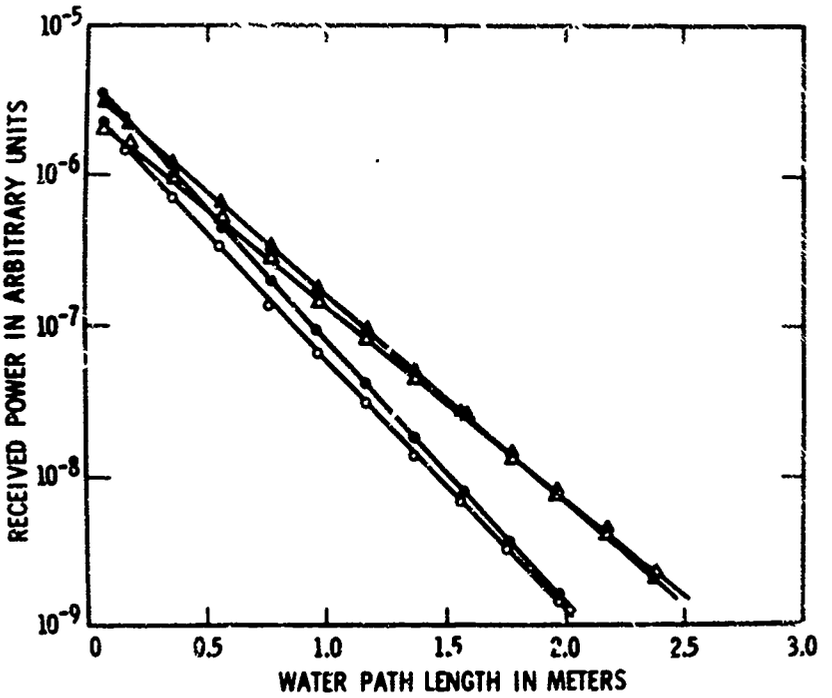

Fig. 5 Received power as a function of water path length for the spring-fed creek water sample. ● - 4880 Å wavelength, at delivery. ○ - 5145 Å wavelength, at delivery, ▲ - 4880 Å wavelength, 48 hours after delivery, △ - 5145 Å wavelength, 48 hours after delivery.

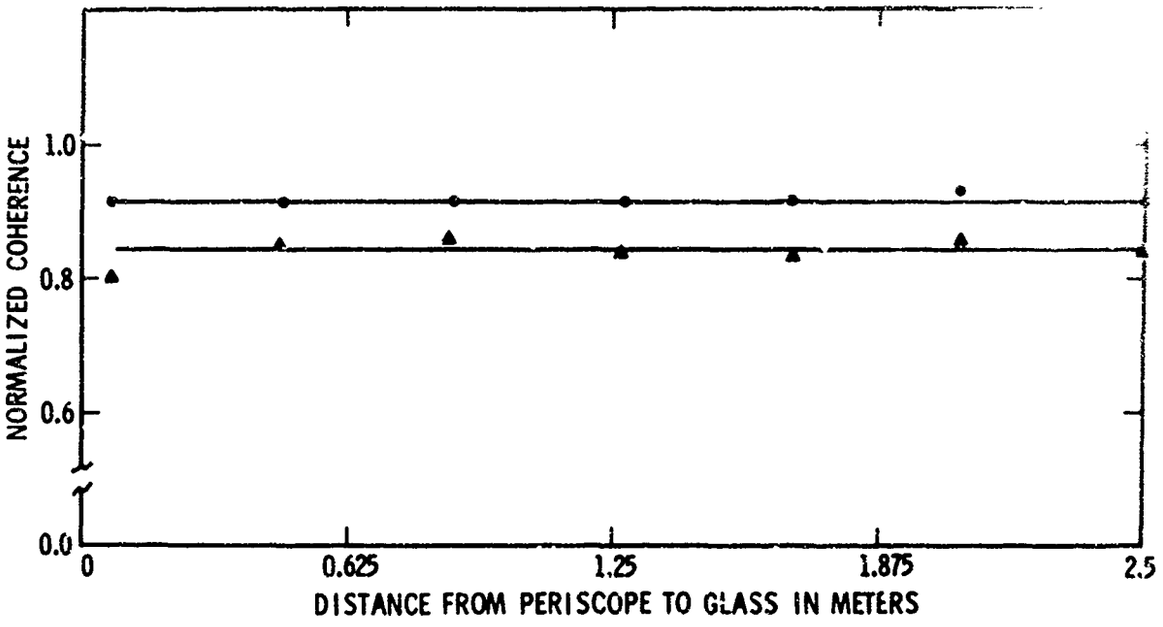

Fig. 6 Magnitude of the normalized degree of coherence for the argon laser as a function of the distance from the periscope to the plate glass window with the tank empty. Pinhole separation distance: ● - 1 millimeter, ▲ - 2 millimeters, wavelength: 5145 Å.

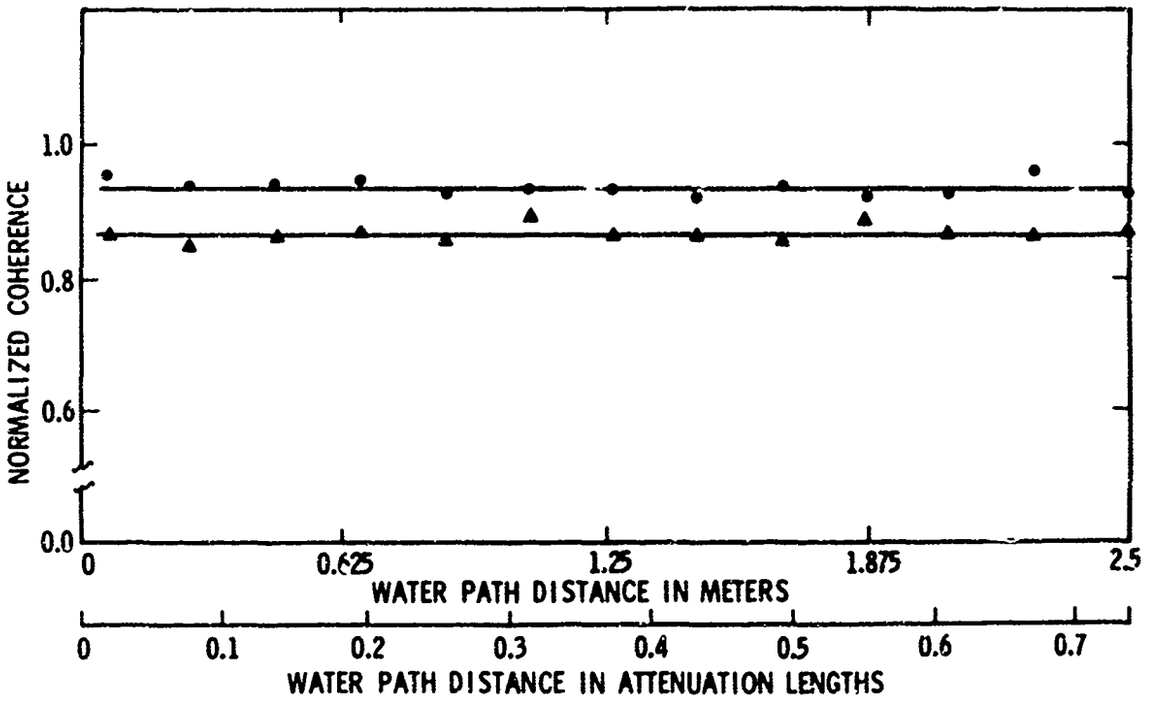

Fig. 7 Magnitude of the normalized degree of coherence for the argon laser as a function of water path distance for tap water. Pinhole separation distance: ● - 1 millimeter, ▲ - 2 millimeters, wavelength 5145 Å.

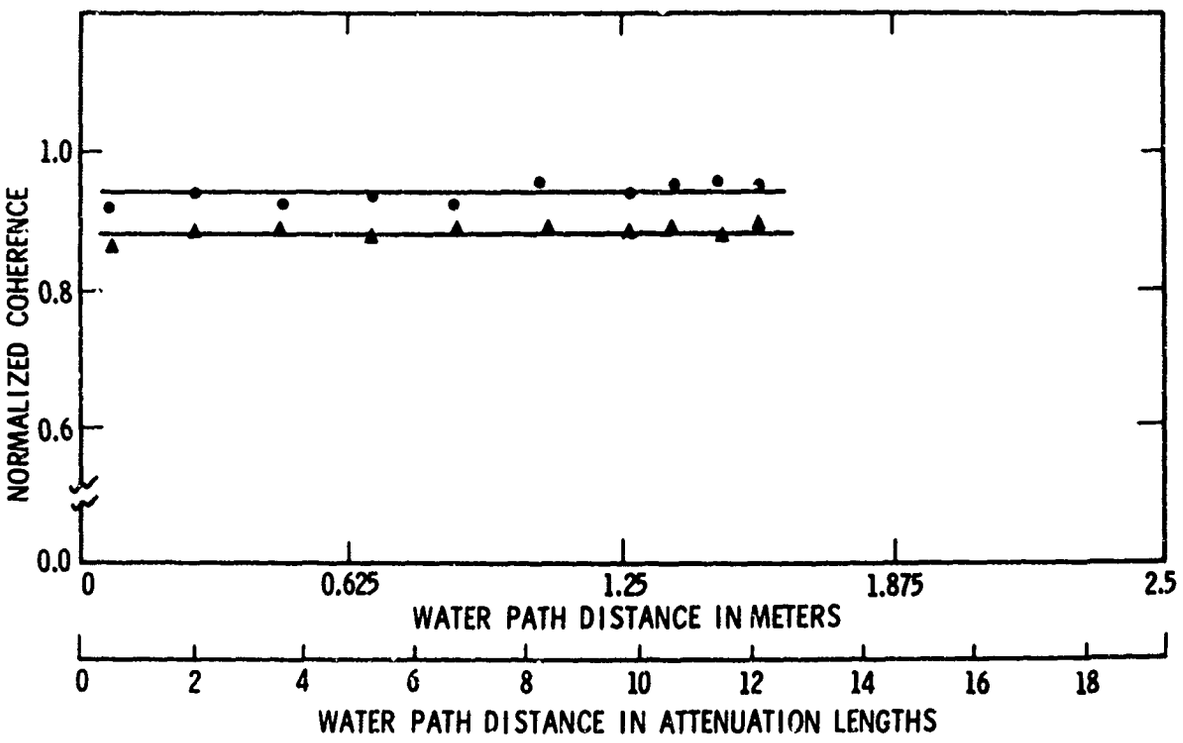

Fig. 8 Magnitude of the normalized degree of coherence for the argon laser as a function of water path distance for the Colorado River water sample. Pinhole separation distance: ● - 1 millimeter, ▲ - 2 millimeters, wavelength: 5145 Å.

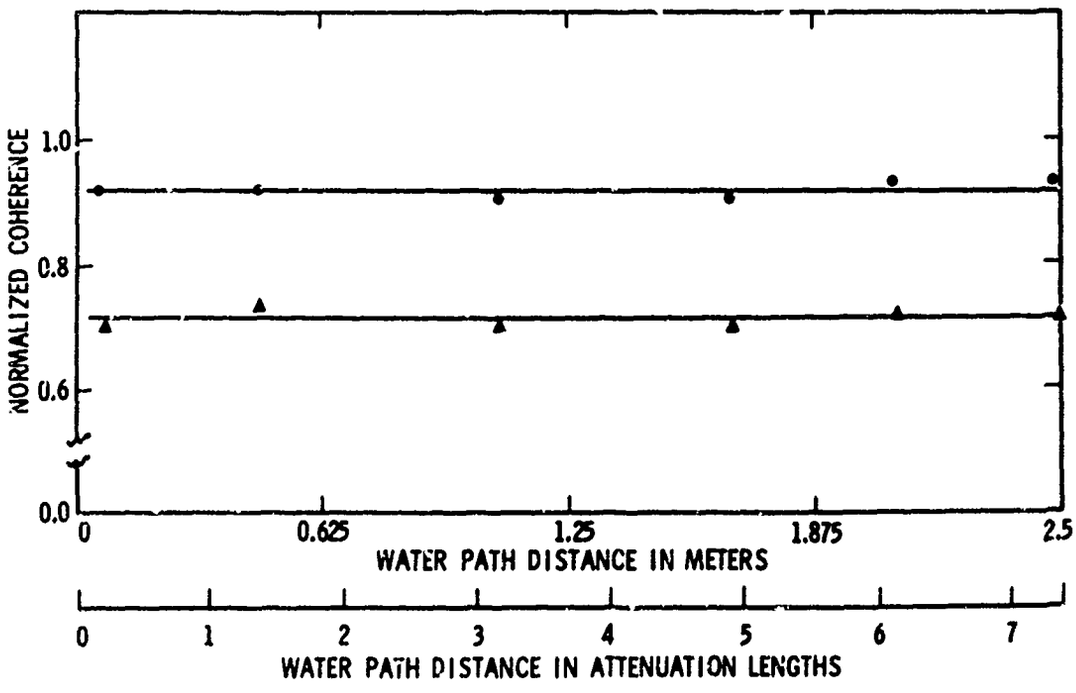

Fig. 9 Magnitude of the normalized degree of coherence for the argon laser as a function of water path distance for the spring-fed creek water sample. Pinhole separation distance: ● - 1 millimeter, ▲ - 2 millimeters, wavelength: 5145 Å.

MONTE-CARLO CALCULATION OF LIGHT TRANSMISSION THROUGH WATER

by

Kenneth R. Hessel and Alfred H. LaGrone

Antennas and Propagation Laboratory
The University of Texas at Austin, Austin, Texas 78712

SOMMAIRE

Les caractéristiques de transmission de la lumière d'un laser à travers l'eau ont été déterminées à l'aide d'une méthode de Monte-Carlo ; cette méthode consiste à calculer les trajectoires de photon pour prédire la répartition du rayonnement sur un plan perpendiculaire au faisceau lumineux principal, à une distance quelconque de la source.

Pour effectuer cette étude, on a supposé que le photon subissait une diffusion anisotrope de la part des particules diffusantes. Les calculs exigeaient d'autre part que l'on connaisse la longueur moyenne d'absorption, la longueur moyenne de diffusion et la probabilité de diffusion de l'eau.

On a procédé à des calculs sur deux échantillons d'eau, à deux distances différentes pour chaque échantillon ; les résultats en sont présentés au cours de l'exposé. Des mesures effectuées en laboratoire révèlent une excellente concordance avec ces résultats.

MONTE CARLO CALCULATION OF LIGHT TRANSMISSION THROUGH WATER*

Kenneth R. Hessel** and Alfred H. LaGrone
Antennas and Propagation Laboratory
The University of Texas at Austin, Austin, Texas 78712

ABSTRACT

The transmission characteristics of laser light through water have been determined using a Monte Carlo method of photon tracing to predict the irradiance distribution on a plane perpendicular to the main beam of light at any distance from the source. Anisotropic scattering of the photon by the scattering particles was assumed. The calculations required a knowledge of the mean absorption length, the mean scattering length and the scattering probability for the water.

Calculations were made for two water samples at two distances for each sample and are reported. Laboratory measurements show excellent agreement with the computed values.

1. INTRODUCTION

Multiple scattering of a photon must be taken into account in any study of the transmission of light through water. While analytical methods have been developed for radiative transfer [1], it is extremely difficult to calculate numerical values when the scattering function is strongly anisotropic. The Monte Carlo method [2], on the other hand, permits the use of anisotropic scatter functions in predicting the distribution of irradiance on a plane perpendicular to a beam of light at any distance from the source.

2. METHOD

The Monte Carlo method is formulated on the assumption that the propagation characteristics of any homogeneous, isotropic body of water can be described in terms of a mean absorption length $\frac{1}{\alpha}$, a mean scattering length $\frac{1}{\beta}$, and a scattering probability, $f(\theta)$, which is a function of the angle measured from the arrival path. The scattering probability is derivable from a volume scattering function $\sigma(\theta)$. Further, the water is assumed homogeneous with scatterers large compared to the wavelength of light yet small compared to the beam diameter.

The parameters required in the Monte Carlo method are directly measurable, or, as noted above, are derivable from a measured function. The quantity $(\alpha + \beta)$ is obtained by measuring the decrease in the on-axis irradiance of non-scattered light with increasing water path length. The absorption coefficient α is determined approximately by using a large aperture detector, a short path (so that back and angle scattering losses are negligible) and by measuring the decrease in irradiance of the combination of both scattered and non-scattered light with increasing water path length. With α and β determined and the irradiance distribution known at a given distance, it is possible to determine the scattering function $\sigma(\theta)$ using the Monte Carlo method and an iterative technique. Basically the method consists of varying $\sigma(\theta)$ systematically from an assumed scattering function [4] until the irradiance distributions determined by the computer coincide with the measured irradiance distributions.

2.1 COMPARISON OF COMPUTED AND MEASURED IRRADIANCE CURVES

The absorption coefficient α, scattering coefficient β, and volume scattering function $\sigma(\theta)$, as well as irradiance distributions across the beam, have been measured by Duntley [3, 4] for various water samples. Fig. 1 shows a scattering function measured by Duntley [4] for a water sample taken from a local lake. Using Duntley's scattering function with his measured $\alpha = 0.73$ nepers per meter and $\beta = 0.606$ nepers per meter for the lake water, the distribution of irradiance perpendicular to the beam was computed at many distances using the Monte Carlo method. The irradiance distribution computed at distances of 3 and 9 meters is shown in Fig. 2 and Fig. 3, respectively. The path of 4000 photons was traced in obtaining each distribution curve. The irradiance scales for the two curves are identical. In both Fig. 2 and Fig. 3 fluctuations characteristic of the Monte Carlo method can be seen. The amplitude of the fluctuations, of course, could have been reduced by tracing the path of a larger number of photons but with a corresponding increase in the time required.

The computed irradiance distribution shown in Fig. 3 compares very well with the irradiance distribution measured by Duntley [4] for the same water at approximately the same distance. Duntley's points are included in Fig. 3 for comparison. Duntley's measurements [5] were for a constant distance from the source (the angle was varied), whereas, the calculated values reported in Fig. 3 are in a plane normal to the path at a distance of 9 meters from the source. This would mean that the computed curve would have a steeper slope than Duntley's measured curve. There were no measured irradiance distributions available for comparison with the computed distribution shown in Fig. 2.

---

*This work was sponsored in part by the National Science Foundation under NSF Grant GA 767.

**Kenneth R. Hessel is now with Sandia Laboratories, Albuquerque, New Mexico 87115

Figure 4 shows a scattering function derived for an impure water sample having $\alpha = 3.6$ nepers per meter and $\beta = 2.0$ nepers per meter. Measurements at 1.07 meters and 1.57 meters were used in deriving the scattering function. Fig. 5 shows the irradiance distribution computed by the Monte Carlo method with the measured irradiance distribution at 1.07 meters. The agreement is good, which simply means that the Monte Carlo parameters for the problem were properly evaluated. Fig. 6 shows the measured and computed Monte Carlo irradiance distributions at 2.17 meters using the parameters obtained by measurement at the shorter distances. The agreement again is good. The good agreement in this case means that the Monte Carlo method, despite the large α and β measured for the water, enables one to significantly extrapolate measured data to useful distances beyond the last measured point.

3. CONCLUSIONS

The Monte Carlo method of predicting irradiance distributions and determining water parameters is quite effective and should contribute significantly in the evaluation of underwater systems designed to operate in the visible portion of the electromagnetic spectrum.

Once α, β and $\sigma(\theta)$ have been determined for a given body of water, it should be possible to accurately predict irradiance distributions to distances at least an order of magnitude longer than the longest measured distribution distance used in the iterative technique.

REFERENCES

[1] Chandrasekhar, Radiacive Transfer (Dover Publications, New York, 1960).

[2] K. R. Hessel, "Theoretical and Experimental Study of the Transmission of Laser Radiation Through Water," Ph. D. Thesis, The University of Texas at Austin, May 1969.

[3] S. Q. Duntley, "Light in the Sea," J. Opt. Soc. Amer., 53, 214-233, Feb. 1963.

[4] S. Q. Duntley, "Underwater Optics," AD No. 631033, 12 March 1966.

[5] S. Q. Duntley, unpublished letter to Mr. Frank B. Isakson dated 12 March 1966.

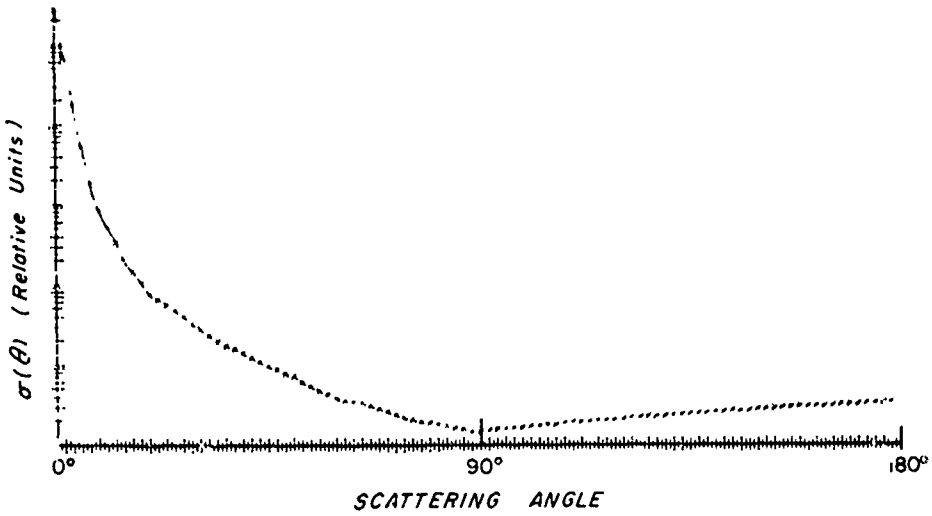

Fig. 1 Duntley's Volume Scattering Function for Lake Water

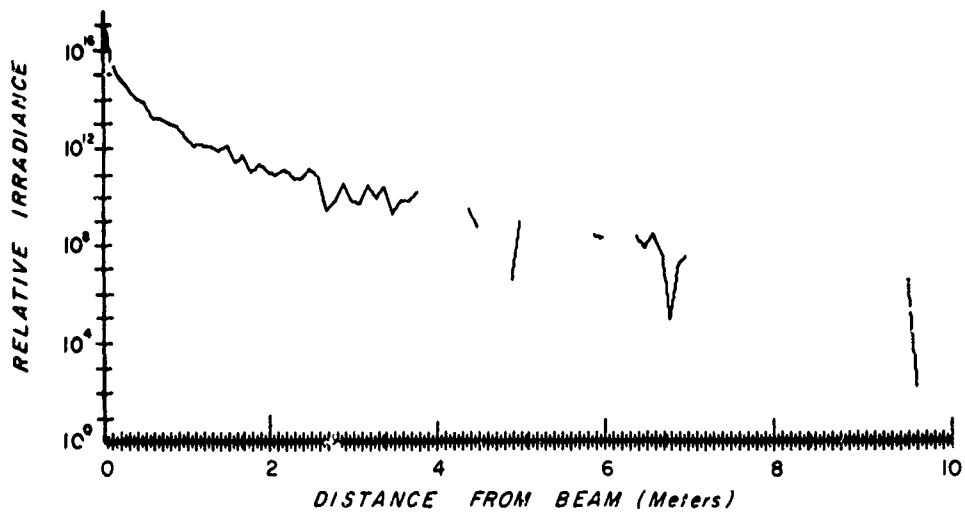

Fig. 2 Irradiance Distribution at 3 Meters for Duntley's Lake Water Sample

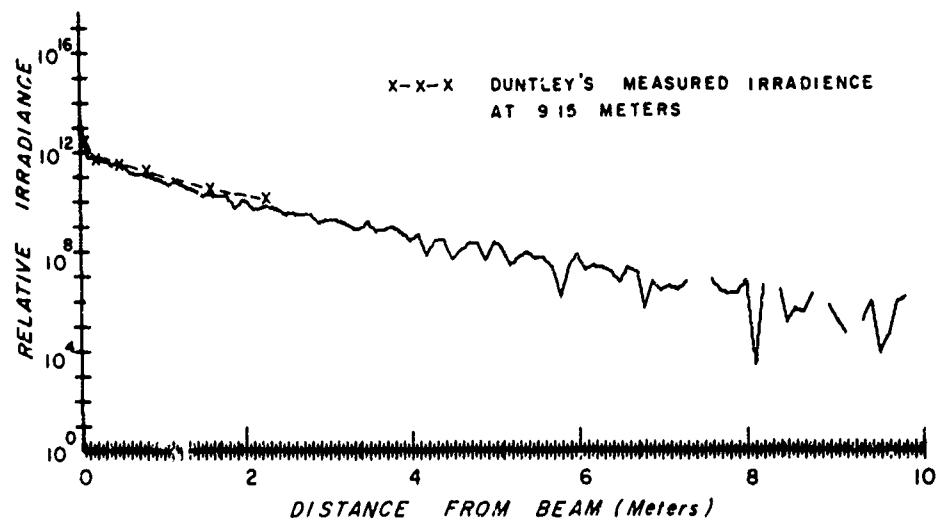

Fig. 3 Irradiance Distribution at 9 Meters for Duntley's Lake Water Sample

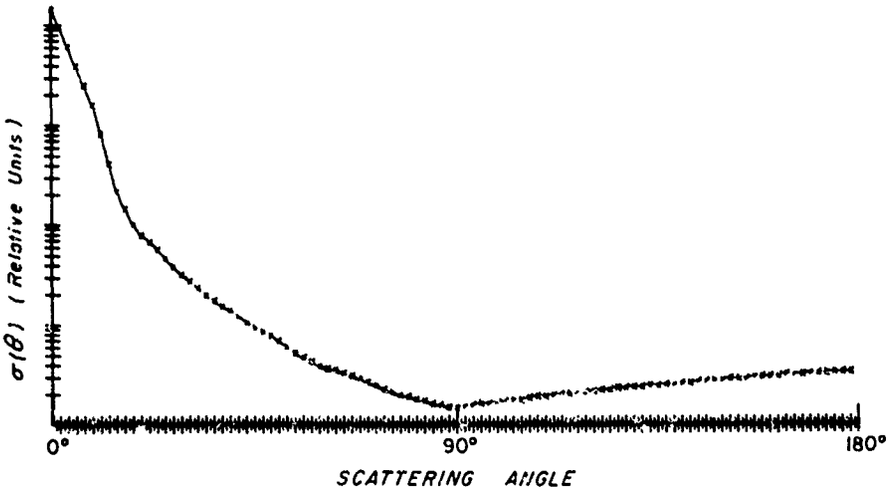

Fig. 4 Volume Scattering Function for Contaminated Tap Water Sample

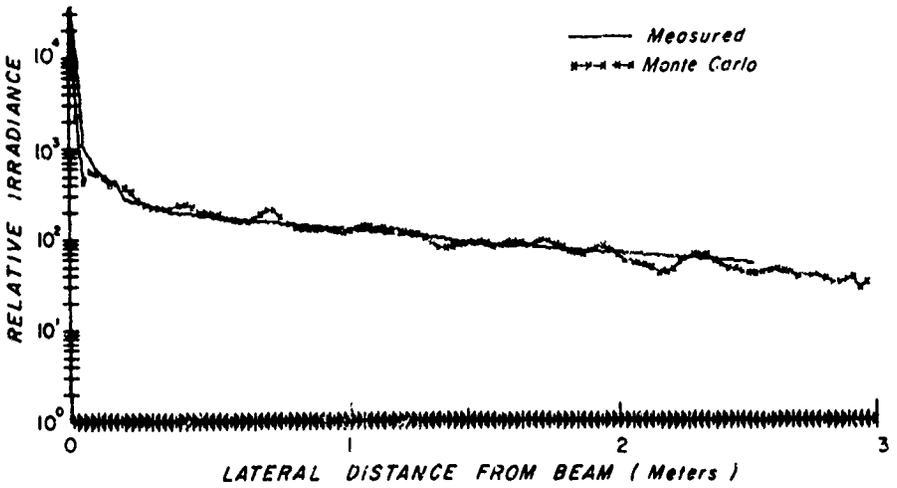

Fig. 5 Measured and Monte Carlo Irradiance Distributions at 1.07 Meters for Contaminated Tap Water Sample

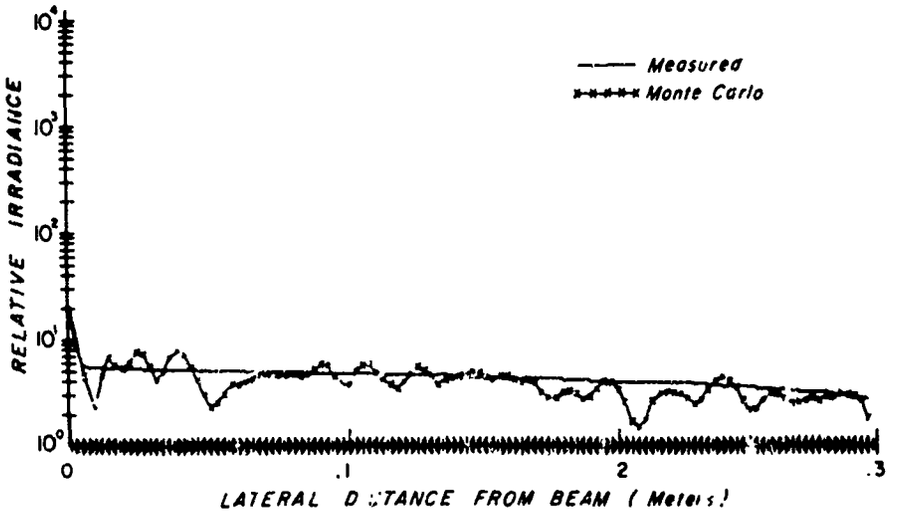

Fig. 6 Measured and Monte Carlo Irradiance Distributions at 2.17 Meters for Contaminated Tap Water Sample

THE ATTENUATION OF COLLIMATED LIGHT BY SEA WATER

by

D.G. Keith-Walker, C.ENG. B.Sc. F.I.E.E.
Chief Engineer

Electronics Research Laboratory,
The Plessey Co.Ltd.,
Martins Road,
Havant, England

SOMMAIRE

L'auteur décrit un programme de travail étendu, mené par le Laboratoire de recherche électronique de la Co Plessey dans le but de déterminer l'atténuation d'un faisceau lumineux collimaté se propageant à travers l'eau de mer.

Il étudie d'abord les facteurs qui affectent l'atténuation de la lumière ; ce sont l'absorption, la diffusion, la longueur d'onde et la divergence du faisceau. Ces facteurs obligent à effectuer une série de mesures sur les propriétés de diffusion et d'atténuation de l'eau. L'auteur décrit la conception et la fabrication de l'équipement nécessaire à la réalisation de mesures extrêmement précises de l'atténuation d'un faisceau collimaté, in situ, c'est à dire dans l'eau de mer ; il expose ensuite certains détails du programme de mesure. Le but de ce programme était l'obtention de profils d'atténuation jusqu'à une profondeur d'environ 300 m pour toute une gamme de turbidité de l'eau de mer, ainsi que pour d'autres conditions.

L'auteur présente enfin un choix de résultats obtenus, en montrant qu'ils sont liés à d'autres facteurs d'environnement.

SUMMARY.

The paper described an extensive programme of work which has been carried out by the Electronics Research Laboratory of the Plessey Company to determine the attenuation of a collimated light beam propogating in sea water.

Initially the factors which affect the attenuation of light are discussed; these are absorption scattering, wavelength and beam divergence. The necessity to carry out a series of measurements on the attenuation and scattering properties of water arises out of the consideration of these factors. The design and construction of the equipment necessary to make highly accurate measurements of the attenuation of a Collimated beam in situ in sea water is presented and followed by details of the measurement programme. This programme was designed to obtain the attenuation profiles down to depths of approximately 300 metres for a range of sea water turbidities and other conditions.

A selection of the results of these measurements are presented and it is shown that they are related to other environmental factors.

1. INTRODUCTION.

The general requirement which initiated the work described in this paper was the determination of the total attenuation of a collimated light beam when passing through sea water; this should be determined for a wide range of sea conditions, geographical locations and depths.

1.1. Aims.

The initial aim of the programme of work was to investigate whether the requirement could be met by the use of results obtained by other workers. It was found that though many workers had studied and measured the attenuation of day light diffusing down through the sea from the surface, the results obtained were, at that stage, no real help in predicting the attenuation of a small collimated beam of light. Such measurements of collimated light attenuation which existed were too restricted to meet our full requirement.

It therefore became necessary to make the main aim of the work the measurement of collimated attenuation in sea water areas and conditions, which would, as far as possible, be representative of more extensive areas. An additional aim was to attempt, on an empirical basis, to correlate the collimated and diffuse attenuation measurements so that the collimated attenuation could be predicted wherever diffuse measurements had been made.

1.2. Approach.

The programme of work to be carried out over a three year period was as follows:

(a) An investigation of the causes of light attenuation in sea water.
(b) The highlighting of the theoretical difference in the attenuation of diffuse and collimated light.
(c) The design and construction of equipment to measure both collimated and diffuse attenuation.
(d) To carry out measurements in reasonably representative sea waters.
(e) To analyse the results and attempt the prediction of collimated attenuation from diffuse attenuation results.

1.3. Comments.

After three years work there is a considerable amount of detail and information which could be disseminated . It is necessary in a paper such as this to reasonably condense the information and for this reason only the collimated attenuation equipment will be described and the presentation of results will be a summary of the total results obtained.

2. THE ATTENUATION MEASUREMENT PROBLEM.

Basically the problem is: what measurements should be made? How and where should they be carried out for the greatest effectiveness? The factors which can affect the attenuation of light are wavelength, absorption, scattering, beam divergence, location, depth, environment and season.

The determination of the optimum wavelength to use was not difficult as information was readily available in the literature that a fairly wide transmission pass band exists for clear ocean water centred on 0.46 micro metres. The other factors were investigated in the measurement programme in a reasonably controlled fashion with the exception of variations due to the season which was determined by the availability of a suitable ship.

2.1. The Attenuation Mechanism.

Figure (1) shows a simple diagram of a collimated beam and the total attenuation coefficient (c) can conveniently be split into two components: the absorption coefficient (a) and the total or integrated scattering coefficient (b). In the case of the attenuation of diffuse light a considerable proportion of light scattered out of a path is replaced by light scattered into it, and the total effective attenuation coefficient (d) will approach the value of the absorption coefficient in the collimated attenuation expression,

2.2. The Required Measurements.

Obviously a direct measurement of the collimated attenuation coefficient (c) should be carried out as this is the prime requirement; however, an important subsidiary measurement is the determination of the diffuse attenuation coefficient (d) under similar conditions, to allow for comparison. As a possible check it was thought worthwhile to obtain an estimate of the collimated beam scattering coefficient (b) are compare the validity of the assumption that:

$$C \simeq d + b.$$

The Measurement Areas.

Ideally measurements would have had to be carried out on a world wide basis at all times of the year; this was obviously impossible and a choice of what was thought to be reasonably representative waters in the proximity of Europe was made. The sea conditions which it was thought would best fulfil this requirement were coastal waters, shallow sea, deep sea under different environmental and geographical conditions and continental shelf waters. The actual areas and the relevant sea conditions are outlined in the section on results of measurement (Section 4).

3. THE MEASUREMENT EQUIPMENT.

The measurements to be made were as follows:

Total collimated attenuation coefficient (c)
Total scattering coefficient (b)
Total diffuse attenuation (d)
Depth
Temperature

The last three measurements are comparatively standard and the methods will not be described here; however, it is worthwhile mentioning the principle of the methods adopted to determine the first two measurements.

3.1. Principle of Methods.

Collimated attenuation coefficient.

Fig.2 shows the collimated path. For a measurement path length of one metre under entirely uncontamminated water conditions of some 100 db/Km attenuation the ratio of light intensity (I_{2/I_1}) is approximately 0.98. To obtain a reasonable degree of accuracy the measurement of I_1 and I_2 has to be made to $\pm$ 0.1%. This is an impossible stability requirement for an equipment which has fixed positions of light source and detector and is calibrated before the measurement. However this order of accuracy can be obtained by physically moving the detector through a distance (Δx) and accurately measuring the maximum and minimum values of light intensity. The method is independent of long term changes in source power, detector sensitivity and window transmission as such changes affect both readings proportionately, and the distance (Δx) need only be known to an accuracy of a few per cent.

Total Scattering Coefficient:

An estimate of the total scattering coefficient can be obtained by making two measurements of the scatter coefficient $\beta(\theta)$ at = 35° and 180° and fitting the standard Jerlov (1) scatter curve to them. The value of the total scattering coefficient (b) can then be obtained by integrating the curve:

$$b = \frac{1}{2\pi} \int_0^{\pi} \beta(\theta) \sin\Theta \, d\Theta$$

3.2. Equipment.

A photograph of the measurement equipment is shown in figure 3. The light source is mounted vertically at the top of the framework and the collimated beam is projected down to the main beam detector mounted within the trolley structure, which is caused to traverse along the beam by a toothed belt drive powered by a fully immersed induction motor. The 35° forward scatter detector is mounted vertically to the left of the source and views the main beam via an angled mirror. The back scatter detector can be seen facing outwards next to the source unit and views a subsidiary beam projected outwards in the same direction. All the detector units contain optical filters centred on 0.46 micrometres. In addition to the optical measurements a pressure transducer monitoring depth and an indicator of maximum and minimum traverse of the main detector trolley is provided.

In use the equipment is suspended from a ten core cable connected in the ship to control, powering and monitoring equipment. The measurements can be made manually from a digital voltmeter, but for normal operation both a numeral print out and a punched paper tape output are used.

Total diffuse attenuation is measured using a separate photo multiplier photometer equipment to determine the illumination profile with depth under daylight conditions. Sea temperature profiles were also obtained using a standard bothythermograph.

4. RESULTS OF MEASUREMENTS.

Figure 4 is a map showing the positions of the measurement areas. In general the procedure carried out was to make a series of measurements, usually along a straight line, in the area of interest. The results presented here show one depth profile for each area which as far as possible is representative of the area; however, in some cases, notably the coastal areas, very considerable variations in average attenuation and profile were experienced within comparatively short distances.

Area A. - Coastal waters of the Western English Channel approximately 15 Km from a comparatively lightly populated coastline. Figure 5 shows no significant structure in the attenuation profile and the water is undoubtedly mixed and contains river contamination.

Area B. - Coastal waters of the Eastern English Channel approximately 50 Km from a heavily populated coastline. Figure 6 shows fairly heavy attenuation at all depths, which even at this distance from the coast is comparatively heavily contaminated. Nearer the coast a constant attenuation of 3,000 db/Km was recorded.

Area C. - Shallow sea (North Sea) some 100 Km from the coast of Scotland. Figure 7 shows an interesting profile with an exceptionally low attenuation trough at 45 metres depth for which we have no

reasonable explanation, though it occurred for other measurements in the area. The average attenuation was less than expected as there is both considerable contamination and plankton activity in the North Sea.

Area D. -Deep sea East of Iceland with cold Greenland currents mixing in. Figure 8 shows a very high surface attenuation dropping below the thermocline to a very low value. The high attenuation in this area is undoubtedly due to the plankton concentration which in this area is above the thermocline. A surface attenuation of 5,000 db/Km was recorded at one position in the area.

Area E.- Deep sea south of Iceland with warm Gulf Stream currents. Figure 9 is somewhat similar to Fig.8, though in this case no thermocline exists.

Area F.- Deep Atlantic Ocean some 300 Km west of the Straits of Gibraltar. Fig.10 shows a profile which appears to be typical of many oceanic areas. The surface layer attenuation is not great but at a depth of some 70 metres, just below the thermocline, it peaks up, indicating a heavy plankton layer. The peak is usually not much more than a few tens of metres deep and below it the attenuation falls to an exceptionally low value sometimes approaching that of distilled water.

Area G.- Atlantic continental shelf water of some 600 metres depth west of the Straits of Gibraltar. In Figure 11 the profile shape is similar to that in the deep atlantic waters but the attenuation peak at 70 metres is considerably larger due to more favourable plankton conditions.

Area H.- Deep Mediterranean waters south east of the Balearic Islands. The profile in figure 12 is almost identical with the deep Atlantic measurement of figure 10, the peak being about 20 metres higher correlating well with the thermocline which is also a corresponding amount higher.

5. DISCUSSION OF RESULTS.

The principle aim of the measurements carried out in this programme was to enable a reasonable prediction to be made of the collimated attenuation in various sea waters of the world. This can be achieved in three ways: the direct results obtained for reasonably representative areas can be extrapolated to other areas; a relationship with diffuse attenuation measurements can be established; lastly, if a relationship with plankton density can be established a knowledge of plankton behaviour would enable attenuation predictions to be made.

In the measurement programme diffuse attenuation measurements were made at all the positions, though full depth profiles were only obtained at some of them. A comparison between averaged results for collimated and diffuse attenuation is shown in figure 13. From this curve it can be seen that above a diffuse attenuation figure of 150 db/Km the collimated attenuation coefficient is twice the diffuse value. Below this attenuation the factor is smaller. An attempt to confirm the assumption that the collimated attenuation was nearly equal to the sum of the diffuse attenuation and the total scatter coefficient met with only partial success. On average the calculated collimated attenuation figure was 25% greater than the measured one but there was a considerable spread in values.

The correlation between collimated attenuation and plankton density has been cited during the presentation of the results in section.4. By way of illustration it is helpful to compare a result (Figure 14) obtained by Menzel and Ryther (2) of the phytoplankton density off Bermuda under similar thermocline conditions to our Atlantic and Mediterranean results.

As a result of the work carried out certain conclusions can be reached:

The collimated attenuation of sea water can be predicted to a reasonable degree of accuracy if diffuse attenuation measurements are available. Also, with a lesser degree of accuracy, predictions can be made for waters where the plankton ecology is understood; this is particularly relevant to open ocean waters. An interesting result to come out of the work was that at depths below 100 metres in deep ocean the clarity of the water closely approaches that of distilled water; this situation exists down to at least 300 metres which was the limit of our measurements.

6. REFERENCES.

1. Tyler, J.E. and Preisendorfer, R.W. 'The Sea' Vol.1. Ch.6. Interscience Publishers. 1962.

2. Menzel, D.W. and Ryther, J.H. 'The Annual cycle of Primary Production in the Sargasso Sea off Bermuda'. Deep-Sea Res. 6. 351-367. 1960.

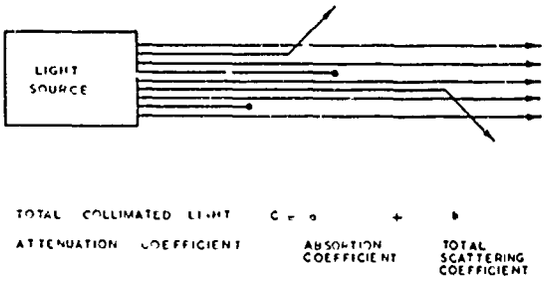

TOTAL COLLIMATED LIGHT ATTENUATION COEFFICIENT = ABSORPTION COEFFICIENT + TOTAL SCATTERING COEFFICIENT

DIFFUSE LIGHT ATTENUATION COEFFICIENT

Fig.1 The collimated beam

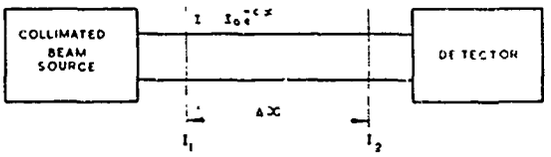

$$c = \frac{1}{\Delta x} \log_e \left(I_1/I_2\right)$$

OR IN db/m $c = \frac{10}{\Delta x} \log_{10} \left(I_1/I_2\right)$

Fig.2 The attenuation coefficient measurement

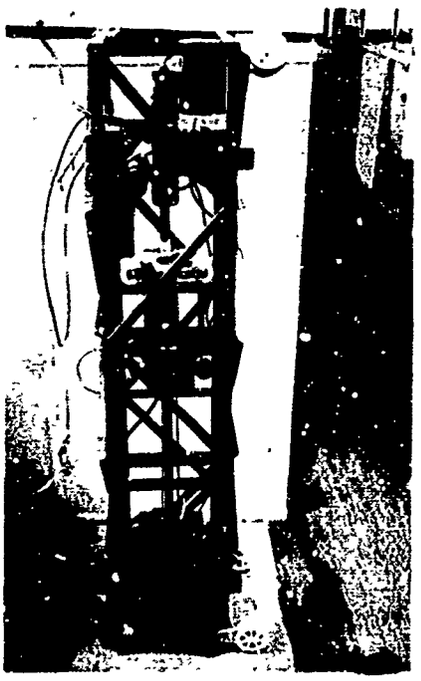

Fig.3 The collimated attenuation equipment

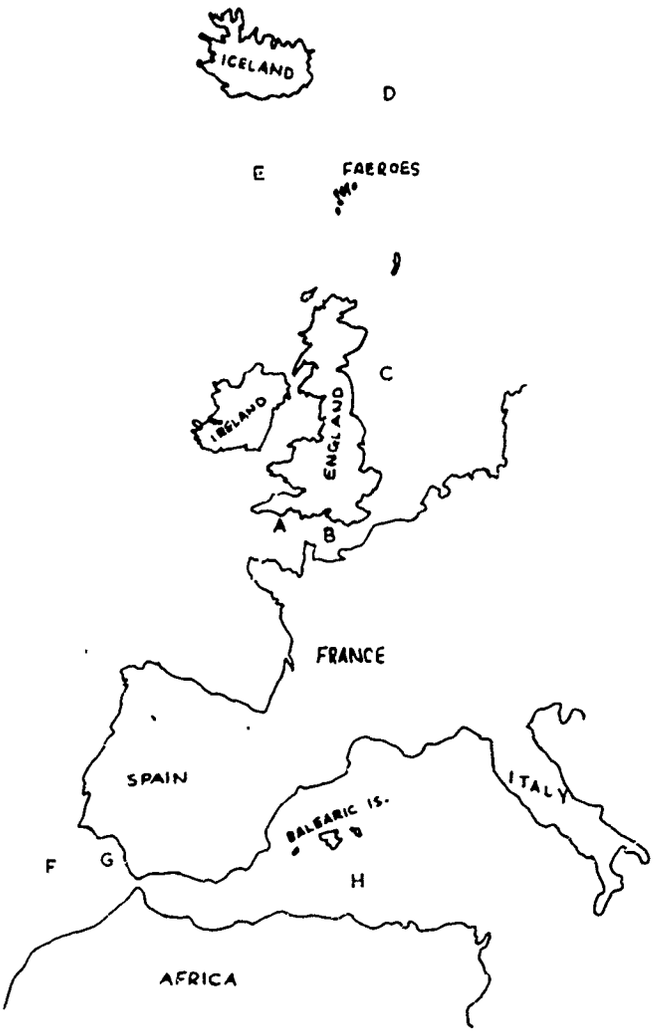

Fig.4 Map of measurement areas

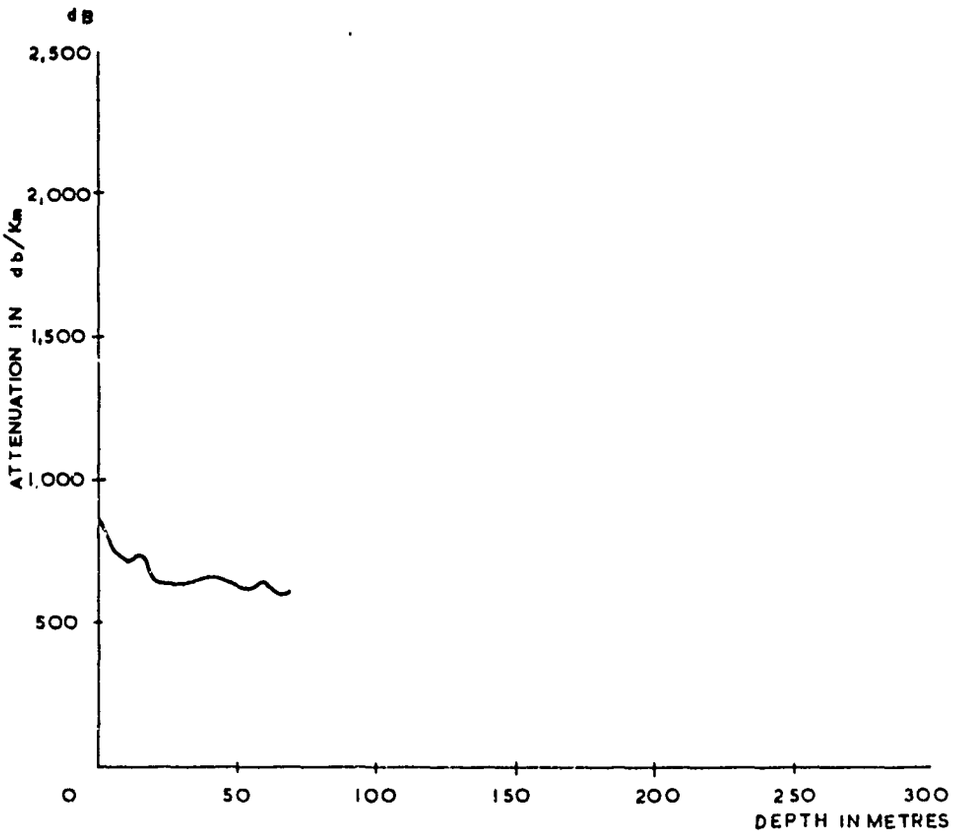

Fig.5 Attenuation profile in area A

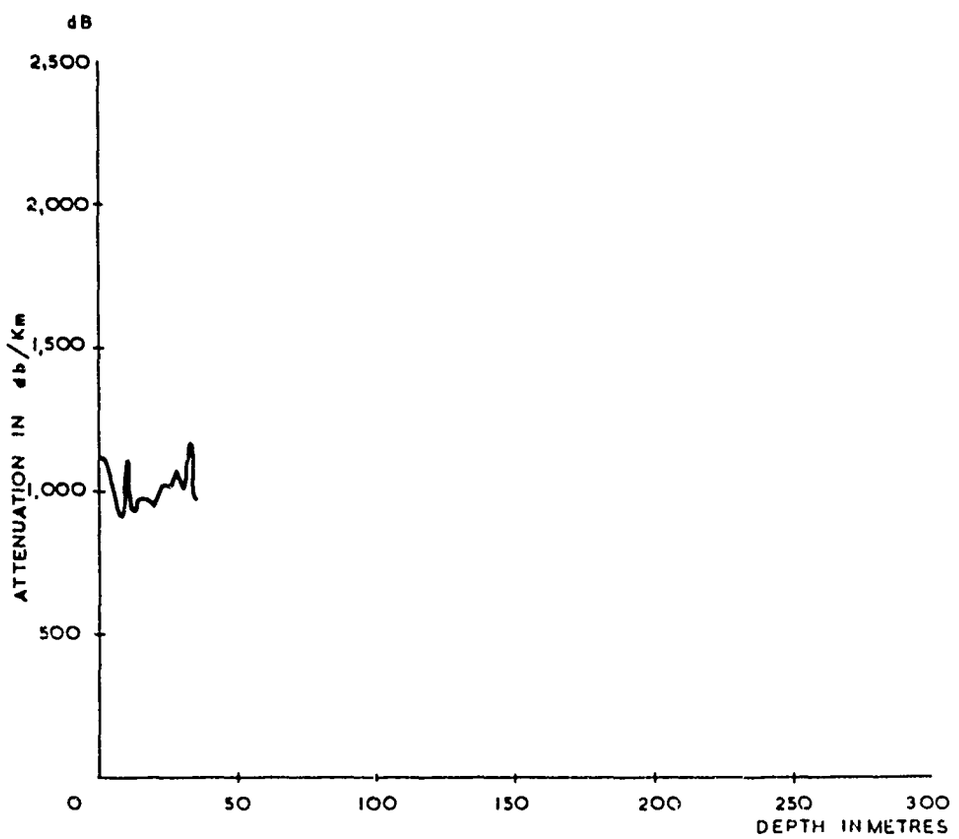

Fig.6 Attenuation profile in Area B

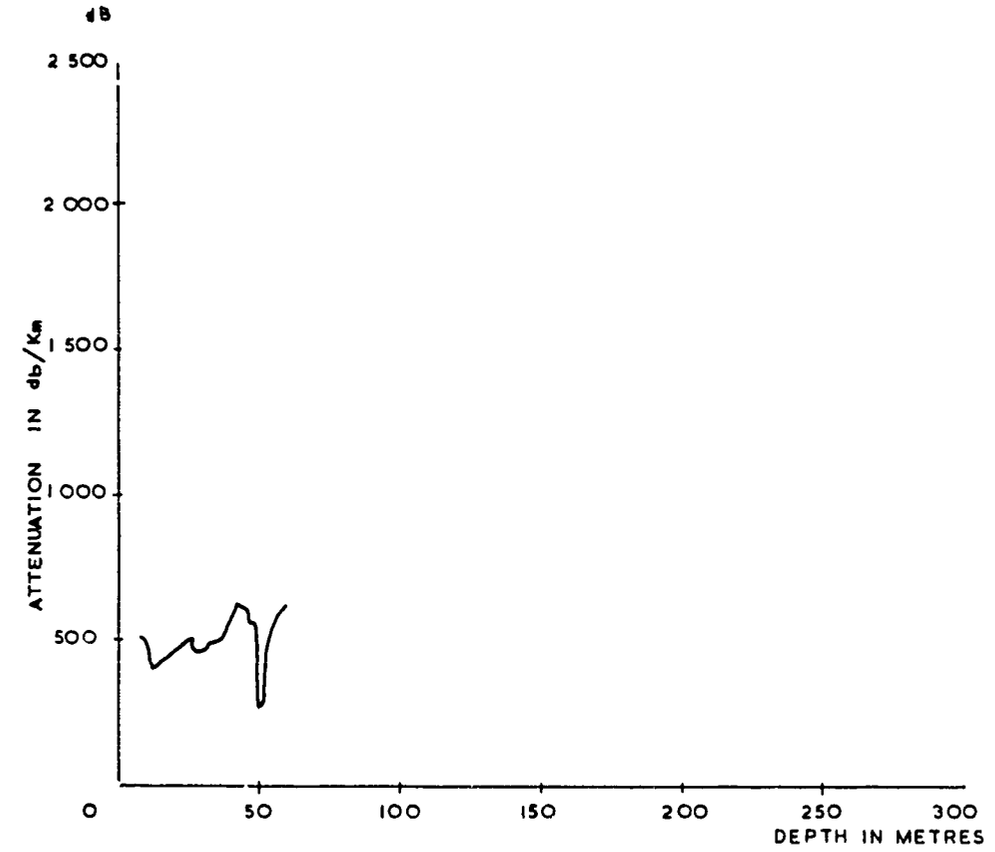

Fig.7 Attenuation profile in area C

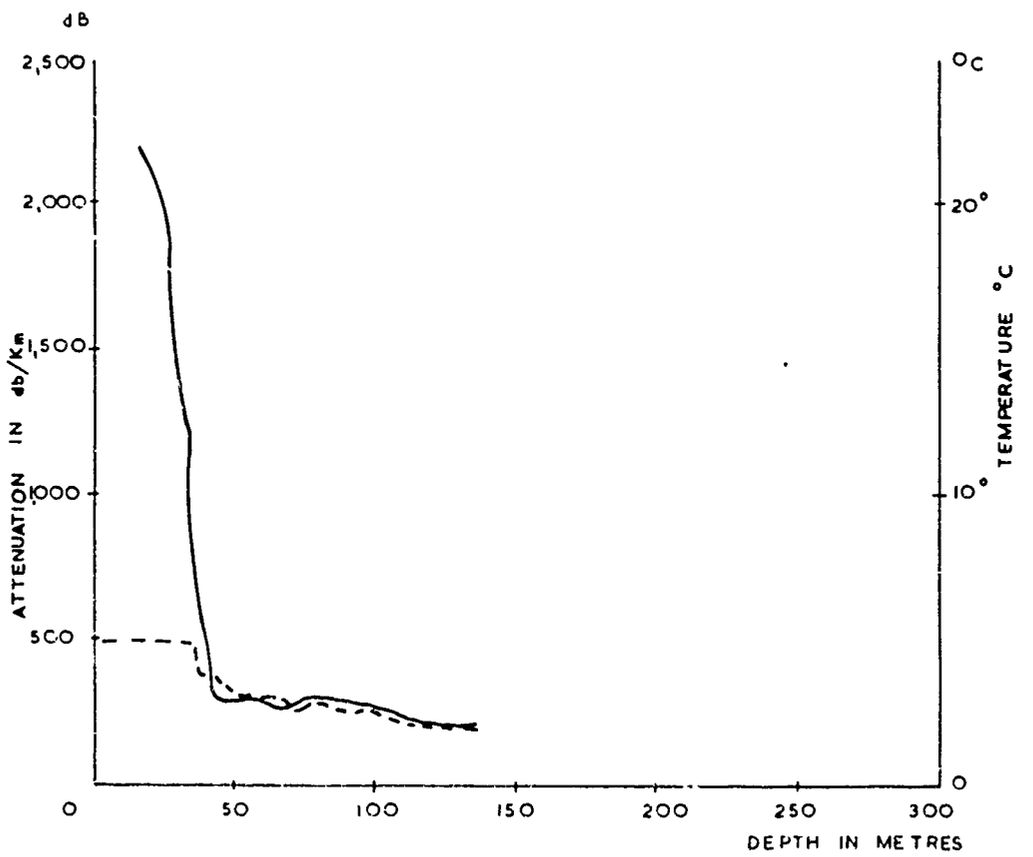

Fig.8 Attenuation profile in Area D

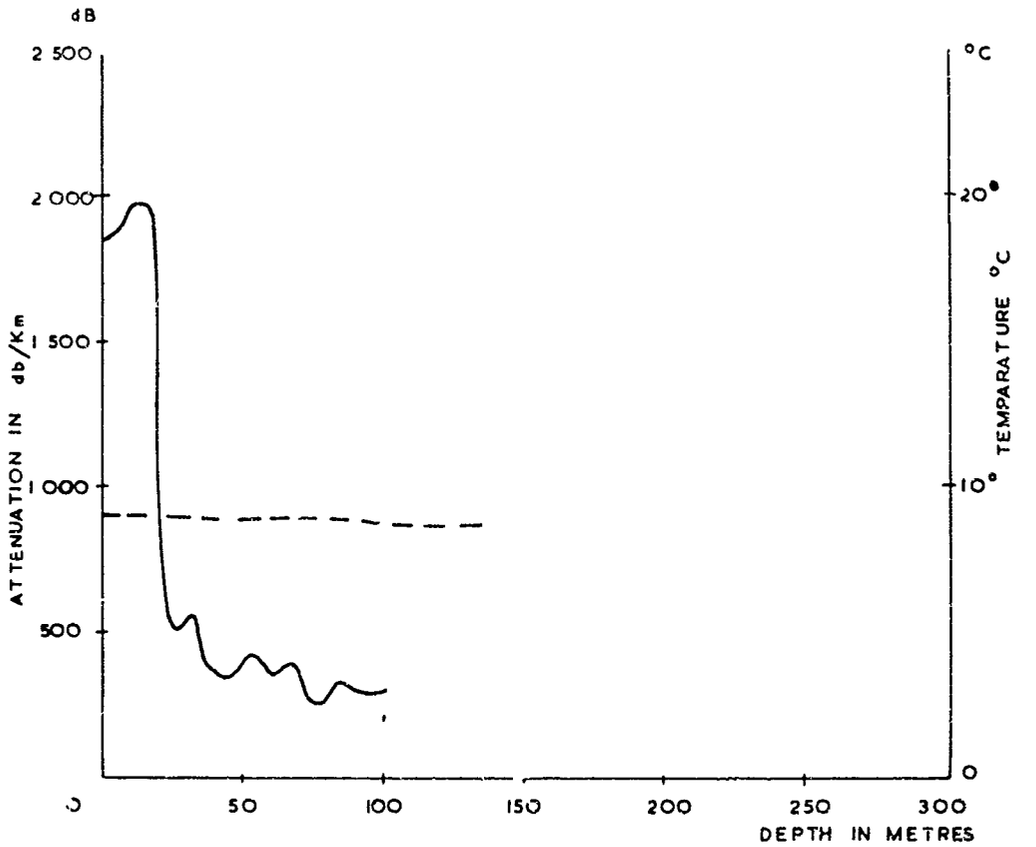

Fig.9 Attenuation profile in area E

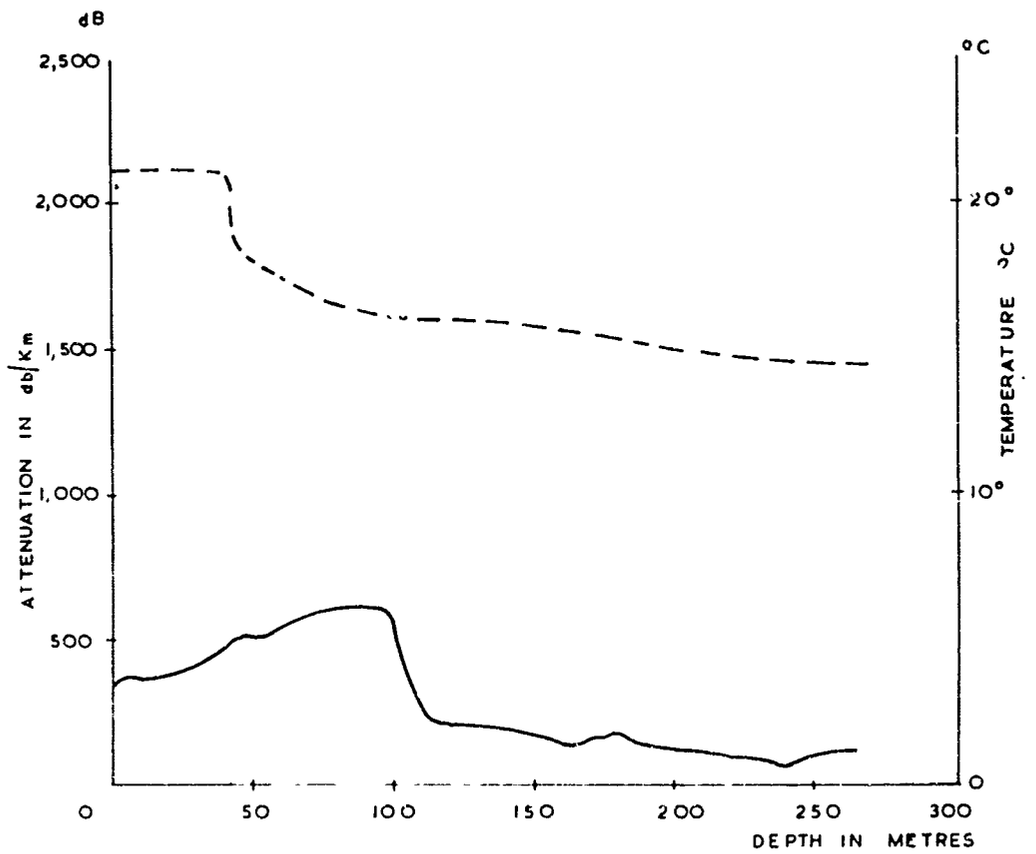

Fig.10 Attenuation profile in area F

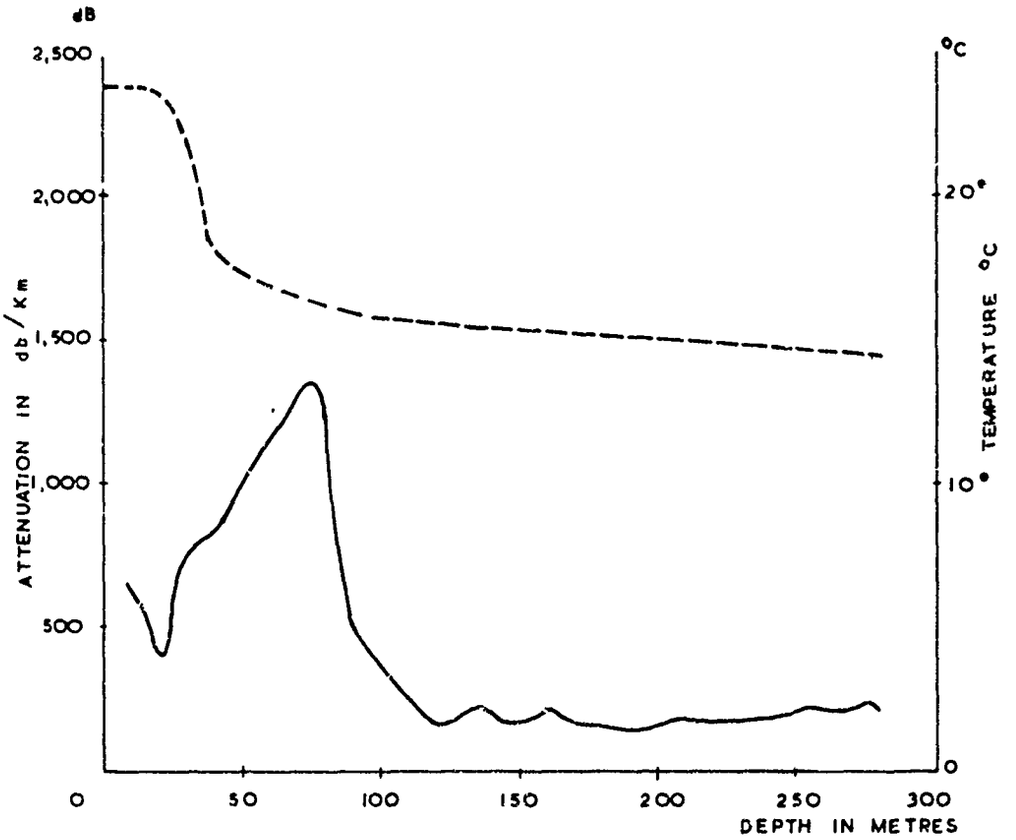

Fig.11 Attenuation profile in area G

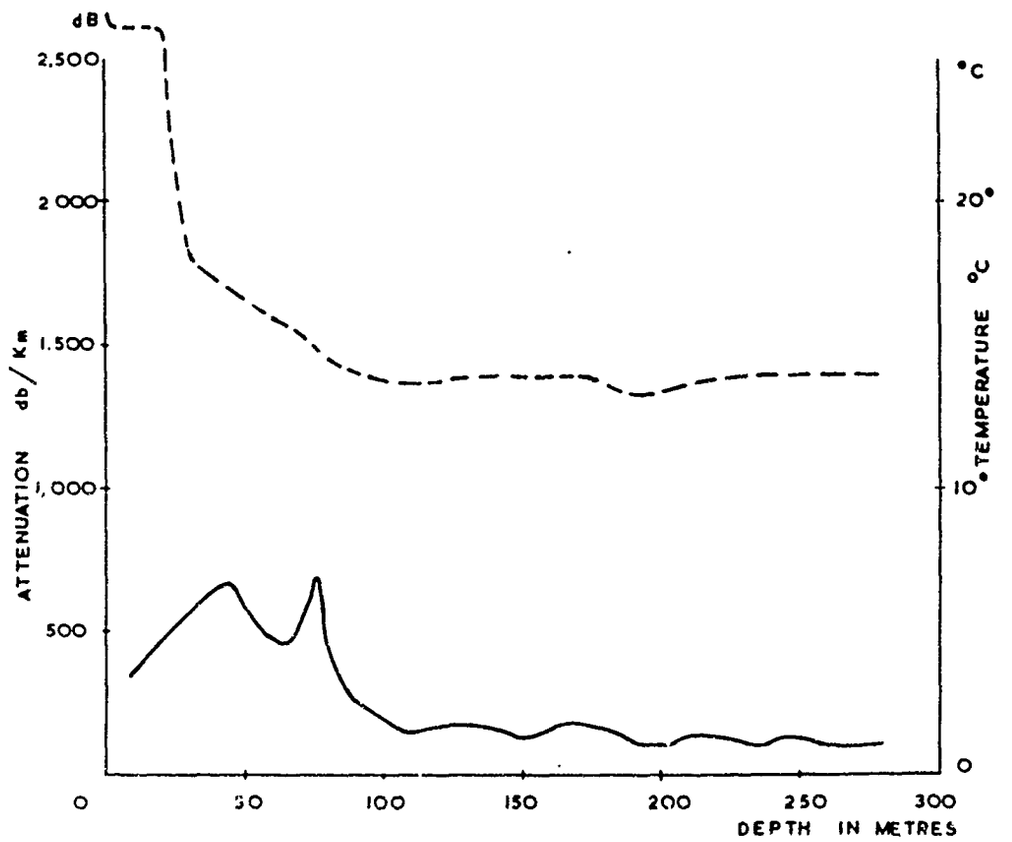

Fig.12 Attenuation profile in area H

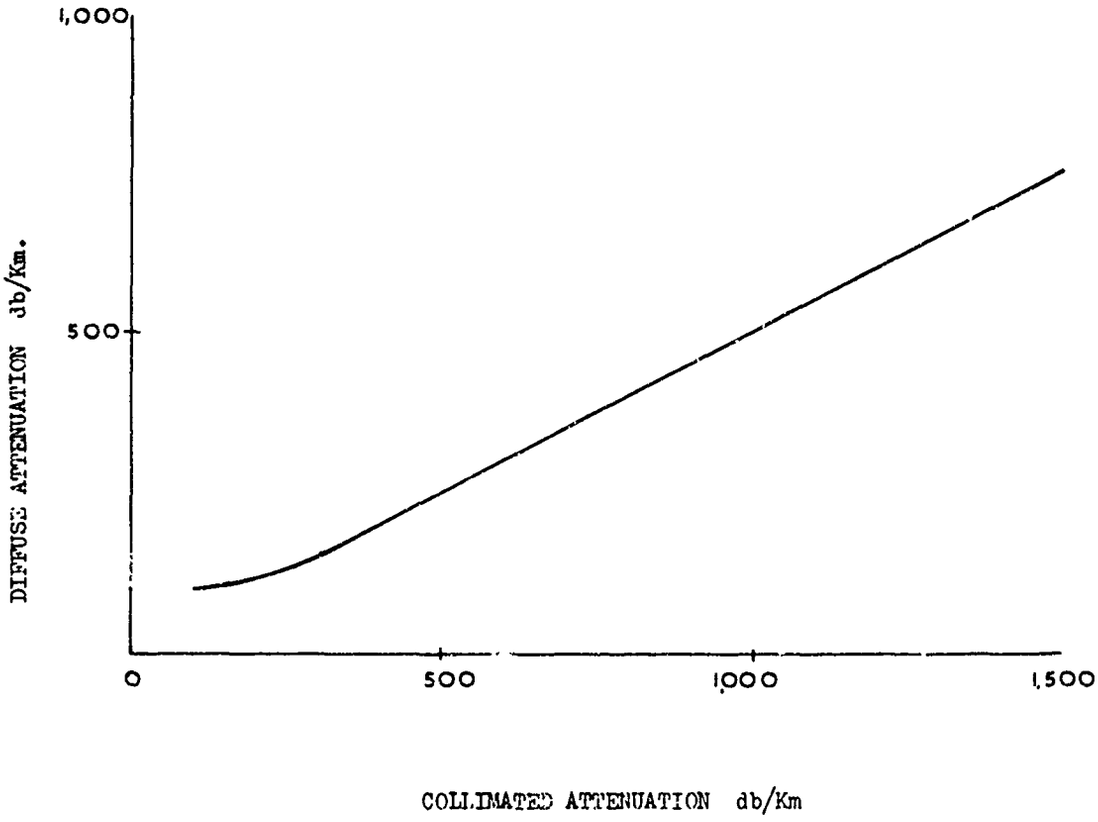

Fig. 13 Diffuse versus collimated attenuation

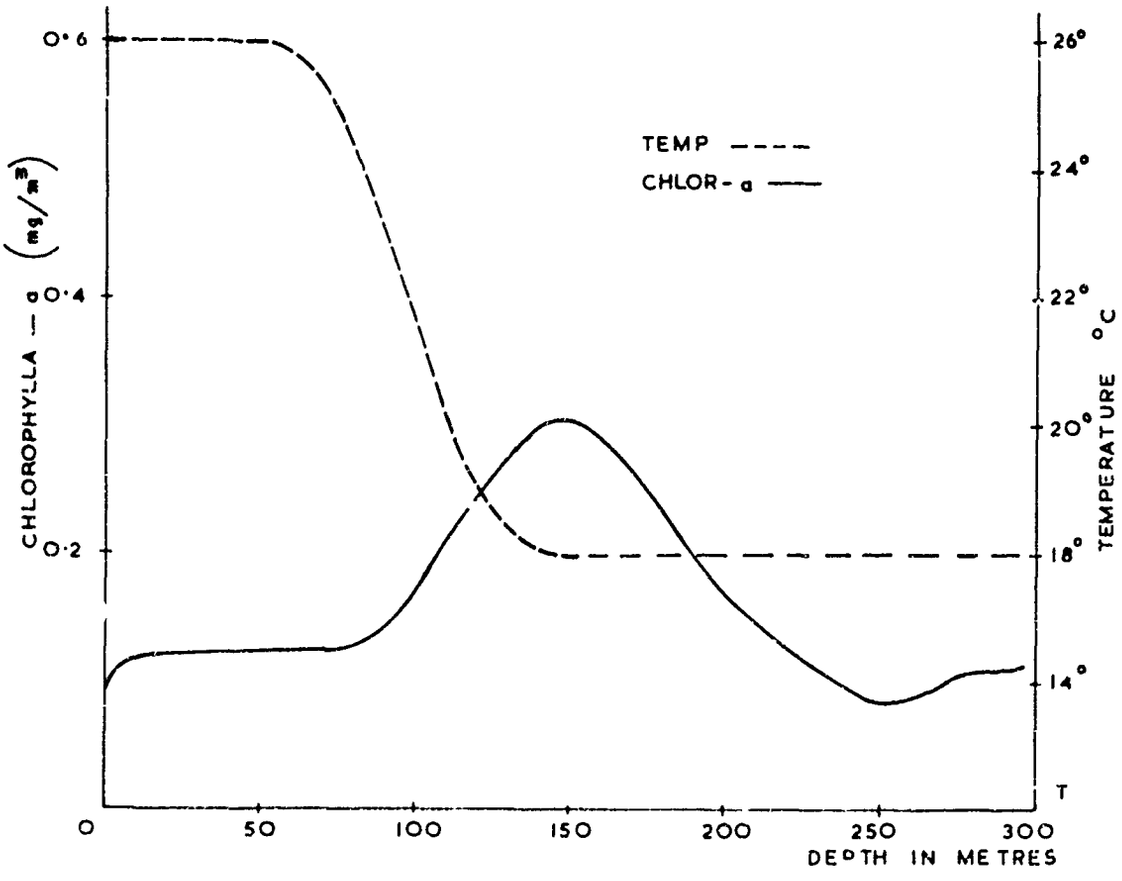

Fig. 14 Plankton density profile

EXAMEN DE RESULTATS EXPERIMENTAUX CONCERNANT LA DIFFUSION DE LA LUMIERE PAR LES EAUX DE MER .

par

André Morel

Université de Paris
Laboratoire d'Océanographie Physique
Villefranche-sur-Mer France

SUMMARY

The degradation of light energy in seawater can be dire tly investigated by surmerging "photometres" and measuring the submarine remainder of daylight at various depths. While they are relatively simple, such experiments are difficult to interpret in view of the complexity of the existing natural conditions : infinite medium, multiple scattering, large size source (sky), superimposed on a variable incidence source (sun). Experiments conducted with an artificial source are easier to interpret, and in particular the possibility of producing an almost parallel light beam allows one to obtain conditions not too remote from the theoretical ones, in which the magnitude absorption and scattering, which cause the attenuation of the initial flow, are defined.

Absorption and scattering are dependent on wavelength. The various studies dealing with absorption coefficient variations in the visible and near ultra-violet range will be reviewed, discriminating between what is ascribable to water, mineral ions, and organic substances in solution in seawater.

In natural seawater, scattering predominates over absorption (except in the infra-red range); scattering itself is the result of molecule scattering and suspended particle scattering.

The spectral dependence of molecule scattering which is theoretically known, has been experimentally established. The direct study of scattering selectivity by particles is delicate, as it involves extremely accurate measurements as far as absolute values are concerned ; one of the indirect methods developed in our laboratory consists in studying selectivity for a given scattering angle, and checking whether the shape of the scattering indicator varies with the wavelength.

The results obtained can be confirmed, at least in the case of sufficiently turbid water, by effecting attenuation measurements in the same spectrum range, and deducting absorption.

EXAMEN DE RESULTATS EXPERIMENTAUX CONCERNANT LA DIFFUSION DE LA LUMIERE PAR LES EAUX DE MER.

André MOREL

Université de Paris,
Laboratoire d'Océanographie physique,
Villefranche-sur-Mer France.

RESUME

Sont présentés les principaux résultats obtenus, relatifs à la diffusion de la lumière par les eaux de mer. Ils concernent la détermination de l'indicatrice, aux angles moyens et aux petits angles, l'étude des variations de cette indicatrice et une interprétation de celles-ci, compte tenu du rôle joué par la diffusion moléculaire ; l'influence de la longueur d'onde est également examinée. Quelques applications sont indiquées qui ont trait au calcul ou à la mesure du coefficient total de diffusion, ainsi qu'aux relations entre propriétés diffusantes et abondance du matériel en suspension.

Cette communication a pour objet de présenter le programme des recherches effectuées dans notre laboratoire, qui concernent la diffusion de la lumière par les eaux de mer. Les principaux résultats obtenus sont brièvement présentés, ou pour certains rappelés ; un aperçu est également donné des orientations actuelles de ce travail. Cependant, il ne s'agit pas d'un état de la question puisqu'en fait nous nous sommes cantonnés à un exposé de nos propres conclusions.

Ce programme a pu être exécuté en grande partie grâce à l'aide financière de la Direction des Recherches et Moyens d'Essais (contrats 63/63, 12/65), à qui nous exprimons ici nos remerciements.

MESURES A ANGLE FIXE ET DETERMINATION DE L'INDICATRICE DE DIFFUSION.

L'étude de la diffusion de la lumière par les eaux de mer a débuté par les mesures systématiques de A. Ivanoff pour lesquelles il a développé une instrumentation adaptée au travail à la mer (1) : le diffusiomètre à angle fixe utilisé permet la mesure de l'intensité de la lumière diffusée à 90° du pinceau incident ainsi que le taux de polarisation. Ce type d'appareil a été par la suite calibré de façon que la mesure puisse être exprimée en valeur absolue : β_{90} (ceci grâce à l'appareil mentionné ci-dessous). Dans le cadre d'études descriptives des océans de telles mesures sont toujours pratiquées (2) (3) (4).

Les premières déterminations d'indicatrice de diffusion, entre 30° et 150°, ont été exécutées en 1962 à l'aide d'un gonio-diffusiomètre Wippler Scheibling (5), modifié par la suite. Il a d'abord été constaté (6) que moyennant certaines précautions (absence de transvasement, ou transvasement sans pollution, agitation de l'échantillon, rapidité de la mesure...) les indicatrices obtenues *in vitro* étaient significatives et comparables à celles obtenues *in situ* par d'autres auteurs (J. Tyler, N. Jerlov) (7) (8) ; la pollution lorsqu'il s'agit d'échantillons très "limpides" recueillis à grande profondeur est évidemment à redouter surtout si l'on songe que de telles eaux sont plus pures optiquement que la plupart des eaux distillées préparées en laboratoire.

Des mesures systématiques (à la longueur d'onde 546 nm) effectuées sur des eaux très variées en Manche et en Méditerranée ont montré que les conclusions faites indépendamment dès 1963 par N.G. Jerlov et S.Q. Duntley (9) (10), au vu des premières indicatrices publiées, devaient être nuancées : ces auteurs en effet notaient que les diverses indicatrices étaient très voisines pour les angles inférieurs à 90° (diffusion avant), mais pouvaient notablement différer pour les angles supérieurs à 90° (diffusion arrière). En réalité les mesures prises en considération étaient toutes relatives à des eaux superficielles où la teneur en particules est toujours relativement élevée, or il a été constaté que dans le cas des eaux très claires de profondeur, la partie "avant" pouvait être, elle aussi, modifiée, la dissymétrie de l'indicatrice étant dans ces conditions considérablement réduite - cf fig. 1, ref. 11 ou fig. 15, ref. 4 -.

La première interprétation des variations de forme observées consiste à invoquer le rôle plus ou moins important joué par la diffusion moléculaire, rôle qui peut ne pas être négligeable même pour la partie "avant" dans le cas des eaux particulièrement limpides. Constatant que la forme de l'indicatrice paraissait pratiquement déterminée par l'intensité même de la diffusion, ou en d'autres termes, que la forme de la courbe variait *grosso modo* régulièrement avec la "limpidité" des échantillons, on a cherché (11) à vérifier l'hypothèse, selon laquelle l'indicatrice résultante pour l'eau de mer obéirait en quelque sorte à une loi de mélange, c'est à dire à l'addition de l'indicatrice constante et symétrique de l'eau pure et de l'indicatrice dûe aux particules, invariable en forme en première approximation, mais variable seulement en magnitude, proportionnellement à la concentration.

S'il en est ainsi, des relations linéaires doivent être trouvées lorsqu'on porte pour divers échantillons les coefficients de diffusion pour un angle θ donné en fonction du coefficient pour 90° par exemple ; la répartition des points expérimentaux semble bien traduire l'existence de telles relations linéaires - cf fig. 2 et 3, ref. 11 -. Les pentes des droites fournissent, pour les particules seules, les coefficients de diffusion relatifs (arbitrairement 1, pour 90°) qui permettent donc de tracer l'indicatrice "moyenne" des particules. Notons que cette méthode est indirecte, car il n'est pas nécessaire de connaître

la valeur de la diffusion moléculaire (celle-ci au contraire en est tirée, ou au moins estimée). La variabilité de l'indicatrice des particules peut aussi être appréciée : elle apparaît seulement notable pour les grands angles ($\theta > 120°$). Cette relative constance de forme est assez surprenante, néanmoins les expériences faites depuis en Atlantique ou en océan Indien l'ont confirmée ; les seules exceptions nettes ont été observées dans le cas d'eaux très fortement chargées d'apports terrigènes.

A peu près simultanément des mesures *in situ*, de la partie avant (1°5 - 14°) de l'indicatrice de diffusion ont été effectuées (λ = 550 nm). Là aussi, et en dépit de conditions très différentes rencontrées en Manche ou en Méditerranée (jusqu'à la profondeur 800 m), cette partie d'indicatrice s'est révélée peut variable (12). Dans ces expériences, les courbes peuvent être directement comparées, car la diffusion moléculaire est toujours négligeable à ces angles.

Ces expériences aux angles moyens et aux petits angles permettent de penser que la notion de courbe moyenne pour présenter l'indicatrice-type des particules marines n'est pas dénuée de signification. Cette indicatrice moyenne a été tracée entre 1° et 150°, en utilisant pour le domaine non couvert par nos mesures (14° - 30°) celles effectuées par N.G. Jerlov jusqu'à 10° -cf fig. 9, ref. 12-. Plusieurs conséquences ont été tirées de l'adoption d'une telle courbe moyenne, elles seront évoquées plus loin.

INFLUENCE DE LA LONGUEUR D'ONDE.

Etude aux angles moyens (de 30° à 150°).

Pour diverses longueurs d'onde (578, 546, 436, 405, 366 nm) on a déterminé les indicatrices de diffusion d'eaux de mer très variées quant à la teneur en particules.

Il est apparu que pour un échantillon donné la valeur des coefficients angulaires, rapportée à ceux du benzène optiquement pur, diminue régulièrement lorsque la longueur d'onde décroit. Ceci implique donc pour les particules une sélectivité de la diffusion inférieure à celle du benzène optiquement pur ; la seconde étant connue il est possible d'évaluer par comparaison la première, sans qu'il soit nécessaire de connaître la diffusion de l'eau elle-même, qui intervient comme une constante (à titre d'exemple, voir la figure 1).

Il ressort de cette étude (13), qu'au moins pour les échantillons étudiés, la dépendance spectrale de la diffusion par les particules serait exprimée par une loi sensiblement en λ^{-1} ; cette loi mal vérifiée pour la retro-diffusion ($\theta > 90°$), peut être appliquée dans le domaine 90° - 30° ; ceci serait une conséquence du fait que l'indicatrice des particules conserve, au moins dans ce domaine, la même forme aux diverses longueurs d'onde (ce qui a pu être établi en utilisant à diverses longueurs d'onde, le procédé décrit dans le paragraphe précédent).

Lorsqu'ont été déterminées les constantes de diffusion de l'eau de mer optiquement pure (voir paragraphe suivant), les points précédents : sélectivité, variation de forme de l'indicatrice, ont pu être repris selon une méthode directe, c'est à dire en soustrayant des valeurs observées pour les divers échantillons, les valeurs de la diffusion moléculaire (tous les coefficients étant exprimés en valeur absolue). Ce procédé demeure délicat pour les eaux très pures où l'erreur expérimentale se reporte intégralement sur la différence et devient en valeur relative très grande. Les résultats obtenus dans le premier temps de l'étude ont été approximativement corroborés de cette manière (14). Les figures 2 et 3 en fournissent l'exemple.

Etude aux petits angles (1° - 25°).

L'étude de l'influence de la longueur d'onde a aussi été étendue au domaine des petits angles ; les mesures étant effectuées en valeurs relatives, les conclusions ne portent donc que sur la forme de cette partie de l'indicatrice. Les principaux résultats de ce travail sont présentés ici même par F. Nyffeler (14) ; ils ont été obtenus soit *in situ* avec l'appareil dont il a été fait mention précédemment (12), soit *in vitro* avec des sources lasers.

Il a été trouvé que la relative invariance de forme déjà constatée, pour la partie de l'indicatrice correspondant aux angles 90° - 30°, subsiste aux petits angles. Cette invariance (au moins approximative) expliquerait que la sélectivité observée pour les coefficients angulaires se reporte sur le coefficient total de diffusion comme W. Burt a pu le montrer en traçant des spectres d'atténuation de particules (où la diffusion joue le plus grand rôle) (15). Un autre exemple est fourni par la figure 4 où le spectre d'atténuation des particules révèle une légère sélectivité, tout à fait comparable à celle observée pour la diffusion.

ETUDE DE LA DIFFUSION MOLECULAIRE.

Afin d'éviter d'avoir recours à des procédés indirects, comme ceux précédemment décrits, pour déterminer exactement les rôles respectifs de la diffusion par les particules et de la diffusion moléculaire, il a paru utile de reprendre l'étude de cette dernière. De plus, si les valeurs concernant l'eau étaient assez controversées, celles concernant l'eau de mer, théoriquement plus élevées, n'avaient jamais été mesurées.

Les procédés de purification de l'eau, des solutions de ClNa, de l'eau de mer naturelle ou artificielle ont été décrits (16). Le fait que l'indicatrice de diffusion mesurée se confonde avec l'indicatrice théorique est pris comme critère de pureté optique -voir figure 2 et 3, ref. 16-. Les valeurs des coefficients de diffusion déterminées pour l'eau sont très voisines de celles prévues par la théorie des fluctuations (17) ; pour les solutions de chlorure de sodium l'accroissement de diffusion dû aux fluctuations de concentration est conforme aux prévisions faites à partir des masses moléculaires des solutés : la diffusion par l'eau de mer optiquement pure est de 10 % supérieure à celle de l'eau -voir fig. 1,

ref. 17- (et environ de 6% supérieure à celle d'une solution de ClNa de même concentration en ion Cl^-).

CONSEQUENCES DE L'ADOPTION D'UNE INDICATRICE MOYENNE.

Puisque la plus grande partie de l'énergie est diffusée aux petits angles -voir fig. 10, ref. 12-, un appareil recevant toute la lumière diffusée entre 0°5 et 10° par exemple, mesure une fraction importante du coefficient total de diffusion b. Cette fraction est évaluée en utilisant l'indicatrice moyenne (elle est de 75 %, pour les angles cités). Les fluctuations des indicatrices réelles autour de l'indicatrice moyenne adoptée sont assez faibles (12) (14) pour qu'au moins une bonne approximation de b soit fournie par cette méthode ; un appareil utilisant ce principe a été mis au point (18).

Une autre conséquence concerne les relations entre coefficients angulaires $\beta(\theta)$ et coefficient total b : ce dernier résulte de l'addition du coefficient relatif à la diffusion moléculaire b_0 constant et connu, et du coefficient b_p relatif à la diffusion par les particules ; b_p est variable, mais n'est plus fonction que de la concentration en particules dès lors qu'on a adopté une indicatrice moyenne. Avec cette hypothèse, on peut calculer* les relations linéaires liant chacun des coefficients $\beta(\theta)$ au coefficient total b (19) ; en raison de la variabilité de "l'arrière" de l'indicatrice, ces relations sont en pratique surtout applicables aux coefficients relatifs aux angles inférieurs à 90° (β_{30}, β_{45} par exemple, ou à la rigueur β_{90}).

Des vérifications satisfaisantes de ces deux méthodes ont pu être faites en comparant pour les mêmes eaux les coefficients b obtenus à partir soit de la mesure β_{30}, soit de la mesure faite avec l'appareil intégrant entre 0°5 et 10° -à titre d'exemple, voir la figure 5- ; on peut noter que dans le cas des eaux les plus claires où b est de l'ordre de $1\ 10^{-2}m^{-1}$, la diffusion moléculaire intervient pour près de 20 % ($0.17\ 10^{-2}m^{-1}$ à 546 nm).

AUTRES DEVELOPPEMENTS DU PROGRAMME.

Sans parler des aspects théoriques qui ne font pas l'objet de cette communication, parmi les prolongements du programme on peut citer les deux points suivants :

Pour appliquer au problème de la pénétration de la lumière du jour les théories du transfert radiatif, simplifiées ou non, il est nécessaire de connaitre l'indicatrice de diffusion (et éventuellement aussi le rôle de la diffusion moléculaire). Les résultats numériques qui concernent l'indicatrice, peuvent soit être repris dans une formulation mathématique, soit être utilisés directement ; c'est cette seconde voie qu'a choisi L. Prieur qui présente ici même (20) quelques résultats de calculs relatifs à cette question.

Si les mesures de diffusion constituent à coup sûr un mode d'estimation du matériel en suspension, elles ne peuvent être réellement utiles dans cette perspective, qu'à la condition de fournir une évaluation quantitative. Des études à la fois pondérale, chimique, et granulométrique des particules en suspension ont été entreprises corrélativement aux mesures de diffusion -voir par exemple la figure 6-, dans le but de déterminer si les relations trouvées (dans le cas des eaux du large au moins) ont un caractère suffisamment permanent et général pour être susceptibles d'une telle application.

* Une erreur numérique s'est glissée dans le calcul présenté ref. 19 : la valeur de l'intégrale normalisée n'est pas 22.5 mais $\pi \times 22.5$; cette omission se répercute sur toutes les valeurs numériques présentées ensuite ; un rectificatif sera prochainement donné.

REFERENCES

(1) Ivanoff, A. "A new water sampler and a new scattering polarizing meter for optical investigation of the oceans". International oceanographic Congress, 1959. Preprint, 553-555.

(2) Ivanoff, A. "Quelques résultats concernant les propriétés diffusantes des eaux de mer". Symposium on radiant energy in the sea. Helsinki. 1960.

(3) Morel, A. "Résultats de mesures de diffusion de la lumière effectuées lors de la croisière n° 25 du navire océanographique "CHAIN". Cah. Océanogr. XVII, 2, 107-121, 1965.

(4) Laboratoire d'Océanographie physique de la Faculté des sciences. "Résultats des observations effectuées en Méditerranée". Cah. Océanogr. XXI, supplément n° 2, 193-263, 1969.

(5) Wippler, C. et Scheibling, G. "Description d'un appareil pour l'étude de la diffusion de la lumière". J. Chim. Phys., 51, 201-205, 1954.

(6) Ivanoff, A., Morel, A. "Au sujet de l'indicatrice de diffusion des eaux de mer". C.R. Acad. Sci., 258, 2873-2876, 1964.

(7) Tyler, J.E. "Scattering properties of distilled and natural waters". Limnol. Océanogr., 6, 451-456, 1961.

(8) Jerlov, N.G. "Optical measurements in the eastern north Atlantic". Medd. Oceanogr. Inst. Göteborg, 30, 1-40, 1961.

(9) Jerlov, N.G. "Optical oceanography". Oceanogr. Mar. Biol. Ann. Rev., 1, 89-114, 1963.

(10) Duntley, S.Q. "Light in the sea". J. Opt. Soc. Am., 53, 214-233, 1963.

(11) Morel, A. "Interprétation des variations de la forme de l'indicatrice de diffusion de la lumière par les eaux de mer". Ann. Geophys., 21, 2, 281-284, 1965.

(12) Bauer, D., Morel, A. "Etude aux petits angles de l'indicatrice de diffusion de la lumière par les eaux de mer". Ann. Geophys., 23, 1, 109-123, 1967.

(13) Morel, A. "Etude pour diverses longueurs d'onde de l'indicatrice de diffusion des eaux de mer". UGGI-IASPO, XIV General Assembly, Berne, 1967.

(14) Nyffeler, F. "Etude de la diffusion de la lumière par l'eau de mer : mesures aux petits angles à l'aide de sources classiques et de sources lasers". A.G.A.R.D., Electromagnetics of the sea, Paris, 1970.

(15) Burt, W.V. "Interpretation of spectrophotometer readings on chesapeake bay waters". J. Mar. Res., 14, 1, 33-46, 1955.

(16) Morel, A. "Etude expérimentale de la diffusion de la lumière par l'eau, les solutions de chlorure de sodium et l'eau de mer optiquement pures". J. Chim. Phys., 10, 1359-1366, 1966.

(17) Morel, A. "Note au sujet des constantes de diffusion de la lumière pour l'eau et l'eau de mer optiquement pures". Cah. Océanogr. XX, 2, 157-161, 1968.

(18) Bauer, D. et Ivanoff, A. à paraître.

(19) Morel, A. "Relations entre coefficients angulaires et coefficient total de diffusion de la lumière pour les eaux de mer". Cah. Océanogr. XX, 4, 291-303, 1968.

(20) Prieur, L. "Pénétration de la lumière du jour dans la mer". A.G.A.R.D. Electromagnetics of the sea, Paris, 1970.

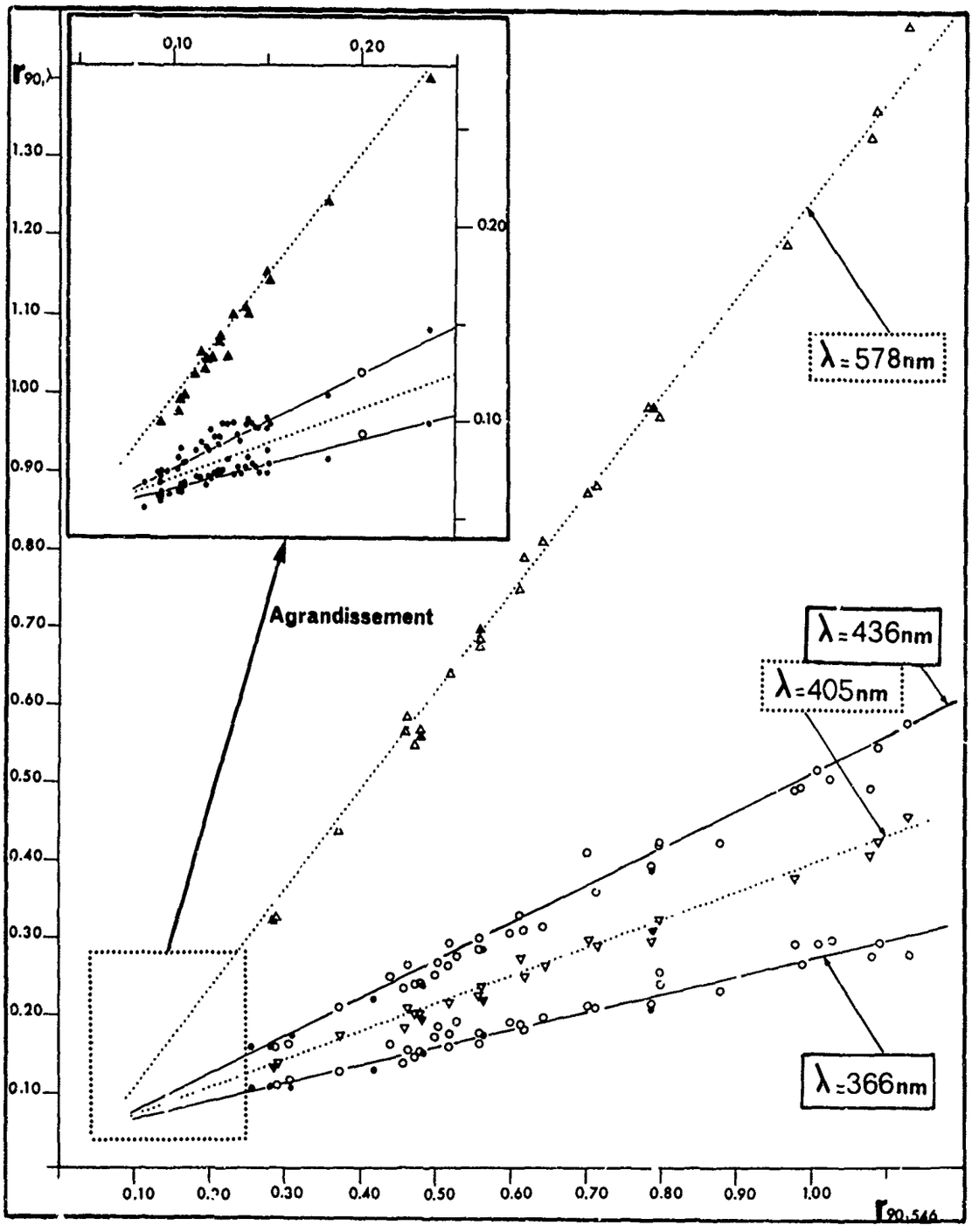

Figure 1 : r désigne le rapport de l'intensité diffusée par l'échantillon à l'intensité diffusée par le benzène optiquement pur ; ce graphique est relatif uniquement à des mesures de diffusion à angle droit (indice 90). Pour chaque échantillon, on porte les r obtenus à diverses longueurs d'onde ($r_{90,\lambda}$) en fonction du r obtenu à λ = 546 nm ($r_{90,546}$). Si la diffusion par les particules est spectralement neutre, les points expérimentaux s'aligneraient sur des droites dont les pentes sont prévisibles : ce sont les inverses des nombres qui caractérisent la sélectivité de la diffusion moléculaire du benzène (cf. 16). Les droites de regression calculées pour les points expérimentaux sont en réalité différentes, et de la différence des pentes on en déduit la sélectivité de la diffusion par les particules, qui pour ces mesures serait la suivante :

λ_{nm}	=	578	546	436	405	366
$(\beta_\lambda / \beta_{546})_{particules}$	=	0.98	1	1.36	1.49	1.54

Sur la figure, les signes blancs correspondent à des échantillons prélevés en Manche, les noirs en Méditerranée, (dans le cartouche agrandi, les mesures à 405 nm ne sont pas portées par souci de clarté).
Des graphiques semblables ont été établis pour d'autres angles de diffusion.

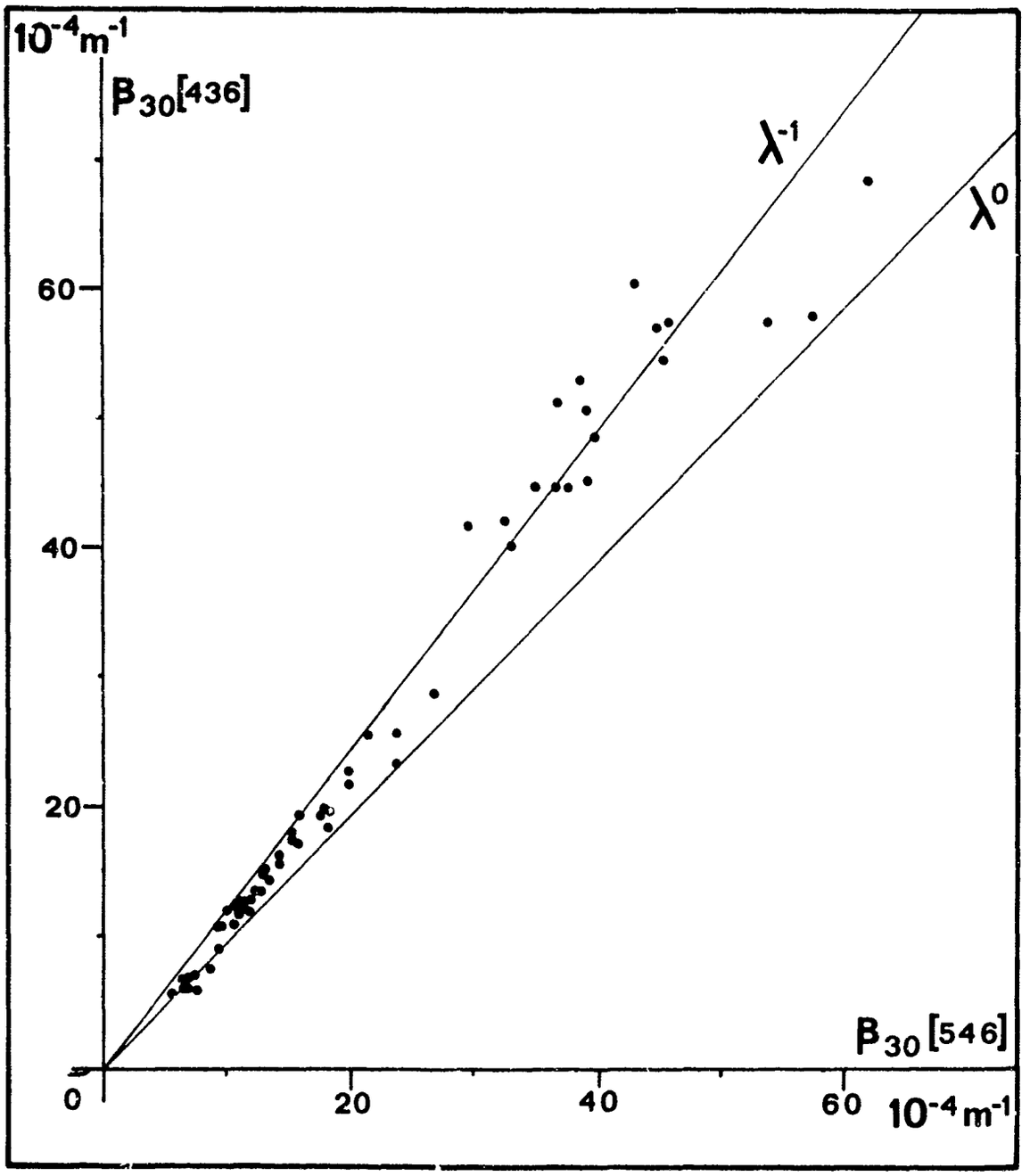

Figure 2 : Coefficients de diffusion à 30° pour les particules seules (après soustraction de la diffusion moléculaire) ; pour chaque échantillon le coefficient à 436 nm est porté en fonction du coefficient à 546 nm ; les droites tracées correspondent à une diffusion spectralement neutre (bissectrice) ou à une sélectivité en λ^{-1}.
Mesures effectuées durant la campagne Hydratlante III (octobre 1968) dans la zone Portugal-Madère, à des profondeurs allant de 0 à 4 000 m.

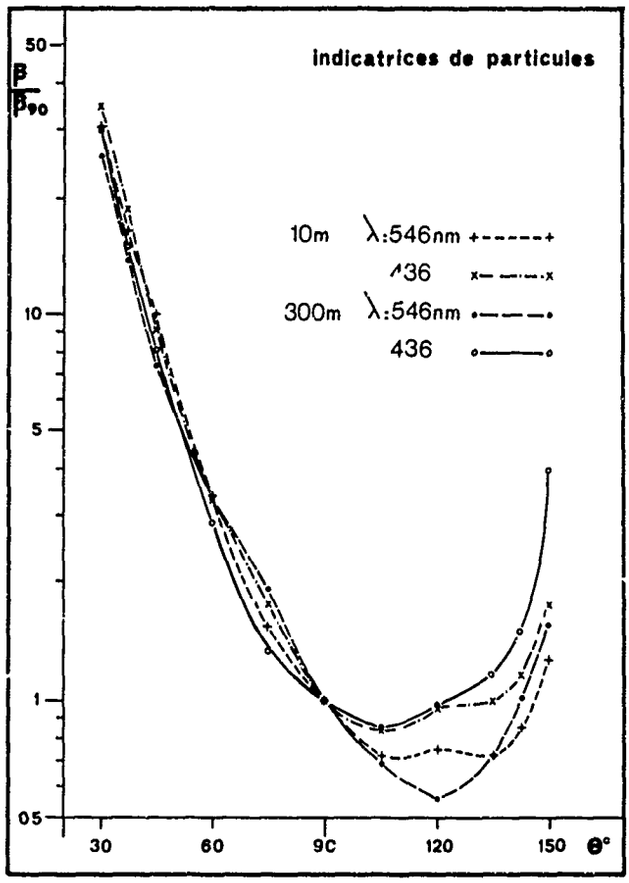

Figure 3 : Indicatrices relatives aux particules seules (déduction faite de la diffusion moléculaire) normalisées à 90°. Prélèvements faits, aux profondeurs indiquées, à la bouée laboratoire mouillée approximativement à 50 nautiques au sud de Toulon (Juin 1969). Les valeurs numériques (à 90°) correspondantes sont :

10 m	λ = 546 nm	$(\beta_{90})_{particules}$	= 3.48 $10^{-4}m^{-1}$
	λ = 436 nm	"	= 4.10 "
300 m	λ = 546 nm	"	= 0.83 "
	λ = 436 nm	"	= 0.99 "

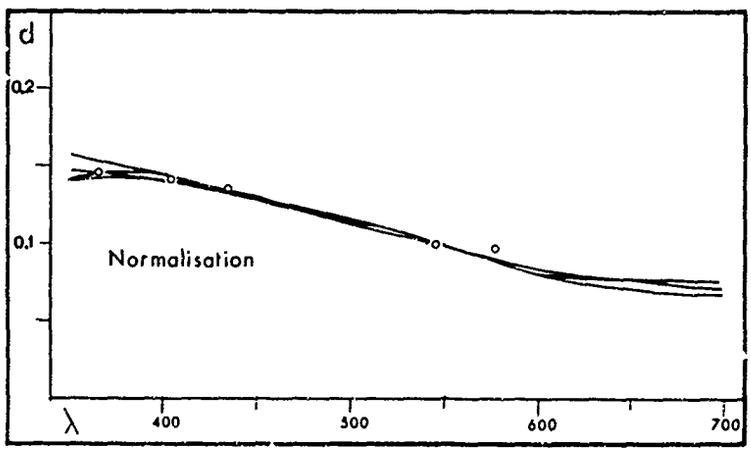

Figure 4 : Spectres d'atténuation de particules marines normalisées à λ = 550 nm ; les mesures sont effectuées sur des eaux de la Manche avec un spectrophotomètre Beckman DK 2 A, en cuves de 10 cm, le blanc étant constitué par la même eau de mer filtrée. Les points figurent les variations spectrales de la diffusion mesurées sur les mêmes échantillons (normalisation à λ = 546 nm).

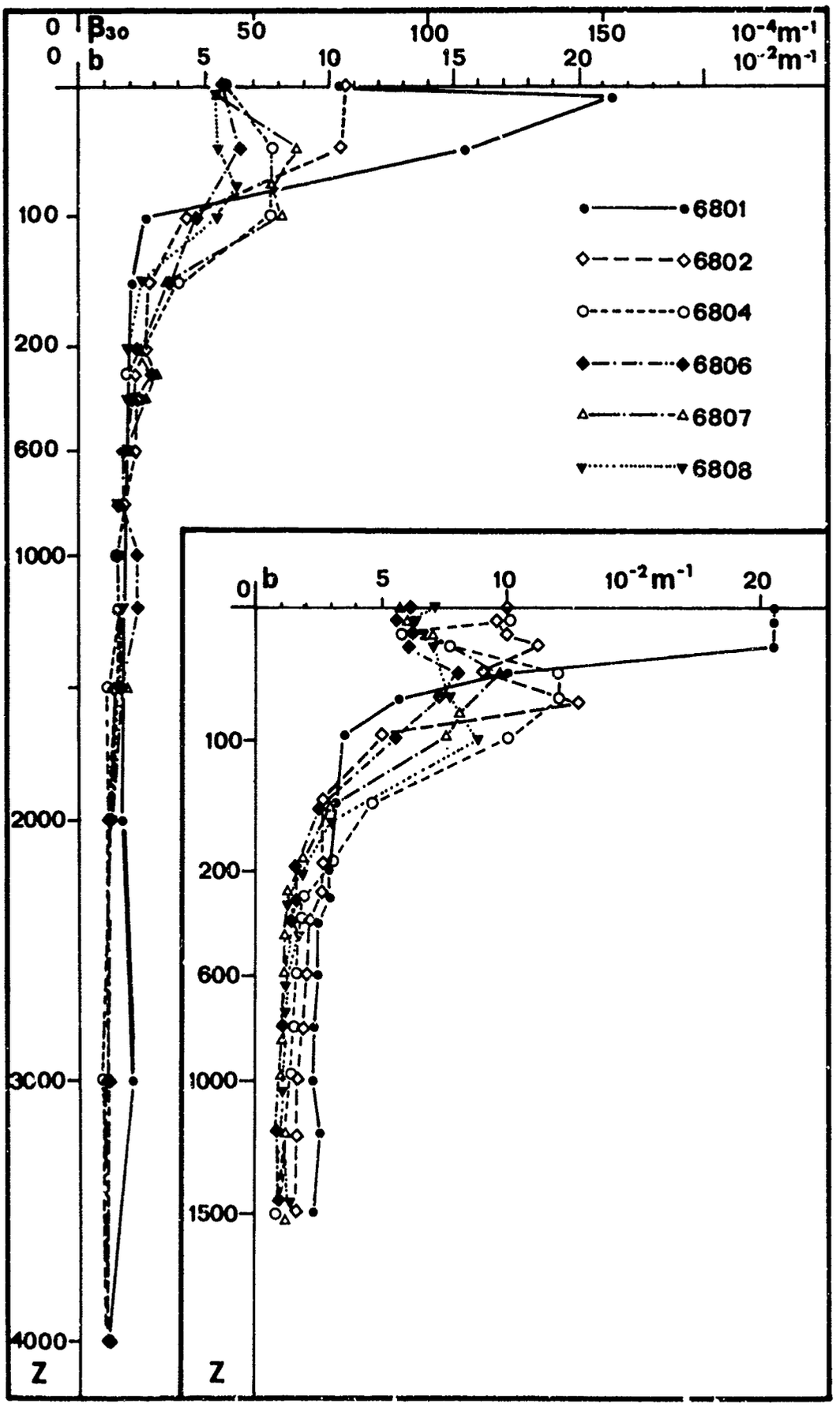

Figure 5 : Campagne Hydratlante III (octobre 1968) : pour diverses stations, profils en fonction de la profondeur du coefficient total de diffusion b déduit de la mesure *in vitro* de β_{30} -partie gauche de la figure- ou de la mesure *in situ* à l'aide du diffusiomètre intégrateur -partie droite- (ces dernières mesures ont été effectuées par D. Bauer).

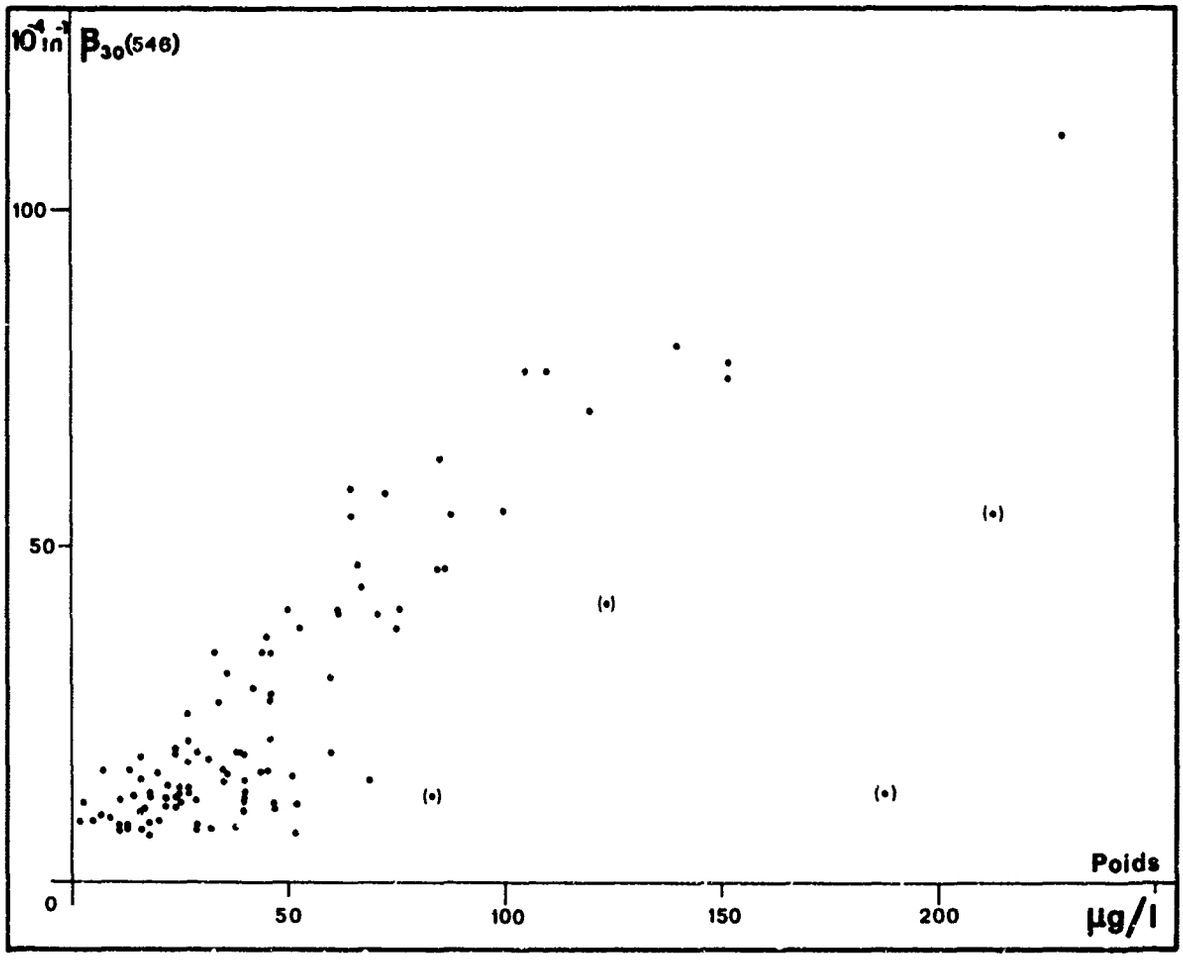

Figure 6 : Campagne Hydratlante III : les mesures du coefficient de diffusion à 30° sont effectuées sur le prélèvement qui est ensuite filtré pour déterminer la concentration en matière particulaire (µg/litre) (mesures effectuées par G. Copin) ; les points entre parenthèses correspondent à des filtrations probablement affectées par des pollutions.

ETUDE DE LA DIFFUSION DE LA LUMIERE PAR L'EAU DE MER. MESURES AUX PETITS ANGLES A L'AIDE DE SOURCES CLASSIQUES ET DE SOURCES LASERS

par

François Nyffeler

Laboratoire d'Océanographie physique
de la Faculté des Sciences de Paris,
Quai de la Darse
06, Villefranche-sur-Mer, France

SUMMARY

Light scattering in seawater near the propagation direction of a light beam has been studied by means of conventional and laser sources. Measurements ware carried out at various wavelengths. Angular scattering coefficients are not measured in absolute values ; nevertheless, it is possible to compare the shapes of the scattering indicators obtained at various wavelengths over the angular area considered.

Such experiments have been carried out in situ with a device especially designed for this purpose (conventional source), and in vitro, with lasers. In situ, it is practically impossible to consider that the indicators obtained for three various wavelengths (459, 555 and 599 nm) are significantly distinct. In vitro, a slight difference is noted between indicators determined at 488 and 632,8 nm. (It should be pointed out that, in this case, measurements are carried out for both wavelengths on the same sample, as opposed to in situ measurements which have to be made successively.)

A comparison of the various series of measurements shows that the seawater scattering indicator shape, for small angles, is practically independent of the light wavelength used ; it does not depend either on light coherence.

The indicators obtained correlate well with those presented by other researchers, and measured either in vitro or in situ by instruments operating at various wavelengths. Therefore, instruments designed for measuring seawater scattering properties could be equipped with laser sources in so far as such sources improve their performance.

ETUDE DE LA DIFFUSION DE LA LUMIERE PAR L'EAU DE MER. MESURES AUX PETITS ANGLES A L'AIDE DE SOURCES CLASSIQUES ET DE SOURCES LASERS.

par François NYFFELER

Laboratoire d'Océanographie physique
de la Faculté des sciences de Paris,
Quai de la Darse
06 - Villefranche-sur-Mer, France.

SOMMAIRE

Une onde électromagnétique est perturbée par le milieu dans lequel elle se propage, l'importance relative des divers phénomènes entraînant cette perturbation dépendant des caractéristiques optiques du milieu et généralement de la longueur d'onde de la lumière. Dans cet exposé, nous allons rappeler brièvement quels sont les phénomènes qui interviennent de manière prépondérante dans l'eau de mer, et présenter des résultats relatifs à la mesure de l'indicatrice de diffusion obtenus in situ à l'aide de sources classiques, et in vitro, à l'aide de lasers.

Cette étude a été en partie réalisée grâce au support financier de la D.R.M.E., dans le cadre du contrat 12/65.

INTRODUCTION

En suspension dans la solution ionique que constitue l'eau de mer se trouvent ce que nous appelerons des "particules marines" dont la concentration varie d'un endroit à l'autre de l'océan. Ces particules sont minérales (apports éoliens, poussières météoriques, apports fluviaux, etc..) et organiques (microorganismes, résidus de décomposition, etc..), leur taille pouvant atteindre plusieurs dizaines de µ.

La propagation d'une onde électromagnétique dans un tel milieu s'accompagne de plusieurs phénomènes que l'on peut ranger en deux groupes : d'une part, ceux qui entraînent une diminution de flux, et d'autre part ceux qui perturbent l'onde lumineuse, modifiant sa direction de propagation, sa phase ou sa polarisation.

Les phénomènes du premier groupe englobant la transformation de l'énergie lumineuse en énergie thermique, en énergie de réaction chimique, ou en énergie lumineuse réémise à d'autres longueurs d'onde par effet RAMAN ou par fluorescence, permettent de définir les propriétés absorbantes de l'eau de mer, alors que ceux du second groupe concernent les propriétés diffusantes de l'eau de mer. Formellement, l'interaction d'une onde électromagnétique avec son milieu de propagation se ramène à une modification du vecteur électrique, que l'on peut représenter (1) à l'aide d'une matrice de transformation ; les éléments de cette matrice sont des fonctions mathématiques dont les paramètres dépendent des propriétés caractéristiques du milieu, notamment de la taille, de la forme et de l'indice des particules en suspension. La connaissance de cette matrice de transformation permettrait de calculer en tout point l'état "actuel" d'une onde à partir de son état initial. Cependant, étant donné la nature des centres diffusants contenus dans l'eau de mer qui sont de tailles, de formes et d'indice fort divers, il est difficile d'envisager la solution du problème de la diffusion par l'eau de mer sur un plan théorique. Dans la plupart des études entreprises, l'aspect expérimental est prépondérant ; ces travaux visent généralement à déterminer les grandeurs les plus caractéristiques du phénomène de diffusion soit : la perte de flux apparente relativement à la direction de propagation, la répartition de l'énergie diffusée ou éventuellement d'autres grandeurs s'y rattachant directement comme par exemple la part relative de la diffusion moléculaire. On trouvera chez JERLOV (2) une bibliographie complète de ces différents travaux.

MOTIVATION

Rappelons que le phénomène de diffusion peut être décrit en introduisant les notions de coefficient angulaire de diffusion (et corrélativement d'indicatrice de diffusion) et de coefficient total de diffusion

Le coefficient angulaire de diffusion $\beta(\theta)$ est défini par la relation

$$dI(\theta) = \beta(\theta)\, E\, dV$$

- $dI(\theta)$: intensité diffusée dans la direction faisant un angle θ avec la direction initiale de propagation.
- E : éclairement sur la face d'entrée du volume diffusant.
- dV : élément de volume diffusant.

L'indicatrice de diffusion est une représentation plane de la répartition de l'énergie entre les différentes directions de l'espace, obtenue en portant dans chaque direction d'un vecteur :

$$\overrightarrow{\beta(\theta)} = \overrightarrow{B(\theta)}\ \overrightarrow{e_\theta}$$

En sommant dans l'angle solide correspondant les intensités relatives à chaque direction θ, on obtient la perte apparente de flux par diffusion qui s'exprime à l'aide du coefficient total de diffusion :

$$b = 2\pi \int_0^\pi \beta(\theta) \sin\theta \, d\theta$$

L'étude de l'indicatrice de diffusion de la lumière par l'eau de mer a été poursuivie par plusieurs auteurs ; comparant l'ensemble des résultats obtenus, DUNTLEY (3) et JERLOV (4) relèvent quasi simultanément en 1963 que pour les petits angles la forme de l'indicatrice varie peu d'une eau de mer à une autre, $\beta(\theta)$ croissant rapidement lorsque θ tend vers 0° ; cette observation a été confirmée ultérieurement par les travaux de D. BAUER et A. MOREL (5) qui ont procédé à des mesures systématiques dans différents types

d'eau, pour des angles compris entre 1°5 et 14° ; mentionnons également les résultats de KOZLIANINOV (6), d'OTCHAKOWSKI (7) qui arrivent à la même conclusion, et enfin ceux de KULLENBERG (8) qui utilise un diffusiomètre équipé d'un laser.

Cette invariance de la forme de l'indicatrice n'est toutefois effective que si la diffusion moléculaire de l'eau pure peut être négligée devant la diffusion due aux particules en suspension, ce qui est le cas pour les angles $\theta < 20°$ environ ; au delà, la diffusion moléculaire intervient de façon d'autant plus sensible que la teneur en particules est faible.

La forme des indicatrices observées montre que c'est au voisinage de la direction de propagation que la plus grande partie de l'énergie est diffusée. Or, si l'on examine l'ensemble des travaux cités ci-dessus, on constate que les mesures aux petits angles sont peu nombreuses et que les longueurs d'ondes utilisées sont différentes. Nous avons donc entrepris deux séries d'expériences dans le but d'examiner d'une part si la forme de l'indicatrice de diffusion aux petits angles varie avec la longueur de la lumière, et d'autre part si elle est modifiée par l'utilisation de sources cohérentes. Les mesures en lumière classique ont été réalisées in situ, à trois longueurs d'onde à l'aide d'un diffusiomètre décrit précédemment par D. BAUER et A. IVANOFF (9) et par D. BAUER et A. MOREL (5). Par suite des difficultés rencontrées dans la mise en oeuvre des lasers, les expériences à l'aide de sources cohérentes ont été réalisées in vitro.

MESURES

Les expériences "in situ" ont été exécutées dans des eaux côtières. Dans la méthode utilisée, les mesures aux différentes longueurs d'onde sont effectuées successivement et correspondent à des "échantillons" différents. Il est donc nécessaire d'appliquer une méthode statistique pour déterminer si les indicatrices moyennes obtenues pour chacune des longueurs d'onde sont significativement distinctes.

Les mesures en lumière cohérente ont été réalisées "in vitro" à l'aide d'un dispositif comprenant deux lasers, une cellule de mesure, et un photomultiplicateur. Ces mesures ayant également porté sur des échantillons d'eaux côtières, les résultats peuvent être comparés directement à ceux obtenus in situ.

RESULTATS

Les indicatrices obtenues à 459, 555 et 599 nm lors des mesures in situ, sont très voisines de celles déterminées par D. BAUER et A. MOREL à l'aide du même appareil pour $\lambda = 550$ nm. L'analyse statistique de nos résultats montre que les trois indicatrices moyennes (cf. fig. 1) relatives respectivement à l'ensemble des mesures à chaque longueur d'onde (17 mesures à chaque λ) ne sont pas significativement distincte au niveau de probabilité $P = 0,95$. On peut donc considérer qu'en moyenne, la forme de l'indicatrice de diffusion ne dépend pas de la longueur d'onde de la lumière.

L'examen des mesures réalisées en laboratoire à l'aide de lasers conduit à la même conclusion. Disposant de deux lasers (488 et 632,8 nm), nous avons par contre pu examiner l'influence de la longueur d'onde non plus seulement d'un point de vue statistique, mais en comparant des mesures exécutées alternativement aux deux longueurs d'onde sur un même échantillon. On constate (fig. 2) que la décroissance de $\beta(\theta)$ en fonction de θ est légèrement plus rapide à 632,8 nm qu'à 488 nm ; cette différence reste cependant très faible. On peut d'autre part remarquer que les mesures sont entachées d'une certaine incertitude découlant de la variabilité du milieu étudié. A titre d'exemple, nous présentons sur la fig. 3 trois indicatrices déterminées sur un même échantillon à 6 h d'intervalle ; les différences observées entre les courbes (qui sont du même ordre de grandeur que celles relevées pour deux mesures consécutives) donnent une indication de la variabilité du phénomène.

Considérant que la forme de l'indicatrice de diffusion ne dépend pas de la longueur d'onde, nous avons alors comparé les deux indicatrices moyennes relatives respectivement à l'ensemble des mesures en lumière classique (51 mesures) et à l'ensemble des mesures en lumière cohérente (15 mesures), entre 1° et 15°. De la similitude des courbes obtenues (cf. fig. 4) on peut déduire que l'utilisation de sources cohérentes ne semble pas modifier la forme de l'indicatrice de diffusion de l'eau de mer.

Une disposition différente des éléments du montage de laboratoire nous a permis d'effectuer des mesures entre 1° et 25°, et ainsi de comparer nos résultats avec ceux d'autres auteurs pour un domaine angulaire relativement étendu. Sur la figure 5, les indicatrices sont normalisées en posant $\beta(20) = 1$. La concordance entre notre indicatrice moyenne et celles proposées par divers auteurs s'avère satisfaisante.

CONCLUSIONS

Dans la méthode utilisée, les coefficients angulaires de diffusion sont déterminés en valeur relative, et l'on ne peut tirer de conclusions en ce qui concerne leur valeur absolue aux différentes longueurs d'onde ; d'autre part, la variabilité du milieu limite la résolution des grandeurs mesurées. Tenant compte de ces restrictions, nous avons cependant établi que pour les petits angles, les variations avec la longueur d'onde de la forme de l'indicatrice de diffusion sont négligeables. Il apparaît que cette forme n'est pas non plus modifiée lorsque l'on opère en lumière cohérente. Ainsi certains appareils destinés à la mesure de la diffusion de la lumière pourraient être équipés de lasers dans la mesure où de telles sources permettent d'en améliorer les performances.

BIBLIOGRAPHIE

(1) VAN DE HULST. "Light scattering by small Particles". John Wiley & sons. New York, 1964, 469 p.

(2) JERLOV, N.G. "Optical oceanography". Elsevier Publisching Company. London, 1968, 194 p.

(3) DUNTLEY, S.Q. J.O.S.A., 53, 1963, pp. 214-233.

(4) JERLOV, N.G. Oceanogr. Marine Biol. Ann. Rev., 1, 1963, pp. 89-114.

(5) BAUER, D. et MOREL, A. Ann. Geophys., 23, 1967, pp. 108-122.

(6) KOZLIANINOV, M.V., Trudy. Inst. Okeanol. Acad. Nauk, S.S.S.R., 25, 1955, pp. 134-142.

(7) OCHAKOWSKI, Y.E. Trudy Oceanol. Acad. S.S.S.R., 77, 1965, pp. 125-130.

(8) KULLENBERG, G. Deep sea Res., 15, 1968, pp. 423-432.

(9) BAUER, D. et IVANOFF, A. C. R. Acad. Sci, 260, 1965, pp. 631-634.

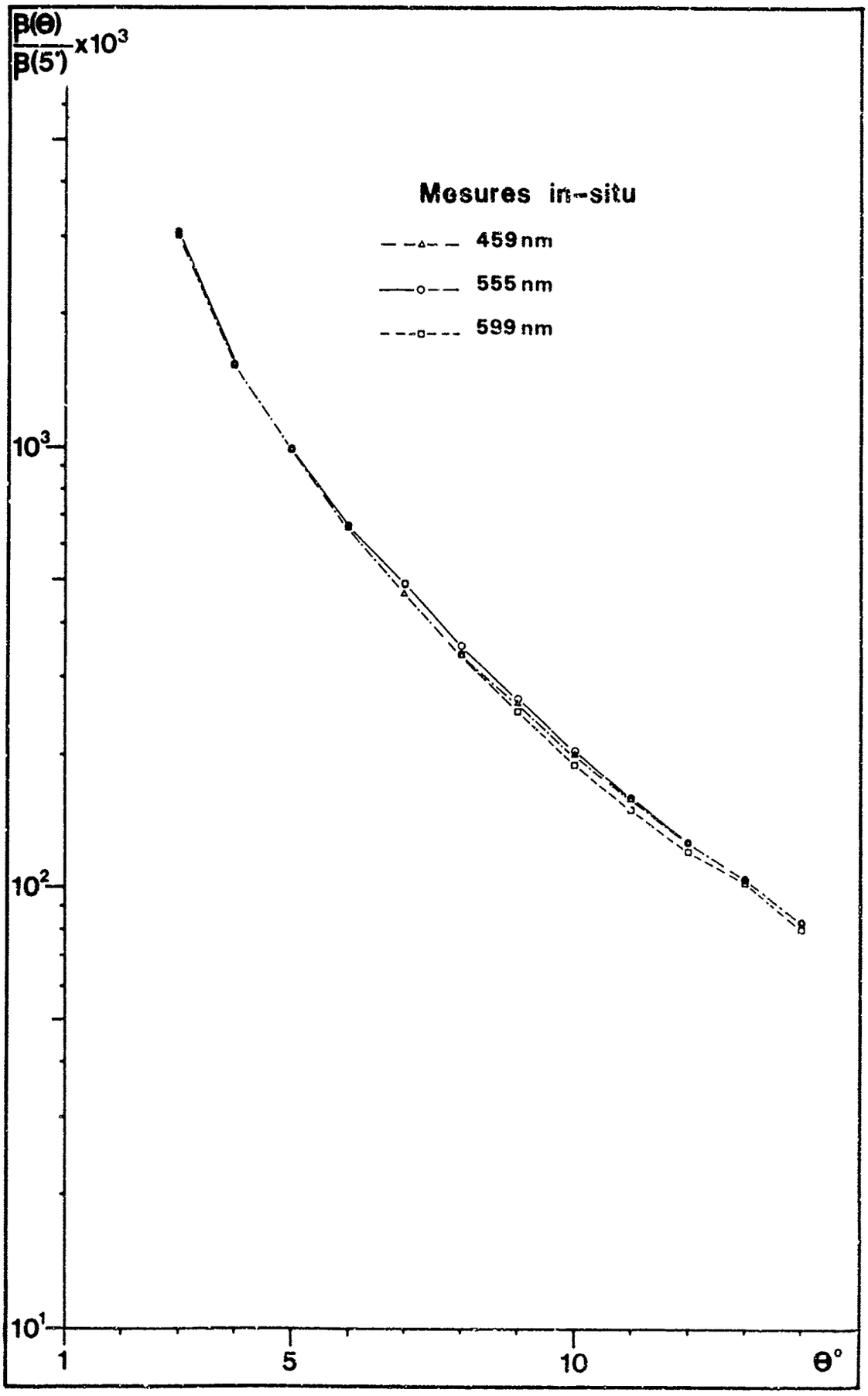

Figure 1 . Indicatrices de diffusion moyennes obtenues à diverses longueurs d'onde.

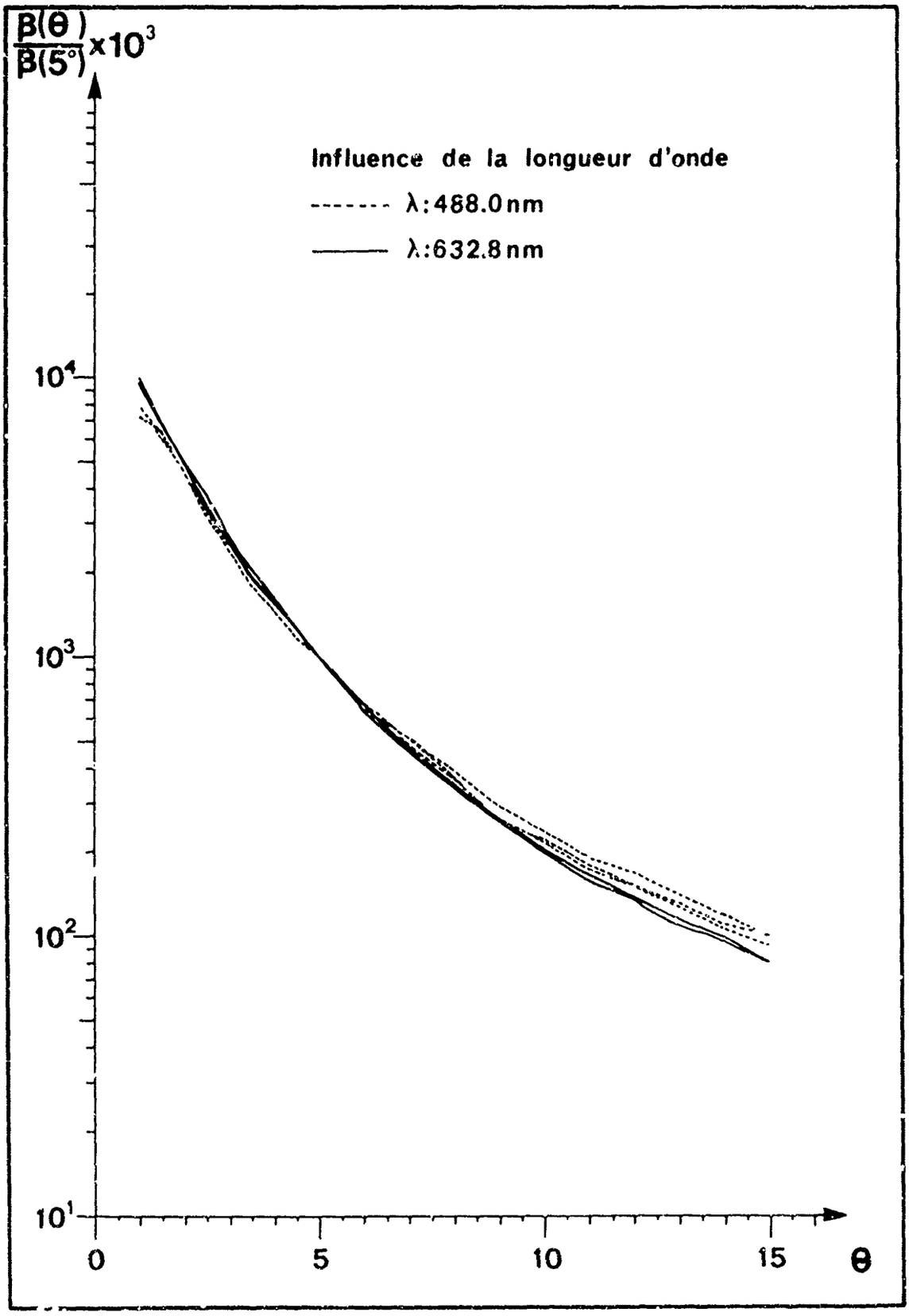

Figure 2. 5 mesures exécutées sur le même échantillon.

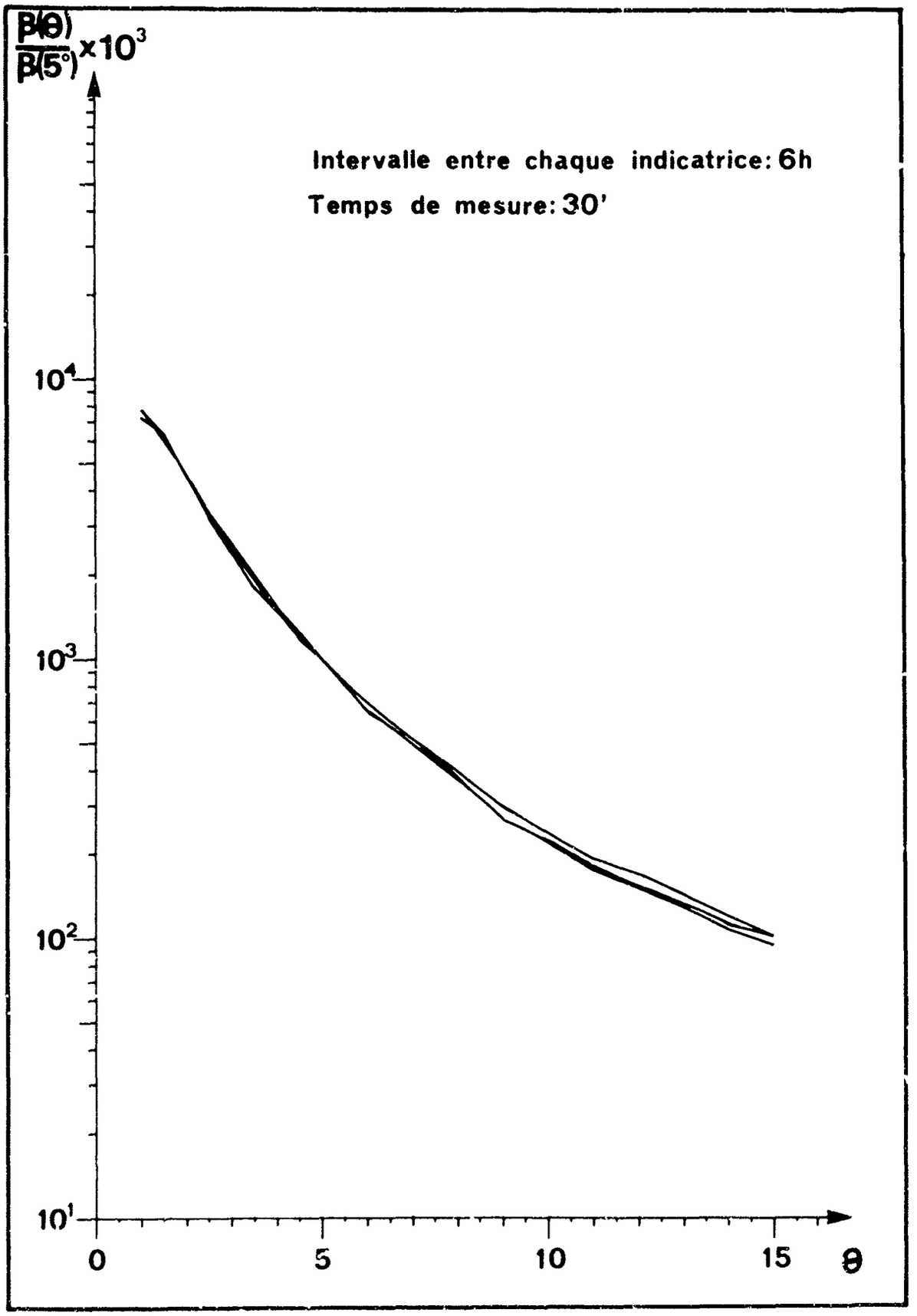

Figure 3. Variabilité du milieu.

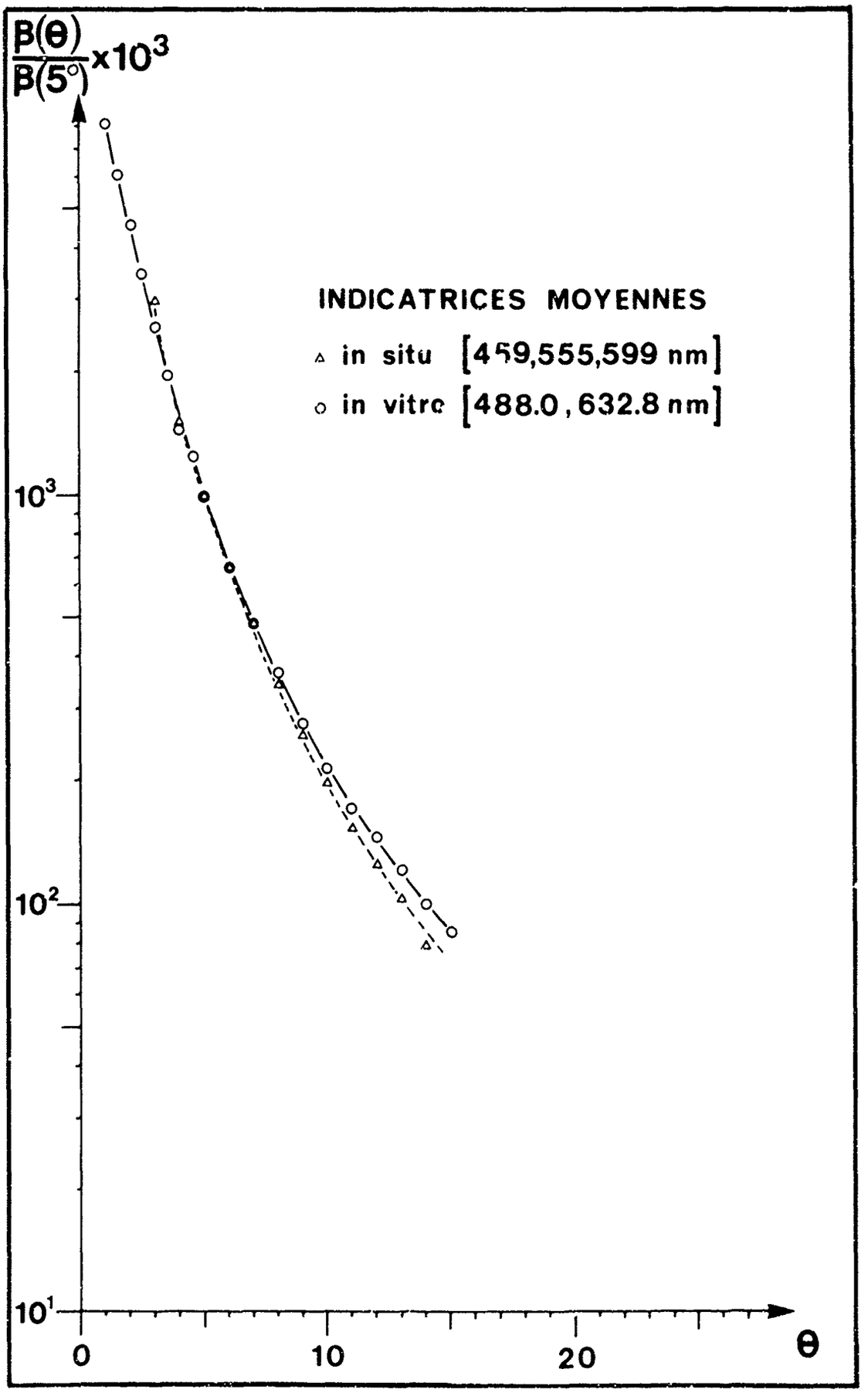

Figure 4. Comparaison des indicatrices moyennes obtenues à l'aide de sources classiques et de lasers.

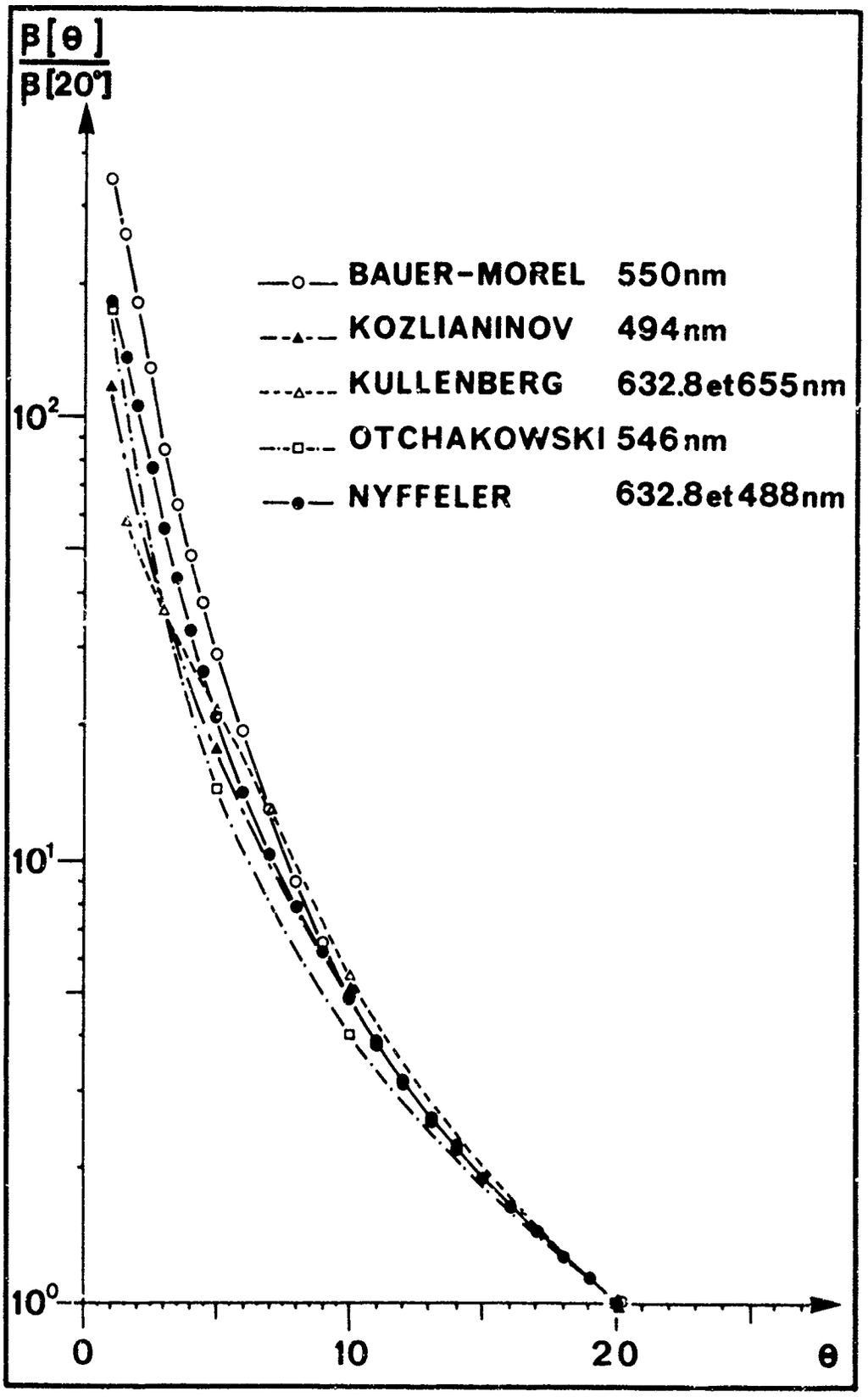

Figure 5. Comparaison avec les résultats obtenus par divers auteurs.

OBSERVATIONS OF LIGHT SCATTERING IN DIFFERENT WATER MASSES

by

G. KULLENBERG

Institute of Physical Oceanography
University of Copenhagen

SOMMAIRE

On a mesuré "in situ" la fonction de diffusion de la lumière à l'aide de deux instruments différents. L'un d eux emploie un laser comme source lumineuse, ce qui permet de mesurer la diffusion sous angle faible (0,5 - 1°). Deux lasers aux longueurs d'ondes respectives de 632,8 et 488 nm ont été utilisés. Le second instrument est un instrument classique pour couches superficielles.

Les fonctions de diffusion, qui correspondent à des eaux marines extrêmement claires (mer des Sargasses) et des eaux côtières troubles (Baltique) ont des formes semblables mais des valeurs différentes. Une grande partie de la diffusion se trouve concentrée en un lobe étroit, situé vers l'avant ; on voit ainsi que la majeure partie de la diffusion est créée par des particules dont la taille est supérieure à la longueur d'onde de la lumière. Dans les eaux claires, la diffusion moléculaire exerce une influence importante sur la fonction de diffusion de la région bleue. On peut observer que la diffusion créée par la matière se présentant sous forme de particules dépend légèrement de la longueur d'onde pour des angles de diffusion importants (40°).

Le rapport entre la diffusion totale sous un angle de 45 ° et le coefficient de diffusion total est quasi constant au large mais varie de façon significative dans les eaux troubles.

OBSERVATIONS OF LIGHT SCATTERING IN DIFFERENT WATER MASSES

G. KULLENBERG
Institute of Physical Oceanography
University of Copenhagen

SUMMARY

In situ measurements of the light scatterance in the Sargasso Sea and in the Baltic are compared. The total scattering functions are similar in shape, with pronounced forward scatterance. In the Sargasso Sea the molecular scatterance has a significant influence which is not the case in the Baltic, proving the Sargasso Sea to be extremely poor in particles.

The particle scatterance is between one and two orders of magnitude stronger in the Baltic. The intense small angle scatterance there is probably caused by large, transparent particles of biological origin. In the Sargasso Sea the particle scatterance is virtually independent of wavelength, while it in the Baltic is strongest in the green part of the spectrum.

An attempt is made to determine discrete particle-size distributions by using the observed scattering functions and calculations by means of the Mie theory. For the Sargasso Sea the distribution $N(r_i) = \text{const.}\ r_i^{-2}$ conforms nicely with the observations. For the Baltic no definite result can be given at present.

INTRODUCTION

The light scatterance has been measured in situ in the Sargasso Sea, where the water is extremely poor in particles, and in the central Baltic, where particles are abundant. The two areas represent extreme conditions encountered in the sea.

The primary aim of the investigation was to determine, and compare the volume scattering functions in different parts of the spectrum. The volume scattering function $\beta(\theta)$ is defined by

$$dI(\theta) = \beta(\theta) \cdot E \cdot dV \qquad (1)$$

where $dI(\theta)$ is the radiant intensity scattered in the direction θ from the incident beam by the volume element dV irradiated by E. The total scattering coefficient b is given by

$$b = 2\pi \int_0^{\pi} \beta(\theta) \cdot \sin\theta d\theta \qquad (2)$$

Instruments used, calibration techniques, and measurements are described by Kullenberg (1, 2), and are therefore only summarized here. Principally two different instruments were used, the β-meter and the laser-instrument. The β-meter (3) utilized a conventional incandescent light source, and optical filters (Schott and Genossen 2 mm BG12, GG5, VG9, RG1; photomultiplier tube with S20 response) were used to isolate the scattered light. The scattering function was measured in discrete steps from 10° to 165° scattering angle. The instrument was used to a maximum depth of 25 m. It is calibrated in the laboratory. The calibration involves uncertainties, and the maximum error is estimated to 20%.

The laser-instrument utilized either a He-Ne laser, $\lambda = 632.8$ nm, or a Ar^+ laser, dominant $\lambda = 488$ nm, as a light source. With this instrument it was possible to measure the small angle (0.5 - 1°, 2.5°, 3-3.5°) as well as the large angle scatterance from the surface to 500 m depth. The small angle scatterance was measured by means of a special optical system (Fig. 1), yielding well defined angular intervals, and effectively eliminating stray light. The instrument was in principle calibrated in situ.

In the Sargasso Sea the observations were carried out while the ship was drifting at about 27°N, 63°W, during a 3 weeks period in March 1966. The β-meter and the He-Ne laser instrument were used, but unfortunately the Ar^+ laser would not function properly. En the Baltic the observations were performed in June 1967 with the ship at anchor for several days at 3 different stations around 55°30'N, 16°30'E. In this case the whole equipment worked well, even though the Ar^+ laser was unreliable.

DISCUSSION OF THE OBSERVATIONS

The observations are presented here only as curves of the scattering functions (Figs. 2, 3, 4), since they are given in a more complete form elsewhere (1, 2).

Total scatterance. Fig. 2 shows total scattering functions obtained with the He-Ne laser as a light source. For the Sargasso Sea the mean values of all observations in the surface layer (10-75 m) are used to determine the scattering function for this layer. For the Baltic the mean values of all observations at station 3 around 10 m and 40 m depth are used. All the functions are smooth, typical of polydispersed systems, and the forward scatterance is very pronounced. This is in general agreement with other results (4, p. 34). The very strong small angle scatterance is also in general agreement with the measurements of Bauer and Morel (5) in the

Mediterranean, even though these authors report a considerably stronger small angle scatterance.

The similarity of the curves representing two extremas encountered in the sea is obvious. The scatterance in the Baltic is between one and two orders of magnitude larger than the Sargasso Sea. The forward scatterance is more pronounced in the Baltic indicating that there are larger particles present.

Although the function obtained at 400 m in the Sargasso Sea, also shown in Fig. 2, is incomplete, it is evident that the scatterance decreases considerably from the surface to this depth. In vitro measurements on water samples from 500 m and 1000 m depth indicate an increase of the scatterance at these depths.

In Fig. 3 the corresponding curves for the blue to blue green part of the spectrum are displayed. For comparison the function obtained by Morel (6) on water distilled three times without boiling is also shown. These measurements were carried out at 546 nm, but have here been transformed to 460 nm, assuming a dependency on wavelength as for molecular scatterance.

Also in this case the curves show a striking similarity, but the forward scatterance is considerably more pronounced in the Baltic. In the Sargasso Sea the molecular scatterance has a significant influence on the shape of the total scattering function in this part of the spectrum, which is not the case in the Baltic. For 90° scattering angle the molecular part amounts to 87% and 38%, respectively, in the two areas. The importance of the molecular scatterance in the Sargasso water is further stressed by comparison with Morel's measurements. The close agreement at large scattering angles is striking, and suggests extremely low particle content. Nevertheless at angles $\leq 60^{\circ}$ tha particles determine the scattering function. The molecular part of the total scattering coefficient is only 10 - 11%. An effect of the molecular influence is also that the total scattering functions are dependent on wavelength.

Particle scatterance. Next the particle scattering functions will be discussed. These (Fig. 4) are obtained by deducting LeGrand's (7) theoretical values of the molecular scatterance from the total scatterance. The wavelengths 510 nm, 525 nm, and 632.8 nm for the Baltic, and 632.8 nm for the Sargasso Sea are shown. For comparison a function obtained by Tyler (8) around 522 nm in coastal water is incorporated.

The very strong forward scatterance shows that in both areas the particle scatterance is determined by particles larger than the wavelength of the light. While it in the Sargasso Sea seems to be virtually independent of wavelength, this is not the case in the Baltic. There the scatterance shows a distinct maximum in the green part of the spectrum, while it is similar in the red and blue parts. This could probably be caused by the abundance of particulate matter of biological origin in the Baltic, and due to selective absorption by this material. One should note that the color of the Baltic water as determined by irradiance measurements is 510 -540 nm in the surface layer (4, p. 149).

The ratio of total scatterance at 45° to total scattering coefficient is practically constant in the purely oceanic region with a mean value of $3.3 \cdot 10^{-2}$. The approximate constancy of this ratio was pointed out by Jerlov (9) for ocean water, and by Tyler (10) for prepared suspensions. In the Baltic the ratio is found to vary considerably, but is generally lower than in the ocean. The ratio has different values for different suspensions (1), and the lower ratio in the Baltic is consistent with a large concentration of biological material. The variation of the ratio further indicates that the suspension in the Baltic contains a wider distribution of particles, both regarding size and origin.

COMPARISON BETWEEN OBSERVED AND THEORETICAL SCATTERING FUNCTIONS

It is well known that scattering measurements on a polydispersed system, usually combined with determinations of the polarisation ratio at at least one angle, can be used to investigate the particle-size distribution (11). The technique is advantageous when the particles cannot be collected for direct observation, which is the case in many astronomical, atmospherical, and oceanographical applications. It is not advisable to use only water sampling and in vitro techniques in studies of particles in the sea, since many particles of primary importance are very delicate and easily break up during the process of sampling (12).

PARTICLE-SIZE DISTRIBUTION MODELS

The present observations have been used for investigating several possible models of the particle-size distribution. The Mie-theory (13) is the theoretical foundation for these calculations. The tables of Ashley and Cobb (14), supplemented with those of Gumprecht and Sliepcevich (15), have been used since they seem to be most appropriate to the present problem. The use of these tables implies that the particles must be distributed in discrete sizes. The relative refractive index m used in the tables is 1.20, which is somewhat higher than the average value of m = 1.17 for minerals in the sea given by Pavlov and Grechushnikov (16). This value could be employed for the Sargasso Sea, where the scatterance is determined by minerals such as quartz, and where the particulate matter of biological origin plays a minor role, (1). On the other hand the m-values in the Baltic probably covers a rather large range due to the presence of biological material. In this case it must be regarded as a rough approximation to use a constant value of m = 1.20.

The range of radii (r_i) is limited to the α-values of the tables. The following values of $\alpha = 2\pi r/\lambda$ have been used, α = 10, 15, 20, 30, 35, and 80, with λ = 632.8 nm. The value of 80 is found in (15), but only for 0° to 3°. However, it is in this region that a few, large

particles can play a decisive role, which is the reason for incorporating the value in the calculations. Guided by the present results and by other observations as summarized by Jerlov (4, p. 25), it is assumed that particles smaller than 1 μm in radius do not contribute significantly to the scatterance. All evidence so far is in favour of such a view.

The total number of particles to include in the models has been estimated by means of the equation

$$b_p = \pi \sum_i N_i \cdot K_i \cdot r_i^2 \qquad (3)$$

where N_i is the number of particles with radius r_i and efficiency factor K_i, and b_p is the particle scattering coefficient. The value of b_p is known from the observations, and thus N_i can be found if K_i and r_i are known. Despite thorough analytical discussions (11) and relevant measurements (17), (18), it is difficult to assign an exact value to K_i. It is well known, and borne out by the measurements mentioned, that the value is approximately 2. Since not much seems to be gained at present in using a more refined value, K_i has been given the value 2 for all radii used in order to simplify the calculations. Even if this is a defect of the models it is not believed to be a serious one. It should be stressed that the values of r_i used in the computations are those corresponding to the α-values given above, supplemented with a few radii deemed necessary to incorporate for the sake of completeness.

As regards the choice of distribution functions, there is no strong evidence in favour of any particular distribution to be used. Particle countings (4, p. 27; 19) usually show more or less well defined intermediate maxima. Therefore two different forms, namely normal and power law distributions, have been used.

First the normal size distribution

$$N(r_i) = \frac{1}{\sigma\sqrt{2\pi}} \cdot \exp\left[-\frac{1}{2}\left(\frac{2r_i - 2\bar{r}}{\sigma}\right)^2\right] \qquad (4)$$

is discussed. Several values of the mean radius ($\bar{r}$) and the standard deviation (σ) have been tried. The best fit is found for $\bar{r} = 3$ and $\sigma = 1.2$ when comparing with the scattering function of the Sargasso Sea surface layer (Fig. 5). The total number of particles used in the model is 360 per cm^3, in the radius range 1.2 - 4.3 μm. The agreement between model and observations is fairly good, but this only shows that the scatterance really is determined by this range of particles. The distribution is narrow, and probably not too representative of oceanic conditions. The total number of particles is low, corresponding to a dry weight of 0.12 mg/l, using the rather high average density 2.5 g/cm^3 for the particulate matter. This mass of suspended matter is considerably lower than the oceanic average of 0.8 - 2.5 mg/l (4, p. 26). It is low compared to direct estimates in the Sargasso Sea as well (20). The conclusion is that a model of the type of eq. 4 is not representative for the Sargasso Sea surface layer.

Next a particle-size distribution of the form

$$N(r_i) = \text{const.} \cdot r_i^{-\xi} \qquad (5)$$

is discussed. Several values of the exponent ξ have been investigated. As regards the Sargasso Sea a model with $\xi = 3$ is compared with the observations in Fig. 6. The total number of particles with radius larger than 1 μm used in the model is 1560 per cm^3, corresponding to a dry weight of 0.08 mg/l, which is a very low value. Although the general agreement between model and observation cannot be denied, the forward scatterance of the model is weaker than the observed.

In Fig. 7 a model with $\xi = 2$ is compared with the same observations. The number of particles larger than 1 μm in radius is 960 per cm^3, yielding 0.24 mg/l dry weight in rather good agreement with other estimates (20). The resemblance between observation and calculation is by far the best in this case. It is noted that the model yields adequate values of the forward scatterance. This model also conforms with the observation that the particle scatterance in the Sargasso Sea is virtually independent of wavelength.

Thus several indications found in the measurements are consistent with this size distribution and it is suggested that it is fairly representative of conditions in the surface layer of the Sargasso Sea.

In the Baltic the scatterance is considerably stronger than in the Sargasso Sea, but the scattering functions are similar in shape. In the Baltic the scatterance is wavelength dependent, there is an abundancy of biological material, the m-values therefore probably covers a large range, and one should expect the particle-size distribution to be wider. The problem thus is more complicated in this area.

The model scattering functions presented above have been compared with the Baltic observations, using a larger number of particles as found from eq. 3, but the agreement is not convincing. Two other models are also investigated. Fig. 8 displays a model with $\xi = 1.5$ together with the surface layer observations in the Baltic. The number of particles larger than 1 μm included in the model is 7240 per cm^3. The distribution is in the present range very similar to a particle-size distribution found by direct counting in the Gullmar fjord (18). Generally agreement between model and observations is good, but there are deviations in details. This is to some degree due to the fact that only part of the larger particles, which are much more abundant here

than in the Sargasso Sea, can be included in the calculations because of the limitations of the tables used, as well as to the fact that the calculations are limited to one m-value only. Thus it is not possible to state at present whether or not this model fits for the Baltic, even if it in a general way conforms with observations.

Hinzpeter (21) argues that in certain areas of the Baltic the particle-size distribution cannot be given by a power law because of the dispersion shown by the scatterance. Thus it is of interest to apply a different type of distribution function. This cannot in a convenient way be done with the tables used so far. Deirmendjian (22) has published a complete set of tables using several continuous models with different particle ranges. With modifications these could be applicable to the present problem.

The continuous size distribution (27, p. 75)

$$dN(r) = a \cdot r^{\xi} \cdot \exp(-d \cdot r^{\gamma})dr, \quad 0 \leq r < \infty \qquad (6)$$

is called a modified gamma distribution. Depending upon the particular values given the constants a, ξ, d, and γ, different models are defined. The calculations are performed for several wavelengths, of which 700 nm suits the present observations at 632.8 nm best.

Fig. 9 shows one of the models, demoted C1 with $\xi = 6$, $\gamma = 1$, together with the Baltic observations. The range of radii is 1 - 14 μm with maximum at 4 μm. The observed small angle scatterance is somewhat stronger than that of the model, while the observed backward scatterance is much weaker than that of the model. Despite this there is an evident general agreement.

In this comparison there is a serious difficulty, since Deirmendjian uses m= 1.33, which is not representative for the particulate matter in the Baltic. How does a change in the value of m affect the shape of the scattering function? An indication of this is found when comparing the scattering function given by Deirmendjian for another of his models, denoted C3, using m = 1.33, with the scattering function for the same model as calculated by means of the tables of Ashley and Cobb for m = 1.20 (Fig. 10). Evidently the general shape of the two functions do not differ very much, but there are considerable differences in details. It is interesting to note that the values of the small angle scatterance are identical. It must be stressed that Deirmendjian uses continuous distributions.

The intense small angle scatterance observed in the Baltic has probably several causes. Some very large particles will give rise to strong scatterance at small angles. With an m-value larger than 1.15 this scatterance is determined by diffraction. As m approaches 1, a departure from the diffraction occurs for large α-values. Not diffraction but the more refraction determines the scattering function at small angles (11, pp. 172-191; 23). Interference between the refracted and the diffracted light will become important, and the phase difference, determined by $\rho = 2\alpha(m-1)$ becomes significant. Constructive interference will cause anamalously strong forward scatterance.

As regards the backward scatterance the value of m probably also is important, and possibly this part of the scattering function can be used to obtain a better understanding of the nature and form of the particulate matter. The discrepancy between models and observations for large scattering angle ($\theta > 90^{\circ}$) is probably an indication of the deviation of the form of the particles from the spherical. A further study of this phenomenon would need more detailed observations.

Finally it should be mentioned that measurements of the polarization ratio have to be included to obtain a complete picture of the scatterance as well as the size distribution and composition of the particulate matter.

CONCLUSIONS

The measurements decribed above are far from complete, and the results in the last section must accordingly be regarded with caution . In the Sargasso Sea the molecular scatterance has an influence which means that the water is extremely poor in particles. This is in accordance with the view that the Sargasso Sea is an art of convergence, implying that the water is relatively old. Nevertheless, the particles present, determine the shape of the scattering function for angles less than 60°. The particles are larger than the wavelength of the light. It is suggested that the wavelength dependency is very weak. A discrete particle-size distribution of the form of a power law shows a scattering function independent of wavelength, and in close agreement with the measurements.

The scattering functions in the central Baltic are similar in shape to those in the Sargasso Sea. Small angle scatterance is more pronounced, showing that the particles on an average are larger than in the Sargasso Sea. It seems probable that the very intense small angle scatterance is caused by large transparent particles. The intensity of the scattered light is much higher, and the molecular scatterance has no significant influence. The particle scatterance is found to be dependent on wavelength, with a pronounced maximum in the green part of the spectrum. This may be caused by biological particulate matter, acting through selective absorption.

The scattering functions of different discrete particle-size distributions have been compared with the observations, but no definite results are obtained. This is probably partly due to the incomplete character of the calculations. To be able to describe the scattering function of such a

complicated polydispersed system as that in the Baltic by theoretical calculations a larger range of α-values is needed for several different values of m. More detailed measurements of the scatterance, and polarization ratio, are necessary to arrive at true values of the particle-size distribution.

ACKNOWLEDGEMENTS.

The author wants to acknowledge fruitful comments on the manuscript by Professor N. Jerlov and Mr. K. Nygård.

REFERENCES

1. Kullenberg, G. "Scattering of light by Sargasso Sea water", Deep-Sea Res., 15, 423 - 432, 1968.
2. Kullenberg, G. "Light scattering in the Central Baltic", Rep. Inst. Phys. Oceanogr. University of Copenhagen, 5, 1969.
3. Jerlov, N. G. "Optical measurements in the eastern North Atlantic", Meddn. oceanogr. Inst. Göteborg, 30, 1 - 40, 1961.
4. Jerlov, N. G. "Optical Oceanography", Elsevier Oceanogr. Ser. 1968.
5. Bauer, D. and A. Morel, "Etude aux petits angles de l'indicatrice de diffusion de la lumière par les eaux de mer", Annls. Géophys., 23, 109-123, 1967.
6. Morel, A. "Etude experimentale de la diffusion de la lumière par l'eau les solutions de chlorure de sodium et l'eau de mer optiquement pures", J. Chém. Phys. 10, 1359, 1966.
7. LeGrand, Y. "La pénétration de la lumière dans la mer", Annls. Inst. océanogr., Monaco 19, 393, 1939.
8. Tyler, J. "Scattering properties of distilled and natural waters". Limn. Oceanogr. 6, 4, 451 - 456, 1961.
9. Jerlov, N. G. "Particle distribution in the ocean", Rep. Swed. Deep-Sea Expedition, 3, 71, 1953.
10. Tyler, J. "Measurements of the scattering properties of hydrosols", J. Opt. Soc. Am. 51, 1289 - 1293, 1961.
11. Van de Hulst, H.C. "Light scattering by small particles", J. Wiley and Sons, 1957.
12. Inoue, N., Nishizawa S., Fukuda M. "The perfection of a turbidity meter and a photographic study of suspended matter and plankton in the sea using an undersea observation chamber", Proc. UNESCO Symp. Phys. Oceanogr., Tokyo, pp. 53 - 58, 1955.
13. Mie, G. "Beiträge zur Optic trüber Medien speziell kolloidalen Metallösungen", Ann. Physik, 25, 377, 1908.
14. Ashley, L. E. and C. M. Cobb, 'Single particle scattering functions for latex spheres in water". J. Opt. Soc. Am., 48, 261 - 268, 1958.
15. Gumprecht, R. O. and C. M. Sliepcevich, "Scattering of light by large spherical particles", J. Opt. Soc. Am. 57, 90 - 94, 1953.
16. Pavlov, V. M. and B. N. Grechushnikov, "Some aspects of the theory of daylight polarization in the sea". U. S. Dept. Comm., Joint Publ. Res. Ser., Rept. 36 (816): 25 - 44, 1966.
17. Jerlov, N. G. and B. Kullenberg, "The Tyndall effect of uniform minerogenic suspensions", Tellus 5, 306 - 307, 1953.
18. Jerlov, N. G. "The particulate matter in the sea as determined by means of the Tyndall meter", Tellus 7, 218 - 225, 1955.
19. Carder, K. L. 'Particles in the Eastern Pacific Ocean: Their distribution and effect upon optical parameters", Ph.D. Thesis, Oregon State Univ., 1970.
20. Parsons, T.R. "Suspended organic matter in sea water". In: M. Sears (Editor), Progress in Oceanography, Pergamon, New York, N. Y., 1, 205 - 239, 1963.
21. Hinzpeter, H. "Messungen der Streufuntionen und der Polarisation des Meerwassers", Kieler Meeresforsch., 18, 36 - 41, 1962.
22. Deirmendjian, D. "Electromagnetic scattering on spherical polydispersions", Elsevier, 1969.
23. Mullaney, P. F. "Application of the Hodkinson scattering model to particles of low relative refraction index", J. Opt. Soc. Am., 60, 4, 573 - 574, 1970.

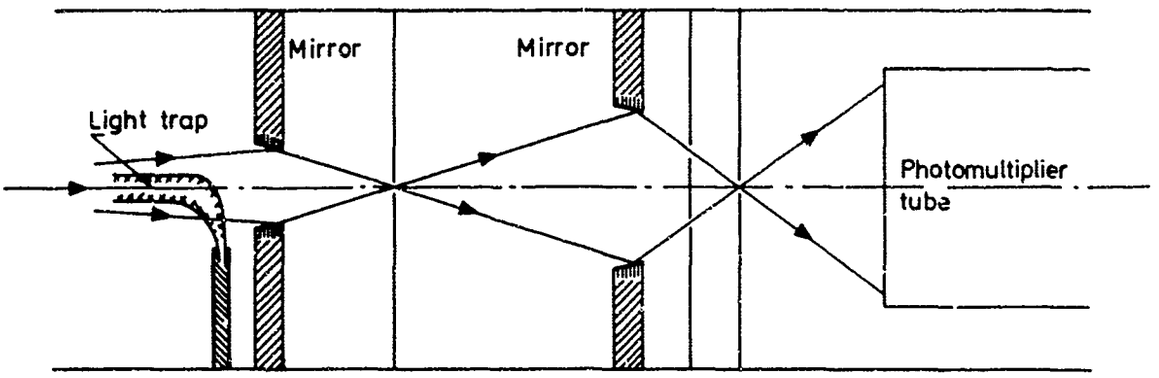

Fig.1 Optical system for measuring small angle scatterance.

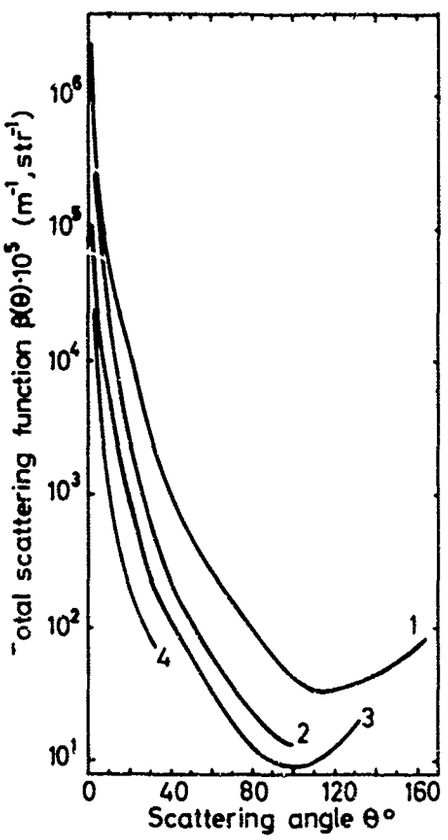

Fig.2 Total scattering functions,
λ 632.8 nm
1. Baltic, 10 m.
2. Baltic, 40 m,
3. Sargasso Sea, 10-75 m,
4. Sargasso Sea 400 m.

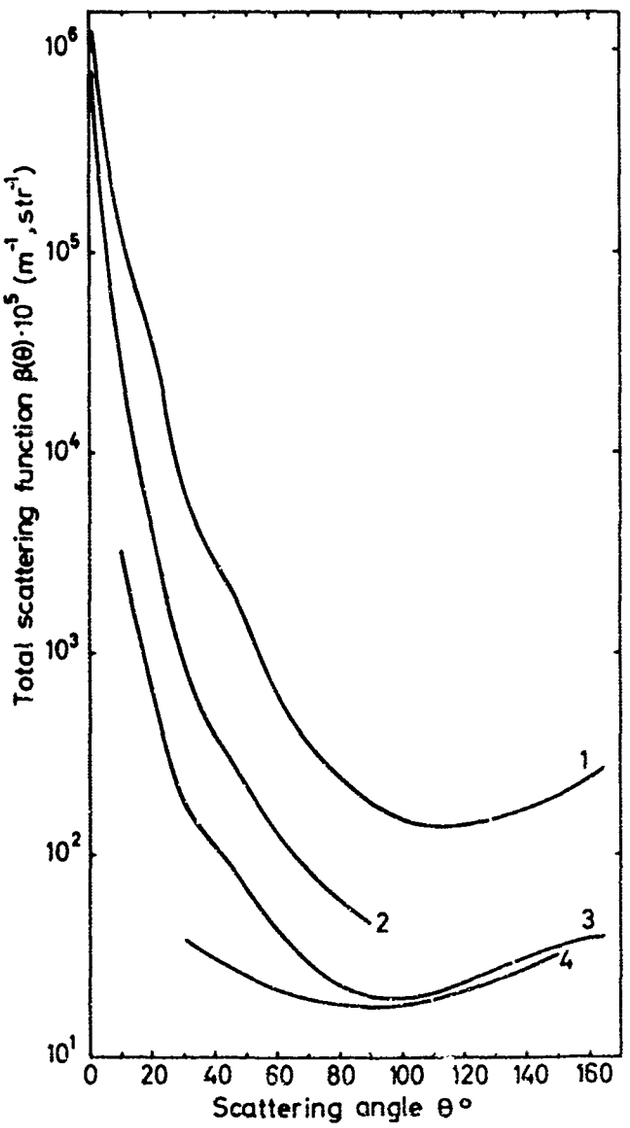

Fig.3 Total scattering functions
1. Baltic, 488 nm, 10 m.
2. Baltic, 488 nm, 40 m.
3. Sargasso Sea, 440-460 nm, 10-75 m
4. Morel (6), 546 nm transformed to 460 nm

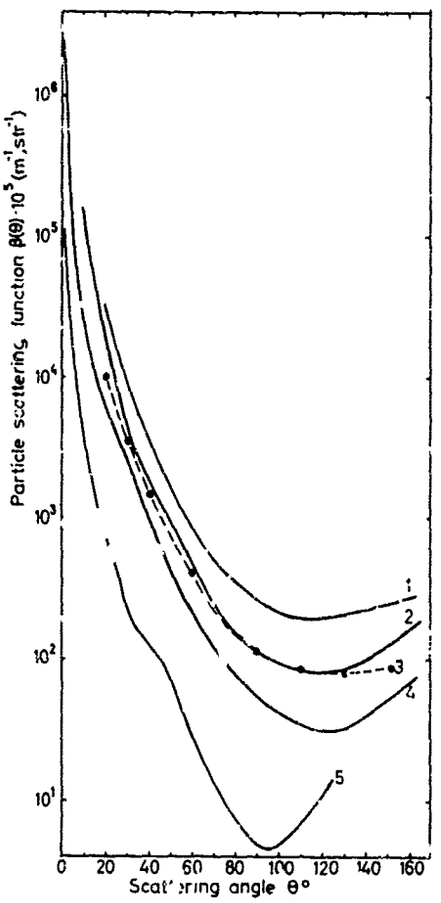

Fig. 4 Particle scattering functions
1. Baltic, 510 nm, 10 m,
2. Baltic, 525 nm, 10 m,
3. Tyler (8), 522 nm,
4 Baltic, 632.8 nm 10 m,
5. Sargasso Sea. 632.8 nm, 10-75 m

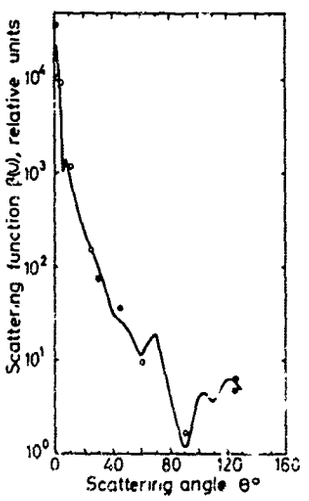

Figure 5 Theoretical scattering function, normal size distribution, compared with Sargasso Sea particle scatterance, 632.8 nm, 10-75 m

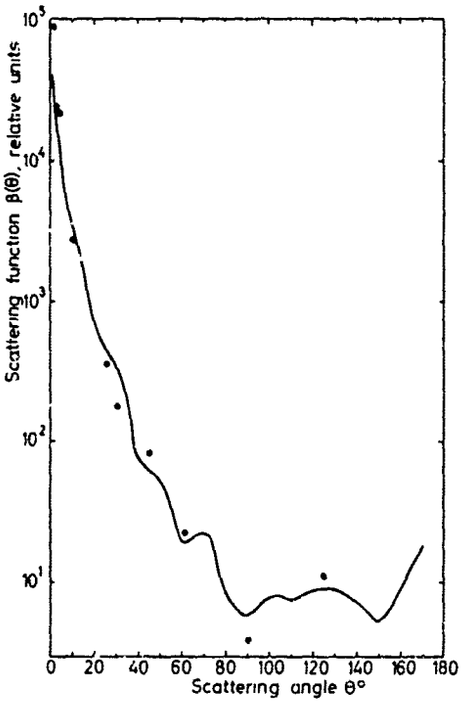

Fig. 6 Theoretical scattering function, power law, exponent 3, compared with Sargasso Sea particle scatterance, 632.8 nm, 10-75 m

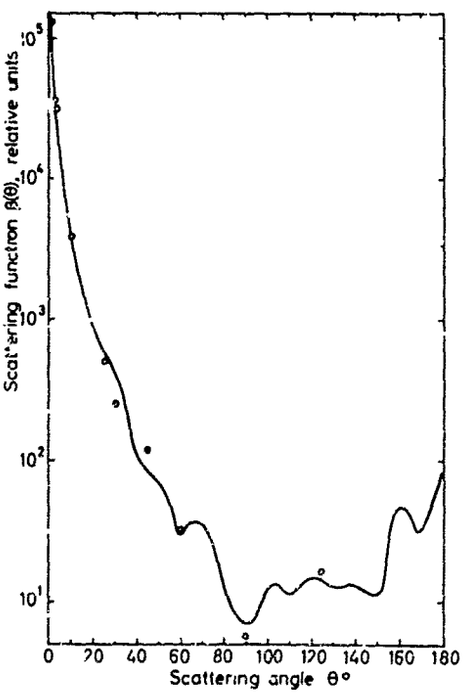

Fig. 7 Theoretical scattering function function, power law, exponent 2, compared with Sargasso Sea particle scatterance, 632 8 nm, 10-75 m

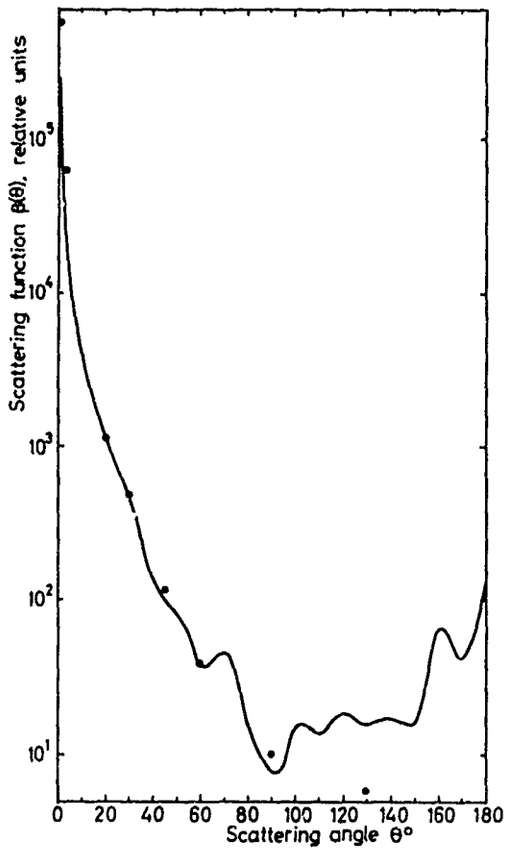

Fig.8 Theoretical scattering function, power law, exponent 1.5, compared with Baltic particle scatterance, 632.8 nm, 10 m

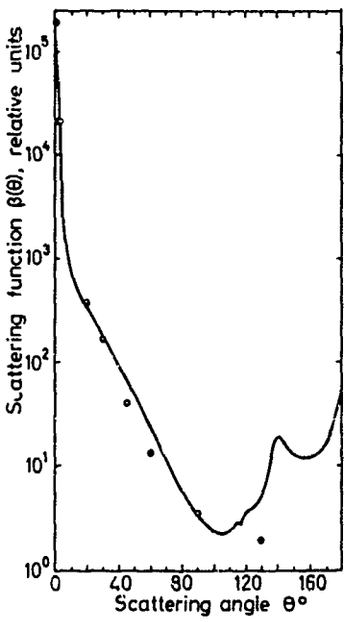

Fig.9 Theoretical scattering function by Deirmendjian, compared with Baltic particle scatterance, 632.8 nm, 10 m

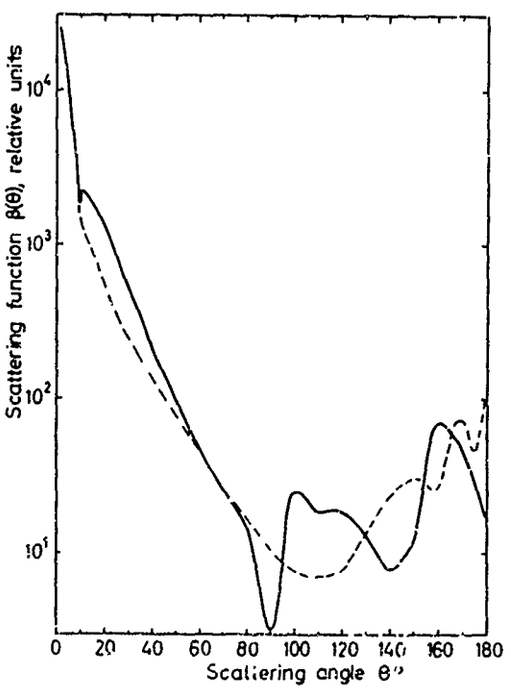

Fig.10 Comparison between theoretical scattering function by Deirmendjian for m 1.33 (dashed), and for m 1.20 (full drawn) by the tables of Ashley and Cobb

PENETRATION DE LA LUMIERE DU JOUR DANS LA MER

par

L. Prieur

Laboratoire d'Océanographie physique
Quai de la Darse
06, Villefranche-sur-Mer, France

SUMMARY

It is interesting to know, either for their own sake or for biological and human purposes, the properties of daylight after it has propagated through seawater over various distances. Such properties are relatively well known on the surface, but they undergo considerable modifications as daylight penetrates through the water, due to the interaction of the electromagnetic waves with the medium. The two optical characteristics of seawater which essentially describe such interaction are selective absorption and scattering. As a result, the spectrum and space distributions of daylight are modified. Therefore, a perfect knowledge of the light energy available in the ocean would require determining these two distributions in each spot ; however, this involves difficult time consuming measurements.

This paper will attempt to demonstrate that partial, however valuable knowledge of the above mentioned phenomena, can be achieved by means of simple and easily handlet instruments. With this purpose in view, first the relationship with the spectrum properties of the measurements already carried out with instruments specifically designed for investigating daylight penetration, will be discussed. Then, in connection with space properties, the "boundary distribution" of luminances and its prediction based on the optical properties of seawater will be considered.

PENETRATION DE LA LUMIERE DU JOUR DANS LA MER .

L. Prieur

Laboratoire d'Océanographie physique
Quai de la Darse
06, Villefranche-sur-Mer, France

SOMMAIRE

La répartition de l'énergie solaire, au sein de la mer, dépend de la répartition de surface et des caractéristiques de l'eau traversée : absorption et diffusion. Après avoir rappelé la nature de la lumière du jour en surface, et examiné les propriétés optiques décrivant l'interaction des ondes électromagnétiques avec le milieu marin dans le domaine du visible, nous dégagerons quelques paramètres qui caractérisent la pénétration de la lumière dans la mer (coefficients d'extinction). A des profondeurs suffisamment grandes, le régime lumineux tend vers une forme limite indépendante du régime de surface et, dans ce cas, existent des relations plus simples entre les coefficients d'extinctions et les caractéristiques optiques ; ces relations sont présentées et vérifiées au moyen de quelques données expérimentales.

1. INTRODUCTION

L'énergie solaire atteignant la surface de la mer, possède une répartition à la fois spectrale et spatiale, qui change avec la nébulosité de la voute céleste et la hauteur du soleil. Lorsqu'elle pénètre en profondeur, la répartition est modifiée par les caractéristiques optiques du milieu que sont l'absorption et la diffusion. Les mesures de décroissance de l'énergie rayonnante pour le spectre visible sont effectuées couramment en Océanographie, mais elles ne présentent jusqu'à présent qu'un caractère descriptif ; en effet, bien que l'équation de transfert de l'énergie soit connue, il n'existe pas de relations simples, suffisamment indépendantes de l'éclairement en surface pour qu'elles soient générales, entre les coefficients d'extinction, qui décrivent la diminution de l'énergie d'une manière globale, et les caractéristiques optiques, qui sont les facteurs physiques responsables de cette diminution.

Cependant, lorsque la profondeur considérée est suffisamment grande, l'effet de la lumière de surface devient très faible, et l'état lumineux ne dépend que des caractéristiques optiques. Dans ces conditions, il est possible de trouver par le calcul, alors simplifié, de telles relations.

2. RAPPEL DES FACTEURS INFLUANT SUR LA PENETRATION DE LA LUMIERE DU JOUR

(Dans tout ce qui suit, on ne tiendra pas compte des phénomènes de polarisation).

2.1. La source

On la considère en général comme la superposition de la lumière solaire directe (provenant d'une source infiniment éloignée), et de celle réémise par la voûte céleste (provenant d'une source étendue). Indépendamment des variations d'énergie en valeur absolue, l'influence respective de ces deux composantes change dans le temps avec la nébulosité et la hauteur du soleil. Ceci entraîne une modification constante et parfois importante de la répartition spectrale et spatiale de la lumière du jour (ciel clair, ciel couvert, etc..), et donc l'impossibilité de schématiser celle-ci sans faire d'hypothèses très simplificatrices, telles que celles de supposer le ciel uniformément éclairé, ou de faire abstraction de la voûte céleste.

2.2. Caractéristiques optiques

Les deux principales caractéristiques sont l'absorption et la diffusion. Elles sont définies pour un pinceau collimaté et caractérisent le milieu marin dans son interaction avec les ondes électromagnétiques.

Le coefficient népérien d'absorption "a" symbolise l'aptitude que possède le milieu à capter l'énergie électromagnétique et à la transformer en une autre forme d'énergie. Cette grandeur intervient surtout pour modifier la répartition spectrale de la lumière, car elle dépend beaucoup de la longueur d'onde. Les radiations de longueurs d'onde supérieures à 650 nm sont absorbées, sinon dans les premiers centimètres, du moins dans le premier mètre, par suite de la forte absorption de l'eau elle même ; et celles de longueurs d'onde inférieures à 350 nm disparaissent plus ou moins rapidement, selon la concentration des matières dissoutes.

La diffusion dans l'eau de mer (caractérisée par son indicatrice angulaire, très pointue vers l'avant, et le coefficient népérien total "b") redistribue dans tout l'espace les radiations provenant d'une direction et modifie donc surtout la répartition géométrique de la lumière. En outre, puisque le milieu considéré est pratiquement infini, ce phénomène intervient un grand nombre de fois dans la pénétration de la lumière du jour : c'est le jeu des diffusions multiples.

En fait, il faut se garder de considérations trop simplistes, car la diffusion, par sa sélectivité, intervient dans la modification de la répartition spectrale ; la répartition géométrique est aussi modifiée par l'absorption, puisqu'une onde diffusée n'est pas, pour autant, soustraite à l'influence de ce phénomène.

3. PARAMETRES DECRIVANT LA PENETRATION DE LA LUMIERE DU JOUR : COEFFICIENTS D'EXTINCTION

Ces coefficients, aisément calculables à partir des mesures photométriques classiques, caractérisent expérimentalement la décroissance de l'énergie solaire dans la mer. Ils dépendent évidemment des facteurs précédemment cités, mais souvent d'une manière complexe.

3.1. Définition

Si G est la grandeur photométrique dont on étudie la décroissance, le coefficient népérien d'extinction relatif à cette grandeur est :

$$K = -\frac{1}{G}\frac{dG}{dz} \tag{1}$$

C'est aussi la pente en coordonnées semi-logarithmiques de la courbe représentative des variations de G avec la profondeur.

3.2.

De la définition, il ressort qu'il y a autant de coefficients d'extinction que de grandeurs photométriques mesurées (I). Les plus utiles sont ceux relatifs à :

- l'éclairement plan ou sphérique à une longueur d'onde ;
- l'éclairement plan ou sphérique énergétique ou photonique dans un intervalle large de longueurs d'onde ;
- la luminance dans une direction et pour une longueur d'onde.

Ces coefficients varient en général avec la profondeur et avec le temps. La figure 1 représente à gauche la décroissance de l'énergie photonique dans le visible, en une station pour deux périodes de l'année, et à droite les coefficients d'extinction. Même lorsque les eaux sont homogènes les coefficients dépendent en principe de la profondeur par suite de l'intervention des diffusions multiples.

Les coefficients d'extinction sont donc commodes pour caractériser la pénétration de la lumière du jour, mais leur interprétation est rendue délicate par leurs variations avec la profondeur, la nature de l'éclairement en surface, et aussi le type de récepteur photométrique utilisé. En outre, les relations qui les lient aux caractéristiques optiques ne sont pas simples, bien que l'équation de transfert de l'énergie au sein du milieu marin diffusant et absorbant soit connue.

4. EQUATION DE TRANSFERT

(Dans tout ce qui suit, la longueur d'onde est fixée).

On sait qu'une forme de l'équation de transfert des ondes électromagnétiques dans un milieu absorbant et diffusant s'écrit pour les luminances et pour une longueur d'onde dans le visible : (II)

$$\cos\theta \frac{dL(z,\theta,\varphi)}{dz} = -cL(z,\theta,\varphi) + b\iint_{4\pi} L(z,\theta',\varphi')\,\beta(\theta,\theta',\varphi,\varphi')\,d\omega' \tag{2}$$

c étant le coefficient d'atténuation :

$$c = a + b \tag{3}$$

$L(z,\theta,\varphi)$ est la luminance dans la direction $(\theta,)$ considérée et à la profondeur z.
$\beta(\theta,\theta',\varphi,\varphi')$ représentant le coefficient angulaire de diffusion en valeur relative pour l'angle α que fait la direction (θ',φ') avec la direction (θ,φ) considérée. Il existe de plus la relation

$$\iint_{4\pi} \beta(\alpha)\,d\omega = 1 \tag{4}$$

Plusieurs auteurs ont déjà résolu l'équation (2) pour des cas voisins de l'eau de mer (III, IV, V), mais les méthodes restent évidemment assez complexes et sont toujours approchées.

Il existe cependant un cas où la résolution est grandement facilitée : lorsque la répartition des luminances ne varie pas avec la profondeur et prend la forme .

$$L(z, \theta,\varphi) = l(\theta)\exp(-kz) \tag{5}$$

k étant indépendant de z, θ, .

L'équation devient alors :

$$l(\theta) = \frac{b/c}{1 - k/c\cos\theta}\iint_{4\pi} l(\theta')\beta(\theta,\theta',\varphi')\,d\omega' \tag{6}$$

Cette relation est valable dans le cas de l'eau de mer pour le régime asymptotique, qui existe lorsque la profondeur considérée est suffisamment grande.

5. REGIME ASYMPTOTIQUE

5.1. Existence

PREISENDORFER, en particulier, a démontré son existence du point de vue théorique (VI), tandis que plusieurs auteurs en ont apporté les preuves expérimentales par des résultats obtenus soit en mer, soit sur des milieux artificiels analogues à l'eau de mer (VII, VIII) ; sur la figure 2, tirée de l'article (VII) sont présentées les courbes représentant en coordonnées semi-logarithmiques, les variations des luminances avec la profondeur pour deux milieux homogènes artificiels différents (b/c). On remarque effectivement qu'elles possèdent la même pente, dans les deux cas, pour la direction verticale 0° et celle éloignée de 30° de cette dernière.

5.2. Paramètres caractéristiques

L'équation (6) montre que, pour une indicatrice de diffusion donnée, le régime asymptotique est complètement déterminé par le choix d'un des trois paramètres, $\lambda(\theta)$, k/c et b/c. En particulier il existe une relation biunivoque entre k/c et b/c qui, d'ailleurs, a déjà été mise en évidence par divers auteurs pour des indicatrices de diffusion parfois assez différentes de celles de l'eau de mer (VII, IX, X, XI, XII). TIMOFEEVA (XI) propose une relation expérimentale de la forme :

(7)
$$k/c = \sqrt{\rho^{\chi}\,(1-\chi)^{\chi}}$$

dans laquelle $\chi = b/c$ et ρ est un facteur qui dépend de l'indicatrice de diffusion du milieu.

5.3. Méthode de calcul utilisée pour trouver la relation k/c, b/c

Après avoir choisi l'indicatrice de diffusion, on fixe le rapport k/c et on procède par itération pour trouver la valeur de b/c. On définit donc une double suite :

(8)
$$l_n(\theta) = \frac{\iint_{4\pi} f_{n-1}(\theta')\,\beta(\theta,\theta',\varphi')\,d\omega'}{1 - k/c\,\cos\theta} \quad ; \quad f_{n-1}(\theta) = \frac{l_{n-1}(\theta)}{l_{n-1}(\theta)}$$

$l_1(\theta)$ est pris arbitrairement et cette suite converge vers une limite $f_e(\theta)$. Alors :

(9)
$$b/c = (1 - k/c) \iint_{4\pi} f_e(\theta')\,\beta(\theta,\theta',\varphi')\,d\omega'$$

5.4. Cas de l'eau de mer

La diffusion de l'eau de mer est la résultante de la diffusion due aux particules et de la diffusion moléculaire de l'eau. L'indicatrice de diffusion moléculaire est connue et fixe, celle due aux particules est pratiquement indépendante du lieu considéré et de la longueur d'onde (XIII, XIV). Seule change la part respective de la diffusion moléculaire et de la diffusion particulaire, c'est à dire le rapport b_m/b_p.

Nous avons choisi comme indicatrice de diffusion due aux particules celle établie par NYFFELER (XV), et comme indicatrice de diffusion moléculaire :

(10)
$$\beta(\theta) = \beta(90)\,(1 + 0{,}835\,\cos^2\theta)$$

Pour trois valeurs du rapport b_m/b_p couvrant tous les cas qu'il est possible de rencontrer en mer, nous avons calculer b/c à partir de $^{m}\,^{p}$ k/c et avons porté les résultats sur la figure 3.

L'examen de cette figure appelle quelques remarques :

- toutes les courbes passent par les points b/c = 1, k/c = 0 ; et b/c = 0, k/c = 1, qui correspondent respectivement à un milieu parfaitement diffusant (sans absorption) et à un milieu parfaitement absorbant (sans diffusion).
- L'influence de la diffusion moléculaire dans l'eau de mer se fait peut sentir sur la relation k/c, /c (elle est beaucoup plus importante sur la répartition asymptotique des luminances non montrées ici).
- Les paramètres ρ (Eq (7)) sont voisins de 0,25 alors que TIMOFEEVA (XI) indiquait 0,23 pour des milieux laiteux.
- Nous avons porté, en outre, des points de mesures effectuées sur des eaux naturelles ; PREISENDORFER (XVI), JERLOV (XVII). Les mesures fournies par TIMOFEEVA (XI) correspondent à des milieux artificiels d'indicatrice de diffusion proche de celle de l'eau de mer. La concordance de ces points expérimentaux avec les calculs theoriques est donc bonne.
- Les calculs ont été menés sans prendre en considération les phénomènes de polarisation. Cependant dans le cas des eaux de mer leur effet doit être faible sur les relations établies (VII).

6. CONCLUSION

Dans les eaux de mer, et dans le cas particulier du régime asymptotique, nous avons montré le lien qui existe entre les coefficients d'extinction caractérisant la pénétration de la lumière du jour et les coefficients relatifs aux caractéristiques optiques des eaux de mer.

Le coefficient d'extinction en régime asymptotique est ainsi une caractéristique optique et à ce titre est indépendant de l'éclairement source qui engendre le régime. En conséquence les résultats trouvés s'appliquent non seulement à la pénétration de la lumière du jour mais aussi à la pénétration des lumières artificielles.

REFERENCES

I .- R.C. SMITH, Limnol. Oceanogr. 13 (3), 1968, p. 423-429.

II .- N.G. JERLOV, Optical oceanography, Elsevier, London, 1968, 194 pp.

III .- J. LENOBLE, Rev. d'opt., 35, 1, 1956, p. 1-17.

IV .- L.M. ROMANOVA, Opt. Spectry, 13, 1962, p. 463-466.
Optika i spektroskopiya, 13, 6, 1962.

V .- R.W. PREISENDORFER, Radiactive Transfert on Discrete Spaces, Pargamon, New York, 1965, 462 p.

VI .- R.W. PREISENDORFER, J. Marine Res., 18, 1, 1959, p. 1-9.

VII .- H. HERMAN et J. LENOBLE, Rev. d'opt., 43, 11, 1964, P. 555-572.

VIII .- V.A. TIMOFEEVA, Izv. Akad. Nauk. S.S.S.R., Ser. Geofiz, 4, 1968, p. 847-850.

IX .- H.H. POOLE, Sci. Proc. Roy. Dublin Soc., 24, 1945, p. 29-42.

X .- J. LENOBLE, Ann. Geophys., 12, 1956, p. 16-31.

XI .- V.A. TIMOFEEVA et F.I. GOROBETS, Izv. Akad. Nauk S.S.S.R., Ser. Geofiz, 3, 1967, p. 291-296.

XII .- L.M. ROMANOVA, Optika i Spectroskopiya, 14, 2, 1963, p. 262-269.

XIII .- A. MOREL, Cahier Océanogr., 20, 4, 1968, p. 291-303.

XIV .- F. NYFFELER, Communication à ce colloque, n° réf. 26.

XV .- F. NYFFELER, Thèse de spécialité présentée à la Faculté des sciences de Paris le 18 décembre 1969. Etude de la diffusion de la lumière par l'eau de mer. Mesures à différentes longueurs d'onde à l'aide de sources classiques et de sources L.A.S.E.R.

XVI .- R.W. PREISENDORFER, On the structure of the light field at shallow depths in deep homogeneous Hydrosols contract N O B S 72039 Task 3, Report n° 3-5, March 1959.

XVII .- N.G. JERLOV et K. NYGARD, Inherent optical properties computed from radiance measurements in the Baltic. Inst. Physical Oceanogr. Univ. Copenhagen, report n° 1, 1968.

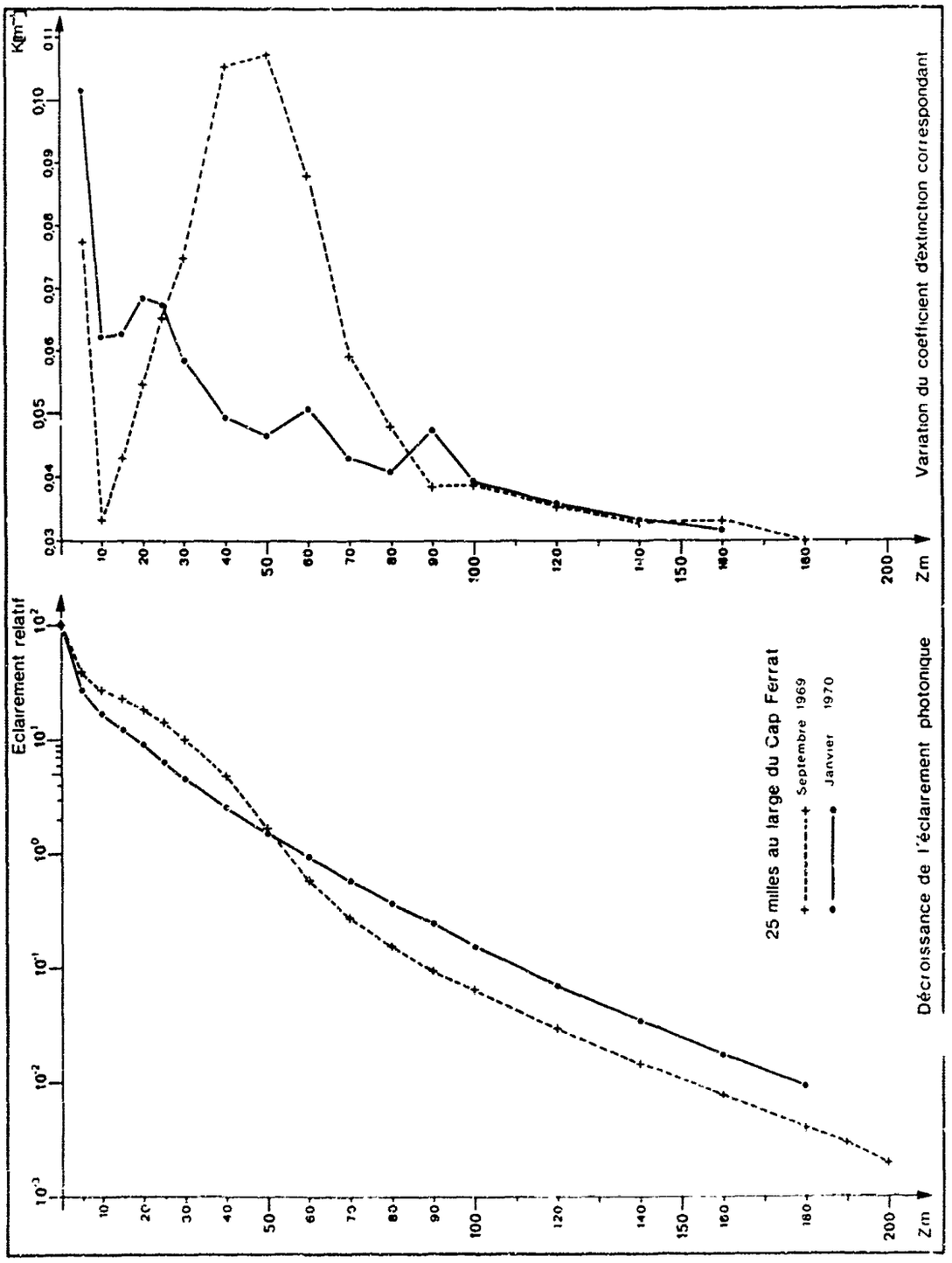
Variation du coefficient d'extinction correspondant
Km⁻¹
Zm
Décroissance de l'éclairement photonique
Eclairement relatif
25 milles au large du Cap Ferrat
Septembre 1969
Janvier 1970
Zm

Figure 1

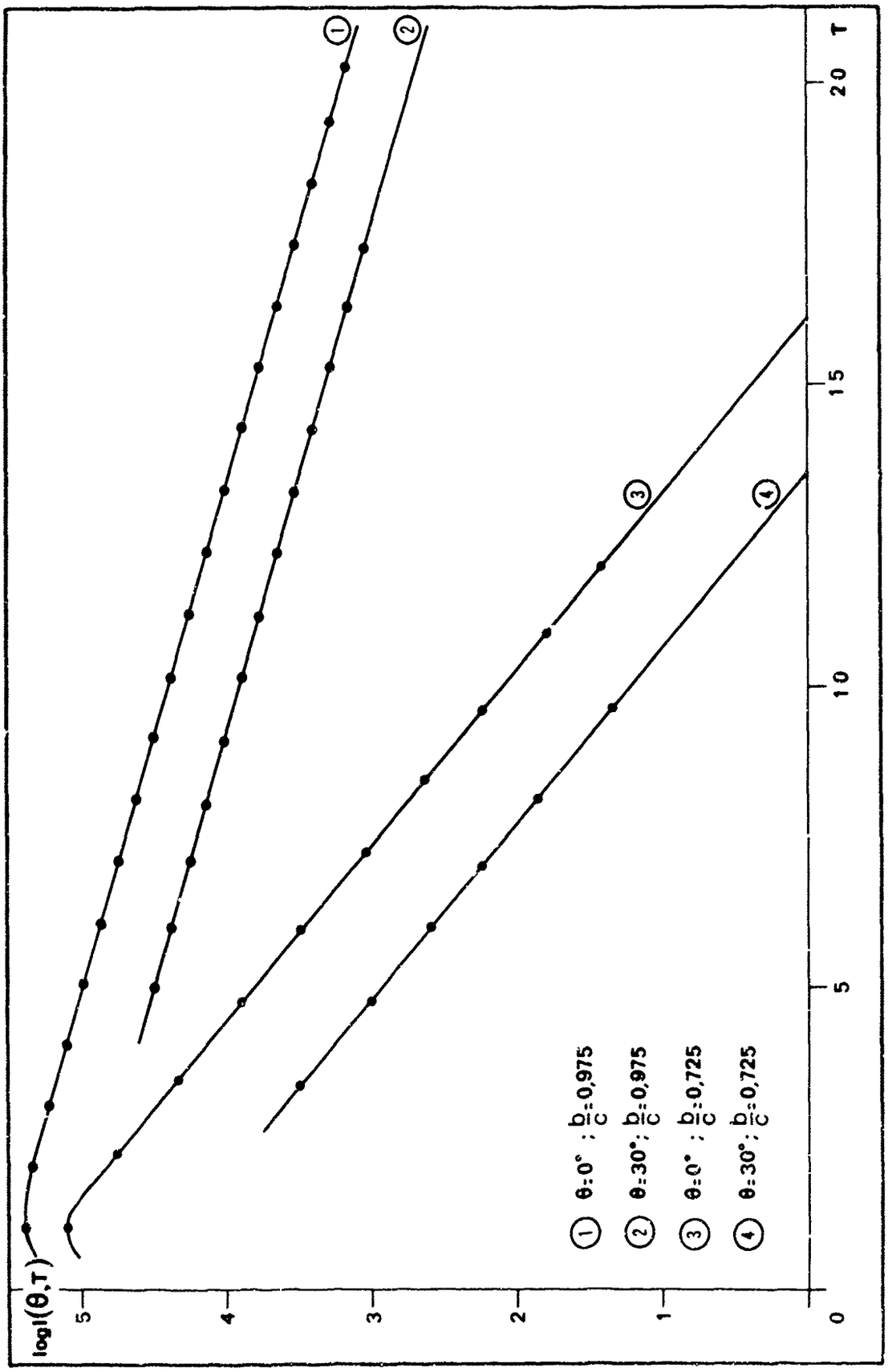
log I(θ,T)
5
4
3
2
1
0
5
10
15
20
T
① θ=0° ; b/c=0,975
② θ=30°; b/c=0,975
③ θ=0° ; b/c=0,725
④ θ=30°; b/c=0,725

Figure 2

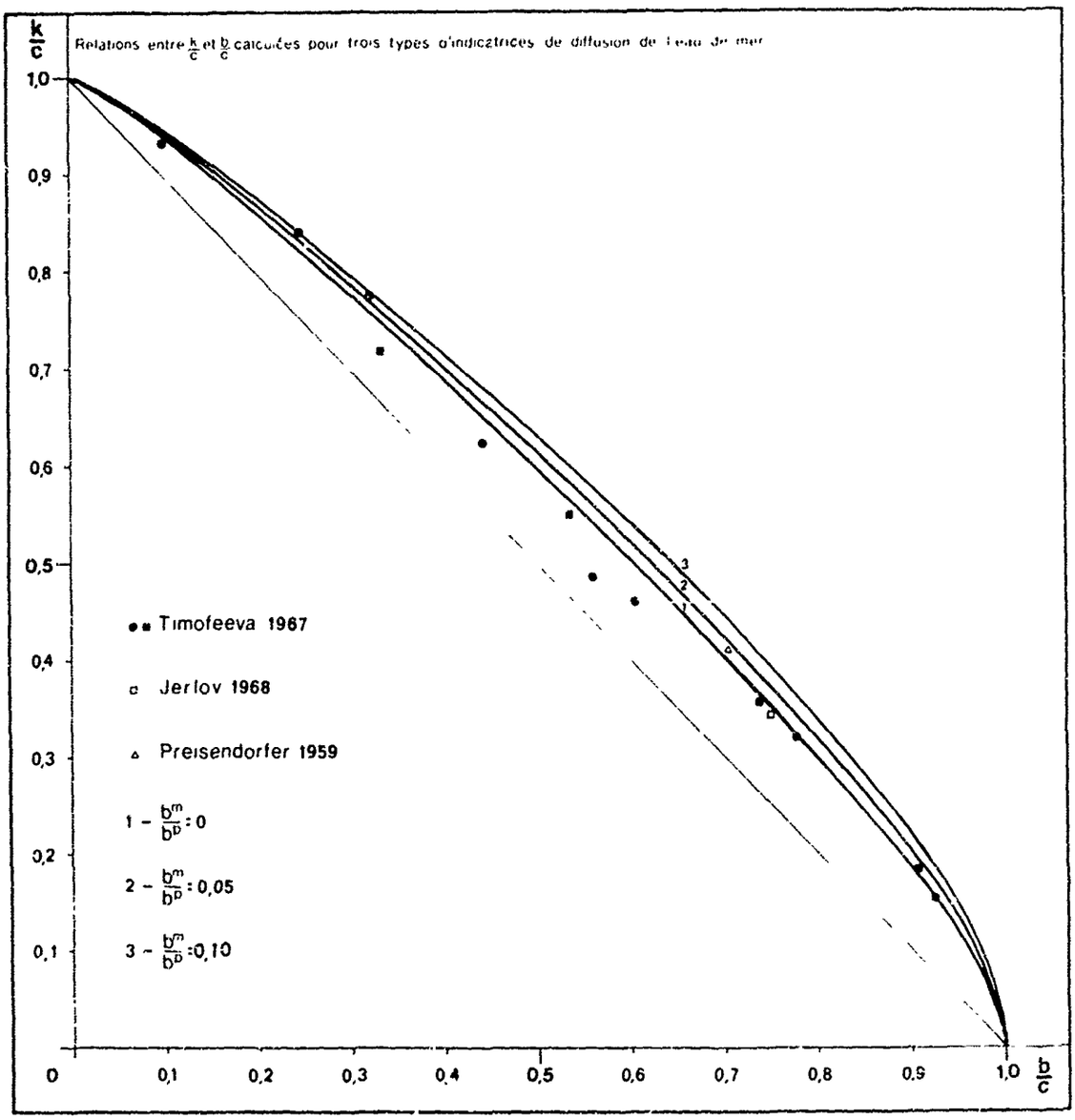
Relations entre $\frac{k}{c}$ et $\frac{b}{c}$ calculées pour trois types d'indicatrices de diffusion de l'eau de mer
k/c
1,0
0,9
0,8
0,7
0,6
0,5
0,4
0,3
0,2
0,1
0
0,1
0,2
0,3
0,4
0,5
0,6
0,7
0,8
0,9
1,0
b/c
Timofeeva 1967
Jerlov 1968
Preisendorfer 1959
1 - $\frac{b^m}{b^p}$: 0
2 - $\frac{b^m}{b^p}$: 0,05
3 - $\frac{b^m}{b^p}$: 0,10

Figure 3

MESURE DE LA TEMPERATURE DE SURFACE DE L'OCEAN AU MOYEN D'UN RADIOMETRE INFRAROUGE

par

Deschamps P.Y., Lecomte P., Vanhoutte J.C.
C.N.E.X.O., Bâtiment P5, B.P. 36
59 - Lille - Distribution

SUMMARY

Within the framework of the general study on the exchanges between the sea and the atmosphere the infra-red radiation of the sea has been measured with a radiometre in the 8-14 μ range.

Divergences between the radiometric surface temperature and the internal temperature, as measured within the first metre, are revealed.

The causes for these divergences are discussed. It is concluded that there exists a cold superficial layer, the temperature of which is at the outside different by 0,3° C from that of the sea mass, in cold and clear weather.

MESURE DE LA TEMPERATURE DE SURFACE DE L'OCEAN AU MOYEN D'UN RADIOMETRE INFRAROUGE.

DESCHAMPS P.Y., LECOMTE P., VANHOUTTE J.C.

C.N.E.X.O., BATIMENT P5, B.P. 36, 59 - LILLE - DISTRIBUTION

SOMMAIRE

Un radiomètre infrarouge de bande passante 8 - 13 microns a été réalisé. Sa précision est de l'ordre de 3/100° C.Des campagnes de mesures ont été effectuées sur la Bouée-Laboratoire du C.N.E.X.O. Au cours de ces campagnes on a mesuré simultanément la température apparente radiative de l'eau, sa température réelle, et le rayonnement du ciel. Les résultats sembleraient indiquer l'existence d'un très léger refroidissement superficiel (de l'ordre de 0,1 à 0,3° C).

1/ INTRODUCTION

Les mesures de température de surface de la mer effectuées au cours des campagnes de Juillet 1967 et Décembre 1967 au moyen d'un radiomètre infrarouge avaient montré que la "température apparente" de surface était en général inférieure de quelques dixièmes de degrés à la température mesurée dans la masse de l'eau, Ref. 1 .

Cet écart est lié à l'état du ciel et il semblait qu'il pouvait s'expliquer en partie au moins par la réflexion du rayonnement du ciel sur la surface de la mer qui n'est pas un corps noir parfait.

Ce point important méritait une étude plus complète, pour laquelle nous avons entrepris 2 campagnes de mesures, en Novembre 1968 et Février 1969.

2/ PROGRAMME

Nous présenterons ici les mesures effectuées en Février 1969.

Le but de la campagne était la détermination du coefficient de corrélation entre ΔT = différence entre la température existant dans la masse d'eau et la température apparente de surface relevée au radiomètre et ΔW = différence d'énergie rayonnée par le ciel et par la mer afin :

1°/ de comparer ce coefficient de corrélation au coefficient théorique obtenu par le calcul pour une réflexion spéculaire sur la surface de l'eau afin de voir si cette réflexion explique complétement le ΔT observé ou si une couche froide existe en surface.

2°/ d'étudier l'influence de l'agitation de l'eau sur le ΔT et sur ce coefficient, notamment en fonction de la vitesse du vent, ce qui semblait suggéré par les travaux de COX et MUNK, Ref. 2 .

3°/ de préciser la correction à apporter par suite de la réflexion sur une éventuelle mesure de la température de surface de la mer par avion, afin de n'avoir plus à tenir compte que d'une correction de transmission sur le trajet atmosphérique.

3/ DISPOSITIF EXPERIMENTAL

Au cours de la campagne de Février 1969, nous disposions d'un radiomètre infrarouge 8-13 μ, ayant une résolution en température de 0,01° C, visant en permanence la mer sous une incidence de 15° mesurant donc une température apparente. Cet appareil ainsi que les méthodes d'étalonnage ont été décrits précédemment, Ref. 3 .

La température interne de l'eau était obtenue par une sonde de platine montée sur un flotteur et raccordée à la centrale de mesures mise au point par J. GONELLA et J. MARTIN. Ref. 4 .

De plus une thermopile permettait de mesurer le rayonnement du ciel. La description de cette thermopile et son étalonnage sont donnés en annexe.

4/ RESULTATS

A titre d'exemple la figure 1 montre des enregistrements simultanés de la température apparente de l'eau mesurée au radiomètre, et de ΔW où l'on peut remarquer une bonne corrélation entre les deux phénomènes lors des passages nuageux. Mais la très grande rapidité des variations dans ce cas montre la difficulté d'un dépouillement systématique.

Les résultats les plus intéressants portent sur la période du 20 au 23 Février où des conditions lentement variables d'état du ciel et de la mer ont permis d'obtenir une bon-

ne observation des phénomènes.
Sur la figure 2 on a reporté la température apparente radiométrique, et la température interne de l'eau. On retrouve qualitativement sur cette figure les mêmes types de variations qu'au cours des campagnes précédentes. On a porté également sur la même figure ΔW exprimé en divisions de l'enregistreur.

5/ DISCUSSION DE LA REFLEXION DU CIEL

a/ Rappels théoriques

Au cours de l'étalonnage, le radiomètre mesure le rayonnement I émis par un corps noir à température T, dans un domaine spectral où il a une transmission τ_λ. Nous appellerons I_λ (T) la luminance énergétique monochromatique du corps noir à la température T.

$$I = \int_o^\infty \tau_\lambda \, I_\lambda(T) \, d\lambda \qquad (1)$$

$$= p \frac{\sigma T^4}{\pi} \qquad (2)$$

où p est le coefficient caractérisant la fonction filtre et qui dépend faiblement de la température T. Ref. 3 .

Lorsque l'on vise la mer qui est un corps noir imparfait ayant une émissivité ε_λ le rayonnement reçu est

$$I' = \int_o^\infty \varepsilon_\lambda \, \tau_\lambda \, I_\lambda(T) \, d\lambda + \int_o^\infty (1-\varepsilon_\lambda) \, \tau_\lambda \, I_{\lambda s} \, d\lambda \qquad (3)$$

$$= \int_o^\infty \tau_\lambda \, I_\lambda(T) \, d\lambda + \int_o^\infty (1-\varepsilon_\lambda) \, (I_{\lambda s} - I_\lambda) \, \tau_\lambda \, d\lambda \qquad (4)$$

où $I_{\lambda s}$ est la luminance énergétique monochromatique du rayonnement émis par le ciel et reçu à la surface de la mer.

Nous définissons une température apparente T_{app}, telle que $I' = p \frac{\sigma T_{app}^4}{\pi}$; cette température obtenue lors de la mesure radiométrique présente donc un écart par rapport à la température réelle de l'eau :

$$\Delta T = T - T_{app}$$

Or nous pouvons écrire dans la limite des approximations faites, Ref. 3

$$I' = \frac{P}{\pi} \sigma T^4 + \frac{P}{\pi} 4 \sigma T^3 \Delta T \qquad (5)$$

d'où nous obtenons en comparant les expressions 2 , 4 et 5

$$\Delta T = \frac{\pi}{p \, 4 \, \sigma T^3} \int_o^\infty (1-\varepsilon_\lambda) \, \tau_\lambda (I_\lambda - I_{\lambda s}) \, d\lambda \qquad (6)$$

Si l'on désire obtenir cette correction sur la température radiative à partir

des mesures effectuées, il faudrait en toute rigueur mesurer $(I_\lambda - I_{\lambda s})$, ce qui suppose une mesure spectrale, puis effectuer le calcul de l'intégrale figurant dans 6 . En fait, la seule donnée qui soit accessible assez facilement aux mesures est la différence ΔW entre les énergies respectivement émises par la mer et le ciel, c'est à dire :

$$\Delta W = W_w - W_s = \int_0^\infty I_\lambda \tau_\lambda \, d\lambda - \int_0^\infty I_{\lambda s} \tau_\lambda \, d\lambda \qquad (7)$$

Remarquons qu'en écrivant cette formule, nous assimilerons la mer à un corps noir. Cette approximation est justifiée pour le calcul du terme correctif ΔW. Dans la formule 7 , τ_λ est la même fonction filtre que précédemment si le même radiomètre sert à mesurer à la fois l'énergie en provenance du ciel et celle émise par la mer.
Dans nos expériences, nous avons utilisé pour mesurer ΔW, la thermopile décrite en annexe et le filtre dont elle était munie durant cette campagne avait une transmission identique au filtre équipant le radiomètre principal; ce n'était pas le cas lors de la campagne de Novembre 1968, ce qui modifie un peu le dépouillement des résultats.

Nous allons définir un coefficient moyen ε tel que

$$\int_0^\infty (1-\varepsilon_\lambda) \tau_\lambda (I_\lambda - I_{\lambda s}) \, d\lambda = (1-\varepsilon) \int_0^\infty (I_\lambda - I_{\lambda s}) \tau_\lambda \, d\lambda = (1-\varepsilon) \Delta W \qquad (3)$$

Il est évident que cet ε dépendra des répartitions spectrales de I_λ qui se modifient très légèrement avec T, et surtout de $I_{\lambda s}$ très variable selon l'état du ciel. L'introduction de ε ne présentera évidemment d'intérêt que si ces variations sont assez faibles, ce que nous verrons plus loin.

b/ Dépouillement des mesures

Comme nous l'indiquons en annexe, la thermopile visant le ciel est étalonnée en visant un bac d'eau dont la surface a une émissivité supérieure à 0,97 entre 8 et 14 μ. L'erreur introduite en l'assimilant à un corps noir est inférieure à la précision des mesures.

Pour une déviation de 1 division, nous avons une variation de K° C de la température du bac au voisinage de la température T de la mer. La déviation d'une division correspond donc à une variation de l'énergie reçue par la thermopile de $\frac{4p\,\sigma T^3}{\pi}$.K. Lorsque l'on vise alternativement la mer et le ciel une déviation de n divisions correspond à une variation d'énergie

$$\Delta W = \frac{4p\,\sigma\,T^3}{\pi}\, nk \qquad (9)$$

De 6 , 8 et 9 nous obtenons

$$\Delta T = \frac{\pi}{p4\,\sigma T^3} (1-\varepsilon)\,\Delta W = (1-\varepsilon)\, nk \qquad (10)$$

En portant sur un graphique ΔT en fonction de n ou de ΔW on doit donc trouver des droites dont la pente va donner le coefficient

$$(1-\varepsilon) = \frac{\Delta T}{nk} \qquad (11)$$

Sur la figure 3 , on a porté ΔT en fonction de ΔW exprimé en micro watts cm^{-2}. sr^{-1}, pour l'ensemble des mesures du 20 au 23 Février 1969 en séparant les résultats en 4 cas

- mer agitée : vent > 22 noeuds
- mer peu agitée : vent 10 à 12 noeuds
- mer peu agitée : vent < 5 noeuds
- calme plat.

Le cas du calme plat comprend trop peu de mesures pour conclure. Mais dans les 3 autres cas, les points s'alignent remarquablement sur des droites comme le prévoit la relation 10 .
De la pente de ces droites on déduit
- mer peu agitée, vent < 5 noeuds $1 - \varepsilon = 0,0192$
- mer peu agitée, vent 10 à 12 noeuds $1 - \varepsilon = 0,0167$
- mer agitée, vent > 22 noeuds $1 - \varepsilon = 0,0147$

Par calme plat, le petit nombre de mesures obtenues semblerait donner $1 - \varepsilon$ de l'ordre de 0,021. Ce coefficient varie notablement en fonction de l'état de la mer. En outre, il semble se confirmer qu'au voisinage de l'incidence normale, l'émissivité de l'eau s'accroît lorsqu'elle est agitée par suite des réflexions multiples à la surface de l'eau, Ref. 5 .

c/ Calcul théorique du ΔT dû à la réflexion

Le coefficient $(1-\varepsilon)$ peut être calculé théoriquement à partir de formule 8 si on se fixe la température de la mer et le rayonnement I_{λ_6} du ciel.
C'est ce que nous avons fait ici pour une mer à 285° K, ce qui correspond à peu près aux conditions de nos mesures, et pour divers modèles de ciel que nous discutons en annexe.

Nous avons pris le cas d'une réflexion parfaitement spéculaire sur une surface plane; ce cas est évidemment extrêmement fictif, mais constitue une première approximation. Le coefficient de réflexion monochromatique nous a été communiqué par L. PONTIER, Ref. 6 .

Nous avons obtenu les résultats suivants :
- Ciel clair T ambiante = 270° K, $1 - \varepsilon = 0,0135$
  " = 285° K, $1 - \varepsilon = 0,0121$
  " = 300° K, $1 - \varepsilon = 0,0108$
- Ciel couvert T ambiante = 270° K, $1 - \varepsilon = 0,0127$
  " = 285° K, $1 - \varepsilon = 0,011$
  " = 300° K, $1 - \varepsilon = 0,003$

On constate que, sauf dans le cas d'un ciel couvert avec une température ambiante très élevée, que nous n'avons pas rencontré au cours de cette campagne de mesure, le coefficient $1 - \varepsilon$ varie peu avec le type du ciel et a une valeur de l'ordre de 0,012.

On retrouve donc bien théoriquement une relation linéaire entre ΔT et ΔW, mais avec une valeur de $1 - \varepsilon$ inférieure à celle déduite des mesures. Cette courbe théorique a été tracée sur la figure 3 elle donne en fonction de ΔW, la correction ΔT à apporter aux mesures. Pour un ΔW et un état de mer donnés, la différence d'ordonnées entre cette courbe et la courbe expérimentale, représente le ΔT réel qui existe entre la température de surface et la température interne; on voit qu'il est pratiquement toujours inférieur à 0,25°.

Les résultats du calcul peuvent être présentés sous une autre forme : sur la figure 4 on a porté le ΔT dû à la réflexion calculé par les formules 8 et 10 en fonction de la température de la mer et pour les divers modèles de ciel considérés.

6/ DISCUSSION DES RESULTATS

Le coefficient $1 - \varepsilon$ calculé pour une surface plane est de l'ordre de 0,012 alors que le coefficient mesuré varie entre 0,021 pour une mer calme à 0,0147 pour une mer agitée. Comment interpréter cette différence?

Pour le radiomètre, les principales causes d'erreur ont été discutées en détail

par P.Y. DESCHAMPS, Ref. 3 . Ajoutons tout de même que les mesures en mer sont moins aisées à effectuer et que de nouvelles causes d'erreurs s'ajoutent aux erreurs instrumentales proprement dites. L'étalonnage n'avait pas pu être effectué avec le corps noir utilisé d'habitude, mais au moyen d'un bac d'eau convenablement agité. Ceci peut introduire une erreur de quelques centièmes de degrés, mais cette erreur n'affecte pas la pente des droites tracées à la figure 3 .

La thermopile du ciel avait été étalonnée au début de la campagne mais avait pris accidentellement l'humidité au cours d'une averse. Il est possible que sa sensibilité en ait été légèrement modifiée. Un étalonnage fait après le retour de la mission indique une baisse de sensibilité de l'ordre de 5/100 ce qui est encore acceptable.

Pour les calculs, ils ont effectués à partir d'un coefficient de réflexion donné par PONTIER, Ref. 6 . Ce coefficient est déterminé avec une précision de l'ordre de 5/100, ce qui entraine une erreur sur la détermination de ε, de l'ordre de 7/100.
Les coefficients de transmission des filtres des deux appareils ont été mesurés à l'aide d'un spectro PERKIN-ELMER modèle 457, au retour de la mission de Février. La précision de cet appareil est de 2 à 3/100 et nous avons trouvé des courbes absolument identiques.
Les calculs sont effectués à partir d'un modèle de ciel dont on a discuté en annexe l'établissement. On peut évidemment étudier en détail l'influence de la forme choisie sur le ε calculé.

7/ CONCLUSION

On a retrouvé au cours de cette campagne une température apparente de surface inférieure à la température interne, mais il semble que la différence s'explique pour une grande part par l'effet de rayonnement du ciel réfléchi.

Si on effectue la correction avec un coefficient de réflexion de 0,012 qui correspond théoriquement à une surface plane d'eau pure, on trouve qu'il reste une différence de température entre la masse et la surface qui est au maximum de 0,30° C par temps clair et de 0,005° C à 0,20° C par temps couvert.

Pour expliquer totalement la température plus froide de surface par la réflexion du rayonnement du ciel, il faudrait admettre un coefficient de réflexion variant de 0,020 par calme plat à 0,014 par mer fortement agitée.

Il reste donc pour conclure définitivement à reprendre l'étude du coefficient de réflexion pour la mer et aussi à effectuer plusieurs séries de mesures sur différentes périodes de l'année.

Actuellement nous pouvons seulement affirmer que s'il existe une couche froide de surface, l'écart de température avec la masse est au maximum de 0,3° C par ciel clair et froid et inférieur en général.

ANNEXE 1

Etablissement d'un modèle de ciel

Il serait intéressant de connaître, en même temps que la température mesurée au radiomètre, le spectre d'émission du ciel. Ceci n'est pas encore possible et nous devons nous contenter d'une mesure globale du rayonnement du ciel dans la bande de transmission du filtre utilisé dans le radiomètre.

Pour calculer le coefficient ε défini par la formule

$$\int_o^\infty (1-\varepsilon_\lambda)\ (I_\lambda - I_{\lambda s})\ \tau_\lambda\ d\lambda = (1-\varepsilon) \int_o^\infty (I_\lambda - I_{\lambda s})\ \tau_\lambda\ d\lambda \qquad (1)$$

nous avons dû nous fixer un peu arbitrairement des modèles de ciel définissant $I_{\lambda s}$ et nous les avons ajustés pour que

$$\int_o^\infty (I_\lambda - I_{\lambda s})\ \tau_\lambda\ d\lambda = \Delta W \qquad (2)$$

ΔW étant mesuré au moyen de la thermopile du ciel.

Rappels sur le rayonnement du ciel

Les principales études relatives à l'émission du rayonnement du ciel entre 8 μ et 20 μ ont été effectuées par SLOAN et COLL (7), OETJEN et COLL (8), BRUSTET et COLL (9).

Tenant compte qualitativement de ces études nous avons bâti des modèles très grossiers, l'un pour ciel clair, l'autre pour ciel couvert, où le seul paramètre est la température au sol.

Pour un ciel clair, et une température T_a au sol, on a pris pour $\lambda < 7{,}5\ \mu$, $I_{\lambda s} = I_\lambda$, I_λ étant la luminance du corps noir à la température T_a. Cette zone correspond à la très forte absorption de la bande 6,3 μ de H_2O.
Pour $7{,}5\ \mu < \lambda < 9\ \mu$, $I_{\lambda s} = \frac{I\ MAX}{6}$; I_{MAX} est la luminance maximale du corps noir à la température T_a. Ceci correspond au début de la fenêtre atmosphérique. Pour $9\ \mu < \lambda < 10\ \mu$, $I_{\lambda s} = \frac{IMAX}{3}$: quoi qu'étant dans la fenêtre atmosphérique, il faut tenir compte de l'absorption par l'ozone. Pour $10\ \mu < \lambda < 12\ \mu$, $I_{\lambda s} = \frac{I\ MAX}{6}$: zone de fenêtre atmosphérique.
Pour $12\ \mu < \lambda < 13{,}6\ \mu$, $I_{\lambda s} = \frac{I\ MAX}{3}$: fenêtre atmosphérique avec quelques raies de rotation de la vapeur d'eau et le début de la bande d'absorption de CO_2 à 15 μ et enfin pour $\lambda > 13{,}6$, $I_{\lambda s} = I_\lambda$: forte absorption atmosphérique due à la bande de rotation de la vapeur d'eau et à la bande 15 μ du CO_2.

Pour un ciel couvert, le rayonnement dans la fenêtre atmosphérique provient essentiellement du nuage et non plus des hautes couches froides. Pour λ de 8 à 9 μ et de 10 à 12 μ, nous avons pris $I_{\lambda s} = \frac{11\ MAX}{12}$. Pour λ de 9 à 10 μ et 12 à 12,8 μ, nous avons pris $I_{\lambda s} = \frac{2\ MAX}{3}$. En dehors de ces valeurs, $I_{\lambda s} = I_\lambda$

Cette répartition spectrale est évidemment arbitraire mais doit s'approcher assez bien de la répartition réelle avec une légère surestimation de l'influence de la température dans la fenêtre atmosphérique et avec une sous-estimation de l'influence de la contenance en vapeur d'eau, donc de la température pour zone de moyenne absorption de la vapeur d'eau.
La figure 7 , montre, pour diverses températures ambiantes, $I_{\lambda s}$ en fonction de λ pour les modèles choisis.

Il est alors possible de tabuler, pour diverses températures ambiantes, pour ciel

clair ou couvert et pour diverses températures de mer, au moyen de la formule 2 , la différence ΔW entre les énergies respectivement émises par la mer et le ciel. Ceci est montré à la figure 8 .
La comparaison avec les quelques points expérimentaux dont nous disposons semble indiquer un assez bon accord avec les calculs, ce qui justifie en partie le choix des modèles. Ce choix est d'autre part justifié par le fait que ε ne varie que lentement avec le ciel et qu'un modèle très approximatif est suffisant pour le calculer.

ANNEXE 2

Thermopile du ciel

Cette thermopile est fabriquée par "KIPP". Elle est constituée de 10 couples manganine - Constantan. Un filtre ayant exactement la même bande passante que le filtre placé dans le radiomètre a été utilisé au cours de la campagne de Février 1969. La figure 5 montre la transmission du filtre fonction de la longueur d'onde. La thermopile a un champ de 20°, un peu plus important que le champ du radiomètre principal (14°). Cette valeur est la plus faible possible compatible avec les exigences de sensibilité de l'appareil. L'ensemble a une constante de temps de plusieurs secondes, du même ordre que le radiomètre. Le signal (en volt) fourni par cette thermopile sous une impédance de 20 Ω est enregistré sur la seconde voie de l'enregistreur utilisé par le radiomètre.

Etalonnage de la thermopile

Lorsque la thermopile du ciel, portée à une température fixe T_a, vise la surface d'un bac d'eau porté à la température de la glace fondante, elle reçoit une énergie

$$W_{273} = \int_0^\infty \varepsilon_\lambda \cdot I_{o\lambda} \tau_\lambda \, d\lambda \qquad (1)$$

Dans cette formule, ε_λ est l'émissivité de la glace fondante, $I_{o\lambda}$ est la luminance monochromatique du corps noir à cette même température, τ_λ est la transmission du filtre à la longueur d'onde . Cette énergie reçue est transformée en chaleur et provoque l'apparition d'un signal

$$S_o = k W_o + C \qquad (2)$$

Si on fait varier la température du bac d'eau, la thermopile reçoit une énergie

$$W_T = \int_0^\infty \varepsilon_\lambda \; I_\lambda \; \tau_\lambda \, d\lambda \qquad (3)$$

I_λ étant la luminance du corps noir à la température de la masse d'eau. Cette énergie provoque un signal

$$S_T = k W_T + C \qquad (4)$$

La valeur de $W_T - W_o$ peut être tabulée en fonction de T; la courbe obtenue est portée sur la figure 6 .
En combinant 2 et 4 , on peut écrire

$$W_T - W_o = \frac{1}{k} (S_T - S_o) \qquad (5)$$

Par cette formule, mesurant S_T et S_o, calculant W_T et W_o on en déduit k exprimé en Volt . W^{-1} cm^2 .sr.

Au cours d'un premier étalonnage, on a fait varier T entre 273° K et 303° K, et on a vérifié la constance de K dans la formule 5 ; les points expérimentaux représentant $(W_T - W_O)$ obtenus à partir de 5 et des mesures, ont été portés sur la figure 6 .

Nous avons choisi de travailler toujours avec des différences d'énergie $(W_T - W_O)$ plutôt qu'avec des valeurs absolues (W_T), car d'assez faibles variations de la température ambiante T_a, déplacent la droite $S_T = k\, W_T + C$, alors que sa pente k reste constante. L'étalonnage doit néanmoins être renouvelé fréquemment.

Mesures

La mesure est effectuée suivant le même principe que l'étalonnage : la thermopile vise le ciel puis une référence. Cette référence, nous avons tout naturellement songé à utiliser la surface de la mer. Dans ce cas, la thermopile reçoit une différence d'énergie $\Delta W = \int_0^\infty (I_\lambda - I_{\lambda s}) \tau_\lambda \, d\lambda$ et donne une variation de signal $\Delta S = k.\Delta W$. Dans cette formule I_λ est la luminance d'un corps noir à la température de l'eau et $I_{\lambda s}$ est la luminance du ciel. En écrivant cette formule, nous faisons l'approximation de considérer la surface de l'eau comme un corps noir. Ceci introduit une erreur de 2/100, inférieure à la précision des mesures.

REFERENCES

1 DESCHAMPS P.Y., LECOMTE P. - Résultats de 2 séries de mesures de température superficielle de la mer au moyen d'un radiomètre - Cahiers Océanographiques (sous presse)

2 COX C., MUNK W. - Measurement of the Roughness of the sea surface for photographs of the sun's glitter - Jl. Optique Society America - Vol. 44 n° 11 p.338

3 DESCHAMPS P.Y. - Etude et réalisation d'un radiomètre infrarouge - Thèse n° d'ordre 114 Lille 1968

4 GONELLA J., MARTIN J. - Centrale de mesures océanographiques - Vol. 18 5 Mai 1966 - Cahiers océanographiques

5 SAUNDERS P.H. - Radiance of sea and sky in the infrared window 800 - 1200 cm^{-1} - Jl. Optique Society America - Vol. 58 n° 5 p.645

6 PONTIER L., DECHAMBENOY C. - Annales de Géophysiques - Vol. 21 p.462 1965

7 SLOAN R., SHAW J.H., WILLIAM D. - Infrared emission spectrum of the atmosphere - Jl. Optique Society America - Vol. 45 n° 6 p.455

8 OETJEN R.A., BELL E.E., YOUNG J., EISNER L. - Spectral radiance of sky and Terrain at Wavelengths between I and 20μ - Jl. Optique Society America - Vol. 50 n° 12 p.1368

9 BRUSTET J.M., CASAMAYOR P., DE LANOUE P., SAPORTE R. - Présentation de quelques travaux de l'équipe de radiométrie (Communication personnelle).

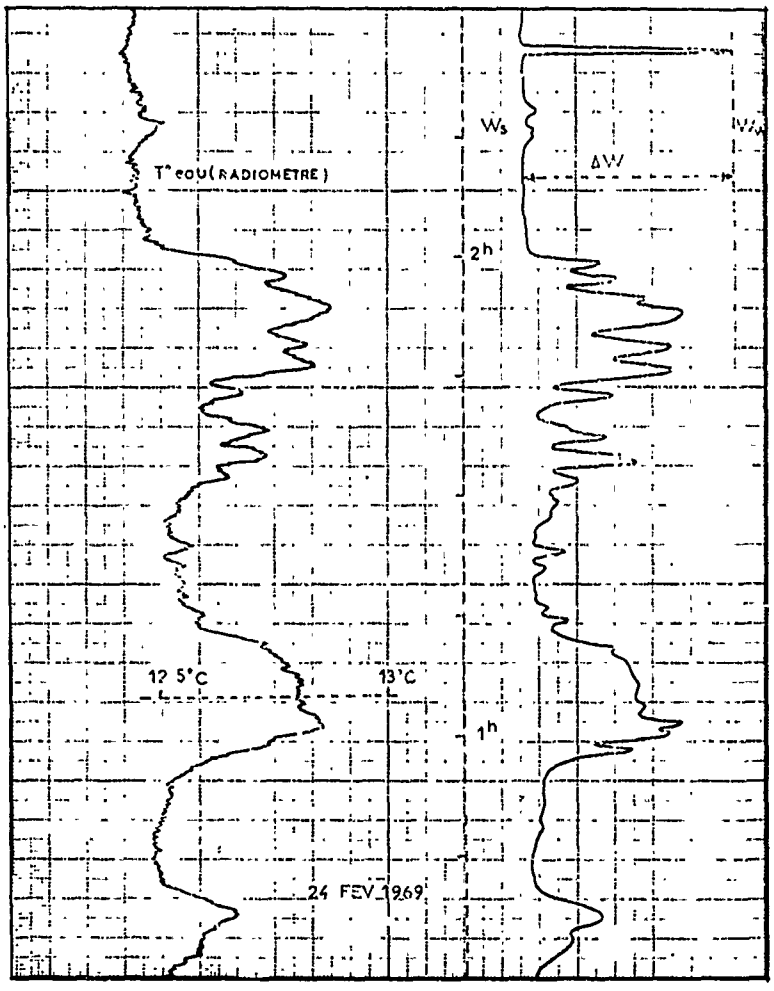

Fig.1 Enregistrements simultanés de la température apparente de l'eau et de ΔW fonction du temps

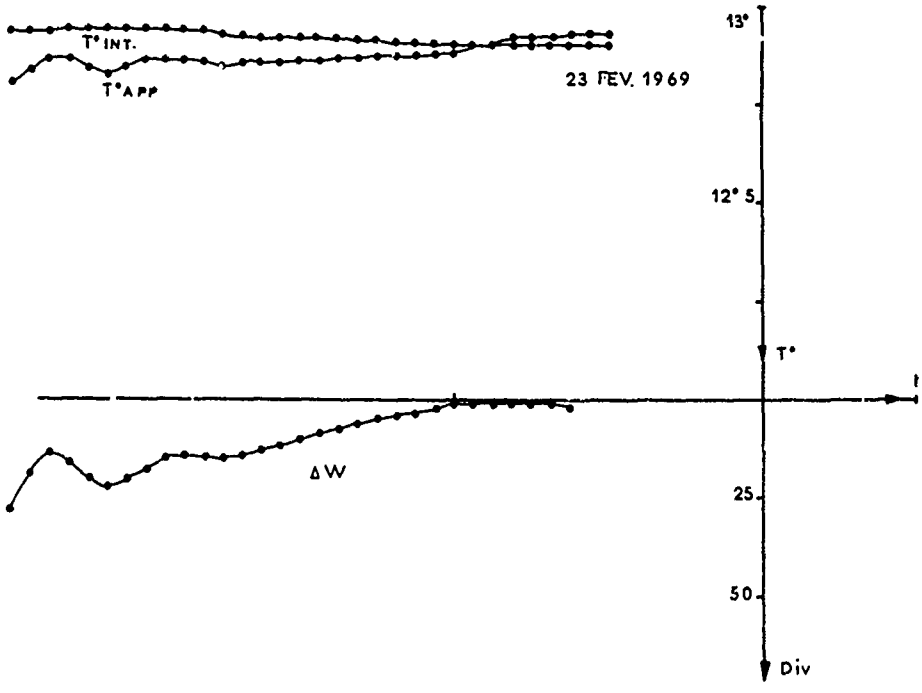

Fig.2 Température apparente, température interne et ΔW fonction du temps.

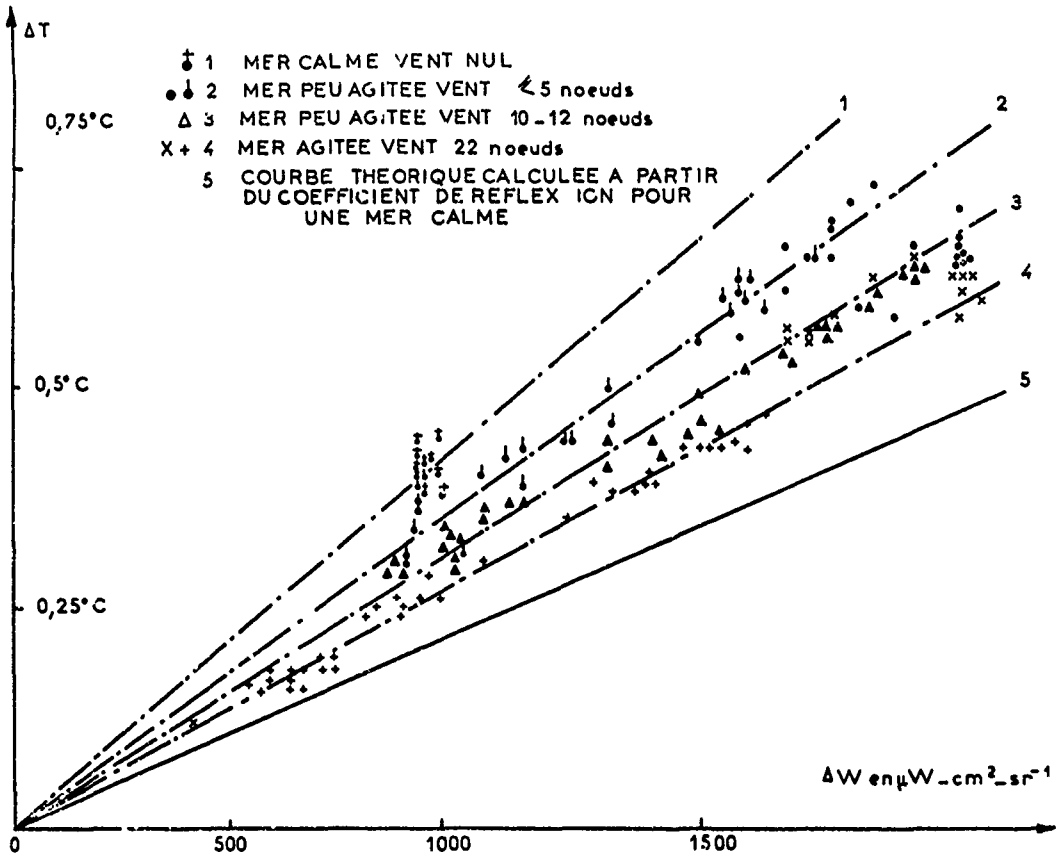

Fig.3 ΔT fonction de ΔW pour différentes vitesses de vent

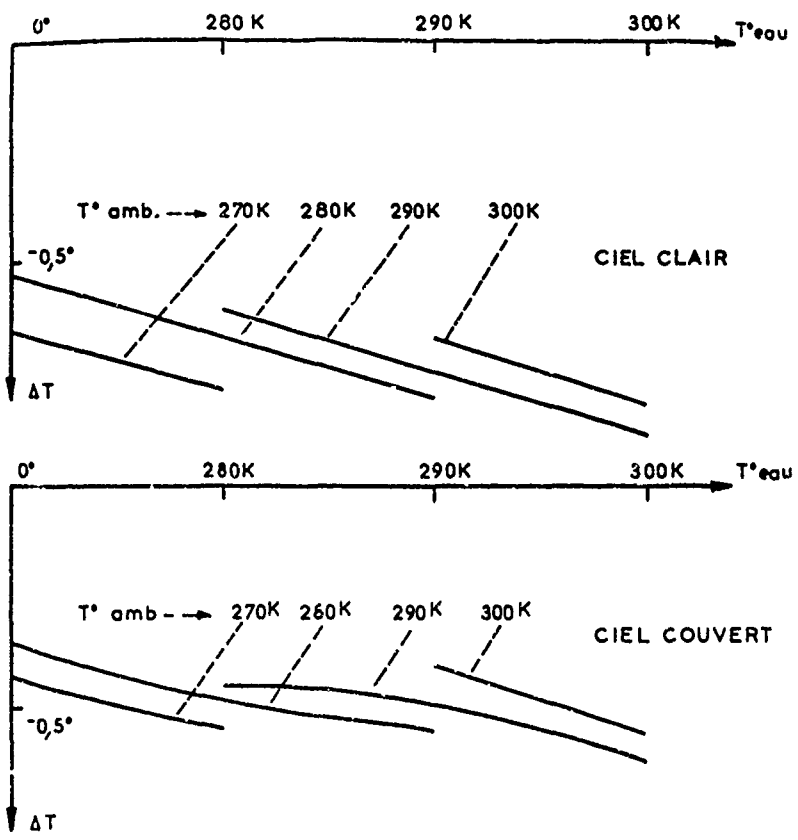

Fig.4 ΔT apparent fonction de la température de l'eau pour différentes températures ambiantes

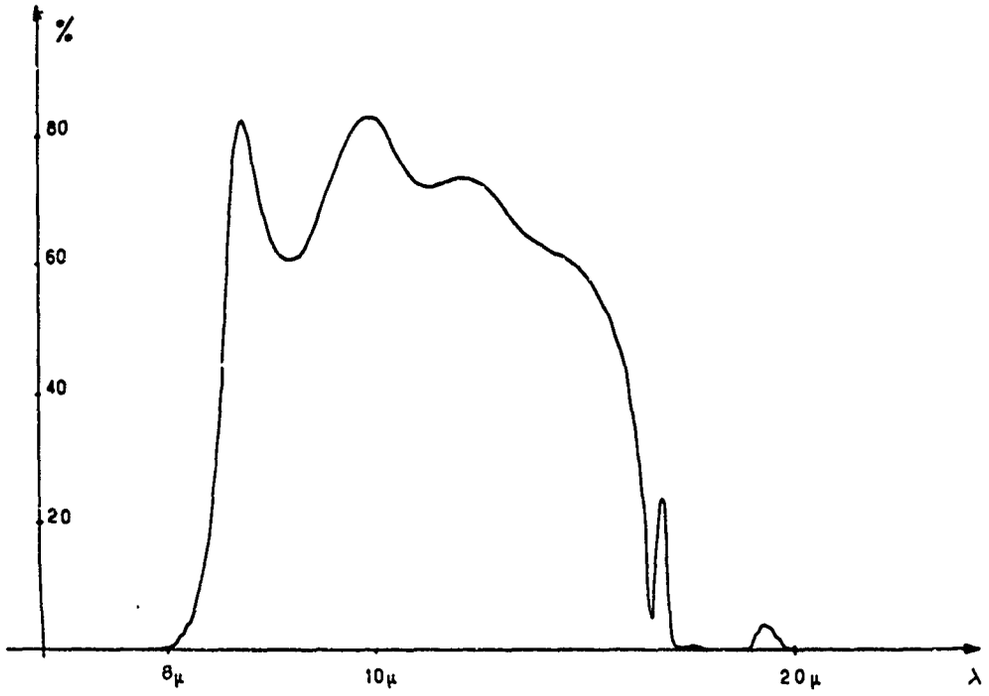

Fig.5 Transmission du filtre fonction de la longueur d'onde

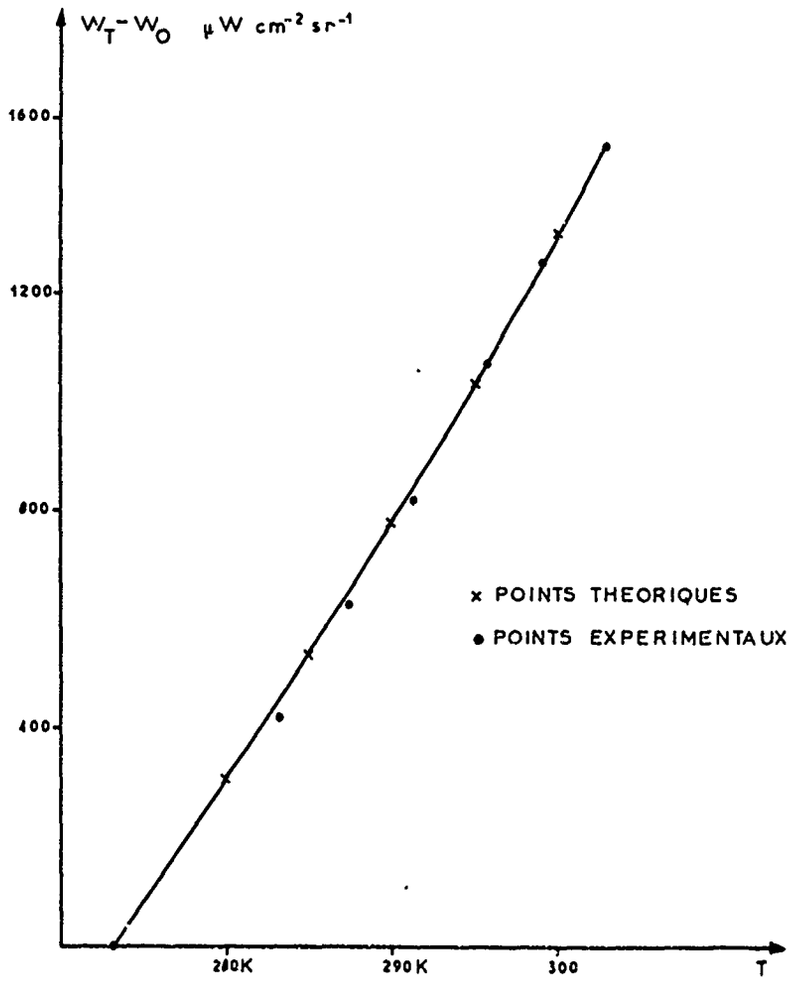

Fig.6 Etalonnage de la themopile du ciel

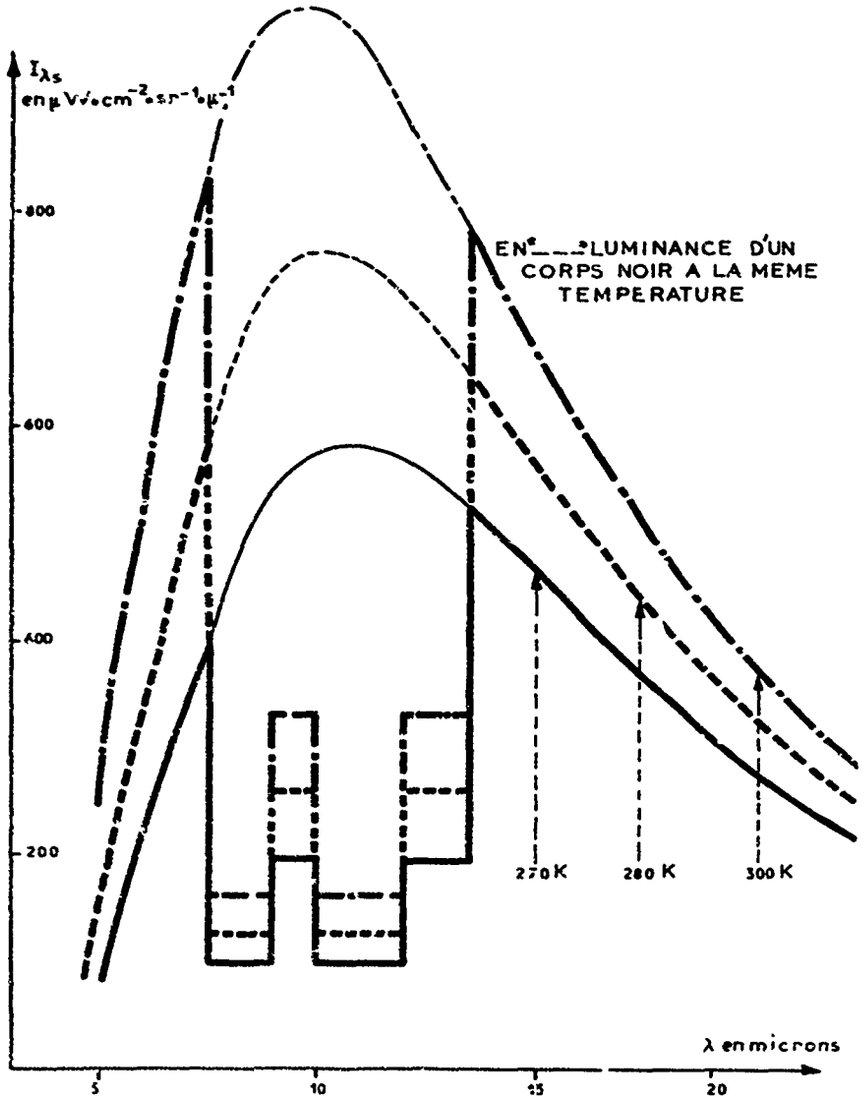

Fig.7 Luminance d'un ciel clair pour différentes températures ambiantes

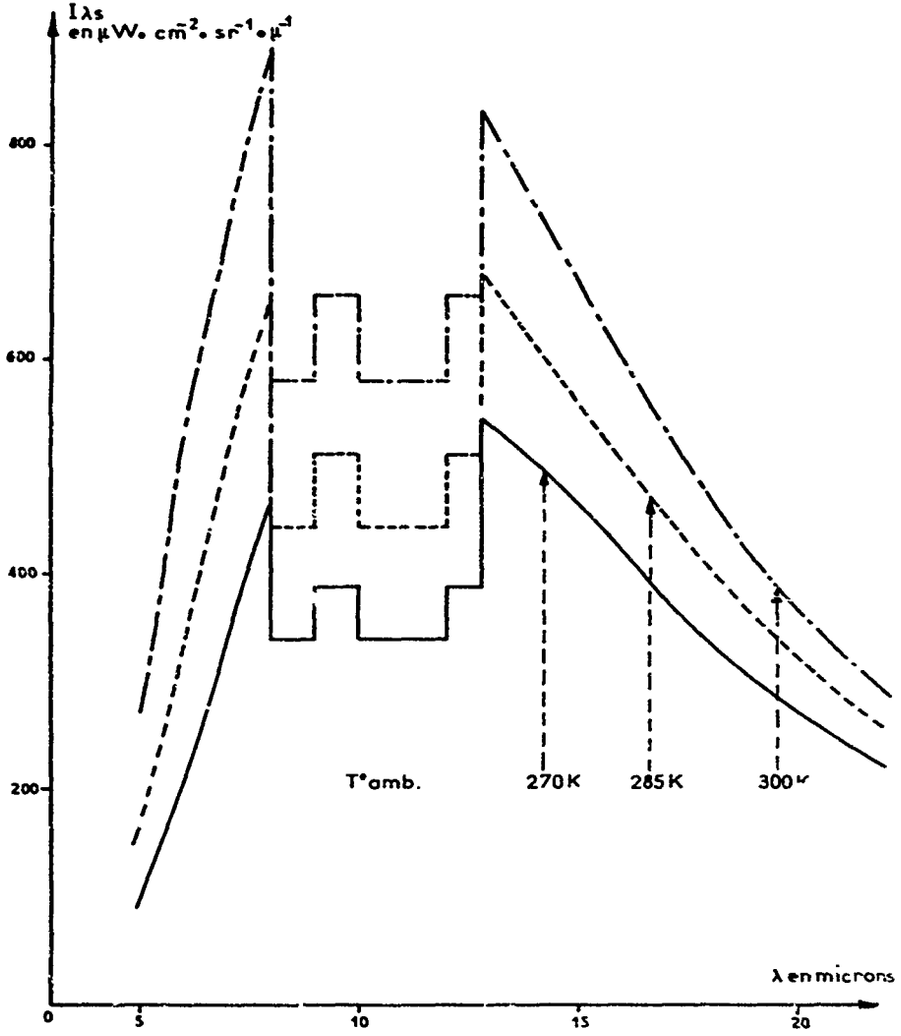

Fig.7 bis Luminance d'un ciel couvert pour différentes températures ambiantes

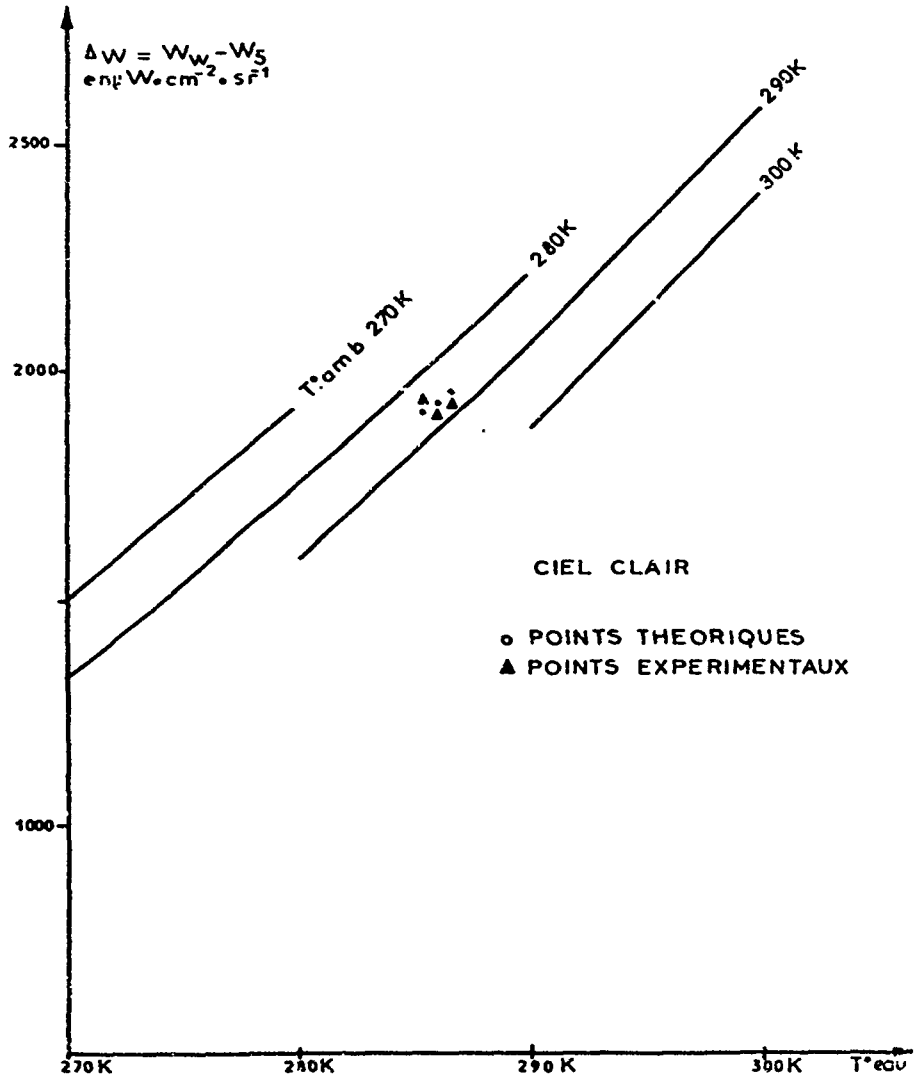

Fig.8 Différence d'énergie reçue sur la thermopile du ciel lorsque celle-ci vise successivement un ciel clair puis l'eau

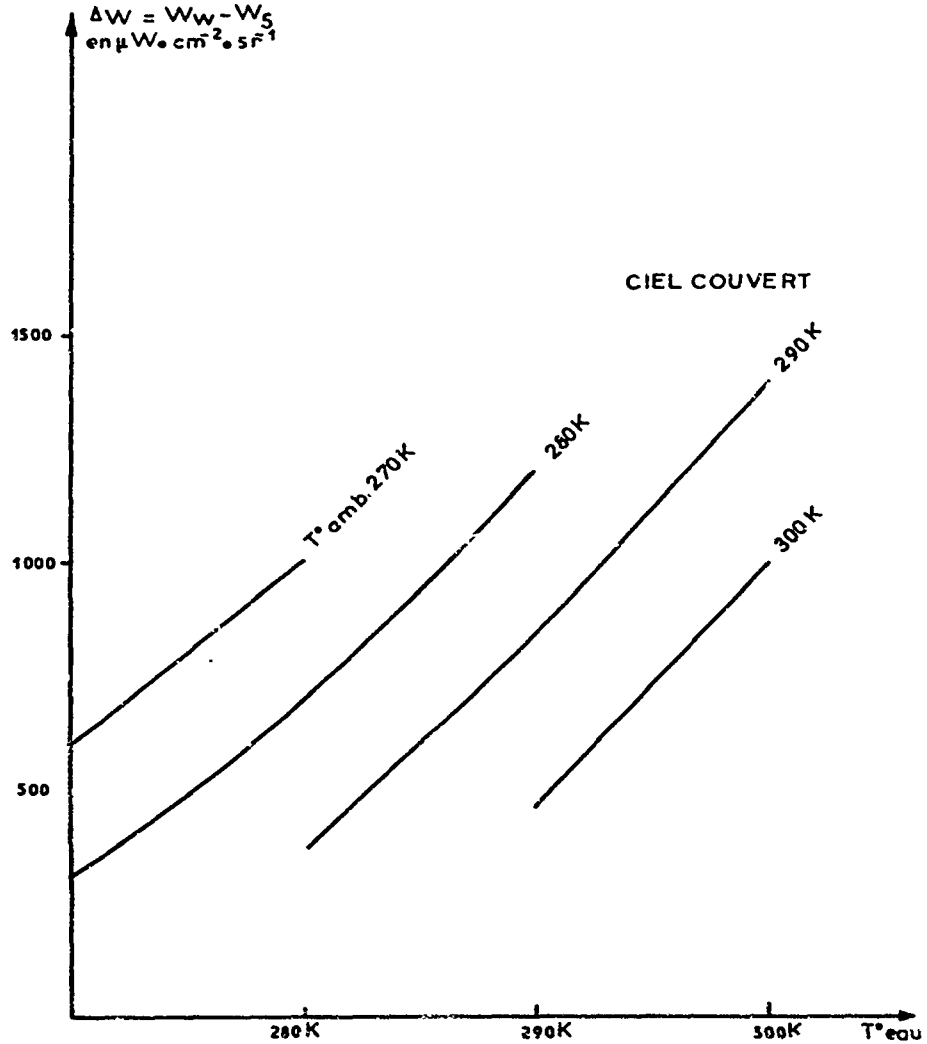

Fig.8 bis Différence d'énergie reçue sur la thermopile du ciel lorsque celle-ci vise successivement un ciel couvert puis l'eau

DISCUSSION ON PAPERS PRESENTED IN SESSION VI
(Experimental Results)

Discussion on paper 27 : "Measurements of the spatial coherence of a laser beam propagating through water", by S.G. VERNADO and A.H. LAGRONE .

Dr. A. WIRGIN : Could you give some more details on the physical processes assumed in your Monte-Carlo technique ? Do you assume small sphere inhomogeneities and geometrical optics interaction with the spheres ?

Dr. A.H. LAGRONE : The Monte-Carlo technique assumes total scattering of a photon in a direction determined by a scattering probability function .
The answer to the second question is "no" for both parts .

Dr. K. PIECH : 1) What was the diameter of the beam at the pinholes, where the complex degree of coherence was measured ?

2) Were any measurements of degree of coherence made at any points outside the beam ?

Dr. A.H. LAGRONE : 2 mm (pinholes were 400μ in diameter)

2) No .

Discussion on paper 30 : "Examen de résultats expérimentaux concernant la diffusion de la lumière par les eaux de mer" par A. MOREL .

Dr. G. KULLENBERG : (from the magnetic tape) I would like to ask you if you don't think there is differences in nature particles, relative refractive index of particles as regard to clear oceanic areas where you have not very much particle material and areas of higher production, where you have a high mass . Don't you think that is difference in the scattering functions and in the backward-scattering ?

Prof. A. MOREL : La plupart des résultats qui ont été présentés ici correspondent, en général, à des mesures effectuées dans des eaux du large, à l'exception de quelques mesures de Manche . Nous avons par ailleurs observé effectivement des différences notables sur des eaux fortement chargées en apports terrigènes ou spéciaux . Nous avons trouvé des différences dans les eaux à la sortie d'un fleuve ou dans les Bahamas sounds . Par contre, en Manche à condition de ne pas prendre de prélèvements à la plage, mais un peu au large, curieusement, nous trouvons que l'indicatrice est quand même très semblable à celle que nous trouvons dans les océans ouverts . Nous sommes nous mêmes très surpris de ce résultat . Il semble que le séjour des particules dans l'eau ait tendance à uniformiser l'ensemble de la population des particules en suspension, qui ont finalement à peu près la même distribution de taille et finalement à peu près les mêmes indices .Quand nous parlons d'indicatrice moyenne, pour une longueur d'onde donnée, ou quand nous parlons d'une invariance de forme lorsque la longueur d'onde varie, nous n'exposons que des lois de première approximation .

Dr. A. WIRGIN : Est-ce que vous avez étudié la polarisation de la diffusion ?

Prof. A. MOREL : (extrait du ruban magnétique) Je n'ai pas présenté d'indicatrice en lumière polarisée, mais des mesures ont été faites entre 30° et 150° des deux composantes verticale et horizontale de la lumière diffusée . Le résultat est le suivant : Le delta "polarization effect" est minimal au voisinage de 90° ou 100° . Il est de l'ordre de 15% en ce qui concerne les particules . Le rapport varie suivant l'importance de la diffusion moléculaire dans l'échantillon .

Cette dépolarisation croît fortement vers 30° où la lumière est complètement dépolarisée . Le delta est égal à environ 80% .

La courbe de delta en fonction de l'angle est relativement symétrique par rapport à 100° .

Discussion on paper 32 :"Observations of light scattering in different water masses", by G. KULLENBERG .

Prof. A. IVANOFF : Some years ago our knowledge on the volume scattering function was very poor indeed, but increase tremendously during the last years . Your results show that the particles scattering function may vary from one water to another one and varies greatly especially in the Baltic . We have found more or less the same volume scattering function in older water .

Dr. G. KULLENBERG : If I compare two extremely areas the Sargass sea and the Baltic, the difference is not so much on the shape of the scattering function but probably on the intensity '.

Prof . A. MOREL : On constate que la courbe N° 5 qui concerne l'indicatrice des particules pour la mer des Sargasses est très nettement différente des autres (N° 1, 2, 3 et 4), en particulier pour la partie arrière '.
Est-ce-que vous ne pensez pas que ayant retranché la diffusion moléculaire à une valeur observée petite la différence apparente entre les courbes est simplement dûe à l'erreur expérimentale '.

Dr. G. KULLENBERG : I don't think its only experimental . I think because these very different water masses you are due to expect different intensities in light scattering . Of course there is a danger in subjecting the relative scattering in this case '. I definitly think that the different particle distributions and different major particles you have in Sargass Sea and in the Baltic will affect the scattering intensity and in some way the form of the function '.

Discussion on paper 33 : "Mesure de la température de surface de l'océan au moyen d'un radiomètre infrarouge", par P.Y Deschamps, P. Lecomte, et J.C. Vanhoutte .

Dr. S. DONATI : What is the reason for the choice of the 8 - 14 μ window for the temperature measurement, and not of, for ex., the 2 - 5 μ region where the most thermographic equipement operate ?

Dr. P. LECOMTE : (extrait du ruban magnétique) En fait, nous avons choisi la fenêtre atmosphérique parce que nous avons voulu rester dans une zone dans laquelle il y a beaucoup d'énergie . On aurait pu travailler à une longueur d'onde plus faible ; mais alors il aurait fallu developper une technique de détection pour laquelle nous n'étions pas encore équipés . Pour nous c'était une question de technologie .

Dr. J. ALBRECHT : Referring to the general field dealt with in this paper, some more information may perhaps be obtained from "radiation balance" investigations conducted by atmospheric research workers for the last four decades . This results in two questions .

1) Refering to the recordings showing sky temperature and sea surface temperature, has any analysis beendone on correlation characteristics related to the fine structure and cloud density effects ?

2) The response time of the equipment should certainly limit the usefulness of results obtained with agitated sea '.

Dr. P. LECOMTE : (extrait du ruban magnétique)
1) Les résultats présentés sont relativement anciens . Après avoir eu pas mal d'ennuis techniques dûs aux tempêtes, nous avons arrêté la série des mesures . Cependant nous avons recueilli une masse de 6000 à 7000 mesures qui sont transcrites sur bande perforée, en vue de leur analyse statistique complète . Malheureusement les paramètres dont nous disposions sont : le rayonnement du ciel, la température apparente de surface, la température réelle de surface, l'humidité et la température de l'atmosphère .
Pour les résultats que nous avons dépouillés de façon vraiment systématique à l'aide d'un ordinateur, la seule corrélation que l'on ait trouvée concerne le ΔT et le ΔW . Cette corrélation est relativement bonne . Elle est indépendante de la différence entre la température de la mer et la température de l'air . Elle est également indépendante de l'humidité ambiante . Elle ne dépend que de l'état de la mer .

2) Votre seconde observation est valable dans le cas des phénomènes qui varient très rapidement . Les phénomènes en cause ne sont pas excessivement rapides . Nous avions une constante de temps de l'ordre de 10 secondes .

LOSS OF OPTICAL RESOLUTION IN SEA WATER BY MULTIPLE SMALL-ANGLE SCATTERING

by

Willard H. Wells
Marion N. Todd

Tetra Tech. Inc., North Rosemead Blvd. 630
Pasadena, California 91107

Loss of Optical Resolution in Sea Water by Multiple Small-Angle Scattering

Willard H. Wells
Marion N. Todd
Tetra Tech, Inc., 630 North Rosemead Blvd., Pasadena, California 91107

Abstract

Multiple scattering of light by particles suspended in liquid can be a cause of degraded optical resolution. This is especially significant when the particles are relatively large and numerous, but most of the scattered power is deflected through very small angles owing to a near match between the refractive indices of the particles and the medium. Formulas which convert the volume scattering function to an image modulation transfer function have been derived and interpreted for this case. This conversion allows one to calculate image degradation given the scattering properties of the medium. The conversion from scattering function to optical transfer function is evaluated for one published scattering function measured in sea water. Graphs of image degradation and beam decollimation are given.

The inverse transform is also derived so that one can calculate the scattering properties given the loss of resolution. The latter is best measured by imaging a set of paralled bar patterns having a wide range of spatial frequencies. We have built and tested a scattering meter based on this inverse transform. Preliminary results are presented.

SOMMAIRE

La diffusion multiple de la lumière par des particules en suspension dans un liquide peut être à la base d'un amoindrissement du pouvoir séparateur, en particulier dans le cas où les particules sont relativement importantes et nombreuses. Cependant, la plus grande partie de la puissance diffusée est déviée suivant de très faibles angles, car les indices de réfraction des particules et du milieu sont très proches. On établit, pour ce cas, des formules de conversion de la fonction de diffusion du volume en fonction de transfert de modulation de l'image.

Cette conversion permet de calculer les propriétés diffusantes si l'on connaît la perte de pouvoir séparateur. La meilleure façon de mesurer ce dernier consiste à tracer un groupe de dessins représentant des barres parallèles possédant une gamme étendue de fréquences spatiales.

La conversion de la fonction de diffusion en fonction de transfert optique est interprétée en général et évaluée pour une fonction de diffusion mesurée dans l'eau de mer et ayant fait l'objet d'une publication.

Les résultats numériques sont comparés aux mesures d'images publiées, et on fournit des graphiques qui sont relatifs à l'étalement du faisceau ou à la décollimation. Ils sont présentés en fonction de la distance sur le faisceau.

When particles having dimensions larger than optical wavelengths are suspended in a liquid that almost matches the refractive index of the particles, then the distribution of scattered light peaks very strongly in the forward direction. In these cases some of the rays which scatter in passage between an object and its image are still useful in image formation, although with degraded resolution. The example of interest here is scattering by transparent organisms in natural waters, in which case the refractive indices nearly match, because the organisms consist mainly of water and organic matter of similar density.

The multiple scattering theory of this case is treated in Reference (1). This theory does not derive the angular distribution of scattered light for a class of particles, but rather regards the distribution as a given (measured or derived) function and applies multiple scattering theory in a form that yields an optical transfer function for images. The inverse transform is also given. The latter provides a means of measuring basic scattering processes indirectly by measuring the loss of resolution in images of bar patterns.

Review of Basic Theory .

The light scattering properties of water are usually expressed as a volume scattering function (VSF), $\sigma(\theta)$. The VSF gives the fraction of the power in a beam that is scattered by angle θ per steradian per unit length along the beam. Improved instrumentation (small-angle-scattering meter built by Visibility Lab., Scripps Institute of Oceanography under Contract N62269-3097, NADC.) has recently extended the measurement of small-angle scattering to angles as small as 0.2°. Such data significantly improve extrapolations of the VSF to zero angle and allow more accurate predictions of the loss of angular resolution as a result of multiple scatter.

Loss of resolution is best expressed by the point spread function or its Fourier transform, the modulation transfer function (MTF). This paper uses the latter with notation $F(\psi, R)$. The precise meaning of this function is best explained with the aid of a hypothetical plane target oriented perpendicular to a line-of-sight from an observer at range R. The target has black-grey-white linear stripes, so that the diffuse reflectance of the target varies sinusoidally at the spatial frequency ν, i.e., ν is the number of black-white pairs per meter, Reference (2). The function $F(\psi, R)$ measures the attenuation of the angular frequency $\psi = \nu R$ (cycles per radian) relative to the attenuation of a uniformly white target. That is, F is the ratio of two attenuations observed as a function of range, the attenuation of the sinusoidal component of apparent target radiance divided by that of the uniform component.

In the small-angle approximation ($\sin\theta \approx \tan\theta \approx \theta$, etc.), the theory of the MTF permits the result of all orders of multiple scattering to be expressed in closed form as given in Reference (1). The explicit results are

$$F(\psi, R) = \exp\left\{[Q(\psi) - \sigma_t]\, R\right\}, \tag{1}$$

where

$$Q(\psi) = 2\pi \int_0^{\Theta} u(\theta)\, J_0(2\pi\psi\theta)\, d\theta, \tag{2}$$

$$u(\theta) = \int_{\theta}^{\Theta} \sigma(t)\, dt, \text{ and} \tag{3}$$

$$\sigma_t = \int_0^{\Omega} \sigma(\theta)\, d\omega = 2\pi \int_0^{\Theta} \sigma(\theta) \sin\theta\, d\theta. \tag{4}$$

Eq. (4) expresses the total small-angle scattering constant σ_t as the integral of the VSF over the solid angle ($d\omega$) up to a limit (Ω) defined by a cone of half-angle Θ. The limit Θ is the maximum acceptance angle of the optics (or other limit as discussed in Reference (1)). The constant σ_t is the fraction of power scattered at all small angles ($< \Theta$) per unit length along a light beam. Eq. (1) can be multiplied by $\exp(-\alpha R)$, where α is the attenuation constant (absorption and large angle scattering). This would convert relative attenuation of the spatial frequencies to absolute attenuation. This separation of $\exp(-\alpha R)$ is possible because all rays have the same length in the small-angle approximation.

The transformation defined by Eqs. (1) through (3) has a wide range of validity within the small-angle restriction already discussed. The VSF is unrestricted with regard to microscopic (unresolvable) correlations and particle interactions. The medium is assumed homogeneous and the particles without preferential alignment (unless it is along an axis parallel to the line-of-sight). Finally, the derivation of the transformation calculates the MTF as though the image were in best focus, which may differ significantly from focus at infinity. That is, of all the rays that emerge from the scattering medium, we have combined the intensities of those that appear to radiate from the same point in the blurred source distribution, not those rays that emerge parallel, nor those that strike a plane at the same position. An exception is the case of an object at infinity viewed through a slab of scattering medium. In this case rays from the same apparent source do arrive parallel.

Interpretation

The interpretation of Eqs. (1), (2), and (3) is straightforward. $Q(\nu)$ is a monotonically decreasing function,

$$\lim_{\nu \to \infty} Q(\nu) = 0.$$

Also in the high frequency limit the MTF expresses the simple exponential decay of the unscattered beam:

$$\lim_{\nu \to \infty} F(\nu, R) = \exp(-\sigma_t R),$$

This limit indicates that all scattered light is lost, insofar as the imaging of the finest detail is concerned. The factor exp (QR) restores some of the scattered power, namely that part which is useful in imaging lower spatial frequencies. Consider again the hypothetical target with sinusoidal stripes. The exp (QR) factor indicates that some of the scattered power is not lost, namely the portion scattered through an angle that is too small to blur the stripes. In the limit of zero frequency, all of the power is restored, i.e.,

$$F(0, R) = 1.$$

which follows from

$$\lim_{\nu \to 0} Q(\nu) = s_t,$$

which can be proven. This limit merely restates the fact that our MTF is normalized to one at zero frequency.

The modulation transfer function at any fixed range will always approach the value exp $(-s_t R)$ is the limit of high frequency. This of course represents a portion of the light that has not been scattered at all, i.e. rays which by chance miss all the discrete scatterers. These unscattered rays always exist in scattering systems that have finite total scattering cross-sections, even though the differential cross-section may have an integrable singularity. The non-zero limit of the MTF corresponds to a delta function at the center of the point spread function. In any real optics or transparent medium the delta function must have a finite width, and the MTF will drop to zero at the corresponding spatial frequency. But this is due to phenomena having an infinite total cross-section, which means that every ray scatters at least once. For example, optical imperfections and turbulent non-uniformities in fluid media give rise to infinite scattering cross-sections. In a full analysis of any real imaging system, the MTF for these phenomena multiplies the scattering MTF to give a resultant MTF that decays to zero in the high frequency limit.

Eq. (1) is easily generalized to give the MTF of a scattering slab, i.e., a scattering medium that begins at a distance R_1 from the target and ends at $R_2 > R_1$. In this more general case Eq. (1) is replaced by

$$F(\nu, R_1, R_2) = \exp\left\{-\sigma_t (R_2 - R_1) + R_2 Q(\nu R_2) - R_1 Q(\nu R_1)\right\} \qquad (5)$$

The following two analytic forms (and linear combinations of them) are convenient for fitting $\sigma(\theta)$ for transformation to Q.

$$\left.\begin{aligned} S_1(\theta) &= A e^{-\theta/T} \\ Q_1(\nu) &= \frac{\nu}{180}\, TA\left[\left(\frac{180}{\pi}\,\frac{1}{2\pi T}\right)^2 + \nu^2\right]^{-\frac{1}{2}} \end{aligned}\right\} \qquad (6)$$

$$\left.\begin{aligned} S_2(\theta) &= B\theta^{-(1+\mu)} \\ Q_2(\theta) &= \frac{\pi B}{\mu(\pi\nu)^{(1-\mu)}}\left(\frac{\pi}{180}\right)^{(1+\mu)}\frac{\Gamma((1-\mu)/2)}{\Gamma((1+\mu)/2)} \end{aligned}\right\} \qquad (7)$$

Conversion factors $\pi/180$ for θ (and T) in degrees and ν in cycles/rad. are shown explicitly, so they can be easily changed for other units.

Evaluation of MTF with an Experimental VSF

Reference (1) evaluates $F(\nu, R)$ for a set of experimental VSF data taken by Morrison (Reference 3) in sea water near the surface at Argus Island near Bermuda on 22 August 1966 with the Scripps small-angle-scattering meter. The water temperature was 28°C, salinity 36.3 to 36.4%, absorption length 2[illegible] meters (=1/a). There is some discrepancy in estimates of the scattering length ($1/\sigma_t$ = 5.0 to 5.6 m) and the attenuation length ($1/\alpha = (\sigma_t + a)^{-1}$).

Recall Eq. (1) and the function $Q(\nu)$ which acts as a negative attenuation constant to restore scattered power at low frequency. This function calculated by Eq. (2) is shown in Fig. (1). For the "numerical" curve, the Hankel transform was performed numerically using a graphical fit to the experimental data for $\theta \to 0$. The "analytic" curve was added for two reasons. The first is to show the effect of a different extrapolation law, within the experimental uncertainty, namely $\sigma(\theta) \sim \theta^{-1.4}$. This accounts for most of the discrepancy between the two curves at high angular frequency where the analytic fit or $\theta^{-1.4}$ is probably the better of the two. The second reason for the analytic case was to show that the dependence on a computer is not essential for calculating MTF. Fig. (2) shows experimental points fitted to

$$\sigma(\theta) \approx \frac{19\ m^{-1} sr^{-1} deg^{1.4}}{\theta^{1.4}} - \frac{3m^{-1} sr^{-1} deg^{0.8}}{\theta^{0.8}} \qquad (8)$$

i.e. two terms of the form of Eq. (6) and none of the form Eq. (7). This function goes negative beyond $\theta = 22^{o}$, as no physical σ can, which accounts for most of the discrepancy between the curves of Fig. (1) at low frequency, where the "numerical" is the better of the two. (More terms in Eq. (8) for a better fit at large angles would eliminate this discrepancy).

Fig. (3) shows the same results except that $\sigma_t - \Omega$ is plotted on a linear scale. This ordinate is not the MTF, but may be converted to it by the expression $F = \exp(-R \times \text{ordinate})$. For example, a sinusoidal target with 1.47 cycles per meter observed at a range of 10 meters would have 14.7 cycles per radian. The relative attenuation of this frequency at this range is $\exp(-0.1 \times 10) = e^{-1}$ from the numerical curve.

Fig. (4) shows the decollimation of an initially collimated beam as it passes through the water. We can represent this case in our imaging formalism by taking the point object that be at ∞, but the scatterers are situated in a finite slab of width w. We obtained these decollimation distributions by performing a numerical Fourier transform to convert the MTF to a point-spread function, which for a source at ∞ is the angular distribution function. The MTF is

$$F(\psi, w) = \exp\left\{\left[\Omega(\psi) - \sigma_t\right] w\right\}$$

which follows from Eq. (5) when $R_1, R_2 \to \infty$ while $R_2 - R_1 = w$. Note that Fig. (4) gives the angular spread of rays at distance w along a collimated beam, not the lateral displacement of rays from one another. Also note that the curves are integrated angular distribution, e.g. the 50% curve shows the angle (as a function of w) which encloses half the power in the beam. This curve clings to the w axis for some distance, because the light travels a ways before half has been scattered through <u>any</u> angle.

<u>Inverse Transformation</u>

The transformation from MTF to VSF is easily derived by using Hankel transform theory to invert Eq. 2. The result is

$$u(\theta) = 2\pi \int \psi \Omega(\psi) J_o(2\pi\theta\psi)\, d\psi .$$

The expression for the complete transformation from $F(\nu, R)$ to $s(\theta)$ then becomes

$$s(\theta) = -2\pi \frac{\partial}{\partial \theta} \left\{\theta \int_o^{\infty} \frac{\psi}{R} \left[\ln F(\psi, R) - \ln F(\infty, R)\right] J_o(2\pi\theta\psi)\, d\psi\right\} . \qquad (9)$$

This expression can be useful in correcting the results of measurements taken with a small-angle-scattering meter. The problem is that any specimen of a scattering medium has a finite length in which some multiple scattering occurs, but the VSF and the basic scattering properties of the particles are defined in the limit of a thin slab specimen in which multiple scattering vanishes.

Note that the existence of the MTF → VSF transformation opens the possibility of measuring small angle VSF's indirectly by the relatively simple technique of scanning images of test patterns that consist of black and white stripes viewed through a specimen of scattering medium. The pattern would include a wide spectrum of spatial frequencies. Coltman (Reference 2) has shown how resolution measurements taken with ordinary black and white stripes can be corrected to achieve the same result as if they were taken with sinusoidally graded stripes. The latter provides a direct measure of the MTF. Eq. (9) then gives the final conversion to the VSF. Recall that the VSF is the more fundamental quantity since it does not depend on the experimental geometry, i.e., on R, or more likely R_1 and R_2 if a scattering specimen is bounded on both ends. Thus the indirect measure suggests a good consistancy check to track down sources of error; viz. take data with more than one set of R_1 and R_2 values and see if they transform to the same VSF within the expected limits of error.

<u>Instrumentation</u>

We designed and built an instrument to measure VSF indirectly through MTF as discussed above. It measures the square-wave modulation transfer function, of a one meter water sample in-situ. A schematic diagram of the instrument is given in Fig. (5) and the instrument which we delivered to the U.S. Naval Undersea Research and Development Center is shown in Fig. (6). As Fig. (5) shows, it is divided into two pressure housings separated by the one meter sample cell. One housing contains the light source, the optical filter, the MTF pattern, the scan motor and collimator. The other pressure housing contains the camera lens, the analysis slit, the photomultiplier detector and its power supply. Although it is not necessary to have a collimated beam in the sample cell, we included collimation to eliminate any dependance of the MTF on the refractive index of the sample medium.

Both housings connect to the control electronics and oscilloscope "top side", i.e. out of the water, through the high pressure penetrators and the water proof cables. The top side electronics contains the low voltage power supplies and controls for the lamp intensity and photomultiplier gain and motor power. The output of the photomultiplier is fed directly to the verticle channel of the oscilloscope. The sweep of the oscilloscope is triggered by a sweep trigger detector which senses the beginning of a MTF sweep.

Frequencies scanned by the square wave pattern are from 0.11 cycles per radian to 8.2×10^3 cycles per radian. The frequency varies as

$$f_n = f_{n-1} e^{-0.035},$$

where f_n and f_{n-1} are the angular frequencies of the nth and (n-1)st bar in the MTF test pattern. The square wave pattern was generated as a circumferential pattern of transparent bars on a black background as can be seen in Fig. (7). The MTF pattern which contains 90 cycles, (one clear and one opaque space) occupies the full circumference at a radius of 38mm. For an analysis slit height of 2mm the angular frequency error is only five percent at all measured frequencies. The analysis slit is one of four transparent slits on an opaque background. The slit widths available are 3×10^{-4}, 10^{-4}, 3×10^{-5} and 10^{-5} radian. wide. The system MTF without water was maximum for a slit width of 3×10^{-5} radian so this slit was used in all measurements made in the laboratory.

Figure (8) contains sample data run on the MTF meter made for the U. S. Naval Undersea Research and Development Center. The first column was run in air and subsequent columns are run in tap water and various mixtures of spunk water (green water taken from a fish pond, not from a hollow stump in the grave yard as in Reference (4)). From the data it can be seen that there is no degradation in the MTF due to the refractive index or the suspended matterin Los Angeles tap water. The pond water, which is relatively clear, shows a marked amount of scatter at small angles as is evident in the data samples. The synchronous scan motor takes 1.66 seconds per revolution. This means that the conversion factor from time scale to angular scale is 3.8 radian/sec. The top photograph in each column of Fig. (8) shows the complete MTF scan. Subsequent traces were made by using the oscilliscope sweep delay to expand the scan at its high frequency end.

Note that the traces have an upward tail at the high frequency end of the trace. This resulted from the fact that the minimum bar width obtainable from our reticle manufacturing technique was 0.03mm. for reliable reproduction. When the bar width reached this dimension it was held constant to the end of the trace. Consequently the average transmission instead of approaching 50% in the limit approaches 25% (for a bar width of 0.030 mm and a line width of 0.010mm).

REFERENCES

Reference (1) Willard H. Wells, Loss of Resolution ir Water as a Result of Multiple Small-Angle Scattering, Journal of the Optical Society of America, Vol. 59, No. 6, 686-691, June 1969

(2) J. W. Coltman, J. Opt. Soc. Am. 44, 468 (1954)

(3) Robert E. Morrison, doctoral theses, Department of Meteorology and Oceanography, New York University (1967)

(4) Samuel L. Clemens "The Adventures of Tom Sawyer", Harper and Brothers, New York, Page 56.

ACKNOWLEDGEMENT

We would like to acknowledge the U.S. Naval Undersea Research and Development Center for permitting us to use data run on the MTF meter which was built for them. We wish to acknowledge Donald M. Rosencrantz of Tetra Tech who successfully managed the building and testing of the instrument under an extremely tight schedule. Also we wish to acknowledge Roy J. Marquedant of Tetra Tech for his designing and testing the control and biasing electronics of the MTF meter, and Mariann Moore for computing.

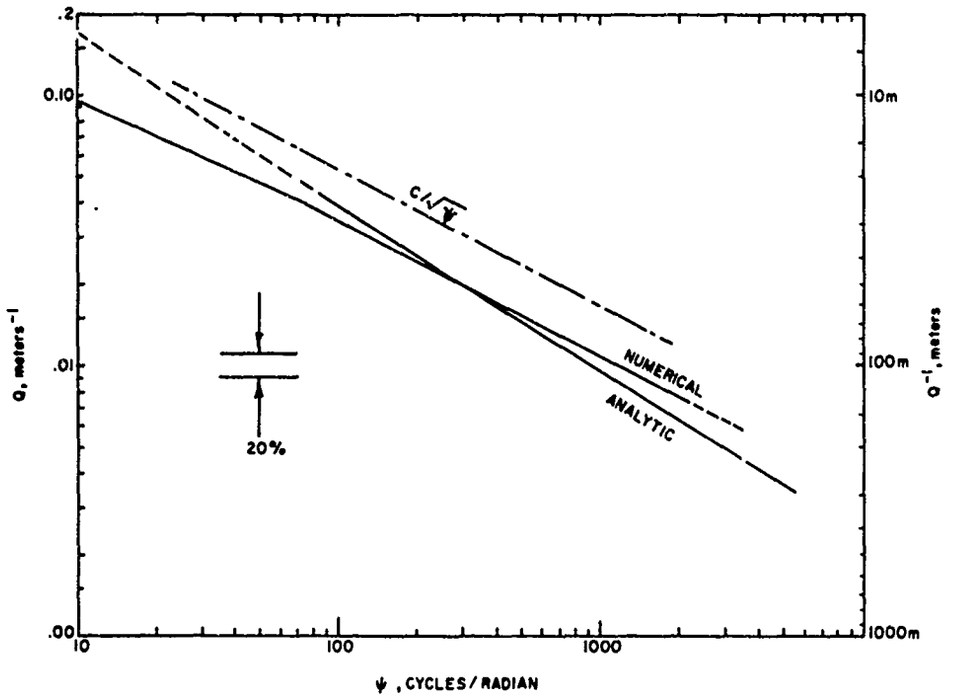

Figure (1) The Q function that defines restoration of low spatial frequencies, see Eq. (1). Two different techniques for fitting and extrapolating experimental data give slightly different results.

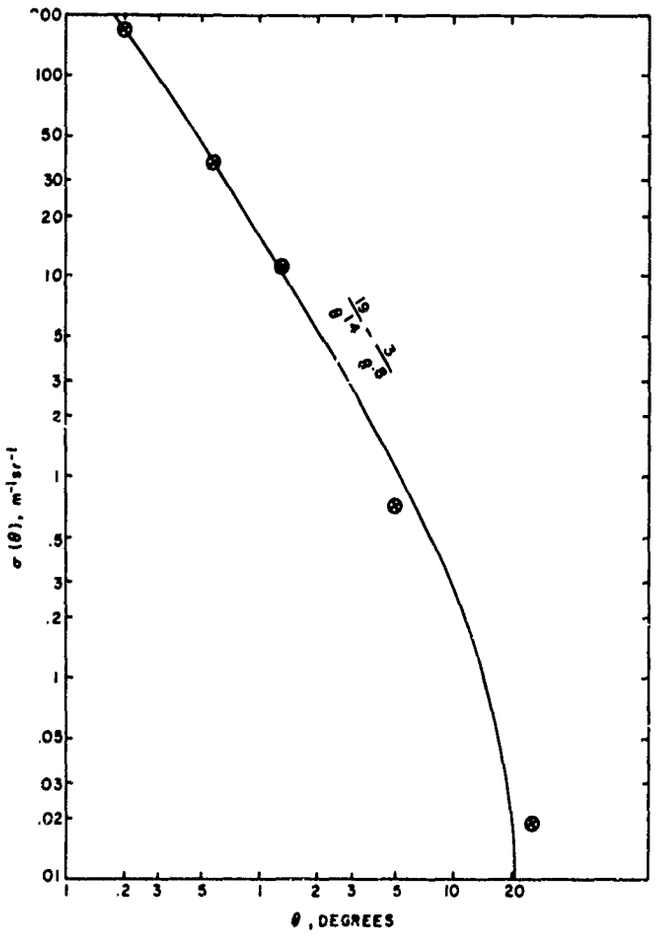

Figure (2) Analytic fit to experimental measurements of Volume Scattering Function $\sigma(\theta)$.

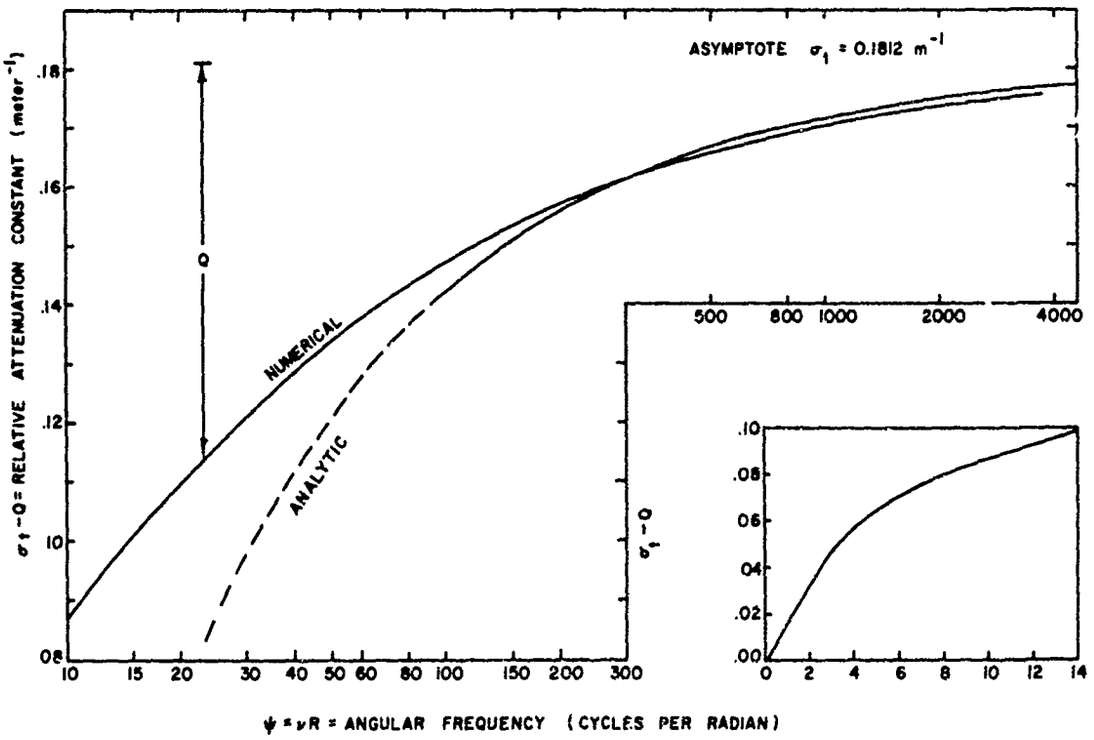

Figure (3) Exponential decay constant expressing the decay of angular frequencies in the field of view, relative to zero frequency. Only the effect of small-angle scatter is considered here. The modulation transfer function = exp (-R xordinate).

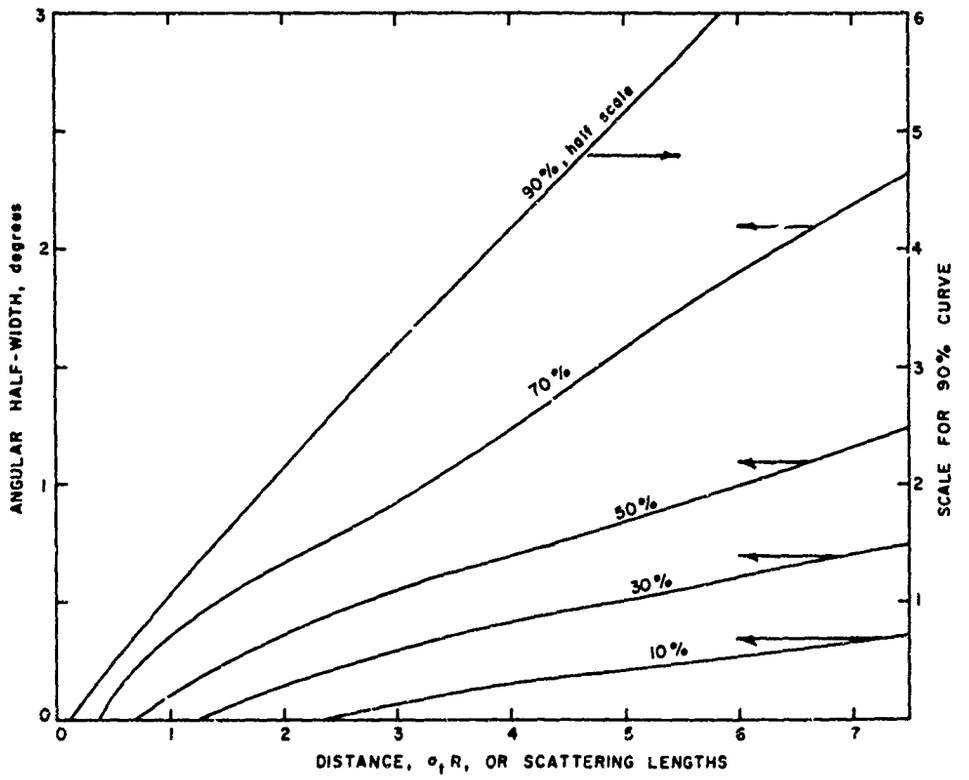

Figure (4) Integrated angular distribution of scattered rays gives the angle which encloses the indicated percentage of the power as a function of distance in scattering lengths. One scattering length 7.7 meters for the technique used in this figure for extrapolating experimental data for very small angle scattering. Attenuation length is shorter, about 5 to 5½ meters.

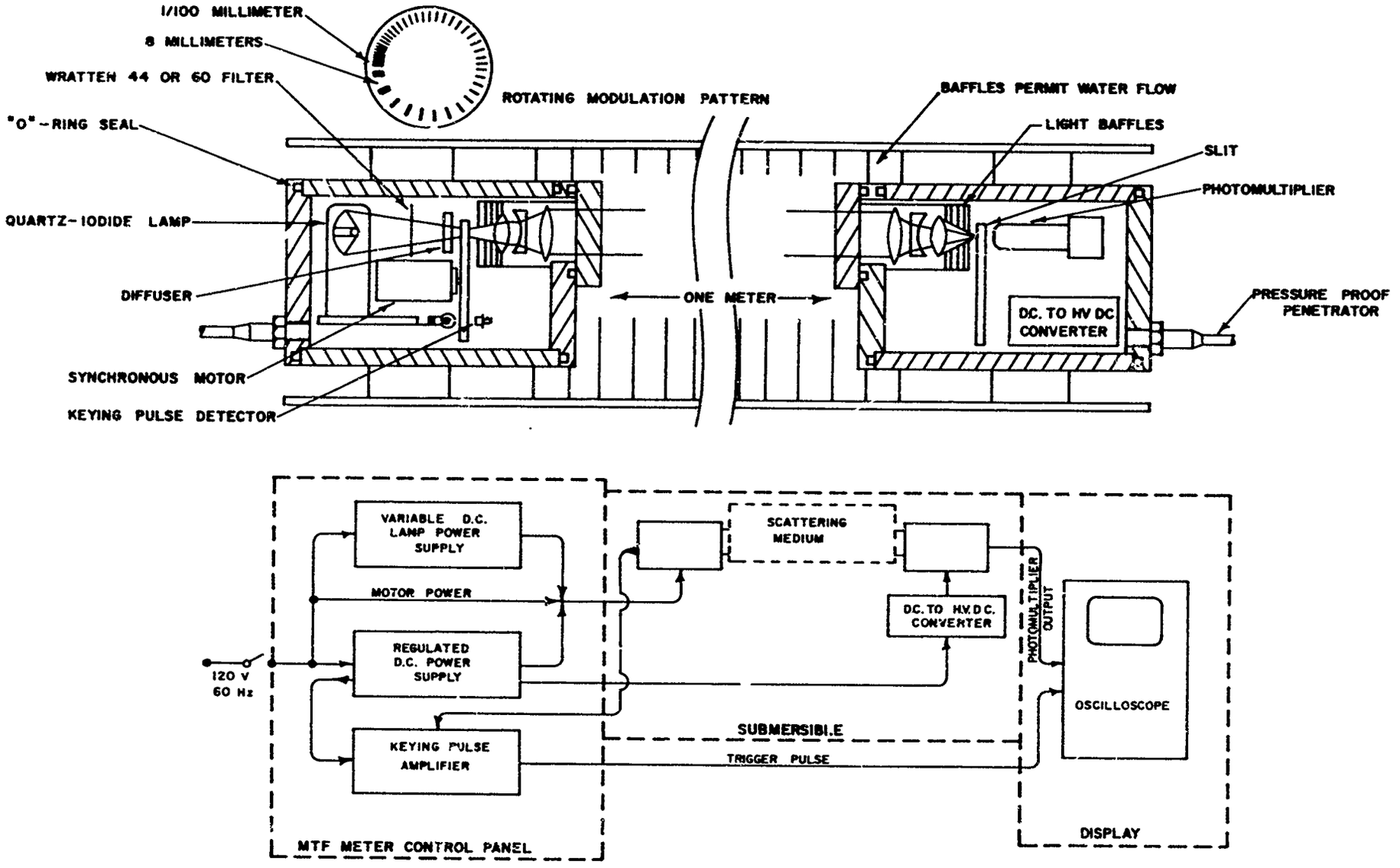

Figure (5) Schematic of operational MTF meter

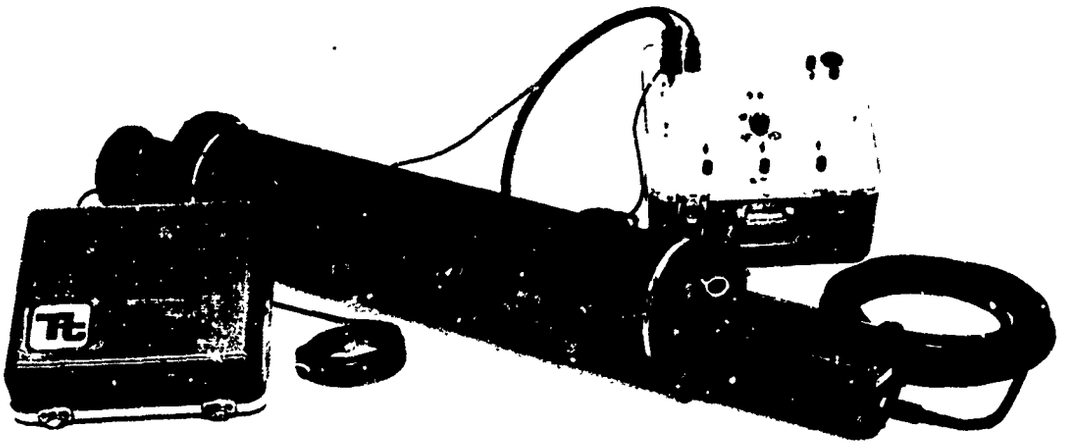

Figure (6) Photograph of the Packaged MTF Meter

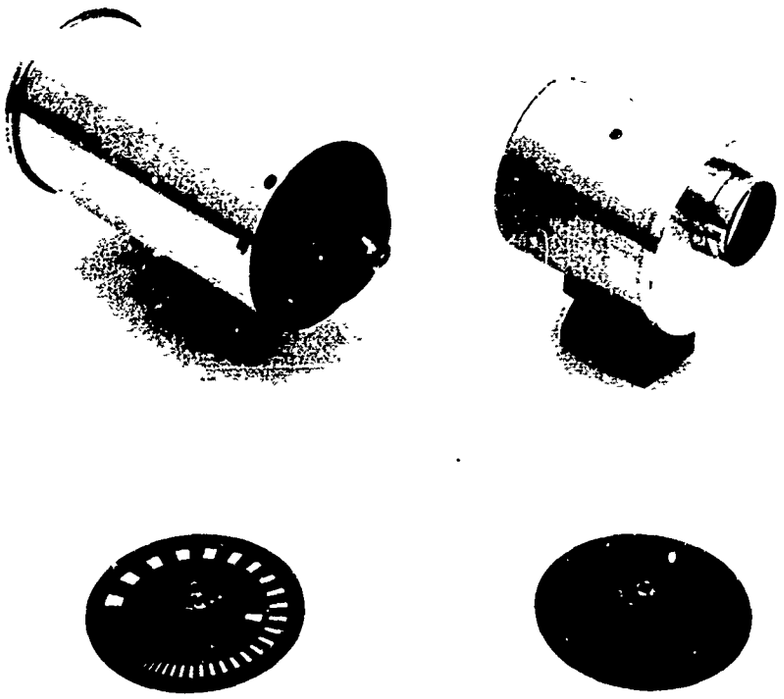

Figure (7) Pattern wheel for MTF meter, analysing slit wheel, and housings for the camera lens and motor/collimator

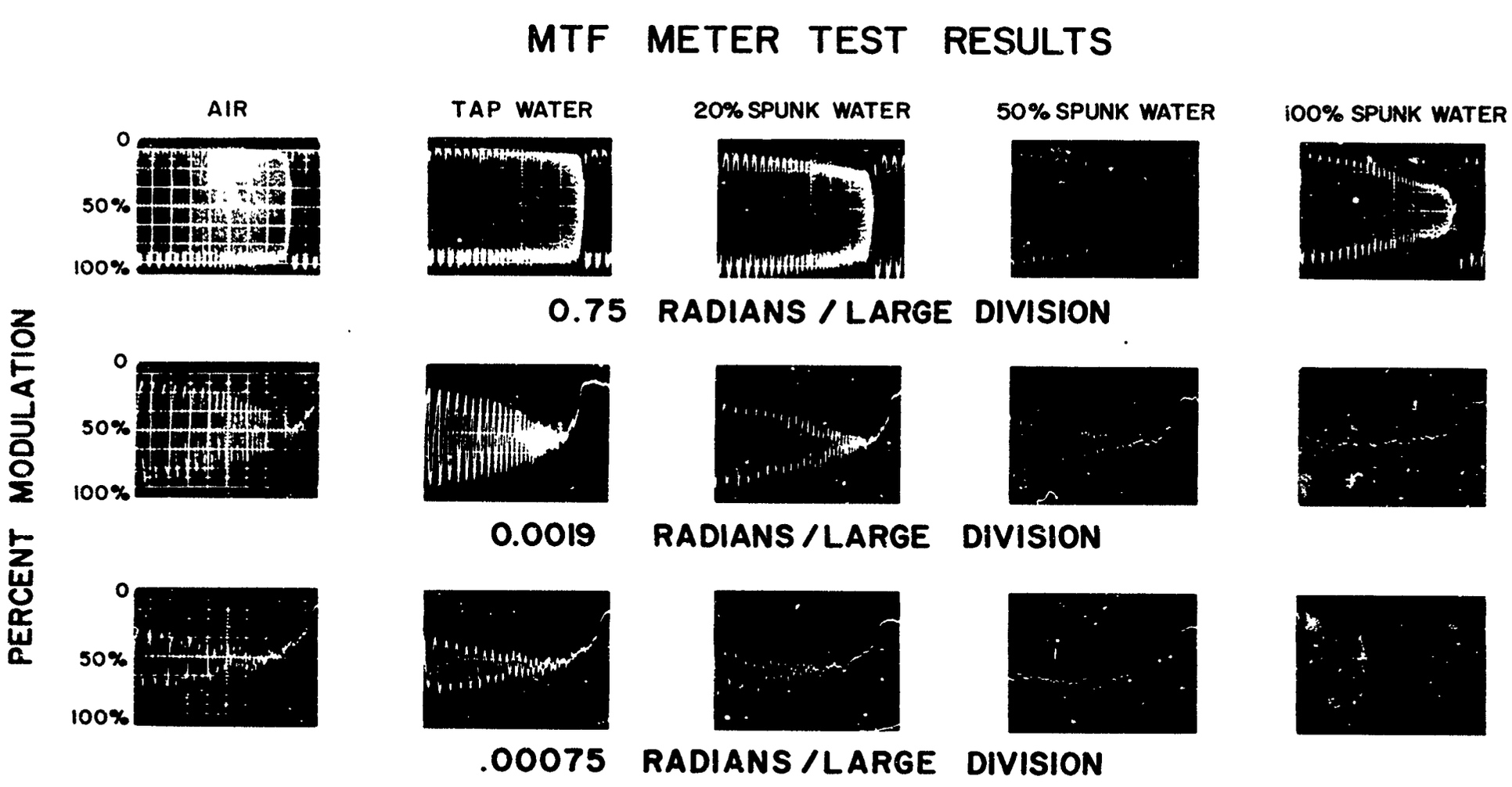

Figure (8) Test results with MTF meter. Top row shows full trace, other rows are expansions of high frequency end of trace.

THE THEORY OF LIGHT SCATTERING IN THE SEA

by

Frank Chilton

Stanford Research Institute
Menlo Park, California

and

W.K. Talley and D.D. Jones
University of California
Davis, California

SOMMAIRE

Au cours de cet exposé seront présentés les résultats de calculs analytiques et basés sur une méthode de Monte Carlo. Ces calculs portent sur la diffusion de la lumière par la turbulence et les particules en suspension dans la mer. Une attention particulière a été consacrée à l'élaboration de règles d'échelle analytique et à la prédiction des spectres d'être observés expérimentalement.

THE THEORY OF LIGHT SCATTERING IN THE SEA

Frank Chilton
Stanford Research Institute
Menlo Park, California

and

W.K. Talley and D.D. Jones
University of California
Davis, California

SUMMARY

Light is scattered in the underwater environment by particles and turbulence. This scattering causes a background radiance at the detector and a substantial loss of resolution over any distance. Absorption strongly attenuates the radiance at a distance.

We have developed a general, potentially complete, model of underwater visibility based on a semianalytic Monte Carlo computation using phenomenological volume scattering functions. A theoretically based parameterization of the volume scattering function provides a shape fit by only two parameters, but capable of describing both turbulence and particles.

Because there was a dearth of experimental information available, the behavior of resolution for different parameter values was studied systematically. A general law or scaling rule for resolution was found.

THE THEORY OF LIGHT SCATTERING IN THE SEA

WHY MODEL VISIBILITY?

The value of a complete (computer) model is its ability to predict the outcome of an experiment, fully instrumented or otherwise, at a reduced time and cost from that required for the actual experiment. The results can be treated exactly the same as the results of experiments to yield "laws of nature" or more restricted predictions.

Our model of underwater optical visibility depends on two components. First, we characterized the single scattering of light in a general way, consistent with both theory and experiment, but so that local or future variations could be accommodated. Second, this model of single scattering is used in a Monte Carlo computation of multiple scattering to yield a model of undersea visibility. The detailed treatment of the model is the subject of Reference 1.

SINGLE SCATTERING

The parameters characterizing the radiance are the scattering length, s^{-1}; the absorption length, a^{-1}; and the attenuation length, $\alpha^{-1} = a^{-1} + s^{-1}$. In our model, it is convenient to scale all dimensions in terms of α^{-1}, the mean free path and to replace a and s by the relative parameter $\zeta = \alpha^{-1}(s^{-1} + a^{-1})$. That visibility in the ocean is generally very poor is best illustrated by noting that good visibility out of the ocean requires say, $\alpha^{-1} \gg$ ten miles. However, in the ocean visibility is considered good if $\alpha^{-1} >$ ten meters. A typical value for ζ is .6 for the ocean.[2] We have used that value in our model although there is no commitment to it. Modification of the value of ζ would not change the qualitative results at all but would change the distance scale for quantitative results.

The source of scattering in seawater is small particulate organic and inorganic matter and that turbulence which alters the index of refraction (salinity and temperature). There is a wide distribution of the sizes of the particulate matter and of the size parameter of the turbulence. The volume scattering function (or differential cross section) is generally sharply peaked in the forward direction. As this is a result typical of diffraction about absorbing or translucent bodies, it is consistent with the fact that a substantial fraction of the particles or cells of turbulence are large compared with optical wavelengths. In this paper, we will use the term diffraction, as in elementary-particle physics, to designate any scattering that is sharply peaked in the forward direction.

The variations of particle-size distribution and turbulence from one location to another and a general lack of knowledge of shape or composition make undesirable a purely theoretical derivation of the volume-scattering function from the formulae of Mie and others[3-5] for scattering from spheres.

Our approach used a phenomenological volume-scattering function, based as firmly as possible on experimental measurements. However, the volume-scattering function has never been measured to angles small enough to be useful in image calculations. It has never been measured even to angles small enough that the radiance is known with certainty to be as much as one tenth of the extrapolated radiance in the forward direction. The difficulty lies in measuring scattering to the sufficiently small angles required ($\lesssim 10^{-3}$ rad). Only the collimation and radiance available with the laser make the experiments possible. Unfortunately, since the image is the bright spot that survives multiple scattering, measurements of the volume-scattering function to well within the half-maximum radiance angle are necessary for precise calculations of imaging. This requirement of small angles for meaningful statements about imaging is reinforced by the realization that the resolution of the eye and of many optical instruments is of the order of 10^{-4} rad. Measurements made with worse resolution detect mostly "blur photons" and few "image photons."

Excellent experimental data are available[2,6] for the volume-scattering function for angles greater than 1^{0}. For smaller angles, we assume that diffraction is the dominant mode, for which a rather general form of the volume-scattering function is $\exp[-\eta(1-\mu)]$, where $\mu = \cos\theta$. This expression is characteristic of the zeroth diffraction maximum in many different situations. For example, it precisely describes diffraction phenomena in high-energy physics.[7] Further, it closely fits the black-disk diffraction formula $|2J_1(kR\theta)/kR\theta|^2$ up to the first zero, if we set $\eta = (kR)^2/2$. The models of scattering by turbulence described by Tatarski[4] also have a $(kR)^2(1-\mu)/2$ dependence and a diffraction appearance. In any event, until experiment permits determination of more than one parameter with precision, our parameter will provide a good characterization.

Note that while small-angle scattering does not distinguish particles from turbulence, the frequency dependence, radiance fluctuations, and polarization degradation are more sensitive.

The volume-scattering function we have used in the piece-wise-continuous function

$$dF/d\Omega = C_1 e^{-\eta(1-\mu)} \approx C_1 \exp(-\eta\theta^2/2) (\theta < \epsilon) \quad (1)$$

$$dF/d\Omega = [C_2/(1-\mu)^b] (\theta > \epsilon), \quad (2)$$

where the angle ϵ is the dividing point between narrow- and wide-angle scattering. Morrison's data[6] are well fitted for $\mu \geq 0$ by $b = 1.08$. The constants C_1 and C_2 are determined by requiring continuity of $dF/d\Omega$ at $\theta = \epsilon$ and by the normalization

$$\int (dF/d\Omega) d\Omega = 1$$

$$2\pi C_1 = \left\{ \frac{1 - \exp[-\eta(1-\cos\epsilon)]}{\eta} + \exp[-\eta(1-\cos\epsilon)] \right.$$

$$\left. \times (1-\cos\epsilon) \frac{1 - [(1-\cos\epsilon)/2]^{b-1}}{b-1} \right\}^{-1} \quad (3)$$

$$C_2 = C_1 (1-\cos\epsilon)^b \exp[-\eta(1-\cos\epsilon)].$$

Some sample volume-scattering functions are shown in Figure 1.

The obvious method of evaluating η, extrapolation of the data of Duntley[3] and Morrison[6] failed. Depending upon the method of extrapolation chosen, values of η can be found ranging from 10^2 to 10^7. Such imprecision in an exponent is strong evidence of the lack of experimental information on small-angle scattering. Analysis of some photographs taken under water by Duntley suggests $\eta \sim 10^6$. Measurements of the particle-size distributions in fjord water[9] can be interpreted to give a calculated value of η. Since diffraction from a sphere is much like diffraction from a disk at small angles,[5,7] we assume that the scattering from the particles will be the same as from a black disk. In this case, $\eta = (kR)^2/2$, where $k = 2\pi/\lambda$, and R is the radius of the particle. Averaged over the particle-size distribution, the value obtained is $\eta \approx 1 \times 10^3$.

Preliminary measurements of small-angle scattering in the sea by R. Honey, G. Sorenson, and G. Gilbert of our laboratory have given $\eta \sim 1 \times 10^8$ in several different environments. This value has two important implications. First, it is much larger than the value obtained from a particle size distribution. Note also that the expectation value of η would be heavily weighted toward larger particles, which are easily visible in the size distribution measurements. Second, this value of η is of the same order as the resolution of optical equipment (and the human eye). This suggests a steep diffraction peak that will always have measured η values of the order of 10^8.

The mechanism to account for such high η values can only be turbulence. Particles that could cause such a high η would be obvious.

In any case, with our model we have explored visibility for a wide range in η. A more meaningful parameter than ϵ is what we call frac, the relative fraction of narrow angle ($< \epsilon$) scatterings. The qualitative behavior of the scattering distributions depends on whether the scattering is narrow angle- or wide angle-dominated. Figure 2 shows the ratio of narrow angle to wide angle scattering, and Figure 3 shows frac for a variety of values of η

VISIBILITY MODEL

Our model was based on semianalytic Monte Carlo calculation of the multiple scattering. The analog Monte Carlo method has the attractive feature of giving an exact modeling of multiple scattering of small numbers of photons and therefore an exact modeling of nature if the volume scattering function is correct.

The semianalytic Monte Carlo method is an improvement over the analog Monte Carlo method. Semianalytic refers to our performing the integrals over the distance into the medium analytically for the first few collisions. This makes the first few collisions equivalent to a new distributed source and improves computation time and accuracy for a given number of photons considerably. We regularly calculated radiances and angular distributions out to 25 mean free paths, with a standard deviation of less than 5%, a prohibitive task if we had been using an analog Monte Carlo method. Further, backscattering is included in the calculations with no additional effort required.

A detailed exposition of the semianalytic Monte Carlo method in our model is given in Reference 1.

RESULTS

Radiance. The radiance of light passing various distances into seawater is given in Figure 4. The distance is given in total mean free paths, α^{-1}. Radiance for several different values of η for $\epsilon=1^{\circ}$ is exhibited. Figure 4 shows that the more narrow angle-dominated the scattering is, the closer it tends to e^{-az}. Also evident is the fact that only at great distances is it possible to distinguish between finite η and purely forward scattering. For example, at 10 mfp only an order of magnitude separates the radiance caused by wide angle-dominated scattering ($\eta=10^3$, frac=0.14) from that caused by narrow angle-dominated scattering ($\eta \geq 10^5$, frac=1). Further, the radiance becomes insensitive to changes of η for values greater than $\sim 10^5$ (frac=1) and for η less than $\sim 10^4$ (frac=0.25). As the radiance continually decreases with distance, the error of measurement increases. Hence, radiance measurement alone is a poor way to try to determine any information about the details of light scattering in seawater. Conversely, to predict anything other than simple radiance, as for imaging, knowledge of the narrow angle portion of the scattering distribution is critical.

Mean Angle. A strong desire to reduce our results to some simple laws or scaling rules places an emphasis on the various moments of the angular distribution. In particular, the average cosine $\bar{\mu}$ appears to have simple properties as a function of distance into the medium.

For wide angle-dominated scattering, $\bar{\mu}(z)$ is presented in Figure 5 for a large range of different values of η and $\epsilon=1^{\circ}$. The dependence on z is quite smooth, becoming linear for $z \geq 3$ (after a few collisions).

For $\eta \geq 10^5$ (frac=1), the scattering is completely narrow angle-dominated. When this occurs, it is more convenient to plot $\eta(1-\bar{\mu})$ as a function of z, as is done in Figure 6. We then find that all curves fall on the same straight line. This appears to be a general property of the diffraction type of scattering. An analytic derivation of this result, with certain approximating assumptions, is given in Reference 1.

We have tried computations in which the wide-angle scattering of Eq. (2) was removed, i.e., $\epsilon=180^{\circ}$. Even for $\eta=10^2$, $\eta(1-\bar{\mu})$ vs z was a straight line, differing only slightly from the universal curve of Figure 6.

The above curves all have the unscattered flux included in the angular distribution. Because the usual oceanographic experiments on light scattering exclude the unscattered beam, we have examined this situation also. Curiously, removal of the unscattered flux from the narrow angle-dominated scattering still produces a straight line plot of $\eta(1-\bar{\mu})$ vs z, but with a different slope.

Angular Distributions. The angular distribution (radiance flux) of the collimated beam is plotted in Figures 7 and 8. It is obvious that the mean cosine, half angle, or some similar parameter is a sensitive function of η and frac, much more sensitive than radiance alone. While Figure 7 dramatically demonstrates the needed precision for angular measurement, it also suggests the difficulties.

LAWS OF VISIBILITY

As is often the case with Monte Carlo calculations of complicated processes, the model is complicated but the results and implications are simple. We can interpret our results to give laws or scaling rules for undersea visibility.

Radiance. Figure 4 demonstrates that the radiance is an exponential function of distance. This functional dependence holds provided that $z>3$ for all volume scattering functions and appears to apply for $z>0$ for narrow angle-dominated scattering.

The value of the exponent depends on the scattering distribution but not in a sensitive way. For narrow angle-dominated scattering, the exponent approximates the absorption parameter, a.

Angular Distribution. The angular dependence of light scattering in the sea also has a simple functional dependence. The mean cosine is the best way to express it.

For the narrow angle-dominated scattering ($\eta>10^5$, frac=1) the rule is particularly simple:

$$\bar{\mu}(z,\eta)=1-0.62z/\eta. \tag{4}$$

Further, this rule appears applicable right up to the origin.

The wide angle-dominated scattering is also characterizable by straight lines in z, providing that $z>3$ (that is, after a few collisions). The equation for these lines is, from Figure 5,

$$\bar{\mu}(z,\eta)\approx 0.83+4.3\times10^{-5}\eta-0.007z, \tag{5}$$

for $\eta \leq 2.0\times10^4$ (frac $\leq$ 0.5).

We know also that angular distributions such as shown in Figures 7 and 8 are nearly exponential in terms of the cosine, at least at small angles. For back scattered light, we are not yet certain of the dependence. We expect to investigate this point further.

Conclusions. We find that the laws of visibility in the sea have a surprisingly simple form considering the complicated scattering from particulate matter and turbulence that is the cause.

The general form for the radiance and for measures of resolution such as $\bar{\mu}$ have been given. The behavior of back scatter has not been fully resolved. These rules can be used for a wide variety of predictions of undersea visibility for any situation that does not depend on the temporal properties of turbulence. Specific versions of our visibility laws will result when more measurements have been made of volume scattering functions in the ocean.

REFERENCES

1. Frank Chilton, Dixon D. Jones, and Wilson K. Talley, "Imaging Properties of Light Scattered by the Sea," J. Opt. Soc. Am. 59, 891 (1969).

2. S. Q. Duntley, J. Opt. Soc. Am. 53, 214 (1963).

3. G. Mie, Ann. Physik 25, 377 (1908).

4. Some models different from that of Mie can be found in H. M. Nussenzveig, Ann. Phys., 34 23 (1965); or M. Fukuda, in Physical Aspects of Light in the Sea, J. E. Tyler, Ed., University of Hawaii Press, Honolulu, 1964.

5. A review is in H. C. van de Hulst, Light Scattering by Small Particles, John Wiley & Sons, Inc., New York, 1957.

6. R. E. Morison, "Studies on the Optical Properties of Sea Water at Argus Island in the North Atlantic Ocean and in Long Island and Block Island Sounds," Ph.D. thesis, New York University (1967).

7. A review of elementary particle scattering is in S. Gasioriwiscz, Elementary Particle Physics, John Wiley & Sons, Inc., New York, 1966, p. 479.

8. V. I. Tatarski, Wave Propagation in a Turbulent Medium, McGraw-Hill Book Co., New York, 1961, p. 70.

9. N. G. Jerlov, Tellus 7, 218 (1955).

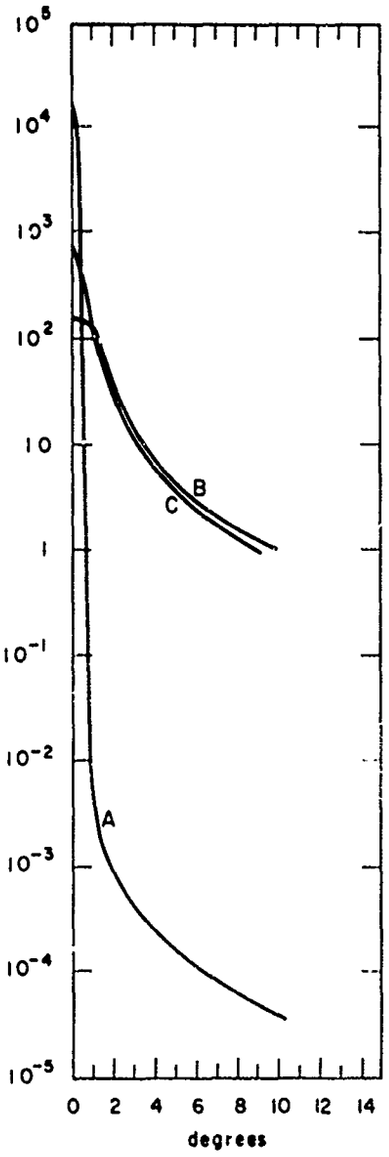

Fig. 1 Typical volume scattering functions. All curves shown have $\epsilon = 1^0 = 17.4$ mrad. The η values are: A, $\eta = 10^5$, B, $\eta = 10^3$; C, $\eta = 10^4$

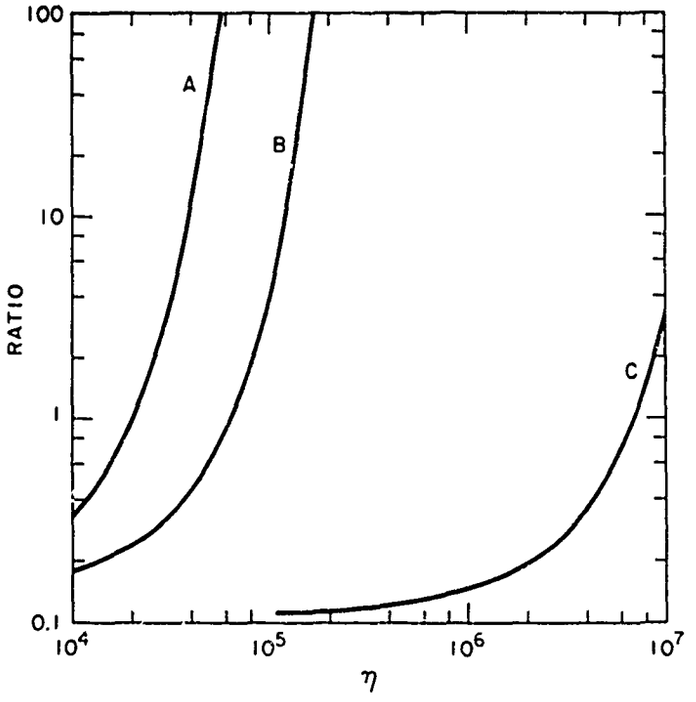

Fig. 2 The ratio of narrow-angle to wide-angle scattering, as a function of η for several values of ϵ: A, $\epsilon = 1^0 = 17.4$ mrad; B, $\epsilon = 10$ mrad; C, $\epsilon = 1$ mrad

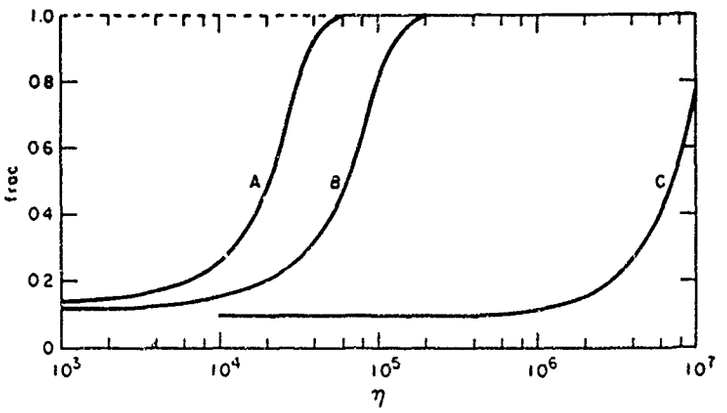

Fig. 3. The fraction (frac) of single scatterings that are narrow-angled as a function of η for several values of ϵ: A, $\epsilon = 1^0 = 17.4$ mrad ; B, $\epsilon = 10$ mrad ; C, $\epsilon = 1$ mrad

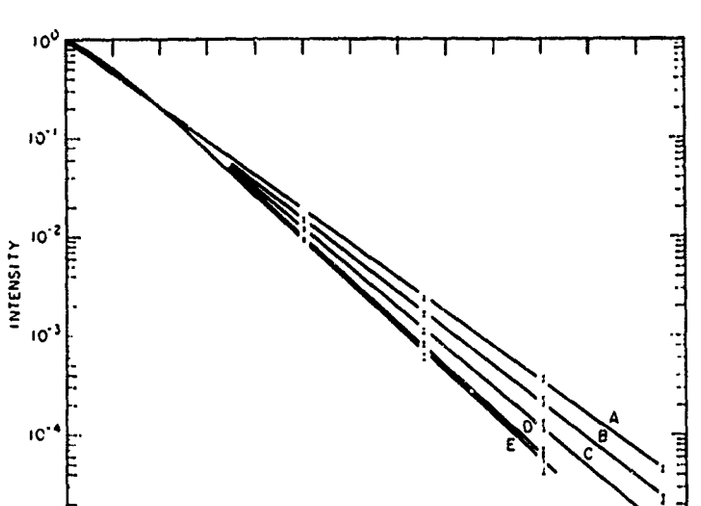

Fig. 4 Radiance as a function of distance for $\epsilon = 1^{\circ} = 17.4$ mrad and different values of η and frac: A, $\eta = 5 \times 10^4$, frac = 1.0 (this curve is approximately $e^{-\alpha z}$); B, $\eta = 3 \times 10^4$, frac = 0.76; C, $\eta = 2 \times 10^4$, frac = 0.50; D, $\eta = 1 \times 10^4$, frac = 0.26; E, $\eta = 1 \times 10^3$, frac = 0.14

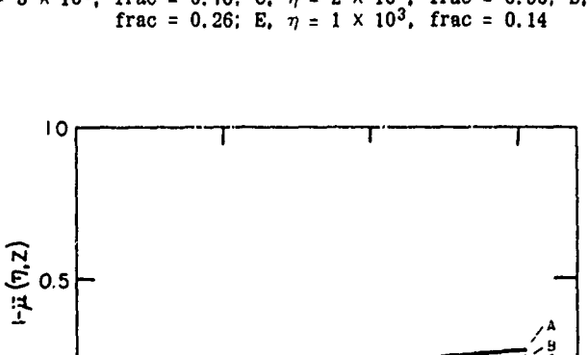

Fig. 5 The average cosine $\bar{\mu}$ as a function of distance for $\epsilon = 1^{\circ} = 17.4$ mrad and several values of η and frac: A, $\eta \leq 1 \times 10^3$, frac = 0.14; B, $\eta = 1 \times 10^4$, frac = 0.26; C, $\eta = 1.5 \times 10^4$, frac = 0.37; D, $\eta = 2 \times 10^4$, frac = 0.50; E, $\eta = 3 \times 10^4$, frac = 0.86; F, $\eta = 4 \times 10^4$, frac = 0.92; G = 5×10^4, frac = 0.98

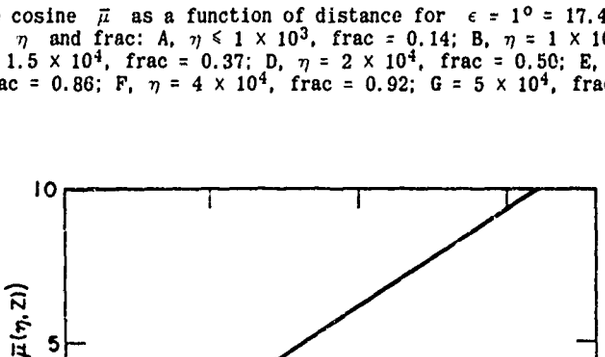

Fig. 6 The average cosine $\bar{\mu}$ for narrow-angle-dominated scattering (frac ≈ 1.0) is displayed as $\eta(1-\bar{\mu})$. The particular case shown had $\epsilon = 1^{\circ} = 17.4$ mrad and $\eta \geq 1.0 \times 10^5$

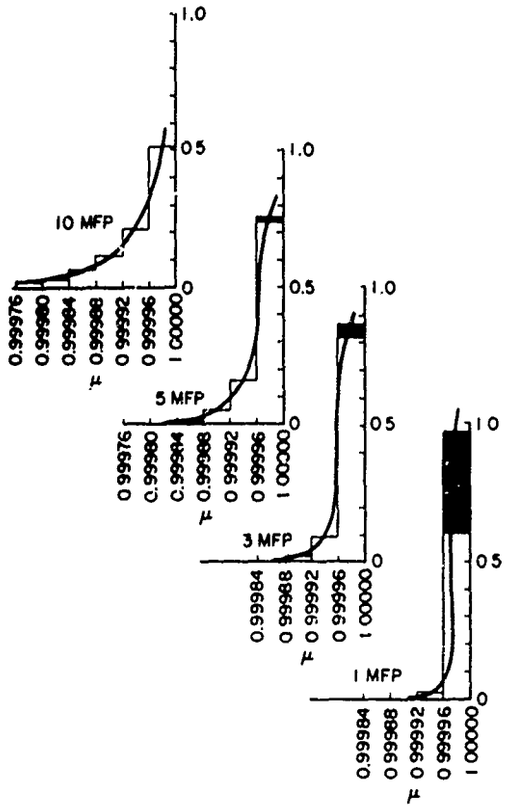

Fig. 7 The angular distributions at several distances for $\epsilon = 1^{o} - 17.4$ mrad and $\eta = 1.0 \times 10^{5}$ (frac ≈ 1.0) . The distances are given in mean free paths (MFP). The shaded areas represent the unscattered flux

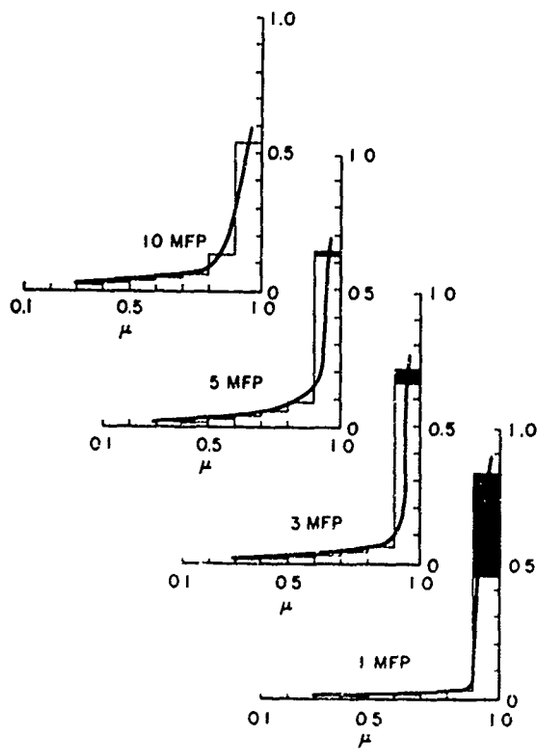

Fig. 8 The angular distributions at several distances for $\epsilon = 1^{o} - 17.4$ mrad and $\eta = 1.0 \times 10^{3}$ (frac 0.14) . The distances are given in total mean free paths (MFP) . The shaded areas represent the unscattered flux

TRANSPORT ANALYSIS OF OPTICAL PROPAGATION IN THE UNDERSEA ENVIRONMENT

by

David L. Feinstein and Kenneth R. Piech

Cornell Aeronautical Laboratory, Inc.
Buffalo, New York U.S.A.

and

A. Leonard
Stanford University
Stanford, California U.S.A.

TRANSPORT ANALYSIS OF OPTICAL PROPAGATION IN THE UNDERSEA ENVIRONMENT *

by

David L. Feinstein and Kenneth R. Piech

Cornell Aeronautical Laboratory, Inc.
Buffalo, New York U.S.A.

And

A. Leonard

Stanford University
Stanford, California U.S.A.

SUMMARY

We investigate the application of the singular eigenfunction expansion technique to the solution of the underwater radiative transport problem. The scalar transport equation is solved by the singular eigenfunction expansion technique for a plane wave incident on a homogeneous half space characterized by a highly anisotropic scattering distribution. An experimental sea-water volume scattering function is treated by a high order expansion in Legendre polynomials. Results for reflected radiance are presented for a 9th order polynomial fit, with undersea radiance distribution given to a 5th order fit. The preliminary results agree qualitatively with experimental measurements of underwater radiance distributions.

1. INTRODUCTION

The propagation of electromagnetic radiation in the undersea environment has become a topic of considerable interest. Detailed analyses are made difficult by the fact that the undersea medium constitutes a random, optically thick medium, with highly anisotropic scattering properties. Some success has been obtained with similar propagation problems in other areas [1,2,3] by formulation in terms of a radiative transport equation. This approach, basically from a flux conservation viewpoint, can yield a significant degree of physical insight and understanding to a problem, frequently enabling one to draw conclusions of a more fundamental nature than otherwise possible.

However, solutions to the radiative transport equation are quite difficult. The equation is basically an integro-differential equation containing a source term expressed in terms of the unknown radiance or flux distribution. Attempts at solutions of the radiative transport equation can generally be classified into three types:

1) approaches applicable to a particular problem or set of conditions -- such as diffusion approximations or small angle scattering approximations,

2) statistical techniques -- such as Monte Carlo, and

3) systematic approaches of an applied mathematical character with varying amounts of analysis -- such as the discrete ordinate or the singular eigenfunction expansion approach.

Each of these approaches has its advantages and disadvantages. Approaches tailored to a single problem can yield rapid solutions, yet are difficult to general more complicated and interesting situations. Statistical techniques such as Monte Carlo [4,5] are os the best way to handle complex geometries and inhomogeneities, but these techniques are difficult .o use for deductions of a general nature, and are also difficult to use in regions where statistics are p or (as in the backscatter direction of a highly forward peaked scattering function). Techniques such as the singular eigenfunction expansion approach, while promising and allowing physical deductions of a general nature, are, however, somewhat difficult to apply in practice because of their high degree of mathematical complexity and difficulties in developing the necessary numerics.

It is our feeling that this latter approach -- that of singular eigenfunction expansions -- has developed to the point where it now promises to be a useful tool for undersea propagation analyses. In this paper we thus consider undersea propagation from the viewpoint of the radiative transport equation formalism, and the singular eigenfunction expansion solution technique. We investigate the usefulness of this approach by considering the description of underwater radiance due to solar illumination. This problem allows a test of the eigenfunction approach in predicting radiance for a highly anisotropic volume scattering function (VSF), as experimental underwater radiance measurements exist for comparison. Since VSF measurements are difficult at small angles, the program also allows a possible determination of effect of small-angle VSF forms on the radiance distributions.

We formulate this problem in terms of the time-independent scalar radiative transport equation with a plane wave incident on a homogeneous, anisotropic scattering half-space. The resulting equation is analyzed using the singular eigenfunction expansion technique. [6,7,8] The anisotropy of the scattering distribution is treated by a high order expansion in Legendre polynomials. In this manner, we can

systematically investigate the effect of the anisotropy. Similar problems are involved in quantitative aerial remote sensing of water pollution [9]. The importance of transport phenomena to these problems has recently been discussed by Feinstein and Piech. [10,11] To check our numerical techniques, [12] we compare our solution for several low order polynomial scattering laws with those given by Chandrasekhar. [1] Finally, we briefly discuss comparisons of our preliminary theoretical calculations based on a scattering law suitable for the undersea environment, with measured underwater radiance distributions. [13,14,15]

The outline of this paper is as follows: In the next section, we formulate the appropriate radiative transport equation, discuss the analytic solution in terms of the singular eigenfunction expansion, and briefly describe the numerical procedures used for the calculations. In the third section, we present the results of these calculations. The final section summarizes the results and conclusions and discusses possible generalizations of the radiative transport formulation of the undersea electromagnetic propagation problem.

2. SOLUTION OF THE RADIATIVE TRANSPORT EQUATION

A. FORMULATION OF PROBLEM

The radiative transport equation for radiance, $I(\underset{\sim}{r},\hat{n})$, in the medium is

$$(n\cdot\nabla)\,I(\underset{\sim}{r},\hat{n}) = -\left(K(\underset{\sim}{r})+\sigma(\underset{\sim}{r})\right)I(\underset{\sim}{r},\hat{n}) + \frac{\sigma(\underset{\sim}{r})}{4\pi}\int d\Omega(\hat{n}')\,p(\hat{n},\hat{n}')\,I(\underset{\sim}{r},\hat{n}') \quad , \tag{1}$$

where we have written the VSF in the form $\sigma(\underset{\sim}{r})\,\frac{p(\hat{n},\hat{n}')}{4\pi}$ with $\frac{1}{4\pi}\int p(\hat{n},\hat{n}')\,d\Omega(\hat{n}')=1$. In Eq. (1) $\sigma(\underset{\sim}{r})$ is scattering per unit length and $K(\underset{\sim}{r})$ represents absorption per unit length. We assume $I(\underset{\sim}{r},\hat{n})$ represents radiance of a given frequency, and that energy exchange between frequencies can be neglected. $d\Omega(\hat{n}')$is a differential solid angle about $\hat{n}'$. Rigorous derivations of Eq. (1), together with a discussion of the range of validity of this equation may be found in the literature. [16,17]

Our intent here is to investigate the solutions of Eq. (1) for a homogeneous half-space with a VSF corresponding to that of seawater. The incident illumination will be assumed to be planar, corresponding to illumination by sunlight. A number of experimental measurements of underwater radiance exist (see for example Ref. 13) together with measurements of the VSF down to small angles. Radiance values can be calculated by extrapolating the measured VSF to zero scattering angle, and a comparison of calculated and measured radiance values can be made. We thus assume the medium under consideration fills the half-space $z \geq 0$, and with the homogeneity assumption write Eq. (1) in the form

$$\left(\mu\,\frac{\partial}{\partial z}+1\right)I^m(z,\mu) = \frac{\tilde{\omega}_o}{2}\int p^m(\mu\cdot\mu')\,I^m(z,\mu')\,d\mu' \quad , \tag{2}$$

where τ is the optical thickness

$$\tau = \int_0^z (K+\sigma)\,dz' = z\,(K+\sigma) \tag{3}$$

and the single scatter albedo $\tilde{\omega}_o$ is

$$\tilde{\omega}_o = \frac{\sigma}{K+\sigma} \tag{4}$$

In Eq. (2) $\mu = \cos\theta$, the cosine of the polar angle. The scattering phase function, p , has also been assumed azimuthally symmetric.

Unless the sun is at the zenith, I will depend on (τ,μ,φ) ; hence we have made the usual expansions:

$$I(\tau,\mu,\varphi) = \sum_m e^{im\varphi}\,I^m(\tau,\mu)$$

$$p(\mu\cdot\mu') = \sum_m e^{im\varphi}\,p^m(\mu\cdot\mu')$$

Since the $e^{im\varphi}$ are orthogonal, Eq. (2) holds for each m with no coupling between different values of m . Eq. (2) thus represents a set of equations describing radiative transport within the model space.

B. METHOD OF SOLUTION

We briefly outline the singular eigenfunction solution technique as applied to Eq. (2). For more details, the reader is referred to the literature. [7,8,12,18] We first assume that the scattering phase function can be expanded as

$$\tilde{\omega}_o\;p(\cos\Theta) = \sum_{\ell=0}^{N}\tilde{\omega}_\ell\,P_\ell(\cos\Theta) \tag{5}$$

where Θ is the scattering angle, and P_ℓ are the Legendre polynomials. We note that the expansion of $p(\cos\Theta)$ in Legendre polynomials is not the only possible procedure. Other basis functions could be utilized, or one could deal directly in the computations with $p(\cos\Theta)$. Use of an analytical expression for $p\cos\Theta$ such as (5), however, allows the analysis to be carried further than in a purely numerical treatment.

Use of the ansatz

$$I^m(x,\mu) = e^{-x/\nu}\ \phi^m(\nu,\mu)(1-\mu^2)^{m/2} \quad , \tag{6}$$

yields the equation for the eigenfunctions, ϕ^m,

$$(\nu-\mu)\,\phi^m(\nu,\mu) = \frac{1}{2}\,\nu \int_{-1}^{+1} p^m(\mu,\mu')\,\phi^m(\nu,\mu')\,dm(\mu') \quad , \tag{7}$$

where ν plays the role of an eigenvalue, and

$$p^m(\mu,\mu') \sum_{\ell=m} c_\ell^m\ P_\ell^m(\mu)\ P_\ell^m(\mu') \quad .$$

In the above $P_\ell^m(\mu)$ are the associated Legendre polynomials divided by $(1-\mu^2)^{m/2}$ and ...

$$c_\ell^m = \tilde{\omega}_\ell\ \frac{(\ell-m)!}{(\ell+m)!} \quad .$$

We have also introduced the notation

$$dm(\mu) \equiv (1-\mu^2)^m\, d\mu \quad .$$

The singular eigenfunction approach is similar to the standard techniques used to solve ordinary differential equations. One just seeks the solutions or eigenfunctions, $\phi^m(\nu,\mu)$, of the homogeneous transport equation (7). The solution for I is then expanded in terms of these eigenfunctions with the expansion coefficients determined by the boundary conditions. The technique is fundamentally no more difficult than that used in ordinary differential equations, but the mathematics is somewhat less familiar because of the singular nature of the eigenfunctions. In general, one may distinguish between two types of solutions of the eigenfunction equation (7), continuum solutions and discrete solutions.

(i) Continuum Solutions

For $\nu \in (-1,1)$ there corresponds a continuous set of singular eigensolutions

$$\phi^m(\nu,\mu) = \frac{1}{2}\,\nu\, g^m(\nu,\mu)\ P\,\frac{1}{\nu-\mu} + \lambda^m(\nu)(1-\nu^2)^{-m}\,\delta(\nu-\mu) \tag{8}$$

where P denotes Cauchy principal value, and

$$\lambda^m(\nu) = 1 - \frac{1}{2}\,\nu\, P\int_{-1}^{1} \frac{g^m(\nu,\mu)\,dm(\mu)}{(\nu-\mu)} \quad , \tag{9}$$

$$g^m(\nu,\mu) = \sum_{\ell=m}^{N} c_\ell^m\, g_\ell^m(\nu)\ P_\ell^m(\mu) \quad , \tag{10}$$

$$g_\ell^m(\nu) = \int_{-1}^{1} \phi^m(\nu,\mu)\ P_\ell^m(\mu)\,dm(\mu) \quad . \tag{11}$$

(ii) Discrete Solutions

For $\nu \notin (-1,1)$ there may exist a set of discrete eigensolutions

$$\phi^m(\pm\,\nu_j^m,\mu) = \frac{1}{2}\,\nu_j^m\ \frac{g^m(\pm\,\nu_j^m,\mu)}{\nu_j^m \mp \mu} \quad , \tag{12}$$

which are the roots of the dispersion relation

$$\lambda^m(z) = 0 \, . \tag{13}$$

The number of discrete roots may be found by the argument principle

$$M = \frac{1}{\pi}\left[\Delta \arg\ \lambda_+^m(\mu)\right]_{0\to+1} \quad , \tag{14}$$

where M is the number of discrete roots with positive real parts and

$$\lambda_{\pm}^{m}(\nu) = \lim_{\varepsilon \to 0^{+}} \lambda^{m}(\nu \pm i\varepsilon)$$

$$= \lambda^{m}(\nu) \pm \frac{1}{2} i \pi \nu g^{m}(\nu, \nu)(1-\nu^{2})^{m} \quad . \tag{15}$$

In Eq. (14) $\left[\Delta \arg \lambda_{+}^{m}(\mu)\right]_{0 \to 1}$ is the change in the argument of $\lambda_{+}^{m}(\mu)$ as μ varies continuously from 0 to 1.

It can be shown that the number of positive roots is limited by[6]

$$M \leq N - m + 1$$

with N the highest order Legendre polynomial occuring. We see that there is at least one real positive root at m = 0 . As $\tilde{\omega}_{o}$ increases, the root tends to infinity and, in general, additional roots appear at ν =1 moving off toward infinity. We also note as the order of the polynomial fit is increased, there is the possibility of additional roots.

Once the eigenfunctions, (8) and (12) have been found, it is necessary to establish the completeness of the ϕ^{m} , so that an expansion of I^{m} in terms of the ϕ^{m} can be properly made and interpreted. Completness of the ϕ^{m} follows from a theorem [6,7,8] which states that an arbitrary Hölder continuous function on [0,1] can be expanded in terms of the ϕ 's as

$$I^{m}(x,\mu) = \sum_{j=1}^{M} a_{j}^{m} \phi^{m}(\nu_{j}^{m}, \mu) e^{-x/\nu_{j}^{m}} + \int_{0}^{1} A^{m}(\nu) \phi^{m}(\nu, \mu) e^{-x/\nu} d\nu \quad . \tag{16}$$

The proof is constructive in that once completeness is proven, it explicitly shows how to calculate the expansion coefficients a_{j}^{m} and $A^{m}(\nu)$. For details of the proofs, the reader is referred to the literature. [6,7,8] We simply quote the results relevant to our problem.

The expansion coefficients may be written terms of the adjoint eigensolutions as

$$a_{j}^{m} = \frac{\frac{1}{\pi} \tilde{\phi}^{m}(\nu_{j}^{m}, \mu_{o}) \mu_{o} H^{m}(\mu_{o})}{(\nu_{j}^{m})^{2} g^{m}(\nu_{j}^{m}, \nu_{j}^{m}) H^{m}(\nu_{j}^{m}) \left.\frac{d\lambda^{m}(z)}{dz}\right|_{z=\nu_{j}^{m}}} \quad , \tag{17}$$

$$A^{m}(\nu) = \frac{\frac{1}{2\pi} \tilde{\phi}^{m}(\nu, \mu_{o}) H^{m}(\mu_{o})(1-\nu^{2})^{m}}{\chi^{m}(\nu) \nu H^{m}(\nu)} \quad , \tag{18}$$

$$\chi^{m}(\nu) = \lambda_{+}^{m}(\nu) \lambda_{-}^{m}(\nu) \quad . \tag{19}$$

The adjoint eigensolutions are given by:

$$\tilde{\phi}^{m}(\nu_{j}^{m}, \mu_{o}) = \frac{1}{2} \nu_{j}^{m} B^{m}(\nu_{j}^{m}, \mu_{o}) + \frac{\frac{1}{2} \nu_{j}^{m} g^{m}(\nu_{j}^{m}, \mu_{o})}{(\nu_{j}^{m} - \mu_{o})} \tag{20}$$

and

$$\tilde{\phi}^{m}(\nu, \mu_{o}) = \frac{1}{2} \nu \left[B^{m}(\nu, \mu_{o}) + \frac{g^{m}(\nu, \mu_{o})}{\nu - \mu_{o}}\right] + \frac{\lambda^{m}(\nu) \delta(\nu - \mu_{o})}{(1-\nu^{2})^{m}} \quad . \tag{21}$$

The H functions are given by

$$\frac{1}{H^{m}(\mu)} = (1+\mu)^{-M} \prod_{j=1}^{M} (1+\mu/\nu_{j}^{m}) \exp\left[\frac{1}{2\pi i} \int_{0}^{1} \ln \frac{\lambda_{+}^{m}(\nu)}{\lambda_{-}^{m}(\nu)} \left\{\frac{1}{\nu+\mu} - \frac{1}{\nu}\right\} d\nu\right] \quad . \tag{22}$$

The $B^{m}(\nu,\mu)$ are given by

$$B^{m}(\nu, \mu) = \sum_{\ell=m}^{N-1} B_{\ell}^{m}(\nu) P_{\ell}^{m}(\mu) \quad , \tag{23}$$

where the B_{ℓ}^{m} are determined by solving the polynomial equations

$$\sum_{\ell=m}^{N-1} B_{\ell}^{m}(\nu') K_{\ell}^{m}(\nu) = -L^{m}(\nu, \nu') \quad , \tag{24}$$

$$L^{m}(z, z') = \frac{1}{(z+z')} \sum_{\ell=m}^{N} c_{\ell}^{m} \left[g_{\ell}^{m}(z) K_{\ell}^{m}(z') - g_{\ell}^{m}(z') K_{\ell}^{m}(z)\right] \quad , \tag{25}$$

$$K_\ell^m(\nu) = \int_0^1 P_\ell^m(\mu)\,\frac{\left[g^m(\nu,\mu) - g^m(\mu,\mu')\right]}{\nu-\mu}\,\mu\,H^m(\mu)\,d m(\mu) + 2\left[\frac{P_\ell^m(\nu)}{H^m(-\nu)}\right]_{AS}\,, \tag{26}$$

where AS means we keep the dominant terms as $\nu \to \infty$.

With the above results, we can write down the final result as

$$I(\tau,\mu,\varphi) = \sum_{m=0}^{N}(2-\delta_{0m})\,I^m(\tau,\mu)(1-\mu^2)^{m/2}(1-\mu_o^2)^{m/2}\cos m(\varphi-\varphi_o) + \delta(\mu-\mu_o)\,e^{-\tau/\mu_o}\left[\delta(\varphi-\varphi_o) - \frac{1}{2\pi}\sum_{m=0}^{N}(2-\delta_{0m})\cos m(\varphi-\varphi_o)\right]. \tag{27}$$

where (μ_o, φ_o) specify the incident wave direction.

The calculations, although quite involved, are actually reasonably straightforward. However, considerable care must be taken to evaluate both the discrete roots and the integrands entering into the calculations of Eq. (16). As roots appear at $\nu = 1$, the integrands vary quite rapidly near $\mu = 1$, and much finer grid spacing is required for evaluation of the integral in this region, with accuracy better than one part in 10^{10} necessary to insure correct results. In addition, calculation of Eq. (23) is difficult for large values of the discrete roots, ν_j. The magnitude of ν_j increases with $\tilde{\omega}_o$. Additional roots, ν_k, appear as N is increased. Hence, the calculations become more difficult as either N or $\tilde{\omega}_o$ is increased. The details of the calculation can be found in Reference 12.

3. NUMERICAL RESULTS AND DISCUSSION

Our ultimate goal is to use measured values of the VSF to predict both reflected and underwater radiance distributions, and to investigate the sensitivity of these distributions to the form of the VSF. In this section, we present some numerical results for radiance reflected from the infinite half-space, and the radiance distribution as a function of depth in the half-space.

The first step in performing the numerical calculations is to fit a polynomial to the VSF. We use the VSF as measured by Tyler.[13] In Figure 1, we show the measured VSF with two polynomial approximations. The VSF is peaked in the forward direction by about four orders of magnitude. We see that the N=3 curve, where N is the order of the fit, is peaked in the forward direction by about a factor of 10, while the N=9 fit is peaked in the forward direction by a factor of about 150. Our computer code for the reflection from the half space presently is operative to N=9, and for the radiance as a function of depth to N=5. We are now in the process of modifying the code to handle arbitrary orders. We feel that to suitably represent the VSF, an N of 50 to 60 will be necessary.

The actual form of the VSF is, of course, not well known for angles $\lesssim 0.1°$ because of experimental difficulties. The solid curve of Figure 1 below such angles is thus an extrapolation. Various approaches to such an extrapolation procedure exist along with several suggested forms for the small angle VSF (cf. Morrison,[19] Wells,[20] and Chilton, Jones and Talley[4]). The VSF need not even be finite at $\theta = 0$.[20] Extension of the polynomial fit to N~50 will hopefully allow determination of the sensitivity of radiance distribution to small angle form.

Although computational time is minimal, the numerical codes are quite involved, hence some verification of the codes is desirable. Before discussing the reflection calculations, let us briefly mention several such checks we have made. Chandrasekhar[1] uses the discrete ordinate technique to solve the problem of reflection from a homogeneous half space for an isotropic, linear, and quadratic (Rayleigh) scattering phase function (analogous to the VSF). The present singular eigenfunction computation reproduces Chandrasekhar's results to the five figure accuracy he has published.[1] As an additional check, one can show from the reciprocity relationship[1] that the eigensolutions must obey the following symmetry laws

$$\mu_o\,\tilde{\phi}^m(-\mu,\mu_o) = \mu\,\tilde{\phi}^m(-\mu_o,\mu).$$

This relationship is satisfied to at least five figure accuracy for polynomial fits to N=9.

In Figure 2 we display backscattered radiance (i.e., $\mu = -\mu_o$, $\varphi = \pi - \varphi_o$). Hence, $\theta = 180°$ corresponds to radiance returning normal to the medium surface.) for the 3rd and 9th order fits as a function of the incident direction with an $\tilde{\omega}_o = 0.721$ (corresponding to Tyler's experimental conditions[14,15]). We observe that the backscattered intensity for the 9th order fit is much less sensitive to angle of incidence than the 3rd order fit (except near grazing incidence). We also observe that the radiance for the 3rd order fit is about 2 1/2 times that of the 9th order fit. This may be attributed to the fact that the 9th order fit is a better approximation by a factor of 15 than the 3rd order fit to the strongly forward peaked VSF. As a result, many more scatterings are necessary on the average for light to be reemitted from the half space. The average optical path is thus longer and considerably more absorption occurs for this greater path length.

In Figure 3 we present reflected radiance distributions for various incident angles for the 3rd order fit to the VSF, and in Figure 4 the 9th order fit to the VSF. We again observe the reduction in radiance from the 3rd to the 9th order fits. With the 3rd order fit, we observe maxima and

minima as a function of θ . This behavior is also observed by Chandrasekhar[1] for low-order polynomial scattering laws. The results for the 9th order fit in Figure 4 still exhibit the extrema, but the amplitudes of the extrema are not nearly as large, indicating that the radiance emitted from the half space for a highly forward peaked VSF is quite diffuse and relatively insensitive to angle of incidence. We also note that for both the N=3 and N=9 fits, the reflected intensity tends to reach a maximum and then decrease as θ approaches 90°. This phenomenon is analogous to limb darkening, and is also observed by Kaper [18] in his eigenfunction solution for the slab for an azimuthally symmetric boundary condition.

In Figure 5 we show the radiance distribution as a function of optical depth, x , from x =1 to 8, for a plane wave incident at 60° from the surface normal. Here, N=5. The curves represent only the scattered radiance at $\varphi = \varphi_0$, i.e., in the plane of the zenith, and the incident wave direction. The unscattered radiance is a decaying exponential in x at 60°. As expected for small optical depths, a maximum occurs about the incident direction. At greater depths in the medium, this maximum moves toward 0°, and the radiance distribution becomes independent of angle of incidence. The observed maximum becomes more pronounced for a given depth as the VSF becomes more strongly peaked in the forward direction, and one must go to larger optical depths before it diffuses. The rate of measured decay of the maximum about the incident angle, coupled with the ability to compute decay as a function of degree of forward peaking, may thus offer an indirect measure of this peaking.

The shift of the maximum to zero degrees is in agreement with the observations of a number of researchers. [13] The general structure of the radiance curves of Figure 5 is also in qualitative agreement with the experimental data of Tyler [14,15] . More detailed comparisons with this data necessitate a better fit to the VSF. This will be reported in a future paper.

4. CONCLUSION

In this paper, we have approached the undersea electromagnetic propagation problem from the point of view of the radiative transport formalism and the singular eigenfunction expansion technique. Our reasons for adopting this approach were detailed in the first section of the paper. While the singular eigenfunction technique is very complex mathematically, we nevertheless feel this approach has developed to the point where it is a useful computational tool for the optical physicist studying undersea propagation phenomena. In addition, this technique possesses the important advantage that it is fundamentally analytical, as opposed to numerical. This characteristic promises to allow a more direct investigation of the physical importance of the various parameters of the problem.

The singular eigenfunction technique was applied to the problem of plane wave illumination of a homogeneous, highly anisotropic, half space. This problem is of interest in a number of fields such as oceanography and remote sensing of environmental pollution. It is also a useful problem for assessing the utility of the singular eigenfunction technique --as measured values of undersea radiance exist for comparison, along with measured values of scattering phase function down to small forward angles. The results of these calculations were presented in Section 3, where the radiance distribution was calculated for reflection from the half space for 3rd and 9th order polynomial approximations to the VSF, and as a function of depth in the medium for a 5th order fit to the VSF. When the polynomial approximation is improved, it will be possible to compare the depth distributions more closely with, for example, the measurements of Tyler. [13]

The above problem corresponds essentially to passive source sensing configurations. Active source systems such as lasers are frequently of great utility, and consequently consideration of this group of problems is of considerable interest. In addition to the vastly different boundary conditions associated with such problems, the coherence characteristics of the types of problems differ significantly. Garrettson[21] has recently solved the pencil beam problem in a homogeneous, isotropic half space by a Green's function approach similar in spirit to our singular eigenfunction technique. The pencil beam approach is fundamentally an intensity transport approach and thus only contains coherence effects implicitly through the optical parameters of the transport equation, such as the VSF. As a result, it does not completely contain or describe interference effects. However, we are presently considering modifications and extensions of the methods presented in this paper employing the formalism developed by Garrettson.[21] With these techniques, one should be able to analyze some aspects of such coherent systems from a radiative transport viewpoint.

In this paper we have formulated the undersea optical propagation problem in terms of the radiative transport equation and investigated the applicability of this approach. The radiative transport equation was solved using the singular eigenfunction expansion technique. Sample calculations were presented for reflected radiance and radiance distribution in the half space, and extensions of the work were discussed. The results indicate that the radiative transport approach offers a useful analytical technique for investigation of undersea optical propagation problems.

ACKNOWLEDGMENTS

The authors are indebted to E.L. Butler of the Cornell Aeronautical Laboratory for his conscientious development of the computer codes and numerical calculations which were so essential to the completion of this work.

FOOTNOTES

+ Supported in part through internal research funds of the Cornell Aeronautical Laboratory, Inc.

1. S. Chandrasekhar, Radiative Transfer, (Dover, New York, 1960).

2. B. Davison, Neutron Transport Theory, (Oxford, New York, 1958).

3. D.L. Feinstein and V.L. Granatstein, "Scalar Radiative Transport Model for Microwave Scattering from a Turbulent Plasma," Phys. Fluids, 12, 2658, (1969)

4. F. Chilton, D.D. Jones and W.K. Talley, "Imaging Properties of Light Scattered by the Sea," JOSA, 59, 891 (1969).

5. C. Funk, "Monte Carlo Simulation of the Underwater Light Field Distribution from a Point Source," Naval Undersea Warfare Center NUWC TN 138 (September 1968).

6. K.M. Case and P.F. Zwiefel, Linear Transport Theory, Addison-Wesley Publishing Co., (Palo Alto, 1967).

7. N.M. McCormick and I. Kuscer, "Bi-Orthogonality Relations for Solving Half-Space Transport Problems," J. Math. Phys., 7, 2036 (1966).

8. S. Pahor, "A New Approach to Half-Space Transport Problems," Nuc. Science and Engin., 26, 192 (1966).

9. A description of some problems associated with aerial remote sensing of water pollution may be found in:

   F.B. Silvestro, "Quantitative Remote Sensing of Water Pollution," "Proceedings of the 1969 Conference of the Institute of Environmental Sciences," 611 (1969).

   K.R. Piech, "How Aerial Photographs Can Identify and Measure Pollutants," Public Works, 101, 68 (March 1970).

   K.R. Piech, "Aerial Detection and Analyses of Water Pollution," (to be published in Water and Wastes Engineering).

   K.R. Piech, F.B. Silvestro, and R.J. Gray, "Industrial Effluent Diffusion in Rivers: A New Approach to Theory and Measurement," "Proceedings of the 1969 Conference of the Institute of Environmental Sciences," 164 (1969).

10. D.L. Feinstein and K.R. Piech, "A Light Transport Problem in Water Pollution," Proceedings of the 1970 Conference of the Institute of Environmental Sciences, 319 (1970).

11. D.L. Feinstein and K.R. Piech, "Multiple Scatter Effects in Remote Sensing of Environmental Pollution," (submitted for publication).

12. F.L. Butler, D.L. Feinstein and A. Leonard, "Numerical Techniques for the Solution of the Scalar Transportation Equation for a Highly Anisotropic Scattering Law," (to be published).

13. S.Q. Duntley, "Light in the Sea," JOSA, 53, 228 (1963).

14. J.E. Tyler, "Scattering Properties of Distilled and Natural Waters," Limnology and Oceanography, 6, 451 (1961)

15. J.L. Tyler, "Radiance Distribution as a Function of Depth in an Underwater Environment," Bull. Scripps Inst. Oceanography, 7, 363 (1960).

16. K.M. Watson, "Multiple Scattering of Electromagnetic Waves in an Underdense Plasma," J. Math. Phys., 10, 688 (1969).

17. P.L. Stott, "A Transpo t Equation for the Multiple Scattering of Electromagnetic Waves by a Turbulent Plasma," J. Phys. A. 675 (1968).

18. H.G. Kaper, J.K. Shultis and J.G. Veninga, "Numerical Evaluations of the Slab Albedo Problem Solution in One-Speed Anisotropic Transport Theory," Report TW-65, Mathematics Institute, University of Groningen, The Netherlands (1969).

19. R. Morrison, "Studies on the Optical Properties of Seawater at Argus Island in the North Atlantic Ocean and in Long Island and Block Island Sounds," Thesis, New York University (June 1967).

20. W.W. Wells, "Loss of Resolution in Water as a Result of Small-Angle Scattering," JOSA, 59, 686 (1969)

21. G.A. Garrettsen, "Green's Functions for Multidimensional Neutron Transport in a Slab " Thesis, Stanford University (August 1969).

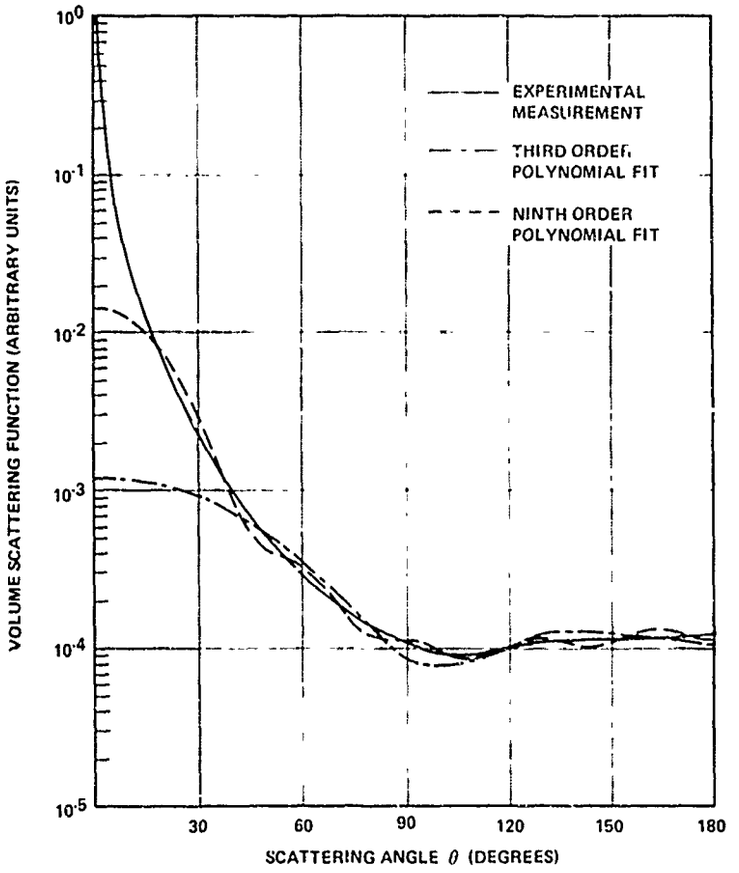

Figure 1 VOLUME SCATTERING FUNCTION

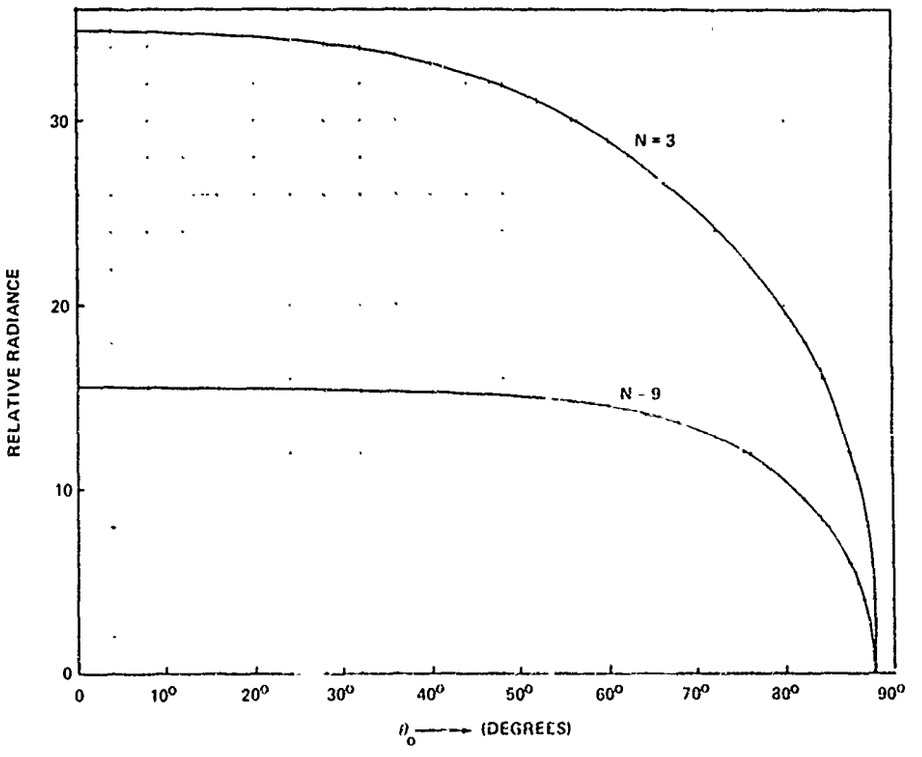

Figure 2 RADIANCE BACKSCATTERED FROM THE HALF SPACE INTO THE INCIDENT DIRECTION ( ) AS A FUNCTION OF INCIDENT DIRECTION

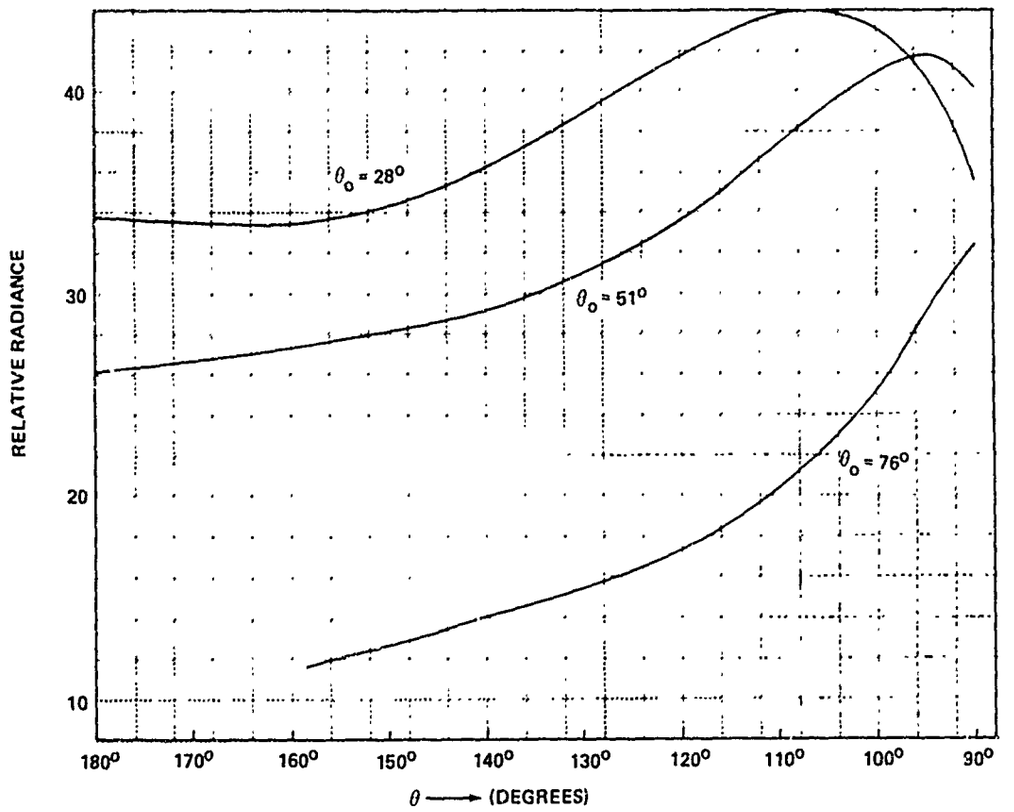

Figure 3 REFLECTION FROM HALF SPACE - 3rd ORDER POLYNOMIAL (N = 3)

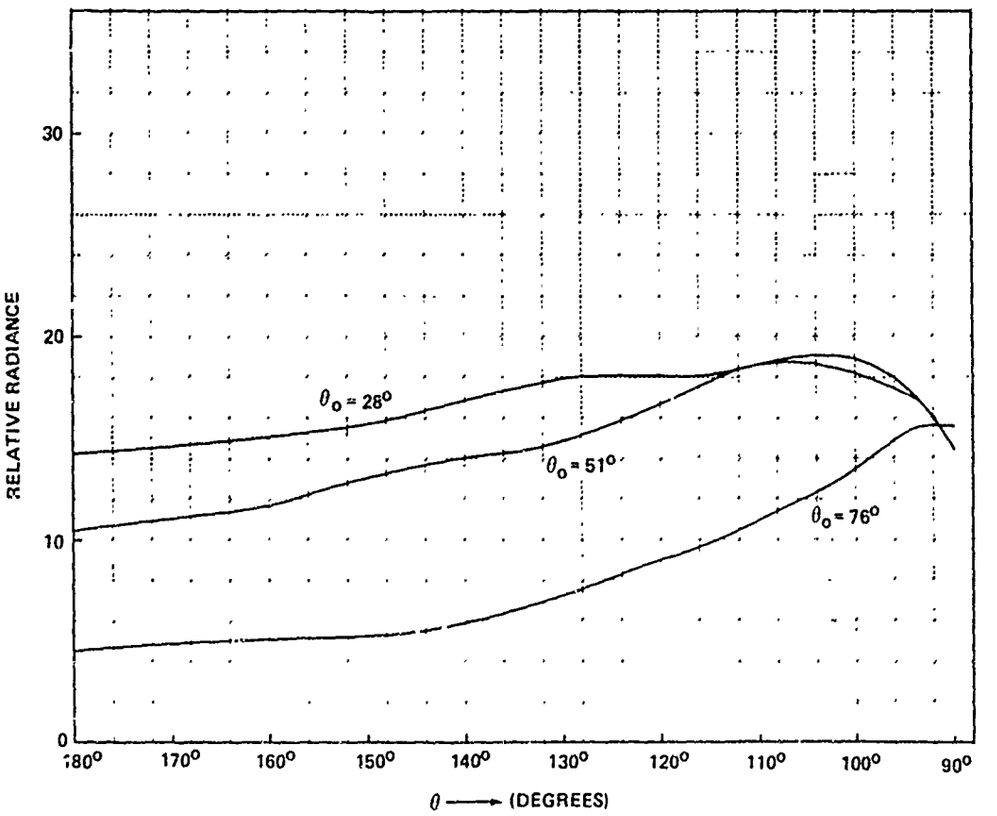

Figure 4 REFLECTION FROM HALF SPACE - 9th ORDER POLYNOMIAL (N = 9)

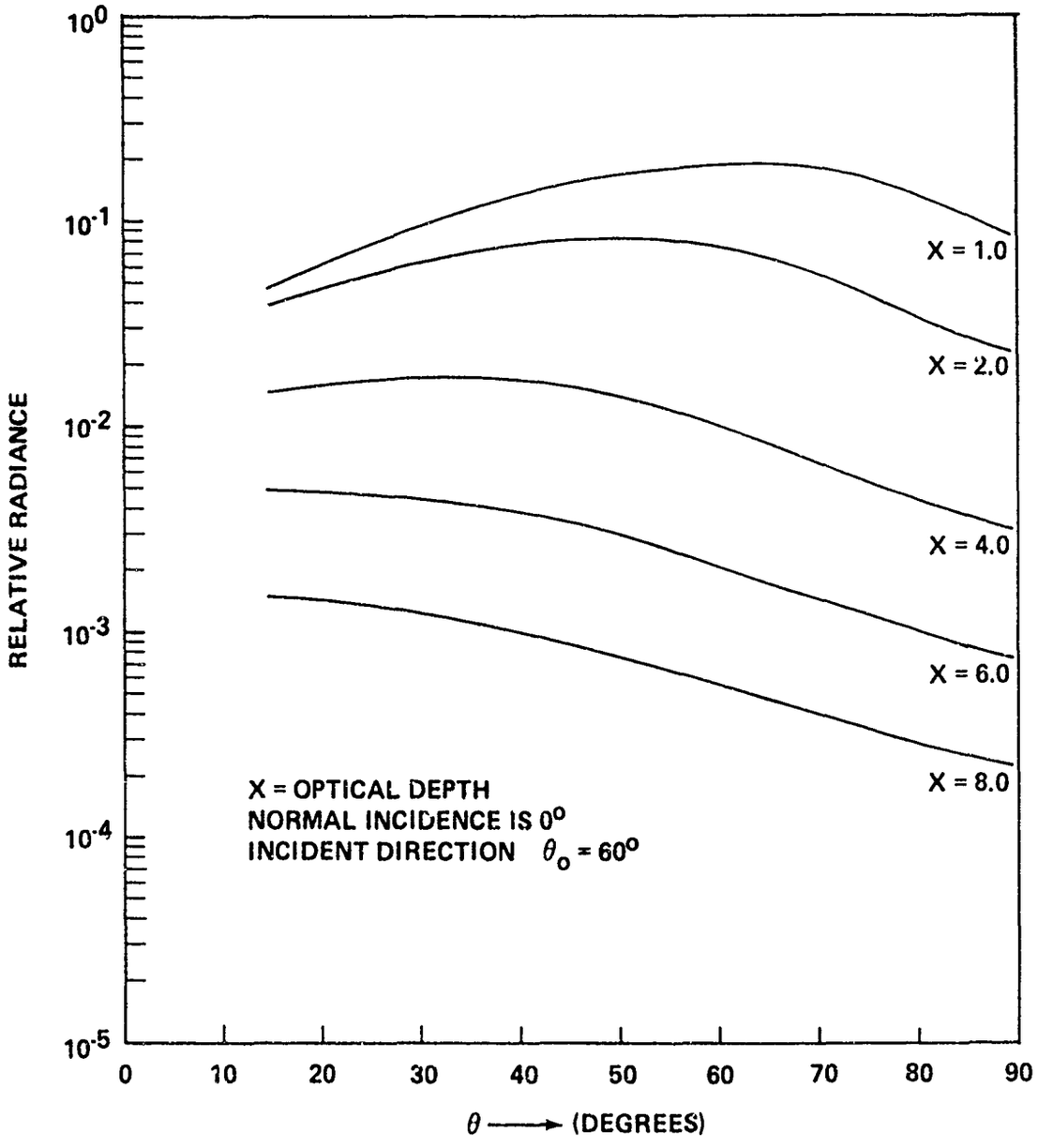

Figure 5 RADIANCE DISTRIBUTION AS A FUNCTION OF DEPTH - 5th ORDER POLYNOMIAL (N = 5)

OPTICAL ABSORPTION AND TURBULENCE-INDUCED NARROW-ANGLE FORWARD SCATTER IN THE SEA

by

Richard C. Honey and Glenn P. Sorenson

Stanford Research Institute
Menlo Park, California

SUMMARY

One of the most fundamentally limiting optical parameters of sea water is the volume absorption coefficient. In typical oceanic waters in which the absorption and scattering coefficients are roughly the same, it has not been a simple matter to measure the attenuation coefficient independent of scattering. A new instrument has been developed to do just this. Basically, it consists of a point source of light and an irradiance detector at a known distance from the point source.

Another parameter in addition to absorption and particulate scattering that can limit the performance of underwater imaging systems is due to fluctuations in index-of-refraction, or optical turbulence. Such fluctuations, resulting from fluctuations in temperature or salinity, occur in the ocean due to a variety of natural causes. Several techniques have been employed to demonstrate the phenomena, including very-narrow forward-angle scattering measurements, propagation of small laser beams through sea water, and motion pictures of back-lighted resolution targets.

OPTICAL ABSORPTION AND TURBULENCE-INDUCED NARROW-ANGLE FORWARD SCATTER IN THE SEA

Underwater visibility is limited by absorption of light by the seawater and by the particles in the water and by the loss of resolution resulting from scattering by particles in the water and from refractive index inhomogeneities in the water. These two limiting factors are the subject of this paper.* The authors gratefully acknowledge the support of the following agencies for portions of the work reported:

1. Naval Undersea Research and Development Center, San Diego, California and the U.S. Navy Deep Ocean Technology Program.
2. Advanced Sensors Office, Advanced Research Projects Agency, Washington, D.C.

ABSORPTION

General

Absorption is apparently a fundamentally limiting factor. Light absorbed by the water and by particles in the water is transformed to heat and is lost as information. Absorption mean free paths for blue-green light range from a few tens of centimeters or less in dirty harbors to tens of meters in very clear ocean water. At other optical wavelengths, absorption mean free paths are much shorter. The fundamentally limiting nature of absorption is often overlooked. For example, if a 1000-Joule pulse is transmitted through very clear water (absorption mean free path = 30 meters), and no scattering whatever occurs, then only a single photon will remain at a range of 1.5 km. Each tenfold increase in transmitted energy adds only 70 m to the range. Imaging requirements and signal-to-noise considerations, as well as target characteristics and scattering in the water, increase the energy requirements of real systems by many orders of magnitude, even in the clearest ocean waters.

The Absorption Meter

Since absorption is the most important single optical characteristic of water, we have developed a simple instrument with which to measure it. The principle of the absorption meter (a-meter) is shown in Fig. 1, a plot of the logarithm of the detector power as a function of range as would be measured by a hypothetical transmissometer or α-meter consisting of a collimated beam source and a receiver with a variable acceptance angle and an aperture very much larger than the beam diameter. As the acceptance angle θ closely approaches zero, the measured power is shown by the lower curve, $e^{-\alpha r}$, where $\alpha = a + s$, and s is the conventional scattering coefficient. As θ increases, so does the measured power. When θ approaches 180°, the power will closely approach e^{-ar}, because all the unabsorbed, forward-scattered photons are measured. The difference in slope between the $\theta = \pi$ and e^{-ar} lines represents the fact that some back-scattered photons are not collected and that the forward-scattered photons travel further than r to reach the detector. These photons, therefore, have a higher probability of being absorbed than if no scattering took place. That is, if no scattering took place, the $\theta = \pi$, the e^{-ar} and the $e^{-\alpha r}$ lines would coincide.

The a-meter itself may be visualized as a spherical system consisting of a point source of light at the center and an irradiance meter positioned as a small section of a sphere of radius r around the source. (The use of a flat, cosine detector instead of a collector shaped as a section of a sphere of radius r introduces negligible error if the area of the detector is very small compared to $4\pi r^2$.) The power at the detector will be approximately proportional to the power at the source (within the bandwidth of the detector and filter, which should be narrow compared to the bandwidth of a water column of length r), proportional to the area of the detector, inversely proportional to $4\pi r^2$, and proportional to e^{-ar}.

There will be a small error due to the scattering in the water, which increases the effective distance traveled by the flux to the detector. That increase in distance depends upon two factors: the scattering coefficient (i.e., the fraction of the flux likely to be scattered between the source and the detector) and the volume scattering function (i.e., the angles over which the scattered flux will be scattered). With reasonable instrument dimensions, this increase in distance and, consequently, the error in the measurement of a are low. For r = 0.5 m, the error in the measured value of a due to scattering is less than 1 percent for likely values of s ($s \leq 0.5$ ln m^{-1} or ≤ 2.2 dB/m) and less than 10 percent even in waters with a scattering coefficient as large as 2 ln m^{-1} or 8.7 dB/m. (Appendix A of Ref. 1). It should be pointed out that these are only errors if they remain uncorrected. They may also be considered as second-order corrections that may be applied to obtain more exact values of a. However, it seems likely that errors of even a few percent can be tolerated in most normal uses.

---

*A third limiting factor commonly dominates underwater imaging system performance: the loss of target contrast that results from the veiling luminance (in the case of daylight illumination) and from backscattering of source light into the detector by the water and particles in the water. Contrast-limiting phenomena and the potential ways of overcoming this limitation, while interesting subjects, are not treated in this paper.

In summary,

$$P_d = P_o A \left(4\pi r^2\right)^{-1} e^{-\underline{a}r} ,$$

where

P_d = Power incident on the irradiance detector (within the bandwidth of the detector and filter)

P_o = Power output of the point source (within the bandwidth of the detector and filter)

A = Area of the detector

$\underline{a}$ = Absorption coefficient (in units of reciprocal length).

This instrument has the important characteristic that it can be self-calibrating. By keeping the light source constant and by simply changing the range, r, of a single detector and noting the new power P_d, the device can be calibrated using the expression

$$a = \frac{2 \ln \frac{r_1}{r_2} + \ln \frac{P_{d_1}}{P_{d_2}}}{r_2 - r_1}$$

Physical Realization

The second generation $\underline{a}$-meter system consists of a rigid underwater frame, on which are mounted two detectors and two self-contained light sources and a deck box for controls. The underwater frame is constructed of square-cross-section black-anodized aluminum tubing fastened at the corners with bracing plates (see Fig. 2). The frame, triangular-shaped for minimum weight and maximum rigidity, is 7 ft. long on each side. The frame rigidly supports two identical free-running pulsed light sources and two photodiode detectors. The bottom light source (Fig. 2), used for the $\underline{a}$ measurement, is positioned between the two detectors to give a precisely-known path difference. If increased sensitivity is required, this path difference is lengthened. The top light source is positioned exactly equidistant from each photodetector, allowing changes in detector characteristics to be closely monitored if they occur. The presence of fish, seaweed, etc., is also indicated by variations in the signals from the upper light source. Pulsed light sources are used in this instrument because they can be much brighter than CW sources, (hence can operate in brighter background conditions), and because they attract far fewer fish. Each light-source system (Fig. 3) consists of an aluminum pressure vessel and an aluminum wand with the xenon strobe lamp supported by polyurethane. The input to the lamp is about 20 J/pulse of 0.5 ms length. The pressure vessel houses the light-source battery power supply, high-voltage pulser, and pulse-frequency oscillator. This circuitry is internally mounted to a rigid framework attached at one end to the pressure-container cover.

The photodetectors are United Detector Technology PIN-10 silicon photodiodes. Each detector is covered with a Lambertian-scattering opal glass diffuser, a blue-green Wratten #61 spectral filter, and a Corning #1-56 infrared blocking filter for calibrations in air. The photodiode and the filter stack are potted in transparent polyurethane, bonded both mechanically and electrically to waterproof male electrical connector (see Fig. 4). The resulting photodiode is strapped to an aluminum plate that may be moved along the side of the triangular frame. The photodiodes have been statically tested to pressures equivalent to 1000 ft. with no damage. Electrical connection with the Deck box is through a single coaxial RG-58 U 50-Ω cable. A female waterproof connector terminates the underwater end of this cable and connects directly to the photodiode. Diode bias voltage supplies of -15 Vdc and 1000-Ω output load resistors are located in the Deck Box; the coaxial cable carries bias to and signal from the photodiode. The two coaxial cables for the photodiodes are the only electrical connection between the Deck Box and the underwater frame.

The Deck Box (Fig. 5) contains the photodetector circuitry and the preamplifier, logarithmic, and digital-logic module circuitry necessary for the real-time signal processing of the absorption coefficient data. The absorption coefficient analog voltage is measured by a digital voltmeter (DVM) with a digital readout display. The signal may also be used to drive a chart recorder to obtain a graphic display of $\underline{a}$ versus time or some other parameter.

The instrument has been tested in the relatively turbid waters of Monterey Bay and the clear oceanic waters of the Pacific (Hawaii) and the Atlantic (Bahamas). Its use will enable realistic estimates to be made of the maximum underwater ranges various optical systems can achieve in the various different ocean waters, and will enable comparisons to be made among instruments and systems tested in different waters, or at different times in the same waters.

SCATTERING

General

The second topic of this paper concerns the scattering phenomena that result in loss of image resolution: scattering by the water and by particles in the water, and by refractive index inhomogeneities in the water. The narrow-angle forward scattering by the water molecules is negligibly low, so only scattering by particles and by refractive index inhomogeneities are of present interest to us. Scattering by particles has been well described by Mie[2] and others.[3] It can be measured at narrow angles by an instrument that we describe later in connection with optical turbulence.

Fluctuations in refractive index (optical turbulence) are commonly present in the atmosphere producing, for example, the twinkling of stars. In the atmosphere, optical turbulence is caused principally by temperature differences associated with individual (mechanically) turbulent eddies. We have now found that optical turbulence also occurs in the sea.

Measurement of Scattering

Figure 6 illustrates a portable, relative short path length version of an apparatus designed to measure very narrow angle forward scattering. It consists of a helium-neon laser ($\lambda = 0.7\mu$) and a long-focal-length camera focused to infinity for the laser wavelength. The laser and camera are mounted on a long, rigid underwater optical bench pointing towards each other. The instrument is quite flexible: Two beam diameters or beam divergences are available from the laser and two focal lengths are available for the camera. Table I summarizes these characteristics. The optical bench can be suspended from spar buoys on the surface to minimize coupling to surface waves. Optical scattering that occurs between the laser and the camera broadens the image on the film plane of the camera. Microdensitometry of the developed film provides intensity profiles across the images, from which scattering angle distributions were calculated. The resolution limit of the system in water was about 50 μrad: this was measured both in air and in a clean, thermally homogeneous swimming pool.

Significant very narrow-angle scattering, as shown in Figure 7, was measured in experiments made with the instrument. In San Francisco Bay the path between the laser and the camera was 68 cm; in the offshore test the path was 183 cm. In both cases the instrument was suspended horizontally, about 1.6 m below the surface (where water well mixed by wave action would be expected). In both cases the scattering was found to be about 100 μrad. Subsequent measurements have been made in a variety of waters over path lengths to about 5 meters.

TABLE I

Characteristics of Narrow-Angle Forward Scattering Device				
Laser beam divergence (full width to $1/e^2$ points)	Camera focal length (mm) Air	U/W	Min. Spot Size (full width to $1/e^2$ points) (mm)	U/W Angular Sensitivity (mm/mrad)
0.8 mrad	400 1200	535 1605	0.32 mm 0.96 mm	0.53 1.6
0.08 mrad (10X telephoto)	400 1200	535 1605	0.032 mm 0.096 mm	0.53 1.6

Single scattering from large particles of diameter d produces scattering angles of the order of λ/d radians; therefore particles of about 7-mm diameter are needed to produce the measured 100-μrad scattering. However, this is at least an order of magnitude larger than the size of the largest particles observed to be present in the water. (Actually only a relatively few particles in the sea are in the range of 10-100 μm; the remainder of the particles apparently increase logarithmically in number with decreasing size.[4]) It was hypothesized that, since the measured scattering was not produced by particles, it must have been produced by refractive index variations in the water.

Optical turbulence in the ocean can be expected on the basis of thermal gradients normally present in the water (as near the surface), salinity gradients normally present in the water (such as due to evaporation or rainfall), the mixing of different water masses, and the slow thermal and saline diffusion rates in water. Changes in temperature or salinity can be simply related to changes in index-of-refraction.[5] Adequate modeling of these effects to describe optical turbulence has not yet been achieved. (In fact, fully adequate modeling of optical turbulence in the atmosphere has not yet been achieved.)

We have recently photographed optical turbulence in the ocean. One technique photographs a back-lighted resolution target. The movies were taken at a range of 1.35 m in waters showing extreme optical turbulence in Hawaii, and much more moderate conditions in the Bahamas. For calibration, the widths of the bars in the middle of the left-hand column correspond to about 1 milliradian. The other technique photographs the image of a small-diameter laser beam incident on a diffuse calibrated target. The sequence in the movie shows the beam from a small Helium-Neon laser (1.4 mm wide to $1/e^2$ points) over a path of 1.1 m in the extremely turbulent conditions encountered in Hawaii. In addition, some scenes showing typical underwater layering and turbulent mixing as made visible using dye tracers will be shown.

We have thus shown that optical turbulence can limit the resolution achievable by undersea imaging systems. Our present investigations involve measurements of the size distributions and refractive index gradients of turbulent eddies in typical oceanic waters, and modeling the effects of this optical turbulence on optical imaging systems.[6]

REFERENCES

1. Gilbert, G.D. "Optical Absorption Meter" SRI Project 7440. Contract N 60530-68-C-1423, April 1969.

2. Mie, G. Ann. Physic, Vol. 25, 377, 1908.

3. Van de Hulst, H.C. "Light Scattering by Small Particles" John Wiley & Sons, 1957.

4. Jerlov, N.G. "Optical Oceanography" Elsevier Publishing Company Amsterdam, 1968.

5. McNeil, Gomer T. "Optical Fundamentals of Underwater Photography" Photogrammetry, Inc. Rockville, Maryland, 1968.

6. Chilton, F., D.D. Jones and W.K. Talley "Imaging Properties of light Scattered by the Sea" Journal of the Optical Society of America. Vol. 59, NO, 8, Part 1, pp. 891-898, August 1969.

7. Sorenson, G.P. and R.C. Honey "Instrumentation for Measuring the Visibility-Limiting Characteristics of Seawater" Society of Photo-optical Instrumentation Engineers. Seminar Proceedings, Vol. 12. "Underwater Photo-optical Instrumentation Applications", February 5-6, 1968.

8. Sorenson, G.P. and R.C. Honey "Underwater Visibility Meter Concept Study" SRI Project 6572, Contract N 60530-67-C-0891, February 1968.

9. G. Sorenson and R.C. Honey "Using Lasers for Undersea Studies" Ocean Industry. Vol. 3, NO. 10, pp. 51-54. October 1968.

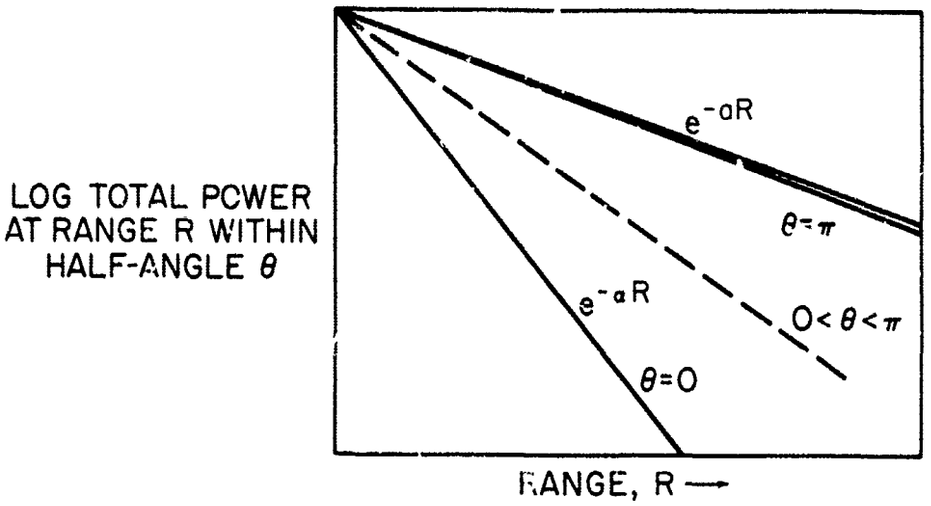

Fig.1 Absorption meter concept

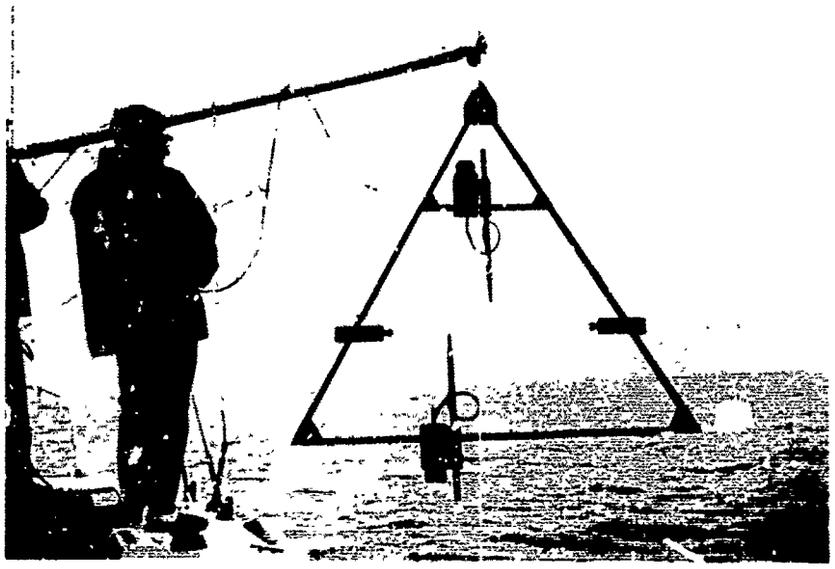

Fig.2 Absorption meter

Fig.3 Underwater strobe light sources

Fig.4 Underwater irradiance detectors

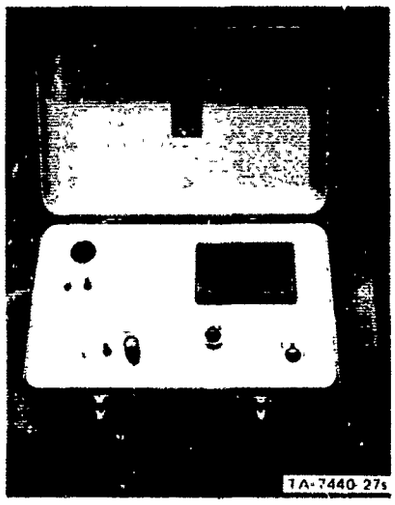

Fig.5 Deck control box

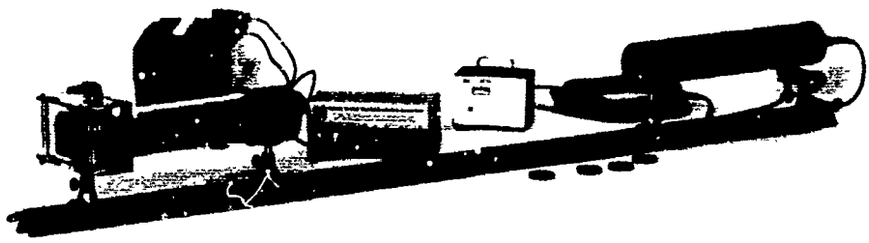

Fig.6 Device for measuring narrow-angle forward scatter

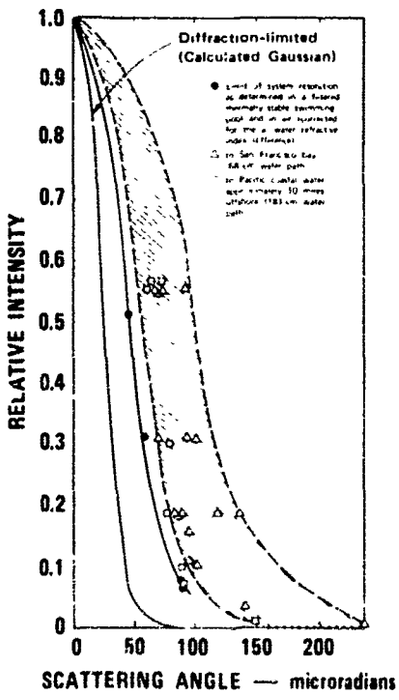

Fig.7 Very narrow-angle forward scattering measurements

DISCUSSION ON PAPERS PRESENTED IN SESSION VII
(Theorical considerations)

Discussion on paper 36 : "Loss of optical resolution in sea water by multiple small-angle scattering", by W.H. WELLS .

Prof. TYLER : I would like to ask a question regarding the extent of scattering function. Can you measure the scattering function to zero direction ?

Dr. W.H. WELLS : The testing diagram we used, has some of the highest frequencies, something like the reciprocal of 25 seconds of arc . But this, is limited only, by the manufacturing cost of the testing diagram . There was not any other limitations as we experimented with this new instrument .

Discussion on paper 37 : "The theory of light scattering in the sea", by R.C. HONEY .

Dr. W. CONDELL : What was the dimensionality for your Monte-Carlo calculation ?

R.C. HONEY : The memory could extract the angle of propagation of a very large number of photons propagating in the same direction, to determine the differences of direction in function of the distance from the axis .

Dr. W. CONDELL : Have you determinate experimentally this parameter "éta" ?

Dr. R.C. HONEY : Yes, I did in every point !

Discussion on paper 38 : "Transport analysis of optical propagation in undersea environment", by D.L. FEINSTEIN and K.P. PIECH

Dr. A. WIRGIN : - What are the boundary conditions that you used ?

Dr. K.P. PIECH : - In addition to plane wave illumination at various angles, we allowed for no refractive effects - i e the infinite half-space above the scattering and absorbing-half space was assumed to have the same index of refraction, but with no absorption or scattering allowed .

Discussion on paper 39 : "Optical absorption and turbulence induced narrow-angle forward scatter in the sea", by R.C. HONEY and G.P. SORENSON .

Dr. A. WIRGIN : - I have two questions : 1 - How do you filter out to have the ambiant daylight in your recepter . 2 - You show a recepter in case in plastic . Do you use a synchronous detection system ?

Dr. R.C. HONEY : - Ambiant daylight is a problem . There are two ways : One of course uses the rolative narrow band filter but that cuts down the amount of energy . The second one uses a pulsed source, much more brighter than the sun . Then the noise is out . Down to 50 or 100 m depth we used a c.w. light source much less bright than the pulsed source and we still had noise problems .

IMAGE DEGRADATION OVER SEAWATER PATHS - A REVIEW

by

J.R. Zaneveld, R. Hodgson, and G.F. Beardsley, Jr.

Dept. of Oceanography, Oregon State University
Corvallis, Oregon 97331 U.S.A.

SOMMAIRE

Lorsqu'un objet situé sous l'eau est vu à travers un système optique immergé formant une image, la qualité de l'image obtenue est toujours dégradée par comparaison avec une image de géométrie située dans l'air. Cette dégradation est le résultat complexe de la diffusion créée par l'eau, des particules en suspension dans cet élément, de l'absorption de la lumière le long de la trajectoire de propagation, et de la géométrie du lieu d'observation. Au cours de ces dernières années, on a consacré une attention considérable à l'expression et à la prédiction de cette dégradation du point de vue de la théorie des communications plutôt que de celui de la physiologie de l'observateur. Les auteurs retracent l'introduction en optique hydrologique, des idées relatives à la théorie des communications, et comparent les divers résultats expérimentaux et théoriques dont il est fait état dans la littérature scientifique. Ils consacrent une attention particulière à trois communications récentes traitant de la prédiction théorique de la fonction de transfert de la modulation par l'eau de mer : J.R.V. Zaneveld et G.F. Beardsley Jr., Josa 59 (4) ; W.H. Wells, Josa 59 (6) ; et F. Chilton, D.D. Jones et W.K. Talley, Josa 59 (8). Ces trois groupes de chercheurs ont eu recours à des techniques analytiques, numériques, et à la technique de Monte Carlo. Les auteurs comparent ces diverses méthodes, leurs limitations ainsi que les résultats auxquels elles ont abouti, et examinent leurs possibilités d'application à des problèmes typiques de visualisation sous-marine.

IMAGE DEGRADATION OVER SEAWATER PATHS - A REVIEW*

by

J. R. V. Zaneveld, R. Hodgson, and G. F. Beardsley, Jr.
Dept. of Oceanography, Oregon State University, Corvallis, Oregon 97331 U.S.A.

SUMMARY

When an underwater object is viewed by a submerged image forming optical system, the quality of the image is always degraded in comparison with the same geometry in air. This degradation is a complicated function of the scattering of the water, the particles in the water, the absorbtion of light along the path, and the geometry of the viewing situation. In recent years considerable attention has been given to expressing and predicting this degradation in the concepts of communication theory instead of the physiology of the observer. This paper reviews the introduction of the ideas of communication theory into hydrological optics, and compares the various experimental and theoretical results that have appeared in the literature. Particular attention is given to three recent papers dealing with the theoretical prediction of the modulation transfer function of seawater: J. R. V. Zaneveld and G. F. Beardsley, Jr., J. Opt. Soc. Amer. 59, 378(1969); W. H. Wells, J. Opt. Soc. Amer. 59, 686(1969); and F. Chilton, D. D. Jones and W. K. Talley, J. Opt. Soc. Amer. 59, 891(1969). These three papers utilize analytic, numerical, and Monte Carlo techniques. The methods, limitations, and results of each paper are compared and the applicability of each approach to typical submarine viewing situations is discussed.

INTRODUCTION

The behavior of light in seawater is governed by its electromagnetic properties. This behavior cannot be predicted on a theoretical basis due to the extremely complicated electromagnetic structure of the materials suspended and dissolved in seawater.

Therefore, any prediction of light behavior in seawater is based on some empirically defined functions which can be considered known. These functions, the volume scattering function and the extinction coefficient, are known as the inherent optical properties of seawater as they are independent of the actual light field. In the ensuing discussion the volume scattering function will be denoted by $\beta(\gamma)$. Jerlov (1968) defines $\beta(\gamma)$ as the radiant intensity from a volume element in a direction γ per unit of irradiance on the volume and per unit volume. The total scattering coefficient b is then given by:

$$b = \int_0^{4\pi} \beta(\gamma)\, d\Omega \qquad (1)$$

where Ω is a solid angle.

The extinction coefficient, c, is the internal attenuance of an infinitesimally thin layer of the medium normal to a beam of light divided by the thickness of the layer.

The scatterers in seawater fall in two classes; those of biological origin and those of geologic origin. The biological particles have a refractive index very similar to that of seawater. A significant fraction of these particles are usually much larger than the wavelengths of visible light. In such a case scattering tends to be peaked very strongly in the forward direction. The particles of geologic origin have refractive indices substantially different from water, but are usually smaller than the biological particles, and hence exhibit scattering that is less strongly peaked in the forward direction. (Duntley, 1963; Pak et al., 1970). Pure seawater, free of all suspensoids, exhibits a volume scattering function approaching that of pure water (Morel, 1966); the backscattering is almost as important as the forward scattering. The intensity of light scattered by pure seawater in the forward region is only a small fraction of that scattered by a typical seawater sample containing suspensoids. The light transmission properties of seawater thus depend greatly on the number, size and type of suspensoids present.

A point source of light is the most elementary light source. If the response of an imaging system in seawater to this light source is known, then the response to all other light sources can be predicted, provided the light source is incoherent and assuming that seawater acts as a linear operator with respect to contrast. Thus, a target may be broken down into several parts, and each part can be acted upon independently by the seawater. The final image will then be the sum of the several parts. The quantity which may be summed is the contrast.

*This work was supported by the Office of Naval Research Contract N00014-67-A 0369-0007

The problem of the theoretical prediction of image degradation in seawater then is to relate the inherent optical properties to the degradation of a point source of light which in turn can be related to the line source response function and to the modulation transfer function.

THE POINT SOURCE RESPONSE FUNCTION

If the quite reasonable assumption of linearity of contrast is made, the problem of describing the information carried by light in seawater is greatly simplified as linear theory may then be successfully applied (O'Neill, 1963). Basic to this theory is the response of a linear system to an elementary source. This response is in various fields called the impulse response, Green's function, or spread function. In this paper we will call the image degradation by a seawater path to the elementary point source of light the point source response function, or more simply the response. If this function is known, the response of seawater to all light sources may be predicted by convolving the object with the point source response to obtain the image.

In our discussion, we will use the following viewing situation (figure 1). Let the coordinates in the object plane be given by x' and y'; and denote the distance from the object plane perpendicular to the object plane by z. In the case of rotational symmetry about the Z axis the distance from the origin in the object plane is denoted by r.

An observer located at a point B on the Z axis when looking at a point in the object observes a light intensity. This observed intensity varies with direction of observation, where each observation direction corresponds to a location in the object plane. Rather than use the local coordinates at the observation point, we will use the coordinates of the object plane. B(x,y,z) then is the light intensity observed a distance z which appears to come from a point x', y' in the object plane.

The point source of light, PS, is defined by:

$$PS(x',y') = \delta(x',y') = 1 \quad \text{for } x'=0, y'=0$$
$$= 0 \quad \text{elsewhere}$$

The response at a distance z from the point source is P(x,y,z).

We then have:

$$B(x,y,z) = \int_{-\infty}^{+\infty}\int P(x'-x, y'-y, z)\, A(x',y',o)\, dx'\, dy' \qquad (2)$$

Where A (x',y',o) is the object, and B(x,y,z) is the image.

THE MODULATION TRANSFER FUNCTION AND THE LINE SOURCE RESPONSE FUNCTION

When testing a linear optical system if a test pattern is used which has spatially sinusoidal variations of intensity, it is found that the output is usually a sinusoidal pattern also, but with changed amplitude and phase (Coltman, 1954). Thus, when a sinusoidal input is used, a strict analogy holds between optical systems and electrical transducers. Clearly, once the response of the system to all spatial frequencies is known the output of the system can be predicted by analyzing the input into its sinusoidal Fourier components and multiplying by the known response and summing the results.

We define the modulation transfer function, MTF(k, z), as the amplitude of the sinusoidal response to a chart with sinsusoidally varying spatial frequency k and unit amplitude at a distance z from the observation plane. We must realize that the MTF does not take into account any possible phase shift of the response with respect to the target.

For most image transmission systems, the MTF is dependent on the wavelength, and seawater systems are no exception. For reasons of notational convenience, the explicit dependence of the various optical properties upon wavelength is not shown in the discussions which follow. However, the reader should keep this dependence in mind and realize that the MTF is not defined for a non-monochromatic case. Note also that the MTF of a seawater system is unaffected by the presence or absence of scattered daylight (spacelight). This spacelight may, however, affect the performance of the final image-detecting equipment. For this reason it can be useful to compute the penetration and the scattering of submarine daylight in the same water types for which the MTF's were calculated, as in Beardsley and Zaneveld (1969).

One previous method of predicting underwater visibility (Duntley, 1969) requires only two measurements of the optical properties of seawater, the beam extinction coefficient c and the diffuse attenuation. With these two values, the range of detectability of a target of known size and contrast can be determined. It is not possible to apply these charts (in their present form) to optical systems other than the human eye. This method also fails to provide information on the resolution of image details. Both of these shortcomings are eliminated when the MTF is known.

Instead of using sinusoidal bar charts to obtain the MTF, it is possible to use the response to a line source of light. The line source of light can be represented by a sequence of delta functions along x'=o in the object plane. This is denoted by $\delta(x')$. The line source response function, L(x, z) is the observed intensity at Z which appears to come from a point x' in the object plane. We can use the fact that the delta function contains all spatial frequencies with equal amplitude, so that its Fourier transform is 1 for all frequencies. Multiplying the Fourier transform of the delta function input by the modulation transfer function then gives the Fourier transform of the line source response function. We thus have:

$$\mathcal{F}[\delta(x')]\,MTF(k,z) = \mathcal{F}[L(x,z)] \qquad (3)$$

Where $\delta(x)$ is the delta function defined by:

$$\delta(x) = 1 \quad \text{for } x = 0$$
$$= 0 \quad \text{elsewhere}$$

and L (x,z) is the response to the delta function input.

The Fourier transform of a delta function is 1 for all k so that:

$$MTF(k,z) = \mathcal{F}[L(x,z)] \qquad (4)$$

This may be inverted to give:

$$L(x,z) = \mathcal{F}^{-1}[MTF(k,z)] \qquad (5)$$

This equation is basic to the prediction of underwater visibility. Since the response to a line source of light is a function only of the volume scattering function and the extinction coefficient of seawater, it then follows that the MTF of seawater is also only a function of these inherent optical properties. Simple geometry then permits us to relate the line and point source response functions as follows (Jones, 1958):

$$L(x,z) = \int_x^\infty P(r,z)\,(r^2-x^2)^{-1/2}\,r\,dr \qquad (6)$$

This equation can be inverted:

$$P(r,z) = -\frac{1}{\pi}\frac{d}{dr}\int_r^\infty \frac{L(x,z)\,r}{x(x^2-r^2)^{1/2}}\,dx \qquad (7)$$

If we now replace L(x,z) in equation (4) by expression (6) and reverse the order of integration we obtain an expression for the MTF in terms of the point spread function:

$$MTF(k,z) = 2\pi\int_0^\infty P(r,z)\,J_o(2\pi k r)\,r\,dr \qquad (8)$$

where J_o is the Bessel function of the first kind and zero order. Equation (8) has the form of a Hankel transform, and so may be inverted:

$$P(r,z) = 2\pi\int_0^\infty MTF(k,z)\,J_o(2\pi k r)\,k\,dk \qquad (9)$$

From the above development we see that optical image degradation may be entirely specified by any one of the three functions: MTF (k,z), P(r,z) or L(x,z). Once one of these functions is determined the other two are also specified. The six equations relating the three functions have the relationship shown in figure 2.

Equation (7) is not easy to use in practice. Marchand (1964) has shown a more practical graphical method to obtain the point spread function from the line spread function.

DISCUSSION OF PAPERS

We will now review the methods of three recent papers which have calculated the image degradation of seawater by either obtaining the MTF or the point source response. The papers will be reviewed in chronological order:

paper 1 J. R. V. Zaneveld and G. F. Beardsley, Jr., Opt. Soc. Amer. 59, 378 (1969).

paper 2 W. H. Wells, J. Opt. Soc. Amer. 59, 686 (1969).

paper 3 F. Chilton, G. D. Jones, and W. K. Talley, J. Opt. Soc. Amer. 59, 891 (1969).

Paper 1 uses a numerical method to solve the equation of radiative transfer for a plane parallel ocean. This implies that the lightfield at a given depth is independent of location. In order for the method to be useful for the MTF calculations, it must be assumed that the target is located at $z = -\infty$. The seawater system then occupies a volume extending from $z = 0$ to $z = \infty$; $-\infty < x < \infty$, $-\infty < y < \infty$ The observing system is located on the z axis at $z = z_0$ (figure 3).

The solution for the lightfield as a function of depth is obtained by conceptually dividing the ocean into thin slabs. It is assumed that each slab is so thin that multiple scattering is not important in the slab. For each case of single scattering, a transmission operator $T(\cdot)$ can be calculated. When $T(\cdot)$ operates on the lightfield entering the thin slab, the lightfield leaving the thin slab is obtained. Thus, if the ocean is divided into N thin slabs, the final lightfield is then approximately given by operating $T(\cdot)$ N times on the lightfield incident at the sea surface. For the purpose of calculations, the icident light field was taken to be an edge gradient i. e. a target which is half white and half black. The line source response then is the derivative of the edge gradient response. When viewing the edge gradient through a seawater path, it is found that the response can be closely approximated by an arc tangent function when looking at the response close to the Z-axis. The derivative of this arc tangent function is the line source response function. The fourier transform of the derivative of the edge gradient response then is the MTF. If the edge gradient response is an arc tangent, then one finds:

$$MTF(k,z) = e^{-k/k_0(z)} \qquad (10)$$

Where $k_0(z)$ depends on $\beta(\gamma)$ and c as well as depth, $k_0(z)$ can be calculated from the edge gradient response.

Using the method outlined above, computer calculations of $k_0(z)$ were made for various shapes of $\beta(\gamma)$, and different values of c and z.

Paper 2

The paper obtains an analytical expression relating the MTF and the volume scattering function. This relation is derived by considering the change in the point source response function when a slab of scatterers is added (see figure 4).

The resultant equation is in the form of a convolution which may be solved using two dimensional Fourier transforms. The result is extended to the case of many thin slabs, which after some manipulation gives:

$$MTF(k,z) = e^{[Q(k,z) - S_t]z} \qquad (11)$$

where:

$$Q(\psi) = 2\pi \int_0^{\theta} u(\theta) J_0(2\pi\gamma\cdot\theta)\, d\theta \qquad (12)$$

$$u(\theta) = \int_0^{\theta} \beta(\gamma)\, d\gamma \qquad (13)$$

$$S_t = \int_0^{\Omega'} \beta(\gamma)\, d\Omega \qquad (14)$$

$$\varepsilon_t = 2\pi \int_0^{\theta} \beta(\gamma) \sin\gamma\, d\gamma$$

Where Ω' is the solid angle corresponding to a cone with half-angle θ.

$\psi = kz$ is the angular spatial frequency in cycles per radiance as observed at a distance z from the target, Φ is a limit set either by a restricted field of view or by the small angle approximation. In seawater $\beta(\chi)$ is highly peaked in the forward direction so that the errors in S_t and will probably be small even when using the small angle approximation.

Equation (12) shows that the MTF for any frequency decays at most like $e^{-S_t z}$. This decay is due to all light scattered between the angles $0 < \theta < \Phi$ as can be seen from equation (15). The light scattered at angles greater than Φ is ignored. Some of the scattered light still retains imaging properties if the scattering angle is not too large. This part of the light is restored to the MTF through the term $e^{Q(kz)z}$. $Q(\psi)$ is a monotonically decreasing function going to zero for high frequencies and going to S_t for zero spatial frequencies. Thus for high spatial frequencies all light scattered loses imaging properties whereas for zero spatial frequency MTF(0) = 1, so that the function is normalized in that manner.

Paper 3

Here again an infinite homogeneous medium with a point source of photons at z = 0 is considered. Given the cosine of the initial flight angle of a photon, μ_0, the probability, $P_0(z, \mu_0)$, of a first scattering occurring in the interval (z, z + dz) is

$$P_0(z, \mu_0) = \left| \frac{b}{\mu_0} e^{-zc/\mu_0} \right| dz \qquad (15)$$

Then for a certain flight path, i. e. a sequence of n scattering events, each with a flight angle characterized by its cosine μ_i, the probability density for an (n + 1) st scattering at z, $P_n(z, \mu_0, \mu_1, \ldots, \mu_n)$, given that for the nth scattering is given by:

$$P_n(z, \mu_0, \mu_1, \ldots, \mu_n) = \left| \int_{-\infty}^{\infty} dz' \left(\frac{b}{\mu_n} P_{n-1}(z - z') e^{-z'c/\mu_n} \right| dz \right. \qquad (16)$$

this equation may be solved:

$$P_n(z, \mu_0, \mu_1, \ldots, \mu_n) = \left| \sum_{i=0}^{n} D_i^n \, e^{-B_i z} \right| dz \qquad (17)$$

where the D_i^n and B_i are functions of the flight path $\mu_0, \mu_1, \ldots, \mu_n$. The P_n are calculated at a particular depth for many flight paths, the scattering cosines being drawn randomly from an appropriate distribution, and the average over these paths is $P_n(z)$, the probability density for the $(n+1)^{st}$ scattering at z. The total scattering density at any position is the sum over all P_n's.

$$P(z) = \sum_{n=0}^{\infty} P_n(z) \qquad (18)$$

The flux of photons $\phi_i(z)$ and the scattering-density functions are related by:

$$P_n(z) = b \, \phi_n(z) \qquad (19)$$

and

$$\phi(z) = \sum_{n=0}^{\infty} \frac{P_n(z)}{b} \qquad (20)$$

The angular distribution, $\bar{u}(z)$, as a function of position is then found by:

$$\bar{u}(z) = \frac{\sum_{i=0}^{N} \mu_i \, \phi_i(z)}{\sum_{i=0}^{N} \phi_i(z)} \cdot \qquad (21)$$

Thus the cosine after the ith collision is weighted by the flux of photons that have suffered i collisions, the weighted cosines are summed over N collisions, and the total is then divided by the total flux at that position. Those photons undergoing more than N collisions contribute an insignificant amount to the total flux and are ignored.

DISCUSSION AND RESULTS

Each of the calculation methods outlined in the previous sections has its theoretical and practical limitations. The viewing situation in paper 1 will not often by encountered in practice. For large distances from the origin the approximation of a target a $z = \infty$ should be less troublesome. Furthermore, the edge-gradient response in the near-forward direction was approximated by an arc tangent function. Although this function fits the data well, it essentially corresponds to a small angle approximation, as for angles greater than 20° from the forward direction the approximation becomes inaccurate. A problem with the comparison of these methods lies in the lack of experimental data. Until such data is available, no real test of these methods is possible.

The limitation in paper 2 lies in the use of the small-angle approximation. The error this approximation introduces probably is small, but cannot be accurately predicted until a comparison with experimental results is available.

A limitation of both papers 1 and 3 is that a separate MTF must be calculated for each range, whereas paper 2 predicts the behavior of the MTF as a function of z.

A problem with the prediction of underwater visibility is the necessity for accurate measurement of the volume scattering function especially in the near-forward direction. Although visibility in general is deteriorated by scattering, near forward scattered light still retains some imaging properties. Thus it is imperative to know the small angle scattering properties of seawater. This makes comparison with experimental results extremely difficult. Only a few attempts have been to directly measure the MTF or the line source response in a seawater viewing situation. (Replogle and Steiner, 1969; Replogle 1966). These results cannot, however, be directly related to the theoretical prediction of visibility due to insufficient measurements of the inherent optical properties.

A theoretical prediction of visibility can now be made only on the basis of an experimental measurement of the volume scattering function, but any prediction is linked to the experimental difficulty in measuring near-forward scattering. On the basis of a Mie - scattering model, Plass and Kattewar (1969) have used a volume scattering function that corresponds to those measured in seawater for the larger angles. This model might be fruitful in predicting forward scattering in seawater. It may well be that eventually visibility will be easier to measure experimentally, from which near-forward scattering can then be predicted.

BIBLIOGRAPHY

G. F. Beardsley, Jr. and J. R. V. Zaneveld, J. Opt. Soc. Amer. 59, 373 (1969)

F. Chilton, D. D. Jones and W. K. Talley, J. Opt. Soc. Amer. 59, 891 (1969)

J. W. Coltman, J. Opt. Soc. Amer. 44, 468 (1954)

S. Q. Duntley, USN Report no. 5-3. Contract Nobs-72039 Task 5 (1960).

S. Q. Duntley, J. Opt. Soc. Amer. 53, 214 (1963)

N. G. Jerlov, Optical Oceanography, Elsevier Publishing Company, Amsterdam (1968)

R. Jones, J. Opt. Soc. Amer. 48, 934 (1958)

E. W. Marchland, J. Opt. Soc. Amer. 54, 915 (1964)

A. Morel, J. Chim. Phys. 10, 1359 (1966)

E. L. O'Neil, Introduction to Statistical Optics, Addison-Wesley Publishing Company, Inc., Reading, Mass. (1963)

H. Pak, G. F. Beardsley, Jr., G. R. Heath, H. Curl, to be published in the Journal of Limnology and Oceanography (1970)

G. N. Plass and G. W. Kattawar. Appl. Opt. 8, 455(1969)

F. S. Replogle and I. B. Steiner, J. Opt. Soc. Amer. 55, 1149 (1965)

F. S. Replogle, Seminar Proceedings, Underwater Photo-Optics (Society of Photo-Optical Instrumentation Engineers, Santa Barbara), p. A.V.-1. (1966)

W. H. Wells, J. Opt. Soc. Amer. 59, 686 (1969)

J. R. V. Zaneveld and G. F. Beardsley, Jr., J. Opt. Soc. Amer. 59, 378 (1969)

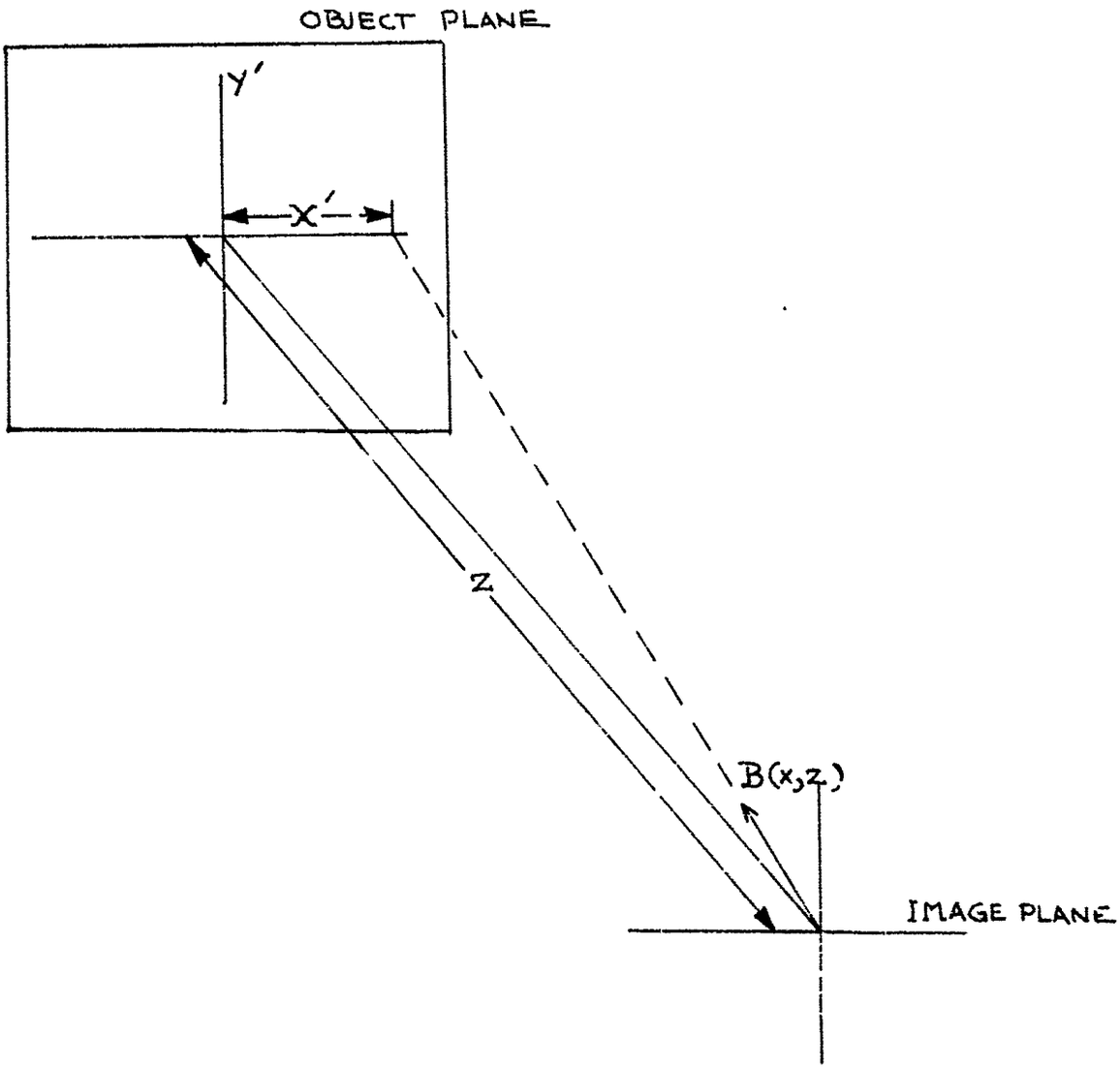

Fig.1 Underwater viewing situation

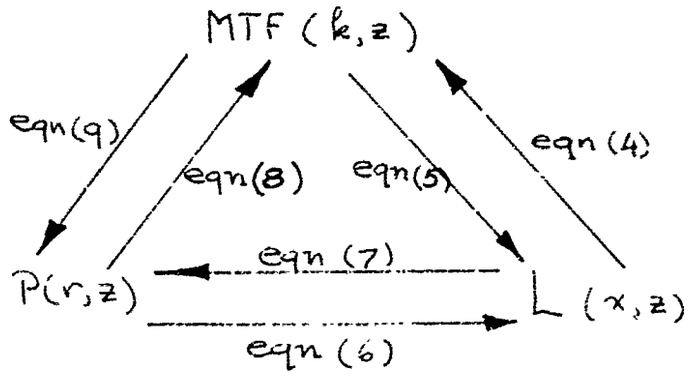

Fig.2 Functional relationships of the modulation transfer function (MTF), the point source response function (P), and the line source response function(L)

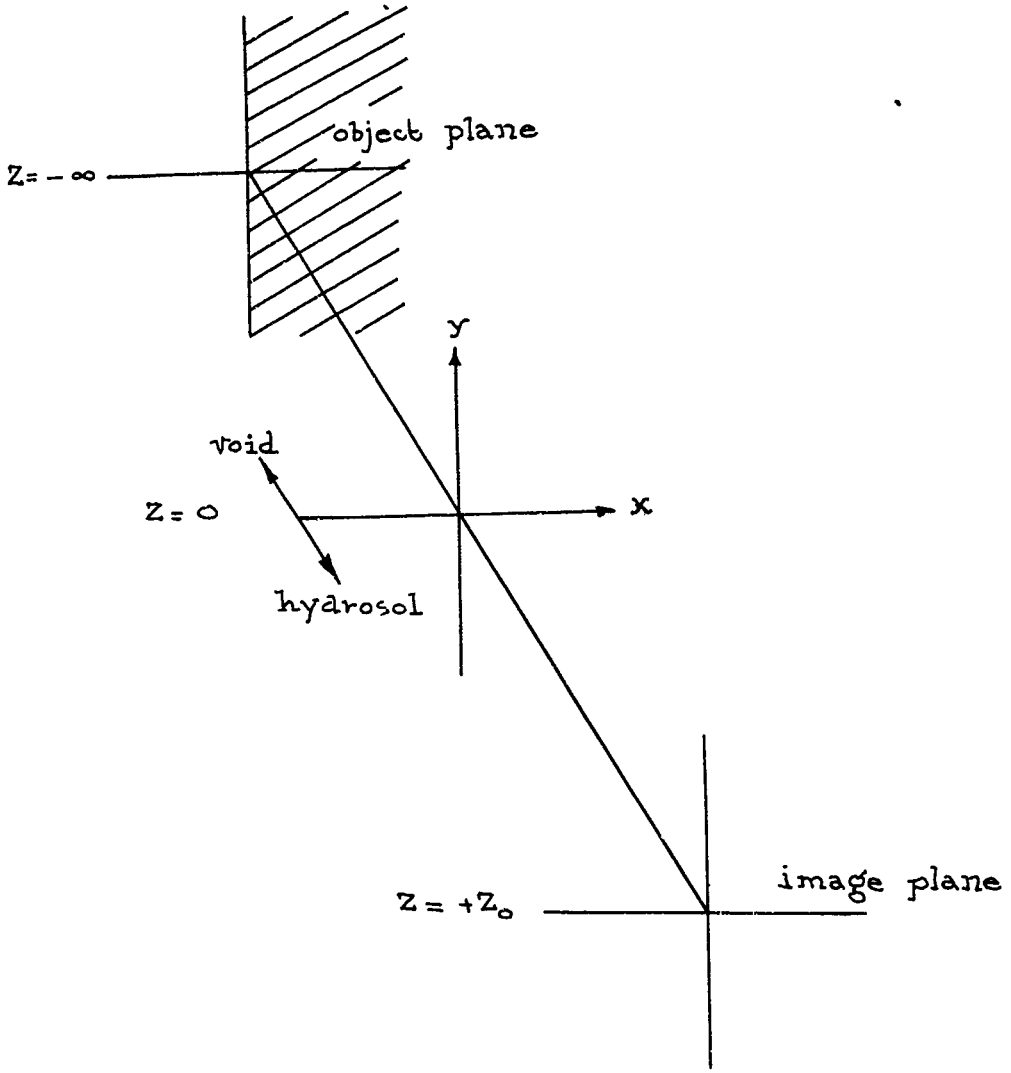

Fig.3 Geometry of the viewing situation used by Zaneveld and Beardsley (1969) for modulation transfer function calculations. The edge gradient target is visible in the object plane

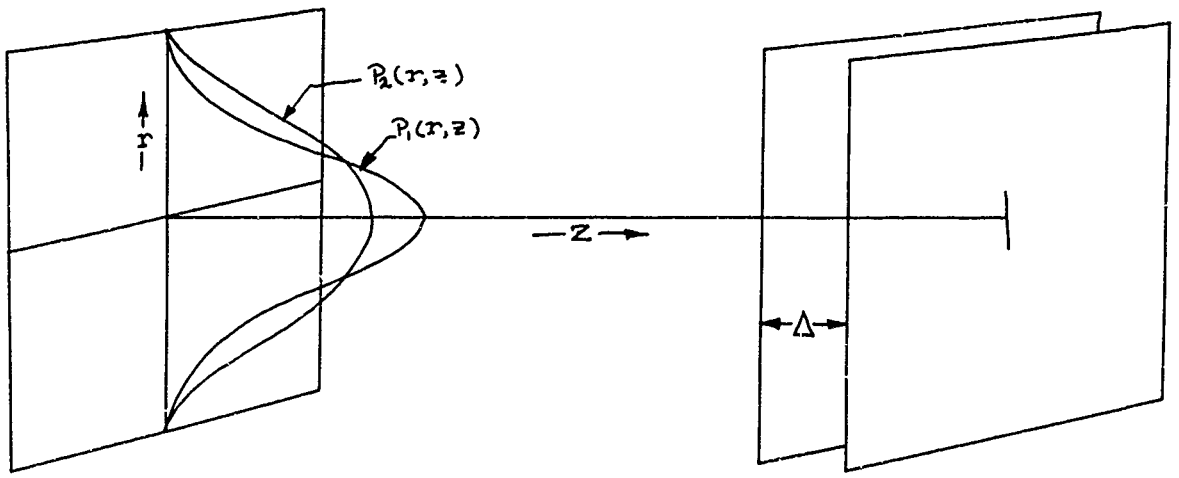

Fig.4 Geometry for derivation of the modulation transfer function from the volume scattering function as used by Wells (1969). The point source response function $P_1(r,z)$ (narrower of the two) spreads to give $P_2(r,z)$ when additional scatterers are added in the slab of width Δ

UNDERWATER OPTICS

by

V.A. Seifert

Naval Photographic Center
U.S. Naval Station
Washington, D.C. 20390

UNDERWATER OPTICS

V. A. Seifert
Naval Photographic Center
US Naval Station
Washington, D.C. 20390

SUMMARY

The Naval Photographic Center has sponsored underwater optical studies and the development of a number of Concentric Dome lenses for 16mm motion picture, 35mm and 70mm format still picture cameras. This report describes validation tests of these developments. Tests were run on an Underwater Calibrator at the Naval Photographic Center and compared with the plane parallel window with an air lens and the Corrector approach. Design criteria are discussed for lens selection depending on the particular application. Test results indicated that lenses designed specifically for underwater photography outperform air lenses adapted for underwater imaging. Resolution and distortion for water lenses was superior for wide angle coverage. The Corrector and Concentric Dome approach resulted in similar results. The Concentric Dome has better structural strength than any plane parallel window or corrector.

INTRODUCTION

Recent advances in the development of underwater photo-optical instrumentation required a closer investigation into the design concept, testing and selection criteria for application. Theory has long preceeded the actual design and construction of underwater optics and their component parts. This development has resulted in three basic approaches for underwater imaging: the plane parallel window with an air lens, the Ivanoff Corrector with an air lens, and the Concentric Dome Window with a lens designed for underwater photography. Along with this development, several questions have arisen; how could theory be verified in the laboratory prior to actual use and how did the results determine the selection of the system? This presentation reviewed some of the theory of primary concern to the optical designer and consequently verified these theories under actual laboratory tests with consideration given to the method of testing, final performance, and design consideration for the selection of a particular optical system.

INTRODUCTION TO THEORY [1]

Oblique rays of light refract at the interface of two media with different indeces of refraction. The refracting angle varies with the wavelength of light causing color dispersion or color distortion(Fig.1) Where θ' is a function of λ (wavelength). Now let us consider an object y and image y'(Fig.2) In order that the object y and the image y' are in an analogous relation to each other,the ratio between y and y' is to be constant:

$$\frac{y'}{y} = c \cdot \frac{\tan \theta'}{\tan \theta} = \text{constant}$$

but since $\frac{\sin \theta'}{\sin \theta} = n_w = \text{constant}$ constant, according to the law of refraction, $\frac{\tan \theta'}{\tan \theta}$ cannot be constant but will vary with the angle θ. This variation means that the larger the incident angle, the more distorted will be the image. This linear distortion, increasing with larger angles of θ, results in color fringes due to the varying index of refraction of white light as a function of λ (wavelength). By observing objects towards the edge of a color transparency, there is a red fringe on the inside, and a blue fringe on the outside of the picture with the rest of the spectrum in between. On black and white film, this will appear as a blurred image with loss of detail or resolution; consequently, the higher the chromatic aberration of a photo-optical underwater system, the lower the overall resolution. This is analogous to air systems.

Angular coverage of an air lens is reduced due to the index of refraction of water. Water attenuation and particle scattering limits underwater photography to close-up work. Most underwater photography is done at distances not exceeding 30 feet (10 meters) except where water is quite clear. In order to get any amount of coverage, wide-angle underwater optics are preferred. On the other hand, the wider the angular coverage, the more chromatic aberration, distortion and image plane curvature resulting in loss of information. In general, it can be stated that some distortion of the image with any air lens is unavoidable.

THEORY

A. CHROMATIC DISTORTION [2],[3]

From the law of refraction:

$$n_w \sin\theta_w = n_g \sin\theta_g = n_a \sin\theta_a$$

or $$n_w \sin\theta_w = n_a \sin\theta_a$$

The subscripts w,g, and a stand for water, glass, and air respectively. A glass interface, separating water from the air lens does not cause any problems as long as the object is at infinity or the object is far and the thickness of the glass is thin.

However, at finite conjugate distances, we have to consider the following relationships:

$$n_{wr} \sin\theta_w = \sin\theta_{ar}$$

or $$n_{wb} \sin\theta_w = \sin\theta_{ab}$$

where subscripts b and r refer to red and blue light. This differentation between colors is

necessary because $n_w = f(\lambda)$ therefore $\sin\theta_{ab} - \sin\theta_{ar} = (n_{wb} - n_{wr})\sin\theta_w$ which indicates that this relationships depends on θ in water; thusly, the larger the angle θ the larger the chromatic aberration.

B. DISTORTION

Looking at a subject y, Fig. 2 at an angle θ, it will refract in a direction θ' forming an image y'. If tan θ is proportional to tan θ' as in Fig. 2, the apparent size will be analogous to actual size.

$$\frac{\tan\theta'}{\tan\theta} = \frac{\frac{\sin\theta'}{\cos\theta'}}{\frac{\sin\theta}{\cos\theta}} = \frac{\sin\theta'}{\sin\theta} \cdot \frac{\cos\theta}{\cos\theta'}$$

however, previously we said that: $n_w \sin\theta = \sin\theta'$

therefore: $\frac{\tan\theta'}{\tan\theta} = n_w \frac{\cos\theta}{\cos\theta'}$, $\theta_w < \theta_a$

n_w = constant for given water temperature, pressure and salinity, but θ and θ' change due to the equation $n_w \sin\theta = \sin\theta'$

therefore $\frac{\cos\theta}{\cos\theta'} \neq$ constant

and, tan θ' is not proportional to tan θ. The distortion of the subject is proportional to $\frac{\cos\theta}{\cos\theta'}$, which changes with θ.

Distortion can be expressed as:

$$\frac{y-y_o}{y_o} \cdot 100 = \left(\frac{\cos\theta}{\cos\theta'} - 1\right) \cdot 100\% \qquad \text{If: } \frac{\cos\theta}{\cos\theta'} > 1 \quad \text{Then: } \frac{\cos\theta}{\cos\theta'} - 1 > 0$$

which means that distortion is always positive.

C. PICTURE ANGLE

The angle of incidence is reduced by the index of refraction of the media. Some immediate solutions to the above mentioned problems would be to replace the glass window by either a concave lens to keep $\theta = \theta'$ which would keep the angle the same but would have structural deficiencies, or use a spherical boundary surface with its center coincident with the principal point or the entrance pupil of the lens. Then there would be:

No refraction
Same Angle
No distortion
No chromatic aberration

Since a curved surface gives a curved picture and the entrance pupil is not a point but of <u>finite</u> physical size, the lens will still have to correct for those problems.

Let us consider the individual optical designs presently used for underwater imaging.

1. Plane Parallel Port

The advantage of such a system is that conventional photographic equipment can be used with some sort of housing to separate camera from water. The angular coverage is reduced to approximately 3/4 of the original lens angle. This system has little or no distortion as long as $\frac{\cos\theta}{\cos\theta'} \approx 1$ chromatic aberration will also be low.

However the useful picture angle would be limited to less than 20°. Larger angular coverage would result in chromatic aberration, distortion and loss of resolution.

2. Plane Parallel Port, using an achromatic window of two types of glass with the same index of refraction but different color dispersion. The cemented surface has to be properly curved such that $\theta'_{red} = \theta'_{blue}$ If some distortion is permissable, a sharp image can be obtained since there is no chromatic aberration. This system, however, cannot correct for distortion. Angular coverage is still reduced by approximately 0.75.

3. Concave Lens

This approach with proper glass selection can correct for distortion and chromatic aberration if the lens is redesigned. The physical construction of such a system is however very impractical due to high underwater pressures.

4. Lens system in combination with a Telescope System.

The picture angle θ' is reduced by n_w getting θ in water. Mathematically the angle reduction is:

$$\text{Tan}\theta = \frac{1 \cdot \cos\theta'}{n_w \cdot \cos\theta} \tan\theta'$$

Therefore is we use a telescope with a magnification of $\frac{1 \cdot \cos\theta}{n_w \cdot \cos\theta'}$, the picture should be the same as in air.

The telescope itself needs a magnification of $\frac{1}{n_w}$ and a distortion of $\frac{\cos\theta}{\cos\theta'}$

A Galileo type telescope is suggested because of simple construction and easier correction for aberrations. Even though the magnification will be slightly different for $\frac{1}{n_w}$ the distortion can probably be eliminated.

This system led to the Ivanoff Corrector which at present time is the most widely used corrected system. (See Fig. 2A)

5. Concentric Lens

When the front nodal point of the taking lens is brought to the center of the concentric lens, rays directed toward the center of the dome are normal to the concentric surface and therefore are not refracted, dispersed or distorted, also, the angular coverage of the taking lens does not change. This permits extreme wide angle photography. The concentric lens produces a virtual and spherical image which is recorded by the taking lens on film. See Fig. 2B.

In practice, the entrance pupil which is of some physical dimension, must be at the center of the dome radius. The taking lens must be able to compensate for the spherical image before recording on film. The degree of curvature of the image is proportional to the radius of the concentric dome.

Preliminary Conclusions

For underwater photography covering more than 20 degrees, some changes have to be made for optical correction, it actually is preferred to have the optical system designed only for underwater photography, not air photography included.

TESTS AND RESULTS

Three basic types of underwater lens systems were tested for comparative analysis along with lenses used in air (4),(5), (6). The three approaches were the plane parallel port, the Ivanoff Corrector and the Concentric Dome. In addition, the Hopkins 45mm f/4.5 underwater lens was evaluated since it was specifically designed for underwater photography using the plane parallel port approach with the taking lens designed to compensate for this problem. All tests were performed under controlled laboratory conditions.

The instrument used to test underwater cameras was an underwater camera calibrator. See Fig.2C. The Calibrator (7) is a precision instrument that provided a known angular array of targets to be photographed by a camera under test. The images of the targets were then read and measured to yield the necessary data for the determination of focal length, distortion, and resolution. Generally, the targets of a camera calibration instrument are located at optical infinity; however, the images presented to the camera by the Underwater Camera Calibrator may be set for any distances from 5 feet to infinity. Thus, a camera focused at 10 feet can be tested with a ten foot object distance. The angles between the targets were 7 1/2 degrees at all object distances.

The purpose of the Camera Calibrator was to provide precise reference direction angles of its targets whereby the interior orientation of a camera may be determined from the measurements made between the recorded images of the targets. Resolution was determined from resolution targets in each collimator. The film distance between the image of the central reference point and the image of any other reference point divided by the tangent of the corresponding angle was equal to the image distance. Distortion can be calibrated as in Fig. 2D. When the collimators were set for infinity the focal length was determined.

In the first series of tests, resolution (8) and distortion was measured for air lenses which subsequently were used in the Underwater Camera Calibrator with an optical flat simulating a plane parallel port. The air lenses were tested in an Air Camera Calibrator based on the same principle as the Underwater Camera Calibrator.

TABLE I
(1)
Resolution (L/mm)

	Summicron AIR		35mm f/2 H2 0		Super-Angulon 21mm f/3.4 AIR		H2 0	
Angle Off-Axis	R*	T*	R	T	R	T	R	T
0°	56	56	56	51	68	68	53	53
7.5°	56	56	51	33	68	68	43	60
15°	39	39	33	21	66	66	33	43
22.5°					56	56	35	33

(1) For 35mm Format
(*) Radia and Tangential

TABLE II
(1)

Angle Off-Axis	Hopkins 45mm f/4.5 H2 0 R	T
0°	65	65
7.5°	65	65
15°	57	46
22.5°	61	38

(1) 35mm Format

Table I gave radial and tangential resolution of two off-the-shelf lenses in air as well as in water. Exposures were made with a Leica M-2 camera, using Kodak Panatomic X panchromatic film at ASA 32, and developed according to manufacturers specifications. The angles were measured from the optical axis out towards the edge of the picture format. Table I shows readily that the air lens did not perform well in water. It was also noticable that air lenses developed strong astigmatism in water. On axis, resolution should have been the same but due to dispersion of the interface between water, glass, and air there was a slight loss. Micro photographs showed the effect of chromatic aberration.

The first picture was the target on axis, whereas picture number two was the target 30 degreen off-axis. The color fringes were quite apparent and according to theory. Additionally, the image was distorted to form an approximate ellipse and theoretically should have been circular as the target on-axis. Picture No. 3 was a blow up micro-photograph of the cross section of the outer ring of picture No. 2, and presented to the viewer the complete visible spectrum because of changing refractive index as a function of wavelength. Picture No. 4 was a further demonstration, that even the most highly corrected air lenses did not perform satisfactorily in water. This picture was taken with a 66mm f/2 apochromat with the target only 7 1/2 degrees off-axis. No matter how well an air lens, in combination with a parallel port, was corrected, there will always be chromatic distortion.

Table II listed the resolution of the Hopkins 45mm f/4.5 underwater lens. Resolution was good for all practical purposes out this lens developed some astigmatism towards the edge of the picture format. If, however, this focal length and aperture is satisfactory, this lens would have been preferred over the air counterparts.

Fig. 3 was the distortion characteristic of the Super-Angulon in air and in water with the distortion curve of the Hopkins lens. The Hopkins lens was excellent out to about 15 degrees followed by a sudden negative distortion but still reasonably when compared to air lenses.

The next series of tests were to compare the plano parallel port to the concentric dome window. The two lenses selected covered 90 degrees, one designed for air and the other for underwater photography. Table III gave the resolution data. The C 88 air lens was used with a KF 28E 70mm format camera and a plano parallel port; the C 201 was used with an underwater Hasselblad. Exposures were made on Kodak Panatomic-X film and developed according to manufacturer specifications. Again the difference was quite apparent. Astigmatism towards the edge of the format caused complete loss of resolution in the tangential direction.

TABLE III
(1)

	Resolution (L/mm)									
Angle Off-Axis	0°		7.5°		15°		22.5°		30°	
Position	R	T	R	T	R	T	R	T	R	T
Elcan C88	29	29	40	33	55	25	29	20	33	0
Elcan C201	77	77	73	63	43	35	49	31	63	43

(1) 70mm Film Format

Fig. 4 gave the distortion characteristics and Pictures 5 through 10 showed the difference in image recording of the two systems out to 30 degrees off-axis.

The last series of tests was to compare the Ivanoff Corrector with a Concentric Dome systems approach. In this case the optics of the underwater camera was specically designed for underwater photography taking into consideration some of the adverse optical effects in water. In order to avoid any limitation of performance put on the lens by either the choice of film or camera, it was decided to test the lenses independtly using Kodak High Resolution Plates. The focal lengths of the lenses were calibrated prior to resolution and distortion measurements. The Ivanoff Corrector was used with a 10.2 f/1.6 Switar and the Concentric Dome Window lens was the 8.9mm f/2.4 Elcan manufactured by E. Leitz, Canada Ltd.

TABLE IV
(1)

	RESOLUTION (1/mm)				
Angle Off-Axis	0°	75°	15°	22.5°	30°
Elcan 8.9mm f/2.4	206	238	386	434	405
Switar 10.2mm f/1.6	210	232	405	N.A.	N.A.

(1) 15 mm Motion Picture Format

TABLE V

	RESOLUTION (L/mm)		
Angle Off-Axis	0°	7.5°	15°
Elcan 16mm f/2.4	96	129	176

(1) 16mm Motion Picture Format

TableIV gave the resolution. At this time figures of resolution beyond 15 degrees off-axis were not available because the mechanical configuration prevented measurements further out. However, in general both systems performed very much alike in resolution and distrotion, Fig. 5.

Table V gave resolution of another concentric dome system using Kodak Micro-file film with an N-9 camera in a system. Resolution was excellent and pictures 11 and 12 showed the difference in recoding of the concentric dome versus a standard air lens wich a plano parallel port.

DISCUSSION OF RESULTS

In general it can be said that the practical tests followed the theory. The difference of air systems adopted for underwater photography as compared to designed underwater optics is obvious. Distortion and loss of resolution for air systems covering more than 20 degrees limits the application of those systems. As a matter of fact a total angular coverage of 10 degrees is more realistic. Optics developed specifically for underwater imaging showed results corresponding to air lens performance. The Ivanoff Corrector and the Concentric Dome approach are sound as far as optical performance is concerned. However, before coming to a final decision it is necessary to look further into the design of the three basic approaches before deciding on a final choice of optics.

DESIGN CONSIDERATION FOR LENS SELECTION (9),(10)

For general underwater amateur photography with limited picture angle, an air lens combination would be suitable in most cases. However, as soon as the underwater photo system was used for photogrammetric purposes or where image size must be correlated to object size, a standard air lens would be insufficient. We know that the index of refraction of water varies with wavelength, temperature, pressure and salinity, for example, see Fig. 6.

How does the variability of the water refractive index effect object to image size correlation? We know that under certain circumstances the refractive index of water can change up to 2%. It also can be seen from the general equation for a thick lens composed of two surfaces

$$\frac{n}{f} = \frac{n''}{f'} = \frac{n'-n}{r_1} + \frac{n''-n'}{r_2} - \frac{n'-n}{r_1} \cdot \frac{n''-n'}{r_2} \cdot \frac{t}{n'}$$

Where f = first focal length
f' = second focal length
n = refractive index of object space
n' = refractive index of lens
n'' = refractive index of image space
r_1 = radius of first surface of lens
r_2 = radius of second surface of lens
t = axial thickness of lens

that the second focal length varies with a change in the refractive index of water except where the first surface of the lens is planar or infinity. However, if a water lens is focused at a finite object distance, a variation in the refractive index of water will cause a change in the object distance focused upon even though the first surface of the water lens is planar.

The following equation determines the revised vertex object distance for a variation in the refractive index of water

$$S_o = \frac{n_o}{\frac{n}{S_n} + \frac{n-n_o}{r_1}}$$

where S_o = vertex object distance for a water refractive index of
S_n = vertex object distance for a water refractive index of
r_1 = radius of first surface of water lens

The vertex object distance is defined as the distance from the first vertex of the water lens to the object.

When the first surface r_1 becomes infinity and

$$S_o = \frac{n_o S_n}{n}$$

Then S_o and S_n have the ratio of their respective water refractive indeces. Furthermore it can be seen that if r_1 and S_n are equal to infinity, S_o is also equal to infinity, thereby indicating no change of focus.

The point of this discussion is to show the drastic change of the vertex object and nodal object distance of a dome lens system with changing index of refraction. For a planar first surface, under the worst change of the refractive index, the vertex object and nodal object distance change two percent, which means about 20mm for an object distance of 5 meters. On the other hand let us assume an object nodal distance of 5 meters or 5000mm with a dome radius of 50mm. D_o is the object nodal distance.

$$S_n = D_o - r_1$$

Substituting $S_n = 5000 - 50 = 4950$mm

Now compare the difference of object vertex distance for sea water with an index of 1.343 and distilled water with an index of 1.333 by substituting the numbers into the formula for vertex object distance

$$S_o = \frac{1.333}{\frac{1.343}{4950} + \frac{1.343-1.333}{50}} \qquad S_o = 2828\text{mm}$$

The revised nodal object distance is

$$D_o = S_o + r_1$$

Substituting

$$D_o = 2878mm$$

This example shows that when an underwater camera with a dome window as part of the lens system is focused for a nodal object distance of 5 meters in seawater, the object focus will shift to almost half when operated in distilled water or water of similar refractive index. The following graph Fig. 7 gives the relationship between vertex object distance and refractive index for various radii of the dome window.

If it is important to minimize the object focus shift, the radius of the first surface should be increased; the least amount of shift occurs when the radius of the first surface is infinity or close to it. Examples of a system using a first surface radius of infinity is the Ivanoff Corrector, the Hopkins f/4.5 underwater lens and any plano parallel port in conjunction with an air lens.

This shift of object nodal distance can become a serious problem for photogrammetric purposes using fixed focus underwater cameras. It will be necessary to know the environmental conditions and the amount of magnitude of the refractive index to arrive at proper data reduction. One simple way to solve this problem is to use short focal length lenses which tend to have a great depth of field or have variable focusing on the camera.

Now let us consider the nodal image distance. The first and second focal lengths vary with change in the refractive index. However, for a dome window lens system the image nodal distance does not change with varying refractive index as long and the first and second nodal points are located at the curvature of the first surface of the lens, see Fig. 8. This is referred to as the concentric condition. This is of particular significance because as long as the image nodal distance remains constant, no mathematical corrections have to be made for analytical calculations.

The camera can be calibrated in any type of water. For an analysis let's investigate the planar condition. The second focal length f' of an underwater lens with a planar first surface remains constant even though the refractive index changes. The first focal length f for index n is

$$f=nf'$$

Then for n_o $\quad f_o = n_o f'$

The difference in first focal length is

$$f-f_o = f' (n-n_o)$$

Since, f' is constant for the planar condition, the difference in the first focal lengths is directly proportional to the difference in the water refractive index. The difference in nodal image distances of d and d_o is approximately equal to the difference in their respective first focal lengths. Therefore, if the refractive index changes by 2% then the image nodal distance and therefore lateral magnification changes by two percent.

Therefore, for a planar condition the object nodal distance does not change but the image nodal distance and lateral magnification changes; for a concentric lens system, the nodal object distance changes but the nodal image distance does not. This alone could establish a criteria of selection of either type of lens systems. Another important criteria is the versatility of the optical system. Plano parallel port systems can be used with any type of lens as long as the picture angle is small. With an Ivanoff Corrector, the versatility is somewhat reduced in that the Corrector has to be made large enough to cover numerous focal length lenses and numerous apertures. This becomes difficult for lenses with large apertures because of the physical size of the corrector. Also, it is desirable to use the Corrector with highly corrected air lenses. Concentric dome windows if properly built can be used with a large variety of lenses, either specifically designed for the camera or standard of-the-shelf systems. One camera presently on the market, handles lenses from 7.5mm to 135mm in focal length lenses for a 35mm format. Additionally, there is the versatility of having a turret behind the dome window for a different angular coverage. Since the virtual image is located at a certain vertex object distance for a given situation, all that is necessary is to make sure that when the lenses are mounted on a turret that their respective entrance pupils fall at the center of curvature of the first surface.

The Concentric Dome has the best phycical characteristics especially for deep ocean photography. The arch cross section is an ideal structural shape to withstand the pressure of external fluids. Glass excels in compression and is inferior in tension. Since the stress involved for this shape is compression, glass performs an outstanding task. In contrast to this, the plano parallel port and Ivanoff Corrector is under tension since the front element is flat.

CONCLUSION

Laboratory tests confirmed the theory that lenses which are designed for underwater photography will outperform lenses designed for air photography and later adapted for underwater imaging. The choice between an Ivanoff Corrector and a Concentric Dome is left up to the individual and their application Ocean bottom photography would prefer a concentric dome window because of its structural shape. The Concentric Dome offers versatility as far as angular coverage is concerned. For hand-held operations, the Ivanoff Corrector and the Concentric Dome offer equal photographic advantages. For photogrammetric work, the concentric approach is recommended. Underwater photoimaging systems should be tested prior to actual use.

REFERENCE: (1) Wakimoto, Z. "On Designing Underwater Camera Lenses, "Papergiven at the Convention of the American Society for Photogrammetry, March 8, 1967

(2) Born and Wolf, "Principles of Optics", The MacMillan Company, New York 1964

(3) Robertson, J.K. "Introduction to Optics", D. van Nostrand Company, Inc.,1959

(4) MIL-STD 150, Photographic Lenses, 1961

(5) NAVPHOTOCEN R&D 68/17 4 Sept 1968

(6) NAVPHOTOCEN R&D 69/36 28 Jan 1970

(7) McNeil, G.T. "Underwater Camera Calibrator", SPIE Journal, v.4, n.3, 1966

(8) NBS Circular 533, "Method for Determining the Resolving Power of Photographic Lenses", 20 May 1953

(9) W. Mandler, "Design Consideration for Underwater Lenses with Water Contact Elements Concentric with the Entrance Pupil"

(10) McNeil, G.T. "Optical Fundamentals of Underwater Photography" 1968

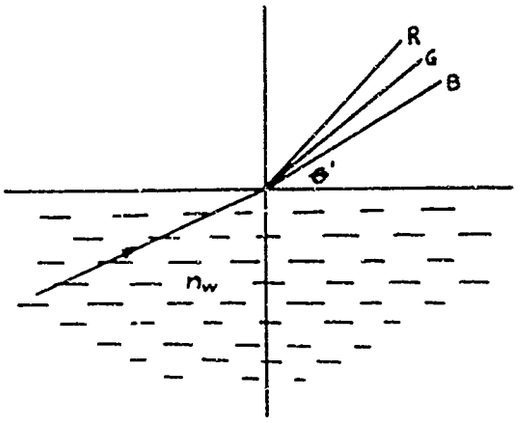

Figure 1

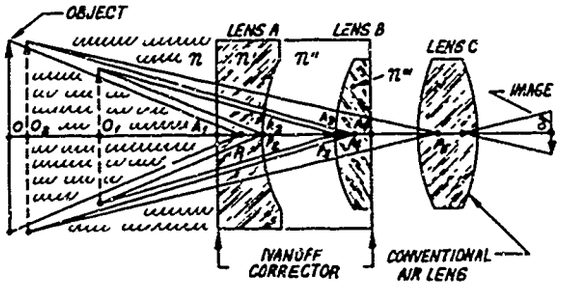

(a) Ivanoff corrector window with air lens

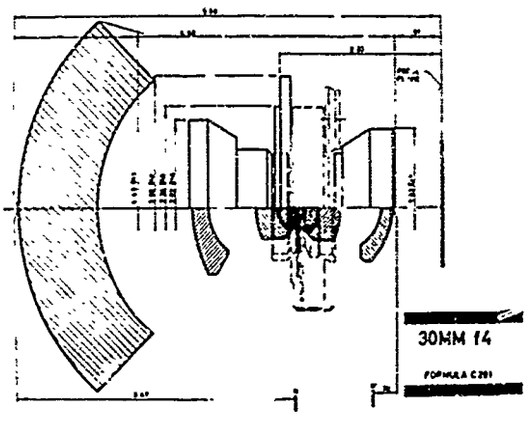

(b) 30mm f/4 concentric dome underwater lens

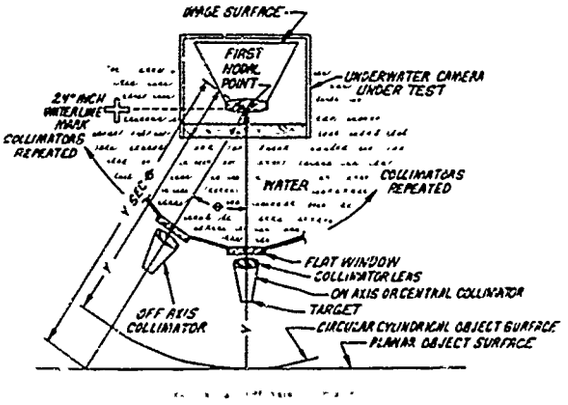

(c) Schematic of underwater camera calibrator

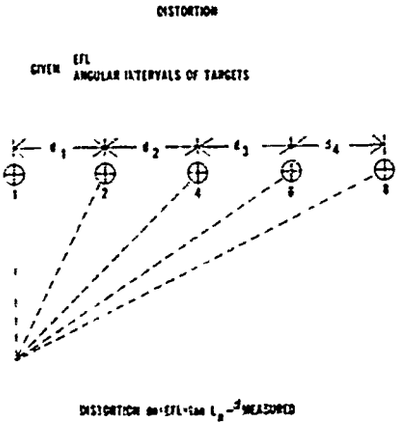

(d) Schematic of distortion measurement

Figure 2

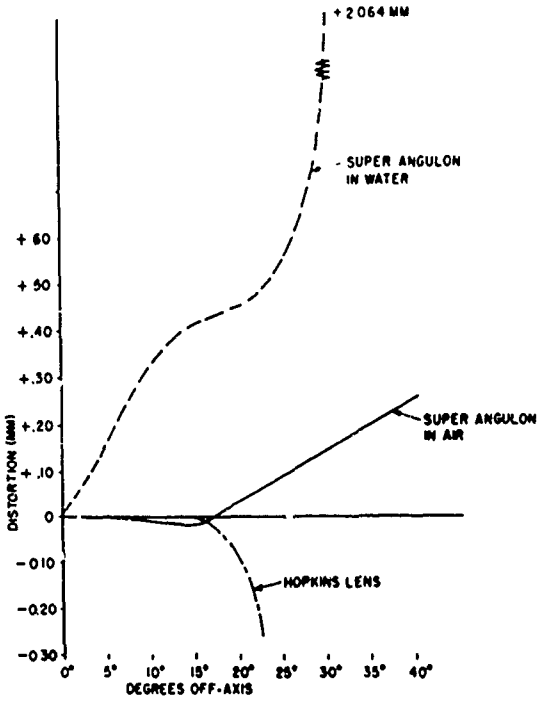

Fig.3 Distortion of lenses

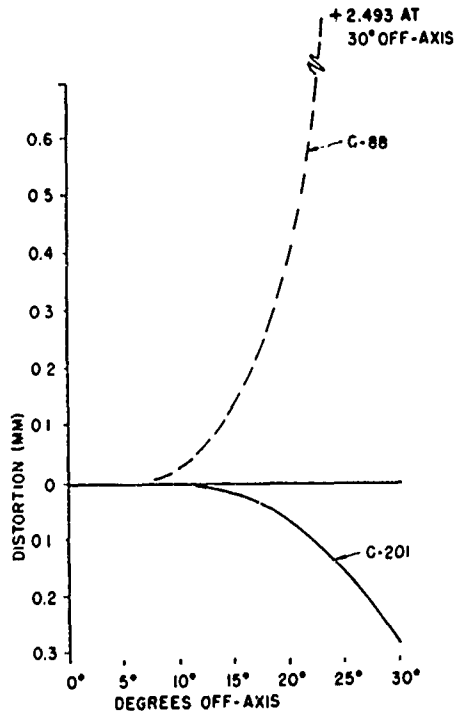

Fig.4 Distortion of lenses

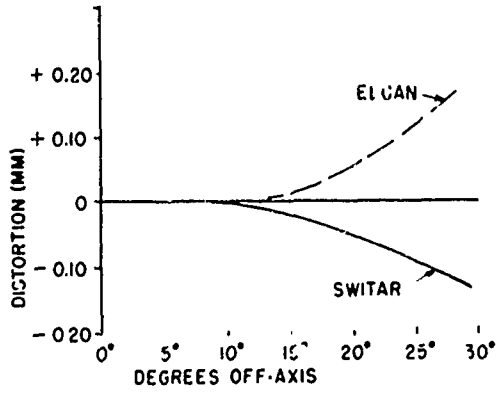

Fig.5 Distortion of lenses

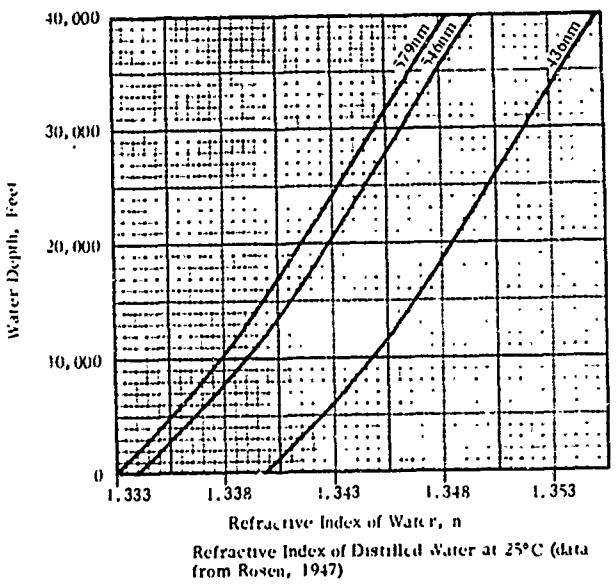

Refractive Index of Distilled Water at 25°C (data from Rosen, 1947)

Fig.6 Index of refraction vs wavelength and depth of water

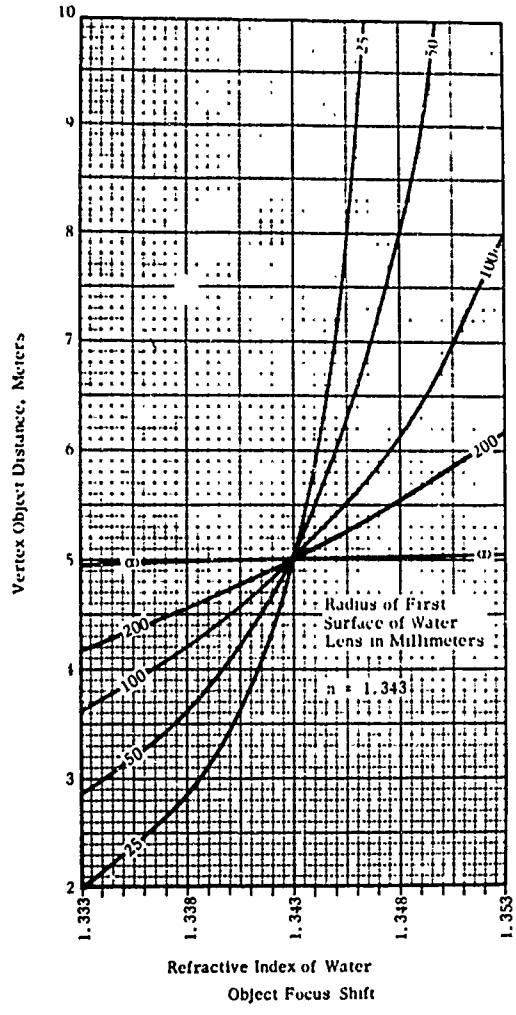

Fig.7 Vertex object distance vs dome radius and index of refraction

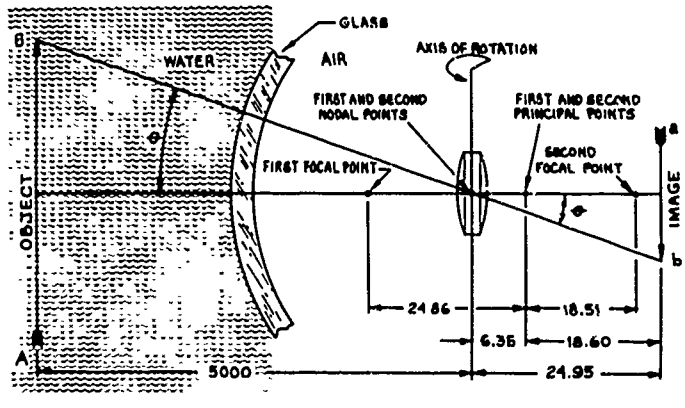

Fig.8 Concentric dome lens system

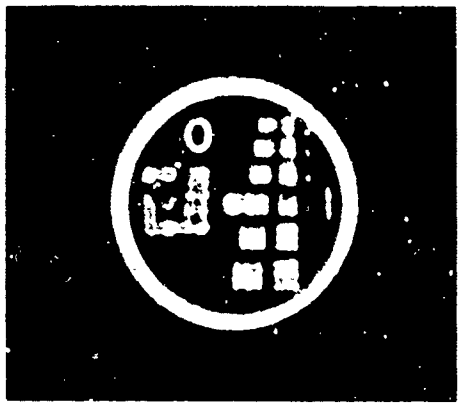

Picture No. 1

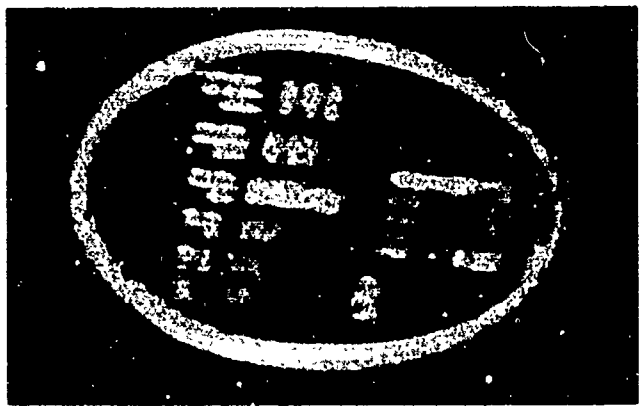

Picture No. 2

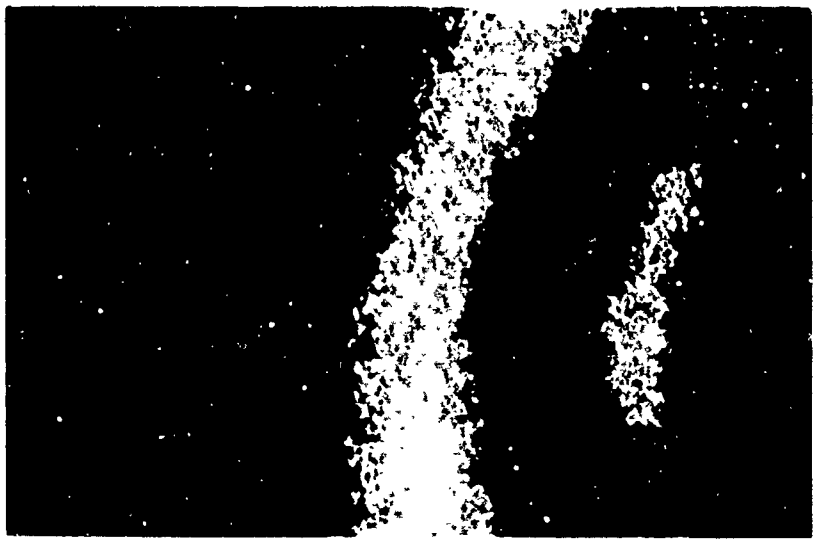

Picture No. 3

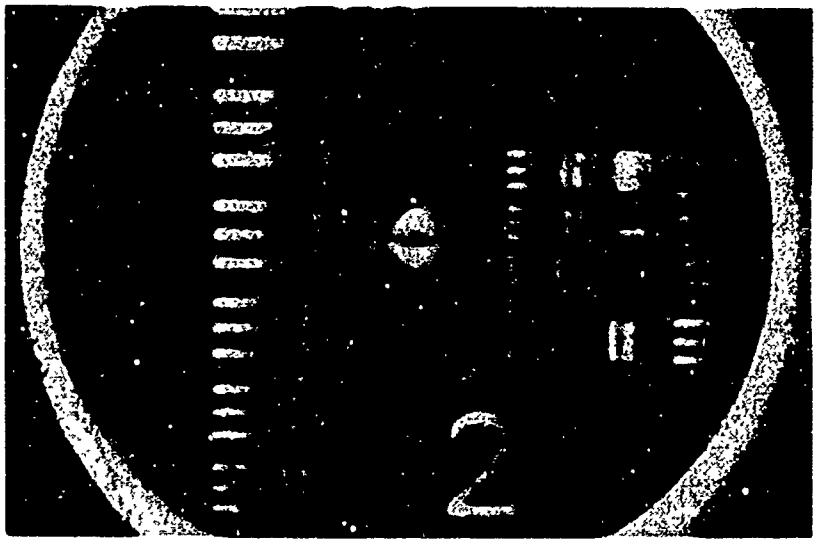

Picture No. 4

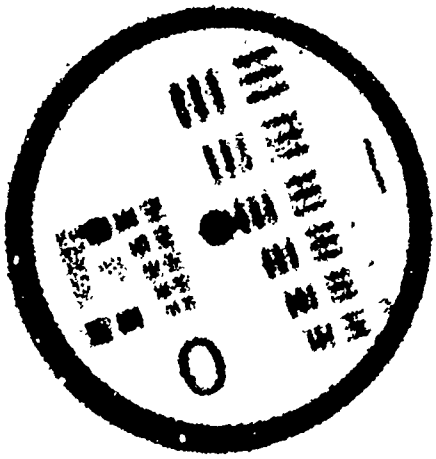

Picture No. 5 C201 on axis

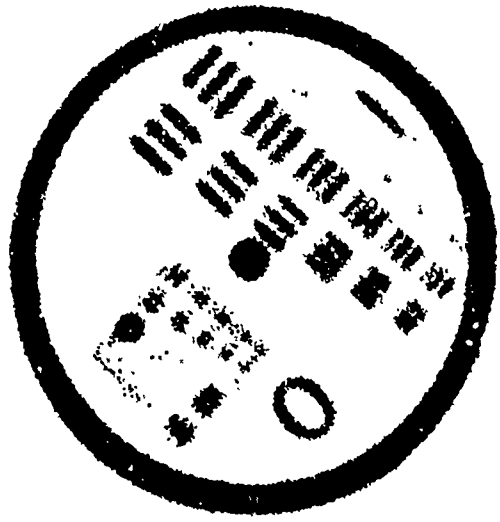

Picture No. 6 C88 on axis

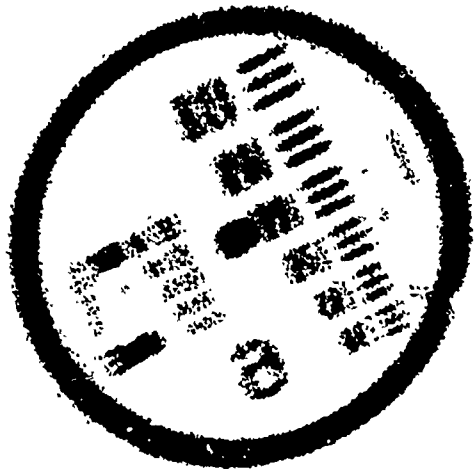

Picture No. 7 C201 22½ degrees off-axis

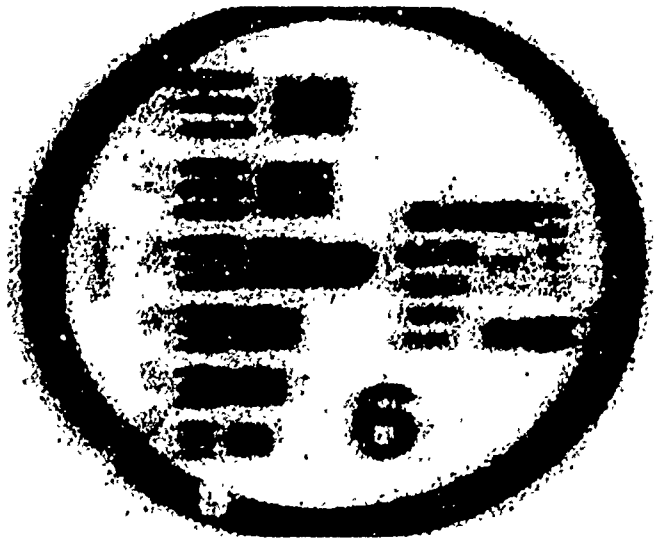

Picture No. 8 C88 22½ degrees off-axis

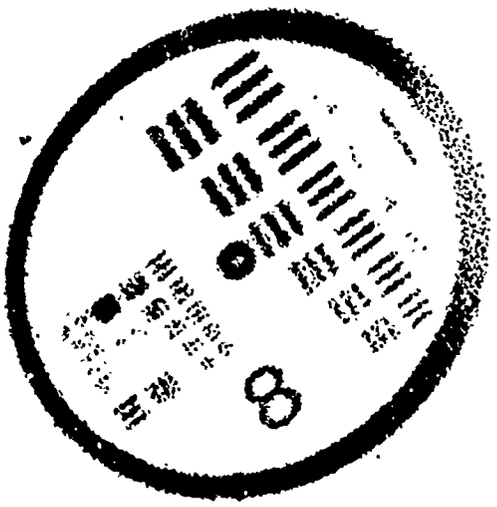

Picture No. 9 C201 30 degrees off-axis

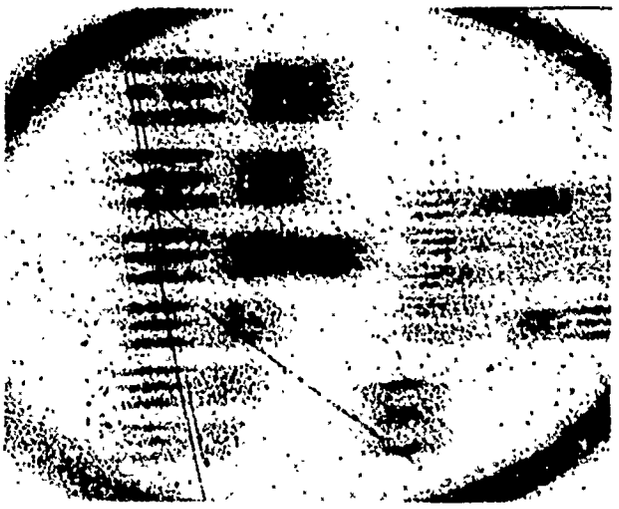

Picture No. 10 C88 30 degrees off-axis

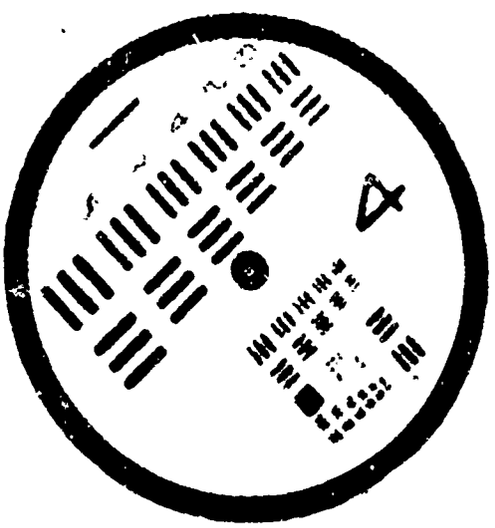

Picture No. 11 Concentric dome 15 degrees off-axis

Picture No. 12 Pluno parallel port 15 degrees off-axis

PROGRAM OF RESEARCH IN OPTICAL OCEANOGRAPHY AT SCRIPPS INSTITUTION OF OCEANOGRAPHY

by

J.E. Tyler

Visibility Laboratory
Scripps Institution Of Oceanography
La Jolla, California

PROGRAM OF RESEARCH IN OPTICAL OCEANOGRAPHY AT SCRIPPS INSTITUTION OF OCEANOGRAPHY

J. E. Tyler
VISIBILITY LABORATORY
SCRIPPS INSTITUTION OF OCEANOGRAPHY
La Jolla, California

SUMMARY

The measurement concepts that have been developed by theory for the purpose of describing the penetration of radiant energy into the ocean are discussed briefly, and new instrumentation which has been developed at the Scripps Visibility Laboratory for the measurement of these concepts in the ocean is described. Some of the specific measurements discussed are the measurement of scattering by particles in the ocean, the measurement of the beam transmittance of a unit path length, and the important measurement of radiance distribution around a fixed point underwater. In the case of radiance distribution, the optical properties that can be derived from this measurement will also be outlined and instrumentation for the independent measurement of some of these derived properties will be discussed.

The program in optical oceanography at Scripps Institution of Oceanography is based on the general theory of scattering-absorbing media. Application of this general theory to the interaction of radiant energy with large bodies of water is, in turn, based on experimentally observable phenomena.

The water volumes used in making measurements of the optical properties of the ocean are generally much larger than the size of the scattering particles in the water and thus the circulation of particles through the measuring volume is not ordinarily detected. Only statistical averages of the microscopic light field are detected. On the other hand, the water volumes employed are generally small compared to many ocean features which are of interest in physical oceanography. This latter fact complicates the application of our optical data to the description of large ocean features.

Within this framwork, and specifically for monochromatic light, the theoretical model defines the significant optical properties, shows the relationships between them, and indicates the various instrumental methods for their measurement.

A major interest of our laboratory is the design and construction of instrumentation capable of accurately measuring the ocean optical properties that are specified by theory.

Beam Transmission Meter

The optical system of Scripps' beam transmissometer produces a cylindrically restricted beam of light between the projector and the detector. All rays within the irradiated path fall within the cylinder defined by the projector aperture and the image of the field stop at the detector. A change in index of refraction of the optical path from that of air to that of water causes the skew rays to converge on the photocell and thus prevents errors that might otherwise be present due to clipping of the beam at the edges of the receiver field stop.

The instrument, Fig. 1, has a one meter folded path. The light source and receiver are both contained in a single water-tight housing. This feature, together with an appropriate shutter mechanism in front of the silicon voltaic cell, permits the operator to standardize the lamp output and check the dark current while the instrument is submerged.

A fundamental difficulty arises in measuring the total attenuation coefficient by means of a beam of light. To properly measure the total attenuation coefficient it is necessary to determine how much image-forming light remains after the light has traversed a water path. Image-forming light is the residual light which has been neither absorbed nor scattered by the medium. In practice, some of the light scattered by the medium appears as forward scattered light within the beam.

Preisendorfer has shown that for this method of measurement of the beam attenuation coefficient the percent error is given by the equation

$$\Delta = 100 \cdot \frac{a^1 - a}{a} = -100 \cdot \frac{2\pi\sigma(0^\circ)}{a}\left(\frac{r}{L}\right)^2$$

Thus the measured value of a approaches the true value of a as the ratio r/L approaches zero. Figure 2 illustrates the form of the error function. Unfortunately the amount of energy in the beam also depends on the solid angle of acceptance of flux from the light source, that is, on $r^2/L2$, and it thus becomes necessary to accept a compromise design. The Scripps transmissometer uses a beam diameter of 20 mm and a path length of 1 meter.

Null-Balance Transmissometer

For measurements at greater depth we have designed and built a null-balance transmissometer with a depth capability of 2000 meters. The optical principle is substantially the same as described previously but this instrument features a null-balance mechanism consisting of a rotating sector mirror arranged so that the light travels the water path and the reference path alternately as shown in Fig. 3. The instrument is continuously balanced by a servo mechanism that drives a circular neutral-density wedge until the optical density of the wedge is equal to the optical density of the water path. The length of the water path can be adjusted to 1/2 meter, one meter, or two meters to accomodate it to a wide range of water types.

Irradiance Meters

The most commonly measured optical property of ocean water is the diffuse attenuation coefficient for downwelling radiant energy. This property is obtained from measurements of horizontal downwelling irradiance in accordance with the equation

$$\frac{H_2}{H_1} = e^{-K\Delta Z}$$

the quantity H_2 (or H_1) being defined by the equation

$$H = \int N \cos \theta \, dw \quad .$$

The integration indicated in this latter equation can be performed by an optical integrator of suitable design. And since there are additional ocean optical properties that depend on the accurate measurement of irradiance for their evaluation, it is a worthwhile exercise to design an accurate optical integrator.

Figure 4 illustrates a cross section of a simple optical integrator for measuring irradiance. A cap of white diffusing plexiglass is cemented to a clear plexiglass base, and the unit is surrounded by a circular light shield that preverts light at angles of incidence of 90° or more from reaching the collector. The dimensions a, b, and c are empirically altered to control the collecting properties of the device and repeated underwater tests are made to determine the accuracy of the cosine form of the collection.

Figure 5 gives the analytical results of a typical collector.

As an additional check this optical integrator with an angular response designated as $f(\theta)$ has been mathematically integrated with experimentally measured radiance distributions and a comparison has been made between

$$\int N \cdot f(\theta) dw$$

and

$$\int N \cos \theta \, dw \quad .$$

The results of this comparison are shown in Fig. 6.

We have built instrumentation using optical integrators of this kind combined with optical filters to achieve sensitivity within specified bandwidths such as the photopic bandwidth of human vision.

Marine Adviser's Transmissometer and Illuminometer

The design concepts for the beam transmissometer and irradiance meter have been incorporated into a general purpose instrument capable of measuring the total attenuation coefficient, the diffuse attenuation coefficient, and the reflectance function.

Spectral Irradiance Meter

The equations describing image transfer through scattering-absorbing media contain both the total attenuation coefficient and the diffuse attenuation coefficient.

The accepted way of evaluating the response of photo detectors in connection with the observation of images through scattering-absorbing media is to integrate the products of detector sensitivity times energy available at each wavelength. Spectral values of the total attenuation coefficient are available in the literature and it is of considerable interest therefore to have spectral values of the diffuse attenuation coefficient.

During the last four years our laboratory has been systematically obtaining spectral data on the diffuse attenuation coefficient of ocean and lake water. The instrument we have used was built for us at Johns Hopkins University but has been extensively altered and improved by our own laboratory. It consists of a photo multiplier tube that observes an irradiance plate through a double-grating monochromator. An early configuration is shown in Fig. 7 which provided for double-beam observation. Prior to 1966 the lower beam shown in the figure was blacked out to provide a means for evaluating the dark current of the phototube, and the upper beam was provided with an irradiance plate.

The bandwidth of this instrument is approximately 6 nm as indicated in Fig. 8, and the internal spurious light is about 10^{-7} of the input flux as illustrated in Fig. 9.

This instrument and its performance have been described in detail in the book "Measurements of Spectral Irradiance Underwater" published by Gordon and Breach, Science Publishers.

Scattering Function Meter

Our interest in the measurement of the volume scattering function has led us to consider many different instrument ideas.

Most recently we have built a small angle scattering meter and a general angle scattering meter. The small angle scattering meter was built after a design by Dr. S. Q. Duntley and is shown in Fig. 10. The projector provides a collimated source of light. Directly in front of the objective lens is a stop which blocks the central portion of the collimated beam leaving only a thin-walled, hollow cylinder of light. At the detector end of this coaxial system the thin-walled, hollow cylinder of flux is blocked by a second stop. By appropriate design of the stops and length of the water path, the angular spread over

which the instrument collects can be controlled. An instrument of this kind was built by our laboratory and used by Dr. R. E. Morrison in connection with his doctoral thesis. Morrison obtained values of the scattering function at four angular settings between 0.126° and 2.86°.

The general angle scattering function meter is shown in Fig. 11. The optical system is illustrated in Fig. 12. This instrument is optically similar to an earlier instrument built for exploratory work in very deep water. In mechanical design, however, the more recent instrument is more compact and simpler to handle. It utilizes a 100 watt tungsten-iodine cycle lamp and an EMI 9524A photo multiplier. The scanning arm travels from 170° to the 0° position. Data is obtained between 170° and 10° and at the 0° position a measurement is made on the attenuated direct beam. This latter measurement gives a measure of the total beam power at the end of every scan. The dark current signal and ambient light signal are also recorded. Figure 13 shows a typical data record. Calculation of the volume scattering function from these data requires correction for changes in the scattering volume with angle.

The total scattering coefficient and also the back- or forwardscattering coefficient can be obtained by integration of the scattering function in accordance with the defining equation

$$S = \int \sigma(\theta) d\omega$$

or

$$S = 2\pi \int \sigma(\theta) \sin\theta d\theta \quad .$$

Measurements of the scattering function at small angles show it to be continuously increasing with decreasing angle. Since $\sin\theta = 0$ at 0°, it is of considerable interest to determine the peak value of $\sigma(\theta) \sin\theta$. Several attempts have been made to do this but the difficulties associated with obtaining accurate values of $\sigma(\theta)$ at small angles and the errors associated with extrapolation to $\theta = 0°$ have left this function in doubt. Morrison obtained a peak value of $\sigma(\theta) \sin\theta$ at about 0.1°, but more recent opinion suggests that as measurements of $\sigma(\theta)$ in the forward direction become more accurately known the peak value of $\sigma(\theta) \sin\theta$ tends to move closer to $\theta = 0°$.

Instruments for Measuring Radiance Distribution

A detailed knowledge of the distribution of radiant energy around each of two or more points at different depths underwater is the most broadly useful information for documenting the light field underwater. From such data it is possible to compute the vector and scalar irradiances at the various depths and from them obtain the diffuse attenuation coefficients for the up- and downwelling stream of radiant energy, the distribution functions, which are a rough measure of the geometrical form of the light field, and the absorption coefficient.

Some time ago our laboratory built a submersible scanning type radiance meter and obtained detailed measurements in lake water of the underwater distribution of radiant energy at various depths under clear, sunny sky lighting and under completely overcast skies. The instrumentation was adequate for the stable operating conditions prevailing at the lake site, but it was hopelessly cumbersome for ocean work.

Within the past year or two our laboratory has designed and built the radiance distribution camera shown in Fig. 14 and 15. As the name implies, this instrument employs photographic film to record and store the radiance information. The instrument uses two 8 mm, f/8, fish-eye Nikkor lenses, one of which observes the upper hemisphere and the other observes the lower hemisphere. This fish-eye lens is ideally suited for the application. The lens has a hemispherical field of view. The projection of the lens conforms to an equidistant projection to within 5 %, i.e.,

$$r^1 = f\theta$$

(where r^1 is the radius coordinate in the image, θ is the zenith angle of the object, and f is the focal length) and the film irradiance is related to the field radiance by the factor $\sin\theta/\theta$ as compared to ordinary lenses which obey the $\cos^4\theta$ law.

The instrument is further equipped with two photocell sensors designed to measure the up-and downwelling irradiance. This information is used to determine correct film exposure and to provide the information necessary to normalize data taken at various depths at the same site.

The operations of the cameras and the exposure of the film are performed by remote control. Two gravity sensing devices located in the submersible unit are included in the film exposure circuit. Their purpose is to prevent exposure of the films if the instrument is out of level by more than a predetermined angle. The instrument also contains a pressure transducer for recording depth.

The radiance distribution camera has been operated at sea several times and we are currently working on the techniques of data reduction

Measurement of the Absorption Coefficient

One of the most interesting results of theory has been the derivation of an equation for calculating the absorption coefficient independent of the scattering. This equation has been called the divergence equation and is given as follows:

$$a = \frac{1}{h}\left[\frac{d\bar{H}x}{dx} + \frac{d\bar{H}y}{dy} - \frac{d\bar{H}z}{dz}\right]$$

where $\bar{H} = H(+) - H(-)$.

If radiance distribution data is available at several depths for homogeneous water and lighting conditions, the absorption coefficient of the water can be immediately calculated from this equation.

We are currently engaged in research involving the determination of the absorption coefficient of water by means of this equation and can say several interesting things about it. The equation is valid for any light field, artificial or natural. However, in a laboratory experiment involving even large tanks of water, the measurable values of irradiance needed to determine the differentials in the equation are all very much alike. Measurements must consequently be made with great accuracy if their differences are to have significance.

Ocean water is uniformly irradiated by the sun and sky over large areas of its surface. The underwater light field can thus be described as horizontally stratified. Under these conditions

$$\frac{d\bar{H}x}{dx} = \frac{d\bar{H}y}{dy} = 0$$

and the divergence equation simplifies to

$$a = \frac{1}{h} \cdot \frac{d\bar{H}z}{dz} \quad .$$

The simplicity of measuring the irradiance components of $d\bar{H}z$ have already been discussed. To measure the absorption coefficient, it is only necessary therefore to devise a simple means for measuring h, the scalar irradiance. Theory tells us that scalar irradiance can be obtained from measurements of spherical irradiance with a uniformly diffusing sphere. Efforts to do this have so far not been satisfactory because a transluscent diffusing sphere is not a good integrating sphere, and there is no way, at present, to know how good the sphere must be to give a satisfactory result.

Our on-going research will, we hope, give us an opportunity to calculate the absorption from radiance distribution information. This can then be compared with values of the absorption coefficient obtained by the use of the best optical integrators we can devise. By measuring the total attenuation coefficient and the scattering coefficient at the same time we hope to check our results by means of the equation

$$c = a + s \quad .$$

Descriptive Oceanography

Another major interest of our laboratory is to describe the underwater light field, both qualitatively and quantitatively, and to confirm the interrelations between the optical properties that are predicted by theory.

Beam Transmission of Ocean Water

The beam transmittance of distilled water as a function of wavelength has been investigated in the laboratory by various workers and the results from several such investigations are combined in Fig. 16, which gives a spectral description of the total attenuation of distilled water from .2μ to 2.5μ. Our immediate interest lies in the portion of the spectrum between about 300 and 800 nm, and since distilled water represents a boundary condition for all natural waters, we are especially interested in knowing if the beam attenuation coefficient has been accurately determined.

Figure 17 exhibits two laboratory determinations of the spectral beam attenuation coefficient. In both cases the work has made use of long path lengths through the water (132 cm for Sullivan, 364 cm for Hulburt) and a short cell of identical materials has been used as a standard. The values obtained by Sullivan are lower than Hulburt's in the blue region of the spectrum being only 67 % of Hulburt's. In the red region of the spectrum Hulburt's values are lower than Sullivan's being only 73 % of Sullivan's. Unfortunately, there is no way to rationalize these differences. If forwardscattering had been present in either experiment it would have resulted in lower values of the total attenuation coefficient. On the other hand, if the distilled water used had been contaminated in either case it would have led to higher values.

We have no immediate plans to undertake distilled water measurements but do plan to measure spectral values of the total attenuation coefficient in ocean waters and will use the data of Hulburt and Sullivan for comparison purposes. On the basis of present information, the minimum expected value of the total attenuation coefficient appears to be .03/m and occurs at about 475 nm.

In addition to measuring transmittance, a beam transmissometer can be used to describe the vertical structure of ocean water and record temporal changes in that structure. Figures 18, 19, and 20 illustrate this use of the beam transmissometer.

Irradiance Transmission of Ocean Water

In ocean water irradiated by sun and skylight only, spectral values of the diffuse attenuation coefficient should be smaller than respective values of the total attenuation coefficient. This statement is based on the fact that the total attenuation coefficient measures losses from absorption and total scattering, whereas the diffuse attenuation coefficient measures losses from absorption and backscattering but not from forwardscattering. The statement can be tested by means of recent data we have obtained for the spectral diffuse attenuation coefficient in exceptionally clean lake water. Figure 21 compares our data for the diffuse attenuation coefficient with values of the total attenuation coefficient obtained by Hulburt. The two sets of data do not conform entirely to expectations, however they do suggest that the difference between c and K will be smaller in the red region of the spectrum where absorption is predominant. This is an effect that can also be surmised from theory.

Measurements of spectral irradiance in various types of water have revealed other interesting features of the underwater environment. Deep water acts like a monochrometer. This is illustrated in Fig. 22, which exhibits spectral irradiance curves for various depths in a single water body down to 600 meters. The curves clearly show the spectral compression due to high attenuation coefficients in the red and near ultraviolet regions of the spectrum. If the integrals of these curves are plotted as log-total irradiance against depth the typical urve in Fig. 23 is obtained. The slope of this curve is steep near the surface, indicating strong, average attenuation near the surface, but after substantial elimination of the red portion of the spectrum the slope becomes nearly constant.

Spectral irradiance data on different types of water show other interesting features of the light field. In the clean water data of Fig. 24 can be seen the relatively high water transmittance between 350 and 500 nm. At about 520 nm, a minor absorption band of water can be seen. This has been previously undetected because of insufficient sensitivity. In water containing large amounts of chlorophyll and yellow substance, the spectral data exhibits strong absorption in the blue and violet regions of the spectrums and at about 670 nm exhibits an absorption band of chlorophyll, Fig. 25.

In waters containing relatively large amounts of chlorophyll, curves of spectral upwelling irradiance show evidence of the red reflectance of the chlorophyll pigment.

Scattering Function

During May and June of this year, Mr. Austin was able to obtain a large amount of data on the volume scattering function of various water types ranging from Sargasso Sea water to water containing about 1 microgram of chlorophyll per liter. Examples of this data have been shown in a previous section.

Most of this data is not yet in final form. However, it is expected to demonstrate the differences in magnitude of the scattering function for different types of water and perhaps will also confirm the suggestion made by Dr. Duntley that the shape of the scattering function is nearly independent of water type.

Radiance Distribution

Measurements of radiance distribution have revealed many of the important optical features of the underwater light field.

As a result of Snell's law, daylight arrives at a point underwater through a 92° cone. If the sky is overcast, the opening of the cone will appear overcast as in Fig. 26.

In Fig. 27, the sun was low in the sky and the zenith was dark. The radiance (6.6° cone angle) of the zenith was measured as a function of depth. It will be seen that for the first 5 meters of depth more flux was being scattered into the zenith path than was being lost by attenuation. In the direction of the sun (the upper curve), flux was being lost at a more rapid rate near the surface than at the greater depths. In the nadir direction, the only observable change is the uniform attenuation with depth.

The data in Fig. 28 was obtained on an overcast day by making four scans in the same vertical plane but at different depths. The first scan (A) was made in air and shows the skyline and other features as noted on the figure. The second scan (B) was made from 2.5 cm below the surface. The edge of the Snell circle is clearly shown at 46.8°, together with the bright ring at 80° to 90°. In scan C the edge of the Snell circle is nearly obliterated by scattered light, and in scan D no further evidence of these surface effects can be seen.

Complete radiance distribution data in the plane of the sun is given in Fig. 29. These data reflect the angle of refraction of the sun's rays, the edge of the Snell circle, the rapid changes in shape, and the trend toward a distribution that is symmetrical about the vertical axis, as well as being symmetrical in azimuth.

These rapidly changing features of the underwater light field with depth support the prediction that the shape of the radiance distribution becomes fixed and that this shape depends only on the scattering and absorbing properties of the water. Figure 30 is another experimental verification of this trend. In the same water the ratio of N_Z/N_N is plotted as a function of depth for both overcast and sunny conditions. It can be seen that the ratio in both cases is approaching the same constant.

APPLICATIONS

Biological

In addition to the use of optical data to detect spacial or temporal variations in ocean water and to support the theory of radiative transfer, we would like to use optical data to quantitatively specify different types of ocean water.

One way to do this is to calculate the trichromatic coordinates from the spectral irradiance data and use the C.I.E. color coordinate system to determine the dominant wavelength, brightness, and purity of the water color. Current research at our laboratory includes work along these lines. We hope to be able to relate the color of the ocean to other ocean variables such as the chlorophyll concentration, amount of yellow substance, etc. In this connection we are also interested in the remote sensing of surface chlorophyll from aircraft or satellites and are currently cooperating with scientists at the Woods Hole Oceanographic Institution in a program of study that measures the optical signal available from different types of ocean water and studies its transmission, first through the air-water interface and then through the atmosphere.

We are also interested and active in research on the interaction of radiant energy with oceanic phytoplankton, in the resulting primary productivity, and in improving the techniques for estimating the

primary productivity of specific ocean areas.

Image Transfer

A continuing interest of our program is the application of ocean optical data to problems of image transfer through ocean water. "Image transfer" in this context refers to human vision, fish vision, photography, or television. In all of these cases the general treatment is the same, but because of different spectral sensitivities of the sensors, the specifics will differ. To simplify the discussion, I will limit myself here to human vision. This limitation means, of course, that all the ocean properties involved must be measured for the photopic bandwidth.

The phenomena of contrast reduction is illustrated by an experiment in which several white sticks are arranged along a track at different distances from the observer. Each stick is partially covered with black cloth. When observed horizontally underwater it can be seen that as the observation distance increases the white portion of the sticks appears to become darker, whereas the black portion appears to become lighter. Ultimately, both black and white portions will melt into the background radiance and disappear from sight.

A colored object may behave in a somewhat different way. For example, a red object is high reflecting, and therefore similar to white, in the red region of the spectrum but low reflecting, and therefore similar to black, in the blue region of the spectrum. As illustrated in Fig. 31, as the observation distance from a red target increases the red reflectance will become darker and the blue reflectance will become lighter. The change in contrast therefore follows a very different pattern than for a plain white target.

The equation for contrast reduction in a scattering-absorbing medium is

$$C_R = C_0 \, e^{-(a+K\cos\theta)R}$$

where C_R is the apparent contrast of an object seen from a distance R and C_0 is its inherent contrast as if the distance R were zero. In this equation we are dealing with contrast against an infinite water background, and contrast is specified by

$$C = \frac{N_0 - N_B}{N_B}$$

where N_0 is the photopic radiance of the object and N_B is that for the water background. N_B can be obtained directly from a knowledge of the radiance distribution at the site of the object, but N_0 is the radiance of the object itself and must either be measured directly or calculated from the gonioreflecting properties of the object in combination with the radiance distribution surrounding the object.

APPENDIX I

Table I

CONCEPTS AND SYMBOLS IN OPTICAL OCEANOGRAPHY

	Units	Vis Lab Symbol	IAPSO Symbol
Volume scattering function	$m^{-1}\Omega^{-1}$	$\beta(\theta)$	$\beta(\theta)$
Backward scattering function	m^{-1}	b	b_b
Forward scattering function	m^{-1}	f	b_f
Total scattering function	m^{-1}	s	b
Radiance at depth Z in direction (θ,ϕ)	watts $m^{-2}\Omega^{-1}$	$N(Z,\theta,\phi)$	L
Scalar irradiance (Downwelling (-), from the lower hemisphere)	watts m^{-2}	h(Z,-)	-
Scalar irradiance (Upwelling (+), from the upper hemisphere)	watts m^{-2}	h(Z,+)	-
Total scalar irradiance	watts m^{-2}	h(Z)	E_o
Irradiance on a horizontal plane from the upper hemisphere (2)	watts m^{-2}	H(Z,-)	E_d
Irradiance on a horizontal plane from the lower hemisphere (2)	watts m^{-2}	H(Z,+)	E_u
Distribution functions	(ratio)	$D(Z,\pm)$	-
Reflectance functions	(ratio)	$R(Z,\pm)$	(1)
Diffuse attenuation coefficient for irradiance from the upper hemisphere	m^{-1}	K(Z,-)	-
Diffuse attenuation coefficient for irradiance from the lower hemisphere	m^{-1}	K(Z,+)	-
Absorption coefficient	m^{-1}	a	a
Ratio of the radiance at the end of a path r to the input radiance	(ratio)	Nr/No	Lr/Lo
Transmittance (for specified path length)	(ratio)	T	T
Total Attenuation coefficient	m^{-1}	c	c

(1) Called "Irradiance Ratio" by IAPSO

(2) Called "downward" and "upward" irradiance by IAPSO

APPENDIX II

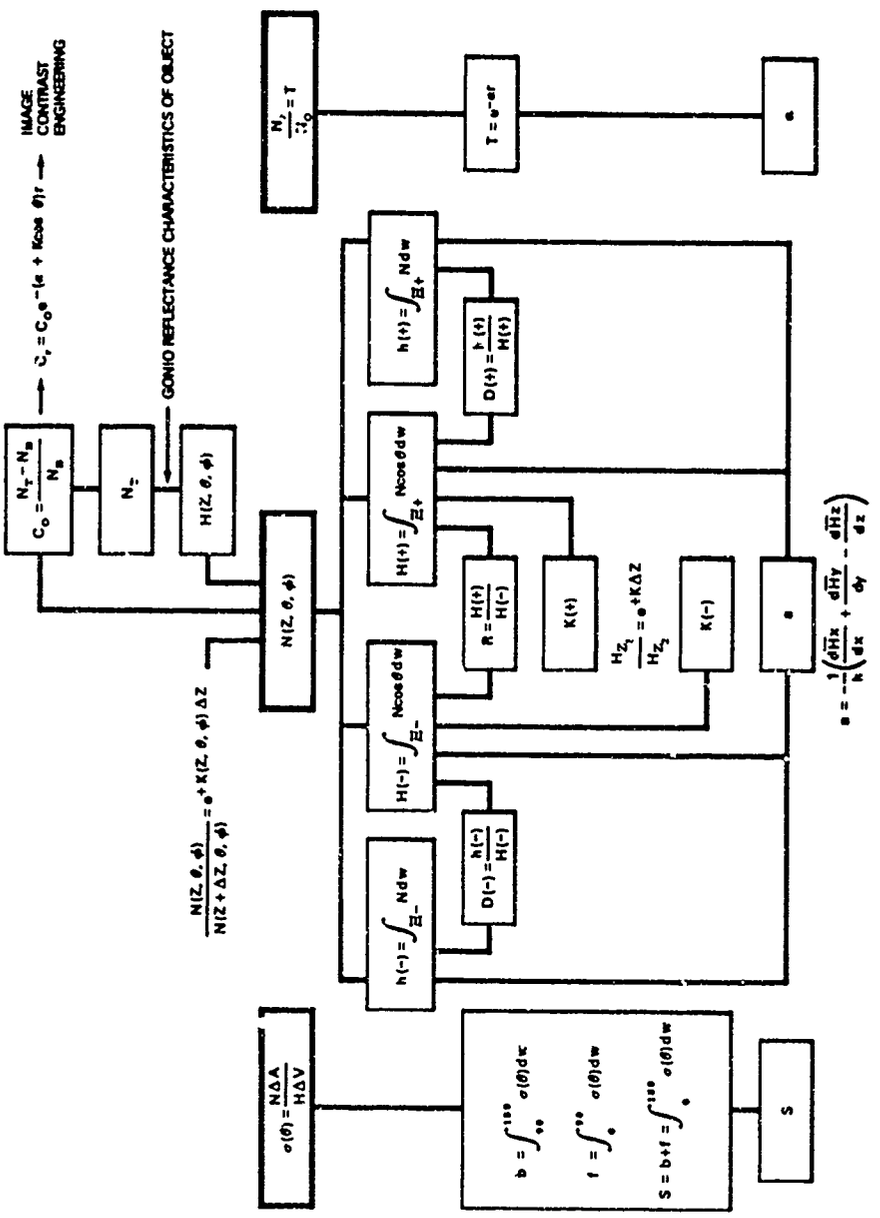

Fig. 1

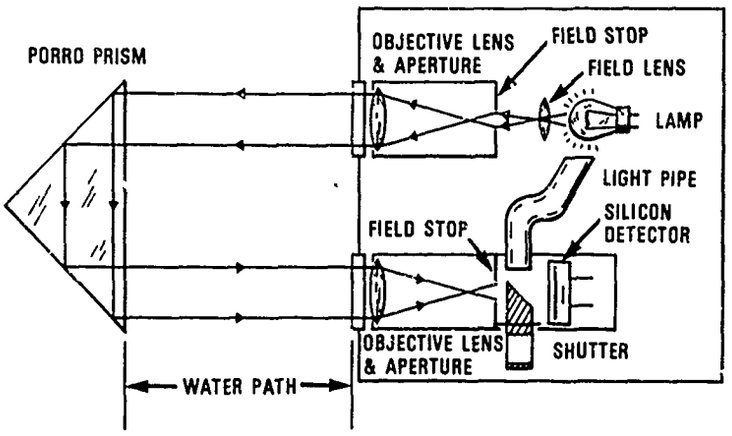

Fig. 1. Transmissometer (or beam transmission meter) designed by T. Petzold and R. W. Austin, S.I.O.

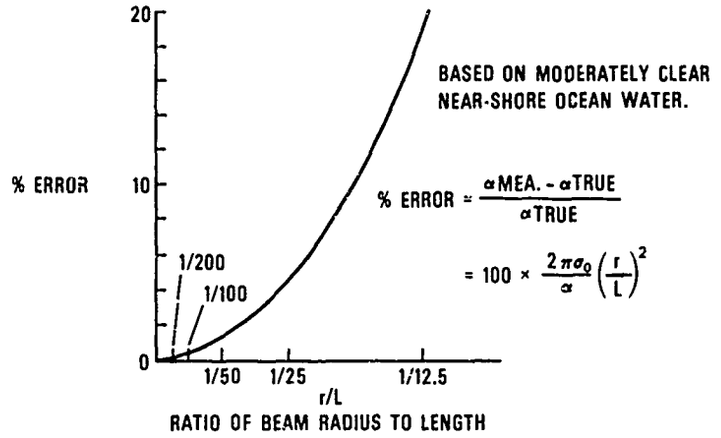

Fig. 2. Error due to the presence of forwardscattered light within the beam of a transmissometer, (after R. W. Preisendorfer, S.I.O.).

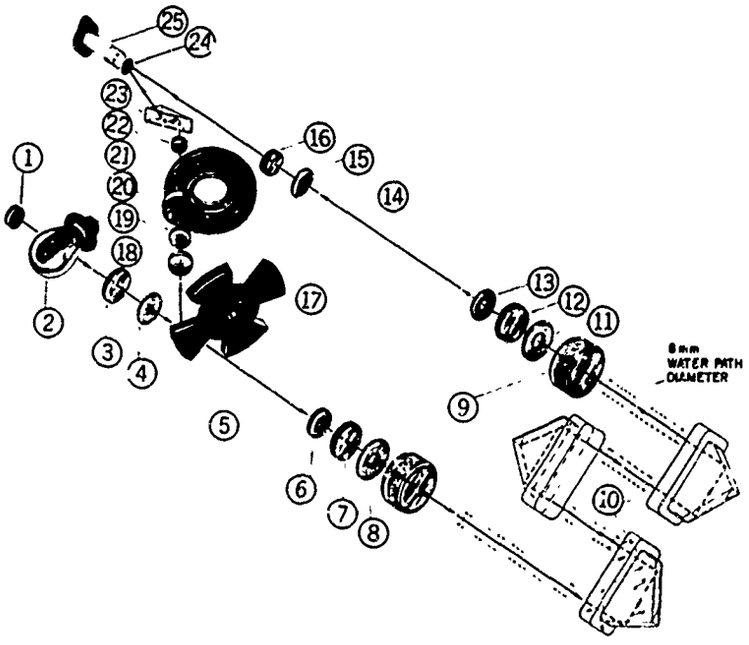

Fig. 3 Optical system of the null-balance transmissometer designed by R. W. Austin, S.I.O.

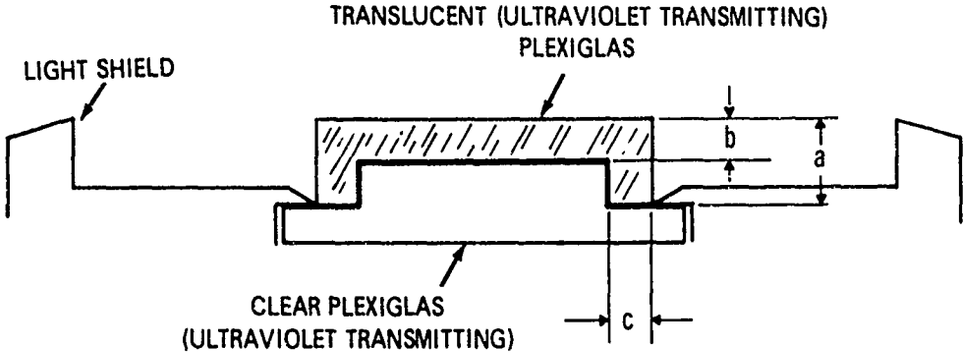

Fig. 4 Cross section of an irradiance collector.

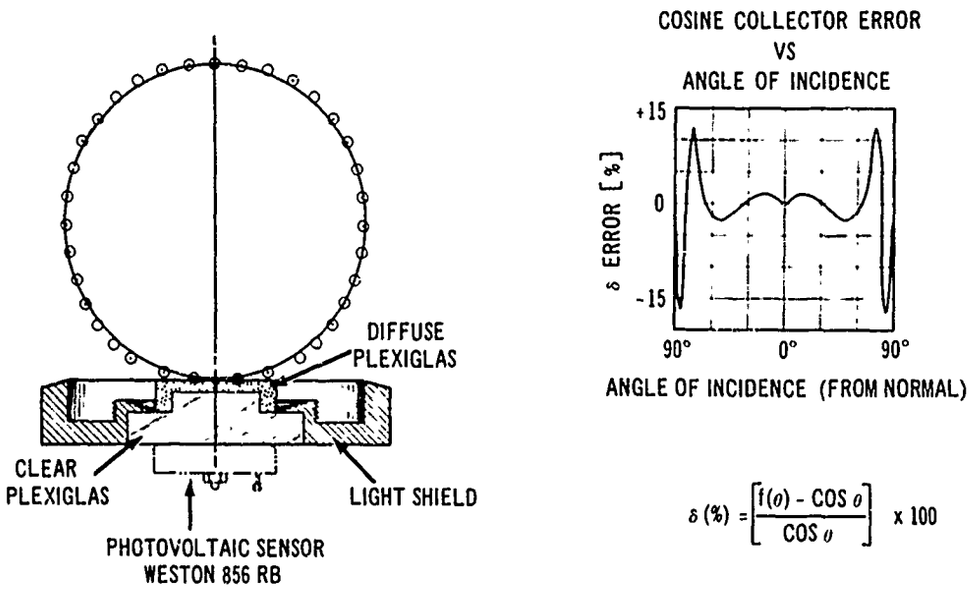

Fig. 5. Illustrating the performance characteristics of a typical irradiance collector, data obtained from underwater experimental tests.

DEPTH (M)	ERROR(%)	
	E(Z,-)	E(Z,+)
4.2	.25 %	-.88 %
10.4	.16	-.88
16.6	-.27	-.93
29.0	-.52	-.89
41.3	-.44	-.94
53.7	-.25	-.92
66.1	-.36	-.93

Fig. 6 Illustrating the performance characteristics of a typical irradiance collector, data obtained by computation.

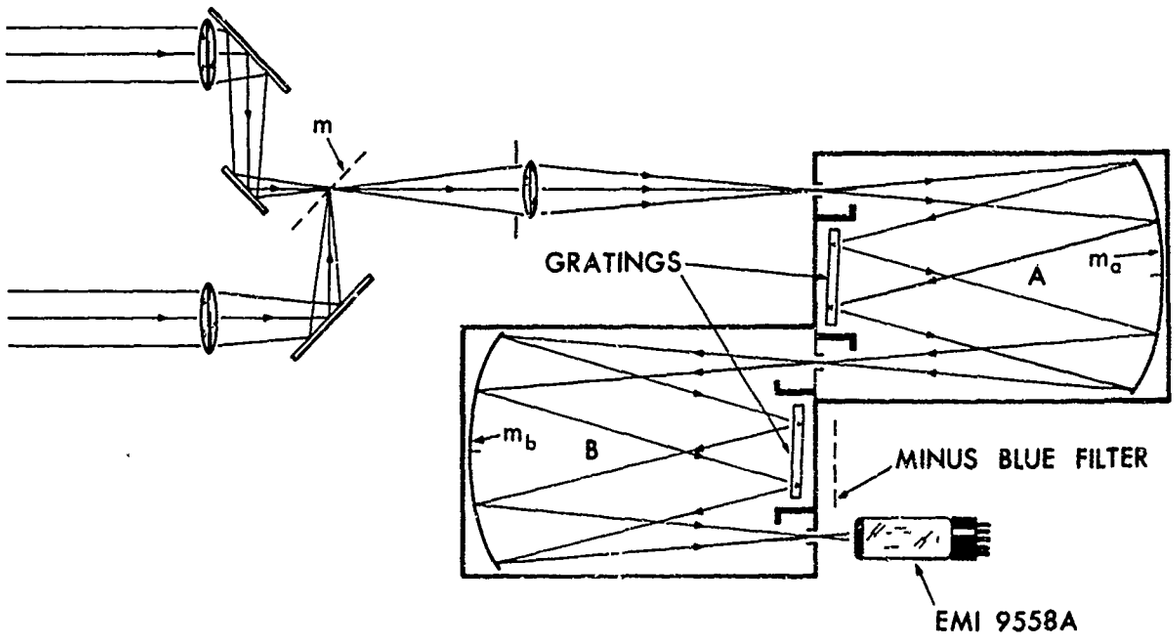

Fig. 7. Optical system of the Scripps spectroradiometer. The two objective lenses at the left in conjunction with the rotating sector mirror, m, provide for double-beam observation.

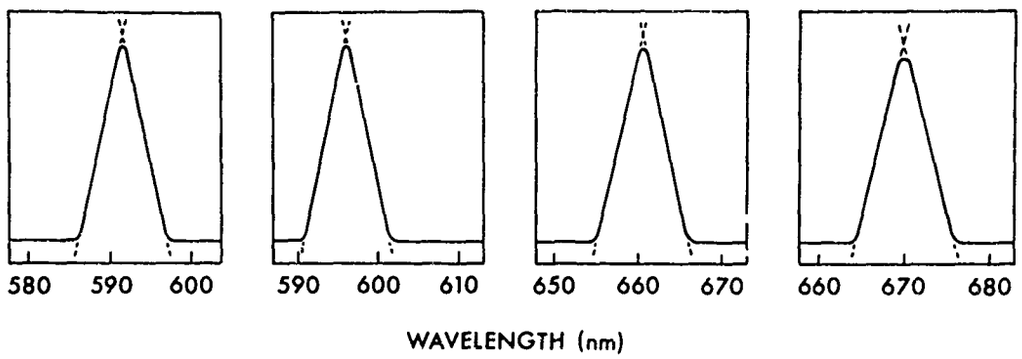

Fig. 8. Typical recordings of spectral bandwidth at four wavelength settings for the Scripps spectroradiometer.

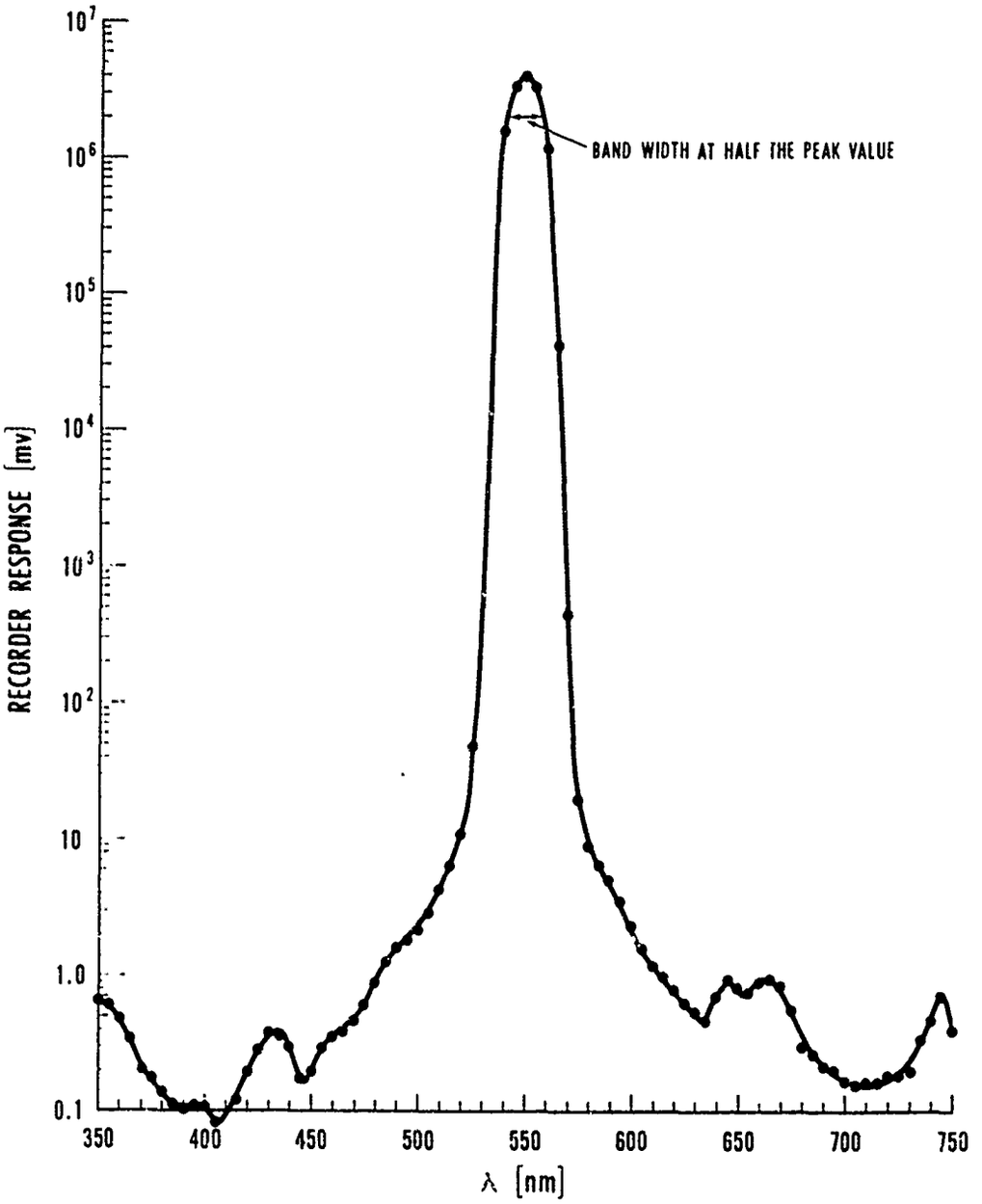

Fig. 9. Direct recording of the stray light present in the blue and red regions of the spectrum when the input to the Scripps spectroradiometer is a broad spectral band in the green region (550nm), as would be the case in typical coastal water.

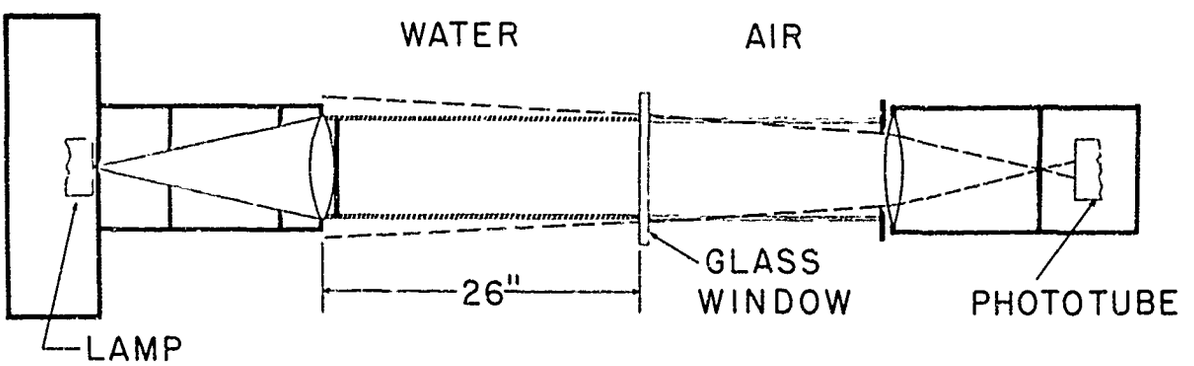

Fig. 10. Optical system of a narrow angle scattering meter, after S. Q. Duntley, S.I.O. The objective lens of the projection system is centrally stopped to yield a thin cylinder of radiant energy - shown cross-hatched over the water path. It is the small angle forward-scatter from this thin cylinder that is collected by the phototube.

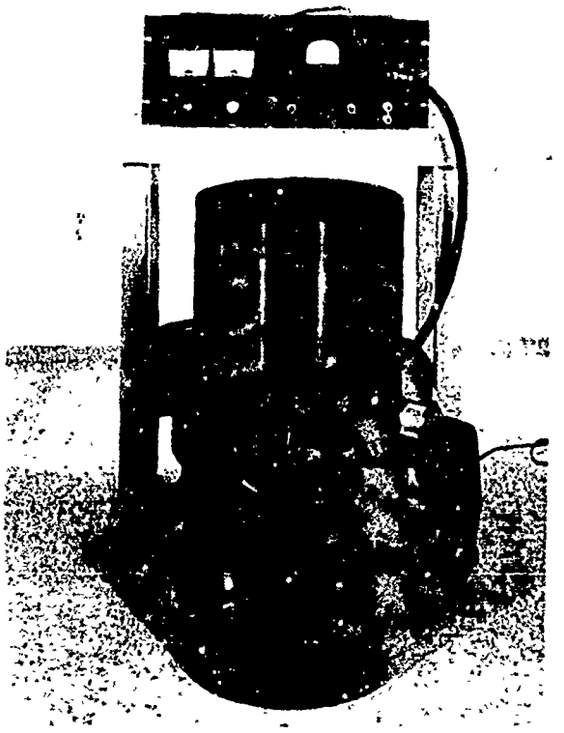

Fig. 11. General-angle scattering meter, after R. W. Austin and T. Petzold, S.I.O.

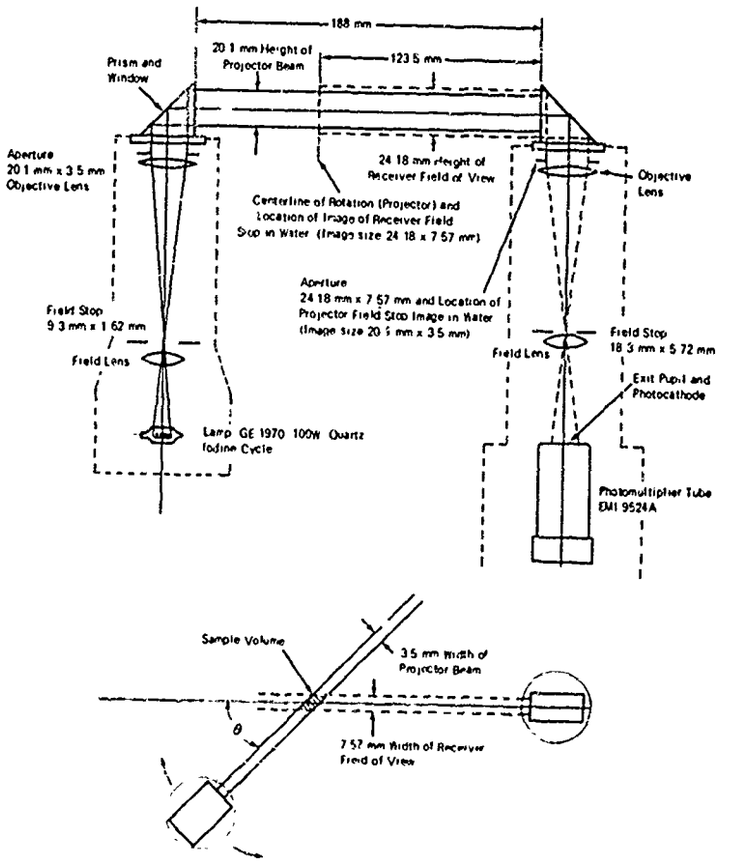

Fig. 12. Optical diagram of the general-angle scattering meter. Upper diagram is side elevation, lower diagram is a plan view.

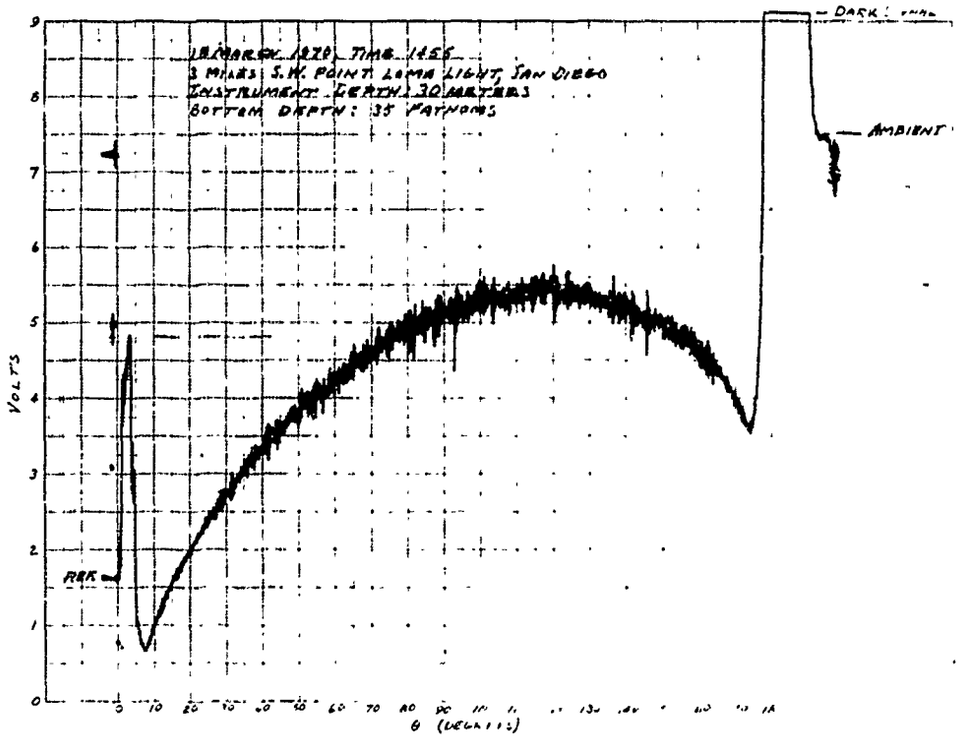

Fig. 13. Data recording from the general-angle scattering meter. Lamp reference level is recorded at the left and ocean ambient light at the right. This data must be corrected for changes in the scattering volume.

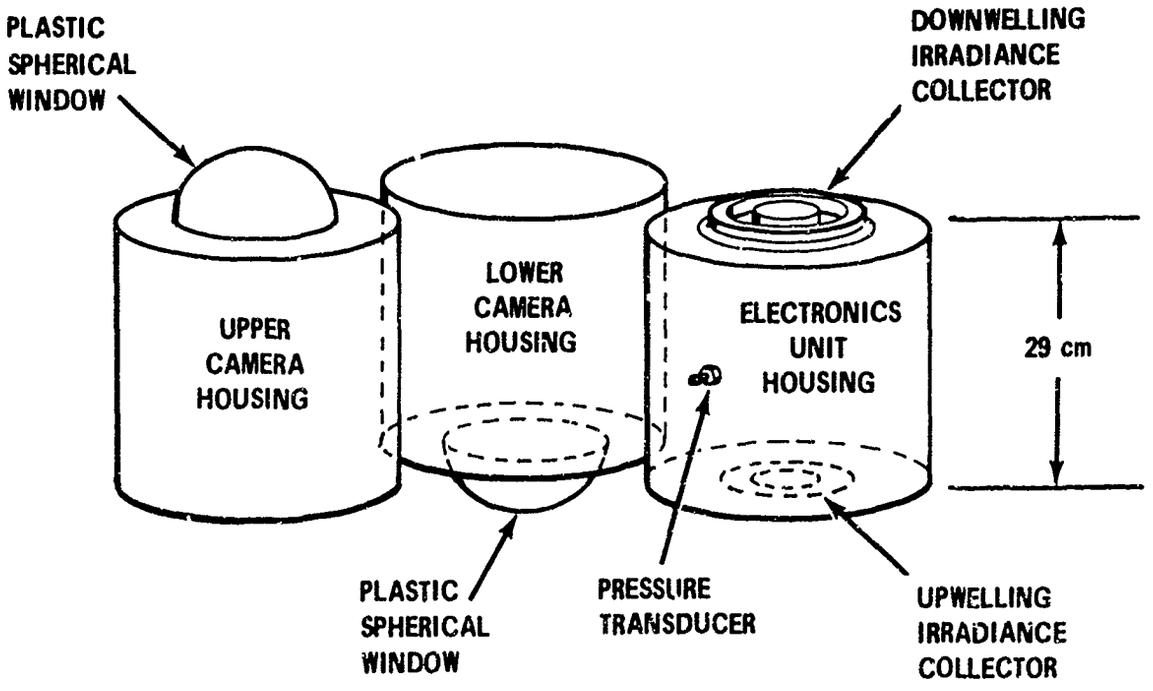

Fig. 14. Diagrammatic arrangement of the radiance distribution camera.

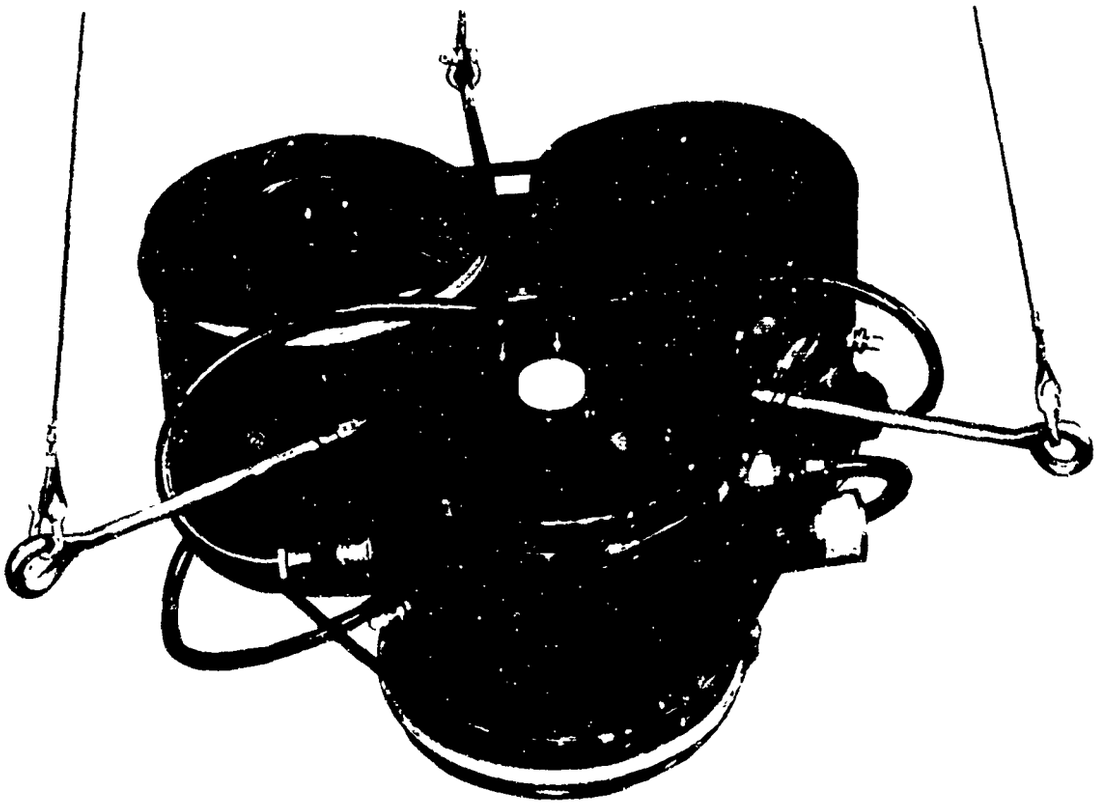

Fig. 15. Radiance distribution camera, after R. C. Smith, J. E. Tyler, and R. W. Austin, S.I.O.

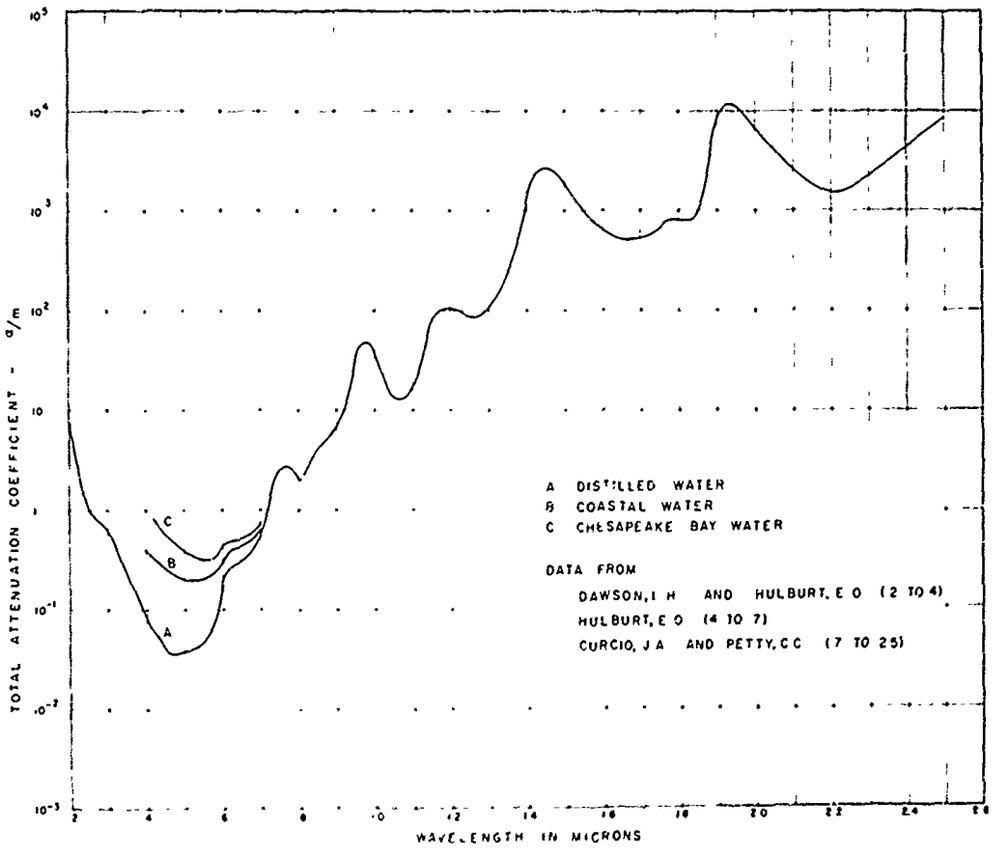

Fig. 16. Laboratory measurements of the spectral beam attenuation coefficient of distilled water.

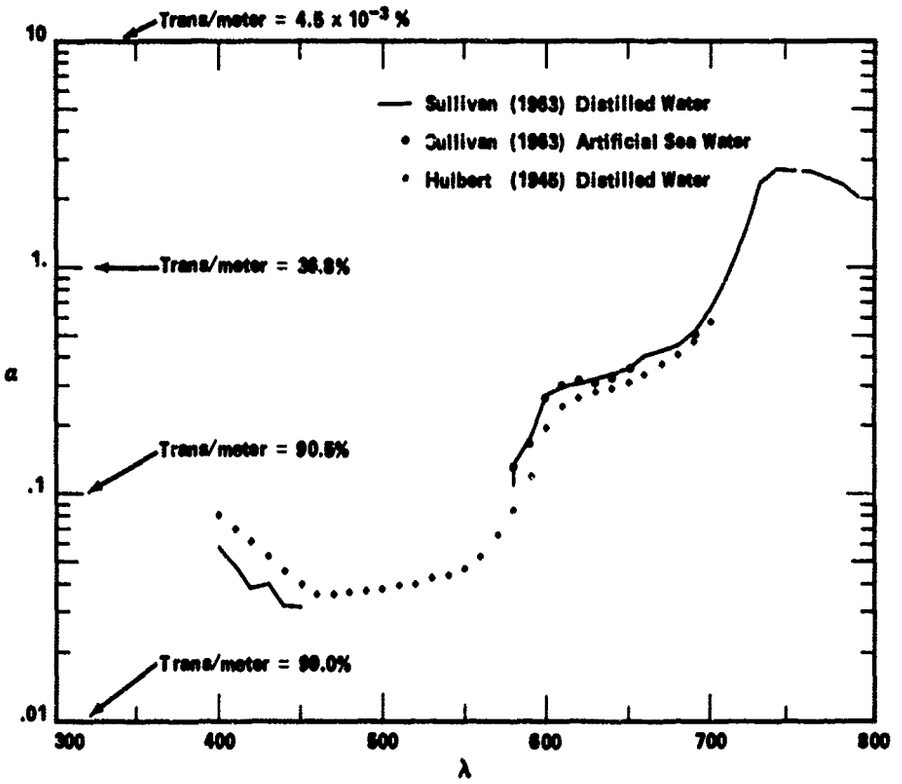

Fig. 17. Laboratory measurements of the spectral beam attenuation coefficients of distilled water.

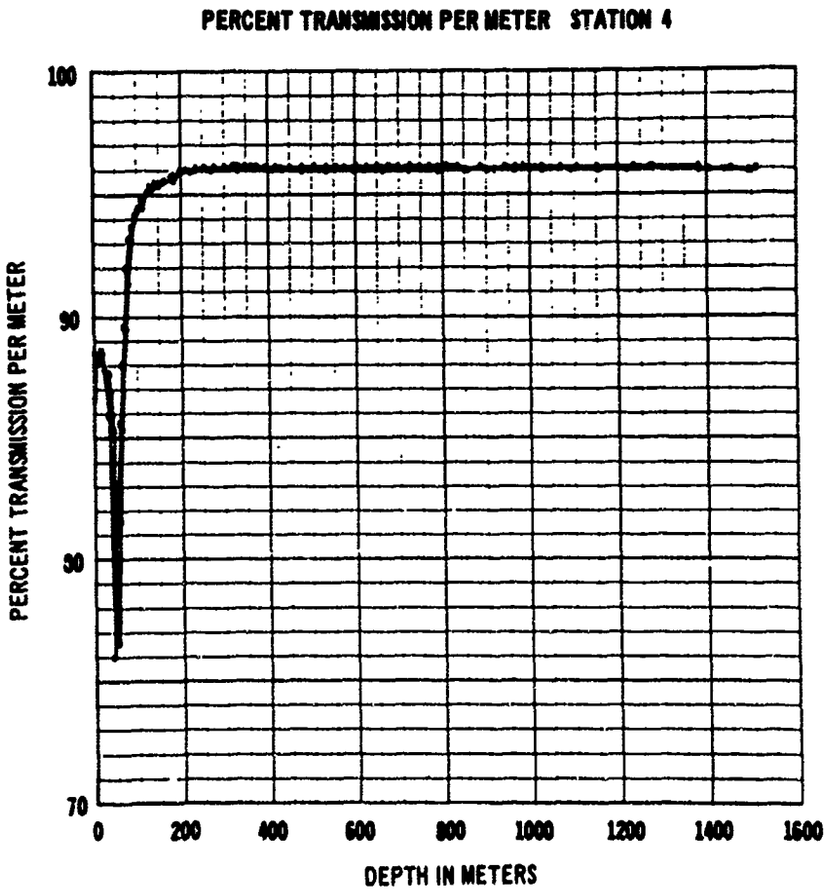

Fig. 18. Beam transmittance vs depth in the Pacific Ocean.

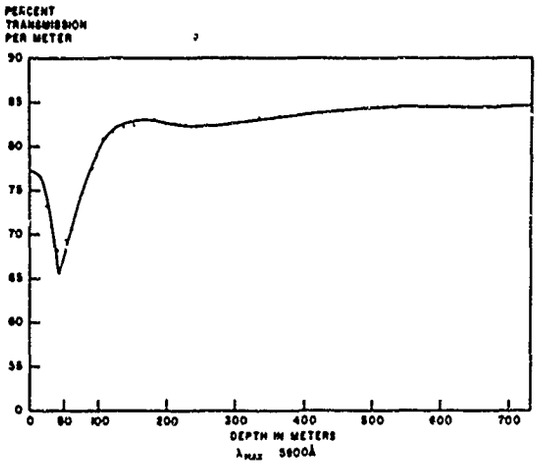

Fig. 19. Beam transmittance vs depth in Pacific coastal water.

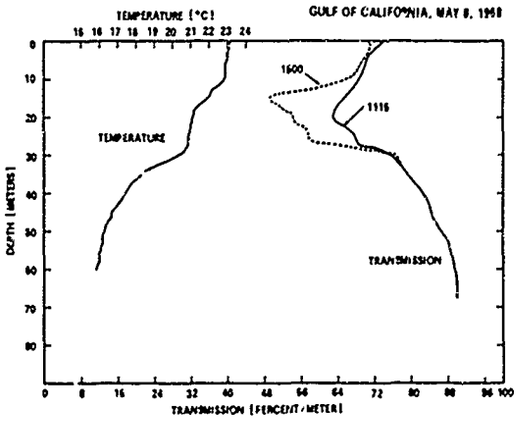

Fig. 20. Change of beam transmittance with depth and time in the Gulf of California.

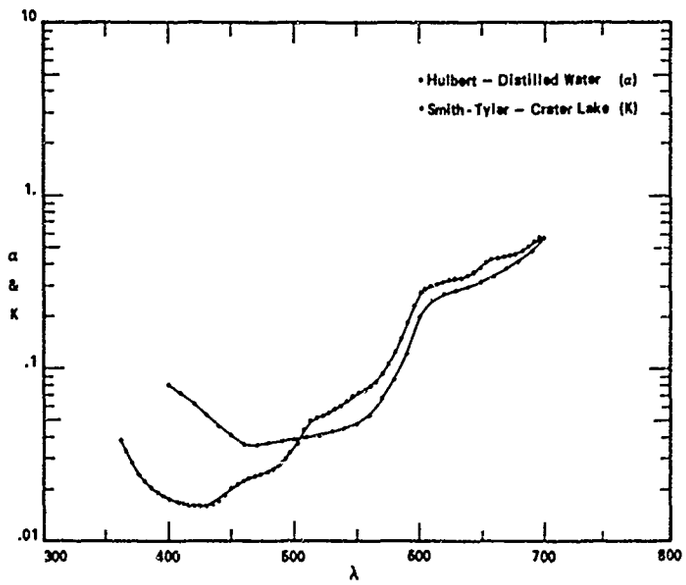

Fig. 21. Spectral values of a (after Hulburt) compared with spectral values of K (after Tyler and Smith). The fact the K is greater than a between 510 and 700 nm probably reflects the fact that the waters were different.

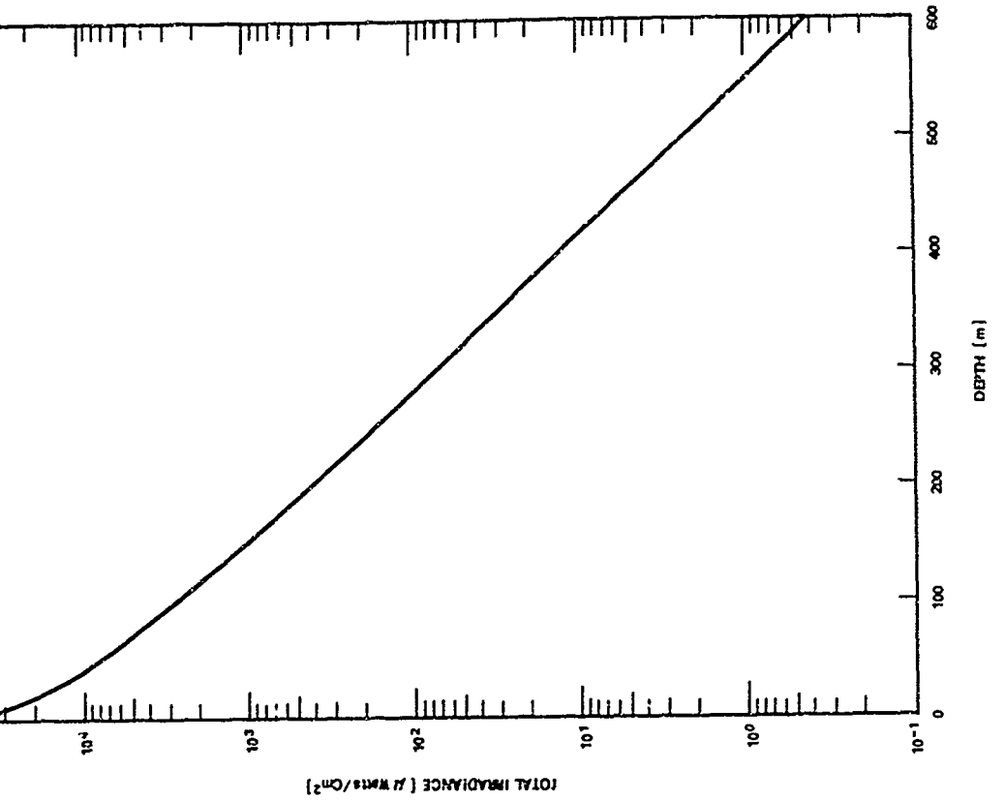

Fig. 23. Total irradiance as a function of depth, calculated from the curves in Fig. 22.

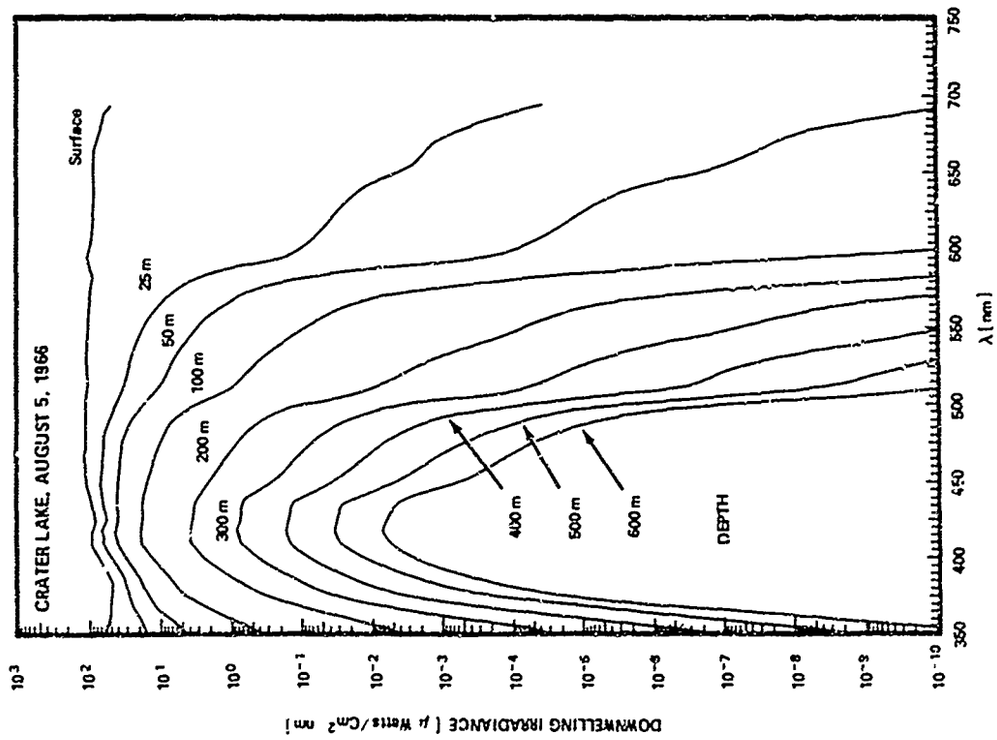

Fig. 22. The variation in spectral bandwidth as a function of depth in clear water.

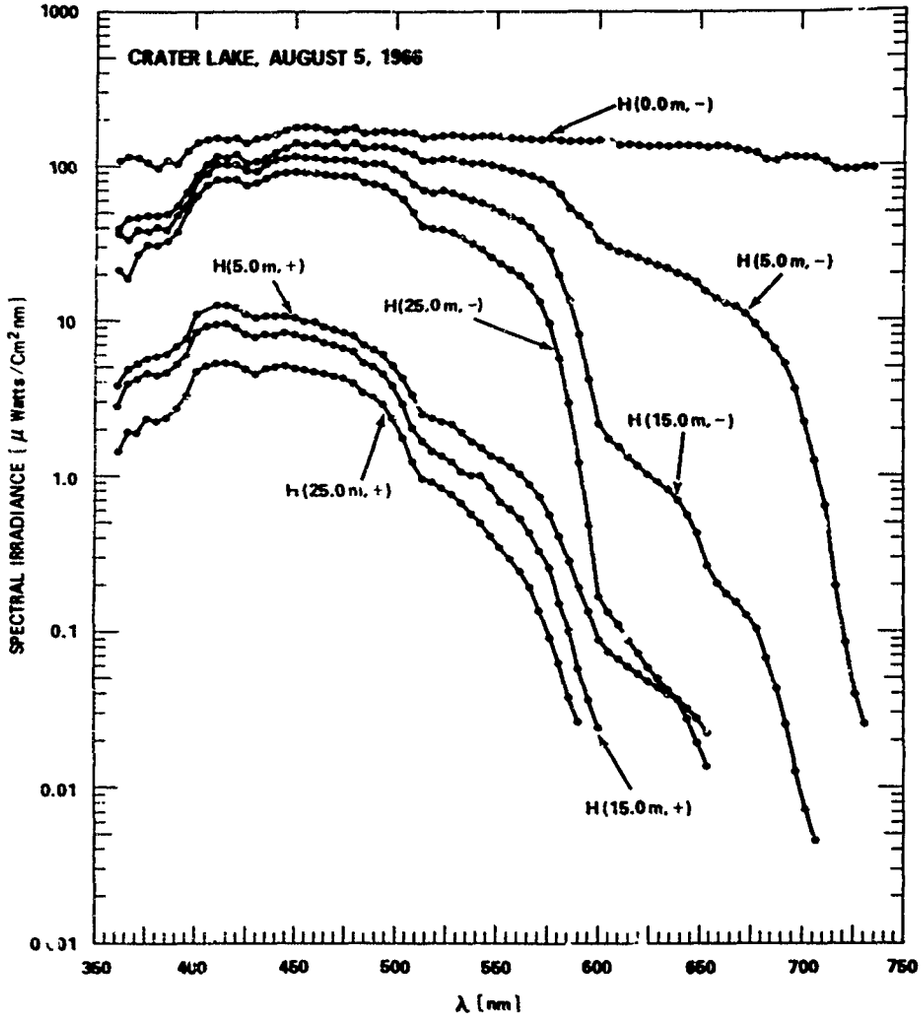

Fig. 24. Spectral irradiance data obtained in the clear water of Crater Lake. The curve marked H(0,0,-) was obtained above the water surface. *

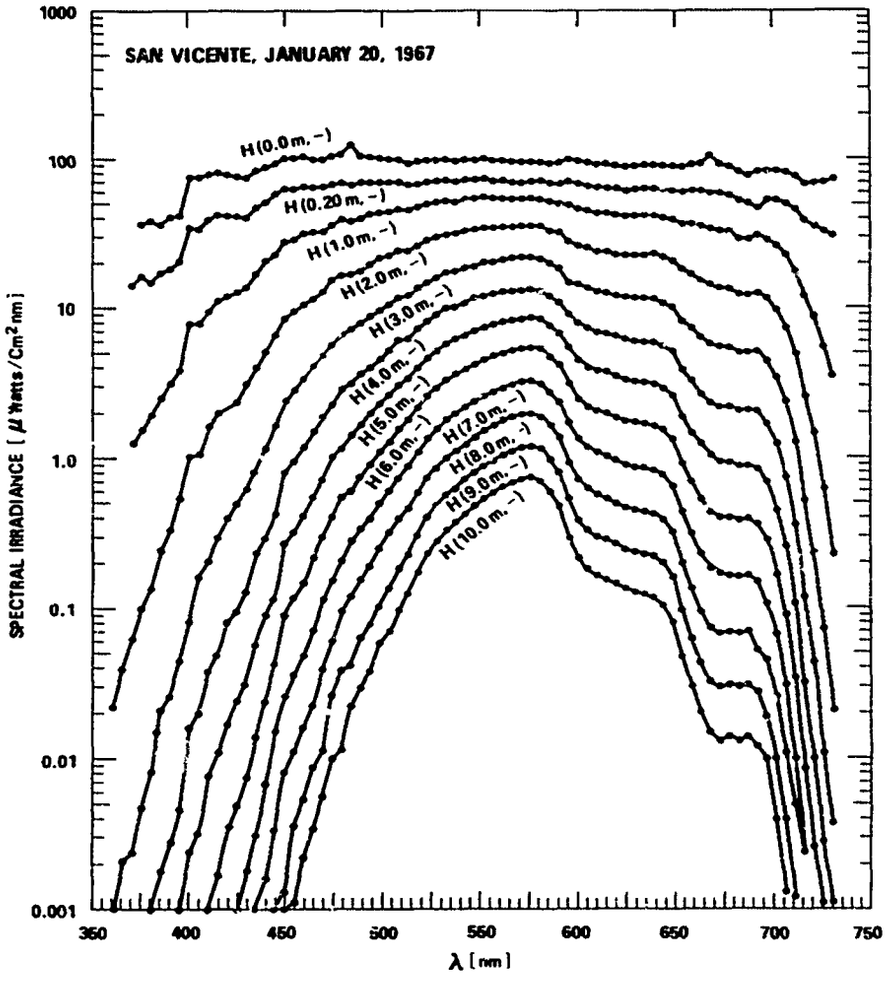

Fig. 25. Spectral irradiance data obtained in San Vicente Lake, San Diego County. The curve marked H(0.0,-) was obtained above the water surfact. *
* See Measurements of Spectral Irradiance Underwater by Tyler and Smith, Gordon and Breach Science Publishers, London, 1970.

Fig. 26. Photograph from underwater showing the Snell circle.

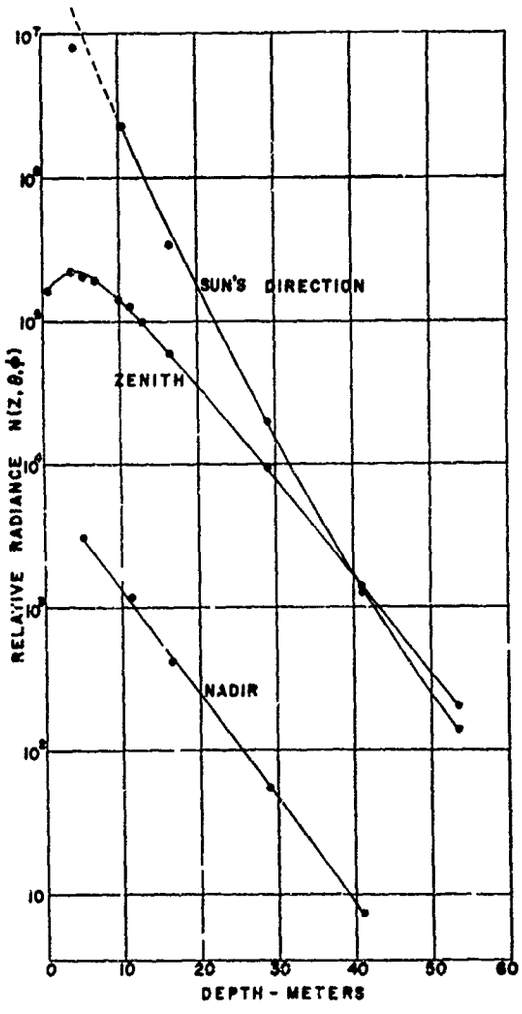

Fig. 27. Radiance in three directions as a function of depth. Clear sunny sky with sun low in the sky and zenith direction consequently darker than sun direction. Note the way the scattered light from bright areas fills in the dark areas as depth is increased.

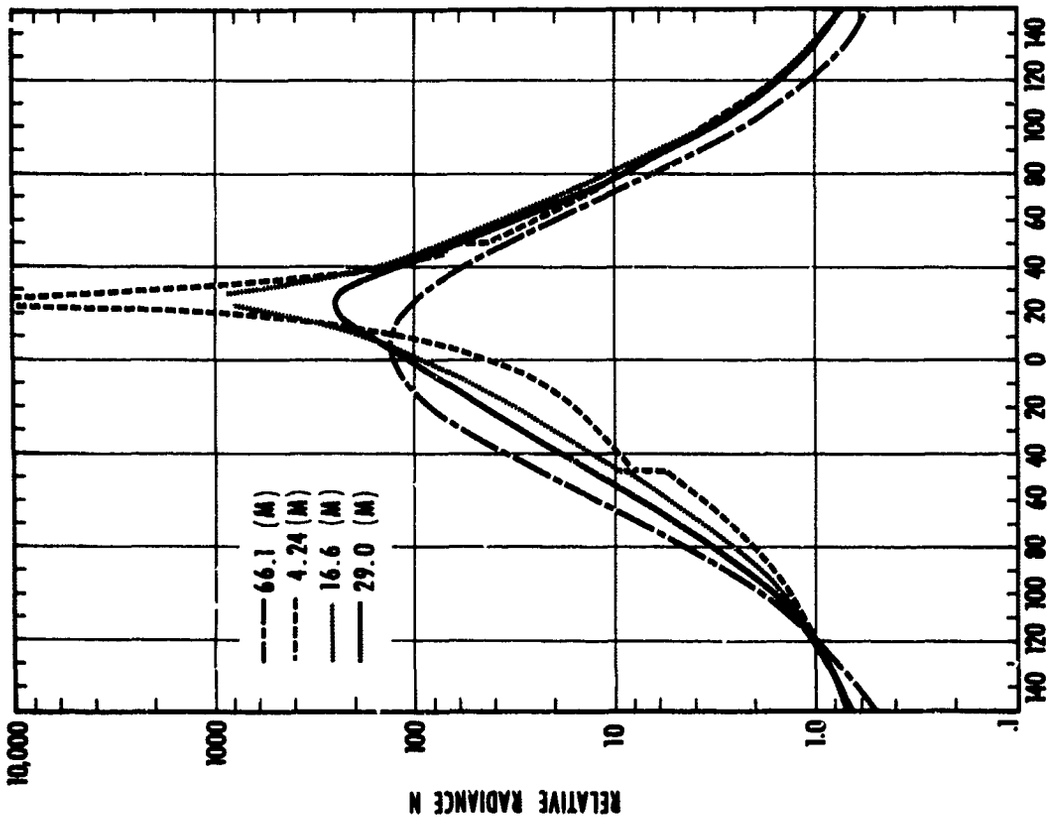

Fig. 29. Radiance distribution in the sun's plane as a function of depth, sunny day. Curves normalized at θ = 120° away from sun.

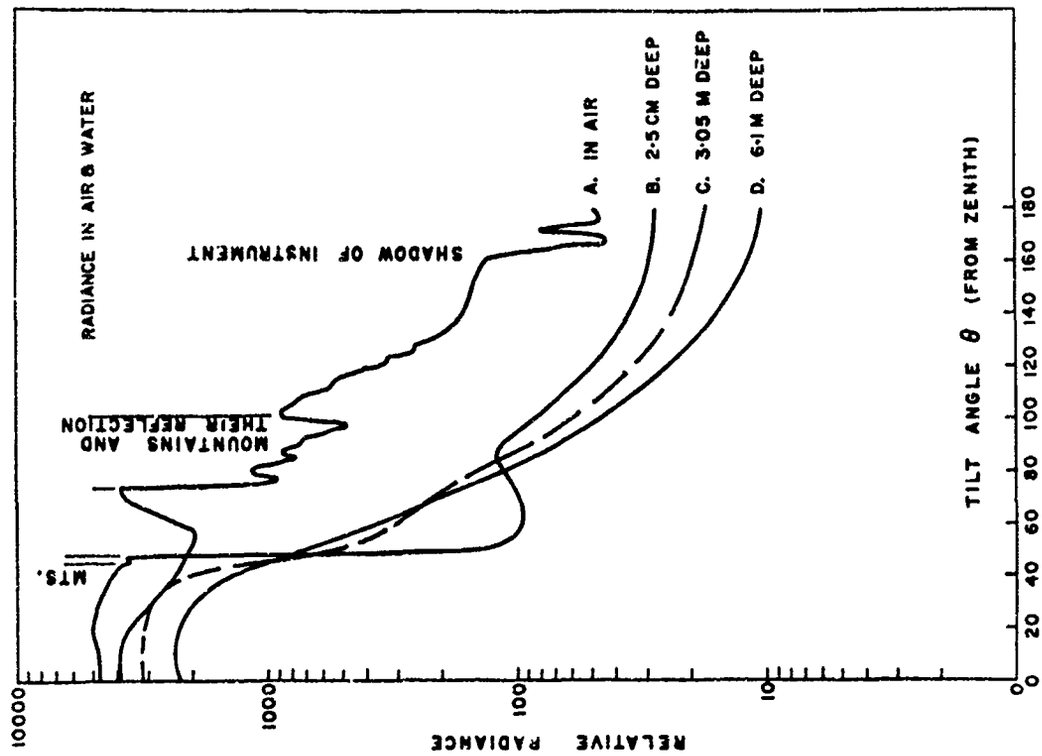

Fig. 28. Radiance distribution in one plane as a function of depth, overcast day.

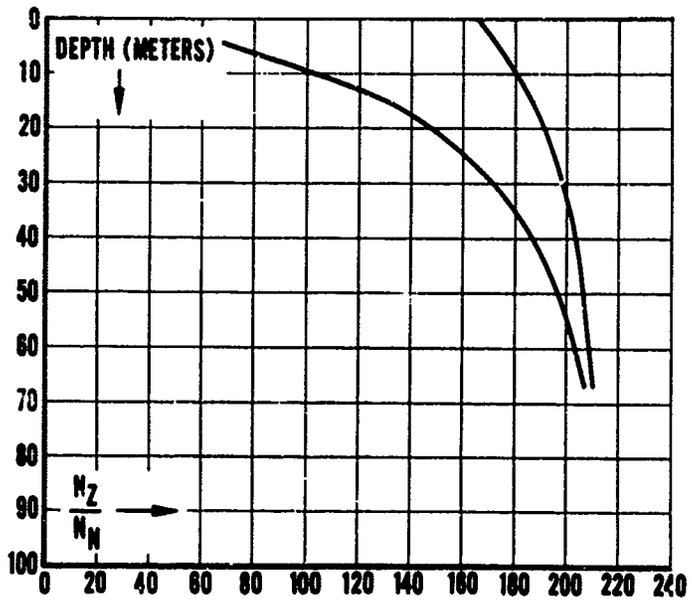

Fig. 30. Ratio of zenith radiance to nadir radiance (N_Z/N_N) plotted as a function of depth in the same water for clear sunny sky lighting (right) and overcast skylighting (left). Both curves are directed toward the same asymptote.

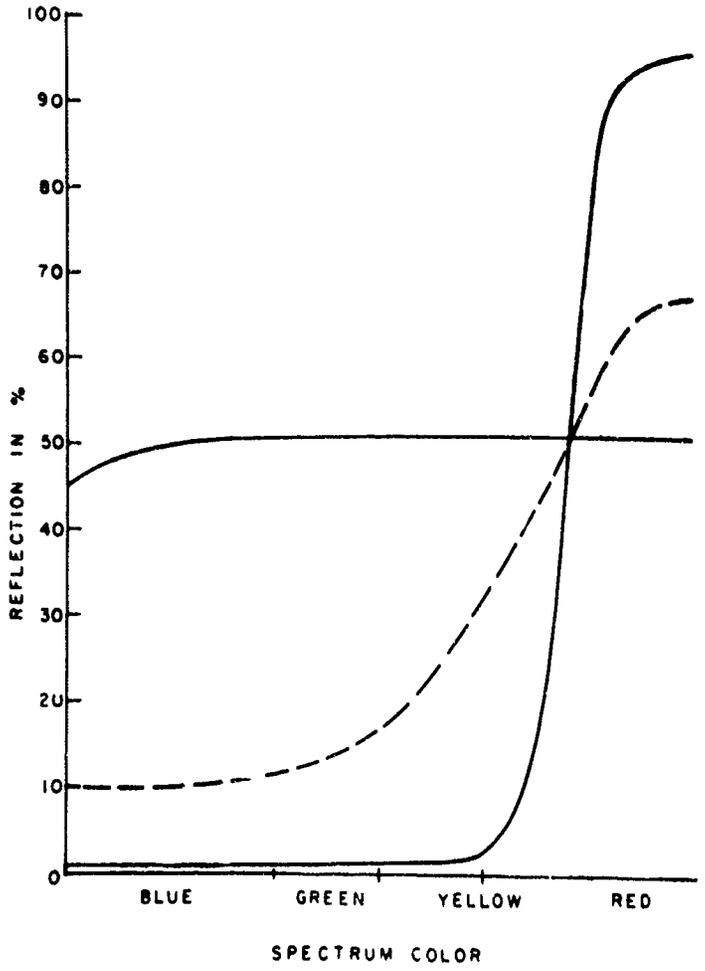

Fig. 31. Change in color of a red object as it is moved horizontally away from an observer. The red object is characterized by the solid curve showing no reflectance in the blue or green regions of the spectrum. The dashed line shows the apparent reflectance when seen through water having strong scattering and absorbing properties. The nearly horizontal solid line shows the reflecting properties of an infinite path of water.

EVALUATION OF UNDERWATER VISIBILITY IMPROVEMENT BY RANGE GATING SYSTEMS

by

S. Donati and A. Sona

Laboratori CISE
Milano, Italy

SOMMAIRE

La vision sous l'eau est limitée par les phénomènes d'absorption et de diffusion de la lumière. L'absorption entraîne une diminution de l'intensité de la lumière qui est fonction exponentielle de l'augmentation de la distance, tandis que la diffusion crée un étalement des faisceaux lumineux en même temps qu'un brouillage des images. On espère améliorer la visibilité en ayant recours à la technique des portes réglables en distance.

Cette technique s'appuie sur l'utilisation d'une source éclairante émettant de courtes impulsions lumineuses (par exemple, un laser commuté) associée à un dispositif d'observation équipé de porte (par exemple un tube convertisseur d'image). La sélection temporelle de la lumière recueillie par le dispositif d'observation équipé de porte permet de rejeter la lumière ambiante et d'accepter totalement la lumière utile émanant des objets observés. Afin d'évaluer l'amélioration de la visibilité sous l'eau que l'on peut obtenir grâce à la technique des portes réglables en distance, nous avons calculé le pouvoir séparateur angulaire et le contraste d'une scène schématique placée à diverses distances. On peut décrire le phénomène de la propagation comme un processus de diffusion multiple, puisque les distances de visibilité sous l'eau correspondent à quelques longueurs d'atténuation. Le processus de diffusion multiple a été étudié à l'aide de la méthode de Monte-Carlo. La trajectoire des photons dans l'espace est déterminée par sélections stochastiques des séquences successives de diffusion, suivant le profil transversal différentiel pour le processus de diffusion élémentaire. On peut ensuite évaluer, pour diverses distances, la luminosité, le contraste et le pouvoir séparateur angulaire d'une cible standard, illuminée ou lumineuse par elle-même. On obtient l'augmentation de la distance de visibilité par une comparaison avec les courbes de visibilité pour l'œil. On a effectué des calculs pour une longueur d'onde $\lambda = 0,48\ \mu$ correspondant à la région bien connue d'absorption minimale. On a supposé que les poids relatifs de la diffusion et de l'absorption étaient respectivement de 60 et 40 %, et que la fonction de diffusion, pour le processus élémentaire était la moyenne des mesures effectuées par plusieurs auteurs et rapportées par Duntley, qui a souligné la grande similitude des résultats obtenus par différents chercheurs en dépit des différences de condition de travail. Les résultats de notre analyse montrent que l'on peut attendre des systèmes de portes réglables avec réponse linéaire (par exemple convertisseur d'image) une amélioration par 2 ou 3 de la distance de visibilité ; de plus, si l'on insère un seuil dans le canal de l'image (par exemple, dans le signal TV d'un système à trame), on pense obtenir une amélioration supérieure.

EVALUATION OF UNDERWATER VISIBILITY IMPROVEMENT BY RANGE GATING SYSTEMS(*)

S. Donati and A. Sona
Laboratori CISE
Milano, Italy

SUMMARY

The underwater propagation problem, including the time dependence, has been studied by means of the Montecarlo method with the aim of evaluating the visibility improvement achievable with range gating techniques. Results are presented for various cases of observation, taking into account powers required from light sources. The different modes of operation are compared and expected performances discussed.

1. INTRODUCTION

Underwater visibility is strongly limited because of absorption and scattering, which reduce apparent radiance, contrast and angular resolution of observed objects. Backscattered light gives the major contribution in contrast loss, and can be almost entirely eliminated with observation systems making use of range gating techniques.

To evaluate the effectiveness of these techniques in improving underwater visibility, the problem of light propagation in presence of multiple scattering must be faced, since the underwater visibility range amounts to about four attenuation lenghts (loosely speaking). In addition, also the time distribution of scattered light must be taken into account to evaluate the performances of range gating systems.

We have chosen the Montecarlo method to treat the multiple scattering time-dependent problem, with the feeling that it was the only method capable of giving practical results of reasonable accuracy without requiring the solution of involved integral equations. As the input data for the Montecarlo calculations we have utilized those from the authoritative work of Duntley[1]. The relative weight of absorption and scattering has been assumed to be 40% and 60% respectively (at 480 nm) and the single scattering function has been assumed according to fig. 12, Ref. (1), averaging among the quoted diagrams and extrapolating linearly between 165° and 180°, where the original diagrams are interrupted.

2. MONTECARLO CALCULATIONS

In a Montecarlo calculation it is important to look for the simplest model of the problem at hand, in order to shorten the computing time as much as possible and meanwhile to obtain numerical results easily utilizable in more complicated cases with few straight supplementary calculations. For this reason, all the symmetries of the propagation process have been fully utilized to settle the model of the problem. As a model, we have chosen a scattering space enclosed in a spherical surface, at the center of which a photon is assumed to start, at time zero, in a "zero angle" direction (Fig. 1). The photon then makes its random zig-zag path and, whether not absorbed, finally reaches the spherical surface where its story comes to an end. The polar coordinates ϑ with respect to the starting direction, the angle ϑ_u at which the path crosses the spherical surface and the total lenght of the path (i.e. the time spent) are the results to be recorded. The Montecarlo computation is made by sorting out in sequence the lenght of path between successive scatterings and the change of direction at each scattering point according to the appropriate probability density functions, so as to build the photon path in space. About 30000 photon paths have been computed in this way, and for each path three results were computed at a time for three different sphere radius, namely R = 3.83, 7.66 and 11.5 attenuation lenghts. The results, stored in three records of 40 x 40 x 40 memory positions, represents in a sampled way the probability $P(\vartheta, \vartheta_u, t)$ that a photon starting at time zero at the center of the sphere, will intersect at time t the spherical surface with the angular coordinates ϑ and ϑ_u. As an example of the Montecarlo results, $P(\vartheta, \vartheta_u, t)$ is plotted versus ϑ in fig. 2 and versus t for some values of ϑ in fig. 3, after an integration on the other variables not indicated. Starting from the $P(\vartheta, \vartheta_u, t)$ which represents the response to a delta source, it is easy to calculate, by means of numerical convolutions, the response to other types of sources, such as a beam giving a uniform illumination over a fixed angular aperture or a Lambert radiator.

Furthermore, if we consider a scene placed on the spherical surface which encloses the propagation space, and viewed by an observer placed at the center of the sphere, it is possible to calculate the radiance received by the observer when the scene is either self-luminous or illuminated by a beam starting from the observation point. In the first case the results are obtained from the Lambert radiator response, in the second through a convolution of the uniform beam and the Lambert radiator response, as discussed in earlier papers (2) and (3).

As an illustrative example, we report some results relative to the case of an illuminated scene. The scene is assumed to consist of a sequence of ten concentric rings, alternatively black and white, and covering and angular field of view of 45° (fig. 4). The black rings are assumed to absorb the collected light, the white ones to re-irradiate the light according to Lambert law with unity diffusion coefficient. The scene is illuminated by an uniform beam of 45° angular aperture and viewed by an image forming optical system.
Since the image of the scene has a circular symmetry, it suffices to consider the radial distribution of light intensity. In fig. 5 we have reported for three scene distances, namely 3.83, 7.66 and 11.5 attenuation lenghts, the intensities of useful light coming from the illuminated rings together with the backscattered light intensities (the sum of the two terms gives the intensity of light actually received). Fig. 5 a refers to the case of no gating: note that the backscattered light, nearly constant for the three ranges considered, becomes very large compared to the useful light from the scene as the distance increases, so that the useful light from the scene soon becomes masked by the background. Fig. 5 b shows the effect of a gating from half the scene distance onward: the intensities of light from the scene are not altered, whereas the backscattered light is so strongly reduced to have still an amplitude comparable to that of the useful light from the scene.

3. VISIBILITY IMPROVEMENT AND POWER REQUIRED

The results obtained through the Montecarlo calculations give the radiance of the viewed scene at the observation point as a function of the angular direction of observation.
They have been analyzed on the basis of visual criteria, since we only consider image-forming systems which display information to a human observer and neglect the problem of pattern recognition or parameter estimation.
Data measured by Blackwell (ref. (4) and preceeding works) are the appropriate starting point: they give the contrast c required for a circular target of given angular diameter α to be resolved when the target is superposed on a uniform background of luminance B. To compare visual data to our radiance curves, we have calculated from the latter the contrast c as a function of the angular resolution α, according to the method discussed in ref. (2). The intersections of the contrast curves with the visual curves give the angular resolution as a function of the illuminating power. Results for some interesting cases of observation are reported in fig. 6-8; all the results presented in the following refer to the visibility of perfectly diffusing objects on an absorbing background.
Fig. 6 shows the angular resolution α of an illuminated scene, plotted against the distance of the scene from the observation/illumination point, measured in attenuation lenghts; the curves are given for some values of the power-parameter $GP/L^2\Omega$, in which:
P = radiant flux of the illuminating source (W),
Ω = solid angle of the emitted radiant flux, assumed equal to the solid angle under which the scene is viewed (stered),
L = scattering lenght (m),
G = radiant gain of the observation system (for example image converter gain) (dimensionless).
The left-hand diagram of fig. 6 refers to the case of no gate, i.e. shows the result of an illuminated scene viewed by the unaided eye; it is apparent that the visibility is lost, even for high illuminating power, a little before five attenuation lenghts. However, the resolving power quickly deteriorates already at about four attenuation lenghts.
The right hand diagram shows the effect of two different gating intervals; here the parameter RET stands for relative excess time of the gate with respect to unattenuated light propagation time t_u, that is $RET = (t - t_u)/t_u$. For the case RET = - 0.5 —∞ , i.e. for a gate from half the distance of the interesting scene up to infinity, it is appearent the strong improvement in visibility. An additional gain is obtained by gating from the scene distance to infinity (RET = 0 —∞) as it is shown in the diagram, whilst a narrow gate (RET = 0—0.05) give only a slight further improvement (this case is not reported in fig. 6).
In fig. 7 are reported the visibility curves of a self-luminous scene, that is one in which the object radiates its own light according to Lambert cosine law. Here the symbols used have the same meaning as in fig. 6, except for Ω which now represents only the solid angle under which the scene is viewed. By a comparison with fig. 6, one can see that the visibility of a self luminous scene with no gate is better of the illuminated one, even gated, at least for equal power-parameters $GP/L^2\Omega$.
Gating of the self luminous scene (results not reported in fig. 7) provides only a minute additional improvement in visibility.
Fig. 8 shows the results attainable with the raster technique. This technique basically consists in a range-gating system employing a narrow-angle illumination beam which is deflected so as to scan the whole scene, while a single detector is made to receive only the light coming from the illuminated spot. To make the estimation of the required power, we assumed that the angular aperture of the illuminating beam is equal to the obtainable resolution, so that the number of point scanned is determined by the operating conditions. By comparing fig. 6 and 8 it is clear that, for equal power-parameters, the resolution achievable with the raster is slightly worse than that corresponding to the range gating system.
The time dependence of the signal received by the detector when the light source emits a light pulse of short duration is reported in fig. 9; in this figure the backscattered light and the useful signals from three target at different distances (3.83, 7.66 and 11.5 attenuation lenghts) are separately plotted. Note that,

though the backscattered light and the useful signal amplitude decrease almost in the same way, the signals are clearly detectable even at the largest distance considered.

The raster techniques allows to exploit sophisticated methods for processing the output signal from the detector, which can be a very sensitive one, like a photomultiplier . For example, non linear techniques may be used to improve the scene contrast by means of background reduction and could allow a reconstruction of the relative intensity of objects at different distances by time dependent amplifier gain.

4. DISCUSSION OF RESULTS

The validity of above-quoted Montecarlo analysis relies on several hypotheses, which must be kept in mind when making a comparison with experimental results:

a) propagation space is assumed to be homogeneous, with a relative weight 60% and 40% for scattering and absorption; the single scattering function (fig. 2) was assumed as an average between measured ones;

b) the viewed objects are perfectly diffusing targets on an absorbing background;

c) the observation system is linear and displays an image directly to the eye.

On the basis of qualitative arguments, the effect of slight deviations from these assumptions may be predicted. For example, were larger the relative weight of absorption, the power required would increase and the angular resolution become better. An increase of backward intensity of the single scattering function would reduce the visibility range of the illuminated scene, gated and not-gated, possibly of the same amount, since amplitude of the corresponding signals have a rate of decrease with range not very different.

Assumption b) was made for characterizing a well-visible, non-cooperative target; however, in an experimental setup the choice of retroreflectors or Scotchlite tapes greatly assists to obtain increased signal amplitudes. In this case, the ranges of both gated and not-gated illuminated scene should increase of the same factor, and when backscattering does not predominate the matter should be that of an additional power gain equal to π times the reflectivity (in 1/sterad) of the reflector.

Hypotesis c) has been selected to assess the performance of simple range gating systems with direct visualization of images to a human observer in real time. Therefore, performances of non-linear photographic films were not studies, even because a comparison with the visual properties of the eye is not straighforward and would require a special analysis.

Some experimental analysis on underwater range gating have been made. Angular resolution and range from the results published by Heckman and Hodgson[5] are shown in fig. 6 as H's. An exact determination of power-parameter is not possible from the photos they have reported, however the comparison would be loose since the target was a Scotchlite tape; at any rate, from published data $GP/L^2\Omega$ is estimated to be in the range 20-150.

As a concluding remark we note that, from results reported in fig. 6, 7 and 8, the visibility range can be improved over a factor of 2 depending on the angular resolution required and/or the available power. The self-luminous scene visibility can be attained, and even overcomed if adequate power or radiant gain is provided. From this last point of view, the raster system is attractive, though it starts from a slightly worse angular resolution, since it enables to obtain a very large gain.

(*) Work supported by the Contract CNR-CISE no. 17.8.3.1. for Development of Technology and Electronics Instrumentation.

REFERENCES

1. Duntley, S. "Light in the Sea" J. Opt. Soc. Amer. 53 (1963), 214.
2. Donati, S. and Sona, A. "Evaluation of the visibility improvement in the fog by the range gating technique", Optoelectronics, 1, (1969), 89.
3. Donati, S. and Sona, A. "Further results on the range gating techniques: visibility in sea water", Optoelectronics 1, (1969) 155.
4. Blackwell, R. " The evaluation of interior lighting on the basis of visual criteria", Applied Optics 6 (1967) 1443.
5. Heckman, P. Jr. and Hodgson, R. "Underwater Optical Range Gating", IEEE J. of Quant. El., QE-3, 11 (1967) 445.

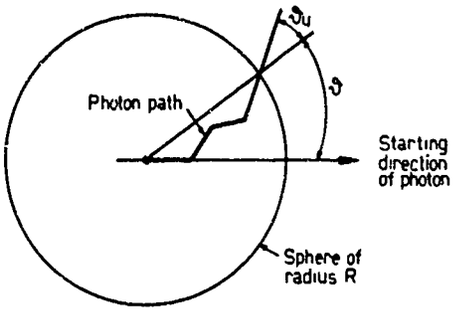

Fig.1 The model of propagation assumed in the Montecarlo calculation. Scattering space is enclosed in a sphe. of radius R (which is measured in number of attenuation lengths). At the sphere center a photon is assumed to start at time zero, and its random path is constructed. When the photon crosses the spherical surfaces at a time t, the variables θ , θ_u and t are recorded as a counting. About 30000 Montecarlo paths were calculated.

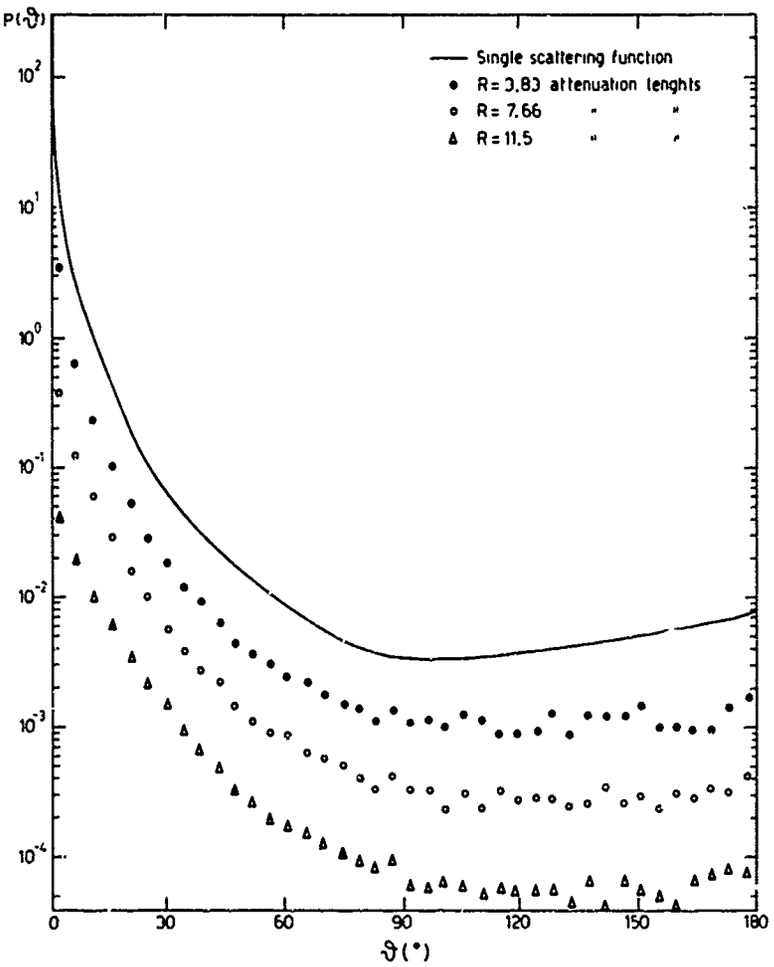

Fig.2 The single scattering function assumed in the calculations and the intensity of light collected per unit solid angle, at angle ·· on the spherical surface (Fig.1) when light is emitted from the sphere center in the ·· 0 direction. Unattenuated light is not included in the diagrams. Three sphere radius, i.e. R 3.83 , 7.66 and 11.5 attenuation lengths are considered

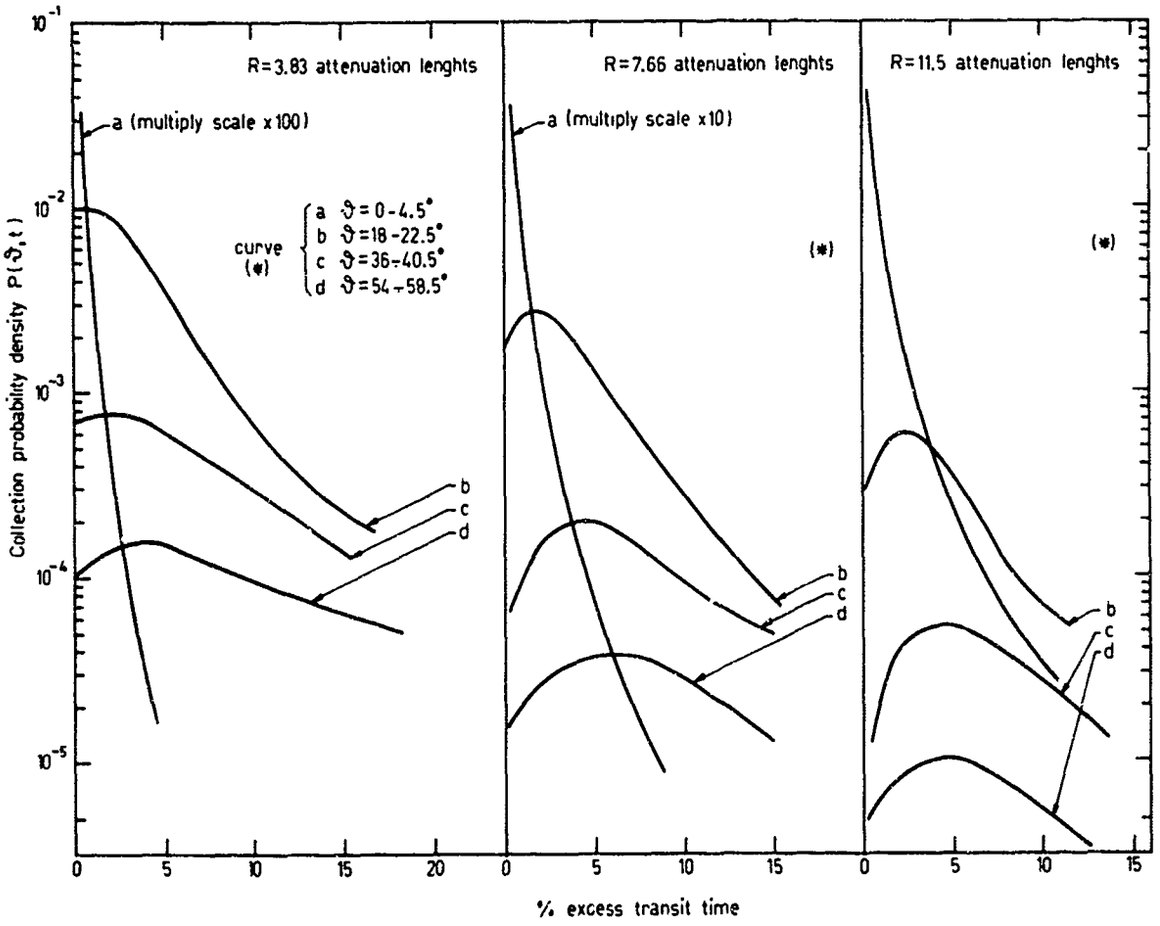

Fig.3 Time distributions of light collected at various point of the spherical surface (unattenuated light is excluded) for three sphere radius cases, as a function of percent excess transit time of light with respect to the unattenuated one

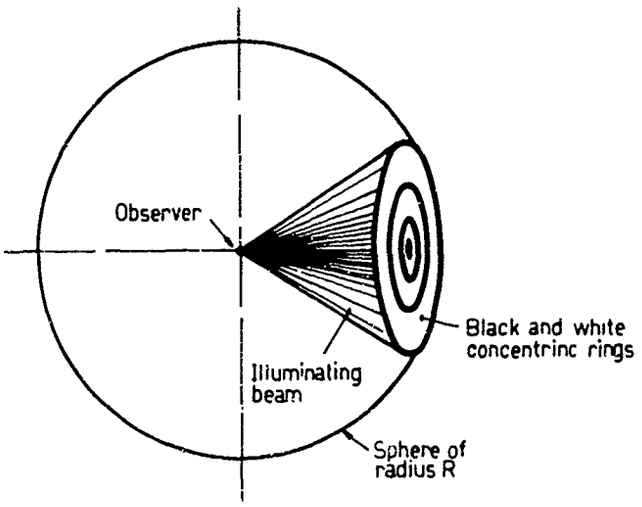

Fig.4 A schematic scene assumed in the calculations. It consists of concentric rings alternately black and white, placed on the spherical surface enclosing the propagation space. The scene is illuminated by a beam starting from the observation point and covering the 45° f.o.v.

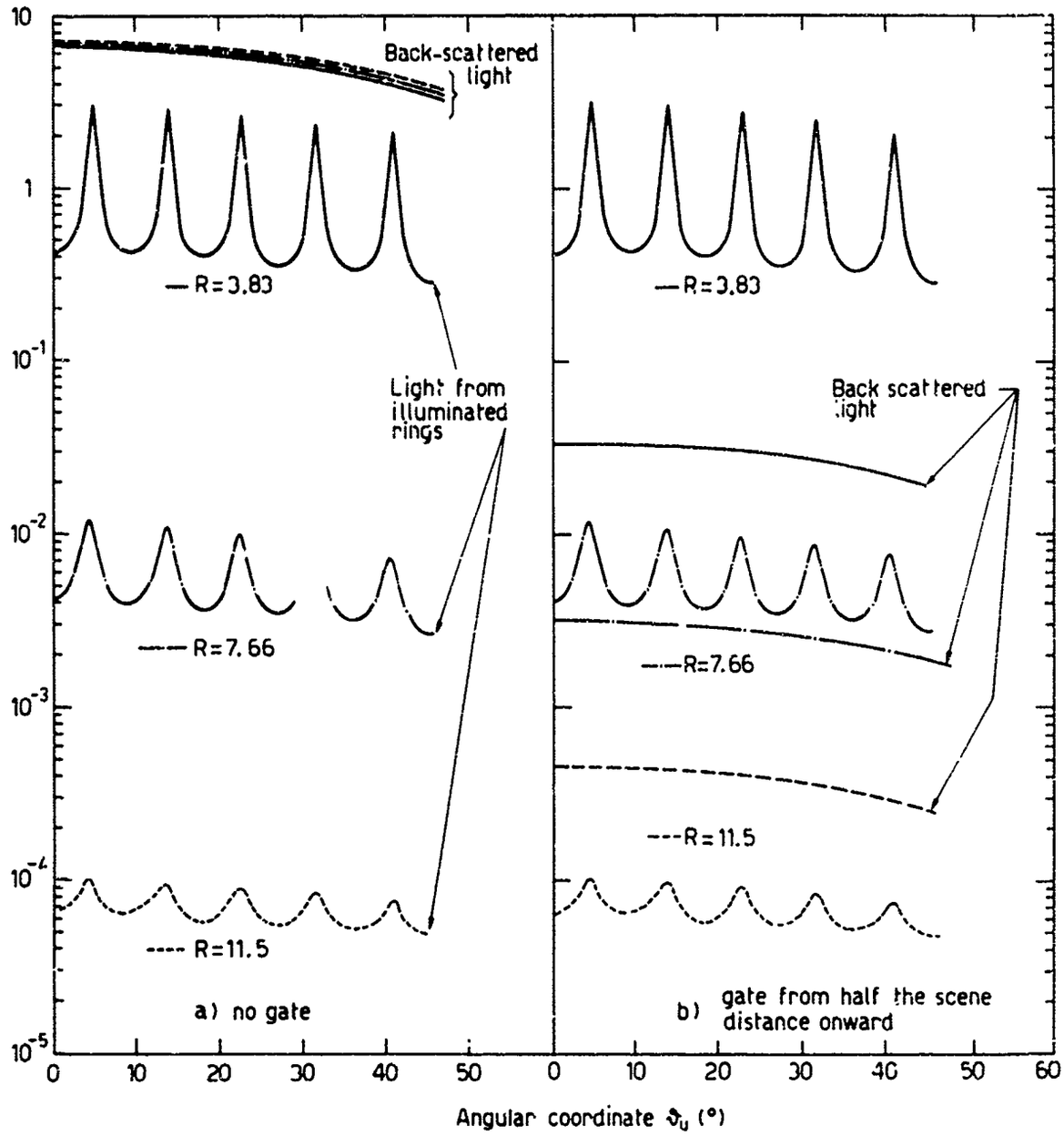

Fig.5 Light intensities in the focal plane of an observation system viewing a scene consisting of rings alternatively black and white (see Figure 4). Light received is splitted in two contributions: the backscattered light (not reaching the scene) and that returning from the rings. Three scene distances R are considered. Case a) refers to no gating on the scene, case b) to a gate from half the scene distance onward

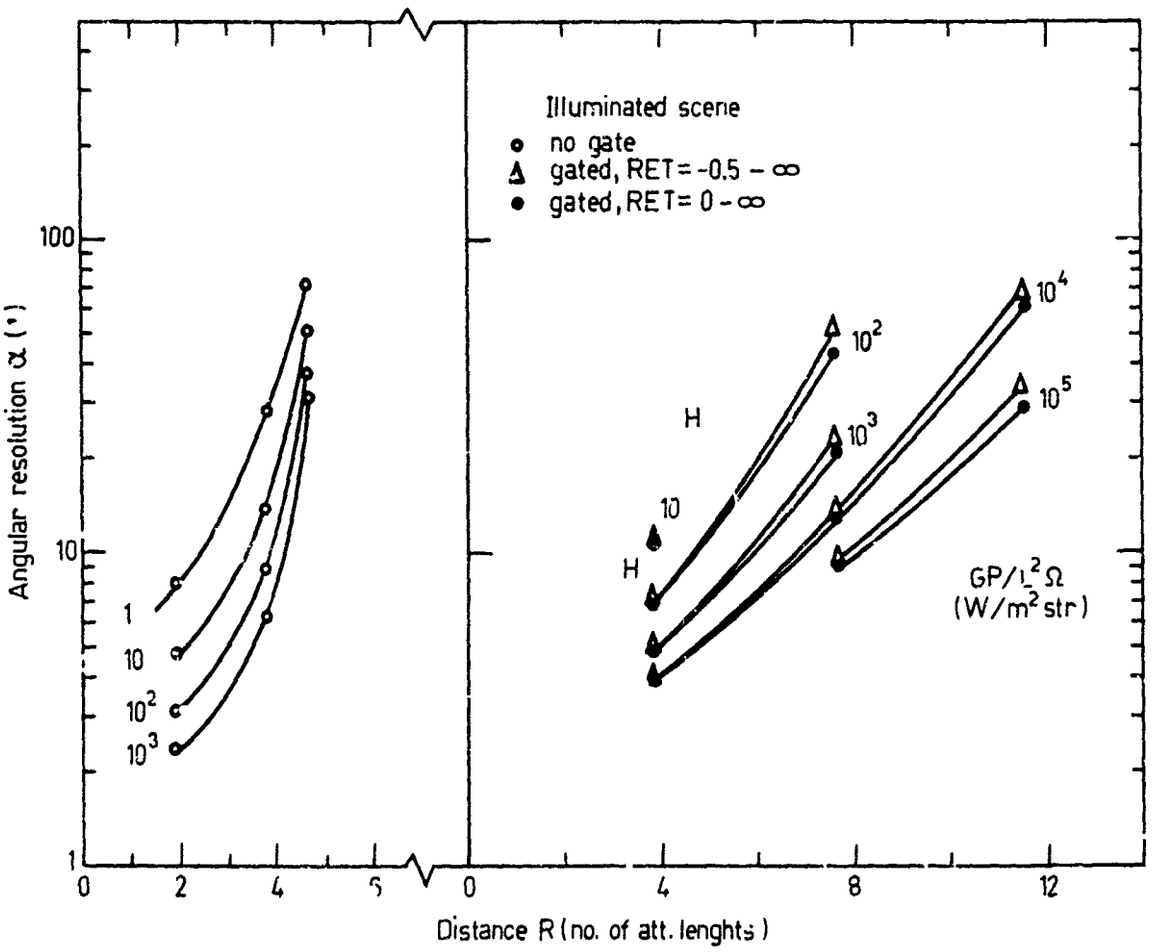

Fig.6 Angular resolution plotted against scene distance for the case of an illuminated scene, both not gated (left-hand diagram) and gated (right-hand one). The parameter $GP/L^2\Omega$ relates to the illuminating power used (see text)

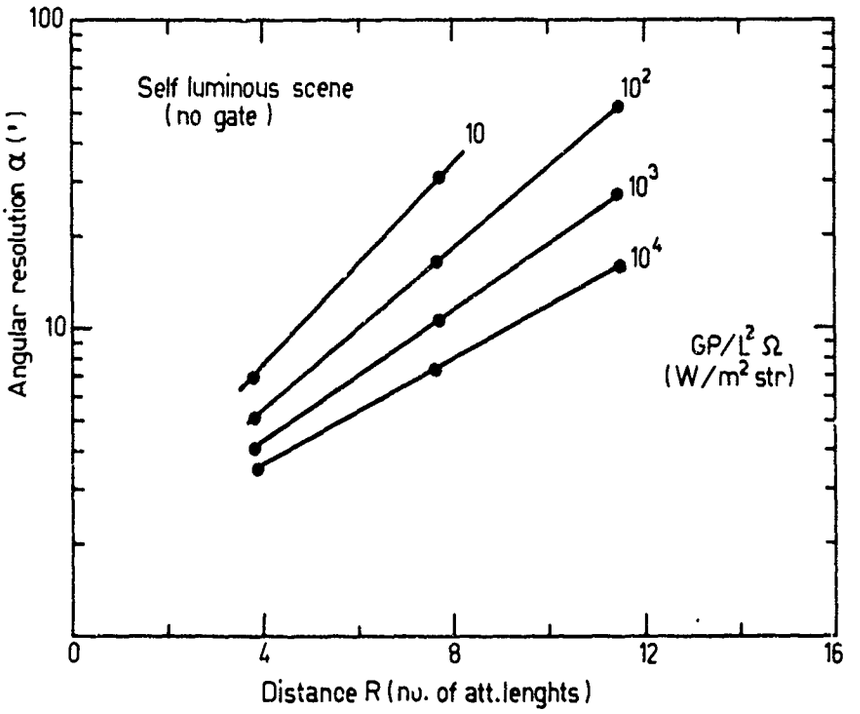

Fig.7 Angular resolution plotted against scene distance for a self-luminous scene, with no gating

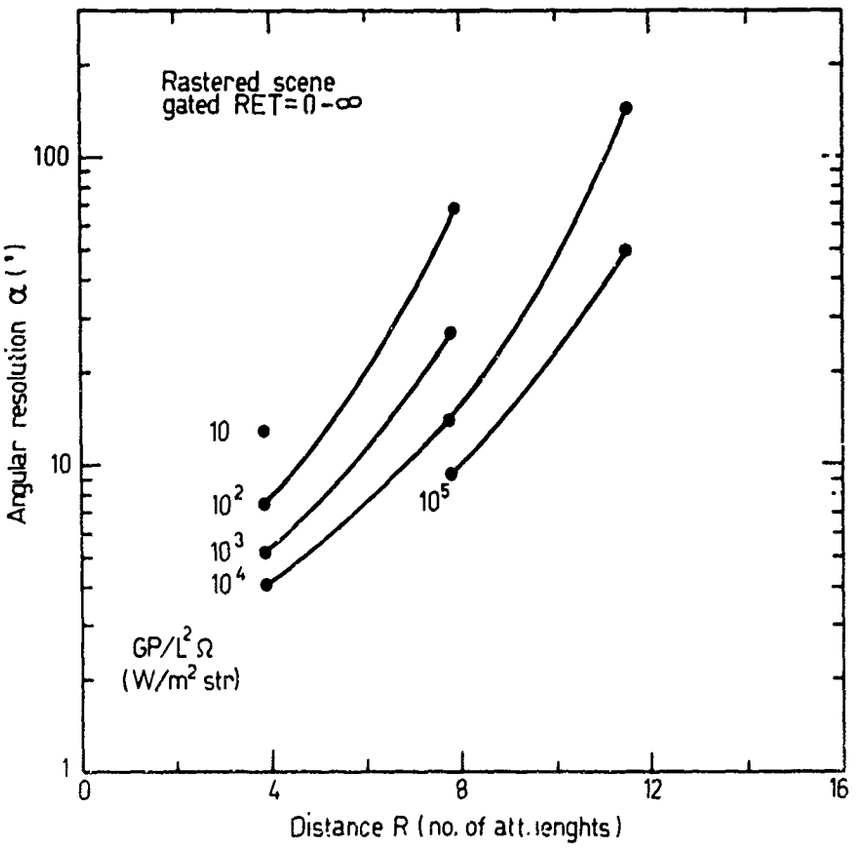

Fig.8 Angular resolution plotted against scene distance for the case of a rastered scene, that is, when the illuminating source is a narrow light beam which scans the scene point by point

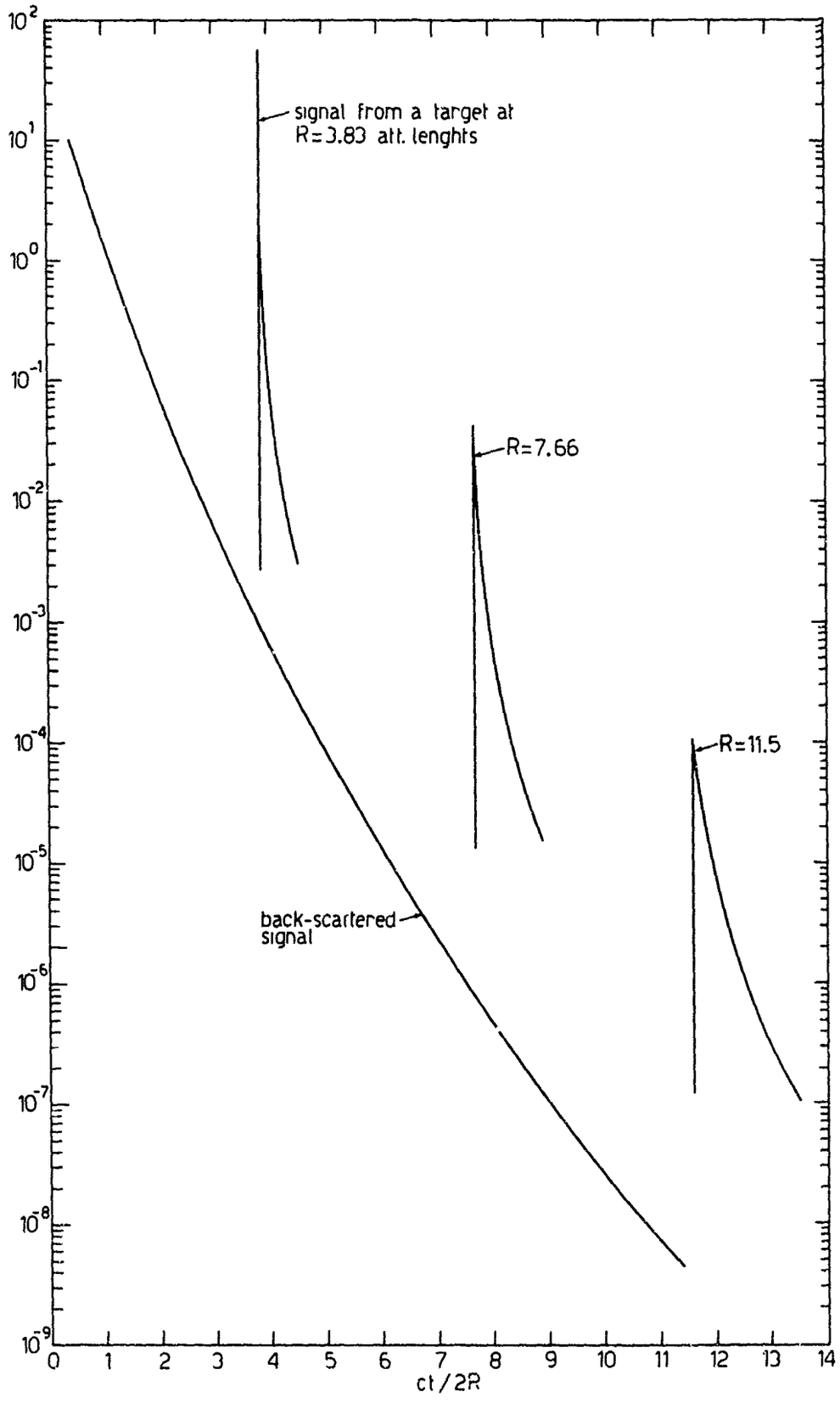

Fig.9 Intensities of light backscattered and of light coming from targets at three distances plotted as a function of their time of arrival at the observation system as a response to a short pulse of illuminating light of narrow angular aperture (raster mode)

SYNCHRONOUS SCANNING

by

H. Hodara and W.H. Wells

Totra Tech. Inc., Pasadena, California

Synchronous Scanning

By
H. Hodara and W. H. Wells
Tetra Tech, Inc., Pasadena, California

The performance of underwater viewing systems is limited by scattering and absorption. Forward scattering contributes to loss of resolution while backscattering reduces contrast (1) or more exactly signal-to-noise ratio (2). In this paper we concentrate on backscatter reduction; forward scattering is treated in a companion paper (3).

Synchronous scanning is based on the old photographer's principle of separating light source and camera to reduce backscatter from the volume of water which lies at the intersection of the light beam and the viewing beam. This is illustrated in Fig. (1). Fig. (1a) shows how a slice of that volume (cross-hatched) intercepts a light ray intended for the target, scatters it back into the camera and fogs film. The photographer's way to reduce backscatter is to increase the base line separation between light and camera Fig. (1b). This approach makes the system unwieldy if we want very large backscatter reduction. A more practical approach though more complex to implement is shown in Fig. (1c). There the base line is cut down to its original dimension, but the beam width is narrowed. The beam now no longer encompasses the entire target and we must scan the light and the camera beams synchronously to cover the target. Hence the name synchronous scanning.

In comparing synchronous scanning with conventional illumination we note that the same field of view is covered by the broad beam instantaneously and by the narrow beam during the scanning time. However, the total backscattering volume is much smaller with the narrow scanning beam as illustrated in Fig. (2). The total backscatter for the static flood beam illumination is the large triangle bounded by the heavy lines. The backscatter for each position of the narrow beam during the synchronous scan is the small cross-hatched triangle. Note that the total area (volume in space) enclosed by the cross-hatched triangle is much smaller than that of the large triangle.

Fan Beams and Pencil Beams

Until a few years ago, synchronous scanning was done with pencil beams, which requires two-dimensional scanning. In 1967 W. Wells proposed using a fan beam. If backscatter is mostly caused by single scattering, approximately the same increase in viewing range is attained with either pencil or fan (4). This is easily demonstrated as follows. Fig. (3) is a strip s of the target illuminated by a fan beam imaged at s' through a fanned angular field of view. The cross section of the two beams labeled 1 and 1' are the same cross sections shown in Fig. (2). In Fig. (3) we see that the backscattering volume which contributes to fogging of the image element s'_2 comes from a pencil beam illuminating the corresponding spot s_2 of the target. In short only those rays contained within the cone embracing s_2 and which scatter only once within the cross-hatched volume of base s_2, contribute to fogging of the image element s'_2. If multiple scattering is predominant, the majority of the rays within the cone subtended by s_2 cross over to some other cone such as the one bounded by s_1 and fog the image at s'_1. This is illustrated in the side view of Fig. (4).

We would like to know the viewing range at which multiscatter becomes significant in degrading the fan beam performance relative to a pencil beam. In Appendix A we estimate the ratios of fractional energy singly and doubly scattered, F_1 and F_2. We find

$$F_1/F_2 \simeq \frac{\sigma}{\beta}\frac{2\pi}{\varphi} e^{-2\sigma x} \qquad \sigma b \ll 1$$
$$\simeq \frac{\sigma}{\beta}\frac{2\pi}{\varphi}\,\sigma b e^{-2\sigma x} \qquad \sigma b \geq 1 \tag{1}$$

Some of the symbols are best explained by referring to Fig. (5). The fan beam has a narrow angle θ and a wide angle φ. The base line separation between source and receiver is b; the attenuation of the water is σ. The beams cross over at a distance x beyond which the water backscatters light into the receiver. The distance x is useful for describing the performance of a synchronous scan. Referring to the geometry of the Fig. (5) we normalize the parameter x with respect to target range, R.

$$r = x/R = (1+\ell/b)^{-1} \tag{2}$$

$\ell = R\theta$ is the width of the strip illuminated by the fan beam at that range, β is the backscatter coefficient, a measure of the fractional energy scattered in the back direction (over 2π steradians) from an elemental volume of water. The volume scattering function, σ is highly peaked in the forward direction, but drops down several orders of magnitude and remains essentially constant at large angles particularly in the back direction (2). We indicate its constant value in that direction by σ_b so that

$$\beta = 2\pi\sigma_b \tag{3}$$

Typical values for β are usually given in terms of σ,

$$\eta \quad \frac{\beta}{\sigma} \sim 10^{-2} \text{ to } 10^{-3} \tag{4}$$

and we shall use these numbers in our calculation. The range at which multiscatter begins to degrade the fan beam performance in relation to a pencil beam is obtained by demanding F_1/F_2 not go below unity, i.e. $F_1/F_2 > 1$. Let us choose typical values for long range in good waters, $\sigma^{-1} \sim 20$m, $\beta/\sigma \sim 10^{-3}$, $\theta \sim 1^{o}$, $\varphi \sim 10^{o}$, $\sigma b \sim 1$. Multiscatter then becomes significant at approximately six attenuation lengths ($6\sigma R$) and beyond it.

Signal-to-Backscatter Ratio

As long as the absorption limit is not reached, the performance of a system is best described in terms of the signal-to-backscatter ratio E_S/E_B, derived in Appendix B.

$$\frac{E_S}{E_B} = \frac{2\rho}{\beta R} \exp[-2\alpha R(1-\varepsilon)] \frac{(1-\varepsilon)}{\int_{\varepsilon}^{1} (u-\varepsilon) \exp[-2\alpha R(u-\varepsilon)] u^{-3} du} \qquad (5)$$

The integral in the denominator can be expressed in terms of exponential-integral functions, Ei, but it comes out in such an awkward form as to render its interpretation useless. The term $\exp[-2\alpha R(1-\varepsilon)]$ in the numerator of equation (5) brings out the backscatter rejection feature of synchronous scan: the effective two way attenuation is smaller than $2\alpha R$ by the factor $(1-\varepsilon)$. The parameter $0 \le \varepsilon \le 1$ in equation (2) is the fraction of the viewing range where the beams cross over. Therefore, we call ε the figure-of-merit of synchronous scanning. Obviously we want ε to be close to unity in order to reject as much backscatter as possible. If we break up the backscattering volume in slices, Fig. (5), only those close to the receiver carry any weight. Although the slices get larger at range, $r^2 x$ their contribution to receiver backscatter diminishe rapidly on account of the relative exponential attenuation, i.e. $\exp[-\alpha(r-x)]$. As ε approaches unity,

$$E_S/E_B\,|_{\varepsilon \to 1} = \rho 2b/\beta R^2 \theta. \qquad (6)$$

The range increases as the inverse square root of the fan beam angle, $1/\sqrt{\theta}$, assuming signal to backscatter ratio and baseline are unchanged. This is confirmed by observing that the average scattering thickness is $R^2\theta/2b$, (Fig. 9) and signal-to-backscatter ratio is inversely proportional to it.

We have computed and plotted E_S/E_B as a function of the number of attenuation lengths αR for several values of the parameter ε. The family of curves is shown in Fig. (6). The ordinate is normalized in terms of the target reflection ρ, and $q=\beta/\alpha$, the ratio of backscatter to attenuation coefficient. These results are self-explanatory.

Depth of Field

A basic limitation in synchronous scanning is depth of field. By that we mean, the range over which the illuminated target remains within the viewing angle of the receiver as illustrated in Fig. (7). The limitation is inherent to this form of scanning if we note that the locus of the points where illuminating and viewing beams overlap 100% is a circle passing through the source and receiver, Fig. (9). We distinguish between front depth of field, δ_F in front of the locus and back depth of field, δ_B behind it. The respective expressions are readily derived,

$$\alpha\,\delta_F = \frac{(\alpha R)^2 \theta}{\alpha b + \alpha R\theta} \qquad (7a)$$

$$\alpha\,\delta_B = \frac{(\alpha R)^2 \theta}{\alpha b - \alpha R\theta} \qquad (7b)$$

As expected, depth of field increases with range but decreases with beam width. Also $\delta_F \le \delta_B$ for all ranges. Obviously when the illuminated spot of size $\ell = R\theta$ equals the base line, b the back depth of field becomes infinite at $R = b/\theta$. The situation of infinite depth of field is not likely to be reached in long range systems. Thus even with a narrow fan beam $\theta = 1^o$, and good backscatter rejection $\alpha b = 1$, the range to target would have to approach $\alpha R = 180/\pi \simeq 60$ attenuation lengths! We have plotted depth of field in Fig. (8) for a base line $\alpha b = 1$, and a beam width $\theta = 10^{-2}$ radian, (a little over $\frac{1}{2}^o$). Front and back depth of field do not differ by much. Back depth of field becomes infinite at 100 attenuation length in this case.

On the same figure we have also plotted the depth of field when the fan beamwidth is ten times as large, $\theta = 10^{-1}$ radians. For this case δ_B is infinite at ten attenuation lengths; the result is of academic interest; with such a broad beam the signal to backscatter ratio would be too small to "see" beyond four or five attenuation lengths.

Photographic Synchronous Scan System

We have developed and built a portable operational photographic system based on the synchronous scan principle. The lamp and the camera are 4' apart, (b=4'). The camera has a wide angle field with a focal plane slit and scanning optics. It was built by Photogrammetry, Inc. and loaned to us by the U.S. Naval Photo Center. The source is a 500 watt lineal Xenon flash lamp which radiates 30 μsec pulses spaced 8 msec apart. The lamp is fixed while the beam fanning cylindrical optics scans over a 120^o angle at a rate of 200^o/sec to match the camera's rate. The lamp and camera have illuminating and viewing beams of 2^o in the narrow angle ($\theta = .035$ radian).

Tests were performed in a swimming pool with controlled quantities of diatomatious earth for scatterers. The pool dimensions are 20' by 40'; the target was hung approximately halfway down the pool and the synchronous scan system was located at one end of the pool. Results in clear water are shown in Fig. (9) together with the geometry of the beam. Only the target and the sides of the pool show. The geometry below explains it since the locus of intersection of the viewing and illuminating beams is tangent to the target and the sides of the pool. This is confirmed by the calculation of depth of field using Eq. (7), $\beta R^2\theta/(b-R\theta)$. The back depth of field is 4.3' which added to the 10' radius is just about the length of the diagonal connecting the center of the circle with the corner of the pool. The

corner of the pool is thus at the extreme of the depth of field where hardly any light reaches the camera. Note that as the beam starts sweeping down, the left side of the pool, the pool's ladder enters the depth of field and becomes visible. The "banding" or stripes are caused by pulsing the xenon lamp. Pulses were used in order to raise the color temperature to 7,000°K with resultant higher efficiency of 12% in the water transmission band.

Figures 10 to 12 compare photographs taken with our system and a conventional Nikonos underwater camera in more turbid water. The same light source was used but the shutter in the Nikonos was left opened for the duration of the beam sweep. The backscatter rejection achieved with synchronous scan is well illustrated in those figures, particularly in the last one, Fig. (12). There the target cannot be seen at all with conventional system while still distinguishable with the synchronous scan. The range in this last photograph is between three and four attenuation lengths as determined from α - meter measurements. The improvement is significant if we bear in mind that visibility with a wide angle system is not more than 1 to $1\frac{1}{2}$ attenuation length. It is worth while at this stage to dispel the old rule of thumb that visibility with conventional systems extends to as much as $2\frac{1}{2}$ attenuation length. This is only true under diffused lighting condition such as daylight. With a conventional lamp situated near the camera, the visibility is limited by loss of contrast at $1\frac{1}{2}$ attenuation lengths.

Adaptive Synchronous Scan

To conclude this paper we would like to propose an adaptive TV synchronous scanning system which eliminates the shortcomings of the present systems. There have been several attempts, none too successful, to design scanning systems that are not depth of field limited. Since the locus of intersection of source and viewing beams scanning at a uniform rate is a circle, an arbitrary shaped object requires one of the beams to sweep with variable speed if that object is to lie at the intersection of both beams during the scan. A typical solution is edge tracking of onethe beam via a servo loop. Systems based on this principle require either excessive bandwidth or are easily thrown out of lock by discontinuities in the field of view.

The system we propose conceived by one of the authors (Wells) does not rely on edge tracking, thus gets around these difficulties. In order to explain its operation consider the receiver to be made up of discrete detecting elements with respective field of views labeled 1 to 5 in Fig. (13a). The narrow light beam shown by a ray in the figure scans from right to left and the light received within each discrete field of view is integrated until a threshold preset by the operator is reached after which the detector cuts off. In the absence of an object, the intensity vs scan angle for each individual detecting element looks like the curves of Fig. (13b). If an object is present within some of the field of views, say elements 3 and 4 in the figure, the intensity in the corresponding detecting elements reach the threshold very sharply at threshold angles earlier in the scan, ψ_A and ψ_B. For each elementary field of view there is a specific one-to-one correspondence between range and scan angles determined by the system geometry, so that knowledge of the threshold scan angles ψ_A, ψ_B determines unequivocally the range to the object within these elementary field of views. A detailed analysis reveals that the principles discussed above apply as well as when either right edges or left edgesare being imaged. As a matter of fact this technique only handles reflectance discontinuities (no continuous tone reflectance) and edges of objects.

In practice, the receiver rather than being made of discrete detecting elements is a TV equipped with adaptive erasure features. To implement the scheme, one measures integrated light intensity in many subdivisions of the field of view by retaining a low resolution memory of the last TV frame of the same scene. In each image increment that is brighter than threshold in the last frame, the integration is cut-off earlier in the new frame; in each increment that was too dim, the integration goes on a longer time. In essence an error loop is set up that feeds cut-off commands to the TV receiver from information received from the low resolution image memory and from integration cut-off times of the preceding frame.

References

1. Wells, W. H. "Loss of Resolution in Water as a Result of Multiple Small Angle Scattering" JOSA, Vol. 59, No. 6 pp. 686-691, June 1969.

2. H. Hodara, and R. J. Marquedant "The Signal/Noise Ratio Concept in Underwater Optics", Applied Optics, Vol. 7, No. 3, pp 527-534, March 1968.

3. W. H. Wells, and M. N. Todd "Loss of Optical Resolution in Sea Water by Multiple Small Angle Scattering" AGARD Technical Specialist's meeting "Electromagnetics of the Sea" June 1970, Paris, France.

4. Final Report - "Investigation of Improved Light Sources for Underwater Photography", U. S. Navy Contract #N00019-67-C-0613, February 26, 1968.

Acknowledgements

We gratefully acknowledge the U. S. Naval Photo Center who sponsored the development and construction of the fan beam synchronous scan.

We are indebted to John Winslow who designed, built, and tested it.

Many thanks to Comer McNeil, builder of the Panoramic Aqua Scan Camera who helped us integrating it into our system.

As usual, Mrs. Mariann Moore exhibited her competence in programming the signal-to-backscatter ratio equation on the IBM 360 and Don Rosencrantz assisted us with the photographs.

Appendix A

Calculation of Single and Double Scatter

Single Scatter

The geometry is shown in Fig. (A-1). The illuminating beam is narrow enough that we only need to represent it by a single ray. The fraction of energy scattered, F_1 is given by the probability that a ray will scatter at a distance x, over a path length, through the scattering volume and within a solid angle $\Delta\Omega$ subtending the receiver aperture of diameter, D

$$\Delta F_1 = \sigma_b \Delta\Omega \bar{\Delta s} e^{-2\alpha x} \tag{A-1}$$

σ_b, the probability of scattering at large angle is also the volume scattering function in the back direction, and is approximately constant in that direction. From the geometry $\Delta\Omega = \pi D^2/4R^2$; $\Delta S = \frac{R^2\theta}{b}$ and

$$F_1 = \sigma_b \frac{\theta}{b} \frac{\pi D^2}{4} e^{-2\alpha x} \tag{A-2}$$

As a check, we calculate the signal-to-backscatter ratio based on single scattering using for the single scattering using for the signal energy Eq. (B-1) in Appendix B.

$$E_s/E = \rho e^{-2\alpha R} \frac{D^2}{4R^2} \tag{B-1}$$

The ratio of these two expressions give the signal-to-backscatter ratio,

$$E_s/E_B = \frac{2\rho b}{\beta R^2 \theta} e^{-2\alpha R(1-\xi)} \tag{A-3}$$

where $\xi = (1+\ell/b)^{-1}$ and $\beta = 2\pi\sigma_b$. (A-3) checks exactly with Eq. (6) in the text as $\xi \to 1$.

Double Scatter

The geometry is shown in Fig. (A-2). The illuminating beam is again represented by a single ray. The probability of double scatter is

$$\Delta F_2 = \sigma^2 ds_1 \Delta s_3 d\Omega \Delta\Omega_2 \tag{A-4}$$

From the figure, $\Delta\Omega_2 = \frac{\pi D^2}{s_2^2}$, $d\Omega = \frac{\varphi s_2 s_3 d\psi}{s_3^2}$, $\Delta s_3 = \frac{\theta s_2}{\sin\psi}$, $b = s_3 \sin\psi$.

The total fraction that is double scattered,

$$F_2 = \iint \frac{\sigma_b^2}{b} \theta\varphi \frac{\pi D^2}{4} d\psi ds_1 \tag{A-5}$$

which reduces after a few manipulations to

$$F_2 = \frac{\pi}{2} \sigma_b^2 \theta\varphi \frac{D^2}{b} \int_0^\infty e^{-2\alpha s_1} \int_0^{\pi/2 - 1/2 \tan^{-1} b/s_1} e^{-\alpha b/\tan\psi'} d\psi' ds_1 \tag{A-6}$$

where $\psi' = \psi/2$. If we make the change of variable $t = (\tan\psi')^{-1}$ we have for $\alpha b \geq 1$.

$$F_2 = \frac{\pi}{2} \sigma_b^2 \theta\varphi \frac{D^2}{b} \int_0^\infty e^{-2\alpha s_1} \int_0^\infty e^{-\alpha b t} \frac{t^2}{1+t^2} dt \tag{A-7}$$

We have assumed that we can integrate ψ from 0 to π without too much error since for $\alpha b \geq 1$ the absorption limits the contribution of that integral in the range $\pi/2 \leq \psi \leq \pi$. Then

$$F_2 = \frac{\pi}{2} \sigma_b^2 \theta\varphi \frac{D^2}{b} \frac{1}{2\alpha} \left[\frac{1}{\alpha b} - \int_0^\infty e^{-\alpha b t} \frac{dt}{1+t^2} \right] \tag{A-8}$$

An upper bound to F_2 is given by the first term in the brackets.

$$F_2 = \frac{\pi}{4} \sigma_b^2 \theta\varphi \frac{D^2}{(\alpha b)^2} \tag{A-9}$$

Single-to-Double Scatter Ratio

Taking the ratio A2 to over A-9 and using $\beta = 2\pi\sigma_b$ we have

$$\frac{F_1}{F_2} = \frac{\alpha}{\beta}\ \frac{2\pi}{\varphi}\ (\alpha b)\, e^{-2\alpha x} \quad (\alpha b \geq 1) \tag{A-10}$$

which is Eq. (1) in the text

For $\alpha b \ll 1$, it can be shown that

$$\frac{F_1}{F_2} = \frac{\alpha}{\beta}\ \frac{2\pi}{\varphi}\ e^{-2\alpha x} \quad (\alpha b \ll 1) \tag{A-11}$$

Appendix B

Derivation of Signal-to-Backscatter Ratio

Calculation of Signal

The source energy is E. The target is lambertian with reflection coefficient, ρ. The energy reflected at the target per unit solid angle is $\rho E \exp(-\alpha R)/\pi$. The energy reaching the receiver within the solid angle subtended by an aperture of diameter, D whose area in $\pi D^2/4$,

$$E_S/E = \rho e^{-2\alpha R} D^2/4R^2 \tag{B-1}$$

For reference purposes, we may want to know the energy density at the detector, $e = E_S/A_I$. A_I is the image area on the detector; for a camera it must exceed the film threshold density,

$$e_{film} = \frac{1.2 \times 10^{-7}}{ASA\#} \ \text{joules/cm}^2 \tag{B-2}$$

Let A be the target area, f the focal distance to the detector, and $F = \frac{f}{D}$ the f-number, then

$$e = \frac{\rho E/A_T}{4F^2}\ e^{-2\alpha R} \tag{B-3}$$

Calculation of Backscatter

From Fig. (5) in the text we see the fraction of energy backscattered at distance, r within the detector's field of view is

$$\frac{A_b}{A(r)} = \frac{R}{r}\ \frac{r-x}{R-x} \tag{B-4}$$

The corresponding energy per unit solid angle is

$$\sigma_b\, dr\, E\, e^{-2\alpha r}\ \frac{A_b}{A(r)} \tag{B-5}$$

σ_b, the volume scattering function in the back direction is approximately constant over 2π solid angle. It is related to the backscatter coefficient $\beta = 2\pi\sigma_b$. The backscattered energy reaching the detectors within the solid angle subtended by its aperture, D^2 in

$$dE_B = \frac{A_b}{A(r)}\ E\, e^{-2\alpha r}\ \frac{\pi D^2}{4r^2}\ \beta\ \frac{dr}{2\pi} \tag{B-6}$$

The fraction of energy backscattered at the receiver is

$$\frac{E_B}{E} = \beta\ \frac{D^2}{8} \int_x^R \frac{R}{r}\ \frac{r-x}{R-x}\ e^{-2\alpha r}\ \frac{dr}{r^2} \tag{B-7}$$

where x is from Fig. (5),

$$\frac{x}{R} = \xi = (1+\ell/b)^{-1} \tag{B-8}$$

Combining (B-1) and (B-7) we get the signal to backscatter ratio after normalization

$$\frac{E_S}{E_B} = \frac{2\rho}{\beta R}\ \exp[-2\alpha R(1-\xi)]\ \frac{1-\xi}{\int_\xi^1 (u-\xi)\exp[-2\alpha R(u-\xi)]\, u^{-3}\, du} \tag{B-9}$$

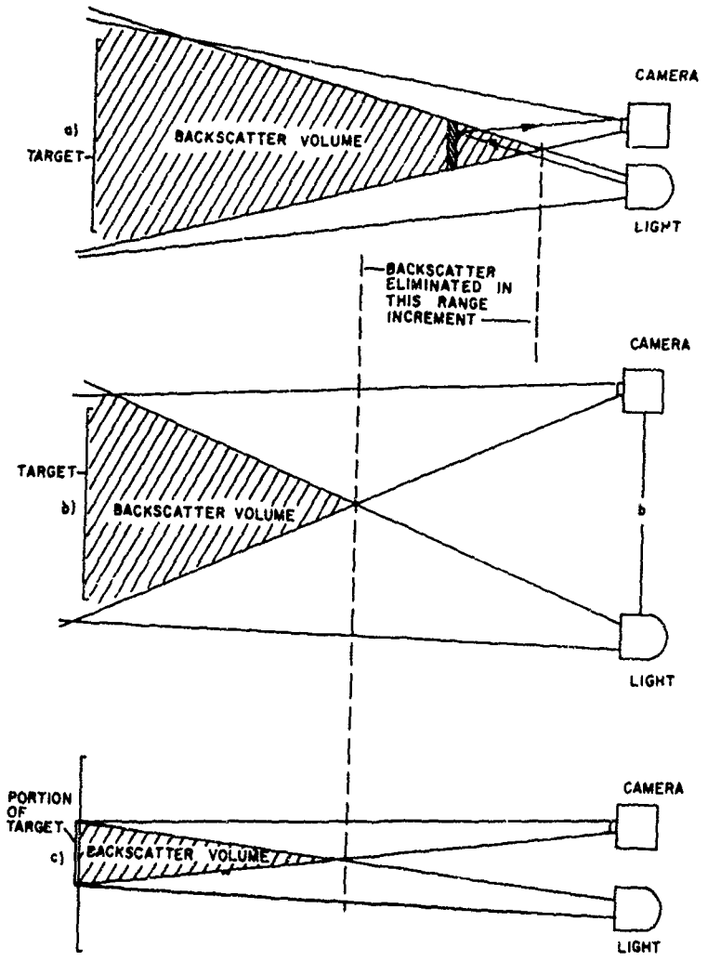

Fig. 1 Backscatter volume geometry

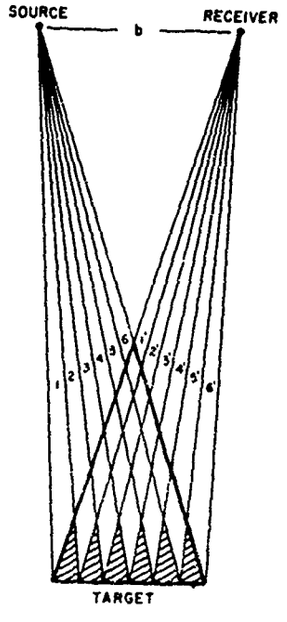

Fig. 2 Comparison of static broad beam and scan narrow fan beam

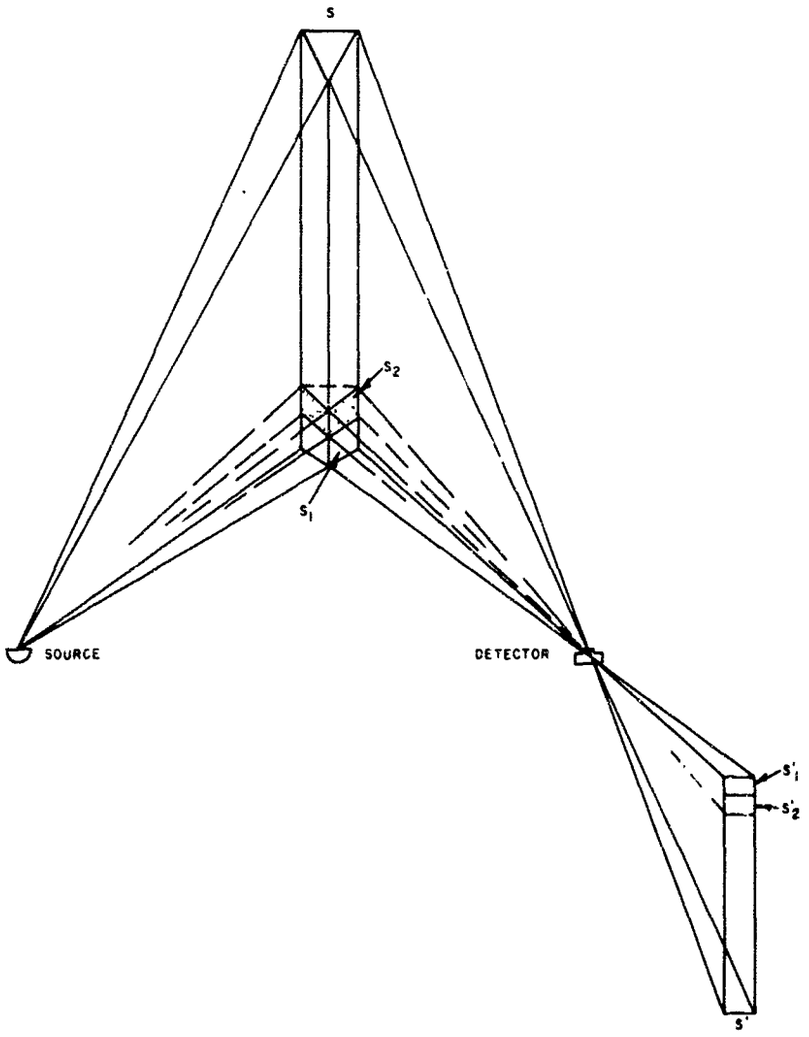

Fig.3 Isometric representation of fan beam scanning

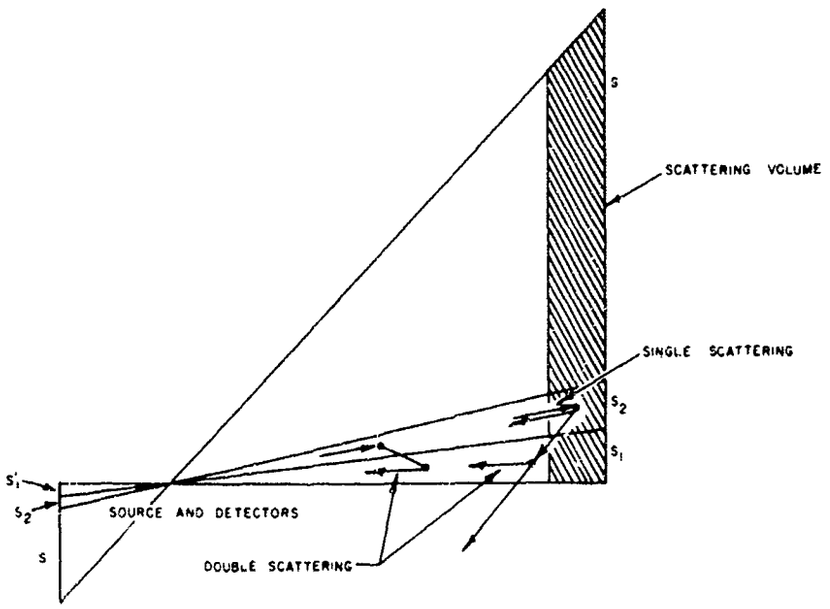

Fig 4 Fan beam side view illustrating effects of single and multiple scatter

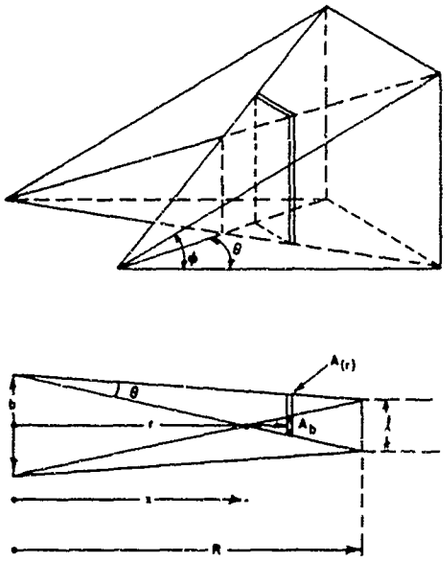

Fig.5 Fan beam synchronous scanning geometry

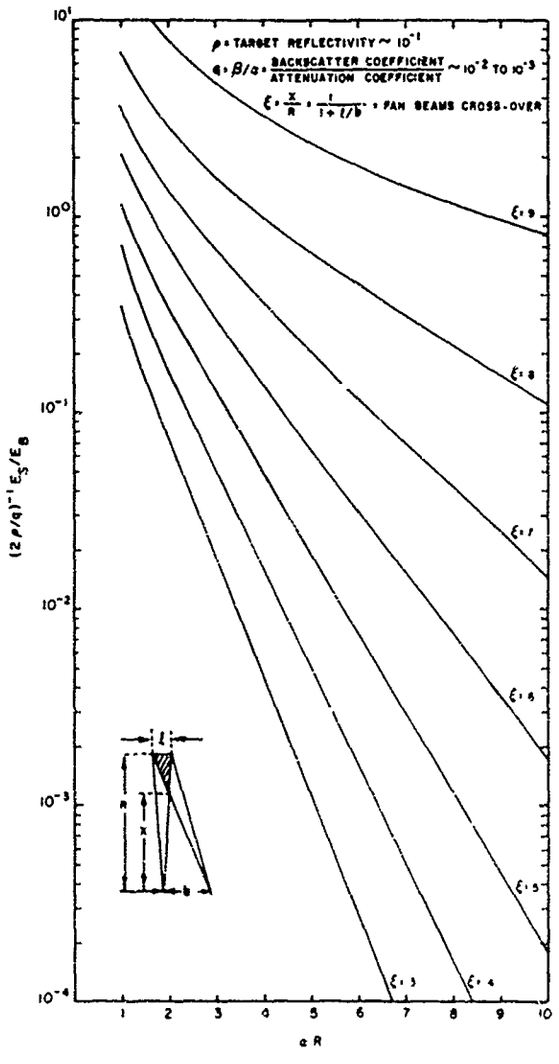

Fig.6 Signal to backscatter dependence on range

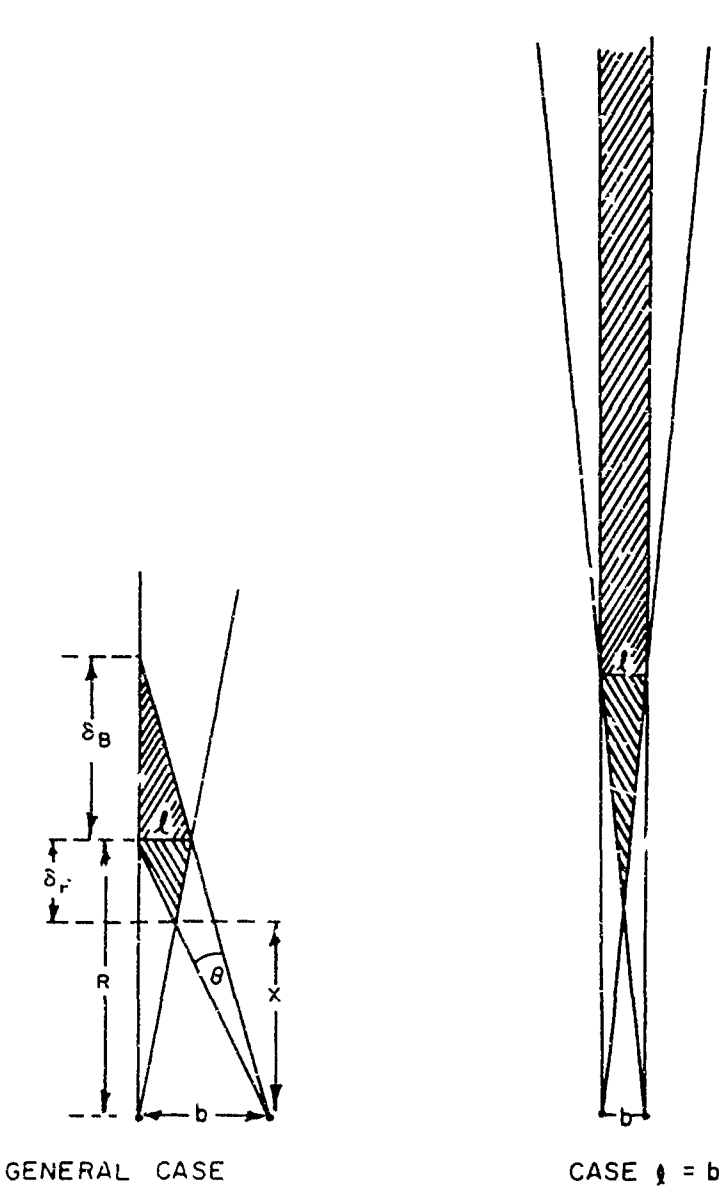

Fig 7 Depth of field geometry

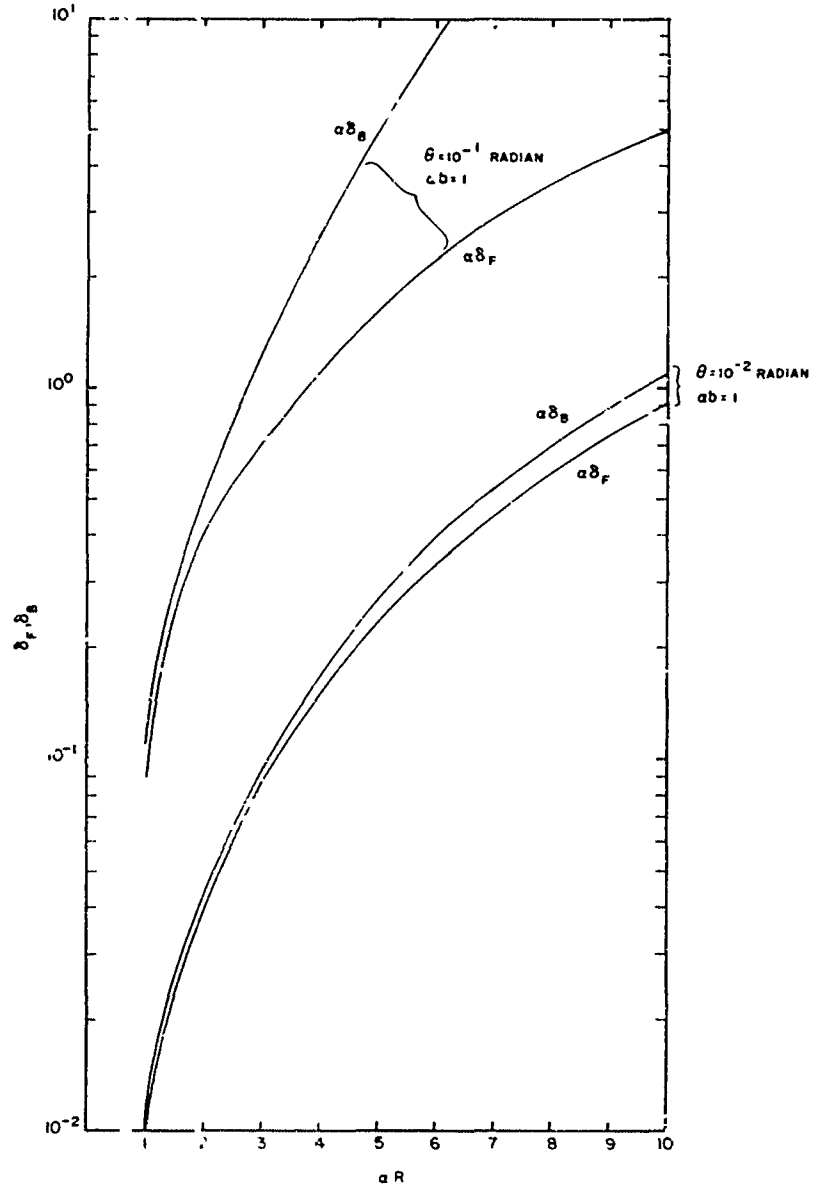

Fig.8 Depth of field dependence on range

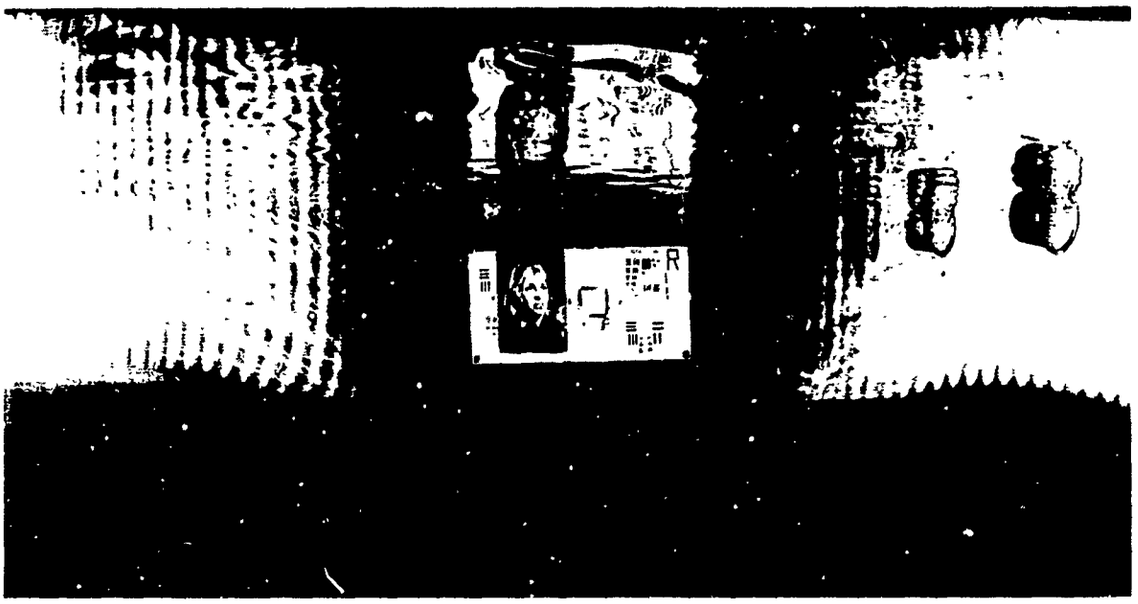

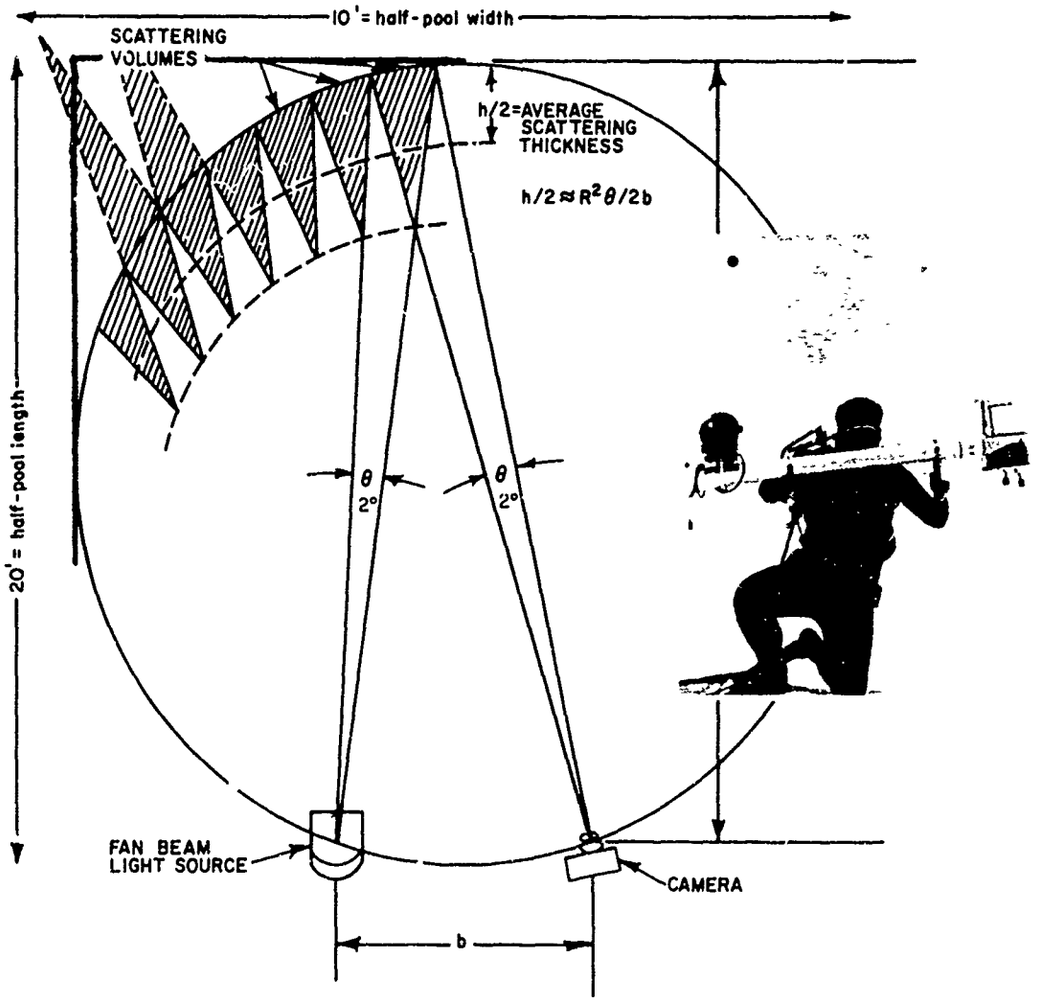

Fig.9 Performance of photographs synchronous scan in clear water

CONTRAST GOOD

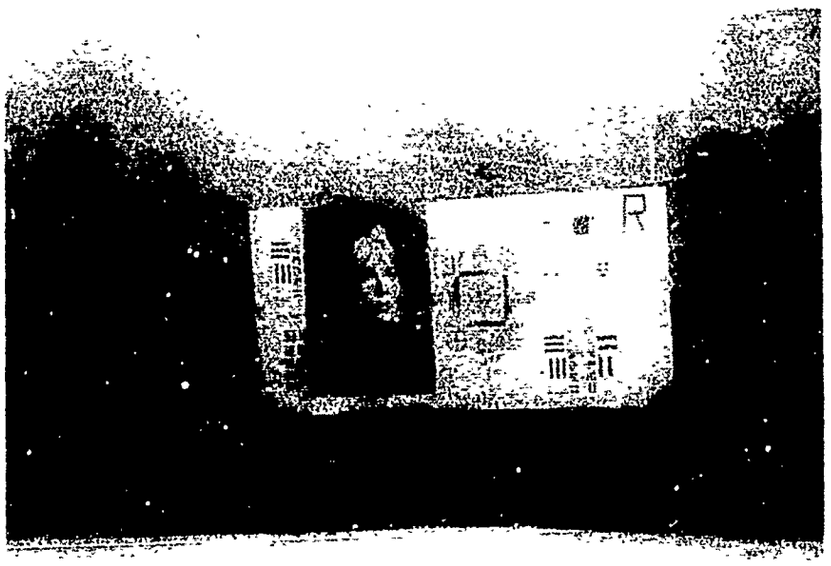

BROAD BEAM LIGHT

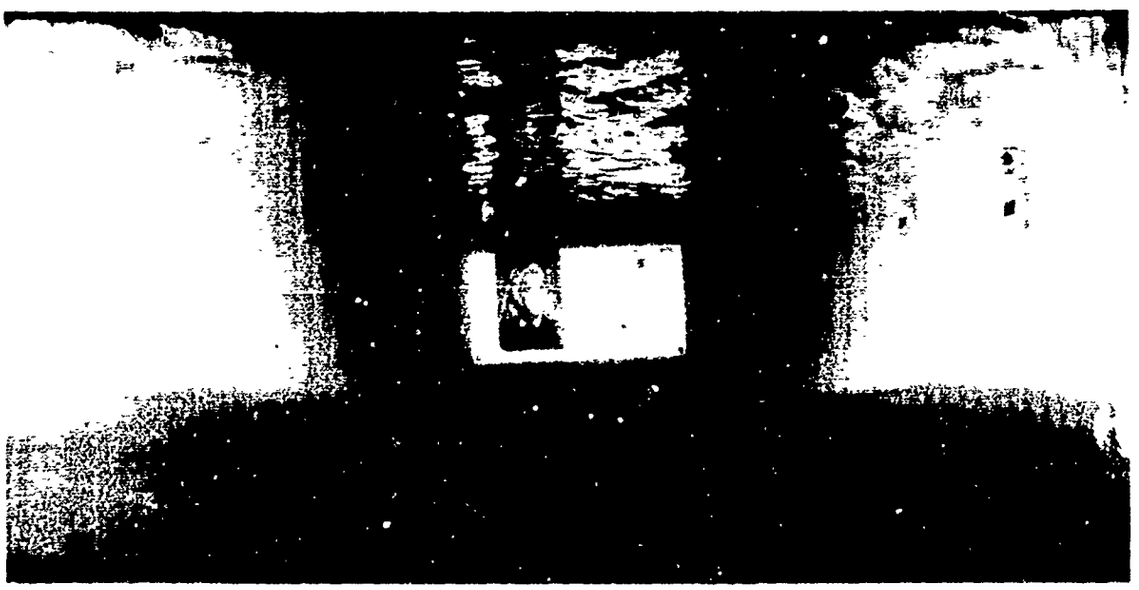

SYNCHRONOUS SCANNED LIGHT

Fig. 10 Photographs comparing synchronous scan and broad beam

TURBID - CONTRAST REDUCED

BROAD BEAM LIGHT

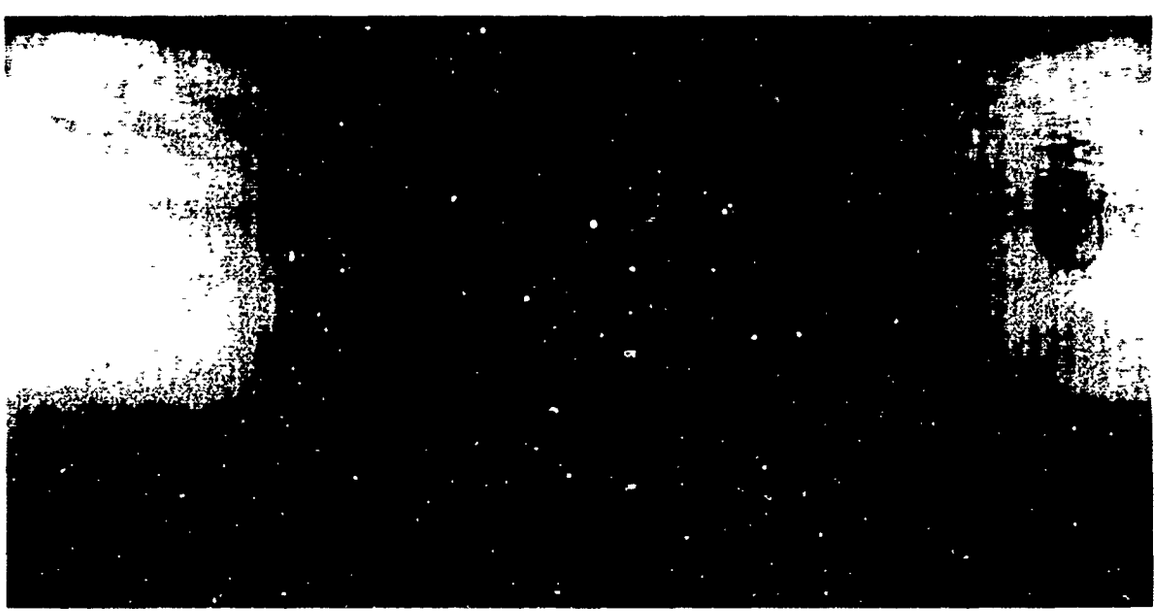

SYNCHRONOUS SCANNED LIGHT

Fig. 11 Photographs comparing synchronous scan and broad beam

VERY TURBID - BACKSCATTER LIMITED

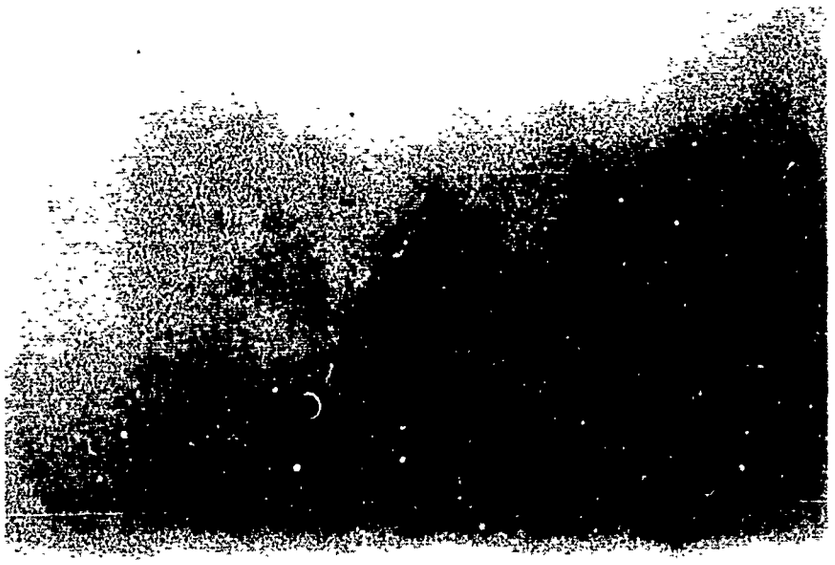

BROAD BEAM LIGHT

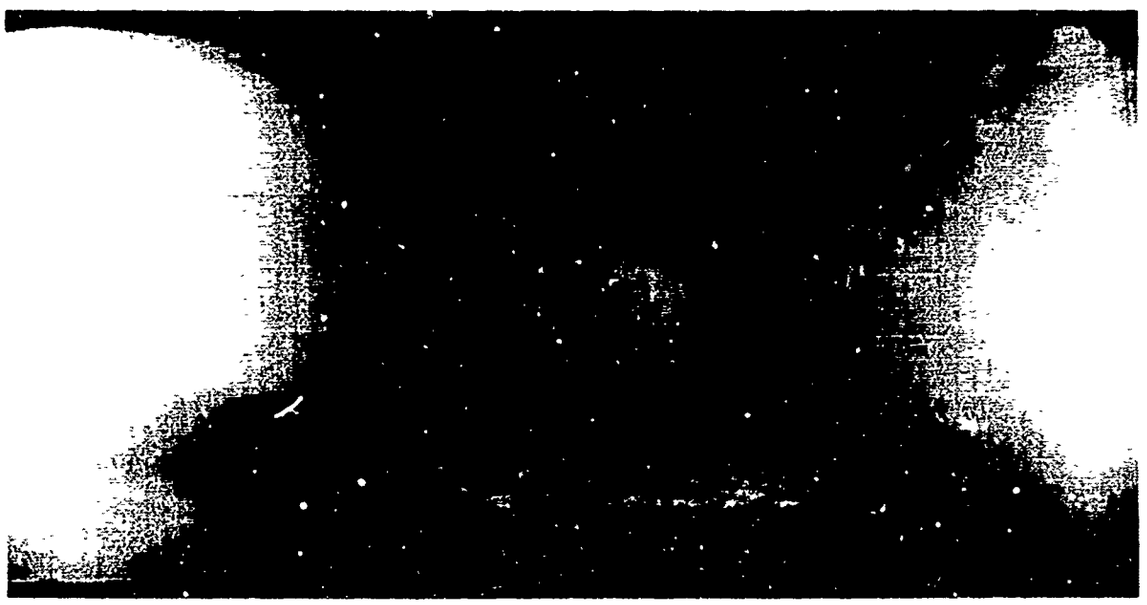

SYNCHRONOUS SCANNED LIGHT

Fig. 12 Photographs comparing synchronous scan and broad beam

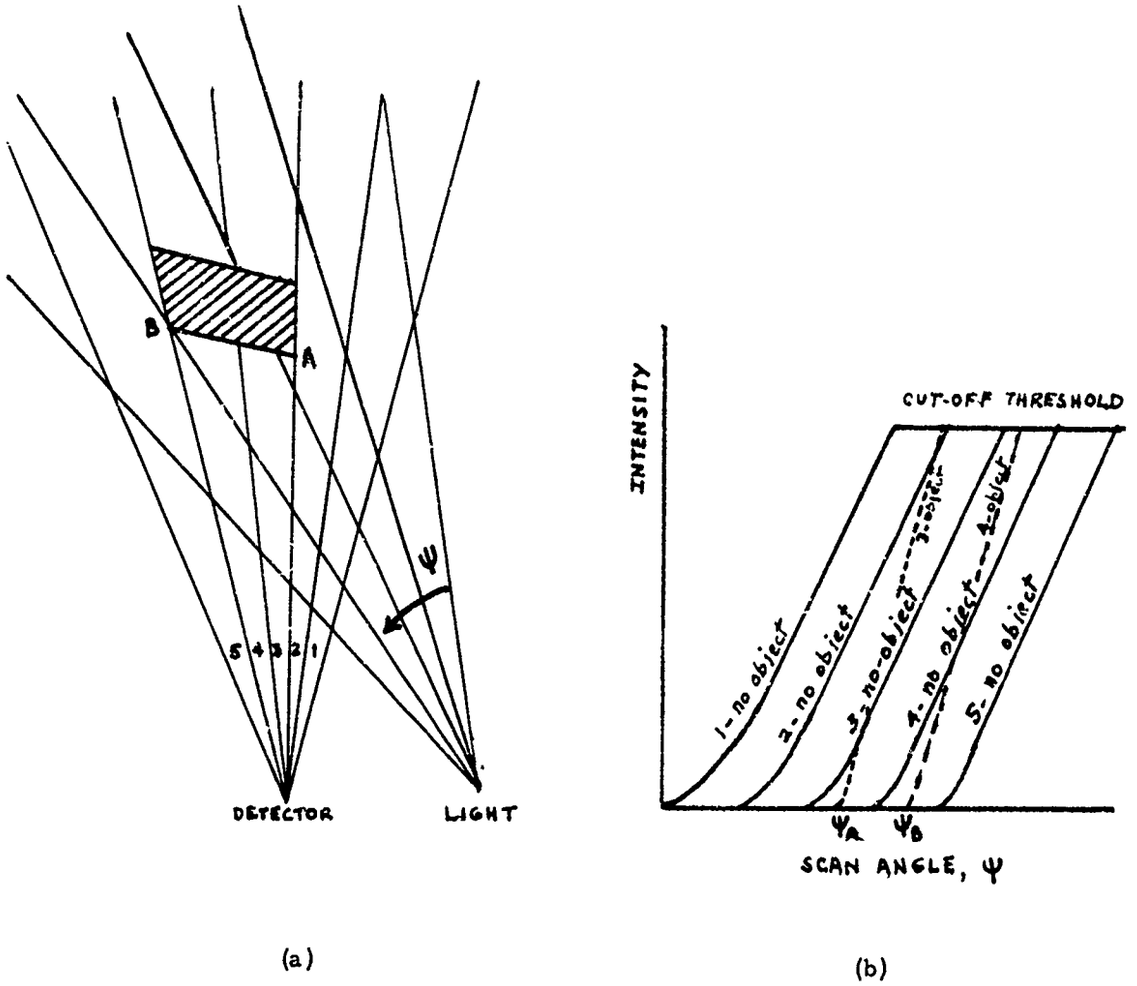

Fig. 13 Adaptive TV scan

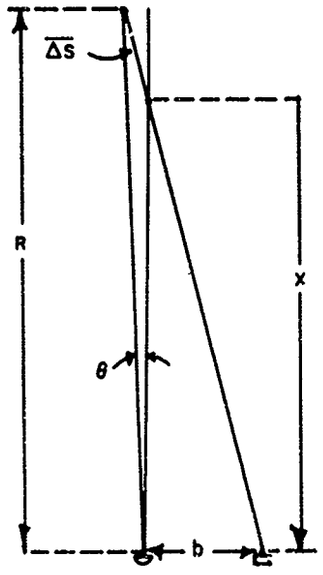

Fig. A-1 Single scatter geometry

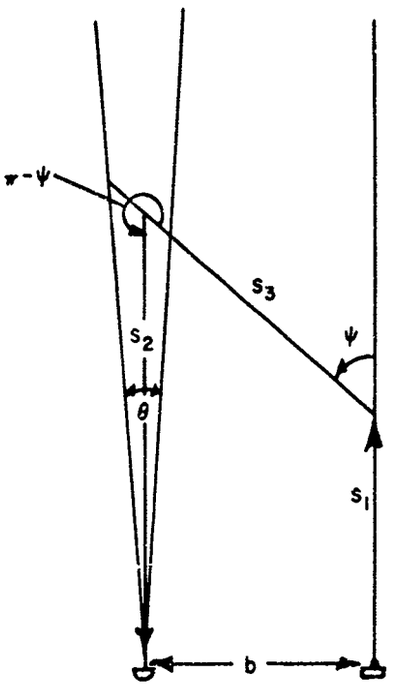

Fig. A-2 Double scatter geometry

DISCUSSION ON PAPERS PRESENTED IN SESSION VIII
(Imagery)

Discussion on paper 44 : " Evaluation of visibility improvement in sea water by range gating systems", by S. DONATI and A. SONA .

Dr. D.L. FEINSTEIN : Could you give us some idea of the computer time necessary for your Monte-Carlo calculation .

Dr. S. DONATI : With our computer (IBM) 1800 a photon story took about 1/3 of second of calculation time .

OPTICS ROUND TABLE DISCUSSION

--

Chairmen : Prof. J. TYLER and Dr. H. HODARA
Rapporteur : C.F. (H) Pierre HALLEY

Plan des discussions

1.- Sur l'application à l'optique océanographique des méthodes générales intéressant la propagation des ondes.

2.- Sur la communication du Dr. MOREL "Résultats expérimentaux sur la diffusion" (papier 30).

3.- Sur la fonction de transfert de modulation (MTF) et des effets non-linéaires.

4.- Sur la diffusion sous petit angle, et de la limite de la fonction de diffusion (VSF) pour un angle nul.

5.- Sur un système de notation international propre à l'optique océanographique.

Un programme de recherches a été présenté par le professeur J. TYLER (papier 43).

OPTICS ROUND TABLE DISCUSSION

Chairmen : Prof. J. TYLER and Dr. H. HODARA
Rapporteur : C.F. (H) Pierre HALLEY

1.- Prof. TYLER : I have several questions I want to discuss, but I am sure you have plenty also.

- C.F. HALLEY : Merci, Monsieur le Président. Je voudrais commencer notre table ronde par un peu de philosophie. J'ai essayé à propos du milieu marin, de réunir des radio-electriciens et des opticiens, ceci parce que j'ai constaté que dans bien des cas il était fructueux de mettre en parallèle les scientifiques de la radio-électricité et de l'optique.

Je constate les difficultés considérables que vous rencontrez en optique dans le milieu marin. Nous sommes, nous les radio-électriciens, les héritiers de l'optique. On a fait une théorie solide électro-magnétique de la radio-électricite, et, partant des concepts de l'optique et de ses principes on a construit un outil très puissant qui permet de résoudre les problèmes de propagation des ondes électromagnétiques dans l'atmosphère comme dans la mer ou dans d'autres milieux. Et je constate que ces méthodes qui sont des démarches assez naturelles de l'esprit, qui partent d'équations de la physique auxquelles on applique les mathématiques ne sont pas, en ce moment tout au moins, praticables dans le domaine de l'optique. Je crois que ce n'est pas dû à la nature électro-magnétique du champ. M. WIRGIN nous disait l'autre jour que, dans un milieu constitué de stratifications avec un interface irregulier et un fond irrégulier, il pouvait faire la théorie de la propagation d'une vibration quelconque, qu'elle soit mécanique élastique ou qu'elle soit électromagnétique. Je dirai la même chose pour ce qui concerne l'atmosphère. On peut faire la théorie d'une vibration mécanique élastique, c'est-à-dire d'une onde de pression ou de perturbation de pression, qu'il s'agisse de la bande sonore, acoustique ou de gravité. On part des équations de la physique, un certain nombre d'équations, par exemple celle des gaz parfaits, celle de l'équilibre hydrostatique, celle des forces appliquées au volume élémentaire de gaz, etc.. sept, huit, neuf. On en écrit autant qu'il y a de variables du champ qu'on puisse concevoir .. Ayant ces équations, la première des choses qu'on fait, en général, c'est de linéariser, en supposant que l'onde dont il s'agit, qu'on ne connait pas encore, est une onde faible qui ne modifie pas le milieu ; après quoi on fait une hypothèse, par exemple du genre W.K.B., et on arrive finalement sous forme matricielle par exemple, à une équation de compatibilité, qui est ce que nous appelons une équation de dispersion, et avec un peu de chance on aboutit aussi à l'indice de réfraction. On arrive même, à condition de se donner un peu de peine, à définir une fonction potentielle. On en dérive les scalaires et les vecteurr du champ. Par exemple, la pression, la densité, la vitesse du gaz, etc.. On définit un rayon, c'est-à-dire une direction de propagation de l'énergie, on précise que le milieu est anisotrope, en présence du champ de gravité et du champ magnétique terrestre, etc. Ainsi, ces excursions de la pensée ne sont pas particulières à l'onde sonore ou à l'onde électromagnétique, ce ne sont que des démarches courantes. Je m'aperçois donc que bien que les théoriciens de l'électro-magnétisme soient les héritiers de l'optique, l'optique ne peut pas appliquer ces méthodes, sans doute parce qu'il s'agit de petites longueurs d'onde, le milieu ne peut pas être considéré comme composé de stratifications homogènes, il n'est pas question d'utiliser les méthodes "full-wave", (toute onde). Il est vrai que le milieu auquel vous avez à faire vous réserve tous les désagréments possibles. Il est turbulent, il est diffusant et la diffusion est anisotrope. On comprend alors que vous soyez obligés presque d'abandonner les concepts usuels et aussi d'en dégager d'autres, comme ce qui a été fait ce matin, je crois par M. HONEY.

Je vous demande M. le Président, s'il n'est pas convenable à une autre échelle, par exemple à une échelle microscopique, d'essayer de dégager des équations fondamentales pour retrouver des théories qui, à l'aide des mathématiques, vous permettraient d'obtenir des résultats très solides, comme ceux que nous obtenons par exemple dans l'atmosphère. Merci, M. le Président.

- Prof. TYLER : Have you any comments on this ?

- Dr. HODARA : Well, I think it is a philosophical question you are asking, actually. I'll answer it in that style.

What makes the problems alike or different is determined by scale sizes, wavelength, λ and refractive index fluctuations, $\langle \Delta n^2 \rangle$. A good example is to compare these quantities for optical waves in atmosphere and water and VHF radio waves in the ionosphere:

optics ($\frac{1}{2}\mu$)	sea	$s/\lambda = 10^6$, $\langle \Delta n^2 \rangle \sim 10^{-9}$
	troposphere	$s/\lambda = 10^3$, $\langle \Delta n^2 \rangle \sim 10^{-12}$
VHF (300 MHz)	Ionosphere	$s/\lambda = 10^3$, $\langle \Delta n^2 \rangle \sim 10^{-12}$

Optics in the atmosphere and VHF in the ionosphere encounter the same types of irregularities so that similar mathematical techniques can be employed. On the other hand, scale size to wavelength ratio for underwater optics and sea water refractive inhomogeneity fluctuation are far enough apart to call for different techniques so what makes the difference is not whether one uses optics or radio but the fact that sea water does not look the same as air to optical waves. There has been in the past a basic difference in the mathematics of optics and radio because optics could only deal with intensities. Since lasers came out a complete merging of classical electromagnetic techniques into optics has taken place. Now we have a whole field of so-called coherent optics which puts all problems of radio and optics on the same common basis. Anyway , why don't we continue this discussion later on Saturday, O.K. ?

- Dr. CONDELL : Do you think it would be safe to say that when the radio physicist solves the sporadic E problem, the optical physicist will have solved the problem of propagation in water?

- Dr. HODARA : Never. The scales we deal with in the water are live ones ! Planktons, etc ... Although a counterpoint exists in the atmosphere. We get radar returns from birds and butterflies, you know.

- C.F. HALLEY : Oui, sans doute. Toutefois je persiste à penser que les études dans un domaine en apparence spécial, comme celui qui nous occupe, participent aux grands courants du progrès de la physique et en dépendent.

2- Prof. TYLER : Are there any questions in connexion with the talks we have had today? Are there any topics you would like to discuss?

I was very much interested in M. MOREL's talk, particularly in some of the questions that were asked him. I think Dr. WIRGIN asked him about polarisation in this gathering and I wonder whether we could, perhaps, spend a few minutes in discussing this point since it may have some very interesting features from the aspect of plankton behaviour.

- Please, M. MOREL.

- Dr. MOREL : Nous avons surtout fait des mesures de polarisation a l'angle de diffusion de 90° dans un premier temps, parce que c'est à cet angle que l'on obtient la polarisation maximale pour la lumière diffusée dans le cas des eaux de mer. On a cherché à savoir si le taux de polarisation était corrélé au coefficient de diffusion : Dans des eaux turbides, par exemple, la dépolarisation était de 20 ou 25 % et décroissait souvent vers 10 % lorsqu'il s'agissait d'eau très claire, on a cherché à savoir si c'était une loi générale. Il semble qu'à 90° ce soit une loi assez générale : Donc en première approximation 20 % serait la dépolarisation caractéristique des particules marines et lorsque les eaux deviennent limpides la dépolarisation décroîtrait vers 10 % qui est caractéristique de la diffusion moléculaire par l'eau (exactement 9 %, ce qui correspond à une polarisation de 83 %). Ensuite, on a cherché à savoir s'il était possible dans certains cas, c'est-à-dire dans les eaux profondes, d'observer quelquefois des particules plus polarisantes, c'est-à-dire des particules très petites qui d'après la théorie de Mie par exemple, donneraient des polarisations très importantes à 90 %. En réalité on n'a jamais trouvé quelque chose de très significatif, on n'a jamais trouvé de dépolarisation inférieure à 10 %. Ensuite, sur des indicatrices de diffusion, au lieu de faire la mesure de l'indicatrice de diffusion entre 30° et 150°, en lumière naturelle, nous avons fait ces mesures, d'une part, en mesurant la composante verticale, d'autre part, en mesurant la composante horizontale. J'ai fait pas mal de mesures, mais je n'ai pas de résultat à présenter de façon statistique.

D'une façon générale, en essayant de soustraire ce qui revient à la diffusion moléculaire, et en considérant ce qui reste, il semble que les particules marines aient un facteur de dépolarisation assez symétrique autour de l'angle 90°, 100°, à cet angle la dépolarisation est de l'ordre de 15 ou 20 % uniquement attachée aux particules. La lumière est pratiquement complètement dépolarisée à 30°, (le taux de dépolarisation est de 85 %). Vers 150° on a une valeur à peu près semblable.

Quand on cherche à interpréter théoriquement ces résultats on est exactement confronté au problème d'interpréter l'indicatrice de diffusion des particules marines en lumière naturelle. C'est le même problème. Notre première conclusion, au vu des courbes de distribution de particules telles que celles qui ont été obtenues par M. BADER à "l'Institut of Marine Science" de Miami et d'autres courbes de distribution de particules obtenues dans notre laboratoire avec un appareillage semblable, est que cette distribution des particules marines présente une courbe croissante vers les petites tailles et ceci d'une façon continue. Si on veut utiliser complètement ces courbes et chercher la bonne explication à la forme de l'indicatrice cela implique d'additionner des indicatrices obtenues par la théorie de Mie dans un intervalle de taille pour lequel les tables ne sont pas calculées actuellement. En particulier, il faudrait jusqu'à des valeurs du paramètre de taille $\alpha = 2\pi R/\lambda$ supérieures à 100 ou 150. D'autre part, les tables actuelle ont été calculées avec des incréments d'indice qui sont trop grands et des incréments de taille aussi trop grands pour être utilisés dans le cas d'une courbe de distribution continue comme celle trouvée expérimentalement. En conclusion, si l'on veut résoudre complètement le problème, il faut d'abord générer des fonctions de Mie, en beaucoup plus grand nombre que celles qui sont disponibles actuellement. Cela représente un très gros programme de calcul qui ne sera sûrement pas fait pour les particules marines, car on n'obtiendra jamais d'argent pour le faire.

- Dr. HODARA : Have you made measurements of depolarisation versus angle ? Can you get them on the board ?

- Dr. MOREL : (exposé au tableau noir : voir note complémentaire N° 1)

Je dois dire que contrairement par exemple à des expériences sur la forme générale de l'indicatrice de diffusion en lumière naturelle, ou sur la question de selectivité de la diffusion pour laquelle j'ai beaucoup de mesures expérimentales, sur la polarisation je n'ai pas un nombre très grand de valeurs expérimentales qui permettraient un traitement statistique de ces données.

- Dr. HODARA : If you have depolarisation, does that mean that you have multiple scattering from this particle ?

- Dr. MOREL : Non, en général si vous éclairez un milieu diffusant en lumière naturelle, quand vous étudiez la lumière diffusée, en diffusion première, elle est seulement partiellement polarisée. Dans le cas de la diffusion théorique de Rayleigh, vous auriez effectivement une polarisation complète à 90° et seulement à cet angle, mais en réalité comme les molécules d'eau sont anisotropes, la lumière n'est pas complètement polarisée à 90°. La dépolarisation est de 9% par exemple dans le cas de l'eau, elle est dans le cas du benzène de 43 %, si j'ai bonne mémoire, c'est-à-dire que la lumière est relativement peu polarisée dans le cas de la diffusion moléculaire du benzène. Et dans le cas des particules, c'est aussi un phénomène de ce genre, si vous éclairez en lumière naturelle, vous observez dans la lumière diffusée un certain taux de polarisation et par exemple, la théorie et l'expérience l'ont montré, vers les petits angles la lumière diffusée est très peu polarisée et à la fin ne l'est plus du tout. C'est-à-dire qu'à partir des angles de 10° par exemple, pour des particules suffisamment grosses, la lumière n'est plus du tout polarisée. Beardsley a fait beaucoup de mesures je crois sur la polarisation de l'indicatrice.

- Prof. TYLER : If one considers the form of the various radiance distribution curves on a sunny day, for example, the maximum of the distribution curve would be slanting towards the rays which are refracted from the sun, and this then becomes a beam of light which is entering a scattering medium. Polarisation will occur at right angles to this beam. Observing this from below the water you will see at least in two directions the angle of polarisation tilted. Now if you go deeper in the water, the same water, and presuming it's homogeneous, the maximum radiance moves towards the zenith, so that all these polarisation factors will tend to become horizontal, and, in fact , from this sort of heuristic argument I would expect polarisation to increase with depth on an overcast day. Do you agree?

- Dr. MOREL : I don't know exactly because I have not done any measurement of this kind of polarisation in water.

- Prof. TYLER : Are there others who would like to make some comments on polarisation?

  Could I ask you about your original thought, did you say something about the activity of plankton ?

- Dr. CONDELL : I presume that it would have to do with the activity of plankton, yes, whether indeed this might not be considered as some type of polar structure which did orient itself, for instance, according to temperature gradiance, to light, to radiance, and so on.

- Prof. TYLER : Well, I would like to say that research has been done on sea weed fucus, and it was found that a larger than expected number of plants oriented in a certain direction under polarised light. With no polarised light, they did not grow this way at all. I think Waterman at Yale has also found some orientation effects with marine animals under polarized light. But somehow I think these effects must all disappear at great depths.

- Dr. HODARA : Has anyone made measurements at any recent date of scattering lengths at great depths who has any values to report ? Measurements of α and σ at great depths ? Has any one made measurements recently and would he like to report on them ?

  For example, on scattering coefficient and attenuation coefficient ?

- Dr. MOREL : We have done some measurements of total scattering coefficient in deep water, but, unfortunately, not of the attenuation coefficient. Total scattering coefficient in deep water (it means at thousand meters depth or more) in the Mediterranean and also in the Atlantic Ocean (near Madeira and the Açore Islands) is often around 1.10^{-2} m^{-1}.

  It means that the molecular scattering in the total coefficient makes something like 16 %, because molecular scattering gives 16 or 17.10^{-4} m^{-1} (at 550 nm).

- Dr. CONDELL : This seems to be a very low number. There are some data from the Atlantic at greater depths. If my memory serves me, I think these numbers are about 0.027.

- Dr. MOREL : For us the minimum value was 0.01, or something like that. By two ways; the first one is with a small angle integrating apparatus which is calibrated against the beam itself, and the other method is an indirect method measuring the scattering function at 30° and, considering that, the ratio between β 30° and b is a constant. And it gives us almost the same value.

- Dr. DONATI : Are there some results on circular polarisation of light in water propagation ? That is, I heard of a method concerning the improvement of visibility that deals with circular polarisation. I was interested in knowing what improvement does it yield in water propagation ?

- Dr. HODARA : I have some results, I don't have them all in my head, but I can send a report. The improvements in reducing backscatter in artificial water, water I made turbid, were of the order of 8 : 1-something like that. These were experiments in a water tank done with a laser and a photo-multiplier so we could get electronic measurements. A year earlier Gary Gilbert measured backscatter improvement with polarisation photographically. We found this method of backscatter reduction very unreliable — because of what Morel said, we get lot of depolarisation. The principle of the method is based on the fact that a target is most of the time depolarising, while the scattering elements supposedly do not. Although measurements were made with linear polarisation circular polarisation gives the same result because circular polarisation is nothing else than a linear superposition of 2 orthogonal linear polarisations.

  The only advantage of circular polarisation is that you do not need to maintain a fixed relative orien-

tation between the source and the receiver.

- : Did you note any difference in the amount of the extinction ratio between the cross-polariser and the circular polariser as a function of separation angle; angle between the source and receiver?

- Dr. HODARA : We made detailed measurements but the rejection of that scatters by polarisation ... is a function of the angle at which you would look at the return so that if you are within a 20 - 30° angle it is quite different from if you were, say, at 90°.

- : Is there any difference between circular and linear polarisation ?

- Dr. HODARA : There is no difference. There should not be any.

- : But you made no measurements, though ?

- Dr. HODARA : Just a couple to satisfy someone else that there's no difference. There is no sense in making those measurements. Linear polarisation measurements should be sufficient to establish the relative improvement in backscatter reduction.

3- Dr. WIRGIN : I have a question about the MTF modulation transfer function. I don't know who mentioned that you could indifferently under the hypothesis of a linear transformation between the image and the object consider the impulse response or the sine wave response to evaluate the image quality. I was wondering if this might not constitute a valid test of the linearity of the ocean medium as an image-forming system. In other words, take, for instance, the impulse response with the point source, measure the image and from that derive the sine wave (MTF) response. Then operate the other way round, see if you come to the same results. I was wondering if a test like this had been made already, because it does not seem to me obvious at all that the ocean medium can be considered as a linear transformer of the images.

- Mr. ZANEVELD : Yes, I think it would be a good test, but it has not been performed. I should say that as far as linearity is assumed this is only linearity in contrast. In other words, if you have two point sources, then the intensity received a distance away will simply be the sum of the intensities received from these two sources. This is all you can say if the linearity of the sea water goes as far as contrast, and I think this is a reasonable assumption. If you have coherent light sources you will probably get some interaction but you won't get the same intensities. So assuming incoherent light sources, you can say that the contrast adds linearly.

- Dr. WIRGIN : There is another reason why it is not so obvious. It seems to me that the radiation characteristics of a point source in water would be very different from that of a beam, because when you reason on a sine wave response, I suppose you are concerned with an infinite wave, whereas in practice you have to consider a beam in water.

Intuitively, it seems to me that the scattering characteristics in water would be very different, specially would be a function of the particles that you encounter and so forth.

- Dr. CONDELL : Perhaps I am a little bit confused.

Whether the light is so-called coherent or incoherent, as long as the index of refraction is not depending on the intensity of light over the range you are using, I don't see how it is possible not to have an MTF meaning in the sense of one-way transmission. Now whether it's a practical use in terms of three part networks or something like that, I think is something else again, but have I missed the point here?

- Dr. WELLS : Well, I quite agree with Dr. CONDELL. It seems as though the linear refractive index principle holds--as you certainly expect it to for weak interaction of light and medium. Maybe we don't mean the same thing by linearity. I have the feeling that there is some communication problem. (Voir note complémentaire 2.)

- Dr. HODARA : I don't think that is what they meant. Somebody brought that up a couple of years ago. It has nothing to do with the change of index of refraction, but I think it has to do with the superposition of the slices when you calculate your modulation transfer functions, some other form of linearity. I know it has nothing to do with what we call usually in electro-magnetics non-linear interaction : the change of the constitutive parameters of the medium with the excitation of the wave.

- Mr. ZANEVELD : But, I think what you are talking about is the medium itself changing due to interaction with light ; what we are talking about is simply the fact that the Fourier type mathematics holds when you are talking about the images in seawater. All this means that you can break it down into its Fourier components, and treat each Fourier component independently. And when you have calculated how each Fourier component decays over a certain distance, then you can add them, and this is what you mean by the linear system. Any linear mathematical system will permit this.

- Dr. WIRGIN : But there can be a difference from the practical measuring point of view because in a point radiating in a scattering medium you can have a situation in which some of the fields are scattered out of the receiver ; it is not effectively received at the position of the receiver, and this will give you a different type of response. In the situation in which you have a beam, which is called plain wave, as an excitation in the medium, it will give you different scattering characteristics and you might have less probability of the fields scattering out of the receptor. So you might be measuring two different things in the end. It can be a factor.

- Mr. ZANEVELD : I think what I mentioned before is that you assume there is a point by point correspondence between the object plane and the image plane. In other words, when you are in the image plane and look at the object plane, you will see a point from which the light appears to come , which means you are looking in one direction only. So if you are talking about a practical problem when you are receiving a signal, the angle might be wider in one case then in some other case. In a theoretical problem you are simply considering a point to point conversion and then the mathematics looks fine.

4 - Dr. HODARA : I think this is a semantic problem. I'd like to ask another question. What are the latest measurements that have been made on the narrow angle of scattering? Does anybody care to report on smaller angles and also, on how this scattering function should approach the axis, the ordinate axis, as the angle becomes smaller and smaller ? Maybe somebody would like to comment on that ?

- Dr. HONEY : In trying to make this kind of measurements and looking back on the data with a clearer understanding of the kind of effects that index of refraction turbulence have on these instruments, I have come to the conclusion --whatever instrument you build, whatever its minimum resolution is-- that you will find under conditions of index of refraction turbulence a peak with that resolution. And of course that kind of resolution is only relevant if you are using it to predict the performance of an optical system with comparable resolutions. But, for instance, in making these measurements that I briefly alluded to in the paper, many times we would see no narrowing or forward scatter at all in well mixed surface layers of the ocean, for instance. And where we did find measurements that were greater than the system of sensitivity, where we did detect these kinds of very narrow angle forward scatter, it was in the regions of, say, 10 miles off the Golden Gate where you would expect or you have reason to suspect that there is a mixing of fresh water with salt water of thermogradient, etc., and the picture seems to be false altogether after the fact that you get measurements and some very narrow angle scatters on some occasions and not on others.

- Dr. WELLS : All the volume scattering functions which I play around with as discussed this morning want to be singular at the origin to about the $\theta^{-3/2}$ power of the angle, which did not particularly bother me since this is an integrable singularity. In other words, in any finite solid angle that the detector subtends you always get a finite scattering probability, which is comforting. We have been computerising the Hankel transform which converts the MTF to volume scattering function or back, whichever way you want to transform it, and these are a little difficult near the singular areas, but you can still perform them all right. I tried to invent a species of particles which would have this singular property and was unable to do so, but I don't really see any reason why the scattering function should not be singular at the origin, not as a result of any one species of particles, but from the distribution of different species. I don't see any reason why there can't be an ever decreasing density of ever larger particles which scatter stronger and stronger in the forward direction, starting with the diatoms and going to the large turbulences. Maybe somewhere inbetween these sizes there is scattering from chemical excretion from minute organisms.

- Dr. HODARA : If this is correct, that is the approach to the origin as $\theta^{-\frac{1}{2}}$ or $\theta^{-3/2}$, it means that Chilton's calculation will take eighth power, it means that he would have to change this "éta" for different angles at the approach of the origin. These two types of functions that were used to fit the volume scattering function are entirely different near their origin, and I would be very curious to know which one is right, if we are interested in narrow angle forward scattering. Because the two $\theta^{-3/2}$ functions obviously don't approach the origin the same way, and perhaps if he was approaching as $\theta^{-3/2}$ it would explain why in Chilton's curve fitting he has to change (éta) to a 2π R/λ value, depending on what type of waters he is in. I noticed this could be anywhere from 10 to the 1/3 to 10 to the 1/8, and it is difficult to adjust an explanation on this. Maybe you have some comments on that ?

- Dr. HONEY : It's true that he picked the symbol "éta" to characterize what happens in a very narrow angle forward direction. He did qualify that, and it is true that it is very easy to pick two or three or whatever number of parameters you want for that purpose; but lacking any better knowledge than there is now about what happens in that forward direction, one seems to be more than adequate and maybe it still is.

- Dr. HODARA : Truly speaking that A would be a function of "éta". It might be, but than you might want to pick a different function.

- Dr. HONEY : The function that they chose is based on the kinds of things that happen in many, many diffraction problems in which narrow angle scattering is important and so it seems like physically a very reasonable choice. But if there is some reason for picking another function, that too is a relatively minor perturbation of the computer program that has been set up.

- Dr. HODARA : By the way, what's the closest narrow angle scattering measured ?

- Dr. HONEY : 50 microradians.

- Mr. ZANEVELD : Yes, I think you probably agree that the scattering due to particles is probably singular at the origin. Now I was wondering whether somebody had some ideas on the scattering due to turbulence ? Perhaps that would be flat at the top and when added in real sea water, then perhaps it would remove the singularity.

- Dr. HONEY : Well, it is not really singular. I don't think any of these things we are talking about are singularities. They are diffractions limited by the size of the beams, of the objects of the instruments you are using to measure them, and that is not a singularity. It just sets a limit to the resolution of the instrument.

- C.F. HALLEY : Monsieur le Président, je signale que le dépouillement de l'enregistrement magnetique sera à peu près impossible si les orateurs ne donnent pas leur nom avant d'exprimer leur opinion.

5 - Dr. CORDELL: Could anybody clear my ignorance about the international notation which has been adopted ?

- Dr. MOREL : I think Prof. TYLER is well placed to answer this question.

- Prof. TYLER : I have with me a table which has listed the optical components followed by the units followed by the IAPSO notation which is the organization which adopted the evaluation units, note : A translation in French of this IAPSO terminology is given by A. Ivanoff, A. Morel, in each Oceanogr. XXII, 5, 457.468, and I also have put into this table symbols which were adopted by the Optical Society of America some years before that, and which, I am sorry to say, we use ourselves. Also on the second sheet of those notes, there is a diagram which we use to illustrate the program we're following. You notice in large outline blocks the three principal measurements which we feel are needed particularly to document ocean water. These are the scattering function, the radiance distribution and the transmission. And then below and above these three are noted the constants and properties which you can derive from each. (voir papier 43, pages 43-7 et 43-8).

- Dr. HODARA : Would any one of you care to end by pointing out or recommending what future work should be carried out, what experiments should be done, what problems - perhaps theoretical or experimental results - are needed to be solved. I think it would be good to summarize this meeting, giving some direction to the meeting by pointing out future areas of research.

- Prof. TYLER : Does anybody feel there might be a way to combine optics and microwaves, for example, as Captain HALLEY suggested, any common field, any common ground that we could stand on ?

- Dr. WELLS : I think you can see a similar complexity --maybe I should call it confusion, or at least argument amongst people -- in the case of the scattering of radar from the sea surface with no consistent, well defined theory.

- Prof. TYLER : Before we close the round table discussion, I would like to say that a lot of very interesting and new information has come to my attention during this meeting. Also, I have been impressed by the way the interpreters have managed in spite of the fact that some of us talk too fast and others talk with an accent. I've been highly impressed by the organization of the auditorium. I would like to say "Thank You" to Captain HALLEY and to others here, as well, who have made this meeting possible. Thank you very much.

NOTE COMPLEMENTAIRE 1 par A. MOREL.

Pour cet échantillon prélevé en Manche, assez turbide (le 7 juillet 1965), (β 90 $\sim 7.10^{-4}$ m^{-1}) la diffusion moléculaire joue un rôle faible, et la polarisation de la lumière diffusée observée peut être pratiquement regardée comme caractéristique des particules marines. La mesure est effectuée, le polariseur étant disposé sur le faisceau incident ; sont portées en fonction de l'angle les composantes horizontales et verticales (données en valeur absolue) selon une échelle logarithmique. Sur la 2ème figure, toujours pour le même échantillon, le facteur de dépolarisation (c'est-à-dire le rapport H/V = δ) est porté en fonction de θ. L'allure de ces courbes est générale ; pour la retrouver dans le cas des eaux claires il faut retrancher l'effet de la diffusion moléculaire ; cette soustraction, ainsi que la perte de sensibilité due à l'introduction du polariseur, font que dans le cas des eaux très limpides, les résultats deviennent hasardeux. (voir figures 1 et 2)

NOTE COMPLEMENTAIRE 2 par P. HALLEY

En électromagnétisme classique, pour résoudre un problème, on écrit les équations du champ qui sont, primo les équations de Maxwell, secundo d'autres équations supplémentaires qui lient entre eux les vecteurs du champ. Si les milieux physiques qui remplissent le domaine du champ sont tels qu'on puisse écrire en tout point des relations linéaires, telles que :

$$D = \varepsilon E, \qquad H = \frac{1}{\mu} B \qquad \text{et} \qquad J = \sigma E$$

, ε μ et σ étant les constantes caractéristiques physiques du milieu au point considéré, on peut dire que les milieux sont linéaires.

Ces caractéristiques peuvent être exprimées sous forme tensorielle. Dans ce cas, chaque composante d'un vecteur du champ peut être représentée par une fonction linéaire des composantes d'un autre vecteur.

De toute manière, si le système des équations, devant lequel on se trouve placé, ne comporte que des équations linéaires, différentielles ou non, on peut dire que l'on considère des effets linéaires. Il en résulte que, en régime sinusoïdal entretenu pur, les nombres qui mesurent les "intensités" d'un des scalaires ou d'un des vecteurs du champ aux différents points du domaine considéré sont indépendants du temps et constituent un ensemble de nombres proportionnels entre eux, dont les proportions sont indépendantes de l'intensité du régime entretenu.

De plus, dans certains problèmes, en régime sinusoïdal pur, on peut définir en chaque point du domaine un vecteur d'onde K, par là, un indice de refraction de phase et un indice d'extinction linéaires. Bien entendu, ceci n'est plus le cas lorsque l'une au moins des équations n'est pas linéaire ; par exemple, lorsque l'expression $J = \sigma E$ doit être remplacée par l'expression plus approchée $J = \sigma_1 E + \sigma_2 E^2$, ou par toute autre expression non-linéaire. Quand on parle d'effet non-linéaire il faudrait préciser quelle équation n'est pas linéaire.

TABLE RONDE D'OPTIQUE
NOTE COMPLEMENTAIRE 1